INORGANIC SCINTILLATORS
and
THEIR APPLICATIONS

Proceedings of the International Conference on

INORGANIC SCINTILLATORS and THEIR APPLICATIONS

Delft, The Netherlands, August 28 - September 1, 1995

SCINT 95

Edited by
Pieter Dorenbos, Carel W.E. van Eijk
Delft University of Technology

Delft University Press

Published and distributed by:
Delft University Press
Stevinweg 1
2628 CN Delft
The Netherlands
Telephone +31 15 2783254
Fax +31 15 2781661

By order of:
Delft University of Technology
Faculty of Applied Physics
Radiation Technology Group
c/o IRI, Mekelweg 15
2629 JB Delft
The Netherlands
Telephone +31 15 2785244
Fax +31 15 2786422

Cover design and idea:
Tieme Dekker and Rob W. Hollander

CIP-DATA KONINKLIJKE BIBLIOTHEEK, The Hague

SCINT95

SCINT95 / ed.: P. Dorenbos, C.W.E. van Eijk. - Proceedings of the International Conference on Inorganic Scintillators and Their Applications, Delft University of Technology, August 28 - September 1, 1995, Delft, The Netherlands
Ill.
with ref.
ISBN: 90-407-1215-8
NUGI: 812
Key words: Inorganic scintillators / Radiation detection / Scintillation crystals / Luminescence

Printed in The Netherlands

Organizing Committee:
Carel W.E. van Eijk (Chairman)
Pieter Dorenbos
Hans Andriessen
José Buurman

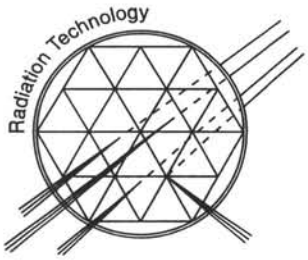

International Programme Advisory Committee:

G. Blasse	Univ. Utrecht
A.V. Gektin	ISC Kharkov
J. Goebbels	BAM Berlin
C. Grabmaier	Siemens Corp. R&D Munich
T. Jones	Hamm. Hosp. London
N.V. Klassen	RAS Chernogolovka
M. Kobayashi	KEK Tsukuba
S. Kubota	Univ. Rikkyo
P. Lecoq	CERN Geneva
J.A. Mares	Inst. Phys. Prague
C.L. Melcher	Schlumberger Ridgefield
W.W. Moses	LBL Berkeley
A. Paans	Acad. Hosp. Groningen
R. Pani	Univ. Rome
C. Pedrini	Univ. Lyon
N.J. Rhodes	DRAL UK
P.A. Rodnyi	Tech. Univ. StPetersburg
U.W. Schiebel	Philips Research Aachen
B. Shulgin	Tech. Univ. Jekatherineburg
J.-M. Spaeth	Univ. Paderborn
S. Tavernier	Univ. Brussels
M.J. Weber	LBL Berkeley
R.T. Williams	Wake Forest Univ.
A. Wojtowicz	Cop. Univ. Torun
C.L. Woody	BNL Long Island

Sponsors:
Delft University of Technology
Radiation Technology Group, DUT
Interfaculty Reactor Institute, DUT
Amcrys-H, Ukraine
City of Delft
Crismatec, France
Delft Electronic Products, The Netherlands
Delft University Fund
Foundation Physica, The Netherlands
Hilger Analytical Ltd., UK
Philips Medical Systems, The Netherlands
Philips Photonics, France
Preciosa, Czech Republic
Shell Nederland B.V., The Netherlands
Siemens AG, Germany

Industrial Exhibition:
Amcrys-H, Ukraine
Crismatec, France
Delft Electronic Products, The Netherlands
Hilger Analytical Ltd., UK
Philips Photonics, France

* keynote paper

* keynote paper

* keynote paper

* keynote paper

* keynote paper

* keynote paper

* keynote paper

* keynote paper

* keynote paper

* keynote paper

PART VII
Light Detection

* keynote paper

Photo: Fotografische Dienst, Facilitair bedrijf, TU Delft

Preface

Inorganic scintillators continue to fascinate us, both from the point of view of materials science and as potential mediators for radiation detection. Although substantial advances have been made in our knowledge, the models describing the scintillation processes, from radiation absorption to light production, are still unsatisfactory in many cases, as are quantitative predictions. Also, materials synthesis and crystal growth processes require our attention. As for the applications, we encounter scintillating crystals, ceramics, glasses, and powders in a large variety of fields, using counting and integrating methods and e.g. position-sensitive photomultipliers and silicon avalanche diodes as light sensors. New techniques have to be developed for new applications.

Inorganic scintillators were the subject of the International Workshop on Heavy Scintillators for Scientific and Industrial Applications, Crystal 2000, held in Chamonix, France, in 1992. As a consequence of the preparations for the large high-energy-physics facilities the attention was somewhat focused on this field. Symposium P of the Materials Research Society meeting, Scintillator and Phosphor Materials, held in San Francisco, in 1994, focused more on the physics and chemistry of scintillating materials. In SCINT95 we tried to combine the fundamental aspects and the applications, with a more uniform distribution of attention over the various fields of application.

On behalf of the Organizing Committee we would like to thank all the participants (~ 160) for their contributions. We thank the members of the International Programme Advisory Committee for their valuable suggestions. We also thank the referees for their work during the conference, which speeded up the publishing of these proceedings considerably. Furthermore, we are very grateful to the sponsors. Without their contributions it would not have been possible to organize the conference with so many participants. We also acknowledge the work of those involved in the organization of the round trip from the border of the FSU to Delft.

Finally we warmly thank the staff of the Aula Congress Office for their continuous support before and during the conference.

The editors,
November 1995

PART I

Scintillators Applied in Detector Systems

PET: THE MOST SPECIFIC AND SENSITIVE MEANS FOR IMAGING MOLECULAR PATHWAYS AND MOLECULAR INTERACTIONS IN MAN - INDICATIONS FOR IMPROVED DETECTOR PERFORMANCE

TERRY JONES
CYCLOTRON UNIT
MEDICAL RESEARCH COUNCIL CLINICAL SCIENCES CENTRE
ROYAL POSTGRADUATE MEDICAL SCHOOL
HAMMERSMITH HOSPITAL
DU CANE ROAD
LONDON W12 0NN
UK

Abstract

This paper explains why PET is the most specific and sensitive means for imaging molecular pathways and molecular interactions in man. Examples are given of its application in clinical research together with a summary of the improvements sought in radiation detector performance to fully exploit the sensitivity offered by Positron Emission Tomography.

SPECIFICITY AND SENSITIVITY OF PET

The use of tracers labelled with gamma ray emitting radioisotopes provides an unique way for studying regional molecular pathways and interactions in man. Positron emittimg radionuclides, such as oxygen-15, nitrogen-13, carbon-11 and fluorine-18 provide the means for substituting natural elements within biochemicals and pharmaceuticals whereby their biological molecular behaviour is undisturbed. This offers an unrivalled specificity for molecular imaging. The paired annihilation photons associated with positron capture allow coincidence detection of the positron emitting tracers within the human body. This electronic collimation removes the need for lead collimation and hence represents a significant increase in the solid angle for detection compared to the case of the *in vivo* detection of single photon emitters. Two additional factors contribute to the sensitivity of PET for detecting low levels of material within the human body. The production of positron emitting radioisotopes by the use of charged particle beam bombardment provides radionuclei with high specific activity. In addition, the use of short lived radioisotopes results in a low amount of stable material being present for a given activity level. As a result of these three components, PET is able to detect Pico Molar concentrations of material within the human body. This is important with respect to the use of tracers to determine molecular sites such as receptors which are biological switches which activate neuro transmission. These are present at the micro or nano molar concentration level. Clearly in order to act as a tracer, the amount of stable material used for delineating such receptor systems needs to be such as not to interfere with the biological activity of the receptors. This results in the need for Pico Molar sensitivity as is offered by PET, to make this a possibility. Even if for biological reasons one could use site saturating doses of a molecule, the problem of identifying specific and non-specific signal becomes of relevance.

This specificity and sensitivity needs to be borne in mind when considering the role of PET in medical imaging. Here structural studies based on density measurements (x-rays) and Milli Molar water concentrations (MRI) need to be compared to the Pico Molar level of sensitivity utilised by PET for studying molecular pathways and interaction. It needs to be mentioned that single photon emission tomogrpahy (SPET) is also a means for molecular imaging. The single photon emitting tracers do not have the same flexibility for radiolabelling physiological, biochemical and pharmaceutical molecules without disturbing their function and hence the

Proc. Int. Conf. on Inorganic Scintillators and Their Applications, SCINT95,
1996, Delft University Press, The Netherlands

degree of freedom for molecular study is less. Nevertheless, for large molecules where the addition of Tc-99^{M}, In-111 or I-123 do not alter molecular function they contribute to the specific role of molecular imaging. It remains however, that the low *in vivo* detection offered by collimated single photon emission systems is far inferior to that offered by the electronic collimation of PET.

The sensitivity offered by PET provides the means to record the tissue kinetic time course of a radiotracer. This is important in that it allows the kinetic rate constants of exchange to be measured between the blood and the tissue targets and pathways of interest. Hence statistically significant short time frame data need to be collected which is possible through the sensitivity of PET.

APPLICATION OF PET IN CLINICAL RESEARCH

An example of how the high specificity and sensitivity of PET is used is the case of the tracer: ^{11}C-labelled diprenorphine [1]. This molecule is selected for the opiate receptors, namely those sites for which morphine is specific and are central to pain sensation and control. The ability to follow the time course of this molecular probe regionally in the brain is a good example of the uniqueness of PET in the area of medical imaging.

When used to its limit of specificity and sensitivity, PET is an expensive and fairly rare speciality. As a research tool its role is seen as: i) obtaining new information in human disease, ii) measuring the effectiveness and action of therapy and iii) assesses drug development and discovery. Within our own programme at the MRC Cyclotron Unit, Hammersmith Hospital, the application of PET in clinical research rests in neurology (movement disorders, epilepsy), psychiatry (schizophrenia, depression, addiction and anxiety), cardiology (heart muscle viability, heart failure and neurocardiology) and oncology (action of anti-cancer agents and therapeutic response).

Before discussing further the use of labelled drugs and biochemicals, it is worth stressing that the high sensitivity of PET has allowed oxygen-15 labelled water to be used most effectively to study small changes in cerebral blood flow when specific activation tasks are undertaken by the human subjects. The short, 2.1 minute half live of oxygen-15 allows repeat measurements to be carried out in the activated and non-activated cerebral states and changes as low as 2% can be reliably measured. This sensitivity has resulted, in our own and other labs experience, in a number of items of new information being reported on the action of the human brain and changes in disease state in scientific journals of the highest quality [2, 3, 4, 5, 6]

Returning to the use of labelled drugs and our own experience in London. The application of carbon 11-diprenorphine has allowed the delineation of those sites in the human brain where the opiate receptors become increasingly occupied by the brain's natural pain killers (endorphines) during the sensation of pain [7]. ^{18}F-L-dopa has been used to determine the viability of transplanted tissue into areas of the brain defective in Parkinsons Disease [8]. A beta blocker, labelled with C-11 (CGP12177) has been used to show how patients with heart failure have reduced beta receptor sites in their heart muscle [9]. There is increasing interest in the use of labelled anti-cancer drugs to determine the dosimetry and time course of these agents especially those introduced at an early stage of clinical trial [10].

At present these tools are used mainly by clinical researchers, however the pharmaceutical industry is becoming increasingly interested in using these specific probes as a means to assess the mechanisms and efficacy of new pharmaceutical agents at an early stage in their development. This has implications in respect to the speed and cost of drug development [11].

THE IMAGING SCIENCE OF PET

In order to address a clinical research or diagnostic question based on functional (parametric) images provided by PET, a number of components have to be systematically considered, all of which contribute to the accuracy of the image itself. These include: i) selection of the biological/pharmacological pathway, ii) the selection of an appropriate tracer molecule and its specific and efficient radiolabelling with a positron emitting radio nuclide iii) pre-clinical studies to ensure that the tracer will provide a specific *in vivo* signal in man iv) the recording of accurate kinetic positron emission tomographic data v) the processing and reconstruction of the recorded data to provide accurate time sequences of tomographic images vi) the voxel by voxel analysis of the kinetic data to provide quantative parametric images of the biological parameters of interest. These steps provide the clinical researchers or diagnosticians with imaging tools, the data from which when applied to man needs to be statistically interrogated for regional changes in function.

This cascade of methodological steps needs to be identified in order to place in context the contribution that the recording of tomographic data has and hence the radiation detectors used in these instruments. The remainder of this paper focuses on this process and leads to identifying those properties of inorganic scintillators that need improvement in order to enhance the accuracy of the data collection.

Modern positron emission tomographs consist of mosaics of detector elements viewed by smaller arrays of photomultipliers. These share the light emitted from the mosaic to identify, through Anger Logic, which elements registered the incident 5ll kev photon. In the accompanying paper by W Moses in these proceedings, details of this process are provided. Currently Bismuth Germanate (BGO) is the scintillator of choice to efficiently stop 511 kev photons and the ratio between detector elements and photomultipliers is typically 8:1. These "blocks" of scintillator mosaics [12] are arranged in circles around the body thereby recording the angular information needed to reconstruct cross sectional tomographic distributions of positron emitting tracers within the human body. In the early design of tomographs, lead or tungsten septa were introduced to reduce the registration of scattered and random coincidences. By using ring or rod sources of positron emitting radioisotopes, it is possible to record a transmission measurement prior to administering the radiotracer. The ratio of coincidence counting between pairs of detectors for the condition when the patient is positioned in the tomograph to that in air provides the attenuation factors for each pair of coincidence detectors. This attenuation correction results in tomographic data that is quantative in that voxal element responses can be callibrated in counts per second per millilitre of tissue per becqueral. As a result, absolute concentrations of radioactitivy in tissues of interest can be recorded. This is important when deriving the amount of tracers sequested in the tissue compared to that administered to the patient or recorded in the blood. The latter is usually measured with a second detector such as a well counter which is also absolutely calibrated in counts per second per millilitre per becquerel.

A principle contribution to the accuracy of the tomographic data is the statistical quality namely the recorded count densities. It is clear that for a given detector array, the principle means for maximising this is to remove the septa and maximise the solid angle for detection by recording all possible coincidence events between the opposing detector elements [13]. Under this condition "scatter becomes the enemy" - E J Hoffman and strategies are needed to correct for the increased registration of scattered coincidences. These still need to retain the quantative accuracy of the tomograph's voxal elements response for measuring concentrations of radioactivity in the tissues. A number of approaches have been adopted to effect this correction. The one developed in our laboratory has been the use of dual energy windows whereby coincidences are recorded in both the 5ll kev photo peak (380-800 kev) and in a second, lower energy 250-380 kev window as a means for monitoring scattered photons within the Compton region. To date, corrections derived from this approach have been successful in quantitating

septa-less data recorded from the brain [14]. It is clear that improvements in energy resolution and the photo peak fraction of a detector is highly relevant in minimising the registration of scattered photons. Corrections derived for scatter introduce statistical deterioration of the data as do corrections for random coincidences undertaken by delayed coincidence circuitry. To account for the statistical effect of such corrections, the term Noise Equivalent Counts NEC has been developed by
Casey Hoffman & Strother [15] who formulated the relationship between NEC and the registered true coincidences, random coincidences and the scatter faction

$$NEC = [T_{tot} (T/S + T)]^2/(T_{tot} + 2fR)$$

Where T_{tot} = total (scattered plus unscattered) counts recorded, T = the unscattered counts, S = scattered counts, f = the fraction of the projection subtended by the object, R = random counts

This formulation has been used to characterise septa-less tomographs and has helped to ensure that increased efficiency is optimally derived in human studies. It has helped to identify the parameters that directly effect the statistical quality of the PET images and points to where improvements are needed in detector performance. Early comparisons between septa and septa-less tomographs demonstrated clearly the effect that random registration has on the NEC [16]. As a result, strategies were pragmatically introduced where the balance was found between the amount of radioactivity that could be administered to achieve useful tomographic data and the loss of effective efficiency (NEC) due to randoms and dead time on the detector. An example of such strategy is the study of regional cerebral blood flow for activation studies. Here it has been shown that there is a loss in NEC of 2% per additional milli curie of $H_2{}^{15}O$ administered [17]. In our experience, gains in NEC by using septa-less data collections amounted to factors of between 3 and 5 for the tomograph as a whole. These are higher for the axial, central locations where factors of 8-10 in gain have been experienced.

The early septa-less tomographs had axial lengths of 10.8 cm and were designed optimally for brain studies where deep side shields could be employed to minimise the registration of singles and hence randoms, and dead time arising from radiation outside the coincidence field of view [13]. However, as the axial lengths of tomographs increase and today, tomographs are typically 16 cm in axial length, and used to investigate the chest and abdominal areas, the effects of out of field radiation increases significantly. In the latest generation of high efficiency, high resolution tomographs, 24 cm axial lengths are used and will be based on block detectors of BGO arrays each element of which is 4.1 millimetre x 4.1 millimetre and 30 millimetre deep. Here ongoing strategies will need to be formulated on how to optimally use the sensitivity of this detector system particularly with effect to the NEC degredation resulting from random registration and dead time arising from out of field activity.

IMPROVEMENTS SOUGHT IN PET DETECTORS

Having discussed the application of PET, the role of the tomograph in recording accurate functional images, particularly with respect to the high sensitivity for recording radioactivity kinetically in man and strategies being developed for tomograhic designs, it is now possible to identify the improvements sought in the detectors of future machines. These centre on maximising the Noise Equivalent Counts (NEC) in order to undertake tracer kinetic studies of low molecular concentrations and to fully utilise of the intrinsic spatial resolution. In this regard the following aspects need to be considered:

- To capitalise on the high solid angle detection by realising depth of interaction information within the detector element itself thereby overcoming problems of parallax.

- Improvements in detector rise and decay times are needed to reduce dead time and the

registration of random coincidences arising from singles from the flux both from within and outside the coincidence field of view. Improved timing resolution is also sought to implement the use of time of flight which would increase the statistical quality of the reconstructed data set.

- Improved energy resolution is sought in order to reduce the registration of scattered coincidences and out of field scattered singles. Improved photo fraction is desirable to distinguish between scatter within the body and in the detector itself.

- Improved packing fraction of detector elements is sought along with the means for recording separately the light emitted from individual detector elements thereby reducing the positional statistical uncertainty associated with the use of Anger Logic and light sharing strategies. Here the use of photo diodes is attractive provided sufficient light can be recorded.

All these sought after improvements point to the need for detectors with more light output and faster rise and decay times while still retaining high density for maximum detection efficiency and minimising scatter within the detection.

References

1. Quantitation of [^{11}C]diprenorphine cerebral kinetics in man acquired by PET using presaturation, pulse-chase and tracer-only protocols. AKP Jones, VJ Cunningham, SK Ha-Kawa, T Fujiwara, Qi Liyi, SK Luthra, J Ashburner, S Osman, T Jones. J Neurosci Methods 51: 123-134, 1994

2. CJ Lueck, S Zeki, KJ Friston, MP Deiber, P Cope, VJ Cunningham, AA Lammertsma, C Kennard, RSJ Frackowiak. The colour centre in cerebral cortex of man. Nature: 340; 386-389, 1989.

3. E Paulesu, CD Frith, RSJ Frackowiak. The neural correlates of the verbal component of working memory. Nature Vol 362: 342 1993

4. G Bottini, E Paulesu, R Sterzl, E Warburton, RJS Wise, G Vallar, RSJ Frackowiak, CD Frith. Nature Vol 376: 778 1995

5. RJ Dolan, P Fletcher, CD Frith, KJ Friston, RSJ Frackowiak, PM Grasby. Dopaminergic modulation of impaired cognitive activation in the anterior cingulate cortex in schizophrenia. Nature in press.

6. DA Silbersweig, E Stern, C Frith, C Cahill, A Holmes, S Grootoonk, J Seaward, P McKenna, S Chua, L Schnorr, T Jones, RSJ Frackowiak. A transient functional neuroanatomy of hallucinations in schizophrenia. Nature in press.

7. AKP Jones, Q Liyi, VV Cunningham, DW Brown, Ha-Kawa, Fujiwara, KF Friston, S Silva, SK Luthra, T Jones, Endogenous opiate response to pain in rheumatoid arthritis and cortical and subcortical response to pain in normal volunteers using positron emission tomography. Int J Clin Pharm Res: 11(6)261-266, 1991.

8. O Lindvall, G Swale, H Widner, JC Rothwell, A Bjorklund, D Brooks, P Brundin, RSJ Frackowiak, CD Marsden, P Odin, S Rehn. Evidence for long-term survival and function of dopaminergic grafts in progressive Parkinsons disease. Ann Neurol 172-180, 1994.

9. DC Lefroy, R de Silva, L Choudhury, NG Uren, T Crake, CG Rhodes, AA Lammertsma, H Boyd. PN Patsalos, P Nihoyannopoulos, CM Oakley, T Jones, PG Camicic. Diffuse reduction of Myocardial Beta-Adrenoceptors in Hypertrophic Cardiomyopathy: A Study with Positron Emission Tomography. JACC 22. No 6: 1653-1660, 1993.

10. DWO Tilsley, RJA Harte, T Jones, F Brady, SK Luthra, G Brown, PM Price. New techniques in the pharmacokinetic analysis of cancer drugs IV Positron Emission Tomography. Cancer Surveys Vol 17: 425, 1993.

11. JM Ritter, T Jones. PET: a symposium highlighting its clinical and pharmacological potential. TIPS (Vol 16): 117, 1995.

12. ME Casey, R Nutt. A multicrystal two dimensional BGO detector system for positron emission tomograph. IEEE Trans. Nucl Sci. NS-33: 570-4, 1986.

13. TJ Spinks, T Jones, DL Bailey, DW Townsend, S Grootoonk, PM Bloomfield, MC Gilardi, ME Casey, B Sipe, J Reed. Physical performance of a positron tomograph for brain imaging with retractable septa. Phys. Med. Biol. No.8, Vol 37: 1637-1655, 1992.

14. S Grootoonk, TJ Spinks, AM Kennedy, PM Bloomfield, D Sashin, T Jones. The practical implementation and accuracy of dual window scatter correction in a NeuroPET scanner with the septa retracted. IEEE Medical Imaging Conference, 2: 942-944. Orlando, IEEE (Piscataway, NJ).

15. SC Strother, ME Casey, EJ Hoffman. Measuring PET scanner sensitivity: Relating count rates to image signal-to-noise ratios using noise equivalent counts. IEEE Trans. Nucl. Sci, Vol 37: 783-788. 1990.

16. DL Bailey, T Jones, TJ Spinks, MC Gilardi, DW Townsend. Noise equivalent count measurements in a neuro-PET scanner with retractable septa. IEEE No3, Vol 10: 256, 1991.

17. DL Bailey, T Jones, JDG Watson, L Schnorr, RSJ Frackowiak. Activation studies in 3D PET: evaluation of true signal gain. p 341-349. In: Quantification of Brain Function. Tracer kinetics and image analysis in Brain PET. editors K Uemura et al. Elsevier Science Publisher B V. 1993.

SCINTILLATORS FOR POSITRON EMISSION TOMOGRAPHY†

William W. Moses and Stephen E. Derenzo, Lawrence Berkeley National Laboratory, University of California, Berkeley, CA 94720

ABSTRACT

Like most applications that utilize scintillators for gamma detection, Positron Emission Tomography (PET) desires materials with high light output, short decay time, and excellent stopping power that are also inexpensive, mechanically rugged, and chemically inert. Realizing that this "ultimate" scintillator may not exist, this paper evaluates the relative importance of these qualities and describes their impact on the imaging performance of PET.

The most important PET scintillator quality is the ability to absorb 511 keV photons in a small volume, which affects the spatial resolution of the camera. The dominant factor is a short attenuation length (≤1.5 cm is required), although a high photoelectric fraction is also important (>30% is desired). The next most important quality is a short decay time, which affects both the dead time and the coincidence timing resolution. Detection rates for single 511 keV photons can be extremely high, so decay times ≤500 ns are essential to avoid dead time losses. In addition, positron annihilations are identified by time coincidence so ≤5 ns fwhm coincidence pair timing resolution is required to identify events with narrow coincidence windows, reducing contamination due to accidental coincidences. Current trends in PET cameras are toward septaless, "fully-3D" cameras, which have significantly higher count rates than conventional 2-D cameras and so place higher demands on scintillator decay time. Light output affects energy resolution, and thus the ability of the camera to identify and reject events where the initial 511 keV photon has undergone Compton scatter in the patient. The scatter to true event fraction is much higher in fully–3D cameras than in 2-D cameras, so future PET cameras would benefit from scintillators with a 511 keV energy resolution <10–12% fwhm.

OVERVIEW OF PET CAMERA DESIGN

The PET camera detects coincident pairs of 511 keV annihilation photons with a circular array of detector modules that encircles the patient as shown in Figure 1, with each detector module potentially in coincidence with each of the detector modules on the opposite side of the ring.

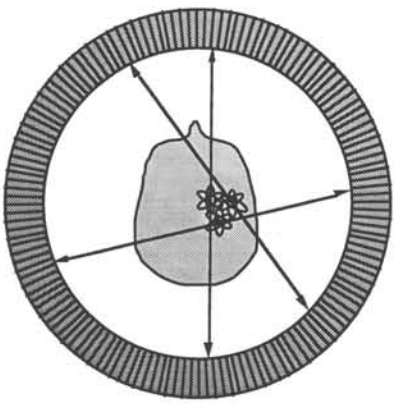

Fig. 1: PET Camera.
The patient is injected with a drug containing a positron emitting isotope, which localizes in a biologically active area in the patient. The isotope decays, and annihilates with an electron from the tissue to form back to back 511 keV photons. These penetrate the patient and are detected via time coincidence in a detector ring that encircles the patient. The decay was then known to occur somewhere on the line connecting the two detector elements, also known as a chord. Using the coincidence rates measured in each chord, the mathematical technique of computed tomography forms a two dimensional image of the isotope distribution (and hence drug distribution) in the plane defined by the tomograph ring.

†This work was supported in part by the Director, Office of Energy Research, Office of Health and Environmental Research, Medical Applications and Biophysical Research Division of the U.S. Department of Energy under contract No. DE-AC03-76SF00098, and in part by Public Health Service Grant No. R01 CA48002 awarded by the National Cancer Institutes, Department of Health and Human Services.

Proc. Int. Conf. on Inorganic Scintillators and Their Applications, SCINT95,
1996, Delft University Press, The Netherlands

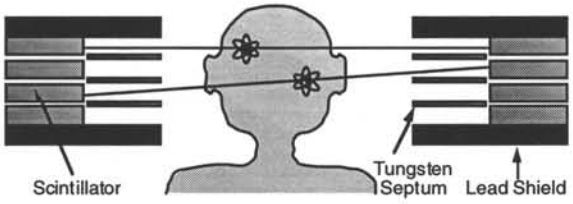

Fig. 2: Multi-Ring Camera. Several rings can be stacked and data simultaneously accumulated to form a 3 dimensional image. Removable tungsten septa reduce Compton scatter from the patient, but decrease the efficiency by limiting the number of cross-plane slices allowed.

Such a ring can then images a two dimensional slice of the activity in that detector plane. Most modern PET cameras contain several stacked detector planes, as shown in Figure 2. This allows several slices (including cross-plane slices, in which the 511 keV photons are detected in different detector rings) to be acquired simultaneously, and the resulting planar images stacked to form a three dimensional image. Interplane tungsten septa collimate the annihilation photons, reducing background from Compton scatter in the patient but limiting the detection efficiency for the cross-plane slices and so the overall detection efficiency. In Fully 3-D PET these septa are often removable so that data from all cross-plane slices can be acquired [1].

PET DETECTOR REQUIREMENTS

The requirements for an individual PET detector module have been described previously [2]. It must identify the 511 keV photons with: (1) high detection efficiency (>85% per 511 keV photon), (2) high spatial resolution (<5 mm fwhm), (3) low cost (parts cost <\$600 / in^2 of "front" surface area), (4) low dead time (<4 μs in^2,where the figure of merit is the product of the detector dead time and the front surface area of the portion of the detector that is dead), (5) good timing resolution (<5 ns fwhm), and (6) good energy resolution (<100 keV fwhm). These requirements are listed in approximate order of decreasing importance.

The first PET detector modules consisted of a single scintillator crystal coupled to a photomultiplier tube (PMT), as shown in Figure 3a. The width and height of the crystal determine the in-plane and axial resolution respectively, while the depth (typically 3 attenuation lengths) determines the detection efficiency. This design has excellent performance, but is expensive (due to the large number of PMTs needed), does not allow small scintillator crystals to be used (due to the minimum size of PMTs), and is difficult to form the crystals into a close-packed two-dimensional array. Therefore, current PET cameras generally use detector modules similar to that shown in Figure 3b [3]. The 511 keV photons interact in the BGO scintillator crystal, and the resulting scintillation light observed by four PMTs. BGO [4] is commonly

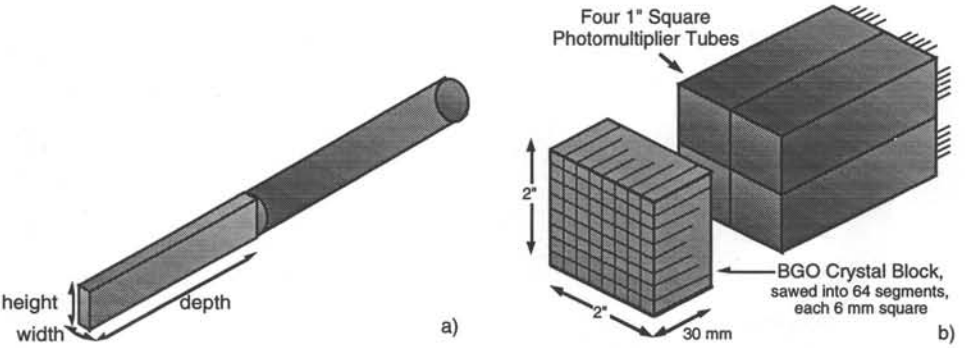

Fig. 3a): Early PET Detector Module. The earliest PET detector modules consisted of a PMT coupled to a single scintillator crystal (at first NaI:Tl, then BGO after its discovery). **3b): Modern PET Detector Module.** Four photomultiplier tubes decode which of the 6x6x30 mm crystal segments the 511 keV photon interacts in. The scintillation light is distributed across the back face of the BGO crystal, where Anger logic (*i.e.* the ratio of the four PMT output signals) determines the segment of interaction.

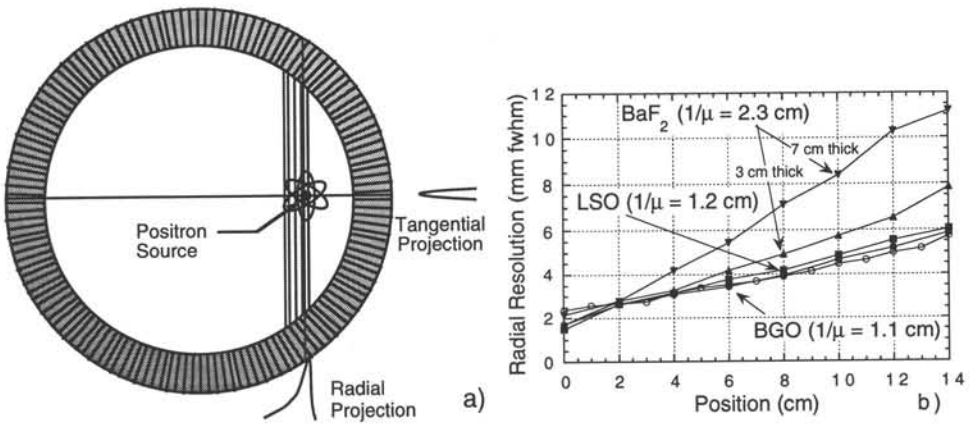

Fig. 4a): Cause of Radial Elongation. 511 keV photons that are incident at an oblique angle can penetrate into the detector ring before interacting and being detected. This causes a blurring that worsens as the source is moved away from the center of the ring. **4b): Effect of Attenuation Length on Radial Elongation.** Monte Carlo simulation of the reconstructed resolution as a function of position for 3 cm deep tomographs made of various scintillators. The closed circles are BGO, the squares are LSO, the triangles BaF_2, and the open circles measured data with a BGO tomograph. The inverted triangles are for a tomograph constructed of 7 cm deep BaF_2 scintillator.

used, as its attenuation length (1.1 cm) is lower than any other commonly available scintillator. The 30 mm depth of the BGO crystal is nearly 3 attenuation lengths, ensuring high detection efficiency. Saw cuts in the BGO define "individual" crystal elements by controlling the light distribution among the four PMTs, and Anger logic (*i.e.* analog ratios among the four PMT signals) is used to determine which of the "individual" crystals the interaction occurred in. The sum of the four PMT signals is used to form a timing pulse (with 3 ns fwhm accuracy) and a measurement of the photon energy (with 100 keV accuracy). The size of the "individual" crystal elements determines the position resolution of the detector module, but a limited number of crystals (typically ≤64) can be accurately decoded due to the limited light output of BGO. The entire module is "dead" for approximately 1 μs after a 511 keV photon interaction while the BGO emits its scintillation light (its decay time is 300 ns), as interaction in any other portion of the module during this time would confuse the Anger logic.

SCINTILLATOR REQUIREMENTS FOR PET

The scintillator requirements for PET are best determined by evaluating their affect on the PET detector requirements listed in the previous section. Using the BGO as a standard, the requirements for a scintillator for PET (all quantities assume 511 keV photon energy), listed in approximate order of decreasing importance, are as follows: (1) short attenuation length (<1.5 cm), (2) high photoelectric fraction (>30%), (3) short scintillation decay time (<500 ns), (5) low cost (<$20/cc), and (6) high light output (>8000 photons/MeV). The remainder of this paper discusses the basis for these requirements in more detail.

Attenuation Length

With any PET detector design, a high detection efficiency (>85%) is necessary, which implies that the detector depth (*i.e.* thickness in the radial direction) be at least two attenuation lengths thick, and preferably three. While this criterion can be met with a scintillator of any attenuation length, a short attenuation length is desired to minimize a resolution degradation artifact caused by penetration of the 511 keV photons into the crystal ring. The origin of this artifact, variously known as radial elongation, parallax error, or radial astigmatism, is shown in

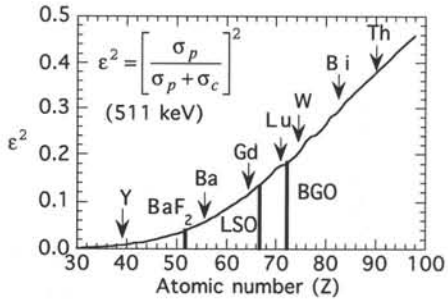

Fig. 5: Double Photoelectric Interaction Probability.
The probability that both annihilation photons interact via the photoelectric effect as a function of effective atomic number. Note the strong increase with increasing atomic number.

Figure 4a. Photons that are normally incident on the detector ring are detected in the crystal that they impinge upon no matter how far they penetrate into the ring before interacting. However, photons that impinge on the detector ring at an oblique angle can penetrate into adjacent crystals before they interact and are detected, which causes mis-positioning errors (*i.e.* events are assigned to chords that do not pass through the source). This spatial resolution degradation increases for objects placed further away from the center of the tomograph ring.

Figure 4b shows the magnitude of this effect for various different scintillator materials. It plots the full width at half maximum (fwhm) of the reconstructed image of a point source as a function of the distance of that point source from the center of the tomograph ring. Data were created with a Monte Carlo simulation of a 60 cm diameter tomograph ring made up of 3x3x30 mm^3 crystals of various scintillators, and validated with a BGO tomograph with the same dimensions (the open circles in Figure 4b). The data show that the resolution is worse at large distances from the center even for BGO (1.2 cm attenuation length), but that the degradation in LSO [5] (1.3 cm attenuation length) is similar to that of BGO. It also shows that a 3 cm thick ring of BaF_2 (2.3 cm attenuation length) has considerably poorer resolution and a significantly reduced detection efficiency. If the BaF_2 thickness is increased to 7 cm (to have a similar number of attenuation lengths as the BGO or LSO tomographs), the degradation becomes severe. This is the main reason that virtually all PET cameras use BGO scintillator.

Photoelectric Fraction

Photoelectric interactions are greatly preferred over Compton scatter, as 511 keV photon interactions that Compton scatter deposit energy in two (or more) locations in the detector ring, frequently separated by >1 cm, and thus reduces the spatial resolution of the detector module. Figure 5 plots the probability that both 511 keV photons interact via a photoelectric interaction as a function of the atomic number. This probability increases rapidly with increasing atomic number, so scintillators containing a large fraction of high Z materials are desired. It is difficult to quantitate the magnitude of this effect, but the similarity of the resolution curves in Figure 4b for BGO (18.5% double photoelectric probability) and LSO (11.6% double photoelectric probability) indicate that the resolution is more sensitive to the attenuation length.

Decay Lifetime

The decay lifetime affects both the timing resolution and the dead time. Assuming that multiple decay lifetime components are present, the dead time is influenced most by the slowest decay component. While the relationship between the decay time and the dead time is difficult to quantitate (especially with multiple decay lifetimes), most PET cameras trigger at the single photoelectron level, so the dead time can be defined as the time that it takes for the scintillation intensity to drop to the level of 1 photon/MeV/ns.

Low dead time is critical as it affects the portion of a PET study known as the transmission scan. This is a scan that is used to correct for the 511 keV photon attenuation

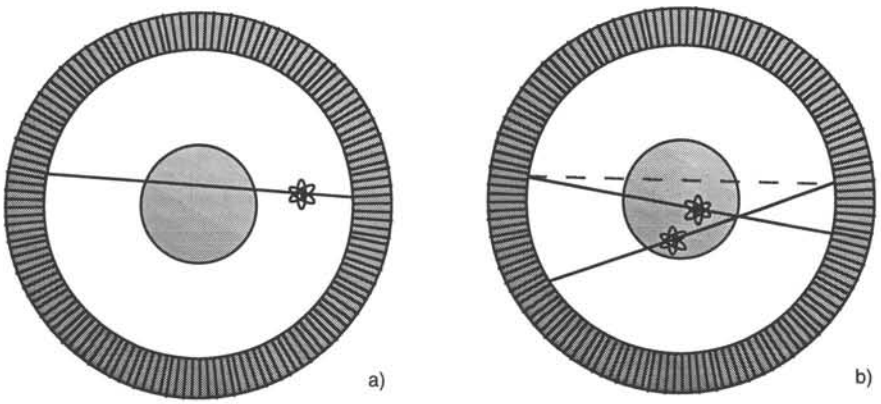

Fig. 6a): Transmission Scans. The attenuation within the patient is measured with an orbiting external source. The correction factor is given by the ratio of count rates with and without the patient in the scanner. **6b): Random Coincidences.** Simultaneous decays can cause random coincident events (dashed line).

within the patient. It is performed with an orbiting external positron source, as shown in Figure 6a — the ratio of the count rate with the patient in the tomograph ring and with no patient gives the attenuation factor on a chord by chord basis. The strength of the external source is presently limited by the count rate in the detector modules closest to the source, which approaches 1 Mhz/in^2. Higher source strengths (1 to 2 orders of magnitude) are desired to decrease the time it takes to perform a transmission scan.

Timing resolution is determined by I_0, the scintillation photon intensity (photons/MeV/ns) immediately after excitation [6]. Again assuming that a scintillator has multiple decay lifetime components, the fastest component usually has the largest affect on I_0. Good timing resolution (<5 ns fwhm) is necessary in order to reduce random coincidences, as shown in Figure 6b. The random coincidence rate is given by $2S^2\Delta t$, where S is the singles rate and Δt is the coincidence window width (typically 10 ns). Randoms become increasingly important when imaging higher activities (such as when imaging with short half-life isotopes) or with fully 3-D PET (which has a much higher efficiency than conventional PET, and random fractions can exceed 50%), as the coincidence rate scales linearly with the activity being imaged (*i.e.* like S) while the randoms rate scales like S^2. Better timing resolution will allow shorter coincidence windows to be used to reduce the random fraction. However, the minimum coincidence width is 4 ns, due to time of flight differences across the tomograph ring.

If the timing resolution is good enough, this decay time difference can be used to localize the position of the annihilation along chord [7]. Tomographs using BaF_2 scintillator have been built using this principle, but are not common. The system-wide coincidence timing resolution is typically 500 ps fwhm (it is difficult to keep the large number of crystals in a PET camera in mutual calibration), which localizes the annihilation to a line segment approximately 8 cm long. While this is considerably greater than the size of the scintillator crystal, the added information can be used by the reconstruction algorithm to reduce noise in the image.

Luminosity

The luminosity affects the timing, spatial, and energy resolution. The affect on timing is simple — for a given decay time, a higher luminosity yields a higher initial intensity I_0 and so better timing resolution, as discussed previously. The effect on the spatial resolution lies in the ability of the block detector module to decode the crystal of interaction, which is limited by counting statistics. With a more luminous scintillator, more crystals can be decoded with the same number of PMTs, allowing the crystal size to become smaller and thus achieve higher resolution. Present BGO based detector modules generate <200 photoelectrons per 511 keV interaction and decode up to an 8x8 array. Figure 7a plots the distribution of the X position

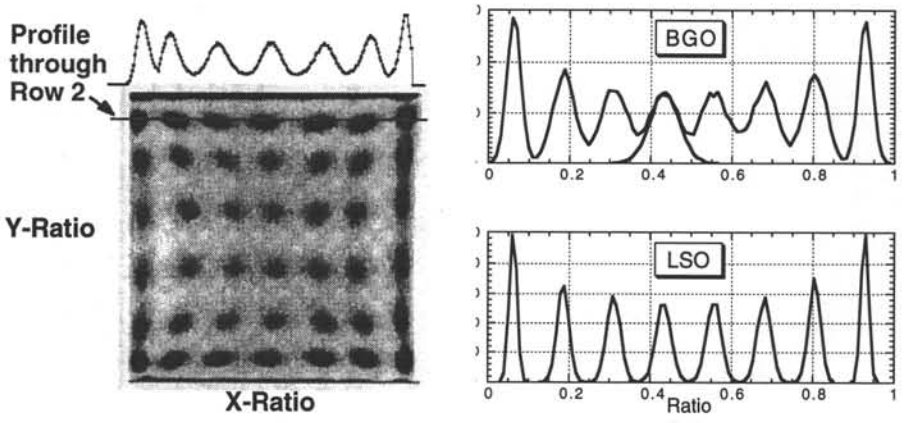

Fig. 7a): Decoding in the Block Detector. The block detector is uniformly illuminated with 511 keV photons, and for each interaction the X and Y position estimators are computed, then plotted as a point on the scatter plot at the left. Distinct dark regions are observed corresponding to crystal positions. A profile drawn through one row shows that there is some overlap between individual crystals. **7b): Dependence on Light Output.** Using a Monte Carlo simulation whose only blurring factor is statistical fluctuations, the overlap between crystals with the same luminosity as BGO is comparable to the experimentally measured overlap, while the overlap between crystals with the same luminosity as LSO is significantly smaller.

estimator (*i.e.* the PMT ratio along one axis) when a 7x8 detector module is uniformly illuminated with 511 keV photons [8]. Seven peaks corresponding to the 7 crystals in this dimension are clearly seen, but there is some overlap and so some crystal mis-identification is present. Figure 7b shows similar distributions acquired from Monte Carlo simulations of an 8x8 array with light outputs equal to that of BGO and LSO, where the only blurring effect is the counting statistics. The peaks overlap significantly when a light output equal to that of BGO is used, but have almost no overlap when the light output of LSO is used.

Higher luminosity can also help reduce background due to Compton scatter in the patient by improving the energy resolution. As the annihilation photons lose energy when they scatter, good energy resolution (for which high light output is necessary) will allow these scattered events to be identified and rejected. With BGO based block detectors, the 511 keV energy resolution is 12%–20% fwhm and a lower energy threshold is typically set at 350 keV. With these parameters, conventional 2-D PET (*i.e.* with septa) has approximately 15% of the coincidences contain scattered photons, while the fraction approaches 50% with fully 3-D PET.

Emission Spectrum

The only requirement on the emission spectrum is that it be a good match to inexpensive PMTs. As this implies PMTs with bialkali photocathodes and borosilicate glass windows, this implies emissions in the range of 300–500 nm.

Materials Considerations

Given that short attenuation length and high effective atomic number are mandatory, the major materials consideration is cost! A commercial tomograph uses approximately 8 liters of scintillator crystal and 500 PMTs. The parts cost of the scintillator and PMTs are each about 25% of the total parts cost, and the next most expensive item is approximately 5% of the total parts cost. Thus, any change compared to the cost of BGO (roughly $20/cc) will have a significant impact on the overall cost of the system.

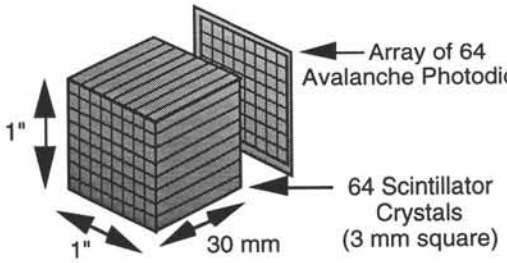

Fig. 8: Solid State Photodetector PET Detector Module.
The module consists of 64 optically isolated scintillator crystals, each 3 mm x 3 mm x 30 mm deep. When a 511 keV photon interacts in any of the elements, the scintillation light is detected by one element of an APD array located at one end of the crystal.

It is also mandatory that the scintillator have good mechanical ruggedness in order to withstand the multiple saw cuts necessary to make the detector. This is one of the major reasons that GSO [9] is not found in modern tomographs. Many of the other materials properties can be compromised — radiation hardness and afterglow are not issues, and hygroscopic crystals can be used (NaI:Tl and CsF have been used reasonably often).

FUTURE DIRECTIONS

Fully 3-D PET

One of the major present directions that significantly affects the scintillator is fully 3-D PET. As mentioned earlier, it places more severe demands on the dead time and energy resolution than conventional 2-D PET. Presently, BGO is the dominant scintillator for 3-D PET, largely because most 3-D scanners are combination 2-D / 3-D scanners (*i.e.* have removable septa) and because no reasonable alternative exists. The majority of the scans performed in a clinical environment are 2-D, as 3-D scans are hampered by relatively poor detector performance and a much larger data set size.

Time of Flight PET

Time of flight PET has long been a desired goal, but has not realized its potential due to scintillator deficiencies. A number of time of flight scanners have been made with BaF_2, but the extreme UV color of the fast light is difficult to work with, and the poor attenuation length and effective atomic number have compromised its spatial resolution or efficiency. A few scanners have also been made with CsF, which has similar problems with poor attenuation length and effective atomic number. Should a scintillator be discovered that combines the high initial luminosity of BaF_2 with short attenuation length, PET would be improved significantly.

Solid State Photodetectors

One of the most exciting potential developments is the replacement of the PMT with a solid state photodetector such as an avalanche photodiode (APD) array, as shown in Figure 8. The successful development of economical, reliable APD arrays would significantly alter the requirements for PET scintillators. First, the lower signal to noise ratio in these devices (compared to a PMT) would require higher luminosity and initial intensity in order to achieve the requisite timing and energy resolution. The fact that each scintillator crystal is an independent detector element greatly reduces the dead time, and so decay lifetimes up to approximately 10 μs can be tolerated. The quantum efficiency of APDs is significantly higher than PMTs, so the limits put on energy resolution by counting statistics are reduced and better energy resolution may be achievable. Finally, silicon based photodetectors have good quantum

efficiency in a different wavelength range than PMTs (400–900 nm rather than 300–500 nm), so it is possible to use scintillators that emit at much longer wavelengths.

CONCLUSION

The most important scintillator property for PET is good stopping power, loosely defined as the combination of short attenuation length and high effective atomic number. The next most important attributes, in order of decreasing importance, are decay lifetime, light output, and cost. Greatly improved PET scanners would result if scintillator materials were developed that had similar characteristics to BGO, but with better energy resolution or shorter decay lifetime. Finally, solid state photodetectors would allow a significantly different set of compromises to be made, but also have tremendous potential for improving PET.

ACKNOWLEDGMENTS

We thank our colleagues working in radiation detection and medical imaging research for the innumerable thought provoking discussions that have lead to this summary. This work was supported in part by the Director, Office of Energy Research, Office of Health and Environmental Research, Medical Applications and Biophysical Research Division of the U.S. Department of Energy under contract No. DE-AC03-76SF00098, and in part by Public Health Service Grant Nos. P01 HL25840, R01 CA48002, and R01 NS29655, awarded by the National Heart Lung and Blood, National Cancer, and Neurological Science Institutes, Department of Health and Human Services.

REFERENCES

[1] Cherry SR, Dahlbom M and Hoffman EJ. 3D PET using a conventional multislice tomograph without septa. *J. Comput. Assist. Tomogr.* **15:** pp. 655–668, 1991.

[2] Moses WW, Derenzo SE and Budinger TF. PET detector modules based on novel detector technologies. *Nucl. Instr. Meth.* **A-353:** pp. 189–194, 1994.

[3] Tornai MP, Germano G and Hoffman EJ. Positioning and energy response of PET block detectors with different light sharing schemes. *IEEE Trans. Nucl. Sci.* **NS-41:** pp. 1458–1463, 1994.

[4] Weber MJ and Monchamp RR. Luminescence of $Bi_4Ge_3O_{12}$: spectral and decay properties. *J Appl Phys* **44:** pp. 5495-5499, 1973.

[5] Melcher CL and Schweitzer JS. Cerium-doped lutetium orthosilicate: a fast, efficient new scintillator. *IEEE Trans. Nucl. Sci.* **NS-39:** pp. 502–505, 1992.

[6] Hyman LG. Time resolution of photomultiplier systems. *Rev. Sci. Instr.* **36:** pp. 193–196, 1965.

[7] Ter-Pogossian MM, Mullani NA, Ficke DC, et al. Photon time-of-flight-assisted positron emission tomography. *J Comput Assist Tomogr* **5:** pp. 227-239, 1981.

[8] Cherry SR, Tornai MP, Levin CS, et al. A comparison of PET detector modules employing rectangular and round photomultiplier tubes. *IEEE Trans. Nucl. Sci.* **NS-42:** pp. 1064–1068, 1995.

[9] Takagi K and Fukazawa T. Cerium-activated Gd_2SiO_5 single crystal scintillator. *Appl. Phys. Lett.* **42:** pp. 43–45, 1983.

YAP:Ce SCINTILLATOR COUPLED TO A POSITION SENSITIVE PHOTOMULTIPLIER FOR HIGH SPATIAL RESOLUTION POSITRON EMISSION TOMOGRAPHY

A. Del Guerra[a,b], F. de Notaristefani[d], G. Di Domenico[b,c], T. Malatesta[e], R. Pani[e], R. Pellegrini[e], A. Turra[a,b], F. Vittori[f], G. Zavattini[a,b]

[a] *Dipartimento di Fisica, Università di Ferrara, via Paradiso 12, I-44100 Ferrara Italy*
[b] *INFN, Sezione di Ferrara, via Scienze, I-44100 Ferrara Italy*
[c] *Dottorato di Medicina Nucleare, Cattedra di Medicina Nucleare, Facoltà di Medicina e Chirurgia, Corso Giovecca 203, I-44100 Ferrara Italy*
[d] *INFN, Sezione di Roma, Dipartimento di Fisica, Università di Roma III, Italy*
[e] *Dipartimento di Medicina Sperimentale, Università di Roma "La Sapienza", Italy*
[f] *Dipartimento di Fisica, Università di Roma "La Sapienza", Italy*

AIM

The aim of these preliminary measurements was to characterise the YAP:Ce [1-3] multicrystal coupled to a position sensitive photomultiplier (PSPMT Model Hamamatsu R2486-06) in coincidence with a BGO crystal to measure the spatial resolution, energy resolution, time resolution, efficiency of the multicrystal at 511 keV and compare these results with those obtained using the same PSPMT coupled to a thin (1 mm) NaI(Tl) crystal. The positron source used was ^{22}Na.

APPARATUS AND METHODS

A scheme of the set-up is shown in figure 1. The YAP:Ce multicrystal is composed of 36 match-like crystals each of dimensions 0.1x0.1x1.0 cm^3, bundled together to form the detector of 0.6x0.6x1.0 cm^3. Each crystal is separated from the adjacent one by a 5μm metallic reflecting layer.

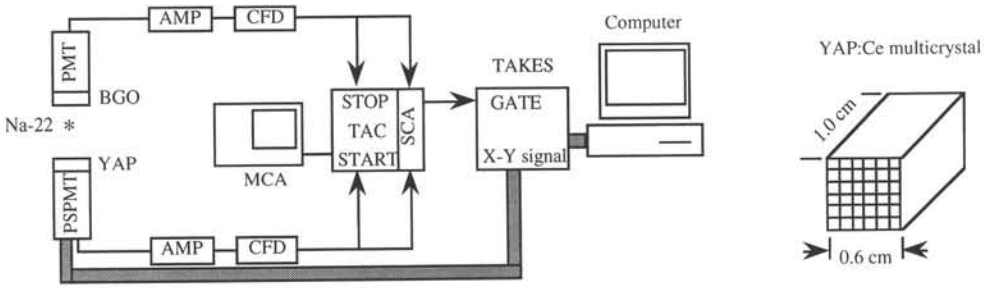

Figure 1: Scheme of the setup and of the YAP:Ce multicrystal. The single YAP:Ce crystals are separated from each other by a 5μm metallic reflecting layer.

The multicrystal is directly put in contact with the PSPMT photocathode. The second detector used for the γ–γ coincidence is a 2.5 cm diameter BGO crystal coupled to a standard photomultiplier. This second (BGO) detector defines the solid angle for the photons incident on the position-sensitive detector.The physical characteristics of the YAP:Ce crystal are listed in

Proc. Int. Conf. on Inorganic Scintillators and Their Applications, SCINT95,
1996, Delft University Press, The Netherlands

Table I and are compared to some commonly used scintillators for PET. The ^{22}Na source was placed near the position sensitive detector (2.8 cm for the NaI(Tl), 2.5 cm for the YAP:Ce) and as far away as possible from the BGO detector (95 cm).

The BGO signal and the signal from the last dynode of the PSPMT are amplified and sent to two Constant Fraction Discriminators (CFD) for fast timing. The thresholds were set so as to select only those events under the photopeak. The logic outputs from the CFDs were sent to a Time to Amplitude Converter (TAC) and then to a Single Channel Analyser (SCA). A time window was set so as to choose the coincidences between the two detectors. The TAC analog output was registered on a Multi Channel Analyser (MCA) to measure the time spread of the YAP:Ce - BGO events and therefore the time resolution of the system.

Table I: Comparison of some physical characteristics of YAP:Ce scintillator with some commonly used scintillators.

Scintillator	NaI(Tl)	BGO	YAP:Ce
Density (gm/cm^3)	3.67	7.13	5.37
Atomic number	11, 53	83, 32, 8	39, 13, 8
Hygroscopic	YES	NO	NO
Photoelectron yield* (511 keV)	2500	300	1000
Scintillation decay time (ns)	230	300	27
Percentage energy resolution at 511 keV, FWHM (%)	7	12	11

* With a standard bialkali photocatode

When a coincidence occurs, the logical SCA output is sent to the gate of a Position Calculator Module (TAKES). Having adjusted the timing between the gate and the analog (X,Y) outputs of the PSPMT, the latter were registered on a memory in the Position Sensitive Module and at the end of the acquisition were down-loaded to a computer for analysis.

The transverse position of the BGO detector was variable within ±2.5 cm which corresponded to ±0.7 mm on the YAP:Ce surface. This permitted us to determine how well two distributions could be distinguished. The centroids of the X,Y and time spread distributions and their FWHMs were then calculated by fitting the experimental data with Gaussian distributions.

Energy spectra of both the detectors were also recorded in coincidence to evaluate the energy resolution and therefore to estimate the mean number of photo-electrons produced at the photo-cathode. The efficiency for 511 keV photons was measured using the same ^{22}Na source. The BGO threshold was placed well above 511 keV so as to detect only the 1275 keV photon also emitted in coincidence by the source but angularly uncorrelated to the 511 keV photons. This permitted us to eliminate the 1275 keV Compton contamination otherwise present in the YAP:Ce spectrum.

The ratio of the coincidence (R_{coinc}) and BGO counting rates (R_{BGO}) yields the following expression for the YAP:Ce efficiency at 511 keV:

$$\varepsilon_{YAP}^{511keV} = \frac{R_{coinc}}{R_{BGO}} \frac{1}{1.8 \cdot \Omega_{YAP}} \qquad (1)$$

The factor 1.8 at the denominator is the ratio of the number of 511 keV to 1275 keV photons emitted by the source, and Ω_{YAP} is ≈ 10%.

A Monte Carlo simulation was also run to verify our understanding of the detector and the spectra obtained. The code used was the general purpose EGS4 code [4] for electron and photon transport.

Estimates of the time spread of the coincidences and of the spatial distribution were made. For the spatial distribution there are several contributions:

i) solid angle defined by the BGO detector - ~ 0.7 mm;
ii) ^{22}Na source dimensions - 1 mm;

iii) mean positron range before annihilation - ~0.5 mm;
iv) deviation from 180° of the 511 keV photons - ~0.5° ;
v) light transport spread before reaching the photocathode ~1.3 mm for NaI(Tl): negligible for YAP:Ce;
vi) intrinsic spread due to the photomultiplier - 0.9 mm.

RESULTS

In fig. 1 there can be seen the spatial distribution of events along the x (fig. 1a) and y (fig. 1b) axis obtained with the YAP:Ce multicrystal set-up. These distributions include the systematic broadening described above.

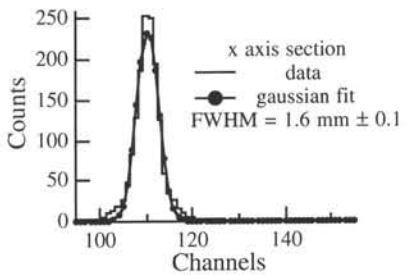

Fig. 1a Coincidence spatial resolution

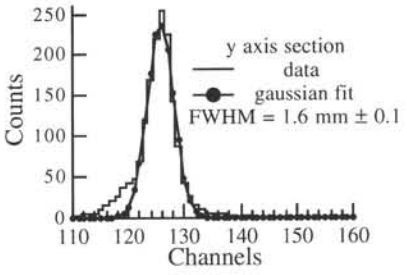

Fig. 1b Coincidence spatial resolution

The time distribution obtained with the BGO-YAP system is shown in fig. 2a. It is compared with a curve obtained with a model based on photo-electron arrival time statistics [5]. This curve depends on the total number of photo-electrons for each scintillator (N_{BGO}, N_{YAP}), on their decay times and on the number of photo-electrons necessary to trigger the electronics (n_{BGO}, n_{YAP}). The decay times are 300 ns for the BGO and 30 ns for the YAP. By fitting the data with the model we obtained the following values for the remaining parameters: N_{BGO}=320, N_{YAP}=100, n_{BGO}=3.6 and n_{YAP}=5.9. These values are consistent with the energy resolutions obtained for each detector.

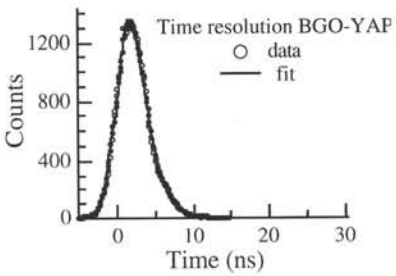

Fig. 2a Coincidence time resolution

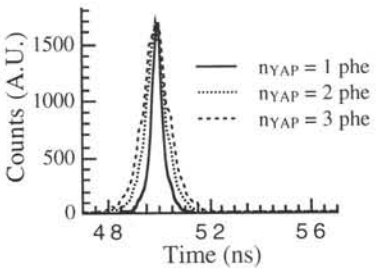

Fig. 2b Coincidence time resolution

By using the values obtained for the YAP we estimated the time distribution for YAP-YAP system which is shown in fig. 2b for different values of the number of photoelectrons needed to trigger the YAP electronics (n_{YAP}).

The results obtained are summarized in the table II.

Table II:

Material	BGO-NaI	NaI(Tl) estimated	BGO-YAP	YAP:Ce estimated
Energy Resolution, FWHM (%)	(11±1)%		(21±2)%	
Time Resolution (ns)	5.1±0.6*	1.8±0.4††	4.6±0.6*	1.3±0.3††
Efficiency			(11.2±2)%	(10.2±0.2)%†
Spatial Resolution, FWHM (mm)	1.8±0.3	1.9±0.3	1.6±0.1	1.7±0.3

* The time resolution of the coincidence is dominated by the BGO contribution, which we estimated [5] (4.2 ± 1.0 ns).

† With EGS4 [4]

†† With the procedure of ref. [5]

CONCLUSION

The results obtained are very promising. The spatial resolution of 1.6 mm is one of the best obtained so far for crystal+PSPMT systems. The use of a longer YAP:Ce crystal (3.0 cm) should help in increasing the efficiency of the detector to acceptable levels. On the other hand a good timing is expected (≈ 2.0 ns FWHM) for a YAP-YAP coincidence system, which could allow to reduce spurious coincidences.

REFERENCES

[1] R. Pani, F. de Notaristefani, K. Blazek, et al., NIM-A348 (1994) 551-558
[2] L. H. Barone, K. Blazek, D. Bollini, et al., NIM-A-360 (1995) 302-306
[3] M.V. Khorzik, O. V. Misevich and A. A. Fyodorov, NIM-B72 (1992) 499-501
[4] W. R. Nelson, A. Hyrayama and D. W. O. Rogers, SLAC-265 (Stanford, CA 94305, 1985)
[5] R. F. Post and L. I. Schiff, Phys. Rev. 80 (1950) 1113

A BGO BASED POSITRON CAMERA FOR HEAVY ION TUMOUR THERAPY CONTROL

J. Pawelke[1], L. Byars[2], W. Enghardt[1,3], H. Geissel[4], B.G. Hasch[1],
K. Lauckner[1], P. Manfraß[1], D. Schardt[4], M. Sobiella[1]
[1] Forschungszentrum Rossendorf, PF 510119, 01314 Dresden, Germany
[2] Byars Consulting, 810 Innovation Drive, Knoxville, TN 37932, USA
[3] TU Dresden, Medizinische Fakultät, Fetscherstr. 74, 01307 Dresden, Germany
[4] Gesellschaft für Schwerionenforschung Darmstadt, PF 110552, 64220 Darmstadt, Germany

ABSTRACT

The in-situ and in-vivo treatment plan verification, beam monitoring as well as dose control during the heavy ion tumour therapy can be performed in principle by measurements of range distributions of β^+-emitting nuclei by means of PET techniques. For this purpose the performance of two different multi-crystal 2D BGO detectors with high spatial resolution as well as the results of in-beam PET experiments using β^+-active and stable heavy ion beams are presented. Following the deduced performance requirements a PET-scanner that is designed for the clinical use in the heavy ion therapy at GSI Darmstadt has been set up.

INTRODUCTION

Due to the high precision that is achievable in tumour conform irradiation with heavy ions [1], methods for verification of the treatment plan, beam monitoring as well as dose control during the therapy are highly desirable for this kind of radiotherapy. This requires non-invasive in-situ measurements of ion beam ranges, which should be possible by means of positron emission tomography (PET). The necessary sources of activity can be provided either by beams of β^+-radioactive ions [2] or by positron emitters generated due to the nuclear fragmentation of the ions of a stable beam in the patient [3].
Caused by its high stopping power for γ-rays, bismuth germanate (BGO) coupled to photomultipliers (PMT) is currently the detector of merit for non-time-of-flight clinical PET applications. However, in practical heavy ion therapy, which was mainly performed at the LBL Berkeley so far, the BGO positron camera PEBA II became considerably activated, so that a clinical benefit was avoided [2]. In preparing the new experimental heavy ion therapy facility at the Gesellschaft für Schwerionenforschung (GSI) Darmstadt [4] a new attempt to apply the techniques of 3D PET was carried out. This involved the evaluation of two different multi-crystal position sensitive BGO detectors with high spatial resolution, the investigation of the background radiation generated in the surrounding of the heavy ion synchrotron SIS at the GSI as well as in-beam PET experiments using beams of β^+-active and stable ions with atomic numbers $6 \leq Z \leq 10$ (i.e. between carbon and neon) with energies of 170 to 500 MeV/u.

EXPERIMENTS AND RESULTS

In a first step we investigated the homogeneity of crystal identification, energy resolution as well as detector efficiency of two small area multi-crystal BGO detectors. For this purpose, a very small limited angle positron camera formed by a pair of each detector type was

Proc. Int. Conf. on Inorganic Scintillators and Their Applications, SCINT95,
1996, Delft University Press, The Netherlands

irradiated with an ^{18}F flood source in between and data were collected in coincidence mode. The geometry of both detector types is depicted in fig. 1.

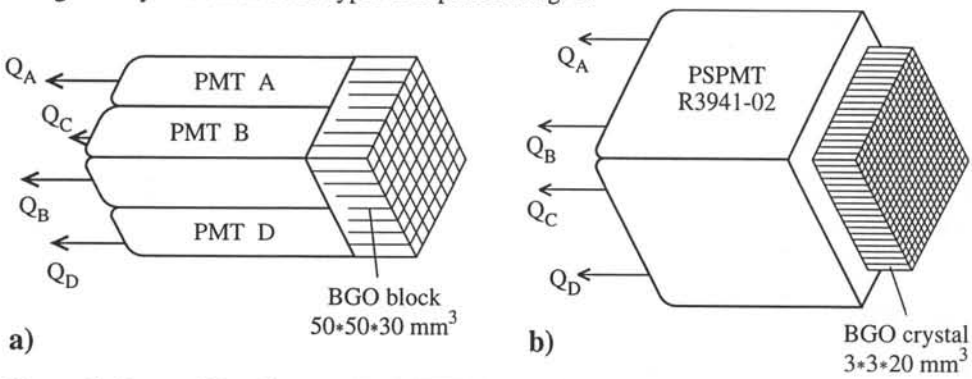

Figure 1: Set up of the Siemens (a) and FZR (b) multi-crystal BGO detectors.

The first detector described in [5] is used in the 950-series of the Siemens/CTI PET scanners and will be called "Siemens detector" (fig. 1a). The second detector was set up at the Forschungszentrum Rossendorf (FZR) following the method of Yamashita [6] for crystal identification and is called "FZR detector". It consists of an array of 18*18 BGO crystals glued on a position sensitive PMT (PSPMT) of crossed wire anode type, Hamamatsu R3941 (fig. 1b). The individual crystals are coated with an anti-reflection film on the plane coupled to the PSPMT and with a reflection paint on all other sides resulting in a pitch of 3.2 mm.

In order to obtain information on the 3D imaging performance two detectors were mounted on a step motor driven handling system which is capable of moving the two detectors independently on a cylindrical surface and simulates an incomplete transaxial tomograph providing gaps for the therapy beam (split ring tomograph) consisting of 34 detector modules. Locating a ^{22}Na point source in the field of view (FOV) of the camera we measured the spatial resolution of the Siemens as well as FZR detectors based tomograph. For this, the annihilation events, i.e. the coordinates of the crystals fired in coincidence and detector positions together, were recorded in list mode by the camera. In an off-line data evaluation, longitudinal tomograms were constructed from these data by backprojection and iterative reconstruction [7] in a 3D image space.

Furthermore, we installed the detector handling system at the beam line at GSI Darmstadt and measured the spatial activity distribution that was generated in a block of polymethylmethacrylate (PMMA) by implantation of β^+-active ions. Our experimental results show that BGO detectors can be operated at focused ion beams without any significant detector activation. However, the registration of the high background of γ-radiation which occurs during the particle extraction from the accelerator had to be suppressed in order to get PET images of appreciable quality acquired directly at the beam of high energetic heavy ions (fig. 2a). The mean range calculated by fitting the projection data to a Gaussian (fig. 2b) can be extracted from several hundreds of registrated annihilation events with an accuracy better than 1 mm, which is essential for the application of the method of an in-vivo treatment plan verification to practical therapy [2].

In further experiments we studied the spatial β^+-activity distribution generated by stopping stable ions in plastic phantoms. The results give rise to the hope for using PET techniques also for on-line therapy monitoring since the distributions show a pronounced peak close to the range of the primary beam particles. Note that there is no significant difference in the shape of the distributions measured with the Siemens or FZR detectors (fig. 3).

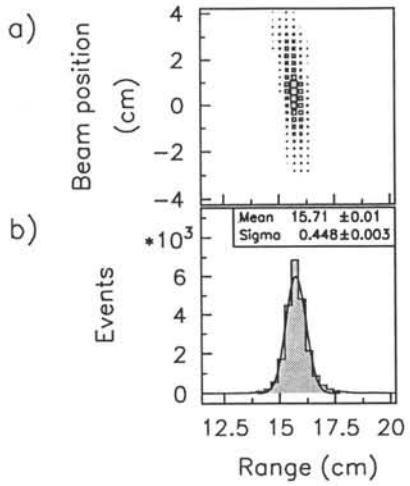

Figure 2: Positron emitter distribution generated by irradiation of a PMMA phantom with a ^{15}O beam (E=382 MeV/u) and measured with the Siemens detectors by means of the simulator: (a) tomogram representing a 2 cm thick slice through the phantom containing the beam axis and (b) range distribution obtained by projection the tomogram onto the range axis.

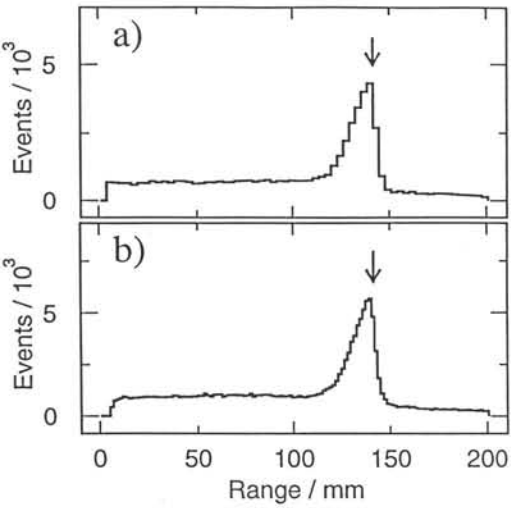

Figure 3: Range distribution of β^+-emitters induced by a ^{12}C beam (E=270 MeV/u) in a phantom of polyethylene measured with the positron camera based on the Siemens (a) and FZR (b) detectors. The range of the primary beam is indicated by an arrow.

The main properties of both BGO detector types are summarized in table 1. The crystal dimensions that govern the intrinsic spatial resolution capability are reduced by a factor of two for the FZR detector in comparison to the Siemens one. It is interesting and frustrating as well to note that this diminishes the FWHM in the images obtained with a point source after reconstruction (point response function PRF) by only about 10 %. Therefore, and due to the higher detector packing ratio and better energy and coincidence time resolution a tomograph based on the Siemens detectors is superior.

Table 1: Main properties of the BGO detectors used for in-beam PET experiments

	SIEMENS	**FZR**
sensitive detector volume (mm^3)	50*50*30	51*58*20
intrinsic spatial resolution capability (mm)	6.25	3.2
511 keV mean energy resolution (FWHM) (%)	20.8±0.5	39.5±5.2
ratio of maximum and minimum detection efficiency	1.8	3.0
sensitivity to gain drift	high	no
detector packing ratio	1.0	0.5
coincidence time resolution (FWHM) (ns)	11	27
transaxial PRF (FWHM, 50 iteration steps) (mm)	4.3±0.1	3.8±0.1

CONCLUSION

A tomograph for clinical use in the heavy ion therapy at GSI Darmstadt requires high reliability. Therefore, it is desirable to use as far as possible components of commercial PET devices as well as the service of an experienced supplier for the set up. Following this a double head positron camera has been set up from components of the PET scanners ECAT EXACT and ECAT EXACT HR of Siemens/CTI, Knoxville TN [8]. The preliminary installation of this device is shown in figure 4. Each head with a sensitive area of 43.2*21.6 cm^2 is set up from 8*4 position sensitive BGO block detectors which are subdivided into 8*8 crystals of 6.25*6.25*20 mm^3 comparable to the Siemens detector described before. It is intended to transfer and integrate the tomograph into the therapy unit at GSI Darmstadt in autumn 1995.

Figure 4: Preliminary installation of the tomograph in the laboratory at the FZ Rossendorf. The detector heads with the analog and digital read out electronics are situated on the table. A flood source for test purpose and the coincidence processor (printed circuit board) are mounted in between in the foreground and background, respectively. On the left hand side both the real time sorter and the SPARC 10 workstation above can be seen. On the right hand side is the VME system for controlling the stepping motor driven linear axis which is connected with the source.

This work is supported by the Bundesministerium für Bildung, Wissenschaft, Forschung und Technologie of the Federal Republic of Germany (grant No 06DR666 2).

REFERENCES

[1] G. Kraft, *Strahlenther. Onkol.* **166**(1990)10-3
[2] J. Llacer, *Nucl. Sci. Appl.* **3**(1988)111-31
[3] W. Enghardt et al, *Phys. Med. Biol.* **37**(1992)2127-31
[4] G. Kraft and G. Gademann(eds.), *Report* **GSI-93-23**(1993)
[5] J.G. Rogers et al, *IEEE Trans. Nucl. Sci.* **NS-39**(1992)1063-8
[6] Y. Yamashita et al, *IEEE Trans. Nucl. Sci.* **NS-37**(1990)589-93
[7] W. Enghardt et al, *Phys. Med. Biol.* **37**(1992)791-8
[8] Siemens Medical System Inc., *Technical Data No.* **A91004-M2330-G009-01-7600**(1993)

STUDYING CATALYST REACTION DYNAMICS WITH A BGO DETECTOR

A.V.G. Mangnus, L.J. van IJzendoorn and M.J.A. de Voigt
Department of Technical Physics, Eindhoven University of Technology, P.O. Box 513, 5600 MB Eindhoven, The Netherlands

ABSTRACT

A detector has been built for the one-dimensional imaging of positron emitter activity profiles in catalyst reactors. The detector consists of two banks with each 10 individual BGO-crystals. The flexibility of the design offers the choice between either a high sensitivity or a low scatter fraction, with an attainable axial resolution of about 3 mm. The variable sensitivity can also be used for experiments with large rate variations.

INTRODUCTION

The routine use of positron emitters like ^{11}C, ^{13}N, ^{15}O and ^{18}F for imaging techniques is at the moment limited to medicine (Positron Emission Tomography [1]), although some industrial applications with positron emitters have been done [2]. The availability of positron emitters of the elements C, N and O makes positron emission also very interesting for chemical studies: many organic molecules can be labeled and the 511 keV photons created upon annihilation of an emitted positron can penetrate the walls of a chemical reactor, which allows the reconstruction of a positron emitter distribution inside a reactor with a detector placed outside the reactor.
In catalyst reactors reactants are adsorbed on the catalyst surface, where intermediates and products are formed. The residence times of reactants, intermediates and products on the surface depend on the concentrations of the different molecules and the reaction rates of the different reaction steps. So measurement of these residence times at different positions in the reactor provides information about concentrations and reaction steps.
The most suitable catalyst reactor for use with positron emitters seems to be the plug flow reactor, which consists of a cylindrical pipe filled with catalyst bed, through which a continuous stream is flowing. The continuous supply and removal of reactants and products puts the reactor in a steady state, in which the concentrations of the different chemical species do not change in time. In this kind of catalyst reactors the concentration gradients in radial direction can mostly be neglected compared to the gradients in axial direction, which means that imaging in axial direction suffices. Reaction dynamics can be studied by injecting a pulse of positron emitter labeled molecules in the reactant flow, without disturbing the steady state of the reactor. A drawback of this technique is the impossibility to discriminate between the different positron emitter labeled chemical species, which means that modelling of the reaction mechanism is required to extract quantitative information about reaction rates.
One-dimensional imaging offers several advantages: there is no tomography needed for reconstruction of the activity profiles, the number of image elements is restricted, which allows acquisition of sufficient data in short sampling times and the detector geometry can more easily be adapted to the reactor size and reaction type. The first dynamical studies with positron emitters in a plug flow catalyst reactor were performed with a medical PET-camera [3]. At the Eindhoven University of Technology a simpler, flexible and less expensive

Proc. Int. Conf. on Inorganic Scintillators and Their Applications, SCINT95,
1996, Delft University Press, The Netherlands

detector especially designed for dynamic catalysis studies has been built. Together with the construction of this Positron Emission Profiling (PEP) detector, the production of positron emitters with the Eindhoven AVF-cyclotron and the radiochemistry for labeling molecules with the positron emitters has been set up [4].
The PEP-detector should be able to measure activity profiles in catalyst beds from a few to 50 cm with a high sensitivity and with sufficiently high reconstruction rates. Design, construction and some performance parameters are already described in [4,5]. In this paper the possibilities for high sensitivity will be discussed and in what way they affect the position resolution and the measurement of activity profiles.

THE PEP-DETECTOR

For reasons of flexibility and sensitivity the PEP-detector consists of two banks with 10 detection elements, each with a BGO-crystal coupled to a photomultiplier. The rectangular BGO-crystals have a size of 5.1 x 20 x 100 mm^3; the smallest dimension is the one in axial direction. Wrapping of the crystals makes the actual axial width 6 mm [5]. The detection elements can individually be positioned in a detector frame, to cope with catalyst reactors of different lengths. With the closest packing the detector length is 60 mm; the maximum length is 500 mm. The distance between the two detector banks can be varied between 72 and 635 mm; the catalyst reactor is positioned midway between the detector banks.
A reconstruction of the annihilation position is made if the energies of both photons detected in coincidence lie in the defined energy window of the detector. The reconstruction position is the point of intersection between the line connecting two crystals in opposite detector banks (line of response) and the catalyst reactor. With two banks of each 10 detection elements there are 100 lines of response, but only 19 reconstruction points: reconstruction points in the middle of the detector have more lines of response. All lines of response are stored; off-line analysis of the activity profiles can be performed with different reconstruction modes.
Sampling of the detector is stationary (no detector movement) to simplify dynamic imaging. Problems with undersampling are not expected, as the injected activity will have passed all the reconstruction points after some time.

MEASUREMENTS

To study the influence of the distance between the two detector banks and of the reconstruction mode on the sensitivity and the position resolution, a 1 mm diameter ^{22}Na source with an activity of 47 kBq was used. The source was moved in axial direction with steps of 0.2 or 0.5 mm along the centre line between the two detector banks. During these measurements the banks consisted of 9 detection elements each, in the closest possible packing (detector length of 54 mm). Only photons with an energy between 370 and 750 keV were used for the reconstructions and there was no reactor present.
In Fig. 1 the effect of the distance between the detector banks on the sensitivity and on the FWHM position resolution for a pair of directly opposite crystals is shown. As expected, the sensitivity is proportional to the inverse of the squared distance ($1/r^2$); for the two extreme distances (72 and 635 mm) a sensitivity change of more than a factor of 50 is reached. The variation of the position resolution is determined by the angular spread of the two annihilation photons. The dotted line is calculated from the position resolution at 72 mm (2.93 mm FWHM) for a FWHM angular spread of 0.5°.

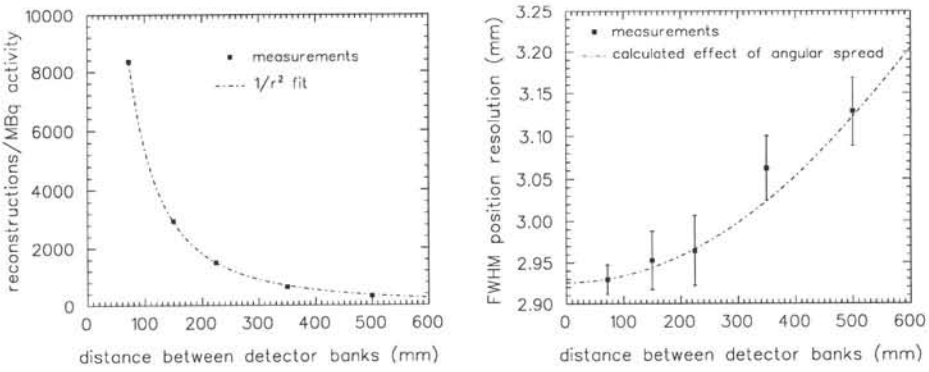

Fig. 1 Measured effect of the distance between the detector banks on the sensitivity (at left) and the position resolution (at right) for a pair of two directly opposite crystals.

The effect of the reconstruction mode on the position resolution is shown in Fig. 2. For a distance between the detector banks of 72 mm, the FWHM position resolution for the reconstruction point in the centre of the detector worsens from 2.93 mm (directly opposite crystals) to 5.5 mm (8th neighbour of the directly opposite crystal). The overall resolution (from the addition of the 9 lines of response for this point) is 3.86 mm; the sensitivity with the 9 lines of response increases with a factor of 8.9 compared to the direct opposite pair. The worsening of the position resolution is due to the larger field of view for the pair with the 8th neighbour: photons from the centre can enter these crystals through the side crystal faces.
With a distance between the banks of 350 mm, the resolution worsens much less: from 3.06 mm to 3.5 mm. The overall resolution with 9 lines of response is 3.31 mm, the sensitivity increases with a factor of 9. Note the higher background for the 72 mm distance; this is due to a higher scatter contribution (Compton events from the 1275 keV γ of the ^{22}Na source).

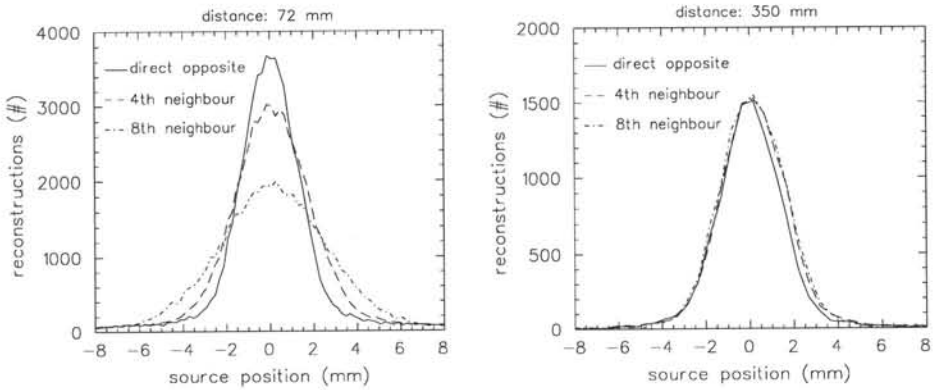

Fig. 2 Measured FWHM position resolution for different combinations of crystal pairs in the two opposite detector banks. At left for a distance between the detector banks of 72 mm, at right for 350 mm.

In these measurements there was almost no scatter in the object. Fig. 3 shows an example of a PEP-experiment with a reactor. The reactor consists of a quartz pipe (diam. 9 mm), surrounded by an aluminum, water-cooled oven (diam. 70 mm). For both measured distributions the distance between the detector banks was 72 mm and all lines of response were used for reconstruction. The difference in activity distributions can clearly be seen.

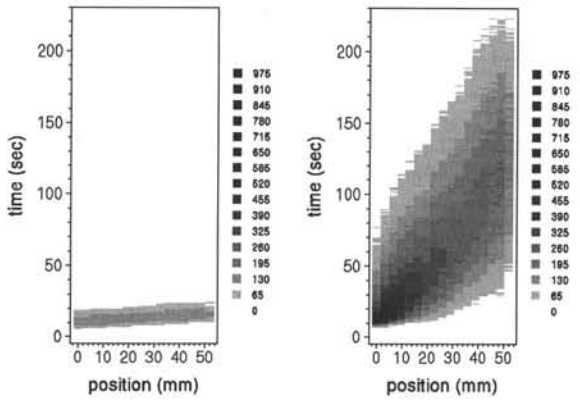

Fig. 3 Measured activity distributions after the injection of ^{11}CO in a pipe filled with non reactive glass beads (at left), and with a 5 cm long platinum exhaust catalyst bed for oxidation of the CO at 130° C (at right).

CONCLUSION AND DISCUSSION

It has been shown that is possible to combine a high sensitivity with an axial resolution of 3 mm for Positron Emission Profiling with 5 cm long catalyst beds. The best way to increase the sensitivity will also depend on scatter in the object, which is strongly dependent on the reactor geometry. The high sensitivity means that even with a low radiochemical reactant yield PEP-experiments can be performed. If a high yield can be obtained, a larger distance between the detector banks can be used (for less scatter contribution); a shorter distance can be used afterwards to see if small amounts of activity remain on the catalyst surface. The variable distance could also be used for decay compensation during the PEP-experiment. This is particularly interesting for experiments with ^{15}O (half-life: 2 min): with a 50-fold increase in sensitivity the reconstruction rate can be kept constant for more than 5 half-lives.

REFERENCES

[1] Simon R. Cherry, Nucl. Instr. and Meth. A 348 (1994) 577.

[2] D.J. Parker, M.R. Hawkesworth, C.J. Broadbent, P. Fowles, T.D. Fryer and P.A. McNeil, Nucl. Instr. and Meth. A 348 (1994) 583.

[3] G. Jonkers, K.A. Vonkeman, S.W.A. van der Wal and R.A. van Santen, Nature 355 (1992) 63.

[4] A.V.G. Mangnus, L.J. van IJzendoorn, J.J.M. de Goeij, R.H. Cunningham, R.A. van Santen and M.J.A. de Voigt, Nucl. Instr. and Meth. B 99 (1995) 649.

[5] A.V.G. Mangnus, L.J. van IJzendoorn, J.J.M. de Goeij and M.J.A. de Voigt, IEEE NSS/MIC Conf. Proc. Norfolk (1995) 333.

PHOSPHORS IN X-RAY COMPUTED TOMOGRAPHY AND FOR THE γ-RAY ANGER-CAMERA

B. C. Grabmaier, W. Rossner, T. Berthold, Siemens AG, Corporate Research and Development, D-81730 Munich, Germany

ABSTRACT

The principles of X-ray computed tomography (XCT) and of the γ-ray Anger Camera are described. Basic specifications for solid state XCT- detectors and the specification for the γ-ray detector are documented. The most suitable phosphors for both applications are discussed.

INTRODUCTION

Phosphors are widely used for the detection of X-rays and γ-rays in medical diagnostic systems. Two important examples are X-ray computed tomography (XCT) and the Anger γ-camera.
Clinical CT visualizes the cross section of the human body by measuring attenuation profiles of an X-ray penetrated body slice at various viewing directions. The efficiency and quality of the X-ray detector is of essential importance and has to be optimized for the distinct CT types and applications.
The Anger γ-camera is the fundamental instrumentation of nuclear medical diagnostics. Physiological studies of the human body using radioactive tracers can be carried out. With the Anger camera the distribution of these radioactive isotopes can be very sensitively determined.

PHOSPHORS FOR X-RAY COMPUTED TOMOGRAPHY

Principle of CT

The principle of CT is based on the detection of a series of X-ray attenuation profiles from several different viewing points, which subsequently allow the reconstruction of cross sectional images of the human body and head. The beam path and collimating system of the fan beam machine with rotating detectors can be seen in Figure 1.The collimating system on the tube side is as close as possible to the patient and helps to limit the X-ray dose to a necessary minimum for the patient. The lamellar collimator of a crystal detector is arranged just in front of the solid state detector elements — gas detectors are self-collimating — and reduces the proportion of diffuse background radiation in the measured signal. The collimator has to be manufactured with extremely high precision.
The measuring system consists of the detectors and the data acquisition system. This facility converts the X-ray radiation attenuated by the object into a scanning signal suitable for computer input.
Figure 2 shows the phosphor with the photosensitive semiconductor detector. See E. Krestel, Imaging Systems for Medical Diagnostics [1] for details.

Proc. Int. Conf. on Inorganic Scintillators and Their Applications, SCINT95,
1996, Delft University Press, The Netherlands

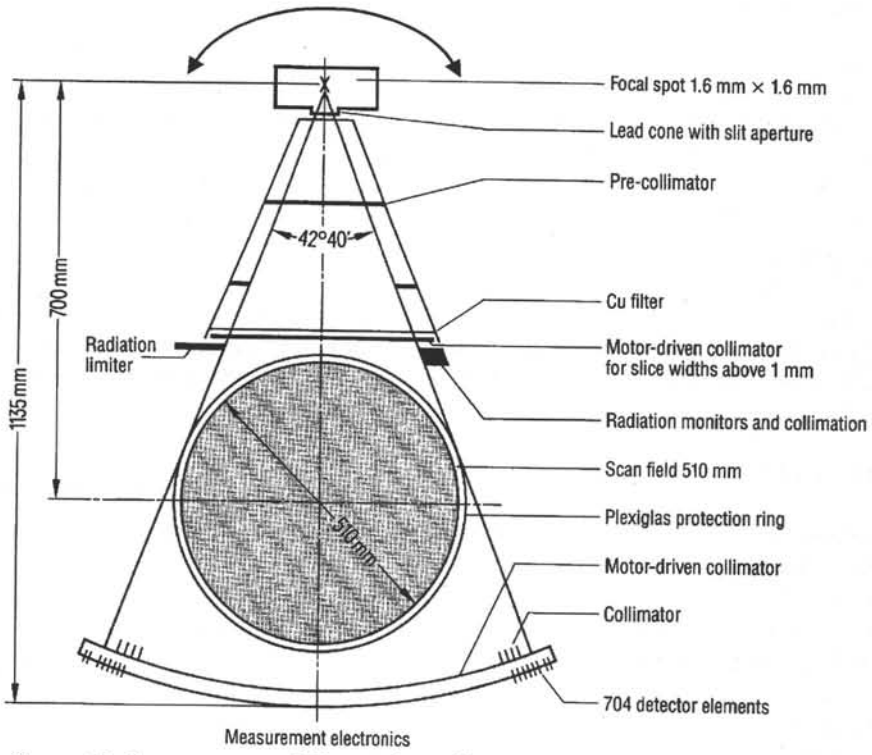

Fig. 1 Geometrical arrangement of X-ray tube, collimators and detector system (when in operation the patient is placed within the Plexiglas protection ring)

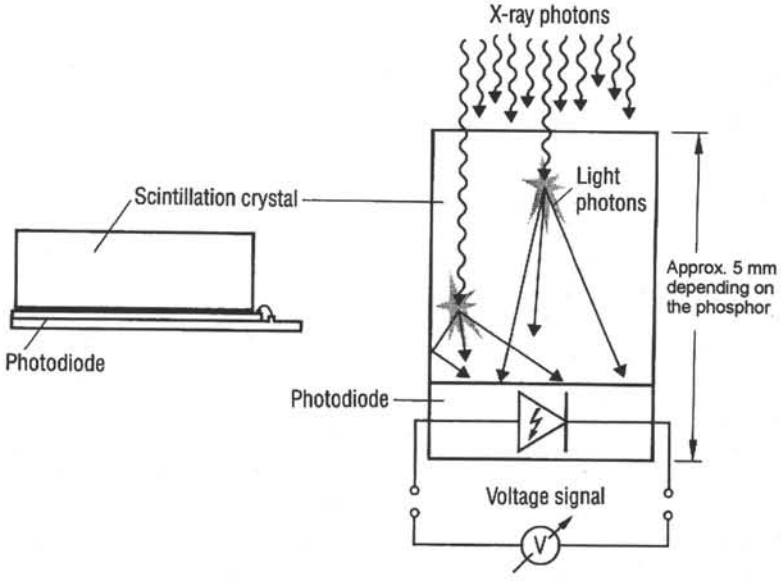

Fig. 2 Scintillation crystal with photo-sensitive semiconductor detector

Basic specifications for XCT

The key feature of CT is not the spatial resolution but the contrast resolution, which should have an accuracy of a few parts per thousand. Very small differences in X-ray attenuation, which are in general a few percent for soft tissue parts, have to be detected precisely whilst CT must simultaneously be able to detect the highest attenuation in the case of bone material. With modern CT installations, a few parts per thousand are recognized within a high dynamic range of up to 10^6.
For solid state detectors, this entails a high light output of the X-ray excited luminescence. The light output is the result of X-ray absorption, the efficiency of the internal luminescent processes and the interior optical quality. As the phosphor is coupled to a photodiode, optical matching of the emission wavelength should be close to the maximum diode sensitivity. To obtain good X-ray absorption, an average atomic number higher than approximately 50 or a density above 4 g/cm^3 are preferred.
Table 1 gives a list of specifications.

X-ray source	
fan shaped X-ray beam	20 - 140 kV
exposure time per element	> 0.75 ms
detected energy dose rate	10 - 100 mGy/s
max. X-quanta per ms and mm^2	$3 \cdot 10^3$ - $1 \cdot 10^8$
Detector arrangement	
scan field	40 - 55 cm
detector elements	≈ 1000
size of one element	≈ 1 mm • 25 mm • h*
Detector characteristics	
dynamic range	$1 \cdot 10^5$
afterglow	$< 1 \cdot 10^{-4}$ after 3 ms
optical quanta per X	≈ 500
linearity	$< 1 \cdot 10^{-3}$
spatial resolution	0.5 - 1 mm
low contrast detectibility	2 - 4 HU**

*h depends on the detector material. The higher the X-ray absorption the lower h is
**HU are Hounsfield units:

$$HU = \frac{\mu - \mu_W}{\mu_W} \cdot 1000$$

μ = attenuation coefficient of the human body
μ_W = attenuation coefficient of water

Table 1 List of specifications for a solid state CT detector

One of the primary requirements for suitable CT phosphors is the rapid response of the emission after the termination of X-ray excitation. The afterglow, in particular, is an extraordinarily critical parameter. If the afterglow intensity exceeds specific limitations, image degradation occurs due to some memory effects. Such limitations are given by the scanning duration for CT imaging. For modern X-ray CT equipment, a single rotation including up to 1000 projections takes about one second. The decay time describes the behaviour of the specific luminescent center, whilst the afterglow is symptomatic of a long

term decrease due to retardation effects. Beside all these physical requirements, the suitability of phosphors depends on a number of technical aspects, such as toxicity, chemical stability, reproducibility, and machining properties.
Fig. 3 shows the CT image of a human abdomen.

Figure 3: Abdomen of the human body

Single Crystals and Ceramic Phosphors for CT

A detailed overview of conventional single crystalline phosphors has been given previously by Farukhi [2] and Grabmaier [3].
Tl activated CsI and self-activated $CdWO_4$ are currently used. Some of the important properties have been measured under the same conditions and are presented in Table 2. They have several drawbacks. CsI:Tl shows an excessive afterglow which cannot be influenced by growth techniques or by codoping. On the other hand, $CdWO_4$, exhibits a short afterglow, a low decay time and a sufficient light output. However, the material is toxic, very brittle and has a tendency to crack parallel to its cleavage plane during machining.
Within the last ten years General Electric [4] introduced the first polycrystalline ceramic scintillator for clinical X-ray detectors. The host material is a composition of Y_2O_3 - Gd_2O_3 with a Gd_2O_3 concentration up to 50 mol%. Gd_2O_3 was chosen because it has a higher X-ray stopping power than the Y_2O_3 . The luminescent dopant is Eu_2O_3 at a concentration of 3 mol%. The luminescence efficiency is high at about 65 % of CsI:Tl. The major emission peak occurs at a wavelength of about 610 nm. The primary decay time of the Eu^{3+}-ion is about 1 ms at room temperature. The afterglow is too high and can be suppressed by the co-dopant Pr^{3+}. As Y_2O_3 - Gd_2O_3 solid solutions have a cubic lattice, the refraction is isotropic and transparent ceramics can be manufactured.
Scanners which operate at scanning times of $\leq$ 1 s per full scan require other scintillators. Therefore Hitachi [5] developed the hexagonal Gd_2O_2S:Pr,Ce,F. The Pr^{3+} activator has a short decay time of $\approx$ 4 µs and a light output of 75% of CsI:Tl. The Ce^{3+} ion reduces the afterglow. A hot isostatic pressing technique is used to transform Gd_2O_2S:Pr,Ce,F powder into a translucent ceramic scintillator.

It is generally believed that the polycrystalline ceramic route offers the greatest potential in discovering new fast speed scintillators.

Phosphor	emission [nm]	rel. light output [%]	attenuation coefficient 150 keV [cm^{-1}]	decay time [µs]	afterglow 3 ms after X-ray turn off [‰]
CsI:Tl	550	100	3.21	1	≈ 100
$CdWO_4$	480	30	7.93	5	< 1
$(Y,Gd)_2O_3$:Eu,Pr	610	65	3.40	≈ 1000	≈ 30
Gd_2O_2S:Pr,Ce,F	511	75	6.86	≈ 3	< 1

Table 2: Some important properties of X-ray phosphors.

PHOSPHORS FOR THE ANGER γ–CAMERA

Principle and Basic Specifications

Clinical diagnosis using nuclear medicine as a tool, has the advantage of yielding a large variety of data about the human body. The size and function of organs can be depicted, i. e. their blood supply or metabolic processes. For this purpose, compounds of radioactive elements such as ^{99m}Tc (140 keV single pulse) are introduced into the body. They are detectable by their emission of γ-rays. H. Anger [6] described a position sensitive detector to observe the distribution of a radioactive tracer in the human body. The principle seems rather simple (Figure 4). The γ-rays hit a scintillator crystal and produce a short shower of photons, which are detected by an array of photomultiplier tubes. From the number of photons recorded by each individual photomultiplier, the spot of the luminescenct event is evaluated.

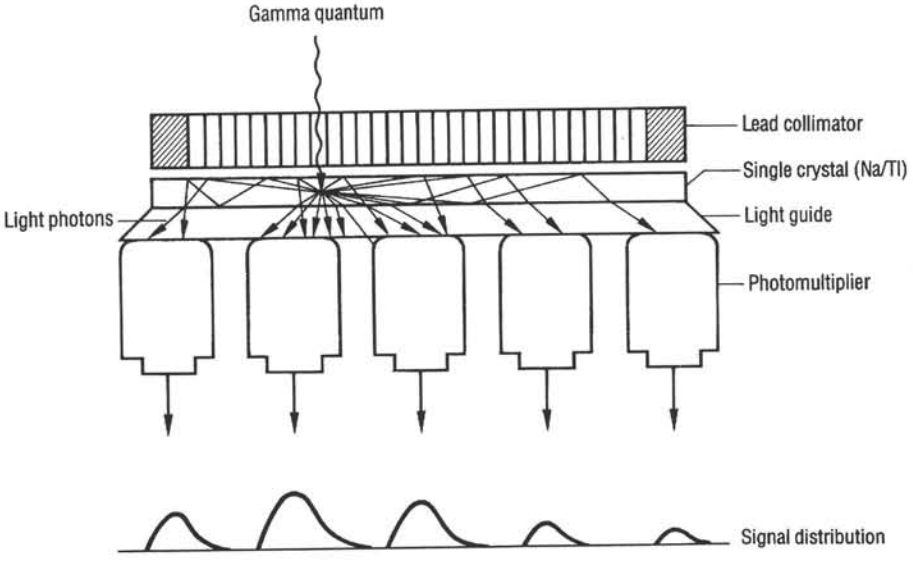

Fig. 4 Measurement principle of the Anger gamma camera

For an efficient working γ-camera, the individual components such as the scintillator crystal, photomultiplier tubes, electronic hardware and the evaluating software, have to fullfill the most precise requirements. The phosphor must have the following properties:

- high light output, this means many photons per γ-pulse.
- high energy resolution
- short decay time
- high transparency
- feasibility of large area plates (400 mm • 600 mm)

Table 3 gives some further details.

spatial resolution	4 mm
energy resolution	9 %
decay time	0.25 µs
γ-quanta per s and mm^2	25
optical quanta per ^{99m}Tc γ-quant	3100

Table 3 Specifications for the detector of an Anger γ-camera

NaI:Tl

These requirements can only be fullfilled by Tl doped NaI. This alkali halide can be grown in waterclear single crystals with diameters up to 500 mm. At approximately 400 °C NaI:Tl can be shaped under high pressure into large area plates. These plates are polycrystalline with statistically oriented grains of 5 - 20 mm. Also this polycrystalline material is waterclear. They are fully equivalent to single crystals with respect to their optical and luminescent properties.
The main disadvantage, however, is the high hygroscopicity of NaI. Even a slight hydration of the surface lowers the light output drastically. A sophisticated canning technology is necessary to keep the scintillator working.

Figure 4 shows the image of a human thyroid as an example of the application of the Anger γ-camera.

Fig. 5 Example for the Anger γ-camera: Thyroid uptake, with the isotope ^{99m}Tc

CONCLUSION

The time required to develop new useful X-ray or γ-ray scintillators can be shortened by an improved understanding of the complex mechanism of the luminescence properties. Careful preparation and advanced processing techniques as well as starting materials of high purity will help to create these new phosphors for application in X-ray CT and in the Anger γ-ray camera.

REFERENCES

[1] E. Krestel: Imaging systems for medical diagnostics
[2] M. R. Farukhi, Workshop on Transmission and Emission Comp. Tomogr. Seoul Korea (1978)
[3] B. C. Grabmaier, IEEE Trans. Nucl. Sci. NS-31 (1984) 372
[4] C. D. Greskovich, D. A. Cusano and F. A. Di Bianca, US Pat. 4,571,312 (1986)
[5] K. Yokota, N. Matsuda and M. Tamatani, J. Electrochem. Soc. 135 (1988) PC 389
[6] E. Krestel: Imaging systems for medical diagnostics

CADMIUM TUNGSTATE DETECTOR FOR COMPUTED TOMOGRAPHY

R. Deych, J. Dobbs, S. Marcovici, B. Tuval
Analogic Corporation, Peabody, MA 01960, USA

ABSTRACT

Recent technology developments in the growth of cadmium tungstate (CWO) have significantly improved the performance of CWO/photodiode x-ray detectors for computed tomography (CT). The high level of crystal stoichiometry and purity achieved today, has brought CWO detector conversion factor to 100 eV/el. The thermal stability of CWO detectors is mostly governed by the thermal quenching of CWO intrinsic emission and was measured to be -0.3 %/°C at 25°C. Investigation of radiation damage effects at small and moderate radiation doses shows excellent radiation hardness of new CWO scintillators. Light output degradation is less than 2.3 % per 1000 R x-ray exposure. Fast CWO crystals with low afterglow have a big potential for developing high speed yet economical CT systems.

INTRODUCTION

The increasing demand for higher quality x-ray computed tomography images can be met by designing x-ray detectors which are more sensitive, stable, and uniform. The ability to reduce image quantum noise makes the solid-state x-ray detectors superior to conventional Xe chamber detectors employed in a majority of the CT scanners in worldwide operation. While solid-state detectors have improved the contrast resolution and dose utilization in modern CT scanners, their instabilities, or signal drift can cause image artifacts.

Recent developments [1] in CWO technology have significantly improved the quality of CWO based detectors. The goal of this paper is to reevaluate the properties of CWO, and compare them with the properties of traditional scintillators and new polycrystalline ceramic scintillators for CT [2,3]. During the work, a substantial amount of innovative, highly accurate series of metrological equipment was developed and used to characterize scintillators and photo-detectors. The analysis was used in the design of the detection system for an Analogic Lightweight CT scanner.

RESULTS AND DISCUSSION

Most of the results presented here were obtained using a tungsten target rotating-anode x-ray tube operating at 120 kV. Single CWO crystals, optically coupled to silicon photodiodes, or assembled detector arrays have been measured using Analogic CT data acquisition systems [4]. P-i-n silicon photodiodes operating in photovoltaic mode, and fast data acquisition systems with 20 bit dynamic range allowed the detection of output currents in the range from 0.5 pA to 0.5 μA.

1. Luminescent properties and conversion factor

According to [1], recent process improvements in CWO crystal growth have reduced to insignificance the crystal self-absorption in the spectral region higher than 420 nm. Due to better stoichiometry and lower impurity content, the light output in currently available CWO

Proc. Int. Conf. on Inorganic Scintillators and Their Applications, SCINT95,
1996, Delft University Press, The Netherlands

crystals is 38% [1] relative to NaI-Tl. This exceeds the light output of yttria-gadolina ceramic, and is marginally lower than that of gadolinium oxisulfide (see Table 1).
We confirmed the main intrinsic emission due to transitions in tungstate groups WO_6 [7,8] of CWO to be located at 495 nm (480 nm[1], 500 nm[7]). The emission spectrum of CWO crystals used in our x-ray detectors does not show any significant contribution of "yellow" emission at 580 nm caused by WO_6 perturbed by lattice defects (oxygen vacancy [8]), and "red" emission at 690 nm. The "red" emission according to [7] arises from recombination at oxygen vacancies, and is responsible for afterglow, which is intrinsically lower than that in ceramic scintillators. Our measurements of optical and luminescent properties of CWO indicate better stoichiometry and purity of crystal. This allows manufacturing of multichannel detector arrays with hundreds of elements showing small variability in detector properties, which is of critical importance for third generation CT scanners

Table 1. Characteristics of scintillators for CT

	CsI-Tl	BGO	CWO	$(Y,Gd)_2O_3$:Eu	Gd_2O_2S:Pr, Ce,F
Type	single crystal	single crystal	single crystal	ceramic	ceramic
Density, g/cm^3	4.52	7.13	7.99	5.9	7.34
Thickness to absorb 99% (90%) of 145 kV x-ray, mm*	**6.1(2.2)**	**2.8(1.2)**	**2.6(1.1)**	**5.8(2.2)**	**2.9(1.1)**
Emission band max, nm	550	480	**495**(580, 690)	610	520
Light output, % NaI-Tl	85	9	38	34	51
Conversion factor, eV/el	45	450	**100**	-	-
Decay time, μsec	1	0.3	2, 15	1000	~2.4
Afterglow, %(msec)	0.5-5(6)	0.005(3)	0.005(3)	0.1(100)	0.01(3)
Temp. stability, %/°C, at 25°C	0.02	-0.15	**-0.30**	<|0.04|	-0.6
Rad. damage, % per (R)	+13.5(450)	-	**-1.8(775)**	-1.0(450)	-

*X-ray spectrum attenuated by 30 cm of water. Results of current paper presented in bold. Data from [1-3,5,6,9] is used.

The image noise in CT is almost entirely determined by x-ray absorption in the scintillating material. As can be seen from Tabl.1 for a 2.6 mm thick CWO element the x-ray detection probability is almost 100 %. The CT system contrast resolution is mostly related to the ability of the detecting system to measure small variations in incident x-ray intensity, and hence it depends on the x-ray detector conversion factor. Using detector quantum noise measurement at 70 keV average x-ray photon energy, for our CWO detectors the conversion factor was calculated to be $K = 0.0100 \pm 0.0005$ el/eV, or 100 ± 5 eV/el. The high detector conversion factor and its uniformity provide very high contrast resolution over a wide range of x-ray attenuation. When taking advantage of low noise electronics as in an Analogic CT scanner, further increases in scintillator light output and conversion factor do not improve contrast resolution. In our opinion light output value can be traded off for other useful properties, such as detector uniformity, and radiation hardness.

2. Temperature dependence of detector gain.

Fig. 1 shows the temperature dependence of CWO single crystal light output and the temperature dependence of CWO/photodiode detector signal. The good correlation between the two data sets proves that the temperature dependence of our detectors is almost entirely due to the temperature dependence of the CWO luminescence. The temperature dependence of the luminescence intensity I(T) under constant excitation above 300 K is explained in terms of

probability of non-radiative transitions by Mott's law $I(T)\sim(1+\omega_0\cdot\exp(-\varepsilon/k\cdot T))^{-1}$, with a frequency factor $\omega_0=4.25\cdot10^6$, and thermal activation energy $\varepsilon=0.49$ eV (Fig.1, solid curve), which is in agreement with ε value of 0.52 eV obtained in [10]. The resulting average temperature coefficient of our x-ray detectors is -0.3 %/°C at 25°C, which is two times lower than that reported for Gd_2O_2S:Pr,Ce,F ceramic light output -0.6 %/°C [3].

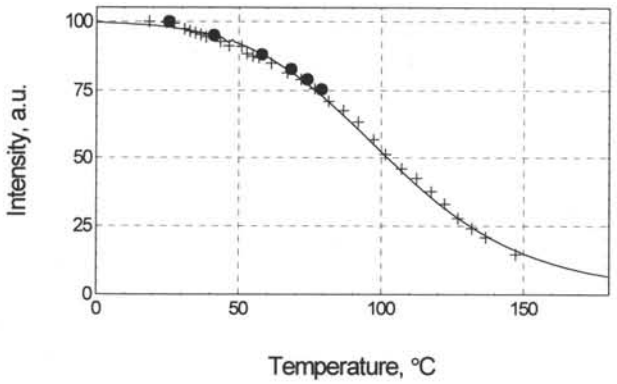

Fig. 1. Temperature dependence of detector output(●), and CWO light output (✦).

This highly uniform and repeatable temperature dependence of CWO scintillators has allowed us to develop consistent temperature corrections for changes in detector sensitivity equivalent to 0.1°C temperature stabilization.

3. Radiation damage.

The exposure rate of unattenuated x-rays impinging on a CT scanner detector is in the range of 1 R/sec. Due to strong x-ray absorption in the photon energy range of 20-140 keV, a rather high dose rate of ~50 rad/sec in a 0.5 mm thick layer at the crystal surface is observed. The non-uniform dose profile and radiation defect accumulation in CWO, as well as in other scintillators for CT, may lead not only to detector gain drift but also to changes in its spectral sensitivity. Both effects cause deterioration of image quality.

In CWO detectors (See Fig. 2a.) short term x-ray exposure in the range of 1000 R causes decrease of gain which spontaneously recovers at room temperature with time constants of 20 min, and 5 hours. Almost 50% of degradation recovers within 1 hour after irradiation. The recovery may be associated with two different types of unstable radiation defects in CWO, yet to be identified. The susceptibility to radiation damage for our detectors has been measured to be in the range of 1.8±0.1 % per 775 R. This value is lower than 2.9 % per 450 R obtained in [2], and 10 % per 2000 R reported in [6], and is practically the same as in yttria-gadolina ceramic (See Tabl. 1.). It is not clear how well the degradation of small size CT elements can be described in terms of deterioration of the scintillator transparency (See e.g.[6,11].). We found that in GSO:Ce based detector (Fig. 2b) radiation causes a positive change in sensitivity, although according to [6] no significant changes in transparency have been detected for doses up to 10^8 rad. This can be interpreted as luminescence yield change, due to changes in generation of emitting states and(or) probability of radiative transitions. Adequate approach in studying the degradation of CT scintillators should include a direct measurement of radiation-induced changes in light output under small and moderate doses.

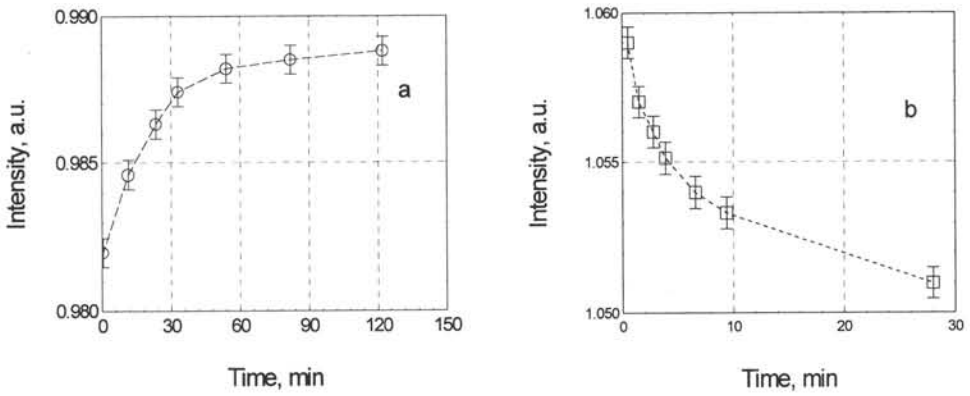

Fig. 2. Degradation and recovery of CWO(a) and GSO:Ce(b) detector gain after 775 R x-ray exposure at room temperature. Intensity equals 1 before exposure.

Radiation damage effects in CWO crystals are strongly affected by preexisting crystal defects, and the excellent radiation hardness of our detectors is explained by improvements in crystal quality. It was pointed out in [12] that the light output and radiation hardness improves in CWO crystals with better stoichiometric composition, and attributed the improvement to the decrease in cadmium vacancies concentration. In our opinion, the experimental data obtained so far suggests low efficiency of intrinsic defect formation by atomic displacement in CWO under x-ray irradiation.

Radiation hardness of CWO x-ray detectors may be further improved by proper crystal doping. It was reported in [13] that introduction of trivalent impurities increases significantly the radiation hardness of CWO crystals without increasing crystal afterglow.

1. D.R. Kinloch, W. Novak, P.Raby, and I. Toepke, IEEE Trans. Nucl. Sci. **41** (1994) 752
2. C.D. Greskovich, D. Cusano, D. Hoffman, and R. Riedner, American Ceramic Society Bulletin **71**(1992)1120
3. M.Yoshida, A.Suzuki, Y.Uchida, M.Yoshida, H.Yamamoto, and Y.Tsukuda, Jap. Journ. Appl. Phys. **27**(1988)L1572
4. B. M. Gordon, Data Acquisition Systems, in :Technical Aspects of Computed Tomography, pp.4113-4159, The C.V.Mosby Company, 1981
5. W. Rossner, and B.C. Grabmaier, Journal of Luminescence **48-49**(1991)29
6. M. Ishii and M. Kobayashi, Prog. Crystal Growth and Charact. **23**(1991)245
7. A.E. Ovechkin, V. D.Ryzhikov, G.Tamulaitis, and A.Zukauskas, Phys. Stat. Sol. (a) **103**(1987)285
8. M.J.J. Lammers, G.Blasse, and D.S.Robertson, Phys. Stat. Sol.(a) **63**(1981)569
9. P. Haque, Internal report, EMI Medical Inc., 1977
10. A.L.Apanasenko, A.V.Kuznichenko, U.B.Govjadovsky, A.E.Ovechkin, V.G.Shevchenko, and V.G.Yakunin, Zh. Prikl. Spectr. **55**(1991)783. In Russian.
11. C.Laviron and P.Lecoq, Nucl. Instr. Meth. **227**(1984)45
12. M.V.Pashkovskii, A.E. Ovechkin, L.L.Nagornaya, O.V.Zelenskaya, and M.M.Batenchuk, Zh. Prikl. Spectr. **4**(1987)781. In Russian
13. L.L.Nagornaya, E.L.Vinograd, I.A.Tupitsina, 1994 IEEE NSS, **1**(1995)88

DEMANDS ON SCINTILLATORS FOR CONE BEAM TOMOGRAPHY

Jürgen Goebbels, B. Illerhaus, H. Staiger, H. Riesemeier
Federal Institute for Materials Research and Testing (BAM)
Unter den Eichen 87, D-12205 Berlin

ABSTRACT

The progress in spatial resolution by several orders of magnitude together with the power of full three dimensional characterization has opened new areas for X-ray computerized tomography (CT). The impact of this nondestructive technique will be felt in the study of rock samples, in the processing and failure detection of advanced composite materials and for in situ observations. All these investigations require for a quantitative analysis a high spatial resolution in the micrometer range at reasonable measuring times. A survey is given which are the demands on detector design. The present state of high resolution CT is shown on some examples together with improvements desirable for the future.

INTRODUCTION

Nondestructive characterisation of materials is becoming more and more important at all stages of new material development and material production. Three dimensional or Cone Beam CT offers the possibility of a complete mapping of the internal geometry and structure of samples in the μm range. To reach this goal depending on the selected X-ray source and experimental configuration different detector designs have be developed.

With microfocus X-ray tubes (focal spot size lower than about 25 μm) a magnification technique can be applied with a moderate demand on the spatial resolution of scintillator screen. But due to the very low intensity of such X-ray tube a high efficiency is needed for an economical application of such an arrangement.

High intensity together with monochromatic energy is available at synchrotron radiation facilities which allow measurements with an parallel beam. To use these possibilities screens with very high spatial resolution are required.

There are very promising starting points for the different detector system solutions like structured X-ray intensifying foils, single crystal plates or scintillating single fibre arrangements. The most important demands on scintillators are:

- Spatial resolution
- Detection quantum efficiency
- Brightness uniformity
- Contrast ratio
- Energy resolution
- Low geometric distortion
- Linearity
- Radiation resistance

Proc. Int. Conf. on Inorganic Scintillators and Their Applications, SCINT95,
1996, Delft University Press, The Netherlands

PRINCIPLE OF 3D- OR CONE BEAM TOMOGRAPHY

Two approaches exist to reach fully 3D-tomography with high spatial resolution. Using a parallel X-ray beam which is available from synchrotron radiation or approximatly with X-ray sources and only low magnification requires detector systems with high spatial resolution. Such a configuration has the advantage that usual 2D-image reconstruction algorithms can be used. Cone Beam tomography requires in connection with a magnifying geometry source spot sizes of lower than 20 μm realized in microfocus X-ray tubes but allows detector systems of medium spatial resolution. A disadvantage is the necessity of the use of cone beam reconstruction algorithms which are in general only an approximation of the mathematical solution.
A scheme of cone beam geometry is shown in fig. 1.

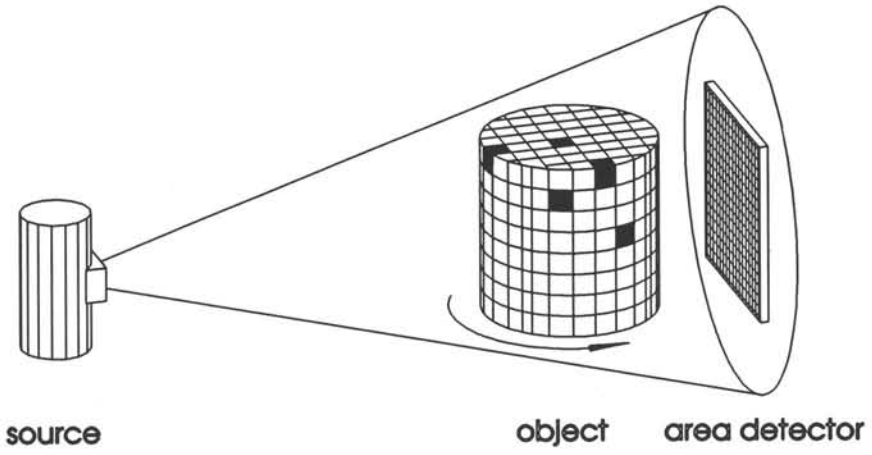

Fig. 1: Principle of Cone Beam Tomography

SPATIAL RESOLUTION

A quantitative description of the spatial resolution of an imaging system offers the concept of Modulation Transfer Function (MTF). The MTF describes the contrast in dependence of spatial frequency. Per definition the height of the MTF is normalized to unity. The spatial resolution of an imaging system is usually defined by $a_0 = 1/2f_0$ with f_0 is the frequency at 10% contrast transfer. Each component of an imaging system can be characterized by an individual MTF. The resultant MTF is the multiplication of the individual MTFs. For an tomographic system the most important components are

$$MTF(f) = MTF_{source} * MTF_{scan\ conditions} * MTF_{detector} * MTF_{reconstruction}$$

The spatial resolution of X-ray sources is in general not a limiting factor of the spatial resolution of the whole system:
Synchrotron radiation is produced as a consequence of radially accelerated charged particles in electron or positron storage rings. These particles travelling at nearly the speed of light

give rise to a very bright beam of electromagnetic radiation, emitted into a very narrow cone of typically 0.1 mrad. This low divergence enables high spatial resolution.

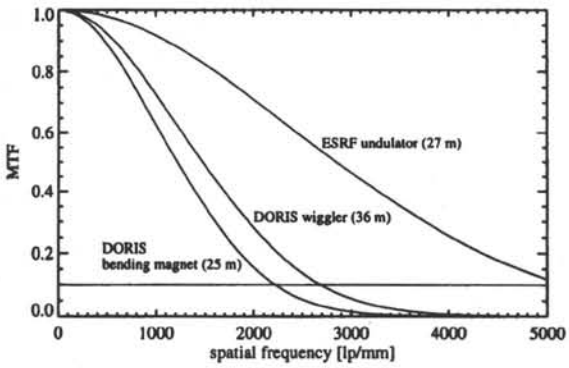

Fig. 2: Calculated MTF of Synchrotron sources

With a linear extension of the source spot of 0.5 - 2.0 mm in horizontal and 0.2 - 0.7 in vertical direction and a distance of 25 - 40 m a parallel beam of about 5 mm height is obtained. Based upon source size and the divergence a spatial resolution was calculated of lower than 0.25 μm for the synchrotron sources DORIS and ESRF, fig. 2 [2].

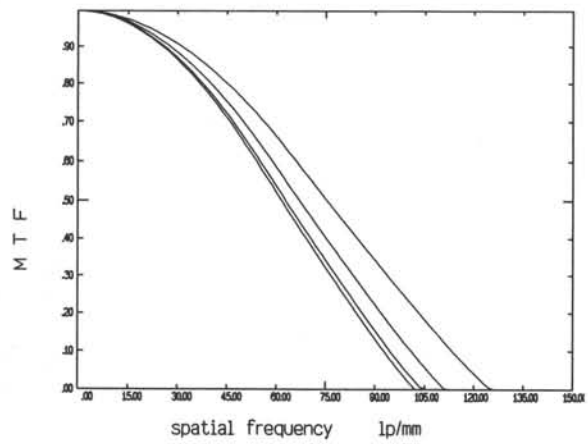

Fig. 3: Calculated MTF of a micro focus X-ray tube (spot size 10 μm) for different magnifications.
The MTF deteriorate with increasing magnification (M =5, 10, 25 and 50 fold, curves from top to bottom)

Microfocus X-ray sources with focal spot sizes lower than 20 μm are available up to 200 kV and with a focal spot of about 15-30 μm up to 320 kV. Assuming a focal spot of 10 μm a spatial resolution of about 5 μm can be achieved (fig. 3) for magnifications between 5 and 50.
From fig. 2 and 3 it comes out that the spatial resolution of X-ray sources is sufficient for a spatial resolution in the object of 5 μm. With synchrotron sources much better values (more than a factor of ten) can can be reached.

How are the conditions for the detector systems:
For the energy range of synchrotron radiation, between 10 and 50 keV, detector systems with high spatial resolution can be achieved decreasing the thickness of the scintillator or by segmentation of the scintillator into very small optically isolated pieces. Busch and al. [2] reported MTF curves of their 2D-detector corresponding to a spatial resolution of 15 μm for an Y_2O_2S:Eu powder sreen, 4 μm for $CdWO_4$ single crystal scintillation screen and an improvement of about two (2.5 μm) using a magnification technique by assymetric Bragg reflection. A similar arrangement was used by Hirano et al. in Japan [3] and by Kinney at al. in USA [4]. With an structured scintillator, phosphor plugs deposited in cellular matrix

a spatial resolution of 1 μm is reported [5].

For cone beam geometry using laboratory X-ray sources an often used detector system is the combination of an image intensifier together with a cooled CCD-camera as readout device. The cone beam tomograph developed at BAM in connection with Sauerwein System Technik is of this kind and its detector system consists of an 12" image intensifier tube together with a cooled CCD-camera of 1024x1024 pixels. Using a 200 kV microfocus X-ray tube a spatial resolution of about 1.7 lp/mm was measured by imaging a lead edge and calculating the MTF from the edge profile [6]. Newer improved high resolution image intensifier has a spatial resolution up to about 3.5 lp/mm [7]. Using a magnifying geometry a spatial resolution between 10 and 20 μm can be reached.

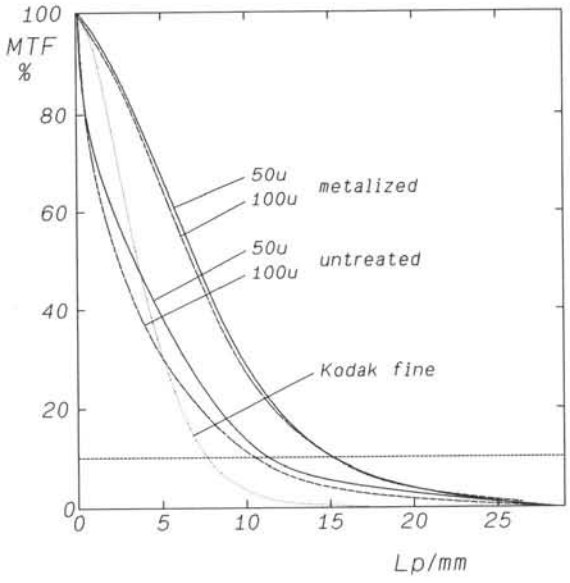

Fig. 4: MTF of structured foils, untreated and metalized (after [8])

A better spatial resolution can be achieved with structured scintillators which are used instead the image intensifier. Fig. 4 shows the MTF of such screens. They consists of a microstructured POM-foil with 10 000 or 40 000 micropyramides per square cm corresponding to a raster of 100 or 50 μm. Screens up to an area of 8 x 10 cm were produced. Each pyramide is filled with a mixture of gadoliniumoxisulfide and PMMA which acts as binder. To reduce the the light scattering between the pyramides through the POM walls some of the foils were metalized befor filling with scintillator material. This improves the MTF significantly from 12 to 15 lp/mm and enables better contrast for lower frequencies. For comparison a commercial fine screen was measured under the same conditions [8].

The limiting resolution at high frequencies plays an important role for detection of small details. For determining density variations the low frequency range of the MTF described by the contrast ratio, is more important.

DETECTION QUANTUM EFFICIENCY

Whereas Synchrotron radiation produces high photon flux even in a very small energy interval the commonly used laboratory sources like mikrofocus X-ray tubes limit the shortening of measuring times. Therefore industrial applications of tomography requires an optimization of the detection quantum efficiency (DQE) of the detctor system.

The definition for the DQE is

$$DQE = A_Q * A_I$$

with the absorption efficiency A_Q and the scintillation factor A_I. This means that an ideal scintillator should absorb all the incident X-rays and convert them into light with the highest possible efficiency. The absorption depends on the thickness of the selected scintillating selected scintillating material. To reach this goal some efforts are necessary if no deterioration of lateral spatial resolution should be done. This means a very high aspect ratio is necessary. An approach to an ideal scintillator are structured screens, scintillating fibre bundles or as in image intensifiers a needle structure of the scintillator material e.g. of CsI. The above mentioned CsI phosphor columns with a high aspect ratio of about 10:1 and with a spatial resolution of about 1 μm stopped about 80 % of 8 keV X-rays [5].

CONTRAST RATIO

The contrast ratio is a measurement of the veiling glare e.g. of image tubes but no simple mathematical relationship exists between the corresponding low frequency part of MTF and the contrast ratio. It is defined as illustrated in fig. 5. as the ratio between the luminance in a given point of the output image if no object is present in the entrance plane (A) and the residual luminance at the same point if the coresponding point in the entrance plane is covered with an X-ray opaque disk (B). Exactly the same exposure rate is assumed [7].

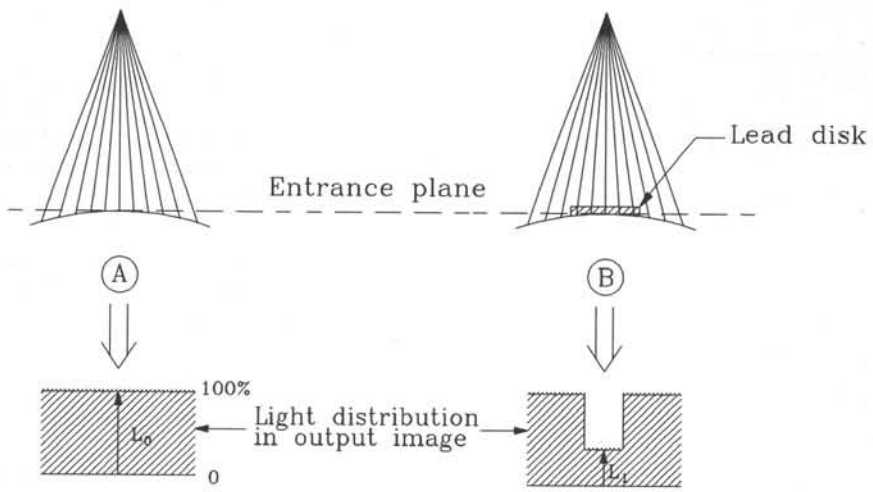

Fig 5: Definition of the contrast ratio

GEOMETRIC DISTORTION

The reconstruction process in tomography requires a carefully alignment of source scan table and detector for a accurately backprojection of the projections. Image intensifier tubes have

a curved surface and therefore a geometric distortion results. By a calibrating procedure this effect can be corrected with subpixel accuracy. Due to the strong influence of stray magnetic fields on the electron trajectories in image intensifier tubes an other type of distortion called S-distortion occurs. Therefore this calibrating procedure must be repeated for each new magnifying geometry.

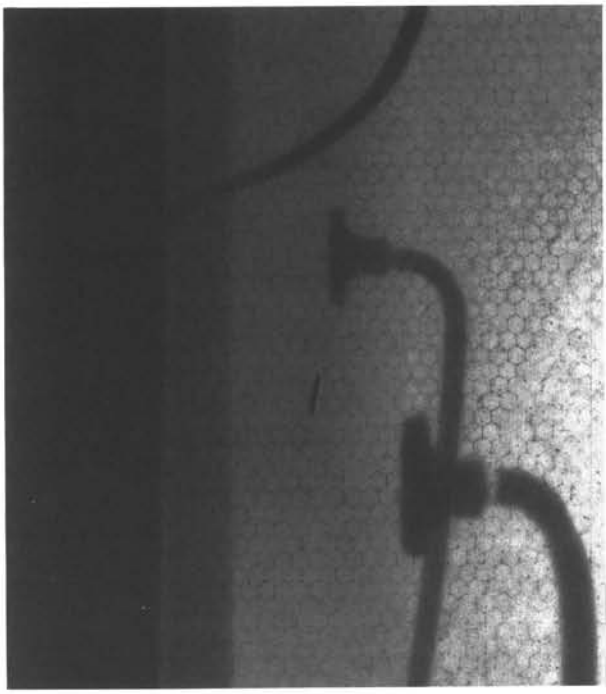

Fig. 6: Digital radiography of bonded wires. The pattern noise of fibre taper must be corrected for tomographic measurements.

No influence of magnetic fields and a much better contrast ratio offers another detector configuration which is tested now for an 3D-tomograph with improved spatial resolution at BAM. Instead of the image intensifier a glass fibre taper with a magnification of 2:1 is used together with a fibre optic entrance of a CCD camera. The front side of the taper is coated with a thin layer of Gd_2O_2S:Tb as scintillator. Fig. 6 shows a radiographic image of bonded wires in a electronic component. The pattern noise ofthe honey-comb structure of the taper which can be clearly seen has to be corrected for a tomographic measurement. First experiments point out a nearly independence patternnoise from incoming photon flux.

EXAMPLES

Two samples measured with the cone beam tomograph should give an example for the sufficient present state of art (fig. 7) and the needs to improve the detector design (fig. 8). Fig. 7 shows a map of three slices taken from a three dimensional data set of a sample of fibre reinforced ceramics - C/SiC - together with a crack which was spreaded after an interlaminar shear strenght test.
The spatial resolution is about 30 μm. For such materials 3D-tomography can be used today to optimize the production process - each carbon fibre bundle should be surrounded by SiC as protection against oxidation - and to observe crack propagation before and after different treatments or bending tests. More details are detectable using monochromatic synchrotron radiation to separate more clearly different phases like C and SiC.

Fig. 8 shows a 3D visualization of the head of a small statue (VA 5010) from Ashur, dated from the last quarter of the 3rd millennium B.C. [9]. The statue has a total height of about 19,5 cm. The diameter of the head is about 3 cm. The basic material consists of a bronze with a high percentage of Tin (over 15 %). The head area has a second outer layer of approximatly pure copper (over 99 %). The goal of the investigation with CT was to separate the Cu-layer from the bronce background e.g. to restitute the primary face of the bronze head and the secondary face of the copper layer. The interference of three opposite effects prohibit a level separation: Beam hardening, limited contrast ratio of the used image intensifier and the lower attenuation of copper against the bronze. The three images of fig. 8 result from different gray level - thresholds set to separate the two faces. But due to the mentioned interference not only the outer secondary face was eliminated. Setting a threshold additionally parts of the inner primary face were strongly disturbed.

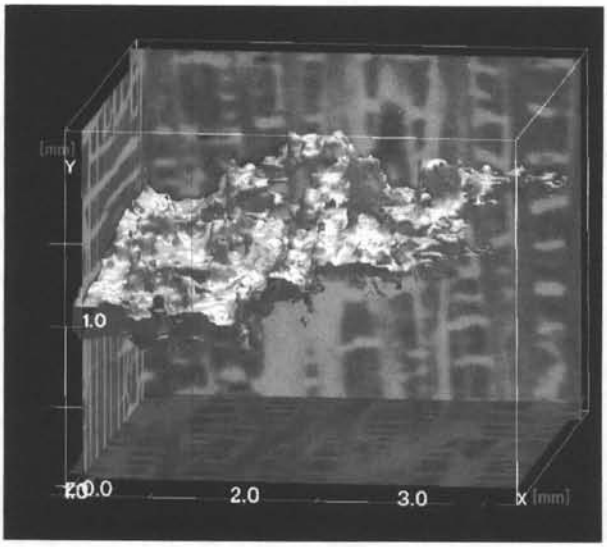

Fig. 7: Three dimensional representation of a load induced crack in a C/SiC sample

A detector system which exhibit a higher contrast ratio that an image intensifier a much better separation should be possible. With a line camera consisting of a CCD-line together with a fibre optic coated with a thin scintillator such improvements are reached today measuring single slices. But there is no area detector available up to now usefull for Cone Beam Tomography.

Fig. 8 Three visualizations of the head of the Statuette VA 5010 from Ashur

CONCLUSION

Whereas most of the outline is focused on high resolution tomography some of the requirements are also important for lower resolution at higher X-ray energies. The advantage of 3D-tomography - completeness inspection at reduced measuring times - opens new possibilities for this kind of tomography, especially for the energy range from 0.3 up to several MeV at a spatial resolution of about 0.1 mm. I believe there are some future aspects for component inspection.

REFERENCES

[2] F. Busch, U. Bonse, O. Günnewig, F. Beckmann
High resolution micro-tomography using synchrotron radiation
International Symposium on Computerized Tomography for Industrial Applications
Berlin, 8-10 June 1994
DGZfP Vol. 44 (1995), 96-103

[3] T. Hirano, S. Eguchi and K. Usami
Study of Quantitative Elemental Analysisof Monochromatic X-ray CT Using Synchrotron Radiation
Jap. J. Appl. Phys. 28 (1989), 135-139

[4] J.H. Kinney, M.C. Nichols, U. Bonse, S.R. Stock, T.M. Breunig, A. Guvenilir and R.A. Saroyan
Nondestructive Imaging of Materials Microstructures Using X-ray Tomographic Microscopy
Mat. Res. Soc. Symp. Proc. Vol 217 (1991), 81-95

[5] H.W. Deckman, J. Dunsmuir, K.L. D'Amico, S.R. Ferguson, B.P. Flannery
Development of Quantitative X-ray Microtomography
Mat. Res. Soc. Symp. Proc. Vol 217 (1991), 97-110

[6] H. Riesemeier, J. Goebbels, B. Illerhaus, Y. Onel, P. Reimers
3-D Mikrocomputertomograph für die Werkstoffentwicklung und Bauteilprüfung
DGZfP Berichtsband 37 (1993), 280-287

[7] P. M. de Groot
Image Intensifier Design and Specifications
Thomson Tubes Electroniques (1991), 34 pp.

[8] W. Bier, A. Guber, K. Schubert, H. Riesemeier
Mikrostrukturierte Röntgenverstärkerfolien für die Röntgendiagnostik
KfK-Nachrichten, 26 (1994), 3-9

[9] Vorderasiatisches Museum Berlin (SMPK)
R.-B. Wartke: Zur Herstellung zweier Kupferstatuetten aus Assur
in "Handwerk und Technologie im alten Orient: Ein Beitrag zur Geshichte der Technik im Altertum"
127-51. Mainz

[10] Yu.M. Protopopov, V.G. Vasil'chenko
Radiation damage in plastic scintillators and optical fibers
Nucl. Instr. Meth. B 95 (1995), 496-500

COMPTON CAMERA BASED UPON YAP:Ce MULTI-CRYSTAL DETECTOR

R.Pani, ^F.de Notaristefani, $F.Scopinaro, *G.J.Royle, "J.E.Fernandez, *R D..Speller , T.Malatesta, ^F. Vittori, R.Pellegrini, +A.Soluri, $G. De Vincentis,
Department of Experimental Medicine Division of Health and Medical Physics - University of Rome "La Sapienza" Italy. (^) INFN Section of Rome Department of Physics - University of Rome "La Sapienza" Italy ($) Department of Experimental Medicine Division of Nuclear Medicine, - University of Rome "La Sapienza" Italy. (*)Department of Medical Physics, University College London United Kingdom . (") Nuclear Engineering Laboratory University of Bologna Italy. (+)ITBM CNR Rome Italy

ABSTRACT

Nuclear medicine studies the functionality of the human body by administering radio-pharmaceuticals. Nuclear medicine imaging suffers, however, from poor spatial resolution, as in SPET and PET applications, and only achieves high sensitivity with the use of positron emitters in PET. Recently YAP camera technology has demonstrated much potential in overcoming the limitations of the Anger camera.
The YAP camera can provide the first step towards a more advanced camera; the Compton Camera, which is potentially capable of carrying out comparable diagnostic information to PET using single photon emitters. In this work a novel Compton camera design is introduced. It is based upon operating the YAP camera and a solid state detector in coincidence to track scattered photons .

INTRODUCTION

Position sensitive detection in Nuclear Medicine is reliant upon the Anger camera. Sensitivity and spatial resolution are key parameters in Nuclear Medicine images. PET can achieve good sensitivity but the current technological limit of spatial resolution (4 - 5 mm) is quite near to the intrinsic limit (1.5 - 2 mm). In addition the high costs of PET and the complicated operation procedures restricts its use at present to research centres. In contrast Single Photon Emission technology has limited spatial resolution and sensitivity but is widely used in hospitals. Current technology allows the possibility for more advanced camera system. The YAP camera is the first gamma camera prototype to achieve intrinsic spatial resolution of 0.7 mm FWHM and detection efficiency comparable to the Anger camera. It consist of a YAP:Ce multi-crystal matrix coupled to a position sensitive photomultiplier tube (PSPMT). It is proposed to develop a Compton camera [1] with high sensitivity and spatial resolution up to 1 mm based upon the YAP camera. The ultimate goal of the proposed camera is to link PET sensitivity with the large diffusion of SPET in hospitals.

THEORY OF COMPTON CAMERA

The theory behind the Compton Camera can be explained in the following way. Consider the case of the two - detector camera. A photon is emitted by a source and undergoes a Compton

Proc. Int. Conf. on Inorganic Scintillators and Their Applications, SCINT95,
1996, Delft University Press, The Netherlands

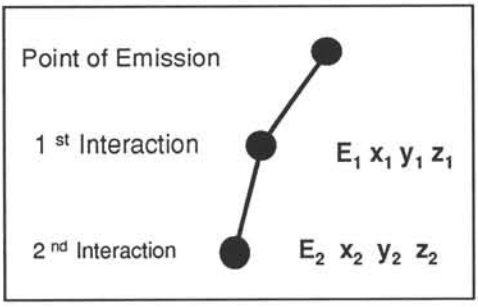

Figure 1 Compton Camera principle

interaction in the first detector (det 1) where it is scattered towards the second detector (det 2) in which it is photoelectrically absorbed. A coincidence detection mode is employed to ensure that the two interactions observed are caused by the same photon. Knowledge of the energy deposited, E , in det 1 by the Compton interaction enables the scatter angle θ to be determined using the Compton relationship (1),

$$\cos\theta = 1 - m_0c^2[1/E' - 1/E] \qquad (1)$$

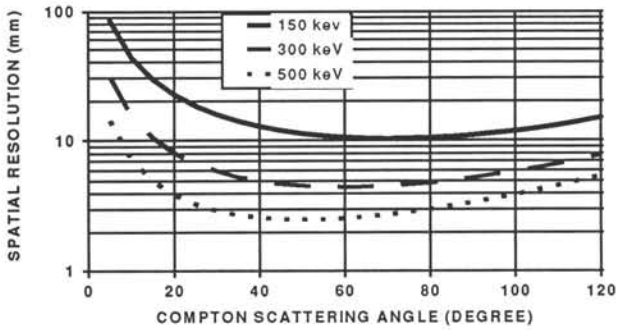

figure 2 Calculated spatial resolution values

where m_0c^2 is the rest energy of the electron and E is the incident energy of the photon. If the coordinates of the first $(x_1y_1z_1)$ and second$(x_2y_2z_2)$ interactions are known together with θ, it follows that the emission point should lie in the surface of the cone, which has a semi-angle θ, the vertex at the first interaction point and the symmetry axis along the line from the second to the first interaction point. The intersection of the cone with the image plane generates a conic section, which is normally an ellipse. The error on the measured energy E' of the scattered photon (which depends on the energy resolution of det 2) causes the error propagation of $\Delta\theta/\theta$. Calculation considers a normalised energy resolution of 1.2 % and 2% at 300 keV and 140 keV, respectively of incident photon energy E. The error on $\Delta\theta$ is very sensitive to the scattering angle with a minimum value at about 60- 80 degrees. It affects spatial resolution as shown in fig. 2 where the curves were calculated at three different incident energies of photon and for a source located at a distance of 10 cm from det 1. Scattering angles between 30 and 90 degree represent the useful detection range of photons. In this simplified approach we assumed that radiation entering det 1 is fully unpolarized. Multiple scattering in the body may produce a consistent fraction of polarized photons which follow an angular distribution law different of Eq. (1) and therefore, should be considered separately [2]. The Compton camera is also suitable for analysing these polarized photons because of the polarization properties inherent to the Compton effect, giving an optimum chance for discriminating single from multiple scattering processes in the body by means of an appropriate strategy.

CAMERA DESCRIPTION

The camera consists of two detectors as shown in fig 3. The first detector is a YAP:Ce multi-crystal matrix coupled to a Position Sensitive Photomultiplier Tube Hamamatsu R2486

through a bundle of fibers. A complete description of a YAP camera prototype can be found elsewhere [3]. The second detector (det 2) consists of a two layer detector: The first layer is CdTe 1 mm thick and the second layer is YAP:Ce multi-crystal matrix 1 mm thick in which the single element cross section is 0.6 x 0.6 mm^2 The YAP:Ce multi-crystal of det 2 covering an area of 100 cm^2 is a circle of 14 cm diameter with a central hole of 2 cm diameter, Det 2 is directly coupled to 4 PSPMTs (Hamamatsu R2487) each with 60 x 60 mm^2 of active area. The hole of the det 2 coincides with the four non active corners of PSPMTs. To simplify calculations the remaining dead areas arising from assembling four PSPMTs together where neglected. When a photon impinges on the detector 1 a Compton photon is generated and escapes from the detector with a probability that will be discussed in the following. The Compton photon emitted under the opportune solid angle is then detected by the second detector. Due to the high photofraction of CdTe it interacts mainly via the photoelectric effect producing x-ray fluorescence at 26.7 keV and 31.8 for Cd and Te K_α respectively with a high yield (ω_k = 0.85). Depending on Compton photon energy and mainly on CdTe detector thickness, characteristic X-rays, escaped forward from CdTe,. interact under photoelectric effect with the second layer of det 2.

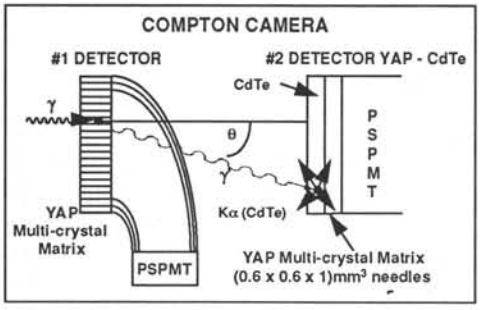

fig. 3 Detection system

At these photon energies the absorption probability in 1 mm of YAP:Ce is almost 1. Finally the Compton camera consists of triple coincidence between three detectors as the following interaction scheme:

1- The incident photon undergoes Compton interaction in det 1. Det 1 provides information only on the interaction position.

2- CdTe layer of det 2 absorbs the scattered photon and records the energy deposited by the scattered gamma ray.

3- The YAP:Ce layer of det 2 records the location within the detector due to CdTe X-ray fluorescence.

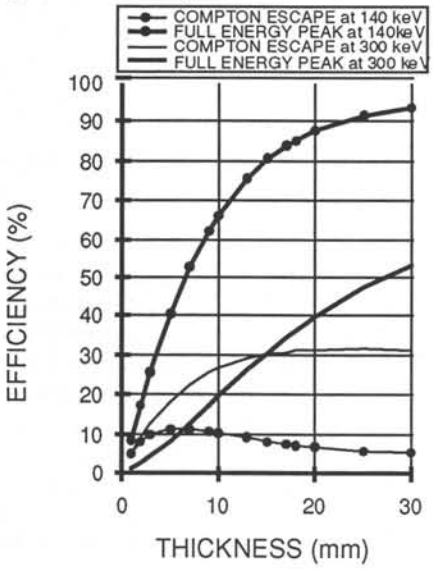

Fig 4 Compton photon escape probability from YAP:Ce multi-crystal detector

RESULTS

When a photon impinges on the det 1 a Compton photon is generated and escapes from the detector with a probability shown in fig. 4 . The calculations were obtained simulating a narrow beam centred in the detector 1 with 140 keV and 300 keV of photon energy respectively. The curves show an efficiency of total Compton escape of about 30% for a detector thickness larger than 15 mm at 300 keV incident photon energy. At 140 keV the efficiency decreases by no more than 12% corresponding to a detector thickness of 7 mm. 10 mm of optimised thickness was chosen for the detector 1. Photon energies of 140 keV and 300 keV were selected for the simulations due to the potential application of the radioisotopes Tc-99m and I-113m.

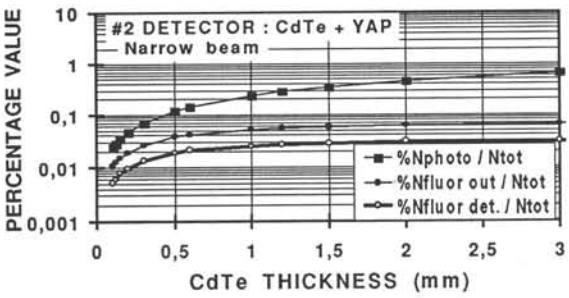

Fig. 5 Compton camera detection efficiency.

A simulation of intrinsic efficiency of the complete detection system is shown in fig 5. %Nphoto/Ntot represents percent values of photoelectric events as a function of CdTe detector thickness. Values are normalised to the number of incident photons on det 1 in narrow beam geometry. %Nfluor out/Ntot represents the percent value of the total number of X-rays escaping from CdTe. %Nfluor det/Ntot is the percent value of CdTe characteristic X-rays escaped and detected by 2nd layer of det 2. 1.2 mm of CdTe is able to carry out an intrinsic efficiency of 0,03%.

CONCLUSION

Table 1 describes the conclusions. The simulation show that the proposed Compton camera has a detection efficiency one order of magnitude greater than the Anger camera, coupled with a significant improvement in spatial resolution.

Table 1	SPATIAL RESOLUTION			
	γ Energy	FWHM (mm) SDD=10 cm	FWHM (mm) SDD=1 cm	SENSITIVITY
COMPTON CAMERA	300 keV	6.5	1.5	$1 - 4 \times 10^{-3}$ (20) *
YAP CAMERA	140 keV	3.3	1.6	2×10^{-4}
ANGER CAMERA	140 keV	10	4 - 5	2×10^{-4}
PET	511 keV	3 - 5	3 - 5	2×10^{-1} *

* Values calculated for a COMPTON CAMERA LITTLE TOMOGRAPH about 20 cm diameter with a cylindrical PHANTOM 20 cm diameter by 20 cm length.

REFERENCES

[1]M.Singh, DE.Gustafson, MJ.Berggren, BK.Gilbert, EL:Ritman Med Phys 4 (1977) 350
[2]J.E. Fernandez, J.H.Hubbell, A.L.Hanson and L.V.Spencer Rad.Phys.Chem. 41(1993) 579
[3]R. Pani, K. Blazek, F. De Notaristefani, P.Maly, R. Pellegrini, A. Pergola , F. Scopinaro, A. Soluri Nucl. Instr. & Meth. A348 (1994) 551

THE LEAD TUNGSTATE CALORIMETER OF THE CMS EXPERIMENT AT LHC

P. Lecoq, CERN, Geneva, Switzerland

Abstract

The CMS experiment (Compact Muon Solenoid) to be installed at the future Large Hadron Collider (LHC) at CERN, is proposing the construction of a scintillator based high resolution homogeneous calorimeter, to meet the performance criteria for the discovery of an intermediate mass Higgs boson in its 2γ decay mode.

A systematic investigation by the Crystal Clear collaboration since 1990 on as many as 25 different scintillator types has led to the conclusion that 3 scintillators could be considered for the construction of this calorimeter, Lead tungstate (PbWO4), Cerium fluoride (CeF3) and high density fluorohafnate glasses.

The relative merits and problems of these 3 candidates will be discussed, as well as the motivations for the final choice of Lead Tungstate by the CMS collaboration. After an overview of the CMS experiment, a description of the present design of the calorimeter will be given, with the present situation of the organisation and the construction plan.

1. INTRODUCTION

The Large Hadron Collider (LHC) to be built at CERN at the beginning of the next century will address one of the key questions in particle physics namely that of the origin of the masses of the particles. This is very likely related to a mechanism of spontaneous symmetry breaking in the electroweak sector of the Standard Model (SM) which must involve a variety of new particles, like Higgs bosons, super symmetric particles, new gauge bosons or Technicolor states [1]. Outside of the Standard Model and its simple extensions, the physics discovery potential should be maintained at a very high level for the detection of possible new phenomena in a completely new energy range, at the 1 TeV scale.

This challenging physics will be very demanding on the detector performances. A study of extremely rare processes will be required to discover the spontaneous symmetry breaking mechanism. High luminosities will be needed and therefore the detectors will have to operate in a particularly hostile environment. Extremely fast (60 MHz interaction rate), highly radiation resistant (10MRad and 10^{14} neutrons/cm^2) and high performance detectors will be required. There is a particular interest in having a very high performance electromagnetic calorimeter for the precise energy measurement of electrons, positrons and photons. Calorimetry based on inorganic scintillators can be considered as a mature technique for such a high quality detector, although the scintillators used in previous experiments (NaI(Tl), CsI(Tl), BGO) do not fulfil the requirements imposed by the future colliders. At LHC the scintillation must be fast and the optical properties must remain unchanged under strong radiation. The pile-up problem is eased by using a dense crystal, allowing a fine granularity.

2. THE CMS DETECTOR

The CMS detector (Fig.1, [2]) has been optimised for the search of Standard Model Higgs bosons in the range from 90GeV to 1 TeV, but it will also allow the detection of a wide range of possible signatures from alternative electroweak symmetry breaking mechanisms. This require the identification and precise measurement of muons, photons and electrons. The goal is to measure these particles with an energy resolution of about 1% over a large momentum range.

At the core of CMS is a high-field superconducting solenoid (4T), with a length of 14m and an inner bore of 5.8m. This leads to a compact design for the muon spectrometer, hence the name Compact Muon Solenoid (CMS).

Proc. Int. Conf. on Inorganic Scintillators and Their Applications, SCINT95,
1996, Delft University Press, The Netherlands

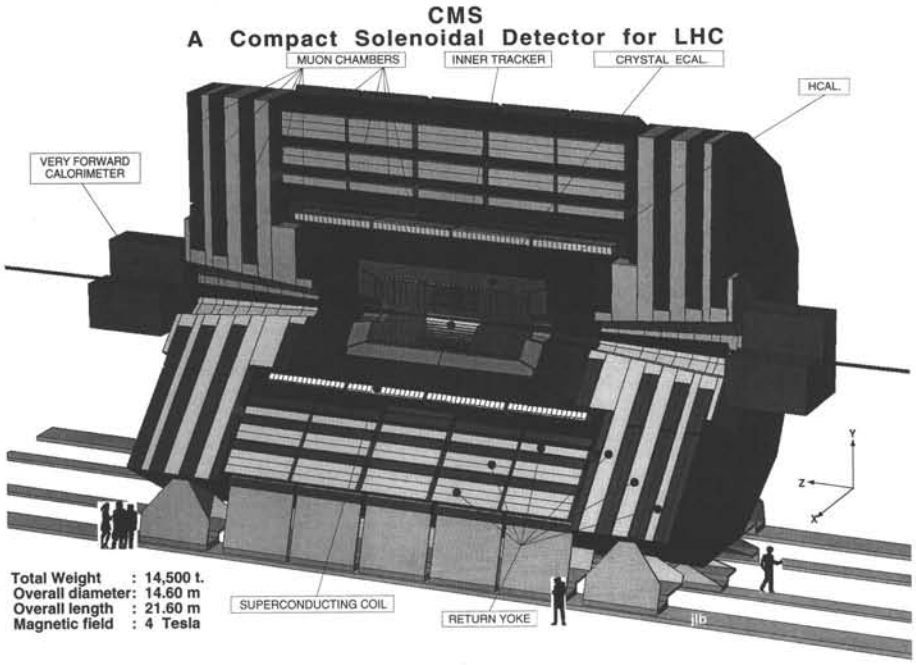

Fig. 1: Three dimensional view of the CMS detector

The large field provides significant benefits for the muon triggering and measurement, calorimeters and inner tracking. Amongst the features relevant for a precision electromagnetic calorimeter (ECAL) are:

• a momentum resolution for electrons of ≈ 0.5% at $p_t \approx 50$GeV matching that of a crystal calorimeter. This is imortant for in situ calibration of the calorimeter cells.

• because of the large inner radius of 1.4m, an important fraction of soft charged tracks curl up and do not reach the ECAL. The pile-up energy entering the e/γ measurement area is reduced. The probability that there is no pile-up in a cell of size $\Delta\eta \times \Delta\phi = 0.1 \times 0.1$ (trigger size) is ≈ 70% at a luminosity of $L = 10^{34}$ cm^{-2}s^{-1}.

• all the calorimetry can be installed inside the coil and hence no material from the coil can spoil the ECAL performance.

The ECAL surrounds the inner tracking cylindrical cavity with a radius of 1.4m and a length of 7m. The geometrical coverage extends to $|\eta| = 2.6$. It will consist of 110,000 Lead Tungstate crystals with a length of 23cm, and an entrance cross-section of ≈ 2 x 2 cm^2. The back cross-section will be slightly bigger due to the pointing geometry. The total Lead Tungstate volume will be 13m^3. The CMS design is described in more details in reference [2].

At high luminosities the calorimeter will operate in hostile environment. A high particle flux leads to problems of radiation damage and energy pile-up. In the CMS geometry the radiation dose (in MRads) and neutron fluence (in units of 10^{13} neutrons/cm^2) are shown in Fig.2. An integrated luminosity of 10^6 pb^{-1}, corresponding to 10 years of operation at a luminosity of $L = 10^{34}$ cm^{-2}s^{-1}, has been assumed.

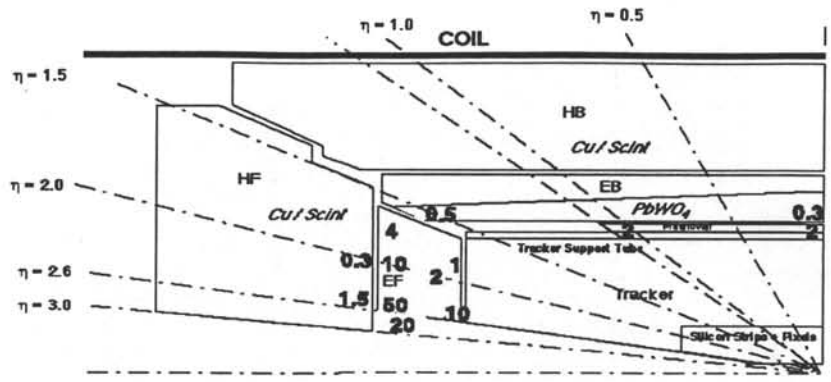

Fig. 2: Radiation dose (MRads) and neutron fluence (x 10^{13} neutrons/cm^2) for an integrated luminosity of 10^6 pb^{-1}, corresponding to 10 years of operation at L = 10^{34} $cm^{-2}s^{-1}$

3. PHYSICS REQUIREMENTS FOR THE CALORIMETER DESIGN

The physics process that imposes the strictest performance requirements on the electromagnetic calorimeter at the LHC is the intermediate Higgs boson decaying into two photons. The natural width in the mass region where this process is dominant (90GeV to 140 GeV) is very small: $\Gamma_H/M_H \approx 10^{-4}$. The observed width is therefore entirely dominated by the instrumental two-photon mass resolution which is given by the formula:

$$\sigma(M)/M = 1/2 \left[\sigma(E_1)/E_1 \oplus \sigma(E_2)/E_2 \oplus \cot(\theta/2) \times \sigma(\theta) \right]$$

where $\oplus$ denotes a quadratic sum, E is GeV and θ is in radians.

The angle between the two photons will be given from the reconstructed impact point of the photons at the entrance of the calorimeter. A dense material and a large radius for the calorimeter will allow a precision which will be negligible compared to the energy resolution.

3.1 Energy resolution

Homogeneous detectors are well known to give excellent energy resolution which is usually parametrised in the following way:

$$\sigma(E)/E = a/\sqrt{E} \oplus b \oplus \sigma_N/E$$

where a is the statistical term (sampling or photostatistics for homogeneous media)

b is the constant term

σ_N is the energy equivalent of noise

The noise term has two sources, namely electronics noise and the pile-up energy. High precision calorimetry at the LHC requires an energy resolution of the order of 0.5% for 100 GeV photons.

An homogeneous calorimeter is not limited by sampling fluctuations and an energy dependant term of the resolution "a" as small as 2% has been currently achieved on several large size

calorimeters. It is much more difficult to achieve a constant term "b" of ≈ 0.5%. On large systems like the L3 BGO calorimeter at CERN, one recognizes usually 3 contributions to the constant term:

$$b = b_L \oplus b_F \oplus b_C$$

The b_L term represents the fluctuations due to the energy leakage. The front leakage due to backscattered particles has a negligible contribution above a few GeV. The rear leakage can be easily controlled by having sufficient material for a full longitudinal energy containment. For the photon energies up to 100 GeV, at least 25 radiation lengths are necessary to maintain the leakage term within reasonable limits (one radiation length is the mean distance over which a high energy electron loses all but 1/e of its energy). The side leakage is more difficult to control. It is determined by the number of cells one has to sum-up to reconstruct the energy. On the other hand this number is limited by the electronic noise and chiefly by the pile-up at LHC if the shower spreads too much laterally. Low noise electronics and high density material will of course limit this contribution. A particular attention must be paid to all gaps, walls, and dead material in front, which may have a important contribution to the leakage term. All leakage contributions can be well reproduced by MonteCarlo and a b_L term of ≈ 0.3% can be achieved with a crystal calorimeter.

The b_F term is associated to non uniformities. They can result from non homogeneities in the active material, like variation of doping concentration in non intrinsic scintillators. Temperature gradient can be the dominant factor of non uniformity when there is a strong dependence of the light yield with the temperature. Lead Tungstate (PWO) for instance has a large temperature coefficient of -1.98% / °C. Crystals like Cerium Fluoride (CeF_3), with a temperature coefficient as small as 1‰ / °C at room temperature will be insensitive to this effect. Other sources of non uniformity are associated to the light collection. Pointing geometry implies cells of pyramidal shape. A strong non uniformity is induced by the focusing effect of these cells, particularly if the refraction index of the medium is high; CeF_3, with an index of 1.6 is here again much better than PWO (n = 2.2). Finally much attention should be paid to avoid large absorption of the light in the medium. This is perhaps the most important problem for crystals with an emission spectrum in the UV like BaF2 and other cross-luminescent crystals, as well as for low density materials because of the long path length of the photons to reach the photodetector. For dense crystals with an emission spectrum in the visible, a b_F term as small as 0.25% is reachable.

The last contribution b_C corresponds to the intercalibration errors. Frequent calibrations with an efficient monitoring system are necessary to maintain this contribution below 0.3%. The L3 BGO has proven that a well designed fibre monitoring system can maintain the intercalibration within 0.3% for long periods of time for more than 10000 crystals. The high luminosity pp machines will also provide excellent means for a continuous calibration of the detector. At LHC a rate of 10 Hz is expected for electron pairs from Z° decays in the central region, which should allow a weekly calibration with about 100 electrons per channel. If there is a good inner tracker, individual e^+ or e^- can be used (E/p matching) at a rate which could be as high as 100 per channel and per day. Finally one should be able to take advantage of the copious number of minimum ionising particles for an almost continuous intercalibration control of all the channels.

Taking all these contributions together it seems that a constant term b = 0.5%, although difficult, is not out of reach for a well designed homogeneous calorimeter.

3.2 Localisation of the two photon vertex

At the LHC the longitudinal position of the interaction vertices will be distributed with an r.m.s. spread of about 53mm. If the mean longitudinal position is used when reconstructing the effective mass a large contribution to the reconstructed width is introduced (about 1.3GeV for a 1.4m calorimeter radius). One way to solve this problem, if the number of pile-up events is not too high, is to take advantage of the hardness of the Higgs production to localise the longitudinal position of the Higgs production vertex. Monte-Carlo simulations show that the production of a Higgs is associated with a certain number of high transverse momentum charged particles, with a distribution which peaks at much higher p_t than for minimum-bias events. A good inner tracker will therefore be used to

reconstruct the vertex from these hard charged particles, which has the largest chance to be at the origin of the emission of the two photons from the Higgs decay.

3.3 Rejection of neutral pions

A good mass resolution would not be essential were it not for a substantial background. There are two major sources of background. One irreducible one arising from different photon production processes and one reducible background from bremstrahlung and jet processes. The di-jet cross-section is seven orders of magnitude larger than the di-photon cross-section so that a very large rejection of the possibility of any di-jet faking a di-photon event is needed if the jets are not to be the source of a formidable background to the Higgs $\rightarrow \gamma\gamma$ signal. The background comes predominantly from energetic π^{o}'s decaying in two photons with a small separation angle. Different isolation cut's can be applied to reduce it, but an intrinsic rejection power of π^{o}'s by the calorimeter can be given if the calorimeter radius is sufficiently large to allow the maximum separation between the two photons from the symmetric decay of high energy π^{o}'s and if the material is dense enough to maintain the showers in the minimum volumes, allowing an easy separation of two nearby photons.

4. THE CHOICE OF THE SCINTILLATOR

A good scintillator for the use at the high luminosity LHC should have:

- a high light yield (a few 100 pe^{-} / MeV of deposited energy)
- an emission wavelength at >300nm where the quantum efficiency of most photodetectors is high
- a short radiation length and Moliere radius (e.g. a high density)
- a short decay time constant (<30ns) with no slow components
- a high radiation tolerance (>5Mrads)
- a good stability of the light emission parameters versus time, temperature, etc...
- good mechanical properties
- an acceptable cost

After a few years of investigations the Crystal Clear collaboration has proposed three candidates for the CMS calorimeter [3]. A comparison of some of the properties of these three scintillators: CeF3, PbWO4 and Hafnium Fluoride Glasses (HFG) is given in Table 1.

4.1 The choice of Lead Tungstate (PWO) crystals

An ideal calorimeter for High Energy Physics would require a dense, fast and radiation hard scintillator. A high light yield comparable to BGO has long been considered as mandatory for a Silicon photodiode readout, the only possible one in a high magnetic field environment. Cerium fluoride (CeF3) is certainly the best candidate known today in this category. Unfortunately the $26m^3$ needed for the CMS ECAL and the absence of large production facilities in the world put the risk factor for this solution at a level which was considered too high. On the other hand, recent developments in the field of other photodetectors like avalanche photodiodes (APD), somehow relaxes the constraints for a very high light yield. The field is therefore open for potentially cheaper solutions, based either on very dense materials like Lead Tungstate (PbWO4) for which a significant volume reduction will be made, or on scintillating glasses for which the production cost is smaller than for crystals. As the production of radiation hard glasses is not yet a mature technology, Lead Tungstate was finally chosen because of its attractive properties.

Table 1 : Comparison of the properties of CeF3, PbWO4, HFG glasses

Properties	CeF_3	$PbWO_4$	HFG glass
Physical & chemical			
Density (g/cm^3)	6.16	8.28	6
Radiation length (cm)	1.68	0.85	1.6
Moliere radius (cm)	2.63	2.19	2.8
Temperature dependence %/°C	0.14	-1.98	-0.15
Hygroscopicity / Chemical Stability	No / good	No / good	No / good
Mechanical Strength	$4kg/mm^2$	$1kg/mm^2$	good
Thermal conductivity (W/°K)		3300	
Specific Heat (J/kg°K)		440	
Index of refraction	1.62	2.2	1.5
Scintillation			
Photon Yield : γ/MeV			
Best crystal, ~$1cm^3$, in 1μsec	2100	140	75
Typical full size crystal in 1μsec	1200	50	25
Typical full size crystal in 25nsec	660	45	15
After glow after 1μsec	No	No	No
Mean decay time	23.4ns	10ns	27.2ns
Radioluminescence peak (λ)	300nm	440-500nm	320nm
Radioluminescence spectrum at 10% of peak intensity	270 to 400nm	360 to 570nm	290 to 360nm
Radiation damage			
Radiation induced scintillation loss	No	No	No
colour centres	Yes	Yes	Yes
Induced absorption length at peak emission for about 500Gy (100Gy/h) on best crystal	> 2m	> 2m	<10cm
Saturation of damage for full size crystal at peak emission (100Gy/h)	<100Gy	100Gy	> 800Gy
Induced absorption length for full size crystal at saturation (100Gy/h)			for 740Gy
1h after irradiation	1.5m	3.3m	0.012m
1 day after irradiation	2.5m	8.4m	0.014m
1 week after irradiation	full recovery	full recovery	0.02m
Induced absorption length at peak emission for about 500Gy (1Gy/h) for full size crystal	No	No	Small
Thermal annealing (conditions)	Significant but incomplete above 250°C	Complete at 150°C	Complete at 260°C
Optical bleaching (conditions)	No	Yes λ>600nm damage at 240nm	Complete : 8 hours Xe lamp (P=0.02W)
Induced absorption length at peak emission for $10^{13}n/cm^2$	>2m	>2m	0.2m
activation after $10^{13}n/cm^2$	0.07 mr/hour		
Growth conditions			
Volume for CMS : $25X_0$, $\|\eta\| \leq 2.5$ (m^3)	26.3	13	24.5
Maximum size produced so far (cm^3)	3x3x28	ø3.6x25	2x3x10
Maximum size required for CMS (cm^3)	3x3x14	3x3x23	3x3x14
Production Method	Bridgman	Czokralski Bridgman	casting, moulding

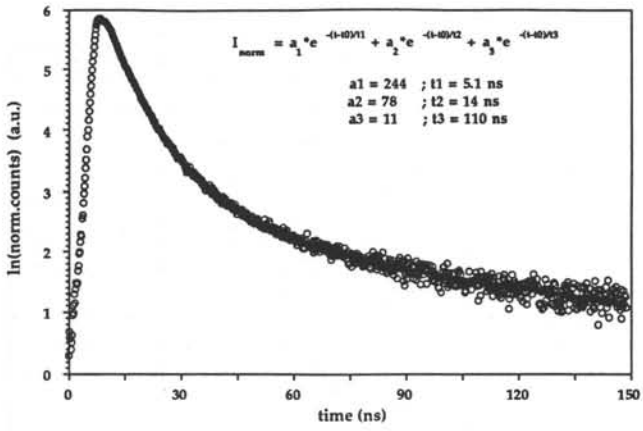

Fig.3 Typical scintillation decay of an undoped PWO crystal

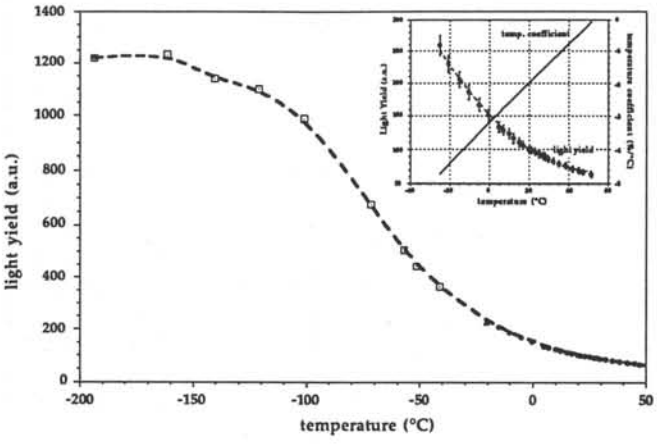

Fig.4 PbWO4 temperature dependence of light yield

Lead tungstate ($PbWO_4$) is a birefringent scheelite type crystal belonging to the space group I4 1/a with a tetragonal unit cell. It is grown from a 50%-50% mixture of Lead oxide (PbO) and Tungsten oxide (WO_3) which melts congruently at 1123°C, without phase transition during the cooling. It is particularly attractive for building a compact calorimeter because of its very high density, leading to a short radiation length and Moliere radius. Moreover, the abundance of the raw material and the relatively low melting point are important parameters for a low production cost. Being non hygroscopic and chemically inert, its handling does not give any problem. The mechanical resistance is somewhat lower than for BGO or Cerium fluoride, but it cleaves less easily than these crystals. The high index of refraction helps the light collection along the crystal but limits the photon extraction efficiency. Because of the light emission mechanism character and the large number of reflections on the lateral faces before collection on the photodetector, the birefringence of Lead Tungstate is not a problem. The properties of $PbWO_4$ are summarised in Table 1 [3-7].

4.2 Scintillation properties

The emission spectrum is rather complex, with generally 2 broad bands at 440nm and 530nm, the relative amplitude of which vary from sample to sample and the stoechiometry. The decay time is strongly non exponential, with a mean value of about 10ns and 90% of the light collected in 100ns. This results from a strong thermal quenching which takes place at room temperature and which has three consequences:

- reduce the light yield to about 50 photons/MeV (large size crystals)

- shorten the decay time to about 10ns with 90% of the light collected in 100ns (Fig. 3)

-produce a strong temperature dependence of the light yield : -1.98%/°C (Fig.4)

These problems which impose the use of avalanche photodiodes (APD) or PM for the readout and a very efficient temperature control system (within a few tenths of a degree), have to be balanced by the very high density of this crystal (8.2 g/cm^3, 1 radiation length = 0.9cm, 1 Moliere radius = 2 cm), which will reduce the volume needed for a crystal calorimeter in CMS by a factor 2 as compared to CeF3. The small light yield of PWO crystals is a problem, not only because the stochastic term of the energy resolution may be increased due to worse photostatistics, but also because of a higher relative contribution to the signal of the leaking charged particles trough the APD. This effect, called the nuclear counter effect, also results in a worsening of the energy resolution. To solve this problem, longer crystals will reduce the rear leakage and larger area APD's will increase the matching factor to the crystal area and therefore increase the effective light yield. It is nevertheless essential that every effort will be made to further increase the light production yield in PWO crystals.

It is well known that variations of stoechiometry are often present in binary oxide crystals grown by Czochralski technique. This is due to the different evaporation rates of the two components but also to the specific characteristics of their phase diagram. The high evaporation rate of WO_3 is at the origin of a progressive change of stoechiometry during the growth and consequently of a variable distribution of the luminescent centres along the crystal. As a result of this, the transmission spectra in different positions along a $PbWO_4$ crystal are function of the position of the sample relative to the seed. On the seed side of the crystal, where the stoechiometry is expected to be correct, the transmission edge is sharper and at shorter wavelengths than for the rest of the crystal. When the distance from the seed increases and the stoechiometry shifts towards a greater PbO concentration, hole O^- centres are created and an absorption band at 350nm shifts the band edge to the green region of the spectrum. Although the emission spectrum is centred relatively far from the absorption edge, this effect results in a slight shift of the scintillation spectrum towards longer wavelengths and in a variation of the light yield along the $PbWO_4$ crystals. The mean decay time seems to be rather uniform along the crystal. This can be explained by the fact that $PbWO_4$ luminescence at room temperature is dominated by the thermal quenching which probably affects equally all emitting centres.

In order to prevent the formation of hole defects on the bottom part of the $PbWO_4$ crystal, a new growth technology based on Nb doping has been developed [8,9]. Nb^{5+} ions progressively replace W^{6+} ions during the growth, thus compensating the tungsten deficiency. Stable ($NbO_3 + F^+$) centres are created which are isoelectronic of the (WO_3 + F) centres. The later are stable defects, present everywhere in the crystal, and responsible of the green emission bands. As a result of this new growth technique, long crystals have been produced which are now structurally and optically very uniform [10].

A second consequence of the doping, is an increase of the light yield of about 20% which has been observed on small size crystals for low doping concentrations (20 to 40ppm). This effect has not been seen on long crystals for which other impurities related to the oxides compete with Niobium in the energy transfer process towards luminescent centres. It is expected that better quality raw materials will help increasing the light yield.

4.3 Radiation resistance

Undoped $PbWO_4$ crystals exposed to ^{60}Co gamma - irradiation present a global reduction of optical transmission, depending on the relative position of the sample in the crystal ingot. Average values of (4±3) m^{-1} after 600 - 700 Gy (3Gy/min) absorbed dose are normally measured for the absorption coefficient of radiation induced defects in the region of the peak emission. The absorption is rather uniform in a large region of the crystal, but in the first few cm near the seed where it is significantly smaller, and in the last few cm where it is higher than average. One can barely distinguish two broad absorption bands at about 400nm and 600nm, which are attributed to O^- related defects.

On the other hand, for $PbWO_4$ crystals doped with Niobium, where O^- defects are compensated, a considerable improvement in radiation hardness was found (Fig.5). Nb doping

provides an uniformisation of radiation sensitivity along the ingot and a strong reduction of it. Typical value of 0.25 to 1 m^{-1} are measured for long crystals after exposure to more than 20000Gy in a LIL 500MeV electron beam. It is worth mentioning that in the case of Nb doped $PbWO_4$ crystals the saturation of the damage as a function of the dose is reached at about 200Gy. When present, the damage recovers at room temperature with two time constants of respectively 2 hours and 20 days. A slight increase in temperature (by 10°C or 20°C) considerably speeds up the recovery process. Optical bleaching can also be efficient at wavelength higher than 550nm. At lower wavelength exposure of PWO crystals can produce some damage.

When exposed to fast neutrons, a very small damage has been observed up to a fluence of about 10^{14} neutrons.cm^{-2}. On the other hand a small phosphorescence can be seen, dying out in 24 hours, which is caused by the activation of ^{186}W in ^{187}W by neutron capture. For the LHC expectefluencees, this effect should be negligeable.

4.4 Crystal production

A systematic evaluation of the production facilities has been made worldwide and has given the CMS collaboration some confidence that the $13m^3$ needed for the CMS calorimeter could be produced before the commissioning of the LHC in 2004.

The standard technology to grow $PbWO_4$ crystals is the Czochralski method with platinum crucibles under atmospheric pressure close to air in composition. In order to reduce stresses, the direction of crystal growth has a deviation from Z axis of about 19°. The differential evaporation rate of PbO and WO_3 is at the origin of a progressive change of stoechiometry during the growth and consequently of a variable distribution of the luminescent centres along the crystal. To compensate for this effect, the crystals are grown at at temperature slightly inferior to the melting point of the stoechiometric $PbWO_4$ compound and the initial melt is made richer in WO_3. With these parameters the growth speed can be as high as 8mm/h. After crystal growth, the crystals are annealed with a low speed temperature variation so that the total necessary time to produce an ingot of $\Phi = 32 \times 220$ mm^3 is 140 hours (72 h -crystal growth and 68 h - annealing). It is possible to grow good quality ingots of larger diameter: $\Phi = 60 \times 220$ mm^3 but the process of annealing aimed at the elimination of intrinsic stress is much longer than for crystals of $\Phi = 32$mm.

Clearly a large effort is still needed to optimise the growth technology and equipment in view of a large and cost effective production. For instance the evaluation of the Bridgman growth technique is interesting from the investment cost point of view as well as for offering a possibility to avoid the tungsten oxide evaporation during the growth. High pressure Czochralski has also to be studied for the same reason. Moreover the cutting and polishing methods are still not optimised and require further R&D work.

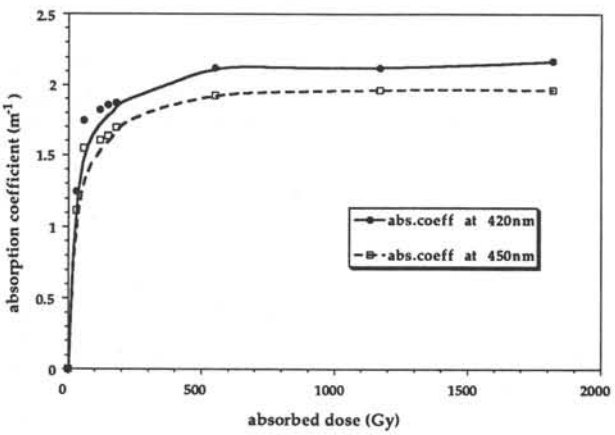

Fig.5 Evolution of absorption coefficient at $\lambda = 420$ nm and $\lambda = 450$ nm with radiation dose in Nb doped $PbWO_4$ crystals

The $PbWO_4$ crystals growth technology is very close to the one used for

niobates and molibdates, which are widely used in different applications, particularly in the military industry. Therefore, a powerful industry basis has been developed in different parts of the world, especially in Russia where large production plants with excellent equipment can be made available for the production of the CMS crystals. A large effort has been initiated to converts existing facilities also in China and in Europe, particularly in the Czech Republic.

5. CONCLUSION

Due to its high density, short decay time, and good radiation hardness, PWO is a good candidate for electromagnetic calorimeter for the future high energy physics experiments. Moreover the large existing infrastructure for mass production (particularly in former Soviet Union) triggered the choice of this crystal for the CMS experiment at LHC. Significant progress have been made in the understanding of the scintillation properties and radiation damage mechanisms. Moreover Nb doping has proven to enhance the optical uniformity and radiation hardness of large crystals. A strong R&D effort is still on the way to define the production parameters for increased and stable light yield on PWO crystals.

The present CMS calorimeter design, with a large radius and a fine granularity, is based on 110,000 PWO crystals representing a volume of $13m^3$. The attractive properties of Lead Tungstate should make this calorimeter an ideal tool for the discovery of an intermediate mass Higgs boson as well as other very rare processes at the LHC.

Acknowledgements

The author would like to express his gratitude to all the members of the Crystal Clear collaboration, as well as to the members of the CMS/ECAL group for their continuous help in this collective effort.

References

[1] For an overview see for instance J.F. Gunion et al., *The Higgs Hunter's Guide*, Addision-Wesley, 1990

[2] The Compact Muon Solenoid Technical Proposal, CERN/LHCC 94-38, 15 Dec 94

[3] TheRD18 Crystal Clear Collaboration status report, CERN/DRDC/94-53, Jan 95

[4] V. G. Baryshevsky et al, NIM A322 (1992) p.231-234

[5] V. A. Katchanov et al, "Beam studies of EM-calorimeter prototype built of PbWO4 crystals", presented at the IV Int.Conf.on Calorimetry in High Energy, Sept.15-19, 1993 Isola Elba, Italy

[6] S. E. Derenzo, W. W. Moses, J. L. Cahon, R. C. C. Perera, Trans. Nucl. Sci. 37(1990), p.203-208

[7] L. Leciejewicz, Zeit. fur. Krist. 121 (1965) 158-164

[8] M. V. Korzhik, V. B. Pavlenko, V. A. Katchanov et al, "The scintillation mechanism in $PbWO_4$ crystals", Presented at MRS Spring Meeting '94, San Francisco, April, 1994; CMS TN/94-317

[9] I. Dafinei, E. Auffray, P. Lecoq, M. Schneegans, "Lead Tungstate for High Energy Calorimetry", Presented at MRS Spring Meeting '94, San Francisco, April, 1994

[10] P. Lecoq, M. Korzhik et al., Lead Tungstate (PbWO4) Scintillators for LHC EM Calorimetry CERN/CMS-TN 94-308, Submitted to Nuclear Instruments and Methods

ELECTROMAGNETIC CALORIMETER FOR KEK B-FACTORY DETECTOR

Kunio Tamai KEK, 1-1 Oho, Tsukuba, Ibaraki, 305 Japan.

Abstract

The electromagnetic calorimeter of the BELLE detector for the KEK B-factory is installed in the outermost position of solenoid field. The calorimeter is composed of a 3m long, 1.25m inner radius barrel section and two endcaps which consist of ~9,000 crystals. The typical size of the CsI(Tℓ) crystal is 30cm length($16.2X_0$) and $\sim 6 \times 6cm^2$ cross section of the truncated pyramid. Each crystal is read out by two PIN silicon photodiodes with $1 \times 2cm^2$ sensitive area.

1. INTRODUCTION

The KEK B-factory is constructed to detect CP-violation in B-meson decay. The accelerator is a two-ring electron-positron collider of energies 8GeV(e^-)×3.5GeV(e^+) in the existing TRISTAN tunnel. The expected luminosity is $10^{34}\text{cm}^{-2}\text{sec}^{-1}$. The BELLE detector is accomodated in the Tsukuba experimental hall at the north collision point.

The main purpose of the electromagnetic calorimeter is to detect γ-rays from B-meson decays with high efficiency and good resolution. Since one third of the decay products are π^0's which decay into γ's having relatively low energy, good performance below 500 MeV is especially important. There are also interesting few body B-meson decays such as $B \to K^*\gamma$ or $B^0 \to \pi^0\pi^0$ which produce high energy γ's up to 4GeV. The high energy π^0 detection requires the separation of two nearby γ's and a precise determination of their opening angle. High energy electron identification relies primarily on a comparison of the charged track momentum measured with central drift chamber and the energy deposited in the calorimeter.

In order to satisfy above requirements, we install a highly segmented CsI(Tℓ) array inside the solenoid magnet. Two silicon PIN photodiodes are used for the readout in the 1.5T field. The complete calorimeter comprises a 3.0 m long, 1.25 m inner radius barrel section and endcaps located at $z = 2.0$ m and $z = -1.0$ m from the interaction point. The overall configuration of the calorimeter is shown in Fig.1 and the geometrical parameters of each section are summarized in Table 1. The total solid-angle coverage is 91% of 4π.

Table 1. The geometrical parameters of the CsI calorimeter

	θ coverage	θ seg.	ϕ seg.	# of crystals
Forward Endcap	11.7° – 31.5°	13	48 – 128	1168
Barrel	32.2° – 128.7°	46	144	6624
Backward Endcap	130.8° – 158.3°	10	64 – 144	1024

Each crystal has a tower like shape and is arranged in a geometry so that it points to the interaction point with a small tilt angle of ~ 1.9°. The entire system contains 8816 CsI(Tℓ) counters and weighs 43 tons. The length of 30cm(16.2 X_0) has been selected to avoid the deterioration of energy resolution at high energy due to the fluctuation of rear shower leakage. The energy resolution at low energy is governed by the electronic noise.

Proc. Int. Conf. on Inorganic Scintillators and Their Applications, SCINT95,
1996, Delft University Press, The Netherlands

We aim at less than 200 keV incoherent thermal noise and less than 100 keV coherent noise picked up in the whole electronics chain. In this article, we will mainly describe the barrel part which is being constructed now.

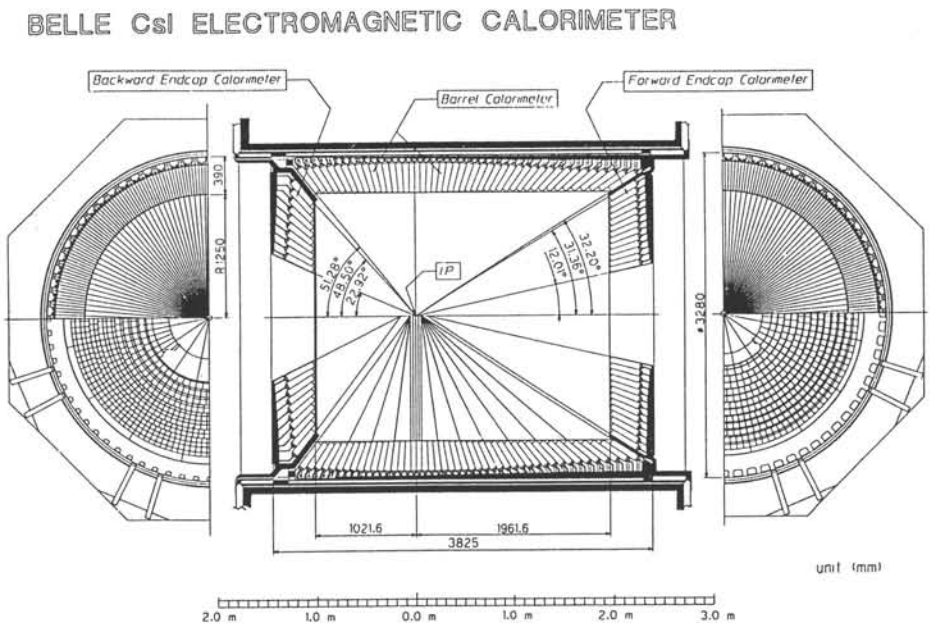

Fig.1 The overall configuration of Electromagnetic Calorimeter

2. CsI(Tℓ) CRYSTAL

The CsI(Tℓ) crystals must satisfy a number of stringent optical and mechanical requirements as in Table 2.

Table 2. Specification of CsI(Tℓ) crystals

Average Light Output	more than 0.27 of reference crystal for all crystals, more than 0.29 for 90% of total crystals.
Light Nonuniformity	less than 9% for all crystals, less than 7% for 90% of total crystals.
Cross Section	within +0 and -200μm from specified size.
Length (L)	within +1 mm and -1 mm from specified length.

The optical properties of each crystal is tested by irradiating with a collimated ^{137}Cs source at 9 points along the crystal and measuring the 662 KeV peak position obtained by a standard bialkali phototube. The light output of the crystal is defined as the average of 9 points with respect to the the light output of a small reference crystal (2.5cm ϕ and 2.5cm long). The (non)uniformity of the light collection is defined by

$$(non)uniformity = \frac{maximum - minimum}{average}. \quad (1)$$

The measurement of the crystal size is done by an automatic device with 20μm precision.

A single CsI(Tℓ) counter will be assembled as in Fig.2. All sides of the crystal, except for the end face for light readout, are covered by a layer of 200μm thick teflon made in Goretex. It is then covered by a layer of aluminized mylar with $\sim$ 25μm thickness for a light and electric shield. Four tapped holes are made on the end face of the crystal to fix an aluminum base plate to the crystal. Small derlin pieces are screwed into the holes and the base plate is fixed to the tapped holes made at the center of the derlin piece using a bolt. Two $1 \times 2cm^2$ photodiodes are glued at the center of crystal end surface via an acrylite plate of 1mm thickness. The use of acrylite plate as a buffer seems usefull as the direct glueing of the photodiode to CsI often fails after temperature cycling. After testing various glues, we decided to use ECOBOND 24 epoxy glue from Grace Japan Co. The curing takes about 3 hours at the room temperature and 200gr of weight is applied on the glue joint during this period. Assembled counters will be precalibrated by cosmic rays.

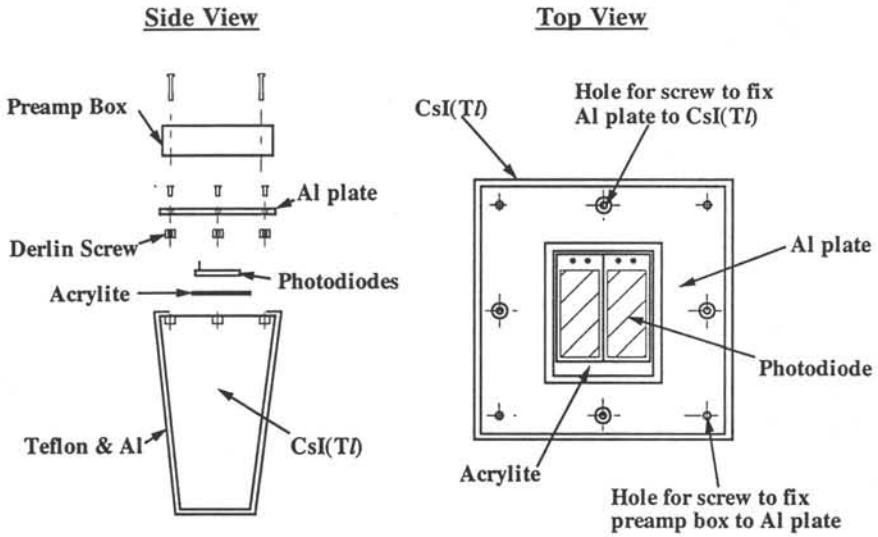

Fig.2 The mechanical assembly of the CsI(Tℓ) Counter.

Barrel crystals are installed in a honeycomb like structure formed by 0.5mm thick aluminum walls stretched between inner and outer cylinders. The outer cylinder forms a rigid structure to support the crystals. The inner cylinder and side walls are made of 1.6 mm thick aluminum to minimize the inactive material in front of the calorimeter. Eight crystals, four rows in θ and two columns in ϕ, are inserted in a cell. The overall support structure will be made gas tight and flushed with dry air to provide a low-humidity (5%) environment for the CsI(Tℓ) crystals. The cooling system by liquid coolant is provided for the preamplifiers which dissipate $\sim$2KW in total.

3. READOUT ELECTRONICS

Each CsI(Tℓ) counter is read out by an independent pair of silicon PIN photodiodes(PD), and charge sensitive preamplifiers attached at the end of crystal. A block

diagram of the readout electronics is given in Fig.3. The two outputs are transmitted by a 10m long 50Ω twisted pair cables to a summing and shaping module. The summed signal is split into the main ADC input and the trigger electronics. The ADC signal is shaped and converted into time information by a charge-to-time(Q-to-T) converter chip. The output of the Q-to-T is transmitted on a twisted pair to a TDC module in the electronics hut for digitization. The trigger signals from ~16 crystals are summed up and shaped for the triggering logic. The maximum energy digitization of the TDC is 18bits and the integral nolinearity is expected to be $\sim 0.1\%$.

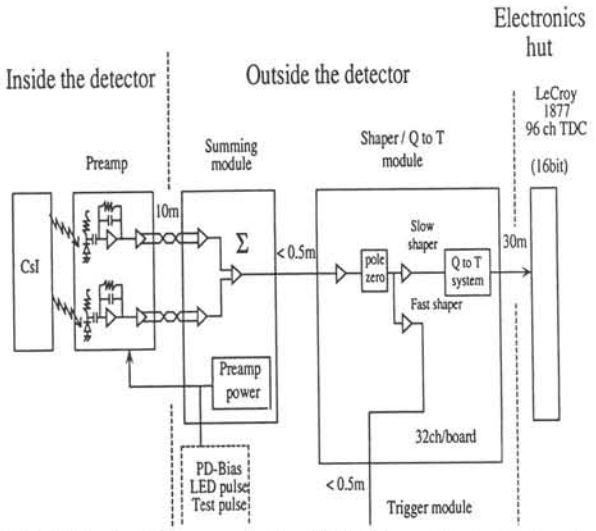

Fig.3 A block diagram of the CsI(Tℓ) readout electronics.

We must take into account the possible failure of the electronics parts, especially the photodiode and preamplifier which are installed in a vessel together with the crystals. The disassembly of the BELLE detector is the only way of access to inside the calorimeter for repairs since the structure supports all inner detectors. The failure analysis of the photodiode and preamplifier was made and confirmed the reliability. Further, a dual readout scheme shown in Fig.3 is adopted to address this part.

PHOTODIODE. Our photodiode 'S2744-08' was developed recently by Hamamatsu Photonics to achieve $\sim 20\%$ higher photo-sensitivity. This has $1 \times 2cm^2$ sensitive area and its 300μm wafer is fully depleted at reverse bias voltage of 70V. The reliability of the photodiode was investigated by operating them at 70V bias and $80C°$ for 500 hours, and by 20 temperature cycles between -20C°(30min.) and 80C°(30min.). The long term stability was independently confirmed at KEK after the same 500 hours operation of 20 samples. No failure was found and an increase of leakage curren(I_d) was less than 0.3nA. The radiation hardness was also checked by γ rays from ^{60}Co. The increase of leakage current at 6Gy and 68Gy exposure are less than 5% and 20%, respectively. No significant change of the capacitance and photo-sensitivity were observed even at 68Gy.

The 14,000 photodiodes were recently purchased. All photodiodes were burned at 70V reverse voltage and at 80C° for 50 hours and inspected before the shipping. We selected a total of 150 samples, 5 or 10 pieces from each production lot, and measured the photo-sensitivity S(mA/W) over all wave lengths. The distribution of photo-sensitivity(S) at

λ =560nm is shown in Fig.4(a). The average and rms spread is $< S >$ =386±6(mA/W). This corresponds to the quantum efficiency of $\epsilon = 85.5 \pm 1.3\%$.

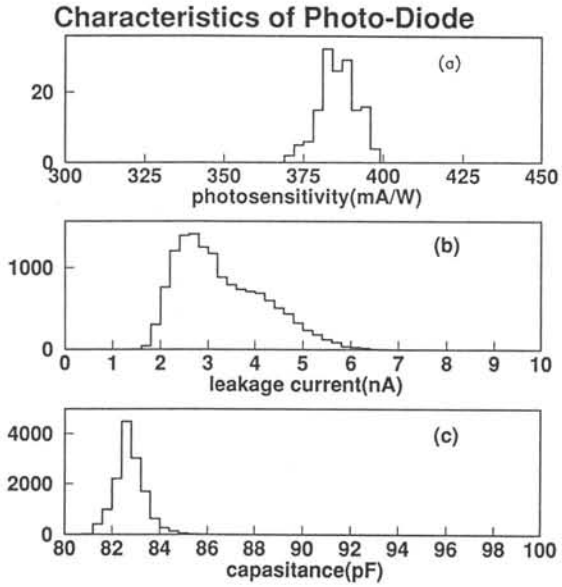

Fig.4 The characteristics of 14,000 photodiodes; (a)photosensitivity S(mA/W), (b)leakage current I_d(nA) and (c)junction capacitance C_j(pF) at 70V bias and 25C°.

We measured the leakege current (I_d) and capacitance (C_j) of all photodiodes at 70V bias voltage and at a temperature of 25C°. The averages and rms are $< I_d >$ =3.31±0.92(nA) and $< C_j >$ =82.8±0.7(pF) . The distributions are given in Fig.4(b) and (c). We observed that the leakage current depends on the production lot; the broad distribution of the current is caused by the lot dependence. All photodiodes satisfy our specification.

PREAMPLIFIER. In designing the charge integration preamplifiers, we have taken care of not only the electronic noise but also the long term reliability and dynamic range of linearity. The circuit is realized in a 4-layer hybrid chip of $1.8 \times 4.5 cm^2$. Each photodiode output is recieved by the two hybrid chips which are accomodated in an aluminium shield case. The two chips are completely independent each other such that the failure of one readout channel does not affect the other. The mother board is equipped with a high luminosity LED of λ =570nm wave length to monitor the response of photodiodes. The shield case is placed just behind the photodiodes to reduce pickup noise and parasitic capacitance due to the readout cable.

As an input FET, we used 2SK932-22 manufactured by SANYO. It has a gate leakage current <1nA, input capacitance of 10pF and transconductance of ~30mS at a drain current of 4mA. The deviation from linearity is shown in Fig.5(a) as a function of preamplifier output voltage. The amplifier covers the linear range of up to 4.6V×1.3pF=6pC, which is equivalent to 8GeV energy deposit in the highest light yield crystal. The deviation from linearity is shown in Fig.5(a) as a function of the output. In Fig.5(b), we show the shaping time dependence of the equivalent noise charge(ENC) for 3 cases; with no load, with 82pF dummy load and with the photodiode. For these measurements, the

^{241}Am X-ray peaks absorbed in the photodiode is used for the calibration. The performance of the hybrid chip is summarised in Table 3. The ENC of 560e corresponds to an energy resolution of 0.2MeV for a crystal with typical light yield. The resolution of the two photodiodes readout as shown in Fig.3 is expected to be below 0.15MeV.

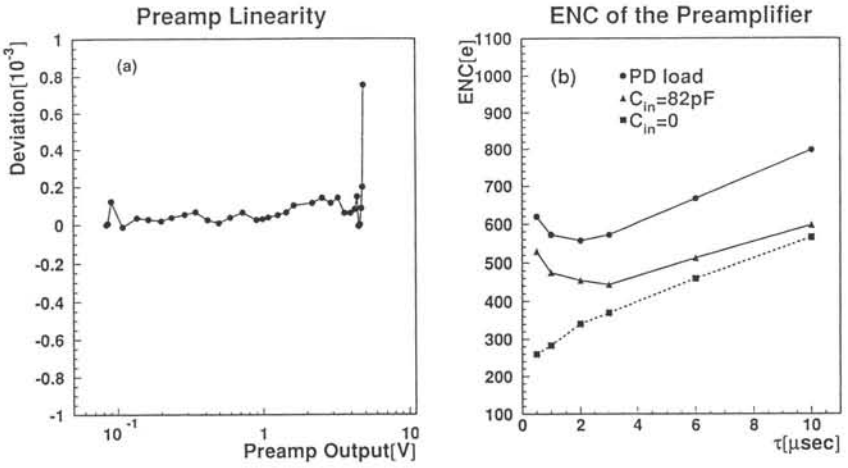

Fig.5 The performance of preamplifier. (a) Deviation from linearity as a function of the preamplifier output voltage. (b) Equivalent noise charge(ENC) as a function of shaping time $\tau(\mu$sec) for different preamplifier loads: a photodiode, capacitance of 82pF and 0pF(=no load).

Table 3. The electronic characteristics of preamplifier.

power	125mW
ENC with a PD ($\tau = 2\mu sec$)	560e
ENC with a PD ($\tau = 1\mu sec$)	575e
decay time	$65\mu sec$
charge to voltage conversion	-1V/1.3pC
dynamic range of the output	$0\sim -4.6$V
nonlinearity in the dynamic range	$< 0.03\%$

The reliability and stabilty of 50 chips and 25 mother boards were examined by (1)10 temperature cyclings, (2)1,050 hours of operation at 85C° and (3)1,000 times on/off switching of the 70V PD bias. The temperature cycle for 25 chips and mother boards is 90C° (30min.)$\rightleftharpoons$ 25C°(5mim.)$\rightleftharpoons$ -40C°(30mim.) and the cycle for the remaining 25 chips is 125C°(30min.)$\rightleftharpoons$ 25C°(5mim.)$\rightleftharpoons$ -40C°(30mim.). No failure was found throughout the tests. The deterioration of the ENC is less than 10% and the change of pulse height is within 0.6% in spite of the hard condition of the test. The prototype satisfies our requirement.

4. BEAM TEST RESULTS AND EXPECTED PERFORMANCE

We performed a beam test of CsI(Tℓ) at the KEK 12GeV proton synchrotron. Crystals were exposed to pion and electron beams between 0.25 and 3.5 GeV. The beams were injected at the center of a 5×6 matrix of CsI(Tℓ) crystals. Two array configurations, a

normal array reproducing central part of the barrel, and a staggered array simulating the edge of barrel, were tested. The beam position on the crystal was measured by a drift chamber with a precision of $\pm$1mm. The energy was obtained by the summation of energies deposited in 5×5 array. The energy resolution for electrons is shown in Fig.6. A negligible deterioration in the staggered array can be seen. The position resolution is shown in Fig.7 which was obtained from the energy weighted mean average position of the crystals plus a minor correction. The position resolution is good near the boundary of the crystals where shower sharing tends to have a large imbalance. The e/π separation capabilities were tested by injecting π^+ and π^- beams at the center of the array. Misidentified pions as electrons are defined as the events, for which the energy deposit is within $\pm 3\sigma_E$ from the expected energy deposit of electrons, where σ_E is the electron energy resolution. The results for π^+ and π^- are shown in Fig.8. The π^- misidentification probability is found to be less than 1% for momenta above 1 GeV/c where the identification is essential for the b flavor tagging. A study is under way to improve the results by taking the diffrence of lateral shower shape for electrons and pions into account.

The effect of materials on the performance of the calorimeter was studied by Monte Carlo simulation. The energy dependence of the resolution is well reproduced by

$$\sigma_E/E(\%) = 0.67/\sqrt{E[GeV]} \oplus 1.8 \tag{2}$$

for the case of no inner detector where the summation $\oplus$ means a quadratic sum. The expected energy and position resolution below 5GeV including all inner detectors are expressed by

$$\sigma_E/E(\%) = 1.26 + 0.63/\sqrt{E[GeV]} \quad if \quad E < 1GeV \tag{3}$$

$$= 1.89 \quad E > 1GeV \tag{4}$$

$$\sigma_x(cm) = 0.728 - 0.242 \ln E[GeV]. \tag{5}$$

The detection efficiency for γ's increases gradually from $\sim$ 70% to $\sim$ 85% as the energy changes from 50MeV to 5GeV.

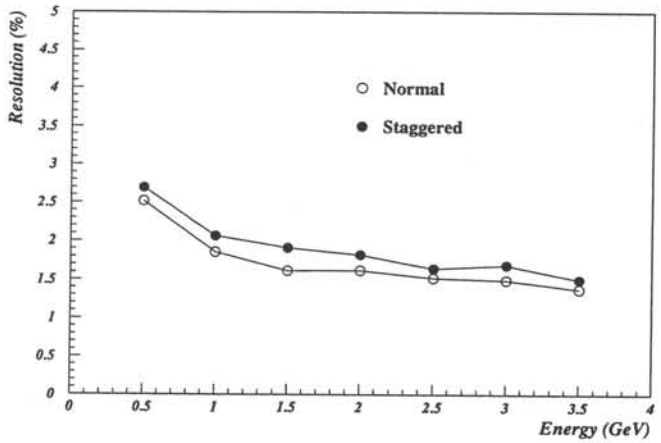

Fig.6 The energy resolution obtained from 5×5 matrix of 30cm long CsI(Tℓ) crystal.

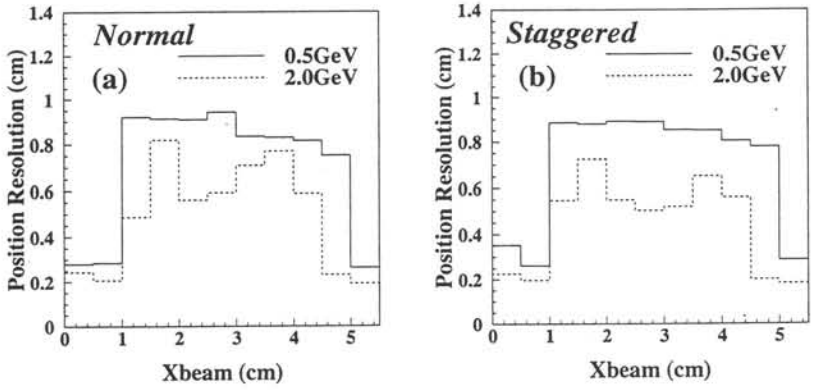

Fig.7 The position resolution dependence on the electron injection point(X_{beam}) of a crystal for (a) normal and (b) staggered array configuration. The surface of crystal is $0<X_{beam}<5.5$cm and the center is $X_{beam} \sim 2.8$cm.

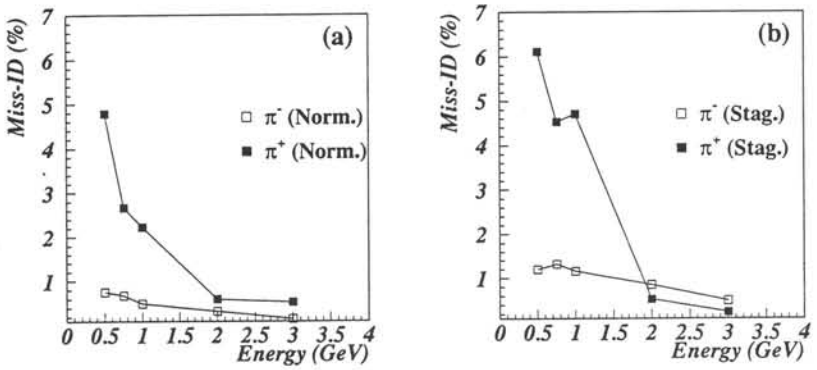

Fig.8 The probability to misidentify a pion as an electron for (a)normal and (b)staggered array configuration.

ACKNOWLEDGEMENT I would like to express my gratitude to companies concerned as well as all members of the electromagnetic calorimeter collabolation and M. Fukushima for continuous efforts in these results.

REFERENCES

1. Technical Design Report; A Study of CP Violation in B Meson Decays, The BELLE Collaboration, KEK Report 95-1, April 1995.

2. Letter of Intent for A Study of CP Violation in B Meson Decays, The BELLE Collaboration, KEK Report 94-2, April 1994.

THE ELECTROMAGNETIC CALORIMETER TAPS
- photon and particle detection with BaF_2 -

R. Novotny
II. Physikalisches Institut, Universität Giessen, D-35392 Giessen, Germany
and for the TAPS-Collaboration: Bratislava,GANIL,Giessen,GSI,KVI,Münster,Valencia

ABSTRACT

The spectrometer *TAPS* - comprising 384 individual plastic and BaF_2 scintillation detectors - is designed to identify and measure high energy photons. The calorimeter has detected photons up to an energy of 15 GeV with high resolution ($\sigma/E = 2.5\%$ at 1GeV). Neutrons and charged particles are identified by pulse-shape (PSA) and time-of-flight techniques (TOF) with high efficiency. The modification into modular plastic-BaF_2-phoswich telescopes allows improved particle spectroscopy at medium energies simultaneously to the photon calorimetry.

THE CONCEPT

The modular detector system TAPS (**T**wo **A**rm **P**hoton **S**pectrometer) has been designed to investigate high energy photons as well as neutral mesons (π^0,η, ω) in relativistic and ultra-relativistic heavy ion collisions or photonuclear reactions, respectively [2]. The point of impact and the total energy of the electromagnetic shower have to be determined precisely. The high multiplicity of hadronic reaction products requires an efficient discrimination against charged/neutral particles. BaF_2 has been the most appropriate scintillator material due to its high light output, fast response and intrinsic selectivity of the pulse-shape to the nature of the impinging probe [3]. The modularity of the device and the flexibility in the geometrical arrangement allow to perform a very broad range of experiments at different accelerator facilities (*CERN-SPS, GANIL, GSI, MAMI*).

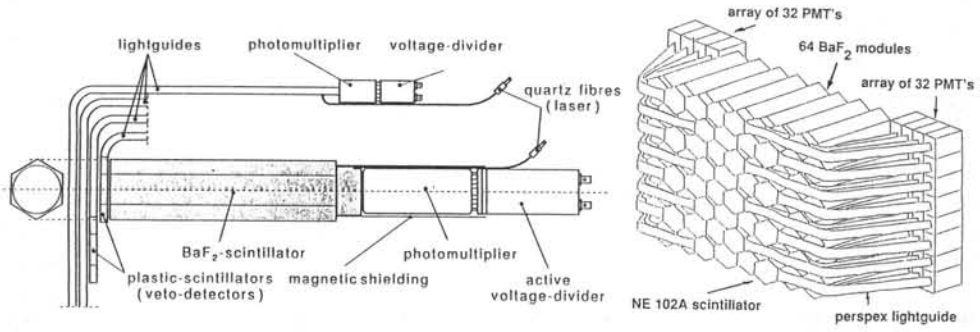

Figure 1: The geometry of the individual module (left). The fully assembled detector block consisting of 64 plastic-BaF_2 scintillator telescopes (right).

Proc. Int. Conf. on Inorganic Scintillators and Their Applications, SCINT95,
1996, Delft University Press, The Netherlands

THE DETECTOR COMPONENTS

An individual detector consists of a 25cm long ($12X_0$) hexagonally shaped BaF_2 crystal (inscribed circle $\varnothing = 5.9$cm) [4] and of a 0.5cm thick plastic scintillator (NE102A) of slightly larger diameter in front. The fully assembled detector and a typical geometrical arrangement of 64 individually read-out telescopes are illustrated in Fig. 1. The optical transmission and the response to low energy γ-sources are carefully measured for all crystals. The obtained averaged specification parameters are listed in Tab. 1 in comparison to the required limits.

PARAMETER		test result	specs
optical absorption length Λ [cm]	at $\lambda = 202$ nm	**41.7**	**18.0**
	at $\lambda = 220$ nm	**76.7**	**28.0**
	at $\lambda = 300$ nm	**488.7**	**292.0**
^{137}Cs (662 keV):	ΔE_{fast} / E [%]	**35.3**	**45.0**
	ΔE_{tot} / E [%]	**11.5**	**12.5**
	amplitude ratio fast/slow (at Δt=40ns)	**9.5**	**7.0**
intrinsic α-radioactivity	[cts/s/module]	**15.9**	**100.0**

Tab. 1: Test results obtained for 450 accepted crystals compared to the required specifications.

The modularity of *TAPS* allows a flexible arrangement. The detectors can be grouped either in blocks mounted on movable towers or placed in a horizontal plane or can form a large annular hexagonal supercluster. The standard charged-particle-veto (CPV) is fixed to the block geometry as shown in Fig. 1. The processing of the BaF_2-signals foresees the determination of the time-of-impact (TOF-analysis) and the integration of the total (2μs) as well as the fast scintillation component (40ns) separately to perform also the pulse-shape analysis in addition.

THE RESPONSE TO PHOTONS AND PARTICLES

The photon response of *TAPS* has been determined in the energy regime up to 800 MeV using monochromatic photons provided by the tagging facility at *MAMI* [5]. The excellent energy resolution for a collimated photon beam (Φ=1.3cm) amounts to $\sigma/E = 0.59\% \; E_\gamma^{-1/2} + 1.9\%$ (E_γ given in GeV) and $\sigma/E = 0.79\% \; E_\gamma^{-1/2} + 1.8\%$ for the fast component, respectively. The point of impact of the photon can be reconstructed from the e.m. shower with a resolution $\Delta x < 2$cm.
The short decay time and high light output of the fast scintillation component allow time resolutions better than σ=85ps. Therefore, particle identification and even energy determination become possible exploiting TOF-technique at a typical distance of 1 - 2m from the vertex using a start counter system. Low and medium energy neutrons, which react via (n,γ)-processes with BaF_2 and induce a signal shape identical to that of photons, can only be identified by TOF. The interaction of high energy neutrons via (n,p)- and (n,X)-reactions can be tagged by PSA of BaF_2 in anticoincidence with the CPV. The total neutron efficiency approaches 17% above 750 MeV kinetic energy of the neutron.
Spectroscopy of light charged particles below 100MeV/u can be performed with resolutions between 2 - 4% (FWHM). At higher energies non-linearities due to quenching and secondary reactions have to be taken into account. Charged pions (π^+) have been tagged by the inspection of the subsequent μ^+-decay of the stopped pion. Particle identification by means of

ΔE-E correlations requires the measurement of the specific energy loss in the CPV. Since the contribution of the fast BaF_2-component diminishes with the increase of the energy density deposited by the ionizing particle the PSA becomes possible. Fig. 2 shows the yield of the fast component as a function of the total light for neutral and charged events. In particular, the lower branch in the spectrum of neutral events represents protons recoiled within the crystal by interacting high energy neutrons.

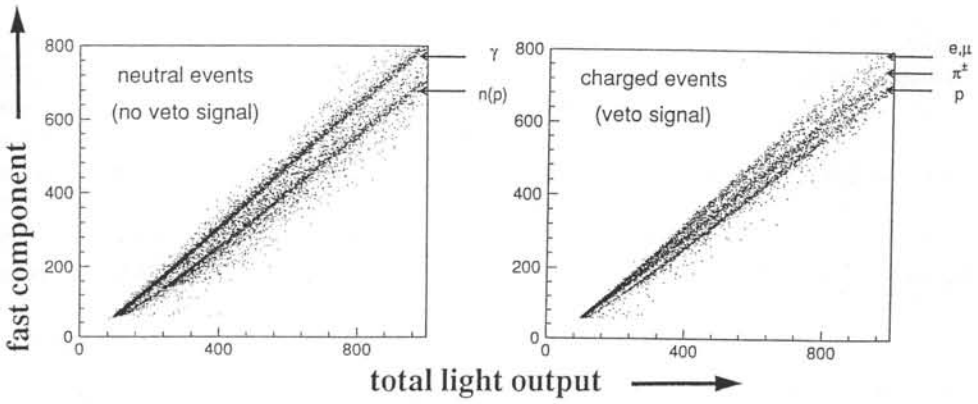

Figure 2: Scatter plot of the fast component versus the total light output shown for neutral (l) and charged (r) events in BaF_2 selected by the CPV. The energy range is approx. 300 MeV.

The particle sensitivity at medium energies improves by a fast plastic scintillator (d=15mm) coupled to the front face of the BaF_2 in phoswich technique. Only the energy loss of charged particles in the plastic layer leads to a substantial increase of the total fast light output and provides mass and charge identification based on ΔE-E correlations. The measurement of neutral events in the BaF_2 remains unaffected. In addition, the individual phoswich modules can be adapted to any geometry such as a large annular hexagonal cluster.

SUMMARY

The spectrometer TAPS - designed for high energy photon detection - is operating successfully since several years and allows high resolution photon and particle spectroscopy due to the excellent and unique properties of the fast inorganic scintillator material BaF_2.

REFERENCES

[1] R.Novotny, IEEE Trans. Nucl. Sci. 38 (1991) 379
[2] R.Novotny et al., Nucl.Instr. and Meth. A262 (1987) 340
[3] manufactured by Dr. K. Korth, Kiel , Germany
[4] A.Gabler et al., Nucl.Instr. and Meth. in Phys.Res. A346 (1994) 168

This work has been supported by BMFT, DFG (SFB 201) and GSI.

THE ROLE OF INORGANIC SCINTILLATORS IN NEUTRON DETECTOR TECHNOLOGY

N.J. RHODES and M.W. JOHNSON
ISIS Facility, Rutherford Appleton Laboratory, Chilton Didcot, Oxon. OX11 0QX U.K.

ABSTRACT

The European Spallation source, ESS, is a proposal to provide the European Community with a state of the art source of neutrons in the 21st century. Based on a 5 MW accelerator, ESS will provide neutron fluxes 30 times brighter than ISIS, the world's most powerful neutron source to date. ESS presents new challenges for neutron scattering instrumentation. This paper describes the role of inorganic scintillators in current neutron detector systems and the detector characteristics resulting from the use of these scintillators. The implications for higher neutron fluxes from ESS for detector performance and desired characteristics of future neutron sensitive scintillators are discussed.

INTRODUCTION

Neutrons provide scientists and engineers with a powerful tool to examine the structure and dynamics of materials on an atomic/molecular scale. Prominent diffraction experiments have included the structure of high temperature superconductors, phase transitions in fullerines and the location of water molecules in the structure of DNA. Inelastic scattering techniques can be used to examine quantum tunneling, molecular translations, rotations, vibrations, lattice modes and transitions within the electronic structure of materials, [1]. Industrial uses of neutrons include the measurement of residual stress in engineering materials and the structure of surfactant monolayers at the air liquid interface, [1,2]

Neutron scattering experiments seek to determine the spatial and temporal distribution of neutrons scattered from samples of interest. Historically neutron scattering instrumentation has been dominated by gas proportional counters. In the last ten years scintillator technology has provided neutron scattering instruments with a range of detectors specifically designed to meet the requirements of individual instruments. This is particularly evident at ISIS, the world's most intense pulsed neutron source. In these detectors the scintillator is viewed by photomultiplier tubes, PMTs, either directly or by fibre optic coded arrays. The PMT outputs are subsequently amplified, discriminated and decoded before passing on to data acquisition electronics. In assessing the performance of these detectors a number of characteristics need to be considered. These include the following:

1) Neutron detection efficiency as a function of energy.
2) Sensitivity to gamma radiation.
3) Intrinsic detector background.
4) Spatial resolution and detector geometry.
5) Pulse pair resolution, ppr.
6) Stability of detector characteristics with respect to time.

Proc. Int. Conf. on Inorganic Scintillators and Their Applications, SCINT95,
1996, Delft University Press, The Netherlands

7) Ease of maintenance.
8) Cost.

Neutron detection efficiency is dependent on the energy of the incident neutrons as shown in Equation 1.

$$Eff = \varepsilon (1 - \exp (- k t / \sqrt{E}) \qquad \text{Equation 1}$$

Eff is the neutron detector efficiency, k is a constant dependent on the neutron absorption cross section and the density of the absorber atom, t is the thickness of the scintillator and E is the energy of the incident neutron. ε is a constant relating the difference between neutron absorption efficiency and neutron detection efficiency. The efficiency with which light is generated from a neutron event, the efficiency of light transmission to the PMTs and the quantum efficiency of the PMTs can all result in a reduction in neutron detection efficiency. Neutron absorption of a sample will generally lead to an (n, γ) reaction. It is extremely important that any neutron detector has a minimal sensitivity to γ radiation to avoid degradation of the neutron scattering data. Pulse pair resolution is a measure of the shortest time interval in which successive neutron events can be individually recorded. It is a means of comparing the temporal response of detectors.

Neutron scattering experiments are typically concerned with neutrons ranging in energy from 1 meV to 100 eV. At these energies the primary ionization of atoms by neutrons is negligible and neutron detection is by the use of neutron capture reactions. The most important neutron capture reaction for scintillator detectors to date is given in Equation 2.

$$^{6}Li + {}^{1}n \longrightarrow {}^{3}H + {}^{4}He \quad 4.79 \text{ MeV} \qquad \text{Equation 2}$$

There are two types of scintillator in common use for the detection of thermal neutrons; GS20(Ce) glass scintillator and zinc sulphide ZnS(Ag)/^{6}Li scintillator, [3,4]. GS20 is a cerium activated aluminosilicate glass containing lithium oxide. ZnS/^{6}Li scintillator is an amorphous mixture of zinc sulphide and lithium fluoride held together with a resin binder. In both these scintillators the lithium compound is enriched to +95% with ^{6}Li. The properties of these scintillators have been described by Spowart, [5,6]. Detectors based on glass scintillator have high neutron detection efficiency and good pulse pair resolutions, ~70 ns, but high gamma sensitivities and intrinsic detector backgrounds. In contrast, ZnS/^{6}Li scintillator detectors can exhibit extremely low gamma sensitivities and intrinsic detector backgrounds. However the pulse pair resolution of these detectors, at 2 μs, is only moderate. Furthermore, the scintillator is opaque and judicious use of detector geometry is required to attain reasonable neutron detector efficiencies without compromising desired detector characteristics. Detector characteristics are not only governed by the choice of scintillator, but also by the manner in which the scintillator is used.

Scintillator technology offers a very flexible medium for optimizing detector characteristics to meet the specific requirements of a neutron scattering instrument. An intricate detector geometry is available, neutron detector efficiency can be tailored to meet the energy ranges of a particular instrument, high pulse pair resolution can be realized, dependent on the choice of scintillator, while advantage can be taken of a solid neutron absorbing medium to minimize parallax errors. These points are illustrated by some of the developments in neutron scintillator detectors described below.

DIRECTLY VIEWED SCINTILLATOR DETECTORS

The SANDALS and IRIS instruments at ISIS both operate linear position sensitive ZnS/^{6}Li scintillator detectors in which the PMTs directly view the scintillator elements. In both these detectors, scintillator elements are contained in aluminized mylar light guides and the PMTs are displaced laterally a half tube diameter from the light guide axis. Neutron events in any one scintillator element are determined by the coincident output from adjacent pairs of PMTs. This PMT arrangement allows detector noise due to random PMT events to be largely eliminated. Essential differences between the SANDALS and IRIS detectors are associated with the arrangement of the scintillator in the detector elements.

The SANDALS elements consist of 20 strips of ZnS/^{6}Li, 200 mm x 10 mm x 0.4 mm stacked one behind the other and separated by crown glass strips of similar dimensions. This arrangement gives a neutron path length through the scintillator element of 8 mm. It yields a high neutron detection efficiency at 10 eV, while maintaining a 10 mm spatial resolution and moderate noise characteristics, Table 1.

In the IRIS detector the scintillator strips are non-overlapping, but are oriented at an angle of 60 degrees to the neutron beam giving a neutron path length of 0.8 mm through the scintillator. This arrangement has a much lower neutron detection efficiency, but the gamma sensitivity and intrinsic detector background are excellent, Table 1.

FIBRE COUPLED SCINTILLATOR DETECTORS

A new scintillator detector for the high resolution powder diffractometer, HRPD, is now being commissioned at ISIS. This detector uses zinc sulphide/^{6}Li scintillator viewed by fibre optic arrays arranged in $^{2}C_{n}$ codes. The use of scintillator technology has allowed concentric detector geometry that accurately approximates the Debye Scherrer cones of diffraction. Such geometry largely eliminates geometrical contributions to the profile line shape of Bragg peaks. In addition, the fibre code has been arranged to enable the data to be collected separately from 60 mm wide orthogonal strips across the detector surface. This yields improved spatial resolution in single crystal diffraction experiments on HRPD. Neutron detector efficiency has been enhanced by configuring individual scintillator elements in a 'V' format. This increases the neutron path length through the scintillator to 1.3 mm, while maximizing collection of the resultant scintillator light. Detector characteristics are given in Table 1.

An example of the excellent signal/noise of this ZnS/^{6}Li scintillator detector was obtained on HRPD from a cadmium sample. Despite the high flux of gamma onto the detector from neutron absorption in the cadmium, diffraction peaks from cadmium were clearly seen as shown in Figure 1. Because of the high neutron absorption cross section of cadmium above 0.3 Angstroms this data is effectively being recorded from the first 40 μm of the sample. No peaks were observed in a similar glass scintillator detector where the background was a factor of 10 higher, Figure 1. This result serves to illustrate the importance of gamma sensitivity and intrinsic detector background in assessing neutron detector performance.

Fibre coding techniques can be extended to give a more conventional two dimensional position sensitive detector as illustrated by the 4096 SXD detectors operating at ISIS. Each detector consists of a single sheet of ZnS/^{6}Li scintillator located onto the front of a mylar light

guide grid. The grid divides the detector into a 64 x 64 array of pixels, each of 3 mm x 3 mm resolution.

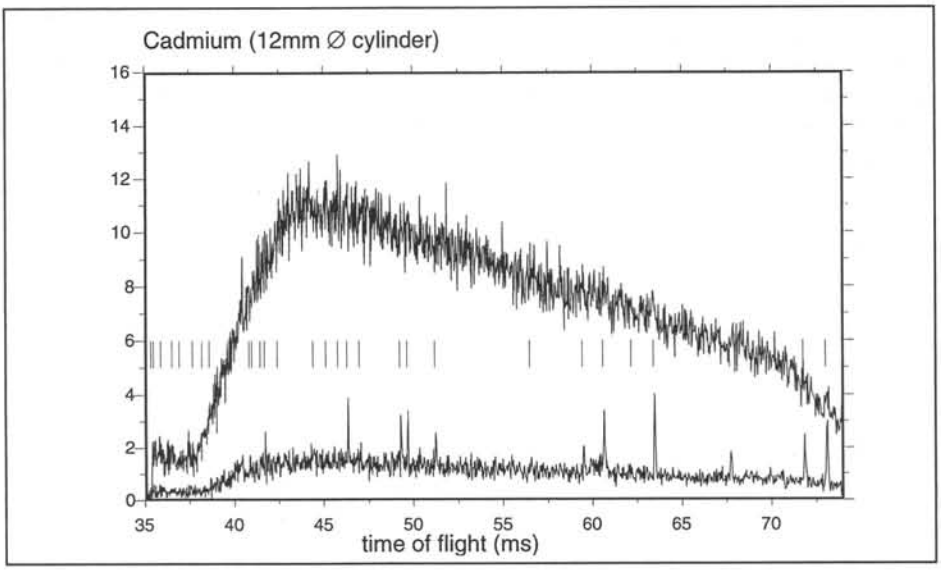

Figure 1. Time of flight spectra recorded on HRPD at ISIS. The lower spectrum is from four ZnS/^{6}Li detector modules and shows Bragg diffraction peaks from a cadmium sample. The upper trace was recorded at the same time using a single detector module of similar geometry, but based on glass scintillator. The trace is dominated by high background and no cadmium data is apparent.

Each pixel is viewed by four 1 mm diameter fibre optic light guides arranged in a quad coincident code. In this manner 4096 pixels are coded by 32 PMTs and associated electronics. Detector characteristics are given in Table 1 and show exceptionally low gamma sensitivities and low intrinsic detector backgrounds. Of prime importance to SXD is the thickness of the active detector element which is only 0.4 mm. Thus a short 250 mm sample to detector distance can be used on SXD without causing a significant parallax error and enabling a large solid angle to be covered.

ANGER CAMERA DETECTORS

At Argonne, [7], and more extensively at Julich, [8,9] the Anger camera principle has been used to provide one and two dimensional position sensitive detectors based on glass scintillator. These detectors use a light disperser designed so that a scintillator event illuminates a small subset of a PMT array. The magnitudes of the illuminated PMT outputs are used to determine the position of an event in the neutron scintillator. Characteristics of these detectors have recently been reviewed, [10]. Neutron detection efficiency and pulse pair resolution are superior to the SXD type detectors described above, but gamma sensitivity and intrinsic detector backgrounds are also high. Julich has also experimented with single crystalline ^{6}LiI(Eu), [8]. This gives 12 times the light output of the glass scintillator and has very low gamma sensitivity. However, ^{6}LiI(Eu) is hygroscopic, encapsulation is required and the decay time constant at 1.2 μs is relatively long.

THE EUROPEAN SPALLATION SOURCE.

The European Spallation Source, ESS, is a proposed third generation source designed to meet the needs of European scientists and technologists in the 21st century. The current status of the project has recently been described by Taylor, [11]. Recommendation that a design study be initiated for a next generation neutron source was given by the Neutron Study Panel in the Large Facilities Report to the Commission of the European Community (CEC) in 1990. In a joint initiative by KFA Julich and Rutherford Appleton Laboratory, a series of meetings was held to explore options for such a source. Meetings on Accelerators, Instrumentation and Techniques, and Target Technologies were carried out from September 1991 to February 1992. These meetings focused on the provision and utilization of an advanced high powered accelerator driven pulsed spallation source and the scientific opportunities it would herald. This study has attracted considerable support throughout Europe. A two year feasibility study to be completed in 1996 is now underway. It is partially funded by the CEC Human Capital and Mobility Programme with the remaining funds coming from the participating institutes including those of Austria, Denmark, Germany, Italy, Netherlands, Sweden, Switzerland and UK. The technical project leader is Dr. H. Lengeler from CERN and the science coordinator is Professor J. Finney from UCL UK. The purpose of this study is to prepare a conceptual design for the accelerator, establish feasibility and reliability, identify areas of research and development required to realize the project and produce a costing at the 20% precision level.

The reference design of the ESS is shown in Figure 2. It is based on an H^- linear accelerator and a pair of accumulator rings. Two 60 mA H^- ion sources feed the linac which accelerates the ions to 1.334 GeV. The H^- ions are then injected into two accumulator rings, converted into protons by the action of a stripping foil and sequentially extracted. The accumulator rings enable the time span of the proton pulse onto the target to be constrained to 1 μs. Two target stations are envisaged, a 50 Hz, 5 MW, high intensity target and a 10 Hz, 1 MW target for high resolution and cold neutron instrumentation.

The benefits of the ESS to the neutron user community have already been discussed [12]. The enhanced temporal brightness of the ESS will allow the source to make a major impact on established fields and substantial contributions to new areas of research. ESS will allow the use of smaller samples and short time kinetic experiments. It will allow higher spatial and temporal resolutions coupled with a wider dynamic range in energy and momentum transfer which are needed to probe more complex systems, for example macromolecular systems and the development of new materials. Under consideration in this paper is the impact of third generation neutron sources like the ESS on future neutron detector systems.

SCINTILLATOR REQUIREMENTS FOR THE FUTURE

There are a number of new detectors based on scintillator technology being developed for the ISIS instruments. These include a two dimensional position sensitive detector for the new reflectometer SURF. Larger diameter optical fibres are being used in a high angle detector for the LOQ diffractometer. Use of a scintillator detector with an active detector thickness of only 0.4 mm will lead to an improved timing resolution for the time focused crystal analyzer. In addition detectors based on 'V' shaped ZnS/^{6}Li scintillators are being developed for a new Paris-Edinburgh high pressure cell detector and for a powder diffractometer for OSIRIS. In both cases the advantage of flexible scintillator geometry offered by scintillator technology is exploited.

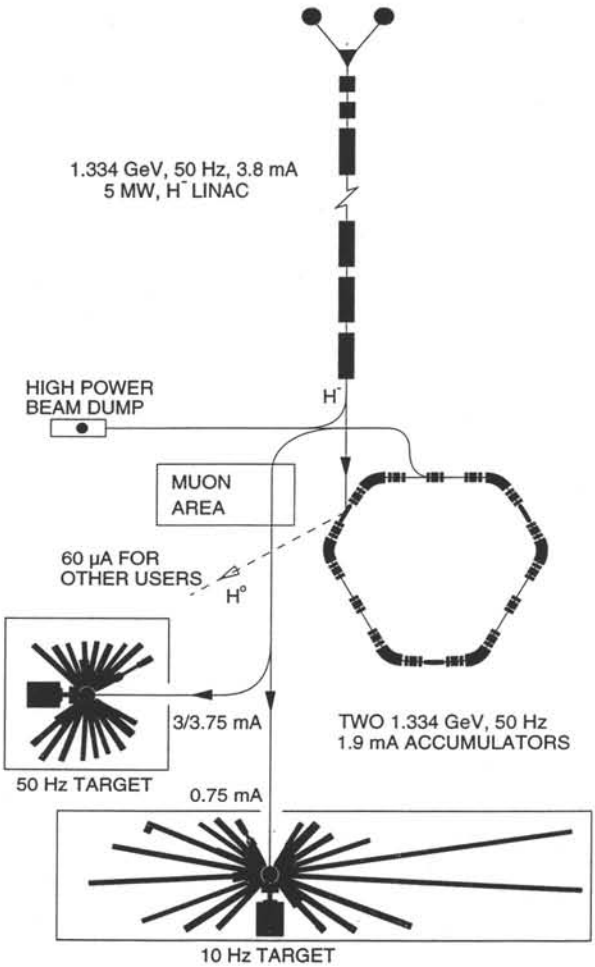

Figure 2. Schematic Layout of the European Spallation Source

Hutchinson has proposed an interesting scintillator detector design for a wide angle neutron detector at the High Flux Isotope Reactor at Oak Ridge. In this detector ZnS/^{6}Li scintillator is coupled to an array of 2 mm x 2 mm wavelength shifting optical fibres. This gives rise to a linear position sensitive detector, 80 mm high with 2.5 mm resolution, [13].

For sources like the ESS current detector technologies will probably be sufficient to cope with the count rates from inelastic instruments. In contrast the elastic instruments are likely to require dead times in the range of 10 - 50 ns, [14]. Existing PMT technology and counting electronics can already cope with these count rates. The limiting feature is the decay time constant of the scintillator. There are a number of scintillators based on cerium activators, [15] which could be made neutron sensitive and which would achieve decay time constants ~50 ns. However a stringent requirement for such systems will be a low sensitivity

to gamma radiation. Experience at ISIS suggests that this should be in the region of 10^{-6} to 10^{-8} for 1 MeV gamma. A mechanism for reducing gamma sensitivities in such scintillators has been proposed, [15]. For instruments with the most demanding resolutions inorganic scintillators with alternative activators or organic scintillators incorporating appropriate neutron absorbers will be required.

CONCLUSION

At the present time ZnS/^{6}Li scintillator is satisfying many of the needs of the ISIS scintillator detector suite. Moderate improvements in transparency, light output and decay time constant of this or a similar scintillator will ensure that these needs are maintained. Construction of the ESS will have a major impact on condensed matter research. New detector systems will have to be developed to cope with the high intensity of this source. For scintillator detectors a substantial improvement in decay time constant is required. However ease of use, and low gamma sensitivity and intrinsic detector background associated with ZnS/^{6}Li scintillator all need to be maintained. The development of such scintillators must become a high priority if the flexibility in detector design currently being enjoyed at ISIS is to be maintained at future neutron sources.

INSTRUMENT	IRIS	SANDALS	HRPD	SXD
MODULES x ELEMENTS	2 x 51	42 x 20	8 x 120	2 x 4096
TYPE	ZnS/^{6}Li SCINT. PAIR CODED	ZnS/^{6}Li SCINT. PAIR CODED	ZnS/^{6}Li SCINT. $^{2}C_{n}$ FC*	ZnS/^{6}Li SCINT. QUAD. FC*
ELEMENT SIZE/MM	50 x 12	200 x 10	45° x 5	3 x 3
NEUTRON EFFICIENCY	36 % at 1A	1.7 x std ^{3}He counter at 10eV	50 % at 1A	20 % at 1A
GAMMA SENSITIVITY	10^{-8}	10^{-5}	10^{-7}	$<10^{-8}$
QUIET COUNT/ ELEMENT/HR	2	360	12	0.06
PULSE PAIR RESOLUTION/μs	2.5	2.5	2.5	2.5

Table 1. Detector characteristics of some of the scintillator detectors operational on ISIS. *FC = fibre coupled. std ^{3}He = a 10 atmosphere, 25 mm diameter, ^{3}He proportional counter. Gamma sensitivities were determined at 1 MeV using a ^{60}Co source.

REFERENCES

1. Proceedings International Conference on Neutron Scattering, Physica B (1995) In the Press
2. M. W. Johnson, Appl. Radiat. Isot. **46** No. 6/7 673 (1995)
3. Levy Hill Laboratories Ltd, 5 Sheffield House, Fieldings Road, Cheshunt, Herts. U.K.
4. NE Technology Ltd, Sighthill, Edinburgh EH11 4BY Scotland
5. A. R. Spowart, Nucl. Instr. and Meth. **75** 35 (1969)
6. A. R. Spowart, Nucl. Instr. and Meth. **135** 441 (1976)
7. R. K. Crawford et al., Proceedings ICANS XI, KEK Report 90-25 **2** 943 (1990)
8. W. Schafer et al., Proceedings ICANS XII, RAL Report RAL-94-025 **1** 200 (1993)
9. M. Heiderich et al., Nucl. Instr. and Meth. **305** 423 (1991)
10. K. D. Muller et al., J. Neutron Research (1995) In the Press
11. A.D. Taylor, Physica B (1995) In the Press
12. Instrumentation and Techniques for the European Spallation Source. Edited by A.D. Taylor RAL Report RAL-92-040 (1992)
13. D. Hutchinson, J. Neutron Research (1995) In the Press
14. M. W. Johnson, RAL Report RAL-92-040 (1992)
15. M.J. Knitel et al., Proceedings LUMDETR'94, Tallinn, Estonia, September 25-29, 1994, M.J. Knitel et al., these proceedings.

$LiBaF_3$, A SCINTILLATOR FOR THERMAL-NEUTRON DETECTION WITH OPTIMAL n-γ DISCRIMINATION

M.J. Knitel, P. Dorenbos, J.T.M. de Haas, C.W.E. van Eijk
Delft University of Technology, Faculty of Applied Physics,
c/o IRI, Mekelweg 15, 2629 JB Delft, The Netherlands.

ABSTRACT. We report on the scintillation properties of a $LiBaF_3$ crystal when irradiated with thermal neutrons or gamma rays. This scintillator exhibits cross luminescence and self-trapped-exciton luminescence. The former does **not** show up under thermal-neutron irradiation, whereas both give a response under gamma irradiation. This offers a unique opportunity for thermal-neutron - gamma discrimination. The effectiveness of the method is demonstrated.

SCINTILLATION PROPERTIES OF $LiBaF_3$

$LiBaF_3$ has a density of $5.24\,g/cm^3$. We studied a polished crystal with a diameter of $7\,mm$ and a thickness of $1.75\,mm$. It contains natural Li. The total linear attenuation coefficient μ_{tot} of this compound amounts $0.399\,cm^{-1}$ for $662\,keV$ gamma rays and $1.26\,cm^{-1}$ for thermal neutrons [1].

The ^{6}Li isotopes present in the crystal have a large capture cross section for thermal neutrons ($25\,meV$, $1.8\mathring{A}$) of 940 barns. In the reaction

$$^6Li + {}^1_0n \rightarrow {}^4_2He + {}^3_1H + Q\,, \qquad (1)$$

the reaction energy Q of $4.78\,MeV$ is shared between the α-particle and the triton. These particles have a range in the material of a few μm. Their kinetic energy is converted into ionisation energy, eventually causing scintillation effects.

Under X-ray excitation the $LiBaF_3$ scintillation spectrum has two components: a) a $100\,nm$ wide band with its emission maximum located near $300\,nm$, which most probably is due to self-trapped-exciton (STE) luminescence, and b) a doublet of narrow bands with emission maxima at $187\,nm$ and $225\,nm$ due to cross luminescence (CRL) [2, 3].

Table 1: Light yields of $LiBaF_3$ upon excitation by 662 keV gamma-rays (column 2) and thermal neutrons (column 3). A reliable estimate of the yield in the slowest component upon thermal neutron irradiation was not possible.

component	γ exc.(ph/MeV)	neutron exc.(ph/neutr.)
$0.8\,ns$	1200	<10
$8\,\mu s$	1600	3500
$> 8\,\mu s$, ms	4500	

In performing scintillation decay studies under excitation with gamma rays from a ^{60}Co source we observe a CRL component with a decay time $\tau = 0.8\,ns$ and an STE component with $\tau \approx 8\,\mu s$. In the scintillation decay curves recorded during irradiation

Proc. Int. Conf. on Inorganic Scintillators and Their Applications, SCINT95,
1996, Delft University Press, The Netherlands

with α particles from a ^{244}Cm source or thermal neutrons the CRL component does not show up. We only observe the component with $\tau = 8\,\mu s$. There is also some emission at the millisecond level, both upon gamma- and thermal neutron irradiation. In table 1, the estimated light yields are presented. The absence of the cross luminescence decay component upon thermal neutron capture offers a unique opportunity for n-γ discrimination.

n-γ DISCRIMINATION

The method is in fact very simple. A gamma ray gives a relatively large fast response at $t \approx 0$. A thermal neutron does not. Thus, to observe neutrons and not gamma rays, signals with a high amplitude at $t \approx 0$ have to be vetoed.

The $LiBaF_3$ crystal is mounted on a Philips XP2020Q photomultiplier tube. One half of the PMT anode signal is sent directly to a charge integrating Q-ADC. The other half is used to determine whether an event is problably a neutron scintillation and if so, to open the gate of the Q-ADC. Two discriminators are used to select the desired events (figure 1):

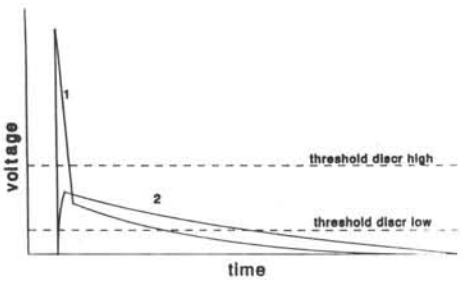

Figure 1: The threshold levels of the discriminators sketched relative to scintillation pulses induced by 1) gamma-rays and 2) thermal neutrons.

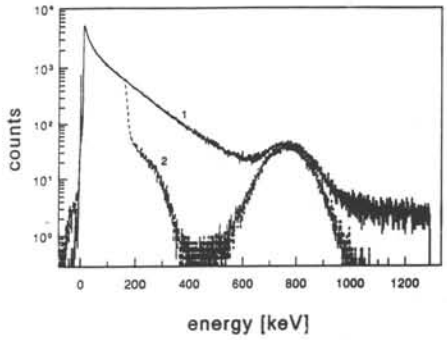

Figure 2: Pulse height spectra of a mixed radiation field with (spectrum 1) and without (spectrum 2) active discrimination against gamma ray induced scintillation events. The spectra are normalised to an effective counting time of 1 hour.

1) The 'low' discriminator that discriminates scintillation events from noise and single photoelectron signals (the threshold voltage level is only a few times larger than the amplitude of a single photoelectron signal).
2) The 'high' discriminator which detects the high amplitude fast scintillation events. If the amplitude of the fast component exceeds the 'high' threshold level, the coincidence unit is blocked for $30\,\mu s$ by a veto signal.

First, the crystal was exposed to radiation from a Pu-Be source surrounded by paraffine and $6\,cm$ of Pb. The shielded source emits a mixed field of thermal neutrons and gamma-/X-rays. Two pulse height spectra were recorded, see figure 2.

In one case (spectrum 1) the veto was switched off so gamma-ray induced scintillation events were *not* discriminated. In the second case (spectrum 2) the veto was on. Both spectra are normalised to an *effective* counting time of 1 hour, to correct for dead time effects. When we discriminate against the gamma-ray induced scintillation events (spectrum 2), a clear well resolved neutron peak is observed at 761 keV which shows that the new pulse shape discrimination method is quite effective. The FWHM of the neutron peak is about 166 keV. CRL pulses caused by gamma-rays and X-rays $< 400\,keV$ do not reach the high threshold level and consequently they are still registered.

How effective is our gamma ray suppression method? To answer this question we define the *detection efficiency* ε_{662} of our detector as the probability that the exposure of the detector to *one* 662 keV gamma quantum yields a count in the thermal neutron peak in the pulse height spectrum (fig 2). The choice of a gamma ray energy of 662 keV is based on the fact that the corresponding photopeak overlaps the thermal neutron peak.

An analogous measurement as described before was performed using the 662 keV gamma radiation from a ^{137}Cs source. Thus we were able to extract the detection efficiency with gamma ray suppression activated: $\varepsilon_{662} \leq 5.7 \cdot 10^{-7}$.

Extrapolation to a $3\,mm$ thick $LiBaF_3$ crystal containing 96% ^6Li gives: $\varepsilon_{662} \leq 1.0 \cdot 10^{-6}$ at a thermal neutron efficiency of $\varepsilon_n = 0.75$.

Unfortunately, the crystal shows some intrinsic, presumably α, activity. About 80 counts/(hour·cm^3) are added to the thermal neutron peak in our pulse height spectrum.

CONCLUSION

The results are very promising and make $LiBaF_3$ crystals interesting for use in thermal neutron scintillation detectors, the more so as a gamma background suppression of the order $10^{-6} - 10^{-8}$ can be a requirement at neutron facilities (nuclear reactors, spallation sources).

Acknowledgements. The authors are grateful to P.A. Rodnyi for providing the $LiBaF_3$ crystal. These investigations have been supported by the Netherlands Technology Foundation (STW).

References

[1] C.M. Lederer, V.S. Shirley (eds.) (1978). *Table of Isotopes*, 7th ed. (New York: John Wiley & Sons

[2] J. Jansons, Z. Rachko, J. Valbis, J. Andriessen, P. Dorenbos, C.W.E. van Eijk (1992). In: *Proc. 12th Conf. Defects in Insulating Materials 2* (eds. O. Kanert and J.-M. Spaeth) pp.1256-1258, World Scientific, Singapore.

[3] P.A. Rodnyi, M.A. Terekhin, E.N. Mel'chakov (1991). *J. Luminescence* 47, pp.281-284

INVESTIGATING ACTIVATION OF SPACEBORNE SCINTILLATOR CRYSTALS

H.E.Evans, P.R.Truscott, C.S.Dyer
Space Department, Defence Research Agency, Farnborough, Hampshire, GU14 6TD, United Kingdom

ABSTRACT

Radiation effects on gamma-ray detector materials in the Low Earth Orbit (LEO) space environment have been investigated by flights of the CREAM (Cosmic Radiation Effects and Activation Monitor) and Shuttle Activation Monitor (SAM) suite of experiments. A selection of the data collected is reviewed and important lessons highlighted. Spectral data from the experiments are compared with the results from detailed simulations which predict the space radiation environment and its consequences. The predicted source spectrum is processed by particle transport codes which account for the spacecraft structure and scintillator. The response of a detector due to the decay of the spallation products generated in the crystal is calculated. New data resulting from the space irradiation of a BaF_2 scintillator crystal will be presented. The applicability of various scintillators including BaF_2 for space radiation measurements will be discussed.

INTRODUCTION

The unique opportunities afforded by spaceflight for X and gamma ray measurements continue to stimulate research aimed at increasing the sensitivity and longevity of detectors and platforms whilst reducing the cost. Since the first balloon-borne experiments, scientists realised the importance of the underlying background and its consequences for the sensitivity. The first few orbiting spectrometers experienced such levels of background so as to confound the data analysis and compromise mission objectives. It was quickly realised that the background components may be split into two categories, prompt and delayed [1].

The prompt component arises from the direct bombardment of the sensitive region of a spectrometer by undesired radiations. All spacecraft are immersed in an unremitting flux of high energy particulate radiation originating from the Van Allen radiation belts (charged particles trapped in the Earth's geomagnetic field), cosmic rays and solar particles. For example a scintillator detector may be bombarded by a whole spectrum of gamma rays as well as charged and neutral particulate radiation. It is possible to veto some of the spurious signals by surrounding the sides and back of a detector with a scintillator working in anticoincidence mode. Careful spacecraft and experiment design can significantly reduce the prompt background contribution effectively increasing instrument sensitivity. This is achievable through a study of the predicted radiation fluxes for a particular orbit and its primary and secondary transmission through a geometric model of the spacecraft.

The delayed background component is caused by nuclear activation reactions of the primary radiation flux with the spacecraft. Some of these, protons and other hadronic particles, are capable of causing nuclear spallation and activation. This is of particular concern to gamma ray astronomers since not only do activated materials local to the detector become a source of gamma-rays but activation of the carefully prepared solid state or scintillation crystal introduces a very important source of background counts. Once again a study of the propagation and interactions of the primary and secondary activating radiation fluxes with their dependence upon the material and geometric composition of the spacecraft [2] can highlight potential conflicts between spacecraft engineering design and scientific objectives.

Once operational, techniques such as active veto shielding, use of a coded mask and pulse shape discrimination can veto many of the spurious signals or at least permit concurrent background analysis [3,4,5,6,7,8,9]. Delayed radiations become a significant background component and have led researchers to consider isotopic enrichment of the detector material [10] or to construct an n-type germanium detector with a segmented cathode which is able to veto beta decay signals from within activated detector crystals [11].

The purpose of this paper is to describe the experimental and theoretical methods which contribute to the ability to predict the background accurately in both well established and modern spaceborne scintillator materials.

Proc. Int. Conf. on Inorganic Scintillators and Their Applications, SCINT95,
1996, Delft University Press, The Netherlands

BACKGROUND PREDICTION

One of the first predictions of activation background measured by a spaceborne scintillator was based on semi empirical cross sections [12,13,14]. Since then, the computer revolution has meant sophisticated Monte Carlo codes may now be utilised to perform detailed transport calculations using predicted primary or secondary particle fluxes incident upon complex geometries representing the whole spacecraft or an individual instrument. The Monte Carlo approach may be too expensive in some circumstances and the relative efficiency of the semi-empirical calculational method retains considerable support.

Activation effects for instruments on large platforms have led to the consideration of the influence of secondary effects in order to make improved predictions [15]. For this purpose the DRA Space Department has developed an integrated software suite for background predictions in a powerful and flexible computer environment.

The first step in a background calculation is the prediction of the source spectra. We shall only consider the main radiations capable of causing activation or spallation. The trapped proton flux is calculated using the UNIRAD [16] code based upon the AP8 model and the IGRF 1975 geomagnetic field extrapolated to the epoch of the AP8 data [17,18,19]. The CREME code is used to predict the cosmic ray proton or alpha particle spectrum [20].

A geometry is then constructed to allow consideration of shielding effects of the spacecraft. The Material and Geometry Editor component of the DRA Integrated Radiation Transport Suite (IRTS) may be used to construct a full 3-dimensional model of a complex spacecraft. This has been done for the analysis of the Gamma Ray Observatory or more recently, the XMM spacecraft. Alternatively, Space Shuttle shielding studies utilise a simple 512 element spherical aluminium shield model which gives the shield thickness as a function of 'look direction' from the Space Shuttle middeck. The internal and external radii of this model are 1.8 and 2.5m respectively to represent the dimensions of the Shuttle middeck.

The IRTS is capable of transporting all primary and secondary cosmic ray and trapped proton fluxes through this geometry [15]. Three different Monte-Carlo codes are incorporated into the IRTS for the transport of nucleon mesons (Light Heavy Ion, LHI, developed from the High Energy Transport Code, HETC) [21], electrons and photons (Electron Gamma Shower, EGS4) [22] and low energy neutrons (Multigroup Oak Ridge Stochastic Experiment, MORSE) [23] through a common geometry description and output format. Therefore a detailed analysis over a broad range of physical interactions is possible since the data output from one transport code is input to the next code until the particles either escape the geometry or their energies fall below some cut-off value. The IRTS is augmented with a Nuclear De-Excitation Model (NDEM) [24] which produces prompt gamma-ray emissions from spalled nuclei, and a soft X-ray and Auger electron model [25] for K shell emissions.

The Evaluated Nuclear Structure Data File (ENSDF) [26] is accessed for radioactive decay information (eg gamma-ray intensities and energies, beta-decay energies and branching ratios). This is used with the BANKER code [27] which computes the mean energy deposition spectra or response function for a particular scintillator resulting from the decay of radioactive nuclei.

EXPERIMENT DESCRIPTION

The DRA has taken part in many studies to validate predictions with experimental evidence. Previous studies have included six Space Shuttle flights of the CREAM (Cosmic Radiation Environment and Activation Monitor) suite of experiments comprising an active monitor, foil packages and one or more scintillator crystals [28,29,30]. The active monitor contains 10 silicon PIN diodes, each 1cm^2 area and 300μm deep, and measures the Single Event Upset (SEU) environment at various pre-

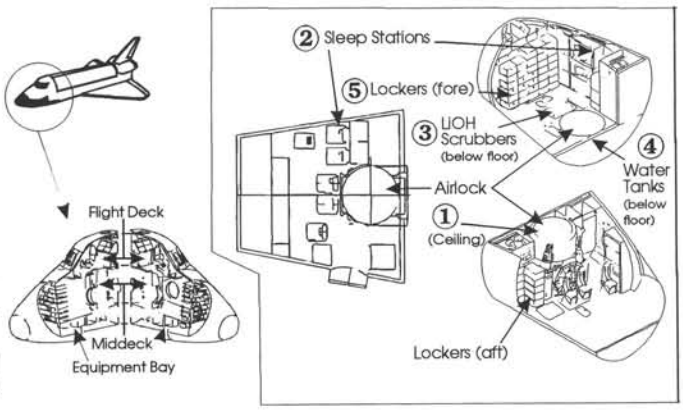

Figure 1 Locations of the CREAM activation foil packs

determined locations within the Shuttle middeck and as a function of time (and hence orbital location). Five identical packages containing foils sensitive to activation by thermal neutrons (gold foil), fast (3-12MeV) neutrons (nickel foil) and epithermal neutrons (tungsten foil) are distributed soon after reaching orbit. These foils are placed at strategic locations around the Shuttle cabin (see figure 1) and interact with the differing neutron radiation fluxes caused by local material distributions. Each foil package also contains thermoluminescent dosimeters collecting data from ionising radiation dose. Finally one or more scintillation crystal samples are flown in a middeck locker throughout the mission alongside one of the foil packs. The CREAM experiments are retrieved as soon as possible after touchdown and counting at a nearby low background counting facility begins. The foil pack activation is measured by high resolution Ge detector systems. The scintillation crystal samples are all mated to their respective PMTs and inserted into a lead castle. Both the internal spectrum detected by the PMT as well as the external spectrum, measured by a Ge spectrometer, are acquired.

The Shuttle Activation Monitor (SAM) experiment was also designed to study the properties of different scintillator materials in Low Earth Orbit (LEO)[31,32,33]. In addition, the two SAM crystals (both cylindrical with 7.6cm diameter and 7.6cm long) were operated in flight to measure the gamma-ray environment in the Space Shuttle.

Table 1 summarises the SAM and CREAM flight experience to date with particular reference to the orbital parameters and scintillation crystal samples.

Table 1 A summary of STS mission orbits with CREAM/SAM experiments

Mission ID	Launch Date	Altitude (nmi)	Inclination (°)	Scintillators flown
STS-28	Aug 89	160	57	SAM NaI, BGO
STS-48	Sep 91	307	57	SAM NaI, BGO and CREAM NaI
STS-44	Dec 91	196	28.5	SAM NaI, BGO and CREAM NaI
STS-53	Dec 92	210/176	57	CREAM NaI
STS-56	Apr 93	160	57	CREAM NaI
STS-68	Oct 94	117	57	CREAM BaF_2, LSO, GSO
STS-63	Feb 95	221/184	51.6	CREAM BaF_2, LSO, GSO

PREVIOUS RESULTS

Figures 2, 3 and 4 present the results from the foil pack experiment during Space Shuttle flights STS-48

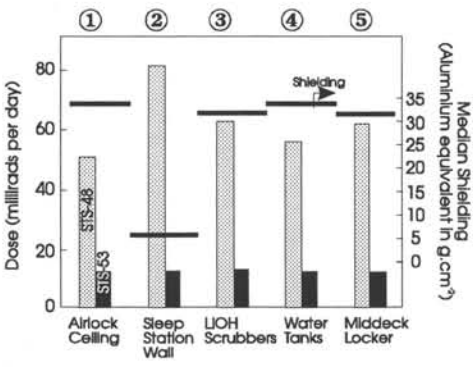

Figure 2 Dose rates in Thermoluminescent dosimeters as a function of location (see figure 1)

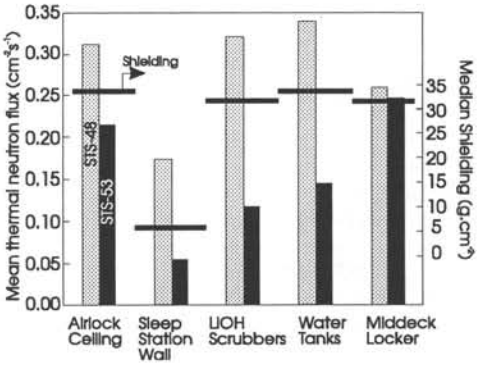

Figure 3 Mission averaged thermal neutron flux estimated from gold foil activation

and STS-53. Figure 2 is the mean dose from TLD measurements in units of millirads per day. Figures 3 and 4 are calculated mission-averaged thermal and fast neutron fluxes from gold and nickel foil activation respectively. Sodium iodide crystal activation during STS-48 and STS-53 can be compared in figures 5 and 6. The solid, jagged line is the internal spectrum measured by mating the crystal to a PMT; the broken lines represent the time-dependent, computer predictions for the internal

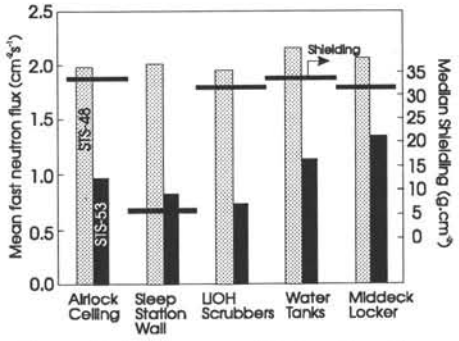

Figure 4 Mission averaged fast neutron flux estimated from nickel foil activation

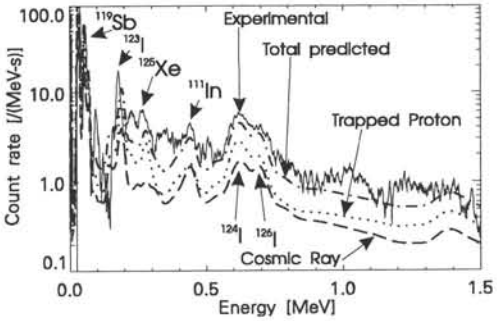

Figure 5 STS-48 NaI internal spectrum 45.96 hours after touchdown with major contributing nuclides indicated

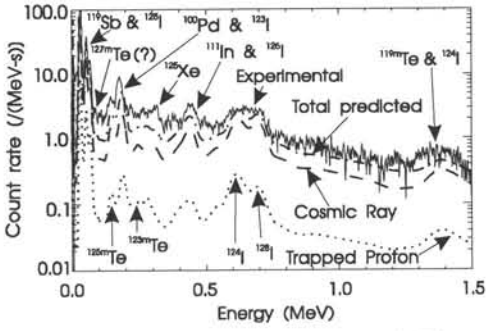

Figure 6 STS-53 internal NaI spectrum 46.25 hours after touchdown. Note the different ordinate scale compared with figure 5

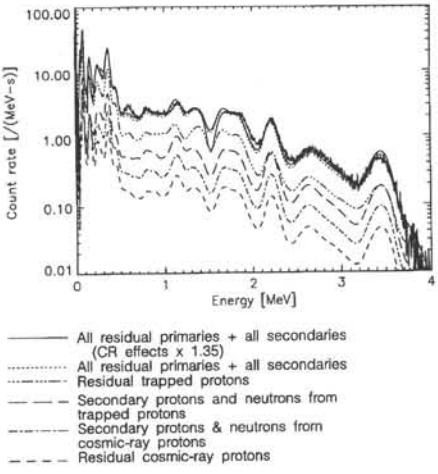

Figure 7 SAM STS-53 internal BGO spectrum 1.86 days after touchdown (jagged curve) compared with predictions. Primary and secondary activating components from trapped-proton and cosmic-ray effects are shown

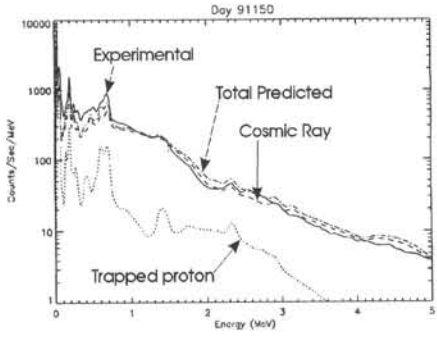

Figure 8 Average background spectrum in OSSE during 5 orbits furthest from SAA on day 150 of 1991 (55 days after launch) compared with predictions.

background. The predictions are further split into the activation from trapped protons and that from cosmic rays. The effects of cosmic-ray alpha-particles have been included by scaling the cosmic ray proton effects by 1.45 [34]

The results of a SAM flight of BGO on STS-48 are presented in figure 7 (taken from [31]). The spectrum (solid curve) was recorded 1.8 days after touchdown and is compared with computer predictions. The predictions are broken down into the trapped proton and cosmic-ray components, which have been further split into the activation resulting from their primary and secondary fluxes.

Figures 8 and 9 show experimental and predicted background spectra observed in OSSE aboard the GRO 55 days and 2 years after launch respectively. These predictions have also been split into trapped-proton and cosmic-ray activation components.

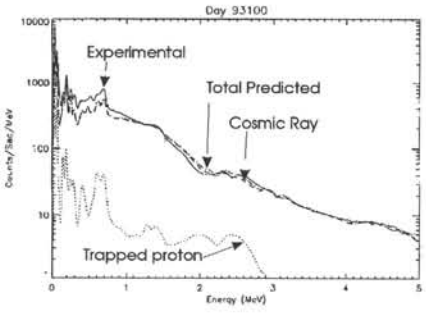

Figure 9 Background spectrum in OSSE compared with predictions for day 100 of 1993 (2 years after launch).

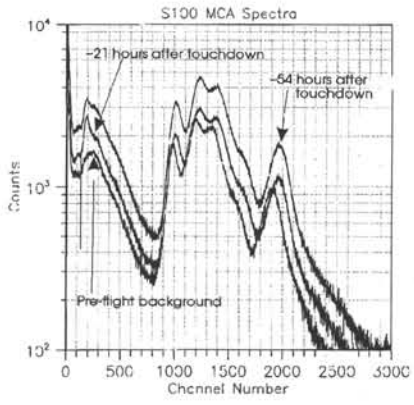

Figure 10 Internal spectra of BaF_2 taken before and after flight aboard STS-63

Figure 10 shows 3 unprocessed spectra from a 1" BaF_2 crystal flown on STS-63. These spectra have not been normalised for live time nor have any background subtractions been performed. The pre-flight spectrum displays a slight energy offset relative to the post-flight spectra due to a gain difference when the crystal, PMT and spectrometer were re-assembled for post-flight measurements. The sensitivity of this scintillator is affected by the naturally abundant Radium isotope which emits several alpha-particles within the crystal, the peaks from which dominate both the pre and post flight background spectra. Nevertheless, evidence of activation is seen in the region of channel ~200 (~250~400keV region from very rough calibrations) by comparing the shape of the spectra in this domain.

DISCUSSION OF RESULTS

The altitude dependence of the radiation flux in the Space Shuttle cabin is clearly evident in figures 2-6. The TLD data in figure 2 indicate no shield dependent dose rates for the lower altitude STS-53 contrasting with STS-48 data where the minimum shielded location (the sleep station wall) receives the maximum dose. This is due to the greater contribution of trapped protons at higher altitudes. Their lower energy compared with cosmic-rays makes them amenable to shielding. Activation foil data from both flights indicate variation of thermal and fast neutron fluxes related to nearby shielding. The thermal neutron flux (figure 3) may be expected to be higher nearer the thermalising materials. Fast neutron flux results (figure 4) have not shown significant station dependence though the data exhibits the altitude dependence. This dependence is interpreted as evidence of the significance of neutrons produced by trapped protons at higher altitudes. Atmospheric albedo neutrons contribute a significant fraction of the neutron flux at lower altitudes.

NaI internal spectra in figure 5 illustrate the dominance of trapped proton over cosmic ray activation effects. The data in figure 6 illustrates the opposite for a lower altitude orbit where the trapped proton flux is 5~7 times lower. The simulation results are accurate enough to be able to identify most of the main spectral features.

BGO activation from the SAM flight aboard STS-48 (figure 7) exhibits the same trapped proton dominant activation. Of particular interest is the prediction of trapped proton secondaries contributing the second biggest fraction of the overall activation, more than either the cosmic ray primary or secondary activation fractions. Note also the greater contribution from cosmic ray secondaries compared with the corresponding primary flux.

Longer term predictions of activation induced background in the OSSE detectors aboard the GRO are also shown to be in close agreement to observations.

Barium Fluoride has been flown but the data remains unprocessed. A detailed IRTS simulation is currently under way. Some of the first results from the LHI (nucleon-meson) transport is in the form of a league table of spallation products. Table 2 is the list so formed when a cosmic-ray proton spectrum is attenuated by the Space Shuttle shielding and incident upon a 1" BaF_2 crystal in a middeck locker. A brief examination reveals most of these products are stable isotopes while only F-18 (a positron emitter), Cs-137, Ba-133, Cs-126 and Cs-127 are unstable. The most prominent gamma decay products of these isotopes lie in the sub 700keV range, in very rough agreement with the observed post-flight internal background spectra.

Table 2 League table results of spallation products from a LHI transport of cosmic-ray spectrum attenuated by the Space Shuttle shielding and incident upon a 1" BaF_2 situated in a middeck locker.

Element	Number of Measurements	Weight of Measurements	Percentage
F-18	3549	3666.022341	4.36%
O-18	2857	2959.7775	3.52%
N-14	2720	2859.765474	3.40%
Ba-137	2635	2747.192806	3.27%
O-16	2393	2513.866198	2.99%
Ba-136	2085	2195.922977	2.61%
C-12	1686	1801.359245	2.14%
O-17	1712	1790.260888	2.13%
N-15	1645	1743.21001	2.07%
Ba-135	1432	1517.670181	1.81%
Ba-134	1276	1350.86689	1.61%
C-13	1145	1205.656347	1.43%
Cs-137	1096	1127.601073	1.34%
Ba-133	874	924.5454863	1.10%
Li-6	823	862.4081417	1.03%
Cs-126	568	753.4139236	0.90%
Cs-127	560	738.2603489	0.88%
Ba-132	697	737.1253898	0.88%

CONCLUSIONS AND FUTURE PROSPECTS

The variety of environmental radiation fluxes and their dependence and effects for different orbits and spacecraft has been demonstrated. Both cosmic-ray and trapped protons are capable of causing activation via secondary particle interactions. Whether trapped proton or cosmic-rays dominate activation effects depends upon orbital altitude, inclination, solar activity and the spacecraft structure. Shielding can reduce trapped proton effects but it enhances cosmic-ray activation.

The success of the IRTS and associated codes over a wide variety of orbital, temporal and spacecraft dependent shielding conditions is encouraging. In particular, the sub 1MeV range where background is most apparent, spectral features may be accurately reproduced by the simulation thereby allowing identification of the culprits causing the background spectrum.

Future flights and ground irradiation experiments will continue to provide tests for the computer predictions. These predictions will provide valuable insights as to the activation properties and hence the background characteristics of well established and modern scintillator materials. A scintillator may one day be found to have some very desirable activation properties enabling highly accurate background predictions and maximum sensitivity during operation in the hostile space environment.

Future challenges to prediction codes include the production of data with finer time detail in order to model the effects of the South Atlantic Anomaly (SAA) (a localised region of higher trapped proton fluxes). The sensitivity of a radiation detection instrument to weak cosmic gamma ray sources is essentially zero during and soon after traversing this region due to the greatly enhanced trapped proton flux and activation effects. Accurate predictions of these effects may lead to the expansion of the 'up-time' of a spectrometer through understanding of the short lived decaying activated nuclides (for example the short lived I-128 in NaI crystals). This finer time detail would also need to include the modulation of the cosmic-ray activating flux as a function of orbital position caused by variations of the geomagnetic field strength.

ACKNOWLEDGEMENTS

This research has been supported by the UK Ministry of Defence and Shuttle flights of the CREAM and SAM experiments were sponsored by the US BMDO and organised by the USAF Space Test Programme. Pre and Post-flight analysis of the SAM detectors for STS-48 was conducted at Lawrence Livermore National Laboratory (LLNL). Miss Jane Flatman and Matthew Cosby are thanked for their help with the data analysis. Terry Sanderson and Dr John Farren of Harwell Laboratory are thanked for the provision of the activation foil packages and analysing the thermoluminescent dosimeters. Dr Gordon Wrenn, Miss Claire Peerless and Ray Hutchins of the DRA are thanked for their assistence regarding the Space Shuttle operations. Dr Penny Haskins and Jack McKisson of Radiation Technologies Inc., Alachua, Florida are thanked for all their support during Shuttle campaigns. Dr Dave Camp of LLNL, Prof. Emmet Bolch and the Environmental Engineering Department of the University of Florida are thanked for the laboratory facilities used extensively during Shuttle campaigns. Finally Dr Cal Moss of Los Alamos National Laboratory is thanked for providing the crystals and associated spectrometer equipment used on STS-68 and STS-63

REFERENCES

[1] Peterson L.E., Geophys.Res.70,(1965),1792
[2] Dyer C.S, Trombka J.I., Seltzer S.M., Evans L.G., Nucl.Inst.Meth.,173,(1980),585
[3] First Compton Observatory Symposium, St.Louis, MO, 15-17 October 1992
[4] Winkler C., Pace O., Volonte S., ESA Journal 17,(1993),207
[5] Labanti C., Rossi E., Shiavone F., Spizzichino A., Traci A., Corba M., Quadrini M.E., Bird A.J., Carter T., Gomm A.J.M., IEEE Trans.Nucl.Sci.,40,4,(1993),879
[6] Forrest D.J., Proc. 'High energy radiation background in space', AIP Conference proceedings 186 (1989),243
[7] Share G.H., Kinzer R.L., Strickman M.S., Letaw J.R., Chupp E.L., Forrest D.J., Reiger E., Proc. 'High energy radiation background in space', AIP Conference proceedings (1989),266
[8] Paciesas W.S., Gregory J.C., Fishman G.J., Proc. 'High energy radiation background in space',AIP Conference proceedings (1989),225
[9] Gruber D.E., Jung G.V., Metteson J.L., Proc. 'High energy radiation background in space',AIP Conference proceedings (1989),232
[10] Gehrels N., Cheung C., Proc. ESA Symp Photon Detectors for Space Instrum 1992
[11] Gehrels N., Cline T.L., Teegarden B.J., Tueller J., Leventhal M., MacCallum C.J., Hewka P.V., Ryge P., IEEE Trans.Nucl.Sci.NS-31,1,(1984),307
[12]Dyer C.S., Morfill G.E., Astrophys and Space Sci., 14,(1971),243
[13]Silberberg R., Tsao C.H., Astrophysical Journal Supplement Series 220(I),25,(1973),315-333
[14]Silberberg R., Tsao C.H., Astrophysical Journal Supplement Series 220(II),25,(1973),335-368
[15]Dyer C.S., Truscott P.R., Evans H.E., Hammond N.D.H., Comber C., Battersby S., IEEE Trans.Nucl.Sci.NS-41,3,(1994),438-444
[16]J.C.L.Debruyn, L.H.Jensen, The UNIFLUX system , ESTEC working paper 1308, (1983)
[17]D.M.Sawyer, J.I.Vette, AP8 trapped proton environment for solar maximum and solar minimum, NSSDC 76-06, National Space Science Data Center, Greenbelt, Maryland, December 1976.
[18]E.G.Stassinopoulos, Charged particle radiation exposure of geocentric satellites , Proc. 'High-Energy Radiation Background in Space', Sanibel Island, Florida, November 3-5, 1987, AIP Conference Proceedings 186, (1989),3
[19]P.D.McCormack, Radiation dose and shielding for the Space Station , IAF/IAA-86-380, (1986)
[20]Adams Jr. J.H., Silberberg R., Tsao C.H., 'Cosmic-ray effects on microelectronics, Part 1: The near-Earth particle environment.' Naval Research Laboratory Memorandum report 4506,(1981)
[21]T.W.Armstrong, B.L.Colborn, A thick target radiation computer code for low-mass heavy ion beams , Nucl.Inst.Meth.169, pps 161-172,(1980)
[22]W.R.Nelson, H.Hirayama, D.W.O.Rogers, The EGS4 Code System , Stanford Linear Accelerator Center, SLAC-Report-265, (1985)
[23]M.B.Emmett, The MORSE Monte Carlo Radiation Transport Code System , Oak Ridge National Laboratory Report ORNL-4972, (1975)
[24]Prael R.E., 'High energy particle Monte Carlo at Los Alamos',LA-UR-85-1243, Presented at the Joint Los Alamos/CEA Monte Carlo Conference, Cadarache, France, April 1985
[25]Hammond N.D.A.,'Fluorescent X-Ray production in the EGS4/PEGS4 element of the RAE Integrated Radiation T4ransport Suite', Document Ref. C21404/S-02/3

[26]J.K.Tuli, Evaluated Nuclear Structure Data File. A Manual for Preparation of Data Sets , National Nuclear Data Center, Brookhaven National Laboratory, BNL-NCS-51655-Rev.87

[27]S.M.Seltzer, 'The response of scintillation detectors to internally induced radioactivity' , Nucl.Inst.Meth., 127, p293, (1975)

[28]Dyer C.S., Sims A.J., Truscott P.R., Farren J., Underwood C., IEEE Trans.Nucl.Sci.NS-39,6, (1992),1809-1816

[29]Dyer C.S., Sims A.J., Truscott P.R., Farren J., Underwood C., IEEE NSREC93, IEEE Trans.Nucl.Sci.NS-40,6,(1993),1471-1478

[30]Dyer C.S., Sims A.J., Truscott P.R., Peerless J., Underwood C., Adv.Space Res.,17,2,(1994),159-162

[31]Truscott P.R., Dyer C.S., Haskins P.S., McKisson J.E., IEEE NSS/MIC94 paper NSS04-03

[32]Haskins P.S., McKisson J.E., Ely D.W., Weisenberger A.G., Dyer C.S., Ramayya A.V., Camp D.C., IEEE Trans.Nucl.Sci.NS-37,3,(1990),1256

[33]Haskins P., McKisson J., Truscott P., Dyer C., Flatman J., Snead L., Rothmann J., Ward T., Camp D., 'Contribution of secondaries to the radiation environment on space missions', Adv.Space.Res.14,10,(1994),943-946

[34]Battersby S.J.R., Quenby J.J., Dyer C.S., Truscott P.R., Hammond N.D.A., Comber C., Kurfess J.D., Johnson W.N., Kinzer R.L., Strickman M.S., Jung G.V., 'Calculation of the induced radioactivity background in OSSE', Proceedings of the Compton Gamma Ray Observatory Symposium, St.Louis, MO, 15-17 October 1992, AIP Conference Proceedings 280,(1993),1107-1111

PART II

Scintillation Mechanisms and Theory

SCINTILLATION MECHANISM: THE SIGNIFICANCE OF VARIABLE VALENCE AND ELECTRON-LATTICE COUPLING IN R.E.-ACTIVATED SCINTILLATORS

Andrzej J. Wojtowicz
Institute of Physics, N. Copernicus University, Grudziadzka 5, 87-100 Torun, Poland,
Chemistry Dept., Boston University, 590 Commonwealth Ave., Boston, MA 02215, USA

ABSTRACT

In this paper we will discuss the basic physics behind the processes of carrier self-trapping and excitation of Ln ions by means of a sequential carrier capture mechanism. We will present experimental results to demonstrate how these effects manifest themselves in the spectroscopy of scintillator materials. Free ion *f-s* promotion energies and a simple band structure model will be used to identify those Ln ions likely to act as hole or electron traps. We will also use a single-configuration-coordinate model (SCC) to include electron-lattice coupling. This model will be then applied to some new scintillator and phosphor systems based on Ln-activation.

INTRODUCTION

It has recently been pointed out that good performance of scintillators depends on high efficiencies of three major steps: energy conversion, energy transfer from the lattice to the activating ion and luminescence [1]. However, more detailed analysis shows that in the case of some newly discovered scintillators even a relatively poor conversion and/or a low quantum efficiency of luminescence ion can be more than compensated by good energy transfer properties leading to a decent light output and a high figure of merit [2].

It has long been known that in photoconductive materials such as ZnS:Ag (broadly used initially as a scintillator and later as a lamp and TV phosphor), the energy transfer mechanism from the host to the activating ion is based on transport of charge carriers (both holes and electrons) and their capture by the ion [3]. Such transport, however, is not always necessary. In $CaWO_4$, also one of the first scintillators and X-ray phosphors, after ionization all initial core holes relax to localized (self-trapped) valence states of the WO_4^{2-} molecular ions, rendering band transport of holes unessential. However, a next step, which is the capture of mobile electrons by the resultant WO_4^{1-} entities and formation of bound anionic excitons, must be (and usually is) very efficient. Exactly the same mechanism must be responsible for the emission of the other prominent and broadly used scintillating material, BGO. In such materials, any competition for holes (*e.g.* from unwanted killer impurities/defects or intentionally introduced dopant ions) would interfere with the process provided there is some band transport of holes. Additionally, electron traps may delay transport of electrons to ionized molecular groups, introducing slow components into the scintillation pulse. In general, in unactivated materials containing molecular ions, the self-trapped anion exciton decay often provides scintillation under ionizing excitation.

An efficient and prompt self-trapping of holes by molecular groups does not, however, inevitably exclude the material as an *activated* scintillator, X- or cathode-ray phosphor. An example is provided by a prominent color TV phosphor, YVO_4:Eu [4]. Fast energy migration in the VO_4^{3-} sublattice combined with an efficient Forster-Dexter type of energy transfer to Eu^{3+} allows efficient luminescence under ionizing excitation [5], despite the expected inability of Eu^{3+} to compete for holes. In other hosts activated by Eu^{3+}, electron trapping by Eu^{3+} and

Proc. Int. Conf. on Inorganic Scintillators and Their Applications, SCINT95,
1996, Delft University Press, The Netherlands

subsequent recombination of the resultant Eu^{2+} with band or self-trapped holes (which would obviously require some degree of hole mobility) may be of importance.

The exceptional example of significance of both band transport and self-trapping of charge carriers is provided by Tl-activated halides. Here, because of self-trapping, only a fraction of the generated holes is captured by Tl^{+} ions (forming Tl^{2+}), the rest forming so-called V_k centers. The good performance of certain halides (*e.g.*, NaI:Tl) seems to be due to a fortunate coincidence of the following facts: i) the Tl^{0} charge state is stable; ii) V_k centers are mobile; and iii) the radiative decay time of the excited Tl^{+} is long enough. These three properties allow efficient recombination of V_k and Tl^{0}, contributing to the prompt component of the scintillation pulse. In addition, at least at room temperature, the trapping (and detrapping) of electrons by Tl^{0}, followed by recombination with the remaining Tl^{2+} ions (in NaI:Tl) also contributes significantly to the fast component in the scintillation pulse [6].

Clearly, charge carrier transport properties are not relevant to the performance of many of the lamp phosphors based on excitation by the fixed wavelength Hg discharge. The excitation, which in most cases makes use of the charge transfer band, is already localized on the activating ion (or molecular group) and the whole process characteristic of the energy-transport-based X-ray, cathode-ray or scintillating material is reduced to essentially the last step, which is creation of the bound exciton.

It has been argued that the scintillation performance of some Ce-activated materials such as fluorides, orthophosphates and orthoaluminates is based on charge carrier transport to the Ce ion [7,8]. On the other hand, the well-documented case of BaF_2:Ce, however, offers a contrary example, strongly suggesting that energy migration employing self-trapped excitons and subsequent energy transfer to the Ce^{3+} *d-f* structure is the dominant mechanism of energy transfer [9]. We hold that this is an exceptional case, which we explain in the forthcoming discussion, and that for most of the new scintillator materials employing fast *d-f* transitions on Ln-ions the scintillation mechanism is more likely based on carrier transport through the lattice preceding self-trapping.

CARRIER TRANSPORT AS ENERGY TRANSFER MECHANISM

The carrier-based energy transfer is based on three consecutive steps. In step 1 a hot band hole moving through the crystal is trapped by a Ln^{n+} ion. Note that in order to bind a hole the ion has to have a filled electronic level in the forbidden energy gap (a hole trap) or, in other words, a stable $Ln^{(n+1)+}$ charge state [10]. After a hole has been trapped there will be a Coulomb potential that introduces empty bound states, enabling the ion to bind an electron and form an ion-bound exciton (step 2). In step 3 the exciton decays, transferring its energy non-radiatively to the electronic structure of the ion. The radiative decay of the excited ion completes the cycle. The sequence of carrier trapping may be reversed, with an electron being trapped first. For this to happen a $Ln^{(n-1)+}$ charge state has to be stable, providing an electron trap [10]. It has been argued [7] that this reversed sequence is likely to yield lower light outputs since holes, which usually relax much faster, may be captured by some killer centers before they stand a chance to be gathered by $Ln^{(n-1)+}$ ions.

It is clear that a carrier transport mechanism based on sequential trapping first of a hole and subsequently of an electron will be efficient and prompt when the following conditions are fulfilled: 1) the hole and electron mobilities are high enough; 2) the Ln^{n+} ion hole capture cross section is high; 3) there is no competition for holes coming from self-trapping or from inadver-

tent impurities; and 4) there is no trapping (or self-trapping) of electrons. These conditions will be elaborated in the following discussion.

Hole and electron mobilities in ionic and molecular materials

It is well known that as long as there is no lattice polarization the mobilities of charge carriers are determined by the widths of their energy bands. It is also well established that while the widths of the conduction band in broad bandgap materials are large enough to ensure decent band electron mobilities, the widths of the valence band are much narrower. The same is true of materials containing molecular groups. Since the localization of a free carrier introduces a loss in stabilization energy of about half the bandwidth, it is clear that holes will be self-trapped much more rapidly. The smaller loss in stabilization energy may be more easily compensated by the gain due to polarization energy introduced by localization of the charge and corresponding adjustment of the surrounding lattice. A relevant discussion of different types of charge-carrier/lattice interaction leading to formation of "dielectric" and "molecular" polarons was presented by Mott and Stoneham [11], who point out that in the case of short-range interactions ("molecular" polaron) there may be some delay in the formation of self-trapped electrons, holes and excitons. This lends some support to the idea of carrier-based energy transfer in these materials despite poor steady-state transport properties. The delay in self-trapping is, in their approach, due to the energy barrier that must be overcome by the system in the configuration coordinate space. This may enable hot hole transport over the lattice to precede self-trapping [12].

Although charge transport parameters in insulator materials are inherently difficult to measure, in some cases it is possible to demonstrate the existence of at least free band excitons by spectroscopic methods. In Fig. 1 we present schematically the appearance of exciton emission and excitation spectra along with the appropriate configuration-coordinate diagrams. In Fig. 1(a) the short range carrier-lattice interaction is strong and transitions in both emission and absorption are between localized states (broad emission and excitation spectra). This is true, for example, in the case of CeF_3, where no Frenkel *d-f* free exciton has been found and both emission and absorption (or excitation) spectra are characteristic of strongly localized *d-f* transitions [13]. In Fig. 1(b), however, the short-range carrier-lattice interaction is weaker and, while emission spectrum is still broad, there is a much narrower band in the excitation spectrum. This is due to the fact that absorption and emission spectra do actually involve different excited states: an excitonic band state (shown by a broken curve) in absorption, and a relaxed self-trapped excitonic state localized in the space of some local configuration coordinate (shown by a solid curve) in emission. Note the energy barrier between these two states: In some cases it may even be possible to have resonance and Stokes-shifted emissions coming from both of these states at the same time [14]. As we will demonstrate later, some Ce-activated scintillator materials clearly belong to the case shown in Fig. 1(b).

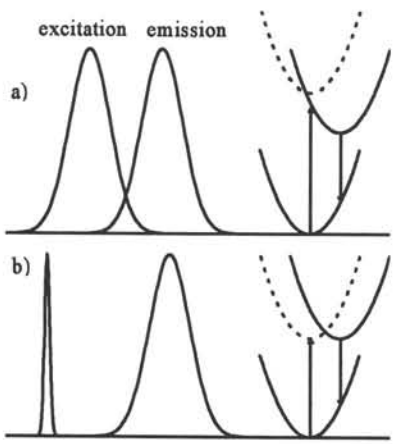

Fig. 1. Excitonic absorption and emission spectra and configuration coordinate diagrams showing electronic and adiabatic energies of the system. a) stronger and b) weaker coupling.

Rare-earth ions as hole and electron traps

Ionization energies of any particular Ln^{n+} ion will strongly increase with n. This increase is predominantly due to the decrease in the Coulomb repulsion term with decreasing number of tightly bound *f*-electrons. Consequently energy levels introduced by the same Ln ion in higher charge states will lie lower in the energy scheme of the material. Which of these levels are occupied and which are not will depend solely on the position of the Fermi level (usually in the middle of the bandgap of an undoped and perfect material). The position of the Fermi level can be intentionally changed to some degree by doping. However, unintentional creation of compensating defects during crystal growth is likely to prevent really large changes in its position. In most cases, therefore, it is reasonable to expect that levels close to the valence band and originating from the valence states of dopant ions are occupied (introducing hole traps) while levels close to conduction band are empty (introducing electron traps).

Let us consider a simple model of the electronic structure of a compound material with the chemical formula AB_3 (where A denotes a tripositive cation and B a singly negative anion or anionic molecular group), doped with some Ln ion. As shown in Fig. 2, we assume in this model that the conduction band originates from the (empty) *d*-, *s*- and *p*-levels of A^{2+}, the valence band originates from the (filled) *p*-levels of B^-, and excitonic bands are due to *s*- and *d*-levels of the A^{3+} cation (neglecting here the possibility of the conduction band being due to B^{2-} and an anionic exciton band originating from the excited $(B^-)^*$ as, *e.g.*, in phosphate materials). In the figure we also show single electron energies of the 2+ and 3+ charge states of the Ln dopant ion. Although the *d*, *s* and *p* levels of Ln^{2+} are likely to merge with the conduction band, a lower lying *f*-level may, if the Fermi level is low enough, introduce an empty level below the conduction band and make the ion an efficient electron trap. Therefore in order to have a Ln ion play the role of an electron trap, the *f-s* promotion energy has to be large enough in comparison to the width of the conduction band. Greater *6s-4f* energy differences in Ln^{2+} favor, therefore, electron trapping by the Ln^{3+} ions. In contrast, smaller *6s-4f* energy differences in Ln^{3+} will increase the probability of having a filled *4f* level of the Ln^{3+} in the forbidden energy gap and avoiding the merging of this level with the valence band, thereby allowing the Ln ion to play the role of a hole trap. Since after trapping a hole the Ln^{4+} ion has all of its corresponding 3+ states empty (and available for electrons) the lower lying *d* and *s* levels of the Ln^{3+} (below the conduction band, at about the energy of host excitons) ensure large capture cross sections for electrons by Ln^{4+}. The proper positions of the filled *4f* level of the unexcited Ln^{3+} and of the *d* and *s* levels of the excited Ln^{3+} therefore lead to efficient radiative recombination of e-h pairs through the Ln^{3+}. Note that most of the energies required to determine positions of the appropriate levels in the forbidden energy gap can be found by spectroscopic measurements [8].

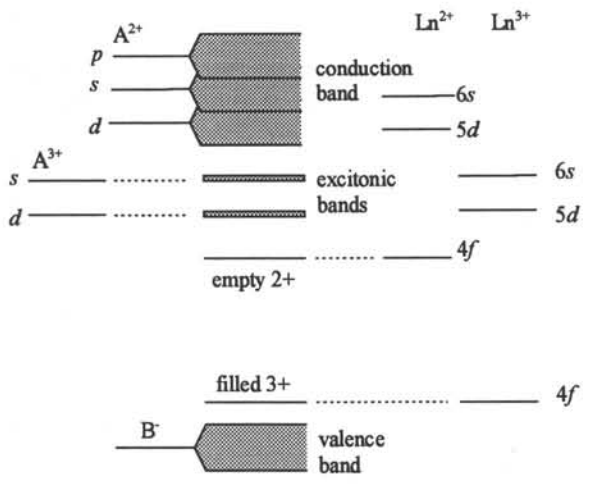

Fig. 2. A schematic band structure model of the compound material doped by Ln^{3+} ions. Energy levels of Ln^{2+} and Ln^{3+} are also shown. For details see text.

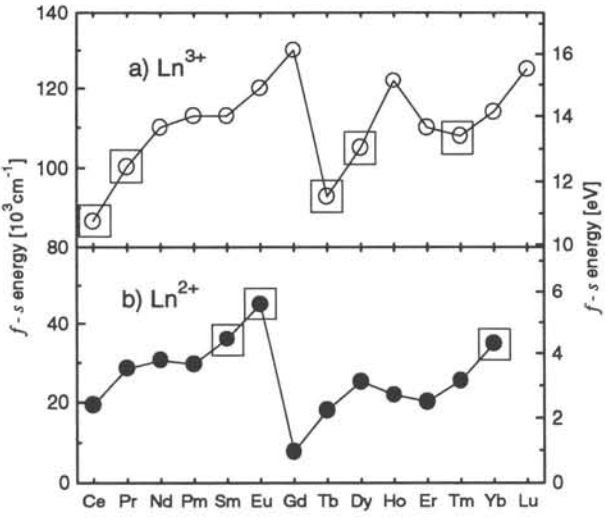

Fig. 3. Energies of f-s promotion for Ln ions in their 3+ and 2+ states. The ions most likely to act as electron or hole traps are indicated by squares.

In Fig. 3 we show *f*-to-*s* promotion energies for 3+ (a) and 2+ (b) Ln ions as calculated by Brewer [15]. As indicated in the figure, Ce, Pr, Tb, Dy and Tm are prime candidates for hole traps while Eu, Sm and Yb are likely to introduce efficient electron traps. It is interesting to note that Ho, Gd, and Lu are very unlikely to introduce hole traps, with the latter two unlikely to introduce electron traps as well. From this point of view it appears that Gd and Lu should be the best candidates for neutral constituents (cations) in the Ln-based materials providing no competition to activating ions.

With Ce, Pr, Tb, Dy and Tm as activators, other Ln inadvertent impurities (especially Eu, Sm and Yb) should be scrupulously avoided, since they may introduce electron traps that would contribute to longer components in the scintillation pulse. One should note, however, that these ions may be very useful in X-ray storage phosphors.

Wojtowicz *et al.* observed previously [8] that although trap levels lying deep in the forbidden energy gap do provide large energy gains upon trapping of carriers, the capture process may nevertheless be severely impeded by energy barriers due to the electron-lattice coupling term in the total Hamiltonian of the system. In this work, a simple one-configuration-coordinate model was introduced and described in detail. Here we summarize the most important conclusions in the case of the hole trap:

1). The optical trap depth ΔE (the energy of an optical transition $Ln^{4+} + h\nu \rightarrow Ln^{3+} + h_v$ which releases a valence hole h_v from the hole trap) is increased by an amount ΔE_x, the relaxation energy relative to the thermal equilibrium depth of the trap, which determines occupancy of the trap under steady state conditions.

2). An energy barrier ΔE_b between $Ln^{3+} + h_v$ (higher energy) and Ln^{4+} (lower energy) states will determine thermally induced rates of capturing holes by the trap:

$$\Delta E_b = \Delta E^2/4\Delta E_x - \Delta E + \Delta E_x, \qquad (1)$$

3). The energy of the photoionization transition E_{ph} (at the maximum of the band) is related to the forbidden energy gap E_g, the relaxation energy ΔE_x and the optical trap depth ΔE:

$$E_{ph} = E_g - \Delta E + 2\Delta E_x. \qquad (2)$$

Although this approach is very simple we were able to demonstrate that it explains the good performance of Ce-activated orthophosphates and orthoaluminates. According to the model, nonradiative recombination involving Ce was found to be highly unlikely, with Ce instead providing a good radiative recombination center for electron-hole pairs in those materials.

Excitons and charge carriers in spectroscopy of $LuAlO_3$:Ce

In Fig. 4 we show emission and excitation spectra of pure and Ce-doped $LuAlO_3$. In emission (under 8 keV X-ray excitation) the pure sample shows a single broad band peaking at about 300 nm (designated STE) and some weak features possibly due to trace contamination by Tb. The spectrum of the Ce-doped sample is more complex, showing a superposition of the 300 nm STE band, strongly quenched with indents clearly caused by Ce-absorption, and a well known band due to Ce and peaking at about 360 nm. The excitation spectra of the 300 nm band shows distinct differences depending on whether Ce is present. In the pure sample the spectrum (solid curve) consists of a single band peaking at about 152 nm with a tail extending toward high energies while, surprisingly, the same emission in the Ce-doped sample shows a different excitation (broken curve), consisting of a much narrower and weaker band peaking at 161 nm. The excitation spectrum of the Ce emission itself is similar to those already published [8,17], and only the short wavelength part of the spectrum is shown in the figure. Note the prominent feature at 156 nm, interpreted in Refs. 8 and 17 as a band-to-band transition.

The spectra shown in Fig. 4 illustrate convincingly some points considered in this paper. While broad absorption bands are typical of the *f*-to-*d* transitions of the Ce^{3+} ion, the 300 nm emission with its narrow excitation components clearly suggests an excitonic origin. We interpret the broad emission peaking at 300 nm as due to self-trapped excitons (STE), with its relatively sharp excitation structure arising from transitions involving band (unlocalized) states. Thus the peak at 161 nm would correspond to creation of free (band) excitons, while shorter wavelength contributions would be due to free electron-hole pairs. The difference in the STE excitation spectra in undoped and Ce-doped samples, showing a strong reduction of free electron-hole pair contribution to STE in the Ce-doped sample, suggests that energy transfer from STE to Ce does not play a major role despite a good overlap between the STE emission and the Ce absorption. The substantial decrease in STE excitation at energies where Ce excitation increases (156 nm) clearly indicates that the Ce-excitation mechanism does not involve STE states but, on the contrary, actually competes with them. Moreover, the decay of the Ce emission is very fast, with only an insignificant slow component [17]. All the evidence is consistent with a Ce-excitation mechanism involving mostly free holes and electrons, while STE are formed both from free electron-hole pairs and band excitons. The Ce hole capture cross section must be relatively large, preventing hole self-trapping in the presence of Ce in $LuAlO_3$. We therefore conclude that the dominant mechanism of Ce-excitation in $LuAlO_3$ under ionizing radiation is consecutive carrier trapping by Ce ions.

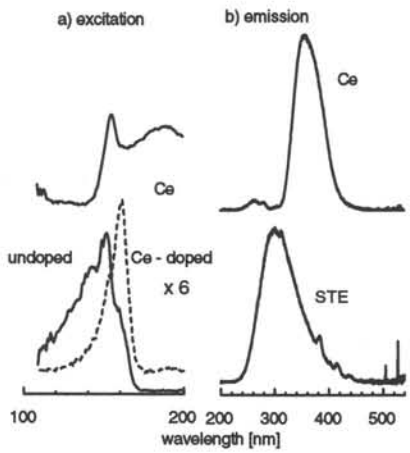

Fig. 4. The emission and excitation spectra of undoped and Ce-doped $LuAlO_3$. The broken curve shows how the STE excitation is changed by the presence of Ce.

Application of the single-configuration-coordinate model

In Table 1 we present parameters of the single-configuration-coordinate (SCC) model for Ce-activated lutetium orthophosphate and orthoaluminate, yttrium oxide and cerium trifluoride. The abbreviations Ce^{3+}/Ce^{4+}, Ce^{4+}/Ce^{3+}, and $Ce^{4+}/(Ce^{3+})^*$ stand for the processes of hole capture, electron capture terminating with the Ce^{3+} ion in its ground state, and electron capture terminating with the

TABLE 1.
The SCC model parameters (in eV)

Scintillator and process	ΔE	ΔE_x	ΔE_h
$LuPO_4$:Ce, E_g=8.27 eV			
Ce^{3+}/Ce^{4+}	3.16	1.09	0.22
Ce^{4+}/Ce^{3+}	7.29	1.09	6.0
$Ce^{4+}/(Ce^{3+})^*$	1.09	1.09	0.27
$LuAlO_3$:Ce, E_g=7.65 eV			
Ce^{3+}/Ce^{4+}	3.44	1.09	0.36
Ce^{4+}/Ce^{3+}	6.39	1.09	4.07
$Ce^{4+}/(Ce^{3+})^*$	0.71	1.09	0.5
CeF_3 E_g=10.eV			
Ce^{3+}/Ce^{4+}	4.48	1.09	1.21
Ce^{4+}/Ce^{3+}	7.7	1.09	6.99
$Ce^{4+}/(Ce^{3+})^*$	1.2	1.09	0.22
Y_2O_3:Ce, E_g = 5.6 eV			
Ce^{3+}/Ce^{4+}	4.96	1.09	1.77
Ce^{4+}/Ce^{3+}	2.82	1.09	0.09
$Ce^{4+}/(Ce^{3+})^*$	-	1.09	-

Ce^{3+} ion in its excited state, respectively. The parameters of the SCC model (ΔE, ΔE_x and ΔE_h) have been discussed in the previous subsections. Optical trap depth ΔE were found using the formula (2) with E_{ph} taken from optical spectra (see Ref. 8 for the case of orthophosphates and orthoaluminates).

We assume that all the materials have the same relaxation energy ΔE_x. In CeF_3 the energy of the bandgap and of the photoionization transition have been taken as 10 and 7.7 eV [18]. The resulting energy barrier for hole trapping at 1.21 eV is significantly higher then in phosphates or aluminates. Although the capture of electron into the excited 3+ state is more likely, it is doubtful whether Ce^{3+} in $Ce(La)F_3$ is able to act as radiative recombination center for e-h pairs. Note also the much higher energy barrier for hole capture in Y_2O_3:Ce, accompanied by a very low barrier for electron capture by Ce^{4+}.

DISCUSSION AND CONCLUSIONS

The approach presented in this paper indicates that certain Ln ions are likely to be efficient luminescence centers under ionizing excitation involving hot band carrier transport through the lattice. In the case of Tb-, Tm-, and Ce-activation (*e.g.*, in oxyhalides known to be efficient X-ray phosphors) the mechanism would very likely be the initial trapping of a hole, followed by electron capture. The same may be true of Eu^{2+} (in BaFCl and BaFBr), where Eu is likely to be an efficient hole trap. Upon formation of a bound exciton the energy of the recombining e-h pair would be transferred to Eu^{2+} and efficient blue *d-f* luminescence would follow. For Eu^{3+} (as in the Y and Gd oxide and oxysulfide TV phosphors) the sequence would probably be reversed, with electron trapping first (into the empty state of Eu^{2+}), followed by hole capture, formation of a Eu^{3+} bound exciton, energy transfer and eventually red Eu^{3+} *f-f* luminescence.

It has been suggested that inherently low scintillation efficiency of CeF_3 is due to inefficient energy transfer from electronic lattice excitations (e-h pairs) and that scintillation derives exclusively from direct excitations of Ce ions [13]. Based on results of photoelectron spectroscopy Pedrini *et al.* have proposed that this may be explained by inability of Ce in cerium trifluoride to capture valence holes [19]. This suggestion is supported by our model, which gives a rather high energy barrier of 1.21 eV for the hole capture process. The apparent difficulty, however, with this interpretation is in the observation that even for very low Ce concentrations the Ce d-f emission strongly dominates over STE emission [7,20]. This would suggest rather high capture cross section of the Ce^{3+}/Ce^{4+} process.

In the case of Y_2O_3:Ce the filled *4f* level lies quite high, indicating a preference toward Ce^{4+} with defect compensation [21]. The SCC model indicates the *d-f* emission from Ce^{3+} to be highly unlikely, and suggests that at higher temperatures Ce may actually play the role of a nonradiative recombination center. At low temperatures, however, some Ce emission may occur, due to the reversed charge transfer transition involving empty 3+ level.

Finally, our mechanistic model can even explain the anomalous behavior of BaF_2:Ce. In the divalent cation host it is very likely that conduction and valence bands as well as the Fermi level are shifted so much on the scale of single electron energies (see Visser *et al.* [22]) that the Ce^{3+} *f*-level is actually in the valence band, thereby preventing hole capture by the ion. Under such conditions holes will self-trap efficiently, and, even if an empty Ce^{2+} level were below the conduction band, it would not be able to compete effectively with electron capture by the self-trapped holes. This would explain why an efficient STE emission persists even with substantial Ce-doping, until the Ce-concentration reaches a high enough level to quench STE emission by a Forster-Dexter type mechanism.

We conclude that transient charge carrier transport in insulating large bandgap materials or materials containing molecular groups may play a significant role determining the performance of these materials as scintillator, X- and cathode ray, and lamp phosphors and certainly deserves more attention of the community involved in the field.

ACKNOWLEDGMENTS

This work was supported by the European Community (Contract No. ERBCIPDCT940037) and the US Department of Energy (DE-FG02-90ER61033). The author is grateful to Prof. C. W. E. van Eijk and his group for their hospitality and help in performing experiments on $LuAlO_3$:Ce. The author gratefully acknowledges a loan of samples and a kind support of Prof. A. Lempicki. Thanks are also due to Prof. C. Brecher who read the manuscript and made many useful comments and suggestions as well as to M. Balcerzyk and D. Wisniewski for their skillful technical assistance. The joint paper giving a full account of experiments performed in Delft will be published later.

REFERENCES

[1]. G.Blasse, in *Heavy Scintillators...*, Crystal 2000 Workshop, Chamonix 1992, p. 85.
[2]. A.Lempicki *et al.*, Nucl. Instr. Meth. A 333 (1993) 304; J. Lum. 60/61 (1994) 942.
[3]. C.C.Klick and J.H.Schulman, Sol. St. Phys. 5 (1957) 97.
[4]. A.K.Levine and F.C.Palilla, Appl. Phys. Lett. 5 (1964) 118.
[5]. G.Blasse, J. Chem. Phys. 45 (1966) 2356.
[6]. H.B.Dietrich *et al.*, Phys. Rev. B 8 (1973) 5894.
[7]. A.J.Wojtowicz *et al.*, MRS Symposium, vol. 348, San Francisco 1994, p. 123.
[8]. A.J.Wojtowicz *et al.*, Conference Record, NSS&MIC, IEEE, Norfolk, 1994, p. 134.
[9]. R.Visser *et al.*, J. Phys.: Cond. Matt. 5 (1993) 1659.
[10]. D. J. Robbins and P.J.Dean, Adv. Phys. 27 (1978) 499.
[11]. N.F.Mott and A.M.Stoneham, J. Phys. C: Sol. St. Phys. 10 (1977) 3391.
[12]. V.N.Kadchenko and M.Elango, Phys. Stat. Sol. (a) 46 (1978) 315; T.A.Green *et al.*, Phys. Rev. B, 39 (1989) 5407.
[13]. A.J.Wojtowicz *et al.*, Phys. Rev. B 49 (1994) 14880.
[14]. K.S.Song and R.T.Williams, *Self-trapped Excitons*, Springer-Verlag, Berlin 1993.
[15]. L.Brewer, J. Opt. Soc. Am. 61 (1971) 1666.
[16]. A.Lempicki *et al.*, Conference Record, NSS&MIC, IEEE, Norfolk 1994, p. 307.
[17]. Torun, Delft and Boston collaboration, to be published.
[18]. C.Pedrini *et al.*, J. Phys.:Condens. Matt. 4 (1992) 5461.
[19]. C.Pedrini *et al.*, MRS Symposium, vol. 348, San Francisco 1994, p. 225.
[20]. R.T.Williams *et al.*, Record of the International Workshop, St. Petersburg 1994.
[21]. M.J.Fuller, J. Electrochem. Soc. 128 (1981) 1381.
[22]. R.Visser *et al.*, J. Phys.: Cond. Matt. 5 (1993) 5887.

ENERGY TRANSFER AND QUENCHING PROCESSES IN CERIUM-DOPED SCINTILLATORS

C. PEDRINI, D. BOUTTET, C. DUJARDIN
Laboratoire de Physico-Chimie des Matériaux Luminescents, Université Claude Bernard Lyon I, Unité de Recherche Associée n° 442 CNRS, 43 boulevard du 11 Novembre 1918, 69622 Villeurbanne cedex (France)
A. BELSKY and A. VASIL'EV
Synchrotron Radiation Laboratory, Physics Department, Moscow State University, 119899 Moscow, Russia

ABSTRACT

The electron-hole pairs→Ce ions energy transfer is qualitatively estimated from X-ray photoelectron spectroscopy in various cerium-doped fluorides and oxides. Surface quenching effects are analyzed in the regions of strong absorption of the lattice and of the cerium ions. Secondary electron excitation quenching is shown to occur when high densities of excitations are produced.

I - INTRODUCTION

In cerium-doped scintillating materials, the energy transfer from electron-hole pairs to cerium ions is of most interest, since most of the energy absorbed by the lattice after X-ray or γ-ray high energy excitation is transformed into separated or correlated electron-hole pairs. Such energy transfer process involves a sequential capture of a hole and then of an electron by Ce centers. The efficiency of the capture of a hole by Ce depends on the energy of the 4f of cerium in the bandgap of the crystal. The X-ray photoelectron spectroscopy (XPS) technique can provide information on the band structures and on the energies of core levels. XPS measurements will be used to explain the low or the high efficiency of a hole capture in cerium-doped fluorides or cerium-doped oxides, respectively.

The luminescence quenching due to surface losses occurs when the radiation penetration depth in the crystal is very small, typically 10nm. Such a process is always important in the fundamental absorption region (10-30 eV) where the lattice usually strongly absorbs, but can be also efficient in the 4f→5d Ce^{3+} absorption region in the case of high Ce concentrations. This quenching will be described in LaF_3-CeF_3 mixed crystals where it can arise in both regions.

The so-called "secondary electron excitation" quenching, attributed to the interaction of closely spaced electron excitations, can be efficient when a high density of excitations is created. Experimental evidences and characteristics of such a process will be presented and discussed. This quenching must be taken into account in the evaluation of the light yield of scintillators.

II - ELECTRON-HOLE PAIRS →Ce IONS ENERGY TRANSFER

1 - Cerium-doped fluorides

XPS measurements provide information about the binding energy of the various orbitals of the crystal ions [1]. We consider only in this paper the valence band region (Fig. 1). In LaF_3, the 4f level of La is not occupied and therefore no peaks are detected besides the 2p levels of F^- ions in the lower energy region. In CeF_3, the 4f peak of Ce (which is occupied by 1 electron) is clearly detected at 3-4 eV above the valence band. The 4f peak of Pr in PrF_3 is stronger since it is occupied by 2 electrons and its binding energy is around 1-2 eV less than the 2p(F^-) level.

XPS spectra of cerium-doped LaF_3 have been recorded for various Ce concentrations. The 4f(Ce^{3+}) peak has been detected for Ce concentrations of more than 10 at %. So the

Proc. Int. Conf. on Inorganic Scintillators and Their Applications, SCINT95,
1996, Delft University Press, The Netherlands

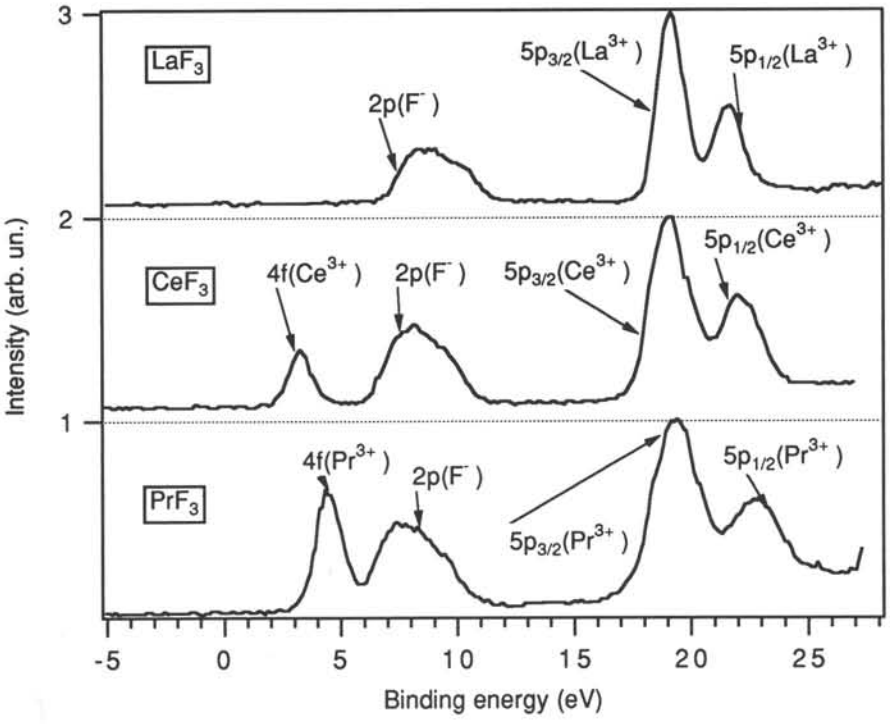

Figure 1 - Photoelectron spectra of various fluorides in the valence band energy region

method cannot provide information about the energy of the 4f(Ce^{3+}) level for Ce weakly doped systems.

From these results, it is clear that the capture of a valence band hole by the 4f(Ce^{3+}) level is most unlikely in fluorides, even if the relaxation of the lattice can substancially reduce the energy difference between the 4f level and the top of the valence band. In region of direct creation of electron-hole pairs with a hole in the valence band (12-16 eV) a deep dip is indeed observed in the fluorescence excitation spectrum of CeF_3 so that the quantum yield is comparable with the scattered light in the monochromator [2]. Therefore separated electron-hole pairs cannot excite Ce ions.

2 - Cerium-doped oxides

XPS spectra of some orthoaluminates are shown in Fig. 2 in the valence band region. Like for LaF_3, the empty 4f(Y^{3+}) level is not observed in the spectrum of $YAlO_3$. On the other hand, the 4f(Ce^{3+}) peak is clearly detected in $CeAlO_3$. It strongly overlaps the valence band and its position in the bandgap is estimated around 1eV above the top of the valence band. Similar results are expected in other cerium based oxides (XPS measurements on Ce_2SiO_5 are in progress) since like for fluorides, oxides containing less than 10 at % Ce do not exhibit 4f(Ce^{3+}) peaks in XPS spectra.

The two spin-orbit components of 4f(Lu^{3+}) in $LuAlO_3$ are very strong as expected since this level is occupied by 14 electrons. The two peaks overlap the bottom of the 2p(O^{2-}) valence band. The role played by this 4f(Lu^{3+}) level in the scintillation mechanism of lutetium based compounds is shown in another paper of the present proceedings [3] and in more details in a paper to be published [4].

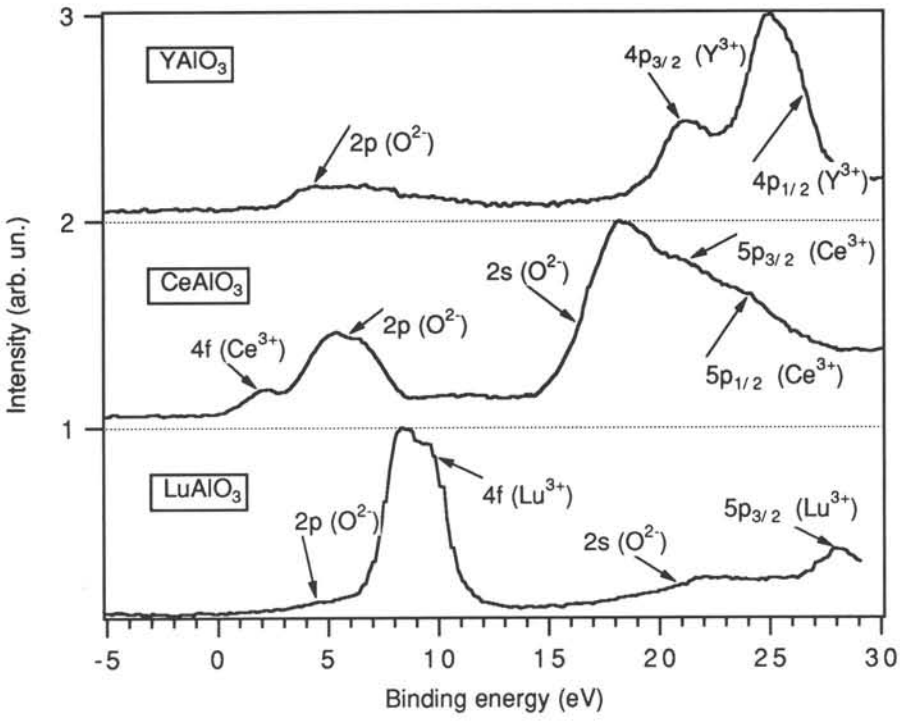

Figure 2 - Photoelectron spectra of various orthoaluminates in the valence band energy region

The location of the 4f(Ce^{3+}) level in the bandgap is very close to the top of the valence band. It is therefore expected that the capture of valence band hole by 4f(Ce^{3+}) is then strongly probable, leading to a relatively high light yield in the region of the fundamental absorption edge of the crystal. The light yield of $LuAlO_3:Ce^{3+}$ at the excitation energy near the beginning of the band to band 2p(O^{2-})→5d(Lu^{3+}) transitions (8.5 eV) is still 50% of the yield obtained under direct excitation of cerium [3]. The strong increase of the luminescence intensity of Lu_2SiO_5:Ce above 6.5 eV [2] is also an indication of the high efficiency of the sequential capture of a hole and then of an electron by Ce centers.

3 - Conclusions

From XPS and fluorescence excitation spectra of cerium-doped fluorides and oxides, the following conclusions can be drawn :

-in fluorides

(i) the capture of 2p(F^-) hole has negligible probability since 4f(Ce^{3+}) level is situated at rather too high energy related to the top of the valence band

(ii) the fluorescence excitation is mainly due to the direct excitation of the 4f(Ce^{3+}) electron after the relaxation of hot electron or core hole

(iii) the efficiency of CeF_3 is the result of the high concentration of Ce ions since the probability of the direct excitation of the 4f(Ce^{3+}) electron after the inelastic scattering of the hot electron or the Auger relaxation of the core hole is high.

-in oxides

The high efficiency of cerium-doped oxides in general and in particular of $LuAlO_3$:Ce and Lu_2SiO_5:Ce is connected with the close energy location of the 4f(Ce^{3+}) level

related to the top of the valence band of the crystal, making the capture of the valence band hole by the luminescent center much easier. Therefore the excitation of cerium through energy transfer from (e-h) pairs is dominant.

III - SURFACE QUENCHING

This effect is connected with the small radiation penetration depth and with the presence of many surface defect centers.

A simple diffusion model of surface losses can be constructed, supposing that the quenching is connected with diffusion of excitation to the surface, where a large number of defect centers makes non-radiative recombinations very likely [5].

The luminescence excitation spectrum can be described by the expression :

$$\eta(h\nu) = \eta_\circ(h\nu)(1 - R(h\nu))\left(1 - \exp(-\alpha(h\nu)d)\right) / \left(1 + \alpha(h\nu)L\right) \tag{1}$$

with

$\alpha(h\nu)$: absorption coefficient

$\eta_\circ$: intrinsic quantum yield determined by bulk process

$R(h\nu)$: reflectivity

d : sample width

$L = (D\tau)^{1/2}$: diffusion length of the excitation with total lifetime τ and diffusion coefficient D

The luminescence decay is described by

$$I(t) = \tau^{-1} \exp\left(-t\left(1 - \alpha^2 L^2\right) / \tau\right)\left(1 - \phi\left(\alpha L (1/\tau)^{1/2}\right)\right) \tag{2}$$

where ϕ is the error function

The decay is non-exponential with a fast starting region

$$I(t) \approx 1 - 2\alpha L (t/\tau)^{1/2} \tag{3}$$

and a nearly exponential behaviour at large times

$$I(t) \approx (\tau/t)^{1/2} \exp(-t/\tau) \tag{4}$$

This model has been applied to the case of CeF_3. The kinetic parameters, like the total integral under the decay curve $I_\circ(h\nu)$

$$I_\circ(h\nu) = \int_\circ^\infty I(t, h\nu) dt \tag{5}$$

and the mean time of luminescence

$$\tau_m(h\nu) = \frac{1}{I_\circ(h\nu)} \int_\circ^\infty t I(t, h\nu) dt \tag{6}$$

are plotted in function of the excitation energy and the resulting curves are compared with the function $1/1+\alpha L$ (with L = 10 nm) which describes the surface quenching (lower part of figure 3). The curves are strongly correlated in the region of energy less than the threshold energy (16

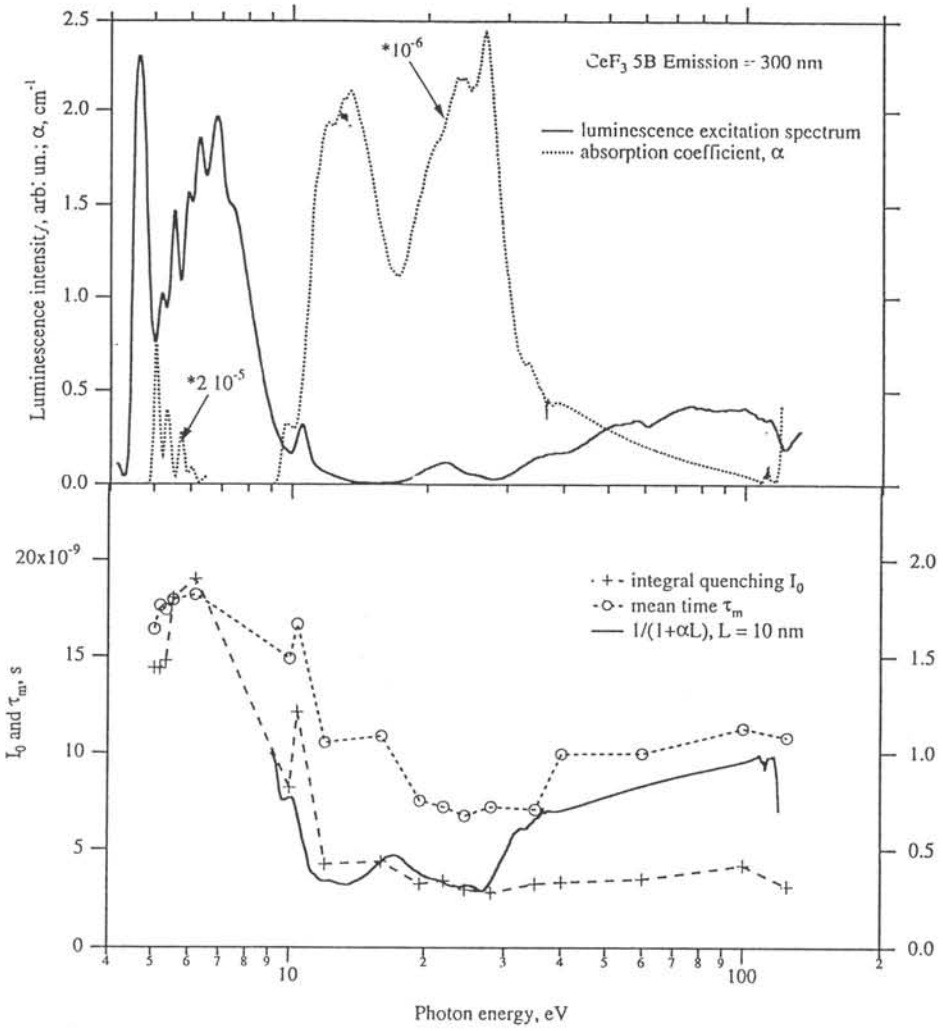

Figure 3 - Upper part : luminescence excitation and absorption spectra of CeF_3 ; lower part : correlation between the surface losses and the kinetics parameters of the scintillation in CeF_3

eV) of the multiplication of the excitations, indicating that the kinetics of the scintillation is mainly governed by the surface quenching effect. Above 16 eV (upper part of figure 3), there is no evidence of the anticorellation between the excitation and the absorption spectra. In this region, the excitation spectrum is indeed strongly modulated by the mechanisms of multiplication of the electronic excitations [2] and the surface quenching is not the dominant process.

In Fig. 4 are pictured the excitation spectra of different cerium-doped LaF_3 systems in the $4f \rightarrow 5d$ Ce^{3+} absorption region. The spectrum of the very weakly doped compound exhibits as expected the five $4f \rightarrow 5d$ bands and reflects the absorption spectrum ; the bands are washed out in the case of 1 at %Ce and the light yield is constant for 10 at %Ce due to the saturation of the fluorescence. The spectrum of LaF_3:50 at %Ce exhibits dips at energies of the absorption peaks and their depths increase with the cerium concentration and is maximum for CeF_3. The best fit using our diffusion model was obtained (using some calculation tricks [6])

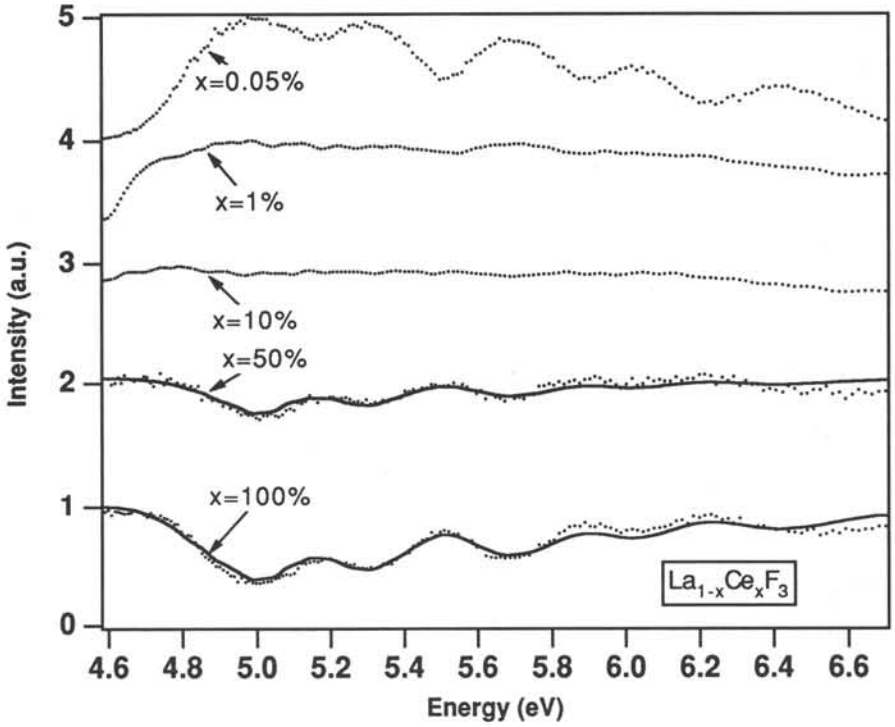

Figure 4 - Excitation spectra of $La_{1-x}Ce_xF_3$ in the 4f→5d cerium absorption region

with $\alpha_{max} = 3.8 \times 10^4$ cm^{-1} for CeF_3. The calculated absorption spectrum, represented in the upper part of figure 3, shows perfect anticorrelation with the excitation spectrum. The absorption coefficient of CeF_3 was used to calculate the absorption spectrum of LaF_3:0.05 at %Ce. A very good agreement with the experimental absorption spectrum was obtained, proving that our diffusion model is consistent. It leads to a very long diffusion length L≈600nm. It is well-known that in ionic crystals, L may vary from 10 to 1000nm. In the region of fundamental absorption, L is usually found around 10 or few tens of nanometers in alkali halides, and it seems reasonable to suggest such a value for CeF_3.

Our model cannot lead to so different diffusion lengths of excitation in the 4f→5d Ce^{3+} absorption and fundamental absorption regions, except of the migration of two kinds of excitations are considered :

(i) in the 4f→5d Ce^{3+} absorption region, where L is about few hundreds of nanometers, we suggest we are dealing with the migration of non-relaxed excitations, like free excitons in ionic crystals.

(ii) in the fundamental absorption region, where L is around 10nm, a cerium ion is ionized with creation of a non-relaxed Ce^{4+} ion and a removed electron. After relaxation, Ce^{4+} captures an electron, and we have shown, using a single configuration-coordinate model and potential curves drawn for various electron-hole distances [6] that this capture is followed by a direct creation of relaxed Ce^{3+} excited ion : this process does not pass through the non-relaxed exciton state. We are therefore dealing with the migration of relaxed excitations. The diffusion length in CeF_3, supposing a dipole-dipole transfer, can be estimated around 7-8nm.

IV - SECONDARY ELECTRON EXCITATION QUENCHING

Such a quenching is attributed to the interaction of closely spaced electron excitations, mainly obtained after Auger relaxation of core holes.

This process can substantially change the fluorescence decay profiles and depends on the excitation energy and on the temperature. I can also lead to a strong variation of the light yield in the X-edge absorption region. Such effects have been shown in previous papers : change of the fluorescence decay profiles of LaF_3:0.05 at %Ce and CeF_3 with the excitation energies around the threshold energy of the multiplication of excitations [2], temperature dependence of the fluorescence decay profiles of CeF_3 under X-ray synchrotron radiation excitation [7], step-wise variation of the light yield of various scintillating materials around the X-edge absorptions in the 7-22 keV region [8].

The general characteristics of secondary electron excitation quenching can be summarized :

(i) it is due to the interaction of closely spaced electron excitations

(ii) it occurs above the threshold of the electron excitation multiplication when the Auger relaxation of core levels begins.

(iii) its magnitude depends on the initial spatial distribution of excited Ce ions, and then on the excitation photon energy

(iiii) it increases near the threshold of the core level transitions, when the relaxation of a core hole results in the production of several electronic excitations surrounding the initially excited ion.

(iiiii) the spatial distribution is not in equilibrium, and depends on the rate of spatial relaxation. The increase of the temperature results in the increase of the migration rate of excitations over the cerium subsystem, and therefore the quenching decreases.

V - CONCLUSIONS

-It is important to use a good energy level diagram of crystals for the description of the mechanisms of scintillation. Two techniques are available : (i) XPS but the 4f level of cerium cannot be detected for Ce concentrations less than 10 at% ; (ii) molecular orbital calculations but there are still problems with reliability.

-It is clear that for high light yield, cerium-doped oxides are potentially much better than cerium-doped fluorides.

-It is important to investigate the region from few eV to 100 eV to study the basic mechanisms of very high excitation. Indeed, fast electrons after the absorption of a gamma-quantum with the energy about megaelectronvolts excite mainly electrons from the highest lying levels with energies from 10 to 100 eV, since the energy loss function is large in this energy region. They can be excited separately by VUV photons as well. Therefore the use of VUV spectroscopy gives the opportunity to analyze the important stage of the energy relaxation in the scintillation process. But it is necessary to take into account the surface quenching which is effective in this region of energy.

-It is important to consider additional quenching due to high densities of excitation, in particular in the estimation of the light output of scintillators. For example, in the case of CeF_3, such effect was estimated to reduce the light output by a factor 0.2-0.5.

REFERENCES

1. J.F. Watts, Vacuum 45, 653 (1994)
2. C. Pédrini, A.N. Belsky, A.N. Vasil'ev, D. Bouttet, C. Dujardin, B. Moine, P. Martin and M.J. Weber, MRS Proceedings, vol. 348, p. 225 (1994)
3. C. Dujardin, C. Pédrini, D. Bouttet, J.W.M. Verweij, A.G. Pétrosyan, A. Belsky, A. Vasil'ev, E.I. Zinin, P. Martin, this conference
4. C. Dujardin, C. Pédrini, D. Bouttet, J.W.M. Verweij, A.G. Pétrosyan, A. Belsky, A. Vasil'ev, E.I. Zinin, P. Martin, to be published in Phys. Rev. B
5. A.N. Vasil'ev and V.V. Mikhailin, Introduction to Solid State Spectroscopy, Moscow, MSU (1987), p. 198

6. A.N. Belsky, A.N. Vasil'ev, V.V. Mikhailin, C. Pédrini, D. Bouttet, C. Dujardin, P. Martin, M.J. Weber, to be published
7. C. Pédrini, B. Moine, D. Bouttet, A.N. Belsky, V.V. Mikhailin A.N. Vasil'ev and E.I. Zinin, Chem. Phys. Lett. 206, 470 (1993)
8. A.N. Belsky, P. Chevallier, P. Dhez, P. Martin, C. Pédrini and A.N. Vasil'ev, Nucl. Instr. and Meth. in Phys. Res. A361, 384 (1995)

X-ray photoelectron spectroscopy of some scintillating materials

D.Bouttet*, C.Dujardin*, C.Pedrini*, W.Brunat**, D.Tran Minh Duc*** and J.Y.Gesland****

* Laboratoire de Physico-Chimie des Materiaux Luminescents, URA 442 CNRS, Universite Claude Bernard Lyon 1, 69622 Villeurbanne Cedex (France)

**BIOPHY Research NOVACITE ALPHA BP 2131, 43 Bd du 11 novembre 1918, 69603 Villeurbanne Cedex (France)

***CENATS Universite Claude Bernard Lyon 1, 69622 Villeurbanne Cedex (France)

**** U.M.C, Université du Maine, 72017 Le Mans Cedex (France)

Abstract: We demonstrate in this paper how XPS measurements on scintillating materials can improve our understanding of scintillation processes. Measurements on CeF_3, PrF_3, LaF_3:10%Ce, $LiLuF_4$, $LuAlO_3$,$CeAlO_3$ and Lu_2SiO_5 compounds are presented.

Introduction: The scintillation efficiency of a crystal is generally described by the product of the efficiencies of (1) β: the energy conversion, (2) S: the energy transfer to the luminescent centers (3), Q: the fluorescence of the emitting center [1]. The first stage is the primary interaction and thermalization of the resulting electrons and holes to e-h pairs with energies roughly equal to the band gap energy Eg. This stage is well described in ref [2]. The third stage depends mainly on the optical properties of the luminescent centers. This generally relies upon radiative transition probability and thermal quenching, both of which can be studied by optical spectroscopy. The second stage (S) strongly depends on the energy level scheme of the system. XPS (X-ray Photo-electron Spectroscopy) is a very powerful surface analysis technique that provides elemental concentrations and chemical informations on the first 10 nm of solid surfaces [3]. Its principle is simple: under photon irradiation, atoms can emit photoelectrons by the photoelectric effect. The measurement of the number of photoelectrons versus their kinetics energy gives the photoelectron spectrum. To draw the energy scheme of compounds, we focus our interest only on the energy position of low energy bounded levels.

Experiment: Energy conservation implies that the kinetic energy (E_K) of the ejected electron is related to the binding energy (E_B) of the atomic orbital from which the electron originates by: $h\nu=E_K+E_B+\Phi_{sp}$ where $h\nu$ is the photon energy and Φ_{sp} the spectrometer work function.

For insulators where charging of the surface occurs and because determination of the position of Fermi levels is quite difficult, internal calibration must be used. This is generally done by setting the C-C component of the C 1s peak of adventitious carbon contamination (always present on surfaces) at 285.0 eV[4]. Energy positions are therefore referenced to this line. The overall experimental accuracy for determining the true value binding energies can be estimated to be about $\pm$0.1-0.2 eV.

Proc. Int. Conf. on Inorganic Scintillators and Their Applications, SCINT95,
1996, Delft University Press, The Netherlands

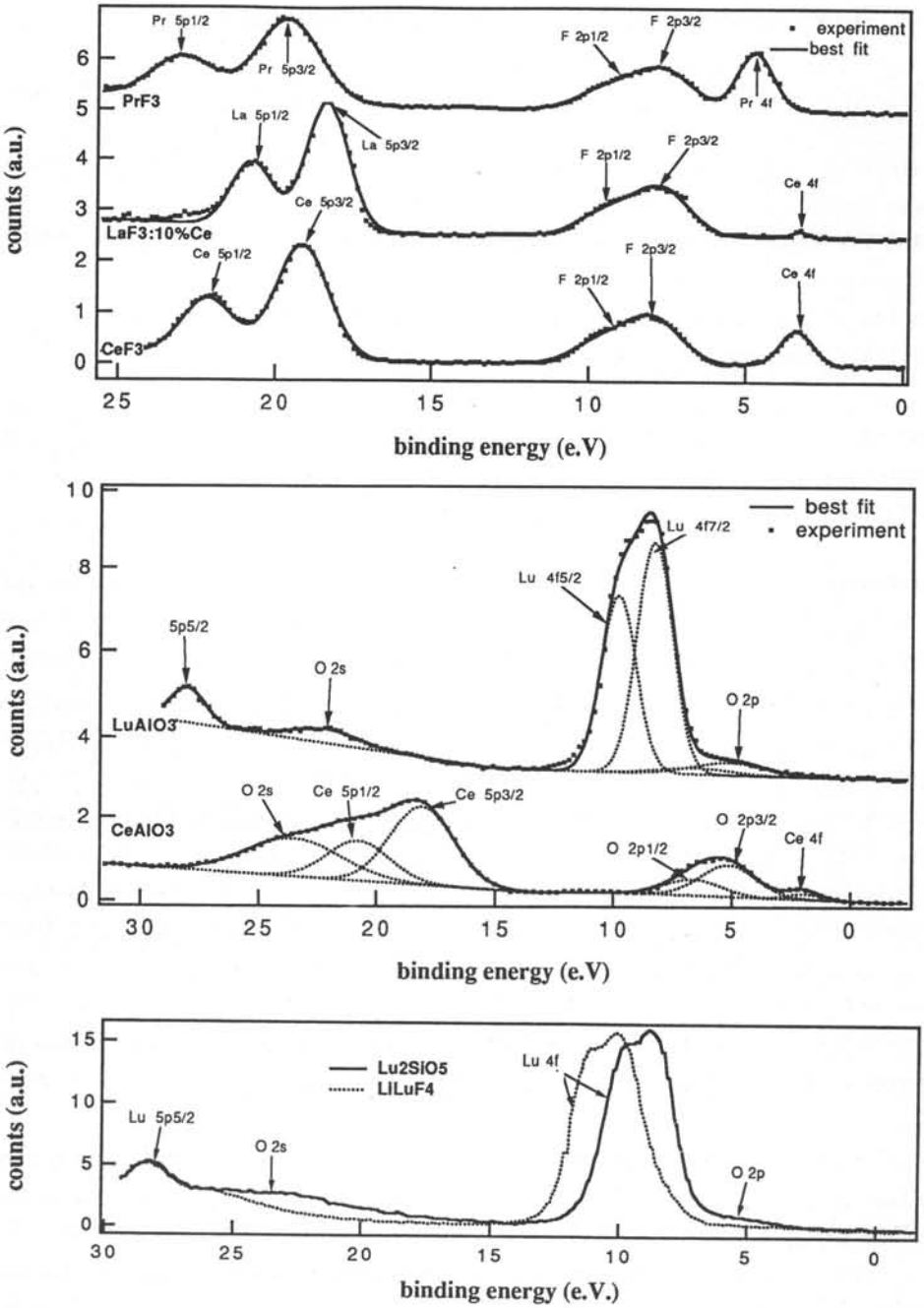

Figure 1: XPS measurements on CeF_3, PrF_3 and LaF_3:10%Ce; $LuAlO_3$ and $CeAlO_3$; Lu_2SiO_5 and $LiLuF_4$

XPS measurements were obtained with the imaging photoelectron spectrometer ESCASCOPE from FISONS INSTRUMENTS [5]. Photoelectron spectra were acquired with a monochromatic Al Kα photon source with a spot size of 1000 μm in diameter. The CAE mode was chosen and gave an experimental energy resolution of 0.7 eV (FWHM) for Ag $3d_{5/2}$. In order to remove the major part of surface contamination, all samples were rinsed in ethanol and hexane before introduction into the instrument.

Results and discussion

-Fluorides compounds: V.U.V spectroscopy of the CeF_3 crystal was best interpreted using its energy scheme diagram [6]. The XPS measurement allow us to locate each level of Ce^{3+} and F^{2-} ions near the valence band. The data show (figure 1-a-) that there is no overlapping between the Ce^{3+} 4f and the F^{2-} 2p. Energy transfer of the thermalized electron hole pair begins by hole trapping by the activator. Therefore, the probability of such transfer is very low, because it involves too many phonons. The only one way to excite cerium is directly by thermalization of a hot electron. The smallest gap between the Ce 5p and the F 2p is around 5-6 eV. It shows that this compound would rather give rise to the Auger process with the Ce 4f --> 5d transition (4.5 eV) than a cross luminescence. CeF_3 and PrF_3 have similar structures which lead to their similar XPS spectra, but it is important to point out the overlap between the Pr 4f and F 2p orbitals. It would increase the hole trapping probability. The energy transfer should then be more efficient than for CeF_3. To study the low doped crystals, we identify the energy position of the based compounds. A spectra of LaF_3:10%Ce^{3+} exhibits a weak peak at exactly the same position as for CeF_3. We can then expect that the localised levels of a few doped compound do not shift significantly from the based compound.

-Oxides compounds: The XPS data of the orthoaluminates $LuAlO_3$, $CeAlO_3$ as well as orthosilicate Lu_2SiO_5 are shown in figures 1-b- and 1-c-. Assignment of the tail around 5 eV for the lutetium oxydes to O 2p is made using a $LiLuF_4$ crystal (the tail does not appear, fig. 1-c-). Lu_2SiO_5 and $LuAlO_3$ crystals roughly give rise to the same band structure near the valence band region. $CeAlO_3$ data allow us to estimate the position of the fundamental level of Ce^{3+} from the valence band in the case of the Ce doped compounds. By this method, an energy scheme of the famous $LuAlO_3$:Ce^{3+} crystal is shown in ref [7].

References

[1] M.J.Weber, To be published in the proccedings of the V International Conference on Calorimetry in High Energy Physics
[2] P.A.Rodnyi, P.Derenbos and C.W.E.Van Eijk, MRS spring meeting (1994) San Francisco
[3] J.F. Watts, Vacuum, Vol. 45, p. 653, 1994.
[4] Practical Surface analysis, Vol. 1, Appendix 2, Ed by D. Briggs and M.P.Seah, Wiley, Chichester, 1990
[5] P. Coxon et al., J. Electron Spectrosc. Relat. Phenem., vol. 52, p. 821,1990
[6] C.Pedrini et.al., MRS spring meeting (1994), San Francisco
[7] C.Dujardin et.al., submitted to IEEE, trans. nuc. science

QUENCHING MECHANISMS OF Ce^{3+} LUMINESCENCE

G. BLASSE
Debye Institute, Utrecht University, Postbox 80 000, 3508 TA Utrecht, The Netherlands

ABSTRACT

Efficient Ce^{3+} scintillators require that the quantum efficiency of the Ce^{3+} luminescence is high. This is not always the case. In $La_2O_3:Ce^{3+}$ and $Gd_2O_2S:Ce^{3+}$, for example, it approaches zero. The possible quenching mechanisms are considered. Most important is quenching via an excited charge-transfer state. From this it follows that efficient Ce^{3+} scintillators will be ionic compounds. A positive effective charge will also suppress quenching, but for scintillators this offers no prospectives in view of the introduction of other quenching sites.

INTRODUCTION

The Ce^{3+} ion is nowadays very popular as a luminescent ion in scintillators. Examples are CeF_3, $Gd_2SiO_5:Ce^{3+}$, $Lu_2SiO_5:Ce^{3+}$, $LuPO_4:Ce^{3+}$, and $LuAlO_3:Ce^{3+}$. This interest in the Ce^{3+} ion is based on the fact that the emission transition is an allowed one ($5d \rightarrow 4f$), so that the radiative decay time is short: values from about 20 ns in the ultraviolet till about 70 ns in the visible have been reported in the literature [1,2]. This variation is due to the occurrence of the emission wavelength till the third power in the expression for the Einstein coefficient of spontaneous emission.

The energy conversion efficiency of a scintillator depends on the efficiency of creating electron-hole pairs, on the efficiency of transfer to the luminescent centre, and on the quantum efficiency of the luminescent centre [1,3]. The latter factor is often left out of the discussion. This, however, is not justified. In this contribution we want to consider the factors which influence the quantum efficiency (q) of the Ce^{3+} ion (see also [4]).

IS $q(Ce^{3+})$ ALWAYS HIGH?

At first sight the Ce^{3+} ion seems to be an efficient luminescent ion which is applied in many luminescent materials [1]. It shows efficient luminescence at room temperature in many solids, like borates, silicates and phosphates. Even in aqueous solution, in polymers and organometallic complexes it may emit efficiently [4].

On the other hand, the Ce^{3+} ion does not emit in titanates, vanadates and tungstates [4], nor, for example, in carboxylic-acid-containing ligands [5]. Even more impressive is the fact that compositions like $Ln_2O_3:Ce^{3+}$ (Ln = Y,La,Gd) and $Ln_2O_2S:Ce^{3+}$ (Ln = La-Lu) do not emit [4,6]. These host lattices would have been promising as scintillators; other ions, like Eu^{3+}, show in these host lattices highly efficient luminescence under ultraviolet and ionizing radiation excitation [1]. To these we may add the low efficiency of Ce^{3+} in Gd_2SiO_5 [7] and $Ln_3Ga_5O_{12}$ [8].

Proc. Int. Conf. on Inorganic Scintillators and Their Applications, SCINT95,
1996, Delft University Press, The Netherlands

From these data we may conclude that $q(Ce^{3+})$ is not always high.

SPECTROSCOPY AND LUMINESCENCE QUENCHING OF Ce^{3+}

The Ce^{3+} has a simple electron configuration in the ground and the lowest excited state, viz. $4f^1$ and $5d^1$, respectively. Considering the lowest crystal-field component of $5d^1$ only, this leads to a simple configurational coordinate diagram (see fig. 1). Luminescence quenching is usually ascribed to a nonradiative transition from the excited to the ground state due to a large parabolae offset [1]. This offset can be estimated from the Stokes shift of the emission. As far as we are aware, this Stokes shift is never so large that it can explain luminescence quenching of the Ce^{3+} ion. Even in water, where the Stokes shift is very large (8000 cm^{-1}), the Ce^{3+} ions shows luminescence. This is contradictory to statements by others, for example [5].

It has also be argued that the quenching is due to a low-energy position of the emitting state. For example, nonluminescent $La_2O_3:Ce^{3+}$ and $Gd_2O_2S:Ce^{3+}$ are yellow, because the lowest 4f-5d absorption band is around some 450 nm (see fig. 2). Some even say that this cannot be Ce^{3+} because this ion is colourless [9]. However, yellow $Y_3Al_5O_{12}:Ce^{3+}$ is used as a luminescent lamp material [1].

Therefore, we have to look for another mechanism. It is obvious to invoke a charge-transfer state for this purpose. This has been done before to explain the quenching action of Eu^{3+} and VO_4^{3-} on the Ce^{3+} emission [1]. Quenching occurs via a charge-transfer state $Ce^{4+} + Eu^{2+}$ and $Ce^{4+} + V^{4+}$, respectively. A more recent quencher is In^{3+} in $(Sc,In)BO_3:Ce^{3+}$ [10].

A very similar phenomenon is responsible for the quenching in $La_2O_3:Ce^{3+}$ and $La_2O_2S:Ce^{3+}$ [4]. Here it is assumed that the emitting level is close to or in the conduction band, so that photoionisation occurs. This is nothing else than creating another charge-transfer state, sometimes indicated as an impurity-trapped exciton state from which return to the ground state is nonradiatvely. It is common that the intensity of the several excitation bands of the Ce^{3+} emission in a given compound decreases for higher energy which can be ascribed to the same effect [8].

This explanation is confirmed by the fact that it is not unique, but has also been observed for the emission of Eu^{2+} [11], Pb^{2+} [12], Bi^{3+}[13,14], and other ions.

CONDITIONS FOR HIGH $q(Ce^{3+})$

The sketched model suggests a "recipe" to find host lattices in which the Ce^{3+} ion shows luminescence with a high quantum efficiency. In order to prevent the negative influence of charge-transfer states, it is imperative to place the Ce^{3+} ion in a site where the bonding is very ionic, so that excited states are at high energy. In fact this simple statement works very well [4]. Another formulation is that host lattices should be applied which show a very wide optical band gap.

Compositions like $La_2O_3:Ce^{3+}$ and $La_2O_2S:Ce^{3+}$ should be considered as rather covalent and their gaps can be observed in the conventional ultraviolet area. It may be questioned why one of the Ce^{3+} ions in $Gd_2SiO_5:Ce^{3+}$ is practically quenched at room temperature. This problem has been attacked in ref. [1]. It should be realized that a better way to describe this silicate is the formula Gd_2OSiO_4 which illustrates that the rare earth ion is coordinated by one or three oxygen ions which do not belong to a silicate

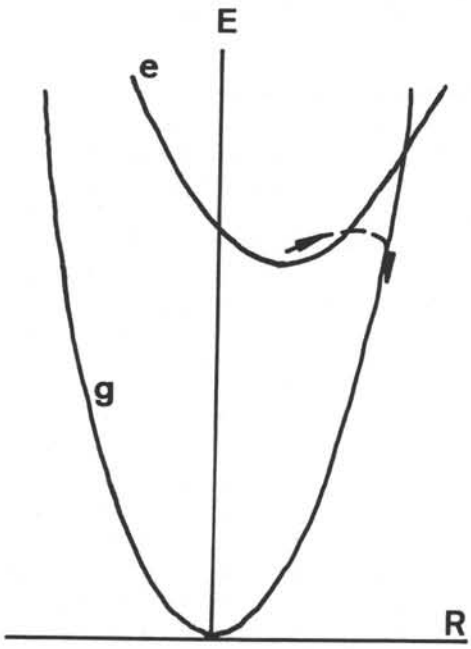

Fig. 1. Configurational coordinate model for Ce^{3+}

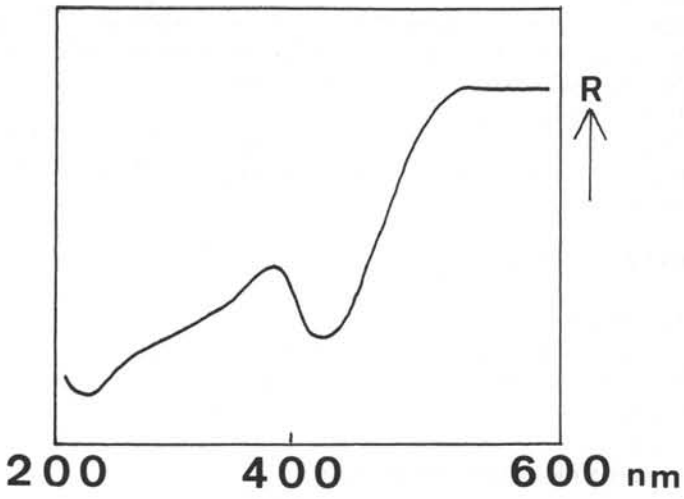

Fig. 2. Diffuse reflection spectrum of $La_2O_3:Ce^{3+}$

tetrahedron. In this way Gd_2SiO_5 contains a Gd_2O-sublattice in which the bonding is comparable to that in Gd_2O_3 (or Y_2O_3 or La_2O_3), where Ce^{3+} does not luminescence. In a similar way Ce^{3+} in $Ca_4GdO(BO_3)_3$ does not luminescence. Nor the oxysilicate nor the oxyborate offer the Ce^{3+} ion an ionic surroundings.

Another way to obtain a high $q(Ce^{3+})$ is to place Ce^{3+} on a site where it is effectively positive, so that the trivalency is stabilized [4]. Examples are $CaS:Ce^{3+}$ and $CaSe:Ce^{3+}$ with efficient Ce^{3+} luminescence in spite of their covalent character. Another example is $CaSO_4:Ce^{3+}$, V^{5+}, the only case where Ce^{3+} and VO_4^{3-} do not quench each others luminescence [15]. However, for scintillators one cannot expect much of such an approach, since the presence of extra positive charges (and consequently compensating extra negative charges) will most probably induce extra electron-hole recombination sites.

In conclusion, efficient Ce^{3+} scintillator luminescence can only be expected if the ion is placed in an ionic surroundings.

REFERENCES

[1] G. Blasse and B.C. Grabmaier, Luminescent Materials, Springer Verlag, Berlin, 1994

[2] G. Blasse, Chem. Mater. 6 (1994) 1465

[3] P.A. Rodnyi, P. Dorenbos and C.W.E. van Eijk, Phys. Stat. Sol. (b) 187 (1995) 15

[4] G. Blasse, W. Schipper and J.J. Hamelink, Inorg. Chim. Acta 189 (1991) 77

[5] S.T. Frey and W. DeW. Horrocks, Jr., Inorg. Chem. 30 (1991) 1073

[6] S. Yokono, T. Abe and T. Hashima, J. Luminescence 24/25 (1981) 309

[7] H. Suzuki, T.A. Tombrello, C.L. Melcher, and J.S. Schweitzer, Nucl. Instr. Methods A 320 (1992) 263

[8] G. Blasse and A. Bril, J. Chem. Phys. 47 (1967) 5139

[9] K. Binnemans and C. Görrler-Walrand, Chem. Phys. Letters 235 (1995) 163

[10] T. Gaewdang, J.P. Chaminade, A. Garcia, M. Pouchard, P. Hagenmuller and B. Jacquier, J. Phys. Chem. Solids 55 (1994) 501

[11] B. Moine, C. Pedrini and B. Courtois, J. Luminescence 50 (1991) 31

[12] H.F. Folkerts and G. Blasse, to be published

[13] G. Blasse, C. de Mello Donegá, I. Berezowskaya and V. Dotsenko, Solid State Comm. 91 (1994) 29

[14] A.M. van de Craats and G. Blasse, to be published

[15] W.T. Draai and G. Blasse, Chem. Phys. Letters 25 (1974) 167

RELAXATION OF ELECTRONIC EXCITATIONS IN WIDE BANDGAP INSULATORS

J.Becker[a], A.N.Belsky[b], D.Bouttet[c], C.Dujardin[f], A.V.Gektin[d], A.Hopkirk[e], S.N.Ivanov[b], I.A.Kamenskikh[b], N.Y.Kirikova[f], V.Klimenko[f], V.N.Kolobanov[b], V.N.Makhov[f], P.Martin[g], V.V.Mikhailin[b], I.H.Munro[e], C.Mythen[e], P.A.Orekhanov[b], C.Pédrini[c], A.Schroeder[a], D.A.Shaw[e], N.Shiran[d], I.N.Shpinkov[b], A.N.Vasil'ev[b], G.Zimmerer[a]

[a] II. Institut fur Experimentalphysik, Universitat Hamburg, Germany
[b] Physics Faculty, Moscow State University, Moscow, Russia
[c] LPCML, Universite Lyon-I, Villeurbanne, France
[d] Institute for Single Crystals, Kharkov, Ukraine
[e] DRAL, Daresbury Laboratory, Warrington, UK
[f] Lebedev Physical Institute, Moscow, Russia
[g] LURE, Orsay, France

ABSTRACT

The article presents the review of recent investigations of luminescent properties of insulating crystals excited in the VUV, XUV and X-ray region carried out by a collaboration on the basis of an INTAS grant 'The luminescence process – a study of the excitation and radiation dynamics of materials using synchrotron radiation'. The sequential steps of the energy conversion of a high-energy photon into a luminescence quantum have been studied: (i) absorption; (ii) multiplication of electronic excitations; (iii) migration during the process of thermalisation; (iv) emission center excitation. These investigations constitute the physical basis for many applications: scintillators, storage screens, dosimetry, etc.

INTRODUCTION

The present revival of the interest to luminescent crystals is to a great extend due to their practical applications in the following fields: scintillator detectors for nuclear spectroscopy, two-dimensional detectors (medical screens, crystallography, radiography, defectoscopy, etc.), and dosimetry.

Different fundamental processes triggered in a solid by the absorption of a high-energy photon are considered. Inelastic electron-electron scattering accouns for the yield of phosphors under high-energy excitation. Understanding of fast luminescent processes of different origin (crossluminescence, CsI-type luminescence, centers affected by the energy transfer) allows to evaluate the limits of the efficiency and decay time of scintillators. Defect creation is linked for practical applications to the efficiency of storage materials and dosimeters. The luminescence excitation technique is useful for investigation of all these processes. The use of synchrotron radiation allows to choose the excitation photon energy in the wide energy region and therefore separately excite different types of electronic excitations in order to investigate the ways of their relaxation.

Proc. Int. Conf. on Inorganic Scintillators and Their Applications, SCINT95,
1996, Delft University Press, The Netherlands

EXCITATION OF SECONDARY PROCESSES IN INSULATORS

Detailed investigation of luminescence excitation spectra and reflection of solids in the VUV and XUV (4–120 eV) with the help of synchrotron radiation have resulted in understanding of some fundamental features of the processes of energy relaxation: multiplication of electronic excitations (EE) due to inelastic electron-electron scattering; genetic recombination of spatially spread excitations after the absorption of a photon; migration of energy to luminescent centers.

Luminescence properties essentially change when excitation energy increases from the beginning of the fundamental absorption, i.e. 10–20 eV, to energies about 100 eV or higher. These modifications seem to be due to the peculiarities of the relaxation of EEs created by high energy photons. The main reason of these alternations is the many-particle interactions in the regions of high EE density. Let us consider the general stages of energy relaxation after VUV or X-ray photon absorption, paying attention on the typical dimensions and duration of different stages and the typical features of EE interactions.

Absorption of a photon with an energy sufficient for the photoionization of the crystal results in the creation of a hole in the valence or core bands and of an electron in the conduction band (Fig. 1). The duration of this stage is about 10^{-16}–10^{-17} s. This stage is responsible for the factor $[1-R(h\nu)][1-\exp(-\alpha(h\nu)d)]$ in the expression for the luminescence quantum yield, $R(h\nu)$ is the reflection coefficient (this part of the factor is significant only for

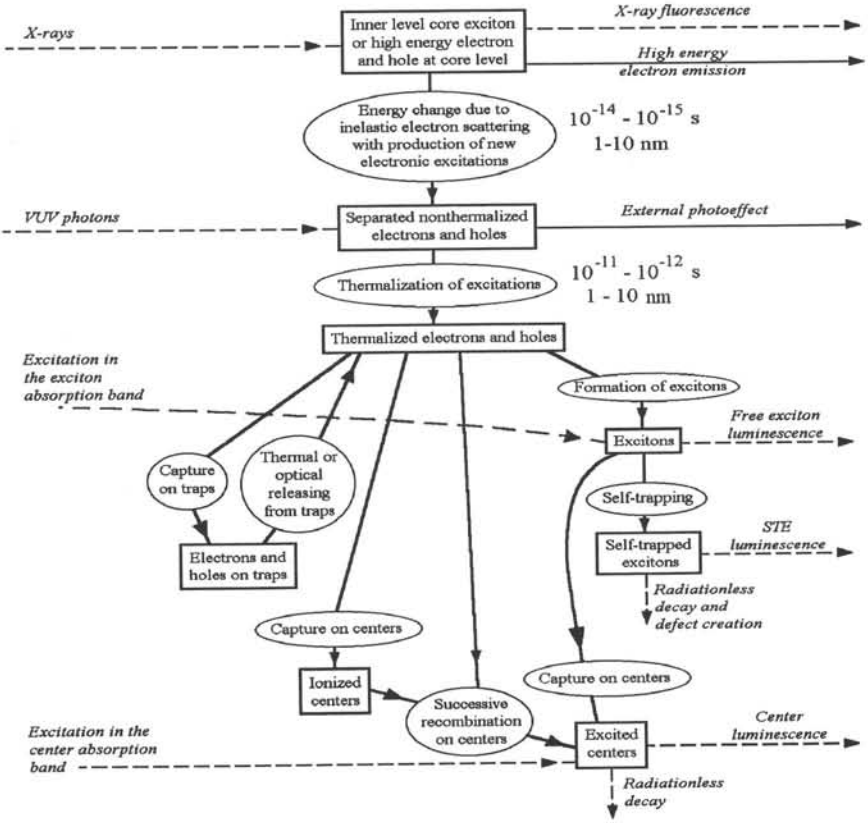

Fig. 1. Elementary processes in an insulator after different types of excitation

VUV region), d is the crystal thickness, $\alpha(h\nu)$ is the absorption coefficient. The initial hole in the core band decays by the Auger mechanism with the creation of secondary EEs of different types within the distance of one to two lattice constants (about 1 nm).

Evolution of the excited region of the crystal created by the absorption of a VUV or X-ray quantum or a fast particle can be subdivided into several stages. The first stage, involving electron-electron inelastic scattering, has a characteristic time of the order of 10^{-15} s and results in the creation of various EEs [1]. The number of such EEs $\beta(h\nu)$ is limited by the ratio of a photon energy to a mean energy required for the creation of one EE, which equals to $E_{EE} = (1.5 \div 3)\ E_g$ for wide-bandgap insulators, E_g being the forbidden gap. Linear growth of $\beta(h\nu)$ with energy is the main reason of the constant luminescence energy yield [2]. EEs after this stage are characterized by their energy and spatial distribution $g_0(E, r; h\nu)$. Both mean energy of hot secondary excitations $E_m(h\nu)$ and mean distance between excitations $r_m(h\nu)$ depends on excitation energy $h\nu$. EE spatial distribution corresponding to this stage is determined by the length of electron-electron scattering which is a function of the electron energy. This function is not monotonous and has a minimum of the order of 1 nm for electron energies about 100 eV. For higher and lower electron energies this characteristic length increases and is about 10 nm both for 10 KeV electrons and 10 eV ones. Such length versus energy dependence results in a substantially non-uniform spatial EE distribution $g_0(E, r; h\nu)$: isolated regions of high EE density with characteristic dimensions of the order of 1–5 nm are created. The same effect is produced by the Auger decay of core holes. When created by relatively energetic electrons, such regions can be quite isolated with the distance to the neighboring ones lager than their characteristic dimension or, on the contrary, they can merge if produced by heavy ions, which create mainly low energy EEs. The total duration of this stage is about 10^{-14}–10^{-15} s.

During the next stage of excited region evolution EEs thermalize with characteristic time of the order of 10^{-12} s and distance 1–10 nm. Energy of the order of $E_{EE} - E_g = (0.5 \div 2)\ E_g$ per one EE is given off as phonons. The spatial distribution of thermalized EEs $g(r; h\nu)$ is formed at this stage. The details of this distribution depend on the distribution function at the previous stage or roughly on mean EE energy $E_m(h\nu)$ and mean distance $r_m(h\nu)$ [3-5].

The next stage is characterized by times of the order of 10^{-9} s and is determined by recombination processes (Fig. 2). In ionic crystals the probability of binding electron-hole pairs into excitons is larger than their direct recombination. Radiationless recombination of excitons and self-trapped holes with electrons leads to the creation of defects. Radiative recombination can result from both annihilation of excitons (upper part of the figure) and with the participation of local levels in the forbidden energy gap created by impurity or intrinsic defects (lower part of the figure, sequential capture of an electron and a hole by a

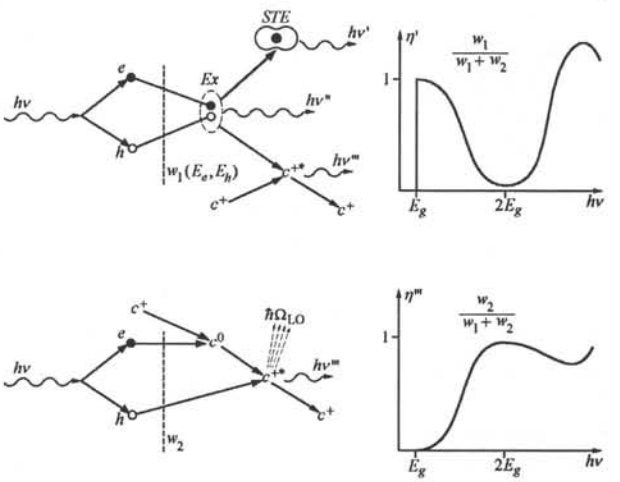

Fig. 2. Two types of recombination channels: excitonic one (upper part) and recombination on a center (lower part). Right graphs display typical energy dependence of the quantum yield of these channels

defect). The probabilities w_i of both channels of recombination depends on the spatial distribution $g(r; h\nu)$ (or $E_m(h\nu)$ and $r_m(h\nu)$). Since binding into an exciton is more sensitive to the distance between an electron and a hole, the volume quantum yield η_v decreases with the mean energy $E_m(h\nu)$ for excitonic channel and increases for recombination one (see right part of the figure, where the quantum yield for these channels is plotted versus photon energy in the beginning of the fundamental absorption region) [4-7]. At the recombination stage not only elementary recombination processes can occur but also more sophisticated ones due to the interaction of EEs in the 'cluster' of excitations (biexcitons, exciton trapped by a hole or radiation defect, etc.).

The diffusion of excitations during this stage can result in so-called surface losses. The factor $1/[1+\alpha(h\nu)L]$ in the quantum yield displays this quenching, where L is the diffusion length during the total excitation lifetime.

Gathering the mentioned above factors, one can combine the formulae for the luminescence quantum yield:

$$\eta = \frac{[1-R(h\nu)][1-\exp(-\alpha(h\nu)d)]}{1+\alpha(h\nu)L}\beta(h\nu)\eta_v\left(E_m(h\nu), r_m(h\nu)\right).$$

The interaction of EEs in the excited regions results not only in modification of the quantum yield, but in the luminescence kinetics and (sometimes) in the alternation of the emission spectrum. The luminescence decay becomes non-exponential for most cases, which is typical for interaction of several excitations [8,9].

Only a few luminescence experiments were performed in the energy region from 40 eV to 3 KeV. Soft X-ray quanta create several EEs in a limited volume due to electron-electron scattering and hole Auger processes. In this region the onset of processes controlled by spatial and temporal correlation of excitations can manifest. Time resolved soft X-ray luminescence spectroscopy is promising in obtaining new features of fast processes.

The scintillation efficiency of wide-bandgap crystals is often described by the formula $\eta=\beta SQ$, where β is the number of secondary EEs, S is the efficiency of the energy transfer and Q is the efficiency of radiation process in the center. This formula is applicable if we suppose three stages of energy relaxation well separated in time. The factors β and SQ have the same origin with that for excitation of luminescence (SQ is replaced in our formulae by η_v). Moreover, luminescence excitation by photons provides additional information about relaxation stages. One can selectively excite electronic states by varying the photon energy, and thus much more information can be obtained about the efficiency of the process which form the factors β and SQ. There are additional factors for photoexcitation which should be taken into account due to strong absorption of VUV and XUV light (the quota of absorbed light and surface losses).

LUMINESCENCE EXCITATION SPECTRA AND DECAY KINETICS

Fig. 3 presents three types of excitation spectra in VUV region. The upper panel displays the excitation spectrum of intrinsic luminescence of $CaWO_4$ [10]. The emission of $CaWO_4$ is due to transitions in WO_4^{2-} complex oxyanion and can be regarded as the emission of self-trapped exciton. The presented spectrum shows that the electron-hole recombination is of excitonic type (compare with upper part of Fig. 2). Activator luminescence of $CaSO_4$:Sm [6] (middle panel of Fig. 3) represents another type of recombination, i.e. successive capture of an electron and a hole by a rare earth ion (compare with lower part of Fig. 2). These two types of

spectra show clear photon multiplication threshold at energies just above $2E_g$ (arrows mark these energies in Fig. 3).

The lower panel of Fig. 3 displays the excitation spectrum of CeF_3 intrinsic luminescence [11]. The emission origins from the transitions between 5d and 4f Ce states. The band structure of this compound differs from that of typical ionic crystals. The absorption due to 4f→5d transitions in Ce subsystem starts from 5 eV, and absorption coefficient reaches 10^4 cm^{-1} above this energy. Fundamental absorption due to transitions from valence fluorine band into conduction band formed by 6s Ce states starts from 11 eV, and absorption coefficient reaches values of 10^6 cm^{-1} in this region. The latter type of transitions is typical for ionic crystals. The luminescence quantum yield is very low in this fundamental absorption region. Thus separated electron-hole pairs are not efficient in the excitation of Ce ions. Since the absorption for energies above 11 eV is mainly due to transitions from F valence band, and the excitation energy for Ce subsystem is more than 5 eV, the photon multiplication threshold is just above the sum of these two values. This type of spectrum confirms supposition that transfer of a hole from F valence band to 4f Ce valence levels has small probability [11], and the main mechanism of excitation of Ce subsystem in the fundamental absorption region is the impact excitation and ionization of Ce ions. This feature result in high value of the mean energy E_{Ce} = 80–100 eV for creation of one excited Ce ion by ionizing particle [12].

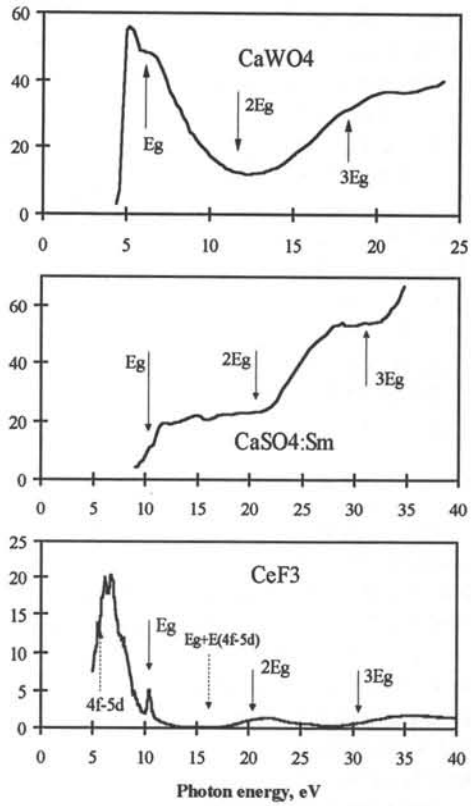

Figure 3. Luminescence excitation spectra of intrinsic luminescence of $CaWO_4$ (upper panel) [10] and CeF_3 [11] (lower panel) and activator luminescence of $CaSO_4$:Sm [6] (middle panel)

Figure 4 presents the excitation spectra of two emission Lu_2SiO_5:Ce (LSO) bands with quite different behavior in the fundamental absorption region ($E_g \approx 7$ eV). This crystal shows two alternative channels of energy transfer to luminescence centers. 510 nm emission band is excited similar to most cerium bands in different matrixes (low yield in the fundamental absorption region, cf. lower panel of Fig. 3), whereas the excitation spectrum of 400 nm band is not typical for cerium activated systems. The yield in the fundamental absorption range is high enough. Such behavior of the excitation efficiency can explain high LSO scintillation yield. The dips at 11, 14 and 34 eV can be connected with lutetium 4f and 5d core states.

In some crystals the activator emission yield increases faster than energy in the region of transitions from core levels (e.g. SrS and BaS doped with Ce) [15]. Such growth of the luminescence yield is observed in $PbWO_4$ crystals as well (Fig. 5) and can be explained in the following way [13].

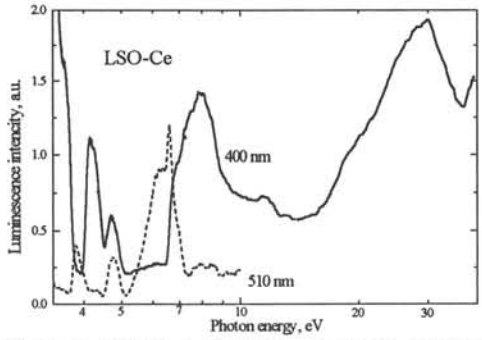

Figure 4. LSO-Ce excitation spectrum for 400 and 510 nm emission bands, 6 K

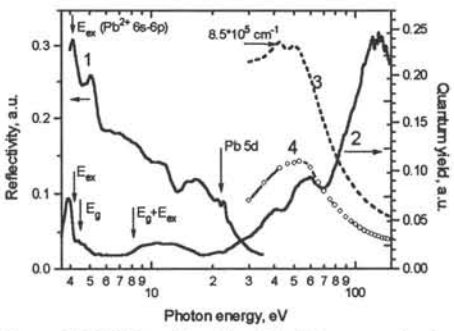

Figure 5. $PbWO_4$ reflectivity (1), 400 nm excitation spectrum (2), RT, total $PbWO_4$ absorption (3) and partial Pb absorption (4) calculated from atomic data

The strong rise of the excitation efficiency starting from 60 eV and the decrease of the absorption coefficient can have the same origin. The transitions into low states of the conduction band are allowed by the energy conservation law only if photon energy is slightly above the ionization energy of one of the valence and upper core bands. In $PbWO_4$ these bands cover the initial 40 eV interval below the top of the valence band closely together. Therefore the mean energy of primary electrons produced by a photon is relatively low for photon energies below 40 eV and increases rapidly with photon energy above 40 eV. Such electrons produce a cascade of secondary electrons and holes. Lead 6s–6p transition is characterized by the very high value of the dipole transition matrix element. Therefore fast electrons can effectively excite 6s lead electrons. The supposition that fast electrons in $PbWO_4$ pass the energy to emission centers in the inelastic scattering cascade more effectively than deep holes in Auger cascade is confirmed by the negative jump of the $PbWO_4$ excitation efficiency at deep core levels [16]. Below the ionization energy of L levels of lead and tungsten ions the largest part of a photon energy converts to electron subsystem, whereas above the ionization threshold the energy of a primary electron decreases by several KeV. Summarizing all these facts, we can conclude that the relaxation of a high-energy electron is more efficient in production of $PbWO_4$ fast luminescence than that of a hole with the same energy.

The other problem which is investigated intensively during last few years is the role of core levels. Core hole in insulators can decay in different ways. We mention here two traditional channels of core hole relaxation, i.e. radiation relaxation with emission of X-ray photon and Auger relaxation. Two specific channels are under discussion during last years. These are radiation relaxation of highest lying core level — crossluminescence (CL) or valence-to-core transitions — and defect formation due to specific relaxation of core holes.

CL can exist only if the possible emission due to radiative relaxation of a core hole into the valence band is not overlapped with fundamental absorption, i.e. if the Auger processes for a core hole from the top of the highest lying core band is energetically forbidden (Fig. 6a). In this case core holes at the top of the core band can decay only radiatively. Excitation spectra for several new CL crystals are presented in Fig. 7. The CL yield can depend on temperature if the absorption is slightly overlaping with the possible emission (e.g. in the case of CsBr).

The de-excitation of some EEs due to Auger cross-relaxation of secondary excitations results in the decrease of the luminescence yield and in modification of the decay. Short component arises in kinetics. This effect corresponds to Fig. 6d, the additional absorption arises from the excitations created by the same or different photons. It was studied in

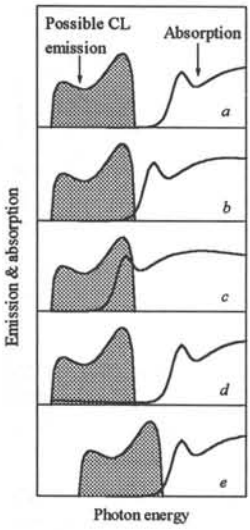

Figure 6. Different cases for overlapping crystal absorption and possible CL emission:

a) Good CL crystal, emission and absorption are not overlapped, Auger decay is forbidden, quantum yield for direct excitation of a core hole $\eta_{direct} \sim 1$
b) Bad CL crystal, emission and absorption are slightly overlapped due to Urbach tail of absorption [15], temperature quenching, $\eta_{direct} \sim 10^{-2} \div 10^{-1}$
c) Non-CL crystal, emission and absorption are strongly overlapped, Auger decay is allowed, $\eta_{direct} \sim 10^{-6} \div 10^{-5}$
d) CL crystal with quenching due to dipole-dipole transfer to correlated excitations, emission spectrum is overlapped by transient absorption, $\eta_{direct} < 1$, non-exponential decay due to energy transfer to spatially separated excitations
e) CL crystal with two core holes at the same ion (cf. case b), possible CL absorption is shifted to higher energies due to hole-hole interaction

traditional crossluminescent crystal, i.e. BaF_2. Decay kinetics under X-ray excitation of different spectral composition and intensity shows such fast subnanosecond component [8,16]. The emission spectrum slightly changes as well. The investigation of this effect after VUV excitation shows that in BaF_2 the fast component appears for excitation phonon energies above $E_c + E_g$, when additional electron-hole pair is created simultaneously with the highest lying core hole [17]. Therefore the core hole is destroyed by Auger process involving these new excitations. The Monte-Carlo simulation of this process shows that the distance between core hole and the nearest excitation decreases significantly for excitation energies above this threshold (32 eV) [18].

CsCl crystal corresponds to the case presented in Fig. 6a. Nevertheless, when two 5p Cs core holes are created after the Auger decay of 4 Cs deep core hole, their correlation energy shifts the possible CL emission (Fig. 6e) and the situation resembles that of CsBr crystal. Anomalous temperature behavior and prominent reduction of the CL excitation efficiency in the range of the transitions from 4dCs states are shown in Fig. 8. The detailed description will be presented elsewhere.

Some effects arising from the interaction of several excitations are connected with core levels. Fast intrinsic luminescence of CsI is an example of such new effects. Fast 300 nm band appears only for excitation energies above 20–30 eV, which is 3 to 5 times greater than the forbidden edge energy (E_g = 6 eV) and its yield increases almost exponentially up to 50 eV [19]. This emission is rather efficient for high excitation photon energies. These arguments allows one to conclude that the creation of specific emission centers is due to interaction of several secondary excitations created by a photon.

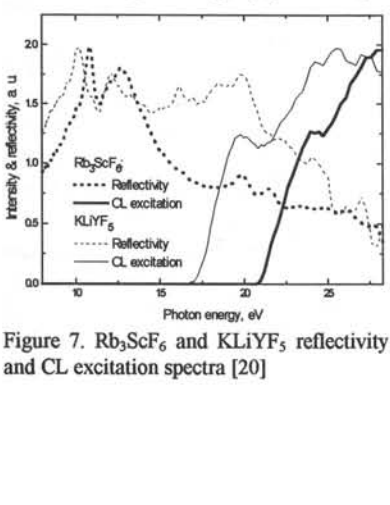

Figure 7. Rb_3ScF_6 and $KLiYF_5$ reflectivity and CL excitation spectra [20]

CONCLUSION

The excitation of insulators using synchrotron radiation in wide continuos spectral region from several electron-volts to several thousands of electron-

volts allows to investigate directly intermediate stages of the transformation of energy of fast particles and high-energy quanta in solids. These stages of energy relaxation significantly determine the efficiency of scintillators, storage screens, detectors, etc. The study of other secondary processes (such as photoelectron emission, desorption, induced absorption) will be very helpful in the investigation of energy relaxation.

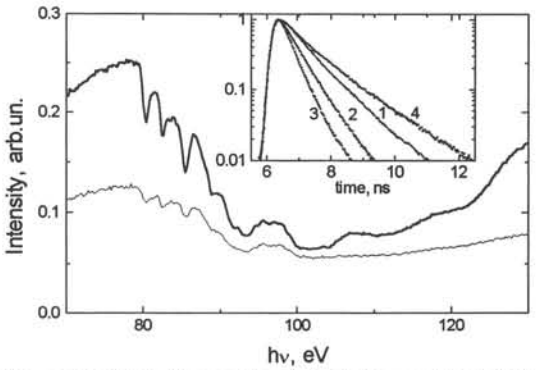

Figure 8. CsCl CL (270 nm band) excitation spectra at 10 K (upper curve) and RT (lower curve) and 270 nm decay curves excited by 100 eV photons at different temperatures: RT (1), 200 K (2), 150 K (3) and 10 K (4)

ACKNOWLEDGMENTS

The authors gratefully acknowledge the support of INTAS 93-2554 grant. The group from Moscow State University also acknowledge the support of RFFI 94-0205695 and ISF JBT100 grants.

REFERENCES

[1] E. R. Ilmas, G. G. Liidja and Ch. B. Lushchik, Optika i Spectrosc., 18 (1965) 453, 631.
[2] A. M. Gurvich et al., Zh. Prikl. Spektrosk., 23 (1975) 158.
[3] V. V. Mikhailin, Nucl. Instr. and Meth., A261, (1987) 107.
[4] A. N. Vasil'ev and V. V. Mikhailin, Introduction to Solid State Spectroscopy, Moscow, MSU (1987).
[5] A. N. Vasil'ev and V. V. Mikhailin, Bull. Acad. Sci. USSR, Phys. ser., 49(9) (1985) 164.
[6] I. A. Kamenskikh, V. V. Mikhailin, I. N. Shpinkov and A. N. Vasil'ev, Nucl. Instr. and Meth., A282 (1989) 599.
[7] A. N. Belsky, I. A. Kamenskikh, V. V. Mikhailin, I. N. Shpinkov and A. N. Vasil'ev, Physica Scripta, 41 (1990) 530.
[8] A. N. Belskiy, V. V. Mikhailin, A. L. Rogalev, S. Stizza, A. N. Vasil'ev and E. I. Zinin, in 2nd European Conference on Progress in X-Ray Synchrotron Radiation Research, Conference Proceedings, Bologna: SIF, v. 25 (1990) 797.
[9] S. Kubota, M. A. MacDonald, I. H. Munro, J. Luminescence, 48&49 (1991) 589.
[10] S. I. Golovkova, A. M. Gurvich, A. I. Kravchenko, V. V. Mikhailin, A. N. Vasil'ev, Phys. Stat. Sol. (a), 77 (1983) 375.
[11] C. Pedrini, A. N. Belsky, A. N. Vasil'ev, D. Bouttet, C. Dujardin, B. Moine, P. Martin, M. J. Weber, Material Research Society Symposium Proc., 348 (1994) 225.
[12] Vasil'ev A. N., NIM B, to be published in 1995.
[13] A.N.Belsky, V.V.Mikhailin, A.N.Vasil'ev, I.Dafinei, P.Lecoq, C.Pedrini, P.Chevallier, P.Dhez, P.Martin, Preprint CERN CMS TN95-073, 1995.
[14] A. N. Belsky, P. Chevallier, P. Dhez, P. Martin, C. Pedrini, A. N. Vasil'ev, NIM, A361 (1995) 384.
[15] I. Davoli, V. V. Mikhailin, S. Stizza, A. N. Vasil'ev, J. of Luminescence, 51 (1992) 275.
[16] A. N. Belsky, I. A. Kamenskikh, A. N. Vasil'ev, A. V. Gektin, C. Pedrini, P. Martin, , Material Research Society Symposium Proc., 348 (1994) 241.
[17] M. A. Terekhin, A. N. Vasil'ev, M. Kamada, E. Nakamura, S. Kubota, Phys. Rev. B52 (1995) 3117.
[18] R. A. Glukhov, A. N. Vasil'ev, Material Research Society Symposium Proc., 348 (1994) 387.
[19] A. N. Belsky, A. N. Vasil'ev, V. V. Mikhailin, A. V. Gektin, P. Martin, C. Pedrini, D. Bouttet, Phys. Rev. B, 49 (1994) 13197.
[20] E.G.Devitsin, N.M.Khaidukov, N.Yu.Kirikova, V.E.Klimenko, V.A.Kozlov, V.N.Makhov and T.V.Uvarova, Radiation Effects and Defects in Solids, 133-134 (1995), to be published

FINAL STAGES OF INELASTIC ELECTRON SCATTERING: INFLUENCE ON SCINTILLATOR EFFICIENCY

A. N. Vasil'ev
Synchrotron Radiation Laboratory, Moscow State University, 119899 Moscow, Russia

ABSTRACT

The paper discusses the influence of the energy distribution of hot secondary excitations in scintillators on the probability of energy transfer to the emission centers. The important energy region is the pre-threshold region, where the probability of strongly inelastic scattering is not high and other channels of relaxation can be essential. The crystals where emission states can be created by electrons in limited energy range (crossluminescent crystals, crystals with rare-earth ions, etc.) are discussed. These processes strongly increase the mean energy necessary to create an emission state.

INTRODUCTION

Efficiency of a scintillator depends on different factors, namely the number of secondary electronic excitations β, efficiency of energy transfer to emission state S and radiative efficiency of the emission center Q. Each of these factors describes the energy relaxation during separated stages, i.e. strongly inelastic scattering with production of new excitations, thermalization with phonon emission, energy transfer and processes in emission centers. In the present paper we analyze some peculiarities of two initial stages. Secondary electronic excitations are produced in electron and hole cascades, which consist of a large number of elementary scattering acts. During the energy relaxation electrons pass through the states with intermediate energies between the threshold of inelastic scattering with production of additional electron-hole pairs (their minimal energy is the forbidden energy gap E_g) and excitons (with energy E_{ex}) and several plasmon energies $\hbar\omega_{pl}$ (this region usually corresponds to electron kinetic energies from 8 to 60 eV). The description of inelastic processes at these energies requires the account for the details of electronic structure and can be performed using the polarization approximation.

INELASTIC ELECTRON SCATTERING

In the framework of this approximation the probability $w_{e\text{-}e}$ of inelastic scattering of an electron is equal to (cf. e.g. [1])

$$w_{e-e}(E_k) \equiv \frac{1}{\tau_e(E_k)} = \frac{e^2\sqrt{2m_e}}{\pi\hbar\sqrt{E_k}} \int_0^{E_k/\hbar} d\omega \, \mathrm{Im}\left[-\frac{1}{\varepsilon(\hbar\omega)}\right] \ln\frac{\sqrt{E_k}+\sqrt{E_k-\hbar\omega}}{\sqrt{E_k}-\sqrt{E_k-\hbar\omega}}, \qquad (1)$$

where E_k is the electron kinetic energy, m_e is the free electron mass, $\varepsilon(\hbar\omega)$ is the dielectric permittivity. Formula (1) is written in the free-electron approximation with neglecting of spatial dependence of the dielectric permittivity.

Figure 1 presents the typical shape of energy loss rate with production of additional secondary excitations (solid line) vs. electron kinetic energy. The threshold of inelastic scattering E_{th} is 2–3 times less than the mean energy for production of an electronic

Proc. Int. Conf. on Inorganic Scintillators and Their Applications, SCINT95,
1996, Delft University Press, The Netherlands

excitation. This mean energy is either about 2–3 E_g or plasmon energy $\hbar\omega_{pl}$, at which the energy loss function has a peak. The threshold of inelastic scattering with production of additional exciton for parabolic bands is roughly estimated as $\frac{2m_e + m_h}{m_e + m_h} E_{ex}$, where m_e and m_h are effective electron and hole masses, respectively, and for heavy holes threshold of inelastic scattering is about exciton energy [2].

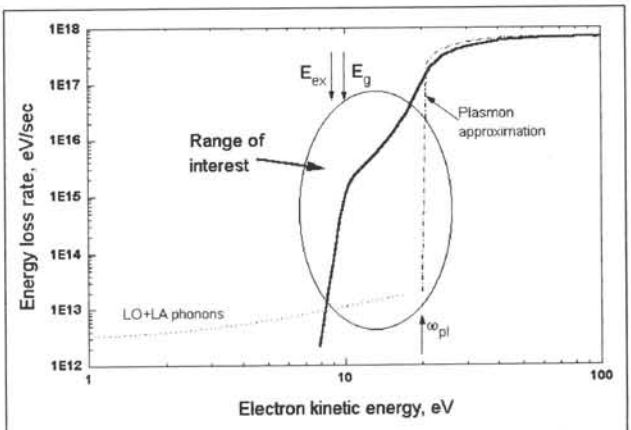

Figure 1. Typical dependence of energy loss rate due to emission of secondary excitations as a function of an electron kinetic energy

ENERGY DEPENDENCE OF THE CREATION PROBABILITY FOR DIFFERENT TYPES OF EXCITATIONS

Formula (1) gives the answer to the question, "What happens to the excitation?". The probability $w_{e\text{-}e}$ defines the rate of the scattering process of a primary electron but says nothing about the products of the scattering. The sense of the integrand in (1) is the energy distribution of longitudinal photons (Coulomb field quanta) with energy $\hbar\omega$, which are immediately absorbed with production of secondary excitations. The probability of production of different types of excitations can be determined in a following way.

When we suppose that individual excitations do not interact strongly, the imaginary part of the dielectric permittivity $\varepsilon_2(\hbar\omega)$ can be considered as a sum of the partial items $\varepsilon_2^c(\hbar\omega)$

$$\varepsilon_2(\hbar\omega) = \sum_c \varepsilon_2^c(\hbar\omega), \quad \mathrm{Im}\left[-\frac{1}{\varepsilon(\hbar\omega)}\right] = \sum_c \frac{\varepsilon_2^c(\hbar\omega)}{\left|\varepsilon(\hbar\omega)\right|^2}. \tag{2}$$

According to eq. (2)., the total probability of electron inelastic scattering can be represented as a sum of partial probabilities

$$w_{e-e}(E_k) = \sum_c w_{e-c}(E_k). \tag{3}$$

Therefore the relative probability of the creation of a certain type of excitation by an electron with kinetic energy E_k is equal to w_{e-c}/w_{e-e}.

When we are interested in the scintillation yield, we have to trace only the production of excitations which produce scintillation emission. In a lot of crystals there are several types of low-energy excitations, but only one is responsible for the observed emission. For instance, in cross-luminescent crystals only highest lying core holes produce fast emission. Therefore it is useful to change the question and ask "What types of excitations can produce the selected type of secondary excitations?". For the case of BaF_2 an electron with kinetic energy above 10 eV can produce additional exciton or electron-valence hole pair (the threshold of $\varepsilon_2^{2pF}(\hbar\omega)$ is about 10 eV). But an electron needs about 18 eV to produce a core

hole which is responsible for cross-luminescence emission (the threshold of $\varepsilon_2^{5pBa}(\hbar\omega)$ is about 17 eV).

For the case of cerium fluoride one is interested in the number of excited cerium ions, since the energy transfer from the fluorine subsystem has low probability. This case will be discussed in details later.

There is an additional factor which modifies the probability of the energy transfer from an electron-hole pair to the emission state. Since recombination probability depends on the distance between an electron and a hole, the spatial correlation due to the creation of this electron-hole pair during the same scattering defines the yield of excited emission states. This spatial correlation is strong for low-energy pairs and becomes weaker for high-energy pairs, when the thermalization length is high enough [3-6].

INELASTIC SCATTERING IN CERIUM FLUORIDE

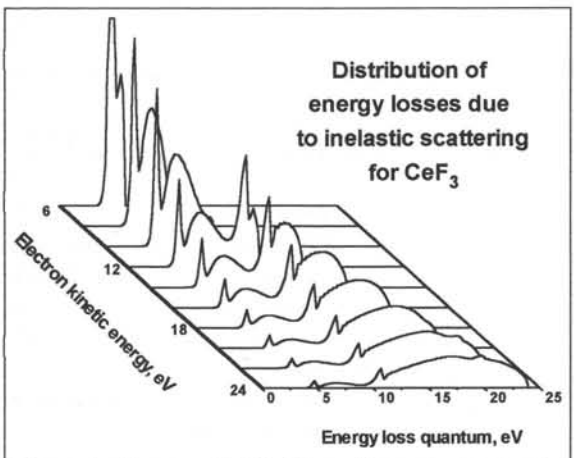

Figure 2. Energy distribution of energy losses for different electron kinetic energies in CeF_3

Figure 2 presents the distribution of the emitted longitudinal phonons over their energies (normalized values of the integrand in formula (1)) for cerium fluoride. The used imaginary part of CeF_3 dielectric permittivity is simulated on the base of simple approximation of density of states and atomic-like partial absorption (cf. details in [2,7]). The main feature of this simple approach is the correct account for the sum rules. Cerium excitations correspond to energy losses in the domain 5 to 10 eV. Figure 2 shows that only electrons with kinetic energy from 5 to 14 eV can effectively produce cerium excitations, whereas electrons with higher kinetic energy produce mainly excitations in fluorine subsystem.

For electron kinetic energies just above the threshold of the production of secondary electrons another relaxation process, the emission of LO and LA photons, cannot be neglected [3,4,8]. Unfortunately the estimation of the probability of such scattering for high electron kinetic energies is difficult. The competition between these two channels of relaxation can change the estimation of the total number of secondary excitations by two times. The account for the phonon emission reduces the strongly inelastic scattering probability by the factor [4]

$$1-\exp\left[-\int_0^{E_k}\frac{w_{e-e}(E')}{w_{e-ph}(E')}\frac{dE'}{\hbar\Omega}\right]. \qquad (4)$$

Figure 3 presents the fraction of "useful" cerium excitations produced by electrons with different kinetic energies. Excited cerium ions are created only by electrons with kinetic energy from 5 to 10 eV, and the probability of this process is strongly reduced when strong phonon relaxation is taken into account. The other type of cerium excitations, ionized Ce^{4+} ions plus electrons cannot be produced on the threshold, and therefore the phonon relaxation

does not influences on their fraction. These results are in agreement with experimental results of CeF_3 fast and slow components, correspondingly [9].

CONCLUSION

The present consideration of the final stages of strongly inelastic electron and hole scattering is important for insulators with complicated band structure which are known to be promising scintillators (systems with localized bands, crossluminescent crystals, etc.). Some results of simulation of energy relaxation in such crystals are reviewed.

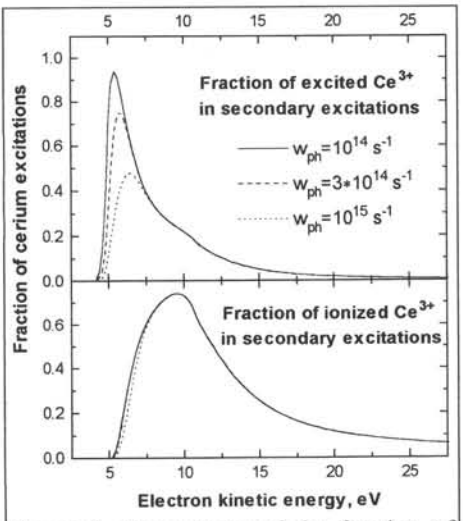

Figure 3. Dependence of the fraction of excited cerium ions and ionized ions produced by an electron, on electron kinetic energy

ACKNOWLEDGMENTS

The author gratefully acknowledges the support of RFFI 94-0205695, ISF JBT100, and INTAS 93-2554 grants.

REFERENCES

[1] R. H. Ritchie, Phys. Rev. 114 (1959) 644.
[2] Vasil'ev A. N., NIM B, 1995, to be published.
[3] Vasil'ev A. N., Mikhailin V. V., Ovchinnikova I. V., Bulletin of the Academy of Sciences of the USSR. Physical Series, v. 49, No. 10, pp. 164-168, 1986
[4] Vasil'ev A. N., Mikhailin V. V., Bulletin of the Academy of Sciences of the USSR. Physical Series, v. 50, No. 3, pp. 113-116, 1986
[5] Belskiy A. N., Kamenskikh I. A., Mikhailin V. V., Shpinkov I. N., Vasil'ev A. N., Physica Scripta, v.41, p.530-536, 1990
[6] Kamenskikh I. A., Mikhailin V. V., Shpinkov I. N., Vasil'ev A. N., Nuclear Instruments and Methods in Physics Research, v.A282, p.599-606, 1989
[7] Glukhov R. A., Vasil'ev A. N., Radiation Effects and Defects in Solids, v. 133–134, pp. 00–00, 1995
[8] Davoli I., Mikhailin V. V., Stizza S., Vasil'ev A. N., Journal of Luminescence, v.51, N5, p.275-282, 1992
[9] Pedrini C., Belsky A. N., Vasil'ev A. N., Bouttet D., Dujardin C., Moine B., Martin P., Weber M. J., Material Research Society Symposium Proceedings, v. 348, pp. 225–234, 1994.

THEORETICAL INVESTIGATION OF THE 4F AND 5D LEVELS OF CERIUM IN LSO, STUDIED WITH HF-LCAO AND THE EMBEDDED CLUSTER SCATTERED WAVE METHOD[1]

J. Andriessen†, A. Sobolev‡, A. Kuznetsov‡, H. Merenga†, P. Dorenbos†,C.W.E. van Eijk†
†Delft University of Technology, Faculty of Applied Physics
c/o IRI, Mekelweg 15, 2629 JB Delft, The Netherlands
‡Ural State University, Experimental Physics Department,
Mira street 19, 620002, Ekaterinburg, Russia

ABSTRACT

Energy levels of cerium defects in LSO were studied using two different methods of approach, the Hartree-Fock and the Embedded Cluster Scattered Wave method. Also a lattice relaxation study of the cerium centres was performed. Evidence is found that the 4f and 5d energy levels of the Ce^{3+} defects are rather low in the gap because of the relaxation of the nn neigbours which is found to be around 5 percent outward. The 4f band of lutetium seems to overlap the valence band, which is found to be 7.3 eV broad.

INTRODUCTION

The study of energy levels of cerium centres in scintillation crystals contributes to the understanding of the processes which play a role in the scintillation process. It gives important quantitative information required to find the most important processes involved. Also it provides a basis for a comparison of the properties of the various crystals.
In an earlier study [1] of a number of crystals it was found that the energy levels of cerium in LSO are particularly hard to calculate. The low site symmetry (C1), the mismatch between the size of cerium and lutetium and the complexity of the crystals are important factors. However LSO is a very interesting scintillation crystal because a very small concentration of cerium ions gives a large light output with a short decay time.
In Table 1 results are listed of a number of similar(oxide) crystals. One may wonder why the tranport in LSO is so efficiënt and why the replacement of for instance yttrium by lutetium enhances the light output by roughly a factor two in YAP and YSO but not in YAG. It is assumed here that there is a relation with the local structure of the cerium defect and the overlapping of electronic energy bands of the host lattice. Also it may be that lattice distortions around the cerium defect play an important role in the transport processes.
This paper is a further contribution in this field and it is part of our currrent research on fast scintillators.
The crystal structure of LSO (Lu_2SiO_5)

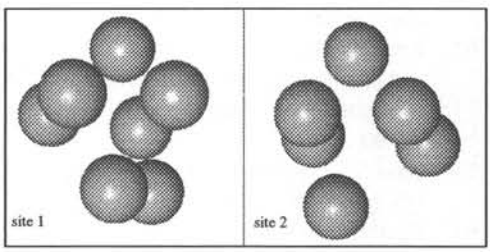

Figure 1. The two sites of cerium in LSO. The balls represent the oxygen nn neighbours.

[1] This work was sponsored by the Stichting Nationale Computerfaciliteiten(NCF) for the use of supercomputer facilities, with financial support from NWO and the Stichting Technische Wetenschappen of the Dutch Foundation for Fundamental Research on Matter (FOM)

contains eight formula units per unit cell. The spacegroup is C2/c. There are two different sites for the lutetium ion [2] of which one has coordination number 7 and the other 6. The local symmetry is c1. In figure 1 a picture is given of the nn neighbours of lutetium at the two sites. Note site 1 and site 2 can be viewed as a distorted octahedron with an extra (silicon bonded) oxygen ion for site 1.
In view of these findings one would expect the excitation spectra of the second cerium centre to consist of two groups of relatively closely packed lines, the lower one being a triplet and the higher one a doublet. Because this is not observed [3] we will assume the cerium populates only the first centre. Another argument for this assignment is that cerium, which is substantially larger than lutetium, fits better into the lattice for site 1: the average Lu-O distance is 2.32 Å for site 1 and 2.22Å for site 2. The estimated [2] ionic radius of cerium is 1.03 Å compared to 0.84 Å for lutetium.

The calculation of 4f-5d energy differences for cerium in ionic crystals looks like a standard routine. Because however the 4f shell is an inner shell and 5d an outer one, the energy difference mostly comes out much too large because of the different levels of approximation used for the two shells. Only a fully relativistic (Dirac-Fock four component) calculation can give useful results. This finding is in contrast with a recent work on cerium in $LaPO_4$ [4] where it was reported that good results on cerium 4f and 5d levels were obtained with small relativistic corrections using the Scattered Wave method, developed by Johnson [5]. Therefore for a number of properties we have made a comparison of our Hartree-Fock results with those of the SW method. This effort was made possible through a visit of one of the authors (A.S) to the group in Delft.

Table 1
Properties of some important oxide type scintillators

Crystal	Ce conc. mol%	λ nm	Light yield phot./MeV	τ nsec
$YAlO_3$ (YAP)	0.2	360	15000/1000	30/10000
$Y_3Al_5O_{12}$ (YAG)	1	550	9000	65
$LuAlO_3$	1	390	25000	10,>200
$Lu_3Al_5O_{12}$	1	300,510	3000,11000	100/long
Y_2SiO_5 (YSO)	-	420	10000	37,82
Lu_2SiO_5 (LSO)	0.1	420	25000	40
$LuPO_4$	-	350	18000	24

A useful trend was found in the 4f-5d energy differences. Whereas the splitting of the 5d level strongly depends on the type of crystal, the average 5d-4f energy difference is fairly constant depending only slightly on the nn Ce-O distances. So only calculations are required for the 5d states. The 4f level splitting can well be approximated by the free ion value and costly relativistic calculations are not required.

In order to find an estimate of the cerium levels in the bandgap it is crucial to know the lattice distortion introduced by the replacement of lutetium by cerium. In our earlier study of cerium in LSO [1] we have shifted the nn neighbours just radially outward by 10 percent in order to simulate the simplest form of lattice relaxation. This gave 4f and 5d energy levels which likely are too low in the bandgap because of the increase of the Madelung potential. Therefore we have attempted a real lattice relaxation using a pair potential model for the LSO lattice.
The studies reported here are calculations (HF or SW) on ionic clusters consisting of the central cerium or lutetium ion surrounded by its nn neighbours. The rest of the lattice is represented by an array of point charges (HF) or a correction to the muffin tin potential(SW). In the SW method also a Watson sphere is used. The errors introduced by these schemes of embedding are unknown.

THEORETICAL MODELS

In the calculations two quantum mechanical models were used. The reason for spending this effort is that every model in some sense has its own results and so by comparing different models insight is given in the reliability of the results.
The models both use a one-particle hamiltonian for obtaining the wavefunctions which describe our state of interest i.e. 4f and 5d of cerium.
The hamiltonian has the simple form:

$$(-\hbar^2/2m\ \nabla^2 + V_c\ (r) + V_x(r)\ )\ \psi_i(\mathbf{r}) = E_i\ \psi_i(\mathbf{r}) \qquad (1)$$

The two models differ in the form of the Coulomb potential V_c and the exchange potential V_x and the way the wavefunction ψ is formulated.

I. The HF LCAO method.

In the Hartree-Fock LCAO method the coulomb as well as the exchange potential are formulated directly using the interaction with all other occupied orbitals in a selfconsistent way, and it requires much computation. The wavefunctions ψ are expanded in terms of a certain chosen set which is fixed. Solving eq.(1) reduces to an eigenvalue problem and good computer codes are available. We have used the non relativistic code Gaussian g92 published by the Carnegie Mellon University[6] and the relativistic code MOLFDIR from the group Theoretical Chemistry of RUG[7]. In our case the method is applied to small molecular clusters of say one cerium ion surrounded by just its nn neighbours embedded in an array of point charges representing the rest of the lattice.

II. The Scattered Wave method.

In the Scattered Wave method [5] the potential V_c is formulated similar as in the HF method with the very important modification that it is forced to have the muffin tin form: it is spherical inside spheres around each nucleus and flat between the spheres. This form of the potential is suited for the scattered wave formalism, which makes use of the spherical waves

in the region between the spheres to obtain solutions of the problem inside the spheres. Most authors in this field use an additional sphere (Watson sphere) around a chosen cluster of ions were the potential is infinite in order to avoid unwanted solutions of the equations. The exchange (correlation) potential V_x is chosen to have the LDA (Local Density Approximation) form in order to include correlation effects. Further the wavefunction ψ is directly obtained by numerical integration in the muffin tin spheres. This formalism is very much less time consuming and in principle one can study much larger clusters than the HF method and one should expect a better description of the solid. This was a motivation for this effort of comparing the results of cerium in LSO. The calculations were done using the code MUSCAT[8].

Lattice relaxation

Because the cerium ion is much larger than the lutetium ion, an estimate of the lattice relaxation was made using the code MOLSTAT[9]. The underlying method is that of Mott-Littleton with shell model. The crystal around the defect is modelled into different regions with different levels of approximation. The ions are described by shell parameters for the polarisation and parameters for the pair potentials. A minimum is found of the electrostatic energy.

RESULTS

In the first place we will compare results for the 4f-5d energy difference of triply ionized free cerium obtained with different methods of approach. The methods are relativistic and non relativistic Hartree-Fock using gaussian basis sets (MOLFDIR and gaussian g92) completely numerical (Desclaux code and Fisher code) and the (numerical) Scattered Wave method implemented in the MUSCAT[8] program. The basis sets are the same as used in reference 1. In table 2 results are given for the orbital and total energies of the 4d and 5d state of Ce^{3+} calculated with different methods.

Table 2
Orbital and total energies of 4f and 5d levels of Ce^{3+}
ion using different methods of approach. Energies are in eV.

Method	ε_{4f}	ε_{5d}	$\Delta\varepsilon$	ΔE_{total}
RHF	-37.8	-29.6	8.2	5.7
HF	-41.8	-30.5	11.3	8.6
SCW*	3.2	10.1	6.9	
ASW	-32.2	-26.2	6.0	10.3

* Calculations done with muffin tin zero

The experimental value for the 4f-5d energy difference is 6.2 eV [10] and so we see only the relativistic calculation gives a useful result if one uses the difference in total energy. Apparently the relaxation of the core electrons on exciting from 4f to 5d modifies the total energy difference to be quite different from $\Delta\varepsilon$. Unfortunately the MUSCAT code does not provide for an evaluation of the total energy. Therefore we have used a similar code ASW [11] to simulate this. The results are given in the last row. The small value of $\Delta\varepsilon$, even better than SCW, increases substantially if one evaluates the total energy difference. This is the

result of the form of the potentials V_c and V_x of eq.(1). The cancellation of the self energy in V_c and V_x is not complete in the SW(LDA) method with the result that particularly the 4f orbital energy is higher compared to the HF value. This effect is completely cancelled however in the evaluation of the total energy. In the HF method one has always a complete cancellation of the self energy and only the effect of core relaxation remains.
However if this lifting of the 4f level is fairly constant in the solid, the SW(LDA) approach is a way of evaluating the 4f-5d energy difference without using a complete relativistic formalism and it explains partly the success of the calculations of reference 4.

Average 4f-5d energy difference

The average 4f-5d energy difference of cerium in ionic crystals is somewhat smaller than the free ion value of 6.2 eV[10]. This experimental fact is explained by the assumption that in the 5d state the wavefunction can lower its energy compared to the 4f state by the larger overlap with the surrounding ions. This means also that the average difference will depend on the nn neighbour distances. For instance in YAP[12] we have an average 4f-5d energy difference of 4.75 eV; in $LaPO_4$, 5.28 eV[4]. There is a certain relation with the average nn neighbour distance: in YAP we have four oxygen neighbours at a rather small distance around 2.3 Å whereas in $LaPO_4$ all oxygen neighbours are at fairly large distances. We will in the following work with the value measured for YAP because the change from YAP to $LaPO_4$ is relatively small.

We have spent a lot of effort to find the dependence of the average 4f-5d energy difference as a function of nn distance. This was done with calculations on a regular CeO_{12} cluster with madelung charges. We have used the HF method in relativistic and non relativistic formalism and also the the SW method.
In figure 2 we show the results. We see that in all three approaches the curve of the 4f-5d energy difference is almost horizontal and so no appreciable distance dependence was found. The small scattering of the points is a result of inaccuracy We call attention to the very large 4f-5d energy difference of the non relativistic HF calculation, the useful SW value and the good RHF value. These findings are in agreement with our calculations on the free ions.

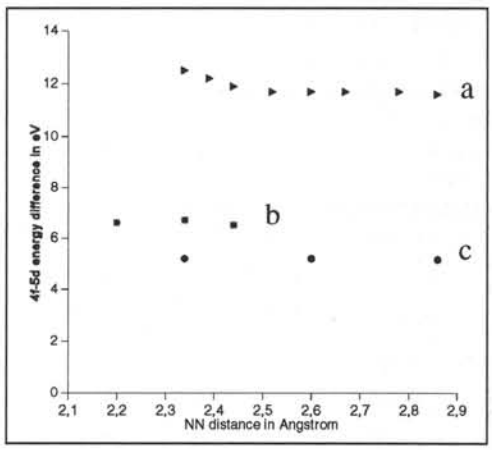

Figure 2. Average 4f-5d energy difference as function of nn distance. a) Non relativistic HF. b) SW. c) Relativistic HF.

LSO model calculations

We come now to the main part of our contribution: calculation of 4f and 5d energy levels in or near the bandgap of the LSO crystal and the positioning of the 4f levels of lutetium.
The results of a cluster calculation depend on the size of the cluster. Therefore we have worked with different cluster sizes. All clusters were embedded in an array of point charges which guarantees a reasonable madelung potential at the sites of the cluster.
We describe the clusters shortly.

CeO_7
Ionic cluster as model for site 1 of LSO. Three radial relaxations were used with 1.0, 1.05 and 1.10 times the lutetium oxygen distances and unchanged madelung charges.
CeO_6
Ionic cluster as model of site 2. Both HF and SW calculations were done using the same relaxations as in the former cluster.
LuO_6
Ionic cluster calculation as model of the host crystal site 2, used as reference for virtuals and for the positioning of the 4f band of lutetium
$Ce(SiO_4)_4O_2$
Large ionic cluster as model of site 2 used for finding cluster size dependence. A minimum was found in the energy on moving all cluster ions except cerium, radially outward with the same amount.

Lattice relaxation
We have done a lattice relaxation study of a point charge model of LSO using pair potentials and polarisation parameters. This calculation done with the MOLSTAT code gave two remarkable results.

Table 3
Energy levels of cerium clusters in LSO using Hartree-Fock and Scattered Wave method. Values are in eV

	CeO_6 HF	CeO_7 HF	CeO_6 SW	$Ce(SiO_4)_4O_2$ HF
relaxation d/d_0 [a]	1.0 1.05 1.1	1.0 1.05 1.1	1.0 1.05 1.1	1.09
ε_{5d}(bottom)	-4.9 -6.8 -8.7	-5.3 -7.5 -9.2	7.9 7.7 7.1	-7.3
ε_{4f}	--	--	4.1 3.0 2.1	
$\Delta\varepsilon_{5d}$	4.9 4.3 3.0[b]	4.3 3.5 2.4[b]	5.6 4.0 3.0	2.7[b]
ε_{val} (top)	-12.5	-12.4	0.0	-12.8
$\Delta\varepsilon_{val}$	9.4	9.3	2.7	7.3
ε_{4f} (Lu)	-16.7	-16.7	--	-16.3

a) d/d0 is the radial relaxation of the neighbouring ion complexes (see text).
b) The numbers are estimates from virtual states (Ce^{4+}).

The pure crystal LSO is not completely stable in the pair potential approach and we had first to change the lattice parameters in order to get a stable LSO. Fortunately the change was not so large. Then we introduced the cerium defect and new positions were found for the ions. The second important result was that the relaxation of the oxygen neighbours is not more than 4 percent or roughly 0.10 Å , a number two times smaller than the difference in radius between the lutetium ion (0.84 Å) and the cerium ion(1.03 Å). So it may be the real relaxation is somewhat larger than calculated with our pair potential model and the error may

be related with the lack of stability in the model for the pure crystal.
Now we come to the results of our HF cluster calculations. A compilation of the resuts of our cluster calculations on LSO is given in table 3 and the results obtained for the positioning of the cerium and lutetium levels in the band gap are visualized in figure 3. Mark in table 3 the large difference between the top of the valence band and 5d. Also the valence bandwidth is remarkable. The positioning of the cerium levels in figure 3 is obtained as follows. From the calculation on the LuO7 cluster we have found an estimate of the bottom of the conduction

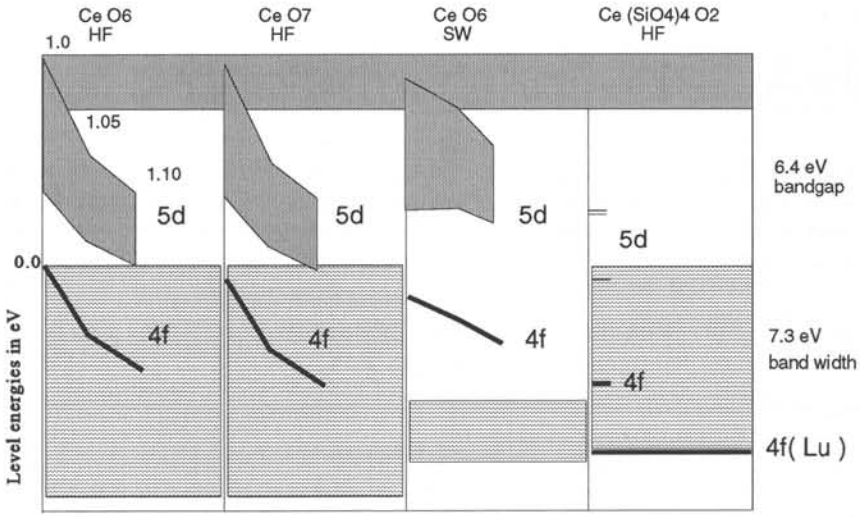

Figure 3. 4f and 5d energy levels of cerium in LSO using different cluster sites and models.
For the HF calculations the valence band is shifted upward to have an expected bandgap of 6.4 eV.

band from the lowest not occupied levels. Now we find the estimated position of the cerium levels just from the difference in orbital energy between these levels and those of the above estimated conduction band. So we have assumed here that the absolute positions of the 5d levels of cerium and the virtual levels are less model dependent than the valence band levels. Therefore we have shifted the valence band levels upward in order to match the expected bandgap of 6.4 eV(the value of YAG). For the results of the SW calculation we have drawn the levels uncorrected in order to show the difference. One can see the far too large bandgap of around 12 eV. The much smaller valence bandwidth of this type of calculation is a result of the averaging in the muffin tin procedure.
Relaxation around the cerium defect directly influences the level position because it changes the madelung potential at the cerium site. Therefore we have marked the levels for the different amounts of relaxation by the percentage outward relaxation of the nn neigbours.

DISCUSSION AND CONCLUSIONS

The calculations of levels of cerium defects in LSO were hard to perform because of several unexpected results. The cluster boundary and the low symmetry introduce low lying oxygen levels which mix strongly with the 5d levels of cerium and makes it hard to choose the right occupation of the orbitals. This is particularly difficult because of the fact that the 5d level splitting is large: at most Ce-O distances the lowest 5d levels are well below the oxygen type levels but for the higher ones this is not true.

Another result of the low symmetry is that in the HF calculations only the lowest 5d level could be occupied because the minimalisation procedure does not allow excited states of the same symmetry. So the higher levels were estimated from the unoccupied levels of an independent calculation for the Ce^{4+} state. In spite of this we have succeeded in performing several useful calculations on cerium defects in LSO with a lot of interesting results.

First we have evidence that the measured excitation spectra[3] are related to only one of the lutetium sites. This is concluded from the local site symmetry and the results of our HF calculations which show the local site symmetry dominates the positioning of the levels.

Second there is good evidence all 5d levels of the cerium are well in the gap of LSO. The third fact is that very probably the relaxation of the neighbours (between 5 and 10 percent) causes the 4f level to be well below the top of the valence band. So Ce^{2+} levels will lie well below the conduction band. It is likely also oxygen type levels are introduced below the conduction band. These levels may be important as trapping centres for electrons excited in the conduction band.

Further the valence band is found to be very broad and this is related to the occurrence of two oxygen bands, one from the Si bonded ones and one from the Lu bonded ones. Next there is good evidence that the 4f band of lutetium overlaps with the oxygen type valence band. This fact becomes even more sure if one realizes that in our model with just one lutetium ion we can not span a band so one has to broaden by at leats 2 eV the lutetium level drawn in figure 3. The overlapping of these bands may be important for an explanation of the fact that the replacement of yttrium by lutetium in a number of crystals almost doubles the light output on X-ray irradiation. However the mechansm is unclear yet. More work on the scintillation processes is needed in order to see if the last two statements really make sense.

REFERENCES

[1] J. Andriessen, P. Dorenbos, C. W. E. van Eijk
Mat. Res. Soc. Symp. Proc., **348**,355(1994)
[2] J.Felsche, Structure and bonding **13,** 99(1973)
[3] H. Suzuki, J. A. Tombello, C. L. Melcher, J. S. Schweitzer, 13
IEEE Trans. Nucl. Sci. **40**,380(1993)
[4] K. C. Mishra, K, H. Johnson, Mat. Res. Soc. Symp. Proc., **348**,367(1994)
[5] K. H. Johnson, Adv. Quant. Chem.,**7**,143(1973)
[6] M. J. Frisch et al., Gaussian™ g92, Pittsburgh , PA, Gaussian, Inc. (1992)
[7] P. J. C. Aerts, Towards Relativistic Quantum Chemisty, PHD Thesis, RUG, 1986
[8] A. V. Bezel, A. B. Sobolev, SCF Multiple Scattering program, Ural State Technical University, 1993
[9] A. N. Varaskin, Sov. J. Struct. Chem. **32,**162 (1991)
[10] W. C. Martin, R. Zalubas, L. Hogan, *Atomic energy levels: The rare earth elements,* Nat. Bur. of Stand.,1978
[11] A. R. Williams, J. Kübler, C. D. Gelatt, Phys. Rev. B **19**,6094(1979)
[12] M. J. Weber, J. Appl. Phys. **44**, 3205 (1973)
[13] M. J. Weber, Solid. State Comm.,**12**, 741(1973)

4F AND 5D LEVEL SPLITTING OF CE^{3+} IN $SRCL_2$:CE, $CECL_3$ AND CEF_3

H. Merenga, J. Andriessen and C.W.E. van Eijk, Radiation Technology Group, Faculty of Applied Physics, Delft University of Technology, c/o IRI, Mekelweg 15 , 2629 JB Delft, The Netherlands.

ABSTRACT

In this paper we present the results of our calculations on $SrCl_2$:Ce and $CeCl_3$ and draw a comparison with our previous results on CeF_3. We show that our method is well capable of giving us an understanding of $SrCl_2$:Ce although the calculated results do not perfectly match the experimental ones due to the uncertainty about the exact geometry. Our method fails to give a good description of $CeCl_3$ because of the limitations of the Hartree-Fock method and the uncertainty about the structure.

INTRODUCTION

The scintillation process in inorganic crystals can be thought of as occurring in three separate stages [1]. The first stage is the absorption of the radiation and the forming of electron-hole pairs. The second stage is the transportation of the electron-hole pairs to the luminescence centres in the crystal. The third stage is the radiative recombination of the electron-hole pairs on the luminescence centres.
In this paper we will focus on a theoretical description of the third stage of the scintillation process in some Ce containing inorganic crystals.
Doping with Ce can provide crystals with good scintillation properties on irradiation with X-rays or γ-rays. The Ce centres show a fast decay (10 ns) and emit photons at wavelengths varying from 300 to 600 nm. Light of these wavelengths can be detected efficiently with current photo multiplier tubes.
We will report here studies on three different crystals: $SrCl_2$:Ce, $CeCl_3$ and CeF_3. $SrCl_2$:Ce is the first chloride we have worked on. We chose this system because of the very high site symmetry of the host material. This high symmetry reduces the costs of especially the relativistic calculations significantly. $CeCl_3$ has the advantage that it is not doped and so the geometry around a Ce site is exactly known. Experimental data on the positions of the 4f and 5d levels in the gap are available. So this system can serve as a benchmark for our method. In a previous paper [2] we have shown that we are able to describe CeF_3 satisfactorily. We incorporate a discussion on CeF_3 in this paper to compare the results with those on $CeCl_3$.

THEORY

Our theoretical model consists of two parts: A material model and a computational model. The material model concerns the representation of the crystal under investigation. The computational model concerns the level of theory used in the calculations.
We are interested in local properties of Ce atoms. These local properties are primarily defined by the direct environment of the Ce atoms. Therefor it suffices to study a small cluster containing only the Ce atom of interest and its closest neighbours. The electrostatic potential due to the rest of the crystal is accounted for by adding a few charges which are optimised to generate the correct Madelung potential at the cluster sites.
All of the relativistically correct calculations were done on the Hartree-Fock-Dirac (HFD) level with the MOLFDIR program package [3]. The non-relativistic calculations were mostly done on the Hartree-Fock (HF) level with the Gaussian 92 program [4].
The procedure we use to calculate the position of the Ce 4f and 5d levels in the gap can be found in detail in reference [2]. We will suffice here with a short description: We assume that the distance between the average of all $4f)^1$ states and the average of all $5d)^1$ states is the same for all crystals of a certain type (say, fluorides or chlorides). So for each type of material we only have to do one Hartree-Fock-Dirac calculation on the average $4f)^1$ state and one on the average $5d)^1$ state of a suitable material to obtain this distance for an entire class of materials. The 5d level splitting can be obtained by a non relativistic Hartree-Fock calculation. The position of the conduction band is determined by the orbital energy of a very diffuse 6s like orbital from a calculation on the host material. The position of the 5d levels is determined by their orbital energies. The position of the 4f levels can then be found by calculating the average 5d energy and subtracting the energy difference between the average 4f and the average 5d levels.
When the cluster contains very diffuse functions (e.g. because of the need for large basis sets for heavy ligands) the 5d orbital energies may be too low. This is caused by the interaction of the orbitals

Proc. Int. Conf. on Inorganic Scintillators and Their Applications, SCINT95,
1996, Delft University Press, The Netherlands

with the edge of the cluster and consequently is an artefact of the material representation of the crystal. In these cases a better way of determining the position of the 5d levels in the gap is taking the difference of the ionisation energy of the lowest Ce $5d)^1$ state and the ionisation energy of the host $6s)^1$ state as the difference between the lowest 5d level and the conduction band.

RESULTS

$SrCl_2$:Ce

In $SrCl_2$:Ce the Ce impurity replaces the Sr atom. The symmetry of the Sr site is very high: O_h. Our cluster will consist of one Ce atom and eight Cl atoms octahedrally distributed around the Ce atom. On some distance of the cluster we put point charges to represent the Madelung potential. The results of the HFD calculations on this system are summarised in the second column of table 1.

Table 1. The results of the HFD and HF calculations on $SrCl_2$:Ce.

	Experiment [5]	original geom.	geom. 1	geom. 2
$E_{4f)^1av-5d)^1av}$ (cm^{-1})	41118	40025		
5d levels (eV)	0.00	0.00	0.00	0.00
		0.00	0.66	0.46
	1.50	1.31	1.73	2.06
	1.61	1.31	1.73	2.06
	1.76	1.46	2.02	2.23

We can see from this table that the energy difference between the average of the $4f)^1$ states and the average of the $5d)^1$ states is quite well reproduced. The 5d levels on the other hand do not compare well with the experimental data. Because the Ce ion has a different formal charge than the Sr ion charge compensation will occur upon doping $SrCl_2$ with Ce. In analogy with BaF_2:Ce [6] we expect an extra Cl^- ion on the 100 axis. We tried to estimate the perturbed geometry with the HADES program [7]. The interaction parameters for the Sr - Cl interaction were extrapolated from the interaction parameters of similar compounds. We performed two different extrapolations and thus got two different sets of interaction parameters. With these sets of parameters we calculated the perturbed geometry due to the extra Cl^- ion. These new geometries have C_{4v} point symmetry. We performed HF calculations on these two systems to obtain the 5d level splitting. The results are listed in the third and fourth column of table 1.
The total spread in the calculated 5d spectra is too big. The second line of the E doublet is experimentally not seen. Comparing these results with the results from the second column of table 1 we conclude that the real geometry around the Ce impurity should be somewhere between the host geometry and geometry 1. Considering that the HADES program has a tendency to overestimate the geometry relaxation this is a reasonable result.
We also calculated the position of all the levels in the gap. The results are based on geometry 1 and we used the alternative method described in the theory section. The results are listed in table 2. Note that the Ce 4f levels are 1.3 eV under the valence band edge. Although this is not impossible it is likely that the levels are still a bit to low, because of the unphysical interaction with the cluster edge.

Table 2. The Ce levels in the gap of $SrCl_2$.

	CB	5d				4f av.	VB
energy (eV)	-0.03	-4.13	-4.32	-5.23	-5.88	-9.74	-8.48

$CeCl_3$ and CeF_3

$CeCl_3$ has a low site symmetry: C_{3h}. The smallest system we can use to represent the crystal is a $CeCl_9$ cluster with a Madelung potential. If we include one extra layer of atoms in the cluster we get a $CeCl_9Ce_8$ cluster. In our calculations on the large cluster we actually used a $CeCl_9La_8$ cluster. This should give approximately the same results but avoids the problems associated with the extra eight unpaired 4f electrons which are present in the original cluster.
In table 3 we have listed the results of our calculations on the small $CeCl_9$ cluster. These calculations consist of a HF calculation on a specified average of states followed by an evaluation of the correct energy expression for all the different states with the molecular orbitals of the calculation on the

average of states. The basis set used for the Ce atom included both 4f and 5d functions. We repeated the calculations with other basis sets. The variations in the results were always less than 5%.

Table 3. The Ce 5d levels for the $CeCl_9$ cluster.

Initial state	HF $5d)^1$ av	HF $4f5d)^1$ av	HF $4f)^1$	Exp. [8]
5d states (eV)	0.00	0.00	0.00	0.00
	0.45	0.43	0.64	0.50
	0.45	0.43	0.64	0.89
	0.67	0.65	0.79	1.20
	0.67	0.65	0.79	

From table 3 we see that the difference in polarisation between the $5d)^1$ average and the $4f5d)^1$ average does not influence the results much. The results based on the $4f)^1$ average state differ much more. But here the Ce 5d levels are unoccupied in the reference state, so the results are less accurate. The calculated 5d level splitting is significantly smaller than the experimental one.
The results of our HF calculations on the larger clusters: $CeCl_9La_2$ and $CeCl_9La_8$ are listed in table 4.

Table 4. The Ce 5d states for the large clusters.

	$CeCl_9La_2$	$CeCl_9La_8$
5d levels (eV)	0.00	0.00
	0.13	0.49
	0.94	0.67

From table 4 it is clear that the results for the large $CeCl_9La_8$ cluster are almost the same as those for the small $CeCl_9$ cluster and still a factor of two too small relative to the experimental results.
The distance between the Ce and Cl ions is very large: 2.966Å. The sum of the ion radii is only 1.03 + 1.80 = 2.83Å. So the interaction between the Ce 5d orbitals and the Cl ions will be small and consequently the Ce 5d orbital splitting will also be small. The nine Cl ions are approximately spherically arranged around the Ce ion. The resulting spherical charge distributions will average and reduce the effect of the point charges surrounding the cluster. To show this we can make the large cluster less spherical by removing six La ions thus obtaining the $CeCl_9La_2$ cluster. The calculated Ce 5d level splitting for this cluster is 50% larger than in the other clusters.
On the basis of the point group symmetry of the Ce site we expect that the 5d spectrum will be split up into three lines by the ligand field. Spin-orbit coupling will further split the spectrum up into five lines. The splitting due to the spin-orbit interaction cannot be more than 0.2 eV. The experimental spectrum does not conform to this expectation. This leaves the conclusion that the crystal structure we use for our calculations is not the same as the crystal structure of the material which gave rise to the experimentally observed spectrum.
In table 5 we list the positions of the Ce levels in the gap. We used the Ce 5d orbital energies obtained from the $CeCl_9La_8$ cluster. We assumed that the conduction band edge is formed by the Ce 6s.

Table 5. The position of the Ce levels in the gap of $CeCl_3$.All entries are in eV.

	CB	5d				4f av.	VB
This work	-0.21	-1.87	-2.02	-2.54	-	-7.03	-7.59
Experiment	0.00	0.00	-0.30	-0.70	-1.20	-5.00	-5.00

CeF_3 is represented by a CeF_{11} cluster. The point group symmetry of this cluster is C_2. The Ce - F distances vary from 2.39 Å to 2.97 Å. So the direct surroundings of the Ce ion are much less spherical than in the $CeCl_3$ case and some of the F ions are very near. We expect therefor a much larger 5d level splitting in CeF_3 than in $CeCl_3$. The results listed in table 6 confirm this.

Table 6. The Ce 5d levels for CeF_3.

	Theory [2]	Experiment [9]
5d levels (eV)	0.00	0.00
	0.31	0.29
	0.71	0.62
	1.00	0.80
	1.40	1.35

The position of the levels in the gap are listed in table 7. The experimental and theoretical results agree within an error bar of 1 eV.

Table 7. The position of the Ce levels in the gap of CeF_3. All entries in eV.

	CB	5d					4f av.	VB
Theory [2]	0.00	-2.31	-2.87	-3.06	-3.40	-3.70	-8.90	-10.14
Experiment [9]	0.00	-1.39	-1.80	-2.10	-2.52	-2.84	-8.00	-10.00

CONCLUSIONS

Our results show that the method we use is able to get reasonable to good results for most systems. If the nearest neighbours of the Ce ion are distributed approximately spherical and if the distance between the Ce ion and its nearest neighbours is very large our method may fail. The reason lies in the limitations of the computational model we use. The HF method is not able to describe the polarisation effects up to the detail required by these kind of systems: The HF method does not describe the tails of the wave functions very well. So at large distances the calculated interaction between the ions will not be correct. Furthermore, in the HF method each electron only feels the average interaction of the n-1 other electrons. So certain types of electron-electron interaction are completely missing.
In principle we can get a correct description in these cases by using a computational method which takes the electron correlation into account. In practice however, these methods can be prohibitively expensive when used on large systems.
In the case of $CeCl_3$ the experimental data are incompatible with the structural data we have. For further research it is imperative to obtain the experimental absorption spectrum of a $LaCl_3$:Ce crystal to verify our suspicion that the current experimental spectrum is an artefact of the preparation of the sample and not the spectrum of a Ce site in bulk $CeCl_3$ or $LaCl_3$.

REFERENCES

[1] J. Andriessen, P. Dorenbos and C.W.E. van Eijk, Calculation of energy levels of Cerium in inorganic scintillator crystals., Conference proceedings of the MRS spring meeting Vol 348, April 4-8 1994, To be published.
[2] H. Merenga, J. Andriessen and van C.W.E. van Eijk, Positions of 4f and 5d energy levels of $Cerium^{3+}$ in the bandgap of CeF_3, YAG and LSO., Radiation Measurements, Int. J. Radiat. Appl. Instrum.., Part D, 1995, To be published.
[3] The MOLFDIR program package is a molecular relativistic quantum chemical program package for doing Hartree-Fock-Dirac and RASCI calculations. It was developed by P.J.C. Aerts, O. Visser and L. Visscher of the Theoretical Chemistry Group of the University of Groningen and H. Merenga of the Radiation Technology Group of the Delft University of Technology. A good description of the program package can be found in: L. Visscher, Relativity and Electron Correlation in Chemistry, Thesis, University of Groningen, The Netherlands, 1993
[4] Gaussian 92, Revision G.2, M.J. Frisch, G.W. Trucks, M. Head-Gordon, P.M.W. Gill, M.W. Wong, J.B. Foresman, B.G. Johnson, H.B. Schlegel, M.A. Robb, E.S. Replogle, R. Gomperts, J.L. Andres, K. Raghavachari, J.S. Binkley, C. Gonzales, R.L. Martin, D.J. Fox, D.J. Defrees, J. Baker, J.J.P. Stewart, and J.A. Pople, Gaussian Inc., Pittsburgh PA, 1992
[5] O.T. Antonyak and N.S. Pidzyrailo, Spectroscopy of Ce^{3+} centers in $SrCl_2$:Ce single crystals, Opt. Spectrosc. (USSR) **60** (1986), 743
[6] R. Visser, J. Andriessen, P. Dorenbos and C.W.E. van Eijk, Ce^{n+} energy levels in alkaline-earth fluorides and cerium-electron, cerium-hole interactions., J. Phys.: Condens. Matter **5** (1993) 5887
[7] A.H. Harker, HADES II/PC: The Harwell Automatic Defect Evaluation System for Personal Computers, 1989, (Harwell: Publications Office)
[8] Shigeru Sato, Optical Absorption and X-Ray Photoemission Spectra of Lanthanum and Cerium Halides, J. of the Phys. Soc. Japan, **41** (1976), 913
[9] W.W. Moses, S.E. Derenzo, M.J. Weber, A.K. Ray-Chaudhuri and F. Cerrina, Scintillation Mechanisms in Cerium Fluoride, J. of Luminescence, 1994, to be published.

CALCULATION OF 4f AND 5d ENERGY LEVELS OF CERIUM IN LiYF4 AND LiLuF4 AND LiBaF3, AN ESTIMATE OF LOCAL DISTORTION

J Andriessen, H. Merenga, C. M. Combes, P. Dorenbos, C.W.E. van Eijk,
University of Technology, Faculty of Applied Physicsc/o IRI, Mekelweg 15, 2629 JB Delft, The Netherlands

The doping of ionic crystals with cerium has provided a number of useful scintillator crystals. The mechanisms which play a role in the scintillation process are quantitatively unknown. The diversity in the light output of the crystals shows the need for data on the atomic level such as level positioning, lattice distortion and changes in the electronic structure of the host crystal by the cerium defect. By comparing such data for all crystals useful trends can be found.
This study is particularly concerned with the lattice distortions introduced by cerium in the crystals $LiLuF_4$, $LiYF_4$ and $LiBaF_3$. The excitation spectra recently measured in our group[1] are accurate enough for obtaining estimated lattice distortions from splitting of the 5d level. The 5d orbital of Ce^{3+} is rather delocalized and interacts strongly with the latttice. The simple crystal field theory using point charges to represent the lattice is not sufficient here. The neighbours have to be presented as real ions and a molecular cluster calculation is required to obtain a realistic picture to compare with experiment.
We have chosen for ab initio HF calculations using a commercial package, the Gaussian™ g92 program[2] . The HF formalism is formulated in the LCAO form with a fixed gaussian basis set. The basis sets are those of reference 3.

LiLuF4 and LiYF4

The spectra obtained[1] for the two crystals are so much the same that one can assume that the local environment of the cerium ion is the same in both crystals. So we have done calculations on the yttrium compound only. The site symmetry for yttrium is S4[4] and it has eight fluorine neigbours. So our molecular cluster was a CeF_8 complex embedded in an array of point charges to quarantee the right madelung potential at the sites of the cluster.
We have included spin orbit interaction in order to have a complete picture of the 5d level plitting.
We have done two calculations. The first one was done with the nominal distances of the yttrium compound and the second one with nn neighbour distances which are 10 percent larger. This is because the cerium ion is substantially larger than yttrium (1.03 Å against 0.94 Å).
The results are given in figure 1. As one can see the first calculation gives clearly a much too large splitting because of the small Ce-F distances. This improves much in the second calculation. The type of the sublevels is noted in the figure and one can see that all sublevels except the fourth have right positions. The difference between xz and yz is determined by spin-orbit interaction because in S4 symmetry they are degenerate. So it seems there is a

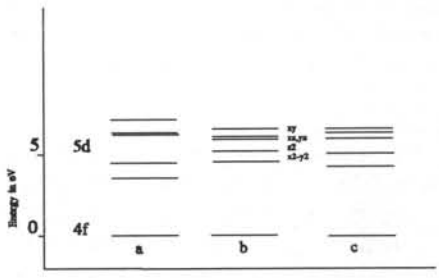

Figure 1 4f 5d levels of cerium in $LiYF_4$. a) Unchanged nn distances. b) 10 percent outward relaxation c) Experimental results[1]

Proc. Int. Conf. on Inorganic Scintillators and Their Applications, SCINT95,
1996, Delft University Press, The Netherlands

distortion of the S4 symmetry because the xz-yz difference is much too large.

$LiBaF_3$

The measurements on cerium in $LiBaF_3$ [1] show two groups of closely packed lines and a splitting of the 5d level which is small. This is understandable because cerium replaces barium and this ion has a coordination number of twelve in a cubic site symmettry. Actually barium is at the centre of a cube with the lithium ion at the corners and fluorine ions at the centres of the twelve edges. This coordination usually has a small crystal field. The occurrence of the two groups indicate the presence of a nearby charge compensation and this is exepected because the barium is only doubly ionized.

Therefore we have done three calculations of which the results together with the experimental data are shown in figure 2. The molecular cluster consisted of the cerium ion surrounded by twelve fluorine neigbours embedded in an array of point charges to quarantee the right madelung potential. Further different forms of charge compensation were used: The first calculation was done on the unmodified cluster showing only two closely packed lines: the cubic field splitting. Spin-orbit interaction was neglected here.

The second calculation was done with an Li^+ ion replacing a nearby Ba^{2+} ion and the third calculation models the charge compensation by a interstitial fluorine ion on one of the cubic axes. One may think of an additional model for charge compensation: the removal of a second neigbour lithium. However this site can not give the right level structure because it does not split the cubic e_g level. The results are shown in figure 2. As one can see only the second calculation gives approximately the right level splitting; it is too small however. The reason may be the neglect of lattice relaxation introduced by the Li^+ defect. We have done some lattice relaxation using the HADES2[5] programs but no useful results have been obtained yet.

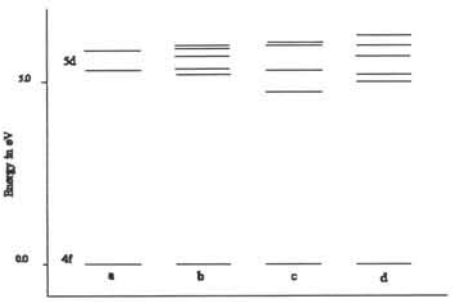

Figure 2 4f and 5d energy levels of Ce^{3+} in $LiBaF_3$ using different models. a) unmodified cubic site. b) Li^+ ion replaces Ba^{2+} c) Interstitial F^- ion. d) Experimental results [1]

CONCLUSIONS

The splitting of the 5d level of Ce^{3+} in $LiLuF_4$, $LiYF_4$ and $LiBaF_3$ clearly reveal information about the local environment. Molecular cluster calculations are useful to obtain this information. The data are not sufficient for obtaining the distortions but are very helpful in choosing between various alternatives.

REFERENCES

[1] C.M. Combes, private communications
[2] M. J. Frisch et al., Gaussian™ g92, Pittsburgh , PA, Gaussian, Inc. (1992)
[3] J. Andriessen, P. Dorenbos, C. W. E. van Eijk,
Mat. Res. Soc. Symp. Proc., **348**,355(1994)
[4] R. E. Thoma, C. F. Weaver, H. A. Friedman, H. Insley, L. A. Harris,
J. Phys. Chem., **65** ,1061(1961)
[5] A. H. Harker, Hades II/PC: The Harwell Automatic defect Evaluation System for Personal Computers(Harwell publication Office 1989)

CLUSTER SIMULATIONS OF EMISSION PROPERTIES OF CsI:Tl AND NaI:Tl SCINTILLATORS

M. Berrondo, J.F. Rivas-Silva* and J.B. Czirr
Department of Physics & Astronomy,
Brigham Young University,
Provo, UT 84602

Abstract

We present electronic *ab initio* calculations of ion clusters simulating two well known thalium-based scintillators, CsI and NaI. We calculate both the absorption and emission energies, the corresponding Stokes shifts and the radiative lifetimes. The cluster model consists of a central cation surrounded by a *single* shell of active ions, with point charges embedding the cluster, simulating the rest of the crystal. The results are within 0.5 eV from experiment. We also compare our results with earlier ones involving larger clusters.

INTRODUCTION

The properties of ground and excited states of doped crystals give information about the spectroscopy of luminescent materials [1, 2]. We can calculate these states modeling the pure crystal as a molecular cluster, replace one ion by the activator, and compute both ground and excited states of the modified cluster, using a relaxed lattice [3]. According to Franck-Condon's principle, absorption is calculated from the electronic ground state minimum, while emission starts at the electronic excited state energy minimum.

We present *ab initio* calculations for the electronic structure of thalium-doped sodium iodide and cesium iodide using a simple cluster model involving only the first shell of anions surrounding the Tl^+ ion, embedded in a sea of point charges. The first crystal is found in the sodium chloride (fcc) structure, while CsI is in the cesium chloride (bcc) structure at room temperature [4]. We have used self-consistent-field (SCF) programs [5] in order to calculate the energy difference between the ground state and the excited state (ΔSCF) [6]. We optimize the geometry of the ground state singlet and lowest triplet states separately. Our calculated Stokes energy shift corresponds to the difference between the two excitation energies.

CLUSTER MODELS

Our simple cluster model consists of a central Tl ion surrounded by a single shell of iodine ions. For NaI there are six nearest neighbors (NN), with a total of 60 electrons and a net charge of -5. This "active" cluster is embedded with 722 point charges ($\pm$ 1), the whole forming a 9×9×9 cube. The fact that we are dealing with the sodium iodide and not other alkali iodides appears only in the distance between point charges, which is held fixed during the whole calculation. CsI has eight NN iodines around the Tl, with a total of 76 electrons in the cluster and a net charge of -7. Next follow two shells of +1 point charges (26 in all), and 56 fractional negative point charges on the surface of a 4×4×4 cube following Evjen's model of an ionic solid. All *ab initio* computations were

Proc. Int. Conf. on Inorganic Scintillators and Their Applications, SCINT95,
1996, Delft University Press, The Netherlands

performed using the gaussian bases and relativistic pseudopotentials of Hay and Wadt [7]. The total number of active electrons is determined by the number of anions in the cluster times eight plus 12 for Tl^+ ($6s5d$ subshells). The basis sets are centered around each of the active ions, but not on the point charges. There are 66 contracted basis functions for NaI:Tl and 82 basis functions for CsI:Tl.

Absorption and emission energies are computed finding the SCF minimum energy nuclear configurations for the electronic ground and first excited states independently. For the ground state, we considered the breathing symmetric mode varying the radial distance corresponding to the first shell, and found the potential energy surface minimum. The triplet state required a more careful study of the different normal modes of cluster deformation in order to optimize the geometry. Only the first shell was displaced, with all point charges fixed.

ABSORPTION AND EMISSION

NaI: The relaxed lattice configuration for the ground state is given by a symmetric dilation of the first shell with respect to the experimental pure crystal configuration of about 0.54 Å. This is approximately the same amount as the difference in ionic radii between Tl^+ and Na^+. A similar breathing mode optimization for the triplet state gives a very small Stokes shift [8]. For the triplet energy minimum, we thus searched along different normal mode relaxations and we found that the optimum configuration corresponds to the tetragonal deformation mode. This implies an *elongation* of 0.43 Å along the tetragonal axis, and a corresponding *contraction* of 0.35 Å from the four iodine ions in the corners of the square forming the plane perpendicular to the fourfold axis. The corresponding calculated Stokes shift is 1.4 eV (see Table I), in excellent agreement with the experimental value of 1.3 eV.

CsI: This case shows a similar behaviour within the bcc geometry. In spite of the fact that the ionic radius of Cs^+ is somewhat larger than that of Tl^+, our calculations show a slight expansion of the ground state of the embedded doped cluster in the ground state, due to the presence of the surrounding point charges. For the triplet relaxed excited state (RES), one of the main diagonals through the thalium ion at the center becomes a threefold symmetry axis. The two corresponding iodines along this axis move *towards* the center a distance of 1.1 Å, while the other six iodines, originally at the corners of the cube, expand by an equal amount. The resulting geometry is that of two staggered symmetric trigonal pyramids in an oblate configuration. Although the ionic displacements seem too large, the corresponding computed emission energy of 2.77 turns out to be in good agreement with the experimental value of 3.09 for the ultraviolet emission band (not involving self-trapped excitons) [9]. The resulting energies are also reported in Table 1. We searched for possible displacements of the Tl^+ ion from its central position in the cluster, without success.

Table 1 presents results for the two Tl^+ activated crystals studied. The second column shows the calculated absorption energy for the singlet ground state optimized geometry. The third column shows the corresponding experimental value. The next two give the emission energy corresponding to the triplet excited state and the experimental emission energy [9-11]. All values in eV.

Table 1 - Excitation Energies (eV)

Crystal	Abs.	Exp.	Emis.	Exp.
NaI:Tl (fcc)	4.94	4.22	3.57	2.89
CsI:Tl (bcc)	5.02	5.0	2.77	3.09

We also calculated the triplet lifetimes, including an effective spin-orbit parameter for the cluster [12]. We first compute the singlet state lifetime and allow for a mixing of the original triplet $|t\rangle$ with the singlet $|s\rangle$, $|t'\rangle = c_1|s\rangle + c_2|t\rangle$. The triplet lifetime $\tau(t')$ is proportional to the singlet lifetime $\tau(s)$, as well as $|c_1|^{-2}$, which, in turn, depends upon the spin-orbit parameter ζ [13]. We use an effective parameter [12] defined as $\zeta = (\zeta_c + n\,\zeta_l)/(n+1)$, where n is the coordination number of Tl^+. This *ansatz* simplifies the calculations, and gives the correct trends. For the central thalium ion, we used the value $\zeta(Tl^+) = 8183$ cm^{-1}, while for the iodine ion we used $\zeta(I^-) = 4000$ cm^{-1} [14].

Table 2 contains the effective parameters (in eV), the calculated triplet lifetimes and the experimental lifetimes values (in μs) [15].

Table 2 - Lifetimes

Crystal	ζ (eV)	τ (μs)	Exp. (μs)
NaI:Tl (fcc)	0.569	0.48	0.22
CsI:Tl (bcc)	0.553	0.76	0.80

As is well known, the spin-orbit effect also splits the ^3P state of the Tl^+ ion excited state into $J = 0$, 1, and 2. The corresponding emissions are forbidden for $J = 0$ and 2. The Tl impurity in the crystal behaves as a deformed ion, presenting a similar behaviour. The calculated atomic charge population is close to one for the ground state configuration. In the RES, this value is reduced, but the spin poulation is 1.7, indicating that the two parallel-spin electrons in the triplet are associated to the Tl impurity.

CONCLUSIONS

The results for excitation and emission of Tl^+ activated alkali halides obtained in this work are surprisingly good. Earlier calculations of NaI:Tl using a much larger cluster [3] are within 7% of our present results. This turns out to be the trend for all the fcc-like alkali halides [16]. The most interesting conclusion seems to be that an *ab initio* calculation using very simple clusters yields reliable numbers, given a judicious choice of the embedded cluster. Actually, for the CsI:Tl case, we tried many different models with larger clusters and we were not able to find the RES minimum, even using singles configuration interaction (CIS) for the optimization. The reason appears to be the presence of *two* consecutive shells of cations surrounding the central Cs (or Tl for the doped case).

The relaxation of the lattice around the Tl^+ ion is not along the breathing mode for the excited triplet state. This is due to the presence of the occupied p orbital in the

sp excited state of Tl^+ defining a preferred axis. This distortion can be understood as a Jahn-Teller effect. In our calculations, the symmetric configuration lies at a saddle point in the potential energy surface, so the search for a minimum energy configuration leads directly to the deformed conformation as the most favorable one.

Regarding the emission process, the thalium centers behave almost as a Tl^+ ion, in contrast to Bi in BGO, where a simple atomic picture is inadequate [17].

ACKNOWLEDGMENTS

Work supported in part by NIH under grant number R01-CA48002-04, subcontract number 4591710 with Lawrence Berkeley Laboratory. One of us (JFR) would like to acknowledge the support from Sistema Nacional de Investigadores - SEP (Mexico).

REFERENCES

[1] W. Hayes and A.M. Stoneham, *Defects and Defect Process in Nonmetallic Solids*, 1st ed. (John Wiley & Sons, New York, 1985).
[2] R.W. Grimes, C.R.A. Catlow and A.L. Shluger, eds. *Quantum Mechanical Cluster Calculations in Solid State Studies*, (World Scientific, Singapore, 1992).
[3] M. Berrondo and J.F. Rivas-Silva, Int. J. Quantum Chem. S29, 0000 (1995).
[4] C. Kittel, *Introduction to Solid State Physics*, 5th ed. (John Wiley & Sons, New York, 1985), p. 92.
[5] M. Frisch *et al.*, GAUSSIAN92, Gaussian, Inc., Pittsburgh, PA. (1992).
[6] W.J. Hehre, L. Radom, P.R. Schleyer, and J.A. Pople, *Ab Initio Molecular Orbital Theory*, 1st ed., (John Wiley & Sons, New York, 1986).
[7] P.J. Hay and W.R. Wadt, J. Chem. Phys. 82, 270 (1985); 82, 284 (1985); 82, 299 (1985).
[8] M. Berrondo, J.F. Rivas-Silva and J.B. Czirr, in *Scintillators and Phosphor Materials*, ed. by M.J. Weber *et al.*, (Materials Research Society, Pittsburgh, PA, 1994) p. 373
[9] V. Nagirnyi, S. Zazubovich, V. Zepelin, M. Nikl and G.P. Pazzi, Chem. Phys. Lett. 227, 533 (1994).
[10] J.B. Birks, *The Theory and Practice of Scintillation Counting*, 5th ed. (McMillan Co., New York, 1964), p. 85.
[11] J.B. Czirr (unpublished).
[12] M. Berrondo and J.F. Rivas-Silva, submitted to J. Phys. Chem. Solids
[13] O. Valée, N.T. Minh and J. Chapelle, in *Spectral Line Shapes*, ed. by B. Wende (Walter de Gruyter, Berlin, 1981).
[14] D. Bramanti and M. Mancini, Phys. Rev. B3 (1971) 3670.
[15] See *e.g.* P.W.M. Jacobs, J. Phys. Chem. Sol. 52 (1991) 35.
[16] M. Berrondo and J.F. Rivas-Silva, to be published.
[17] M.J. Weber, A.C. West, C. Dujardin, B. Rupp, M. Berrondo, and J.F. Rivas-Silva, these Proceedings.

* On leave from IFUAP (Mexico).

ENERGY RESOLUTION, NON-PROPORTIONALITY, AND ABSOLUTE LIGHT YIELD OF SCINTILLATION CRYSTALS

P. Dorenbos, M. Marsman, C.W.E. van Eijk
Delft University of Technology, Faculty of Applied Physics,
c/o IRI, Mekelweg 15, 2629 JB Delft, The Netherlands.

ABSTRACT For 11 different scintillators, the influence of the absolute light output and non-proportional response on the obtainable energy resolution for the detection of γ-quanta was studied. The scintillation process in NaI(Tl) was simulated with Monte Carlo techniques.

INTRODUCTION

In scintillator research one is particularly interested in the scintillation emission spectrum, the scintillation decay time, and the absolute scintillation light yield. The latter is usually expressed in terms of the number of photons created in the crystal per unit of absorbed ionizing energy (photons/MeV). A high light output is needed to obtain good timing properties and a good energy resolution. Quite soon after the discovery of NaI(Tl) and CsI(Tl) scintillators it was found that their light yield is not proportional with the γ-quantum energy [1]. It was also realized that a non-proportional response influences the obtainable energy resolution [2, 3]. Unfortunately, studies on non-proportional response and its influence on the energy resolution received little attention during the past 15 years.

In this work a compilation of the absolute photon yield, the photoelectron yield in PMTs with bialkali photocathodes, and the energy resolution for the detection of 662 keV γ-quanta, is given for 11 different scintillators. The relation between absolute light output, non-proportionality and energy resolution was studied by means of Monte Carlo simulation of the scintillation process. First results on NaI(Tl) are presented.

ENERGY RESOLUTION

Suppose γ-quanta of energy E_γ are detected by means of a scintillator optically coupled to a photomultiplier tube (PMT). The average total charge $\overline{Q_0}$ contained in the anode pulse delivered by a photomultiplier tube then equals:

$$\overline{Q_0} = \overline{N_{ph}}\,\overline{p}\,\overline{M} \tag{1}$$

where $\overline{N_{ph}}$ is the mean number of photons created in the scintillator upon absorption of the γ-quantum. $\overline{p}$ is the average transfer efficiency and represents the probability that a photon from the scintillator results in the arrival of a photoelectron at the first dynode which subsequently undergoes the full multiplication in the PMT. $\overline{M}$ is the mean electron multiplication factor of the PMT.

The energy resolution R is now defined as the full width of the peak in the pulse height spectrum at half the maximal intensity (FWHM) divided by the mean pulse height.

Proc. Int. Conf. on Inorganic Scintillators and Their Applications, SCINT95,
1996, Delft University Press, The Netherlands

We will distinguish four separate contributions to R which are related according to:

$$R^2 = R_{np}^2 + R_{inh}^2 + R_p^2 + R_M^2 \tag{2}$$

R_{np} is the contribution due to the non-proportional response of the scintillator, R_{inh} is connected with inhomogeneities in the scintillation crystal causing local variations in the scintillation light output. The transfer resolution R_p is related to the variance in p. R_p is determined by many technical parameters of the scintillator PMT combination. For example; possible self absorption of scintillation light in the crystal, non-uniform reflectivity of the reflecting covering of the crystal, non-uniform photocathode properties, etc. The combined effect of the above three contributions is often named scintillator resolution R_s defined as $R_s^2 = R_{np}^2 + R_{inh}^2 + R_p^2$.

R_M is the photomultiplier resolution which can be written as [4, 5]

$$R_M = 2.35\sqrt{\frac{1 + v(M)}{\overline{N_{ph}}\overline{p}}} \tag{3}$$

where $v(M)$ is the fractional variance in the multiplication M. For multistage linear focussed photomultiplier tubes with an enhanced first dynode and a bialkali photocathode, $v(M)$ is typically 0.1 to 0.2 [5].

For an ideal detector system and perfect crystal quality, R_{inh}, R_p, and $v(M)$ will vanish and the resolution is determined by R_{np} and the Poisson statistics in the number of photoelectrons, i.e. $\overline{N_{ph}}\overline{p}$. Note that R_{np} and N_{ph} are fundamental properties of the scintillator and their values are determined by the physical processes occurring in the crystal upon absorption of γ-quanta. In the literature on scintillators, data on N_{ph} are frequently reported. The value for R_{np} can not be measured directly and its contribution to the overall energy resolution is usually not known.

In Table 1, a review is presented of the energy resolution, photoelectron yield, and light yield obtained with scintillators optically coupled to a photomultiplier tube. All data pertain to the case of full absorption of 662 keV gamma quanta in the scintillator. Equations (2) and (3) were used to calculate the values of R_s and R_M in Table 1. For more details, see [5]

Table 1 shows that for relatively low light output crystals like $Bi_4Ge_3O_{12}$, BaF_2, $Gd_2SiO_5(Ce^{3+})$, and $YAlO_3(Ce^{3+})$, Poisson statistics in the number of photoelectrons, i.e. R_M, gives the dominant contribution to the overall energy resolution. For the high light output crystals $NaI(Tl^+)$, $CsI(Tl^+)$, $CsI(Na^+)$, and $Lu_2SiO_5(Ce^{3+})$, the scintillator resolution appears more important. $Lu_3Al_5O_{12}(Sc^{3+})$ and $K_2LaCl_5(Ce^{3+})$ combine a large light output with a small value for R_s, consequently, despite a lower light yield, the energy resolutions obtained with these crystals are comparable or even better than that of $NaI(Tl^+)$ crystals.

ABSOLUTE LIGHT YIELD AND NON-PROPORTIONALITY

The absolute light yield of a scintillator can be expressed as [18]

$$N_{ph} = N_{eh}SQ = \frac{E_\gamma}{E_{eh}}SQ \tag{4}$$

Table 1: Photon yield (N_{ph}), photoelectron yield ($\overline{N_{ph}\bar{p}}$), and energy resolution (R) determined at 662 keV gamma excitation of scintillators optically coupled to photomultiplier tubes with bialkali photocathodes. The references in column 7 pertain to the data in columns 3 and 4. See also ref. [5].

crystal	N_{ph} 10^3 ph/MeV	$\overline{N_{ph}\bar{p}}$ phe/662 keV	R %	R_M %	R_s %	ref.
NaI(Tl^+)	38-43	6,230	6.5	3.1	5.7±0.2	[6]
CsI(Tl^+)	65	3,240	7.3	4.3	5.9±0.3	[7]
CsI(Na^+)	42	5,740	7.4	3.3	6.6±0.3	[8]
$CdWO_4$	≈28	2,380	6.8	5.2	4.4±0.4	[6]
$Bi_4Ge_3O_{12}$	9	960	9.3	8.1	4.2±0.6	[9]
BaF_2	11	1,590	7.7	6.2	4.6±0.5	[10]
$Gd_2SiO_5(Ce^{3+})$	8.5-10	1,250	7.8	7.3	2.7±1.0	[11, 12]
		1,480	7.8	6.6	4.2±0.5	[8]
$YAlO_3(Ce^{3+})$	14,3	1,900	7.2	5.7	4.4±0.5	[13]
$Lu_2SiO_5(Ce^{3+})$	23	3,360	7.9	4.4	6.6±0.4	[14]
$Lu_3Al_5O_{12}(Sc^{3+})$	23	2,320	6.5	5.1	4.0±0.4	[15, 16]
$K_2LaCl_5(Ce^{3+})$	28	3,900	5.1	3.9	3.3±0.4	[17]

N_{eh} is the number of electron-hole pairs present in the ionization track created by the absorbed γ-quantum, S is the transfer efficiency of e-h pair energy to the luminescence center, Q is the quantum yield of the luminescence center. E_{eh} is the average energy needed to create a thermalized e-h pair. It can be written as βE_g with β a constant and E_g the energy gap between the upper valence band and the conduction band of the inorganic scintillator crystal. For a review on the theories about the value for β and experimentally determined values, we refer to [18].

Eq.(4) expresses a light output which is proportional to the energy of the γ-quantum. That this is in general not the case is demonstrated in Figure 1 which shows response curves for NaI(Tl^+), $Lu_2SiO_5(Ce^{3+})$, and $K_2LaCl_5(Ce^{3+})$. The light output per unit energy (N_{ph}/E_γ) is plotted against E_γ. It is normalized to unity at E_γ = 662 keV. For NaI(Tl^+) one observes that as the gamma ray energy decreases from about 1 MeV to 60 keV, the (relative) light yield gradually increases by about 15 %. Then the yield drops by about 5% near 35 keV and below 30 keV the yield appears to increase again. It was suggested by Engelkemeir [1] that the change in yield near 35 keV is associated with the K-shell absorption edge at 33.2 keV of the iodine ions in the NaI host crystal. Also changes in the light yield near the L absorption edges of iodine (≈5 keV) were observed [19]. CsI(Tl^+) and CsI(Na^+) show proportionality curves quite similar to the one of NaI(Tl^+) [5]. $Bi_4Ge_3O_{12}$, $Gd_2SiO_5(Ce^{3+})$, and $CdWO_4$ show proportionality curves which resemble the one of $Lu_2SiO_5(Ce^{3+})$ [5]. From 1 MeV to 100 keV the response of LSO is quite constant, the response drops a few percent near the K-shell binding energy of Lu ions (63 keV), and a large drop in the response occurs at energies near the L-shell binding energy (≈10 eV), see Figure 1. $K_2LaCl_5(Ce^{3+})$, shows a constant response down to 10 keV. Similar curves have been observed for $YAlO_3(Ce^{3+})$ and $Lu_3Al_5O_{12}(Sc^{3+})$ and

more or less also for BaF_2 [5].

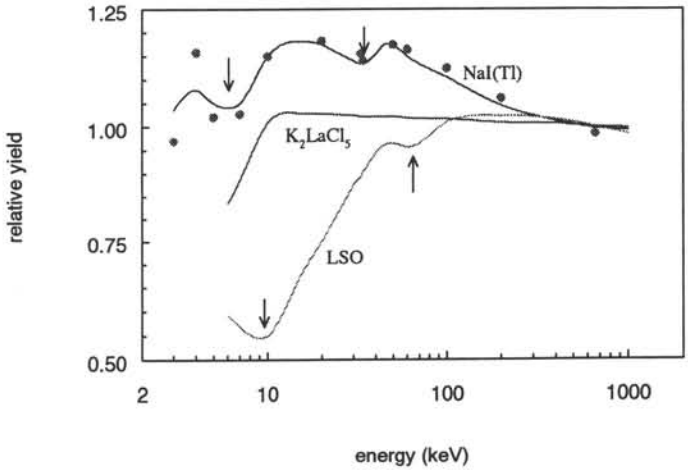

Figure 1: Response curves of NaI(Tl^+), $Lu_2SiO_5(Ce^{3+})$(LSO), and $K_2LaCl_5(Ce^{3+})$, normalized to unity at E_γ=662 keV. The experimental data points, not shown in the Figure, for NaI(Tl^+) can be found in [3]. For $K_2LaCl_5(Ce^{3+})$ and $Lu_2SiO_5(Ce^{3+})$ see [5]. The data points are results from Monte Carlo simulations of the scintillation process in NaI(Tl^+). The arrows show the position of K-shell and L-shell binding energies.

The changes in the light output of a scintillator when the γ energy crosses the binding energy of electrons in the K-shell or L-shell of the ions in the host material, were explained by Zerby, *et al.* [2]. It is related to the non-proportional response of the scintillator to fast electrons. A γ-quantum absorbed by the photoelectric interaction with an electron in a K-shell produces a fast photoelectron. The subsequent decay of the hole in the K-shell produces relatively low energy Auger electrons and X-ray fluorescence. The X-rays are again absorbed in the crystal, they also produce energetic electrons. As a result a collection of n fast electrons is created of energy $E(e_i)$ with e_i representing the i^{th} electron. The photon yield is then given by:

$$N_{ph} = \sum_{i=1}^{n} Y(E(e_i))E(e_i) \tag{5}$$

with Y(E) the response of the scintillator to energetic electrons of energy E. If the energy of the γ-quantum is just below the K-shell binding energy, a different collection of energetic electrons will be created resulting in a different photon yield.

Whether a γ-quantum is absorbed by the photoelectric effect either in the K-shell or the L-shell of an atom or by Compton scattering on loosely bound electrons is a statistical process. Also the creation of Auger electrons and X-ray fluorescence is a statistical process. Different γ-quanta of the same energy will, therefore, not produce the same collection of fast electrons. As a consequence N_{ph} fluctuates. The relation with R_{np} is given by:

$$R_{np} = 2.35\sqrt{v(N_{ph})} \tag{6}$$

with $v(N_{ph})$ the fractional variance in N_{ph}.

In order to understand the non-proportional response of scintillators to γ-quanta one should study the non-proportional response of scintillators to fast electrons. An elegant experimental technique to measure response curves to fast electrons was recently proposed by Valentine and Rooney [20]. Using a Compton spectrometer configuration and a collimated γ-ray beam incident on a scintillator, the energy deposited in a Compton scattering event can be calculated. The light output of the scintillator can then be studied over a wide range of electron energies.

Stopping power equations of fast electrons in matter show that the energy loss $\frac{dE}{dx}$ of electrons increases with decreasing electron energy. As was already proposed by Murray, *et al.* [21], it is likely that non-proportional response of the scintillator to fast electrons is related to the electron-hole pair density in the ionization track.

Assuming that the electron-hole pair density ρ, defined as the number of e-h pairs per nm ionization track length, is proportional to the energy loss of the ionizing fast electron, i.e.

$$\rho = \frac{1}{\beta E_g} \frac{dE}{dx} \tag{7}$$

one can generalize Eq.(4) to

$$N_{ph} = \int_{track} \rho(x) S(\rho) Q(\rho) dx \tag{8}$$

where x represents some length coordinate which runs over all the tracks caused by the collection of fast electrons created in the scintillation event. The dependence of S and Q on ρ is in this model responsible for non-proportional response.

SIMULATION OF THE SCINTILLATION PROCESS IN NaI(Tl)

Figure 2 shows results from a simulation study on the creation of ionization tracks by γ-quanta in NaI(Tl). E_g of NaI is 5.9 eV and for β a value of 2.5 was assumed. Further details on the simulation method can be found elsewhere [22]. The spectra of Figure 2 contain 230 channels spaced equally on a logarithmic scale. The contents of a channel represents the number of electron-hole pairs n_{eh} created per MeV absorbed γ-quanta energy which are created in sections of the tracks with an electron-hole pair density between ρ and $\rho + \Delta\rho$, where $\Delta\rho$ represents the width of the channel. The integrated contents of all channels equals $6.78 \cdot 10^4$ e-h pairs. The electron-hole pair density spectra show that as the γ-quantum energy increases, an increasing part of the ionization track contains a low e-h pair density. Relatively low energy Auger electrons and δ-electrons created by a primary energetic electron are responsible for the apparent maximum near densities of 1.0 e-h pairs/nm.

In order to calculate the response curve of NaI(Tl) to γ-quanta from electron-hole pair density spectra, knowledge of the product $S(\rho)Q(\rho)$ is necessary which is closely related to the scintillation mechanism. Over the years, considerable effort has been put in the elucidation of the scintillation mechanism of NaI(Tl^+), see for example [23]. Several mechanisms are active: i) electrons and holes recombine to form a Self-Trapped-Exciton (STE)-like state which is quenched at room temperature, ii) electrons and holes recombine at a Tl^+ center yielding luminescence, and iii) an electron is trapped at a Tl^+ forming Tl^0 and a hole is trapped to form a Tl^{2+}. Tl^0 is not stable at room temperature; its

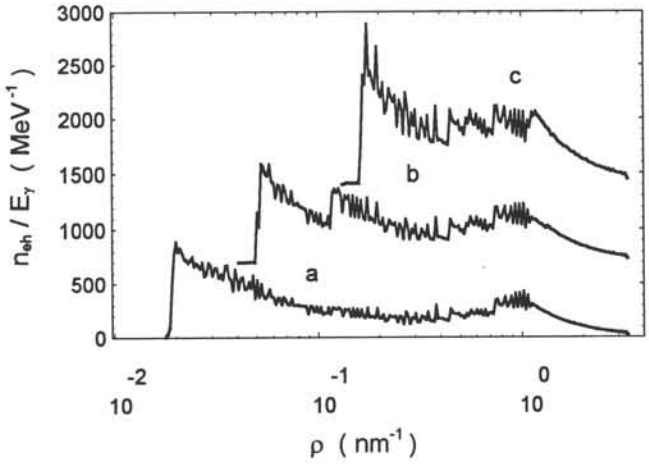

Figure 2: Average electron-hole pair density spectra of ionization tracks produced by total absorption of a) 662 keV, b) 100 keV, and c) 20 keV γ-quanta in an infinitely large NaI(Tl) scintillator. For illustration purposes, spectra b) and c) are offset by 700 and 1400 MeV^{-1}, respectively. The spectra are averaged over 500 γ-quanta interactions.

lifetime is about 0.35 μs. After de-trapping of the electron it can recombine with Tl^{2+}, thus contributing to the scintillation pulse; it can also be re-trapped in a Tl^{+} ion.

With the phenomenologically chosen SQ-curve of Figure 3 and the simulated electron-hole pair density spectra, the light output of NaI(Tl^{+}) was calculated for values of E_γ between 2 and 662 keV, see Figure 1. A reasonable agreement with the experimental data can be observed.

Above a critical e-h pair density (ρ_q) of about 0.68 e-h pairs/nm, SQ is proportional to ρ^{-1}. This is the region of prompt quenching, where via mechanism i) e-h pairs are lost in the scintillation process. Michaelian and Menchaca-Rocha [24] studied the ion-induced scintillation response of NaI(Tl). The response as a function of ion velocity and the type of ion was explained by introducing a critical energy deposition density. For energy densities larger than 0.23 J/g, corresponding with 1 e-h pair/2750 nm^3, e-h pairs were assumed to be lost before exciting Tl^{+} centers. The results of our simulations on the γ-induced scintillation response are consistent with those of the ion-induced responses if one assumes that electrons and holes are thermalized within a radius of 24 nm around the ionization track produced by the γ-quanta.

Below the critical density SQ is proportional to $\rho^{0.2}$. The reason for the increase of SQ with increasing e-h pair density is unclear. One may speculate that with increasing density, the Tl^{2+} concentration created via mechanism iii) also increases. Trapping of electrons originating from Tl^{0} by Tl^{2+} yielding luminescence instead of retrapping in Tl^{+} or being lost due to quenching centers then becomes more probable.

To study the effects of non-proportional response on the energy resolution, i.e. the values for R_{np}, electron-hole pair density spectra of totally absorbed 662 keV γ-quanta were determined. For each γ-quantum the photon yield N_{ph} was calculated and the results are shown in the spectrum of Figure 4. The events yielding a pulse height of 386 are caused by those γ-quanta which were absorbed by the photoelectric effect in the

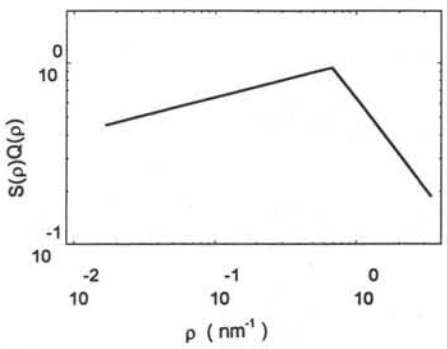

Figure 3: Luminescence efficiency SQ as a function of e-h pair density ρ employed for calculation of non-proportional response and R_{np} of NaI(Tl$^+$).

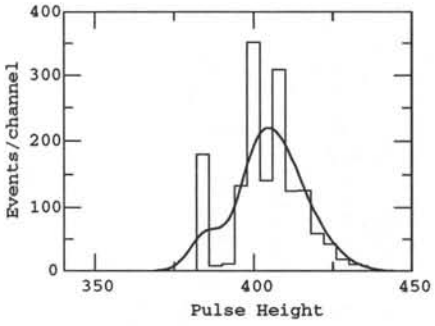

Figure 4: Simulated pulse height spectrum of 1500 totally absorbed 662 keV γ-quanta in NaI(Tl$^+$). The smooth continuous curve shows the pulse height spectrum after folding in 3.1% photomultiplier resolution.

K-shell of the iodine ions. The other events are due to γ-quanta absorbed by means of multiple Compton scattering processes. One observes that the pulse height distribution is certainly not a Gaussian distribution, consequently the definition of R_{np} in Eq.(6) and Eq.(2) will only hold approximately. The convolution of the simulated pulse height spectrum with a Gaussian shape pulse with a FWHM of 3.1% is also shown in Figure 4. The 3.1% corresponds with the photomultiplier resolution R_M, see Table 1. The resulting total absorption peak shows a width (FWHM) of 5.6% and a shoulder on the low energy side of the peak. In conclusion, the simulation shows that the maximal obtainable energy resolution for the detection of 662 keV γ-quanta with a (infinitely) large NaI(Tl) crystal and a PMT with a bialkali photocathode amounts to 5.6%. 3.1% contribution stems from R_M and R_{np} is roughly 4.7%.

Simulation studies on other scintillators than NaI(Tl$^+$) have not been performed yet. It is already clear though, that by assuming a constant value for SQ below the critical density and by choosing other values for ρ_q, non-proportionality curves resembling those of $Lu_2SiO_5(Ce^{3+})$ and $K_2LaCl_5(Ce^{3+})$ are obtained.

Summarizing, i) absolute light yield, ii) non-proportional response to γ-quanta, iii) non-proportional response to fast electrons, and iv) the obtainable energy resolution are all related to one and the same SQ-curve. The SQ-curve, i.e. the luminescence efficiency as a function of electron-hole pair density, is determined by the scintillation mechanism.

References

[1] D. Engelkemeir, The Rev. of Scientific Instr. 27(8) (1956) p.589.

[2] C.D. Zerby, A. Meyer, R.B. Murray, Nucl. Instr. and Meth. 12 (1961) p.115.

[3] D.W. Aitken, B.L. Beron, G. Yenicay, H.R. Zulliger, IEEE Trans. on Nucl. Sci. 14(1) (1967) p.468.

[4] J.B. Birks, "The Theory and Practice of Scintillation Counting", (Pergamon Press 1967).

[5] P. Dorenbos. J.T.M. de Haas, C.W.E. van Eijk, expected to appear in IEEE Trans. on Nucl. Sci. 42(16) Part II (1995).

[6] D.R. Kinloch, W. Novak, P. Raby, I. Toepke, IEEE Trans on Nuclear Science 41(4) (1994) p.752.

[7] P. Schotanus, R. Kamermans, P. Dorenbos, IEEE Trans. on Nucl. Sci. 37(2) (1990) p.177.

[8] E. Sakai, IEEE Trans. on Nucl. Sci. 34(1) (1987) p.418.

[9] K. Okajima. K. Takami, K. Ueda, F. Kawaguchi, Rev. Sci. Instr. 53(8) (1982) p.1285.

[10] Y.C. Zhu, J.G. Li, Y.Y. Shao, H.S. Sun, B.Z. Dong, G.P. Zhou, Zp. Zheng, F.Z. Cui, C.J. Yu, Nucl. Instr. and Meth. A244 (1986) p.577.

[11] C.L. Melcher, J.S. Schweitzer, T. Utsa, S. Akiyama, IEEE Trans. on Nucl. Sci. 37(2) (1990) p.161.

[12] C.L. Melcher, J.S. Schweitzer, R.A. Manente, C.A. Peterson, IEEE Trans. on Nucl. Sci. 38(2) (1991) p.506.

[13] J.A. Kierstead, S.P. Stoll, C.L. Woody, Mat. Res. Soc. Symp. Proc. Vol. 348 (1994) p.469.

[14] C.L. Melcher, private communications, Sept. 1994.

[15] N.N. Ryskin, P. Dorenbos, C.W.E. van Eijk, S. Kh. Batygov, J. Phys.: Condens. Matter 6 (1994) 10423.

[16] N.N. Ryskin, P. Dorenbos, C.W.E. van Eijk, Stratech report TUD-SCIR-94-03, Delft University of Technology (1994).

[17] J.C. van't Spijker, P. Dorenbos, J.T.M. de Haas, C.W.E. van Eijk, H.U. Güdel, K. Krämer, presented at the LUMDETR'94 symposium, September 25-29, 1994, Tallinn, Estonia. To be published in a special issue of Radiation Measurements (1995).

[18] P.A. Rodnyi, P. Dorenbos, C.W.E. van Eijk, Phys. Stat. Sol. (b) 187 (1995) p.15.

[19] K. Brunner, W. Hink, Nucl. Instr. and Meth. 82 (1970) p.269.

[20] J.D. Valentine, B.D. Rooney, Nucl. Instr. and Meth. A353 (1994) p.37.

[21] R.B. Murray, A. Meyer, Phys. Rev. 122 (1961) p.815.

[22] M. Marsman, P. Dorenbos, C.W.E. van Eijk, presented at the SCINT'95 conference, to be found in these proceedings.

[23] H.B. Dietrich, A.E. Purdy, R.B. Murray, R.T. Williams, Phys. Rev. B. 8(12) (1973) p.5894.

[24] K. Michaelian, A. Menchaca-Rocha, Phys. Rev. B 49(22) (1994) p.15550.

A THEORETICAL APPROACH TO THE NON-PROPORTIONAL GAMMA ENERGY RESPONSE OF SCINTILLATORS

M. Marsman, P. Dorenbos, C.W.E. van Eijk
Delft University of Technology, Faculty of Applied Physics, c/o IRI, Mekelweg 15, 2629 JB Delft, The Netherlands.

ABSTRACT The response of a scintillator as a function of absorbed γ energy is calculated by Monte Carlo simulation of the scintillation process. The response is given in terms of the e-h pair density distribution in the ionization track.

INTRODUCTION

The scintillation process can be divided in four steps: i) absorption of the γ quantum resulting in the creation of energetic electrons, ii) energy loss of the energetic electrons to the atomic electrons of the scintillator resulting in ionization tracks, iii) energy transport from the ionization track to luminescence centers through charge migration processes and iv) radiative decay in the luminescence center.

It was realized by Zerby *et al.* [1], that the non-proportional response of scintillators to γ energy results from a non-proportional response to energetic electrons. According to Murray *et al.* [2], the latter is likely to be related to the e-h pair densities in the ionization tracks. The relationship between e-h pair density and luminescent e-h recombination at luminescence centers, is closely related to the scintillation mechanism.

The calculation of the e-h pair density in the ionization tracks by Monte Carlo simulation of the first two steps in the scintillation process is the subject of this work. The calculation of the scintillation response from these e-h pair densities -the last two steps in the scintillation process- is discussed in reference [3].

THE PRIMARY ELECTRON SPECTRUM

We will consider the interaction of a γ quantum with the scintillator resulting in the creation of energetic electrons in the crystal, through: i) photoelectric absorption and ii) Compton scattering. Further energetic electrons are created through: iii) Auger electron emission, iv) the reabsorption of characteristic X-rays -both by-products of photoelectric absorption- and v) absorption of Compton scattered photons. Their number and individual energies depend strongly on E_γ, the energy of the γ quantum. The energetic electrons, created through i), ii), iii), iv) and v) by a single γ quantum, will be called the primary electrons of this quantum.

The average distribution of the energy of a γ quantum amongst its primary electrons, the so-called *primary electron spectrum*, can be calculated by Monte Carlo simulation of the above mentioned interactions. The necessary interaction cross sections for the simulation of i), ii), iv) and v) tabulated for all elements over a wide range of E_γ, were taken from Plechaty *et al.* [4]. Probabilistic determination of the distribution of γ energy amongst primary electron and scattered photon in case of Compton scattering was based on the differential Klein-Nishina cross section. Figure 1 shows the calculated primary electron spectrum corresponding to events of total absorption of a 100 keV γ quantum, in NaI(Tl^+). The intense lines at 67 keV, 23 keV and the two lines below 5 keV are the products of respectively photoelectric

Proc. Int. Conf. on Inorganic Scintillators and Their Applications, SCINT95,
1996, Delft University Press, The Netherlands

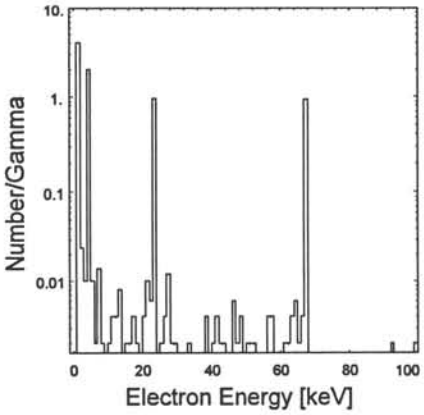

Figure 1: The average primary electron spectrum produced by total absorption of a 100 keV γ quantum in a NaI(Tl$^+$) scintillator.

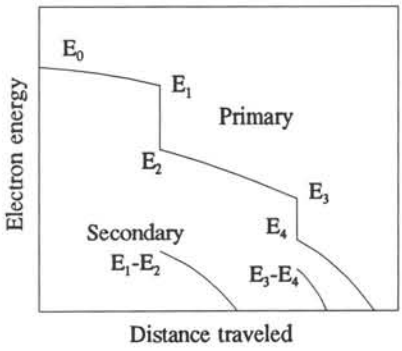

Figure 2: Schematic illustration of the electron energy vs. path length in the hybrid model [5].

absorption in the iodine K-shell, reabsorption of the iodine K_α X-ray in the iodine L-shell and Auger decay of iodine L- and M-shell holes.

THE e-h PAIR DENSITY DISTRIBUTION

The creation of ionization tracks in scintillators, by (primary) energetic electrons, can be studied by Monte Carlo simulation of e-e interactions, using the 'hybrid' model of Murata *et al.* [5], which incorporates the generation of secondary energetic electrons.

The relationship between the energy of an energetic electron and its distance traveled, shown in Figure 2, illustrates some of the properties of this model. The electron energy decreases continuously, at the rate dE/dx, predicted by a stopping power equation, unless a knock-on collision occurs. This stopping power equation takes into account only the energy loss of the energetic electron due to e-e interactions involving an energy transfer below a certain cut-off value, ε_c. Inelastic e-e scattering events which involve an energy transfer exceeding ε_c, so-called knock-on collisions, are treated separately. These knock-on collisions correspond to the creation of fast secondary electrons, also known as δ-rays, and show as discrete drops in the electron energy in Figure 2. The probability of the occurrence of knock-on collisions and the energy distribution of the resulting secondary energetic electrons are determined by the differential inelastic e-e scattering cross section given by the Møller theory [5]. The local e-h pair density ρ in the ionization track, defined as the number of e-h pairs per nm ionization track length, is assumed to be proportional to the specific energy loss given by the stopping power equation.

The ionization track of an energetic electron is constructed segment by segment by repeating the following procedure. i) Starting with the electron energy, the program calculates the probabilities of occurrence, in this segment, of a knock-on collision and of the continuous slowing down process. ii) Probabilistic determination is made of whether or not a knock-on collision occurs. iii) If no knock-on collision occurs then the specific energy loss, dE/dx, is calculated using the stopping power equation and a probabilistic determination is made of the segment length, Δl, based on the mean free path of the energetic electron, calculated from the Rutherford cross section for elastic scattering and the Møller cross section for inelastic

scattering. The amount of energy the energetic electron loses in this segment and consequently the number of e-h pairs created, is given by the product of Δl and dE/dx. iv) If a knock-on collision does occur then a probabilistic determination of the amount of energy lost by the energetic electron -equal to the amount of energy with which the secondary electron emerges- is made, based on the Møller cross section. The secondary electrons resulting from knock-on collisions are treated the same way as the energetic electrons that created them and may undergo knock-on collisions themselves and will form ionization tracks.

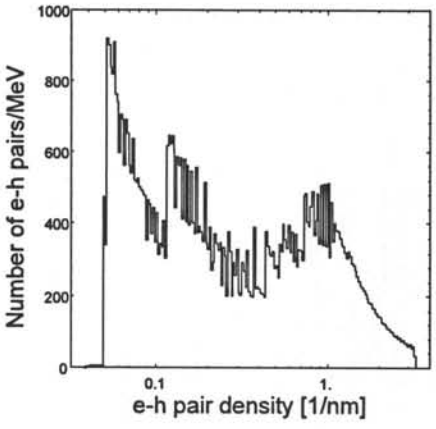

Figure 3: The e-h pair density distribution calculated from the primary electron spectrum of a 100 keV γ quantum, absorbed in a NaI(Tl$^+$) scintillator.

Instead of reconstructing the true spatial form of the trajectories of an energetic electron, and its secondaries, which would involve storing the segment lengths, the angles between successive segments and the amount of energy lost in each segment, it was chosen to describe the ionization track in terms of its *e-h pair density distribution spectrum*. One channel in this spectrum contains the number of e-h pairs n_{eh} in the track which are created in segments of the track with an e-h pair density between ρ and $\rho+\Delta\rho$. The width of the channel, $\Delta\rho$, varies such that the spectrum consist of 230 channels equally spaced on a logarithmic scale. Figure 3 shows the e-h pair density distribution calculated from the primary electron spectrum of a 100 keV γ quantum, absorbed in NaI(Tl$^+$). The maxima in Figure 3 in the regions $0.05<\rho<0.1$, $0.1<\rho<0.2$ and $0.5<\rho<2$ tie in with respectively the lines at 67 keV, 23 keV and the two lines below 5 keV in the primary electron spectrum of Figure 1.

THE SCINTILLATION RESPONSE

The scintillation response was calculated from the e-h pair density distribution by choosing an approximated luminescence efficiency curve, $S(\rho)Q(\rho)$, which relates the fraction of electrons and holes that move away from the ionization track and recombine radiatively at luminescence centers to the e-h pair densities in the track. Further details on these calculations and the results for the case of a NaI(Tl$^+$) scintillator can be found in reference [3].

REFERENCES

[1] C.D.Zerby, A.Meyer, R.B.Murray, Nucl. Instr. and Meth. 12 (1961) p.115.

[2] R.B.Murray, A.Meyer, Phys. Rev. 122 (1961) p.815.

[3] P.Dorenbos, M.Marsman, C.W.E.van Eijk, "Energy resolution, non-proportionality and absolute light yield of scintillation crystals", to be found in these proceedings.

[4] E.F.Plechaty, *et al.*, "An integrated system for production of neutronics and photonics calculational constants - volume VI : Photon Cross Sections 1 keV to 100 MeV", California University, Livermore California, Oct 1968

[5] K.Murata, D.F.Kyser, C.H.Ting, J. Appl. Phys. 52(7) (1981) p.4396.

ON THE RELATION BETWEEN PROMPT LUMINESCENCE AND THERMO-LUMINESCENCE (TL) PROPERTIES OF SOME MATERIALS.

K. Meijvogel[1)], A.J.J. Bos[1)], P. Dorenbos[2)] and C.W.E. van Eijk[2)]
[1)] Interfaculty Reactor Institute, Delft University of Technology
[2)] Radiation Technology Group, Delft University of Technology
Mekelweg 15, 2629 JB Delft, The Netherlands

ABSTRACT

Measured prompt and TL light yields of several scintillators and TL materials are presented. The results show a very low TL light yield for scintillators. TL materials have comparable prompt and TL light yields. A simple model is given which describes the process from the absorption of ionising radiation to the emission of a photon.

INTRODUCTION

Scintillators and TL materials convert energy, absorbed during interaction of ionizing radiation with matter into visible light. The difference between the two types of materials is the time scale of light output. A scintillator immediately emits the photons during irradiation, whereas a TL material stores the energy, which can be released in the form of visible light, when the material is thermally stimulated. In addition the prompt luminescence in scintillators decays relatively fast, whereas the prompt luminescence of TL materials decays relatively slow[1]. In gaining a theoretical understanding of the processes involved in thermoluminescence the measurement of intrinsic properties can be helpful. In addition comparative measurements are also valuable in the search to new and better TL materials. In this paper experimental results are presented of the absolute prompt and TL light yield and emission spectra of some well known scintillators and TL materials. The numbers give some insight in the processes involved in the light production.
The prompt light yield Y_{pr} is defined as the number of photons emitted immediately after irradiation ($\tau <$ 1s) per unit absorbed energy:

$$Y_{pr} = \frac{N_{ph,pr}}{E_{absorbed}} \tag{1}$$

where $E_{absorbed}$ is the energy absorbed during interaction and $N_{ph,pr}$ is the number of prompt photons.
The TL light yield Y_{TL} is defined as the number of TL photons per unit energy absorbed emitted during heating:

$$Y_{TL} = \frac{N_{ph,TL}}{mD} \tag{2}$$

with $N_{ph,TL}$ the number of TL photons emitted during heating of a given sample, m the irradiated mass of the sample and D the average absorbed dose.
After the absorption of ionizing radiation different processes can be distinguished.Interaction of ionizing radiation with matter creates a number of electron-hole pairs in the material. With n_{eh} we denote the number of e-h pairs per unit absorbed energy. When an electron-hole pair is thermalized, the three following processes can take place: trapping in trapping centres with an efficiency η_{tr}, radiative recombine (scintillation) with an efficiency η_{lum} and radiationless recombination with an efficiency η_{loss}. This leads to the following equation:

$$\eta_{tr} + \eta_{lum} + \eta_{loss} = 1 \tag{3}$$

When thermally stimulated, a fraction η_{TL} of the trapped charge carriers recombine under emission of a TL photon after transportation to a luminescence centre. Due to selfabsorption TL photons escape from the TL material with an efficiency η_{esc}. The prompt and TL light output can be now written with the following

Proc. Int. Conf. on Inorganic Scintillators and Their Applications, SCINT95,
1996, Delft University Press, The Netherlands

TL material with an efficiency η_{esc}. The prompt and TL light output can then be written as:

$$Y_{pr} = n_{eh}\eta_{lum}\eta_{esc} \quad , \quad Y_{TL} = n_{eh}\eta_{tr}\eta_{TL}\eta_{esc} \tag{4}$$

EXPERIMENTAL DETAILS

TL light output is measured with a calibrated Harshaw 2000 reader. The calibration procedure is described by Meijvogel *et al.*[2] TL emission spectra were recorded with a home built facility [3]in the 200-750 nm wavelength range with a resolution of 19 nm, whereas prompt spectra were measured with an X-ray excitation setup[4] and compared with a BaF_2 crystal to determine the prompt light output in the 100-540 nm wavelength range. TL readouts were performed using a linear heating profile up to 673 K. Dimensions of the samples, heating rate and the temperature range in which the TL response is integrated are given in Table 1.

RESULTS AND DISCUSSION

Table 1. Prompt and TL light yields for several scintillators and TL materials. The light yields are 'as measured' i.e. not corrected for thermal quenching in the luminescence centres. The temperature range is given, in which the TL emission is integrated. The TL emission wavelengths are those at the top of the most important TL emission bands. The prompt light yield is the yield in the 100-540 nm range.

Material	Physical size	Annealing procedure	Dose [mGy]	Temperature range [K]	Heating rate [K s^{-1}]	TL emission wavelength [nm]	Prompt Light Yield [ph MeV^{-1}]	TL Light yield [ph MeV^{-1}]
LiF:Mg,Ti (Harshaw)	variable, single crystals	1h 673 K	19	460-550	6.0	410	180±20	70±23
LiF:Mg,Ti (TLD100)	3.2x3.2x0.9mm samples	1h 673 K	19	460-540	6.0	410	460±30	106±20
LiF:Mg,Cu, P (GR200)	ø4.5x0.9mm samples	10 min 513 K	6.4	428-513[1]	3.0	370	330±40	2700±530
CaF_2:Dy (TLD200)	3.2x3.2x0.9mm samples	1h 673 K	8.1	390-543	6.0	475,575	7200±300 (STE 5500)	17000±350 0
CaF_2:Tm (TLD300)	3.2x3.2x0.9mm samples	1h 673 K	8.1	410-610	6.0	370,475	8400±500 (STE 5600)	1000±200
Al_2O_3:C (Russia)	ø5.0x1.0 mm single crystals	1h 673 K	7.0	410-543	6.0	410	15300±600	2800±230
CaF_2:Eu	single crystal	-	1040	330-470	1.0	435	22000	5
BaF_2(pure)	single crystal	-	6760	350-610	1.0	310,370,480	11000(STE)	6
BaF_2:Ce	single crystal	-	6760	350-650	1.0	315,400	13000	12
LSO:Ce	single crystal	-	5.8	330-450	6.0	415	24000	2500

[1] At the end of the heating plateau

All results are summarized in Table 1.The highest TL light yield is found for CaF_2:Dy. Its value is only a factor 2.6 less that the theoretical upper limit [1]. This indicates that all processes (trapping, transfer, luminescence) run down very efficiently. The large error in this value is caused by the relatively large error on the quantum efficiency of the PMT at the 570 nm line of the Dy emission. In this material the prompt light yield is also high, although the prompt emission shows not only characteristic Dy lines, but also self trapped exciton (STE) luminescence at 300 nm (Figure 1). Like CaF_2:Dy, CaF_2:Tm shows an equally strong STE luminescence, together with the characteristic Tm lines.

The highest prompt luminescence of a TL material is found for Al_2O_3:C. The prompt luminescence spectrum is the same as the TL emission spectrum (Figure 2, main peak at 410 nm) what means that the luminescence centre during irradiation (scintillation) is the same as during heating (TL). This suggests that the high light yield (prompt and TL) of this material is caused by a efficient transfer to the luminescent centre.

The measured prompt and TL light output of LiF:Mg,Ti (TLD-100) are of the same order of magnitude. The emission of TL photons from pressed and sintered samples as is the case with TLD-100 is not isotropic.

With the given size of the sample and the TL-reader set-up this results in a much better light collection (factor 1.8) than in case of single crystals. The emission spectra do not differ (single emission band at 410 nm).

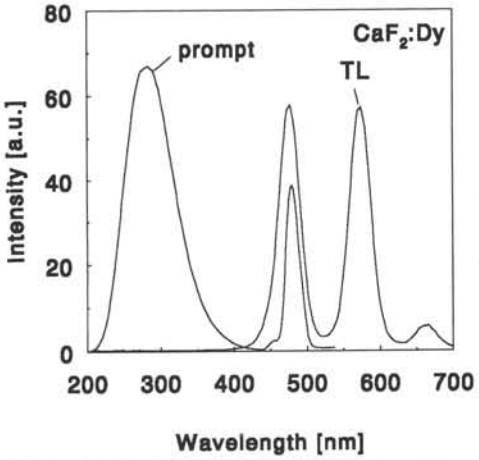

Figure 1. Prompt and TL emission spectrum of CaF_2:Dy.

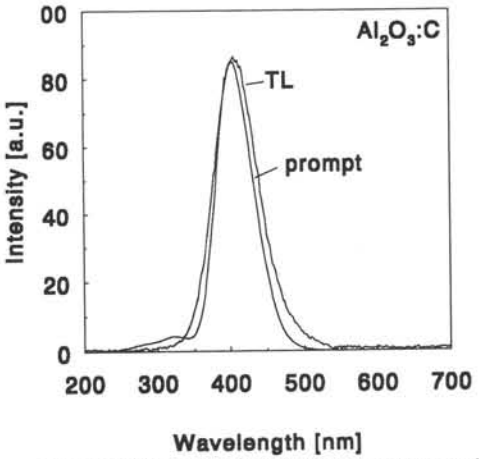

Figure 2. Prompt and TL emission spectrum of Al_2O_3:C

The TL light output for GR-200 is a factor 27 higher than for TLD-100. This factor agrees with values reported from measurements of relative efficiencies. GR-200 is less transparent to its own photons than TLD-100 which means that η_{esc} is smaller. The TL light output is an order of magnitude larger. This means that for GR-200 the product of η_{tr} and η_{TL} must be much higher than for TLD-100. The relatively low prompt luminescence indicates a high trapping efficiency η_{tr}.
As expected the scintillators show a very low TL light yield. For three materials used in this investigation the TL light yield is lower than 20 photon per MeV absorbed dose. Obviously η_{tr} is low and almost all created e-h pairs recombine directly after irradiation. The TL emission of CaF_2:Eu peaks at 435 nm and that of BaF_2:Ce at 315 and 410 nm. The TL emission spectrum of 'pure' BaF_2 shows several lines of different impurities (at ppm level) in the material. On the other hand, the TL light output of LSO:Ce is considerable and can be related to the afterglow of the material [5]. The value in table 1 was taken from a readout recorded 5 minutes after irradiation. Enlarging the time resulted in less TL light output

SUMMARY

The absolute TL light yield of several well known TL materials ranges from 100 to 17000 photons per MeV absorbed energy, whereas for scintillators it is less than 20 photons MeV^{-1}. A simple theoretical model can describe the process from absorption of energy from ionising radiation to the emission of photons. TL materials show prompt luminescence which is roughly of the same order of magnitude as the thermoluminescence, indicating that an efficient TL material also has to scintillate reasonably well.

REFERENCES

1. Pető, Á. and Kelemen, A., Radiat. Prot. Dosim. (submitted)
2. Meijvogel, K., van der Burg B., and Bos, A.J.J,. Radiat. Prot. Dosim. (submitted)
3. Piters, T.M., Meulemans, W.H. and Bos, A.J.J., Rev. Sci. Instrum, 64, 109-117, 1993
4. Dorenbos, P., de Haas, J.T.M., Visser, R., van Eijk, C.W.E. and Hollander, R.W., IEEE Trans. Nucl. Sci.. 40(4), 424-430, 1993.
5. Dorenbos, P., van Eijk, C.W.E., Bos, A.J.J. and Melcher, C.L., J. Phys.: Condens. Matter 6, 4167-4180, 1994

PART III

Intrinsically Pure Scintillators and Phosphors

ORIGIN OF THE 4.1-eV LUMINESCENCE IN PURE CsI SCINTILLATOR

H. Nishimura, M. Sakata, T. Tsujimoto and M. Nakayama
Department of Applied Physics, Faculty of Engineering, Osaka City University
Sugimoto, Sumiyoshi-ku, Osaka 558, Japan

The spectra and decay times of the 4.1-eV luminescence in a pure CsI scintillator, which were measured in a wide temperature range (4.5-300 K) by using two-photon spectroscopy, are discussed in comparison with the results of the well-known 4.3- and 3.7-eV luminescence associated with the self-trapped excitons (STE's). We conclude that the 4.1-eV luminescence is intrinsic: The origin is the on-center STE responsible for the 4.3-eV luminescence (not the off-center STE responsible for the 3.7-eV luminescence).

1. INTRODUCTION

Of all available scintillators, CsI is one of the most extensively used materials: CsI:Tl and CsI:Na have high luminescence efficiencies (45 and 85 %), but the decay times are long (1 and 0.6 μs) because of the triplet transitions, and pure CsI (4.1-eV band) has a short decay time (15 ns), but the efficiency is small (5 %). From the viewpoint of applications, pure CsI with fast timing characteristics has widely been investigated [1-8]. However, the origin of the 4.1-eV band, even for the question of whether it is intrinsic or extrinsic, has long been uncleared.

There are several interpretations proposed for its origin: (1) Inter-atomic transition between the $I^-(5p)$ valence band and the $Cs^+(5p)$ core band (cross luminescence) is proposed by Kubota *et al.* [4], (2) radiative decay of free excitons bound to a defect is proposed by Abdrakhmanov *et al.* [7], and (3) radiative decay of the STE's responsible for the 3.7-eV luminescence is proposed by Gwin and Murray [1] and by Chen *et al.* [3].

Pure CsI is well-known to have two luminescence bands (4.3- and 3.7-eV bands) ascribed to the STE [9-14]. For the STE, a cluster composed of two nearest neighbor I^- ions and 12 neighboring Cs^+ ions with D_{4h} point symmetry (upper left in Fig. 1) has been considered [10, 11]: A free hole formed optically is trapped by the two I^- ions to form V_k center to which a conduction electron is bound to form a STE. Since the $Cs^+(6s)$ and $Cs^+(5d)$ conduction bands are very close in energy to each other [15,16], the STE states composed of the $6s$ and $5d$ electrons, which are represented by $^{1,3}\Gamma_2^-$ and $^{1,3}\Gamma_4^-$ (Fig.1), can be assumed to be both stable.

Based on the assumption, Iida *et al.* [11-13] have ascribed the 4.3-eV band to the $^3\Gamma_4^-$ state, and the 3.7-eV band to the $^3\Gamma_2^-$ state: These spin-triplet states are mixed with the allowed $^1\Gamma_5^-$ state with π polarization (perpendicular to the V_k axis) by spin-orbit interaction. Tsujimoto *et al.* [17] have studied the effect of hydrostatic pressure on the 4.3- and 3.7-eV bands, and concluded that the 4.3-eV band does not arise from the $^3\Gamma_4^-$ state, but arises from the $^{1,3}\Gamma_2^-$ states in the on-center STE with D_{4h} symmetry, and the 3.7-eV band arises from the $^{1,3}\Gamma_1$ states in the off-center STE with C_{4v} symmetry. In the present paper, we conclude that the 4.1-eV band arises from the same state ($^{1,3}\Gamma_2^-$) as the 4.3-eV band.

Proc. Int. Conf. on Inorganic Scintillators and Their Applications, SCINT95,
1996, Delft University Press, The Netherlands

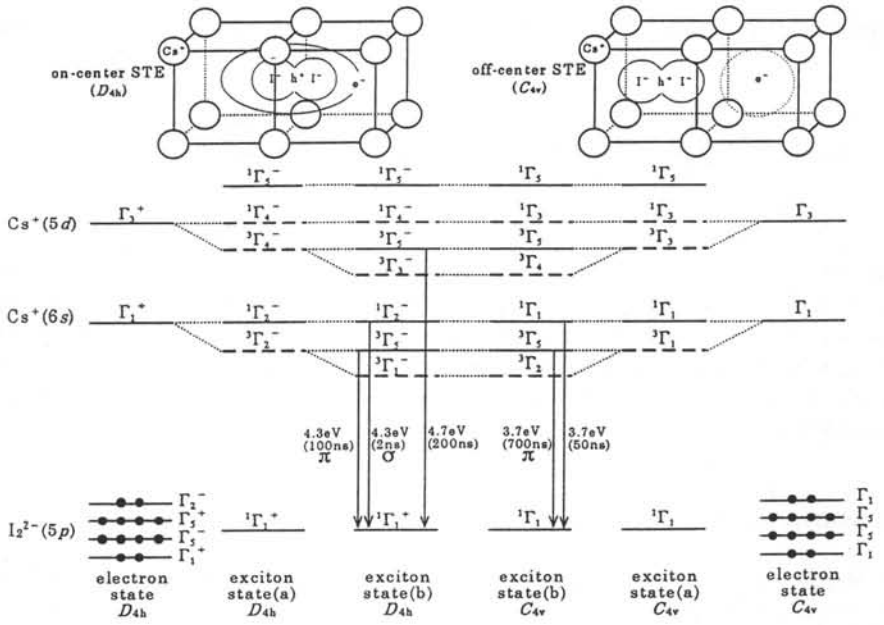

Fig.1. Energy states of electrons and excitons in D_{4h} and C_{4v} point symmetries; (a) without spin-orbit interaction, (b) with spin-orbit interaction. Broken lines indicate forbidden states.

2. EXPERIMENTAL PROCEDURES

We used a conventional method of two-photon spectroscopy: A tunable dye laser (PRA LN-102) pumped by a pulsed nitrogen-gas laser (PRA LN-100) with a peak power of 250 kW was used as the light source. The time duration of the dye laser pulse (we used BBQ as the dyestuff) was nominally 0.2 ns. We used a quartz-prism monochromator (Carl Zeiss M4QIII) and a photomultiplier tube (Hamamatsu R-955) for measuring the luminescence spectra, and a box-car integrator (Stanford SR-250) for the time-resolved spectra. These spectra were corrected for the sensitivity of the detecting system. Luminescence decay times were measured by using a 500MHz digitizing oscilloscope (Tektronix TDS-520) and a photomultiplier tube (Hamamatsu R-1546). The time resolution of the detecting system was 1 ns.

The pure CsI crystal used in the present study was obtained from Harshaw Chemical Co. Samples with a typical dimension of $5\times5\times2$ mm^3 were cooled by heat conduction, and the temperatures were measured by an Au(Fe)-Cu thermocouple attached to the sample holder.

3. RESULTS AND DISCUSSION

Figure 2 shows the luminescence spectra of a pure CsI crystal observed at various temperatures under the two-photon absorption of 3.18-eV light. The arrows indicate the peak positions of the 4.3- and 3.7-eV bands. The 4.1-eV band appears strongly at 290 K. As temperature falls, the band shifts to higher energy and the intensity decreases, but below 8 K the band appears strongly again at 4.3 eV, which suggests that the 4.1- and 4.3-eV bands have the same origin. On the other hand, the intensity of the 3.7-eV band increases with decreasing temperature, but is weak again at 4.5 K, and the peak energy shifts to lower. We note that the 4.1-eV band appears under two-photon absorption of 3.18-eV light. Similar result has already

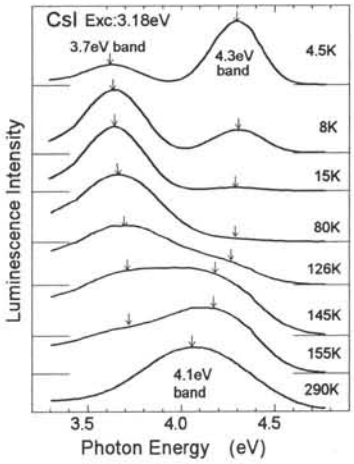

Fig.2. Luminescence spectra measured under two-photon absorption of 3.18eV light.

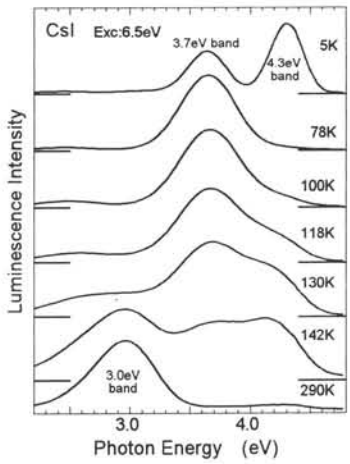

Fig.3. Luminescence spectra measured under one-photon absorption of 6.5eV light.

been reported by Chen *et al.* [3]: They found that the excitation-threshold energy for the 4.1-eV band was 5.49 eV, corresponding to the 2p-exciton energy. These results are not favorable to the interpretation (cross luminescence) proposed by Kubota *et al.* [4] for its origin.

Several authors have reported that the 4.1-eV band is not excited by the low energy photons (<10 eV) [4,8]. We have not observed the band either under one-photon absorption of 6.5 eV light (Fig. 3). Although the spectra measured by one-photon and two-photon excitations are similar to each other at low temperature, they are very different at high temperature: The 4.1-eV band is replaced by the 3.0-eV band.

We first assume that STE's are mobile by hopping motion at high temperatures, and lots of STE's are captured by defects to emit the luminescence associated with the defects. In the two-photon excitation, STE's are formed inside the crystal where defects are rather a few, so that lots of STE's decay radiatively to emit the 4.1-eV band, while in the one-photon excitation, STE's are formed near the crystal surface where lots of defects are populated, so that lots of STE's are bound to defects to emit the 3.0-eV band associated with a defect. Thus we conclude that if the crystal is perfect, the 4.1-eV band must appear strongly, irrespective of the way of excitations. At low temperature, the STE's are not mobile, so that the spectra are less sensitive to the population of defects (the way of excitations). The next question to be discussed is what kind of STE it is.

Considering the identity of the 4.1-eV band with the 4.3-eV band in origin, we first discuss the origin of the 4.3-eV band. Iida *et al.* [11-13] have assigned the 4.3-eV band to the ${}^3\Gamma_4^- \rightarrow {}^1\Gamma_1^+$ transition, on account of its π polarization, long decay time (100ns) and magnetic circular polarization. In the present study, we found that the decay curve of the 4.3-eV band was composed of a 2 ns component in addition to the 100 ns component (Fig. 4). The time-resolved spectra at 4.5 K confirmed that the 2 ns component as well as the 100 ns component belonged to the 4.3-eV band (Fig. 5). The appearance of the 2ns component is not favorable to the model proposed by Iida *et al.*, since the singlet transition ${}^1\Gamma_4^- \rightarrow {}^1\Gamma_1^+$ is symmetry forbidden. Thus the 2 ns component should be assigned to the ${}^1\Gamma_2^- \rightarrow {}^1\Gamma_1^+$ transition, and the 100 ns component to the ${}^3\Gamma_2^- \rightarrow {}^1\Gamma_1^+$ transition. This interpretation is consistent with the polarization property of the 4.3-eV band reported by Pellaux *et al.* [13]: The 4.3-eV band is π polarized at 5 K where the 100 ns component is dominant, and is σ polarized above 11 K where the 2 ns component is dominant.

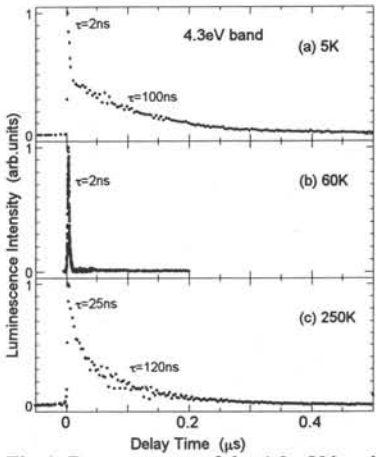

Fig.4. Decay curves of the 4.3-eV band.

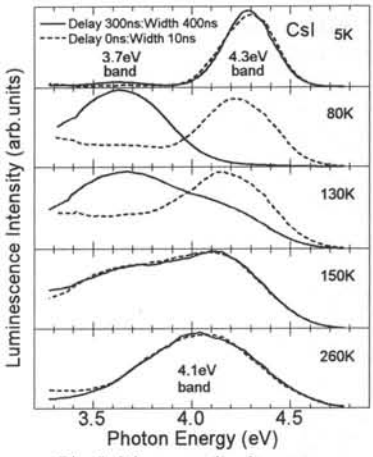

Fig.5. Time-resolved spectra.

We thus conclude that the initial state of the 4.3-eV band is the $^{1,3}\Gamma_2^-$ states. Since no other STE state whose energy is lower than the $^{1,3}\Gamma_2^-$ states is left, the initial state of the 3.7-eV band should also be the $^{1,3}\Gamma_2^-$ states, but the lattice configuration is different; on-center for the 4.3-eV band and off-center for the 3.7-eV band.

In the recent studies on the STE's in the alkali halides with the NaCl structure, it has been confirmed that the STE's are occasionally stable in off-center configuration as well as in on-center one [18-21]: The on-center STE consists of an electron trapped by a V_k center (I_2^-), in which the electron and hole are populated on the I_2^{2-} center, while the off-center STE consists of a nearest-neighbor pair of F and H centers, in which the electron and hole are separated from each other to form a Frenkel pair (F and H pair). Figure 6 shows a diagram of adiabatic potential-energy surfaces of the singlet and triplet states for both types of STE's. The energy surfaces are cut along the off-center axis Q_2.

The $^{1,3}\Gamma_4^-$ states, on the other hand, must play less important role on the luminescence process, since the states lie higher in energy than the $^{1,3}\Gamma_2^-$ states (Fig. 1). Several authors have reported that the 6*s*-exciton state shifts to higher energy under hydrostatic pressure, and the 5*d*-exciton state shifts to lower energy to cross each other at 0.5 GPa [17,22,23]. In other words, the lowest energy-exciton state is the 6*s*-exciton state below 0.5 GPa, and is the 5*d*-exciton state above 0.5 GPa. Tsujimoto *et al.* [17] have reported that the 4.3 and 3.7-eV bands disappear above 0.5 GPa and a new luminescence band appears with a decay time of 200 ns at 4.7 eV, and that the 4.7-eV band should be assigned to the $^3\Gamma_4^- \rightarrow {}^1\Gamma_1^+$ transition. It is noted that the 4.7-eV band has originally been reported by Laisaar *et al.* [24].

Figure 7 shows the decay times of the 4.3- and 3.7-eV bands as a function of temperature. The 3.7-eV band consists of two slowly decaying components (0.6 and 20 μs at 5 K) due to the triplet transition ($^3\Gamma_1 \rightarrow {}^1\Gamma_1$) in the

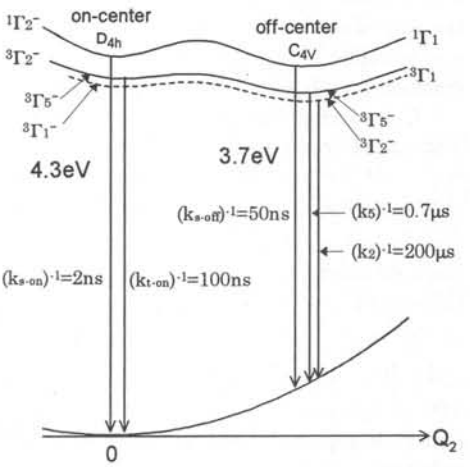

Fig.6. Adiabatic potential-energy surfaces for the singlet and triplet STE states in CsI.

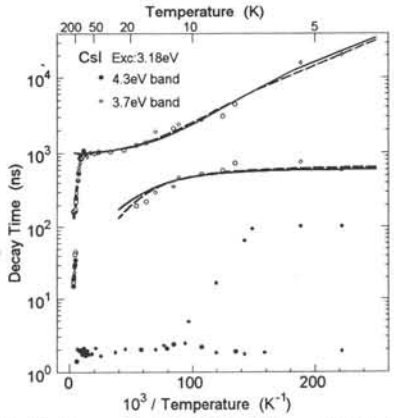

Fig.7. Decay times of the 4.3- and 3.7-eV bands as a function of temperature.

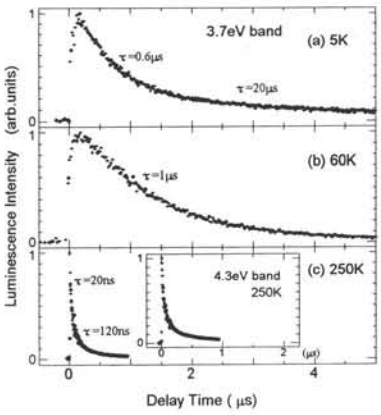

Fig.8. Decay curves of the 3.7-eV band.

off-center state. Typical decay curves are shown in Fig. 8. No quickly decaying component due to the singlet transition is observed: It may be hidden in a delay part. We note that the decay time is shorter when the luminescence is emitted from the $^3\Gamma_2^-$ state in the on-center state (100 ns) than when it is emitted from the $^3\Gamma_1$ state in the off-center state (0.6 and 20μs), probably because of larger overlapping of the wave functions of the electron and hole in the on-center STE than in the off-center STE [25,26].

The decay time of the triplet component (100 ns) of the 4.3-eV band decreases abruptly above 6 K (Fig. 2) in accordance with the intensity decrease. Since the 3.7-eV band is enhanced above 6 K (Figs. 2 and 9), the triplet STE's seem to relax from the on-center state to the off-center state on the triplet surface. The decay curves shown in Figs. 4 and 8 support this interpretation: The rise time of the 3.7-eV band is equal to the decay time (100 ns) of the 4.3-eV band at 5 K. The same result has first been reported by Nagli and Karklinya [14]. These results suggest that the potential barrier between the on-center and off-center states is small on the triplet surface. On the singlet surface, on the other hand, the potential barrier must be much larger, since the decay time and intensity of the 2-ns component of the 4.3-eV band remain constant up to 160 K. According to Matsumoto *et al.* [27], the same situation for the potential barrier realizes in most alkali halides.

The 4.3-eV band is enhanced above 100 K with two slowly decaying components whose decay times are the same as those of the 3.7-eV band, and the intensity of the 3.7-eV band is reduced (Fig. 9). These results suggest that a thermal activation of STE's occurs from the off-center state to the on-center state on the triplet surface above 100 K. A similar thermal activation of STE's is likely to occur on the singlet surface, since the 4.3- and 3.7-eV bands have a common quickly decaying component (30 ns at 200 K) above 200 K (Fig. 10), and since the 3.7-eV band almost disappears above 200 K (Figs. 2 and 9). In the thermal activation, the radiative transition to the ground state must occur mainly at the on-center state with a larger radiative decay rate rather than at the off-center state, so that the intensity of the 4.3-eV band increases, and the decay time decreases with increasing temperature.

Next we estimate the radiative decay rate at the $^3\Gamma_1$ state in the off-center STE. The decay times of the 0.6 and 20 μs components are interpreted by the population changes of STE's in the $^3\Gamma_1$ state. This triplet state splits into two sublevels by spin-orbit interaction: $^3\Gamma_5$ and $^3\Gamma_2$ states in the C_{4v} point symmetry (Fig. 1). Since the $^1\Gamma_5$ state with π polarization mixes into the $^3\Gamma_5$ state by spin-orbit interaction, the triplet state is partially allowed, whereas the $^3\Gamma_2$ states is of pure triplet. Thus the STE's in the off-center configuration decay radiatively

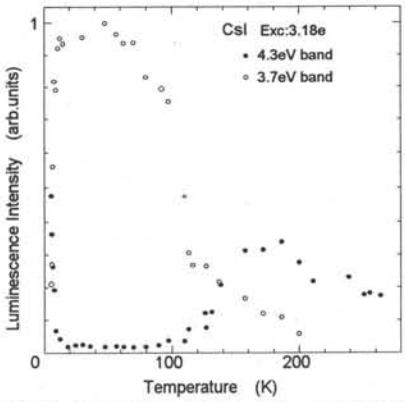

Fig.9. Intensities of the 4.3- and 3.7-eV bands as a function of temperature.

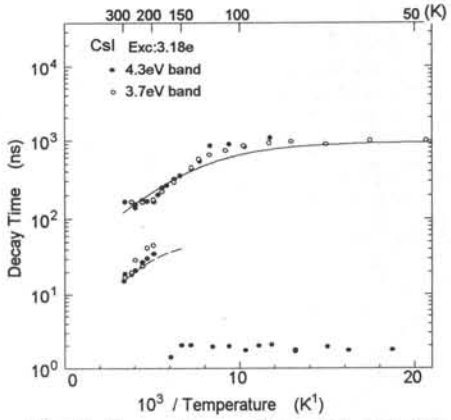

Fig.10. Decay times of the 4.3- and 3.7-eV bands as a function of temperature.

through the $^3\Gamma_5$ state with π polarization, and the $^3\Gamma_2$ state acts as a trapping state for the STE's.

We now assume that the populations of STE's on the $^3\Gamma_5$ and $^3\Gamma_2$ states, n_5 and n_2, decay in accordance with the following rate equations based on one-phonon process:

$$dn_5/dt = -n_5\left\{k_5 + k_{52}(\bar{n}+1)\right\} + n_2 k_{25}\bar{n} \quad , \tag{1}$$

$$dn_2/dt = -n_2\left(k_2 + k_{25}\bar{n}\right) + n_5 k_{52}(\bar{n}+1) \quad , \tag{2}$$

where $\bar{n}$ represents the phonon occupation number; $\{\exp(E_{52}/k_BT)-1\}^{-1}$, E_{52} is the energy separation between the $^3\Gamma_5$ and $^3\Gamma_2$ states, k_5 and k_2 are the decay rates from the $^3\Gamma_5$ and $^3\Gamma_2$ states to the ground state, k_{52} and k_{25} are the transition rates of STE's from the $^3\Gamma_5$ state to the $^3\Gamma_2$ state, and the reverse. Solving Eqs.(1) and (2) under an initial condition ($n_5=n_0$ and $n_2=0$ at $t=0$), we obtained n_5 to be given by the sum of two exponential decay parts. The solid curves in Fig. 7 represent the best fits of these two decay parts to the data. The values of several parameters obtained by the fittings are given in Table I(A). A few values obtained by Lamatsch *et al.* [9] in a thermal activation model [Table I(B)] agree well with our results, but some of our results are unreasonably large:12.6 for k_{25}/k_{52} is much larger than the expected value 2, being the statistical weight of two final states, and further 2 meV for E_{52} is much larger than 0.495 meV obtained by Falco *et al.* [12] from the magnetic circular polarization.

To solve these discrepancies, we adopt Orbach model based on two-phonon process *via* an intermediate state I lying above the $^3\Gamma_5$ and $^3\Gamma_2$ states instead of above one-phonon model. In the Orbach model [28], $k_{52}(\bar{n}+1)$ and $k_{25}\bar{n}$ in Eqs.(1) and (2) are replaced by $k_{52}\bar{n}_{5I}(\bar{n}_{2I}+1)$ and $k_{25}\bar{n}_{2I}(\bar{n}_{5I}+1)$. Here, $\bar{n}_{5I}=\{\exp(E_{5I}/k_BT)-1\}^{-1}$ and $\bar{n}_{2I}=\{\exp(E_{2I}/k_BT)-1\}^{-1}$, and E_{5I} and E_{2I} are the energy difference between the $^3\Gamma_5$ and I states and between the $^3\Gamma_2$ and

Table I. The values of several parameters obtained in the one-phonon process (A) and those in the two-phonon process (C), and those reported by Lamatsch et al. (Ref.9) (B).

	E_{52}	E_{5I}	E_{2I}	k_5^{-1}	k_2^{-1}	k_{52}^{-1}	k_{25}^{-1}	k_{25}/k_{52}
A	2meV	–	–	0.9μs	70μs	1.8μs	0.14μs	12.6
B	2meV	–	–	0.6μs	65μs	–	–	–
C	0.5meV	0.9meV	1.4meV	0.7μs	0.2ms	1.7μs	0.7μs	2.4

I states. Fitting the solutions of these equations to the data (broken curves in Fig. 7), we obtained the reasonable values for k_{25}/k_{52} (2.4) and for E_{52} (0.5 meV). These values are given in Table I(C).

Next we discuss the thermal activation of STE's from the off-center state to the on-center state. We assume Boltzmann distribution for the STE's on both states; $n_{on}/n_{off}=\exp(-E_d/k_BT)$. We also assume a weak nonradiative process with a rate of $k_n\exp(-E_a/k_BT)$ on account of the gradual decrease of the intensity of the 4.3-eV band at high temperatures (Fig. 9). Based on this model, we obtained a mean-decay rate τ^{-1} of the STE's on the triplet surface, and that on the singlet surface to be

$$\tau^{-1} = \frac{\exp\left(-E_d/k_BT\right)\left\{k_{on} + k_n \exp\left(-E_a/k_BT\right)\right\} + k_{off}}{\exp\left(-E_d/k_BT\right)+1}, \qquad (3)$$

where E_d represents the energy difference between the on-center and off-center states, and k_{on} and k_{off} the radiative decay rates at each state. The solid and broken curves in Fig. 10 represent the best fits of Eq.(3) to the data for the triplet and singlet transitions. The values of several parameters obtained by the fittings are given in Table II.

The radiative decay rates are much larger at the on-center state than at the off-center state; 100 ns and 600 ns on the triplet surface, and 2 ns and 50 ns on the singlet surface (Table II). These results are reasonable, because the overlapping of the electon-wave function and hole-wave function is larger in the on-center configuration than in the off-center one. In other words, the off-center states lose the inversion symmetry, resulting in the smaller radiative decay rates there. Thus the luminescence arising from the on-center state becomes dominant at high temperatures. The red shift of the peak energy (4.3 → 4.1 eV) is caused by the thermal expansion of the lattice, and the blue shift of the 3.7-eV band (3.6→3.7 eV) is a feature of the luminescence due to off-center STE's [29].

The nonradiative process considered in Eq.(3) is probably caused by the hopping motion of STE's, since strong luminescence due to defects appears at high temperatures at the expense of the intensities of the 4.3- and 3.7-eV bands, when the sample contains lots of defects.

It has been reported that the 4.1-eV band has 1 μs component of decay time at room temperature [6]. The intensity of this component is fairly large; about 50 % of the total. We observed that the time resolved spectrum at 1 μs was spread over a wide energy region (4.6-3 eV), and was far from the spectrum of the 4.1-eV band. We thus exclude the 1 μs component from the 4.1-eV band.

Finally we discuss how we can improve the alkali-halide scintillators. The existence of the off-center STE state is not favorable to scintillator with short decay time and high quantum yield, because the off-center state acts as a trapping state for the on-center STE's, and further the state acts as a precursor of defect formations such as F and H centers, leading to radiation damage. To remove the effects caused by the off-center state, we must find materials in which the off-center state is not stable. NaI and NaBr are well-known to be such materials [19, 20]. In the materials, however, the hopping motion of the STE's occurs rather at low temperatures [30], so that the STE's are captured by defects to emit the luminescence associated with the defects, before the STE's emit their own luminescence with short decay times (1.2 and 1.6 ns for the singlet transitions in NaI and NaBr [31]). Thus it is difficult to observe the STE

Table II . The values of several parameters in Eq. (3).

	k_{on}^{-1}	k_{off}^{-1}	E_d	k_n^{-1}	E_a
Singlet	2ns	50ns	60meV	2ns	60meV
Triplet	100ns	0.9μs	25meV	20ns	25meV

luminescence in these materials at room temperature, unless the materials are of extremely high quality. To reduce the nonradiative decay rate of STE's, we have to develop new methods such as alloying the materials.

In conclusion, the singlet and triplet STE states in CsI are stable both in the on-center and off-center configurations. The STE's are in thermal equilibrium both on the singlet and triplet surfaces at high temperatures. The 4.1-eV luminescence in the pure CsI scintillator arises from the $^{1,3}\Gamma_2^-$ states in the on-center configuration. The quickly decaying component (15 ns at 290 K) is assigned to the singlet $^1\Gamma_2^- \rightarrow {}^1\Gamma_1^+$ transition, and the slowly decaying component (100 ns at 290 K) to the triplet $^3\Gamma_2^- \rightarrow {}^1\Gamma_1^+$ transition. To improve the alkali-halide scintillators, new materials in which off-center STE's are not stable, and the hopping motion of on-center STE's hardly occurs, should be found.

REFERENCES

[1] R.Gwin and R.B.Murray: Phys. Rev. **131**(1963)508.
[2] T.Towyama, I.Morita and M.Ishiguro: J. Phys. Soc. Jpn. **25**(1968)1133.
[3] C.H.Chen, M.P.McCann and J.C.Wang: Solid State Commun. **61**(1987)559.
[4] S.Kubota, S.Sakuragi, S.Hashimoto and J.Ruan (Gen): Nucl. Instrum. Methods **A268** (1988)275.
[5] B.K.Utts and S.E.Spagno: IEEE Trans. Nucl. Sci. **37**(1990)134.
[6] P.Schotanus, R.Kamermans and P.Dorenbos: IEEE Trans. Nucl. Sci. **37**(1990)177.
[7] M.Abdrakhmanov, S.Chernov, R.Deich and V.Gavrilov: J. Lumin. **54**(1992)197.
[8] A.N.Belsky, A.N.Vasil'ev and V.V.Mikhailin: Phys. Rev. **B49**(1994)13 197.
[9] H.Lamatsch, J.Rossel and E.Saurer: Phys. Status Solidi **B48**(1971)311.
[10] J.U.Fischbach, D.Frohlich and M.N.Kabler: J. Lumin. **6**(1973)29.
[11] T.Iida, Y.Nakaoka, J.P.von der Weid and M.A.Aegerter: J. Phys. **C13**(1980)983.
[12] L.Falco, J.P.van der Weid, M.A.Aegerter, T.Iida and Y.Nakaoka: J. Phys. **C13**(1980)993.
[13] J.P.Pellaux, T.Iida, J.P.von der Weid and M.A.Aegerter: J. Phys. **C13**(1980)1009.
[14] L.E.Nagli and M.N.Karklinya: Sov. Phys. Solid State **31**(1989)2116.
[15] K.Teegarden and G.Baldini: Phys. Rev. **155**(1967)896.
[16] Y.Onodera: J. Phys. Soc. Jpn. **25**(1968)469.
[17] T.Tsujimoto, H.Nishimura, M.Nakayama, H.Kurisu and T.Komatsu: J. Lumin. **60/61** (1994)798.
[18] C.H.Leung, G.Brunet and K.S.Song: J. Phys. **C18**(1985)4459.
[19] R.T.Williams, K.S.Song, W.L.Faust and C.H.Leung: Phys. Rev. **B33**(1986)7232.
[20] K.Kan'no, K.Tanaka and T.Hayashi: Rev.Solid State Sci. **4**(1990)383.
[21] K.S.Song and R.T.Williams: *Self-Trapped Excitons* (Springer-Verlag, Berlin, 1992).
[22] D.W.Lynch and A.D.Brothers: Phys. Rev. Lett. **21**(1968)689.
[23] A.I.Kuznetsov, A.I.Laisaar, V.S.Shcherbakov and G.S.Zavt: JETP Lett. **40**(1984)899.
[24] A.I.Laisaar, V.S.Shcherbakov and A.I.Kuznetsov: High Pressure Res. **3**(1990)78.
[25] K.S.Song and L.F.Chen: J. Phys. Soc. Jpn. **58**(1989)3022.
[26] R.T.Williams, Hanli Liu, G.P.Williams,Jr. and K.J.Platt: Phys. Rev. Lett. **66**(1991)2140.
[27] T.Matsumoto, M.Shirai and K.Kan'no: J. Phys Soc. Jpn. **64**(1995)291.
[28] R.Orbach: Proc. R. Soc. London Ser. **A264**(1961)458.
[29] S.Suzuki, K.Tanimura, N.Itoh and K.S.Song: J. Phys. Condens. Matter **1**(1989)6993.
[30] S.Nagata, K.Fujiwara and H.Nishimura: J. Lumin. **47**(1991)147.
[31] T.Matsumoto, T.Kawata, A.Miyamoto and K.Kan'no: J. Phys. Soc. Jpn. **61**(1992)4229.

INTRINSIC AND IMPURITY LUMINESCENCE OF CRYSTALS WITH ELPASOLITE STRUCTURE

Voloshinovskii A.S., Rodnyi P.A.*, Mikhailik V.B., Pashuk I.P., Antonyak O.T. and Pidzyrailo M.S.
Lviv State University, 8 Kyrylo and Mefodiy str., Lviv, 290005, Ukraine
**Technical University, 29 Politekhnicheskaya str., St.Petersburg, 126251, Russia*

Abstract The luminescence properties of pure and Ce-doped complex chlorine crystals $Cs_2NaLaCl_6$, Cs_3LaCl_6, $Cs_2NaCeCl_6$ and $Cs_2NaLaCl_6$-Ce were studied under pulse high-energy excitation. The emission features are related with self-trapped exciton (STE), core-valence and Ce^{3+}-luminescence. The main peculiarities of the core-valence luminescence are explained in frame of cluster approach. Unusual temperature behavior of Ce-emission decay time is revealed at pulse X-ray excitation. Possible excitation mechanism for Ce-emission is considered to be the result of interaction of Ce^{3+}-ions with V_k-centers, which are created at the temperature decay of STE, and core holes or excitons.

INTRODUCTION

Today the interest is renewed to application of fast and efficient scintillation detectors in science, medicine and industry [1]. Two types of luminescence are estimated to be the most promising routes for the search for fast scintillators [2]: i) 5d-4f emission in RE-ions and ii) core-valence luminescence (CVL) caused by radiative recombination of valence electrons and uppermost core holes, created by ionizing radiation in some ionic crystals, containing K^+, Rb^+, Cs^+ and Ba^{2+} cations [3].

The compounds exhibiting both mentioned emission simultaneously are of particular interest. The combination of CVL-active matrix with RE-doping may lead to increasing general intensity of the fast emission response. Here we present the results of luminescence studies for pure and doped complicated halide compounds with elpasolite structure demonstrating the mentioned properties.

RESULTS AND DISCUSSION

Intrinsic luminescence of elpasolite crystals

The single crystals $Cs_2NaLaCl_6$, Cs_3LaCl_6, $Cs_2NaCeCl_6$ and $Cs_2NaLaCl_6$-Ce were grown from a melt by means of Bridgman technique. The emission spectra and decay time peculiarities were measured under the pulsed X-ray excitation (pulse HWFM 1-5 ns, anode voltage 35 kV, pulse frequency 100 kHz) using a right angle geometry. The UVPS measurements were performed using the synchrotron radiation of the storage ring at Daresbury Laboratory as excitation source.

Figure 1 demonstrates the ultraviolet photoelectron spectroscopy (UVPS) data for $Cs_2NaLaCl_6$. The Fermi level position E_f and binding energies are assessed from comparison of our data with these of the UVPS studies on RE trihalides [4]. One can see an energy gap between valence $3pCl^-$-band and $5pCs^+$-outermost core band, which is suitable for radiative transitions between valence and core band [3]. Such core-valence transitions with fast decay time ($\tau = 1.7$ ns, $T = 77$ K) were observed in $Cs_2NaLaCl_6$ crystals in UV-spectral range at X-ray pulsed excitation [5]. The CVL nature of the observed emission is confirmed by existence of the threshold near 14 eV in the excitation spectrum coinciding with the onset of the interband transitions between core and conduction band [6]. This value is very close to that observed in other cesium halide compounds exhibiting the CVL [3].

Proc. Int. Conf. on Inorganic Scintillators and Their Applications, SCINT95,
1996, Delft University Press, The Netherlands

Fast emission spectrum of $Cs_2NaLaCl_6$ measured at pulse X-ray excitation (time gate 1 ns) demonstrates two maxima of comparable intensities at 4.1 and 4.7 eV (Fig.2a, curve 1). The steady-state X-ray luminescence spectrum of the crystals at 77 K displays the emission band centered at 2.7 eV (Fig.2a, curve 2). The luminescence decay time at this temperature may be estimated as being close to 10^{-6} s, which is characteristic for the radiative decay of the self-trapped excitons (STE). STE luminescence is characterized by very strong temperature dependence of luminescence intensity. Contrary, the luminescence intensity of fast decay component varies slightly in the temperature range from 77 to 295 K. Only some broadening of the CVL spectrum and redistribution of the luminescence intensity is detected as the temperature arises. Hence, the spectral and kinetic features of the fast emission and its thermal stability confirms that the fast intrinsic luminescence of $Cs_2NaLaCl_6$ crystals is due to radiative interband transitions between the Cs-core and Cl-valence band.

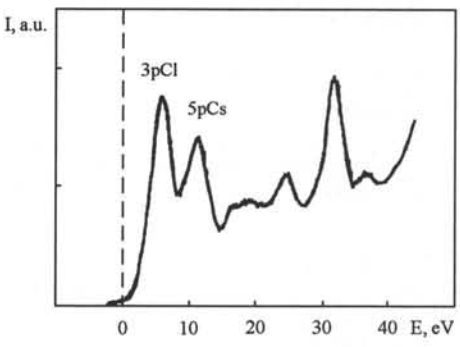

Fig. 1: UVPS data of $Cs_2NaLaCl_6$ crystals. The binding energy positions are counted out relative to the Fermi level E_f.

It is interesting to emphasize the similarity of the CVL spectra of $Cs_2NaLaCl_6$ and $CsCaCl_3$ crystals. As can be seen from comparison of Fig.2a and 2b, (curves 1) the position of maxima of luminescence bands and the widths of the fast X-ray luminescence spectra are very resembling. The similarity of the fast X-ray luminescence spectra of compounds with different structure and composition suggests that core-valence transitions occur within same elementary cesium-chlorine cluster. In $CsCaCl_3$ crystal, which has the perovskite structure, and in $Cs_2NaLaCl_6$ with elpasolite structure, the Cs^+-ions are surrounded by 12 Cl^--ions. In both cases a similar cluster $[CsCl_{12}]$ participates in the process. Hence, the core-valence transition is a local phenomenon, and the emission is due to a recombination of excitation in the local region of the crystal and it can be described by a molecular cluster approach.

The cluster approach with different quantum-mechanical calculation schemes was used for spectral calculation of real crystals [7, 8]. Our model calculations of CVL spectra have shown the dependence of CVL spectra on the ion environment of CVL-active cation [9]. One emission band is observed for the cluster $[CsCl_6]$, where coordination number n is equal to 6. There are two emission bands for cluster $[CsCl_8]$ ($n = 8$), and more complicated spectrum shape is obtained for cluster $[CsCl_{12}]$.

Cluster approach gives a possibility to explain the CVL emission features of other investigated elpasolite crystals.The fast emission spectrum of Cs_3LaCl_6 crystals (Fig.2c, curve 1) contains unresolved high-energy emission band appearing due to the presence of CVL active cesium ions in the two different positions with coordination number n equal to 12 and 6. The superposition of spectra from core-valence transitions in cluster with n equal to 6 and 12 just gives the observed unresolved emission band.

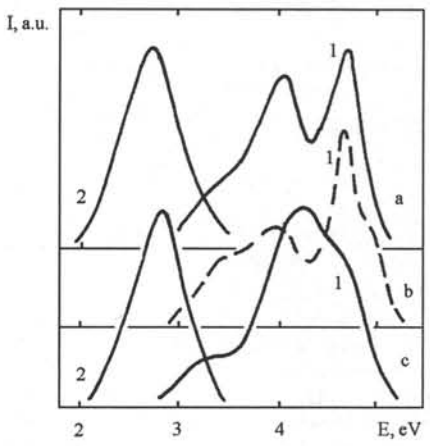

Fig. 2: Normalized (1) fast and (2) slow emission components of the X-ray luminescence spectra for (a) $Cs_2NaLaCl_6$, (b) $CsCaCl_3$ and (c) Cs_3LaCl_6 crystals measured at 77 K.

Luminescence of Ce-containing elpasolite crystals

Taking into consederation that the light yield of CVL is equal to about 1%, we have doped the crystals by Ce-ions to increase the total fast scintillation light output of elpasolites.

The photoluminescent bands of 370 and 405 nm in the emission spectra of $Cs_2NaLaCl_6$-Ce crystals are shifted in long-wave range in comparison with those in other wide-band gap halide crystals. The position of the excitation spectra (maximum at 340 nm) is suitable for the excitation by nitrogen and XeCl lasers. The luminescent decay curve at optical excitation is exponential ($\tau = 26$ ns, $T = 77$ K).

The X-ray luminescence spectra are of interest, because we observed both the CVL and Ce-luminescence (Fig.3a). At 77 K the intensities of the CVL and Ce-emission are comparable. But the contribution of Ce-emission significantly varies at increasing the temperature (Fig.3b). The temperature escalation causes increasing both the emission intensity and the decay time. The decay time changes from 40 ns at 77 K to 160 ns at 340 K (Fig.3c).

Contrary to the previous crystal, in $Cs_2NaCeCl_6$ crystals the Ce-ions are the component of crystal, but not the admixture. However, the photoluminescence spectra and the excitation spectra of this crystal are very similar to those of Ce-doped $Cs_2NaLaCl_6$. The decay time at the optical excitation is equal to 38 ns at 77 K. The photoluminescence intensity is slowly changed as the temperature rises. At X-ray excitation the CVL observed in the previous crystals is absent, and only Ce-emission is observed. The X-ray luminescence spectra and the decay time are sensitive to temperature changes, as in the case of $Cs_2NaLaCl_6$ crystals. As the temperature rises the X-ray luminescence intensity increases, and the τ rises from 20 ns at 77 K to 100 ns at 340 K.

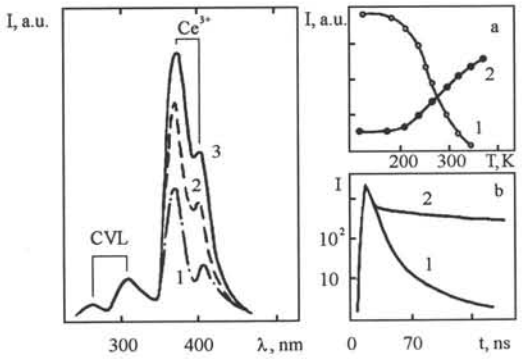

Fig. 3: (a): X-ray luminescence spectra of $Cs_2NaLaCl_6$-Ce at (1) 77, (2) 260 and (3) 340 K. (b): Temperature dependence of (1) STE and (2) Ce-emission for $Cs_2NaLaCl_6$-Ce. (c): X-ray emission decay pulses at (1) 77 and (2) 340 K.

Let us consider the tentative mechanism of Ce-emission in the studied crystals. In the temperature range of 77-200 K, where the STE is stable, the probability of electron-hole recombination with creation of STE exceeds that of recombination with Ce-centers. In this temperature range the intensity of STE-emission exceeds considerably the Ce-emission. In the range of temperature decay of STE ($T > 200$ K) we observed the increase in the impurity luminescence and the decay time. Such emission features make it possible to consider the mechanism of Ce-emission at high temperature as follows. The Ce-luminescence is caused by the recombination of V_k-centers, arisen at the temperature decay of STE, with Ce-centers. In this case the rising part of the luminescence pulse is determined by the probability of V_k- and Ce-centers recombination. The decay time of luminescence is determined by statistics of such recombinations. The temperature increase accelerates the delocalization and the decay of STE and by this promotes the interaction of the decay products with Ce-centers. It leads to the increase of Ce-emission and decay time in the crystals under investigation.

Hence, the Ce-emission at high energy excitation could be used as a special test for halide excitons presence in the investigated crystals. Taking into consideration that Ce-emission in $CeCl_3$, LaF_3 and LaF_3-Ce does not exhibit the above mentioned temperature dependence the existing of halide excitons in these crystals is doubtful.

Finally, it is necessary to underline the significant difference between the decay time curves at the X-ray excitation and the excitation in the range of outermost core band ($h\nu = 20$ eV) at 295 K. The latter curve is similar to that for the X-ray excitation at

77 K (fig 3c, curve 1), where Ce-emission is determined by the recombination with hot electrons and holes. The emission pulse shape observed at the excitation in core band points out the absence of recombination of V_k- and Ce-centers. It can be explained in the following way. The excitation of core band is connected with the creation of core excitons. These excitons interact with the Ce-centers before their decay through the CVL or STE creation. It is possible to observe this effect in the systems with the CVL, for which the probability of deactivation of core holes is relatively small ($\tau \sim 10^{-9}$ s). In alternative case, the deactivation occurs through the fast Auger-decay ($\tau \sim 10^{-12}$ s), and the excitation of Ce-centers by core excitons and holes has very low probability. Hence, the CVL-active systems allow us to study the mobility of the outermost core excitons and core holes.

ACKNOWLEDGEMENTS

The work was supported in part by Joint Committee ISF-Ukraine Grant K6N100. The authors are grateful to Prof.I.H.Munro (Daresbury Laboratory) for given possibility for UVPS measurements and Mr.S.Downes for assistance.

REFERENCES

1. C.W.E. van Eijk, Record of the International Workshop Physical Processes in Fast scintillators Sept.30-Oct.3 1994. Ed. by P.A.Rodnyi and C.W.E. van Eijk S.Petersburg, Russia, 1994, p.1-12.
2. G.Blasse, IEEE Trans.Nucl.Sci. 38 (1991) 30.
3. P.A.Rodnyi, Sov.Phys.Solid State 34 (1992) 1053.
4. K.-H.Park and S.-J.Oh, Phys.Rev.B 48 (1993) 14833.
5. A.S.Voloshinovskii, A.G.Dmitriev, V.B.Mikhailik and P.A.Rodnyi, Sov.Phys.Solid State 34 (1992) 1998.
6. E.N.Mel'chacov, I.H.Munro, S.V.Petrov et al, Abstracts of X Feofilov Symposium on Spectroscopy of Crystals Activated by Rare Earth and Transitional Ions. S.Petersburg, Russia, 1995, p.22.
7. J.Andriessen, P.Dorenbos and C.W.E. van Eijk, Mol.Phys. 3 (1991) 535.
8. A.B.Sobolev, Sov.Phys.Solid State 31 (1993) 1111.
9. A.S.Voloshinovskii, V.B.Mikhailik, P.A.Rodnyi et al, Sov.Phys.Solid State 36 (1994) 911.

LUMINESCENCE QUENCHING STUDIES IN CeF_3 AND CeF_3-LaF_3 WITH SYNCHROTRON RADIATION

M.A.Terekhin[1,2], I.A.Kamenskikh[3], V.N.Makhov[4], V.A.Kozlov[4], I.H.Munro[2], D.A.Shaw[2], C.M.Gregory[2] and M.A.Hayes[2]

[1] Russian Research Centre "Kurchatov Institute", Moscow 123182, Russia

[2] Daresbury Laboratory, Warrington, Cheshire WA4 4AD, UK

[3] Moscow State University, Moscow 117234, Russia

[4] Lebedev Physical Institute, Moscow 117924, Russia

ABSTRACT

The quenching mechanisms for fast luminescence in CeF_3 and CeF_3 - LaF_3 crystals have been studied by means of time-resolved VUV-spectroscopy using synchrotron radiation. The luminescence decay of these crystals reveals at least three mechanisms of quenching: the first one, conventional for VUV region, where the radiation penetration depth is very small ~ 10 nm, results from surface losses; the second one is due to the energy transfer to defect centres in the bulk of the crystal (very pronounced in CeF_3 - LaF_3) and the third one, the least studied, is attributed to the interaction of closely spaced electron excitations (secondary electron excitation quenching).

INTRODUCTION

For the successful use and manufacture of fast scintillator materials which have wide practical applications both in high energy physics and medicine the understanding of fundamental processes responsible for quenching of the luminescence is crucially important. In the wide band gap scintillator crystals, CeF_3 and BaF_2, an unusual type of quenching of prompt intrinsic luminescence under moderate intensity VUV excitation has been observed recently [1,2]. It is assumed that the effect is associated with a non-radiative energy transfer between the VUV excited luminescence centre (the $(Ce^{3+})^*$ or $5pBa^{3+}$ core hole) and the nearest electron excitations created by the same absorption process [3].

The aim of this research is to extend our investigations into the effects of luminescence quenching in pure CeF_3 and mixed CeF_3 - LaF_3(10%) crystals, paying especial attention to non-radiative energy transfer between the luminescent centre Ce^{3+} and the nearest secondary electron excitations.

EXPERIMENTAL PROCEDURE

CeF_3 - LaF_3 crystals with a concentration of 10% LaF_3 were grown by the Stockbarger-Bridgeman method in a fluorine atmosphere. Crystals were cleaved just prior to their installation into the cryostat. The CeF_3 sample was a high purity powder with a total impurity concentration of less than 20 ppm.

Synchrotron radiation from the SRS (Daresbury Laboratory) was used as a light source. The excitation and emission spectra were measured in multibunch operation while luminescence decay curves were derived in singlebunch mode of the SRS on station 3.1, using a 1 m Seya-Namioka monochromator covering the VUV photon range 5 - 35 eV [4]. The luminescence was observed via interference filters and a visible/UV monochromator (SPEX Minimate) with a resolution of 5 nm. Low temperature measurements were performed using an UHV continuous flow helium cryostat (Oxford instruments) with temperature controller (model ITC4) . The residual pressure in the sample chamber during collection of experimental data was $2 \cdot 10^{-7}$ Pa.

Proc. Int. Conf. on Inorganic Scintillators and Their Applications, SCINT95,
1996, Delft University Press, The Netherlands

RESULTS AND DISCUSSION

The luminescence spectrum of CeF_3-LaF_3 has four main features (unshown) at wavelengths 290, 310, 325, and 390 nm. The first two bands correspond to emission from the 'normal' (unperturbed) Ce^{3+} in the cation position [5-8] while the later two are associated with Ce^{3+} perturbed by some impurity or intrinsic defects, e.g. O^{2-} or (and) an anion vacancy in its first co-ordination sphere [7,8]. The same situation has been observed in pure cerium fluoride and CeF_3 activated by the divalent cations Ca^{2+}, Cd^{2+}, Ba^{2+} where the broad emission band of 'perturbed' Ce^{3+} luminescence was in the spectral region 320-380 nm [1,8,9]. Luminescence studies of pure CeF_3 powder have revealed very small contribution the perturbed Ce^{3+} emission.

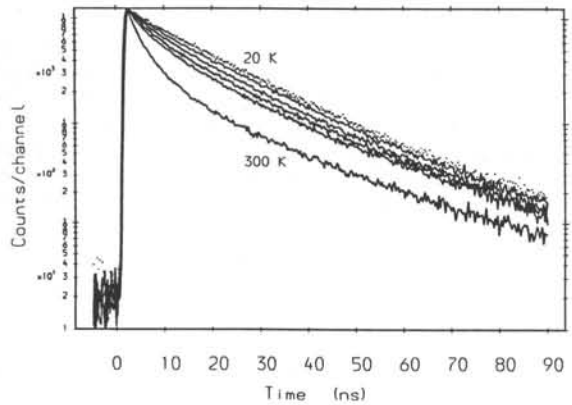

Fig.1. Decay curves for normal Ce^{3+} emission for E_{ex} = 8.4 eV in CeF_3 - LaF_3(10%) at T = 300, 200, 150, 100 and 50 K The lifetime increases steadily from 300 (the lowest) to 50 K (upper) curve (—). The top curve is CeF_3 at T = 20K (·····).

Fig.1 demonstrates the temperature dependences in the range 20 - 300 K for decay curves of the normal Ce^{3+} emission in CeF_3 - LaF_3 crystals and their asymptotic approach to the decay curve of pure CeF_3 at 20 K (top curve Fig.1). The deviation from one exponential decay law for CeF_3 - LaF_3 is supposed to be mainly associated with non-radiative resonance energy transfer from normal $(Ce^{3+})^*$ to perturbed Ce^{3+} [7,8,10]. For pure CeF_3 the time decay slightly decreases with temperature, without any significant changes (unshown). The later effect is successfully explained in terms of surface losses [2].

In the excitation region, corresponding to the Ce^{3+} absorption from 5 to 10 eV, the radiation penetration depth is rather high and the surface losses are smaller than in the region of transitions involving the fluorine states (E > 10 eV [11]). Both these cases are illustrated in fig.2 for CeF_3 - LaF_3 at low temperature, when the non-radiative energy transfer between normal and perturbed Ce^{3+} could be ignored. It is clearly seen that at lower energy 12.4 eV (Fig.2.) the shortening of the decay is not so strong in comparison with that at 20.7 eV, despite a decrease in the absorption coefficient from $1.6 \cdot 10^6$ to $1.2 \cdot 10^6$ cm^{-1}. The changes in absorption coefficient were estimated by the Kramers-Kronig analysis of the reflectivity spectrum for s-polarised light of crystal CeF_3 measured in [11]. Therefore there must be an additional quenching mechanism if neither surface losses nor resonance energy transfer to perturbed Ce^{3+} - centres could decrease the decay time so strongly. We suggest that it is the non-radiative energy transfer between the normal excited Ce^{3+} and the nearest secondary electron excitation that is responsible for generating the strong luminescence quenching. The closely spaced secondary electron excitations are created above the energy region from 15 to 17 eV for CeF_3 as a result of inelastic scattering of the fast electron on Ce^{3+} ions (i.e. impact excitation of Ce^{3+} ions [12, 13]).

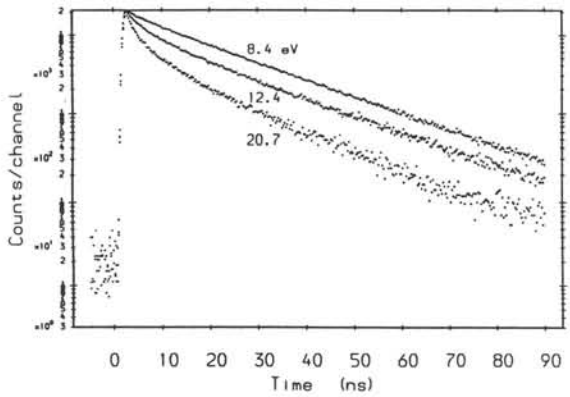

Fig.2.Decay curves of normal Ce^{3+} emission from CeF_3 - LaF_3 (10%) at 20K. E_{ex} = 8.4 upper, 12.4 centre and 20.7 eV lower curve respectively.

The assumption that the dominant mechanism of quenching changes between 12.4 and 20.4 eV is confirmed by Fig.3, where the temperature dependence of decay curves in CeF3 with excitation above and below the threshold energy for impact excitation of Ce3+ ions, is presented. The effect of temperature on the decay curves is reversed in these two cases. For an excitation energy at 12.4 eV (two upper curves in Fig.3), when the surface losses are assumed to be dominant, the luminescence quenching is greater at room temperature than at 20 K. Two mechanisms of the surface quenching are

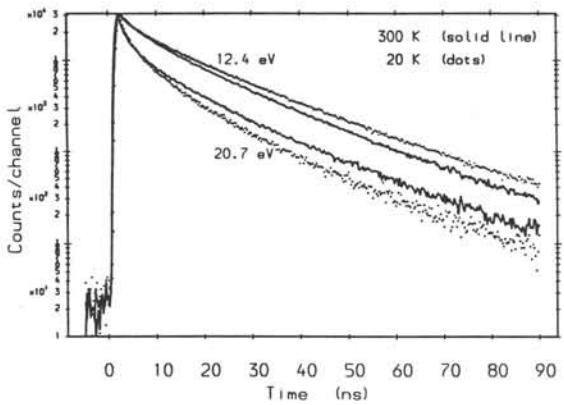

Fig.3. Decay curves for normal Ce^{3+} emission from CeF_3 at E_{ex} = 12.4 eV (the upper two curves) and 20.7 eV (the lower two curves). T = 300 K (—), 20 K (·····).

postulated [2]: namely, resonance and (or) diffusion energy transfer from electron excitations to the quenching centres, the concentration of which is much larger near to the surface than in the volume of a crystal. Thus we can conclude that the faster decay of the luminescence with temperature, at an excitation of 12.4 eV, is associated with the increasing diffusion mobility of electron excitations. The reverse effect with temperature is observed at an excitation energy of 20.7 eV when the secondary electron excitation at a distance ~ R_0 from $(Ce^{3+})^*$ can be created such that secondary electron excitation quenching can take place. In the latter case the rise of electron excitation mobility with temperature will increase the mean distance R between $(Ce^{3+})^*$ and electron excitation created in the same absorption process which reduces the probability of secondary electron excitation quenching.

CONCLUSIONS

The quenching due to the interaction with geminate secondary electron excitations has been identified in pure CeF_3 and CeF_3-LaF_3 crystals. In these fast scintillators the Ce^{3+} luminescence is quenched by the nearest electronic excitation (excited Ce^{3+}, electrons or hole etc.) created by the same absorption process, as a result of inelastic scattering of the hot photoelectron (or Auger decay of core hole). It has been shown that secondary electron excitation quenching effect takes place once the excitation energy is sufficient for the creation of secondary electron excitations and obviously starts with the threshold of the electron multiplication in the scintillator. The magnitude of secondary electron excitation quenching seems to decrease with the mobility of the electronic excitations.

The surface losses are traditionally assumed to be the main mechanism of luminescence quenching with VUV excitation but this work demonstrates that such is not always the case. For CeF_3 and CeF_3 - LaF_3 at an excitation energy of 20.7 eV, secondary electron excitation quenching effect is more significant than near surface losses.

The understanding of this quenching effect is extremely important for practical scintillator applications particularly those where the scintillator detectors are operated in the VUV and soft X-ray regions where the mean free path of photo and secondary electron excitations is very small.

ACKNOWLEDGEMENTS

The experiments have been carried out at EPSRC Daresbury Laboratory (Molecular Science Division). The work was supported by the Science and Engineering Research Council of Great Britain in the framework of UK-Russian collaboration on synchrotron radiation. The authors would like to thank Dr A.N.Vasil'ev for valuable discussions and Dr T.V.Uvarova for the growth of the CeF_3 - LaF_3 crystals.

REFERENCES

1. I.A.Kamenskikh, M.A.MacDonald, V.N.Makhov, I.H.Munro, V.V.Mikhailin and M.A.Terekhin NIM A348 (1994) 542
2. M.A.Terekhin, A.N.Vasil'ev, M.Kamada, E.Nakamura and S.Kubota , Phys.Rev. B 52 (1995) 3117.
3. I.A.Kamenskikh, I.H.Munro, M.A.MacDonald, V.N.Makhov and M.A.Terekhin SYNCHROTRON RADIATION, Daresbury Annual Report 1991/92 (1992) 36.
4. R.J.Cernik , Daresbury Annual Report 1993/1994 (1994) 265.
5. L.R.Elias, Wm.S.Heaps and W.M.Yen Phys.Rev. B8 (1973) 4989.
6. D.F.Anderson NIM A287 (1990) 606.
7. C.Pedrini, B.Moine, J.C.Gacon and B.Jacquier J.Phys.:Condens.Mater4(1992) 5461.
8. M.Nikl and C.Pedrini Sol.St.Comm. 90 (1994) 155.
9. M.Nikl, J.A.Mares, E.Mihokova, A.Beitlerova, K.Blazek and J.Jindra Sol.St.Comm. 84 (1993) 185.
10. A.J.Wojtowicz, M.Balcerzyk, E.Berman and A.Lempicki 1994 Phys.Rev. B49 14880
11. C.G.Olson, M.Piacentini and D.W.Lynch Phys.Rev. B18 (1978) 5740.
12. Yu.M.Aleksandrov, V.N.Makhov and M.N.Yakimenko Sov. Phys.- Solid State 29 (1987) 1902.
13. E.N.Melchakov, P.A.Rodnyi and M.A.Terekhin Optika i spectroskopia 69 (1990) 1069.

TIME-RESOLVED OPTICAL ABSORPTION AND LUMINESCENCE IN LaF_3 AND CeF_3 IRRADIATED BY 1-MeV, 20-ns ELECTRON PULSES

Y. Zhang, R. T. Williams, C. Itoh,* and K. Tanimura*
Department of Physics, Wake Forest University, Winston-Salem, NC 27109 USA
*Department of Physics, Nagoya University, Furo-cho, Chikusa, Nagoya 464-01 Japan

Time-resolved optical absorption and luminescence spectra have been measured in pure LaF_3 and CeF_3 following irradiation by 1-MeV, 20-ns electron pulses at temperatures from 10 to 574 K. In LaF_3 below room temperature, the absorption at all times from 0.5 μs to ~ 1 min is comprised mainly of the three bands with peaks near 580, 420, and 310 nm which are known from prior steady-state spectra. The 580-nm band, believed to be due to the F center, is the most prominent in this temperature range. In LaF_3 above room temperature, this F-center band is absent even at 0.5 μs after the electron pulse, but bands near 390 nm and ~ 300 nm are prominent for times of order 10 ms, vanishing almost completely in about 1 minute. Transient absorption data in CeF_3 illustrate in real time the shift of absorption strength from the 2.1-eV band to a ~2.9-eV band at 230 K. Luminescence studies showed that excitation is efficiently transferred from the LaF_3 host to 4 ppm Ce impurities at low temperature and high temperature, but not in the middle range near room temperature. Time dependence of the broad 370-nm luminescence band which is seen most clearly in the middle temperature range was measured.

EXPERIMENT

The LaF_3 and CeF_3 crystals were grown at Optovac in 1994 and 1993, respectively, from 99.999% starting material. On the basis of ultraviolet absorption spectra, the LaF_3 has low oxygen content and only ~ 4 ppm cerium impurity. The transient absorption spectra in this work were measured by recording transmission of a 1-μs xenon lamp flash occuring at a controllable delay after the electron pulse from a 1-MeV, 20-ns febetron [1] Marx-bank field emission device at Nagoya University. The crystals were oriented with c-axis parallel to the electron beam and the probe beam passed through at 30° to the c axis. The spectra were recorded with an optical multichannel analyzer (OMA). Luminescence spectra were measured with a delayed-gate intensified OMA. The intensity of the lamp flash, electron pulse, and luminescence were monitored for each shot and were used for normalization and correction of the absorption data. The electron fluence was limited to keep induced peak optical density below about 0.1 to avoid build-up of significant permanent absorption at low temperature.

RESULTS AND DISCUSSION

Figure 1 shows the radiation-induced absorption spectra in LaF_3 measured 0.5 μs (upper trace) and ~ 1 min (lower trace) after the electron pulse at several temperatures from 10 to 289 K; and 5μs, ~ 30s, from 296 to 574 K. From 10 K through 119 K, the spectra display the three bands at 580, 420, and 310 nm which have been observed

Proc. Int. Conf. on Inorganic Scintillators and Their Applications, SCINT95,
1996, Delft University Press, The Netherlands

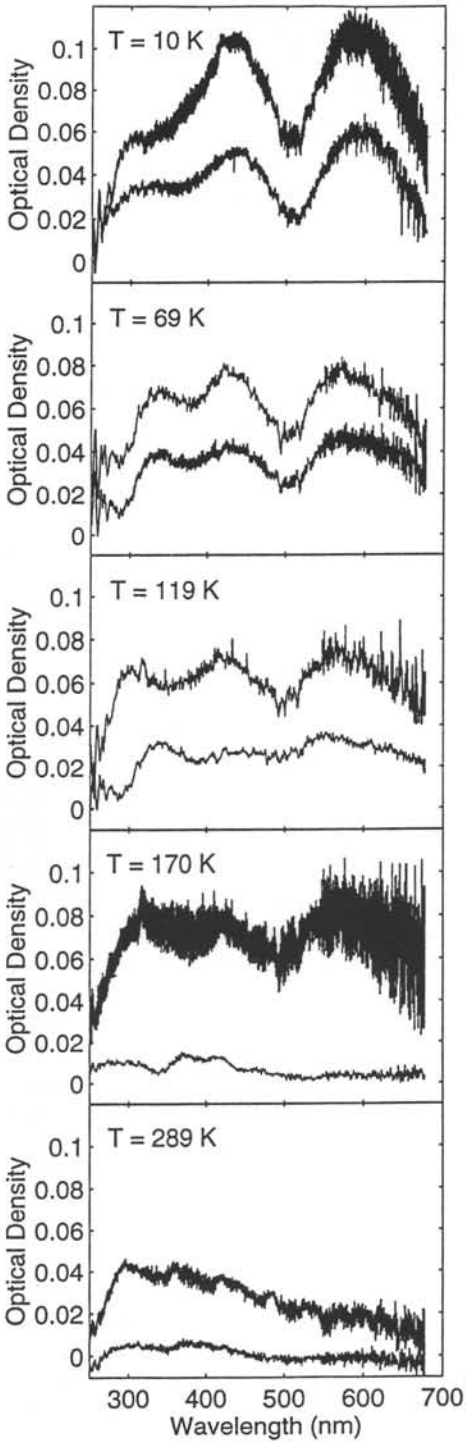

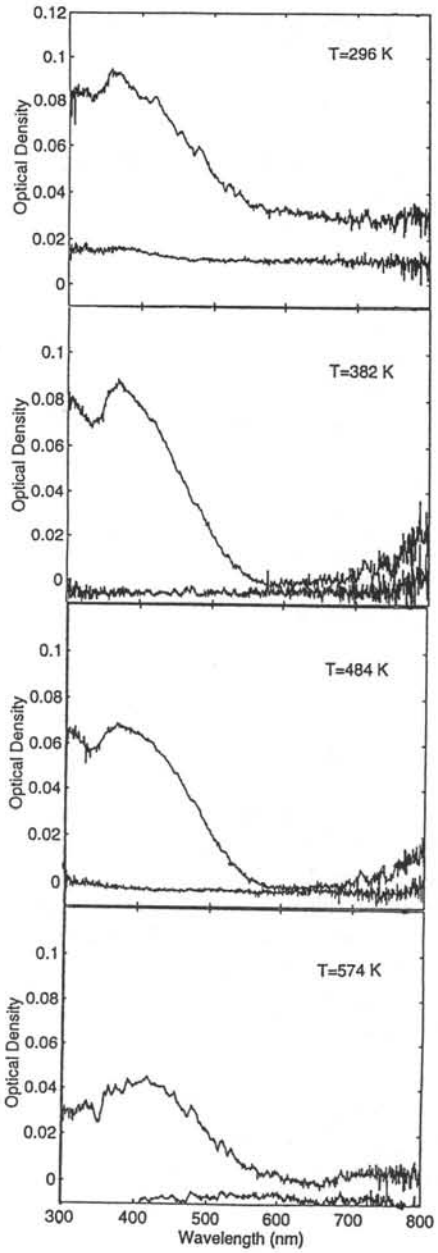

Fig. 1 Radiation-induced absorption of LaF_3 measured 0.5 μs after electron pulse (upper trace) and ~ 1 min afterward (lower trace) at temperatures labeled 10-289 K; 5 μs and ~ 1 min for temperatures 296-574 K.

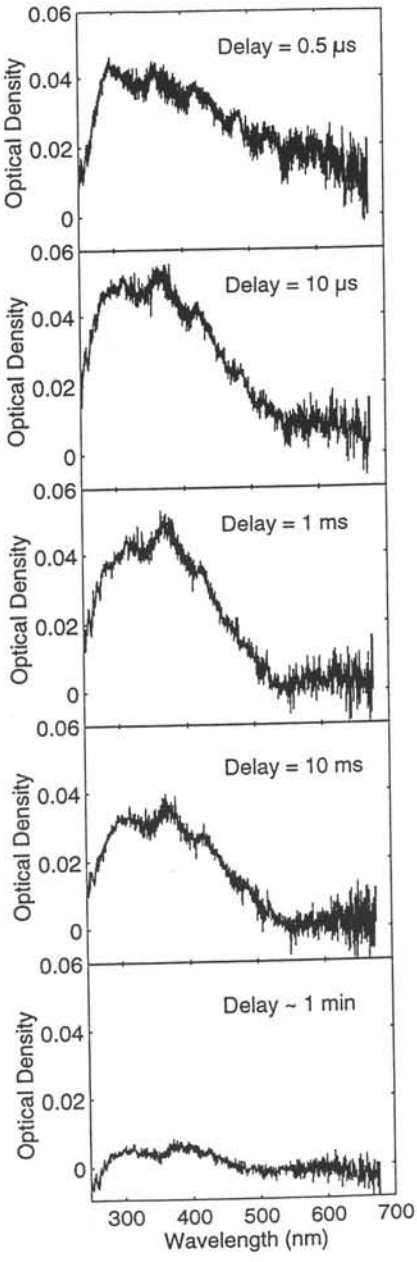

Fig. 2 Absorption spectra of LaF_3 at 289 K, at the indicated times after electron pulse.

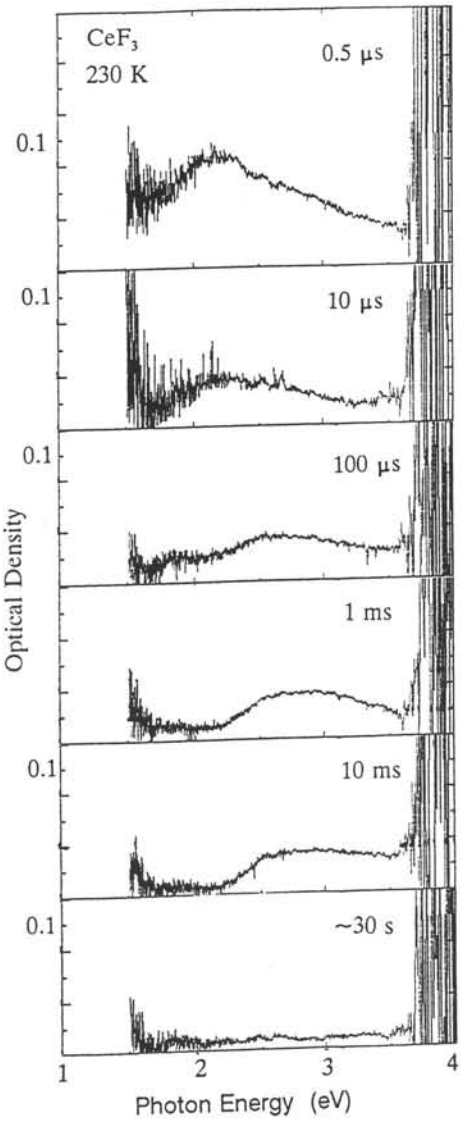

Fig. 3 Absorption spectra of CeF_3 at 230 K, at the indicated times after electron pulse.

previously in steady-state experiments. [2-4] At 10 K and 69 K, the stable spectrum remaining after 1 min preserves the same basic shape as the 0.5 μs spectra; i.e. there are no significant new bands in the low-temperature transient spectra. However, above about 170 K the absorption becomes almost entirely transient, with only a small absorption remaining at 1 min. At 289 K, the absorption near 580 nm decays within ~10μs, leaving mainly three blue/ultraviolet bands at 300 nm, 365 nm, and 420 nm, as shown in Fig. 2. Above room temperature, only bands at about 300 nm and 390 nm are seen in the transient spectra, and negligible absorption survives at 1 min. The 580-nm band which dominates the spectrum at low temperature and has been attributed to F centers completely vanishes even in the 5-μs transient spectra. The 390-nm band lasts for times of order 10 ms from 296 to 574 K, and almost nothing is observable after ~ 1 min.

Transient absorption in CeF_3 was also studied. Figure 3 illustrates that at 230 K, the spectrum observed consists primarily of the 2.1-eV peak which has been attributed to the F center. Within 1 ms, it decays and a 2.9-eV peak appears. These main bands in the visible transient spectrum are not the same as observed in steady state of irradiated CeF_3 annealed to the corresponding temperatures [5] but our 2.1-eV transient band is similar to the F center band polarized $\perp$ c axis suggested in Ref. [3].

Part of the motivation for undertaking this work was that the existence of self-trapped excitons (STEs) in LaF_3 has been suggested [6], and EPR evidence for V_k centers has been found [4]. In alkali halides and alkaline earth fluorides, STEs exhibit quite strong transient absorption spectra distinct from those of stable defects. The present measurements show reasonably strong transient absorption in LaF_3, but it is not obviously different from defect bands seen in steady state. Below 415 K, extrinsic fluorine vacancies exist mainly on the F2, F3 sublattices of LaF_3, whereas above 415 K, vacancies significantly populate the F1 sublattice [7]. Perhaps a faster absorption measurement than 0.5 μs could track the F-center spectra in this interesting range.

Acknowledgments

RTW was supported in Nagoya by a fellowship of the Japan Society for the Promotion of Science. The work of YZ and RTW was partially supported by NSF grants DMR-9206745 and DMR-9510297. We thank B. C. McCollum of Optovac for preparation of the samples.

References

[1] manufactured by Varian Inc.

[2] A. J. Wojtowicz, A. Lempicki, D. Wisniewski, C. Brecher, R. H. Bartram, C. Woody, P. Levy, S. Stoll, J. Kierstead, C. Pedrini, D. Bouttet, and Cz. Koepke, **Scintillator and Phosphor Materials**, MRS Symp. Proc. Vol. 348 (1994), p. 455.

[3] E. Radzhabov and A. I. Nepomnayashikh, to be published.

[4] E. D. Thoma, H. W. Shields, Y. Zhang, B. C. McCollum, and R. T. Williams, in these Proceedings.

[5] L. E. Halliburton and G. J. Edwards, **Scintillator and Phosphor Materials**, MRS Symp. Proc. Vol. 348 (1994), p. 423.

[6] W. W. Moses, S. E. Derenzo, M. J. Weber, A. Ray-Chaudhari, and F. Cerrina, J. Luminescence **59**, 89 (1994).

[7] A. F. Aalders, A. F. M. Arts, and H. W. de Wijn, Phys. Rev. B**32**, 5412 (1985).

OXYGEN IMPURITY IN CERIUM FLUORIDE SCINTILLATION CRYSTAL

Gang Chen, Shaoxia Ren, Chunshen Zhang, Chuiping Li, Xiaohong Chen
Beijing Glass Research Instituete, Beijing 100062

ABSTRACT

Experiments have shown that some cerium fluoride crystals have absorption peaks in UV range. The wavelength of these peaks overlap that of the crystal's scintillation light. Therefore, the light output of the crystals is reduced by self absorption. The longer the crystal, the more obvious the decrease. The decrease is not uniform between the two ends of the crystal suggesting uneven impurity distribution. Two different annealing conditions were performed to understand the effects of oxygen impurities in cerium fluoride crystal. One crystal was annealed in a humid atmosphere and another was embedded in cerium oxide powder. In order to reduce oxygen impurities so that cerium fluoride crystal's light output and radiation hardness are maximized, the cerium fluoride raw material synthesis technique, crystal growth parameters, and the vacuum condition are all of importance.

1. INTRODUCTION

Cerium Fluoride(CeF_3) crystal has been identified as a good scintillator candidate for applications of high energy physics experiments and nuclear medicine[1,2]. It has a high density to yield a short radiation length, is not hygroscopic and has sufficient fluorescence with short decay lifetime. The radiation damage of CeF_3 has also been investigated. CeF_3 seems to be a highly radiation resistive crystal[3]. However, two strong absorption bands at 340 nm and 385 nm appeared in the transmission curves of some crystals after irradiation[4]. The effects of doping some metal ions on the properities before and after irradiation were investigated. Some ions such as Ba^{2+} ion are able to improve the radiation resistance[5]. OH^- and O^{2-} ions are correlated with some absorption bands, which was first reported by Gao Ming[6]. This paper reports the futher result on their effects in the crystal and the growth technique issues to reduce their contents in the crystal.

2. EXPERIMENT

The raw material of CeF_3 was compounded with the solution of $Ce(NO_3)_3$ and HF acid. The collected sediment of CeF_3 powder from solution was purified and dried. This material was then redried and mixed with PbF_2 as an oxygen scavenger before the growth

$$Ce(NO_3)_3 + HF \rightarrow CeF_3 + HNO_3$$

Proc. Int. Conf. on Inorganic Scintillators and Their Applications, SCINT95,
1996, Delft University Press, The Netherlands

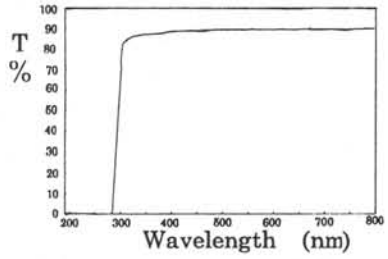

Fig.1 Transmission spectra of CeF_3 crystal

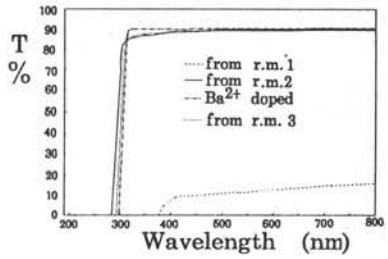

Fig.2 Transmission spectra of CeF_3 grown from different raw material

Table 1. Relation between the CeF_3 Crystal Property and Its Raw Material

Raw Materialfrom	Vendor 1	Vendor 2	Vendor 3
Marked Purity	99.99%	99.95%	99%
Color	white	light yellow	yellow
Crystal Length	50mm	50mm	50mm
Optical Quality	bad	good	good
Scintillation	bad	good	good
Absorption BandEdge	---	285 nm	288 nm

Two different annealing conditions were performed to further understand the effects of oxygen impurities in cerium fluoride crystal. One crystal was annealed in a humid atmosphere. And another was embedded in ceriun oxide powder annealed in a high vacuum. Fig.5 shows the transmission of CeF_3 crystal before and after heat treatment under humid air. The effect from H_2O in the air is weak at 300 ℃ and becomes much stronger at the temperture of 420 ℃ .Some white and opaque substances were formed. This is mainly the results of the folowing chemical reaction:

$$CeF_3 + H_2O \rightarrow Ce(OH)_xF_{3-x} + HF\uparrow$$

Here "x" ranges from 1 to 3. $Ce(OH)_xF_{3-x}$ decomposes at a higher temperture to CeOF which is a yellow substance. The other heat treatment was to embed samples in ceriun oxide powder annealed at 400 ℃ in a high vacuum. The resulting transmission curve is shown in Fig.6. An absorption band at 340nm was caused by the CeO_2 powder. The surfaces of the crystal after the treatment was changed to a yellow color. After repolishing the surfaces, its transmission level recovered back to that of original sample. It means that the treatment within CeO_2 affects the crystal surfaces only and oxygen diffusion is slow at 400℃.

process. The crystals were grown by the Bridgman method in high vacuum environment followed by a suitable annealing technique to prevent cracking of the crystal ingot. Transparent and crack-free crystal ingots with maximum size of $35 \times 35 \times 300$ mm^3 were grown in our laboratory. The samples for investigating the effects of oxygen ions were annealed in different oxygen environment. Transmission curves were measured with a HITACHI UV-3210 spectrophotometer.

3. RESULTS AND DISCUSSION

Fig.1 is a typical transmission curve of a CeF_3 crystal. Its absorption band edge is at 285nm. The highest level of the transmission is 89.1% at visible range. The raw materials from 3 sources for crystal growth were investigated to compare their effects on crystal transmission. Table 1 and Fig.2 shows the relation between the crystal property and the raw materials. The crystal grown from Vendor 3 with a 99 % purity only has a good transmission while the crystal from Vendor 1 with a 99.99% has a poor transmission. A similar phenomenon is also here while the purity of raw material from Vendor 2 is 99.95%. It means the transmission level is not related with the purity which usually means the content of metal ion impurities in the raw material. Because the contents of some anions such oxygen ions can not be measured in CeF_3, the purity of the raw material noted by vendors does not take into account the contents of oxygen ion impurities as well as the metal ions. So it is possible the transmission level of the crystal is related with the contents of anion impurities. On the other hand, the wavelength of the absorption bands is related to the listed purities as illustrated in Fig.2. The higher the purity is, the shorter absorption edge is, when crystals is good enough. Doping one weight percent Ba^{2+} moves the band to longer wavelengths. It was deduced in Reference 4 that the band edge position is strongly coupled to the density of fluorine vacancies in the lattice which changes the local crystal field seen by the Ce^{3+} ions.

Another typical curve is shown in Fig.3 which is slanting towards short wavelegths with two wide absorption bands. The wavelength of these bands overlap that of the crystal's scintillation light. Therefore, the light output of the crystals is reduced by self absorption. A Cerium Oxide doped crystal makes clear the effects of oxygen impurities as shown in Fig.4. It has a similar curve as shown in Fig.3.

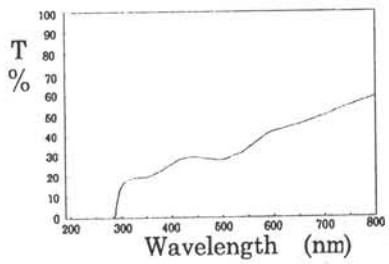

Fig.3 Another Transmission curve of CeF_3 crystal

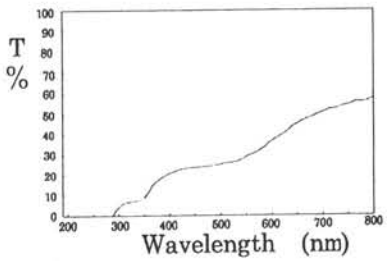

Fig.4 Transmission spectra of cerium oxide doped CeF_3 crystal

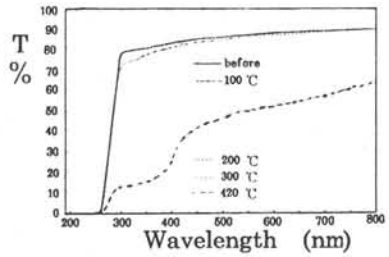

Fig.5 Transmission spectra of CeF_3 crystal before and after heat treatment under humid air

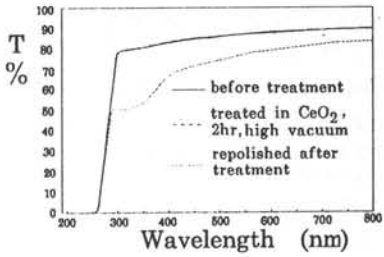

Fig.6 Transmission spectra of CeF_3 crystal before and after heat treated in CeO_2 powder

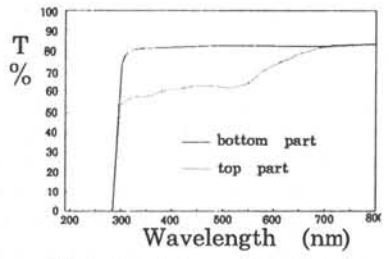

Fig.7 Transmission spectra at bottom and top parts along a long crystal

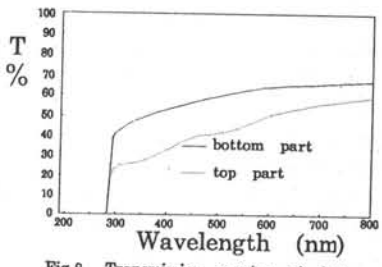

Fig.8 Transmission spectra at two two parts along the long crystal after 10 Mrd gamma irradiation

Figs.7 and 8 show that the absorption bands are not uniform between the two ends of the crystal that we infer it was caused by impurity distribution. It is revealed that crystals with oxygen impurities also exhibit increase radiation damage.

Studies of the harmful effects of OH^- and O^{2-} on the radiation resistance of BaF_2 crystals have been carried out successfully[7,8]. Summarizing the works of CeF_3 crystal we find that the reduction of oxygen impurities, the cerium fluoride raw material synthesis technique, crystal growth parameters, and the vacuum condition are all of importance to insure the light output of CeF_3 and radiation hardness are maximized.

REFERENCE

[1]. D.F. Anderson, IEEE Trans. Nucl. Sci. NS-36(1989)137.
[2]. W.W.Moses and S.E.Derenzo, IEEE Trans. Nucl. Sci. NS-36(1989)173.
[3]. M.Kobayashi et al., Nucl. Instr. and Meth. A302(1991)443.
[4]. Futher Results on Cerium Fluoride Crystals, Crystal Clear Collaboration, Feb., 1993
[5]. G.I. Britvich et al., Nucl. Instr. and Meth. A308(1991)509, A321(1992)64
[6]. Gao Ming et al., Nucl. Instr. and Meth. A348(1994)163
[7]. G.Chen et al., Internal Note, GEM TN-92-78
[8]. L.Y.Chen, M.Gu, L.M.Wang et al., Internal Note, GEM TN-92-129

F AND V_K CENTERS IN LaF_3, CeF_3 CRYSTALS

E.Radzhabov and A.I.Nepomnyashikh
Vinogradov Institute of Geochemistry, Academy of Sciences, Siberian Branch, Favorskii street 1a, P.O.Box 4019, 664033 Irkutsk, Russia, e-mail:eradzh@igc.irkutsk.su

Abstract. Optical absorption properties of additively colored in calcium vapor and X-irradiated crystals with tysonite structure, LaF_3 and CeF_3, were studied in 1.5-5.5 eV energy range. Photobleaching with 1.9 eV light and dichroism of the absorption bands were investigated.

The absorption band at 3.75 eV which annealed above 80K is observed in X-irradiated LaF_3, similar to the V_k-centre-bands observed in other fluorides. No such band is observed in X-irradiated CeF_3. For X-irradiated LaF_3 and CeF_3, at temperature below 110K the photo-bleachable, dichroic bands are observed: for two bands near 2 eV -band perpendicular to c-axis, near 2.7 eV -band along c-axis.

In additively colored CeF_3 absorption bands at 1.7 eV, 2.15 eV are observed. These bands can be attributed to F centers. F centers occupying the vacancies of fluoride F(1) layers in X-irradiated crystals and F-centers occupying all fluoride vacancies in additively colored crystals are proposed to be observed. Additive coloration upon heating in calcium vapor did not produce any new absorption band in LaF_3 crystals while formation of metallic inclusions, most likely La precipitates were observed.

INTRODUCTION

Lanthanide trifluorides have rather complicated crystal lattice of tysonite type. Each lanthanide ion surrounded by 11 fluorine ligands. There are three different types of fluoride ions in the crystal cell, with different Madelung potentials [1]. F(1) fluorides build fluoride layers in the lattice; F(2), F(3) fluorides build mixed La-F layers. The lanthanide trifluorides containing Ce, Nd, Pr are the promising materials for scintillators. In spite of their chemical simplicity the defects created by ionizing radiation are not well understood.

V_k centers in LaF_3, CeF_3 crystals were studied by ESR [2]. It was found 3-line hyperfine pattern in ESR of LaF_3 following x-ray irradiation, with g= 2.00 and total splitting of 1740 Gauss when B is along the c axis. These values correspond closely with the parameters of V_k centers in other fluoride crystals and authors tentatively assign this as the V_k resonance. This ESR signal anneals at about 70 K [3].

The optical absorption spectra of the Co^{60} irradiated crystals at 77 K are formed by many absorption bands in the 1.5-4 eV range with broad maxima at 1.7 and 2.4 eV. The investigation of transformation of these centers shows that the observed absorption bands have to be assigned to electronic centers [4].

In this paper the optical absorption spectra of F and V_k centers as well as optical dichroism of their absorption were studied in CeF_3 and LaF_3.

EXPERIMENTAL

The crystals were grown by Stockbarger method. Purification from oxygen was obtained by addition of PbF_2 to the extent of about 1-3 wt. %. The mixture is slowly heated under vacuum up to melting point. Crystals are grown under vacuum 10^{-3} - 10^{-4} torr.

The crystals were additively colored in calcium vapor in vacuum above 700°C. The samples were placed into stainless steel tube and evacuated to near 10^{-2} torr. The 0.2 - 0.4 g of metallic calcium is placed into another boat. Then the samples were heated 2-3 hours at 700-950°C. Apart from alkaline-earth fluorides a metallic layer, probably calcium, forms on the surface of LaF_3 and CeF_3. Nevertheless both crystals were colored. The coloration depth was

Proc. Int. Conf. on Inorganic Scintillators and Their Applications, SCINT95,
1996, Delft University Press, The Netherlands

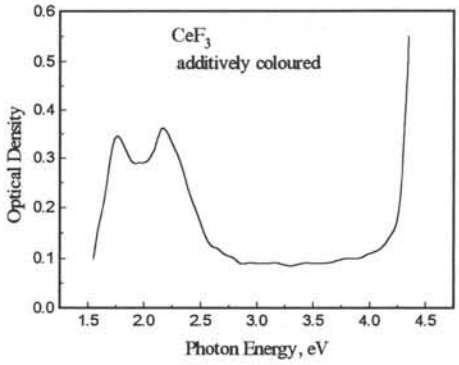

Fig 1. Optical absorption of additively colored CeF_3 crystal at room temperature.

about 1-2 mm per hour at 750°C . After slowly cooling the samples were sawed and polished. Before measuring the additively colored crystals were annealed at 700 to 900°C for about 5 min. and rapidly cooled in air. To avoid the contact with air under annealing the sample (particularly CeF_3) was surrounded by Cu foil. Nevertheless the additional polishing is necessary for CeF_3.

X-irradiation was produced by W tube operated at 40 kV, 40 mA. All absorption spectra were measured at 80 K. Photobleaching was done by 200 W halogen lamp through filter with 1.9 eV high energy edge.

RESULTS

Additive coloration

Results of the coloration were sharply different in LaF_3 and CeF_3. LaF_3 crystals have a metallic shine after the coloration. Into microscope one can see a metallic inclusion more than 10 μm. These inclusions are probably precipitates of metallic La. No new absorption bands were seen in spectra of additively colored LaF_3. These metallic precipitates disappeared above 950°C but no absorption bands appeared after quenching.

CeF_3 crystals were blue colored after additive coloration. Apart from LaF_3 no precipitates were observed into microscope in these crystals. Two main absorption bands at 1.7 and 2.15 eV appeared in CeF_3 samples quenched from 900°C (Fig.1). No dicroism of these bands was observed at room temperature. After long storage at room temperature the bands at 2.5, 2.7 eV also are appeared. The additive coloration disappeared above 900°C .

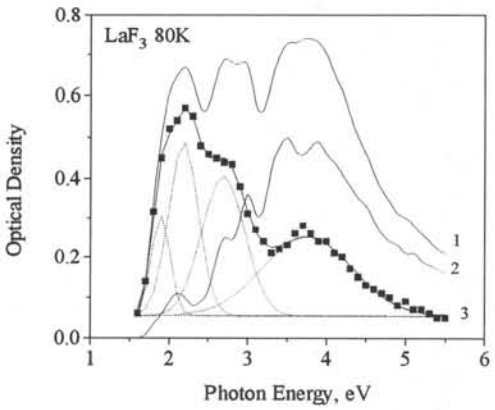

Fig. 2 Photobleaching of x-irradiated LaF_3 by 1.9 eV light at 80 K. Curve 1 - after X-irradiation , curve 2 - after subsequent 1.9 eV light irradiation, curve 3 is difference of curves 1 and 2. Curve 3 fitted by four gaussians (dashed curves).

X-ray irradiation

LaF_3 The X-irradiation of the crystals leads to the creation of electronic centers as well as hole centers. Several absorption bands are created by X-irradiation at 80K (Fig.2). The 3.75 eV band in LaF_3 was disappeared below 115 K. The glow peak observed during this process. Moreover after X-ray irradiation the crystals had a slight blue luminescence in the dark. The 3.75 eV and other bands were slightly decreased with keeping at 80K. All other bands are extremely easy photobleached simultaneously by 1.9 eV light or light from 2.2 or 2.7 eV bands. Therefore all three bands belong to one type center. The 1.9 and 2.2 eV centers are oriented perpendicular to the c-axis and 2.7 eV - along the c-axis (Fig.3).

CeF_3 Some bands at 1.5-3 eV region disappear at 90-120 K temperatures in the X-irradiated CeF_3 crystals. Similar to LaF_3 the low energy transitions at 1.7, 2.1 eV are oriented perpendicular to the c- axis and 2.6 eV centers - along the c-axis. This bands can be easy photobleached by red light.

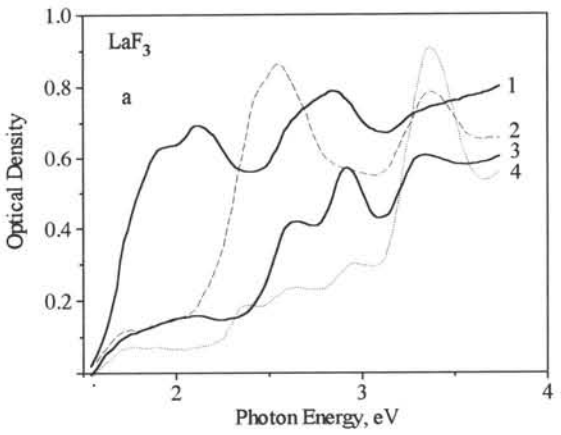

Fig 3. Dichroism of absorption of LaF_3 crystals at 80 K. Curves 1,3 were measured perpendicular to c-axis, curves 2,4 - parallel to the c axis. Curve 1, 2 were measured after X-irradiation , curves 3 and 4 were measured after subsequent bleaching with 1.9 eV light.

DISCUSSION

Additive coloration

In many additively colored crystals the quenching procedure leads to appearance the single F centers rather than F center aggregates. Therefore it may be suggested that the 1.7, 2.15 eV bands in quenched additively colored CeF_3 belong to F centers.

X-ray irradiation

LaF_3 The V_k center ESR spectrum in LaF_3 [2] closely matched the spectra of V_k centers in other fluoride crystals. One can expect that the ultraviolet V_k absorption band has to be in the range of 3.5-4 eV as in other fluorides. Therefore we assume that the absorption band at 3.75 eV with halfwidth 1.1 eV belongs to the V_k centers.

The ESR spectrum of V_k centers is annealed above 70K [3]. Our experimental results show that the V_k centers absorption band slowly annealed at 80K. Possibly at 80K experiments we see the only V_k and F centers which are spaced in the lattice good enough to survive during 1 hour of x-irradiation.

We assume that the 1.9, 2.2 and 2.7 eV in X-irradiated LaF_3 are bands of the F centers as these bands are closed to F centers bands in CeF_3 and show similar dichroism.

CeF_3 No absorption band at V_k region (3-4 eV) in CeF_3 is annealed within 80-120K. This is consistent with absence of the V_k spectrum in ESR of CeF_3 [2].

The 1.7, 2.1 eV bands are rather close to 1.7 ,2.15 eV bands of F centers in additively colored CeF_3 crystals. The smaller 2.6 eV band which can be seen apparently only in dichroism spectrum (see Fig.4) also belongs to this centers. Therefore the absorption bands at 1.7, 2.1 and smaller 2.6 eV band in X-irradiated CeF_3 belong to the F centers.

F-centers absorption

Although the actual unit cell has trigonal symmetry and six molecules, we shall make use of the simpler hexagonal unit cell with only two molecules (see also [5]). Fluoride ions have three different symmetry positions in the lattice. The F(2) and F(3) fluorides have the same positions in hexagonal unit cell. The F(2) (or F(3)) and F(1) sites have a D_{3h} and C_{3v} symmetries respectively. Due to low symmetry of the crystal structure the 1s-2p absorption band of F centers has to be splitted into two bands. F center has allowed $A_1 \rightarrow A_1, A_2''$ ($E \parallel c$) and $A_1 \rightarrow E, E''$ ($E \perp c$) transitions.

It is known from crystal field theory that overlapping of central ion orbital with negative ligands leads to increase of its energy [6]. Owing to the calculation of F centers in BaFCl, SrFCl [7] one can conclude that the overlapping with positive ion orbitals also leads to the similar result. Considering the p_x, p_y, p_z orbital overlapping with nearest ions we can qualita-

tively estimate the order of A and E states for both fluoride sites. The p_z orbital of F center in mixed F(1), F(2) layers are not overlapped with surrounding ions (Fig.4). The p_x,p_y orbitals sufficiently overlap with three La^{3+} ions. Therefore the E'' level has to be at higher energy than A_2'' level. The reverse order of A_1 and E levels is estimated for F center from fluoride F(1) layer (see Fig.4).

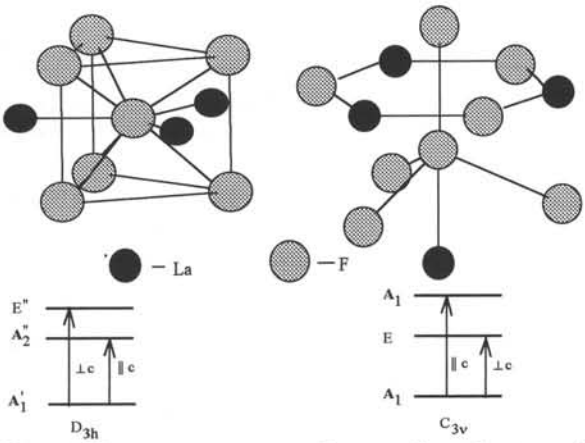

Fig. 4 Nearest environment for two fluoride sites of LaF_3 hexagonal lattice. The left picture belongs to the F(2), F(3) fluoride sites from mixed layer. The right picture belongs to F(1) sites from fluorine layer. The symmetry groups and possible order of energy levels are shown at the bottom.

Experimental results are shown that in X-irradiated crystals F centers occupied one type of fluoride vacancies, possibly F(1) vacancies. The difference in F centers absorption of X-irradiated and additively colored CeF_3 crystals is obviously caused by the occupation of both type anion vacancies in additively colored samples at room temperatures.

CONCLUSION

The V_k centers have 3.75 eV absorption band. The centers were observed only in LaF_3.

F bands are shown in the Table. The F centers' transitions near 2 eV oriented perpendicular the c-axis and transitions near 2.7 eV oriented along the c-axis in x-irradiated LaF_3, CeF_3 crystals. It is assumed that the F centers occupy the vacancies at fluoride F(1) layers in X-irradiated crystals.

Crystal	Coloration procedure	Absorption, eV	Orientation to c-axis	T, K
CeF_3	additive	1.7, 2.15		295
CeF_3	X-ray	1.7, 2.2 2.6	perpend. paralell	80
LaF_3	X-ray	1.9, 2.1 2.7	perpend. paralell	80

ACKNOWLEDGMENTS

This work was partially supported by a grants N 26072, 28052 from State Committee of Education of Russia. The authors are grateful to Figura P., Mironenko S. and Krasin A. for preparation of crystals. The authors are also grateful to professor Williams R.T. for informing them of the results of a paper prior to publication.

References

1. Van Gool W. and Piken A.G.1969 *J.Mater.Sci.* **4** 95
2. Williams R.T., Thoma E.D. and Shields H.W. 1994 *Record of the International Workshop Physical Process in Fast Scintillators (PHYSCI-94) (St.Petersbourg State Technical University, St.Petersbourg)* p 49
3. Williams R.T. 1995 private communication
4. Sheulin A.S., Korolev N.E. and Ryskin A.I. 1994 *Record of the International Workshop Physical Process in Fast Scintillators (PHYSCI-94) (St.Petersbourg State Technical University, St.Petersbourg)* p 70-74
5. OlsonC.G., Piacentini M. and Lynch D.W. 1978 *Phys.Rev.B* **18** 5740
6. Murrell J.N., Kettle S.F.A. and Tedder J.M. 1978 The Chemical bonds, J.Willey & Sons, N.Y. 382 p.
7. Lefrant S. and Harker A.H. 1976 *Sol.St.Communications* **19** 853

OPTICAL AND EPR STUDIES OF LaF_3 AND CeF_3 UNDER X-RAY IRRADIATION

E. D. Thoma, H. Shields, Y. Zhang, B. C. McCollum*, and R. T. Williams
Department of Physics, Wake Forest University, Winston-Salem, NC 27109 USA
*Optovac, North Brookfield, MA 01535 USA

The EPR spectrum of the V_k center in LaF_3 is presented, and its probable site is suggested. Luminescence of LaF_3 (4 ppm Ce) was measured from 33 K to 700 K, revealing that host-to-Ce energy transfer operates well at low and high temperatures, but is inhibited near 300 K in favor of a weak, broad 360-nm luminescence band. The 7-line "F-center" EPR resonance in CeF_3 is shown to be comprised of two independent defects with triplet and quartet hyperfine patterns of equal splitting.

Figure 1 shows the EPR spectrum (9.27 GHz) of LaF_3 before and after x-ray irradiation at 25 K. The irradiation was for 30 minutes at 40 kV, 10 mA, filtered by 0.5-mm fused silica. The LaF_3 crystal was grown at Optovac from 99.999% starting material using methods chosen to minimize oxygen impurity, and was determined to contain 4 ppm cerium impurity. The crystal was oriented with its c axis along the magnetic field for the measurement of Fig. 1. It can be seen that the x-irradiation induces a 3-line hyperfine pattern at $g \approx 2.0$ having approximately 1:2:1 intensity distribution, consistent with two equivalent spin-1/2 (fluorine) nuclei. The magnitude of the splitting, 870 Gauss, is very close to V_k-center hyperfine splittings in alkali fluorides and several other fluoride compounds. As the crystal's c axis was rotated away from the magnetic field direction, the outer lines moved in slowly and split slightly, indicating that the defects have multiple orientations making small equal angles with the c-axis. We have surveyed the possible fluorine-fluorine pairs in the LaF_3 structure, as summarized in Table 1. Only one type of pair, the first entry in Table 1, satisfies the condition of making a small non-zero angle (15°) with the c axis. It turns out also to be the pair with the smallest fluorine-fluorine separation (2.568 Å). There are 3 orientations of such pairs making 15° angles with the crystal c axis, as illustrated in Fig. 2. Within the LaF_3 structure, these pairs are composed of one fluorine from each of the F1 puckered layers flanking a La-F2-F3 mixed layer. (F1, F2, F3 denote the three different types of fluorine sites in LaF_3).

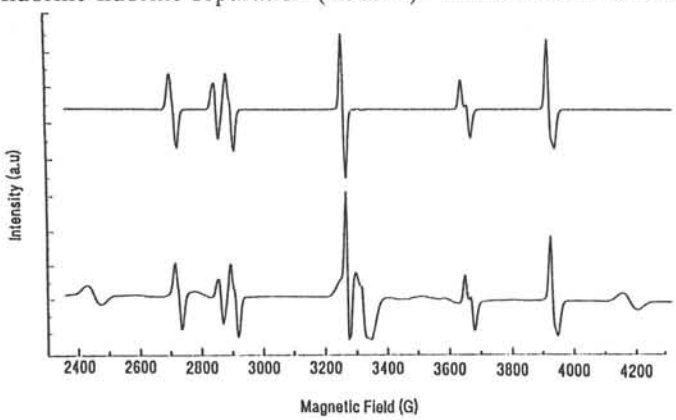

Fig. 1 EPR spectra before (top) and after (bottom) x-irradiation of LaF_3 at T = 25 K. Magnetic field parallel to c axis.

Proc. Int. Conf. on Inorganic Scintillators and Their Applications, SCINT95,
1996, Delft University Press, The Netherlands

	DISTANCE(Å)	θ_c(deg)	NUMBER OF ORIENTATIONS	NUMBER OF PAIRS
F1---F1(min)	2.568	15.0	3	6
F1---F1(4--1)	2.687	63.6	3	6
F1---F1(10--1)	2.734	64.1	3	6
F2---F2(min)	3.767	0	1	2
F2---F2	4.254	77.2	1	2
F3---F3(min)	3.767	0	1	1
F1---F2(min)	2.701	50.7	6	12
F1---F2	2.868	46.8	6	12
F2---F3(min)	4.175	83.5	3	12
F1---F3	2.754	63.2	6	12

Table 1 Fluorine ion pairs which might be the sites of hole self-trapping.

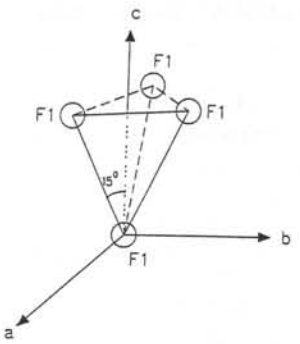

Fig. 2 Illustration of the three orientations of F1-F1(min) pairs.

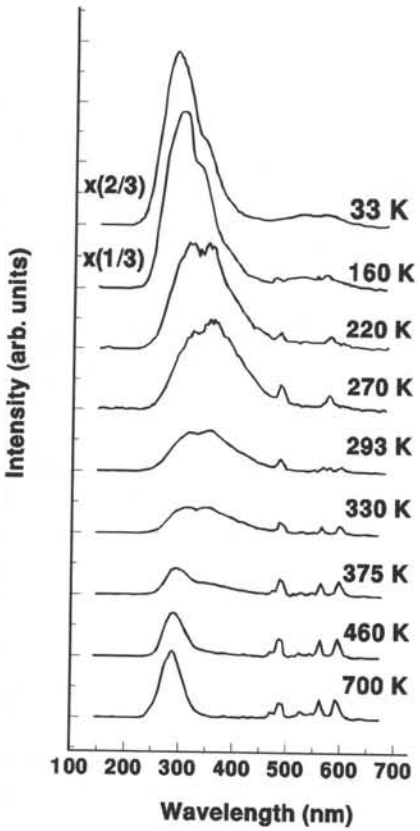

Fig. 3 Luminescence of LaF_3 (4 ppm Ce) excited by x rays at the temperatures shown. Note reduced scale at low T.

The notations (4-1) etc. refer to specific positions in the unit cell, discussed in a more detailed paper.[1] The V_k EPR resonance vanishes when temperature is raised above about 65 K, which we take to be the temperature threshold of V_k mobility.[2]

Figure 3 shows x-ray excited luminescence of LaF_3 (4 ppm Ce) from 33 K to 700 K. At low temperature, the spectrum is dominated by the very dilute Ce impurity. Around room temperature, the 300 nm Ce^{3+} 5d-4f luminescence vanishes, leaving a weak, broad 360 nm luminescence band suggested by Moses et al [3] to be due to self-trapped exciton luminescence. The (non-exponential) lifetime of this luminescence has been measured [4] as roughly 10 μs at 296 K. Continuing to higher temperature, it is seen that the cerium impurity luminescence returns to dominate the spectrum once again. This seems not consistent with quenching of the cerium excited state at room temperature, but consistent with inhibition of energy transfer from the LaF_3 host to dilute Ce impurity at room temperature. We suggest that the excitation (exciton or charge carriers) may have band mobility at low temperature, which is inhibited by thermally activated trapping near room temperature. At sufficiently high temperature, hopping mobility of the trapped excitations or carriers could restore energy transfer to the dilute Ce impurity, as observed.

Figure 4(a) shows the radiation-induced EPR resonance near g = 2 in CeF_3, suggested to be due to F centers.[5] Figure 4(b) shows that by selective annealing to 135 K, four lines of the 7-line pattern disappear first. There are two independent defects; one giving a triplet hyperfine pattern and the other a quartet, with the same hyperfine splitting of 22 G and the same g-value. One is a spin interacting with two equivalent fluorine nuclei and the other a spin interacting with three equivalent fluorine nuclei. Cerium has no nuclear spin, so these cannot be the nearest-neighbor cations interacting with an F-center electron. In the next-nearest shell (fluorines) there are more than 3 equivalent neighbors, and one expects very weak overlap of the electron wavefunction there. The identification of this resonance is somewhat problematic at present.

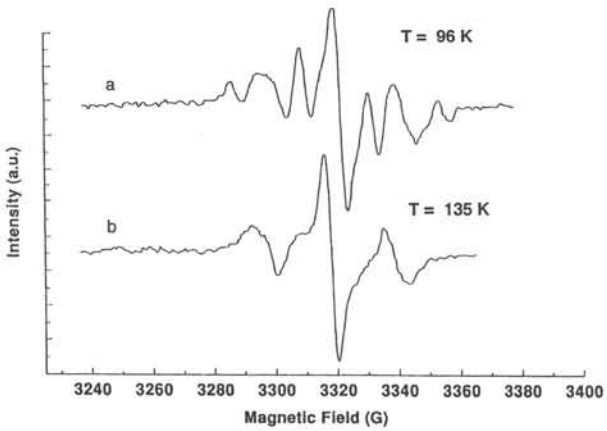

Fig. 4 EPR spectra of radiation-induced defects centered at g ≈ 2.0 in CeF_3, measured at 96 K (top) and at 135 K (bottom). The lower spectrum was shifted -5 G for display.

Acknowledgments

This work was supported by NSF grants DMR-9206745 and DMR-9510297. We thank D. L. Alov for helpful discussions.

References

[1] E. D. Thoma, H. W. Shields, Y. Zhang, B. C. McCollum, and R. T. Williams, to be pub.

[2] We first presented the V_k EPR resonance in LaF_3 in an oral report at the International Conference on Physical Processes in Scintillators (PHYSCI94), St. Petersburg, Oct. 1994. In that report, the annealing temperature was over-estimated as ~ 100 K, due to too-rapid heating. The present value of 65 K is correct.

[3] W. W. Moses, S. E. Derenzo, M. J. Weber, A. Ray-Chaudhari, and F. Cerrina, J. Luminescence **59**, 89 (1994).

[4] Y. Zhang, R. T. Williams, C. Itoh, and K. Tanimura, in these proceedings.

[5] L. E. Halliburton and G. J. Edwards, in **Scintillator and Phosphor Materials**, MRS Symp. Proc. Vol 348 (1994), p. 423.

LUMINESCENCE PROPERTIES OF RARE EARTH TRIFLUORIDES

N.Yu.Kirikova, V.E.Klimenko and V.N.Makhov
Lebedev Physical Institute, Moscow 117924, Russia

ABSTRACT

Emission properties of pure rare earth trifluorides have been studied under pulsed vacuum UV and X-ray synchrotron radiation excitation. Emission bands in the vacuum UV (150-180 nm) spectral range were detected for NdF_3, ErF_3 and TmF_3. The bands are due to the allowed $5d \rightarrow 4f$ transitions in rare earth ions and have subnanosecond decay times. Measurements of excitation spectra in the vacuum UV spectral range clearly demonstrate that the process of impact excitation is the dominant one for the excitation of the $5d \rightarrow 4f$ emission in rare earth trifluorides.

INTRODUCTION

Since 1989 cerium fluoride crystal has been considered as one of the most promising fast scintillator for applications in high-rate detectors of ionizing radiation [1,2]. Besides CeF_3, some other rare earth (RE) trifluorides with parity-allowed $5d \rightarrow 4f$ radiative transitions can be discussed as possible fast scintillators with decay times in nanosecond range. During last years a demand for vacuum ultraviolet (VUV) scintillators has been arised for radiation detectors which employ photosensitive gases (like TMAE or TEA) sensitive to VUV photons. This has led to a search for new scintillating materials emitting in the VUV range. In particular, it was found [3] that similar to Nd^{3+} doped LaF_3 crystals [4] NdF_3 has an emission band situated in the VUV region and having decay time less than 1 nsec. In the present work emission properties of all RE trifluorides (exept PmF_3) have been studied in the spectral range 120–520 nm.

EXPERIMENT

All measurements have been carried out under synchrotron radiation excitation at the S-60 (Lebedev Physical Institute, Moscow) electron synchrotron. Emission spectra (in the range 120–520 nm) and decay curves were measured under soft X-ray ($E \sim 1$ keV) excitation using 0.5 m Seya-Namioka-type analyzing monochromator. The spectral resolution of the monochromator was about 2 nm. Measurements were performed at temperatures 90 and 300 K. All emission spectra were corrected on the monochromator/detector response function and are presented in units 'emitted photons per constant wavelength interval'. The details of the set-up for emission excitation spectra measurements were presented elsewhere [5].

All samples were high purity powders with the concentration of the uncontrollable rare earths and other metals admixtures of about 0.0005–0.001 % and mostly contaminated with oxygen being present with the concentration of about 0.02–0.05 %.

RESULTS AND DISCUSSION

Unlike CeF_3, most of other RE trifluorides emit in visible and UV spectral regions only narrow lines which are due to parity-forbidden $4f \rightarrow 4f$ transitions with decay times much longer than in CeF_3. For example for PrF_3 (Fig.1) there were detected several emission bands which are due to transitions from the highest $^1S_0$ level to different levels of the ground $4f^2$ configuration of Pr^{3+}: $^1S_0 \rightarrow {}^1I_6$ (400 nm), $^1S_0 \rightarrow {}^1D_2$ (337 nm), $^1S_0 \rightarrow {}^1G_4$ (273 nm), $^1S_0 \rightarrow {}^3F_4$ (253 nm), $^1S_0 \rightarrow {}^3H_4$ (217 nm). The decay times of all these bands exceed or are of the order of 100 ns. Nevertheless the weak 217 nm band has the admixture of the fast component the fraction of

Proc. Int. Conf. on Inorganic Scintillators and Their Applications, SCINT95,
1996, Delft University Press, The Netherlands

which increases strongly at lowering temperature from 300 to 90 K. This is probably due to the fact that the lowest excited 5d4f state lies very close to the $^1S_0$ state of the 4f configuration and a weak 5d4f $\rightarrow$ 4f^2($^3H_4$) band is observable in this spectral range. Another possible reason of the fast emission at 217 nm is the admixture of Nd^{3+} ions in PrF_3.

Several emission bands with subnanosecond decay times were observed in the UV and vacuum UV range for NdF_3 (Fig.1). The bands are due to radiative transitions from the lowest level of the excited 4f^{2}5d configuration to various levels: $^4I_{15/2,13/2,11/2,9/2}$ (173 nm), $^4F_{9/2,7/2,5/2,3/2}$ (217 nm), $^4G_{11/2,9/2,7/2,5/2}$ (247 nm) of the ground 4f^3 configuration. The decay time of these bands is less than 1 ns that can be seen from Fig.2 where decay curves for 217 nm band of NdF_3 and 220 nm band of BaF_2 (well-known cross-luminescence band with decay time 0.8 ns) are shown for the comparison.

No intrinsic emission bands were detected for SmF_3, EuF_3, HoF_3 and YbF_3 in the studied spectral range. For GdF_3 (Fig.3) several narrow bands (with long decay times) were observed in the UV range which are due to 4f $\rightarrow$ 4f intraconfiguration transitions to the ground $^8S_{7/2}$ state from different excited levels: 312 nm ($^6P_{7/2}$), 278 nm ($^6I_{7/2}$), 254 nm ($^6D_{9/2}$), 217 nm and 206 nm. In TbF_3 the multiplet band around 495 nm was detected (the lines at 488, 493 and 498 nm were resolved) which is due to 4f intraconfiguration transitions $^5D_4 \rightarrow {}^7F_6$ (ground state) and a very weak emission due to $^5D_3 \rightarrow {}^7F_6$ transitions was observed near 400 nm. In DyF_3 the band centered near 460 nm and consisting of several narrow lines was detected which is due to $^4F_{9/2} \rightarrow {}^6H_{15}$ (ground state) transitions.

Emission properties of RE trifluorides for RE's with almost completely filled 4f-shell should be similar to those of RE's from the beginning of the lanthanide's series because they have similar energy levels scheme (but with the reversed order of terms with the different value of the total momentum J) of the ground 4f configuration. In particular, similar to the case of the impurity emission of RE^{3+} ions in different matrices [6,7], 5d $\rightarrow$ 4f radiative transitions can be observed for some "heavy" RE trifluorides. In our measurements the emission bands in the 150$\div$180 nm spectral region were detected for ErF_3 and TmF_3 (Fig.4). The bands have doublet-like structure, the shortwavelength subbands being the dominant ones. The intensity of the bands is several times higher at 90 K compared with that at 300 K and the shortwavelength subbands are more dominant at low temperature. Decay times of the bands are similar to those of NdF_3 and lie in the nanosecond range. Thus these bands can be attributed to the interconfiguration transitions from the lowest levels of excited 4f^{n-1}5d configuration to different terms near the ground state of the 4f^n configuration. Various narrow bands due to 4f $\rightarrow$ 4f transitions (with longer decay times) are also observed in ErF_3 and TmF_3 in the UV and visible ranges but their intensities are much lower than those of VUV bands.

LuF_3 has a wideband emission (FWHM = 1.2 eV) centered near 265 nm at 300 K. At 90 K the maximum of the band is shifted to shorter wavelength and is situated near 235 nm. The emission intensity is higher by a factor of 10 at 90 K compared with that at 300 K and a doublet structure of the band can be observed (with the splitting equal to about 0.35 eV). The decay time of this emission is rather long (definitely longer than hundreds nanoseconds) and cannot be measured by used set-up. The ground state of Lu^{3+} ion with completely filled 4f-shell is $^1S_0$ (only one term) and its first excited configuration is equivalent to that of Pr^{3+} (4f5d). The most probable nature of this band is some kind of the exciton emission in LuF_3.

The process of impact excitation of the RE^{3+} ions emission seems to play the dominant role among all possible mechanisms of emission centers excitation in RE trifluorides [3,8-14]. The effect is clearly observed in excitation spectra [3,8-10] as a sharp increase of RE^{3+} emission intensity at photon energies above 15$\div$17 eV corresponding to the threshold of this process: $E_{th} \simeq E_g + E_R$, where E_g is the band gap ($\simeq$ 10$\div$11 eV) and E_R is the energy of the direct optical excitation of the RE^{3+} emission. While the efficiency of the "recombination" mechanism of RE^{3+} emission excitation (which should occur at photon energies $E_g < h\nu < E_{th}$) is usually very low just after the energy of 'hot' photoelectron becomes high enough ($h\nu >$ 12-13 eV) for the creation of the separated electron and hole. The effect is well pronounced for the excitation of 5d

$\rightarrow$ 4f emission in CeF_3, NdF_3, TmF_3 and 4f $\rightarrow$ 4f emission in PrF_3. But in EuF_3, GdF_3, TbF_3 and HoF_3 the efficiency of the "recombination" mechanism of the 4f $\rightarrow$ 4f emission excitation is also rather high. The competition of different mechanisms of RE^{3+} emission excitation depends probably on the position of energy levels of RE^{3+} ion in the bandgap.

CONCLUSIONS

The nanosecond VUV emission (in the range 150-180 nm) for three RE trifluorides (NdF_3, ErF_3, TmF_3) has been detected using pulsed synchrotron radiation excitation. These compounds can be recommended as possible fast VUV scintillators. Their densities are: 6.51 (NdF_3), 7.82 (ErF_3), 7.95 (TmF_3) g/cm^3 [15]. ErF_3 and TmF_3 have two modifications of the lattice structure. Nevertheless ErF_3 has the temperature of the phase transition close to the melting point, i.e. it is possible to obtain large crystals of ErF_3 (of both modifications) [15]. Besides ErF_3 is relatevily cheap (comparable with CeF_3) [15] and so it can be regarded as promising fast scintillator with the emission in the VUV range.

ACKNOWLEGEMENTS

The authors would like to thank V.A.Antonov for provoding the samples. The support of the INTAS 93-2554, ISF N9Y000 and ISF N9Y300 Grants is gratefully acknowleged.

REFERENCES

1. D.F.Anderson, IEEE Trans. Nucl. Sci **NS-36** (1989) 137.
2. W.W.Moses and S.E.Derenzo, IEEE Trans. Nucl. Sci. **NS-36** (1989) 173.
3. Yu.M.Aleksandrov, V.N.Makhov, T.V.Uvarova and M.N.Yakimenko, Sov.Phys. - Lebedev Inst. Rep. **6** (1990) 46.
4. P.Dorenbos, C.W.E. van Eijk, R.W.Hollander and P.Schotanus, IEEE Trans. Nucl. Sci. **NS-37** (1990) 119.
5. Yu.M.Aleksandrov, V.N.Kolobanov, V.N.Makhov, T.I.Syrejshchikova and M.N. Yakimenko, J.Appl. Spectrosc. **36** (1982) 659.
6. K.H.Yang and J.A.DeLuca, Appl.Phys.Lett. **29** (1976) 499.
7. K.H.Yang and J.A.DeLuca, Phys.Rev **B17** (1978) 4246.
8. Yu.M.Aleksandrov, V.N.Makhov, M.N.Yakimenko, Sov.Phys.- Solid State **29** (1987) 1092.
9. Yu.M.Aleksandrov, V.N.Makhov, M.N.Yakimenko, Nucl.Instr.& Meth. **A282** (1989) 597.
10. Yu.M.Aleksandrov, V.N.Makhov and M.N.Yakimenko, Rev. Sci. Instr. **63** (1992) 1466.
11. V.N.Makhov, in "Heavy Scintillators for Scientific and Industrial Applications", Proc. "Crystal 2000" Int. Workshop, 1992, p.167.
12. I.A.Kamenskikh, M.A.MacDonald, V.N.Makhov, V.V.Mikhailin, I.H.Munro and M.A. Terekhin, Nucl. Instr. & Meth. **A348** (1994) 542.
13. A.J.Wojtowicz, M.Balcerzyk, E.Berman and A.Lempicki, Phys.Rev. **B49** (1994) 14880.
14. A.N.Vasil'ev, in press.
15. B.P.Sobolev, in "Crystal Fluorides for Radiation Detectors", 1994, p.93.

FIGURE CAPTIONS

Fig.1. Emission spectra of CeF_3, PrF_3 and NdF_3 at 300 K.
Fig.2. Decay curves of the emission of NdF_3 (217 nm) and BaF_2 (220 nm) at 300 K under X-ray excitation.
Fig.3. Emission spectra of GdF_3, TbF_3 and DyF_3 at 300 K.
Fig.4. Emission spectra of ErF_3, TmF_3 and LuF_3 at 90 K.

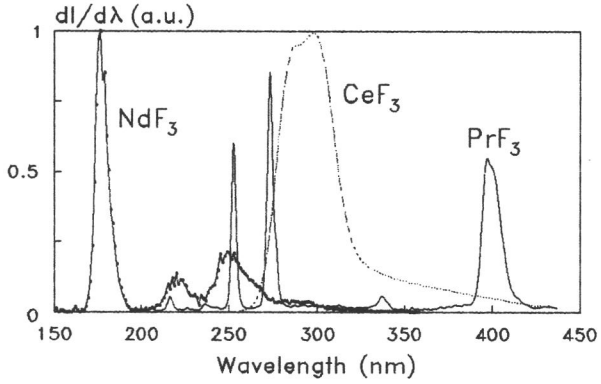

Fig.1.

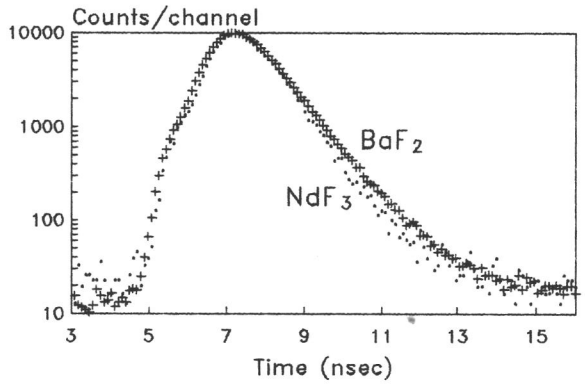

Fig.2.

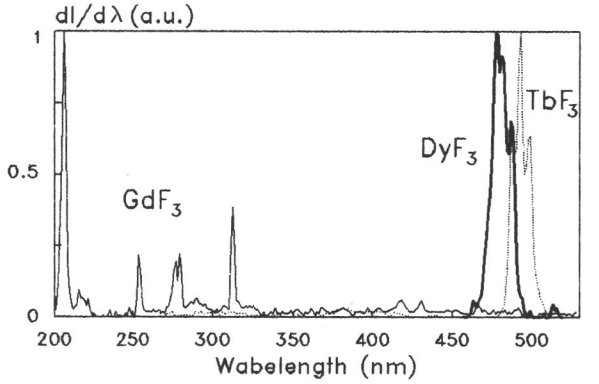

Fig.3.

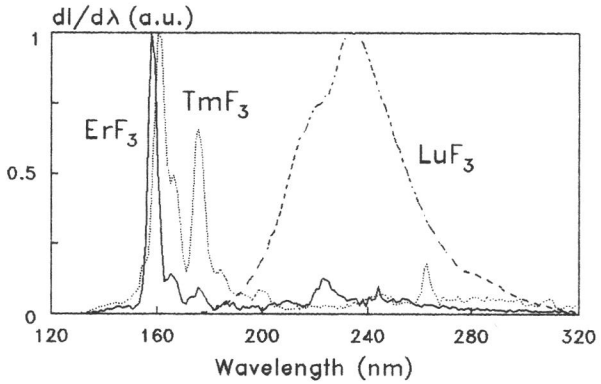

Fig.4.

NEW FEATURES OF CORE-VALENCE TRANSITIONS IN IONIC CRYSTALS

P.A.Rodnyi, Experimental Physics Department, State Technical University,
Polytechnicheskaya 29 , 195251 St.Petersburg , Russia

INTRODUCTION

In recent time both investigators and practicing engineers have come to the conclusion that non-doped crystals such as BaF_2, CsF, CeF_3 etc. can be used as scintillators. In such crystals there is no problem of an uniform impurity distribution throughout the sample. Besides, pure compounds possess usually higher radiation hardness as compared to doped ones. It is well known that intrinsic luminescence in halide crystals has usually excitonic nature. The excitonic luminescence is quenched below room temperature for most of the crystals. The new type of luminescence associated with hole transitions between upper core and valence bands possesses stability of parameters within a wide temperature range [1]. High thermal stability, short decay time (0.6 - 3.0) ns and relatively high light yield of the crystals with core-valence (CV) transitions show that they are promising materials for the fast scintillators.
The CV luminescence has been revealed [2] and clarified [3] for BaF_2 in the beginning of the eighties. Recently a possibility of light amplification due to population inversion between the valence and upper core bands in BaF_2 has been demonstrated [4]. A short decay component (0.4 ns) of CV luminescence has been discovered in BaF_2 at VUV excitation [5]. At irradiation by Ar-ions, the BaF_2 exhibited a decay time as short as 240 ps [6]. The model of CV transitions has been checked for a number of alkali halides crystals: KF, RbF, CsF, CsCl and CsBr [7]. Next step was the investigation of CV transitions in ternary [8] and mixed [9] compounds.
This paper presents some recent results of CV luminescence investigation obtaining in St.Petersburg State Technical University in collaboration with Daresbury Laboratory and Lviv Technical University.

EXPERIMENTAL

A pulsed X-ray tube (40 kV, 0.1 A, pulse duration 1 ns, frequency 20 kHz) together with the single photon counting method was used for X-ray excitation and detection of light emission in the UV and visible region. Vacuum ultraviolet and X-ray excitation was performed at SRS at Daresbury Laboratory (pulse duration 130 ps, the periods were 2 and 240 ns in multibunch and singlebunch modes respectively). A 1 m Seya-Namioka monochromator with 1200 and 2400 grooves/mm gratings was used, the wavelength resolution being about 0.8 nm for all measurements. The luminescence was detected at a right angle to the beam through the secondary monochromator or appropriate filters with the help of quartz-window R1688-01 photo-multiplier. The quantum yield as a function of excitation energy was corrected for the excitation light spectrum and the beam current of SRS.

RESULTS AND DISCUSSION

The increase of light output of CV luminescence is one of the important tasks. We undertook fforts to solve this problem changing and complicating the crystal compositions. Two types of

Proc. Int. Conf. on Inorganic Scintillators and Their Applications, SCINT95,
1996, Delft University Press, The Netherlands

crystals have been studied: 1)The crystals containing CV-active ions (Cs^+, Rb^+, Ba^{2+}) as one of the cations, e.g. compounds with perovskite and elpasolite structure. These crystals display the intrinsic CV luminescence; 2) The crystals containing the CV active ions as activators and possessing so-called impurity CV luminescence.

The investigations showed that some perovskite-structure crystals such as $CsCaCl_3$ and $RbCaF_3$ give higher light yield comparing with corresponding binary crystals (CsCl, RbF). The elpasolite-structure crystals $Cs_2NaLaCl_6$ and Cs_2KLaCl_6 also exhibit large light yield. The complex crystals also allow to vary the emission wavelength and slightly the decay time.

It is established now that the shape of the CV luminescence spectrum is related to the symmetry of nearest-neighbour anionic environment of the CV-active ion [1]. More detailed understanding of the nature of radiative CV transitions has been obtained for the Cs-doped chlorides on the basis of a cluster calculation by means of the scattered-wave X_α method [10]. The crystals with co-ordination number 6, 8 and 12 should give one, two and three emission bands, respectively. This statement has got a row of experimental confirmations [7,9,11]. Thus, for one type of transitions (5pCs $\rightarrow$ 3pCl), by varying the composition of the radiative cluster $[CsCl_6]$, $[CsCl_8]$, $[CsCl_{12}]$ different emission spectra can be obtained.

The incorporation of CV-active ions in crystals without CV luminescence also gives possibility to vary the luminescent parameters. Figure 1 the presents luminescence excitation spectrum for a pure $KCaCl_3$ crystal (curve 1) for which the condition for creation of CV luminescence is not fulfilled It can be compered with the spectrum for a $KCaCl_3$-RbCl crystal (curve 2). One can see that the crystal $KCaCl_3$-RbCl displays a threshold near 17 eV typical for 4pRb $\rightarrow$ 3pCl transitions.

The two upper core bands (4pRb and 3pK) of $KCaCl_3$-RbCl crystal do not overlap and therefore the CV luminescence has low efficiency. Large efficiency of CV luminescence can be obtain in a crystal with overlapping upper core bands (5pCs and 4pRb). For instance, the intensity of X-ray excited luminescence of Rb_{1-x} Cs_xCaCl_3 at $x > 0.04$ is higher than that of CsCl [9].

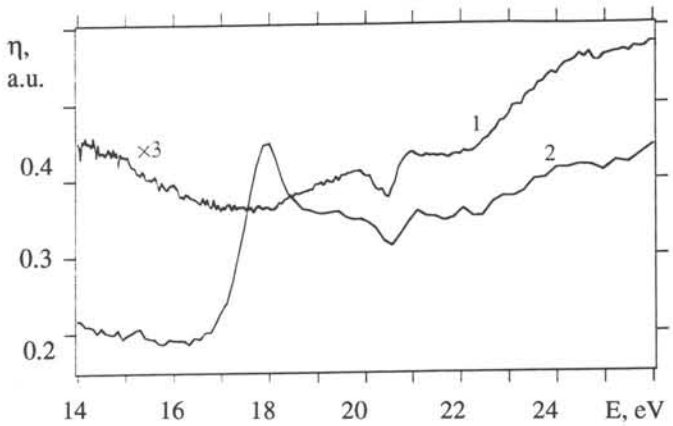

Fig.1

Luminescence excitation spectra of undoped (1) and Rb (3%) doped (2) $KCaCl_3$ crystals at 295 K

Particular attention should be given to the yield dips at 20.4 eV (Fig.1), i.e. in the region of 3pK core excitons creation. Similar dips have been observed in the yield spectra of some alkali halides, CaF_2 [12] and $RbCaCl_3$ [9]. The effect is most pronounced for 2pNa, 3pK and 3pCa core excitons. The mechanism of decay of core excitons becomes clear from photoelectron spectroscopy experiment [13].It has been found that the nonradiative decay of the 2pNa core excitons in sodium halides occurs through the following process: the core hole forming a core

exciton recombines with a valence electron which is excited to the continuum state. Two valence holes and one band electron (trion) are produced in the final stage of this core-exciton decay. An electron excited from 2pNa level to higher excited states without having a chance to recombine directly with hole. So the dips in luminescence excitation spectra (Fig. 1) can be associated with nonradiative decay of 3pK core excitons.

The first measurements of intrinsic (excitonic) luminescence excitation spectra in X-ray region have revealed a stepwise decrease of light yield near of K-absorption edge in CaF_2 [14], KBr [15] and KCl [15,16]. Authors explained the spectral features in terms of X-ray fluorescence [14,15] or F-centre production [16]. Of some interest is the study of CV luminescence excitation spectra near the K-edge in scintillator crystals. We have chosen to study two typical CV scintillators CsCl and $RbCaF_3$ which do not possess an exitonic emission at room temperature. In CsCl crystal (emission bands 4.4 and 5.2 eV), the stepwise decrease of light yield near the K-edge of Cs (35.9 keV) has been detected. The decrease of CsCl light yield (17%) is less than in case of excitonic luminescence (more than 50% in KCl [16]). The decay time of CV luminescence (0.9 ns) is the same below and above the K-edge. The CsCl crystal keeps an almost exponential decay of emission over three orders of magnitude and very low level of afterglow is observed.

The $RbCaF_3$ crystal possesses a large energy yield (about 1%) of 4.3 eV emission band at X-ray excitation . The excitation spectrum of $RbCaF_3$ also displays a stepwise decrease in the Rb K-edge region (15.2 keV). One can see from Fig.2 that below and above the K-edge the light yield increases linearly, i.e. the relative yield is constant. The decay time of $RbCaF_3$ luminescence (2.8 ns) does not change in the used range of energy of incident quanta.

The obtained data show that the K-edge stepwise decrease is typical for both kinds of intrinsic luminescence: CV and excitonic ones. Little is known concerning the detailed physics and nature of this phenomena. It is clear that the efficiency of X-ray fluorescence in X-ray excited

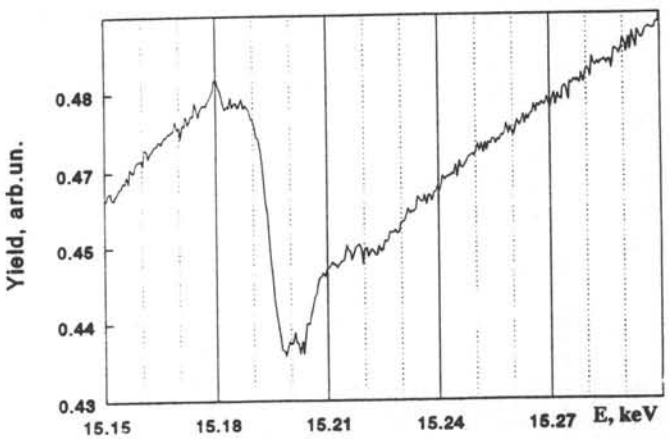

Fig.2

Luminescence excitation spectra of $RbCaF_3$ around the absorption K-edge of rubidium

crystals is too small to explain the observed decrease of intrinsic luminescence [16]. Another possible reason of the phenomena is the increase in the F-centre formation yield above the K-edge which has been detected in a KBr crystal [17] but not studied for other compounds.

It should be noted that scintillation efficiency of a crystal strongly depends on the separation of electron and hole capable to take part in the recombination process. Mobility of holes in ionic crystals is significantly less than one for electrons. That is why the carrier separation is determined by the energy spectrum of the created electrons. The energy distributions of secondary electrons at excitation below and above the K-edge are different due to a distinction of hole decay cascade involving Auger effect and recombination process [18]. It is

known that a crossing of K-edge causes a distinct shift in the secondary electron spectrum. Quite recently [19] it has been shown using Monte Carlo simulation for NaI-Tl that at energy of incident quanta 33 keV i.e. below iodine K-edge (33.164 keV), roughly 35% of energy is distributed amongst secondary electrons with energy less than 5 keV. For energy of X-rays 34 keV, this value decrease to 17% [19]. This distinction would have a profound impact on the light yield of a scintillator around the absorption K-edge. On the other hand, the narrow minimum in the yield spectrum of $RbCaF_3$ (Fig.2) points to the fact that nonradiative decay of core excitons like for VUV excitation can play a role in creation of the stepwise decreases in X-ray region.

REFERENCES

1.Multicomponent Crystals Based on Heavy Metal Fluorides for Radiation Detectors / ed. by B.P.Sobolev, Barcelona, 1994.

2.N.N.Ershov, N.G.Zakharov and P.A.Rodnyi, Opt. Spectrosc. **53** (1982) 89.

3.Yu.M.Aleksandrov, V.M.Makhov, P.A.Rodnyi, Sov. Phys. Solid State, **26** (1984) 2865.

4.M.Itoh and H.Itoh , Phys. Rev. **B46** (1992) 15509.

5.Y.Nunoya, J.Ruan (Gen) and S.Kubota, Nucl. Instr.and Meth. in Physics Research **A337** (1994) 632.

6.K.Kimura and J.Nada, Phys.Rev. **B 48** (1993) 15535.

7.P.A.Rodnyi and M.A.Terekhin, Phys. Stat. Solidi (b) **166** (1991) 283.

8.A.P.Shpak, O.A.Gluke, A.G.Dmitriev, P.A.Rodnyi, A.S.Voloshinovskii and S.M.Pidzyrailo, J. of Electron Spectroscopy and Related Phenomena, **68** (1994) 335.

9.P.A.Rodnyi, I.H.Munro, M.A.Macdonald, E.N.Mel'chakov, S.S.Kotelnikov and A.S.Voloshinovskii, Nucl. Instr. and Meth. in Physics Research, **B88** (1994) 407.

10.A.S.Voloshinovskii, V.B.Mikhailik, P.A.Rodnyi, S.V.Syrotyuk, A.P.Shpak and A.N.Yares'ko, Sov. Phys. Solid State, **36** (1994) 911.

11. A.S.Voloshinovskii, V.B.Mikhailik, S.V.Syrotyuk, P.A.Rodnyi, Phys. Stat. Solidi (b), **172** (1992) 739.

12.J.H.Beamount and A.J.Bourdilon, J.Phys. C **9** (1976) L479.

13.M.Kamada, D.Aita, K.T.Ishikawa and K.Tsutsumi, Phys.Rev. **B36** (1987) 4962.

14.A.Bianconi and D.Jackson, Phys. Rev. **B17** (1976) 2021.

15.M.Yanagihara, Y.Kondo, T.Hanyuu and S.Yamaguchi, Solid State Commun. **68** (1988) 345.

16.Y.Kondo, S.Hoshina, M.Yanagihara, H.Kimura, T.Hanyuu and S.Yamaguchi, Solid State Commun. **80** (1991) 431.

17.B.R.Sever, K.Kristianpoller and F.C.Brown, Phys.Rev. **B34** (1986) 1257.

18.P.A.Rodnyi, P.Dorenbos and C.W.E.van Eijk, Phys. Stat. Solidi (b) **187** (1994) 15.

19. M.Marsman, A Theoretical Approach to the Nonproportional Response in the Detection of Gamma Quanta by Scintillators, Delft TU, June 1995.

EFFECT OF QUENCHING PROCESSES ON DECAY OF FAST LUMINESCENCE FROM BaF_2

R.A.Glukhov[1], M.Kamada[2], S.Kubota[3], E.Nakamura[2], S.Ohara[2], M.A.Terekhin[4], A.N.Vasil'ev[1]
[1] Physics Department, Moscow State University, Moscow 119899 Russia
[2] Institute for Molecular Science, Myodaiji, Okazaki 444 Japan
[3] Rikkyo University, Nishi-Ikebukuro 3 Tokyo 171 Japan
[4] RRC 'Kurchatov Institute', Moscow 123182, Russia

ABSTRACT

The problem of two types of luminescence quenching and non-exponential decay kinetics due to interaction with surface states and with secondary excitations is studied for barium fluoride both experimentally and theoretically.

INTRODUCTION

Luminescence excited in VUV region usually have a non-exponential decay. There are several mechanisms of the luminescence quenching, i.e.

(i) dipole-dipole transfer from an electronic excitation (EE) to the surface centres;
(ii) diffusion of EEs to the surface with the following decay at the surface 'killers' (the quenching centres of recombination, the concentration of which is large at the surface);
(iii) dipole-dipole interaction between different EEs produced by the same excitation photon;
(iv) the same processes between EEs created by different exciting photons; etc.

This luminescence quenching is affected by the following energy transfer parameters:

- the photon penetration depth $1/k_{\text{eff}}(h\nu)$, which determines the initial spatial profile of the excitation distribution, $k_{\text{eff}}(h\nu)$ is the absorption coefficient for photons with energy $h\nu$;
- the total diffusion length $L = \sqrt{D\tau}$. This parameter controls the motion of EEs towards the surface, D is the diffusion coefficient, τ is the total EE lifetime;
- the dipole-dipole transfer distance R_0, which characterises the interaction between different EEs;
- the electron mean free path $l(E)$, which determines the mean distance between different EEs after inelastic scattering.

The process (i) is controlled by the ratio between R_0 and $1/k_{\text{eff}}(h\nu)$; (ii) — L and $1/k_{\text{eff}}(h\nu)$; (iii) — R_0 and $l(E)$; (iv) — R_0 and the mean distance l_m between EEs created by different photons. The aim of this work is to study the role of different quenching mechanisms of fast luminescence in wide-forbidden-gap insulators in a broad energy range of exciting photons. We investigate this problem both experimentally and theoretically.

EXPERIMENTAL PROCEDURES

In order to investigate the role of these types of quenching we have studied the decay curves of the BaF_2 cross-luminescence (CL) (fast nanosecond fluorescence band 220 nm) excited by photons with different energies (from 16 to 90 eV) at different angles of incidence (from 12^0 to 87^0). The variation of the angle of incidence changes the penetration depth as:

Proc. Int. Conf. on Inorganic Scintillators and Their Applications, SCINT95,
1996, Delft University Press, The Netherlands

$$1/k_{\mathrm{eff}}(h\nu,\theta)[\mathrm{cm}] = \frac{1.38\cdot 10^{-5}}{h\nu[\mathrm{eV}]\cdot\sqrt{\sqrt{\left(\varepsilon_1-\sin^2\theta\right)^2+{\varepsilon_2}^2}-\left(\varepsilon_1-\sin^2\theta\right)}}, \qquad (1)$$

where $\varepsilon_1(h\nu)$ and $\varepsilon_2(h\nu)$ are the real and imaginary parts of dielectric permittivity, respectively. This fact allows one to separate processes of type (i) and (ii) from that of (iii). The variation of the excitation energy changes not only the penetration depth, but also modifies the number and spatial distribution of secondary excitations due to the processes of EE multiplication, i.e. creation of new electronic excitations after inelastic scattering of a primary EE. Luminescence decay curves following the SR pulses were measured at UVSOR storage ring using devices described in Ref. [1, 2].

MONTE-CARLO SIMULATION

To investigate the role of quenching due to the dipole-dipole interaction between different EEs produced by the same excitation photon we have performed the Monte-Carlo (MC) simulation of the evolution of the excited region arising in the BaF_2 after the absorption of a VUV photon. The crystal is assumed to be uniform. So surface effects are not taken into consideration. We neglect some effects connected with excitons and more complex excitations, but partial account of these effects is present due to account for the Coulomb interaction between charged particles. Probabilities of elementary events involved in the relaxation process was calculated on the basis of simulated dielectric permittivity with account for the sum rules and simplified rectangle density of electron and hole states. The electron-phonon scattering rate is assumed to be energy independent (about 10^{14} s^{-1}). For more details concerning the MC simulation we refer to [3, 4].

This MC scheme allows one to evaluate the number of core holes $n(0)$ that is responsible for the CL, the number of quencheres $c(0)$ (these excitations represent all other types of EEs which can accept the core-hole energy) and the spatial distribution of secondary excitations produced in the relaxation process during 10^{-12} s after the absorption of an exciting photon, which is characterised by the two-particle n-c distribution function $G(r,0)$. So we can evaluate the CL intensity [3]:

$$I(t) \propto \int_{-\infty}^{t} I_b(t') e^{-(t-t')/\tau_r - Q(t-t')} dt', \qquad (2)$$

where $I_b(t)$ is the excitation bunch profile, τ_r is the radiation time for CL, $Q(t)$ is the quenching rate, which is connected with the non-radiative quenching as

$$Q(t) = -c(0)\int d^3r \frac{K(r)}{K(r)+\tau_r/\tau_c} G(r,0)\left[1-\exp\left(-\frac{t}{\tau_c}-\frac{K(r)t}{\tau_r}\right)\right], \qquad (3)$$

where τ_c is the radiative lifetime for quenchers, $K(r)=\left(R_0/r\right)^6$ is the probability factor of the dipole-dipole transfer from core holes to quenchers.

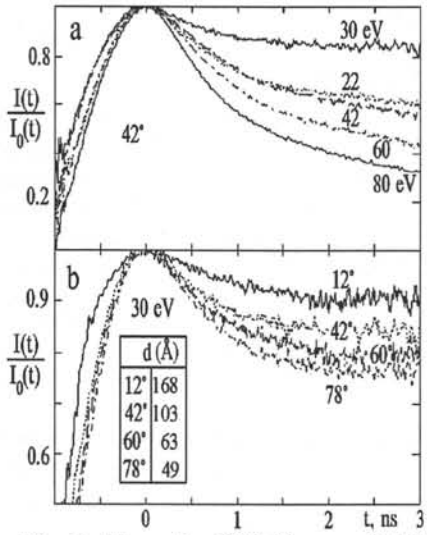

Fig. 1. The ratio $I(t)/I_0(t) = \exp(-Q(t))$ for BaF_2 at different excitation energies: (a) — 42°; 30 eV, 22eV, 42eV, 60eV, 80 eV; and different incidence angles: (b) — 30eV; 12°, 42°, 60°, and 78°. The values of the penetration depth d are presented in the figure. $I_0(t)$ is the convolution shown in Fig. 2, curve g.

RESULTS AND DISCUSSION

Surface quenching

For excitation energies below 30 eV only a primary electron can interact with a core hole. This type of quenching should not be very intensive. The main effect at these energies is due to the high absorption coefficient, it reaches 1.5×10^6 cm^{-1} (the penetration depth is 7 nm) [5]. For grazing angles of incidence the effective penetration depth can reach 3 nm. Thus, we conclude that the kinetics in this energy region is determined either by the diffusion to the surface or by the dipole-dipole transfer to the surface 'killers'. Formula (1) shows that the strong dependence on the angle can exist only for $\varepsilon_2 \leq 1$, whereas for $\varepsilon_2 > 1$ the angle dependence is weak. There are both such regions for photon energies below 30 eV [6]. Fig. 1 shows the strong angle dependence for $h\nu$ = 30 eV (where $\varepsilon_2 \leq 1$). Using the data from Ref. [6] and formula (1), one can obtain the values for the penetration depth $1/k_{\text{eff}}(h\nu,\theta)$, which is depicted in Fig. 1. At the energy $h\nu$ = 22 eV (where $\varepsilon_2 > 1$) the decay is much faster (Fig. 1), but the angle dependence is very weak (it is within the experimental errors). This fact correlates with weak angle dependence of the penetration depth (4.4 nm for $\theta = 12^\circ$, and 3.7 nm for $\theta = 78^\circ$).

There is an additional criterion to distinguish different types of quenching. Theoretical analysis of the surface quenching problem predicts that the asymptotic behaviour of the decay curves for different $k_{\text{eff}}(h\nu,\theta)$ differs only in pre-exponential factor [7]. Therefore the ratio of the curves for different penetration depth should be constant in the case of the surface losses. Such behaviour of decay curves is observed at $h\nu = 30$ eV, see Fig. 1 (b).

Quenching caused by secondary excitations

Fig. 2 presents the normalised CL decay curves for different energies. The conventional model of the CL, involving the radiative transition of the valence band electron to the uppermost core hole, predicts the single exponential decay law. The single exponential decay curve, calculated as the convolution of the excitation profile and exponential curve with $\tau_r = 0.92$ ns, is also displayed in Fig. 2. The kinetics is non-exponential for all energies. The deviation from the single exponential law increases with photon energy above 30 eV where the penetration depth $1/k_{\text{eff}}(h\nu,\theta)$ increases several times. Thus, the quenching effect cannot be attributed to the surface quenching. Therefore, these curves demonstrate the role of the quenching due to the increase of the mean number of secondary excitations. This conclusion is approved by MC simulations. The concentration of quenchers in the dipole-dipole interaction region of radius R_0 is directly proportional to the excitation energy in the region from 40 to 90 eV (see Fig. 3 (a)). The behaviour of the curves calculated from the pair distribution function

$G(r,0)$ using eqs. (2,3) (Fig. 3 (b)) is similar to the experimental one (Fig. 2). This fact confirms the validity of our supposition concerning the nature of CL quenching mechanism above 30 eV.

CONCLUSIONS

The present investigation shows that there are at least two different mechanisms of the luminescence quenching (the surface quenching and the energy transfer to the excitations produced by the same photon). The relative importance of these processes depends on the excitation energy: at energies below 30 eV the surface quenching dominates (which is demonstrated by the angle-of-incidence dependence of decay curves), whereas at higher energies the main quenching process is the energy transfer from the core hole to other electronic excitations, whose number increases linearly with the energy as it was shown by means of MC simulation.

Experimental data and theoretical calculations in the wide region of excitation energy allow one to separate different quenching mechanisms in ionic crystals.

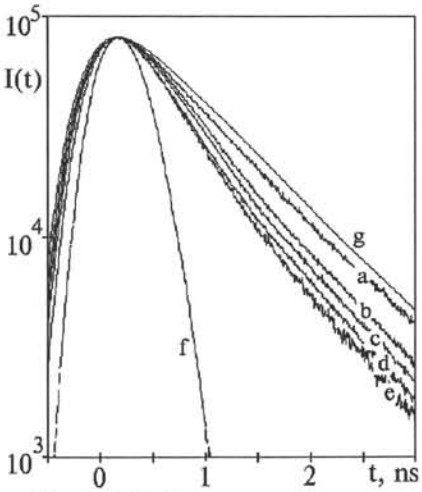

Fig. 2. BaF_2 fluorescence decay curves for different excitation energies: (a) — 30 eV; (b) — 40 eV; (c) — 52 eV; (d) — 70 eV; (e) — 90 eV; (f) — excitation profile; (g) — $I_0(t)$, i.e. the single exponential decay curve (τ = 0.92 ns) convoluted with the excitation profile. The radiation time τ_r is determined by fitting the asymptotic behaviour of the slowest decay curve (a).

REFERENCES

[1] S. Kubota, J. Ruan(Gen), M. Itoh, S. Hashimoto, and S. Sakuragi, Nucl. Instr. & Meth., A289, 253 (1990).

[2] M. A. Terekhin, A. N. Vasil'ev, M. Kamada, E. Nakamura, S. Kubota, Phys. Rev., B52, 3117 (1995).

[3] R. A. Glukhov, A.N.Vasil'ev, Material Research Society Symposium Proceedings, v. 348, 387, (1994).

[4] R. A. Glukhov, A.N.Vasil'ev, Radiation Effects and Defects in Solids, v. 133–134, (1995), in press.

[5] C. Tarrio, D. E. Husk, and S. E. Schnatterly, J. Opt. Soc. Am. B 8,1588 (1991).

[6] M. Yuri, N. Kanadaka, T. Kambe, S. Sato, H. Kato, H. Fukutani, J. Phys. Soc. of Jap. 61, 1829 (1992).

[7] A. N. Belsky, I. A. Kamenskikh, V. V. Mikhailin, A. N. Vasil'ev, in press.

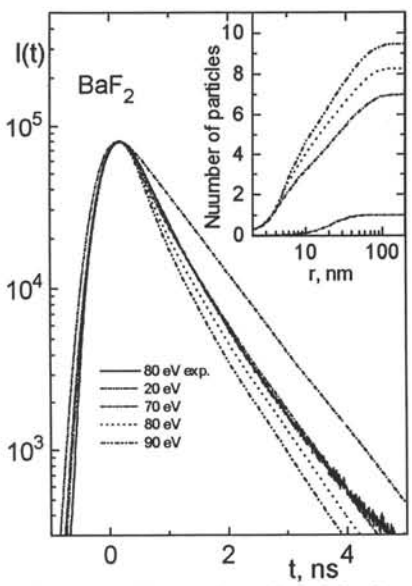

Fig. 3. (a) The number of particles in a sphere around the core hole vs sphere radius; (b) decay curves of CL from the Monte-Carlo simulation

THE TEMPERATURE DEPENDENCE OF CROSSLUMINESCENCE IN CsF

V.N.Makhov [1], I.A.Kamemskikh [2], M.A.Terekhin [3,4], I.H.Munro [4], C.Mythen [4] and D.A.Shaw [4]

[1]Lebedev Physical Institute, Moscow 117924, Russia
[2]Moscow State University, Moscow 117234, Russia
[3]RRC "Kurchatov Institute", Moscow 123182, Russia
[4]Daresbury Laboratory, Warrington, Cheshire WA4 4AD, UK

ABSTRACT

The spectroscopic and temporal characteristics of crossluminescence of CsF have been studied across the temperature range 20 to 300 K following vacuum ultraviolet (12 to 40 eV) synchrotron radiation excitation. The temperature behaviour of the crossluminescence bandwidth is well described by taking into account the electron-phonon interaction with the phonon frequency equal to Debye frequency. Crossluminescence decay kinetics in CsF reveal a non-monotonic dependence on temperature with the longest mean decay time being observed at about 150 K. The results can be well explained in terms of a model incorporating different mechanisms for crossluminescence quenching.

INTRODUCTION

Though discovered more than 10 years ago [1,2] the crossluminescence (CRL) phenomenon (known alternatively as Auger-free luminescence or as core-valence radiative transitions) is not well described by any existing theoretical models. In particular the non-exponential decay kinetics and complicated temperature dependence of the emission characteristics of CRL are only poorly explained. The non-exponentiality of CRL decay is usually attributed to various mechanisms for CRL quenching namely to near-surface quenching and to quenching resulting from the interaction with near neighbouring excitations [3-7].

Many experimental and theoretical studies [8-12] ascribe the wideband CRL emission to the recombination of valence band electrons with localised core holes, more correct to radiative transitions in "molecular complex" (cluster) arising after lattice relaxation around the localized core hole. However the role of free core holes in the CRL process is not yet certainely revealed. The emission bands due to radiative transitions involving free states of the core hole (and valence band electron) are expected to be very narrow [13] (of the order k_BT, where k_B is Boltzmann constant). The CRL spectrum of CsF where several rather narrow (less than 50 meV) bands have been observed seems to fit such a description.

EXPERIMENT

The spectral and time characteristics of CRL of CsF have been measured in the temperature range from 20 K to 300 K under VUV excitation by synchrotron radiation in the photon energy range from 12 eV to 40 eV. Measurements were carried out using a 1 m Seya-Namioka monochromator on station 3.1 at the SRS. The emitted light was analysed using a secondary visible/UV monochromator with a resolution of 5 nm or alternatively was selected using interference filters. The samples were mounted in a continuous flow helium cryostat (Oxford Instruments) with temperature controller ITC4. Standard single-photon counting was used for time-resolved measurements using "single bunch mode" operation of the SRS (using an XP2020Q photomultiplier as detector). The samples were high purity powders installed into the cryostat prior to vacuum pumping. The pressure in the cryostat was about 10^{-7} Pa.

RESULTS AND DISCUSSION

The CRL emission spectrum of CsF (Fig.1) consists of several emission bands, the 3.1 eV band being the dominant one. The latter band shows a strong dependence on temperature, the main changes being observed in the temperature range above 100 K. The characteristics of

Proc. Int. Conf. on Inorganic Scintillators and Their Applications, SCINT95,
1996, Delft University Press, The Netherlands

three narrow bands situated near 4.0 eV are independent on temperature within an accuracy of our measurements. At T < 50 K a strong emission band at 4.6 eV appears which is due to the emission of self-trapped excitons [14]. These results are similar to those obtained in [15] using X-ray excitation (in the temperature range T > 80 K).

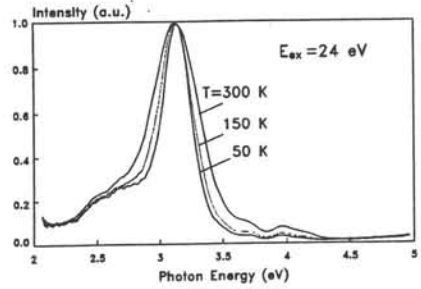

Fig.1. Crossluminescence emission spectrum of CsF at different temperatures. Excitation energy is 24 eV. Spectra are corrected to the monochromator/ detector response function and normalized to their maxima.

The 3.1 eV wideband emission is obviously due to transitions in the localized 'molecular cluster'. Taking into account the electron-phonon interaction the temperature dependence of the 3.1 eV band width can be written as [16]:

$$\Delta E = \Delta E_0[\coth(h\omega/2k_BT)]^{1/2} \qquad (1)$$

where ΔE_0 is bandwidth at T=0 K, ω the characteristic frequency of the local vibrational mode (frequency of phonons). The observed temperature dependence of the 3.1 eV band width is quite well described by this formula with the vibration frequency equal to Debye frequency ω_D (Fig.3) the value of which for CsF is $h\omega_D$= 24 meV (θ_D=276 K) [17].

The CRL decay law was observed to be non-exponential at all excitation energies and temperatures (Fig.2). The shape of the decay is the same for all CRL emission bands. At excitation energies between 14 and 25 eV, as is the case for other CRL crystals, the non-exponentiality of the decay seems to be the result of non-radiative surface losses [4-6]. At hν > 25 eV the processes of electronic excitations multiplication can influence on the kinetics of the CRL decay [5-7].

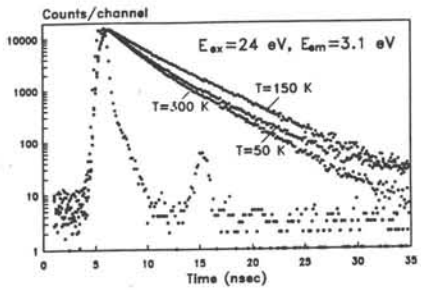

Fig.2. Crossluminescence decay curves of CsF at different temperatures. Excitation energy is 24 eV. Emission energy is 3.1 eV. The measured time profile of synchrotron radiation excitation pulse is also shown.

The temperature dependence of the CRL decay was measured at an excitation energy of 24 eV (i.e. before possible quenching due to multiplication processes is activated). Unlike the results obtained at X-ray excitation [15] it was found (Figs. 2 and 3) that decay kinetics of CRL in CsF at VUV excitation exhibit a strong and non-monotonic dependence on temperature, the longest mean decay time being observed at about 150 K. The temperature dependences of the decay kinetics are essentially the same for the 3.1 and 4.0 eV bands.

To characterise the quenching value of CRL from its kinetics we use the value of time for the decrease of the emission intensity by a factor of 10 ($I(t)/I_{max}$= 0.1). The temperature dependence of this parameter (Fig.3) is consistent with that of the integral quantum yield $\int I(\lambda,t)d\lambda dt$ of CRL.

Both migration and resonance energy transfer to the non-radiative surface states can lead to a non-exponential decay (quenching) of CRL. In the latter case, the decay of donor emission (CRL) can be described by the "Forster" formula [18]:

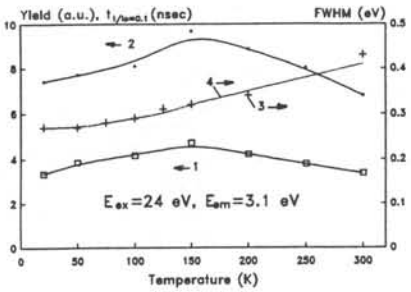

Fig.3. Temperature dependence of crossluminescence characteristics of CsF: 1 - the total light yield, 2 - $\tau_{1/10}$ of the 3.1 eV band, 3 - the measured FWHM of the 3.1 eV band, 4 - the calculated FWHM of the 3.1 eV band. Excitation energy is 24 eV.

$$I(t) = I_0 \exp(-t/\tau - at^{1/2}), \quad (2)$$

$$\text{where } a = 4/3\ \pi^{3/2} C_A R_0^3 \tau^{-1/2}, \quad (3)$$

τ is the radiative liftime, C_A the concentration of acceptor centres (surface states) and R_0 the interaction radius. Parameter a characterises the 'amount of quenching'. The decrease in the CRL bandwidth should result in a decrease of quenching because R_0 depends on the overlap integral, Ω, of the donor emission spectrum D(E) and the absorption spectrum A(E) of acceptor:

$$R_0 \sim \Omega^{1/6}, \quad (4)$$

$$\text{where } \Omega = \int D(E)*A(E)/E^4 dE, \quad (5)$$

$$a \sim R_0^3 \sim \Omega^{1/2}. \quad (6)$$

In the range from 150 to 300 K, the increase of quenching with temperature correlates with the change in the width of the 3.1 eV band. Our estimations show that to explain the observed dependence of quenching in this temperature range the value of the interaction radius should change approximately by a factor of $R_0(300\ K)/R_0(150\ K) = 1.7$ (the overlap integral Ω - by a factor of 25). The CRL radiative lifetime which fits such behaviour is $\tau = 4.6$ ns. Thus the process of resonance energy transfer to the surface states can give a reasonable explanation for the observed correlation between changes of the CRL bandwidth and the decay kinetics across the temperature range 150 to 300 K.

In the range from 20 to 150 K, although only small changes of the spectral parameters of the CRL spectrum (further lowering) are observed, the quenching increases with decrease in temperature reaching, at 20 K, approximately the same value as at T = 300 K. Such behaviour of CRL quenching could be reasonably well described in terms of an activation barrier between free and localized states of the core hole [19,20]. As a consequence of such model the mobile free core holes have a large free path (i.e. large effective interaction radius R_0) before localization at low tempetrature that leads to the large near-surface losses of core holes and to the increase of CRL quenching. Large mobility of the core holes at low temperature can result also in the increase of CRL quenching due to the interaction of the core holes with impuruties, defects, self-trapped excitons, etc.

As mentioned earlier, the shape and temperature dependence of decay kinetics are similar for different CRL emission bands. These experimental facts suggest that all observed emission bands in the CRL spectrum of CsF should belong to the same radiative state of the core hole (cluster) and are probably due to transitions to different final states of the hole in the valence band or (for high-energy narrow bands around 4.0 eV) to some defect or impurity levels situated near the top of the valence band. Thus the observed decay kinetics of CRL in CsF under VUV excitation can be described in terms of the radiative decay of the localized core hole (cluster) distorted by different mechanisms of CRL quenching. Nevertheless the existence of radiative transitions involving free states of the core hole remains an unresolved problem.

CONCLUSIONS

The temperature dependence of the CRL characteristics of CsF have been studied under VUV sunchrotron radiation excitation. The CRL emission spectrum shows a strong dependence on temperature, the main changes occuring in the range T > 100 K. The temperature dependence of the width of the main (3.1 eV) CRL emission band can be well described by taking into account the electron-phonon interaction with the frequency of phonons responsible for the emission broadening equal to Debye frequency.

CRL decay kinetics in CsF reveal a non-monotonic dependence on temperature, the longest effective decay time being observed at about 150 K. The process of resonance energy transfer to the quenching surface states is probably responsible for the observed correlation of changes of CRL bandwidth and decay kinetics in the temperature range from 150 K to 300 K. The increase in the mobility of free core holes can explain the increase of CRL quenching with diminishing temperature in the range 20 K to 150 K.

ACKNOWLEGEMENTS

The work was supported by the Council for the Central Laboratory of the Research Councils of the United Kingdom in the framework of UK-Russian collaboration on synchrotron radiation, the International Association for the Promotion of Cooperation with Scientists from the Independent States of the Former Soviet Union (INTAS), Agreement No. 93-2554, and the International Science Foundation, Grant No. N9Y000. The authors would like to thank A.N.Belsky, A.L.Rogalev and A.N.Vasil'ev for valuable discussions.

REFERENCES

1. Yu.M.Aleksandrov, V.N.Makhov, P.A.Rodnyi, T.I.Syrejshchikova and M.N. Yakimenko, Sov.Phys.-Solid State **26**(1984)1734.

2. J.A.Valbis, Z.A.Rachko and J.L.Jansons, Sov.Phys.-JETF Letters **42**(1985)172.

3. A.N.Belsky, V.V.Mikhailin, A.L.Rogalev, S.Stizza, A.N.Vasil'ev and E.I.Zinin, Proc. 2nd European Conf. on Progress in X-ray Synchrotron Radiation Research, Bologna 1991, p.797.

4. S.Kubota, M.MacDonald and I.H.Munro, J.Lumin. **48-49**(1991)589.

5. I.A.Kamenskikh, M.A.MacDonald, V.N.Makhov, I.H.Munro, V.V.Mikhailin and M.A.Terekhin, Preprint DL/SCI/P882E of Daresbury Laboratory, August 1993, Nucl.Instr. and Meth. **A348**(1994)542.

6. M.A.Terekhin, A.N.Vasil'ev, M.Kamada, E.Nakamura and S.Kubota, UVSOR Activity Report 1993, p.32, Phys.Rev. **B52** (1995) .

7. R.A.Glukov and A.N.Vasil'ev, Proc. MRS Symp.**348**(1994)387.

8. Yu.M.Aleksandrov, I.L.Kuusmann, P.Kh.Liblik, Ch.B.Lushchik, V.N.Makhov, T.I.Syrejshchikova and M.N.Yakimenko, Sov.Phys.-Solid State **29**(1987)587.

9. I.F.Bikmetov and A.B.Sobolev, Sov.Phys.-Solid State **33**(1991)155.

10. J.Andriessen, P.Dorenbos and C.W.E. van Eijk, Mol.Phys. **74**(1991)535.

11. A.S.Voloshinivskii, V.B.Mikhailik, S.V.Syrotyuk and P.A.Rodnyi, Phys.Stat.Sol. (b) **173**(1992)739.

12. J.Andriessen, P.Dorenbos and C.W.E. van Eijk, Nucl.Tracks Radiat.Meas. **21** (1993)139.

13. A.L.Rogalev, Thesis, Moscow MSU, 1992.

14. W.Hayes and I.B.Owen, J.Phys.C **10**(1977)L197.

15. A.N.Belsky, V.V.Mikhailin, A.L.Rogalev, A.N.Vasil'ev and E.I.Zinin, Abstr. EURODIM'94 Int.Conf., Lyon 1994, p.296.

16. S.Tanaka, H.Fujita, K.Fujiwara, S.Nagata, M.Nakayama, H.Nishimura, T.Komatsu and S.Hasimoto, UVSOR Activity Report 1990, p.125.

17. S.Narain, Phys. Stat. Sol. (b) **182**(1994)273.

18. Th.Forster, Z.Naturf. **A4**(1949)321.

19. N.Yu.Kirikova and V.N.Makhov, Sov.Phys.-Solid State **34**(1992)1557.

20. V.N.Makhov, J.Becker, L.Frankenstein, I.Kuusmann, M.Runne, A.Schroeder and G.Zimmerer, Rad.Effects and Defects in Solids **133-134**(1995).

LUMINESCENCE AND RADIATIVE DECAY OF LOW ENERGY ELECTRONIC EXCITATIONS IN LiB_3O_5

I.N. OGORODNIKOV, A.Yu. KUZNETSOV, A.V. KRUZHALOV
Urals State Technical University, Experimental Physics Department
620002, Ekaterinburg, Russia; e-mail: ogo@kef.rcupi.e-burg.su

Abstract. – The results of study on luminescence and radiative decay of the low energy electronic excitations in the large LiB_3O_5 single crystals are reported. It was shown that the luminescence at 295 nm is excited by photons with energy exceeded band gap, by an electron beam, by X–ray and also in recombination processes. Four peaks of thermoluminescence at 130, 180, 240 and 330 K are revealed, their parameters are fixed, and the origin of the trapping and recombination centers are determined. The most acceptable models of recombination processes and the origin of the LiB_3O_5 luminescence are discussed.

1. INTRODUCTION

Crystals of lithium triborate LiB_3O_5 (LBO) are reported to be a comparatively modern material for nonlinear and integrated optics [1]. Several primary physical, chemical [2] and nonlinear [3] properties of LBO have been studied. Recently Scripsick *et al.* [4] have published some results of preliminary studies on point defects in small LiB_3O_5 crystals obtained from China. However, nearly nothing is known about luminescence manifestation and scintillation properties of LBO.

Preliminary investigations of both luminescence and interaction of the electronic excitations with point defects in LBO crystals was the goal of the present work.

2. EXPERIMENTAL DETAILS

Nominally pure LiB_3O_5 single crystals of high optical quality grown by the advanced flux method at 834 –810 $^{\circ}C$ [5] were studied. The dimensions of such grown crystals were $50\times40\times25$ mm^3 on the average. The main crystallographic characteristics are in a complete agreement with that reported previously by König and Hoppe [6]. For the measurements of the X-ray-induced luminescence (RL), the thermostimulated luminescence (TL), the cathodoluminescence (CL), and the optical transmission spectra the samples were produced in the form of polished plane-parallel plates ($10\times10\times1$ mm^3) with the crystallographic {001} axis square to the large surface of the plate. Experimental instruments and methods were described in our previous works [7, 8, 9].

3. RESULTS

3.1. Luminescence spectrum

LBO crystals have a wide band of optical transparency (160 – 3500 nm) [1, 4]. We studied the optical transmission from visible range to the edge of the fundamental absorption. Transmission spectra show that the crystals have a high transparency right up to fundamental absorption and have no optical absorption bands, (Fig. 1). Optical excitation in the band of transparency causes no photoluminescence. On the contrary, excitation by photons with energy, exceeding the band gap, leads to strong UV-luminescence, (Fig. 1). The luminescence yield at 290 K amounts to 30% compared to that for luminescence of BeO crystals at 250 nm. The RL spectrum represent a wide complex band with the maximum intensity at about 290 to 305 nm, (Fig. 1), differing at various temperatures because of the changing intensities of the elementary bands. The complex band was divided at least into two Gaussian sub-bands. At 290 K the spectral positions of the sub-band maxima were 295 and 350 nm, FWHM were 64 and 107 nm, ratio of the maximum intensities of sub-bands was ~4. Also a weak shoulder is present near 250 nm,

Proc. Int. Conf. on Inorganic Scintillators and Their Applications, SCINT95,
1996, Delft University Press, The Netherlands

(Fig. 1). In Fig. 2 the temperature dependence of the RL intensity at 290 nm $I_S(T)$ is given in Arrhenius coordinates. The maximum occurred for a temperature of 240 K. As the temperature is decreased below 240 K the RL intensity decreases in the regions from 240 to 130 K and from 120 to 77 K with the activation energies of 65 and 10 meV. Above 240 K a temperature quenching of the luminescence proceeds. Assuming the Mott's law, the activation energy of quenching is 295 meV.

3.2. Decay kinetics of luminescence

The time response of the CL at 294 nm, after excitation by a short (15 ns) electron pulse contains several components. There are a short exponential component with lifetime τ_f approximately equal to the excitation pulse-time, and slow components in the millisecond range. Measurement of the fast component using the statistical one-photon method, under excitation with α-particles permitted to determine more precise value of τ_f = (4±1) ns. Excitation by intense synchrotron radiation with extremly short (0.43 ns) pulses give the value of τ_f =1 ns [9]. The lifetime and the intensity of the fast component in the 77 to 650 K region are temperature independent.

Fig. 3 represents the normalized spectra of the fast- and long-time components for two different temperatures. The spectral band of the slow component has the shape like that for RL: the principal band – at 300 nm (300 K) or 310 nm (77 K) – and long-wavelength "tail". The contribution of the long-wavelength "tail" increases when cooling the crystal (Fig. 3). On the contrary, the shape of spectral band of the fast component has no dependence on temperature at 77 – 650 K. It contains two well defined bands: at 300 and 250 nm, and also a long-wavelength "tail" weakly dependent on temperature, (Fig. 3).

Analysis of the long-time decay kinetics showed that, in the examined time and temperature ranges, the time response of the CL intensity $I(t)$ may be described by the sum of an exponential function (τ =10–40 μs), and a hyperbolic one. Whereas the hyperbolic dependence may be precisely singled out all over the 77–500 K region, the exponential component is present only in the 77–180 K temperature region. In this connection the main attention was paid to the hyperbolic constituent part of the long-time CL kinetics: $I(t) = I_0/(1 + t/\tau)^p$, where I_0 –initial intensity, τ –hyperbolic lifetime, p –kinetics order; In Fig. 2 the temperature dependencies of the initial intensity $I_0(T)$ and hyperbolic lifetime $\tau(T)$ are given in Arrhenius coordinates.

In the temperature region between 77 and 180 K the $I_0(T)$ curve behaves similarly to $I_S(T)$. The activation energy of corresponding process at 120–180 K is ~67 meV. Over the 200–350 K region the $I_0(T)$ curve substantially differs from $I_S(T)$, (Fig. 2). The value $I_0(T)$ increases by not 1.5 but 3 orders of magnitude; the $I_0(T)$ and $I_S(T)$ curves reach their maxima at the different temperatures (~300 K and 240 K). Above this temperatures the slopes of the both curves are different, (Fig. 2).

3.3. Thermally stimulated Luminescence

Non-irradiated LBO crystals do not show TL. For crystals irradiated by X-ray at 77 K four main TL peaks result from thermal decay of radiation defects, in the region between 77 and 600 K, (Fig. 4). The most effective defect formation was observed at 77 K. TL spectra of the most intensive peaks at 130 and 240 K are close to that for RL at 290 nm. This implies the probable participation of radiation defects in the excitations of the UV-luminescence. It should be noted that the temperature dependence of the RL, and the glow curve are somewhat correlated. Luminescence at 290 nm rises in the temperature region of the main TL peaks at 130 and 240 K, and a maximum of the luminescence intensity is at 240 K.

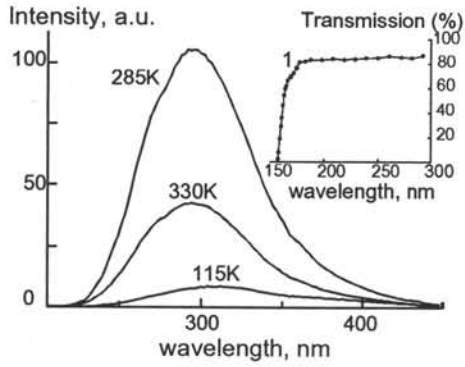

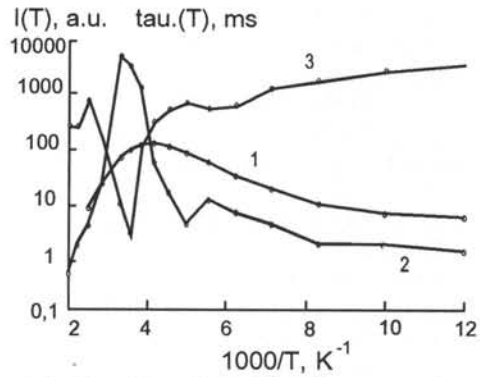

Fig. 1. Transmission spectrum near the fundamental absorption edge –(1) and spectra of the X-ray induced luminescence of LiB_3O_5 at different temperatures

Fig. 2. Temperature dependencies of the X-ray induced luminescence –(1), and of the decay kinetics parameters (initial intensity –(2) and hyperbolic lifetime –(3))

We believe that the rise of $I_0(T)$ at T>180 K and the TL peak at 240 K are due to the decay of common trapping centers, but the thermal quenching of the RL at T>240 K is due to another reasons. It is necessary to consider that the main recombination centers in LiB_3O_5 are stable to temperatures just higher than the decay temperature of the trapping centers, causing the TL peak at 240 K.

3.4. Recombination Processes

As grown LiB_3O_5 crystals have no paramagnetic defects and optical absorption bands. Exposure to ionized radiation of any kind at room temperature does not lead to the appearance of additional optical absorption or paramagnetic centers. Only a small TL peak at 330 K is observed (Fig. 5). Manifestations different from above are observed after irradiation at 77 K. Irradiation by an electron beam (an energy is ~150-200 keV, a flux is $\sim 10^{13}$ electrons·cm^{-2}) leads to the effective creation of paramagnetic centers, namely B^{2+} electron and O^- hole trapped centers [7], and to appearance of radiation induced optical absorption in a wide band at 360 nm [8]. Optical excitation at 360 nm causes no photoluminescence.

The most likely models for these defects may be the following. From ESR the O^- center represents a hole trapped at an anion site, and the non-pared spin of the center interacts with the nucleus giving I =3/2 (^{11}B or ^7Li) spin. This leads to the typical four-lines ESR spectrum [7]. Also from ESR data [7], the electron B^{2+} center is caused by the trapping of an electron on a boron ion siting in an interstitial position. Studying the temperature dependence of the ESR-signals from O^- and B^{2+} centers and radiation-induced optical absorption band, it was shown that each decrease on the annealing curves occurs in the regions of the main TL peaks at 130 and 240 K [7, 8].

4. CONCLUSION

The preliminary study of the UV-luminescence and recombination processes in LiB_3O_5 crystals was carried out. It was shown that luminescence is excited by photons with energy exceeding band gap, by electron beam, by $X-$ray and also in recombination processes; has no dependence on the excitation mode; has the fast exponential component ($\tau_f \approx 1 \div 4$ ns) independent on temperature over the range between 77 and 650 K. Also the B^{2+} and O^- centers were revealed. These centers take part in the recombination channel of the UV-luminescence excitation in LiB_3O_5.

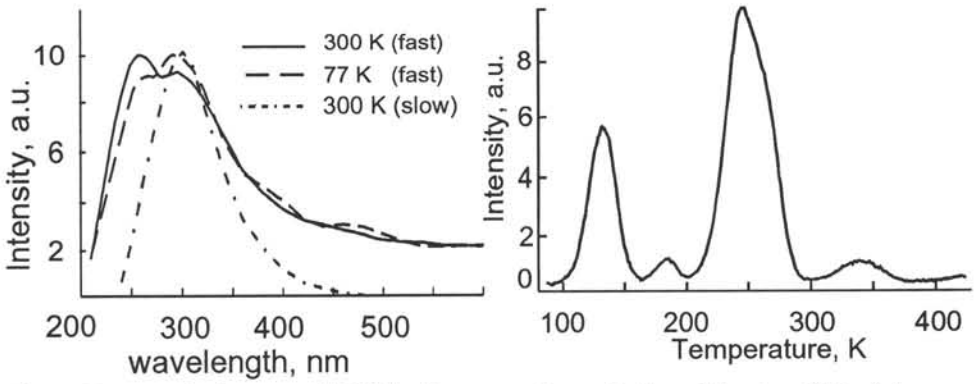

Fig. 3. Time-resolved spectra of LBO luminescence after excitation with a short (15 ns) electron pulse (fast component) and 1 ms later (slow component) at room temperature and at 77 K.

Fig. 4. Thermally stimulated luminescence of LiB_3O_5 after X-ray irradiation. Heating rate is 0.3 $K \cdot s^{-1}$.

It may be noted that broad-band luminescence with such properties and large Stokes shift are observed in wide band gap oxide dielectrics and are usually assigned to: (1) the radiative annihilation of self-trapped excitons (low-symmetry crystals, namely BeO, Al_2O_3, $YAlO_3$ and etc.); (2) the direct radiative recombination of electrons on trapped hole centers.

Acknowledgment. – All examined LBO crystals were grown and put at our disposal by V.A. Maslov. The authors wish to express their gratitude to him for providing the research material.

REFERENCES

1. Chen C., Wu Y., Jaing A., Wu B., You G., Lin S. (1989) *J. Opt. Soc. Am. B-Opt. Physics*. **6** (4). 616-625.
2. Shuqing Z., Chaoen H. and Hongwu Z. (1990) *J. Cryst. Growth*. **99**. 805-810.
3. Ukashi T., Lane R.J., Bosenberg W.R. and Tang G.L. (1990) *Appl. Phys. Lett*. **57** (10). 980-982.
4. Scripsick M.P., Fang X.H., Edwards G.J., Halliburton L.E., Tyminski J.K. (1993) *J. Appl. Phys*. **73** (3). 1114-1118.
5. Maslov V.A., Olkhovaya L.A., Osiko V.V. and Shcherbakov E.A. (1992) In: *Oral Presentation Abstracts. ICCG-10. Tenth Int.Confer. on Crystal Growth*. p.11. Sheraton Harbor Island Hotel, San Diego.
6. König H., Hoppe R. (1978) *Z. Anorg. Allg. Chem*. **439**. 71-79.
7. Ogorodnikov I., Kudyakov S., Kuznetsov A., Ivanov V., Kruzhalov A., Maslov V., Olkhovaya L. (1993) *Pisma v Zhurnal tekhnicheskoi Fiziki*. **19** (13). 77-80. (in Russian)
8. Ogorodnikov I., Ivanov V., Maslakov A., Kuznetsov A., Maslov V. (1993) *Pisma v Zhurnal tekhnicheskoi Fiziki*. **19** (16). 42-47. (in Russian)
9. Ivanov V.Yu., Kuznetsov A.Yu., Ogorodnikov I.N., Pustovarov V.A., Kruzhalov A.V. (1995) *Nuclear Inctruments and Methods in Physics Research*. **A359**. 339-341.
10. Victorov L.V., Kruzhalov A.V., Shulgin B.V. (1982) *Pribory i technika experimenta*. **2**. 171-174.

MECHANISMS OF FAST UV-SCINTILLATIONS IN OXIDE CRYSTALS WITH SELF-TRAPPED EXCITONS

I.N. OGORODNIKOV, A.V. KRUZHALOV, V.Yu. IVANOV
Urals State Technical University, Experimental Physics Department
620002, Ekaterinburg, Russia; e-mail: ogo@kef.rcupi.e-burg.su

Abstract. – Study and discuss of the mechanisms of fast UV-scintillations in oxide crystals with self-trapped excitons by the example of BeO.

1. INTRODUCTION

To date the most effective inorganic crystalline scintillators are among the activated scintillators. For example, the early effective scintillations crystalline detectors on the base of the $NaI - Tl$ and $CsI - Tl$ systems were put by Hofstadter et al. more than 40 years ago. However, up to now this scintillators would remain as before as the excellent scintillators among the ones based on the oxides and fluorides. Under extremely high power ionizing radiation the energy transport to the activators may be destroyed owing to the radiation damage and defect creation processes. In this situation the crystalline systems with the fast ultraviolet intrinsic luminescence may be preferable. Unfortunately, the known effective mechanism of creation and of radiative annihilation of self-trapped excitons (STE) in alkali halide crystals can not be used in scintillators because of its low-temperature origin.

Wide band gap oxide crystals exhibit often the strong intrinsic ultraviolet luminescence attributed to radiative annihilation of STE (e.g. BeO, Al_2O_3, Y_2O_3, $Y_3Al_5O_{12}$ etc.). From the viewpoint of scintillators these groups of oxides reveal the different properties. For example, MgO have no scintillations, whereas BeO [1], Y_2O_3, $Y_3Al_5O_{12}$ [2] are reputed to be moderately good fast UV-scintillators (Table 1). These facts allow us to suggest that the intrinsic luminescence of STE determines the scintillation properties in the certain of simple wide band gap oxides. Because beryllium oxide is intermediate on the symmetry group between the cubic and low-symmetry oxides, it may be the most representative crystal for understanding of the origin of the fast scintillations in oxides.

Table 1: Scintillation properties of the selected oxides with STE under excitation by ^{137}Cs

Crystal	C_r, %	τ, ns	Z_{eff}	λ_m, nm
BeO	15	18	7.3	250
Y_2O_3	36	28	35.7	370
$Y_3Al_5O_{12}$	27	100	29.5	260

Note: C_r-efficiency to $NaI - Tl$; τ-decay time; λ_m-emission band maximum.

2. EXPERIMENTAL RESULTS AND DISCUSSION

2.1. Scintillation properties of BeO

The experimental instruments and methods as well as the samples were described previously in our works [3, 4]. Beryllium oxide single crystals show a moderately good scintillation efficiency C_r of 33-65% and B_A of 23-30% with respect to $CsJ:Tl$ (table 2). The absolutely energy yield of radioluminescence ρ was 4.1-6.7%. The time response curve of the α and β scintillations of radioluminescence devides into three components with the rise-time less than 1 ns, the initial intensities ratio of 1:(0.2-0.3):(0.02-0.07) and the decay-time of (10-18) ns, (130-320) ns and (1.4-3.2) μs. The moderately high contribution of the inertial luminescence with the life-time longer than 10 μs is the typical feature as well. The value of $(\rho - \eta)/\eta$ for the inertial part is about 0.3 (BeO) or 0.5 ($BeO:Li$). As the temperature decreases the life-time of the inertial constituent and its contribution into the scintillation will increase. It was revealed, that the trapped

Proc. Int. Conf. on Inorganic Scintillators and Their Applications, SCINT95,
1996, Delft University Press, The Netherlands

carriers from shallow traps can participate in the tunnel recombination process, which effectively proceeds below the temperatures of 200 K (BeO) or 350 K ($BeO:Li$) with the time-constant of $\approx(10^{-5}-10^{-4}$ s). The rate of the thermally stimulated ionization increases and contribution from the shallow trap decreases respectively as the temperature decreases. These facts indicate that shallow traps give a significant contribution into the scintillation pulse over the low temperature region. The α and β scintillations in BeO crystals have a commom spectral band matched almost exactly with that for the UV-steady-state luminescence at 4.9 eV [3, 4].

Table 2: Scintillation properties of the BeO single crystals

Crystal	Ex-ci-tat.	T, K	Parameters of scintillations										
			C_r, %	B_A, %	η, %	ρ, %	R, %	$t_{0.5}$, ns	τ_1, ns	τ_2, ns	τ_3, μs	$\frac{I_2}{I_1}$	$\frac{I_3}{I_1}$
$BeO:Li$	α	300	48	27	5.1	6.1	21	15	18	290	1.92	0.25	0.07
BeO	α	300	36	26	3.1	4.4	20	8	12	190	1.46	0.30	0.04
BeO	β	300	65		5.1	6.7		7	10	130	1.40	0.35	0.05
BeO	e^-	300		28				40	50		3.2		0.02
BeO	e^-	77		28				50	70		33		0.4
$CsJ:Tl$	α	300	100	100		7.1	11	–	480	1600	–	0.06	–
$CsJ:Tl$	β	300	100	100		11.3	9.9	–	820	5700	–	0.16	–

Note: C_r and B_A - the efficiency to $CsI-Tl$ by using the registration systems on the base of the FEU-71 type PMT; with time-resolution of 1 μs and 4 ns, respectively. η - scintillation efficiency; ρ - energetic yield of radioluminescence. R - normalized energetic resolution. $t_{0.5}$, τ_1, τ_2, τ_3 - FWHM and decay-times of components of scintillation. I_2/I_1, I_3/I_1 the ratio of the initial intensities of components

2.2. Luminescence spectra of BeO

It is known that in BeO there are two intense broad luminescence bands at 4.9 and 6.7 eV (Fig. 1). A typical feature of these luminescences at temperatures from 150 to 230 K is a quenching of the 6.7 eV band and an associated increase of the 4.9 eV band. The latter band is stable on further heating to 750 K [3]. The current model assigns these bands to radiative annihilation of STE of two kinds: STE(4.9) and STE(6.7), respectively [7]. The hole components of both STEs are in the form of the O^- ion-type small-radius polarons, which differ in the directions of the $Be-O$ bonds [8]. The crystallographic structure of BeO determines the 'axial' (i.e. parallel to the optical C axis) and 'non-axial' orientation of these bonds [3]. In Ref. [8] it was demonstrated that STE(6.7) and STE(4.9) are based on the axial and non-axial configuration, respectively. According to the results of spectral and kinetic studies [3, 7] the STE(6.7) appears predominantely when the free exciton relaxes, whereas the STE(4.9) arises in the recombination of electrons with holes in the form of a small radius polaron. The characteristics of the 4.9 eV luminescence inherit no properties from the recombination centers [3].

The time response of the 6.7 eV triplet luminescence at temperature below 150 K is described by the exponential function with decay-time of 340 μs [7]. According to Ref. [8], the 4.9 eV luminescence exhibits a complicated decay kinetics: a temperature independent exponential component with life-time of 29 ns and several inertial components which can be described by a hiperbolic law. As a rule, the inertial components have a strong temperature dependence of both intensities and life-time in microsecond region (Fig. 2). So, only the fast luminescence of STE(4.9) may be sutable for the scintillation applications.

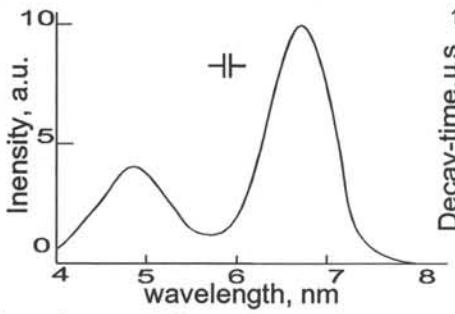

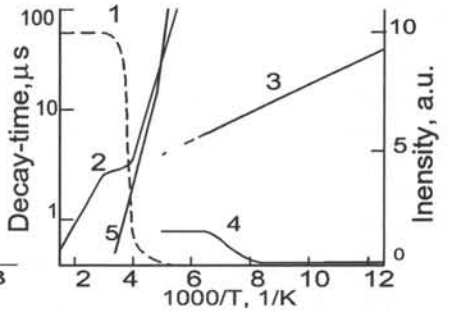

Fig. 1. Spectra of the steady-state luminescence of BeO at 77 K

Fig. 2. Temperature dependence of the decay-times (2,3,5) and initial intensities (1,4) of the first (1,2) and second (3,4) slow microsecond components of the 4.9 eV luminescence and decay-time of the 6.7 eV luminescence (5) from BeO under the 15 ns electron beam excitation.

2.3. Decay kinetics of the fast STE luminescence

Study of the fast luminescence of BeO was carried out by the use of the X-ray spectroscopy experimental station of the VEPP-3 storage ring, described in detail in Ref. [6]. Under excitation by synchrotron radiation pulses the initial stage of the decay kinetics of BeO in the region 250-500 nm contains two exponential components: a fast component with τ_1 =2.0±0.1 ns and a slower component with τ_2 =45±2 ns [9]. The decay parameters were determined by the convolution method [10]. The spectrum of the fast component is shifted relative to the spectrum of slow component or the coinciding steady-state luminescence spectra (Fig. 3). The quantum yield and decay time of the fast component are only slightly temperature dependent in the experimental temperature range 77-600 K and they are virtually identical to the temperature dependence of steady-state $X-$ray luminescence [5]. The doping with heterovalent (Al and B) or isovalent (Zn and Mg) impurities has no effect on the relative yield of the short component. Likewise, synchrotron radiation with excitation density in the range 10^{14}-$6{\cdot}10^{16}$ photons/s·cm^2 had no observable effect on the intensity ratio of the components. There are no deviations from a linear relation between the excitation density and the peak intensity of the luminescence pulse. This indicates that saturation processes do not occur. The strong polarized synchrotron radiation allow us to study the orientation effects [9]. The short component is observed predominantely with parallel orientation of the optical **C** axis of the crystal relative to the electric vector of the synchrotron radiation. For $\mathbf{E}\perp\mathbf{C}$ the contribution of the short component is significantly smaller (Fig. 4). Polarized measurements show that the degree of polarization for the short (2 ns) component ($P = +70\%$) is significantly different from that for the slow component (45 ns) or steady stte luminescence ($P = -50$-60% [7]). The available data do not allow us to attribute the fast luminescence to the impurity or intrincic defects. The electronic structure of BeO does not contain any prerequisites for associating it to corel-valence transitions. However, the situation is very similar to the manifestation of triplet and singlet STEs in the inert-gas crystals, where the spectra of these excitons are virtually identical [11].

According to a number of recent papers (see, e.g., Ref. [12]), a similar picture is also observed for NaI crystals, where the states of the singlet (τ_1 =1.2 ns) and triplet (τ_2 =110 ns) STEs have virtually identical energetics. For the other oxide crystals Al_2O_3 and $Y_3Al_5O_{12}$ the short components with τ <50 ns were associated in Ref. [2, 12] to transitions from split triplet nonequilibrium states. However, the decay parameters and the polarized and orientation characteristics of the fast luminescence in BeO make it

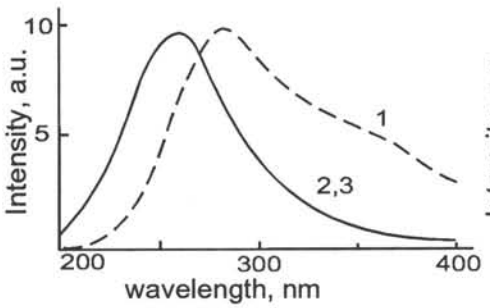

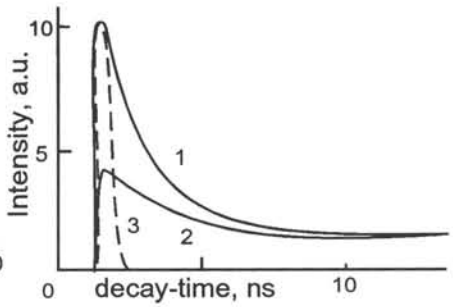

Fig. 3. Time-resolved (1,2) and steady-state (3) luminescence spectra of *BeO* with excitation by synchrotron radiation at 300 K (**E**||**C**). 1-spectrum of the fast component, obtained as the difference of spectra measured at the moment of excitation pulse and with a delay of 40 ns; 2-spectra measured with a delay of 40 ns.

Fig. 4. Decay kinetics of the luminescence of oriented *BeO* crystals at 300 K (λ =350 nm), 1-(**E**||**C**), 2-(**E**$\perp$**C**) and the exciting pulse of synchrotron radiation - (3).

impossible to explaine this luminescence in such a model. Based on its properties, it is logical to associate the fast (2 ns) luminescence in *BeO* to the luminescence of singlet STEs.

So, beryllium oxide single crystals demonstrate good decay-time properties and moderately good scintillation efficiency. The origin of the final stage of the fast scintillations in *BeO* is associated with the radiative annihilation of STE(4.9).

Acknowledgment. – The authors are grateful to B.V. Shulgin, V.A. Pustovarov and E.I. Zinin. All examined *BeO* crystals were grown and put at our disposal by V.A. Maslov.

REFERENCES

1. Ogorodnikov I.N., Ivanov V.Yu, Kruzhalov A.V. (1994) *Fizika tverdogo tela.* **36** (11). 3287-3298. (in Russian)
2. Kuznetsov A., Namozov B., Mürk V. (1985) *Fizika tverdogo tela.* **27** (10). 3030-3037. (in Russian)
3. Ogorodnikov I.N., Ivanov V.Yu., Kruzhalov A.V. (1995) *Radiation Measurements.* (in press)
4. Shulgin B.V., Kruzhalov A.V., Ogorodnikov I.N. *et al.* (1988) *Zhurnal Prikladnoi spectroskopii.* **49** (2). 286-291. (in Russian)
5. Giniyatullin K.N., Malysheva A.F., Kruzhalov A.V. *et al.* (1982) *Trudy Inst. Fiz. Akad. Nauk Est.SSR* **53**. 71-82.
6. Zinin E.I., Pustovarov V.A., Rogalev A.L. *et al.* (1989) *Proc.VUV-89.* Irkutsk. p.282.
7. Ivanov V.Yu., Pustovarov V.A., Kruzhalov A.V. *et al.* (1989) *Nucl. Instrum. Methods Phys. Res.* **A282** 559-564.
8. Gorbunov S.V., Ivanov V.Yu., Antsigin I.N., Kruzhalov A.V., and Shulgin B.V. (1991) *Radiat. Effects and Defects in Solids.* **119-121**. 893-900.
9. Pustovarov V.A., Ivanov V.Yu., Kruzhalov A.V., Zinin E.I. (1994) *Fizika tverdogo tela.* **36** (5). 1523-1526. (in Russian)
10. Pustovarov V.A., Betenekova T.A., Zinin E.I. *et al.* (1991) *Nucl. Instrum. Methods Phys. Res.* **A308** 203-204.
11. Itoh M., Hashimoto S., Ohno N. (1991) *J. Phys. Soc. Japan.* **60** 4357-4361.
12. Mürk V.V. and Ismailov K.M. (1993) *Fizika tverdogo tela.* **35**. 498-503. (in Russian)

X-RAY LUMINESCENCE OF GALLIUM GARNETS

A.E.Nosenko, V.N.Shevchuk, and A.S.Voloshynovskii
Department of Physics, Lviv State University
Dragomanov Str. 50, Lviv 290005 Ukraine

Abstract Luminescence properties of nonactivated $R_3A_2Ga_3O_{12}$ ($R=R^{3+}$-rare-earth ion, A=Ga or Sc) and $Ca_3Ga_2Ge_3O_{12}$ garnets under pulsed X-ray excitation ($\Delta t \cong 1.5$ ns) in the temperature range 80÷300 K and in the spectral range 200÷600 nm have been studied. By the photons counting method the decay of luminescence kinetics is investigated.

INTRODUCTION

Using of garnet crystals in detectors of ionizing radiation stimulates the investigation of their luminescence properties. In this aspect yttrium aluminium garnet [1] is most investigated. Gallium garnets are insufficiently investigated. Only some information about UV-luminescence (UL), in particular, of undoped gadolinium gallium garnet crystals are presented in [1-4].

The present work is performed with the aim to search for scintillation materials with ultrashort decay time of emission relaxation τ and in connection with problem of fast luminescence nature in complex oxides and their correlation with photoinduced "matrix rare-earth ion – ligand" charge transfer. Latter forms unusual photoconductivity spectra of rare-earth gallium garnets [5] in 200÷400 nm range. Here, the intrinsic luminescence and luminescence of matrix R^{3+} (R=Nd,Sm,Gd) ions in nonactivated garnet $R_3A_2Ga_3O_{12}$ (A=Ga or Sc), $Ca_3Ga_2Ge_3O_{12}$ and $Y_{3-x}Er_xSc_2Ga_3O_{12}$ (x=0.25) crystals in the temperature range T=80÷290 K and in spectral range λ=200÷650 nm under pulsed ($\Delta t \cong 1.5$ ns) X-ray excitation are investigated. The previous data of this investigations were presented in [6]. The X-ray luminescence (XL) and its decay time are investigated by the photons counting method [7]. Time characteristics of the fast XL ($\tau \cong 0.5$ ns) are determined with allowance of the excitation impulse form [8]. Crystals were grown by the Czochralsky method.

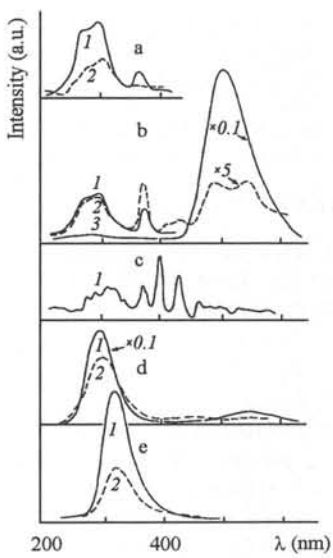

Fig. 1: The spectra of X-ray luminescence of some gallium garnets. Curve a) are corresponding to GdGa-garnet, b) – GdScGa, c) – NdGa, d) – YErScGa and e) – CaGaGe. Temperature of the measurements are: 80 K – curves 1a-e and 3b; 130 K – 2a and 2e; 220 K – 2b; 290 K – 2d.

EXPERIMENTAL RESULTS

In all investigated crystals the low-intensity UL in 250÷400 nm range is observed (Fig. 1). In the case of Sc-garnets the XL spectra contain additional wide nonelementary bands in the visible 400÷650 nm range. The XL spectra of NdGa-garnet in this region also contain narrow peaks which are connected with transitions in Nd^{3+} ion. The series of bands connected with Gd^{3+} ion *f-f*-transitions in the Gd-garnet cases coincided with intrinsic emission region of the crystals. Detailed XL spectra consideration gives possibility to identify UV-peaks structure and to compare narrow peaks with corresponding transitions from ^6I, ^6P excited states of Gd^{3+} ions. Very little intensity of UL make it impossible to discover the detailed structure of narrow peaks.

Proc. Int. Conf. on Inorganic Scintillators and Their Applications, SCINT95,
1996, Delft University Press, The Netherlands

Table. Lines of the most intensive X-ray luminescence at 80 K in gallium garnet crystals.

garnet	emission range (nm)	λ (nm)
NdGa*	270 - 480	260, 275, 290, 310, 320, 337, 367, 397, 430, 458
SmGa	270 - 400	
GdGa	250 - 350	280, 320
	370 - 400	380
GdScGa	250 - 350	280, 320
	370 - 400	380
	410 - 650	440, 505, 560
YErScGa	250 - 380	305
	470 - 620	550
CaGaGe	275 - 400	320

*) The emission peaks are compared with the luminescence spectra of other Nd^{3+} doped garnets [1,9].

The additional XL peak at 380 nm is typical for the Gd-garnets. The nature of this peak is not connected with the $4f^7$-shell in Gd^{3+} ion. The spectral positions of the observed most intensive luminescence bands of garnets in the investigated range are presented in the Table.

With increase of temperature the intensity of the observed XL peaks is decreased. The long-wave luminescence (400÷650 nm) of the Sc-garnets is quenched at 300 K. This is also observed in the CaGaGe-garnet luminescence. The intensity and correlation of UL components of all crystals are determined by crystal temperature and lattice defects. Thus the UL in GdGa-garnet is practically quenched e.g. at Sm-impurity introduction in place of Gd at the 1:10 ratio. The similar decreasing of f-peaks intensity is observed in photoconductivity spectra [5]. The maximum XL yield corresponds to maximum intensity of the photocurrent. The temperature quenching of XL is accompanied by photoconductivity increasing.

Investigation of UL decay time profiles (Fig. 2) at 80 K give value of $\tau \leq 0.5$ ns (the most fast component). In the case of rare-earth garnets the parameter τ is characterised by small temperature quenching. Practically for all investigated crystals as following from Fig. 2 long-time UL contribution is characteristic.

For the long-wave luminescence of Sc-garnets τ is $\cong 10^{-7}$ and $\cong 10^{-9}$ s at 80 and 290 K correspondingly. The curves of XL decay (UL and long-wave luminescence) at 80 K are nonexponential as a rule (except UL of Gd-garnets) and at 290 K XL decay is exponential. This confirms the complex character emission of crystals. It is due to contributions of some processes of different nature.

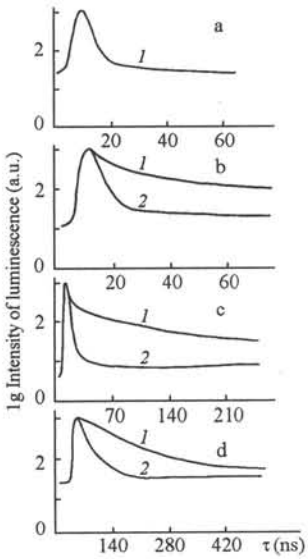

Fig. 2: The decay time profiles of luminescence for the GdGa-garnet (curve a), CaGaGe (b), YErScGa (c) and GdScGa (d) at 80 K (curves 1a-c), 100 K (1d), 170 K (2d) and 290 K (2b,c). In the GdGa-garnet case measurement is made in integral operation. In other cases measurements are at 320 nm (b), 300 nm (c) and 530 nm (d).

CONCLUSIONS

The contents of cation sublattice of nonactivated gallium garnets decisively determine the XL spectra of the crystals. So, in the case of Sc-garnets the long-wave luminescence in 400÷650 nm range is observed. In the other cases considered above this emission is not observed. Value of τ and its temperature dependence in the UL case are different for rare-earth and CaGaGe-garnets. In the latter case UL is most intensive and experienced of considerable temperature quenching. The UL is ultrafast ($\tau \leq 1$ ns) for all crystals at 290 K. The investigated XL peaks are complex. The answer as relating to the luminescence nature, the contribution and existence of recombination processes with participation of short life defects, shelf-trapped excitons luminescence, core-valence luminescence need of subsequent investigations. Because of temperature dependence of the XL it is possible to only indicate what contribution of core-valence luminescence in emission spectra of the investigated crystals is being discussed.

REFERENCES

1. S.Kh.Batygov, Yu.K.Voron'ko, N.G.Margiani, and N.N.Ryskin, in: Spectroscopy of oxides crystals for quantum electronics, Proc. IOFAN. vol. 29, Nauka, Moscow. P.101-140 (1991) (in Russian).
2. V.A.Andrijchuk, L.G.Volzhenskaja, Ya.M.Zakharko, and Yu.V.Zorenko, Fiz. tverd. tela. **29**, 232 (1987).
3. A.N.Belskii, Sh.Vishnevskii, E.I.Zinin, V.N.Kolobanov, M.Kuchera, V.V.Mikhailin, P.A.Orekhanov, and A.L.Rogalev, in: Proc. IX Vsesojuzn. Conf. VUV-91. Tomsk, 28-30 may 1991. Moscow State University, Moscow. P.80 (1991).
4. V.N.Kolobanov, V.V.Mikhailin, P.A.Orekhanov, A.L.Rogalov, and E.I.Zinin, in: Proc. VIII Conf. RPhCh-8. Tomsk, 10-12 novemb. 1993. Tomsk Politekhnich. University, Tomsk. Part 2, p.17 (1993).
5. A.E.Nosenko, and V.N.Shevchuk, Zhurn. tekhn. fiz. **63**, 69 (1993).
6. A.E.Nosenko, V.N.Shevchuk, and A.S.Voloshynovskii, in: Intern. Symp. Luminescent detectors and transformers of ionizing radiation LUMDETR-94. Tallinn, Estonia, September 25-29, 1994. Vol. of Abstracts. Tallinn, Institute of geology Estonian Academy of Sciencies. P. 79 (1994).
7. A.S.Voloshynovskii, A.G.Dmitrijev, V.B.Mikhailik, and P.A.Rodnyi, Fiz. tverd. tela. **34**, 3730 (1992).
8. A.S.Voloshynovskii, V.B.Mikhailik, S.V.Myagkota, N.S.Pidzyrailo, and I.P.Pashuk, Ukr. fiz. zhurn. **38**, 1012 (1993).
9. A.Niklas, and W.Jelenski, Phys. stat. sol. (a). **77**, 393 (1983).

SELF-SHRINKED EXCITONS IN COMPLEX OXIDES

V. Mürk
Institute of Physics, Riia 142, EE2400 Tartu, Estonia

Abstract. The specific features of self-shrinked excitons in complex oxides are discussed. The low point symmetry of the crystal`s lattice is supposed to cause the coexistence of different ways of exciton relaxation. The generation stage of self-shrinked excitons, their role in relaxation processes and the character of radiative transitions are described on the basis of the experimental data obtained.

INTRODUCTION

Wide-gap insulators are usually characterized by a strong electron-phonon coupling that leads to a remarkable lattice relaxation and to electron excitation self-trapping. In the well-known case of alkali halides the identity of self-trapped excitons created either recombinationally or directly through excitation of unrelaxed excitons has played an important role in the determination of the exciton`s structure. High point symmetry of these simple crystals together with a strong chemical bonding in the relaxed state of an exciton seem to be the causes of such, in fact unique, behaviour of self-trapping processes. In a general case we cannot expect such identity of both kinds of self-trapped excitons. To separate these two cases we will use here, according of Sumi`s classification [1], the term `self-shrinked exciton` (SSE) for an exciton trapped as a whole, whereas the term `self-trapped exciton` (STE) will be used for the one, which can be created recombinationally. In the case of alkali halides apparently only hypotetical one-halogen excitons are true SSEs. Evidently because of the high probability of interchannel scattering such SSEs are here observable only as short-lived intermediate states of exciton relaxation. The possibility of coexistence of both kinds of relaxed excitons appears even when very simple assumptions are made [2] . A fundamental reason for this is connected with a different character of lattice relaxation induced by either uncharged or charged electron excitation. This difference may be of a decisive importance in the case of low point symmetry when the self-trapping of, e.g., hole (i.e. the first stage of the creation of STE) disturbs essentially the Coulomb stability of the lattice, in contrast to the case of SSE. The complex spatial structure of the majority of wide-gap insulators (which leads to low point symmetry of ions` positions and, respectively, to large option of different ways of lattice distortion) may cause, therefore, in some cases, high stability of several final stages of relaxation. As a result, at least two bright intrinsic luminescence bands of an essentially different origin may occur in the emission spectrum. Among these the SSE emission has some properties, which may be of interest from the view-point of scintillation processes. We will discuss here the data obtained for some complex oxides, although the model developed here can obviously be applicable for other complex compounds as well.

SSE EMISSION

In a number of different complex oxides it has been shown by several authors that some bright bands of supposedly intrinsic luminescence cannot be created in slow recombination processes (thermoluminescence etc.) [3-5]. This means that these emission centres are excitable only

Proc. Int. Conf. on Inorganic Scintillators and Their Applications, SCINT95,
1996, Delft University Press, The Netherlands

through exciton-like mechanisms (i.e. simultaneous participation of both unrelaxed electrons and holes is needed). In contrast to cross-luminescence, these emissions are excitable on the edge of transparency region and exhibit decay times characteristic of relaxed emission centres. Some examples of such,in fact SSE emission are given in Table 1.

Table 1. Luminescent features of complex oxide crystals

Crystals	Edge of intr.transitions	SSE emission band	Recomb.lum. band
Al_2O_3 (sapphire)	9.0 eV	7.5 eV	3.8 eV
Y_2O_3 (yttria)	6.05 eV	3.45 eV	-
$YAlO_3$ (YAP)	8.0 eV	5.9 eV	4.2 eV
$Y_3Al_5O_{12}$ (YAG)	7.0 eV	4.9 eV	4.2 eV
$Y_3Ga_5O_{12}$ (YGG)	6.0 eV	4.1 eV	?
$Lu_3Al_5O_{12}$ (LuAG)	7.3 eV	5.1 eV	4.5 (?)

The relaxed state of SSE can be described by a set of three kinds of levels having a triplet character [6] . Radiative decay times usually lie in the range of about 30 ns, 300 ns, and some tens of microseconds, respectively. The evident reason of such uniformity seems to be connected with the circumstance that in all these cases the main features of SSE are determined by excited states of the oxygen ion. Usually the population of these levels is determined by thermal equilibrium between two lowest levels and, therefore, the yield of the fastest emission from the upper level is low (some percent of the total yield of unquenched SSE emission). Thermal quenching of the main part of the emission takes place from the intermediate level and is accompanied by a respective decrease of the decay time. Although this decay time can be fast enough at room temperature, the yield of such quenched SSE emission is too low to be of interest for usual applications. However, in some cases the population of SSE levels may be more favourable. As it was shown for sapphire and YGG [6,7] , the population of all three kinds of levels is almost equal and the quenching of each population takes place independently. As a result, there exists a temperature interval where SSE emission consists of only the fast component with a relatively high yield (about 0.3 of the total yield).

GENERATION STAGE

The investigation of excitation spectra has shown that SSE excitation spectra (being placed entirely in the region of intrinsic absorption) differ strongly from excitation spectra of any recombination luminescent processes. In Fig.1 we demonstrate the spectra recently obtained for LuAG and YGG (see also [3,8,9] for the cases of sapphire, YAP and YAG). The low-energy side of the SSE excitation spectra is formed by competition between the Urbach tail of intrinsic absorption and impurity- or defect-induced additional absorption. The region of most efficient excitation of SSE correlates with the exciton peculiarities of absorption spectra. In the higher-energy region of electron-hole transitions, where the well-known processes of surface losses disturb usually the shape of excitation spectra, more accurate information gives the ratio of different excitation spectra (e.g. the ratio of those of SSE and either STE or other recombination luminescence), as it is shown in Fig.2. In addition to the exciton absorption region, such `spectrum of ratio` shows one more region of an efficient excitation of SSE, which is placed in the region of multiplication of electron excitations. This peak reflects the creation of exciton by hot photoelectron [10]. High relative efficiency of such a process cannot

evidently be affected by crystal imperfections and this fact confirms once more the intrinsic origin of the presumed SSE emission. At the same time, the SSE excitation efficiency is non-vanishing also in the region of pure electron-hole transitions, which shows that there exists some probability to form exciton from unrelaxed (or partially relaxed) electrons and holes. Although such probability is not very high, both these mechanisms give together relatively high efficiency of the SSE emission observed in scintillation process. As shows the study of SSE decay times, the efficiency of the creation of SSE in scintillation process does not depend on the temperature (at least up to 300 K), whereby the SSE emission yield decreases at high temperatures through intracentre quenching. As follows from the creation mechanisms of SSE emission, its generation stage is limited by fast processes of electron and electron-lattice relaxation and, therefore, no afterglow can be observed here.

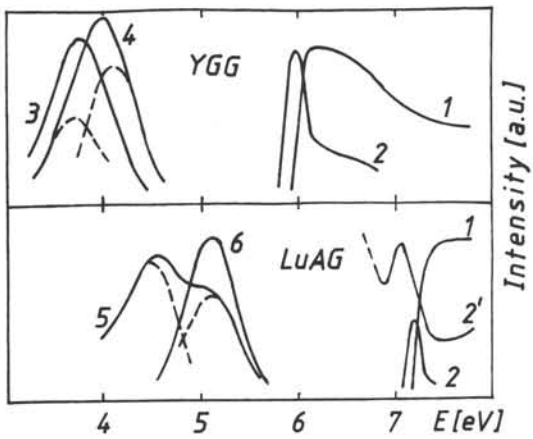

Figure 1. Excitation spectra (1) of the SSE emission and (2) of the recombination luminescence (2' - of the Tb emission) at 5 K.
Luminescence spectra and their distribution in elementary bands: at excitation at 5 K by the 5.9 eV (3) and 7.7 eV (4,6) photons and at pulsed X-ray excitation at 190 K (5) and 5 K (6).

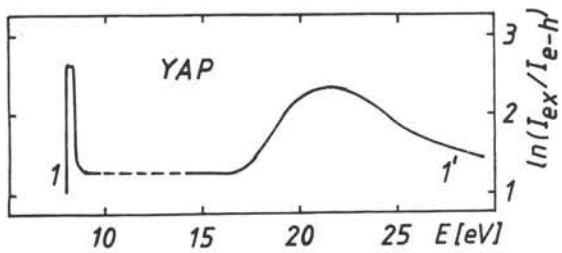

Figure 2. Spectrum of the ratio of intensities of the SSE and recombination emissions (the 5.9 eV band with respect to the 4.2 eV one) at 5 K (1,1') according to [8,10], respectively.

SSE CHANNEL IN RELAXATION PROCESSES

At low temperatures the SSE channel determines the relaxation of a remarkable part of scintillation energy. This channel plays also an important role at high temperatures, determining the behaviour of relaxation even when SSE emission is already strongly quenched. The quenching of SSE emission is accompanied by a respective increase of the intensity of recombination emissions and, e.g. in some garnets, by the increase of thermoluminescence

storage [11] . The latter shows that in this case thermal decay of SSE is connected with thermoionization after which electrons and holes participate in recombination processes. It is possible, in principle, that SSE transforms at high temperatures into some other kind of SSE or STE simply over the barrier between the respective adiabatic surfaces. Probably such situation is realized in sapphire, where the 3.8 eV STE emission shows a `delayed` rise time [12] . The scheme in Fig.3 can illustrate the specificity of coexistence of SSE and recombination channels when these both relaxation branches are characterized by different lattice distortions. The character of this coexistence obviously depends on the relative position of the unrelaxed exciton and electron-hole states (which reflects the complex energy structure) and on the magnitude of lattice relaxation (i.e. the softness of the lattice) in both these cases and, therefore, the mechanism of branching of relaxation between SSE and the recombination channel must be carefully checked in each compound under consideration. In particular, among the crystals discussed, the states of excitons and of the electron-hole continuum are overlapped in YAG crystals, whereas the exciton states are somewhat shifted downwards with respect to the electron-hole ones, being the lowest states of electron relaxation in sapphire and Y_2O_3. Moreover, in the latter case no manifestations of the STE channel were observed either.

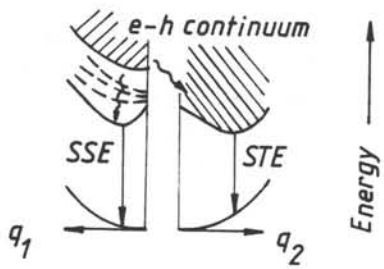

Figure 3. A scheme of relaxation processes in complex oxides. Different configuration coordinates, q_1 and q_2, are used to illustrate different relaxation ways. Two different e-h continuums reflect complex energy structure of the crystals under consideration.

This work is supported by the Estonian Science Foundation Grant No 943.

References

[1] Sumi A., *J.Phys.Soc.Japan* **43** (1977) 1286.
[2] Kuznetsov A.,Abramov V.,Mürk V,Namozov B, *Sov.Phys.Solid State* **33**(1991) 1126.
[3] Kuznetsov A.I.,Namozov B.R.,Myurk V.V., *Sov.Phys.Solid State* **27**(1985) 3030.
[4] Batygov S.Kh.,Voronko Yu.K,Margiani N.G.,Osiko V.V.,Ryskin N.N.,Strelov V.I.,Timoshechkin M.I., *Opt.Spectrosc.(USA)* **67** (1989) 360.
[5] Batygov S.Kh. et al. *Preprint No 53,General Phys.Inst.,Moscow* 1990, 30 p.
[6] Mürk V.V.,Ismailov K.M., *Phys.Solid State* **35** (1993) 259.
[7] Mürk V., Ryskin N. and Ismailov K. *Record of the Intern.Workshop PHYSCI`94, TUD-SCIR-94-04, Delft, the Netherlands*, p. 125.
[8] Mürk V,Kuznetsov A,Namozov B,Ismailov K. *Nucl..Instr.and Meth.***B 91**(1994) 327.
[9] Mürk V.,Yaroshevich N., *J.Phys.:Condens. Matter* **7** (1995) 5857.
[10] Lushchik Ch.,Frorip A.,Lushchik A.,Mürk V,Kirm M.,Martinson I. *MAX-LAB activity report 1993, National Laboratory Lund,Sweden*, 1994, p.166.
[11] Ismailov K.M.,Mürk V.V. *(Sov.)Phys.Solid State* **34** (1992) 165.
[12] Mürk V.V.,Kuznetsov A.I.,Namozov B.R.,*Phys.Status Solidi (a)* **63** (1981) K131.

RELAXATION PROCESSES IN Y_2O_3 AND Sc_2O_3 CRYSTALS

V. Mürk and O. Svinarenkov
Institute of Physics, Riia 142, EE2400 Tartu, Estonia

Abstract. The decay times of the Y_2O_3 and Sc_2O_3 intrinsic emissions are measured by means of the pulsed X-ray and photo-excitation in the wide temperature range. The specifity of relaxation of electron excitations in both crystals, induced by the complex electron structure is discussed.

INTRODUCTION

The oxide crystals, being widely used in practice, have,as a rule, a complex crystalline and an energy structure, where the valence band, being mainly formed from oxygen orbitals, contains on its top a set of narrow subbands of a nonbonding character. This inhomogeneity of the valence band of complex oxides has earlier been proposed to be responsible for the specifity of relaxation in several Al-containing oxides [1,2] .The aim of this work is the search of the peculiarities of relaxation processes in the region of the intrinsic absorption of Y_2O_3 and Sc_2O_3 crystals,where manifestations of the d-type states of the conduction band in relaxation processes can be expected to be observable. For these two crystals, which have a very similar crystalline structure and physical properties, a distinct exciton absorption peak has been observed only in the first one, that has been ascribed [3] to the difference in the origin of the conduction band bottom (i.e. a d-like one for the Sc_2O_3 and probably an s-like one for the Y_2O_3).

EXPERIMENTAL

The luminescence and thermoluminescence excitation spectra were investigated in a wide temperature interval down to 5K by using traditional VUV methods [2] .For time-resolved luminescent measurements an X-ray facility with a variable pulse duration [4] and a VUV discharge lamp [5] were used.

DECAY TIMES

The temperature dependences of the decay time of a supposedly intrinsic luminescence indicate a similarity of emitting centres in both crystals at the temperatures above 100 K (see Fig.1). At low temperatures the 3.45 eV exciton emission of Y_2O_3 crystal exhibits usual features, characteristic of self-shrinked exciton emission in a number of oxide crystals [4] . At the same time the decay time of an analogous exciton emission of Sc_2O_3 at 3.55 eV increases rapidly up to very high values and at 5 K this supposedly intrinsic emission is characterized by a strong afterglow [3] . Although during this the total yield of emission remains, the more precise measurements have shown that the band of this slow emission is shifted somewhat in the low-energy side with respect to the usual position. Due to decrease of the pulse amplitude, the fast (about 70 ns) component of the 3.55 eV emission becomes clearly

Proc. Int. Conf. on Inorganic Scintillators and Their Applications, SCINT95,
1996, Delft University Press, The Netherlands

observable on the background of the slow emission at low temperatures. The first manifestations of such drastic change in the structure of the Sc_2O_3 emission, observed early at intermediate temperatures [3] , were supposed to be connected with the formation of the special kind of self-trapped excitons called by Toyazawa an exciton dichotomy (see for details in [6,7]). In some sense such excitons are similar to the off-centre self-trapped excitons in alkali halides [8] , where the electron and hole, which form an exciton, are essentially separated in the crystal lattice.

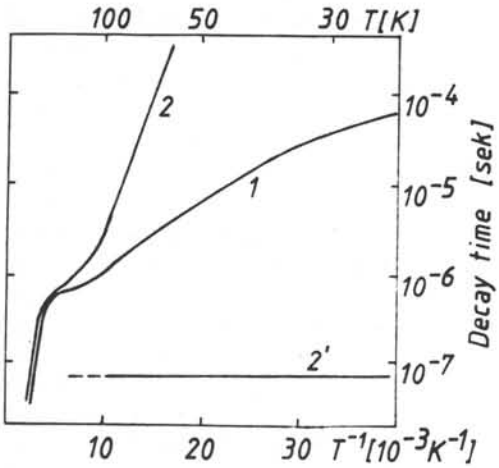

Figure 1. Temperature dependences of the decay time (1) of the 3.45 eV emission in Y_2O_3 and (2,2') of the two components of the 3.55 eV emission in Sc_2O_3.

EXCITATION SPECTRA

A comparison of intrinsic luminescence excitation spectra of different Y_2O_3 crystals shows that the relaxation properties of the electron excitations created by photons in the spectral interval of about 1 eV around the exciton absorption peak differ from those for electron excitations of higher energy (see Fig.2, where two extreme cases of excitation spectra are given). As shows the investigation of theromoluminescence excitation spectra, the energy region where the excitation spectra of the 3.45 eV emission strongly depend on the crystal quality is the region of the electron-hole transitions.This indicates that the behaviour of the excitation spectra depends here on the competition between the `mounting` of excitons from electrons and holes and the trapping of charged carriers by the lattice defects. The features of such electron excitations of the Y_2O_3 crystal are similar to those of the main electron excitations of Sc_2O_3 crystals, which give rise to a supposedly intrinsic 3.55 eV emission.

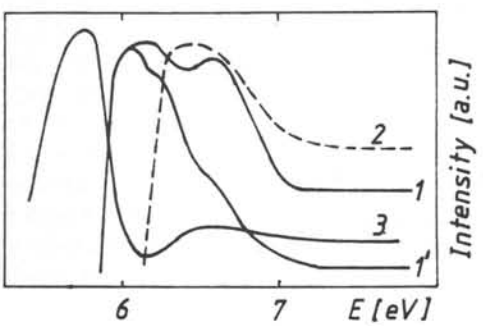

Figure 2. Luminescence excitation spectra at 5 K (1,1') for the 3.45 eV exciton emission in two different Y_2O_3 samples, (2) for the 3.55 eV emission in Sc_2O_3, and (3) for the defect emission at 2.8 eV in Y_2O_3.

DISCUSSION

In the Sc_2O_3 crystals the slow, in fact recombination, relaxation channel giving rise to the 3.55 eV emission is very efficient, in contrast to that in the Y_2O_3 crystal, where it seems to be strongly disturbed by the crystal imperfections. This means that in Sc_2O_3 either electrons or holes self-trap giving the cores of formation of recombination self-trapped exciton. Only relatively weak fast component of the Sc_2O_3 emission represents probably the exciton relaxation channel at low temperatures. As at high temperatures the recombination channel transforms here entirely into the exciton one, the states of respective self-shrinked excitons turn out to be the lowest relaxed states of intrinsic excitations (in contrast to an opposite case in, e.g., garnets [2]). However the lowest unrelaxed electron states of Sc_2O_3 are evidently the states of the d-electron and p-hole continuum. In Y_2O_3 the exciton states are the lowest states in the both relaxed and unrelaxed cases. Thus, this different position of exciton states with respect to the continuum ones reflects here obviously the different position of the s-conduction band with respect to the d-one. Although the bottom of the conduction band may have the d-character in the both crystals,the s-conduction band (participating in the formation of the s-p-exciton) must lie very close to the conduction band bottom namely in the Y_2O_3 crystals..

This work is supported by the Estonian Science Foundation Grant No 943.

References

[1] Kuznetsov A I, Namozov B R, Myurk V V, *Sov.Phys.Solid State* **27**(1985)3030.
[2] Mürk V, Yaroshevich N, *J.Phys.:Condens. Matter* **7** (1995) 5857.
[3] Abramov V.N.,Ermoshkin A.N.,Kuznetsov A.I.,Mürk V.V. *Phys.Status Solidi (b)* **121** (1984) K59.
[4] Mürk V V, Ismailov K M, *Phys.Solid State* **35** (1993) 259.
[5] Mürk V.V.,Namozov B.R. *Trudy Inst.Fiziki AN Est.SSR* **55** (1984) 180.
[6] Kuznetsov A I, Abramov V N, Mürk V V, Namozov B R, *Sov.Phys.Solid State* **33** (1991) 1126.
[7] Sumi A, *J.Phys.Soc.Japan* **43** (1977) 1286.
[8] Song K.S.,Williams R.T. *Self-trapped excitons, Springer Series in Solid-state Sciences (ed. by M.Cardona) **105** ,Springer-Verlag Berlin Heidelberg*, 1993.

□

THE LUMINESCENCE OF LEAD AND BISMUTH COMPOUNDS

G. BLASSE, H.F. FOLKERTS and J. ZUIDEMA, Debye Institute, Utrecht University, Postbox 80.000, 3508 TA Utrecht, The Netherlands.

ABSTRACT

The luminescence of lead- and bismuth-containing eulytites is described. In the case of lead it is possible to study the isolated Pb^{2+} ion. This allows to elucidate the so-called s^2 ion effect, which is also of importance for $Bi_4Ge_3O_{12}$. Crystal structures in which this effect occurs also (stuffed tridymite) or does not occur (barite) are also included. Finally other types of lead compounds are mentioned ($PbGe_3O_9$, $PbWO_4$ and $PbTiO_3$), including the luminescence of $BiTaO_4$ ($d=9.1$ g.cm^{-3}).

INTRODUCTION

Due to their high density lead, and especially bismuth compounds are serious candidates as scintillators. Well known are, for example, $Bi_4Ge_3O_{12}$, $PbWO_4$ and $PbSO_4$. On the other hand, the factors which determine their luminescence properties are by no means well understood. In this paper an attempt is made to contribute to a solution of this situation. A large number of compositions are described. The details of their luminescence properties will be discussed elsewhere.

EXPERIMENTAL AND RESULTS

Powder samples were prepared by conventional techniques [1] and checked by X-ray powder diffraction. Measurements of their photoluminescence properties were performed on a spectrofluorometer equipped with a liquid helium cryostat as described elsewhere [2].

Table I presents the results of the present study. It may be clear that they relate to three crystal structure types in which the Pb^{2+}/Bi^{3+} concentration is either 100 or a few percent. The emission and excitation spectra consist of broad bands which implies that the spectral maxima as well as the values of the Stokes shift are only reliable estimates. In a few cases more than one luminescent centre has been observed. The values of the quenching temperatures can only be considered as a rough estimate.

DISCUSSION

All optical transitions involved are ascribed to the Pb^{2+}/Bi^{3+} ion [1] . This implies that this study is only related to the last step of the scintillation process, viz. the emission from the luminescent centre. The efficiency of electron-hole pair creation and the transfer efficiency is here not considered.

Proc. Int. Conf. on Inorganic Scintillators and Their Applications, SCINT95,
1996, Delft University Press, The Netherlands

Table I. Some data on luminescent compounds containing lead or bismuth. Spectral data at 4.2 K.

Composition	Emission maximum (nm)	Excitation maximum (nm)	Stokes shift ($10^3 cm^{-1}$)	Crystal structure	Quenching temperature (K)	Ref.
$PbGa_2O_4$	590	265	21	s.t.[a]	350	[3]
$SrGa_2O_4$:Pb	360/430	280	8/13	s.t.	>300	[4]
$PbAl_2O_4$	475	250	19	s.t.	>300	[3]
$SrAl_2O_4$:Pb	310	250	8	s.t.	>300	[4]
$Bi_4Ge_3O_{12}$	480	260	18	eul.[b]	>300	[3]
$Pb_4(PO_4)_2SO_4$	470	255	18	eul.	150	[5]
$Ba_4(PO_4)_2SO_4$:Pb	360	245	13	eul.	300	[5]
$Sr_4(PO_4)_2SO_4$:Pb	350	250	12	eul.	300	[5]
$Ba_3La(PO_4)_3$:Pb	365	250	11	eul.	>300	[6]
$Ba_3Bi(PO_4)_3$	400	290	10	eul.	100	[5]
$Pb_3Bi(PO_4)_3$	350/385	255/275	11/11	eul.	100/300	[5]
$Pb_3La(PO_4)_3$	vis.[c]	270	-	$Pb_3(PO_4)_2$	-	[5]
$PbSO_4$	335	220	15	bar.[d]	300	[7,8]
$SrSO_4$:Pb	315	210	15	bar.	>300	[4]
$BaSO_4$:Pb	340	220	16	bar.	>300	[9]

a: stuffed tridymite
b: eulytite
c: several bands over the whole visible region
d: barite

The emission of Pb^{2+}/Bi^{3+} is due to the $^3P_{0,1} \rightarrow {}^1S_0$ transition. The excited state can be strongly influenced by the host lattice. Table I shows the following effects:
a.Dilution of the Pb^{2+}/Bi^{3+} ion concentration with ions with noble-gas configuration has sometimes no influence at all (barite structure), but in other cases its influence is dramatic (stuffed tridymite, eulytite structure).
b. This influence is most conspicious in the positions of the emission maxima as a consequence of the variation of the Stokes shift, i.e. of the relaxation in the excited state.
c. Crystalchemical considerations show that a high value of the Stokes shift, i.e. a long wavelength emission, can be correlated to an off-centre position of the Pb^{2+}/Bi^{3+} ion in its coordination polyhedron. This aspect will now be discussed in more detail.

Ions with s^2 configuration, like Pb^{2+} and Bi^{3+} (both $6s^2$), favour a strongly asymmetric coordination (the so-called lone-pair effect). Examples are $Bi_4Ge_3O_{12}$ (Bi-O 2.16 Å on one side and 2.60 Å on the other [10]) and $Pb_4(PO_4)_2SO_4$ (Pb-O 2.43 Å and 2.66 Å, respectively [11]). The consequence of such a configuration is a large Stokes shift of the emission, long wavelength emission, and a low quenching temperature. This explains why the emission of $Bi_4Ge_3O_{12}$ is quenched at 300 K for about two thirds [1]. A very extreme case is $Bi_2Ge_3O_9$ with a quenching temperature of 130 K and a Stokes shift of more than 20.000 cm^{-1}; actually the short and the long Bi-O distances are even more different than in $Bi_4Ge_3O_{12}$ (2.14 Å and 2.74 Å, respectively) [12].

In the stuffed tridymite structure the large cations (Sr^{2+}, Pb^{2+}) occupy the large interstices in the tridymite sublattice. Noble gas ions do so in the centre of the site, but s^2 ions offcentre. Table I shows the dramatic change in the Pb^{2+} luminescence. The samples with low lead concentration show the characteristic Pb^{2+} emission in the ultraviolet, because the Pb^{2+} ions substitute for on-centre Sr^{2+}. The lead compounds, however, have off-centre Pb^{2+} ions as has been shown crystallographically, and the Stokes shift is more than doubled. Although not clear from Table I, the quenching temperature of the emission of the lead compounds is lower than that of the doped samples [3,4].

In the barite structure, on the other hand, the coordination of Sr^{2+}, Ba^{2+} and Pb^{2+} is nearly the same and so is the luminescence. This is very similar to results observed for the alkaline-earth and lead carbonates [13].

An interesting case is that of the eulytite structure of which $Bi_4Ge_3O_{12}$ is the most well-known representative. Barbier [11, and references cited there] has performed an interesting study of that crystal structure. It turns outs that $Bi_4Ge_3O_{12}$ is an exceptional case, because it is fully ordered. Other compounds with this structure show disorder, however. Whereas the ideal eulytite structure shows only one site for oxygen, $Pb_4(PO_4)_2SO_4$ shows two oxygen positions which are only partly filled. There are two types of tetrahedra possible. There is some indication that P and S show short-range order. In the eulytites $Sr_3La(PO_4)_3$ and $Ca_3Bi(PO_4)_3$ there is not only disorder on these oxygen sublattices, but also on the larger cation sublattice. Only in an ordered structure all off-centre positions can be expected to occur in phase. Disorder will counteract the off-centre effect.

The luminescence data for $Bi_4Ge_3O_{12}$ and $Pb_4(PO_4)_2SO_4$ (see Table I) are similar, confirming the close-to-ordered situation in $Pb_4(PO_4)_2SO_4$. The lead concentration in this compound can be diluted with noble-gas ions which is not possible in $Bi_4Ge_3O_{12}$. The off-centre position gets lost, and in fact the Stokes shift decreases and the quenching temperature goes up. In the even more disordered $Ba_3La(PO_4)_3$ the Pb^{2+} luminescence is similar to that in $M(PO_4)_2SO_4$ (M=Sr,Ba).

Interestingly enough, $Pb_3Bi(PO_4)_3$ does not show luminescence as expected for a eulytite with only s^2 ions. The spectra point to on-centre Pb^{2+} and on-centre Bi^{3+}.

Obviously the disorder prevents long-range order of off-centre positions. The low quenching temperature of the Pb^{2+} luminescence of $Pb_3Bi(PO_4)_3$ is striking. This is probably due to quenching via an excited "Pb^{3+}-Bi^{2+}" state which cannot be at high energy in view of the ionization potentials involved.

On-centre Bi^{3+} ions are found in $Ba_3Bi(PO_4)_3$ with luminescence characteristics which are very different from $Bi_4Ge_3O_{12}$. The small Stokes shift suggests a high thermal quenching temperature. This is not observed (see table I). Probably energy migration to quenching centres plays a role [1].

The instability of the eulytite structure is demonstrated by the fact that the composition $Pb_3La(PO_4)_3$ could only be obtained with the $Pb_3(PO_4)_2$ structure. Similar observations have been made for other eulytite compositions [14,15]. This means that the lead positions of the latter structure are occupied by (67% Pb^{2+}, 22% La^{3+}, and 11% vacancies). In fact the emission spectrum consists of many overlapping Pb^{2+} emission bands. The present results yield information on the relation between chemical composition and luminescence of s^2 ions in the eulytite structure.

In the compositions dealt with above the electrons of the Pb^{2+} centre are always localized. This is not the only possibility. In $PbGe_3O_7$, $CsPbCl_3$, and $Bi_{12}GeO_{20}$, for example, the s^2 ion levels broaden into energy bands [1]. Usually the quenching temperature of the luminescence is then lowered considerably. Cases in between are $PbWO_4$ and $PbTiO_3$ [1,2]. No doubt a very exciting compound in this class is $BiTaO_4$ ($d=9.1\ g.cm^{-3}$) [16]. It occurs in two modifications with different luminescences. The α phase contains Bi^{3+} in its favoured off-centre position which implies stabilization. The luminescence is due to the tantalate sublattice. In the β-phase the Bi^{3+} ion is on-centre, i.e. destabilized. The luminescence transition is now of a bismuth-tantalate charge-transfer type like in $PbWO_4$ and $PbTiO_3$. Due to its high density $BiTaO_4$ may be of interest for certain applications: since the quenching temperature is below room temperature, the decay is expected to be fast, but the light output low.

REFERENCES

[1] G. Blasse and B.C. Grabmaier, Luminescent Materials, Springer Verlag, Berlin, 1994
[2] H.F. Folkerts and G. Blasse, Chem. Mater. 6 (1994) 969
[3] C.W.M. Timmermans and G. Blasse, J. Solid State Chem. 52 (1984) 222
[4] H.F. Folkerts, F. Ghianni and G. Blasse, unpublished
[5] H.F. Folkerts, J. Zuidema and G. Blasse, unpublished
[6] H.S. Kiliaan and G. Blasse, J. Electrochem. Soc. 136 (1989) 562
[7] G. Blasse, Chem. Phys. Letters 35 (1975) 299
[8] W.W. Moses, S.E. Derenzo and P.J. Shlichte, I.E.E.E. Tr. Nucl. Science 39 (1992) 1190
[9] H.F. Folkerts, M.A. Hamstra and G. Blasse, to be published
[10] A. Durif and M. Averbuch-Pouchot, C.R.Ac. Sci. Paris II 295 (1982) 555
[11] J. Barbier, Eur. J. Solid State Inorg. Chem. 31 (1994) 163
[12] C.W.M. Timmermans, O Boen Ho and G. Blasse, Solid State Comm. 42 (1982) 505
[13] H.F. Folkerts and G. Blasse, submitted to J. Phys. Chem. Solids
[14] J. Barbier and D. Maxin, J. Solid State Chem. 116 (1995) 179
[15] M.F. Hoogendorp, W.J. Schipper and G. Blasse, J. Alloys Compounds 205 (1994) 249
[16] M. Wiegel, W. Middel and G. Blasse, J. Mater. Chem., in press

DENSE LEAD AND BISMUTH SCINTILLATORS

M. J. Weber, A. C. West, C. Dujardin*
Lawrence Berkeley National Laboratory, Berkeley, California USA 94720

B. Rupp
Lawrence Livermore National Laboratory, Livermore, California USA 94550

M. Berrondo, J. F. Rivas-Silva
Brigham Young University, Provo, Utah 84602 USA

ABSTRACT

Scintillation intensities of dense lead and bismuth compounds at 300 K are reported relative to BGO. For luminous materials the Pb and Bi site asymmetry is quantified using a principal axis transform of the charge distribution and correlated with the Stokes shift of their emission. Preliminary results of *ab initio* cluster calculations of electronic structure are also presented.

INTRODUCTION

Lead and bismuth are the heaviest nonradioactive elements in the periodic table. Luminescent compounds of these elements can have short radiation lengths and large photoelectric fractions and therefore are attractive for use in detectors for calorimetry in high energy physics [1] and for medical imaging (PET).[2] In the search for new inorganic scintillators, a large number of lead and bismuth compounds have been investigated [3,4] but thus far none have exhibited a light yield superior to that of $Bi_4Ge_3O_{12}$ (BGO). We have extended this survey using crystal diffraction databases [5,6] to identify dense Pb- or Bi-based hosts. The results are summarized in Table 1 where compounds are grouped by scintillation light output relative to that of BGO. Samples were generally in the form of powders or polycrystalline materials. All measurements were performed at room temperature using a pulsed x-ray apparatus and detection techniques described elsewhere.[7] The scintillation spectra were not characterized. At this stage our

Table 1. Reported scintillation intensity at room temperature for lead and bismuth compounds relative to that of $Bi_4Ge_3O_{12}$ [from references [3,4] and from this work (*)].

10–100% BGO	1.0–10% BGO	≤ 1% BGO
$Bi_4Ge_3O_{12}$	$PbCO_3$	Bi_2O_3, Bi_2CO_5, $BiPO_4$, $Bi_2(SO_4)_3$, $BiBO_3$, $Bi(OH)_3$,
$Bi_4Si_3O_{12}$	$PbWO_4$	BiF_3, $BiCl_3$, $BiBr_3$, BiOCl, BiOBr, *$BiKF_4$, *BiK_4F_7,
$PbSO_4$	*$Bi_2Al_4O_9$	*Bi_3KF_{10}, *Bi_4KF_{13}, *$BiHfF_7$, *$BiNa_4I_7$,*$Bi_2Cs_3Br_9$,
*$PbHPO_4$	*$Pb_5(PO_4)_3F$	*Bi_2BaF_8, $Bi_{12}GeO_{20}$, $Bi_{12}SiO_{20}$, $Bi_4Ti_3O_{12}$, $Bi_2Ti_2O_7$,
*$PbAl_2O_4$	$PbCl_2$	Bi_2WO_6, $Bi_2W_2O_9$, $Bi_2W_3O_{12}$, $Bi_2Na(WO_4)_2$, $BiNO_4$,
	*PbOHCl	$Bi(MoO_4)_3$, *$Bi_2Sn_2O_7$, $Bi_2Sn_3O_9$, $Bi(C_2H_3O_2)_3$,
	*PbOHBr	$Bi_{12}PbO_{20}$, $BiPbFO_2$, PbF_2, $PbCl_2$, $PbBr_2$, PbI_2,
	*PbOHI	$Pb(NbO_3)_2$, $PbSO_3$, PbC_2O_4, $Pb(OH)_2$, $Pb(VO_3)_2$,
		PbB_3O_7, $PbZrO_3$, Pb_2SiO_4, $Pb(NO_3)_2$, $PbSeO_4$,
		$PbSiO_3$, $PbTiO_3$, *$PbHfO_3$, $PbTa_2O_6$, $PbMoO_4$,
		$Pb_2P_2O_7$, $Pb_3P_2O_8$, $Pb(NbO_3)_2$,$Pb(ClO_4)_2 \cdot H_2O$

Proc. Int. Conf. on Inorganic Scintillators and Their Applications, SCINT95,
1996, Delft University Press, The Netherlands

intent is to survey and screen those materials operating at room temperature that warrant further spectroscopic studies and growth efforts.

Although the luminescence properties of various Pb- and Bi-doped materials and lead and bismuth compounds have been investigated for many decades and most of the spectroscopic features are generally understood [8], our ability to predict efficient room-temperature Pb or Bi luminiscence is still limited and new features continue to be reported (see, for example, [9]). The number of Bi and Pb compounds exhibiting intense photo- or x-ray-excited luminescence at 300 K is small. The structure and spectroscopic properties of several of these compounds are given in Table 2. ($T_{1/2}$ is the temperature at which the luminescence is reduced to one-half of its low temperature value.) Of the bismuth oxide–germanium oxide system, only the compounds with large germania content exhibit luminescence. Similar behavior is observed for the Bi_2O_3–SiO_2 system. The 1:2 compounds of the bismuth aluminate and gallate systems and the 1:1 compounds of the lead aluminate and gallate systems exhibit intense luminescence at room temperature.[10] Although their densities are not high, there are other compositions, particularly the 2:1 compound $Bi_4Al_2O_9$, that warrant investigation. Many different lead phosphate compositions exist with a wide range of densities. The 3:1 compound in Table 2 is moderately dense but has a quenching temperature of only 150 K; no significant luminescence was detected for several other lead phosphates down to liquid helium temperatures.[11]

Table 2. Structure and spectroscopic properties of lead and bismuth compounds.[10-15]

Compound	Density (g/cm^3)	Oxygen CN: (distances – Å)	Stokes shift (eV)	Quench $T_{1/2}$ (K)
Bismuth:				
$Bi_{12}GeO_{20}$ (6:1) *(cubic)*	9.2	7: 2.07–3.19	1.0/1.5	25/140
$Bi_4Ge_3O_{12}$ (2:3) *(cubic)*	7.1	6: 2.16–2.62	2.25	270
$Bi_2Ge_3O_9$ (1:3) *(hexagonal)*	6.2	6: 2.14–2.75	2.5	120
$Bi_3B_5O_{12}$ (3:5) *(orthorhombic)*	6.2	6: 2.12–2.68	2.1	150
$Bi_2Al_4O_9$ (1:2) *(orthorhombic)*	6.2	6: 2.24–2.78	2.2	280
Lead:				
$PbAl_2O_4$ (1:1) *(monoclinic)*	5.5	6: 2.27–3.27	2.4	>300
$PbGa_2O_4$ (1:1) *(monoclinic)*	6.6	6: 2.28–3.30	2.6	290
$PbSO_4$ *(orthorhombic)*	6.4	8: 2.63–2.93	2.2	>300
$PbHPO_4$ *(monoclinic)*	5.6	6: 2.35–2.87	≈2.9	220
$Pb_3(PO_4)_2$ (3:1) *(monoclinic)*	7.5	8: 2.54–2.97	1.5	150

SITE ASYMMETRY

Blasse and co-workers have noted that luminous Pb and Bi compounds generally have Pb or Bi ions with asymmetric coordination polyhedra. For such off-center sites, large displacive relaxation may occur in the excited electronic state resulting in large Stokes shifts. We have quantified the asymmetry by forming a matrix of the coordinates and charges of the surrounding ions. The program SEXIE [16] was used to identify the coordination shells. Note that even when there is no symmetry of the surrounding ligands, it is still possible to define a principal axis system.[17] Using a simple point charge for the ligands, the coordination matrix is diagonalized using a Jacobi transformation, thus yielding a set of three

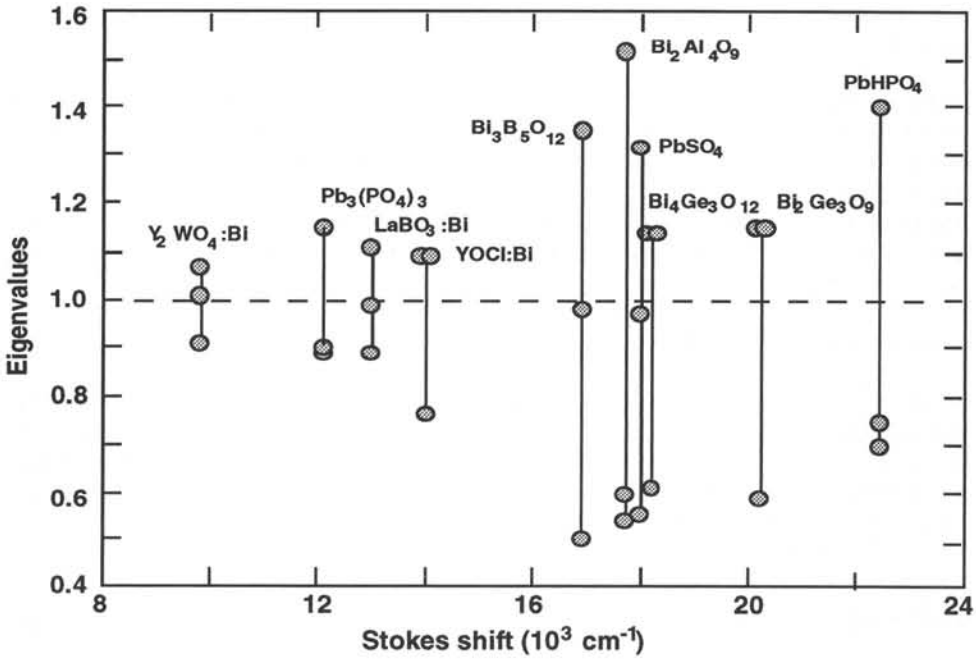

Figure 1. Eigenvalues of a principal axis transformation of the nearest neighbor charge distribution for Pb and Bi materials as a function of the Stokes shift of their luminescence

eigenvalues (renormalized to 1 for a spherical charge distribution) which are the semi-axes of the charge ellipsoid. The results for several Pb and Bi compounds are shown in Fig.1. Large Stokes shifts correlate with large distortions of the charge distribution. What is needed is guidance in predicting the quenching temperature. As can be seen from Table 2, there is not a clear correlation between charge asymmetry, Stokes shift, and quenching temperature.

CLUSTER CALCULATIONS

We have begun using *ab initio* calculations of ion clusters to simulate the electronic structure of BGO and BSO crystals. (In an early investigation of BGO, a $(BiO_6)^{9-}$ cluster was treated using molecular orbital theory.[18]) We have tried several different clusters and embedding approaches. To date the most meaningful results have been obtained with a cluster consisting of a Bi ion surrounded by six O and three Ge. The cluster was saturated with fifteen H atoms. The total number of valence electrons was 80. All computations were performed using gaussian bases and Hay-Wadt pseudopotentials which include relativistic effects necessary for heavier atoms. We first optimized the cluster configuration for the ground state minimizing the total self-consistent-field (SCF) energy. The final ground state configuration is very close to that of the known crystal structure. Excited states are treated using a singles configuration interaction calculation. We re-optimized the cluster geometry for the excited triplet state to obtain the emission energy and Stokes shift. In the lowest excited state the Bi moves slightly towards the center of the cluster, but one of the nearest neighbor oxygens binding the Bi with a Ge moves an unexpectedly large 1.1 Å away from the Bi. (This behavior was confirmed from calculations of bismuth trihalide molecules.) A large Stokes shift is predicted but is larger than observed because the absorption energies are about 20% larger than the experimental

values and the emission energies are 10% lower. We also estimated the lifetime of the lowest excited state using a spin-orbit term to mix singlet and triplet. The calculated lifetime of BGO is about five times longer than that of BSO. Experimentally it is found to be three times longer. The computed Mulliken atomic charge on Bi for the triplet state is close to 1.5 instead of the formal charge of +3. This partially covalent binding between Bi and the three closest oxygens implies an approximate C_{3v} symmetry, thus the 3P state of Bi^{3+} is split into two electronic states. At the same time, the spin population is almost evenly split between the Bi and the displaced oxygen. In this case a molecular orbital picture of the excitation is more appropriate. These results are in contrast to those obtained for other $6s^2$ ion scintillators, such as NaI:Tl, where the thallium was found to behave almost as a Tl^+ ion.[19]

ACKNOWLEDGMENTS

We are indebted to P. Berdahl and D. Perry (LBNL, Berkeley) and B. Sobelov (Institute of Crystallography, Moscow) for samples used in this work. This work was supported in part by the Director, Office of Energy Research, Office of Health and Environmental Research, Medical Applications and Biophysical Research Division of the U.S. Department of Energy under contract No. DE-AC03-76SF000098, and by Public Health Service Grant R01 CA48002 awarded by the National Cancer Institute, Department of Health and Human Services. One of the authors (C. D.) acknowledges the support of a NATO grant.

* Permanent address: Laboratoire de Physico-Chimie des matériaux Luminescents, Université Claude Bernard Lyon 1, URA 442 CNRS, Villeurbanne Cedex, France

REFERENCES

1. P. Lecoq, "The Lead Tungstate Calorimeter of the CMS Experiment " (these proceedings).
2. W. W. Moses, "Scintillators for Positron Emission Tomograaphy" (these proceedings).
3. S.E. Derenzo, W.W. Moses, et al., *IEEE Trans Nucl Sci*, **NS-37**, 203 (1990) and *IEEE Nuclear Science Symposium Conference Record* 91CH3100-5, **1**, 143-(1991).
4. S.E. Derenzo, W. W. Moses, M. J. Weber and A. C. West, in *Scintillator and Phosphor Materials*, (Materials Research Society Symposium Proceedings Vol. **348**, 1994), p. 39.
5. NIST Crystal Data Identification File (1993), International Centre for Diffraction Data, Newtown Square, PA, U.S.A.
6. Inorganic Crystal Structure Database, FIZ, Karlsruhe, and GMELIN Insitute, Frankfurt.
7. S. C. Blankespoor, S.E. Derenzo, et al., *IEEE Trans.Nucl. Sci.* **NS-41**, 691 (1994).
8. G. Blasse and B. C. Grabmeier, *Luminescent Materisls* (Springer Verlag, Berlin, 1994).
9. G. Blasse, H. F. Folkerts and J. Zuidem, (these proceedings).
10. C. W. M. Timmermans and G. Blasse, *J. Solid State Chem.* **52**, 222 (1984).
11. G. Blasse, E. W. J. L. Oomen, and J. Liebertz, *Phys. Stat. Sol. (B)* **137**, K77 (1986).
12. G. Blasse and O Boen Ho, *J. Lumin.* **21**, 165 (1980).
13. C. W. M. Timmermans, O Boen Ho, G. Blasse, *Solid State Commun.* **42**, 505 (1982).
14. G. Blasse and G. J. Dirksen, *Mater. Chem. Phys.* **12**, 551 (1985).
15. G. Blasse, *Phys. Stat. Sol. (B)* **143**, K131 (1987).
16. B. Rupp, B. Smith and J. Wong, *Comp. Phys. Commun.* **67**, 543 (1992); A. E. Tabor-Morris and B. Rupp, *Comp. Phys. Commun.* **82**, 21, (1994).
17. S. Brawer and M. J. Weber, *J. Non-Cryst. Solids* **38&39**, 9 (1980).
18. R. Moncorge, B. Jacquier, et al., *J. Lumin.* **12/13**, 467 (1976)
19. M. Berrondo, F. F. Rivas-Silva and B. Czirr (these proceedings); M. Berrondo and F. Rivas-Silva, *Int. J. Quantum Chem.* **S29** (in press).

PART IV

Tungstate Scintillators - $PbWO_4$

$PbWO_4$ SCINTILLATOR. CURRENT STATUS OF R&D

M.V.Korzhik, Institute for Nuclear Problems, Minsk, Belarussia..

ABSTRACT

The present status of $PbWO_4$ scintillator development to be applied for the CMS Electromagnetic Calorimeter will be discussed. Special attention is paid to the origin of the coloration in the crystals and to the peculiarities of crystal structure.

INTRODUCTION

Recently, lead tungstate crystals, $PbWO_4$ (PWO) which is a fast and dense scintillator, have found an application in the electromagnetic calorimetry [1-6] for future experiments with the new LHC Collider. This crystal has been under investigation for some decades, but till now its properties are still debated in the literature [7-9]. A significant progress in the improvement of the scintillation properties is still obtained to date [10]. However some problems which came up during its investigation still should be solved.

Coloration of the crystals.

Two wide absorption bands with maximums λ=350 and 420 nm appear in the crystals. Their intensities are strongly dependent on the crystal growth conditions, purity of the raw materials, and stochiometry variation in the melt. These bands have a strong effect on the scintillation properties of the full size elements giving a decrease of light yield and a worsening of the light yield uniformity.

Light yield improving

Although further light yield improving is strongly dependent on the suppression of the absorption bands mentioned above, there are two ways which should be investigated. The first one is the increase of the contribution from green luminescence centers to the scintillations. The second one is the increase of the role of blue luminescing centers with simultaneous strong suppression of the 420 nm absorption band. Perhaps, some compromise between these two directions will be acceptable.

Scintillation kinetics

It was established that the fast components in the PWO scintillations mainly origin from blue emitting centers and partly from green luminescing ones. The latter ones give also some rise to the middle fast components (~15÷40 ns), but red luminescing centers do not make a contribution to

Proc. Int. Conf. on Inorganic Scintillators and Their Applications, SCINT95,
1996, Delft University Press, The Netherlands

the scintillations [11]. Strong influences of the purity of the raw materials and the number of the recrystallizations on the appearance of slow components have been observed.

Radiation damage in PWO scintillators

PWO crystals, which are grown under different growth conditions, show a decrease of the transmission under ionizing radiation irradiation. An additional wide absorption band with maximum at 620 nm usually appears under irradiation. With compensation of some sorts of point structure defects by Nb doping, a global improvement of the PWO radiation hardness has been detected. Unfortunately, the radiation induced afterglow [12] still exists in the crystals. Parameters of this afterglow are related with the presence of some color centers in the crystals.

Mechanical properties

To build the CMS Electromagnetic Calorimeter, producers have to increase the yield of the crystals after treatment to the level not less than 90%. To date this yield is less the 70%. Casual fragility after crystal growth and fragility of the annealed crystals under machining are the reason for this poor yield. It indicates that annealing as well as machining procedures are still not optimized.

Raw materials specification

The purity of the raw materials strongly relates with all items mentioned above. Due to the limitations in the price of scintillators that will be acceptable for CMS, it will be impossible to use for the mass production very pure and expensive raw materials. Nevertheless, all unwanted impurities have to be specified and omitted from the raw materials. It was found that Mo, Fe, and some other trivalent and divalent impurities lead to a worsening of the PWO scintillation properties.

To date the following PWO scintillation properties, see Table 1, have been obtained.

Table 1. PWO scintillation properties

Light yield, phe⁻/MeV	Emission maximum, nm	Decay time, ns(%)	Radiation hardness
12-16 (full size) 30-40 (20×20×10 mm^3)	500	2,5/14/150 (40,30,30)	available for the CMS

The scintillation properties of PWO crystals are originating mainly from luminescing centers based on regular WO_4^{2-} and irregular (WO_3+F) centers [4,9]. Their contribution to the scintillation efficiency and scintillation kinetics strongly depends on the presence of other points structure defects and energy transfer processes in the crystals. These energy transfer processes may create quenching of luminescence, but can also be responsible for afterglow and the appearing of slow

components. The point structure defects that are involved in these processes can be due to the presence of additional impurities or host matrix defects. An additional coloration of PWO crystals is still existing mainly due to the presence of an absorption band around λ_{max}=420 nm. This band overlaps the spectrum of luminescence and has a typical maximum absorption coefficient of about k =0.05 cm^{-1} and leads to a relative decrease of light yield by a factor of two for scintillation elements with 200 mm length or more. So, special attention is paid to the origin of the coloration of the crystals and crystal structural peculiarities. Thus motivated, we have investigated PWO structural peculiarities and the influence of doping PWO with ions that, by *a priori* estimation, can effect (worse or improve) PWO scintillation properties.

SAMPLES AND EXPERIMENTAL METHODS

Investigated crystals were grown by the Czochralski technique in platinum crucibles in an atmosphere close to air in composition with some lead deficiency in the melt. Details of crystal growth technology are given elsewhere [4]. Dopants Nb, Yb, Mg, or Bi were introduced in the form of oxides into the melt. Crystals with different impurities were grown in separate crucibles, but all doped ones, excluding Bi doped crystals, contained in addition the same amount of Nb. Samples have been prepared from the top part of the ingots that were annealed in air. Other parts of the ingots were used for preparing of the scintillation elements. Equipment for spectroscopic measurements and measuring scintillation parameters are described elsewhere [13].

Detailed investigation of the crystal structure has been carried out using experimental facilities of the University of Technology (Annecy le Vieux) with the following technique. For suitable X-ray analysis, single crystals were extracted by mechanical means. The intensities of 4340 reflections were collected by a CAD-4 automatic four circle difractometer in a θ -2 θ scan mode using a graphite monochromator and MoK_{α} radiation (50 kV, 30 mA). The data collection was performed in half of the sphere of the reciprocal space up to 30° in θ. The lattice parameters have been determined from 25 reflections where a= 0.7719(1) and c= 1.2018 nm. Scans of ψ for 7 reflections were carried out for empirical absorption correction. Data reduction and absorption correction with the scans of ψ data were performed with the structure determination system MOLEN [14]. Examinations of the systematic extinction have the unique space group P4/nnc. Examination of the Patterson maps revealed the Pb and W heavy atoms positions. Then Fourier maps revealed the oxygen positions. Finally, the least squares refinement of the position and isotropic thermal parameters converged using F values of 89 independent reflections with $I > 3\sigma$. The final mean value of R ($=\sum|\Delta F|i\sum F_e$) was 0.056. All structure solutions and refinements were performed using the MOLEN system [15].

$PbWO_4$ CRYSTAL STRUCTURE

$PbWO_4$ crystals occur in nature as tetragonal stolzite [16], sheelite type, and monoclinic raspite [17]. A high pressure form has also been prepared under high temperature [16]. Previously, in analog to $PbMoO_4$ the structure of $PbWO_4$ has been claimed as a pure sheelite structure. It was found that together with the pure sheelite structure, new phases can be obtained by the variation of the crystal growth conditions. The sheelite type $PbMoO_4$ is characterized by a square lattice of identical columns of Pb and Mo atoms parallel to the Z axis, each column being made by a regular stacking of Pb and Mo atoms. The X ray precession photographs of $PbWO_4$ (small crystals of

approximate size 100×100×100 μm^3) showed a structure with a tetragonal symmetry, but with a unit cell parameter a = 7.719A, which is $\sqrt{2}$ times larger than the a parameter of the sheelite type structure. Refinement of X-ray diffracted intensities have revealed that each column is made of Pb atoms only or W atoms only, with each W column located at the center of a square of four Pb columns. W atoms fully occupy one crystallographic site with four oxygen atoms as first neighbors. The Pb(1) site, which is not fully occupied, is surrounded by a regular square antiprism of eight O(1) atoms. For Pb(2) that is just on top of Pb(1) along the Z axis, the regular square antiprism of O(2) atoms has a larger size. Pb(3) has an identical coordination of eight oxygen atoms, but the polyhedra is an irregular antiprism. Atomic positions, occupation factors and isotropic temperature factors are given in Table 2. Table 3 presents the interatomic distances in such kind of $PbWO_4$ crystals. Thus, in crystals grown with some lead deficiency, oxygen and lead sites are not fully occupied which gave a formula $Pb_7W_2O_{(32-X)}$ with x= 3.2(8).

Table 2. Structural parameters of lead tungstate

Atom	Site	X	Y	Z	Occupancy	B*eq
Pb(1)	2a	1/4	1/4	1/4	0.5(1)	2.1(2)
Pb(2)	2b	1/4	1/4	3/4	1.0	0.7(1)
Pb(3)	4c	1/4	3/4	3/4	1.0	0.9(1)
W	8f	0	0	0	1.0	0.3(1)
O(1)	16k	0.037(5)	0.181(5)	0.086(4)	1.0	0.3(1)
O(2)	16k	0.653(5)	0.095(5)	0.096(4)	0.80(5)	2.0(3)

Table 3. Interatomic distances in PbWO4 crystals, Å

W-2O(1)	W-2O(2)	Pb(1)-8O(1)	Pb(2)-8O(2)	Pb(3)-4O(2)	Pb(3)-4O(1)
1.762(8)	1.808(8)	2.623(7)	3.331(8)	2.328(7)	3.012(8)

IMPURITIES AND POINT STRUCTURE DEFECTS IN THE CRYSTALS

An important consequence that was obtained from structure data is the existence of lead and oxygen deficiency in the crystals grown under conditions mentioned above. The deficiency of lead in Pb(1) positions is compensated by the deficiency of oxygen in O(2) sites that coordinate Pb(1) ions in the second coordinating sphere. So, in agreement with [4] the irregular WO_3 groups connected with oxygen vacancies V_o or F centers (V_o+2e^-) based on them exist in crystals. On the other hand, the lack of Pb ions leads to the creation of hole centers (O^-), which are localized near W tetrahedra. Additional hole centers near W arise in crystals grown in an atmosphere close in composition to air, due to oxidization of Pb^{3+} ions. Thus, two types of host matrix defects, hole and F centers. dominate in undoped crystals.

An additional doping of the crystals causes a significant redistribution of the host matrix defects and, by this way, helps to understand the origin and possible effects of different defects on the crystal scintillation properties. Let us consider the possible influence of ions with different valencies at Pb and W ion sites in the host. Single valency ions on a lead site will lead to the

creation of O^- hole centers near W tetrahedra. Ions with variable valence $2+ \leftrightarrow 3+$ at a site of lead will provide the same effect as Pb ions and will create hole centers. Ions with a smaller valency at a W site such as 5+, on the contrary, will prevent the creation of the hole centers near tetrahedra. Other ions that can create tungsten compounds with the same valence as Pb or W can lead to the appearance of a local crystal structure change. With our crystal growth conditions being established in eightfold oxygen coordination, Bi ions mainly will be localized in the trivalent state, Yb ions, having a variable valency will be stabilized in two or three valence states, but with domination of the trivalent state, and Mg ions will be in 2+ state only. Nb ions will be localized in oxygen tetrahedra in the 5+ state, or will compensate W ion deficiency, or will simply replace one.

SPECTROSCOPY OF PWO DOPED CRYSTALS

With Bi doping of the PWO crystals an increase of the absorption band peaked at 420 nm has been detected. At the same time, spectra of the radio luminescence as well as scintillation kinetics have the same shape as described in [4]. With an additional optimized procedure of the vacuum annealing at 1000 °C, a yellow coloration of Bi doped crystals can be significantly decreased. After this bleaching, these crystals have a light yield about two times less than the yield of a typical PWO crystal, and their spectroscopy is different. The same effect of the absorption increase is observed with Yb activation of the crystals. With increase of the Yb content, the absorption bands with maximums λ=350,420 nm peak intensity increase, and red luminescence excitation spectra are detected. Excitation luminescence spectra of Yb doped crystals are very close to those of Bi doped crystals annealed in vacuum. The scintillator light yield in this crystal is suppressed significantly as indicated by the scintillation kinetics. Mg activation does not change the typical optical transmission, luminescence, and luminescence excitation spectra of the PWO crystals, but reduce the light yield of scintillators.

We already noted [18] that Nb activation of the PWO leads to some increase of the transmission in the near UV region (λ ~350 nm) as the Nb content increases in the crystals. It indicates that presence of Nb ions suppresses the absorption band with a maximum at 350 nm, but it does not act on the band with maximum at 420 nm. The transmission, luminescence, and luminescence excitation spectra of Nb doped crystals are different from the spectra of undoped crystals mainly by the absence of red luminescence and their excitation bands in the spectra and by the appearance of a new green luminescence band slightly shifted into the yellow region relatively to the ones of (WO_3+F) centers. Although the 420 nm absorption band is also present in Nb doped crystals, these crystals exhibit a better transmission and lesser coloration. In addition Nb doped crystals show a better radiation hardness. The radiation induced absorption band with maximum at 620 nm in undoped crystals, does not appear in Nb doped crystals. So we conclude that the decrease of radiation damage in PWO:Nb crystals is related with the suppression of the 350 nm absorption band of color centers. The effects mentioned above were observed at a Nb content of a few tens of ppm. By increasing the Nb content until several thousands of ppm, an additional strong suppression of green luminescence is observed. The band maximum of γ-ray excited luminescence is shifted to the blue region and the light yield is three - four times less than the light yield of undoped crystals. With Nb doping, the green luminescence in PWO crystals is a superposition of at least three bands. Luminescence kinetics of these combined bands under photo excitation depends on the Nb content in the crystals. Table 4 shows the data of the luminescence (λ_{lum}=520, λ_{exc}=313,337 nm) kinetics versus Nb content. The (WO_3+F) centers of luminescence are mainly

excited by 313 nm light, but the band connected with Nb doping appears in the kinetics under 337 nm excitation. is. With a Nb concentration of ~ 1000 ppm or more, a component with a decay time up to hundred nanoseconds appears. This component, having a contribution to the total kinetics of about 10-15%, becomes slower and slower when the Nb content increases. For Nb contents of a few tens of ppm, the kinetics is close to that of undoped crystals. The scintillation pulses measured with XP1911 or XP2020 Philips photomultiplier tubes of Nb doped crystals with a Nb content of some tens of ppm did not exhibit a slow component [6]. In comparison with undoped crystals where the main contribution in the scintillation kinetics is due to components with $\tau_{1,2} \approx 3$, 20 ns, the components with $\tau_{1,2} \approx 2.5$, 14 ns dominate in Nb doped crystals.

Table 4. Parameters of green luminescence kinetics under photo excitation of undoped and Nb doped crystals

Nb content, ppm	λ_{exc}, nm	Decay time τ_1, ns	Decay time τ_2, ns	Decay time τ_3, ns
undoped	313 337	1.8 4.3	16.5 17.3	- -
~30 ppm	313 337	2 3,5	18 24	
~1000 ppm	313 337	1,1 0.5	4.5 6.2	47.6 70.3
~10000 ppm	313 337	1.1 1.2	5.3 11.5	54.5 104

We have already specified the defects present in PWO crystals with oxygen deficiency [9]. It was also shown [10] that green luminescence consists of two bands with maximums close to each other. This is in good agreement with two possible anion vacancies or F centers based on them in O(2) position only. An important role of the Pb^{2+} ions on the scintillation properties was found [4,19]. The appearing of a wide absorption band in the blue region in different crystals related with molybdenum and tungsten with a structure different from $PbWO_4$ was noted. The absorption band with a maximum of about 420 nm was detected in $PbMoO_4$ crystals. Its intensity varied with crystal growth conditions and purity of the raw materials [20]. The same band was observed in $BaGd_2(MoO_4)_3$ crystals doped with Eu which has a variable valence $2+ \leftrightarrow 3+$ like Yb ions [21]. These crystals were grown in air with some deficiency of divalent Ba ions.

Obtained data show that the 420 nm absorption band is caused mainly by trivalent ions in Pb sites. At the same time, the absorption band with a maximum at 350 nm, present in undoped crystals, disappears with Nb activation. So, we conclude that the origin of this band is the presence of cation vacancies. Two defects are responsible for these bands. Both are hole centers, but one is due to charge uncompensated W linked with localization of 3+ ions in Pb site, and the other is due to O^- hole centers near cation vacancy V_k (Pb) at Pb sites. This interpretation of the 350 nm absorption band is in agreement with data obtained for Nb activated crystals. Nb^{5+} ions localized in W^{6+} sites, compensate the O^- centers arising near V_k (Pb). This is clearly indicated in transmission spectra of Nb doped crystals. The red luminescence, that has an excitation band at 350 nm and exists in undoped crystals, is also suppressed by Nb doping [18]. Although we did not activate PWO by 1+ ions, it was found that Na^{1+} activation of the crystals leads to the appearance of a red luminescence [8]. The creation mechanism of the hole center with 1+ ion activation is

similar to the one created by a lack of Pb. Another impurity with valence 3, 4+ that can be stabilized in W sites generates O^- hole centers too. Fe ions, being in crystals grown in the conditions mentioned above, will replace W ions having a maximal valency state of 3,4+. So they will generate O^- centers with absorption bands near 350 nm. The influence of Mg activation becomes clear from the results mentioned above. Mg^{2+} ions replace or compensate a lack of Pb^{2+} ions. The last one leads to the reducing of oxygen vacancies and so green luminescing centers based on them appear. These crystals, having the same spectroscopy as the undoped crystals, at the same time have the shifted blue luminescence under γ-excitation due to the decrease of a contribution of green luminescence in the total spectrum.

CONCLUSIONS

Scintillation and spectroscopic PWO data show that further improving of their parameters strongly depends our understanding of the origin of point structure defects in these crystals. Although the necessary dimensions of the crystals to produce scintillators for the CMS Electromagnetic Calorimeter are already achieved, the key of the mass production lies still in the raw materials specification. For the current period of R&D this is the main task and it has to be solved as soon as possible.

ACKNOWLEDGMENTS

Author thanks CMS Collaboration and LAPP (Annecy le Vieux) for the support of this research and very appreciative to V.Kachanov, J.-P.Peigneux, P.Lecoq, I Dafinei ,E. Auffray, A.Fedorov, A.Annenkov, V.Ligun, O.V.Missevich, G.Yu.Drobyshev and many others for illuminating discussions.

References

1. V.B.Baryshevsky et al.,NIM A322(1992) 231.
2. M.Kobayashi, M.Ishi, H.Yakagi. in "Heavy Scintillators"Frontieres, 1993, 375.
3. V.A.Kachanov et al, "Beam stadies of EM-calorimeter prototpe built of $PbWO_4$ crystals ", precented at IV Int.Conf.on Calorimetry in High Energy, Isola Elba, Italy, 1993.
4. M.V.Korzhik, V.B.Pavlenko et al, "Spectroscopy and origin of radiatng centers in $PbWO_4$ single crystals" LAPP-EXP-94.01,January,1994.
5. P.Lecoq, I.Dafinei, et.al., CERN-PPE/94-225,1 December1994.
6. A.A.Fedorov, M.Korzhik, et al., "Progress in PWO scintillating crystals" LAPP-EXP-94.25.
7. F.A.Kroger, "Some aspects of the luminescense of solids", Elsivier, 1948.
8. J.A.Groenink, G.Blasse, Journ.Solid . State . Chem.,39(1980)9.
9. M.V.Korzhik, V.B.Pavlenko, V.A.Kachanov et.in" Scintillator and phosphor materials" Edited by M.J.Weber,P.Lecoq, R.C.Ruchti et al. Mat. Rec. Sosiety Symp.Proc., V.348, p.99-104, 1994.
10. P.Lecoq, I.Dafinei, E.Auffray, M.Schneegans, M.V.Korzhik, V.B.Pavlenko et al., Lead tungstate (PbWO4) scintillators for LHC EM calorimetry (To be published in NIM in 1995).
11. P.Lecomte, F.Nessi-Tedaldi, S.Pirro, L.Pacciani (privat communication).
12. C.Woody (privat communication).

13. M.V.Korzhik, J.P.Peigneux, V.B.Pavlenko et al., (to be published in Phys. Stat .Solidi in 1995).
14. C.Kay Fair, MOLEN, Structure Determination Sustem, Enfar Nonius, Delft, Netherlands(1990).
15. T.Fudjita, I.Kawadaand K.Kato, Acta Cryst. B 33(1977)162.
16. P.W.Richter, G.J.Kruger, and C.W.F.T.Pistorios, Acta Cryst., B32(1976)928.
17. T. Fujita, I.Kawada, and K.Kato, Acta CrystB33(1977)162.
18. KorzhikM.V., J.P.Peigneus et al "Further Progress inLead Tungstate Crystals " LAPP- EXP-94.24, December ,1994.
19. A.N.Belsky, V.V.Mikhailin, A.N.Vasil'ev et. al., "Fast luminescence of undoped $PbWO_4$ crystals", CERN/PPE report CMS TN /95-073.
20. E.G.Reut, Phys. Tverdogo tela, 23(1981)2514 (In Russian).
21. B.I.Zadneprovski, V.A.Nephedov, G.L.Achmetova, I.S.Bikov Razvedka i Ochrana Nedr, 3(1995)14 (In Russian).

LUMINESCENT PROPERTIES OF THE LEAD TUNGSTATE SINGLE CRYSTAL

V.Kolobanov[2],J.Becker[1],M.Runne[1],A.Schroeder[1],G.Zimmerer[1], V.Mikhailin[2], P.Orekhanov[2],I.Shpinkov[2],P.Denes[3],D.Renker[4], B.Red'kin[5],N.Klassen[5],S.Shmurak[5]

[1]Institut fur Experimental physik der Universitat Hamburg, Germany, [2]Lomonosov University, Moscow, Russia, [3]Princeton University, USA, [4]Paul Scherrer Institute, Switzerland, [5]Institute of Solid State Physics, Chernogolovka, Russia

Insulating crystals with a complex oxianion $XO_4^{(2-)}$, where X is a transition metal ion, are known to be efficient X-ray scintillators due to a set of favourable properties: high chemical stability and radiation hardness, high stopping power and efficiency of X-ray energy conversion into the intrinsic or impurity luminescence, possibility to grow large uniform transparent crystals, etc.

The crystals of the lead tungstate should be mentioned separately, as they have a high absorption of the hard electromagnetic radiation and an outstanding radiation hardness. Intrinsic luminescence of $PbWO_4$ with decay times of less than 10^{-8} sec, which was observed under X-ray excitation, was the subject of the present investigation.

The crystal of lead tungstate ($PbWO_4$ – PWO) was grown using Czochralski technique from especially synthesised PWO raw material. The synthesis was made from superpure PbO and WO_3 powder ("Red Chemist" – St. Petersburg) by two stage thermal diffusion and subsequent milling. In the case of exact stoichiometry ratio of initial components one stage crystallisation process turned out to be sufficient for the production of rather good crystal (light yield about 140 photons per MeV and rather sharp transmission increase in the spectral range of 310 –320 nm.

The main part of the results of the measurements performed at the SUPERLUMI station of HASYLAB, DESY [1]. The working range of the primary monochromator was 30 to 350 nm with the spectral resolution not less than 10^{-3}. The photon flux at the sample was up to 10^{12} 1/sec. We have measured the spectra of the intrinsic luminescence emission and excitation of the lead tungstate, lead fluoride and magnesium orthosilicate. For the measurements of the emission spectra a monochromator BM50 was used either with a PMT or a position-sensitive detector.

The surface of crystal was polished mechanically. Subsequent annealing was applied (T~700°) to remove structural distortions, produced by mechanical treatment. It was hard to obtain good cleaved surface of the sample, so we measure the reflection from mechanically polished surface. The effect of the crystal surface conditions was studied by the luminescence measurements performed at the polished and cleaved surfaces.

Reflection and luminescence 430 nm excitation spectra of PWO measured at liquid helium temperature are presented at fig.1, details are shown at fig. 2 and fig. 3.

The reflectivity of PWO at RT has a peak at 4.22 eV, which at cooling to LHeT resolves into a doublet peaking at 4.25 and 4.35 eV. We attribute this feature to a molecular-type exciton of the complex oxianion. Intrinsic 430 nm luminescence excitation spectrum at LHeT also has an onset above 4.1 eV, the yield monotonously increases with the energy of excitation. At 5.45 eV the yield increase faster. Thus the forbidden energy gap of PWO can be evaluated as not less than 5 eV.

Proc. Int. Conf. on Inorganic Scintillators and Their Applications, SCINT95,
1996, Delft University Press, The Netherlands

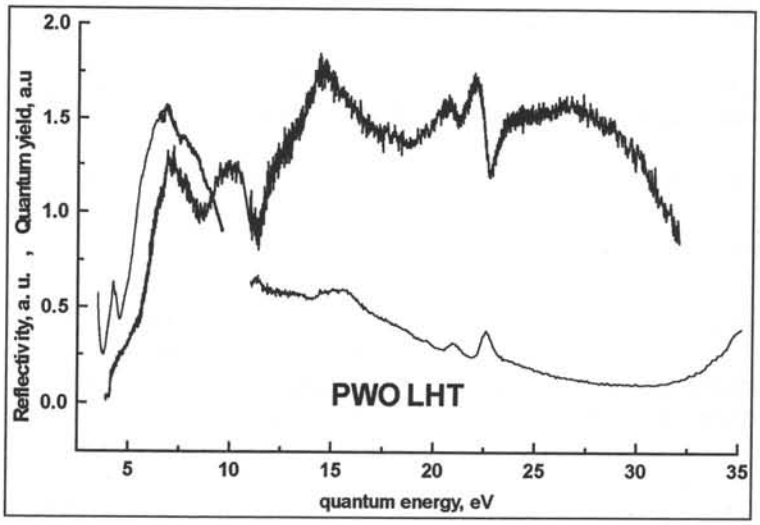

Figure 1. Reflectivity and luminescence excitation spectra(bold) of $PbWO_4$

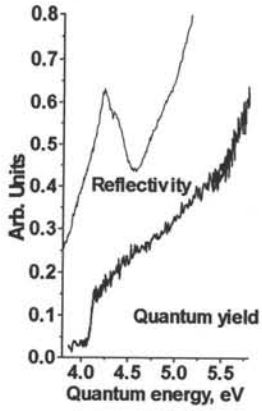

Figure 2. Reflectivity and luminescence quantum yield near the fundamental adsorption edge of PWO

The features of the reflectivity spectrum at high energies can be attributed to the transitions within the complex oxianion [2]. On the smooth background of the reflectivity spectrum two sharp peaks at 20.8 eV and 22.5 eV are observed. In the reflectivity spectrum of the lead fluoride (fig. 3) measured under the same conditions two similar peaks at close energies were observed. This fact allows to attribute these features to the transitions involving the 5d Pb core level, the separation between the peaks is in a reasonable accord with the data for a free lead ion.

The emission spectra of the lead tungstate have been measured at the excitation in the fundamental absorption range (for 11.7, 14.1 and 20,7 eV excitation). At LHeT the emission spectrum consists of a broad non-elementary band with the maximum at 430 nm and the halfwidth of 90 nm.

Like reflectivity, the luminescence excitation spectrum of the lead tungstate for the 430 nm band has a steep rise corresponding to the onset of the transitions between the orbitals of the oxianion WO_4^{2-} [2].

Spectral features at high energies can be explained in frames of "genetic recombination" model [3]. Decrease of quantum yield at 7 eV shows the excitonic type of energy transfer to luminescence centres. Minimum at 8.4 eV and maximum at 10 eV can be due to nonelementary structure of valence band. Raise of quantum yield at 11.4 eV connected with the beginning of photon multiplication (creation of two electron-hole pairs by single photon).

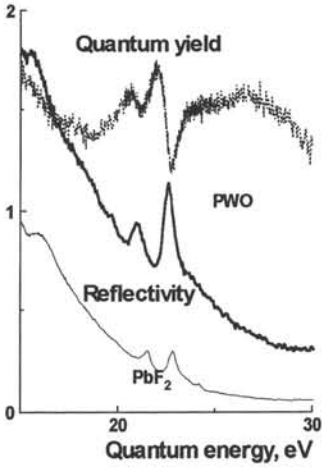

Figure 3. Pb core levels in the luminescence quantum yield of PWO and in the reflection spectra of PWO and PbF_2.

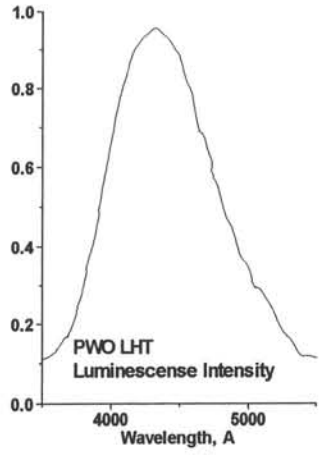

Figure 4. Emission of PWO at liquid helium temperature

At higher energies a smooth increase of the luminescence yield with weak features is observed. Transitions involving the 5d lead core level show up as two dips at 20.8 and 22.5 eV. Comparison of the emission spectra reveals that at wavelengths shorter than 400 nm the spectra are different for the excitation below or above the lead edge. When the transitions from the lead core-level are involved, the emission spectra show weak additional band peaking at 350 nm. The same UV additional band were found under the exitation the same PWO cristal by X-rays and 80 MeV protons at PSI accelerator [4]. Short wavelength shift of the PWO emission can be due to relative increase of the role of Pb states.

Conclusions

1. Reflectivity of PWO single crystal at LHT shows the prominent double exciton structure at 4.25 eV. - 4.35 eV
2. Additional weak UV emission band with maximum about 350 nm is observed under excitation above 23 eV (transition from 5d level of Pb).
3. Correlation between the scintilation yield under proton excitation and the short-wavelength shift of the emission spectrum was obtained for different crystals.
4. The relative intensity of the PWO UV emission band spectrum increases with the energy of excitation (VUV – X-rays –charged particles).

Acknowledgement

Authors from Moscow University would like to thank International Science Foundation and Russian Fundamental Investigation Foundation for financial support.

References

1. G.Zimmerer. Status report on luminescence investigations with synchrotron radiation at HASYLAB. Nuclear Instruments and Methods in Physics Research A 308 (1991) 178-186.
2. R.Grasser et al. Optical Properties of $CaWO_4$ and $CaMoO_4$ Crystals. Phys. stat. sol. (b) 69, 359 (1975)
3. Belskiy A.N.et al., Physica Scripta **41** (1990) 530
4. P.Denes et al. Optical and Scintillation Properties of $PbWO_4$ Crystals. Abstracts of Int. Workshop on Physics Processes in Fast Scintillators PHYSCI-94, St Petersburg 1994, p N1.

SPECTRAL STUDIES OF LEAD TUNGSTATE SCINTILLATORS

Shmurak S.Z., Klassen N.V., Gurov A.F., Kolchin A.A., Konovalov N.T.,Schekoldin V.N.,
Sidorov N.S., Sinitsyn V.V., Red'kin B.S.,Rybchenko S.I
Institute of Solid State Physics, 142 432, Chernogolovka, Moscow Region, Russia

Many publications are devoted to optical spectra of $PbWO_4$ [1-5]. Luminescence spectra as well as excitation spectra of luminescence have been studied in a wide temperature range. Models of light emission centers have been proposed. On the other hand, influence of stoichiometry and structural disturbances, gamma irradiation, various surface treatments on spectral characteristics and gamma scintillation effectiveness were not studied in detail. Our paper presents additional information in this field.

Reut [3] studied influence of surface on luminescence quantum yield of lead molibdate. It was shown, that at 77 K the yield is constant in the wavelength range 250-370 nm for the cleaved surface, whereas for the surface polished mechanically it is decreased during wavelength change from 370 to 270 nm by 6 times and in the spectral range 270-200 nm remains constant. It was noted at [3], that the influence of the surface on the quantum yield existed for $CdMoO_4$ and for $PbWO_4$.

Our paper studies in more detail the influence of surface treatment on optical spectra of $PbWO_4$. It is shown, that the changes of luminescence spectrum with processing variations are weak, whereas luminescence excitation spectrum at 300 K is changed significantly.

Fig.1 demonstrates luminescence excitation spectra (LES) at 500 nm for mechanically and chemical-mechanically polished surfaces. As it is seen, chemical polishing (CP) results in creation of a new band in LES with a maximum at 280 nm, its intensity increases with the removal of the surface disturbed layer (SDL). As it is seen from fig.1, LES maximum is shifted with CP to shorter wavelengths.

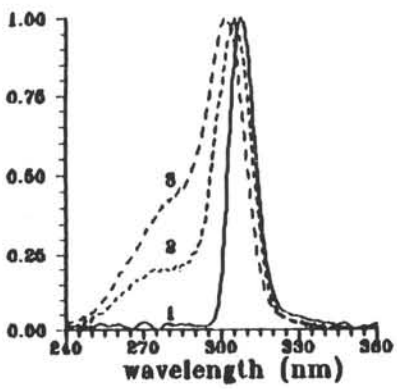

Fig.1. LES at 300 K. 1- mechanical polishing; 2,3- chemical polishing : 2-50 mcm, 3-100 mcm

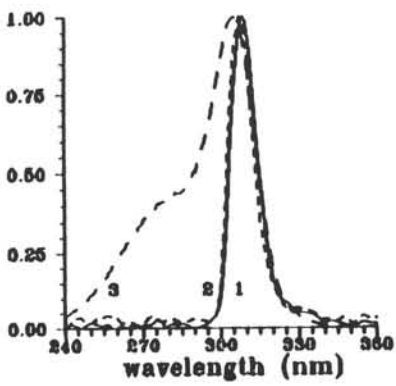

Fig.2.LES at 300 K. 1,3-mechanical polishing, 2- annealing, 3- mechanical polishing after annealing

Proc. Int. Conf. on Inorganic Scintillators and Their Applications, SCINT95,
1996, Delft University Press, The Netherlands

LES studies for chemical-mechanically polished surfaces of $PbWO_4$ gave an estimation of the thickness of a surface layer, disturbed by mechanical polishing. It turned out to be about 100 mcm, thus the disturbances of surface by the mechanical polishing are essential.

Analogous changes of LES were found after annealing of the mechanically polished crystal, made at 650°C during 2 hours at the air atmosphere (fig.2). The band with a maximum at 280 nm appears as well and the shift of the main maximum to shorter wavelengths is observed. Hence the annealing removes the disturbances, made by mechanical polishing and is equivalent to the chemical polishing.

Our annealing procedure changes the structure of the surface layer without changes in the crystal volume. This is confirmed by repeated mechanical polishing of the annealed crystal, which reconstructs the initial LES (curve 2 at Fig.2).

The maximum position (280 nm) of the bands, appearing after chemical polishing or annealing is confirmed by Gaussian expansion of the spectral curves at Figs. 1 and 2.

It's worth to emphasize, that for 77 K the influence of variations of surface treatment on LES is much weaker. For 450 nm luminescence wavelength any difference in LES is not seen, whereas for the luminescence at 500 nm slight differences are observed in the range about 280 nm.

The results presented above let us to conclude, that studies of luminescence excitation spectra can be used as a method for estimation of a surface quality and determination of a disturbed layer existence.

Fig. 3 demonstrates LES (luminescence at 500 nm) for crystals, grown from the powders of stoichiometry composition (C), with WO_3 0.3% excess (W) and PbO 0.3% excess (Pb). As is can be seen from the spectra (and from Gaussian expansion as well) LES for "W" and "Pb" crystals have additional bands in longwavelength region with a maximum at about 330 nm. In addition the main LES maxima are shifted from 307 to 312 nm. The longwavelength intensity for W crystal is 3 times stronger, than for Pb crystal. At the same time the luminescence spectra practically coincide for all the crystals, having a maximum at 500 nm.

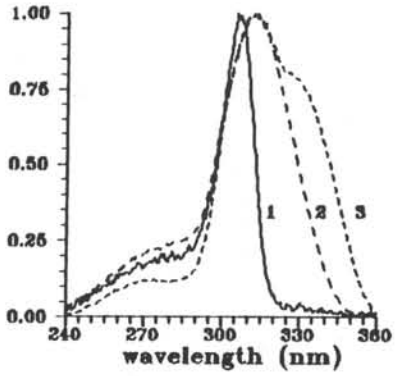

Fig.3.LES,300 K. 1-stoichiometric powder, 2-0.3% PbO excess, 3-0.3% WO_3 excess.

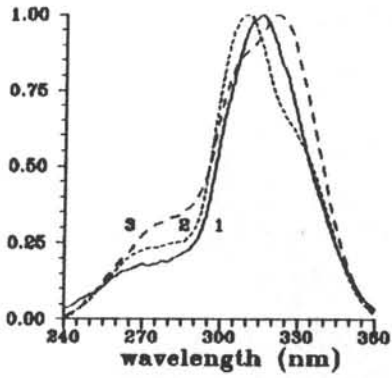

Fig.4. LES of gamma irradiated $PbWO_4$. 1-before irradiation, 2- 1 Mrad dose, 3 - 10 Mrad dose

Gamma irradiation shifts LES to longer wavelengths as well and enhances the band with maximum at 325-330 nm by 3 times (it is determined by Gaussian expansion) - Fig.4.

Comparison of LES spectra at Figs. 3 and 4 shows, that irradiation gives the same changes, as doping.

These results demonstrate the ability of LES studies to analyze the stoichiometry of lead tungstate crystals.

At least for some of the crystals small deviations from stoichiometry enhance light yield of gamma scintillations: 0.3% doping either with PbO or with WO_3 the yield is increased by 20% but further deviation from stoichiometry leads to the yield fall down.

For some crystals gamma irradiation dose induces nonmonotonous variations of scintillation light yield: after 1 Mrad the yield falls to 91%, after 10 Mrad returns almost to the initial value, further irradiation again decreases the light yield of gamma scintillations.

It is well known, that the irradiation dose increase enhances the crystal light absorption. So the light yield growth with P increase can most probably show the creation of new light emission centers. Due to the increase of concentration of defects during gamma irradiation the number of WO_4^{2-} centers, positioned in defect sites, grows. This can be an additional argument for an assumption [4], that WO_4^{2-} groups, situated at disturbed sites, are the main light emission centers.

Two stable modifications of $PbWO_4$ are known - stolzite (sheelite) and raspite. In spite of the fact that raspite is presented in literature as low temperature stable modification of lead tungstate, all our attempts to get this phase either by the melt growth (and subsequent cooling) or by low temperature growth from solutions gave sheelite modification only. So we studied mineral raspite crystals, found in Australia. Dimensions of the samples being at our disposal were $0.2x0.2x0.1mm^3$.

Luminescence spectra (LS) either at 300 K or at 77 K have maximum at 520 nm (Fig.5). In distinction to sheelite modification at 77 K in raspite LS a band 420 - 450 nm is absent (at excitation in the range 220-370 nm). The excitation spectrum was measured at 77 K only (because of too weak emission at room temperature). It is shown at Fig.6 . Hence we can assume, that a band about 520 nm in luminescence spectrum of stolzite is connected with centers, which have the same local configuration as in raspite.

Big number of luminescence spectra modifications, described in papers [4,5] can be explained as a result of metastability of sheelite phase at 300 K, due to which a lot of local neighboring configurations of WO_4^{2-} tetrahedrons can be present.

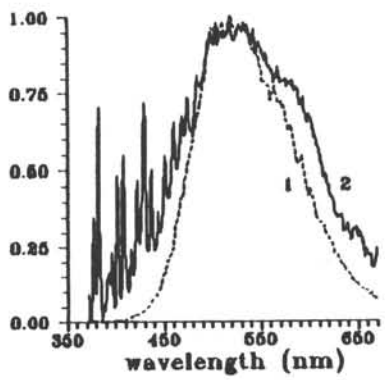

Fig 5.Raspite luminescence spectra, 337 nm excited. 1-77K,2-300K. Narrow lines at the left -belong to exciting nitrogen-laser.(Curve 2 magnified by 20)

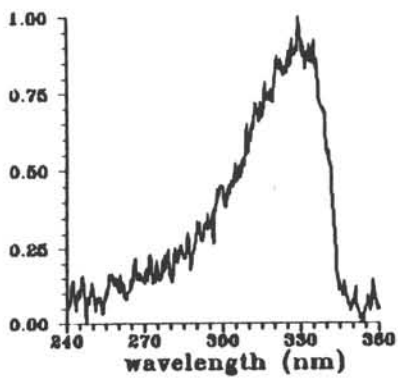

Fig.6. Luminescence excitation spectrum of raspite at 77 K (for emission at 500 nm).

Due to sheelite metastability at room temperature generation of some new intermediate structures is possible (as it was observed at ZnS, SiC, etc.). We have found a new phase of lead tungstate, giving anomalies of temperature expansion and specific heat in the range - 50° C - + 30°C (Fig.7). At the same temperature interval an abrupt change of interatomic spacing is observed. To clarify the nature of the new phase additional studies are necessary. But anyway the existence of this phase can be a key to understanding of multivariant set of emission centers in $PbWO_4$.

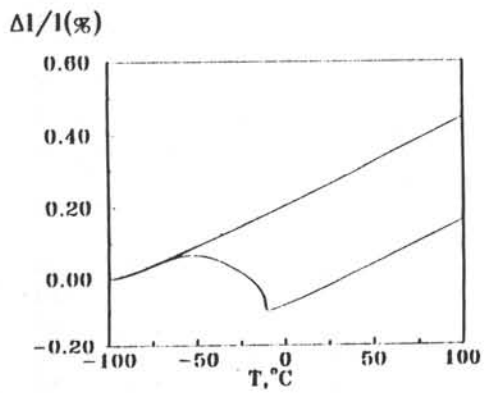

Fig.7.Relative elongation of $PbWO_4$ during heating. Upper curve -without keeping at 77K, lower - 10 hours keeping at 77K

In addition the existence of structural transformation, starting about 200 K, can better explain unusually abrupt fall down of lead tungstate light emission yield at temperatures higher than 200 K. Nonstability of regular lattice, induced by the probability of the structural transformation, can produce additional effective channels of nonradiative recombination of electron excitations. So the search of the ways to stabilize lead tungstate structure can result in improvement of its scintillation light yield at room temperature.

We would like to thank Fersman Museum of Mineralogy RAS (N 78522) for providing single crystal $PbWO_4$ of raspite modification.

The work was supported by INTAS grant 93-1239.

REFERENCES

1. Blasse G.,Bril A., Philips res.rep., V.24, 275 (1983).
2. Van Loo W., Phys. Stat. Sol. (a), V.27, 565 (1978).
3. Reut E.G., Optika I Spectroscopia, V. 50, 821-823 (1981).
4. Korzhik M.V.,Pavlenko V.B., Katchanov V.A., Peigneux J.P.,Poulet M. MRS 1994 Spring. Meeting Scintillators and Phosphor Materials. S-Francisco, Apr. 1994. Edited by M. Weber, P. Lecog, R.C. Ruchti, C. Woody, W.M. Yen, R.-Y. Zhy. V.348, 285-290 (1994).
5. A.S.Voloshinovsky, M.A.Krisjuk, L.L.Nagornaya, S.G.Nedelko, J.A.Tupuzina. PHYSCI 94. Physical Processes in Fast Scintillators. Record of the International Workshop. St.-Petersburg., Russia, September 1994. Edited by P.A.Rodnyi and C.van Eijk.

LUMINESCENCE AND SCINTILLATION OF $PbWO_4$ SINGLE CRYSTALS

[a]M.Nikl, [a]K.Polak, [a]K.Nitsch, [a]E.Mihokova, [b]P.Lecoq, [b]I.Dafinei
[c]P.Reiche, [c]R.Uecker, [d]O.Jarolimek
[a]Institute of Physics CAS, Cukrovarnicka 10, Prague, Czech republic
[b] Div. PPE, CERN, Geneva, Switzerland
[c]Institute for Crystal Growth, Rudower Chaussee 6, Berlin, Germany
[d]Preciosa Crytur Ltd, Palackeho 1175, Turnov, Czech republic

$PbWO_4$ luminescence and decay kinetics are measured in 4.2 – 300 K range showing separately blue and green components at low temperatures. At 295 K both UV and γ–excited decays exhibit very slow components down to ms time scale, which are related mainly to the green component. Large differences in X–ray excited emission spectra of PWO are found comparing the samples from different producers.

1. INTRODUCTION

Luminescence of $PbWO_4$ (PWO) has been already investigated in the past by several laboratories. At present, there is strongly increased interest in this material in connection with its choice as scintillating medium for crystal calorimeter for LHC project in CERN.

At 4.2 K emission of PWO single crystals is dominated by the bands peaking in blue (425 nm) and green (515 nm) region of spectra. Blue emission was ascribed to regular WO_4 group [1], while the green one is related to the defect WO_3 group [2], possibly with F centre nearby [3]. Also red PWO emission is reported [3] ascribed to Pb^{3+} and depending strongly on the purity of starting raw materials and on the growth technology.

It is the aim of this contribution to demonstrate general photoluminescence (PL) and decay kinetics features of recent PWO single crystal samples in a broad temperature range. Furthermore, X–ray excited emission spectra of PWO grown by several different laboratories are compared at 295 K (RT). PL and scintillation decay kinetics are studied in ns – ms time scale.

2. EXPERIMENTAL

Emission spectra and PL decay kinetics measurements were performed using Spectrofluorometer 199S (Edinburgh Instrument), for the details see [4], scintillation kinetics was measured using ^{22}Na radioisotope and coincidence method. All spectra are corrected and ns decay times are extracted from the decays using deconvolution procedure.

Recently grown PWO samples (Czochralski method) were cut from single crystal boules, shaped into plates or rhombohedra and polished. Following samples were measured:

1) PWO 643 (0.04% of Nb^{5+} in the crystal), grown in Bogoroditsk, Russia [3];
2) PWO 892 (a few tens of ppm of Nb^{5+} in the crystal), Bogoroditsk;
3) PWO Pr, undoped,grown by K.Nitsch in collaboration with Inst.for Cryst.Growth, Berlin;
4) PWO Ch, undoped,(Bridgman method), Shanghai Institute for Cryst., China;
5) PWO T , undoped, grown by O.Jarolímek, Preciosa Crytur, Turnov, Czech rep.

Proc. Int. Conf. on Inorganic Scintillators and Their Applications, SCINT95,
1996, Delft University Press, The Netherlands

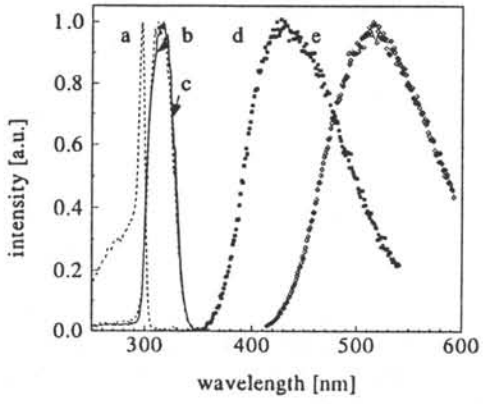

Fig.1 Excitation(a,b,c) and emission (d,e) PWO spectra.
a)λ_{em}=400nm,4.2K; b)λ_{em}=400nm,295K.
c)λ_{em}=560nm,4.2K; d)λ_{ex}=290nm,4.2K;
e)λ_{ex}=315nm,4.2K.

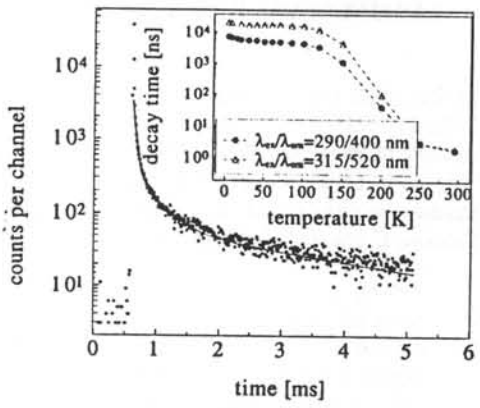

Fig.2 PL decay of PWO at RT,λ_{ex}=240nm and λ_{em}=520nm
In the inset, temperature dependence of fast emission component decay times is given.

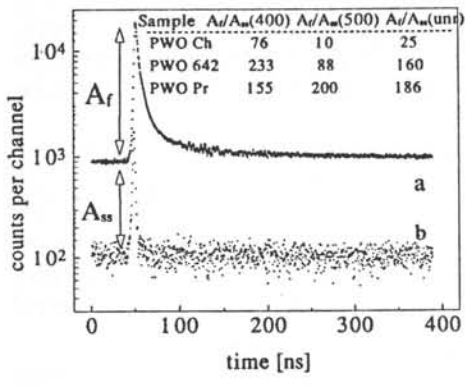

Fig.3 Spectrally unresolved scintillation decay of PWO Ch at RT(a) and "no crystal" measurement (b) (see the text)

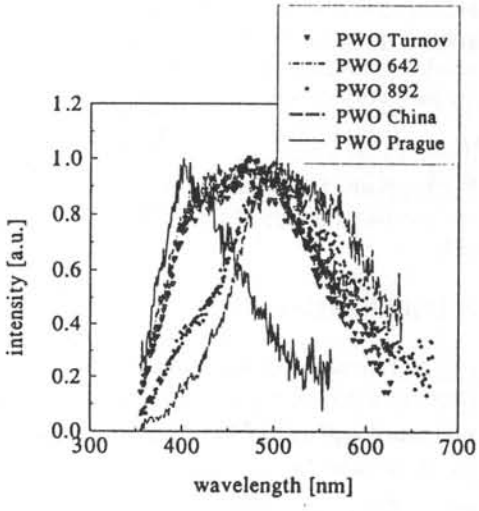

Fig.4 X-ray excited emission spectra of PWO at RT manufactured by different producers.

3. RESULTS AND DISCUSSION

PL spectra of PWO are shown in Fig.1. Different excitation spectra (a,c) enable to separate blue (d) and green (e) emission components at 4.2 K, which is not possible at RT where excitation spectra almost coincide (the green component one is temperature independent). PWO PL decay kinetics excited in the lowest energy excitation bands show single exponential behaviour up to about 200 K, their temperature dependence is given in the inset of Fig.2. At T> 200 K mainly green component decay exhibits slower non-exponential processes in the decay tail, the decay times in the inset of Fig.2 are extracted from the initial decay part. Under shorter wavelength excitation (λ_{ex} < 250 nm) rather slow non-exponential decay extended to ms time scale is observable at all the temperatures (at RT in Fig.2).
Spectrally resolved scintillation decay at RT shows similar to PL decay times in its initial part (2-3 ns) and slower non-exponential part is present as well, which can be fitted by another two exponentials with decay times typically 20-30 and 100-200 ns. However, scintillation decay is extended to much longer time scale, which is shown in Fig.3. Two decay curves presented are obtained in the same experimental conditions incl. accumulation time, with (a) and without (b) PWO sample. Hence, true dark count level can be deduced from (b) and the difference A_{ss} is clearly given by the contribution of radiative decay processes in PWO crystal, which are slow in comparison with the average "repetition rate" of ^{22}Na excitation γ-photons. Measuring stopping rate of starting photomultiplier, average frequency about 50 kHz, i.e. 20 μs between the subsequent excitation events is obtained. This finding coincides with the above shown very slow PL decay in Fig.2 under band-to-band excitation, because (apart from the initial space distribution) in both cases free carriers are created in the sample after absorption of excitation photon(s). To learn about spectral distribution of these "super slow" components, scintillation decay was measured spectrally unresolved, at 400 and 500 nm and the ratio A_f/A_{ss} was calculated (Fig.3). X-ray excited emission spectra of all the samples studied are given in Fig.4. In spite of high crystal quality, there are big differences in emission spectra. Comparing table in Fig.3 and related emissions in Fig.4, one important consequence can be formulated:

The relative intensity (importance) of super slow radiative decay components increases with increasing content of the green component in the overall scintillation emission spectrum.

In conclusion, important issues regarding PWO scintillation properties important for LHC application can be formulated:
1.Fast(2-3 ns) scintillation component is related mainly to the PWO blue emission component.
2.Mainly green emission centres are responsible for the presence of very slow radiative processes in the overall scintillation decay, which might be harmful for high-repetition rate application (pile-up effects).
3.Slower non-exponential part of PL and scintillation decay is extended down to ms time scale. It can not be ascribed to superposition of several exponentially decaying emission centres, but probably it is related to the free carrier recombination decay kinetics of II. order.

Literature.

1. W.van Loo, phys.stat.sol (a) 27, 565 (1975) and 28, 225(1975).
2. J.A.Groening, G.Blasse, J.Sol.St.Chem. 39, 9 (1980).
3. P.Lecoq et al, "Lead tungstate Scintillators for LHC EM calorimetry",accepted in NIM A.
4. K.Polak, D.J.S.Birch, M.Nikl, phys.stat.sol (b) 145, 741 (1988).

LEAD TUNGSTATE CRYSTALS FOR CALORIMETRY AT LHC

Yu.Borodenko, S.Burachas, K.Katrunov, W.Martinov, L.Nagornaya V.Ryzhikov,
Yu.Vostretsov,I.Tupitsina,V.Manko
Institute for Single Crystals Acad.of Sci. of Ukraine
60 Lenin av.,310001,Kharkov,Ukraine

Abstract

The effect of growth and thermal annealing conditions on scintillation and optical properties of crystals is discussed. The light output of more homogeneous $PbWO_4$ crystals, 160-230 mm in length, is shown to be > 60-70ph/MeV.

I.INTRODUCTION

Scintillators on the basis of the $PbWO_4$(PWO) crystals started to be considered as most suitable for the creation of compact total absorption detectors in electromagnetic calorimeters for LHC after large optically homogeneous scintillator elements were obtained in 1992 [1]. Lead tungstate single crystals possess a number of unique physico-chemical properties. However the main difficulty in their application for the mentioned purposes, especially in combination with photodiodes is low light output. The effect of stoichiometric and impurity defects on luminescence and scintillation characteristics of PWO was studied in [2]. The works on the study of the effect of PWO growth conditions on these characteristics [3], published before, show that even minor deviations in the technological process of growth lead to a significant variation of their luminescence characteristics. These variations are especially revealed when growing long crystals. The purpose of this paper is to find the way of improving scintillation parameters, transparency and uniformity of crystals over their length. A particular attention was paid to the effect of growth conditions and thermal treatment on these characteristics.

II.EXPERIMENTAL

PWO single crystals 32 mm in diameter and 200-250 mm long were grown by the Czochralski method in platinum crucibles with HF heating. The raw powder was prepared by solid phase high temperature synthesis of the stoichiometric composition of lead and tungsten oxides. The obtained crystals were used to prepare scintillation elements in the form of parallelepipeds or cubes, 20×20×160-230, 20×20×50, 20×20×20 mm^3. All the surfaces of the samples were polished.

III.RESULTS AND DISCUSSION

The investigations of PWO scintillators (20×20×160 mm^3) carried out before by the authors [4] showed that shortening of the cycle of thermal treatment of crystals in the oxidizing atmosphere (e.g. in air) at the stages of growth, post-growth annealing and annealing to eliminate thermal strain increases the light output . Typical for these crystals is a less pronounced coloration and absence of light absorption in the region of 430 nm. Besides, it is shown in [5] that the probability of obtaining colorless PWO crystals is higher if they are grown from iridium crucibles in argon. However, this information seems to be not so convincing since the final result (transparency of the PWO samples) was estimated by the combination of technological factors including in particular annealing of the samples in air at 900°C. Nevertheless, the expediency of growing PWO in the atmosphere with a reduced content of oxygen is evident. Some experiments on growing crystals in the reducing, oxygen containing and inert (Ar,N_2) atmospheres at lowered to ~5×10^{-2} torr pressure were carried out. The growth

Proc. Int. Conf. on Inorganic Scintillators and Their Applications, SCINT95,
1996, Delft University Press, The Netherlands

experiments at a lowered pressure in the medium close in its composition to air ensured the improvement of light output and optical transparency of PWO crystals. However, as a result of intensive evaporation of the melt and violation of the stoichiometry the crystals became optically inhomogeneous and had different spectral-luminescence characteristics over the length. To achieve better homogeneity the authors tried to grow crystals under a pressure in the inert gas (Ar,N_2).

The comparative data on transparency and homogeneity of PWO crystals

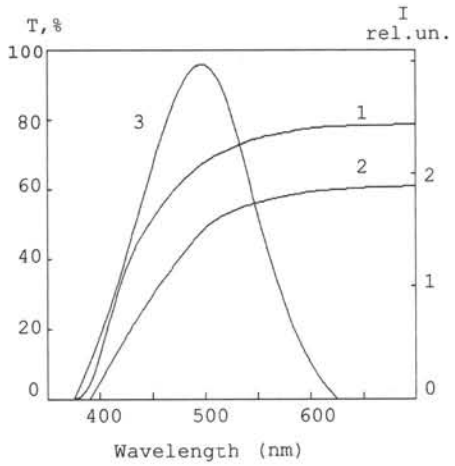

Fig.1 Transmission (1,2) and emission (3) spectra of PWO single crystals:
1-grown in the inert atmosphere
2-grown in the oxidizing atmosphere

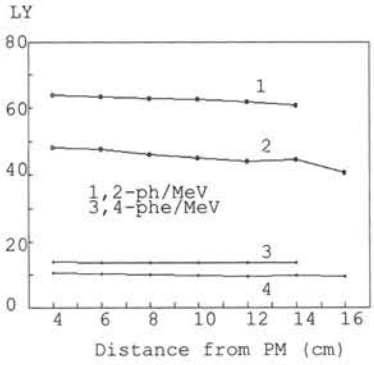

Fig.2 Light Yield of PWO single crystals ($20x20x160\ mm^3$)
1,3-grown in the inert atmosphere
2,4-grown in the atmosphere close to air

grown in the oxidizing and inert atmospheres are shown in Fig.1. As one can see crystals obtained in the inert gas have much higher transparency in the region of the intrinsic luminescence and homogeneity over the crystal length. To eliminate post-growth thermal strain as well as to improve optical characteristics the experiments on the selection of conditions and regimes of PWO thermal annealing were carried out. The effect of the atmosphere and annealing temperature on optical transparency of crystals and position of the X-ray luminescence maximum was studied. Chosen were the optimal atmosphere and double-stage annealing, which on some crystals increased the light output by 15-20%. The study of the anisotropy of PWO luminescence properties showed that the maximum emission intensity is achieved at the irradiation normal to the plane (001) or (104). It was also found that diffusion and heat conduction of PWO crystals are higher in the direction |001| as well. However, in spite of this fact the authors believe that the growth of PWO in the direction |100| is preferential from the viewpoint of their better adaptation to the typical for the Czochralski method thermal fields in the crystallizer as well as due to a higher diffusive mobility at posterior thermal treatment especially in the case of low temperature annealing. On the basis of the mentioned investigations technological methods for the growth and thermal annealing of crystals close to optimal were elaborated. As-grown crystals, 200-250 mm in length, were taken to cut out scintillation elements, 20×20×160-230 mm3 and $20\times20\times20\text{-}50mm^3$ in size.Fig.2 shows light output uniformity values for the crystals 160 and 230 mm in length. The data on the light output of the mentioned elements are presented in Table.The analysis of the data shows that the method for

growing long PWO crystals developed in this work gives the possibility to get scintillation elements with sufficiently -high light output (~60-70 and 180-230 ph/MeV for crystals 20×20×160-200mm^3 and 20×20×20mm^3 respectively). The nonuniformity of light output did not exceed 5-10% (Fig.2).Using the studied scintillators, 20×20×160 mm^3, fabricated were detectors with photodiodes as radiation receivers. The size of the matrix was 3×3 elements. The energy spectrum of the detector at the irradiation with the electron beam 5 GeV is shown in Fig.3. It confirms the possibility to detect radiation ,especially under lower temperature, by means of photodiodes provided scintillators with the improved light output characteristics and luminescence shifted to the longewave region are used.

Light output of the PWO single crystals

Dimensions	Wrapping	LY (ph/MeV)
10×10×10	teflon	200÷230
20×20×20	teflon	160÷185
20×20×50	teflon	70÷100
20×20×160÷230	teflon	60÷70

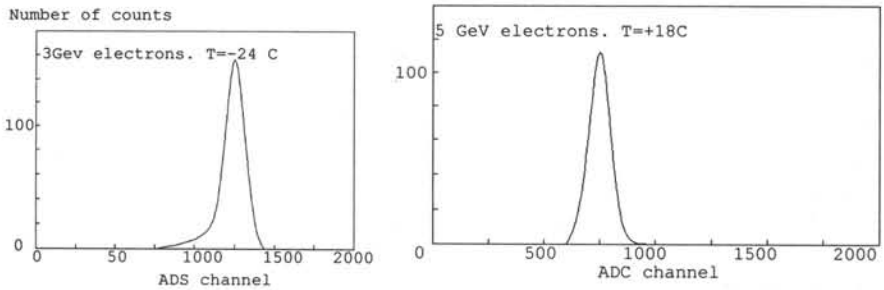

Fig.3 Energy spectra of PWO crystals with PD-PA systems

IV.CONCLUSIONS

A possibility to optimize the preparation conditions for the scintillators on the basis of PWO crystals, 160-230 mm in length with improved scintillation parameters (60-70 ph/MeV), better homogeneity is shown in this paper. The idea of fabricating detection assemblies with photodiodes as radiation receivers for the registration of high power radiation is discussed.

REFERENCES

[1] L.Nagornaya,V.Ryzhikov"Fast scintillators based on large "heavy" tungstate single crystals",Proc.of Int. Workshop Crystal 2000, Chamonix, France, 1992 p.367.

[2] L.L.Nagornaya, V.D.Ryzhikov,I.A.Tupitsina "$PbWO_4$-Based Fast Heavy Scintillator for the Total Absorption Detectors of EM Calorimeters" Proc. of the Nuclear Science Symposium & Medical Imaging Conference San Francisco,California USA,1993,v.1,p.156,Lowell Klaisner,Guest Editor

[3] P.Lecoq, I.Dafinei et.al. "Lead tungstate ($PbWO_4$) scintillators for LHC EM-calorimetry" Preprint CERN-PPE/9-225, 14December94,CMSTN/94-308. Sub. to NIM

[4] L.L.Nagornaya, V.D.Ryzhikov,I.A.Tupitsina et.al."Development of Large Heavy Fast $PbWO_4$ Scintillators",submited to IEEE Nucl. Trans

[5] R.Oeder, A.Scharmann, D.Schwabe and B.Vitt,J.of Crystal Growth,43(1978)N4, p.537

IMPURE AND DEFECT LEAD TUNGSTATE SINGLE CRYSTALS: X-RAY AND PHOTOLUMINESCENCE PROPERTIES

S.G. Nedel'ko[(1)], A.S. Voloshinovskii[(2)], M.O. Krisjuk[(1)], Z.T.Moroz[(2)] ··M.V. Pashkovskii[(2)]
[(1)]Taras Shevchenko Kyiv University, Kyiv, Ukraine
[(2)]Ivan Franko State University, Lviv, Ukraine

1. INTRODUCTION

For well-known reasons, full attention has been given during the past years to $PbWO_4$ (PWO) [1-4]. At the present stage of investigations we are comparing our results for crystals which were grown in different laboratories and under various conditions. Such investigations, as we hope, will give us trustworthy results.

2. EXPERIMENTAL RESULTS

In Fig. 1 X-ray luminescence spectra at room temperature are presented. Curve 1 corresponds to continuous excitation, the other ones correspond to pulsed excitation. The blue band gives the main contribution to the emission, but under continuous excitation the blue-green band is present as well. Decay curves given at the bottom of Fig.1 confirm the more slow character of the decay of the blue-green band. Estimation of the decay time (τ) gives until 20 ns $\tau_f = 4.5$ ns for the exponential part of the curve; and the effective decay time is $\tau_s = 20$ ns for decay of the blue-green components in the range from 40 to 150 ns. We note that the X-ray luminescence spectra are practically the same for all our samples. In the photoemission spectra (Fig. 2a), the well-known bands in the blue (with main maximum at λ_{max} =427 nm), the blue-green (λ_{max}=500 nm) and the yellow-red (from 550 to 750 nm) spectral region can be observed.

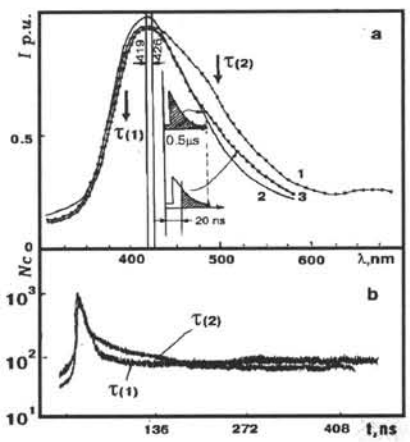

Fig.1. a). Room temperature luminescence spectra of PWO crystals under (1) continuous and under (2,3) pulsed X-ray excitation. Registration conditions under pulsed excitation are shown schematic.

b). Decay curves of the X-ray luminescence at room temperature Registration is in the regions indicated by the arrows in Fig.1a.

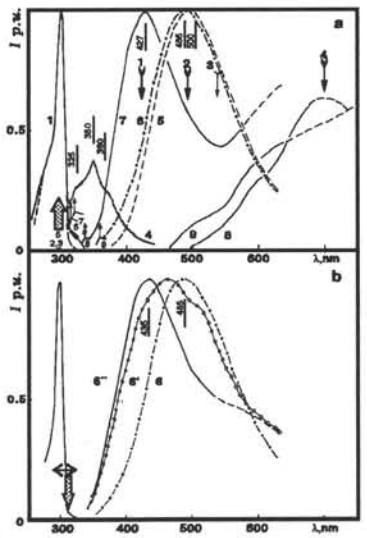

Fig.2. Room temperature photoexcitation (1-4) and photoluminescence (5-9) spectra of the PWO crystals at several registration and excitation wavelengths.

Proc. Int. Conf. on Inorganic Scintillators and Their Applications, SCINT95,
1996, Delft University Press, The Netherlands

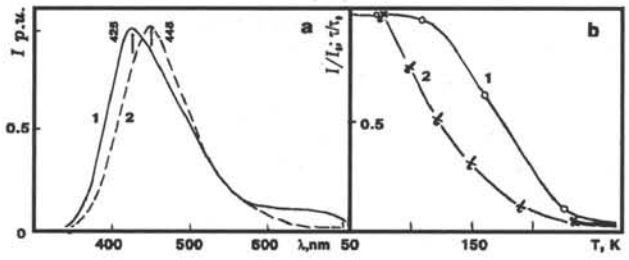

Fig.3. a) X-ray luminescence spectra of PWO crystals at room temperature (1), and 77K (2).
b) Temperature dependence of the peak intensity (1) and decay time (2) of the X-ray excited luminescence bands (in percents).

Correlation between the excitation and emission spectra allows us to suggest that the blue-green emission is easily excited within the short wavelength band with a peak position near 300 nm. The blue emission is excited in the range 310-330 nm and the yellow-red emission is excited both in the short wavelength band, as mentioned above, and in the bands in the whole near ultraviolet region, see curve 4 Fig. 2a.

Comparison between the spectral properties of different crystals allows us to say that all crystals have the above mentioned characteristics. At the same time some differences are present, but analysing them is very complicated. This is connected with the superposition of bands both in luminescence and excitation spectra. Furthermore, we are not certain of the existence of the emission band with maximum at 465-475 nm.

It is interesting that by varying the wavelength within small limits around λ=311 nm or changing the width of the slit of the exciting monochromator, we can obtain different maximum positions for the luminescence bands (Fig. 2b).

With decreasing temperature, only the blue emission band was observed in the X-ray excited luminescence. Its maximum shifts towards the long wavelength region (436-475 nm). The band becomes more symmetrical at the expense of an attenuation of its long wavelength side. The half width of the band decreases and the weak wing in the yellow-red region disappears too, see Fig.3a. These changes are accompanied by an increasing emission intensity. The increase of the intensity follows the classical Mott law (Fig. 3b).

Decay curves (integral over the spectrum) strongly change with decreasing temperature. While at room temperature only the beginning of the decay is exponential (τ = 4 ns), at 77 K the decay takes place practically in accordance with an exponential law with τ=1μs. The temperature dependence of the decay time does not agree with the temperature dependence of the intensity, although some correlation is observed (Fig.3b).

The maximum of the blue band in the photoluminescence spectra is located in the same region as the one in the X-ray luminescence spectra at the same temperature. The location of its maximum (510-515 nm) is practically unchanged with decreasing temperature.

Photoexcitation spectra at low temperatures are more pronounced and detailed, and consequently they are more informative. Typical excitation spectra obtained at 4.2 K are shown in Fig. 4, where all excitation peaks are obvious. It is noted that we, especially for the excitation spectra, base the discussion on the spectral data obtained at the low temperatures. These spectra provide real energy levels for the absorption transitions which are luminescence active.

3. BRIEF DISCUSSION

Below we will present, in our point of view, the most important features.

1. The X-ray excited luminescence band lies in the blue spectral region for temperatures ranging from 4.2 to 300 K.

2. Within the boundaries of blue-green, yellow and red regions of the photoluminescence spectrum at least two bands can be found. So, there are bands with peaks located at 510 and 530; 560 and 600; 700 and 750 nm for the blue-green, yellow and red spectral region, respectively.

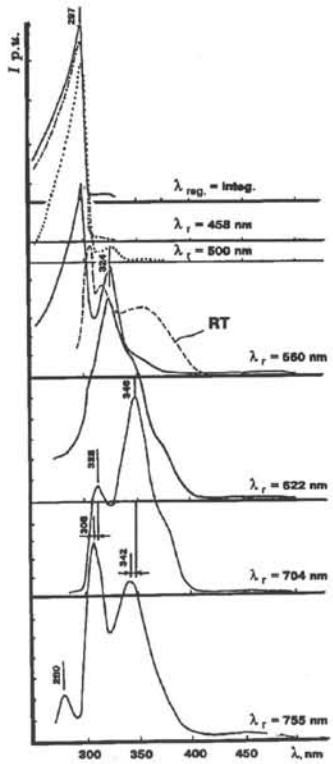

PWO crystals measured in various spectral regions of luminescence. T = 4.2 K.

3. Doubling of the bands is also present in the photoexcitation spectra. There are, for example, bands with peak positions at 305 and 308, 342 and 348 nm. Moreover, it is possible to combine the excitation peaks into the pairs 308 - 342 nm, 312 - 348 nm. They dominate in the registration of the red emission at various spectral regions. There are the following combinations averaged over the numerous measurements

- (280;290) nm - excitation of the blue emission with λ_{max} = 435-445 nm
- (305;320) nm -excitation of the blue-green emission with peak position at 510 and 530 nm.
- (324;380) nm - in general, excitation of the yellow emission with maxima 560 and 600 nm.
- (308;342) nm - excitation of the red emission with λ_{reg} = 700 nm.
- (312;348) nm - excitation of the emission with λ_{reg} = 750 nm.

4. Therefore, there is the very interesting effect: that the position of the photoexcitation of the blue emission changes with the blue-green one if the temperature goes from 4.2 (77) K $\Leftrightarrow$ 300 K and back. This indicates that the bands have a common origin. The excitation bands are considerably narrower then the luminescence bands. This is quite uncharacteristic for transitions in local molecular luminescence centres in solid state matrices.

Our investigation carried out on other crystals such as alkali halides (AHC) with impurities of tetrahedral molecular anions (MA) like CrO^{2-}_4, ReO^{-}_4, VO^{3-}_4, etc, and investigations on ionic and covalent crystals with SO^{2-}_4, CrO^{2-}_4, VO^{3-}_4 anions in regular crystal sites [5,6] allows us to make conclusions about the formation of complex molecular luminescence centres in such systems. Their composition includes MA and an anion vacancy trapped electron or MA and an electron belonging to the impurity ion that compensates the excess charge of the MA. This electron forms a relatively stable bond with the MA. The bond is stronger in the excited state of the centre. The created complex is characterised by two wells in the potential curve. We will call such a complex: the ion-polaron pair. The trapped electron plays the role of localised polaron. With increasing temperature, the polaron releases itself and it can transfer the excitation energy. Complex formation manifests itself by the appearing of the red luminescence bands connected with the short wavelength luminescence band. In the region of the vibrational modes, the bonding electron-phonon modes arise. Raman scattering shows a resonance character. The internal modes of the tetrahedral groups distort too. This fact evidences the distortions of the tetrahedral molecular group [5,6].

We suppose that the formation of such type of centres takes place in PWO crystals too, and that they cause the blue-green and red luminescence bands. Taking into account recent references [1-3] and our experimental data, we have constructed the following preliminary model of luminescence centres in PWO.

Free complex Frenkel excitons of $(Pb^{2+}\text{-}WO^{2-}_4)^*$ type are created by X-ray quanta or photons with 280-296 nm wavelength. The stable bond between lead and oxygen ions stimulate the complex character. This fact is well known for systems containing oxygen (see, for example [7]). Excitons rapidly localise themselves or "auto localise" on lattice defects, for example, on the distorted tungstate groups or on the oxygen vacancies. First the blue luminescence centres are formed. The internal modes of the complex centres cause a very rapid localisation of the excitons. Therefore, blue luminescence band dominates in the spectra. With the exciton localised on an anion vacancy, the transfer of an electron from Pb towards the anion vacancy becomes possible. This process becomes more likely at higher temperatures, and it causes the transfer of excitation energy from exciton to the "vacancy-WO_3 group" pair which results in blue-green or red emission. The second type of green-red centres (Fig. 5) origins from other types of oxygen vacancies.

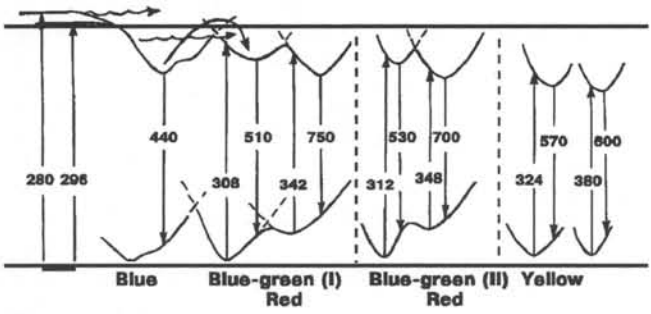

Fig.5. Energy levels diagram of the emission centres of PWO crystals

Thus, the spectral behaviour is determined to a great extent by the lead cation, oxygen vacancies and distorted tungstate groups. The exciton is supposed to origin from the lead's electron excitation. Therefore substitution of the Pb^{2+} ion on the other one must influence the blue emission. The bonding of the trapped electron with the tungstate group remains and determines the properties of the green-red centres. These centres can exist in other tungstates too. The yellow luminescence bands of lead tungstate may be connected with the transitions in interstitial oxygen anions, as it was supposed recently for cadmium tungstate crystals. These conclusions are in good agreement with the increasing contribution of such bands in spectra of crystals grown with an excess of tungsten.

Very strong similarity between the spectra, especially excitation spectra, of cadmium tungstate crystals with bismuth impurities and spectra of lead tungstate crystals confirms the indicated suppositions [8]. The considered models neither contradict with the data obtained for PWO crystals with impurities of transition row elements such as Ti, Cr, V. For some of them the blue-green emission band dominates while the blue band is almost absent. The intensity of the blue-green band increases 3-5 times under X-ray excitation and 10-20 times under photoexcitation, but at the same time the intensity of slow decay components increases.

4. CONCLUSIONS

1. The attempts of systematisation of PWO crystals with their luminescence spectra obtained at the same λ_{ex} require a special approach.

2. A scheme of luminescence centres of PWO crystals has been suggested. It is noted, that the scheme is still open for further experimental confirmation.

REFERENCES

1. Korzhik M.V., Pavlenko V.B., Timoshenko T.N., Kachanov V.A., Singovsky A.V., et. al.(1994). Spectroscopy and origin of radiating centers in $PbWO_4$ single crystals. LAPP.-EXP-94.01.

2. Nagornaya L.L., Ryzhikov V.D., Vostrerov U.Ia., at. al. Fast heavy scintillators on the basic of tungstate single crystals. Vol. of Abstracts. International Symposium "Lumdetr'94". Tallin.(1994). P.75.

3. Denes P., Klassen N., et. al. Optical and scintillation properties of $PbWO_4$ crystals. Record of the Workshop "PHYSCI 94". St. Petersburg. (1994). P. 118-124.

4. Voloshinovskyi A.S.,Krisjuk M.A., Nagornaya L.L., Nedelko S.G., Tupitsina I.A. Temperature investigations of lead tungstate single crystals (1994). (in ibid.).P.134-141.

5. Nedelko S.G.,Podshivajlov M.I. et.al. Electron vibrational interactions in doped luminescent centres "molecular anion - defects" in ion and heterodesmic crystals". Zhurnal prikladnoi spectroscopii. (1991). V.55. P.838-844.

6.Bilyi M.U.,Nedelko S.G., Chukova O.V. The luminescent properties of alkaly metal chromates. Zhurnal pricladnoi spectroscopii. (1995). V.62, P.241-250.

7.Rawson H. Inorganic glass-forming systems. (1967). Acad.Press. L. & N.-Y.

8.Nedelko S. Optical engineering bulletin. (SPIE). (1995). N2. P.23-27.

STRUCTURE DEPENDENCE OF THE EMISSION IN $PbWO_4$.

D.L.Alov, N.V.Klassen, N.N.Kolesnikov, S.Z.Shmurak
Institute of Solid State Physics, Chernogolovka, Russia

Luminescence from stolzite and raspite structure forms of $PbWO_4$ was examined. The observed results support the attribution of two emission bands (430 and 520 nm), usually detected in the luminescence spectra of pure $PbWO_4$ crystals, to the emitting centers in two different structure environments.

INTRODUCTION

Crystallographically, tungstate phosphors ($MeWO_4$) normally exist in two structure modifications: scheelite-type ($I4_1/a$, C_{4h}^6) and wolframite-type ($P2/c$, C_{2h}^4), depending on the size of the metal ion (Table)[1, 2]. Lead tungstate appears exceptional among

Table. Structure of different tungstate phosphors

Ion radius, 10^{-8} cm	Wolframite	Scheelite
$0.66 \leq r \leq 0.97$	(Mg,Fe,Mn,Zn,Cd)WO_4	
$0.99 \leq r \leq 1.34$		(Ca,Sr,Ba)WO_4
1.20		$PbWO_4$
1.20	$PbWO_4$	

these compounds because it has been detected in both structure forms: stolzite (scheelite-type) and raspite (wolframite-type). Stolzite structure is common for all $PbWO_4$ crystals produced by the high temperature melting techniques. Raspite structure was observed in the natural crystals found in Broken Hill, Australia[3].

A similar situation is observed in the optical properties of tungstate phosphors. Luminescence of the pure compounds of different structure groups (studying at proper conditions: low temperature, fundamental excitation) comes to be in two different spectral regions: scheelite-tungstates emit at 400–440 nm, wolframite-tungstates emit at 500–520 nm[2]. In addition, exciton positions (detected as inflections in the reflection spectra) are different for different tungstates: scheelite-type compounds have the exciton peaks at 240–250 nm; whereas the wolframite-type have them at 290–300 nm[2, 4]. Lead tungstate looks exceptional again. Though the exciton position is observed near 250 nm[4] the cut-off in the transmission spectrum occurs at 320 nm (for thick crystals)[5]. In addition, the emission spectrum substantially changes when the excitation comes across the spectral point 290 nm[2]. Thus the emission occupies the spectrum range from 400 nm to 550 nm and more to the red[6].

Such peculiarities of $PbWO_4$ were known, but not explained, long before this material fell under close attenion due to its selection as a candidate for the electromagnetic calorimeter in LHC. But no recent investigators emphasize the obvious connection of the optical peculiarities with the crystal structure. Nevertheless, we believe this may lead to some important conclusions able to explain the results in radiation hardness, light yield and, possibly, mechanical properties of the real $PbWO_4$ crystals.

Proc. Int. Conf. on Inorganic Scintillators and Their Applications, SCINT95,
1996, Delft University Press, The Netherlands

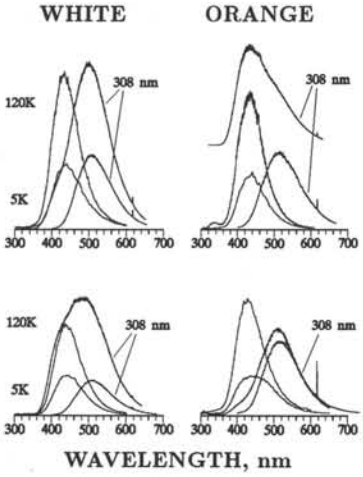

Figure 1. Photoluminescence of different $PbWO_4$ crystals at different temperatures (5 K, 120 K) and under different excitation (222 nm, 308 nm).

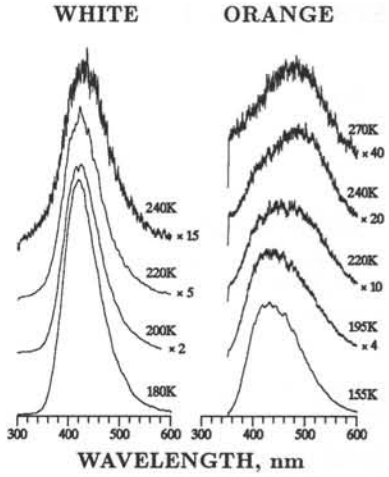

Figure 2. Temperature dependences of the photoluminescence of different $PbWO_4$ crystals: white and orange. Excited by 222 nm

EXPERIMENT AND DISCUSSION

$PbWO_4$ crystals studied by us were pure (not doped specially with other elements) crystals grown in different places by Czochralski melting technique. Depending on the crystal growth conditions (and, perhaps, stoichiometry) the produced crystals may have the color either white or orange (more or less intense). X-ray structure analysis detects all of them to be scheelite-type.

Under the excitation by 308 nm radiation (excimer laser on XeCl), the conditions close to those which are commonly used by many authors to analyze $PbWO_4$ crystal properties, crystals may display very different luminescence spectra (see Fig.1). However, under the excitation by 222 nm (excimer laser on KrCl) the observed spectra are very similar for all crystals, both white and orange (Fig.1). Because the exciton position is lower than the radiation used (thus the excitation is fundamental) we may conclude that we observe at 430–440 nm the main emitting states characteristic for this material.

The observed similarity breaks when the temperature rises and the emission begins to quench. Whereas the emission of white crystals quenches keeping the same spectrum (Fig.2), the emission of orange crystals is redistributing to the band at 500 nm. As a result, the emission of various crystals will occupy the wide spectral region from 400 to 550 nm. But they may all be decomposed as consisting of two bands with the maxima at 430 and 500 nm.

A crucial point for the resulting conclusions was the observation of the luminescence of raspite $PbWO_4$. The studied samples were from Broken Hill, Australia. Some of those crystals had the raspite structure, while others were scheelites. Fig.3 shows the corresponding spectra of these crystals. The spectrum of the raspite sample coincides with the 500 nm band observed in all presented samples (Fig.1, 308 nm excitation). The spectrum of a scheelite-type crystal from Broken Hill is very close to that taken on the most orange of the studied samples (Fig.1, Fig.2).

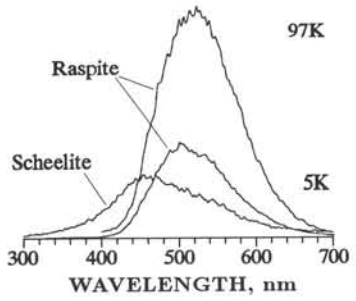

Figure 3. Photoluminescence of different $PbWO_4$ crystals from Broken Hill, Australia. Excitated by 222 nm.

Thus, we could suppose that the 500 nm band in scheelite-type $PbWO_4$ crystals may be due to the presence of raspite inclusions in the tested samples. However, X-ray structure analysis didn't observe raspite as a large bulk constituent in our samples. On the other hand, it is accepted to treat[2, 4, 6] that the emission in $PbWO_4$ is due to the defect states of the crystal lattice. In this case it is the local crystal symmetry of the defect state environment which is most important for all processes taking place on these states. Raspite structure may be treated as the distortion of the scheelite structure[1]. The unit cell volume difference between raspite and stolzite $PbWO_4$ is very small (0.5%[3]). We suppose that the raspite-type local distortions of very small size may be produced in the synthesized $PbWO_4$ crystals during the growth process and/or subsequent treatment. It is the defect states existing in these distorted volumes which are responsible for the observation of the 500 nm band in the stolzite $PbWO_4$. These states give for the excitations more deep levels than the main volume (430 nm) and become relatively more occupied when the temperature rises because of the activated migration of excitations. When the temperature is low the migration is shut down and primarily the defect states in the majority structure (stolzite) will be populated. Thus the emission will be detected at 430 nm.

CONCLUSIONS

The spectral variability of luminescence in $PbWO_4$ crystals is explained by the assumption that the emitting defect states may exist in two different local structure environments: scheelite-type and wolframite-type.

REFERENCES

[1] L.N.Demianec et al. Izv.Akad.Nauk SSSR,Neorgan.Mat., v.3, p.2221 (1967)

[2] F.A.Kröger. "Some aspects of the luminescence in solids", Elsevier, 1948
M.V.Pashkovski. "Effect of structure defects on the physical properties of tungstates", Visha skola, 1978 (in Russian)

[3] T.Fujita et al. Acta Cryst. B**33**, p.162 (1977)

[4] E.G.Reut. Izv.Akad.Nauk SSSR, Ser.fizich., v.49, p.2032 (1985)

[5] W. van Loo. Phys.Stat.Sol.(a) **27**, 565 (1975)

[6] M.V.Korzhik et al. In "Scintillator and phosphor materials", Proceedings of the MRS 1994 Spring Meeting, MRS Pittsburg, USA, p.285

CHARACTERISTICS OF SCINTILLATING $PbWO_4$ CRYSTALS PRODUCED AT DIFFERENT GROWING CONDITIONS

M.V.Belov, E.G.Devitsin, V.A.Kozlov, L.S.Popov, S.Y.Potashov
Lebedev Physical Institute, 117924 Moscow, Russia

V.A.Nefedov, B.I.Zadneprovsky
All-Russian Research Institute of Synthesis of Mineral Raw Materials, Alexandrov, Vladimir region, Russia

Abstract

The characteristics of heavy scintillating $PbWO_4$ crystals produced at different growing conditions have been studied. All crystals were grown in All-Russian Research Institute of Synthesis of Mineral Raw Materials.

The measured light yield of the best sample (3.85) was 6.4 % of that of BGO crystal. Decay times were established to be $\tau_1 = 2.2$ ns, $\tau_2 = 7.9$ ns, $\tau_3 = 33.9$ ns.

All samples were irradiated by γ-quanta from a powerfull ^{60}Co source up to doses of 460 krad and 7 Mrad. For colourless samples almost selfannealing after 2 weeks of the exposure is seen.

1 Introduction

Starting with the first communication from S.Derenzo et al. [1] the intensive studies on scintillation properties and radiation hardness of $PbWO_4$ crystal are being carried out [2-4]. For this scintillating crystal used in e.m. calorimetry optical nonuniformity along the full size crystal and shift of emission spectra for different parts of undoped crystal were observed [4]. The introduction of Nb allowed to obtain more optical uniform crystals and increased its radiation hardness [4]. However, for $PbWO_4$ doped with Nb wide absorption band around 420 nm is observed which slightly decreases the crystal light yield. Note, that even for the best $PBWO_4$ samples light yield doesn't exceed 5 % from that of BGO crystal.

2 X-ray phase and scintillation characteristic studies

Crystals have been grown by Czochralski method in a resistive heating setup using platinum crucibles. The mechanical mixture of PbO and WO_3 oxides taken in stoichiometric ratio is used as a charge.

Crystals 90-100 mm long and 20-22 mm in diameter have been obtained. Crystal colour varies from bright orange-yellow to slight lemon-yellow and almost colourless depending on oxidizing potential of gas atmosphere. Therefore, X-ray phase studies of grown material and initial lead oxides are performed taking into account that phase content of crystals itselves and lead content in charge components may produce a colour of $PbWO_4$. The studies were performed using DRON-4-07 diffractometer (CuK_α-irradiation, Ni-filter). The data obtained indicate that the phase inhomogenity and yellow colour centers happen during crystal growing and are substantially caused by oxygenic processes in a melt as well as by form of the lead oxide present. Our results allow to consider the creation of colour centers as a consequence of transition into three valent state of part of lead in melt and its further re-entry into crystal yielding defects involving Pb^{3+}.

The initial crystals have been cut up to cylindrical samples with the following dimentions: 11.0 mm in diameter and 10.0 mm long for spectral studies. The butt surfaces of the samples

Proc. Int. Conf. on Inorganic Scintillators and Their Applications, SCINT95,
1996, Delft University Press, The Netherlands

have been polished. The same way a BGO sample for comparison is manufactured. Transmission spectra in visible and close UV regions (280 - 900 nm) are recorded on spectrometer "Specord-M 40". X-ray luminescence spectra are obtained using special setup based on KSVU-2 assembly (MoK_α irradiation, PMT-100) in the range of 330-750 nm. X-ray luminescence spectra of crystals are presented as a broad structureless asymmetric band. Luminescence intensity is maximum for material from crystal head part and decreases with shift of selecting zone to the rear part of a crystal without changing in wavelengh of spectrum maximum. The comparison of samples cut from the same parts of different crystals shows that for the most crystals X-ray luminescence intensity of middle and bright coloured materials is higher than for slight yellow and colourless ones. It is shown that the observed shift of maximum of X-ray luminescence spectra of crystals is a consequence of the decrease of number of green luminescence centers.

For measuring the $PbWO_4$ light yield samples were coated with white teflon tape and coupled to XP-1911 photomultiplier by "Rhodorsil" optical grease. The signal from the samples irradiated by ^{137}Cs source enters the amplifier and then ADC ORTEC AD811. Pulse height spectra for all samples under investigation are presented in fig. 1. It is evident that photopeaks corresponding to yellow colour samples (for example, 3.E) have a smaller amplitude than those of colourless ones (for example, 3.85).

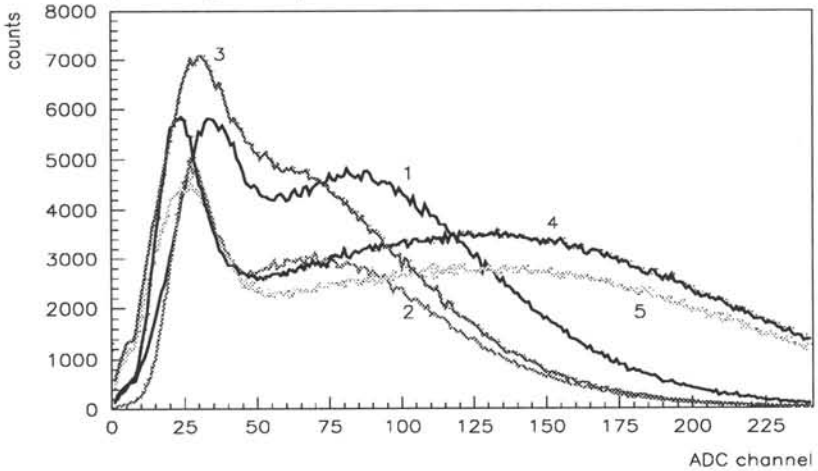

Fig.1 *Pulse height spectra of different $PbWO_4$ crystals (10 mm in diameter, 10 mm long) obtained using ^{137}Cs source : 1 - sample 1.6; 2 - sample 1.E; 3 - sample 3.E; 4 - sample 3.8; 5 - sample 3.85.*

Absolute light yield of $PbWO_4$ samples was measured by comparing it with that of BGO crystal of the same size. For this comparison the $PbWO_4$ 3.85 sample was chosen and QDC KA-010 was used having gate width of 400 ns. When measuring BGO pulse height spectrum the attenuation was 16 dB. Spectra for $PbWO_4$ and BGO are shown in fig. 2. By comparing these spectra one can calculate that $PbWO_4$ 3.85 sample light yield is 6.4 % of that of BGO sample. Note that in accordance with S.Derenzo et al. [1] light yield of $PbWO_4$ is 3.6 % and with M.Kobayashi et al. [3] it is 4.4 % of that of BGO.

Decay times were measured by means of "separate scintillators" method using YAP scintillating crystal and ^{60}Co source [5]. PMT signals enter constant fraction discriminator ORTEC 463 and then 1024 channel TDC KA-317. To approximate initial data the function consisting of a sum of three exponents and a line reflecting background was chosen. Decay times are τ_1=2.6(34.3%), τ_2=10.8(38.9%), τ_3=76.9(28.4%) ns (yellow sample 3.E) and τ_1=2.2(28.4%), τ_2=7.9(47.6%), τ_3=33.9(23.9%) ns (colourless sample 3.85). It is evident that colourless $PbWO_4$ samples have shorter decay times compared with yellow ones (especially τ_3). Our results on

decay time measurements of colourless PWO crystals are similar to [4].

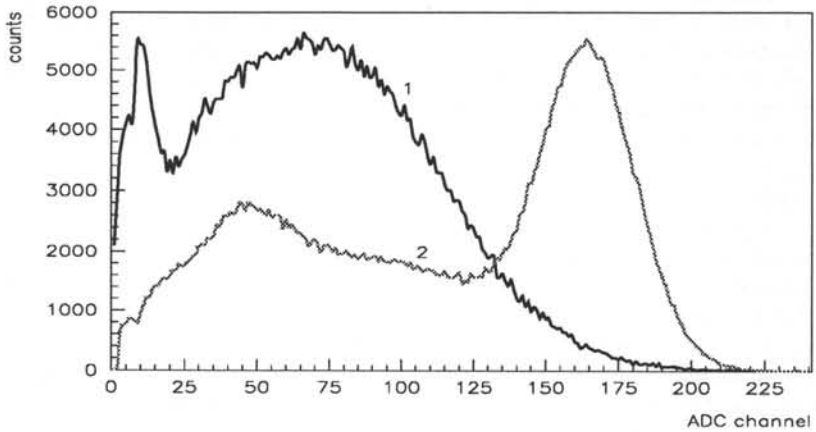

Fig.2 *Comparison of pulse height spectra of $PbWO_4$ and BGO crystals (10 mm in diameter, 10 mm long) obtained using ^{137}Cs source : 1 - $PbWO_4$ (sample 3.85); 2 - BGO (attenuation 16 dB).*

3 Radiation hardness measurements

Radiation hardness of $PbWO_4$ samples was studied using ^{60}Co source (maximum power is about 1 krad/s). All $PbWO_4$ crystals were sequentially irradiated with two doses: 460 krad and 7 Mrad. Transmission spectra measurements were performed just after irradiation. Some results are plotted in figs. 3 and 4. From the analysis of the spectra one can conclude that with the increase of the irradiation dose the transmission drops down for yellow coloured samples (for example, 3.E) (fig.3).

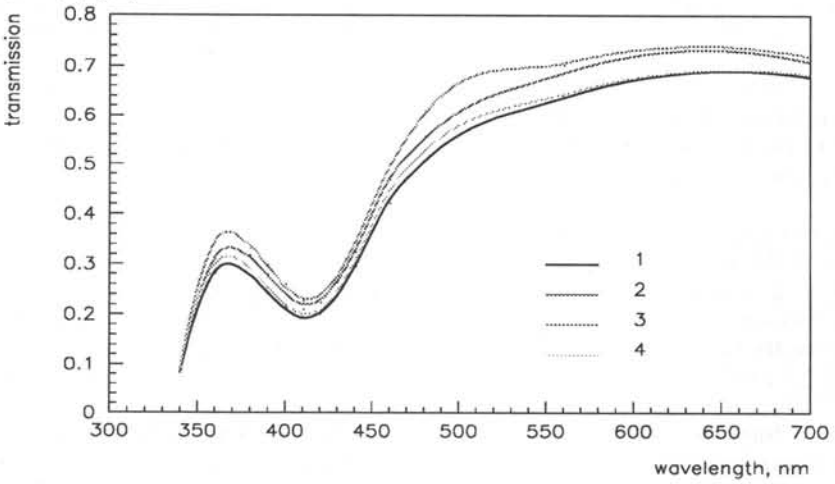

Fig.3 *Transmission spectra of $PbWO_4$ crystal (sample 3.E - 10 mm in diameter, 10 mm long): 1 - before irradiation; 2 - after 460 krad (^{60}Co source); 3 - after 7.0 Mrad; 4 - selfannealing after 2 weeks after irradiation.*

Evidently the saturation of radiation damages has taken place because the difference in

transmission for two doses is small. The behaviour of radiation damages of colourless crystals is different. After the samples were irradiated by a low dose the decrease in transmission is about 5 %. After the high dose irradiation the transmission increases. In addition, the transmission spectra of all samples were measured within 2 weeks after high dose irradiation (7 Mrad). The self annealing of radiation damages is quite pronounced for all samples and the transmission is completely recovered for the sample 3.85 (fig. 4).

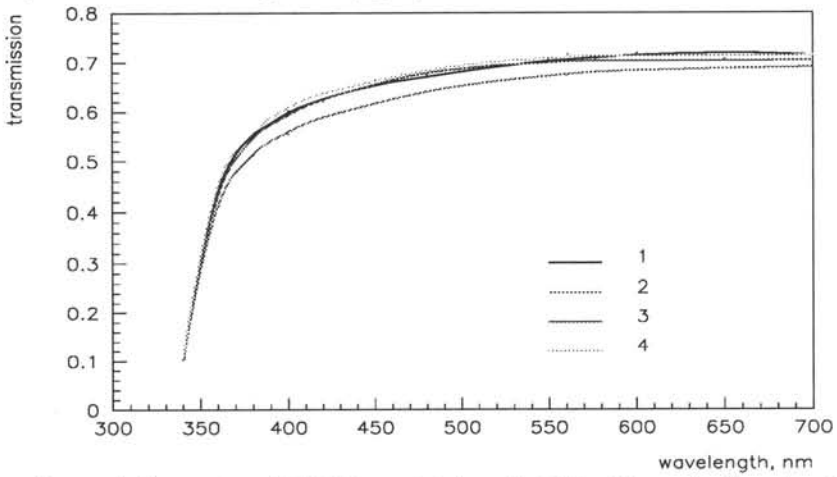

Fig.4 *Transmission spectra of $PbWO_4$ crystal (sample 3.85 - 10 mm in diameter, 10 mm long): 1 - before irradiation; 2 - after 460 krad (^{60}Co source); 3 - after 7.0 Mrad; 4 - selfannealing after 2 weeks after irradiation.*

4 Conclusion

The process of creation of colour centers in $PbWO_4$ crystal is a consequence of transition into 3 valent state of part of lead in a melt and its further re-entry into the crystal yielding defects involving Pb^{+3}.

The shift of maximum of X-ray luminescence spectra of the crystals is a concequence of the decrease of a number of green luminescence centers.

Colourless samples of $PbWO_4$ crystal have higher light yield, shorter decay times and better radiation hardness compared with colour ones.

References

[1] **S.E.Derenzo et al.** // IEEE Trans. Nucl. Sci. NS-37(1990)203;

[2] **V.G.Baryshevsky et al.** // Nucl. Inst. Meth. A322(1992)231;

[3] **M.Kobayashi et al.** // Nucl. Inst. Meth. A333(1993)429;

[4] **O.V.Buyanov et al.** // Nucl. Inst. Meth. A349(1994)62; **A.N.Annenkov et al.** "Progress in $PbWO_4$ scintillating crystal" // LAPP Preprint LAPP-EXP 94-25, 1994; **A.N.Annenkov et al.** "Lead tungstate ($PbWO_4$) scintillators for LHC EM-calorimetry" // CERN/PPE report, CMS TN/94-308; **I.Dafinei et al.** "Lead tungstate for high energy calorimetry" // CERN/PPE report, CMS TN/94-317;

[5] **M.Moszynski and B.Bengtsen** // Nucl. Inst. Meth. 142(1977)417.

RESISTANCE OF LEAD TUNGSTATE AND CERIUM FLUORIDE TO LOW RATE GAMMA IRRADIATION OR FAST NEUTRONS EXPOSURE

R. Chipaux, O. Toson
CEA, DSM/DAPNIA, CE-Saclay, F-91191 Gif sur Yvette cedex, France,

ABSTRACT

We present here the results of recent low dose rate gamma irradiation of lead tungstate and cerium fluoride long crystals, and, for lead tungstate only, fast neutron exposure. For the low rate tests, recovery processes are taking place during irradiation and, compared to the usual high rate tests, only a very low damage is noticed, if any. No saturation effect is observed in these previously irradiated samples. For the neutron tests, a very small variation with fluence is not excluded, after a fast saturation at low fluence. The samples tested here are very resistant.

INTRODUCTION

The experiments proposed for the future high-energy particles accelerators like the Large Hadron Accelerator (LHC) in construction at CERN, Geneva, will have to support a high radiation environment during all their life. An important part of the R&D effort of the collaborations is devoted to the study of the radiation resistance of all the detector's components : detection media, photodetectors, electronics, mechanics, etc. The exact dose and fluence levels will depend on the final designs of the experiments, but their order of magnitude have already been well established. For example, the Compact Muon Solenoid (CMS) [1] electromagnetic calorimeter (ECAL), in which the active elements will be lead tungstate scintillating crystals, will suffer some 5 kGy (0.5 Mrad) and 10^{13} fast neutrons cm^{-2}, at the maximum of energy deposition and over the first ten years of operation. In the forward electromagnetic calorimeter, levels from 3 to 10 higher are foreseen.

This radiation environment is characterised by a simultaneous presence of ionising radiations (mainly gamma rays) and hadronic fluxes (neutrons and protons). This situation is quite close to the one encountered in and near nuclear reactor cores, but with rates of some 6 orders of magnitude lower. In order to simulate this environment, we use, in Saclay, both the nuclear reactor ULYSSE, with which we simulate a LHC-like ambience [2,3], and the ^{60}Co source COCASE, which allows us long term irradiation on large volumes of materials at realistic dose rates.

EXPERIMENTAL

The longitudinal optical transmissions of the crystals studied here were measured with a Perkin-Elmer Lambda 19 spectrometer before and after irradiation. In the $PbWO_4$ crystals, two optical paths were always clearly distinguishable because of their birefringence and length. The usual induced absorption coefficients $\varepsilon = \log(T_0/T)/\ell$ were calculated from the transmission spectra.

Low dose rate gamma irradiations

We have recently implemented in Saclay a ^{60}Co source named COCASE, designed for low rate experiments. The dose rate is approximately 0.25 Gy/h at 1 m from the source. A dosimetry is made with alanine dosimeters supplied and analysed by CEA/DAMRI. The doses given here are the equivalent doses in air, with a precision of 10 %.

Proc. Int. Conf. on Inorganic Scintillators and Their Applications, SCINT95,
1996, Delft University Press, The Netherlands

One sample of cerium fluoride, (20 x 20 x 78 mm^3) and one of lead tungstate (of projective shape, (18.1 x 18.1) to (20.8 x 20.8) x 214 mm^3) were irradiated at a rate of ≈1 Gy/h since December 1994. The crystals were taken out after 0.3, 0.9, 2.4 and 4.3 kGy for the measurements reported here. Irradiation is scheduled up to 10 kGy.

The CeF_3 crystal is referenced CF638 in the Crystal Clear data base and comes from Optovac. The $PbWO_4$ one is numbered PW826 in the CMS data base, and is a niobium doped sample (40 ppm) coming from Bogorodisk.

Both have been previously exposed to a high rate (≈3 Gy/mn) irradiation. CF638 has

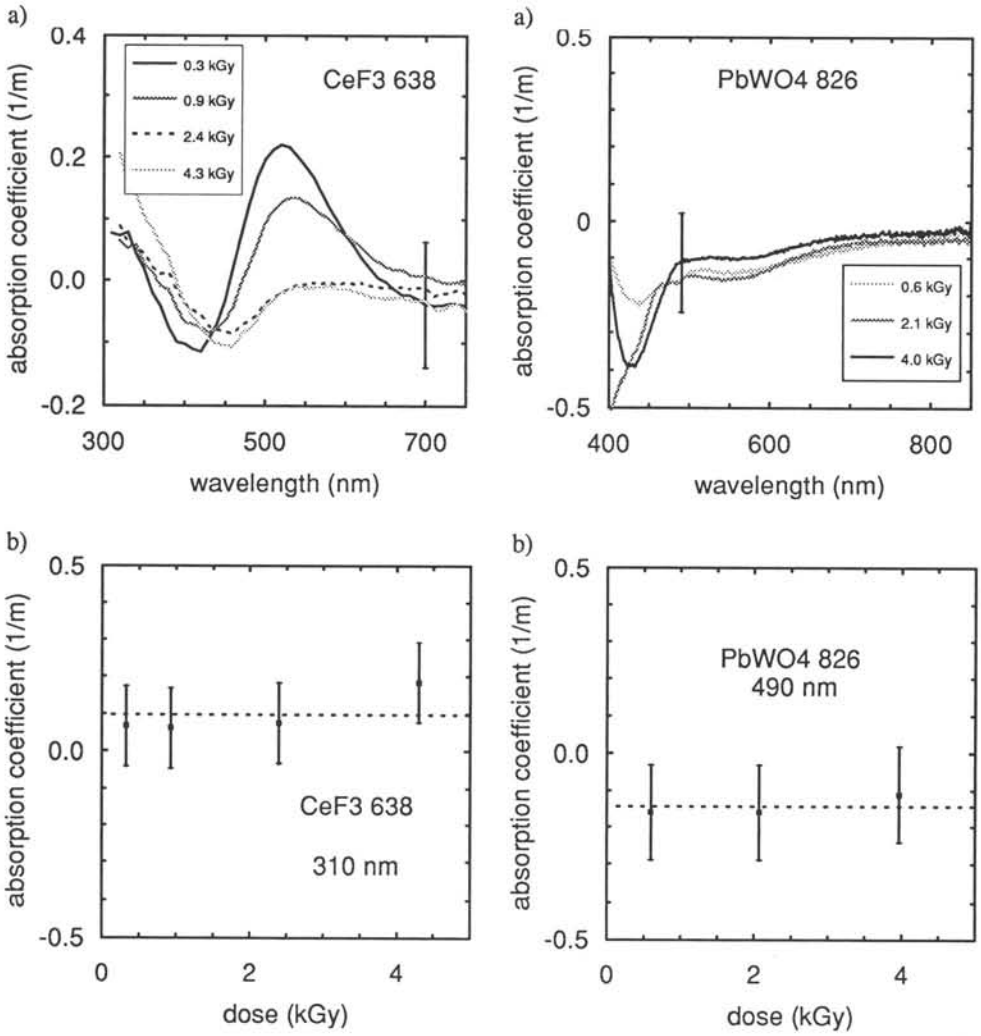

Figure 1 : Induced absorption coefficient in CF638 after low dose rate gamma irradiation :
a) as a function of wavelength ;
b) as a function of dose, at the maximum of emission.

Figure 2 : Induced absorption coefficient in PW826 after low dose rate gamma irradiation (referenced to the 1st dose data) :
a) as a function of wavelength ;
b) as a function of dose, at maximum of emission.

been exposed by step to 540 Gy in August 1994. The induced absorption coefficient at 310 nm was ≈ 1 m^{-1} just after the last irradiation, and recovered to ≈ 0.3 m^{-1} within one day. Then a slower recovery process occured (0.2 m^{-1} after one month) [4]. PW826 has been exposed in the same way to 1.8 kGy in September 1994. No effect was clearly distinguishable, with $-0.5 \leq \varepsilon \leq 0.5$ m^{-1} at 490 nm [5].

As shown in figure 1, an absorption band appears in CF638, around 500 nm, after the first 300 Gy. This band vanishes when the dose increases. This variation might be related to the modification of room temperature during the experiment, (it began at 14°C in winter, to end at 30°C, or even more, in summer...), leading to faster recovery process. In any case the induced absorption coefficient remains below 0.2 m^{-1} at any wavelength, and is almost negligible at the wavelength of peak emission (figure 1b).

PW826 seems to present two different crystalline orientations in the bulk, separated by a weakly refracting plane, and to have a slight defect of parallelism between its two small faces. This, in addition to the intrinsic birefringence and index dispersion of lead tungstate, induces difficulties to collect all the transmitted light in such a long sample. For that reason, the reference transmission, measured before irradiation, was not correct below 520 nm, leading to artificial structures in the following absorption spectra. If we take as reference the data at the first dose, we observed that the transmission remains practically unchanged (figure 2).

As mentioned, the two crystals have been irradiated before this test, and not submitted to thermal or similar 'hard' annealing. That could explain the absence of any saturation effect at low dose.

Neutron irradiations

We have irradiated in the reactor ULYSSE a long $PbWO_4$ crystal by a procedure already described [3]. This piece, of parallelipipedic shape (20 x 20 x 180 mm^3), is referenced as PW739 in the CMS data base. It is also a niobium doped (35 ppm) crystal coming from Bogorodisk.

This crystal has been previously irradiated to 100 kGy (10 Mrad) by 500 MeV electrons from the LiL at CERN [6,7]. 4 days after this irradiation, the induced absorption coefficient was 1.4 m^{-1} at 490 nm, and decreased to about 1 m^{-1} within one month ; the remaining damage

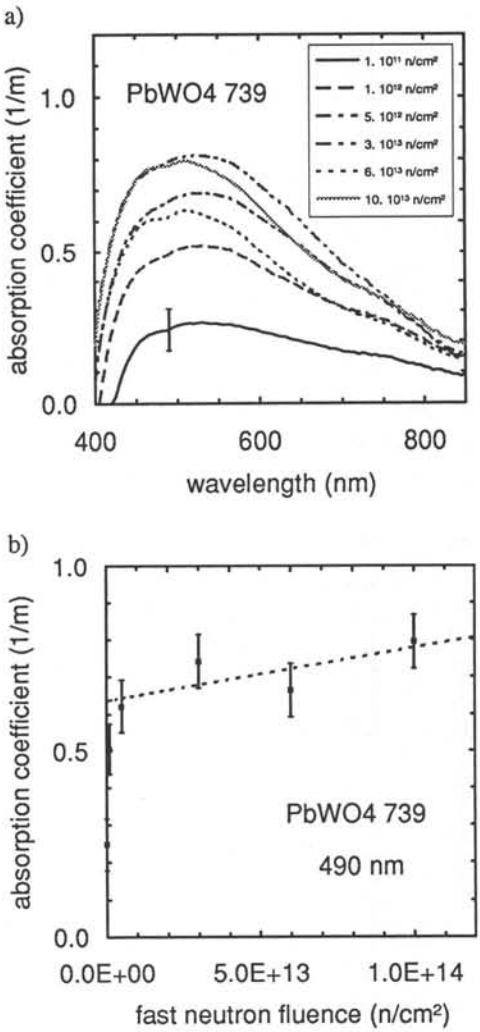

Figure 3 : Induced absorption coefficient in PW739 after the 6 steps of neutron irradiation :

a) as a function of wavelength ;
b) at 490 nm, as a function of integrated fast neutron fluence.

disappeared after a 6 hours annealing at 220°C [5].

In the present test, a cumulated fluence of 10^{14} fast neutrons cm^{-2} and a total dose of 12.5 kGy were reached in 6 steps (10^{11} ; 10^{12} ;5.10^{12} ; 3.10^{13} ; 6.10^{13} and 10^{14} fast neutrons cm^{-2}). To allow the decay of the induced radioactivity, the measurements were made between one week and one month after irradiation, depending on fluence.

As shown in figure 3, the sample exhibit a small degradation of the transmission properties after the two first irradiations (i.e. below 5.10^{12} fast neutrons cm^{-2} and 625 Gy). Unlike the two preceding crystals, PW739 has been thermally annealed before this test. The initial induced absorption coefficient is slightly lower that the one induced after its previous electrons irradiation. Then a saturation regime occurs, with maybe a slight increase of the damage with the fluence Φ. A linear regression on the four last values give $\varepsilon = (0.64 \pm 0.05) + (0.14 \pm 0.09)\ 10^{-14}\ \Phi\ m^{-1}$ at 490 nm. This variation is at the limit of significance and should be confirmed. It could indicate creation of defects by fast neutrons.

Measurements, not reported here, were also made in polarised light, but no effect of the light polarisation has been observed.

CONCLUSION

It is confirmed here that, in lead tungstate, pre-existing defects are activated very rapidly by radiation, leading to an initial degradation followed by a saturation. This initial damage is any way rather small, but seems permanent, except after thermal annealing. Further studies are needed to understand what are these defects, if and how they can be reduced, etc.

After this initial variation, the permanent (or quasi-permanent) damage, which is the only type seen in this work, is practically absent, confirming that both cerium fluoride and lead tungstate can be very radiation resistant, and, from that point of view, good candidates for high luminosity crystal calorimetry.

ACKNOWLEDGEMENTS

This work was carried out in the frame of CMS and Crystal Clear collaborations. We are indebted to J. Safieh, G. Dauphin and the operating team of the ULYSSE reactor (CEA/INSTN), as well as J.-L. Faure, P. Micolon and P. Rebourgeard (CEA/DAPNIA), for their support.

REFERENCES

[1] CMS collaboration, "The Compact Muon Solenoid", Technical Proposal, LHCC/P1, CERN/LHCC 94-38, 15 dec 1995.

[2] Crystal Clear Collaboration, *Nucl. Instr. and Meth.*, **A332** (1993) 373-394.

[3] R. Chipaux et al., *Nucl. Instr. and Meth.*, **A345** (1994) 440-444.
R. Chipaux et al., in *Proc. Symp. scintillator and phosphor mater., MRS '94 Spring meeting, San-Francisco, USA, 4-8 avril 1994,* eds. M.J. Weber, P. Lecoq, R.C. Ruchti, C. Woody, W.M. Yen and R.-Y. Zhu, pp 481-486.

[4] Crystal Clear Collaboration, "'Crystal Clear Collaboration' Status Report", CERN-DRDC/94-53 (1994).

[5] E. Auffray and I. Dafinei, personnal communications and these proceedings (1995).

[6] J.P. Merlo et al, "Radiation hardness tests using the LiL beam facility", CMS TN/94-262 (1994).

[7] A. Fyodorov et al., "Progress in $PbWO_4$ scintillating crystal", LAPP-EXP/94-25 (1994), to appear in *Radiat. Meas.*

A STUDY OF THE OPTICAL AND RADIATION DAMAGE PROPERTIES OF LEAD TUNGSTATE CRYSTALS

C.L. Woody, J.A. Kierstead, S.P. Stoll
Brookhaven National Laboratory [1]

R.Y. Zhu, D.A. Ma, H.B. Newman
California Institute of Technology

ABSTRACT

A study has been made of the optical and radiation damage properties of undoped and niobium doped lead tungstate crystals. Data were obtained on the optical absorbance, the intensity and decay time of the scintillation light output, and the radioluminescence and photoluminescence emission spectra. Radiation damage was studied in several undoped and niobium doped samples using ^{60}Co gamma ray irradiation. The change in optical absorption and observed scintillation light output was measured as a function of dose up to total cumulative doses on the order of 800 krad. The radiation induced phosphorescence and thermoluminescence was also measured, as well as recovery from damage by optical bleaching and thermal annealing. An investigation was also made to determine trace element impurities in several samples.

INTRODUCTION

Lead tungstate ($PbWO_4$) is a new scintillating material which is of great interest for use in high energy electromagnetic calorimeters. It has a very high density (ρ = 8.3 g/cm^3), short radiation length (X_o = 0.9 cm) and small Moliere radius ($R_M \approx$ 2 cm), and has a scintillation light output which peaks between 450-550 nm with a decay time in the range from 5-15 ns. It is presently being considered for use in two large, high resolution electromagnetic calorimeters, one for the CMS experiment and the other for the ALICE experiment, at the Large Hadron Collider at CERN. In order to meet the stringent demands of these two experiments, the crystals are required to be of high purity, produced uniform light output, and, in the case of CMS, be resistant to radiation damage up to several megarads.

We have carried out a study of the optical and radiation damage properties of a number of undoped and niobium doped crystals obtained from sources in the former Soviet Union. A total of seven samples, measuring typically 2 × 2 × 21 cm^3, were measured in all. In this paper, we will mainly discuss the results for two particular samples (number 767 and 768), both of which are Nb doped, and were part of a group of crystals prepared for study by CMS. These two samples, which were grown under similar conditions, showed very different properties, particularly with respect to radiation damage. Other samples, both undoped and Nb doped, have shown similar behavior, some exhibiting good radiation hardness and others not. We will compare a number of differences observed in samples 767 and 768 in order to attempt to identify which of these properties could be relevant in determining the important optical and radiation damage properties of $PbWO_4$. Additional information on an undoped sample can be found in ref.[1].

[1] Research supported by the U.S. Dept. of Energy under Contract No. DE-AC02-76CH00016.

Proc. Int. Conf. on Inorganic Scintillators and Their Applications, SCINT95,
1996, Delft University Press, The Netherlands

OPTICAL AND RADIATION DAMAGE PROPERTIES

The initial (pre-irradiation) transmission spectra for samples 767 and 768 are shown in Figure 1. Sample 767 showed a distinct absorption band in the region around 430 nm, while sample 768 exhibited only a shoulder. Sample 767 also contained a small ($\sim$ 2 cm long) region of inhomogeneity near the center of the crystal at one end which produced much higher absorbance near the center than near the edges.

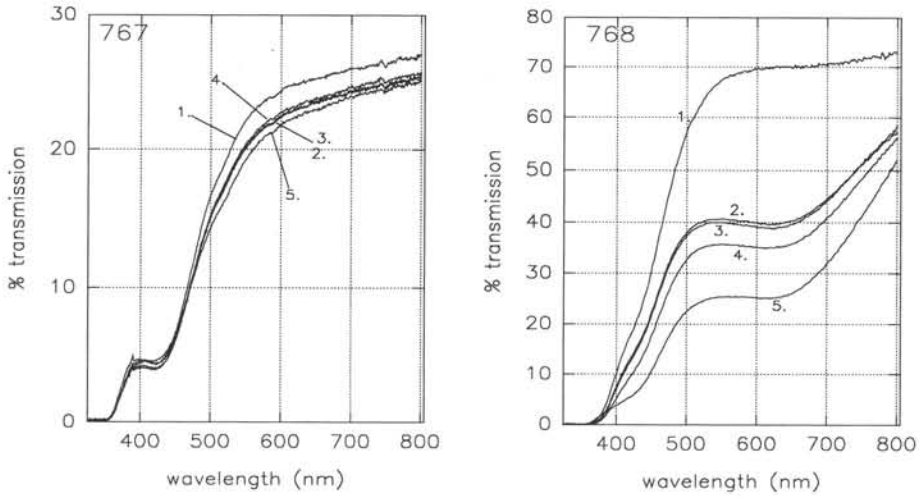

Figure 1: Transmission spectra as a function of radiation dose for samples 767 and 768. Cumulative doses for 767 are 1 - initial, 2 - 2.6 Krad, 3 - 7.6 Krad, 4 - 18.2 Krad, 5 - 769 Krad. Dose rate was 120 rad/hr for doses 2 through 4 and 3.5×10^4 rad/hr for dose 5. Cumulative doses for 768 are 1 - initial, 2 - 2.4 Krad, 3 - 11 Krad, 4 - 20 Krad, 5 - 834 Krad. Dose rate for dose 2 through 4 was 132 rad/hr and 3.6×10^4 for dose 5.

The spectral light output of both samples was compared by measuring the radioluminescence and photoluminescence emission spectra. The radioluminescence was measured using ^{60}Co gamma ray excitation, and the photoluminescence was measured using UV excitation at a wavelength of 315 nm. For sample 767, the photoluminescence was also measured for other excitation wavelengths from 250-350 nm, and no dependence of the emission spectrum on the excitation wavelength was found. Figure 2 shows the spectra measured for the two crystals after correcting for phototube quantum efficiency and monochrometer grating efficiency. The radioluminescence peaks at around 515 nm for sample 767, while sample 768 shows a lower peak at around 486 nm. Although the photoluminescence appears to peak at longer wavelengths (527 nm for 767 and 513 nm for 768), at least part of this shift can be attributed to self absorbance in the crystal. Decay times measured for the radioluminescence showed two major components in the range of 2-3 ns and 15-20 ns, along with a third slow component with a decay time of several hundred nanoseconds.

Both samples were irradiated using ^{60}Co gamma rays up to a maximum total dose of 769 krad for sample 767 and 834 krad for sample 768. In both cases, the initial irradiation was carried out at a low dose rate ($\sim$ 120-130 rad/hr), in order to study any

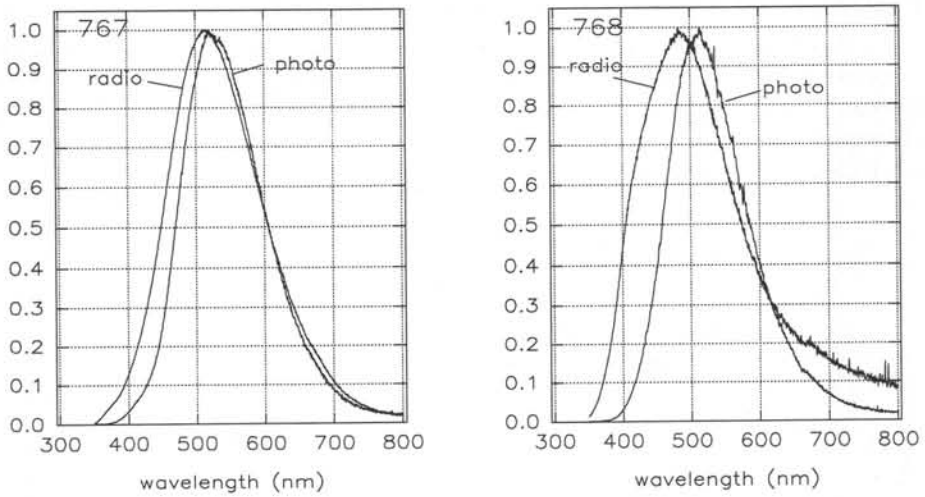

Figure 2: Radioluminescence and photoluminescence emission spectra for samples 767 and 768. All spectra have been corrected for phototube quantum efficiency and monochrometer efficiency and normalized to one at their peak.

rapid changes which may occur in either sample. As shown in Fig. 1, sample 768 damaged quickly, exhibiting a series of strong, broad absorption bands in the region between 400 and 700 nm, and continued to damage with increasing dose. This damage was similar to that which was observed in undoped samples [1]. On the other hand, sample 767 showed very little damage, both at the initial low dose rate, and at the higher dose rate up to the maximum dose. The light output of both samples measured before irradiation on a 2" dia. phototube was $\sim$ 8 photoelectrons per MeV. After the initial dose, the light output from sample 768 was not measurable due to the increased self absorbance and interference from radiation induced phosphorescence. However, the light output from sample 767 was measurable even up to the maximum dose, as shown in Figure 3. The light output measured approximately 30 minutes after the final dose showed a slight decrease of about 15%, but recovered to its original value within 5.5 hours. Sample 768 showed a natural recovery in its transmission with a time constant of $\sim$ 160 hours. Optical bleaching using light in the 600-700 nm range produced significant recovery when applied immediately after irradiation, and thermal annealing for several hours at a temperature of 200 °C produced slightly more recovery.

Figure 3 also shows the radiation induced phosphorescence in samples 767 and 768 measured as a function of time shortly after irradiation. The apparent lower phosphorescence intensity in sample 768 was at least partly due to its higher induced absorption. The time constant for the phosphorescence decay was approximately 6-7 minutes for both samples. Both samples also exhibited a modest thermoluminescence signal which showed several peaks in the temperature range from 50-300 °C. However, in absolute terms, the thermoluminescence signal was several orders of magnitude less than for many other materials, such as BaF_2 or undoped CsI.

A trace element analysis was performed on both samples using Particle Induced X-ray Emission (PIXE) and Glow Discharge Mass Spectroscopy (GDMS) in order determine

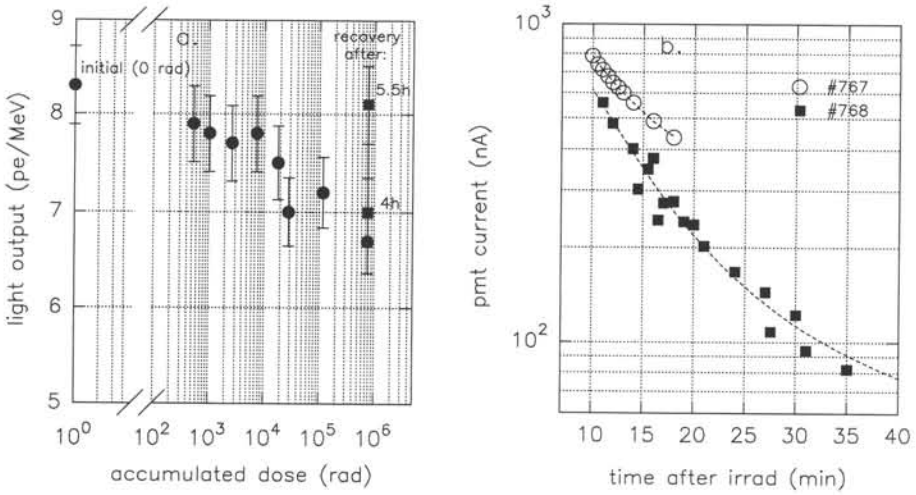

Figure 3: (a) Light output vs accumulated dose for sample 767. Except where indicated, all points were measured approximately 30 minutes after irradiation. (b) Phosphorescence intensity vs time for samples 787 and 768. A fit to spectra give decay times of 6.0 and 6.7 minutes for samples 767 and 768, resp.

the stoichiometry of the crystals and to search for trace element impurities. The results showed that both crystals were essentially stochoimetric $PbWO_4$, although there was an indication that the W/Pb ratio varied by $\sim 5\%$ from one end of the crystal to the other. A survey of 77 elements show similar levels of impurities in the few ppm to sub ppm level in both samples, although sample 767 showed a significantly higher level of sodium than 768 (9.6 ppm vs. 1.8 ppm).

CONCLUSIONS

A study of a number of lead tungstate crystals has revealed a large sample to sample variation in many of their properties. The optical transmission varies considerably, and some samples show sizable regions of visible inhomogeneities. The radioluminescence spectra also vary from crystal to crystal, with the peak occurring in the 480-520 nm range. The scintillation decay time shows two major components in the 2-3 ns and 15-20 ns range, along with a third slow component in the several hundred nanosecond range. Some samples, which do not necessarily show the best optical transmission before irradiation, exhibit particularly good radiation hardness. Initial trace element analyses carried out on samples having very different characteristics have shown no high level impurity content and similar levels of trace element impurities. Further work is under way to attempt to correlate these results with the optical and radiation damage properties of the crystals.

REFERENCES

[1] J.Kierstead et.al., Proceedings of the *Symposium on Scintillator and Phosphor Materials*, Materials Research Society, Vol. 348 (1994) 475.

SCINTILLATION CHARACTERISTICS AND RADIATION HARDNESS OF PWO SCINTILLATORS TO BE USED AT THE CMS ELECTROMAGNETIC CALORIMETER AT CERN

E. Auffray[1], I. Dafinei[1*], F. Gautheron[1], O. Lafond-Puyet[1], P. Lecoq[1], M. Schneegans[2]
1) CERN, Geneva Switzerland, 2) LAPP, Annecy France, *On leave from IFA Bucharest Romania

ABSTRACT

Since the $PbWO_4$ (PWO) crystal was selected as the baseline option for the Electromagnetic Calorimeter (EC) of the future Compact Muon Solenoid (CMS), a very intense research activity was dedicated to a better understanding of its scintillation properties. Nevertheless the low light yield of this crystal and the complexity of the luminescence mechanism lead to contradictory results and interpretations. In this paper, results on the scintillation characteristics (luminescence spectra, decay time, light yield) and radiation hardness of PWO crystals having a geometry close to the CMS design ($23 \times 2.38 \times 2.05$ cm^3) and produced in industrial conditions are presented.

INTRODUCTION :

After the choice of the $PbWO_4$ crystals for building the electromagnetic calorimeter of CMS detector at the future LHC collider at CERN [1], a large effort and progress have been made on the production of long crystals (up to 2.38x2.38x23 cm^3), in terms of scintillation properties, optical quality and radiation hardness as well as mechanical properties. In this paper, the results, based on the study of more than 100 crystals with geometry close to the CMS design, will be summarised . We particularly focus on spectroscopic properties as well as on radiation hardness.

TRANSMISSION PROPERTIES :

For all the crystals, the optical transmission has been measured transversally with a 2 cm step along the growth axis from 300nm to 700nm. In this region of wavelength, the theoretical transmission of $PbWO_4$ varies from 70% to 75 % assuming a variation of refraction index from 2.75 to 2.24 for ordinary index and from 2.5 to 2.15 for extraordinary index. Above 500nm, all crystals have a similar transmission close to the theoretical transmission. Below 500nm, the behaviour of optical transmission can be classified in 3 types, called type 1, 2, 3 (figure 1) depending on the slope of the transmission edge and its uniformity for transversal measurements all along the crystal.

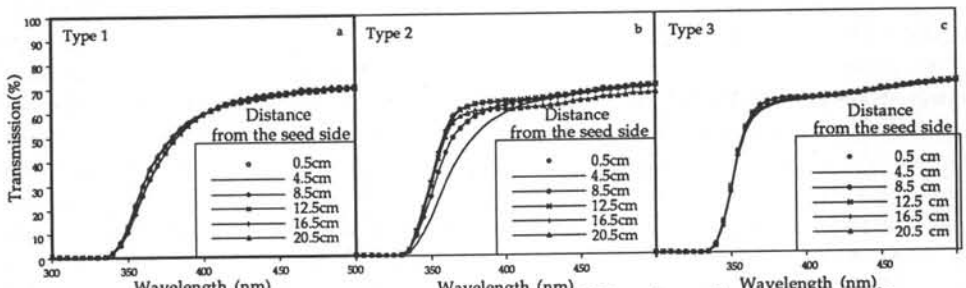

Fig. 1.The 3 behaviours of transversal transmission below 500nm observed on $PbWO_4$ crystals

For the type 1, the transmission edge increases smoothly from 350nm to 400nm independently of the position along the growth axis. The smooth form of the transmission edge reveals the presence of an intrinsic absorption band at 350nm. For the type 2, a position dependence of the transmission edge along the growth axis can be observed. At the seed part of the crystal, the transversal transmission is of the first type, whereas at the bottom part, the transmission edge increases much

Proc. Int. Conf. on Inorganic Scintillators and Their Applications, SCINT95,
1996, Delft University Press, The Netherlands

more steeply from 350nm to 400nm. For type 3, the transmission edge increases all along the crystal like the bottom part of crystal type 2 (steeply from 350nm to 400nm). In this case, the absorption band at 350nm is absent. It was observed that undoped crystals are generally of the first type transmission, while Nb doped crystals are of the third type. This observation shows that Nb doping suppresses the absorption band at 350nm. In addition, an absorption band at 420nm has been observed for certain crystals independently of the transmission type.

In the following, the notation of crystals transmission will refer to the 3 types defined above.

LUMINESCENCE PROPERTIES :

The luminescence properties of $PbWO_4$ are known since a long time [2] and consist of a blue emission ascribed to regular lattice $(WO_4)^{2-}$ group and a green emission related to the (WO_3) group possibly associated with a F-centre [3] . The ratio between the intensities of these two emissions as well as their decay kinetics may vary in a broad range depending on the crystal growth conditions, the thermal treatments made after growth and on doping. As a consequence, scintillation spectra and decay time values reported by different authors are sometimes contradictory. Careful measurements made on industrial scale produced $PbWO_4$ crystals shown that the fast scintillation decay is accompanied by a slow component in some of the samples and in this case a shift to the green of the scintillation spectrum is present. The effect, firstly put in evidence as an unusual rise of the background in scintillation decay measurements, is not due to an afterglow as it was thought at the beginning. Heating of these samples at 100°C for 5h did not change their scintillation decay characteristics. It is also worth mentioning that the green emission is not the only responsible for a slow component in $PbWO_4$ scintillation decay. Slow component of the decay was also put in evidence in the blue component of both undoped and Nb doped $PbWO_4$ crystals. Migration of excitation on various kinds of defects can affect both green and blue components resulting in a slowing down of the scintillation decay. For the moment, in $PbWO_4$ crystals produced in industrial scale a tendency of light yield increase on the basis of the slow component is noticeable (figure 2).

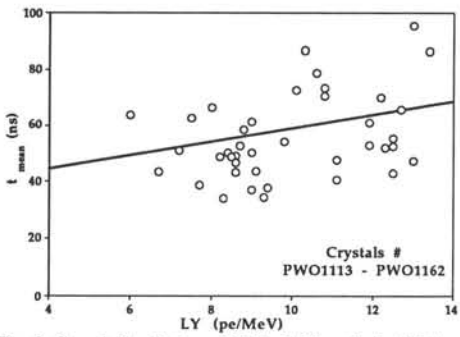

Fig. 2. Correlation between light yield and scintillation mean decay time for PWO scintillators

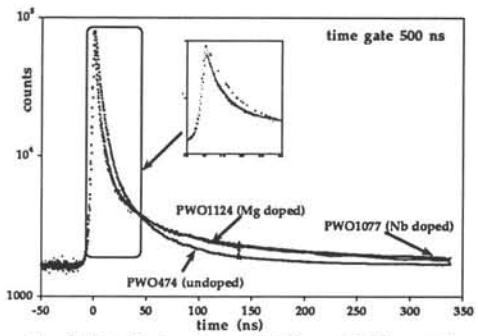

Fig. 3. Scintillation decay of different PWO crystals

Work is on the way in order to obtain a PWO scintillator with an enhanced light yield without the accompanying effect of increased slow component contribution, by growing $PbWO_4$ crystals doped with a divalent metal (figure 3). Table 1 gives the values of the mean decay time resulting from a 3 exponential fit of the scintillation decay measured in a 500ns time gate of three PWO samples (undoped, Mg doped and Nb doped). The decay time as well as the relative intensity of each component is also given for integral and wavelength resolved measurements. In this last case, interferential filters with $\Delta\lambda = 20$ nm were put in front of the R1668 Hamamatsu PM used to detect the light coming from the PWO sample. Though faster in the first nanoseconds, Nb doped PWO crystals have a more important slow component which makes the mean decay time greater. This lengthening of the decay is obviously due to a larger contribution of the green component. A stronger contribution of the fast component in the blue (400nm) region is noticeable in the case of Mg doping. The red component is in this case extremely weak, at the limit of detection of our setup.

Table 1. Wavelength resolved scintillation decay characteristicsfor doped and undoped $PbWO_4$ crystals

crystal	λ (nm)	t1 (ns)	t2 (ns)	t3 (ns)	I1 (%)	I2 (%)	I3 (%)	t mean(ns)
undoped	integral	5.1	22	88	53	31	16	24
	400	4.3	15	241	63	31	6	22
	450	6.1	35	349	65	28	7	39
	500	7.4	44	961	44	44	12	141
	550	7.0	39	128	26	61	13	42
	600	4.5	29	55	15	33	52	39
Nb doped	integral	3.9	19	149	30	25	45	72
	400	3.7	34	294	76	10	14	49
	450	5.3	49	335	44	24	31	119
	500	8.8	43	228	26	30	45	117
	550	11.3	37	194	18	28	53	116
	600	8.9	25	140	7	34	59	92
Mgdoped	integral	2.8	16	117	34	26	41	53
	400	2.7	11	70	72	17	10	11
	450	2.8	15	107	36	25	39	47
	500	3.3	18	91	20	29	51	53
	550	2.6	19	94	7	34	59	62

LIGHT-YIELD :

The light yield presented in this paper is defined as the number of photons extracted from the crystal and impinging on the photocathode of a XP2262B Philips photomultiplier with quantum efficiency of 13% in the wavelength region of the emission of $PbWO_4$, when excited by a Co^{60} source.

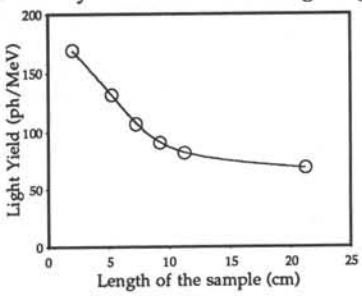

Fig. 4. Dependence of the light yield with the length of crystals

An improvement of the light yield of a factor 1.5 has been observed between long crystals produced in 1994 (undoped) and long crystals produced in 1995 (Nb doped), due to an improvement of the raw material purity and growth conditions control as well as Nb doping (which has been found to be good for increasing the radiation hardness [4]). Today, long $PbWO_4$ crystals ($20.5x20.5x210mm^3$) grown with good raw material and Nb doped with a concentration of 30ppm have a light yield of 80ph/MeV in comparison with a light yield of 50ph/MeV for the undoped crystals produced in 1994 of same dimensions. For small crystals, the typical value is 200ph/MeV. In order to understand the origin of the difference between the light yield of large crystals and small crystals, a long crystal has been shortened in several steps, and the light yield has been measured for each length of this crystal. The dependence of the light yield with the length of the sample (figure 4) shows that the factor of 2.4 observed between the light yield of small samples ($2x2x2cm^3$) and the one of long samples ($20.5x20.5x210mm^3$) is essentially due to the absorption by the crystal of emitted light. Moreover, this result shows that the light production process is uniform along the crystal which is confirmed by the fact that several identical pieces cut from a long crystal have the same light yield.

RADIATION DAMAGE :

Several long PWO crystals have been irradiated with a Co60 source at a dose rate of 3Gy/mn. A correlation between the transmission type and the radiation hardness has been found (figure 5). For crystals with transmission type 1, a grey coloration appears after irradiation due to the presence of two large and intense absorption bands at 400nm and 600nm. On the other hand, for the crystals with a transmission type 3, an extremely weak effect is observed. For crystals with transmission type 2, a gradient of the damage is observed. For the part of the crystal characterised by transmission type 1, a radiation damage is observed, whereas for the other part of crystal characterised by a transmission type 3, the effect is much lower. This result shows a significant correlation between the radiation hardness and the presence of the intrinsic absorption band at 350nm. The fact that Nb doping suppress this absorption band at 350nm might be an explanation for the radiation hardness improvement in Nb doped PWO crystals.

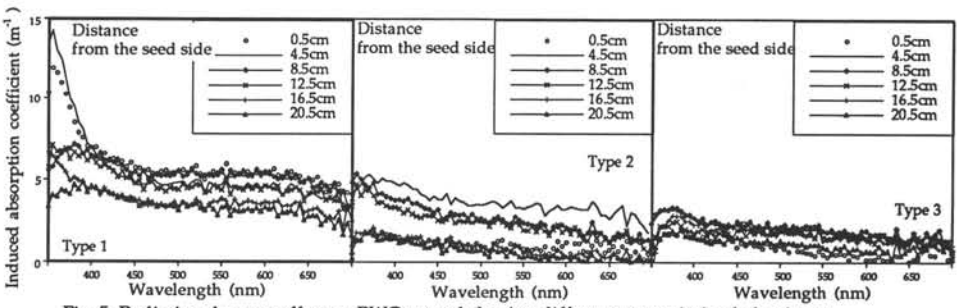

Fig. 5. Radiation damage effect on PWO crystals having different transmission behaviours

After irradiation, all crystals present a recovery of the damage at room temperature. The recovery of the induced absorption can be described by a sum of 2 exponentials with time constant of typically 40 hours and of 50 days respectively (figure 6).

Furthermore, a strong correlation has been observed between the recovery of the light yield and induced absorption after irradiation (figure 7). This demonstrates that the scintillation is not affected by irradiation. The loss of the light yield observed after irradiation is only caused by absorption effect.

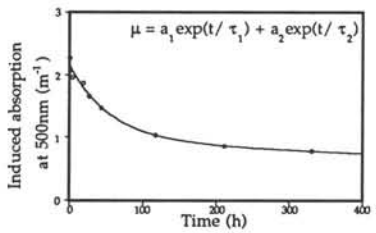

Fig. 6.Recovery of induced absorption after irradiation

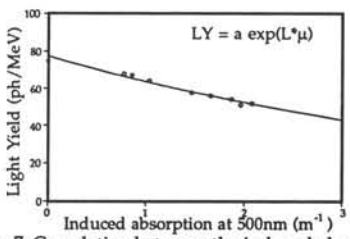

Fig. 7. Correlation between the induced absorption at 500nm and the light yield after irradiation

CONCLUSIONS

In less than one year from the selection of $PbWO_4$ crystal as the baseline option for the EC of the CMS, important progress was made in production of large optical quality crystals with a good radiation hardness and acceptable light yield and light yield uniformity. An increase of the light yield was also observed, which is unfortunately related in some cases to the contribution of a slower component of the scintillation decay. Studies are on the way for a better understanding of the nature of this slow component in order to obtain fast scintillators with a sufficiently high light yield.

ACKNOWLEDGEMENTS :

The authors want to thank all members of the Crystal Clear and CMS collaborations for the fruitful discussions and the very efficient exchange of information. The very good collaboration spirit with the crystals producers (Bogoroditsk plant in Russia, SIC and BGRI in China, Crytur in the Czeck republic was also greatly appreciated.

REFERENCES :

[1] The Compact Muon Solenoid Technical Proposal, CERN/LHCC 94-38, LHCC/P1, 15, Dec.1994
[2] F.A.Kröger, Some aspects of the luminescence of solids (Elsevier, Amsterdam, 1948) Chap. 3
[3] P.Lecoq et al, Nucl.Instrum.and Meth in Phys.Res.A, ref. NIMA 10151, 1995, to be published
[4] E.Auffray, I.Dafinei, P.Lecoq, M.Schneegans, "Scintillator and Phosphor Materials", MRS Symposium Proceedings, vol.348, (1994), p 217 - 224

FURTHER STUDIES ON EXCITATION-EMISSION SPECTRA, RADIATION DAMAGES AND MECHANICAL PROPERTIES of $PbWO_4$

Masaaki KOBAYASHI[a)], Mitsuru ISHII[b)], Kenji HARADA[b], Yoshiyuki USUKI[c)], Hideki OKUNO[d)], Hajime SHIMIZU[e)] and Tatsuya YAZAWA[b)]

a) KEK, National Laboratory for High Energy Physics, Tsukuba 305, Japan,
b) SIT, Shonan Institute of Technology, Fujisawa 251, Japan,
c) Furukawa Co., Kamiyoshima, Yoshima, Iwaki 970-11, Japan,
d) INS, Institute for Nuclear Study, University of Tokyo, Tanashi 188, Japan,
e) Department of Physics, Yamagata University, Yamagata 990, Japan.

ABSTRACT

There are two types of crystals with respect to luminescence. Type A gives a primary emission at around 410-430 nm (blue) with a second one around 500 nm. Type B gives the primary emission at 480-500 nm (green). The apparent emission of Type B can be due to phosphorescence which is peaked at around 500 nm with an order of magnitude larger intensity than scintillation and the decay constant of about 15 ms. The cause for the phosphorescence may be Mo. We also determined the cleavage plane (011) and measured the thermal expansion coefficients and flexural strength.

1. INTRODUCTION

In recent years, $PbWO_4$ has attracted [1-5] much interest as a very dense, fast and possibly radiation-hard material for γ -ray detectors at high energies. There remain some problems to be solved;

(1) The discrepancy in the emission wavelength between 420-440 nm (blue)[1] and 480-500 nm (green)[3,5] has to be solved.

(2) It is necessary to reduce the yellowish colour, without degarading the other scintillating characteristics.

(3) The radiation hardness has to be improved. The effect of recently proposed Nb-doping[6] on scintillation characteristics has to be examined.

(4) Mechanical properties of $PbWO_4$ have to be studied.

We compared 15 $PbWO_4$ crystals grown in different conditions, and also measured some mechanical parameters. We will give a brief summary of the result in a limited space by omitting the result on transmission, decay constant and radiation damages, where the result was not striking.

The test samples from Furukawa and Russia[7] are listed in Table 1. The nominal purity of raw materials was 99.99% except for No.3. No.5-7 are typical Russian samples of the best quality at different times of 1993-95.

2. RESULTS ON LUMINESCENCE

We found two types of crystals with respect to luminescence. The one (Type A) has the blue emission at around 410-430 nm (the excitation at 330 nm), while the other (Type B) green at 480-500 nm (310 nm). Although the conclusion is the same, we present here the emission from deep inside (deep emission) rather than from the surface. Most of Furukawa samples except

Proc. Int. Conf. on Inorganic Scintillators and Their Applications, SCINT95,
1996, Delft University Press, The Netherlands

Table 1 Summary for 15 $PbWO_4$ samples tested. λ (em) =emission wavelength in nm. I denotes relative light intensity only within each category.

Sample	Thick (mm)	Mfg. Co.	UV-exc. λ (em)/I	Phosph. λ (em)/I	X-ray exc. λ (em)	γ -ray I	Remarks
No.1	9.5	Furukawa	424/16	--/<0.2	430	74	
No.2	9.6	〃	425/16	--/<0.1	435(510)	69	twice crystall.
No.3	9.7	〃	423/14	--/<0.2	430(505)	83	5N material
No.4	9.9	〃	420/8	--/<0.2	430(505)	69	Cl-added
No.5	10	Russia	498/90	490/<0.8	490	88	less coloured
No.6	9.2	〃	498/300	490/1.2	505	121	whitish
No.7	10	〃	490/320	490/2.5	500	102	
No.8	6.7	Furukawa	425/5	--/<0.2	435	132	3-times crystall.
No.9	10	〃	425/6	--/<0.2	430(520)	85	
No.10	10	〃	425/7	--/<0.2	430(495)	71	Cs-added[1]
No.11	10	〃	500/120	500/0.8	505	100	Mo-doped
No.12	~5	〃	500/65	--/<0.4	500(440)	143	Cl-doped
No.13	10	Furukawa	414/7	--/<0.1	425(510)	66	Nb-doped
No.14	9.6	Russia	490/420	490/18	505	144	〃
No.15	20	〃	425/7	--/<0.1	435(510)	68	〃

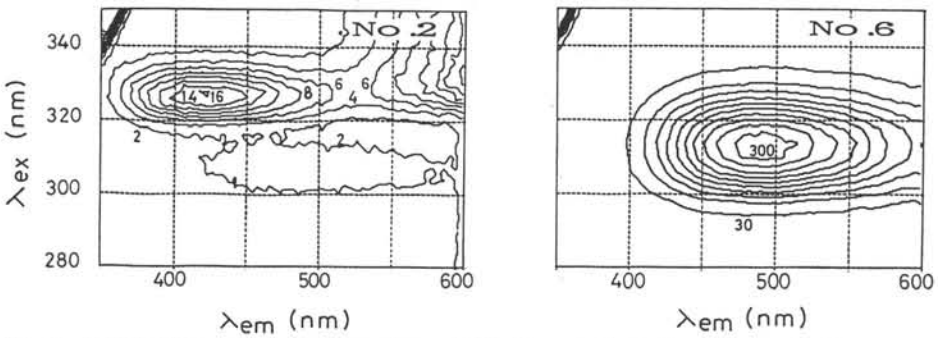

Fig. 1 Excitation-emission spectra of No.2 and No.6 for UV-excitation.

PWO:Mo belong to Type A, while most of Russian ones Type B. Type B gives an order of magnitude larger emission than Type A if measurement is made in a dc mode (i.e. integrated mode). As an example, No.2 and No. 6 are compared in Fig. 1. No systematic effect of Nb-doping was found.

Type B samples emit phosphorescence peaked at around 500 nm with a decay constant of roughly 15 ms. Its integrated intensity should be an order of magnitude larger than the scintillation in order to explain the large UV-excited luminescence and almost the same scintillation intensity. The emission and decay time spectra of No.6 sample are given in Fig. 2. The cause for the phosphorescence may be Mo. In fact, only PWO:Mo (No.11 sample) among the Furukawa samples clearly belongs to Type B. Among several samples for which the GDMS was examined, Type B samples (No.5, No.7, No.14) showed Mo contamination as large as 20 ppm.

We studied radioluminescence due to X-rays (Cu, 50kV, 30A). As seen in Fig. 3, Type A samples have a peak at around 420-430 nm with a second peak or shoulder at around 500-510 nm, while Type B samples only at around 500-510 nm, in consistency with photoluminescence. The 420-430 nm emission may be hindered behind much larger phosphoresence at 500-510 nm.

The scintillation light output was estimated within a precision of about 20% by measuring the γ -rays from ^{60}Co using a PMT and a PHA with a gate time of 1μ s (see Table 1). We see that the light output was roughly the same for all the samples.

Fig. 2 (a)Phosphorescence and (b)its decay time spectra for No.6.

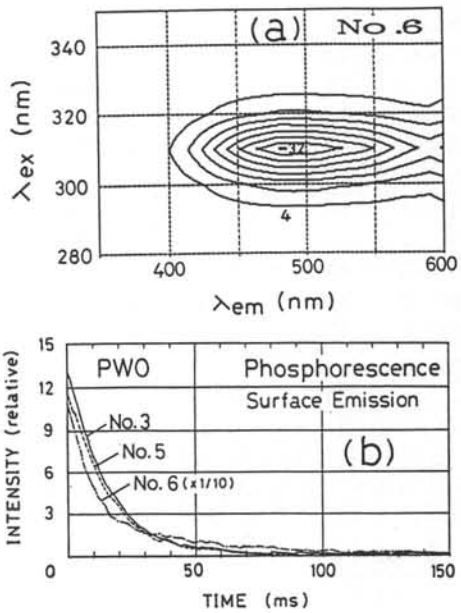

Fig. 3 Radioluminescence spectra due to X-ray excitation.

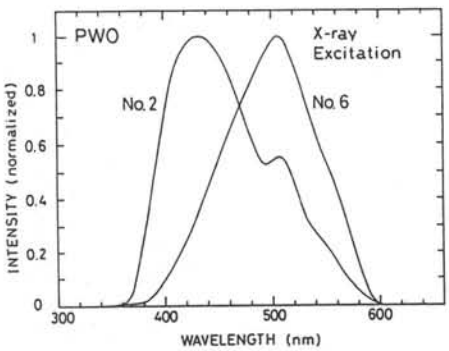

3. RESULTS ON MECHANICAL PROPERTIES

All the cleavages are weak compared with $CdWO_4$, and compatible with the (101)/(011) plane from the X-ray diffraction spectrum.

Thermal expansion coefficients were obtained by measuring the lattice constants from X-ray diffraction angles at different temperatures. The average coefficients between room temperature and 900 °C were 29.5 x 10^{-6}/°C and 12.8 x 10^{-6}/°C along the [001] and [100]/[010] axes, respectively.

Bending test was carried out in a conventional 4-point loading configuration. The flexural strength was between 26.8 and 31.7 MPa for the stretching direction along [010] and [001], while 18.5 MPa along the normal to the cleavage plane.

References

1) M. Kobayashi et al., Nucl. Instr. Meth. A333(1993)429.
2) V.G. Baryshevsky et al., Nucl. Instr. Meth. A322(1992)231.
3) O.V. Buyanov et al., Nucl. Instr. Meth. A349(1994)62.
4) S. Inaba et al., Nucl. Instr. Meth. A359(1995)485.
5) M.V. Korzhik et al., "Spectroscopy and origin of ---", LAPP-Exp-94.01.
6) A. Fyodorov et al., "Further progress in PWO crystals", preprint(Minsk).
7) Supplied by M. Korzhik (Minsk).

Measurements of light yield, optical properties and radiation damage of undoped $PbWO_4$ crystals

S. Baccaro^, L. M. Barone°, B. Borgia°, F. Castelli*, F. Cavallari°, F. de Notaristefani°, M. Diemoz°, R. Faccini°, A. Festinesi^, E. Leonardi°, E. Longo°, M. Mattioli°, M. Montecchi^, G. Organtini°, S. Paoletti°, S. Pirro°, E. Valente°

^ ENEA-INN, Casaccia, Roma (Italy)
° Dip. di Fisica, Univ. "La Sapienza", Roma - INFN Sezione di Roma (Italy)
* Dip. di Chimica, Univ. "La Sapienza", Roma (Italy)

Abstract This paper describes a set of measurements performed on $PbWO_4$ crystals. The light yield of small and large size crystals was measured under stabilised temperature conditions. A systematic investigation on the optical properties of small and large monocrystals was performed. The transmission, luminescence and excitation spectra are reported. Emission decays and time resolved spectra detected by a single photon time correlation method were measured. The radiation damage behaviour of undoped crystals is presented for gamma and neutron irradiation, at different absorbed doses.

1. Light yield measurement on $PbWO_4$ crystals

In order to measure the light yield properties of PWO crystals a radioactive source is employed to cause ionization in the crystals. The measurement setup consists of an XP2262B photomultiplier tube in contact both with a small crystal PWO-522 (2x2x1 cm^3) and a LED for calibration purposes. The radioactive source is collimated using a conical Pb shield on the crystal face opposite to the one in contact with the PMT. Because of the strong dependence of the light yield with temperature (see below) the measurements were performed inside a climatised chamber [1]. We used three different gamma sources, namely ^{22}Na, ^{137}Cs and ^{60}Co. In order to extract the number of photoelectrons emitted per deposited MeV (N_{phe}/MeV) we used several techniques. The results are reported in Table 1. In the first column we report the results obtained modeling the Compton background as a Fermi-Dirac distribution and a poissonian for the photopeak [2]. This is our preferred method.

Table 1

	N_{phe}/MeV Dirac+Poisson	N_{phe}/MeV Dirac+Gauss	N_{phe}/MeV Gauss	N_{phe}/MeV σ/E (Dirac+Gauss)	Fit Stability Dirac+Poisson	Fit stability Dirac+Gauss
^{22}Na	15.35 ± 0.12	14.25 ± 0.25	14.25 ± 0.25	14.50 ± 1.20	0.35%	1.5%
^{137}Cs	15.45 ± 0.10	15.15 ± 0.20	14.30 ± 0.20	14.35 ± 0.90	0.3%	3%
^{60}Co	15.35 ± 0.10	15.10 ± 0.20	14.10 ± 0.20	15.80 ± 0.90	0.1%	0.8%

In column 2 the fit was done using a gaussian approximation for the photopeak using the calibration factor given by the LED. In column 3 the fit was repeated using only the right part of the spectrum, i.e. not including the Compton background in the fit. In column 4 we used the same technique as in column 2, but the number of photoelectrons is evaluated from the width of the gaussian rather than from its mean. As can be seen from the last two columns the stability of the fit varying the starting point of the fit over a reasonable range is much better for the first method.

1.1 - Temperature dependence of the LY

The temperature dependence of the scintillation light using a ^{137}Cs source was then studied [1]; measurements were corrected for the light intensity variation of the LED with temperature. We made a series of runs at different temperatures between -5 and +20 °C. Around T = 18 °C, we obtain

$$\frac{\Delta LY}{LY} = -2.3 \pm 0.3 \ \%/\,°C$$

in agreement with [3].

Proc. Int. Conf. on Inorganic Scintillators and Their Applications, SCINT95,
1996, Delft University Press, The Netherlands

1.2 - Decay times

We performed this analysis in two different ways: using a Le Croy 9450 sampling oscilloscope and delaying the gate of the ADC [1]. With the sampling oscilloscope, we also studied the signal profile for three different temperatures (Fig 1). The three curves are normalized to the same peak value. What can be seen is a suppression of the slow component when the temperature increases, in agreement with [3].

1.3 - Results on long crystals

The results on long crystals PWO-691 (undoped, 2x2x21 cm, tapered) and N70 (undoped, 2x2x23 cm, parallel faces) were obtained using both cosmic rays and γ-sources [1].

1.3.1 - Results with cosmic rays

We studied the light collection on PWO-691 using cosmic muons. A simple muon telescope was realized using 3 small scintillators in coincidence between them and a 5 cm thick Pb absorber. We measured the longitudinal uniformity of the light collection by moving the crystal between the coincidence scintillators.

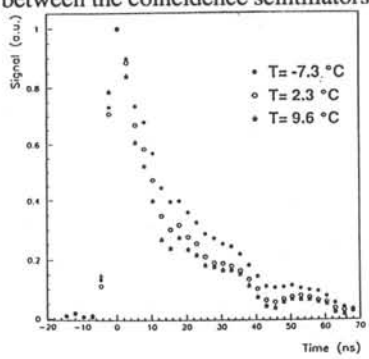

Fig. 1: PWO decay time for three temperatures The light signal is excited by a ^{137}Cs source. The curves are normalized to the peak value.

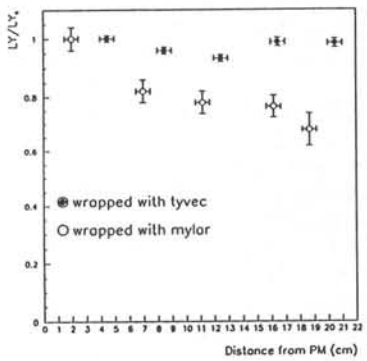

Fig. 2: Light uniformity in a 22 cm long crystal wrapped by tyvek or aluminised mylar.

Two different wrappings have been used, namely mylar and tyvek. The two results shown in Fig. 2 are normalized to 2 cm distance from the PM. In this set of measurements the temperature was not monitored.

1.3.2 - Results with γ-sources

Due to the poor light yield of PWO to observe a signal from ^{137}Cs sources one must increase the sensitive area as much as possible. We therefore connected the PM on the side of the crystal as shown in Fig. 3. Three measurements have been made on the left end, on the centre and on the right end side. A ^{137}Cs source with collimator has been used. In all the three positions, the axis of the collimator and the axis of the PM laid on the same line. The results obtained at T = -7.4 °C are shown in the Table II.

Table II

PM Position	Left	Center	Right
Signal (Phe)	7. 4 ± 0.2	6.5 ± 0.3	7.3 ± 0.3

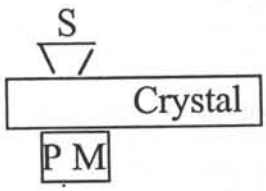

Fig. 3: PM and crystal arrangement for light yield measurements.

The small difference between centre and sides is probably due to the fact that the bases of the crystal were wrapped and therefore there is a greater probability to collect more photons near

the bases than at the centre. Comparing the results obtained on the small size crystal with the above one at the same reference temperature we observed a difference of a factor ~3 in the ligth yield. This difference can hardly be understood as an effect due to light collection. Further investigations are needed.

2. Optical properties measurements and radiation damage

2.1 -Transmission and fluorescence measurements

The transmittance measurements were carried out with a double beam spectrophotometer in the range of 190-850 nm. Optical measurements were performed on the lead tungstate of 1 cm length (PWO-527). The measurements of fluorescence excitation and emission have been performed with a fluorescence spectrophotometer equipped with an excitation monochromator in the 200-700 nm range, and an emission monochromatoro in the 220-800 nm range. The spectra are recorded at excitation wavelengths of 280 nm and 310 nm. The broad emission peak appears at 517 nm [1]. The $PbWO_4$ (PWO-527) crystal was irradiated at the Cobalt source Calliope with a dose rate of 0.78 Gy/s at ENEA-Casaccia near Rome. After the initial transmission spectrum measurement before irradiation, the crystal was exposed to γ radiation up to 76.2 kGy. When comparing crystals before and after irradiation it is often useful to calculate the induced absorption coefficient defined as: $\mu = 1/L \ln (T_0/T)$, where T_0 is the initial optical transmission before irradiation, T is the optical transmission after irradiation and L is the crystal length, in our case L = 0.01 m. Fig. 4 shows the behaviour of the induced absorption coefficient as a function of the absorbed dose; the curve shows saturation about after 10 kGy. The irradiated crystal at a maximum dose (76.2 kGy) was measured by a fluorimeter. The emission and excitation spectra do not show any appreciable shift of the peak wavelengths. The $PbWO_4$ (PWO-527) crystal was also irradiated at TAPIRO reactor (ENEA). After fast neutron irradiation at 10 Mrad, corresponding to a fluence of 10^{16} n/cm^2, the qualitative activation analysis is performed and reported in Table III [11.

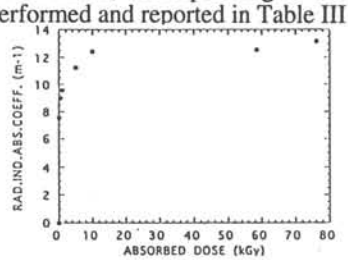

Fig. 4: Radiation induced coefficient vs. absorbed dose.

Table III

ELEMENT	%
185 W	76.0
181 W	9.3
187 W	8.2
203 Pb	2.5
182 Ta	2.4
99 Mo	1.5
181 Hf	0.1

2.2 - Emission decay and time resolved spectra

Emission decays were measured using the single photon time correlation tecnique [4], with an apparatus which uses as a source a 10 ps argon sinchronously pumped Rh6G dye laser and has subnanosecond time resolution. Crystal PWO-691, its growth axis vertically oriented, was excited with vertically and horizontally polarized light at 295 and 590 nm. Emission at 440 and 480 nm was collected at 90° relative to excitation. However, emission was monitored essentially from the crystal surface when exciting at 295 nm and from the center of the crystal when exciting at 590 nm, a condition which seems more important with respect to highly penetrating radioactive excitation. In the latter case, in order to favour two photon excitation, the laser beam was focussed on the crystal and the linearity of the emission signal with the square of the laser intensity was verified with calibrated filters. Measurements were performed with two time bases, 50 ns and 1 μs so that the very slow component could be isolated. Decays were fitted to a sum of three exponentials and the results are shown in Table IV.

Table IV

Exc	Pol	Emiss	A_1	t_1	A_2	t_2	A_3	t_3	χ^2
295	H	440	17240±102	1.04±0.01	1969±92	3.67±0.08	75±1	133±34	1.50
295	V	440	17070±85	1.13±0.01	1690±84	4.35±0.12	165±2	164±5	1.01
295	H	480	16780±150	1.06±0.01	1732±76	5.7±0.2	249±5	144±4	1.33
295	V	480	17490±88	1.125±0.009	1638±47	6.7±0.2	346±6	161±2	1.14
590	H	440	4252±59	1.17±0.04	576±83	4.0±0.3	26±1	66±2	1.03
590	H	480	4409±49	1.22±0.02	383±31	6.2±0.4	67±2	55±4	1.00
590	V	480	742±43	1.1±0.1	95±51	4.0±1.3	9±1	46±5	1.05

Time resolved emission spectra were recorded at 8 nm resolution into two time windows, 15 ns width without delay relative to the exciting laser pulse and 0.5 μs width with 0.1 μs delay. The spectra, called fast and slow respectively, are shown in Fig. 5 together with the steady state spectra.

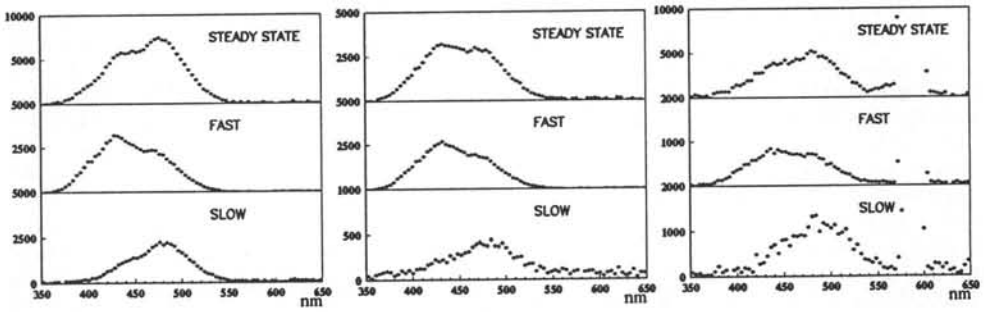

(a) (b) (c)

Fig 5. Time resolved spectra at (a) λ_{exc}=295 nm vertical polarization, (b) λ_{exc}=295 nm horizontal polarization, (c) λ_{exc}=590 nm horizontal polarization. Spectra are the result of summing 20 scans for excitation at 295 nm and 150 scans at 590 nm. The signal for vertically polarized excitation at 590 nm was too weak to be recorded.

All data are consistent with the emission due to three main components. Despite of some overlap between the emission bands, it is clear that the very slow component is peaked at ~485 nm (green band), while the fast components, which are not separated in the spectra, are peaked at ~430 nm (blue band).When exciting at 295 nm, changing polarization from vertical to horizontal yields a decrease of the total signal (at least one order of magnitude) and a decrease of the slow component contribution with respect to the fast components. Thus, the steady state spectrum is more similar to the fast spectrum for horizontal polarization. These results are consistent with the large polarization of the green band reported for measurements at low temperature [5]. When exciting at 590 nm, total signal intensity and slow component relative contribution decrease with changing polarization from horizontal to vertical, which is the inverse relative to the 295 nm excitation. Furthermore, the slow component lifetime decreases drastically to ~1/3 of the values measured at 295 nm. Correspondingly, the slow component relative contribution to the total emission decreases also. Concerning the mechanism of the biphotonic process for the excitation at 590 nm, the changes observed with the different polarizations seem to rule out double photon absorption and indicate, as a possible mechanism, a process of crossed polarized second harmonic generation, due to the non linear polarizability of the medium [6], followed by absorption. Comparison of the data at the two excitation wavelengths indicate that differences exist between the bulk and the surface of the crystal, the slow decay being due to different centers or to the same centers in different enviroments. The values of the decay constants for the bulk appear to be more consonant for the use of such crystal as EM calorimeter. A more detailed account of the data and a more precise discussion will be given somewhere else [7].

References

[1] - S. Baccaro, F. Castelli, M. Diemoz, A. Festinesi, E. Longo, L. Nencini, G. Organtini, S. Pirro, CERN-CMS-TN/95-065 (1995).
[2] - *Fitting radioactive sources absorption spectra in scintillators* ,INFN Report (in prep.).
[3] - I. Dafinei, E. Auffray, P. Lecoq, M. Schneegans, CMS TN/94-317 (1994).
[4] - W.R Ware, in *Creation and detection of the exited state*, edited by A. A. Lamola (Marcel Dekker, New York,1971) vol. 1A.
[6] - A. Yariv, Quantum Electronics (Wiley, New York,1968).
[5] - J.A. Groenink and G. Blasse, J. Solid State Chem. 32, 9 (1980)
[7] - *Emission decay and time resolved spectra of PWO crystals*, INFN Report (in prep.)

Measurements of refractive index on $PbWO_4$

S. Baccaro*, L. M. Barone^, B. Borgia^, F. Castelli•, F. Cavallari^,F. de Notaristefani^,
M. Diemoz^, R. Faccini^, A. Festinesi*, E. Leonardi^, E. Longo^, M. Mattioli^,
M. Montecchi*, G. Organtini^, S. Paoletti^, E. Valente^

(*) ENEA - INN, Casaccia, Roma (Italy)
(^)Dipartimento di Fisica, Università "La Sapienza", Roma - INFN - Sezione di Roma (Italy)
(•) Dipartimento di Chimica, Università "La Sapienza", Roma (Italy)

Abstract This note reports the work carried out in order to determine the optical properties of $PbWO_4$ crystals We performed transmission and reflectance measurements at normal incidence in the range (320-850) nm with polarised light and measurements of the separation angle (γ) between the ordinary and extraordinary rays with laser beam in the wavelength range mentioned above.

1 - Introduction

Crystals of $PbWO_4$ will be used in the electromagnetic calorimeter of the CMS experiment at LHC (CERN). The behaviour of the electromagnetic (e.m.) wave generated in the crystal depends on the boundaries and on the refractive index (N) of the crystal. If the crystal is isotropic the refractive index N is a complex number depending only on the e.m. wavelength. Observations on the propagation of laser beam through $PbWO_4$ crystal lead us to consider $PbWO_4$ an optically anisotropic medium of uniaxial kind. For such a material, N depends also on the orientation of the electrical vector **E** of the e.m. wave and it can be represented by an index ellipsoid having two equal principal axes (ellipsoid revolution) [1]. The values of N along the two equal principal axes and along the third principal axis are respectively named ordinary (n_{ord}-ik_{ord})and extraordinary index (n_{ext}-ik_{ext}). This note describes a procedure for the determination of the crystal index ellipsoid. The proposed method requires the transmission (T) and reflectance (R) measurements at normal incidence with polarised light and the measurements of the separation angle (γ) between the ordinary and extraordinary rays at various wavelengths. We investigated undoped and doped crystals: PWO-522 (1 cm length, undoped), PWO-N30 (23 cm length, undoped) and PWO-1024 (21.5 cm length, 30 ppm Nb^{5+} doped).

2 - Theory

2.1 - Propagation of a plane e.m. wave in uniaxial crystal

Let us consider a plane interface air-uniaxial crystal and a plane monochromatic e.m. wave travelling with the wave front parallel to the interface. The optical axis of the crystal makes the β angle with the interface and it is lying on the Γ plane that is orthogonal to the interface. Respect to the Γ plane, assuming k<<n, the $E_{\perp}$ wave experiences n_{ord} and travels through the crystal according to the usual laws of an isotropic medium (ordinary ray). The $E_{//}$ wave experiences the refractive index n_{mix} given by equation (1) and it travels through the crystal as extraordinary ray. The γ angle between the propagation directions of the extraordinary and ordinary ray [2] is given by equation (2)

$$n_{mix} = n_{ord}\sqrt{\sin^2\beta + \frac{n_{ext}^2}{n_{ord}^2}\cos^2\beta} \quad (1) \qquad \gamma = a\tan\left(\frac{n_{ord}}{n_{ext}}\tan\beta\right) - \beta \quad (2)$$

Both the orientation of the Γ plane and the γ angle can be easily determined by examining the propagation of a laser beam hitting orthogonally on a crystal surface if $0 < \beta < 90°$ and the crystal is long enough to allow the separation of the extraordinary from the ordinary beams.

2.2 - Transmittance and reflectance spectrophotometric measurements at normal incidence with polarised light.

The normal incidence transmittance and reflectance of a polarized plane wave are given by equation (3) where $n=n_{ord}$ and $n=n_{ext}$ respectively for orthogonal and parallel polarization (n_{air} = 1 and $k << n$ are assumed) [1]. The $PbWO_4$ samples are hexaedron and the measurements of T and R involve not only the entrance air-crystal interface, but also the opposite one. Taking into account that for our sample n ~ 2 and k ~ 0, T and R can be approximated [2] with

Proc. Int. Conf. on Inorganic Scintillators and Their Applications, SCINT95,
1996, Delft University Press, The Netherlands

equation (4)

$$t = 1 - r \qquad r = \left|\frac{n-1}{n+1}\right|^2 \quad (3) \qquad\qquad T \equiv t^2 e^{-\alpha d} + t^2 r^2 e^{-3\alpha d} \qquad (4)$$

$$R \equiv r + t^2 r e^{-2\alpha d}$$

where the absorption coefficient α is defined as $\alpha = 4\pi k/\lambda$. The $T_{//}$ and $R_{//}$ measurements can suffer from the displacement of the extraordinary ray respect to the ordinary ray. Concerning only R, the measurement is performed at quasi-normal incidence (~7°) and the distance between the first and the second interface contributions depends linearly on the crystal thickness d. For long crystal (d ~20 cm) the second contribution does not reach the detector so that $R = r$. For smaller length (about less than 1 cm) the second contribution is well detected.

3 - Experimental method

We measured R and T by a Lambda 9 and a 340 Perkin Elmer double beam spectrophotometers respectively, where a polarisator was placed on the beam, before the sample. The linear polariser transmits in the (320-2300) nm range. In both devices the beam is deviated by mirrors and its s polarisation intensity is greater than the p polarisation. To optimise the signal to noise ratio, the measurement is always performed with the beam totally s-polarised. The crystal is oriented so that **E** of the beam is orthogonal or parallel to the Γ plane.

4 - Results and discussion

In the case of PWO-522, the sample dimensions are 2x2x1 cm. Only the two 2x2 cm^2 faces are polished and are used for the optical measurements. The 1 cm length of the sample does not allow to distinguish the extraordinary from the ordinary ray and no information about the Γ plane is available.The second surface contribution of R was entirely detected. Assuming the crystal to be isotropic, we searched for the (n (λ), α (λ)) solutions of T and R (equations (4)) in the range 330-850 nm by a numerical method; n (λ) is reported in Fig. 1. The absorption coefficient α increases strongly near 350 nm.

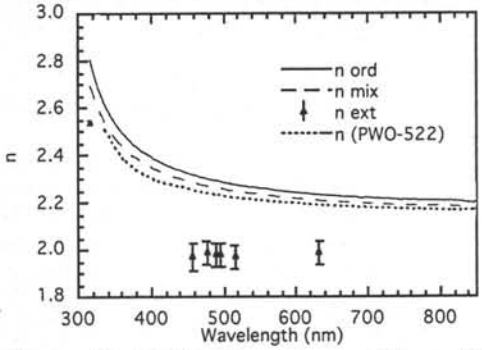

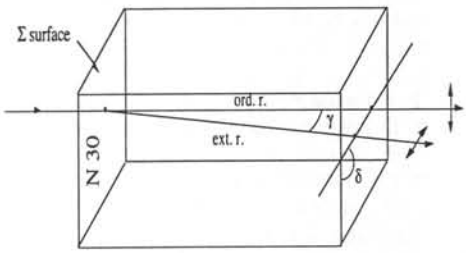

Fig. 1: n(λ) of PWO-522 sample, $n_{ord}(\lambda)$, $n_{mix}(\lambda)$ and n_{ext} at 320 nm and at the Ar and HeNe laser wavelengths for PWO-N30 sample.

Fig.2: Splitting of a laser beam impinging orthogonally on the (2x2) cm surface (Σ) closest to the N30 mark. In the direction of the wave propagation, the Γ plane makes the δ = 100° ± 1° angle with the N30 marked surface.

In the case of PWO-N30, the sample dimensions are 2x2x23 cm^3 and all the faces are polished. Fig. 2 shows the splitting of a laser beam impinging orthogonally on the 2x2 cm^2 surface (Σ) closest to the N30 mark. The second column of Table 1 lists the γ angle at the wavelength of Ar and HeNe lasers. In the direction of the wave propagation, the Γ plane makes the δ angle with the N30 marked surface equal to 100° ± 1°. In the examined wavelength range, $R_{//}$ is always lower than $R_{\perp}$, therefore n_{ext} is lower then n_{ord}. The crystal length is such that the 2nd surface contribution on R is not detected, then $R_{//} = r_{//}$ and $R_{\perp} = r_{\perp}$. The $n_{ord}(\lambda)$ and $n_{mix}(\lambda)$ are calculated from $r_{\perp}$ and $r_{//}$ (equation (3)) considering $k = 0$ and they are shown in Fig. 1. Moreover their values at the Ar and HeNe laser wavelengths are listed in the 3rd and 4th columns of Table 1.

Table 1 - Crystal PWO-N30

λ (nm)	γ (deg)	n_{ord}	n_{mix}	n_{ext}	α (cm^{-1})
457.9	2.61 ± 0.07	2.32 ± 0.01	2.30 ± 0.01	1.97 ± 0.06	$(4.9\pm0.2)10^{-2}$
476.5	2.37 ± 0.07	2.31 ± 0.01	2.28 ± 0.01	1.99 ± 0.05	$(3.8\pm0.2)10^{-2}$
488.0	2.37 ± 0.07	2.30 ± 0.01	2.27 ± 0.01	1.98 ± 0.05	$(3.2\pm0.2)10^{-2}$
496.5	2.37 ± 0.07	2.30 ± 0.01	2.27 ± 0.01	1.98 ± 0.05	$(2.9\pm0.2)10^{-2}$
514.5	2.37 ± 0.07	2.29 ± 0.01	2.26 ± 0.01	1.97 ± 0.05	$(2.6\pm0.2)10^{-2}$
632.8	1.93 ± 0.07	2.24 ± 0.01	2.22 ± 0.01	1.99 ± 0.05	$(1.9\pm0.2)10^{-2}$

The β angle and n_{ext} can be determined from the knowledge of γ, n_{ord} and n_{mix}. Minimising the propagation of the experimental error [2] we obtained $\beta = 72° \pm 2°$ and n_{ext} reported in the 5th column of Table 1. At the other wavelengths where γ is not known, n_{ext} could be computed by equation (1) but the error is very large for a β angle close to 90°. A better evaluation of n_{ext} can be obtained from the measurement of R on a large surface 2x23 cm^2 with **E** almost parallel to the optical axis. Unfortunately the compartment of Lambda 9 spectrophotometer does not allow the position of the sample in this way. We tried to rotate the light polarisation, instead of the sample, but the spectral measurement was noisy because of the weak signal. We kept only the measurement at 320 nm, where the crystal is not transparent, and we obtained $n_{ext} = 2.54 \pm 0.01$. At the same wavelength $n_{ord} = 2.80 \pm 0.01$, so that $n_{ord}-n_{ext} \sim 0.26$. Taking into account the results reported in Table 1, the difference $n_{ord}-n_{ext}$ seems to be about a constant in the considered wavelength range. The PWO-522 refractive index is comprised between n_{ord} and n_{ext}. To obtain information on the imaginary part of refractive index, the transmittance measurement is necessary. By our instrument it was possible to measure only $T_{\perp}$ because $T_{//}$ was seriously affected by the displacement of extraordinary ray as described at the end of section 2.2. The absorption coefficient computed from $T_{\perp}$ by eq. (4), using the previously determined n_{ord} data, is reported in Table 1 and it is lower than α of PWO-522. As an example α_{N30} (λ = 500 nm)=(2.8 ± 0.2) $10^{-2}cm^{-1}$ and α_{522} (λ = 500 nm)=(6.8 ± 0.4)$10^{-2}cm^{-1}$. In the case of PWO-1024, the sample dimensions are 2x2x21.5 cm^3 and all faces are polished. The Γ plane makes $\delta = 57° \pm 1°$ with the 2x21.5 cm^2 marked surface and $\beta = 76° \pm 2°$. Both n_{ord} and n_{ext} result equal inside the experimental error to those of PWO-N30, and we can conclude that the 30 ppm Nb^{5+} doping affects the real part of the crystal refractive index by less than 0.01 (the experimental error).

5 - Conclusions

For long crystals (one dimension about 20 cm) it is possible to determine the optical axis orientation and the ordinary and extraordinary refractive index by means of the propagation of laser beams and by reflectance and transmittance measurements with polarised light at almost normal incidence. The $PbWO_4$ extraordinary refractive index is lower than the ordinary one and both seem not to be affected by a 30 ppm Nb^{5+} doping. For both the long crystals the position of the identification mark, placed on a side of a great surface, and the optical axis are oriented in the same way. Moreover the angles between the growth axis and the optical axis are very similar and they are in a good agreement with the value reported in the paper of P. Lecoq et al. [3]. The $T_{//}$ measurements was seriously affected by the displacement of the extraordinary ray. Work is in progress on the determination of imaginary part of the extraordinary refractive index.

6 - References

[1] Born, M. and E. Wolf, *Principles of Optics*, 3th edition, Pergamon Press, Oxford (1965).

[2] Baccaro, S., L. M. Barone, B. Borgia, F. Castelli, F. Cavallari, F. de Notaristefani, M. Diemoz, R. Faccini, A. Festinesi, E. Leonardi, E. Longo, M. Mattioli, M. Montecchi, G. Organtini, S. Paoletti, E. Valente, "Optical properties of lead tungstate ($PbWO_4$) crystal for LHC em-calorimetry", INFN Report (in press) (1995)

[3] Lecoq, P., I. Dafinei, E. Auffray, M. Schneegans, M.V. Korzhik, V.B. Pavlenko, A. A. Fedorov, A.N. Annenkov, V. L. Kostylev, V. D. Ligun, CERN-PPE/ 94-225, CMS-TN/ 94-308 (1994).

OPTICAL PHONON SPECTRA OF GAMMA RAYS IRRADIATED $PbWO_4$ SINGLE CRYSTALS

Bazhenov A.V., Klassen N.V., Red'kin B.S, Smirnova I.S., Shmurak S.Z.

Institute of Solid State Physics, Russian Acad. Sci.,
Chernogolovka, Moscow distr., Russia, 142432

Sample preparation.

$PbWO_4$ single crystals have been grown by means of standard Czochralski method from the stoichiometric melt in platinum crucible. Pulling rate was 3 mm/hour. As-grown crystals were 20 mm in diameter and 20 cm long. Main part of our measurements has been performed with undoped crystals of 1x1x1 cm^3. X-ray analysis has shown the dominant tetragonal crystallographic structure of crystals with some features discussed in [1].

Optical phonon spectrum.

Optical phonon spectrum of $PbWO_4$ single crystals has been studied by means of far-infrared spectroscopy. Fig.1a presents measured room temperature reflectivity spectra for the incident electric field polarized perpendicular to the fourfold axis C, E⊥C, and E∥C. Spectra are identical to those measured earlier in [2]. Spectra of Fig.1b are optical conductivity spectra calculated from the reflectivity ones using Kramers-Kronig analysis. Optical conductivity spectra are similar to the absorption spectra and their maxima correspond to the spectral positions of the transverse optical (TO) phonon frequencies.

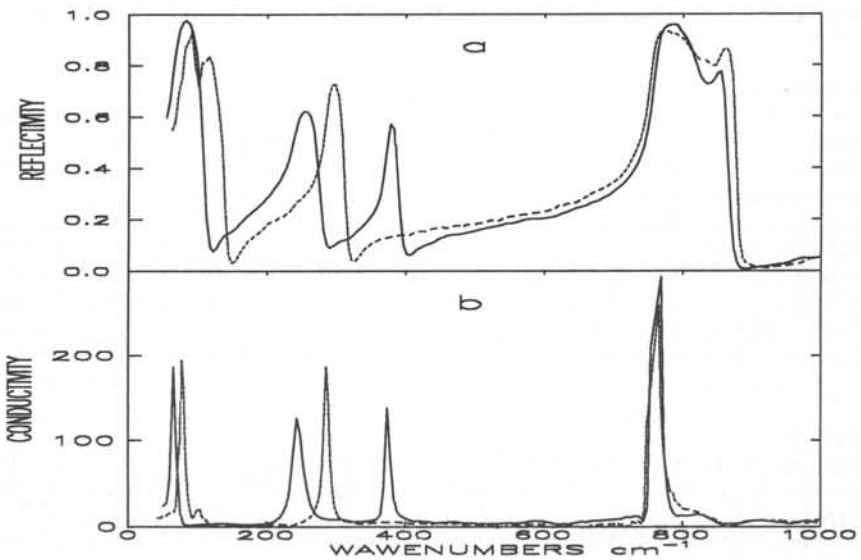

Fig.1. Polarized reflection spectra and optical conductivity of $PbWO_4$ single crystals for E⊥C (dashed line) and E∥C (solid line). T=300K.

Proc. Int. Conf. on Inorganic Scintillators and Their Applications, SCINT95,
1996, Delft University Press, The Netherlands

Theoretical analysis of optical modes.

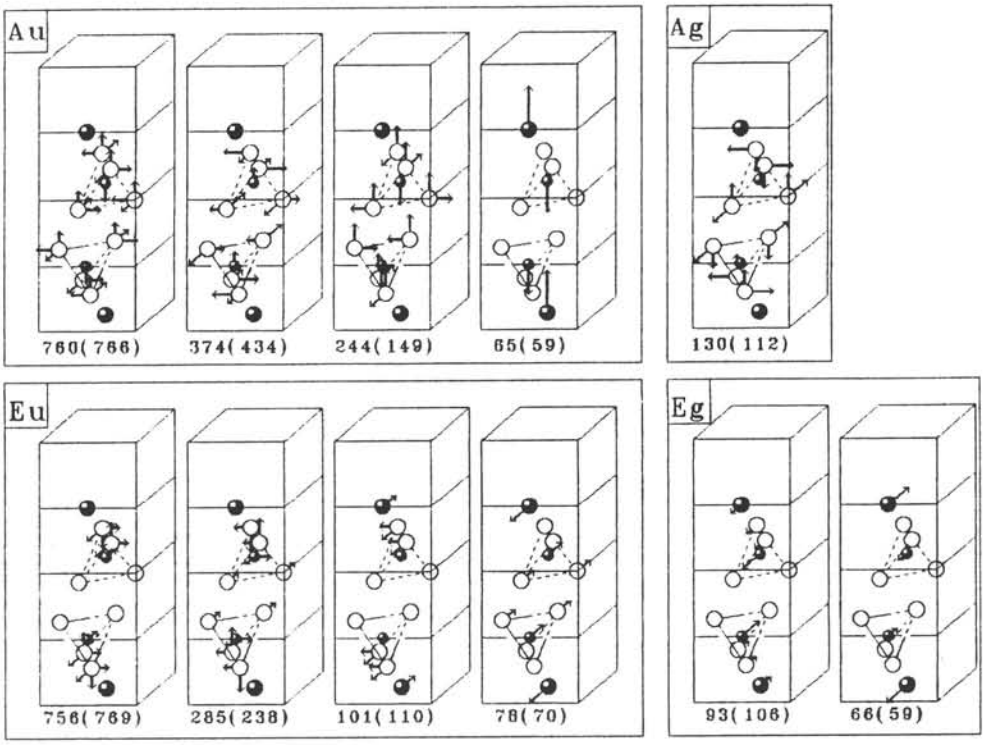

Fig.2. Infrared active A_u and E_u normal modes of $PbWO_4$. Low-energy Raman-active modes (Ag, Eg) are presented too. Experimental TO-frequencies [cm^{-1}] and the result of theoretical calculations (in brackets) show the assignment of modes.

The twelve ions of the tetragonal unit cell of $PbWO_4$ yield a total of 33 optical vibrational normal modes:

$$\Gamma=4A_u+3B_u+4E_u+3A_g+5B_g+5E_g$$

13 modes of A_g-, B_g- and E_g-symmetry are Raman active. They can not be observed in reflectivity spectra of perfect single crystal. 3 B_u modes are silent. So, four A_u modes and four double degenerate E_u modes are infrared active in polarizations E||C and E⊥C respectively (Fig. 1). Moreover, reflectance spectra of Fig. 1 permit to evaluate the charge of oxygen ions **Z**0. Kramers-Kronig analysis has shown **Z**0=-1.2 e.

The theoretical calculations in frame of "rigid ions" approximation have been performed for assignment of optical modes. Fig.2. shows infrared active A_u and E_u normal modes of $PbWO_4$. The description of the modes is complex, due to the mixing of different internal-displacement coordinates, but a few general statements are possible. Arrows show the displacements of ions that give the main contribution of the force constants to the potential energy of the normal mode. The O-W-O stretches determine the high-frequency modes 760 and 756 cm^{-1}. The bending of W-O gives 374, 244 and 285 cm^{-1} frequencies. All these modes correspond to the relative motions of ions of WO_4-tetrahedron. Pb practically does not take part in these modes. Pb together with W are responsible for low-frequency modes 101, 78, 65 cm^{-1}.

Gamma rays irradiation.

The change of the phonon spectrum due to gamma rays irradiation (Co^{60} source) with dose up to 10^7 rad has been investigated. Any influence of irradiation on the phonon modes derived by oxygen and W ions motions of WO_4-tetrahedron has not been observed (energy from 240 to 760 cm^{-1}). So, we may conclude that WO_4-tetrahedron does not disturb under this gamma rays irradiation.

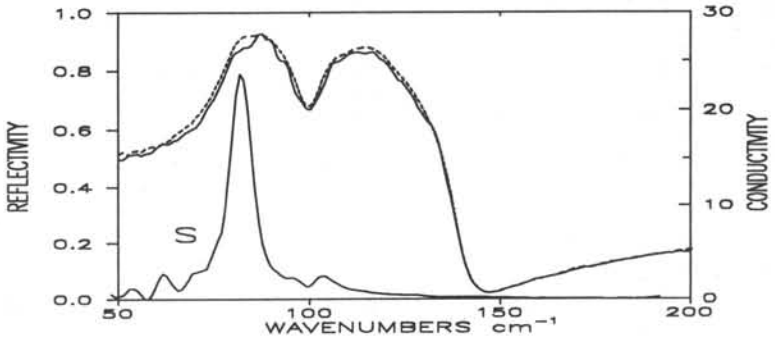

Fig.3. Influence of gamma rays irradiation on the reflectance spectrum of the $PbWO_4$ single crystal for E⊥C at T=300K: Dashed and solid lines are the reflectance spectra before and after 10^7 rad gamma-irradiation respectively. Solid line S is the difference of optical conductivities before and after gamma-irradiation and demonstrates the irradiation induced local phonon modes.

It has been found that after irradiation new local phonons occur near low-energy optical modes (50-140 cm^{-1}) dominated by motion of Pb-ions with some contribution of W-ions. Fig.3 shows the appearance of local modes near 130, 85 and 60 cm^{-1} as a result of gamma rays irradiation. It should be noted that these frequencies are close to the Raman-active Ag and Eg modes shown on Fig.2. The strongest local modes 85 and 60 cm^{-1} are determined by Pb and W ions motion. Taking into account the stability of the WO_4-tetrahedron we have concluded that gamma rays irradiation distorts the Pb sublattice of $PbWO_4$ single crystals. Break of local symmetry due to the Pb ions displacement seems to be responsible for the observation of the forbidden Raman active modes.

Another possible explanation of the observed effects may be the change of the position of WO_4-tetrahedra as a whole with respect to the Pb sublattice. It seems improbable due to the absence of O-derived Raman active local modes (757, 770 cm^{-1}) in infrared spectra of gamma rays irradiated single crystals.

The spectrum of local phonons and their oscillator strengths depend on crystal history and its doping. For example these modes have been observed in W-doped single crystals. Some kinds of heat treatment have been responsible for generation of these local modes.

It is essential that irradiation induced local phonons have been observed in crystals with high and low stability of gamma-scintillation with respect to gamma rays irradiation. We suppose that decrease of light output of gamma-scintillation may be determined by formation of macroscopic Pb-clusters. The last process strongly depends on crystal doping.

The work was supported by INTAS Grant No. 93 1239.

1.N.V.Klassen, FR-A-13.
2. J.M.Stencel, E.Silberman, J.Springer, and E.A.Jones, Phys. Rev.B 14, 5435 (1976).

SPECTRAL-KINETIC AND THERMOSTIMULATED STUDIES OF $MeW0_4$ SINGLE CRYSTALS

L.Nagornaya,A.Apanasenco,I.Tupitsina
Institute for Single Crystals Acad.of Sci. of Ukraine
60 Lenin av.,310001,Kharkov,Ukraine

Abstract

The results of the investigation of spectral-kinetics and thermostimulated characteristics of the $CdWO_4$ and $PbWO_4$ single crystals in the widely temperature range are discussed.It is supposed the excitation of the green luminescence centers is mainly of recombination nature. The role of the impurities defects of the formation the trapping of carriers and their influence for high afterglow $CdWO_4$ are discussed.

1.INTRODUCTION

Tungstate single crystals those of cadmium and lead have been studied for a long time [1]. However, the origin of the luminescence centers and mechanisms of their excitation remain the subject for discussion up to now. In practice, however, in this type of crystals this problem is complicated because of the presence of different defects. It should be noted that the luminescence characteristics of tungstates are very sensitive to the peculiar features of the synthesis. In particular this concerns lead tungstates. Perhaps, this account for the divergence in the results of different authors. Therefore, the main attention in this paper was paid to the growth of $PbWO_4$ and $CdWO_4$ crystals with stabilyty properties and the study of the effect of different type defects on their optical-luminescence characteristics. Being different in the structural type of lattice (scheelite and wolframite) lead and cadmium tungstate respectively, have much in common in the spectroscopic aspect.This allows to find out a similarity of the main processes and indentify structural defects.

Different kinds of the luminescence centers in $PbWO_4$ single crystals were considered in the papers by Kroger [1], Blasse [2], Loo [3], Reut [4], Lekoq [5]. These authors are unanimous in the idea that regular or isolated tungstate groups [1,2] or transitions in Pb^{2+} are responsible for the luminescence in the blue part of the spectrum. The green luminescence is connected either with defective tungstate groups [1] or with the charge transfer Pb^{3+}-WO_4^{3-} [3]. There is also no consensus of opinions on the structure of the luminescence centers and mechanisms of the radiative process in $CdWO_4$ crystals. Most authors consider the isolated WO_6^{6-} group as a center of the blue-green luminescence in $CdWO_4$.

2.EXPERIMENTAL

The crystals were grown by the Czochralski method in platinum crucibles under optimal conditions. The crystals used were of a difinite stoichiometric composition, nominally pure or doped with the impurities. The samples for investigations were in the form of disc (diameter 15 mm and thickness 2-3 mm). All the surfaces of the samples were polished

3.RESULTS AND DISCUSSIONS

It is known , that the x-ray luminescence spectra of lead and cadmium tungstate crystals at room temperature look like broad nonelementary bands with the emission in the region of 3.2-1.9 eV. The main maximum of $CdWO_4$ X-ray luminescence spectrum is only 2.5 eV. It is presented in a wide temperature range (80-400K) and does not strongly depend on the stoichiometric composition. Besides, additional (covert) maximums in the region of

Proc. Int. Conf. on Inorganic Scintillators and Their Applications, SCINT95,
1996, Delft University Press, The Netherlands

2.9,2.17-1.9 eV appear on the emission curve. It is known [6], that for cadmium tungstate crystals temperature dependences of the intensity and the decay constant (τ) of the luminescence band 2.5 eV in the temperature range of 80-270K change insignificantly. Only with further temperature rise there are the exponencial decay of the XL intensity and dramatic drop in the decay constant due to the thermal quenching processes .

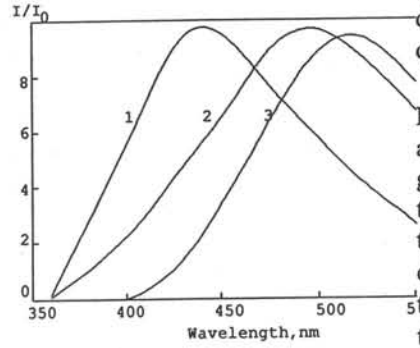

Fig.1The spectra of XL (1,2) and TSL(3)of the impurity free $PbWO_4$. (1)-T=80K,(2)-=300K

The position of the XL maximum in $PbWO_4$ strongly depends on the growth conditions and stoichiometric composition of crystals. If the growth conditions for $PbWO_4$ allow to maintain their composition close to the stoichiometric one the XL maximum is 2.9eV (PWO1). Formation of defects in the oxygen sublattice at growing leads to the shift of the maximum of their emission towards the long wavelength part 2.6-2.5 eV (PWO2).This being so the blue luminescence of PWO1 is preserved in the low temperature part of the spectrum. However, the green maximum (2.6 eV) is shifting towards the short wavelength (blue part of the spectrum) at lowering the temperature (Fig. 1). Temperature dependences of the XL intensity of $PbWO_4$ in different spectral regions and $CdWO_4$ are shown in Fig.2 (in the blue part - curve 1(PWO1) and curve 2 (PWO2), in the green one - curve 3 (PWO2), curve 5 - $CdWO_4$. After the crystal has accumulated the energy (x-ray irradiation at 80 K) the rise in the intensity of the green component is observed (curve 4). It is particularly pronounced at T>160K where thermal quenching of the blue XL begins. This is confirmed by the data on temperature dependence of the decay time of blue and green XL components . The rise of the green component amplitude begins at T~160K. This probably explains the shift of the XL spectrum maximum at T>160 K (Fig.1). To exclude the energy accumulation influence, a temperature dependence of the blue and green XL decay time and intensity has been measured, under impulse excitation. We have investigated the same results. It may be assumed that there occurs a transfer of the excitation energy from the blue luminescence centers to the green ones which is enhanced as blue luminescence quenching proceeds. This is in good agreement with the conclusions of Loo [3] from his photoluminescence studies of these crystals.

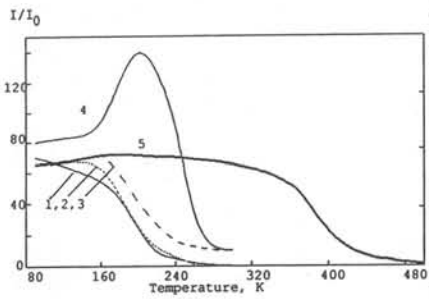

Fig.2 XL temperature dependence $PbWO_4$ (1-4) and $CdWO_4$ (5) in the blue(1,2) and green (3.4) parts of the spectrum.(1-3)without an accumulated energy (4) - after energy accumulated.

The dose dependence of the green XL intensity in PWO may serve as a proof of the recombinational mechanism of its excitation. Perhaps, while the shallow traps are filled, the recombinational flow through the centers of the green luminescence rises, which can be seen from (Fig.2,curve 4). The recovery of the initial intensity of green XL occurs after the emission of the last temperature peak of thermostimulated luminescence (TSL) (Fig.3).

Since the blue XL component does not depend on the degree of traps filling one can assume that the mechanism of its excitation is not recombinational.

It is known that the doping of $CdWO_4$ crystals does not produce an impurity luminescence [7]. Doping the crystals with heterovalent impurities (mainly trivalent) only changes the corelation of seperate peaks intensities in $CdWO_4$ luminescence band. Doping lead tungstate crystals with the impurities influences their spectral composition in the same way. Unlike X-ray and photoluminescence the thermostimulated processes in $CdWO_4$ and $PbWO_4$ are extremely sensitive to the faultness of crystals. In the undoped samples of both

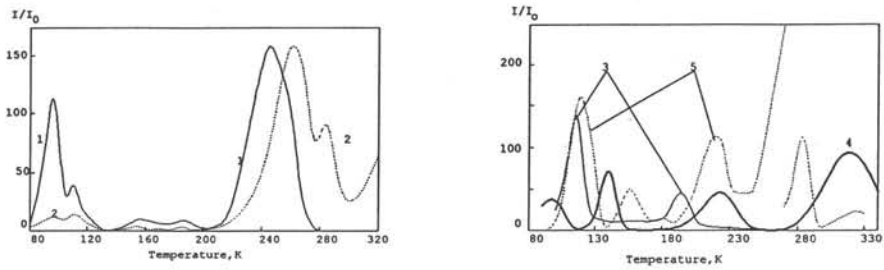

Fig.3 TSL (1,3,4) and TSC (2,5) curves of the undoped (1,2) $PbWO_4$ and doped with Nb (3,5)and Yb(4)

types of the temperature range of 80-350 K 6-7 peaks of thermoconduction (TSC) and 5-6 peaks of TSL are observed with the spectral composition in the blue-green and red regions of the spectrum. The position and intensity of the TSL peaks strongly depend on the stoichiometric composition of the crystals (Fig.,4). The presence of TSC naturally proves a seperate localization of free electrons

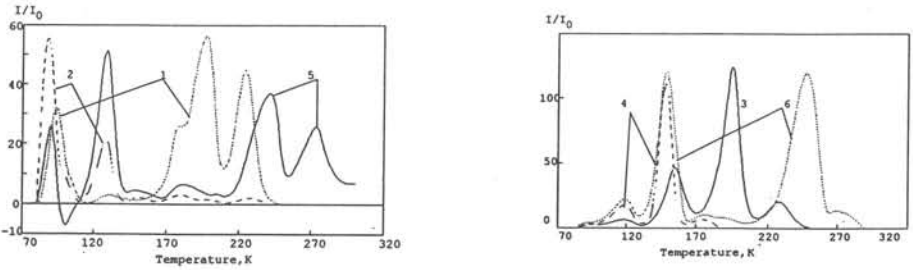

Fig.4 TSL(1-4) and TSC(5,6) curvers of the $CdWO_4$ crystals with an excess W (1,2,5) and Cd (3,4,6) in the red(1,3) and blue(2,4) regions of the spectrum

and holes. However the number of TSL peaks is too large (over 6) to be explained by the ionization of simple point defects. In the closed-packed structures of tungstates the presence of the Frenkel defects and interstitial impurity centers can be disregarded. Therefore, it can be assumed that shallow traps are either aggregates of point defects or localization of carriers proceeds in different coordination spheres near the point defects. The addition of isovalent impurities replacing the cations (Ca^{2+}) or anions (Mo^{6+}) does not change significantly the form of the TSL and TSC curves when compared with the undoped lead and cadmium tungstate crystals. A different situation is observed when heterovalent impurities are added to the crystals. The single and trivalent elements (Li^{1+}, Bi^{3+}, Ho^{3+}, Eu^{3+}, Sm^{3+},ets.) in the concentration of 10^{-3} mas.% lead to a full transformation of the shallow traps structure in cadmium tungstate crystals. TSL peaks, typical of the undoped crystals, disappear and

intensive peaks characteristic of this impurity energy emerge. So in the Ho^{3+}, Li^{1+} and Bi^{3+} - doped samples the main TSL peaks at about 125,155,175 K, respectively, are present (Fig.5). It was shown together with Tale [8], that the emptying of the Li-related traps at 155K results mainly in blue-green luminescence . Thus, the spectral composition of the glow corresponds to that of X-ray excited luminescence, whereas the emptying of the Bi-related traps results in the yellow luminescence band . The distinction in the spectral composition of the recombinational luminescence indicates that Li and Bi impurity ions act as traps for different charge carriers. Let us note that unlike the undoped crystals these TSL peaks do not coincide with TSC ones . That means that the TSL in the doped samples of $CdWO_4$ proceeds without a release of the trapped carriers. It may be supposed that shallow traps in such doped crystals are located in the vicinity of the impurity ion. According to the abovesaid concept on the structure of shallow traps as aggregates of vacancies one may assume that the impurity concentrates vacancies ensuring the trapping of the carriers around itself. This can be an explanation for a high afterglow typical of $CdWO_4$ crystals doped with rear-earth elements.

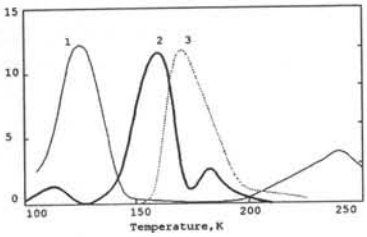

Fig.5 TSL curvers of the $CdWO_4$crystals doped with Ho(1), Li(2) and Bi(3).

A similar effect is observed at doping lead tungstate crystals with Yb^{3+} ions (Fig.3). Here also suppressed are the low temperature peaks typical of the undoped crystals but an intensive high temperature peak (T=320K) appears. The luminescence of the latter is accompanied by the annealing of the induced optical absorption. The addition of a pentavalent impurity (Nb^{5+}) to $PbWO_4$ leads to the emergence of intensive TSC peaks which weakly correlate with TSL.

4.CONCLUSIONS

It was found that the shift of the XL band in $PbWO_4$ towards the green part with the temperature rise is connected with a possible transfer of the excitation energy from the intrinsic centers of blue luminescence to those of green luminescence. The excitation of the latter is mainly of recombination nature.

On the basis of the TSL and TSC spectra study an assumption was made that the structure of shallow traps and impurity centers is mainly determined by the point defects and their aggregates.It can also be inferred that the heterovalent impurities in $PbWO_4$ and $CdWO_4$ crystals form complexes with the point defects.

ACKNOWLEDGEMENTS

The research discribed in this publication was made possible in part by Grant № K6M100 from the International Science Foundation.

REFERENCES

[1]F.A.Kröger"Some Aspects of the luminescence of Solids",Elsevier,1948[2] J.A.Groenink, G.Blasse, J. Sol.St.Chem.39(1980)9. [3] W.Van Loo,Phys. Stat. Sol(a) 27 (1975) 565 [4] B.Reut , Izvestiya AN SSSR.Ser.phys.49(1985)N10,p.2032.[5] P.Lecoq et.al."Lead tungstate scintillators for LHC EM-calorimetry" Subm. to NIM. [6] A.E.Ovechkin, V.D.Ryzhikov, G.Tamulaitis et.al. Phys. Stat.Sol.(a)103(1987)285 [7] I.Ya.Kushnirenko et.al.,Ukrainskii physichnii journal37(1992)N7,976 [8]V.Tale,I.Tale"Heterovalent impurity traps in CdWO4"Proc.of LUMDETR'94,Tallinn,Estonia,25-29 September 1994 .p.113

TRAP CENTERS AND RECOMBINATION LUMINESCENCE IN TUNGSTATES

M.Springis, V.Tale, I.Tale§, M.Barboza Flores* and L.L.Nagornaya***
Institute of Solid State Physics University of Latvia, 8 Kengaraga Str. LV1063, Riga, Latvia
*Centro de Investigacion en Fisica, Universidad Sonora, Apdo.Postal 5-088, Hermosillo, Sonora, 83190 Mexico.
**Institute for Single Crystals, Acad.Sci of Ukraine, 60 Lenin Av., Kharkhov, Ukraine
§) On leave from: Institute of Solid State Physics University of Latvia

ABSTRACT

The nature of thermostimulated electron - hole recombination in $CdWO_4$, $CaWO_4$, $ZnWO_4$, $PbWO_4$ has been discussed on the basis of investigations of the emission spectra of thermostimulated luminescence (TSL) and activation energy spectra of traps by the fractional glow technique (FGT)., Heterovalent dopants Li, Bi and Ho in $CdWO_4$ results in formation of localized electronic states. Bi in $CdWO_4$ acts as luminescence centre too. Most of the trapping centres in all tungstates investigated have single energy levels. It is proposed that blue-green and yellow luminescence occurs by recombination of released holes and electrons, respectively, at intrinsic luminescence centers of different structure related to the tungstate groups.

INTRODUCTION

The presence of impurities in tungstate scintillators may cause the formation of a new luminescence or color centres. The first investigations of the thermostimulated luminescence (TSL), activation energy spectra of thermostimulated recombination processes indicated that heterovalent impurities Li, Bi, Ho in $CdWO_4$ may act as traps for charge carriers [1]. On the basis of difference of the TSL spectral composition (TSL spectra) in peaks caused by Li^+ and Bi^{3+} related traps it was proposed that monovalent and trivalent impurities in $CdWO_4$ form acceptor- and donor-like trapping centers for charge carriers respectively [1]. A number of single monoenergetic kinds of trapping centres are present in nominally pure $CdWO_4$ scintillator crystals. Similar results have been observed in undoped $PbWO_4$ [2].
In the present paper the recombination luminescence and parameters of corresponding trapping centers, extended to different tungstates as well as to the liquid helium temperatures (LHeT) are discussed. The effect of irradiation with X-rays or uv-light on TSL has been compared.

EXPERIMENTAL

Single crystals of $CdWO_4$, $CaWO_4$, $ZnWO_4$ and $PbWO_4$ were grown by the Chochralski method in an atmosphere close to air. The luminescence excitation and emission spectra including spectral composition of TSL have been monitored using a model FluoroMax SPEX spectrofluorometer equipped with 150W Xe-arc light source, f/3.2 plane-grating Czerny-Turner type monochromators with a dispersion of 4.25 nm/mm. Signal detector - R152P PMT 180-680nm response. The luminescence emission spectra are not corrected for the spectral distribution of the PMT response. Spectral investigations were carried out in a model APD-CRYOGENICS closed cycle optical helium temperature cryostat. TSL spectra were monitored during linear heating with a rate at 0.1 K/s. The FGT measurements have been performed using oscillating heating-cooling at a linear rate at ±0.15 K/s, the increase of the maximal sample temperature, T_{n+1}-T_n, from the current temperature oscillation to the next one being $0.5 \times 10^{-2}\ T_n$ K. Thus, the trap emptying was monitored at logarithmic heating

Proc. Int. Conf. on Inorganic Scintillators and Their Applications, SCINT95,
1996, Delft University Press, The Netherlands

rate $\ln(T/T_0)$=const.x t. Experimental details of the FGT, calculation of the mean activation energies, $E(T)$, frequency factors, $s(T)$ and trap spectra are considered in [3].

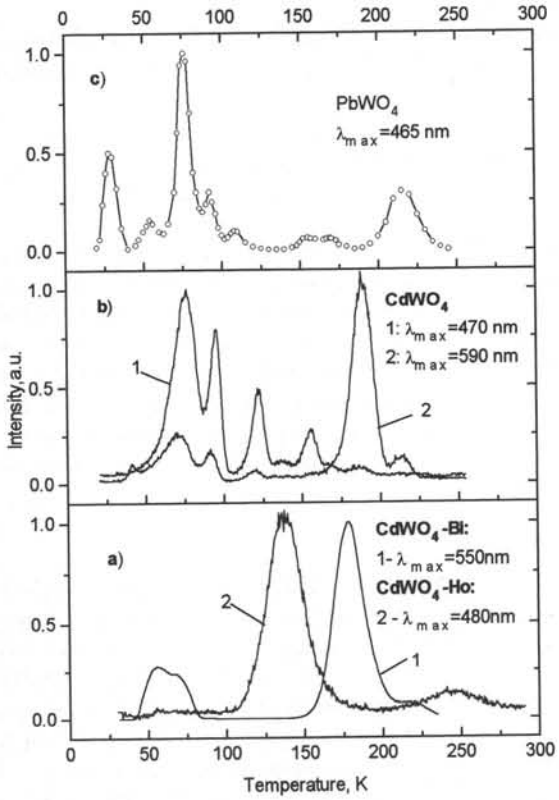

Fig 1. TSL of Cd- and Pb- tungstates excited at 11K by photons hν: a); b) - 320nm; c) - 305 nm for 20 s.

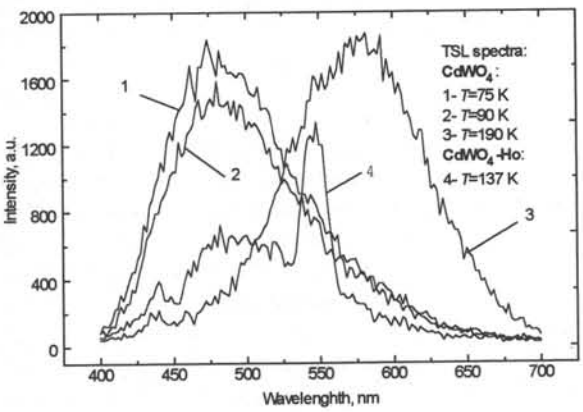

Fig.2 TSL spectra of $CdWO_4$ and $CdWO_4$-Ho.

RESULTS AND DISCUSSION

TSL curve of nominally pure $CdWO_4$, photo-irradiated by photons in the spectral region of intrinsic absorption (hν<330 nm) at 11K, is represented by a number of peaks starting from 39 K (Fig.1,b). The TSL emission spectrum in the low temperature peaks (39-150 K coincides with spectrum observed by the X-irradiation and corresponds to the blue-green luminescence band (Fig.2). TSL spectrum in the high tem perature (150 - 250K) peaks corresponds to the yellow luminescence band reported in [4]. Thus, it is possible to conclude that the ther-mostimulated recombination process have different nature in theses two temperature regions. Doping with Li sufficiently affect the TSL of $CdWO_4$. As observed recently in [1], presence of Li ions results in the appearance of new TSL peak at 155K and completely suppression of the low temperature peaks, observed in undoped crystals. The emptying of the Li-related traps at 155 K results in the blue-green luminescence.

Doping with Bi results in both the appearance of a new TSL peak at 179 K followed by suppression of the low temperature TSL peaks (Fig.1,a) as well as appearance of a new luminescence band at 530 nm (Fig.3, curves 3-6) in all TSL peaks by photo as well as by X-ray excitation. Besides by X-ray excitation in the high temperature

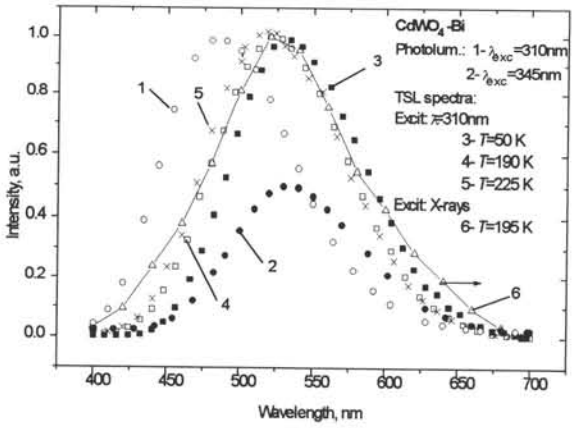

Fig.3TSL and photoluminescence spectra of $CdWO_4$-Bi

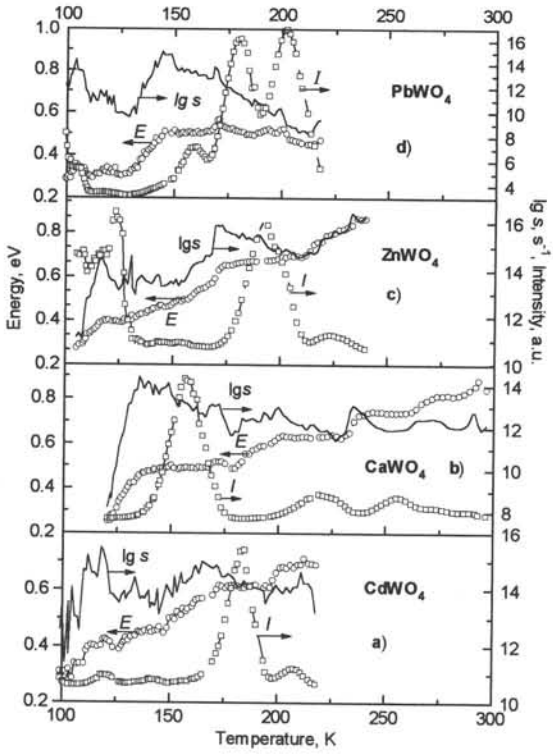

Fig.4. FGT spectra of tungstates X-ray irradiated at 80K.□□□ - glow intensity; ooo - mean activation energy; ____ - frequency factor.

TSL peaks at 179 and 245 K the yellow luminescence band at 600 nm is present (Fig.3, curve 6). Photo-excitation in the spectral region of the intrinsic absorption results only in the blue-green luminescence band Fig.3, curve 1), while intrinsic Bi-luminescence at 530 nm (Fig.3, curve 2) has excitation band at 345 nm.

Li^+ and Bi^{3+} ions in $CdWO_4$ substitute for Cd. The distinction in the spectral composition of the recombination luminescence indicates that Li and Bi impurity ions act as traps for different charge carriers. In the case of local or non-local charge compensation of the Me^+ and Me^{3+} impurity doping by some intrinsic defects it can be expected that impurity ions irrespective of the sign of excess charge will act as traps for one kind of charge carriers. Thus, it is reasonably to assume that Li^+ and Bi^{3+} ions in $CdWO_4$ form acceptor- and donor-like centers and, respectively, act as hole and electron traps giving rise to the corresponding TSL peaks.

Selective photo-excitation of the Bi^{3+}- centers results in creation of all characteristic TSL peaks. Thus, photo-ionization of Bi^{3+} ions takes place and ionized Bi luminescence centers are created being stable at least to temperatures of the highest TSL peak at 245K. The difference in the TSL emission during emptying of the Li^+- and Bi^{3+}- related traps can be explained by difference in the recombination mechanism as follows. The blue-green luminescence arises by recombination of free holes with electrons localized at intrinsic defects related to the WO_6 group. The yellow luminescence occurs by recombination of free electrons with holes localized at tungstate groups which lack one oxygen ion [4]. Recharge of

the Bi^{3+} during excitation and formation of stable Bi^{2+} and Bi^{4+} electron traps and ionized luminescence centres explains that the Bi- luminescence can dominate both in electron and hole thermostimulated recombination stages.

In Ho-doped $CdWO_4$ additional to the blue-green luminescence occurs intrinsic luminescence of Ho ions (Fig.2). Our investigations of the Ho- and blue-green luminescence excitation spectra show that the Ho- luminescence is present due to the reabsorption of the blue-green luminescence (See reabsorption caused decrease of the luminescence intensity in the luminescence spectrum of $CdWO_4$ -Ho in the 450 nm region, curve 4 Fig.2).

The presence of well-pronounced steps in E(T) corresponding to each of the TSL peaks investigated starting from 80 K, indicate that similar to undoped and Li-, Bi- doped $CdWO_4$ the trap spectrum of nominally pure $CaWO_4$ $ZnWO_4$ and $PbWO_4$ is represented by single monoenergetic traps (Fig.4). It should be mentioned that in the $PbWO_4$ the main light sum is accumulated by traps stable below liquid nitrogen temperatures (Fig.1,c). The trap parameters are represented in Table.

$ZnWO_4$		$CaWO_4$		$CdWO_4$		$PbWO_4$	
T_{max}, K	E, eV	T_{max}, K	E, eV	T_{max}, K	E, eV	T_{max}, K	E, eV
140	0.39	158	0.49	130	0.41	135	0.33
170	0.65	240	0.63	141	0.44	160	0.51
200	0.69	260	0.74	160	0.56	178	0.52
240	0.75	275	0.82	183	0.6	203	0.49
				207	0.68		

CONCLUSIONS

In $CdWO_4$ heterovalent dopants results in formation of localized electronic states. Defects present in nominally pure $CdWO_4$, $CaWO_4$, $ZnWO_4$ and $PbWO_4$ as well as known impurities Li, Bi, Ho in $CdWO_4$ act as relatively shallow traps for charge carriers, stable only below room temperatures. Experimental results indicate that the blue-green and yellow luminescence in $CdWO_4$ arises by recombination of free electrons and free holes, respectively, at intrinsic luminescence centers of different structure. Both intrinsic luminescence centers are related to the tungstate group of $CdWO_4$. The trap spectrum of nominally pure $CaWO_4$ $ZnWO_4$ and $PbWO_4$ is represented by single monoenergetic traps.

This work is supported in part by Latvian Council of Sciences, (Latvia, Grant No.93.783) and in part by CONACyT (Mexico, Grant No. D1520-E9201), DGISCA-SEP (Mexico), FOMES (Universidad de Sonora, Mexico) Dr. I.Tale is grateful to CONACyT for a Catedra Patrimonial de Excelencia Nivel II grant.

REFERENCES

1.Tale V., Tale I., L.L.Nagornaya. Radiat. Eff. and Defects in Solids, 1995, **133-134** (in press).

2. Auffray E., Dafinei I., Lecoq P., Schneegans M. Radiat. Eff. and Defects in Solids, 1995, **133-134** (in press).

3. Tale I.Phys. status solidi (a), 1981, **66**, 65-75; Proc. Sov. Acad. Sci., phys. sci.,1981, **45**, 245-252 (in russ.).

4. Lammers M.J.J., Blasse G. and Robertson D.S. Phys. stat.sol. (a), 1981, **63**, 787-791.

PART V

Impurity Activated Scintillators and Phosphors

CRYSTAL GROWTH AND SCINTILLATION PROPERTIES OF THE RARE EARTH OXYORTHOSILICATES

C. L. Melcher, J. S. Schweitzer, C. A. Peterson, R. A. Manente, H. Suzuki
Schlumberger-Doll Research, Ridgefield, CT 06877-4108, USA

Abstract

The rare earth oxyorthosilicates, $Ln_2(SiO_4)O$, melt congruently at ~2170 - 2320K and crystallize in either monoclinic C or monoclinic P structures, depending on the size of the rare earth ion. Typically the Czochralski technique is used to grow single crystals from Ir crucibles in either an inert or slightly oxidizing atmosphere. The Y, Gd, and Lu compounds are of interest as scintillators due to their good transparency at visible and ultraviolet wavelengths. The most effective activator for scintillation is Ce in which the scintillation emission arises from a fast, allowed 5d to 4f transition in the trivalent Ce ions. Scintillation light yields range from ~10,000 photons/MeV for $Y_2(SiO_4)O$:Ce ("YSO") to ~27,000 photons/MeV for $Lu_2(SiO_4)O$:Ce ("LSO"). The emission wavelength, 400 - 500 nm, and to a lesser degree, the decay time, 30 - 60 ns, are influenced by the crystal field at the Ce site. For $Gd_2(SiO_4)O$:Ce ("GSO"), the decay time is slowed by a nonradiative Gd to Ce energy transfer between overlapping levels that excites the Ce centers.

INTRODUCTION

The rare earth oxyorthosilicates have the chemical formula $Ln_2(SiO_4)O$, where Ln can be any of the 14 lanthanide elements or Y or Sc. These materials were studied first in powder form and subsequently as single crystals. They melt congruently at ~2170 - 2320K and crystallize in either monoclinic C or monoclinic P structures, depending on the size of the rare earth ion [1]. The compounds with larger rare earth ions (La $\rightarrow$ Tb) form a monoclinic P structure, and the smaller rare earth ions (Ho $\rightarrow$ Lu, Y, and Sc) form a monoclinic C structure. ($Dy_2(SiO_4)O$ exists in both forms.) Each structure consists of (SiO_4) tetrahedra with extra non silicon-bonded oxygens and two crystallographically independent rare earth sites. The two rare earth sites in the monoclinic P structure have oxygen coordination numbers of 7 and 9, while the two rare earth sites in the monoclinic C structure have oxygen coordination numbers of 6 and 7. Properties such as refractive index and density vary with atomic number (Table 1).

Table 1. Physical properties of the rare earth oxyorthosilicates from [2],[11].

	Melting point (K)	Density (g/cm^3)	Index of ref. (ave.)	Crystal structure
$Sc_2(SiO_4)O$	2220	3.49		C2/c
$Y_2(SiO_4)O$	2200	4.45	1.792	C2/c
$La_2(SiO_4)O$	2200	5.49		$P2_1/c$
$Ce_2(SiO_4)O$		6.11		$P2_1/c$
$Nd_2(SiO_4)O$	2250	6.00		$P2_1/c$
$Sm_2(SiO_4)O$	2210	6.38		$P2_1/c$
$Eu_2(SiO_4)O$	2250	6.51		$P2_1/c$
$Gd_2(SiO_4)O$	2170	6.77	1.888	$P2_1/c$
$Tb_2(SiO_4)O$	2180	6.93	1.890	$P2_1/c$
$Dy_2(SiO_4)O$	2190	7.20	1.887	$P2_1/c$
$Dy_2(SiO_4)O$	2190	6.66	1.830	C2/c
$Ho_2(SiO_4)O$	2190	6.80	1.826	C2/c
$Er_2(SiO_4)O$	2250	6.96	1.820	C2/c
$Tm_2(SiO_4)O$	2230	7.07	1.819	C2/c
$Yb_2(SiO_4)O$	2250	7.28	1.817	C2/c
$Lu_2(SiO_4)O$	2320	7.41	1.808	C2/c

Proc. Int. Conf. on Inorganic Scintillators and Their Applications, SCINT95,
1996, Delft University Press, The Netherlands

Powders doped with various activators including Ce, Tb, Eu, Dy, Tm, Sb, and Bi have been synthesized and studied as possible lamp phosphors, CRT screen phosphors, and storage phosphors [3],[4],[5],[6]. The wavelength and decay time of the emission depend on both the host lattice and activator. Cerium activators tend to produce a blue emission with a decay time of 30-60 ns while other activators such as Tb and Eu produce longer wavelength emissions with longer decay times.

Single crystals have been grown by a number of techniques including the hydrothermal method [7], flux growth [8], the Verneuil method [9], zone refining [10], and the Czochralski method [11],[12],[13]. Both pure crystals and crystals doped with activators including Ce, Tb, Eu, Sm, Nd, and Tm have been grown and characterized for possible applications such as CRT faceplates [14], lasers [15], gamma-ray detectors [16],[17], and neutron detectors [18]. The Czochralski technique has been used to grow single crystals of $Ln_2(SiO_4)O$ where Ln = Y, Gd, or Lu for use as scintillators. Since the low atomic number and density of $Y_2(SiO_4)O$ ("YSO") results in low detection efficiency for x-rays or gamma rays above ~100 keV, most attention has been given to $Gd_2(SiO_4)O$ ("GSO") and $Lu_2(SiO_4)O$ ("LSO") [19],[20]. Although Ln = La would also seem to be an attractive candidate for a scintillator material, growth of single crystals has not yet been achieved.

A promising new area is that of the mixed rare earth compounds. Recent investigations show that single crystals comprising solid solutions of two rare earths, such as $(Gd,Y)_2(SiO_4)O$:Ce and $(Lu,Gd)_2(SiO_4)O$:Ce, can be grown [21],[22]. While the density and atomic number of these materials vary smoothly between the end member values, the crystal structure is either purely monoclinic P or monoclinic C depending on the relative amounts of small and large rare earth cations. Scintillation properties such as emission wavelength, light output, and decay time, are affected by the local environment of the luminescence centers as well as energy transfer through the crystal lattice. Thus, the opportunity exists to design scintillation materials with properties tailored to match the requirements of specific applications by adjusting the mix of two or more rare earths.

CRYSTAL GROWTH

Rare earth oxyorthosilicate scintillator crystals are typically grown by the Czochralski technique using stoichiometric proportions of Ln_2O_3, SiO_2, and CeO_2 of at least 99.99% purity. The powders are loaded into an iridium crucible either in loose or compressed form in batches or in a continuous feed. The crucible is inductively heated, and diameter control can be achieved by monitoring the rate of weight change of either the crystal or the crucible [23]. A flowing atmosphere of N_2 or $N_2 + O_2$ is used. GSO is grown with oriented seed crystals to reduce cracking along the cleavage plane [24]. YSO and LSO boules can be grown in various crystallographic directions. Following growth, boules are cooled over a period of ~10 - 60 hours. Table 2 summarizes the growth conditions used for these materials.

Table 2. Typical crystal growth parameters.

	YSO	GSO	LSO
Rotation rate (rpm)	6 - 30	6 - 60	20-65
Pulling rate (mm/hr)	0.5 - 2.0	0.5 - 2.0	0.5 - 5.0
Max. diameter (mm)	25	62	35
Max. length (mm)	60	300	100

Although YSO, GSO, and LSO can be grown under similar conditions, the occurrence of defects depends strongly on the material. Both YSO and LSO boules tend to have relatively few defects visible to the naked eye regardless of the pulling rate or rotation rate. On the other hand, GSO boules tend to have numerous voids concentrated near the growth axis. The density of voids is lower in boules grown with high rotation rates and low pulling rates [24]. In addition, the growth atmosphere affects GSO more noticeably than YSO or LSO. GSO

boules grown in an atmosphere of N_2 + 3000 ppm O_2 have relatively smooth transparent surfaces while the boules grown in pure N_2 have a frosty white appearance evidently due to numerous defects and cracks. However, LSO boules grown in pure N_2 have a similar appearance to LSO boules grown in N_2 + 3000 ppm O_2. GSO boules often display cracks along the (100) cleavage plane which appear during cooling. On the other hand, YSO and LSO boules, which have no cleavage plane, are much less prone to cracking.

Brandle et al. [14] have shown that the distribution coefficients of dopants in YSO and GSO vary systematically with the ionic radius of the dopant relative to the ionic radius of the host rare earth cation. Since Ce^{+3} is larger than Gd^{+3}, Y^{+3}, and Lu^{+3}, the Ce distribution coefficients are expected to be less than one in these hosts. Figure 1 shows the distribution coefficients reported by various authors for several dopants in YSO and GSO. Note that the distribution coefficient of Ce in GSO appears to depend on the growth atmosphere. A value of 0.56 is reported for crystals grown in N_2 + O_2, while values of 0.7 to 0.9 are reported for growth in pure N_2. The distribution coefficient reported for Ce in YSO ranges from 0.25 to 0.34. The distribution coefficient of 0.22 for LSO is low, as expected, due to the relatively large size of Ce^{+3} compared to Lu^{+3}.

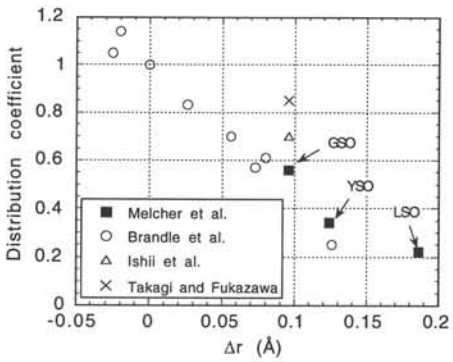

Figure 1. Distribution coefficients of various rare earth dopants in YSO, GSO, and LSO, display a clear correlation with the difference between ionic radius of the dopant and rare earth host ion. Data is taken from refs. [13],[14],[16],[25].

SCINTILLATION PROPERTIES

The luminescence emission in cerium-doped materials arises from 5d - 4f transitions in Ce^{+3}. The 5d level is split into sublevels by the crystal field of the host lattice. Excitation and absorption bands result from transitions between these sublevels and the 4f ground state, but the luminescence emission comes primarily from the lowest 5d level. The ground state itself is split by spin-orbit coupling. The details of the luminescence mechanism in Ce-doped rare earth oxyorthosilicates have been studied by Ishibashi [26], Suzuki et al. [27],[28], Rachko et al. [29], Buracas et al. [30], Sekita et al. [31], and Baryshevskii et al. [32],[33].

Figure 2 shows absorbance spectra of Ce-doped YSO, GSO, and LSO. The absorption bands correspond to transitions from the 4f ground state to the 5d sublevels of Ce^{+3}. The energies of the 5d sublevels, and consequently the wavelengths of the absorption bands, are influenced by the crystal field of the host lattice. YSO and LSO, which have a monoclinic C crystal structure, have similar absorption bands while GSO, which has a monoclinic P crystal structure, has absorption bands at somewhat different wavelengths due to the different crystal field at the Ce^{+3} site. In addition, absorption lines are seen in the GSO spectrum due to 4f-4f transitions in Gd^{+3}; the strongest one is located at 275 nm. As noted earlier, these materials have two rare earth sites, and consequently, two cerium luminescence centers, Ce1 and Ce2. The band structures of these two centers cannot be distinguished in the room temperature spectra shown here, although they can be seen at low temperature [28].

Figures 3 and 4 show excitation and emission spectra of YSO, GSO, and LSO. The excitation bands match the Ce^{+3} absorption bands showing that the emission comes from Ce^{+3}. The emission spectra of YSO and LSO are nearly identical since they have the same monoclinic C2/c crystal structure and similar activator sites. On the other hand, the GSO emission spectrum peaks at a longer wavelength reflecting the monoclinic $P2_1/c$ crystal structure. Studies of the excitation and emission bands at low temperature (~11K) has allowed the identification of the two distinct Ce luminescence centers and are discussed in more detail by Suzuki et al. [27,28]

The time decay of the luminescence emission under gamma-ray excitation (scintillation) is shown in Figure 5. The decays can be approximated by exponentials with time constants of 40 ns for LSO, 42 ns for YSO, and 56 ns for GSO. In addition, GSO has a secondary component of ~ 600 ns. The decay times are somewhat longer than the calculations of Hoshina [34] for the lifetime of Ce^{3+} in a cubic crystal field but similar to the experimentally observed lifetime of Ce^{3+} in numerous other phosphors and crystals. For YSO and LSO, direct excitation of Ce^{3+} by UV light produces the same decay times, while in GSO direct excitation of Ce^{3+} results in significantly shorter decays (see discussion below).

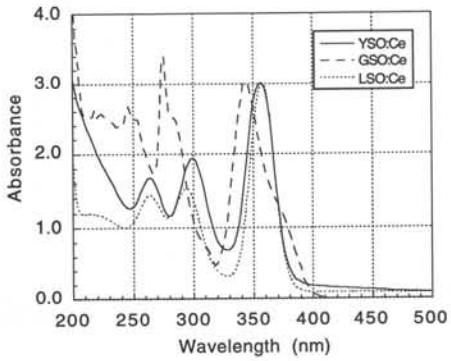

Figure 2. Absorbance spectra of YSO, GSO, and LSO doped with Ce.

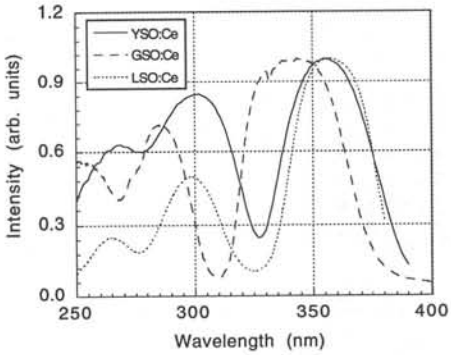

Figure 3. Excitation spectra of YSO, GSO, and LSO doped with Ce. The intensity was monitored at the peak emission wavelength.

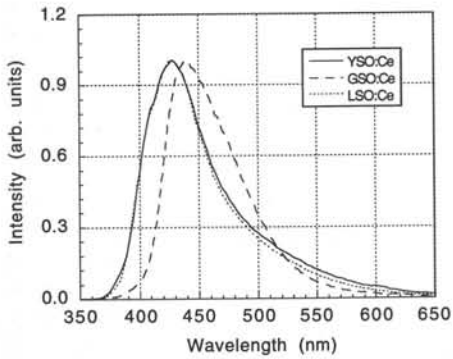

Figure 4. Emission spectra of YSO, GSO, and LSO doped with Ce under gamma-ray excitation. Intensities are normalized to unity.

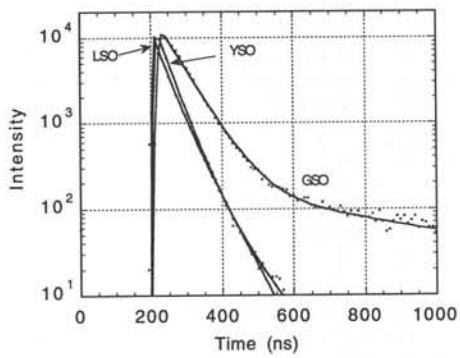

Figure 5. Scintillation decay time of YSO, GSO, and LSO doped with Ce under gamma-ray excitation.

Unlike the simpler cases of YSO and LSO where the scintillation properties depend almost solely on the properties of the Ce^{3+} luminescence centers, the complex scintillation properties of GSO cannot be explained simply by the luminescence emission of the Ce^{3+} activator. As in YSO and LSO, two types of excitation and emission spectra and decay constants are observed, probably corresponding to Ce^{3+} ions located at the two different rare earth lattice sites (Ce1 and Ce2). At room temperature, the Ce1 emission dominates with a decay constant of 22 ns, whereas the weak Ce2 emission has an even shorter decay of 5 ns. Under gamma-ray excitation, GSO has two decay constants (56 ns and 600 ns for 0.5 mol% Ce), both of which are considerably longer than the intrinsic Ce^{3+} decay and both of which are strongly dependent on Ce concentration. These results suggest that a relatively slow energy transfer from the Gd^{3+} sub-lattice to the Ce^{3+} activator plays a role in the scintillation process.

The energy transfer from Gd to Ce was investigated by Suzuki et al. [21],[35] by exciting the Gd absorption and analyzing the time-dependence of the subsequent Ce^{3+} emissions. When the ^6I_J states of Gd^{3+} (at 275 nm) were excited, a build-up in the Ce^{3+} decay was observed; when the ^6P_J states of Gd^{3+} (at 313 nm) were excited, the Ce^{3+} decay showed a long decay component. The observed build-up and the long decay component suggest that the slow gamma-ray excited decay constants are due to the energy transfer from Gd to Ce.

This model, illustrated by the energy level diagram in Fig. 6, was confirmed by using the decay curves measured with UV excitation to decompose the gamma-ray excited decay curve into three components. These three components are the prompt emission from $Ce1^{3+}$, the $Ce1^{3+}$ emission populated through the ^6I_J states of Gd^{3+}, and the $Ce1^{3+}$ emission populated through the ^6P_J states of Gd^{3+}. Therefore, the slow decay constants observed under gamma-ray excitation are due to the energy transfer from the ^6I_J and ^6P_J states of Gd^{3+} to the 5d states of the Ce^{3+} activator as seen in Fig. 2. The dependence of the decay constants on Ce concentration can be explained by the dependence of the transfer rates from Gd^{3+} to Ce^{3+} on Ce concentration.

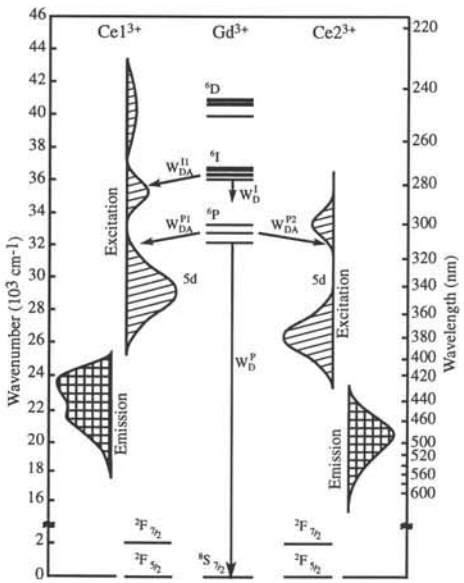

Figure 6. Energy levels of Gd^{3+}, $Ce1^{3+}$, and $Ce2^{3+}$. $W_{DA}{}^{I1}$ indicates the effective transfer rate from the ^6I_J multiplets of Gd^{3+} to $Ce1^{3+}$; $W_{DA}{}^{P1}$ represents the rate from the ^6P_J multiplets of Gd^{3+} to $Ce1^{3+}$; and $W_{DA}{}^{P2}$ indicates the rate from the ^6P_J multiplets of Gd^{3+} to $Ce2^{3+}$.

The radiation resistance of GSO and LSO have been studied by Kobayashi and co-workers who have found that these scintillators are among the most radiation resistant

scintillators known [36],[37]. For crystals with cerium doping of 2.5%, the reduction in transparency is less than a few per cent for a dose of 10^9 rads of ^{60}Co gamma rays.

The natural radioactivity of LSO must be considered in certain applications. ^{176}Lu is present with 2.6% abundance in natural Lu. The beta decay of this isotope leads to a number of gamma rays below 1 MeV, and therefore LSO crystals have an inherent gamma-ray background of about 300 counts per second per cm^3 of crystal.

CONCLUSIONS

The scintillation properties of the YSO, GSO, and LSO are summarized in Table 3. GSO and LSO have received the most attention for gamma-ray applications due to their higher density and atomic number, but YSO is a viable candidate for low energy gamma-ray and x-ray detection. LSO is preferred over GSO in most cases due to its significantly higher light output, faster decay time, and better machinability. The longer decay components of GSO are a disadvantage for timing applications, and its cleavage plane makes fabrication of complex detector shapes difficult. In some applications, the natural radioactivity of LSO may make one of the other rare earth oxyorthosilicates preferable.

Table 3. Scintillation properties.

	YSO $Y_2(SiO_4)O:Ce$	GSO $Gd_2(SiO_4)O:Ce$	LSO $Lu_2(SiO_4)O:Ce$
Best light output (photons/MeV) (NaI:Tl = 38,000)	9200	12,500	27,000
Best energy resolution at 662 keV (%)	9.0	7.0	7.9
Peak emission wavelength (nm)	420	430	420
Decay time (ns)	42	56, 600	40
Eff. atomic no.	35	59	66
Density (gm/cm^3)	4.45	6.7	7.4
Hygroscopic ?	no	no	no
Rugged ?	yes	no	yes

In order to assess the potential for further improvements in these scintillators, it is useful to compare the theoretically predicted maximum light output of YSO, GSO, and LSO, with the actual measured light output following the guidelines of Lempicki [38]. According to Lempicki, the scintillation efficiency (light output) of a crystal may be defined as the fraction of the gamma-ray energy deposited in the crystal which is converted into luminescence. This conversion occurs in three steps: the creation of electron-hole pairs, the transfer of energy to the luminescence centers, and the emission of light from the luminescence centers. Thus, the scintillation efficiency η is given by

$$\eta = \beta * S * Q \qquad 0 \leq \eta, \beta, S, Q \leq 1$$

where β is the efficiency of electron-hole creation, S is the transfer efficiency, and Q is the quantum efficiency of the luminescence centers. According to the theory developed by Robbins [39], β is a function of the band gap, the static and high frequency dielectric constants, and the longitudinal optical phonon energy. No suitable theory currently exists to calculate S so it is inferred once the other variables are known. Q is the ratio of the radiative transition rate to the radiative + nonradiative rate, and η is determined from the number of luminescence photons created by gamma rays of known energy.

In the case of LSO, the scintillation parameters may be calculated as follows. From measurements of the band gap and the dielectric constants together with the longitudinal optical phonon energy from the literature, β is found to be 0.35. The quantum efficiency of the Ce luminescence centers is measured to be very close to unity at room temperature, and the

scintillation efficiency is measured to be ~0.38. Thus, the transfer efficiency S must be ~1.0. Therefore, the scintillation performance of LSO is already near the theoretical limit since both S and Q are close to the maximum theoretical value of 1 and β is a fixed property of the material. (See Table 4.)

The transfer efficiency for YSO and GSO may be calculated in a similar way. The factor β is virtually the same as for LSO, while the quantum efficiencies of the luminescence centers is again obtained from the luminescence lifetimes. As seen in Table 4, the lower scintillation efficiency of GSO results from lower transfer efficiency as well as lower quantum efficiency, and the lower scintillation efficiency of YSO results primarily from lower transfer efficiency. For comparison, the table also shows that the high light output of NaI(Tl) and CsI(Tl) results from efficient energy conversion β as well as efficient energy transfer S, and that BGO suffers from low quantum efficiency at room temperature.

Table 4. Scintillation efficiency.

crystal	β	S	Q	η
LSO	0.35	1.0	1.0 (Ce1) 1.0 (Ce2)	0.38
GSO	0.35	0..86	0.9 (Ce1) 0.1 (Ce2)	0.17
YSO	0.35	0.37	1.0 (Ce1) 1.0 (Ce1)	0.13
NaI(Tl)	0.88	0.59	1.0	0.52
CsI(Tl)	0.97	0.99	1.0	0.96
BGO	0.69	1.0	0.13	0.094

REFERENCES

[1] J. Felsche, The crystal chemistry of the rare-earth silicates, in *Structure and Bonding* V13, Springer-Verlag, 99-197 (1973).

[2] *Phase Diagrams for Ceramists: 1969 Supplement*, E. M. Levin, C. R. Robbins, and H. F. McMurdie, eds., The American Ceramic Society (1969).

[3] A. H. Gomes de Mesquita and A. Bril, Preparation and cathodoluminescence of Ce^{3+}-activated yttrium silicates and some isostructural compounds, Mat. Res. Bull. **4**, 643-650 (1969).

[4] I. A. Bondar, A. A. Kolpakova, L. Ya. Markovskii, A. N. Sokolov, L. E. Tarasova, and N. A. Toropov, Rare earth activated luminophors based on yttrium and gadolinium silicates, Izvestiya Akademii Nauk SSSR **33**(6), 977-981 (1969).

[5] P. J. Born, D. S. Robertson, and P. C. Smith, A study of phosphors in the yttrium oxide-silicon dioxide phase system. J. Mat. Sci. Lett. **4**, 497-501 (1985).

[6] J. Holsa, K. Jyrkas, and M. Leskela, Site selectively excited luminescence of Eu^{3+} in gadolinium, yttrium and lutetium oxyorthosilicates, J. Less Common Metals **126**, 215 (1986).

[7] B. A. Maksimov, Yu. A. Kharitonov, V. V. Ilyukhin, and N. V. Belov, The crystal structure of the Y oxyorthosilicate $Y_2(SiO_4)O$, Dokl. Akad. Nauk SSSR, **183** (5), 1072 (1968).

[8] G. Buisson and C. Michel, Serie isomorphe d'orthosilicates (T_2SiO_5) et d'orthogermanates (T_2GeO_5) de terres rares, Mat. Res. Bull. **3**, 193-198 (1968).

[9] N. A. Toropov, I. A. Bondar, A. N. Lazarev, and Yu. I. Smolin, Rare earth silicates and their analogues (in Russian), Nauka, Leningrad (1971).

[10] P. A. Arsenev, I. N. Raiskaja, and R. K. Sviridova, Spectral properties of neodymium ions in the lattice of Y_2SiO_4O crystals, Phys. Status Solidi (a) **13** (1), K45 (1972).

[11] G. V. Anan'eva, A. M. Korovkin, T. I. Merkulyaeva, A. M. Morozova, M. V. Petrov, I. R. Savinova, V. R. Startsev, and P. P. Feofilov, Growth of lanthanide oxyorthosilicate single crystals and their structural and optical characteristics, Izvestiya Akademii Nauk SSSR, Neorganicheskie Materialy, **17**(6), 1037-1042 (1981).

[12] A. P. Kulesskii, A. M. Korovkin, A. V. Kruzhalov, L. V. Viktorov, and B. V. Shul'gin, Radioluminescence and scintillation properties of monocrystals of silicates of yttrium and rare earth elements, Zhurnal Priklanoi Spektroskopii, **48** (4), 650-653 (1988).

[13] C. L. Melcher, R. A. Manente, C. A. Peterson, and J. S. Schweitzer, Czochralski growth of rare earth oxyorthosilicate single crystals, J. Crystal Growth **128**, 1001-1005 (1993).
[14] C. D. Brandle, A. J. Valentino, and G. W. Berkstresser, Czochralski growth of rare-earth orthosilicates (Ln_2SiO_5), J. Crystal Growth **79**, 308-315 (1986).
[15] R. F. Belt and J. A. Catalano, Growth of cerium-doped rare earth silicates for tunable lasers, in *Tunable Solid-State Lasers II*; Proceedings of the OSA topical meeting, A. B. Budgor, L. Esterowitz, and L. G. DeShazer, eds. (Springer Series in Optical Sciences, V. **52**) 94-101 (1986).
[16] K. Takagi and T. Fukazawa, Cerium-activated Gd_2SiO_5 single crystal scintillator, Appl. Phys. Lett. **42**(1) 43-45 (1983).
[17] C. L. Melcher, J. S. Schweitzer, T. Utsu, and S. Akiyama, Scintillation properties of GSO, IEEE Trans. Nuc. Sci. **37** (2), 161-164 (1990).
[18] P. L. Reeder, Neutron detection using GSO scintillator, Nucl. Instr. Meth. **A340**, 371-378 (1994).
[19] C. L. Melcher and J. S. Schweitzer, A promising new scintillator: cerium-doped lutetium oxyorthosilicate, Nucl. Instr. and Meth. in Phys. Res. **A314**, 212-214 (1992).
[20] C. L. Melcher, Lutetium orthosilicate single crystal scintillator detector, U.S. Patent No. 4,958,080, (1990) and No. 5,025,151 (1991)
[21] H. Suzuki, T. A. Tombrello, C. L. Melcher, and J. S. Schweitzer, Energy transfer mechanism in $Gd_2(SiO_4)O$:Ce scintillators, IEEE Trans. Nucl. Sci. **41**(4), 681-688 (1994).
[22] S. Akiyama, T. Utsu, H. Ishibashi, C. L. Melcher, and J. S. Schweitzer, Single Crystal Scintillator, U.S. Patent No. 5,264,154 (1993).
[23] R. A. Manente, C. L. Melcher, C. A. Peterson, J. S. Schweitzer, M. A. Singelenberg, and F. J. Bruni, A Macintosh-based system for Czochralski crystal growth, Scientific Computing and Automation, Jan. 1994.
[24] T. Utsu and S. Akiyama, Growth and applications of Gd_2SiO_5:Ce scintillators, J. Crystal Growth **109**, 385-391 (1991).
[25] M. Ishii, H. Ishibashi, and S. Akiyama, in: Extended Abstracts 9th Intern. Conf. on Crystal Growth (ICCG-9), Sendai, 251E11 (1989).
[26] H. Ishibashi, Mechanism of luminescence from a cerium doped gadolinium orthosilicate (Gd_2SiO_5) scintillator, Nuc. Instr. Meth. in Phys. Res. **A294**, 271-277 (1990).
[27] H. Suzuki, T. A. Tombrello, C. L. Melcher, and J. S. Schweitzer, Light emission mechanism of cerium doped lutetium oxyorthosilicate, IEEE Trans. Nucl. Sci. **40**(4) 380-383 (1992).
[28] H. Suzuki, T. A. Tombrello, C. L. Melcher, and J. S. Schweitzer, UV and gamma-ray excited luminescence of cerium-doped rare-earth oxyorthosilicates, Nucl. Instr. Meth. **A320**, 263-272 (1992).
[29] Z. A. Rachko, I. A. Tale, V. D. Ryzhikov, J. L. Jansons, and S. F. Burochas, Cathodoluminescence mechanism of crystalline Gd_2SiO_5:Ce, Nucl. Tracks Radiat. Meas. **21**(1), 121-124 (1993).
[30] S. Buracas, S. Jursenas, V. P. Martinov, V. D. Ryzhikov, and G. Tamulaitis, Photoluminescence of Ce-doped Gd_2SiO_5 scintillators, Phys. Stat. Sol. (A) **133**, 541-546 (1992).
[31] M. Sekita, Y. Miyazawa, T. Akahane, and T. Chiba, Optical studies of Ce-doped Gd_2SiO_5 single crystals, J. Appl. Phys. **66**(1), 373-378 1989.
[32] V. G. Baryshevskii, M. V. Korshik, M. G. Livshits, A. S. Lobko, B. I. Minkov, M. L. Meil'man, V. I. Moroz, V. B. Pavlenko, and A. A. Fedorov, Scintillation characteristics of $Gd_2SiO_5:Ce^{3+}$ crystals, Vestsi Akad. Navuk BSSR, Ser. Fiz. Energet. Navuk, No. **4**, 114-117 (1991).
[33] V. G. Baryshevskii, D. M. Kondratiev, M. V. Korzhik, V. B. Pavlenko, and A. A. Federov, Mechanism of scintillations in cerium-doped gadolinium orthosilicate Gd_2SiO_5:Ce crystals, J. Luminescence **60/61**, 956-959 (1994).
[34] T. Hoshina, 5d-4f Radiative Transition Probabilities of Ce^{3+} and Eu^{2+} in Crystals, J. Phys. Soc. Japan, **48** (4), 1261-1268 (1980).
[35] H. Suzuki, T. A. Tombrello, C. L. Melcher, C. A. Peterson, and J. S. Schweitzer, The role of gadolinium in the scintillation processes of cerium-doped gadolinium oxyorthosilicate, Nucl. Instr. Meth. **A346**, 510-521 (1994).
[36] M. Kobayashi and M. Ishii, Excellent radiation-resistivity of cerium-doped gadolinium silicate scintillators, Nucl. Instr. Meth. **B61**, 491-496 (1991).
[37] M. Kobayashi, M. Ishii, C. L. Melcher, Radiation damage of a cerium-doped lutetium oxyorthosilicate single crystal, Nucl. Instr. and Meth. **A335**, 509-512 (1993).
[38] A. Lempicki, A. J. Wojtowicz and E. Berman, Fundamental limits of scintillator performance, Nucl. Instr. and Meth. **A333**, 304-311 (1993).
[39] D. J. Robbins, On predicting the maximum efficiency of phosphor systems excited by ionizing radiation, J. Electrochem. Soc. **127** (1980) 2694.

DENSE, FAST, RADIATION-TOLERANT FLUORO-HAFNATE GLASS SCINTILLATORS FOR ELECTROMAGNETIC CALORIMETERS IN HIGH ENERGY PHYSICS

Hobson P R, Imrie D C, Price T
Department of Physics, Brunel University, Uxbridge, UB3 4PH, UK

Bell K W, Brown R M, Cockerill D J A, Flower P S, Grayer G H, Lintern A L, Sproston M
Rutherford Appleton Laboratory, Chilton, Didcot, OXON OX11 0QX, UK

McKinlay K J, Parker J M
Department of Engineering Materials, University of Sheffield, Sheffield, UK

ABSTRACT

Over 200 different compositions of heavy metal fluoride glasses have been produced and evaluated as possible candidates for the active medium in homogeneous electromagnetic calorimeters for high energy particles. Promising glasses, based on mixtures containing hafnium fluoride, have densities of 6 g cm^{-3}, radiation lengths of 1.6 cm, and good optical transmission from the UV to the IR. Glasses containing the Ce^{3+} ion are fast scintillators, with properties similar to those of pure cerium fluoride crystal. We have made glasses which have up to 14% of the light yield of CeF_3, fast scintillation characterised by typical exponential decay constants of 10 ns and 25 ns, and a temperature dependence of light yield of -0.4%/°C over the range -10°C to 60°C. We have carried out a detailed investigation of the effects of gamma irradiation (up to doses of 6 kGy) on the optical transmission, and systematic studies into the role of indium and other elements on radiation tolerance and light yield. Some glasses have shown complete optical annealing of radiation-induced absorbance when exposed to UV light.

INTRODUCTION

Almost all current and planned experiments in particle physics incorporate detectors for measuring the directions and energies of high energy electrons and photons - so called electromagnetic calorimeters (often abbreviated to ECAL). The technologies employed in these detectors fall into one of two categories; 'sampling' and 'homogeneous'. In sampling detectors many layers of an active medium (plastic scintillator, gas or liquid ionisation device, semiconductor diode) are interleaved with a dense material having high atomic number, such as lead or tungsten. Homogeneous detectors have been constructed using silicate glass loaded with barium or lead; large, dense scintillating monocrystals of materials such as sodium iodide, caesium iodide or bismuth germanate; or a dense liquified noble gas such as krypton. As a rule of thumb, homogenous detectors give better energy resolution but are more expensive when compared with their sampling counterparts. Furthermore, among the available homogenous media, heavy silicate glasses are cheaper than crystals but give somewhat inferior energy resolution.

The work described here was motivated by the desire to develop a new homogenous medium for high energy electromagnetic calorimetry, which would give an energy resolution approaching that of crystals, at a significantly lower cost. The particular application in mind was the CMS (Compact Muon Solenoid) experiment at the LHC (Large Hadron Collider) recently approved for construction at CERN. The calorimeter for such an experiment must be fast (signals of 25 ns duration or less), dense (a radiation length of 2 cm or less), radiation hard (able to survive a dose of 10 kGy) and realisable on a large scale (tens of cubic metres of detector are required). The most promising materials we have investigated are glasses based on the hafnium fluoride matrix.

FLUORIDE GLASSES

Heavy metal fluoride glasses were discovered in 1974 [1] in the course of investigations of crystalline laser hosts. Many of these glasses have very good optical transparency, and interest focused on their potential for use in extremely low loss optical fibres for communications. A formulation which has

Proc. Int. Conf. on Inorganic Scintillators and Their Applications, SCINT95,
1996, Delft University Press, The Netherlands

been extensively studied is ZBLAN (ZrF_4, BaF_2, LaF_3, AlF_3, NaF) which is relatively stable against crystallisation during production, allowing kilogram scale blocks to be cast.

Fluoride glasses readily accept transition metals and lanthanides into the matrix, offering the possibility that they might be made to scintillate by doping with a fluorescent ion such as Ce^{3+}. ZBLAN has a radiation length of 2.7 cm which is too long for applications at LHC. Nevertheless, it might have proved of interest for other particle physics experiments, however, our early work showed that replacing lanthanum with cerium did not result in a measurable scintillation yield from this glass [2]. Mixtures based on HfF_4 rather than ZrF_4 also form stable glasses and these have much shorter radiation lengths (typically 1.6 cm). Furthermore, in 1992 Devitsin et al [3] showed that doping with CeF_3 at the level of a few molar percent produces a significant scintillation yield and this has led us to concentrate our investigations on these materials.

GLASS PRODUCTION

Glass samples were prepared at Sheffield University from their component metal fluorides, which were in the form of small crystals or powders (HfF_4 was obtained from Johnson Matthey [4], Merck [5] and Moscow [6], all other metal fluorides were supplied by Merck). Typically, 10 g batches were prepared giving 20 x 10 x 6 mm^3 finished samples. The glass production techniques are described in greater detail elsewhere in these proceedings [7].

LIGHT YIELD

The scintillation yields were measured relative to a CeF_3 crystal using a secondary charged-particle beam at the proton synchrotron accelerator of the ISIS neutron spallation source at the Rutherford Appleton Laboratory. The beam line was tuned to accept protons with a mean momentum selected in the range from 540 to 750 MeV/c. At these momenta the protons are below threshold for directly producing Cherenkov light in the sample (the threshold is 840 MeV/c for a refractive index of 1.5). This is an important consideration since even a small contribution from Cherenkov photons can bias fits to scintillation decay curves. Scintillation light was detected by a Thorn EMI 9814QKB photomultiplier. The photomultiplier signal was recorded on a 1 G Sample/s digital oscilloscope, using a gate width of 500 ns.

For a given basic glass composition, the light yield was found to increase monotonically with cerium content up to the maximum concentration that could be incorporated into a stable glass. Typically, a glass containing cerium fluoride at a concentration of 5% (molar) gives a light output per MeV of

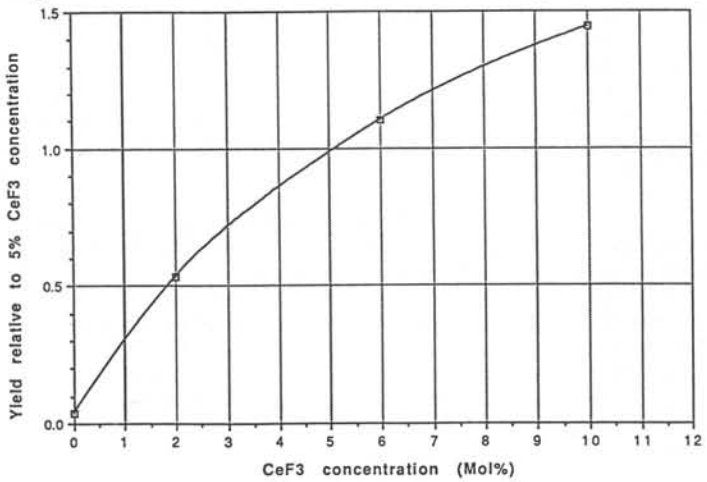

Figure 1 The measured light yield plotted against CeF_3 concentration, for a set of glasses of composition 'HBCeAN'. The yield has been normalised to unity for 5% CeF_3 concentration.

energy deposited which is approximately 10% that of a cerium fluoride crystal. Figure 1 shows the variation of light yield with cerium fluoride concentration for a set of glasses with a composition HBCeAN.

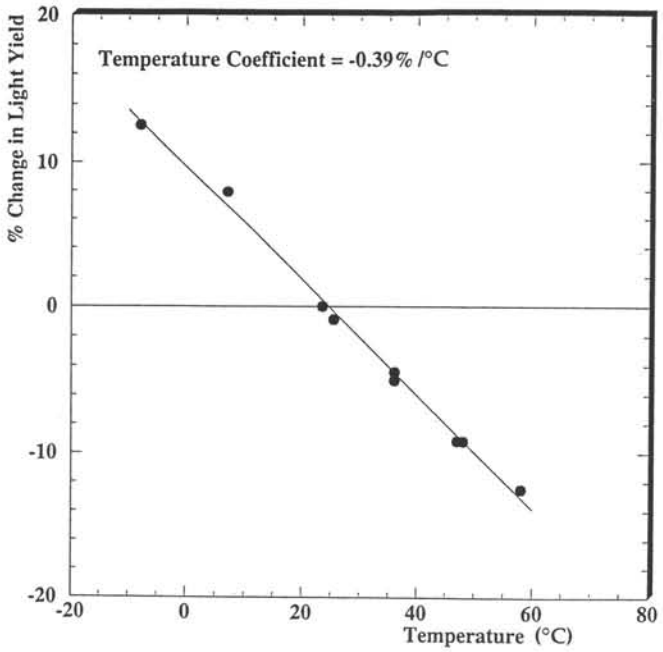

Figure 2 The measured variation of light yield with temperature for a fluorohafnate glass doped with CeF_3.

With the aid of a Peltier cooling/heating device, a set of measurements was made for one of the samples (HBCeA), at temperatures in the interval from -10 to + 60°C. The light yield was found to decrease linearly with increasing temperature over this range by approximately -0.4%/°C (figure 2).

DECAY TIME SPECTRA

Scintillation decay time spectra were obtained by two methods. In one approach, several thousand individual digitised wave forms, recorded with protons at ISIS, were summed to give an average pulse shape. The other measurement, performed at Brunel University, used a standard delayed single-photon technique, with an additional multi-photon veto logic. The sample was excited by an annihilation photon from a 10 μCi Na^{22} positron source, the other photon was detected in a BaF_2 crystal which started a fast time-to-amplitude converter. The data were collected over a time window of 2000 ns, with a single-photon timing resolution of 1.40 ns.

Figure 3 shows a typical decay time distribution obtained with protons. In the range from 0 to 250 ns, the curve is well fitted by the sum of three exponentials:

$$I(t) = I_0(ae^{-t/\tau_1} + be^{-t/\tau_2} + ce^{-t/\tau_3})$$

where $\tau_1 = 11$ ns, $\tau_2 = 25$ ns, $\tau_3 = 62$ ns and the coefficients a, b and c are in the ratio 0.16:1.0:0.26.

Since the three terms are strongly correlated in the fit, the decay spectrum is more usefully characterised by considering the fraction of the light yield contained within a given time interval. Integrating under the curve, one finds that 53% of the light is emitted in the first 25 ns. This result is very similar to that obtained with a single crystal of CeF_3.

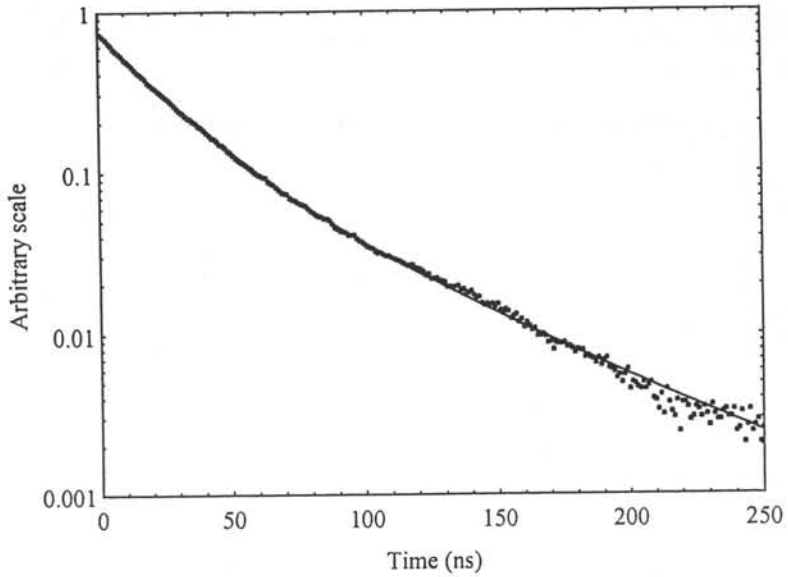

Figure 3 The measured decay time spectrum for scintillation light from a sample of Ce doped fluorohafnate glass (HBCeALi). The smooth curve is a fit to the data and is the sum of three exponential terms: $I(t) = I_0(ae^{-t/\tau_1} + be^{-t/\tau_2} + ce^{-t/\tau_3})$ where $\tau_1 = 11$ ns, $\tau_2 = 25$ ns, $\tau_3 = 62$ ns and the coefficients a, b and c are in the ratio 0.16:1.0:0.26.

TRANSMISSION AND EMISSION SPECTRA

Emission spectra have been measured using X-ray (~ 9 keV) and ultraviolet light (284 nm) excitation, with similar results. Figure 4 shows the fluorescence spectrum obtained for a fluorohafnate glass (HBCeA) containing CeF_3 at a concentration of 8% (molar). The spectrum is dominated by an emission band centred at 320 nm, which is attributed to radiative transitions from the lowest excited 5d-level of Ce^{3+}, to the 4f ground state.
The optical transmission as a function of wavelength is shown on the same plot. It can be seen that the emission spectrum lies close to the band-edge. Good optical transmission just above the cut-off is therefore crucially important for detectors using large blocks of glass, if significant self absorption of scintillation light is to be avoided.

RADIATION DAMAGE

Radiation damage in glasses is characterised by the development of optical absorption bands which result from the creation and population of defects known as colour centres. The development of these absorption bands is consistent with the irradiation creating and populating new defect sites and the sites relaxing either spontaneously or as a result of irradiation, or both. The absorbance at a particular wavelength saturates as a function of dose.

In an LHC experiment the radiation dose in the electromagnetic calorimeter will be dominated by electromagnetic showers produced by high energy photons from π^0 decays. As a result, the dose will vary with depth in the calorimeter (being greatest at the position of the average shower maximum) and will be higher close to the direction of the colliding beams (the 'forward' regions) than at larger angles with respect to this axis (the 'central' region). The estimated dose in the central region, averaged over the first eight radiation lengths of the detector, is 0.4 kGy/year. In order to investigate the ability of our glasses to withstand these large radiation levels, samples were irradiated with a 4 Ci Co^{60} source at Brunel. Doses of up to 6 kGy were delivered in 5 days (at a dose rate of 12 m Gy/s), corresponding to more than 10 years of operation in the central region at LHC.

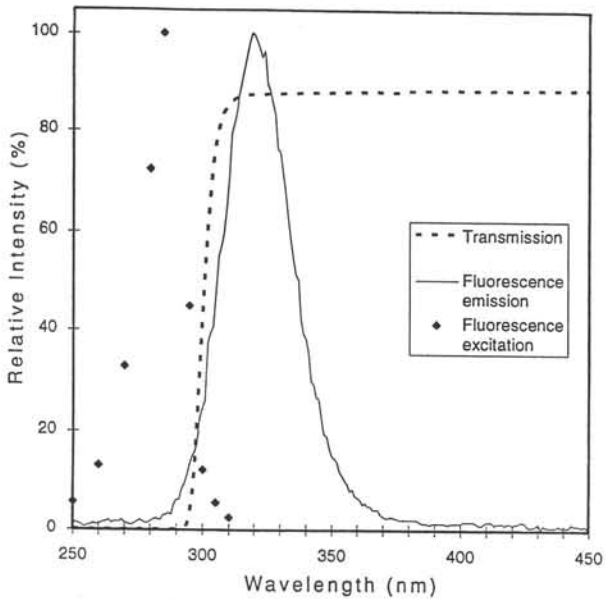

Figure 4 Fluorescence excitation and emission spectra for a cerium doped fluorohafnate glass together with the optical transmission measured for the same sample.

All undoped fluorohafnate glasses studied proved to be quite susceptible to radiation damage, the internal transmission at 325 nm of a 5 mm thick sample typically falling to 5% of its initial value after 6 kGy. Studies were therefore made to determine the effect of various dopants (Fe, Ga, Nb, In, Pr, Nd, Sm, Eu, Gd, Ho, Er, Yb, Lu) on radiation hardness. In some cases the effect was quite dramatic. Thus for example adding 1.5% (molar) of EuF_3 to HBLA resulted in a glass which exhibited negligible damage at wavelengths above 400 nm for doses in excess of 6 kGy. Unfortunately strong damage was still observed in the Ce^{3+} emission region from 300 to 350 nm.

The dopant which was found to minimise radiation damage in the Ce emission region is indium, the magnitude of the effect depending quite sensitively on the concentration (figure 5). Curve II in this figure shows how the radiation-induced optical attenuation (at 350 nm), measured immediately after a dose of 2.4 kGy (Co^{60} γ-ray), varies with indium concentration. The addition of indium has the undesired effect of reducing the light yield from Ce doped glass, as can be seen from curve I. However, for an indium concentration of 0.5%, which maximises the radiation hardness, the loss in light yield (from a small sample) is only 30%.

Since the radiation dose received by a calorimeter at LHC would be spread over the ten year lifetime of the experiment, the effect of thermal annealing over a long interval at room temperature should also be taken into account. Curve III in figure 5 shows how the radiation-induced attenuation length varies with indium concentration for a much larger dose (7 kGy delivered in 7 days) followed by storage for 4.5 months in the dark at room temperatures. Comparing curves II and III it can be seen that self annealing largely offsets the effect of the bigger radiation dose for indium concentrations of 0.8% and above. At lower indium concentrations self annealing occurs to a greater degree and this is particularly evident for the point at 0.2% concentration. However, the optimum indium concentration still appears to be close to 0.5%, even allowing for self annealing.

The above studies were performed using small samples of glass (typically 1 cm^3). In order to obtain a better understanding of how the results would translate to the performance of a glass calorimeter, the effect of irradiation on light yield was measured using a much larger block of glass (HBLALi doped with 0.5% InF_3). The block was 13 cm (8.2 radiation lengths) long with a rectangular cross section (3 x 1 cm^2). For the light yield measurements it was wrapped in Tyvek and a 2" phototube was

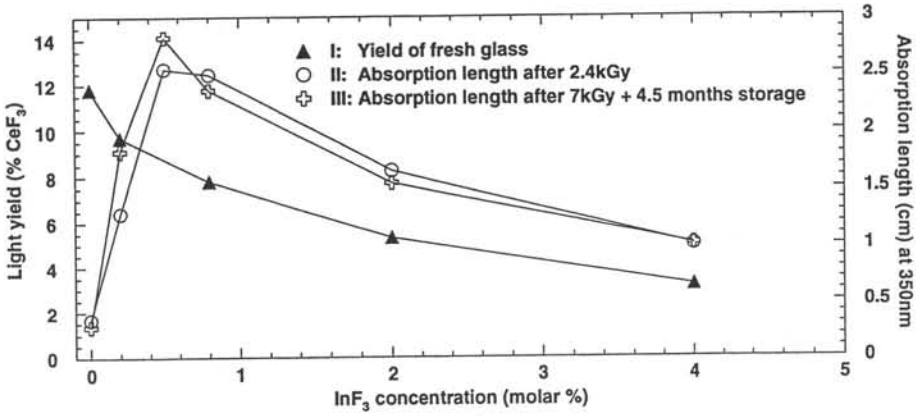

Figure 5 The effect of InF_3 doping on the light yield and radiation hardness of a glass with basic composition 'HBCeAN', containing 5% (molar) CeF_3.
Curve I (triangles) shows the variation of light yield versus InF_3 concentration. The yield is normalised to the yield obtained from a crystal of CeF_3 of similar dimensions to the glass samples.
Curve II (open circles) shows the variation of radiation-induced optical attenuation at 350 nm, measured immediately after a dose of 2.4 kGy. (Co^{60}-γ).
Curve III (crosses) shows the optical attenuation induced by a dose of 7 kGy, followed by 4.5 months storage in the dark at room temperature.

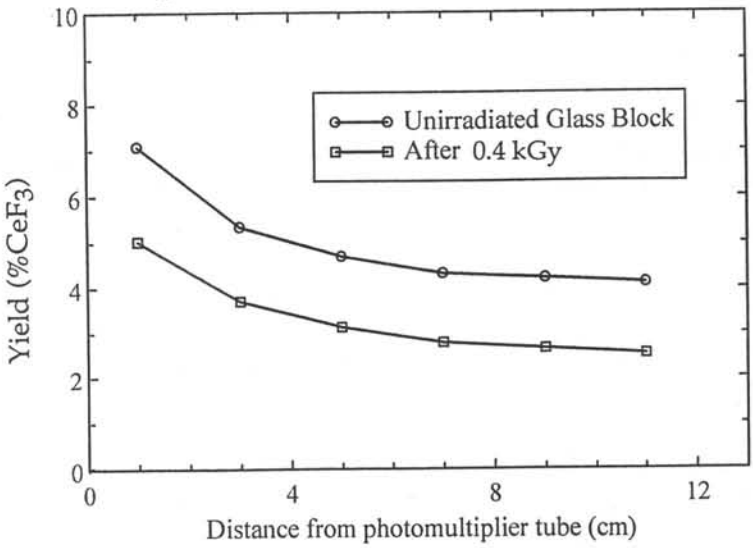

Figure 6 The light yield as a function of position along the length of a block (dimensions 13 x 3 x 1 cm^3) of fluorohafnate glass (HBCeALi) doped with 0.5% (molar) InF_3.
The upper curve was obtained before irradiation. The lower curve was measured immediately following a 0.4 kGy dose (Co^{60}-γ) delivered approximately uniformly over the volume of the block.

mounted on one end. The proton beam was directed through the 1 cm dimension at several points along the length. The block was then irradiated with a dose of 0.4 kGy in 40 hrs (~ 1 year dose at LHC), delivered approximately uniformly over the whole volume, and the light yield remeasured.

The results are shown in figure 6. Both before and after irradiation the light yield shows a strong variation as a function of distance from the phototube in the region close to the tube, whereas further from the tube the yield varies rather slowly. The loss of light from the far end following irradiation is 35%. A full sized detector would be 3 times longer than the block tested, however, the radiation dose at LHC falls off rapidly after the first 8 radiation lengths. On the basis of these data we conclude that this particular glass would satisfactorily survive one year of operation in the central rapidity region at LHC. However, ten years of operation would require some method of *in situ* annealing to be devised.

OPTICAL ANNEALING

All the glasses were stored and irradiated in complete darkness to avoid any possibility of photo-induced bleaching. After spontaneous recovery of absorbance had stabilised, several glasses were illuminated with light from a 150 W Hg arc lamp. Interference filters were used to select the 365 nm, 435 nm and 577 nm lines in the Hg spectrum. Lines above 400 nm were observed to cause little measurable change in absorbance, but the 365 nm line was extremely effective in reversing the radiation induced optical damage in some fluoride glasses. Some glasses were found to recover fully (figure 7); whereas others, including those doped with indium, recovered only partially.

Complete optical annealing of radiation damage in a scintillating fluoride glass has previously been reported by the Crystal Clear Collaboration[8].

PROTOTYPE GLASS DETECTOR

A composite block of glass (13 x 3 x 3 cm^3), fabricated from three plates similar to that used for the irradiation study, has been tested in a high energy electron beam at CERN. The beam was directed on to the centre of the front face and the light was detected with a 2" phototube (9814QKB) mounted on the rear face. The measured response to 10 and 50 GeV electrons was found to be in good agreement with that predicted by a GEANT [9] simulation of the energy deposition in this detector (figure 8).

CONCLUSIONS

We have demonstrated that cerium doped fluorohafnate glass could be used as the active medium in a high performance electromagnetic calorimeter for many particle physics applications. Radiation damage would be a limitation to use in the harsh environment at LHC although this might be overcome by optical annealing *in situ*.

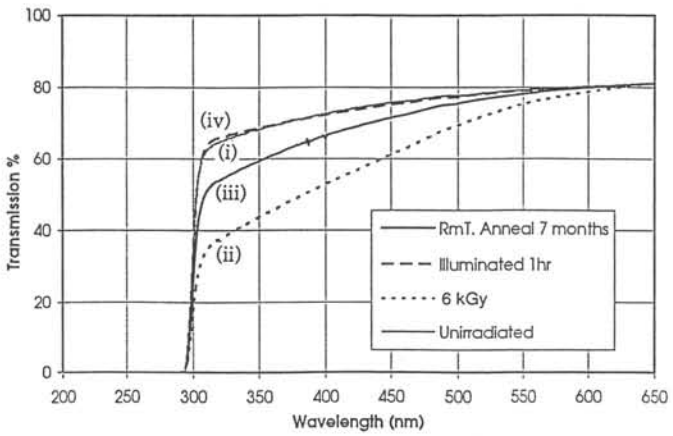

Figure 7 The measured external transmission of a fluoro-hafnate glass; (i) unirradiated, (ii) after 6 kGy, (iii) after annealing in the dark at room temperature for 7 months (where strong recovery is observed), and (iv) after illuminating with a mercury arc lamp for one hour. The glass has fully recovered after one hour of optical annealing.

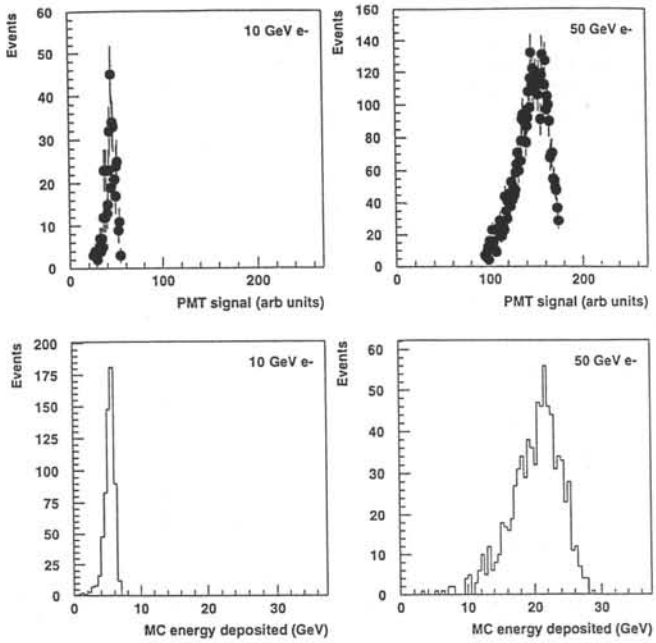

Figure 8 The measured (upper) and Monte Carlo simulated (lower) response of a composite glass block of CeF_3-doped fluorohafnate glass to 10 GeV and 50 GeV electrons. The block was 3 x 3 cm^2 in section and 13 cm ($8.2X_0$) long.

ACKNOWLEDGEMENTS

We thank E G Devitsin, V A Kozlov, V N Makhov and S U Potashov from the Lebedev Institute and L N Dmitruk from the General Physics Institute in Moscow for many helpful discussions, for supplying some of the HfF_4 raw material and for suggesting the glass formulation used for the CERN beam tests. We are grateful to S Sheikh from the Department of Physics at Brunel University, for measuring the fluorescence spectra of the HBCeA glass and to B W Kennedy for analysing data recorded at ISIS.

This work has been supported by the UK Particle Physics and Astronomy Research Council.

REFERENCES

[1] Poulain Mi., Poulain Ma., Lucas J., Brun P., Mat. Res. Bull. (1975) 12, 243-246
[2] Hobson P R., in Heavy Scintillators for Scientific and Industrial Applications, de Notaristefani F et al., (eds), Editions Frontieres, Gif-sur-Yvette, (1993), 343-347
[3] Devitsin E G. et al., in Heavy Scintillators for Scientific and Industrial Applications, de Notaristefani F. et al., (eds), Editions Frontieres, Gif-sur-Yvette, (1993), 401-406
[4] Johnson Matthey Chemicals, Orchard Road, Royston, Herts SG8 5HE, UK
[5] Merck Ltd., Merck House, Poole BH15 1TD UK
[6] All-Russian Institute of Chemical Technology (Prof. Fedorov)
[7] Hobson P R. et al., The industrial production of large, inexpensive blocks of scintillating fluorohafnate glass, to be found elsewhere in these proceedings
[8] Auffray E., Dafinei I., Lecoq P., Schneegans M., in Scintillator and Phosphor Materials, Materials Research Society Symposium Proceedings, 348 (1994), 217-224
[9] R Brun and F Carminati, GEANT Detector Description and Simulation Tool, CERN Program Library Long Writeup W5013, (1993)

DENSE Ce^{3+}-ACTIVATED SCINTILLATOR MATERIALS

M. J. Weber, S. E. Derenzo, C. Dujardin,* W. W. Moses
Lawrence Berkeley National Laboratory
University of California
Berkeley, CA 94720 USA

ABSTRACT

Several very dense hosts for Ce^{3+} are identified and their scintillation characteristics at 300 K are reported. Included are simple oxides, aluminates, borates, tantalates, BGO, and fluorides.

INTRODUCTION

Cerium-activated scintillator materials have received renewed interest for many applications because of the favorable spectroscopic properties of Ce^{3+} and the ability to incorporate Ce^{3+} into many different host materials.[1] Many of these materials combine high light yield, favorable emission wavelength, fast fluorescence decay, and temperature stability which make them attractive for use in detectors for high energy physics [2] and medical imaging.[3] Whereas the former application is tolerant regarding light output, the latter requires the highest scintillation efficiency. High density and good stopping power are important for both applications. Cerium-activated materials with increasingly higher densities have been developed in recent years, lutetium-based compounds being of particular current interest. We have used crystal diffraction databases [4] to identify potential hosts for Ce^{3+} having densities in the range $\gtrsim$ 7-10 g/cm^3. Here we present preliminary results for several very dense Ce-activated materials. Samples were generally powders or polycrystalline materials. All scintillation measurements were performed at room temperature using a pulsed x-ray apparatus and techniques described elsewhere.[5] Decay kinetics are reported but luminescence spectra have not been characterized. At this stage our intent is to survey and screen those materials operating at room temperature that warrant further spectroscopic studies and growth efforts; optimized cerium concentration, precise measurements of scintillation light output, or studies of other important properties such as radiation damage, afterglow, etc. have thus not been made.

LUTETIUM OXIDES

The properties of three lutetium oxide compounds are listed in Table 1. Since for applications such as PET a large photoelectric fraction is desirable, the photoelectric length (attenuation length divided by photoelectric fraction) for 511 keV photons is given. Simple Lu_2O_3 is a very dense material, but preparation of single crystals is difficult because of the very high melting point (2740 K). Attempts to prepare samples of Ce-activated Lu_2O_3 in the form of fibers have been made using the laser-heated pedestal growth technique; for a discussion of their optical properties we defer to reports presented elsewhere in these proceedings.[7] The properties of an additional high density oxide and of an oxysulfide of potential interest are included in Table 1, however no samples were available to test. A broad red emission from Ce^{3+} in the oxysulfide Lu_2O_2S has been reported at temperatures <170 K.[8] Thermal quenching of the luminescence at higher temperatures limits the usefulness of this material.

Proc. Int. Conf. on Inorganic Scintillators and Their Applications, SCINT95,
1996, Delft University Press, The Netherlands

Table 1. Properties of high density Ce^{3+} hosts for 511 keV photons.

Compound	Crystal system	Density (g/cm^3)	Attenuation length (cm)	Photoelectric fraction (%)	Photoelectric length (cm)
Lu_2O_3	cubic	9.4	0.93	38.1	2.43
$LuLaO_3$	orthorhombic	8.2	1.17	31.7	3.68
Lu_2O_2S	hexagonal	8.9	0.99	37.0	2.67
$Lu_3Al_5O_{12}$ (3:5)	cubic (garnet)	6.7	1.41	29.0	4.87
$LuAlO_3$ (1:1)	orthorhombic	8.4	1.10	32.1	3.44
$Lu_4Al_2O_9$ (2:1)	monoclinic	~8.5	1.06	34.9	3.04
Lu_3BO_6 (3:1)	monoclinic	7.4	1.20	41.3	3.28
$LuBO_3$ (1:1)	hexagonal	6.9	1.32	37.2	3.91
$LuTaO_4$ (1:1)	monoclinic	9.8	0.90	37.8	2.37
Lu_3TaO_7 (3:1)	cubic	~10	~0.87	~39	~2.3
$LuPb_2TaO_6$	orthorhombic	10.1	0.77	45	1.70
$LaTaO_4$ (1:1)	monoclinic	7.8	1.22	31.6	3.86
$LaTa_3O_9$ (1:3)	tetragonal	8.1	1.12	34.8	3.21
$LaTa_5O_{14}$ (1:5)	orthorhombic	8.2	1.09	35.7	3.04
$LaTa_7O_{19}$ (1:7)	orthorhombic	8.3	1.07	36.2	2.72
$Bi_4Ge_3O_{12}$	cubic	7.1	1.21	46.0	2.63
LuF_3	orthorhombic	8.3	1.10	34.2	3.22
Lu_3KF_{10}	cubic	6.9	1.39	30.7	4.51
$BaLu_2F_8$	monoclinic	6.9	1.35	32.2	4.18

LUTETIUM ALUMINATES

The properties of three compounds of the lutetium oxide-aluminum oxide system are included in Table 1. Of these, the cubic garnet phase can be grown most easily. Obtaining the more dense perovskite phase free of the garnet phase requires more care.[8] As evident from several papers in this volume, the orthoaluminate $LuAlO_3$ has been the subject of intense study.

We have investigated the slightly more dense 2:1 compound $Lu_4Al_2O_9$. A sample was grown by Airtron from a stoichiometric melt doped with 0.75 at.% Ce using the Czochralski technique. The growth was well behaved but the single crystal decomposed during cooling. The x-ray pattern indicated that it was not single phase and Lu_2O_3 was also present. The x-ray excited decay could be fitted with three components having time constants and percentages of 0.3 ns (12%), 3.3 ns (22%), and 45 ns (66%). The intensity was less than that of BGO.

LUTETIUM BORATES

Properties of two lutetium borates are presented in Table 1. A powdered sample of the 1:1 compound $LuBO_3$ doped with 1% Ce was prepared by D. Keszler (Oregon State University) and exhibited good light output (greater than that of BGO) and decay kinetics characterized by

4 ns (9.2%), 28 ns (32%), 335 ns (59%). This is a promising compound. It undergoes a phase transition at 1310 °C from the calcite to the valerite-type structure. Thus far we have been unable to obtain a good sample of the more dense 3:1 compound Lu_3BO_6 . An x-ray pattern attributable to this phase was obtained but was contaminated with other compounds.

TANTALATES

The properties of several Lu and La tantalates are given in Table 1. $LuTaO_4$ is a known phosphor material with an absorption peak at about 220 nm and intense emission at 330 nm arising from a charge transfer transition of the TaO_6 group. It has also been doped with Nb or Bi for emission at longer wavelengths [9,10] and with several trivalent lanthanide ions.[11] Varying relative amounts of tantalate and dopant emissions are observed and depend on the specific transitions involved. We have measured an x-ray excited decay time of 1.87 μs for a pure $LuTaO_4$ powder sample. A polycrystalline sample doped with 0.5% Ce grown from the melt by B. Chai (CREOL) exhibited a weak luminescence (less than BGO) with a decay that could be fitted approximately by three time constants of 59 ns (6%), 344 (27%), and 1.03 μs (67%). Powdered samples of $LuTaO_4$:Ce prepared by C. Torardi (Du Pont) in a reducing atmosphere to minimize the presence of Ce^{4+} also exhibited a weak scintillation output; for the most concentrated sample (3% Ce) the output was very weak and fast. All samples had a pale yellow coloration. Samples of the more dense 3:1 compound Lu_3TaO_7 do not luminesce under x-ray excitation [12]; no Ce-doped samples of this compound or the ultra-dense lutetium-lead tantalate in Table 1 have been prepared.

The lanthanum tantalates are not as dense as the lutetium compounds but the La site is a much better size fit for Ce than Lu. The absorption edge of $LaTaO_4$ is at 260 nm. Luminescence associated with the tantalate group has been observed at low temperatures (77 K) [10]; only weak x-ray excited luminescence is observed at 300 K.[12] Luminescence has been reported for $LaTaO_4$ doped with Eu^{3+} and Tb^{3+} with little transfer from the tantalate group evident from excitation spectrum.[13] A polycrystalline sample of $LaTaO_4$ doped with 0.2% Ce exhibited a decay of 1.8 ns (61%) and 75 ns (39%). Thsi material undergoes a phase transition at 600 °C. Corresponding decays from.a polycrystalline 0.5% Ce sample of the more dense $LaTa_3O_9$ were 1.7 ns (29%) and 35.3 (71%). This material melts at 1850 °C snd shows no phase transition dureing cooling. Neither compound exhibited strong scintillation output (< BGO).

BISMUTH GERMANATE

$Bi_4Ge_3O_{12}$ (BGO), while not as dense as some of the other materials in Table 1, is of interest because it has a smaller photoelectric length than most of the other materials. Several trivalent lanthanide ions have been added to BGO in small quantities (< 1 at.%) for studies of spectroscopic and defect properties and to increase radiation stability.[14] BGO has the eulytite structure; intense UV-excited Ce^{3+} luminescence has been reported from several phosphate-containing eulytites, e.g., $Sr_3La(PO_4)_3$.[15] The fundamental band gap of BGO is near that expected for the Ce^{3+} 4f–5d splitting. The large Stokes shift of the BGO emission, however, is unfavorable for energy migration to Ce. A crystal doped with a nominal 0.2% Ce was measured and exhibited an initial decay component (~20%) having a lifetime of ~30 ns in addition to the ~300 ns decay observed in undoped BGO. The total light output from this sample was reduced slightly with respect to that of undoped BGO. Growth in a reducing environment is required to minimize the formation of Ce^{4+}.

LUTETIUM FLUORIDES

The properties of several Lu fluorides are included at the bottom of Table 1. LuF_3 is attractive from the viewpoint of density but is difficult to prepare. Samples of $BaLu_2F_8$ were prepared by B.Sobelov (Institute of Crystallography). Undoped $BaLu_2F_8$ exhibits a very fast luminescence which is believed to be due to a core-valence transition associated with Ba; the decay time was 0.86 ns. The scintillation light was about one-third of that of BaF_2, which is reasonable in view of the smaller cation percentage of Ba. A sample of $BaLu_2F_8$ doped with 3% Ce had an x-ray excited decay characterized by two components: 6.3 ns (28%) and 39 ns (72%). The rise time of the Ce luminescence was consistent with radiative transfer of cross luminescence from the host.

ACKNOWLEDGMENTS

We are indebted to the people and organizations cited for the samples used in these studies. This work was supported in part by the Director, Office of Energy Research, Office of Health and Environmental Research, Medical Applications and Biophysical Research Division of the U.S. Department of Energy under contract No. DE-AC03-76SF000098, and in part by Public Health Service Grant R01 CA48002 awarded by the National Cancer Institute, Department of Health and Human Services. One of the authors (C. D.)* acknowledges the support of a NATO grant.

* Permanent address: Laboratoire de Physico-Chimie des matériaux Luminescents, Université Claude Bernard Lyon 1, CNRS URA 442, Villeurbanne, France.

REFERENCES

1. C. W. E. van Eijk, J. Andriessen, P. Dorenbos, and R. Visser, *Nucl. Instr. and Meth.*. **A348** (1994) 546.
2. P. Lecoq, *IEEE Trans. Nucl Sci.* **40**, 409 (1993).
3. S.E. Derenzo, W. W. Moses, M. J. Weber and A. C. West, in *Scintillator and Phosphor Materials*, (Materials Research Society Symposium Proceedings Vol. **348**, 1994), p. 39.
4. NIST Crystal Data Identification File (1993), International Centre for Diffraction Data, Newtown Square, PA, U.S.A.
5. S. C. Blankespoors, S.E. Derenzo, et al., *IEEE Trans.Nucl. Sci.* **NS-41**, 691 (1994).
6. See papers by W. Schaik, et al., and S. Claeys, et al. in these proceedings.
7. S. Yokono, T. Abe and T. Hoshina, *J. Lumin.* **24/25**, 309 (1981).
8. A. G. Petrosyan, G. O. Shirinyan, K. L. Ovanesyan and A. S. Kuzanyan, *J. Cryst. Growth* **52**, 556 (1981).
9. L. H. Brixner, *Mater. Chem. Phys.*, **16**, 253 (1987).
10. L. H. Brixner, *Inorgania Chimia Acta*, **140**, 97 (1987).
11. G. Blasse, G. J. Dirksen, L. H. Brixner and M. K. Crawford, *J. Alloys Comp.* **209**, 1 (1994).
12. C. Torardi (private communication).
13. G. Blasse and A. Bril, *J. Lumin.*, **3**, 109 (1970).
14. See M. V. Korzhik, A. P. Kudryavtseva, S. V. Lyubetskii, et al., *Zh. Prikl. Spectrosk.*, **57**, 299 (1992) and references cited therein.
15. M. F. Hoogendorp, W. J. Schipper and G. Blasse, *J. Alloys Comp.* **205**, 249 (1994).

EPR STUDY OF CERIUM-DOPED $YAlO_3$ SINGLE CRYSTALS

H.R. Asatryan[1], J. Rosa[2], S.A. Smirnova[3], J.A. Mareš[2], P. Malý[4] and J. Kvapil[4]
[1]Institute of Physical Research of National Academy of Armenia, 378410, Ashtarak -2, Republic of Armenia.
[2]Institute of Physics, Czech Academy of Sciences, Cukrovarnická 10, 16200 Prague 6, Czech Republic.
[3]VNIISIMS, Institutskaya st., Aleksandrov, Vladimir Region, 601600, Russia.
[4]Preciosa Crytur Ltd., Palackého 175, 51119 Turnov, Czech Republic.

EPR spectra of Ce^{3+}, Er^{3+} and Nd^{3+} ions in $YAlO_3$ crystal lattice are presented. These spectra can be described by spin Hamiltonian with an effective spin S = 1/2 and rhombohedric symmetry. The g factors for all studied ions and the constants of hyperfine interaction for Nd^{3+} and Er^{3+} were obtained. We conclude that all resonances which are upon the interest in this paper, belong to the RE^{3+} ions replacing the Y^{3+} cations in the $YAlO_3$ lattice. Some additional resonant lines with intensities 100 - 1000 times less than Ce^{3+} main line were observed and interpreted as spectra of defect-related Ce^{3+} centres.

1. INTRODUCTION

$YAlO_3$ crystals doped by rare earth^{3+} ions (RE^{3+}) as Nd^{3+}, Ce^{3+}, Er^{3+} etc. belong to the most studied laser and scintillator crystals [1-4]. Yttrium orthoaluminate (or yttrium aluminium perovskite (YAP)) is studied for more than 25 years and, especially scintillator applications of this crystal (YAP:Ce^{3+}) appears more significant during last years. YAP:Ce^{3+} multidetector arrays are tested in SPECT cameras [5] and another perovskite crystal $LuAlO_3$:Ce [6] appears as promising scintillator for positron emitting tomography (PET medical imaging). Generally, for characterisation of impurities in the crystals various methods are used as luminescence and scintillation studies [2,4], electron microanalysis [4] and also electron paramagnetic resonance (EPR) [7].

EPR is the effective method for the detailed studies of structure, lattice location and charge state of point defects and impurities in the crystals. Up to now this method was rarely used for studies of RE^{3+}-doped YAP crystals. Only EPR spectra of Cr^{3+}, Fe^{3+} and Gd^{3+} in YAP were reported in the papers [7,8]. The aim of this paper is to show the results of detailed measurements on YAP:RE^{3+} crystals and to interpret them by the presence of Er^{3+}, Nd^{3+} and Ce^{3+} in YAP lattice. Especially, Ce^{3+} EPR spectra are correlated with the luminescence studies of YAP:Ce crystals where various nonequivalent centres are observed [4].

2. EXPERIMENT AND SAMPLES

Single crystals YAP doped with Ce^{3+} and containing also other trace impurities as Er^{3+}, Nd^{3+}, Cr^{3+}, Fe^{3+} and Mo^{3+} have been studied by EPR method. The concentrations of Ce^{3+} and some of other uncontrolled impurities were determined by EMA method [4]. In the studied crystals, Ce^{3+} ions were found from trace concentrations up to ~0.3 at. %. Er^{3+} and Nd^{3+} concentrations are less than ~0.01 wt. %. The crystals were grown either by Czochralski method in Mo crucibles (by Preciosa Crytur Ltd. in Turnov, Czech Republic) or by the

Proc. Int. Conf. on Inorganic Scintillators and Their Applications, SCINT95,
1996, Delft University Press, The Netherlands

Bridgman horizontal one again in Mo crucibles (by VNIISIMS in Alexandrov, Vladimir Region, Russia). The EPR measurements were performed at 9.24 Ghz in a standard EPR spectrometer in temperature range 4 - 77 K. An Oxford Instruments ESR-9 cryostat system was used.

YAP single crystals samples for EPR studies were carefully cut along [100], [010] and [001] crystallographic axes (after orientation by x-ray roentgenographic analysis with an accuracy up to 0.5^0 for all three lattice axes). The dimensions of the samples were 1.5 x 2 x 5 mm^3. Angular dependences of EPR spectra were carried out in all the main crystals planes (001), (010) and (100).

3. RESULTS AND DISCUSSION

The example of EPR spectrum of YAP crystal containing Er^{3+}, Nd^{3+} and Ce^{3+} ions is presented in Fig. 1 for magnetic field of parallel orientation to the crystallographic axis [100]. As an example of HF structure of Er^{3+} is also shown (see inset of Fig. 1). The weak, wide resonance line at ~280 mT can be assigned to the Mo^{3+} ion. Comparison of the hyperfine component intensities and splitting of observed EPR spectrum of YAP crystal corresponds to the natural abundance of individual ions, their nuclear spins and magnetic moments. Hyperfine structure of the EPR spectrum is generally nonequidistant for both Er^{3+} and Nd^{3+}. The single intense line without hyperfine structure (with two magnetically nonequivalent positions) with extremaly small g factors components in the [100] and [010] directions (0.395, 0.338, respectively) can be attributed to Ce^{3+} ions occupying Y^{3+} positions in YAP single crystals, because the correlation between cerium concentration and EPR line intensities is observed. In Fig. 2 experimental and fitted angular dependences of EPR spectra of Er^{3+}, Nd^{3+} and Ce^{3+} ions are shown. These spectra can be fitted by spin Hamiltonian of rhombic symmetry. The directions of Er^{3+}, Nd^{3+} and Ce^{3+} centres are oriented in such a way that their y axes are parallel with crystal axes [001] while z and x axes are lying in the plane (001).

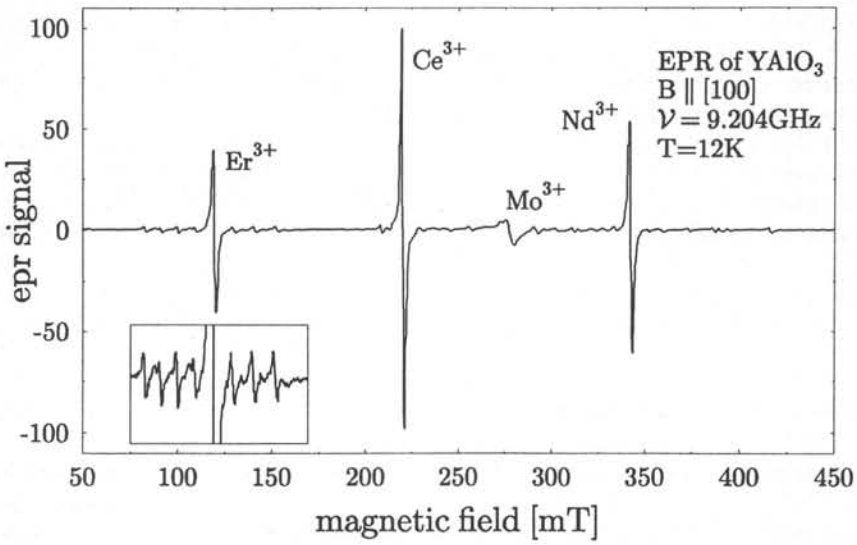

Fig. 1. An example of the EPR spectrum in $YAlO_3$. **B** | [100], n = 9.24 Ghz, T = 12 K (inset - the HF structure of Er^{3+} is displayed).

Ce^{3+} EPR spectrum exhibits no HF structure but other lines (having their intensities 100 - 1000 times in magnitude weaker in comparison with the main lines) are observed around the main lines. Angular dependences of these weaker EPR lines are similar to the main ones. Weak EPR lines grouped around two main magnetically inequivalent lines of Ce^{3+} centres are interesting namely in connection with already reported existence of inequivalent Ce^{3+} centres in YAP lattice in luminescence studies [4]. These "satellite" lines can be in our case also ascribed to Ce^{3+}-based centres on similarity of (i) g factors, (ii) angular dependences and (iii) the linewidth of resonant lines of the main and satellite lines. Satellite line intensities are 100 - 1000 times smaller than that of the main line and their all three magnetic axes show rather small departures from the directions of equivalent axes of the main Ce^{3+} centres. We interpret these centres as defect-related Ce^{3+} centres induced by another local distortion of the crystal field. The most probable is situation at which Al^{3+} ion is positioned at Y^{3+} site next to the substituted Ce^{3+} centre. Such effects was already reported for EPR studies of YAG:Ce crystal. Similar effects are not observed for Er^{3+} and Nd^{3+} ions.

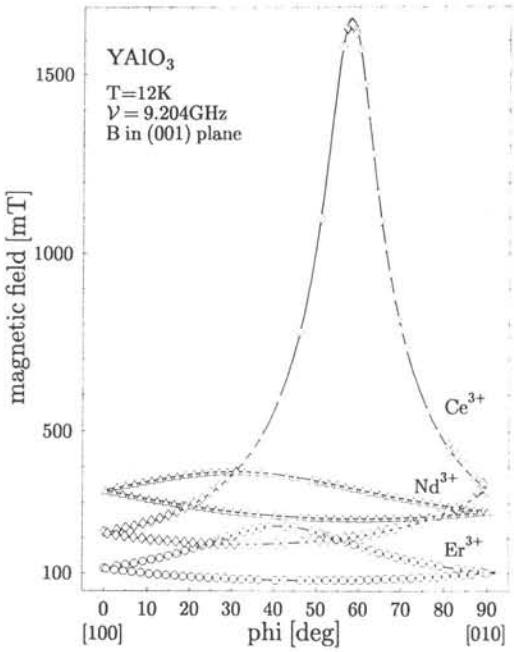

Fig. 2. The angular dependence of RE^{3+} resonance fields in $YAlO_3$, **B** in the (001) plane. n = 9.24 Ghz, T = 12 K. Circles, diamonds and triangles - measured data for different RE^{3+} ions, smooth lines - calculations.

Besides the two above mentioned spectra of Ce^{3+}-related centres, we have observed the third, relatively intense, type of Ce^{3+}-related resonances, study which are in progress. The intensity of these Ce^{3+}-related lines is a few tenths of the whole intensity of Ce^{3+}-related spectra. This value gives an estimate of the ratio between nonequivalent and main Ce^{3+}-centres concentration and seems to be higher than the number derived from the luminescence spectra in (one tenth [4]).

REFERENCES

[1] A.A. Kaminskii, Laser crystals (Moscow, Nauka, 1975).
[2] G. Blasse, Chem. Mater. 6 (1994) 1465.
[3] M. Ishii and M Kobayashi, Prog. Cryst. Growth Char. Mat. 23 (1992) 245.
[4] J.A. Mareš, M. Nikl, C. Pedrini, B. Moine and K. Blažek, Mat. Chem. Phys. 32 (1992) 342.
[5] R. Pani, F. de Notaristefani, K. Blažek and P. Malý, private communication.
[6] J.A. Mareš, M. Nikl, J. Chval, I. Dafinei, P. Lecoq and J. Kvapil, Chem. Phys. Lett. 241 (1995) 311.
[7] A. Abragam and B. Bleany, Electron paramagnetic resonance of transition ions (Clarendon Press, Oxford 1970).
[8] J.P. van der Ziel, F.R. Merrit and L.G. Van Uiterit, J. Chem. Phys. 50 (1969) 4317.

LUMINESCENCE OF Ce OR Pr DOPED GADOLINIUM ORTHO-ALUMINATE AND CERIUM ORTHO-ALUMINATE CRYSTAL FIBERS GROWN BY THE LASER HEATED PEDESTAL GROWTH METHOD

J.W.M. Verweij, C. Madej, H.L. Lautesse, C. Pedrini, B. Moine, M.Th. Cohen-Adad and G. Boulon, Laboratoire de Physico-Chimie des Materiaux Luminescents, Universite Claude Bernard Lyon I, Unite de Recherche associee au CNRS n° 442, Bât 205, 69622 Villeurbanne cedex, France

ABSTRACT. $GdAlO_3$:Ce (GAP-cerium) crystals are compared with crystalline fibers of the same chemical composition. We have grown these fibers with the Laser Heated Pedestal Growth (LHPG) technique. For comparison we have also grown undoped $GdAlO_3$, $GdAlO_3$:Pr and $CeAlO_3$ crystalline fibers. These last two also prove to be very interesting: the Pr^{3+} ion shows luminescence due to a 5d - 4f (dipole allowed) transition like Ce^{3+} and consequently this luminescence is fast. $CeAlO_3$ does not show the problems that often hamper crystals with a Gd-sublatice: energy migration to impurities is much lower in this crystal than it is in the GAP-cerium crystal. Furthermore the density penalty in going from Gd to Ce is relatively low. The potential of this material as an efficient scintillator crystal is therefore very good.

INTRODUCTION

In the search for efficient and fast scintillation crystals $GdAlO_3$:Ce(GAP-cerium) is one of the latest members of the Rare-earth/Alumina mixed compounds to gain considerable interest. A fair amount of research has already been conducted on this material [1,2,3], but not all properties are known [3]. The crystalgrowth of R.E.-ortho aluminates is also still relatively troublesome. Because of this, we have used the LHPG method to grow a number of fibers. Ce and Pr doped $GdAlO_3$ fibers are grown now without difficulty. Undoped $GdAlO_3$ and $CeAlO_3$ are grown also but not yet with the same success. The fibers are single crystal but contain one or more impurities, which (severely in the case of $CeAlO_3$) hamper the luminecence of these fibers. It is to our knowledge the first report of the growth of a single crystal of $CeAlO_3$. It is also the first time we tried to grow these fibers and because of this we are optimistic about further results.

EXPERIMENTAL METHODS.

The single crystal fibers of Gadolinium ortho-aluminate were grown by the laser-heated pedestal growth (LHPG) method. This technique is developed in 1975 [4] and it is now a well established technique for the growth of single crystal fibers (SCF). The fibers where grown as described before [5].

Proc. Int. Conf. on Inorganic Scintillators and Their Applications, SCINT95, 1996, Delft University Press, The Netherlands

Preparation of feed rods for the LHPG of $GdAlO_3$ fibers began by weighing stoichiometric amounts of Gd_2O_3(Cerac, 99,9 %), Al_2O_3 Cerac, corundum -325 mesh, 99,99 %) and dopant (CeO_2 Alpha Products 99,9 % or Pr_2O_3 Cerac 99,9 % -325 mesh) to a total of ~ 25 grams. About 0.5% (weight) Chemplex Spectroblend briquetting agend was added and this mixture was ground in a ball mill for 15 minutes. The powder was then cold pressed into 25 mm diameter pellets of appropriate thickness and fired in air at 150^0C for 1 hour 650^0C for 3 hours and 1450^0C for 6 hours followed by slow cooling. From the resulting hard pellets square feed rods of 2.5 X 2.5 mm could easily be cut with a diamond saw. The powders which could not be fired with a briquetting agent ($CeAlO_3$ grown in this series of fibers for comparison can not be fired in air or any atmosphere that containes the smallest amount of oxygen: if such an atmosphere is used it decomposes to CeO_2 and Al_2O_3) posed some more problems. After mixing and milling the mixture was fired in either $Ar/5\%H_2$ or $80\%N_2/20\%H_2$ at 1450^0C untill X-ray powder diffraction showed the sample to be single phase. Then the powder sample was poured in a latex tube of 3 to 4 mm diameter which after sealing was pressed in a hydrostatic press with a pressure of 800 to 1500 bar. The resulting feed rods were not as hard as the sintered rods and not of constant diameter but since they did not have to be cut this was not a major problem. Fibers could be grown of reasonable stable diameter (~ 2 mm) after which a second pull further improved the quality. This system is currently being improved in order to minimalise the contamination problems of crystals grown at high temperatures.

The structure of the fibers was verified by X-ray powder diffraction.

Roomtemperature excitation and emission spectra and lifetime measurements were made at the SuperACO positron storage ring of LURE (Orsay University) using synchrotron radiation in the range of 4 to 120 eV and a pulse width of ~ 0.1 ns. Absorption and emission spectra at various temperatures and better resolution were made using conventional laser and spectrophotometer equipment.

RESULTS

Spectra of the undoped $GdAlO_3$ fibers show that the ^8S to ^6I and the ^6P to ^8S excitation and emission transitions do not differ from those observed earlier for bulk grown crystals [6] and crystalline powders [7]. The speed with which the fibers are grown does not seem to influence the energy levels of the incorporeted luminescent ions. However an additional broad band is observed in the excitation spectrum and there is a corresponding band in the emission spectrum. The origin of this transition is not yet clear.

Spectra of the GAP-cerium fibers and bulk grown crystals are almost exactly the same. Absorption and excitation spectra show no differences for the Ce^{3+} 4f to 5d transition. However time resolved excitation and emission spectra show some small differences. With a short gate time, the excitation bands of the

crystalline fibers are shifted a bit to a higher energy, while with a longer gate time the emission band is shifted to lower energy compared to the bulk grown crystals. From this we conclude that the crystalline fibers contain more Ce^{3+} ions on distorted sites than the bulk grown crystals. This is a result of the speed with which the crystalline fibers are grown (up to 90 mm/hour). No additional excitation or emission bands are observed in the Ce-doped crystalline fibers.

The emission spectrum of $GdAlO_3$:Pr shows three broad bands. These bands correspond to transitions from the lowest crystal-field component of the 4f5d configuration to the ^3H_J and the ^3F_J levels. In the visible some emission lines are observed: these are due to transitions of the ^3P and ^1I levels to the $^3H_4$ ground state. The absorption spectrum shows that the f-d absorption band edge is at around 44.000 cm^{-1}. At lower energy the Gd^{3+} absorption lines are observed superimposed on a broad absorption band (possibly Ce^{3+}). These absorptions distort the emission spectrum because they are situated in the Pr-emission band, but the spectra correspond well with measurements done earlier on $YAlO_3$:Pr [8]. Therefore we think it is fair to estimate the Stokesshift at 1600 cm^{-1} and the decay time at certainly less than 10 ns.
Next to the broad absorption band (which is possibly Ce^{3+}) no other bands are observed in the emission spectra.

The spectra of the $CeAlO_3$ fibers are a bit more complex. The absorption spectrum of an undiluted material like this would of course not show different bands because of the strength of the absorption transition of Ce. However, the spectra made of a 0.5 mm thick sample show a band with the absorption edge at the longer wavelength side at ~ 490 nm. This is not an absorption band of the Ce^{3+} ion. We do not know the nature of the absorption transiton but it has also been observed in $GdAlO_3$:Ce powder [9] and the intervalence charge transfer transition between Ce^{3+} and Ce^{4+} [10] is a strong possibility. As a result of this very strong absorption we had some difficulty studying the underlying Ce^{3+} excitation and emission bands. Upon excitation at ~ 260 nm we observed a Ce^{3+} emission band with a maximum at 308 nm. We also observed a band with a maximum at 440 nm. Excitation spectra of this band and the Ce^{3+} band at 308 nm are clearly different, but they are overlapping each other. The emission band at 440 nm resembles the anomalous emission band observed earlier in the undoped $GdAlO_3$ fibers. Unfortunately it is not possible to compare the corresponding excitation spectra of both bands because in the $CeAlO_3$ fiber this excitation band is obscured by both the Ce^{3+} excitation band and the (possible) Ce^{3+} to Ce^{4+} intervalence charge transfer transition.

However we consider this material, $CeAlO_3$, a promising material for further study of the scintillating mechanisms in Rare Earth ortho-aluminates. The emission of Ce^{3+} is at a relatively high energy and the Stoke shift is small (2800 cm^{-1}). This means an efficient luminescence from this material is very well possible. It will also have a short decay time. Next generations of $CeAlO_3$ crystals will doubtlessly be of better quality and these

will enable us to compare the luminescenc of this material in more detail with other Ce-doped R.E.-aluminates.

DISCUSSION AND CONCLUDING REMARKS

Comparison of GAP-Ce crystalline fibers and bulk grown crystals shows that the fibers are less perfect crystals than the bulk grown ones. The effect of the difference in crystal quality however is not of great importance, because the luminescence data are almost exactly the same. The Gap-Pr fiber shows very promising results and should be studied more intensely in the future. The data of the undoped $GdAlO_3$ And $CeAlO_3$ fibers are more troublesome. Considering however that the precise stoichiometry of these crystals is not yet known, these first results are promising and since the impurity is most probably an excess of one of the components we think that this can be resolved easily. Particularly because we employ the fast (and also cheap) LHPG method.

REFERENCES

1] P. Dorenbos, E. Bougrine, C.W.E. van Eijk and M.V. Korzik, presented at the 'Eurodim 94' Seventh Europhysical Conference on Defects in Insulating Materials, July 1994, Lyon, France, to be published in Eurodim 94 conference proceedings in Radiation Effects Defects Solids.

2] J.A. Mares, M. Nikl, C. Pedrini, D. Bouttet, C. Dujardin, B. Moine, J.W.M. Verweij and J. Kvapil, presented at the 'Eurodim 94' Seventh Europhysical Conference on Defects in Insulating Materials, July 1994, Lyon, France, to be published in Eurodim 94 conference proceedings in Radiation Effects Defects Solids.

3] G. Blasse and B.C. Grabmaier in Luminescent Materials (Springer Verlag, Berlin, 1994) Ch. 9

4] C.A. Burrus and J. Stone J. Appl. Phys. 49, (1975) 318

5] A. Brenier, A.M. Jurdic. J.W.M. Verweij, M.T. Cohen-Adad and G. Boulon, submitted to Optical Materials.

6] J.A. Mares, C. Pedrini, B. Moine, K. Blazek and J. Kvapil Chem. Phys. Letters 206 (1993) 9

7] A.J. de Vries, W.J.J. Smeets and G. Blasse Mat. Chem. Phys. 18 (1987) 81

8] C. Pedrini, D. Bouttet, C. Dujardin, B. Moine, I. Dafinei, P. Lecoq, M. Koselja and K. Blazek Optical Materials 3 (1994) 81

9] J.W.M. Verweij, M.Th. Cohen Adad, D. Bouttet, H. Lautesse, B. Moine and C. Pedrini Chem. Phys. Letters 239 (1995) 51

10]W. van Schaik, S. Lizzo, W. Smit and G. Blasse J. Electrochem. Soc. 140 (1993) 216

Fluorescence and scintillation properties of Cerium doped Lutetium orthoaluminate

C.Dujardin, C.Pedrini, D.Bouttet, J.W.M. Verweij
Laboratoire de Physico-Chimie des matériaux Luminescents, Université Claude Bernard Lyon1, Unité de Recherce associée CNRS n°442, bat 205, 69622 Villeurbanne cedex (France)
A.G.Petrosyan
Institute for physical research, Armenian National Academy of Science
378410 Ashtarak-2 (Armenia)
A.Belsky, A.Vasil'ev
Synchrotron Radiation Laboratory, Physics Department, Moscow State University, 119899 Moscow (Russia)
E.I.Zinin
Budker Institute of Nuclear Physics, Novosibirsk (Russia)
P.Martin
LURE, Bât. 209D, Centre Universitaire Paris-sud, 91405 Orsay (France)

Abstract

Optical and V.U.V. spectroscopy has been performed on an orthoaluminate $LuAlO_3:Ce^{3+}$ crystal grown using the Bridgman technique. The analysis of the excitation spectra, as well as the decay time in the V.U.V. region up to 50 eV, allow us to describe the main processes of scintillation involved in this crystal.

-I- Introduction

Scintillating materials have a variety of applications. Some of them, such as medical imaging techniques P.E.T. need scintillating materials with high light yield, fast decay time and high density to get a high stopping power. For fast scintillation, cerium activated materials are good candidates due to the electric-dipole allowed transition d-->f of the Ce^{3+} [1]. $YAlO_3:Ce^{3+}$ gives rise to a high light yield around 26000 photons/Mev but its density is only 5.35 g/cm^3. Substition of Y to Lu increases the density to 8.34g/cm^3 and the first measurements on this crystal gave rise to very good properties for scintillation application [2,3].

Results and discussion

The experimental details for data acquisition and crystal growth are describe in reference [4].

-optical spectroscopy

Proc. Int. Conf. on Inorganic Scintillators and Their Applications, SCINT95,
1996, Delft University Press, The Netherlands

In figure 1 are pictured absorption and emission spectra of the LuAlO3:Ce^{3+} crystal. The absorption gives rise to 3 peaks in the range between 260 and 320nm. These 3 peaks are connected to the transion 4f-->5d (3t2). We cannot see the other 2 peaks coming from the transition 4f-->5d (2e) because of the strong increase of the absorption coefficient even using very thin sample (270µm). This band is identified between 250nm (5 eV) and 210nm (6 eV) using excitation measurements (figure 2). At 360 nm, the absorption coefficient is not zero while no luminescence of Ce^{3+} is detected. This phonomenum is probably connected to Ce^{4+} presence [5]. Fluorescence spectra under U.V. excitation (290nm) give rise to two non-resolved band at room temperature (figure 1). These two bands are characteristic from the spin orbit splitting of the 4f Ce^{3+} ($^2F_{7/2}$ and $^2F_{5/2}$ separated by roughly 2000 cm^{-1}). This crystal does not contain any garnet phase in accordance with the X-ray diffraction measurements.

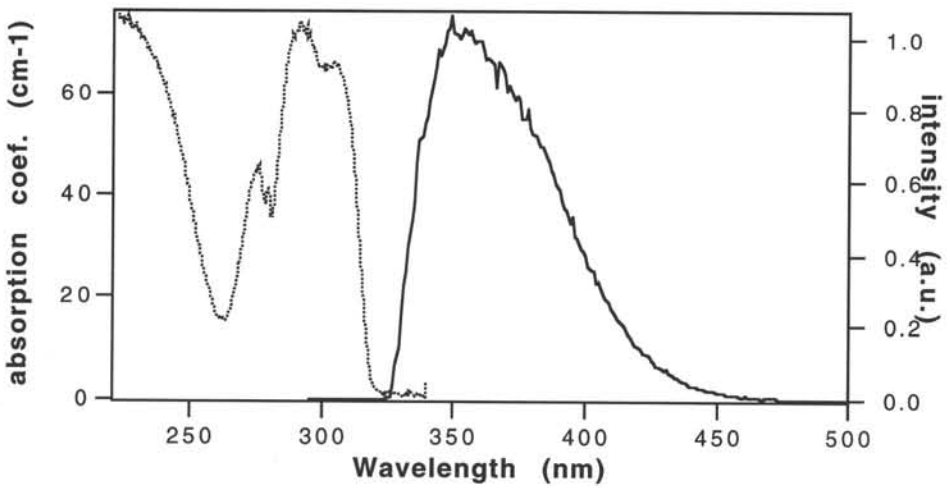

Figure 1: Absorption at liquid helium temperature (dash line) and emission at room temperature (exc 290nm, solide line) on LuAlO3:Ce^{3+}

- Mechanisms and kinetics

Excitation as well as absorption spectra from 4 eV up to 50 eV are shown in figure 2. The kinetics for several excitations from 4 eV to 40 eV are plotted in figure 3.

The excitation spectra exhibits two bands between 3.5 and 6 eV corresponding to intracenter mechanisms, which have been discussed above. The decay time in this region (4.6 eV) is a single exponential with a time constant around 19 ns. The region between 6 and 7 eV accounts for charge transfer from 4f(Ce^{3+}) to 5d(Lu^{3+}). Excitaton formation and valence band to conduction band transitions are expected above 7 eV. A strong increase of the light yield is observed at the fundamental absorption edge. At this energy, the exciton or closed electron-hole pairs are created which result in energy transfer to Ce^{3+}. For excitation energy between Eg and 2Eg, a hot hole or hot electron is created which can migrate by forming a separated

electron-hole pair. When the energy gap between the fundamental of the activator and the top of the valence band is large (several eV) hole trapping is forbiden and the light yield drops to zero which was observed with CeF_3 [6]. In $LuAlO_3:Ce^{3+}$, the light yield does remain quite high which means that the hole trapping is efficient. This confirms fully our XPS measurements performed on $LuAlO_3$ and $CeAlO_3$ which allow us to estimate the energy distance between $4f(Ce^{3+})$ and $2p(O^{2-})$ to be approximately 1 eV [7]. The situation is very similar with the electron trap. In doped crystal the migration of e^- and h^+ leads to a slow component in the kinetics. At 8.7 eV the lifetime measurement exhibit a slow component. The maximum efficiency is at 7.9 eV which is close to the exciton formation region. It means that the probability of tranfer to Ce^{3+} is greater from the exciton or close electron-hole pair than from separated electron-hole. For this energy, the kinetic does not exhibit any rise time. The rise time appears for excitation at 12 eV. For XPS measurements, we located the begining of the 4f (Lu^{3+}) around 3.7 eV below the top of the valence band. An excitation of 12eV is then able to excite an electron from the 4f (Lu^{3+}) to the conduction band. Then the migration of the hole to a Lu^{3+} near a Ce^{3+} leads to an Auger process where the hole is filled by the 2p (O^{2-}) electron with simultaneous excitation of the Ce^{3+} ion. For higer energy excitation, the anticorrelation between the excitation and the absorption (due to the diffusion of the excitation to the surfac) make the interpretation of the excitation shape difficult (figure 2). Nevertheless, we observe a strong increase of the light yield at 18 eV which can be correlated to the multiplication process. The plateau at 25 eV match well with an excitation from a $2s(O^{2-})$ and $5p(Lu^{3+})$ to the conduction band. The increase of the light yield for energy larger than 40 eV is clearly connected with the multiplication process since no core level are involved before 60 eV $(6s(Lu^{3+}))$.

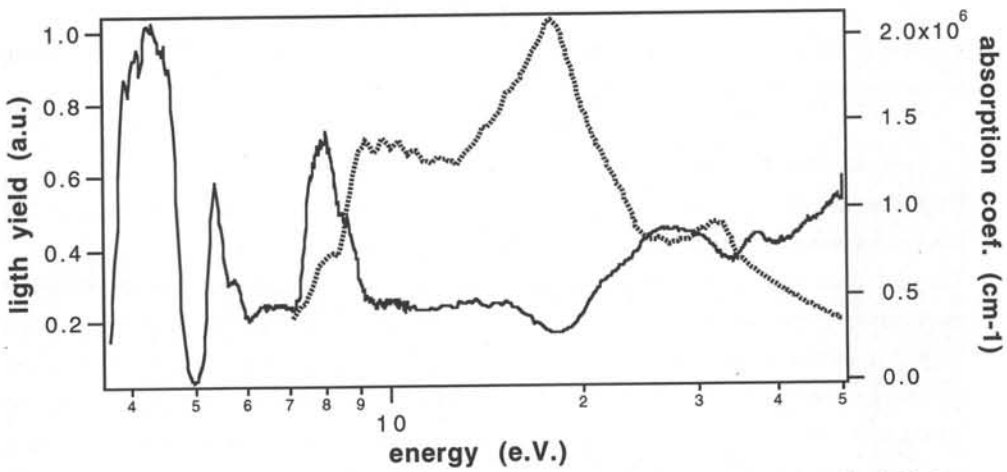

Figure 2: Excitation spectra (emission 380nm, solid line) and absorption spectra (dash line) at room temperature on $LuAlO3:Ce^{3+}$

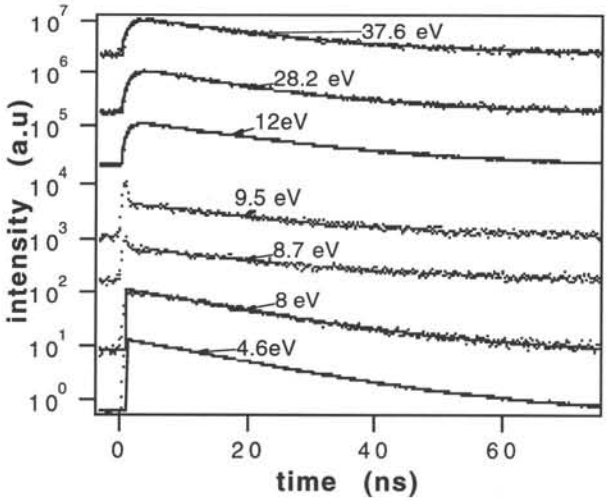

Figure 3: Kinetics measurements on $LuAlO_3:Ce^{3+}$ at room temperature (dots) and best fits obtained (solid line)

- Light yield measurement

The light yield measurement on a rectangular crystal (0.45x0.45x0.9 cm^3) using 511 keV excitation gave rise to around 8200 photons / MeV which is much lower than the light oupout of 32000 photons / MeV obtained by Lempicki et al.[3].

Conclusion

Using XPS and optical spectroscopy we located the core level, as well as the position of the Cerium level in the forbidden band. The carefull analysis of the excitation spectra and the kinetics allow us to identify the processes for those excitation. More work needs to be done with coincidence fluorescence to determine the multiplication threshold. This work is currently in progress.

Refrences

[1] M.J.Weber, To be published in the proceedings of the V International Conference on Calorimetry in high energy physics

[2] W.W.Moses, S.E.Derenzo, A.Fyodorov, M.Korzhik, A.Gektin, B.Minkov and V.Aslanov, IEEE Trans. Nucl. Sci. NS-42 (submitted for publication)

[3] A.Lempicki, M.H.Randles, D.Wisnieswski, M.Balccerzyk, C.Brecher and A.J.Wojtowicz, IEEE Trans. Nucl. Sci. NS-42 (submitted for publication)

[4] C.Dujardin, C.Pedrini, D.Bouttet, J.W.M. Verweij, A.G.Petrosyan, A.Belsky, A.Vasil'ev, E.I.Zinin and P.Martin, IEEE Trans. Nucl. Sci. (submitted for publication)

[5] E.G.Gumanskaya, O.A.Egorycheva, M.V.Korzhik, S.A.Smirnova, V,B.Pavlenko and A.A.Fedorov, Opt.Spectrosc. (URSS) 72 (1992) 215

[6] C.Pedrini, A.M.Belsky, A.N.Vasil'ev, D.Bouttet, C.Dujardin, B.Moine, P.Martin and M.J.Weber, Materials Research Society Symposium Proceedings, vol.348 (1994) p.225

[7] D.Bouttet, C.Dujardin, C.Pedrini, W.Brunat and D.Tran Minh Duc, this conference

Cerium-Doped Aluminate Scintillators

A. Lempicki [*], C. Brecher [*], D. Wisniewski [*†] and E. Zych [*°]

[*] *Dept. of Chemistry, Boston University, Boston, MA 02215*
[†] *Inst. of Physics, N. Copernicus University, Torun, Poland*
[°] *Dept. of Chemistry, Wroclaw University, Wroclaw, Poland*

Abstract

The present status of the $LuAlO_3$:Ce (LuAP) scintillator is reviewed and its performance compared to that of $YAlO_3$:Ce (YAP). The light output of LuAP, at this stage of development, appears to be limited by two factors: insufficient Ce concentration and the presence of a parasitic absorption. Both LuAP and YAP show a dependence of light output on thickness, indicating that YAP also suffers from parasitic absorption.

Introduction

While the scintillation properties of $LuAlO_3$:Ce (LuAP) crystals have been reported previously [1], the understanding of its behavior is still fragmentary at best. The interest in this material derives from the high light yield of its analog $YAlO_3$:Ce (YAP). Substitution of Lu for Y, without changing the structure, substantially increases the density (from 5.55 to 8.34 g/cm^3) and shortens the decay time (from 24 to 18 ns). As reported in Ref. 1, the various optical spectra of LuAP are nearly identical to those of YAP, allowing the latter, with its longer history of development [2-5], to serve as a benchmark against which to measure its denser counterpart.

In the present paper we deal with two deficiencies of LuAP, namely the fact that its measured light output thus far is lower than has been observed in corresponding YAP samples, and that the actual value obtained is dependent on the dimensions of the specimens. Having discovered a similar size dependence in YAP, we claim that in absence of size information, the assignment of a single output value to either of these two materials is totally meaningless.

Materials and Experiments

The LuAP specimens on which we report were cut from boules grown by Litton Airtron by the Czochralski method, with Ce concentrations in the melt ranging from 0.25% to 1.5%. The crystals were optically clear, colorless and single-phase. The YAP samples were cut from a disk, also grown by the Czochralski method, by Union Carbide. The LuAP specimens were subjected to post-growth heat treatment at moderate temperatures (1200 C) in air, vacuum and Ar/H_2, the details of which will be published elsewhere. Light output measurements were performed by comparing photopeak positions with that of BGO, using a Cs gamma source. Emission spectra were taken under optical, γ-ray and X-ray (8 keV) excitation. Decays were obtained by the standard photon correlation method.

Results

Fig. 1 gives the emission spectra from two LuAP plates of different thickness, excited by 8 keV X-rays from one side and measured by an integrating detector from the other side. The penetration depth of the X-rays is estimated to be on the order of 10 microns, so that the emitted light traverses an essentially unexcited crystal before being detected. Note first that as the thickness increases the spectrum shifts to longer wavelength, the material acting as an optical filter. At wavelengths between 330 and 370 nm, the differences between the light signal from the thin (1.0 mm) and thick (5.2 mm) samples were used to derive an effective absorption coefficient, which is plotted in the insert and compared with the absorption actually measured. The excellent agreement between measured and derived

Proc. Int. Conf. on Inorganic Scintillators and Their Applications, SCINT95,
1996, Delft University Press, The Netherlands

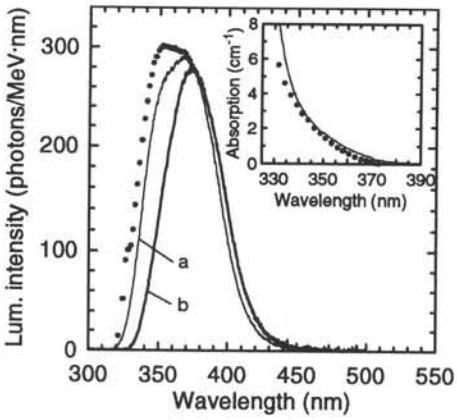

Figure 1. Emission spectrum of $Ce_xLu_{1-x}AlO_3$ (LuAP, $x=0.0011$), excited by 8 keV X-rays, as function of thickness: (a), 1.0 mm; (b), 5.2 mm. Dotted curve shows emission corrected to remove parasitic absorption. Insert shows measured (solid) and calculated (dotted) absorption profiles.

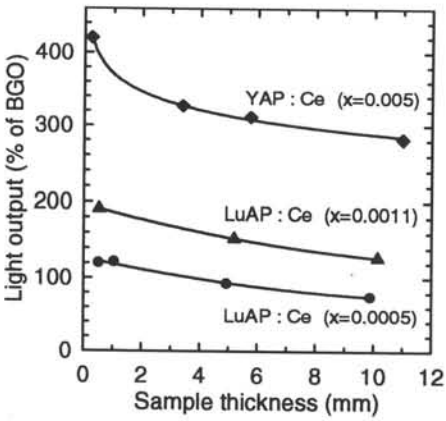

Figure 2. Measured light output of cerium-doped LuAP and YAP under γ-excitation, as function of sample thickness. Note also the scaling with atom fraction of Ce (x), with the measured value in YAP more than four times that in the higher LuAP specimen.

absorption curves confirms that the major part of the thickness-dependent spectral variations can be explained as an absorption effect. Thus, by using this absorption coefficient we can correct the emission of the 1.0 mm sample to what it would be if the absorption were not present. This is shown on the main figure by the dotted curve. The remarkable consistency of these results offers strong presumptive evidence that the loss of light output with thickness is a direct result of the tail of the absorption, between 320 and 370 nm. Although some absorption remains even in the thinnest specimen, the maximum light output measured on such specimens is a good representation of what can be expected from LuAP if the absorption could be removed. Note also that the light output under γ excitation, shown on Fig. 2, indicates a similar thickness dependence, although necessarily less pronounced since in the latter case the light is emitted throughout the bulk of the specimen.

The source of the absorption is far from clear. One possibility is self absorption by Ce. However, while this could have a similar effect on the *shape* of the spectrum, it should not cause a loss of *total light output*, instead simply shifting intensity from the short to the long wavelength components of the Ce doublet, as is the case in CeF_3 [6,7]. This is contrary to the results shown in Fig. 1, where the total light emitted by the 5.2 mm specimen, as measured by the area under the curve, is more than 15% smaller than that from the 1.0 mm specimen. This is true despite the fact that the spectrum of the thicker specimen shows a small *increase* in intensity above about 380 nm. This "gain" of light output at the longer wavelengths serves as an indication of the upper limit of possible self absorption, which comes out at least an order of magnitude less than the total absorption actually observed. Moreover, any greater amount would necessarily cause a substantial and measurable lengthening of decay times with increasing thickness. This is not observed for any thicknesses ranging from 1 to 17 mm.

We did not have the opportunity to perform similar X-ray measurements on YAP, nor are we aware of any comparable study of light output *vs* thickness. However, under bulk excitation from a Cs γ source a pronounced shift of the emission spectrum to lower energies, similar to that in LuAP, was observed for the thicker YAP specimens as well. Moreover, as seen in Fig. 2, the light output from YAP shows a similar dependence on thickness.

(To allay any suspicions of a systematic experimental error, similar measurements performed on comparable plates of BGO showed no thickness dependence whatever.) Note that for the thinnest sample, the light output of YAP amounts to a phenomenal 420% of BGO, significantly higher than has ever been reported in the literature [4]. Taking this as a benchmark, the portents for LuAP are favorable indeed.

Seeking to ascertain why the light output of YAP is so much higher for all thicknesses, we performed mass-spectrometric analyses of the crystals. The dependence of light output on the Ce concentration (as atom fraction relative to lutetium) is shown on Fig 3. The fact that in the YAP specimen the cerium content is more than four times higher than in LuAP, must be at least part of the answer. Note also that the shape of the curve suggests that even somewhat higher output is achievable, reaching saturation in the vicinity of $x = 0.01$.

In Fig. 4 we explore the feasibility of using the intensity of the absorption at 300 nm, close to the maximum of the first *4f - 5d* transition in Ce^{3+}, as a measure of the real Ce^{3+} concentration. Since the oscillator strengths of the transition are different in the two materials, it is necessary to correct the YAP value (open circle) by multiplying by the ratio of the decay times of the corresponding emission. The resulting linear relationship confirms the validity of using the absorption as a concentration monitor. Note that the true concentrations, as measured, indicate that only some 10% of the Ce concentration in the melt actually becomes incorporated into the LuAP lattice.

It is a remarkable fact that for both YAP and LuAP the excitation spectra go to zero at 250 nm but the absorptions do not [1,3,5]. This provides a clear indication of the presence of an unwanted absorbing species, variously interpreted as due to Ce^{4+} or other defects. Russian workers studying YAP report a correlation between the depth of the absorption valley at 250 nm and the light output [5,8], which they express in terms of a parameter *s*, defined as the ratio of the absorption constant at 310 nm (the peak of the first absorption band of Ce^{3+}) to that at 250 nm. The light output was shown to be a monotonic function of the parameter *s*, suggesting that the parasitic absorption may be simply the tail of a more intense absorption at shorter UV wavelengths, superimposed on the *4f* $\rightarrow$ *5d* Ce emission. We attempted and *completely failed* to find a similar correlation in LuAP, using a number of 1 mm samples, both as grown and after undergoing a variety of heat treatments. With $1.5 < s < 5$ we find a totally random collection of light outputs, between 110 and 260% of BGO. For the YAP crystal we find $s \approx 9$, but this high value is due mostly to the much stronger peak absorption at 300 nm rather than a lower value in the valley at 250 nm. At the present time *s* does not appear to be the proper parameter to

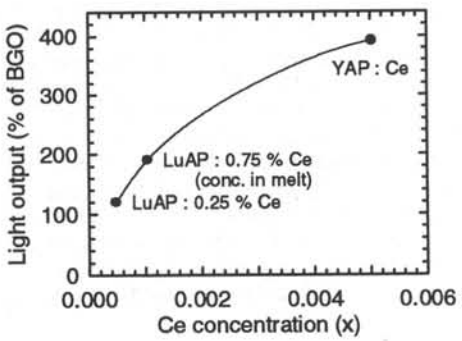

Figure 3. Light output of LuAP and YAP under gamma excitation, as function of Ce atom fraction (x). Curve suggests saturation at $x = 0.01$. Melt concentrations indicate a distribution coefficient of only about 0.1.

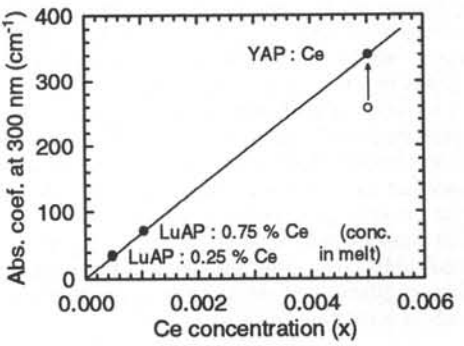

Figure 3. Intensity of 300 nm absorption in LuAP and YAP as function of Ce atom fraction (x). Open circle shows intensity before correction for oscillator strengths as indicated by decay time difference (see text).

describe the behavior of LuAP. Other factors, not describable by this parameter, evidently play a dominant role.

Conclusions

It is abundantly obvious that YAP and LuAP are in many respects almost identical materials. Both of them suffer from a parasitic absorption, suspected but not proved to be connected with Ce^{4+}. The presence of absorbing but non-emitting species in both is undeniable, and is the main cause of the thickness dependence of light output. The fact that in thin specimens YAP can achieve a light output of 34,000 photons/MeV, some 420% of BGO is very encouraging. If this intrinsic value, not much influenced by the parasitic absorption, could be obtained in larger size LuAP crystals, such a scintillator would have no peer. Future efforts must therefore be directed at increasing the Ce^{3+} concentration and the reduction of the parasitic absorption.

While we can make the general statement that heat treatments of LuAP, whether in oxidizing or reducing atmospheres, can more than double the light output, the reasons are as yet undetermined. It is possible that correlation with the parameter *s* is simply obscured by the low light output and will become more evident when the concentration of Ce is increased. It is noteworthy too that we found no evidence of phase instability at temperatures above 1200 C. While heating can introduce a milky appearance to the samples, we found this to be merely a thermal etching of the surface, readily removed by polishing.

Acknowledgments

We thank. C. W. E. Van Eijk and his group for their hospitality and assistance in performing the X-ray experiments in Delft; A. J. Wojtowicz for discussions and arranging the visit of one of us (D. W.) to Delft; and M. Kokta of Union Carbide Corp. for providing the YAP crystal. We acknowledge the support of the US Dept. of Energy, Grant DE-FG-02-90ER61033, and the European Economic Community, Grant ERBCIPDCT940037.

References

[1] A. Lempicki, M. H. Randles, D. Wisniewski, M. Balcerzyk, C. Brecher, and A. J. Wojtowicz, 1995: "$LuAlO_3$:Ce and Other Aluminate Scintillators", *Conference Record, IEEE Nucl. Sci. Symp. & Med. Imag. Conf.* (Norfolk VA, USA, Oct. 1994), pp. 307 - 311.

[2] V. G. Baryshevsky, M. V. Korzhik, V. I. Moroz, V. B. Pavlenko and A. A. Fyodorov, 1991: "$YAlO_3$:Ce: Fast-Acting Scintillators for Detection of Ionizing Radiation", *Nucl. Instr. & Meth.* **B58**, pp. 291 - 293.

[3] M. V. Korzhik, O. V. Misevich, and A. A. Fyodorov, 1992: "$YAlO_3$:Ce Scintillators: Application for X-Ray and Soft γ-Ray Detection", *Nucl. Instr. & Meth.* **B72**, pp. 499 - 501.

[4] W. P. Trower, 1994: "Cerium-Doped Yttrium Aluminum Perovskite (YAP): Properties of Commercial Crystals", *Scintillator and Phosphor Materials, MRS Symp. Proc.* (San Francisco CA, USA, April 1994). Editors: M. J. Weber, P. Lecoq, R. C. Ruchti, C. Woody, W. M. Yen, and R. Y. Zhu. Materials Research Society, Pittsburgh PA, USA. Vol. 348, pp. 131 - 136.

[5] E. G. Gumanskaya, O. A. Egorcheva, M. V. Korzhik, S. A. Smirnova, and E. B. Pavlenko, 1992: "Spectroscopic Properties and Scintillation Efficiency of Ce-Doped $YAlO_3$ Single Crystals", *Opt. Spectrosc.* **72**, pp. 215 - 217.

[6] A. J. Wojtowicz, M. Balcerzyk, D. Wisniewski, and A. Lempicki, 1994: "Scintillation Light Trapping and Radiation Damage in CeF_3", *IEEE Trans. Nucl. Sci.* **41**, pp. 713 - 718.

[7] A. J. Wojtowicz, M. Balcerzyk, E. Berman, and A. Lempicki, 1994: "Optical Spectroscopy and Scintillation Mechanisms of $Ce_xLa_{1-x}F_3$", *Phys. Rev. B* **49**, pp. 14880 - 14894.

[8] V. G. Baryshevsky, M. V. Korzhik, B. I. Minkov, S. A. Smirnova, A. A. Fyodorov, P. Dorenbos, and C. W. E. van Eijk, 1993: "Spectroscopy and Scintillation Properties of Cerium Doped $YAlO_3$ Single Crystals", *J. Phys.: Cond. Matter* **5**, pp. 7893 - 7902.

LUMINESCENCE AND SCINTILLATION MECHANISMS IN Ce^{3+}-DOPED $RE^{3+}AlO_3$ PEROVSKITE CRYSTALS

J.A. Mareš[1], M. Nikl[1], J. Chval[1], J. Kvapil[2], J. Giba[2] and K. Bla□ek[2]
[1]Institute of Physics, Czech Academy of Sciences, Cukrovarnická 10, 16200 Prague 6, Czech Republic.
[2]Preciosa Crytur Ltd., Palackého 175, 51119 Turnov, Czech Republic.

$RE^{3+}AlO_3$:Ce perovskite crystals are characterized by fast ($\tau \sim 10$ - 30 ns) Ce^{3+} fluorescence peaking in the UV between 300 and 400 nm. Here, we present the latest results of fluorescence and scintillation studies of new promising scintillator $LuAlO_3$:Ce. This crystal is characterized by fast fluorescence and scintillation decays (both lifetimes are $\tau \sim$ 17 ns) and also its light yield is high (up to 30000 photons/MeV). These results show that properties of $LuAlO_3$:Ce crystal are better in comparison with other perovskites $YAlO_3$:Ce and $GdAlO_3$:Ce.

1. INTRODUCTION

Modern applications of scintillators (medical imaging systems, new generation of energy calorimeters for high energy physics etc.) demand quite new or improved scintillating materials [1-3]. Ones of the most studied materials are either Ce^{3+}-doped or Ce^{3+}- concentrated ones as e.g. CeF_3 [4]. From various Ce^{3+}-doped crystal scintillators the most important and promising ones turn to be orthoaluminates as $YAlO_3$ [5], $GdAlO_3$ [6] and $LuAlO_3$ [7-9].

Ce^{3+}-doped lutetium orthoaluminate $LuAlO_3$:Ce (or lutetium aluminium perovskite, abbr. LuAP) is a new scintillator characterized by (i) high density (ρ = 8.34 g/cm^3), (ii) high light yield (up to 32000 photons/MeV [7]) and (iii) short fluorescence and scintillation decay time ($\tau \sim$ 17 ns) [9]. These properties can result in scintillator applications where fast timing and high counting rates, good energy resolution and stopping power are necessary as γ detection or PET systems [1,3,8]. The only disadvantage of $LuAlO_3$:Ce is a high cost of Lu but there are extrapolations that due to applications of Lu-compounds the price of Lu will decrease in the next years [8].

The presented paper summarizes and compares photoluminescence, x-ray excited luminescence and scintillation decays of various $LuAlO_3$:Ce crystals including Lu garnet phase. Properties of $LuAlO_3$:Ce are also compared with those of other perovskite ($YAlO_3$:Ce and $GdAlO_3$:Ce).

2. EXPERIMENTAL

$LuAlO_3$:Ce crystals were grown by the company Preciosa Crytur Ltd. in Turnov, Czech Republic by Czochralski method (the prepared boules were ~ 8 cm long and about 1.5 cm in diametr but they exhibit a tendency to cracking).

We have studied three different $LuAlO_3$ crystal samples, two of them were pure $LuAlO_3$:Ce ones having different Ce concentrations, the third one was $Lu_3Al_5O_{12}$:Ce garnet phase. Ce concentrations are ~ 0.04 at. % or ~ 0.16 at. % for two studied $LuAlO_3$:Ce crystals (sample 1 and sample 2, respectively) but the sample 2 contains ~ 9.3 at. % of Gd.

Proc. Int. Conf. on Inorganic Scintillators and Their Applications, SCINT95,
1996, Delft University Press, The Netherlands

Fluorescence spectra and decays of $LuAlO_3$:Ce crystals (and $Lu_3Al_5O_{12}$:Ce phase) were measured on the spectrofluorometer Model 199S Edinburgh Instruments [11]. Scintillation decay kinetics has been studied at CERN under β^+ Na^{22} excitation source using coincidence method of Bollinger and Thomas [12].

3. RESULTS AND DISCUSSION

Spectroscopic properties of $YAlO_3$:Ce and $GdAlO_3$:Ce are characterized by broad emission, excitation and absorption bands with emissions peaking in the near UV (5d $\rightarrow$ 4f transitions). We have studied these crystals and the most important results are given in [5,6] in details. Especially, $YAlO_3$:Ce scintillator has good light yield (~ 17000 photons/MeV) and is radiation hard [3,5] but its density is rather low (ρ = 5.35 g/cm^3). Now, the most promising scintillator seems $LuAlO_3$:Ce crystal.

Excitation and emission spectra of two variously Ce-doped $LuAlO_3$ crystals are presented in Figs 1 and 2, respectively. Ce^{3+} broad emission bands are peaking at $\lambda_p \sim 350$ nm (sample 1) and at $\lambda_p \sim 362$ nm (sample 2) under x-ray excitation at room temperature (RT). Additional narrow emission bands towards shorter wavelengths ($\lambda_p \sim 288$ nm and 308 nm) are observed on sample 1. Under photoexcitation, Ce^{3+} emission spectra of both $LuAlO_3$:Ce crystals are roughly the same peaking at ~370 nm at RT, but for $LuAlO_3$:Ce crystal (sample 2) Ce^{3+} ground state splitting is easily observable even at RT ($\delta \sim 1850$ cm^{-1}) while at LNT δ ~2070 cm^{-1}. Weak emission bands peaking either at $\lambda_p \sim 477$ nm (sample 1) or at $\lambda_p \sim 425$ nm (sample 2) are probably caused by Ce^{3+} inequivalent centres.

Ce^{3+} excitation spectra of $LuAlO_3$:Ce crystals are presented in Fig. 1 (curve a) and in Fig. 2 for λ_{em} = 370 nm and λ_{em} = 420 nm. The transitions to three Ce^{3+} excited energy levels (broad bands peaking at $\lambda_p \sim 305$ nm, $\lambda_p \sim 290$ nm and $\lambda_p \sim 275.4$ nm) are observed coinciding also with Ce^{3+} absorption spectra in $LuAlO_3$:Ce crystals. Two other weak excitation bands in the UV (positions $\lambda_p \sim 230$ nm and $\lambda_p \sim 210$ nm) could be also due to Ce^{3+} ions but the shape of the excitation spectra below 260 nm can be influenced by the overlap of several absorption bands caused by unwanted impurities (e.g. by Eu^{3+} emission of which was observed on $LuAlO_3$:Ce crystal sample 1 [9]).

Ce^{3+} fluorescence and scintillation decay curves mainly consist of fast and slow components. Ce^{3+} fast fluorescence decay component for λ_{em} =370 nm and spectrally unresolved scintillation decay are almost exponential with practically the same lifetimes $\tau_{uv} \sim 18$ ns and $\tau_{sc} \sim 17$ ns for $LuAlO_3$:Ce. However, besides the fast components we have also observed long parts of decays having lifetimes $\tau > 1$ μs [9] in the scintillation decay. Under UV excitation λ_{ex} = 280 nm for λ_{em} = 310 nm the very long decay time $\tau_l \sim 2.36$ ms was observed on sample 1. $LuAlO_3$:Ce crystal sample 2 exhibits also long decay components and its lifetime shortens from $\tau \sim 900$ ns at LNT to $\tau \sim 400$ ns at RT.

Gd^{3+} ion plays important role in $LuAlO_3$:Ce crystals. Two additional narrow emission lines in the UV peaking at $\lambda_1 \sim 287.5$ nm and $\lambda_2 \sim 308$ nm (see Fig. 1 curve b) are probably due to Gd^{3+} transitions $^6I_{7/2} \rightarrow {}^8S_{7/2}$ and $^6P_{3/2} \rightarrow {}^8S_{7/2}$, respectively. If we excite Gd^{3+} directly (into $^6I_{7/2}$ level at $\lambda \sim 280$ nm) we have observed for $\lambda_{em} \sim 310$ nm ($^6P_{3/2} \rightarrow {}^8S_{7/2}$ Gd^{3+} transition) long lifetime $\tau \sim 2.36$ ms which is typical Gd^{3+} fluorescence lifetime. Another indication of Gd^{3+} in trace concentrations in sample 1 are fluorescence and scintillation lifetimes [9]. Slow components ($\tau > 300$ ns or in the μs range) in the spectrally unresolved Ce^{3+} scintillation decay or in fluorescence decays are probably due to emission coming either separately from Gd^{3+} ions or due to $Gd^{3+} \rightarrow Ce^{3+}$ energy transfer. Gd^{3+} emission lines were not observed in the x-ray excited emission spectrum of $LuAlO_3$:Ce crystal sample 2 and this could be either due to

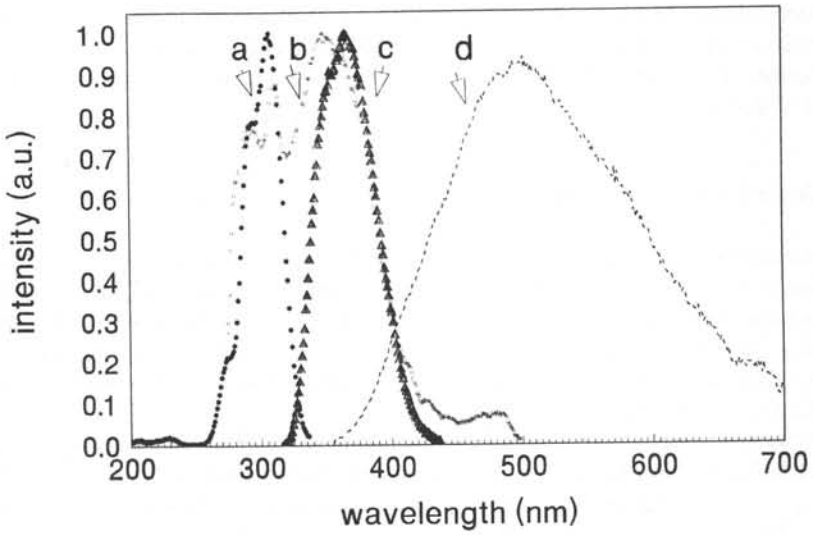

Fig. 1. Excitation (a) and emission (b,c) spectra of $LuAlO_3$:Ce (sample 1-trace concentrations of Gd^{3+}) at RT for λ_{em} = 380 nm (curve a), for x-ray excitation (Mo anticathode, 35 kV, curve b) and λ_{ex} = 290 nm (curve c). The x-ray excited emission spectrum of BGO crystal (curve d) was taken under the same conditions as that of $LuAlO_3$:Ce (curve c), both at room temperature.

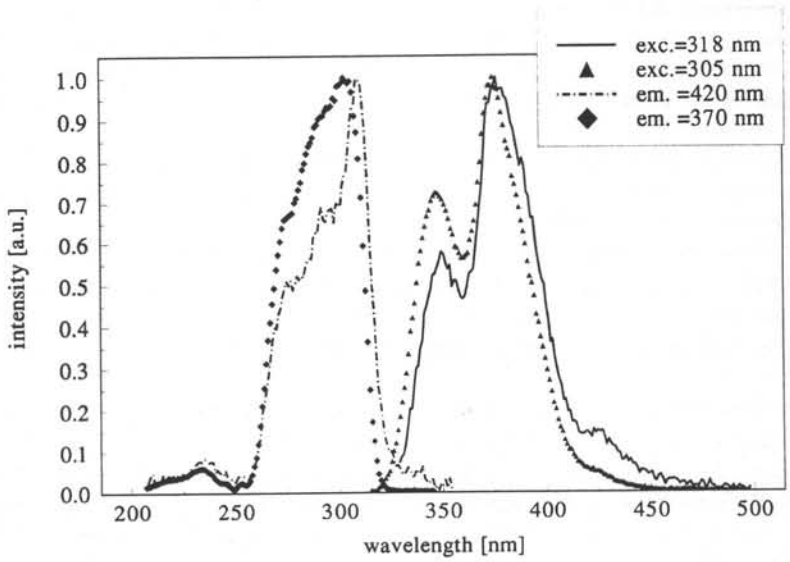

Fig. 2. Emission and excitation spectra of $LuAlO_3$:Ce crystal (sample 2 - Gd content ~9.3 at. %) at LNT for different excitation and emission wavelengths.

higher Ce^{3+} concentration or due to efficient energy migration among Gd^{3+} ions (Gd^{3+} content is ~ 9.3 at.%) and its subsequent capture at Ce^{3+} acceptor centres. That is probably why in the Ce^{3+} fluorescence decays of sample 2 the long component has appeared {τ_l(RT) ~ 405 ns and τ_l (LNT) ~ 900 ns}. We can conclude that presence of Gd^{3+} ions result in (i) long components in Ce^{3+} scintillation and fluorescence decays (unappropriate influence on $LuAlO_3$:Ce as fast scintillator) and (ii) stabilization the perovskite phase in the growth process and prevention of cracking of the $LuAlO_3$:Ce crystals as was also observed by Moses et al. [8].

X-ray excited emission spectra in the same experimental conditions and with equally shaped crystals of BGO and $LuAlO_3$:Ce were performed in order to compare their lights yields (e.g. see Fig. 1). For $LuAlO_3$:Ce crystal sample 1 the light yield of about 10000 photons/MeV can be deduced in such a way. For $LuAlO_3$:Ce crystals sample 2 the comparison results in the light yield ~ 30000 photons/MeV. These values are valid for small measured $LuAlO_3$:Ce crystals.

Luminescence of the measured $LuAlO_3$:Ce crystals is free of luminescence of Lu garnet phase. The third measured sample was pure $Lu_3Al_5O_{12}$:Ce garnet which is peaking at λ_p ~ 535 nm with lifetime τ_g ~ 60 ns. Its first Ce^{3+} broad excitation band is lying in the blue range at λ_p ~ 430 nm the other Ce^{3+} broad excitation bands are in the UV at λ_p ~ 335 nm and λ_p ~ 230 nm.

While in $YAlO_3$:Ce crystal the scintillation lifetime is almost twice longer in comparison with the fluorescence one [2,5], scintillation and fluorescence decay studies of $LuAlO_3$:Ce crystals have shown that there is no substantional difference between fast Ce^{3+} components of the decays (τ_{sc} ~ 17 ns and τ_f ~18 ns). Taking into account that the observed light yields of $LuAlO_3$:Ce crystals are high (l.y. up to 32000 photons/MeV are almost twice higher than l.y. of $YAlO_3$:Ce which is ~ 17000 photons/MeV) probably no significant nonradiative processes are present during intermediate electron and hole transfer process. The similarity between Ce^{3+} scintillation and fluorescence decays in $LuAlO_3$:Ce crystal show that the scintillation excitation processes are much faster than the Ce^{3+} decay time τ ~ 18 ns. The scintillation processes include recombination of e^- (electrons) and h (holes) ($Ce^{3+} + h \rightarrow Ce^{4+}$) followed by $Ce^{4+} + e^- \rightarrow (Ce^{3+})^{ex}$ scintillation mechanism.

REFERENCES

[1] M. Ishii and M. Kobayashi, Prog. Cryst. Growth Charact. Mat. 23 (1992) 245.
[2] S. Anderson, P. Lecoq et 80 authors, NIM Phys. Res. A332 (1993) 373.
[3] Materials of Crystal Clear Collaboration 1992 - 1995, CERN, Geneve, Switzerland.
[4] G. Blasse, Chem. Mater. 6 (1994) 1465.
[5] J.A. Mareš, M. Nikl, C. Pedrini, B. Moine and K. Blažek, Mat. Chem. Phys. 32 (1992) 342.
[6] J.A. Mareš, M. Nikl, C. Pedrini, D. Bouttet, C. Dujardin and B. Moine, to be published in J. Rad.Eff. Def. (1995).
[7] A. Lempicki, M.H. Randles, D. Wisniewski, M. Balcerzyk, C. Brecher and A.J. Wojtowicz, to be published in IEEE Trans. Nucl. Sci. (1995).
[8] W.W. Moses, S.E. Derenzo, A. Fyodorov, M. Korzhik, A. Gektin and V. Aslanov, to be published in IEEE Trans. Nucl. Sci. (1995).
[9] J.A. Mareš, M. Nikl, J. Chval, I. Dafinei, P. Lecoq and J. Kvapil, Chem. Phys. Lett. 241 (1995) 311.
[10] A.A. Kaminskii., A.G. Petrosyan, A.A. Makrosyan and G.O. Shironyan, Phys. Stat. Sol. (a) 125 (1991) 353.
[11] K. Polák, D.J.S. Birch and M. Nikl, Phys. Stat. Sol. (b) 145 (1988) 741.
[12] M. Bollinger and G.E. Thomas, Rev. Sci. Instr. NS-32 (1961) 1044.

LuAP, A NEW FAST SCINTILLATOR[1]

M.Moszyński, D.Wolski, T.Ludziejewski
Sołtan Institute for Nuclear Studies, PL 05-400 Świerk-Otwock, Poland
A.Lempicki[1)], C.Brecher[1)], D.Wiśniewski[1,2)] and A.J.Wojtowicz[1,2)]
[1)] Chemistry Department, Boston University, MA 02215, USA
[2)] Institute of Physics, N.Copernicus University, PL 87-100 Toruń, Poland

Abstract

The scintillation properties of LuAP (lutetium aluminum perovskite, $LuAlO_3$) have been investigated at three different levels of Ce doping: 0 %, 0.25 % and 0.75 %. The light yield, in photoelectrons per MeV, was measured as 122±20 phe/MeV, 1300±100 phe/MeV and 2850±200 phe/MeV, respectively. The light pulse shapes were largely exponential, with a decay constant of 16.0±1 ns for all the samples studied. However, in all cases an additional slow component, amounting to about 10±3 % of the total light, was also found, characterised by a time constant of 74±7 ns. The sample doped with 0.75 % Ce showed an energy resolution of 9.3 % for the 662 keV full energy peak from a ^{137}Cs source. The high detection efficiency of the material for γ-rays (because of its high density of 8.4 g/cm³) is confirmed by a photofraction of about 13 % for a specimen with a volume of only 0.05 cm³. The time resolution for ^{60}Co γ-rays at a 1 MeV threshold was measured as 160 ps, somewhat poorer than that expected. Nevertheless, the high light yield, fast light pulse, high detection efficiency for γ-rays and high time resolution make this material a very attractive scintillator, particularly, in positron emission tomography.

1. INTRODUCTION

Crystals characterised by a high detection efficiency for γ-rays are of special interest in a number of scintillator application. Rivalling the well-known GSO:Ce [1,2] and LSO [3,4], a new material LuAP:Ce was recently proposed [5,6] as particularly attractive because of its high density (8.34 g/cm^3), a short decay time (17 ns), and high light yield (expected to be above 20.000 photons/MeV). Although the advantages of replacing Y by Lu in the YAP crystal lattice have been recognised for several years [7], the first successful development and examination of the new scintillator was reported by Lempicki et al in the past year [5]. The crystals were grown by the Czochralski technique, with conditions carefully controlled to avoid contamination of the LuAP with other aluminate phases [6].

The aim of the current work was to study the basic scintillator properties of the LuAP, recognising that the material is still in the process of development. We report new measurements of the light yield and pulse shape, and studies of energy and time spectrometry to gain a preliminary assessment of the material capabilities in various applications.

2. EXPERIMENTAL RESULTS

The studies reported here were carried out on several specimens of LuAP, one sample doped with 0.25% and two others with 0.75% Ce, and an undoped sample. Two samples doped

[1]Support for this work was provided by the Polish Committe for Scientific Research, Grant No. 2-P302-096-07, US DOE, Grant DE-FG02-94ER81702 and US DOT, Contract DTRS-57-94-C-00175

Proc. Int. Conf. on Inorganic Scintillators and Their Applications, SCINT95,
1996, Delft University Press, The Netherlands

with 0.75% Ce were differently treated in the post growing process. The crystals were somewhat irregular in shape with linear dimensions of 6 to 8 mm and thickness of 0.5 to 1 mm. All the spectrometry measurements were performed with the crystals coated with Teflon tape and coupled to the XP2020Q photomultiplier with the calibrated radiant sensitivity characteristic working with the B' voltage chain [8].

2.1. Light yield

The number of photoelectrons per energy unit (phe/MeV) was measured by comparing the position of the 662 keV full energy peak from a ^{137}Cs source with that of the single photoelectron peak. The photoelectron yield of 1300±100 phe/MeV, 2670±200 phe/MeV and 2850±200 phe/MeV were measured for the sample doped with 0.25% and two samples doped with 0.75% Ce, respectively. The undoped sample showed a much lower light yield of 122±20 phe/MeV. From these values, the light output in photons per energy unit (ph/MeV) can be estimated from the quantum efficiency of the XP2020Q equal to 25% in the region of 300 to 400 nm of the wavelengths, giving a value of 11320±1500 ph/MeV. This value requires two assumptions: first, that very little of the light emitted by the 1 mm thick crystal is lost, and largely compensated by the amount reflected back from the photocathode and detected on second pass; and second, that all photoelectrons emitted by the photocathode of the XP2020Q are actually collected. Departure from these assumptions would mean that the true light output should be even higher than measured, but we feel that the value obtained is reasonably reliable. The measured light yield is still lower than that expected [5,6], however, it is comparable to 2700 phe/MeV found for the YAP:Ce crystal as reported in Ref. [9].

2.2 Light pulse shape

Light pulse shape studies were performed by means of the single-photon method [10,11] using an XP2020UR photomultiplier. The time response of the system was calibrated by means of the Cherenkov light produced in the photocathode by ^{60}Co γ-rays following the method used in Ref. [10]. The FWHM of the prompt spectrum was measured as 500 ps.

An uncoated LuAP crystal was optically coupled to the XP2020Q photomultiplier in the reference counter and irradiated by γ-rays from a ^{137}Cs source. The time distribution of the light pulse from LuAP doped with 0.75% Ce is shown in fig. 1. Note the very intense fast component with the decay time constant of 16.0±1 ns, followed by a slower component, with a decay time constant of about 74.4±7 ns and an intensity about 10±3 %. The insert shows the initial part of the light pulse on expanded time scale. The initial fast rise of the pulse is defined by the 500 ps time response of the system. It is interesting to note that all the LuAP specimens, including the undoped

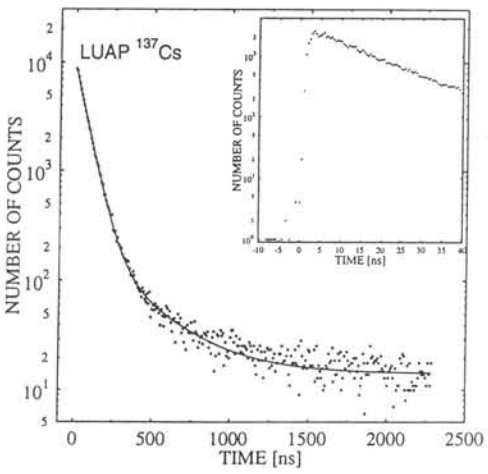

Fig.1 Light pulse shape measured for the sample of LuAP doped with 0.75% Ce. In the insert an initial part of the light pulse is shown presenting a fast rise of the light pulse.

one, displayed the same light pulse shape. The measured 16 ns decay time of the main component agrees well with the value reported in Ref. [5].

2.3. Energy spectrum

Fig. 2 shows the energy spectrum obtained from the LuAP sample doped with 0.75% Ce, when irradiated with the 662 keV γ-rays from a ^{137}Cs source. Note the intense full-energy peak in the spectrum with an area of about 13% of the total. This high photofraction, from a sample whose volume was only about $0.05cm^3$, confirms the high detection efficiency of the LuAP scintillator. The energy resolution of this peak, in terms of FWHM, was about of 9.3%. Note a weak bump shifted down from the peak. It was reduced considerably due to the post growing, heat treatment of this sample. The other sample showed a double peak with the effective energy resolution of 16.8 %, reflecting inhomogeneities in the crystal.

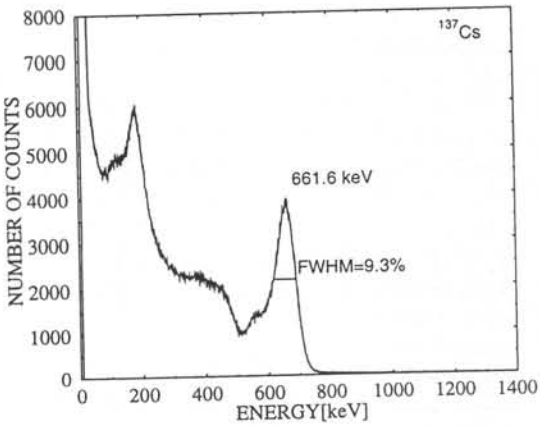

Fig.2 The energy spectrum for the 662 keV γ-rays from ^{137}Cs source.

2.4. Timing study

The timing capabilities of the LuAP scintillator were also investigated. These measurements were carried out on the sample doped with 0.75% Ce coupled to the XP2020Q photomultiplier, using a ^{60}Co source, with energy thresholds set at 1 MeV and 100 keV. The reference counter was provided by a BaF_2 crystal 2.5 cm in diameter and 1.2 cm thick, coupled to an XP2020URQ photomultiplier. For the 1 MeV energy threshold, the time resolution of the reference counter was 80 ps. The time spectra of LuAP measured here were compared with those measured on LSO crystal [4].

Fig. 3 presents the time spectrum of LuAP with the energy thresholds at 1 MeV. The resultant total time resolution of 180 ps, when corrected for the contribution from the reference counter, yields a time resolution (FWHM) for the LuAP counter of about 160 ps. This value is the same as that measured for the LSO crystal [4], and is somewhat poorer than the value of 110 ps calculated [10] according to the Hyman theory [11], taking into account the measured light pulse shape and number of photoelectrons. Note however, that the light pulse of LuAP is faster than that from LSO by almost a factor of three, with a light yield only about 30 % lower, leading to the expectation of considerably better time resolution. Clearly, further studies are necessary, perhaps with larger specimens.

Fig. 4 shows the time spectrum measured for the energy threshold set at 100 keV. The resultant time resolution of 295 ps (necessarily a higher value than was obtained at the higher energy threshold) confirms the high speed of the LuAP scintillator.

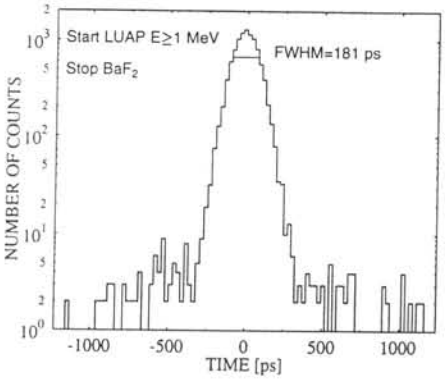

Fig.3 The time spectrum measured with ^{60}Co source for the energy threshold set at 1 MeV.

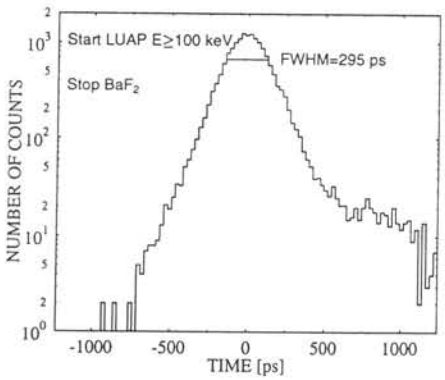

Fig.4 The time spectrum measured with ^{60}Co source for the energy threshold set at 100 keV.

3. CONCLUSION

Although the LuAP scintillator is still in the early stages of materials development, the present study shows a number of its advantages. A high detection efficiency for γ-rays, a high speed of the light pulse, a good and possibly improvable light yield, and a consequently good time resolution and energy resolution make LuAP a prime candidate to replace BGO in positron emission tomography. Since this new material shares with all other lutetium compounds the disadvantage of an underlying background caused by the presence of the natural admixture of radioactive ^{176}Lu, it limits possible future application to those using small volume crystals, to high counting rate experiments and measurements of high energy γ-rays of several MeV. In PET applications, of course, coincidence counting techniques make the additional background completely inconsequential.

REFERENCES

1. K.Takagi and T.Fukazava, Appl. Phys. Lett. 42(1983043.
2. H.Ishibashi, K.Shimizu, K.Susa and S.Kubota, IEEE Trans. on Nucl. Sci. NS36(1989)170.
3. C.L.Melcher and S.Schweitzer, IEEE Trans. on Nucl. Sci. NS39(1992)228.
4. T.Ludziejewski, K.Moszyńska, M.Moszyński, D.Wolski, W.Klamra, L.O.Norlin, E.Devitsin and V.Kozlov, IEEE Trans on Nucl. Sci. in press.
5. A.Lempicki, M.H.Randles, D.Wisniewski, M.Balcerzyk, C.Brecher and A.J.Wojtowicz, IEEE Trans. Nucl. Sci. in press.
6. W.W.Moses, S.E.Derenzo, A.Fyodorov, M.Korzhik, A.Getkin, B.Minkov and V.Aslanov, IEEE Trans. Nucl. Sci. in press.
7. A.A.Kaminskii, A.O.Ivanov, S.E.Sarkisov, I.V.Mochalov and L.Li, Sov. Phys. JETP 44(1976)516.
8. By courtesy of Philips Photonics.
9. S.I.Ziegler, J.G.Rogers, V.Selivanov and I.Sinitzin, IEEE Trans. on Nucl. Sci. NS-39(1992)158.
10. M.Moszyński, Nucl. Instr. and Meth. A324(1993)269.
11. M.Moszyński, T.Ludziejewski, D.Wolski. W.Kiełek, W.Klamra and V.V.Avdieichikov, Nucl. Instr. and Meth. to be published.
12. L.G.Hyman, Rev. Sci. Instr. 36(1965)193.

ENERGY TRANSFER IN RE-DOPED FLUOROPEROVSKITES

N.Shiran, V.Komar, A.Gektin, I.Krasovitskaya, E.Vinograd
Institute for Single Crystals, National Academy of Sciences of Ukraine,
60 Lenin Ave., Kharkov 310001, Ukraine

ABSTRACT

Optical and scintillation properties of Ce-doped $KMgF_3$ crystals have been studied. At least three types of emission centers were found, depending on the dopant concentration. One such center type having 355 nm emission and 27 ns decay time provides the scintillations yield of $KMgF_3$(Ce) crystals comparable to that of pure CsI crystals.

INTRODUCTION

For $KMgF_3$ crystals fast (0.8 ns) scintillation pulses in the UV-range (140-200 nm) are associated with core-valence transition [1]. Use of those crystals in the scintillation technique is limited because of their low radiation resistance ($<10^4$ Gy) [2]. This effect as was shown by us [3] to be associated much with the presence of oxygen traces which are particularly difficult to remove from fluorides.

It is known that the introduction of RE dopants (Ce and La) into fluorides (e.g. into BaF_2 [4]) allows to shift the fast UV- emission to longer wavelengths and to suppress the slow component of luminescence.

This work deals with the study of RE dopants effect on the optical, thermoluminescence and scintillation properties of $KMgF_3$ crystals.

EXPERIMENTAL

$KMgF_3$ crystals were grown from the chemically obtained raw material of the precise stoichiometric composition by the Bridgman method in graphite crucibles under inert atmosphere. The RE dopant (Ce and La) concentration in the melt was varied from 0.01 to 2%. For pure and RE-doped single crystals absorption, excitation, photo- and X-emission and thermoluminescence spectra as well as scintillation characteristics were measured.

RESULTS

In X-luminescence spectra of $KMgF_3$(Ce) crystals, a series of overlapping bands with maxima in the 290-460 nm range are revealed besides of the core-valence emission in the 140-200 nm region. The intensities relations are influenced substantially by the dopant content. Starting from photoexcitation and luminescence spectra (Fig.1), at least three types of emission centers can be discriminated. First, at low concentrations (0.05% Ce) an emission in the 290-325 nm region occurs excited in the 200-250 nm one. Second, at 0.05 to 1% Ce concentrations and at the excitation mainly in the 280 nm range, an intensive luminescence is generated with λ_{max} =355 nm. The absorption at λ_{max} =273 nm is corresponding to these centers (Fig.2 A).

The crystals with a dopant concentration mentioned above scintillate under an ionizing irradiation. The decay time is 27 ns. The light yield increases in proportion to the Ce content (Fig.3). The scintillation efficiency is close to that of pure CsI crystals.

It should be noted that, as is seen in Fig.2, the Ce absorption band in as-received $KMgF_3$(Ce) crystals (λ_{max} =273 nm) is overlapped with the F-center one in irradiated pure

Proc. Int. Conf. on Inorganic Scintillators and Their Applications, SCINT95,
1996, Delft University Press, The Netherlands

$KMgF_3$ crystals. Besides, in the Ce-doped crystals, the light excitation occurs in the 200-250 nm region, i.e. where oxygen in $KMgF_3$ absorbs [3].

At Ce concentrations exceeding 0.1%, along with UV emission bands mentioned above, a blue luminescence excited in the 200-250 nm range is observed.

Doping of $KMgF_3$ by La results only in X-luminescence near 300-320 nm and in an additional absorption band with λ_{max}= 208 nm.

Irradiation of pure $KMgF_3$ crystals and those doped by Ce and La by equal doses with the subsequent measurement of induced F and F_n absorption bands as well as thermostimulated luminescence demonstrated that the radiation resistance of doped specimens exceeds significantly that of pure ones.

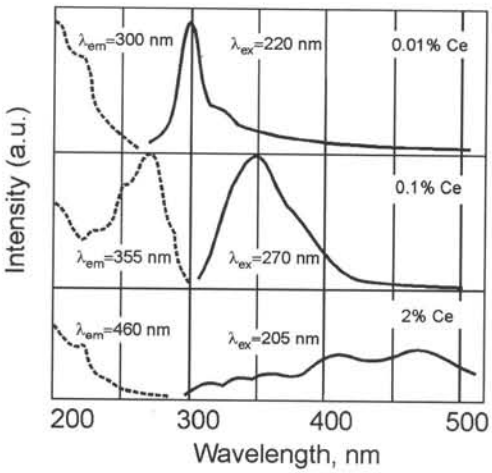

Fig.1. Excitation (dushed line) and emission (solid line) spectra of $KMgF_3$(Ce) crystals with different dopant concentrations.

DISCUSSION

A correlation of the results obtained with the ESR data [5] shows that Ce^{3+} ions can form at least three types of emission centers.

1. A Ce^{3+} ion in a K^+ point with the charge compensation by a vacancy positioned in the place of a K^+ ion nearest to the Ce^{3+} one. These centers are positioned along C_4 axis. The centers of that type ($Ce^{3+}_{K^+}\upsilon_c^-$) are prevailing in $KMgF_3$ crystals with small Ce concentrations and are responsible presumably for the luminescence having maximum in the 290-325 nm range (λ_{exc} =200-250 nm).

2. The second type of Ce^{3+} centers is due to the substitution of Mg^{2+} by Ce^{3+} and the charge compensation by an interstitial F_i^- ion. Such centers are positioned about C_2 axis. It is just this type ($Ce^{3+}_{Mg^{2+}}F_i^-$) which appears to be associated with a longer-wave UV luminescence (λ_{max} = 355 nm) causing short decay time scintillations.

3. The third center type is Ce^{3+} O^{2-} one. There, a Ce^{3+} ion occupies the position of K^+ one, near an O^{2-} ion, that replaced of fluoride. In this case, the luminescence has a maximum in the 410-460 nm range

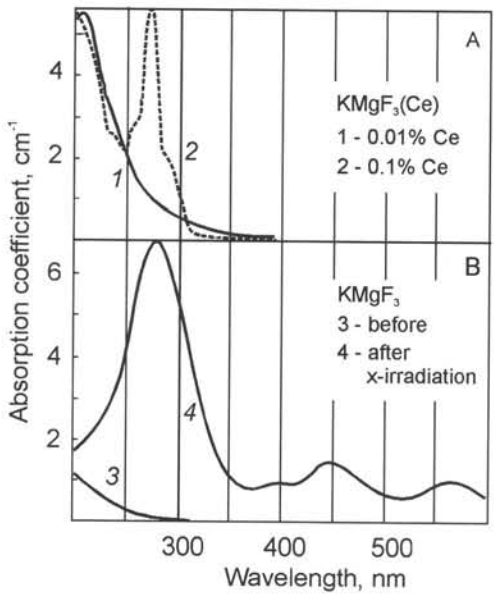

Fig.2. Absorption spectra of Ce-doped (A) and pure (B) $KMgF_3$ crystals.

(λ_{exc} ~208-250 nm) i.e. in the scintillation region characteristic for cerium-containing oxide-type materials.

It can be supposed that, in all cases listed above, the luminescence is associated with radiative transitions within Ce^{3+} ion, distinction between spectral and kinetic characteristics of the emission being due to features of energy transfer to a luminescence center. Therewith, possibilities of the energy transfer are diverse and not restricted to above mentioned cases. Other effective electron traps are also existing in $KMgF_3$, first of all, the color centers of radiative origin. Particularly, the dopant excitation bands are found to be overlapped with F center absorption. That points to the fact that transitions associated with F centers excitation are realized therein with subsequent relaxation resulting in the Ce ion luminescence.

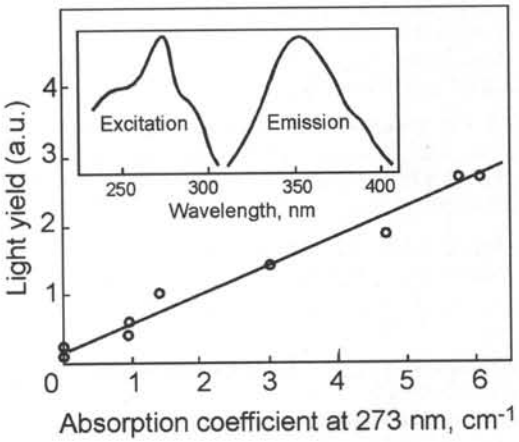

Fig. 3. Light yield as a function of Ce-concentration in $KMgF_3(Ce)$. β ^{207}Bi, 975 keV; time gate 100 ns. Inset: excitation and emission spectra of Ce-component with 27 ns decay time.

The coincidence of the excitation bands of Ce-ion luminescence with those of oxygen absorption allows to suggest the energy transfer to the UV-luminescence of Ce with simultaneous afterglow suppression. It seems that Ce and La-ions bind the oxygen, thus contributing also to the suppression of energy storage in $KMgF_3$-crystals.

CONCLUSION

It should be noted, as a conclusion, that the diversity of Ce^{3+} emission centers and the presence of various electron traps causes the complex character of the luminescence. Therewith, the spectral and kinetic characteristics of the emission are determined to a great extent by features of the energy transfer to a Ce^{3+} center. It is suggested that scintillations

(λ_{max} = 355 nm) are due to transitions in $Ce^{3+}_{Mg^{2+}}F_i^-$ centers.

REFERENCES

[1] J.L.Jansons, V.I.Krumins, Z.A.Rachko and J.A.Valbis. Crossluminescence of KF and related compounds, Solid State Comm., 67 (1988) 183.

[2] A.F.Buzulutskov, G.I.Britvich, V.I.Kochetkov, M.V.Mityagin, L.L. Vistin and I.P.Zibrov. Study of the $KMgF_3$ scintillator radiation damage, Nucl.Instr.Meth., A322 (1992) 235.

[3] A.V.Gektin, V.K.Komar, N.K.Shiran, V.V.Shlykhturov et al. Radiation damage of pure and doped $KMgF_3$ crystals, IEEE Trans.Nucl.Sci., 42, (1995), N4.

[4] P.Schotanus, P.Dorenbos, C.W.E.Van Eijk and H.L.Lampfers. Supression of the slow scintillation light output of BaF_2 crystals by La^{3+} doping, Nucl.Instr.Meth., A281 (1989) 162.

[5] J.Jbragimov, J.J.Fazlizhanov, V.L.Falin and V.A.Ivanov. Ce^{3+} ESR in $KMgF_3$ crystals, Russia, Phys.Solid State, 34 (1992) 3261.

CERIUM-DOPED LUTETIUM-BASED SINGLE CRYSTAL SCINTILLATORS

W.P. Trower, M.V. Korzhik*, A.A. Fyodorov*, Physics/Virginia Tech, Blacksburg, USA.
S.A. Smirnova, All Russia Institute for Crystal Synthesis, Alexandrov, Russia.
V.A. Aslanov, Institute for Single Crystals, Kharkov, Ukraine.

ABSTRACT

We report on the spectroscopic and scintillation properties of Ce^{3+}-activated compounds and single lutetium-based crystals. Special attention is paid to scintillators grown from Lu_2O_3-Al_2O_3 using Czochralski and horizontal Bridgeman techniques.

INTRODUCTION

Lu_2SiO_5 activated with Ce^{3+} ions [1] was the first of a new family of fast, bright, dense, lutetium-based scintillators. Later perovskites and monoclinic crystals were discussed [2]. In addition to these oxides, cerium doped lutetium orthophosphate crystals have been proposed [3]. The lutetium-based crystals investigated to date have a density greater than 6.2 g/cm^3; Ce^{3+} ions emit mainly in the near-ultraviolet to green region. Light yields up to ~27,000 photons/MeV; signal rise times less than ~500 ps; and dominant fast component scintillation decay times less than ~40 ns [1-9] have been obtained. Although lutetium is the second least abundant of the rare earths, and therefore expensive, the advantages of lutetium-based crystals make them the current scintillator-of-choice for the next generation of high resolution medical radiology equipment. However, this preference will only be realized if the technological, physical, and operational problems pertaining to these scintillators can be understood and solved.

Lu_2SiO_5:Ce SCINTILLATORS

From spectroscopy [9] studies, LuSO luminescence has been shown to originate in two Ce^{3+} ion sites. The LuSO crystal structure is a close analog of the well-investigated Y_2SiO_5 [11]. The Y^{3+} ions are replaced isomorphously by Ce^{3+} ions which are located in two different sites with nonequivalent oxygen distorted octahedral coordination. So the two LuSO luminescence centers may result from two nonequivalent Ce^{3+} lattice sites. In frame of this suggestion, the shape of the total Ce^{3+} luminescence band has to be the same from crystal to crystal because the activator distribution coefficient between coordinations does not depend on the Ce concentration at typical contents of ~$1{\cdot}10^{19}$ cm^{-3}. We have found that the LuSO luminescence spectral shape varies from crystal to crystal and identified a correlation between the luminescence band shape and the scintillation parameters.

LuSO luminescence is a superposition of at least two bands peaked near 410 and 470 nm [10], with both bands contributing when excited by ionizing radiation. However, even with similar activator concentration we have found that the relative contribution of each band can vary

Proc. Int. Conf. on Inorganic Scintillators and Their Applications, SCINT95,
1996, Delft University Press, The Netherlands

significantly from crystal to crystal. The long wave luminescence contribution to the total spectrum is defined as the ratio of the luminescence intensity at 470 nm, I_S, to its band maximum at 430 nm, I_T. There is no correlation between this ratio and the cerium content in the crystals, as can be seen in Fig. 1(a). Even at small activator concentrations, between 0.06 and 0.3 % by weight, the ratio I_S/I_T changes from 0.5 up to 0.8. This indicates that the appearance of the long wave luminescence band depends on the crystal growth conditions. From this we conclude that the long wavelength luminescence is not from Ce^{3+} ions in regular lattice positions but it is connected with Ce^{3+} ions located in disordered lattice positions, or spatial lattice defects. Therefore, the number of these luminescence centers is correlated with the presence of structural defects near the cerium activator.

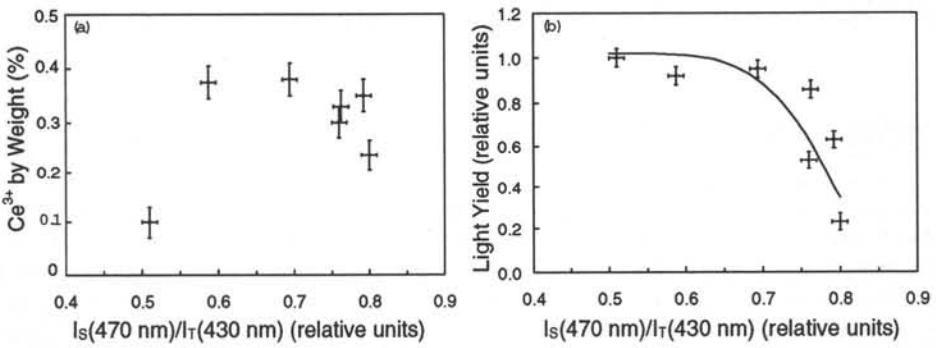

Figure 1. γ-ray excited LuSO luminescence ratio, I_S/I_T, at 300 K versus (a) the cerium content and (b) the light yield.

An increase of the long wavelength band ratio causes a decrease of the LuSO light yield, as can be seen in Fig. 1(b). This light yield suppression is not related to the dominant Ce^{3+} short-wavelength luminescence band quenching observed for LuSO scintillation kinetics, where different I_S/I_T produce insignificant changes in the kinetics. However, in other cerium activated oxide matrices, like YAP, light yield varies strongly with the activator concentration, especially at low concentrations < $1 \cdot 10^{19}$ cm^{-3} [12]. For this case, even some fraction stabilization of Ce ions in irregular sites decreases the total light yield. With diminishing long wavelength luminescence light yield, we have found that the energy resolution of the 662 keV γ-ray photopeak in pulse height spectra measured with LuSO crystals with the smallest I_S/I_T ratio is ~10 % while a crystal with the largest I_S/I_T ratio gives markedly worse energy resolution. We also found a satellite peak near the photopeak in samples with a strong long wavelength luminescence which is not connected with the characteristic X-ray escape peak in lutetium-based scintillators [6]. Since long wavelength luminescence centers degrade LuSO scintillation properties, their presence must be minimized before this scintillator can become commercially interesting.

$LuAlO_3$:Ce SCINTILLATORS

LuAP, which was proposed would be a good scintillator [2,7,8], is now also being actively investigated [13-15]. Although YAP and LuAP have very similar spectroscopic properties, LuAP scintillation kinetics is faster than the decay under photoexcitation. This indicates that the activator luminescence quenching processes in lutetium aluminum perovskite are stronger than in YAP.

The reason of LuAP crystal growth problems lies in the difficulty of obtaining its single crystal state from Lu_2O_3-Al_2O_3 oxide. Garnet, $Lu_3Al_5O_{12}$, and monoclinic, $Lu_4Al_2O_9$, phases [16] as a rule are present or dominate in the crystals although authors of [8] were successful in growing LuAP. Mixed $Lu_3Al_5O_{12}$(40%)-$Lu_4Al_2O_9$(60%) crystals with Ce have an absorption spectrum which clearly exhibits the garnet (λ = 340, 440 nm) and the monoclinic (λ = 370 nm) phase Ce^{3+} ion absorption bands. The last band is strongly split by the crystal field into 365 and 380 nm components. Although the Ce^{3+} ion in the monoclinic phase has a luminescence maximum at 440 nm, it is significantly quenched by the overlap with the garnet phase Ce^{3+} absorption band. At the same time. the monoclinic phase if present in LuAP has to provide an effective suppression of Ce^{3+} luminescence in the perovskite phase. From the perovskite, garnet, and monoclinic phase Ce^{3+} spectroscopic data; it appears that the garnet and monoclinic phases in LuAP crystals can lead to significant decrease of scintillation efficiency. This effect is even more important than that of efficiency decrease by Ce^{4+} ion generated color centers.

(Lu-Y)AlO_3:Ce SCINTILLATORS

We have attempted to obtain lutetium crystals with a perovskite structure by growing solid solutions of (Lu_x-Y_{1-x})AlO_3 crystals. Yttrium aluminum perovskite has a wider stability region in the Y_2O_3-Al_2O_3 phase diagram than LuAP. The Y^{3+} ion radius is very close to that of lutetium. Both perovskites have similar melting points and so dissolve into each other.

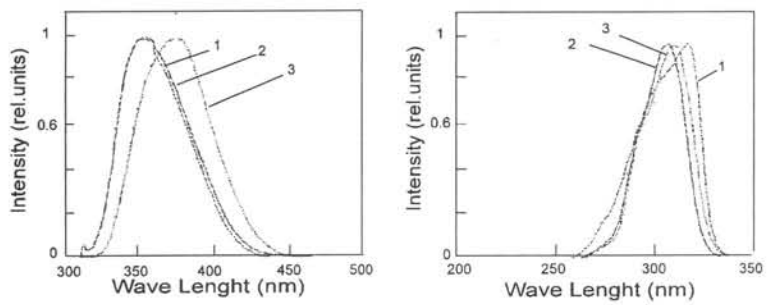

Figure 2. Normalized (a) luminescence (λ_{exc} = 300 nm) and (b) luminescence excitation (λ_{lum} = 350 nm) spectra for (1) YAP, (2) ($Lu_{0.5}$-$Y_{0.5}$)AP, and (3) LuAP.

The luminescence and luminescence excitation spectra of YAP, ($Lu_{0.5}$-$Y_{0.5}$)AlO_3, and LuAP, are similar, as can be seen in Fig. 2. However, in the Ce^{3+} luminescence band in (Lu-Y)AP

there is a shift to a short wavelength region. Adjusting the crystal growth parameters, we obtained a $(Lu_{0.5}\text{-}Y_{0.5})AlO_3$:Ce scintillator with a density of 6.3 g/cm^3, a luminescence band maximum at 342 nm, a light yield of 14,200 photons/MeV, and decay times of 4.6 (33%), 22 (52%), and 83(15%) ns. With the optimization of the crystal growth technology, we believe that $(Lu_{0.8}\text{-}Y_{0.2})AlO_3$ can be reliably produced which will then be promising for application medical radiology.

CONCLUSIONS

Although lutetium-based scintillators are technically, if not economically, promising for future applications in medical radiology, none of them have yet been sufficiently optimized and therefore, implementation is not imminent. First, a research program should establish the LuSO growth technology to minimize the presence of Ce^{3+} ions in irregular positions in the crystal host matrix. Second, although LuAP technology is only beginning to be developed, special attention should be paid to the presence of additional phases, especially the monoclinic phase, which will significantly degrade LuAP scintillation properties. Third, the new (Lu-Y)AP scintillator has the advantages of both YAP and lutetium-based crystals and so a possible future application in medical radiology, especially PET, should be investigated.

References

1. C.L. Melcher, US Patent 4,958,080 (1990) and 5,025,151 (1991).
2. V.G. Baryshevsky, D.M. Kondratiev, M.V. Korzhik, V.A. Kachanov, B.I. Minkov, V.B. Pavlenko, and A.A. Fyodorov, Nucl. Tracks Radiat. Meas. 22 (1993) 111.
3. A. Lempicki, E. Berman, A.J. Wojtowicz, M. Balcerzyk, and L.A. Boatner, IEEE Nucl. Sci. Conf. Rec. (1994) 141.
4. C.L. Melcher and J.S. Schweitzer, Nucl. Instrum. Meth. A314 (1992) 212.
5. C.W.E. Van Eijk, J. Andriessen, P. Dorenbos, and R. Vissier, Nucl. Instrum. Meth. A348 (1994) 546.
6. N.N. Ryskin, P. Dorenbos, and C.W.E. Van Eijk, in Proc. EURODIM-94, in press.
7. W.W. Moses, S.E. Derenzo, A.A. Fyodorov, M.V. Korzhik, B.I. Minkov, and A.V.Gektin, IEEE Nucl. Symp. Conf. Abst. NSS09-04 (1994).
8. A. Lempicki, M.H. Randles, D. Wisniewski, M. Balcerzyk, C. Brecher, and A.J. Woitowicz, IEEE Nucl. Symp. Conf. Rec. (1994) 307.
9. A.A. Fyodorov, V.B. Pavlenko, M.V. Korzhik, W.P. Trower, and R.F. Zuevski, Radiat. Meas. in press.
10. H. Suzuki, T.A. Tombrello, C.L. Melcher, and J.S. Schweitzer, Caltech bb-115 1(1993) (unpublished).
11. I.N. Kurkin and K.P. Chernov, Phys. Status Solidi B101 (1980) 233.
12. V.G. Baryshevsky, M.V. Korzhik, V.I. Moroz, A.A. Fyodorov, and S.A. Smirnova, Nucl. Instrum. Meth. B58 (1991) 291.
13. D. Bouttet, C. Dujardin, C. Pedrini, J.W.H. Verweij, A. Belsk, A.N. Vasiliev, E.I. Zinin, A.G. Petrosian, and P. Martin, CERN CCC-1/02/95 (1995) (unpublished).
14. J.A. Mares, M. Nikl, J. Chval, I. Dafinei, P. Lecoq, and J. Kvapil, Chem. Phys. Lett. 214 (1995) 311.
15. M.V. Korzhik and W.P. Trower, Appl. Phys. Lett. 66 (1995) 2337.
16. S. Smirnova, in these proceedings.

LEVELS OF Ce ION IN THE YAG ENERGY STRUCTURE

V. Mürk and N. Yaroshevich
Institute of Physics, Riia 142, EE2400 Tartu, Estonia

Abstract. The excitation spectra of different luminescent processes are studied in the YAG:Ce and YAG:La crystals. The manifestations of the near-impurity excitations are observed in the luminescence excitation spectra at 6.7 eV in both crystals. The investigation of the thermo-luminescence excitation spectra has shown that the upper level of the split d-multiplet of the Ce ion lie in the YAG conduction band. The model of the electron states involved in the process of energy transfer to the scintillating Ce ion is proposed.

INTRODUCTION

The YAG:Ce crystal is one of the well-known fast scintillators and, therefore, it is important to understand in detail the processes of energy transport and the location of the Ce levels with respect to energy bands of host crystal. Although there exist a number of theoretical and experimental works, which consider different aspects of these problems, the situation is still far from clarity [1,2]. The electron excitations and their relaxation in the YAG host crystal have earlier been investigated in detail [3] and it was of interest to use the same methods to study the specificity of the interaction of YAG intrinsic excitations with scintillating Ce ions. Of special interest was a comparison with the experimental data obtained earlier for YAG:La crystals, where the impurity ion, being very similar to the Ce one, has a closed shell configuration and cannot, therefore, itself take part in luminescent transitions.

EXPERIMENTAL

The properties of relaxation of electron excitations have been studied in YAG:Ce and YAG:La (both 0.1 at %) single crystals by using different VUV spectroscopy methods in the temperature interval from 5 to 300 K (see for the details in [3,4]).

LUMINESCENCE EXCITATION SPECTRA

In the excitation spectrum of the Ce emission together with the well-known five excitation bands (corresponding to the f-d transitions of the last optically active electron of a three-valent Ce ion [5]) the selective band of the so-called `near-impurity` excitation is observed at about 6.7 eV adjacent to the YAG intrinsic absorption edge (see Fig.1).The investigation of the temperature dependence of excitation spectra shows that in this case the competition with the exciton relaxation channel (giving rise the 4.9 eV emission) plays the same decisive role as for other analogous emissions of a recombinational character in YAG crystals [3]. In addition to the Ce intracentre emission the UV recombination luminescence band at about 4.5 eV is observed as well. However in contrast to the similar emission of the YAG:La crystals, the excitation efficiency in the 6.7 eV band seems to be divided between the Ce and Ce-induced luminescence bands. Evidently this reflects here the possibility of further relaxation of `near-

Proc. Int. Conf. on Inorganic Scintillators and Their Applications, SCINT95,
1996, Delft University Press, The Netherlands

impurity` excitation on the levels of impurity ion. In the YAG:La crystal evidently no such possibility exists and, therefore, the 4.5 eV band is there the main band of recombination emission.

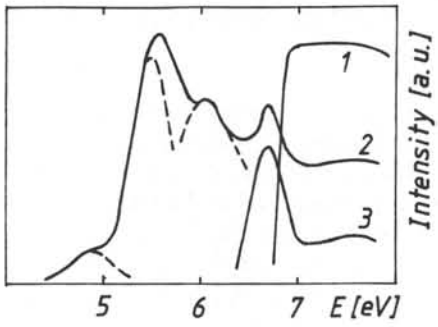

Figure 1. Luminescence excitation spectra for the YAG:Ce (1,2) and YAG:La (1,3) crystals at 5 K for (1) the 4.9 eV self-shrinked exciton emission, (2) the Ce emission and (3) the La-induced recombination emission at 4.5 eV. Three high energy excitation bands of the Ce ions are shown according to [5].

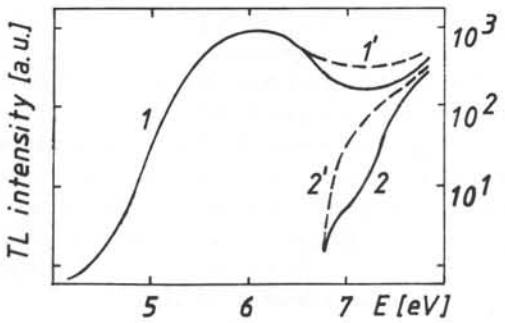

Figure 2. TL photoexcitation spectra for the YAG:Ce (1,1') and YAG:La (2,2') crystals, irradiated at 5 K (1,2) and 150 K (1',2').

THERMOLUMINESCENCE EXCITATION SPECTRA

The thermoluminescence (TL) excitation spectra were earlier investigated for the case of doping with the closed shell ions (e.g. three-valent La or Sc ions [3,4,6]). Although these ions induce in the host matrix respective trapping levels, which are very efficient recombination centres, no TL is excitable in the YAG transparency region (see Fig.2). In contrast to the case of a YAG:La crystal, the strong peak of the TL excitation is observed at 6.05 eV (i.e. it coincides with the transitions on the upper excited level of the split d-multiplet of the Ce ion). The temperature independence of the TL excitation efficiency for this peak shows that the 6.05 eV level lies in the YAG conduction band. Simple Gaussian shape of this peak indicates that only one upper level of the Ce d-multiplet is involved in such very efficient process of the self-ionization. As the other levels of the d-multiplet are non-active in TL processes, it gives one a possibility to determine experimentally the position of the Ce ion levels with respect to the host matrix energy bands.

DISCUSSION

Thus, in the case of the Ce doping we have a complex set of both Ce and Ce-induced (or, generally speaking, induced by a large rare-earth ion in the host matrix) levels which are

involved in the energy transfer to the scintillator's emitting level. The model which could describe the relaxation processes in the YAG:Ce crystal is given in Fig.3. As it was shown for the YAG host crystal [4,7], the exciton channel itself plays no role in the energy transfer to recombination centres at moderate impurity concentration, although electrons and holes, which originate from thermoionized (at high temperatures) excitons participate, naturally, in the ordinary recombinations.

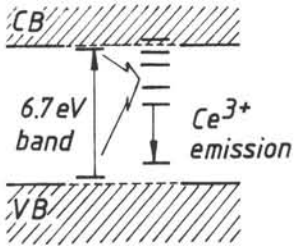

Figure 3. A position of the Ce and Ce-induced levels with respect to the YAG conduction (CB) and valence (VB) bands. The arrow indicates possible non-radiative transfer of excitation energy from the states of the near-impurity excitation to the Ce ion.

This work is supported by the Estonian Science Foundation Grant No 943.

References

[1] Ermakov G.A.,Ljubchenko V.M.,Smirnova C.A.,Shabaltai A.A. *Inorg.Mater.***24** (1988) 682.
[2] Merenga H., Andriessen J., van Eijk C.W.E. *Record of the Intern.Workshop PHYSCI'94,TUD-SCIR-94-04, Delft, the Netherlands,* p. 50.
[3] Mürk V, Yaroshevich N, *J.Phys.:Condens. Matter* **7** (1995) 5857.
[4] Ismailov K.M. and Mürk V.V. *(Sov.)Phys.Solid State* **34**(1992)165.
[5] Tomiki T.,Akamine H,Gushiken M,Kinjoh Y,Miyazato M,Miyazato T,Togokawa N, Hiraoka M.,Hirata N.,Ganaha Y.,Futemma T. *J.Phys.Soc.Japan* **60**(1991)2437.
[6] Mürk V.,Namozov B.,Yaroshevich N.*Radiation Measurements* **00** (1995) 000.
[7] Mürk V., Yaroshevich N. *Phys.Status Solidi (b)* **181** (1994) K37.

Emission, efficiency and decay properties of $Y_3Al_5O_{12}$ (Cr, Mn, Co) scintillators

V.I. Solomonov, S.G. Mikhaylov
Institute of Electrophysics, Russian Academy of Science
620019, Ekaterinburg, Russia
S.I. Krylov, L.V. Victorov
Experimental Physics Department, Urals State Technical University
620002, Ekaterinburg, Russia

Abstracts. - The results of study on scintillation properties of $Y_3Al_5O_{12} - Me$ (Me=Cr, Mn, Co, Fe, Ni, V) single crystals under α, β and e-beam excitation are reported.

1. INTRODUCTION

$Y_3Al_5O_{12}$ Single crystals are known as X-ray phosphors [1] and scintillators [2,3]. But it was no data about e-beam scintillation properties of $Y_3Al_5O_{12}-Me$ single crystals. In this work we present some results of (^{239}Pu)-, (^{90}Y-^{90}Sr)- and puls-electron beam excitation measurements on $Y_3Al_5O_{12}$ single crystals, which were doped by Me= Cr, Mn, Co, Fe V, Ni. (The crystals were presented by M.I. Timoshechkin, Institute of General Physics RAS and Kh.S. Bagdasarov, Institute of crystallography RAS). For high current (j=200±100 A/cm^2) excitation we used the compact electron accelerator of RADAN type, (2 ns, 160-200 keV).

2. RESULTS AND DISCUSSION

The results for α -, β- scintillation of $Y_3Al_5O_{12} - Me$ are in Table 1. The compounds $Y_3Al_5O_{12} - Me$ are the α- β- scintillation materials.

Using the high power e-beam excitation the spectra were recorded at 2 modes:

- pulse recording of spectra with the storage time 1 ms and the delay time ±1 ms (fine structure of bands was appeared well), solid curves in Fig 1,2;
- nearly continuous registration during 3s with averaging of spectral information on 15 pulses of electron beam with the pulse repetition of 5 Hz,- dashed curves in Fig 1,2.

The position of emission bands, decay time (long componens only); time of rise and types of transitions for $Y_3Al_5O_{12} - Me$ are presented at Table 2.

The pulse-e-beam excitation give fine spectral-emission resolution, which is for 3-4 orders higher than X-ray -exitation. It gives the possibility to analyze some details of spectra of d-elements in $Y3_Al_5O_{12}$ (Cr, Mn, Co, Fe, V, Ni).

Cr^{3+}. The emission bands of Cr^{3+}-ion, Fig 1, Table 2, correspond to dublet R-line and their Stockes and anti-Stockes sattelites N and S lines with exponential decay. There are 3 additional lines 628, 642 and 663 nm, which correspond to optical transition $^2T_{1g} - {}^4A_{2g}$ in Cr^{3+}-ion.

Mn^{2+} and Mn^{4+}. There are the emission red dublet R and R′ lines and U-band (to 610 nm), and additional band 587 nm with thin structure, Fig. 2.

Co^{2+}. There are two main emission bands 483 (500) nm and 585 nm, which correspond to transition in Co^{2+} ions. It was difficult to find the Co^{3+}- band due to another impurities.

Fe^{3+} There is IR emission bands 790 nm ($\Delta\lambda$ =90 nm), with lines 773, 789 and 804 nm (probably $^4T_{1g} - {}^6A_{1g}$ transition).

Proc. Int. Conf. on Inorganic Scintillators and Their Applications, SCINT95,
1996, Delft University Press, The Netherlands

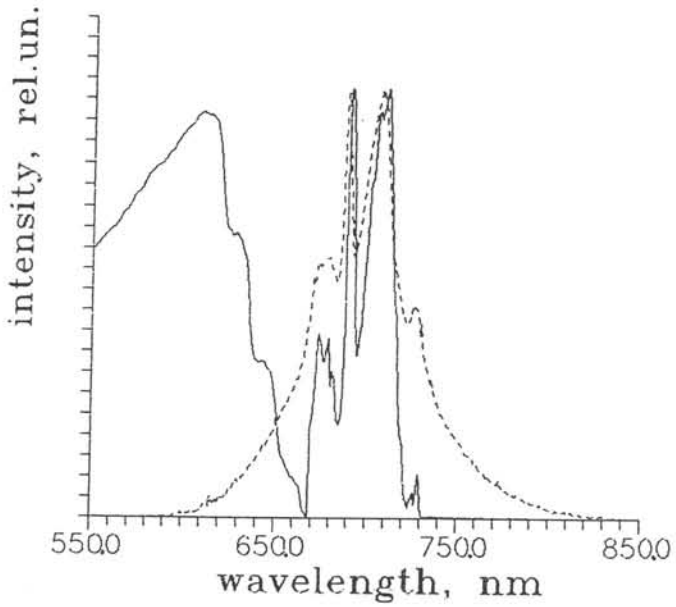

Fig.1.

The luminescence spectra of $Y_3Al_5O_{12}+Cr^{3+}$ under high power e-beam excitation for the pulse recording (solid curve) and nearly continuous registration (dashed curve).

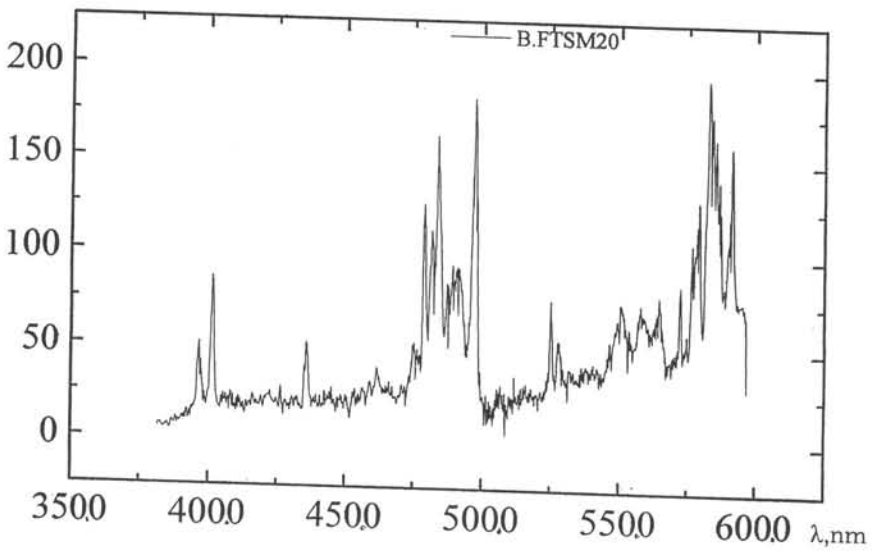

Fig.2. The luminescence spectra of $Y_3Al_5O_{12}$-Co under high power e-beam excitation

V^{3+}. There are the 3 red emission bands: 620 ($\Delta\lambda$ =150 nm), with lines 603, 616, 632, 653 and 686 nm ($^1A_1$, $^1T_2 - {}^3A_2$ transitions) and IR-band 720 nm ($\Delta\lambda$ =100 nm) with lines: 692, 705, 708, 723 and 741 nm ($^3T_1 - {}^3A_2$ transitions).

Ni^{2+}. There are the emission band 420 nm ($\Delta\lambda$ =100 nm) and band 605 nm (with lines 605, 585 and 568 nm).

The $Y_3Al_5O_{12}$ (Cr, or Mn, or Co, or Fe) compounds are the materials for high power e-beam registration. The pulse-e-beam excitation give fine spectral-emission resolution, which is more higher (for 3-4 orders) than $\alpha-$, $\beta-$ or X-ray exitation. The high current e-beam excitation method may be used as a new scintillation spectroscopy method of solids.

Table 1: Scintillation properties of $Y_3Al_5O_{12}$ for integral emission (α, β- exitation):

Activator	Exc.	Efficiency, % to $CsI-Tl$	Absolute Efficiency, %	Decay, ns	
				τ_1	τ_2
Cr	α	9	1.75	110	700
	β	45	8.3	–	–
Mn	α	9	1.45	25	112
	β	45	7.0	–	–
Co	α	4.5	0.3	(37)*	(180)*
	β	22	1.5	–	

* weak distortional signal

Table 2: Emission and decay properties of $Y_3Al_5O_{12}$ for pulse-e-beam excitation

Activator	λ-emission, nm		Transition	Decay, μs		Time of rise, μs
				τ_1	τ_2	
Cr^{3+}	728	(726)	$^2E_g \rightarrow {}^4A_{2g} - \hbar\omega_x$	0.66	107	2.5
	710	(706)	$^2E_g \rightarrow {}^4A_{2g} - \hbar\omega_x$	1.13	243	2.5
	690	(681)	$^2E_g \rightarrow {}^4A_{2g}$	1.34	238	15
	679	(674)	$^2E_g + \hbar\omega_x \rightarrow {}^4A_{2g}$	111	1.47	3
Mn^{4+}	671	(667)	$^2E_g \rightarrow {}^4A_{2g}(4)^*$	2.5	1282	1.4
	645	(642)	$^2E_g \rightarrow {}^4A_{2g}(6)^*$	3.0	1182	1.3
Mn^{2+}	618	(601)	$^4T_{1g} \rightarrow {}^6A_{1g}(6)^*$	(2.4)		2.5
	590	(579)	$^4T_{1g} \rightarrow {}^6A_{1g}(6)^*$	(3.8)		2.5
Co^{2+}	483	(500)	$^2T_1(^2H) \rightarrow {}^4T_1(6)^*$	880	22	2.8
	585		$^2T_1(^2H) \rightarrow {}^4T_1(6)^*$	64	904	2.8

* coordination number

Acknoledgements. – This work was made in authority with B.V. Shulgin. The authors are grateful to M.I.Timoshechkin and Kh.S. Bagdasarov.

REFERENCES

1. Yu.K. Voronko, V.I. Denker, V.V. Osiko et al. Doklady Akademii Nauk SSSR, 1969, **188**(6). 1258-1260.
2. B.V. Shulgin, L.V. Victorov et al. Radiatsionno-stimulirovannye yavleniya v tverdykh telakh. Sverdlovsk, Urals Polytechnical Institute, 1979, **1**. 24-31.
3. L.V. Victorov, B.V. Shulgin, V.Yu. Yakovlev, M.I.Timoshetschkin. Issledovaniya vzaimodeistviya izlutschenija s vetshestvom. Karaganda, University, 1981. 3-13.

SCINTILLATION PROPERTIES OF Pr^{3+} DOPED $Lu_3Al_{5-x}Sc_xO_{12}$ CRYSTALS

P. Dorenbos, J.T.M. de Haas, C.W.E. van Eijk
Delft University of Technology, Faculty of Applied Physics, c/o IRI, Mekelweg 15, 2629 JB Delft, The Netherlands.

N.N. Ryskin, E.V Zharikov, A.A. Kiryukhin
General Physics Institute, 117317 Vavilov street, Moscow, Russia

ABSTRACT The scintillation properties of crystals of $Lu_3Al_{4.8}Sc_{0.2}O_{12}$ doped with Pr^{3+} were studied at room temperature by means of X-ray and γ-ray excitation. Besides host lattice luminescence, fast luminescence (τ=8 ns) due to 5d-4f transitions in Pr was observed. The dominant decay components are however relatively slow; i.e. several hundreds of ns.

INTRODUCTION

Recently [1] we reported on a new scintillator material $Lu_3Al_{5-x}Sc_xO_{12}$ (LAG:Sc) garnet crystals. It has a density of 6.7 g/cm^3 and shows an efficient scintillation emission at 270 nm. A maximal light yield of 22,500 photons/MeV with a main decay time of 610 ns was observed for a Sc concentration of $x = 0.2$. The luminescence was attributed to the decay of excitons localized near Sc^{3+} centers. The scintillator coupled to an XP2020Q photomultiplier tube (PMT) shows an energy resolution of about 6.5 % for 662 keV γ-quanta. In an attempt to shorten the scintillation decay time and to shift the emission to wavelengths detectable with glass window photomultiplier tubes, LAG:Sc crystals doped with Pr^{3+} were grown. Pr^{3+} was chosen as activator ion because in garnet crystals its 5d-4f absorption band overlaps the host lattice emission band. So transfer of excitation energy to Pr was anticipated. Furthermore Pr^{3+} ions often show fast luminescence due to dipole allowed transitions.

RESULTS AND DISCUSSION

Two crystals of $Lu_{3-y}Pr_yAl_{4.8}Sc_{0.2}O_{12}$ were grown by the Optical Zone Melting Technique at the General Physics Institute in Moscow. The Pr concentration was estimated after growth from the intensity of the optical absorption lines. It amounted to y=0.0008 and y=0.01 within an estimated systematic uncertainty of a factor of two. For the methods to determine the X-ray excited emission spectra and to register pulse height spectra with an XP2020Q PMT we refer to [2]. Gamma ray excited scintillation decay spectra were determined using the single photon counting technique employing the multiple hit method [2, 3].

The optical absorption spectra of the Pr doped samples reveal absorption bands at 190, 240, and 280 nm. The latter two are surely caused by transitions from the ground state of Pr^{3+} to excited states of the 4f5d configuration. Excitation in these bands pro-

Proc. Int. Conf. on Inorganic Scintillators and Their Applications, SCINT95,
1996, Delft University Press, The Netherlands

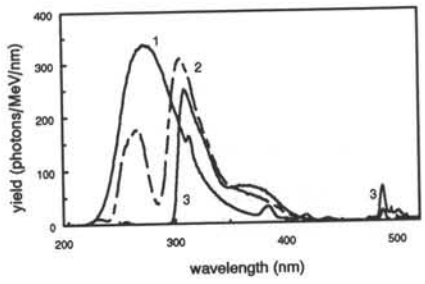

Figure 1: X-ray excited luminescence spectra of $Lu_{3-y}Pr_yAl_{4.8}Sc_{0.2}O_{12}$ crystals. Spectrum 1) y=0.0; spectrum 2) y=0.0008; spectrum 3) y=0.01.

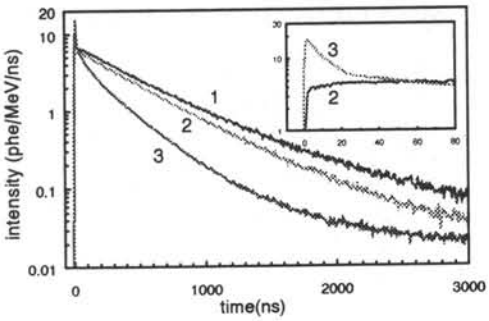

Figure 2: Scintillation decay spectra of $Lu_{3-y}Pr_yAl_{4.8}Sc_{0.2}O_{12}$ crystals. Spectrum 1) y=0.0; spectrum 2) y=0.0008; spectrum 3) y=0.01.

duces characteristic Pr luminescence. Transitions from the lowest 5d4f state to levels of the $4f^2$ configuration produce wide emission bands between 300 and 400 nm. Transitions within the $4f^2$ configuration cause narrow emission bands near 490 nm. These spectroscopic properties are very similar to those of $Y_3Al_5O_{12}$ crystals doped with Pr^{3+}, see for more details [4, 5, 6].

Under X-ray excitation, LAG:Sc (x=0.2) luminesces at 270 nm with an integral light yield of 22,500 photons/MeV, see Figure 1 and [1]. Doping with a small amount of Pr causes the appearance of the Pr^{3+} related 5d4f-$4f^2$ luminesces between 300 and 400 nm. In addition, one observes between 250 and 280 nm a remnant of the host lattice luminescence. $4f^2$-$4f^2$ luminescence occurs near 490 nm. Increasing the Pr content to y=0.01 causes the almost complete disappearance of the host emission, only Pr emission remains. The X-ray excited photon light yield of the several emission bands are compiled in Table 1. The overall light yield decreases from 22,500 ph/MeV for the undoped to 10,700 ph/MeV for the sample with y=0.01. There may be some loss of light yield due to thermal quenching of the Pr emission, an observation which was also made for YAG:Pr samples [2, 5].

From the position of the total absorption peak in pulse height spectra of a ^{137}Cs source, the number of photoelectrons created per MeV of γ-ray energy in an XP2020Q PMT was determined. Results are compiled in Table 1. With the effective quantum efficiency of 20% of the PMT and an estimated light collection efficiency of 90%, the phe yields are consistent with the light yields obtained from the X-ray excited emission spectra. For the sample with y=0.01, we also determined phe yields at excitation energies of 59.9 keV (^{241}Am), 32 keV (^{133}Ba), and 17.4 keV (X-rays from a Mo target). Within error (10%) they showed the same phe yield/MeV as with 662 keV excitation.

γ-ray excited decay time spectra of the three samples are shown in Figure 2. The decay spectrum of the sample without Pr is dominated by a 610 ns decay which accounts for 98% of the light output, the rest has a decay time of 3.3 μs [1]. Doping with a small amount of Pr^{3+} changes the decay. After about 70 ns the pulse reaches its maximal

Table 1: X-ray excited photon yields due to host, 5d-4f, and 4f-4f luminescence in photons/MeV. Photoelectron yields of $Lu_{3-y}Pr_yAl_{4.8}Sc_{0.2}O_{12}$ crystals. Photoelectron yields were measured with an XP2020Q PMT; the employed shaping time is indicated in parenthesis.

	X-ray excitation			662 keV excitation
Pr^{3+}-conc.	emission band			yield
y	host	5d-4f	4f-4f	(phe/MeV)
0	22,500	–	–	4,150 (10μs)
0.0008	4,800	14,000	200	3,000 (3μs)
0.01	–	10,000	700	1,800 (3μs)

value. At times longer than about 100 ns, the decay can be described with a sum of two decay components; i.e. τ=400 ns (20%) and τ=620 ns (80%). The 620 ns component is attributed to STE emission and Pr emission excited via radiative energy transfer from the STE to Pr. The 400 ns component is attributed to Pr luminescence excited via non-radiative (i.e. multipole-multipole or exchange) interactions with STEs localized on Sc sites. The value of the rise time is indicative for the excitation rate of the Pr ions. Increasing the Pr contents to y=0.01 results in a decay curve characterizable by three exponentially decaying components; i.e. 8.3 ns (9%), 86 ns (14%), and 386 ns (77%). We attribute the fast one to direct trapping of electrons and holes in Pr^{3+} ions followed by prompt 5d4f-$4f^2$ luminescence. The slow decay components are attributed to Pr ions excited via energy transfer from the excitons on Sc.

References

[1] N.N. Ryskin, P. Dorenbos, C.W.E. van Eijk, S. Kh. Batygov, J. Phys.:Condens. Mater 6 (1994) p.10423.

[2] P. Dorenbos, J.T.M. de Haas, C.W.E. van Eijk, R.W. Hollander, IEEE Trans. on Nucl. Sci. 40(4) (1993) p.424.

[3] W.W. Moses, Nucl. Instr. and Meth. A336 (1993) p.253.

[4] P. Dorenbos, R. Visser, C.W.E. van Eijk, N.M. Khaidukov, M.V. Korzhik, IEEE Trans. on Nucl. Sci. 40(4) (1993) p.388.

[5] M.J. Weber, Solid State Comm. 12 (1973) p.741.

[6] M.L. Meilman, A.I. Kolomitsev, A.M. Keverkov, Kh. S. Bagdasarov, Opt. Spectrosc. (USSR) 57(2) (1984) p.145.

Eu^{3+} LUMINESCENT CENTERS IN $Ca_3Ga_2Ge_3O_{12}$ CRYSTALS

A.E.Nosenko, L.V.Kostyk, V.V.Kravchishin
Department of Physics, Lviv State University
Dragomanov str. 50, Lviv, 290005, UKRAINE

Abstract. Spectral - luminescence properties of Eu^{3+} doped relatively new easy-melted $Ca_3Ga_2Ge_3O_{12}$ garnet crystals have been investigated. It is shown that at least three Eu^{3+} activator centers are occurred in concentration range from 0.1 to 3 at.% in given compound. The mechanism of formation of different type is investigated.

INTRODUCTION

Rare-earth (RE) activated crystals with a garnet structure have been intensively studied because of their application as luminescent and solid state laser materials [1-3]. The garnet unit formula is $\{A_3\}[B_2](C_3)O_{12}$ and a space group O_h^{10} - Ia3d. Garnets have three kinds of cation sites, dodecahedral {c}, octahedral [a] and tetrahedral (d). The {c}, [a] and (d) positions are occupied by trivalent cations in aluminate and gallate garnets and divalent, trivalent and tetravalent cations respectively in germanate and silicate garnets. In terms of the crystallochemical approach, it is most probably that trivalent RE doping ions occupy dodecahedral {c}-positions in garnet structure. It should be noted one type of activator center with site symmetry D_2 mainly occur in aluminate (gallate) garnets. In germanate and silicate garnets, where heterovalent replacement of doping ions is realized, this mechanism become complicated. In this case one can find multicenter phenomenon [4].

This paper reports on the experimental studies of spectral-luminescence properties of Eu^{3+} ions in $Ca_3Ga_2Ge_3O_{12}$ crystals. Received interest to study the spectral-luminescence properties of crystals doped by Eu^{3+} ions is due to the practical needs in effective phosphors. On the other hand, Eu^{3+} ions is often used as a structural microprobe to study its nearest surroundings.

EXPERIMENTAL

The Eu^{3+} doped $Ca_3Ga_2Ge_3O_{12}$ single crystals with high crystalline perfection were grown by the Czochralski technique in flow of dry oxygen in a platinum crucible. The concentration of Eu^{3+} impurity ions ranged from 0.1 to 3 at.%. Optical absorption spectra were recorded by UV-VIS spectrophotometer.Luminescence and excitation spectra were obtained with a grating spectrometer SDL-2. Excitation was achieved by 150 W xenon lamp. Measurements were carried out at 300 and 80 K. Starting composition of the melt was in accordance with the scheme: $(Ca_{1-x}E_x)_3\ Ga_2(Ge_{1-x}Ga_x)_3O_{12}$.

RESULTS AND DISCUSSION

The transparency region of pure $Ca_3Ga_2Ge_3O_{12}$ crystals extend from ~ 0.240 to 6 μ, that allows us to investigate electron transitions of Eu^{3+} impurity ions. Figure 1 shows the absorption spectrum in the region 36000-26000 cm^{-1}.

Proc. Int. Conf. on Inorganic Scintillators and Their Applications, SCINT95,
1996, Delft University Press, The Netherlands

Absorption spectrum of given crystals consists of narrow lines of f-f transitions in Eu^{3+} ions and strong absorption at near UV - region, which is due to the broad charge-transfer band O^{2-} - Eu^{3+} overlapped with the intense absorption of the fundamental absorption edge. The transition $^7F_0$ - $^5D_0$ is observed at 17230 cm^{-1} as a weak fracture in the samples with maximum concentration of activator (about 3 at.%) only (Inset on Fig. 1). The relatively intense group of lines due to transition $^7F_1$ - $^5D_0$ was observed in absorption spectrum at 17100-16600 cm^{-1} at 300 K. Two intense line are recorded at 18968 and 19030 cm^{-1} due to $^7F_0$ - $^5D_1$ transitions.

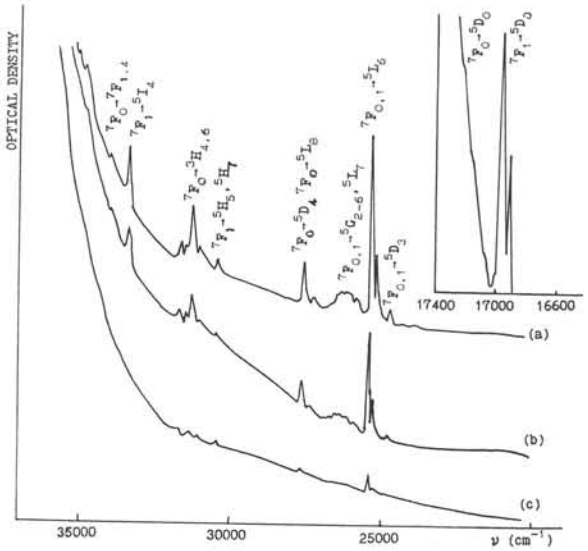

Figure 1. RT absorption spectra of $Ca_3Ga_2Ge_3O_{12}$ crystals activated with (a) 3 at.%, (b) 1 at.% and (c) 0.1 at.% europium. Inset: magnification of the $^7F_{0.1}$ - $^5D_0$ region.

The excitation spectrum of Eu^{3+} luminescence correlates well with the absorption spectrum. This spectrum consists of the broad charge-transfer band O^{2-} - Eu^{3+} peaked at about 260 nm and narrow lines of f - f transitions in Eu^{3+} ions (Fig. 2a). Luminescence spectra of $Ca_3Ga_2Ge_3O_{12}$:Eu crystals are observed in the region between 580-730 nm and mainly due to the transition $^5D_0$ - $^7F_{0.4}$ in Eu^{3+} (Fig. 2 b). An absence of emission from higher ^5D levels can be due to efficient multiphonon relaxation or to quenching by cross relaxation. Under UV lamp excitation, there is only a red luminescence indicating that all the Eu ions are in trivalent oxidation state. It is known, that number, relative intensities, and the splittings of lines associated with $^5D_0$ - ^7F_j transitions give information about site symmetry and number of Eu^{3+} sites [5,6]. The complete degeneration lifting and relative low ratio between line intensities of magnetic dipole transition $^5D_0$ - $^7F_1$ and electric dipole transition $^5D_0$ - $^7F_2$ (Fig. 2 b) indicate low symmetry sites with no inversion center. In view of crystal structure one expect that Eu^{3+} activator ions are incorporated into host lattice replacing Ca^{2+} ions at the site of D_2 symmetry in the dodecahedron. The heterovalent isomorphism is realized in given compound. The positive effective charge Eu^{3+} requires the formation of charge compensating defects. One could expect the most probable defects compensating excess charges of Eu^{3+} impurities to be "antisite" defects $Ga_{(d)}^{3+}$. This is Ga^{3+} ions replacing the tetrahedral sites of Ge^{4+} ions according to the scheme: $\{Ca_{1-x}TR_x\}_3[Ga]_2(Ge_{1-x}\ Ga_x)_3O_{12}$.

High volatility of GeO_2 dioxide during growing of $Ca_3Ga_2Ge_3O_{12}$ crystals promotes the appearance of such type defects. Really, direct technique such as neutron diffraction confirms the presence of antisite defects Ga^{3+} in $Ca_3Ga_2Ge_3O_{12}$ crystals. As a result in addition to single Eu^{3+} center the different types of associations ($Eu_{\{Ca\}}^{3+}$ +$Ga_{(Ge)}^{3+}$) and their clusters can appear. As it is shown in [4] using thermodynamical point of view, at least six different types of activator centers can be formed in Nd^{3+} doped $Ca_3Ga_2Ge_3O_{12}$ garnet crystals.

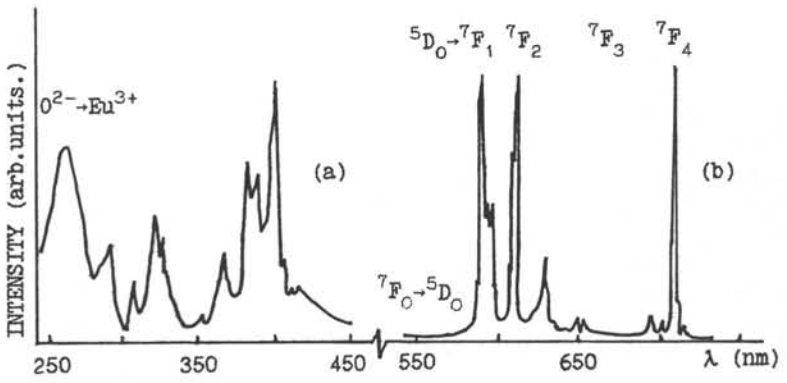

Figure 2. Excitation (a) and luminescence (b) spectra of $Ca_3Ga_2Ge_3O_{12}$: Eu^{3+} (C=3 at.%) recorded at 300 K (λ_{exc} = 260 nm, λ_{em} = 590 nm).

Structure, composition and concentration of these centers depend on total activator concentration in given compound. In order to elucidate of the possible formation of difference Eu^{3+} centers in $Ca_3Ga_2Ge_3O_{12}$ the detail investigation of Eu^{3+} emission for various activator concentrations ($C_{Eu^{3+}}$ = 0.1 - 3 at.%) in a spectral region 570-600 nm ($^5D_0$ - $^7F_{0,1}$ channels) was performed (Fig. 3). From Fig. 3 the following remarks can be made:

luminescence lines are inhomogeneously splitting and broadening;

the $^5D_0$ - $^7F_1$ transition is mainly composed of at least eight well separated lines. This indicates that spectrum is complex and is due to more than one type of Eu^{3+} activator centers;

the $^5D_0$ - $^7F_0$ transition is composed of a single narrow line peaking at 580.1 nm and is obviously observed in crystals with maximum Eu^{3+} concentration (3 at.%);

the relative fluorescence lines intensities and their number vary with change of activator concentration. Such fact could be explained by change of concentration of different types of Eu^{3+} centers.

Thus, it can be concluded that Eu^{3+} activator ions form a several type centers in $Ca_3Ga_2Ge_3O_{12}$ crystals. It should be noted that the all type of activator centers are excited simultaneously under exciting lamp light and the observed fluorescence spectra are complicated. The individuals of different activator centers are difficult to separate in given case. The analysis of absorption spectra in the line groups $^7F_0$ - $^5H_{4,6}$ at 80 K was done using the concentration series technique [8]. The concentration dependences of peak absorption coefficient of lines have showed the three systems of parallel curves reproduced the concentration dependences of corresponding centers.

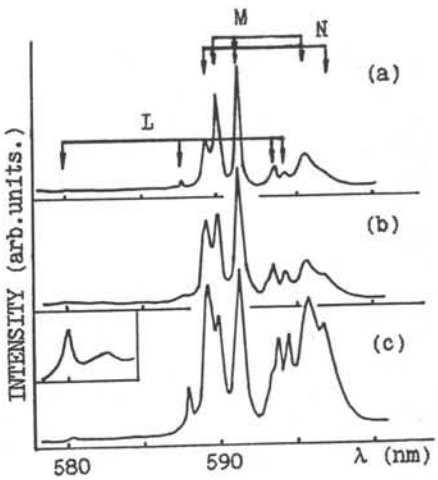

Figure 3. Emission spectra of Eu^{3+} in $Ca_3Ga_2Ge_3O_{12}$: Eu^{3+} (a) 0.1 at.%, (b)1at.%, (c) 3at.% under 395 nm excitation at 300 K. Brackets show lines of different activator centers, and marks are denoted according with [7]. Inset: magnification of the $^5D_0$ - $^7F_0$ region.

This result indicates that mainly three types of centers are revealed in concentration range 0.1 - 3 at.%. This conclusion is in agreement with data obtained in [7] for $Ca_3Ga_2Ge_3O_{12}$: Eu^{3+} crystals at concentration of Eu^{3+} ions about 0.05 at.%. Three different types of centers were isolated in [7]:

single M-center with local symmetry D_2 ;

L-pair center with local symmetry C_2 (Eu^{3+} plus charge compensation defect Ge_{Ge+3} in first coordination sphere);

N-pair center with local symmetry C_{2v} (Eu^{3+} activator plus Ga_{Ge+3} in more distant coordination sphere).

We have labeled the individual lines of different centers in Fig. 3 using the data obtained in [7]. As it is follow from Fig. 3, luminescence spectrum at $C_{Eu3+} = 0.1$ at.% exhibits dominant lines of single M-centers. When increasing the activator content in crystals the concentration of N and L centers is enhanced. The concentration of single M-center is obviously decreased with respect to the lines of N- and L type centers in luminescence spectrum at concentration $C_{Eu3+} = 3$ at%. So, quality and quantity of different types of Eu^{3+} activator centers depend on the total concentration of activator. The narrow line at 580 nm (Inset on Fig. 3 c) due to $^5D_0$ - $^7F_0$ transition is connected with L-type center only and is observed in samples with sufficient concentrations of L-centers.

It should be noted, that Eu^{3+} luminescence efficiency under excitation into the f - f levels is high. The efficiency under charge-transfer excitation is somewhat lower as follows from excitation spectrum (Fig. 2). The radiationless losses at charge-transfer excitation depend on concentration. Intensity of charge-transfer excitation related to the intensity of f - f excitation is more for high Eu^{3+} concentration. For a low activator concentration the efficiency under excitation charge-transfer band is lower. Therefore, the losses are higher in samples, where single centers with D_2 symmetry are predominant and a lower in samples, where pair centers ($Eu_{Ca3+} + Ga_{Ge3+}$) are predominant. This can be explained by decreasing of positive effective charge in pair defects ($Eu_{Ca3+} + Ga_{Ge3+}$) and agrees with the model suggested in [9].

REFERENCES

1. A.A.Kaminskii, L.A.Aminov, V.L.Yermolaev et. al., in: Physics and spectroscopy of laser crystals. chap., Nauka, Moskow (1986).
2. O.A.Keda, M.V.Vasylenko, L.B.Viktrov et.al. Zh.Prikl. Spectr. 41. 867 (1984).
3. S.Kh.Batygov, Yu.K.Voron'ko, N.G.Margiani and N.N.Ryskin, in: Spectroscopy of oxides crystals for quantum electronics, Proc IOFAN, v. 29, Nauka, Moscow, P. 101 (1991).
4. Yu.K.Voron'ko, S.B.Gessen, Yes'kov et. al. Izv. Akad. Nauk. SSSR, Ser. Neorg Mater, 24, 818 (1988).
5. M.Buijs and G.Blasse J.Solid State Chem., 71, 296 (1987).
6. J.Dexpert-Ghys, M.Fancher and P.Caro. J. Solid State Chem., 47, 27 (1982).
7. Yu.K.Voron'ko, N.A.Yes'kov, L.M.Yershova, A.A.Sobolov, C.N.Ushakov. Optika and spectr., 70 1038 (1991).
8. Yu.K.Voron'ko, A.A.Kaminskii and V.V.Osiko. Zh.Eksper. Teor.Fiz., 49, 724 (1965).
9. G.Blasse, Van Der Voort, W.J.Shipper and W.Van.Schaik, Proceeding ICDIM 92, Schloß, Nordkirchen, Germany, August 16-26, p. 240 (1992).

TIMING PROPERTIES OF GSO AND LSO SCINTILLATORS[1]

M.Moszyński[1)], T.Ludziejewski[1)], D.Wolski[1)],
W.Klamra[2)], and V.V.Avdiejchikov[3)]
[1)] Soltan Institute for Nuclear Studies, PL 05-400 Świerk-Otwock, Poland
[2)] Royal Institute of Technology, Department of Physics
Frescati, S-104 05 Stockholm, Sweden
[3)] Joint Institute for Nuclear Research, 141980 Dubna,
Moscow Region, Russian Federation

Abstract

Light pulse shape, number of photoelectrons per energy unit and time resolution for a 1x1x1 cm^3 GSO crystal coupled to an XP2020Q photomultiplier were studied and compared with similar measurements done earlier for LSO. The observed time resolution, FWHM equal to 703 ps for the energy threshold set at 1 MeV on ^{60}Co γ-spectrum is inferior compared to that for LSO because of the slow rise of the light pulse of GSO and a lower light yield. The time resolution obtainable with the GSO and LSO crystals was discussed in terms of the Hyman theory of timing.

1. INTRODUCTION

In spite of the fact that a number of papers discuss different properties of the new scintillators, there is a lack of a systematical study of their timing properties. Within the frame of this work the study of the obtainable time resolution with GSO scintillator [1,2] was carried out. Light pulse shape and the number of photoelectrons per energy unit lost by γ-rays were measured as the factors determining the time resolution for the scintillators. Then a simlar set of data measured recently for LSO scintillator in this same experimental conditions, presented in ref. [3], was used to discuss the timing with LSO and GSO crystals based on Hyman theory of timing [4].

2. EXPERIMENTAL DETAILS

All the studies were carried out for two samples of GSO crystals with the dimensions of 10x10x10 mm^3 and 10x10x1 mm^3. The concentration of Ce in the studied GSO samples was determined by X-ray fluorescsence analysis to be 1.0 ± 0.2 mol% and 0.53 ± 0.1 mol%, respectively. The crystals coated with a teflon tape were used in the study. The measurements were done with the XP2020Q photomultiplier with the radiant photocathode sensitivity of 74 mA/W working with the B' voltage chain [5]. The energy resolution of 9% for the 662 keV γ-line from a ^{137}Cs source was measured for the thick sample.

All the details concerning LSO crystals are presented in ref. [3]. The timing study was done for the 5x4x14.5 mm^3 sample with Ce concentration of 0.22 % , see ref. [3].

[1] Support for this work was provided by the Polish Committee for Scientific Research, grant No. 2-P302-096-07

Proc. Int. Conf. on Inorganic Scintillators and Their Applications, SCINT95,
1996, Delft University Press, The Netherlands

3.RESULTS

3.1 Number of photoelectrons

The number of photoelectrons per energy unit was measured by comparing the position of the 662 keV full energy peak from a ^{137}Cs with that of the single photoelectron peak. The photoelectron yield of 1280±80 phe/MeV and 1600±100 phe/MeV were measured for the 10x10x10 mm^3 and 10x10x1 mm^3 samples, respectively. The measured values are in good agreement with those found in refs. [6,7].

The number of photoelectrons for the LSO crystal considered in this work was measured in ref. [3] to be 4200±300 phe/MeV.

3.2. Light pulse shape

The light pulse shape studies were performed by means of the single photon method [19,20]. The XP2020UR photomultiplier [8] was used to detect single photons. The uncoated GSO scintillator was optically coupled to the XP2020Q photomultiplier, to produce a reference signal, and was irradiated by γ-rays from a ^{137}Cs source.

Fig. 1 presents the light pulse shapes measured for both the crystals. The solid curves in fig. 1 are a result of a fit using a sum of two exponentials plus uniform background. The decay times of the fast component equal to 41.1±2.0 ns and 64.2±3.5 ns for the thick and thin GSO crystals, respectively, are in a good agreement with the decay times measured for the different Ce content in the GSO samples, refs [1,2,7]. In the insert of fig.1 a more detailed shape of the fast component of the GSO light pulse is shown. The solid line represents a result of two exponential fit to reflect a finite rise of the light pulses. The poor accuracy of the fit shows the difficulties to describe the GSO light pulse in the way as above. An observed serious slowing down of the initial decay of the light pulse was interpreted in ref. [9] by the energy transfer from Gd to Ce.

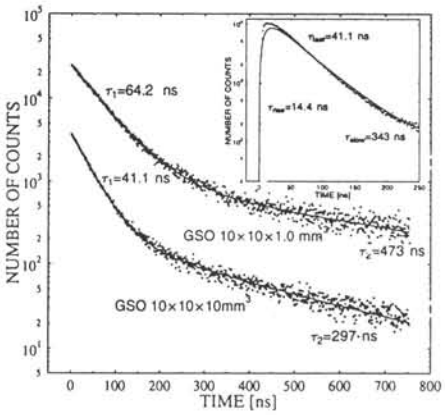

Figure 1 Time distribution of light pulses produced by γ-rays in the GSO crystals.

3.3. Timing studies

The timing studies of the GSO scintillator were carried out with the 10x10x10 mm^3 crystal coupled to the XP2020Q photomultiplier. The reference counter consisted of a NE111 plastic 2.5 cm in diameter and 1 cm in height coupled to the XP2020UR photomultiplier. Its time resolution for a narrow energy window set at 1 MeV of ^{60}Co γ-spectrum was equal to 80 ps [8]. The time resolution measurements were performed for a ^{60}Co source. The time spectra measured with the GSO were compared to that measured previously in the same conditions with the 5x4x14.5 mm^3 LSO scintillator, following ref. [3].

Fig 2 presents the comparison of the time spectra measured with GSO and LSO crystals for a ^{60}Co source and the energy threshold set at 1 MeV. It shows much inferior timing properties of the GSO crystal. The time resolution of the GSO is worse by factor of 4.4, taking for the LSO the time resolution corrected for the contribution of the reference counter [3].

To understand the observed difference one has to analyze the time resolution taking into account the characteristics of the scintillator which affect the timing, the light pulse shape and the number of photoelectrons. The decay time constants of both the crystals are approximately the same, 41.1 ns for GSO (see fig. 1) and 46.6 ns for the LSO crystal, see ref. [3]. The number of photoelectrons measured for the LSO with the same XP2020Q photomultiplier equal to 4200 phe/MeV, see ref. [3], is higher than that determined for GSO as 1280 phe/MeV. However, it leads only to difference by factor of 1.8. Thus, one has to pay attention into difference of the light pulse shapes. Both the pulses are presented in linear scale in fig. 3, normalised at their decay. The LSO light pulse exhibits a pure exponential decay with very fast initial rise, see ref. [3]. The GSO light pulse is slower. One observes a finite rise time of about 4 ns and delay of the decay reflected in the rounded maximium of the pulse. The comparison of the light pulses presented in fig. 3 seems to explain qualitatively the larger degradation of time resolution for GSO than that resulting from the lower light yield.

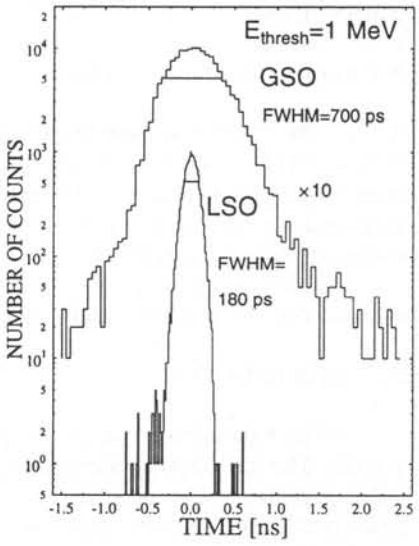

Figure 2 The comparison of the time spectra measured with the GSO and LSO crystals for ^{60}Co γ-rays and energy threshold set at 1 MeV.

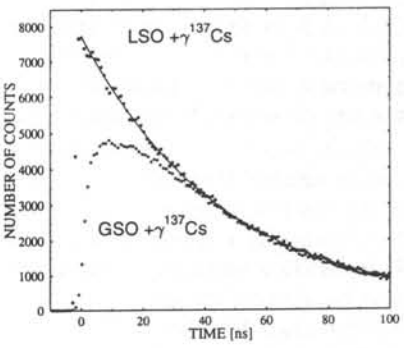

Figure 3 The light pulses of GSO and LSO presented in a linear scale and normalised at their decay.

An approximate quantitative analysis of the time resolution for the LSO and GSO can be based on the Hyman theory of timing [4]. The prediction of the Hyman theory are presented in ref. [4] as series of plots showing the normalised time resolution to the number of photoelectrons, N and to the decay time constant τ of the light pulse as a function of the triggering fraction of the anode pulse. The plots were calculated for the different parameters of the photomultiplier and scintillator. Let pay attention to the plot in fig. 4, following fig. 4f of ref. [4], which corresponds well to the parameters of the counter consisting of LSO scintillator and XP2020Q photomultiplier. The plots were calculated for the σ = 1 ns, which is a satisfactory value for the standard deviation of the single photoelectron response of the XP2020 and τ=48 ns close to decay time constant of the LSO. Since the best time resolution

for the $\sigma'/\sigma=1/2$ is not improved for a lower time jitter, σ', then 0.5 ns [4], it can be used to find the normalised time resolution equal to 0.1. It can be recalculated to the time unit taking $\tau=46.6$ ns and N=5250 phe, corresponding to the mean accepted energy in the measurement. Thus one will find $\delta t=66$ ps and FWHM=156 ps. Note an excellent agreement of the calculated time resolution with that measured in ref. [3].

A similar analysis for GSO is only approximate since the Hyman theory considers the light pulse of the two exponential form. It was shown in fig. 2 that this description weakly reflects the real shape of the GSO light pulse. The estimation of the time resolution for GSO was based on the plots presented in figs 6 and 7 of ref. [4], taking the rise time constant of the light pulse of 8.2 ns and 16.4 ns, respectively. The time resolution of 700 ps and 999 ps was calculated for both the cases, respectively. Note measured time resolution of 700 ps. It suggests that for timing discussion a better rise time constant of the GSO pulse is of 8.2 ns. No doubt that a more accurate description of the GSO pulse introduced to the Hyman theory will allow to find a full agreement.

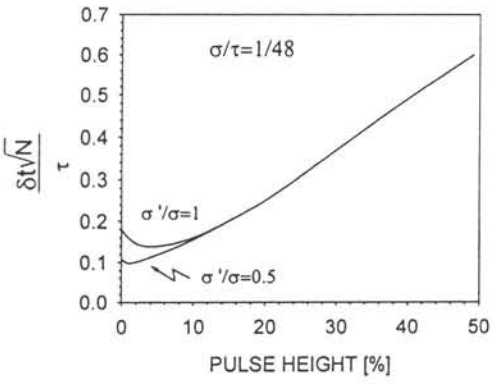

Figure 4 The normalised time resolution acc. to ref.[4] versus the triggering fraction of the photomultiplier pulse.

The presented experiment and comparison with the Hyman theory show that the time resolution of the LSO is controlled by its decay time constant and the number of photoelectrons. In the case of GSO it is strongly influenced by the finite rise time and slowing down of the light pulse by the energy transfer from Gd to Ce.

REFERENCES

1. K.Takagi and T.Fukazava, Appl.Phys.Lett. 42(1983)43.
2. H.Ishibbashi, K.Shimizu, K.Susa and S.Kubota, IEEE Trans. on Nucl. Sci. NS36(1989)170.
3. T.Ludziejewski, K.Moszyńska, M.Moszyński, D.Wolski, W.Klamra, L.O.Norlin, E.Devitsin and V.Kozlov. IEEE Trans on Nucl. Sci. in press.
4. L.G,Hyman, Rev. Sci. Instr. 36(1965)193.
5. Philips Photonics, Photomultiplier Catalog, 1982.
6. S.I.Ziegler, J.G.Rogers, V.Selivanov and I.Sinitzin, IEEE Trans. on Nucl. Sci. NS-39(1992)1588.
7. P.Dorenbos, J.T.M.deHaas, C.W.E.vanEijk, C.L.Melcher and J.S,Schweitzer, IEEE Trans. on Nucl. Sci. NS-41(19940735.
8. M.Moszyński, Nucl. Instr. and Meth. A324(1993)269.
9. H.Suzuki, T.A.Tombrello, C.L.Melcher and J.S.Schweitzer, IEEE Trans. on Nucl. Sci.NS-41(1994)681.

LUMINESCENCE PROPERTIES OF CERIUM-DOPED GADOLINIUM OXYORTHOSILICATE CERAMIC SCINTILLATORS

W. Rossner*, R. Breu**
* Siemens AG, Corporate Research and Development, D-81730 Munich, Germany
** Fachhochschule Munich, Lothstr. 34, D-80335 Munich, Germany

ABSTRACT

The luminescence characteristics of polycrystalline, highly-dense ceramics of cerium-doped gadolinium oxyorthosilicate are reported. The fundamental luminescence features of the ceramic samples are nearly identical to those of single crystals. The ceramics doped with ≥0.5 mol% Ce do not exhibit a secondary decay as reported for single crystals. The drawback of the ceramic is the low optical quality of the bulk dominated by optical scattering. This is the main reason for the observed low light yield and broad photopeak of the pulse-height spectra from these ceramics for gamma radiation from Co^{57}.

INTRODUCTION

In recent years, interest has increased in cerium-doped gadolinium (GSO:Ce) and lutetium oxyorthosilicate scintillators for high energy radiation detectors [1]. These scintillators have very attractive properties such as high densitiy, high light output, short decay time and good spectral matching to most photodetectors. It has been reported that single crystals have been grown which are up to 20 cm in length and 6 cm in diameter [2]. However, there have been some problems with the production of single crystals relating to the high melting point, low pulling rate, cerium segregation, anisotropic thermal expansion and easy cleavage. For that reason and, moreover, for general feasibilty, we investigated the fabrication and the properties of polycrystalline, ceramic oxyorthosilicates. GSO:Ce was chosen as a typical example. In the present work, the luminescence properties of cerium-doped GSO ceramics, according to $Gd_2O(SiO_4)$:Ce, with cerium concentrations varying from 0.25 to 5 mol% were investigated and compared with single crystal data.

EXPERIMENTAL

The test samples were fabricated using advanced ceramic technology starting with a precipitated cerium-doped Gd_2O_3 and a nanometer-scaled SiO_2 powder, followed by a solid state reaction at 1400 °C, high energy milling, isostatic powder pressing and pressureless sintering of powder compacts at temperatures from 1650 °C to 1750 °C. The sintered bodies were cut in 20 mm diameter sample disks with thicknesses of 0.5-2 mm. An uniform surface quality was established for all test specimens by grinding. The luminescence properties of the samples were measured by various techniques. For emission and excitation spectroscopy at room temperature a spectrofluorophotometer (Shimadzu RF5001.PC) was used. Time-

Proc. Int. Conf. on Inorganic Scintillators and Their Applications, SCINT95,
1996, Delft University Press, The Netherlands

resolved spectroscopy was performed with a pulsed ArF-excimer laser with a wavelength of 193 nm (6.4 eV) and an OSMA-gated photodiode array. The laser pulse width (FWHM) was about 30 ns und the pulse decay time below 10 ns. For the time-resolved measurements, the samples were located in reflecting position at a 48° angle realtive to the laser beam. Excitation with X-rays was carried out with a tungsten tube operating at 50 kV and 20 mA for emission spectroscopy, and a Co^{57} source (122 keV) for pulse-height spectra measurements.

RESULTS AND DISCUSSION

Without optimizing the ceramic processing, a relative density of the ceramic bulk of at least 99.7 % was achieved . The ceramic microstructure (Fig. 1) shows an average grain size of 7 µm, nearly equiaxed grains with a statistical crystallographic orientation, residual pores with an average size of about 1 µm and several micorcracks. The measured samples were nearly colorless and opaque. As tested by standard X-ray diffraction analyses, the ceramics were single phase within the experimental error. Due to the non-translucent optical character of the GSO ceramic, the optical transmittance is very low. For a quantitative description of the optical properties of the ceramic, the Kubelka-Munk theory was used which revealed an absorption coefficient of about 1 cm^{-1} and a scattering coefficient of 45 cm^{-1} in the visible range. The very high value for the optical scattering coefficient compared to a typical single crystal value (<1 cm^{-1}) is the result of residual micropores and microcracks, and the grain boundaries. Due to the anisotropic index of refraction of GSO and the statistical grain orientation within the ceramic, the grain boundaries themselves cause optical scattering which is determined by the absolute change of the refraction index from one grain to the neighboring one.

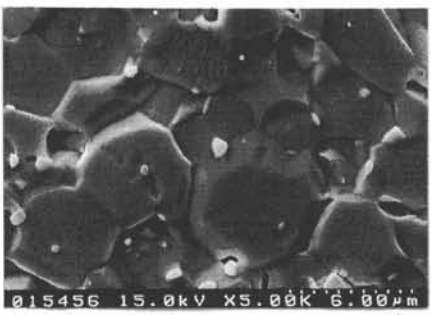

Fig. 1: Characteristic microstructure of GSO: Ce ceramic sintered at 1750°C

In Fig. 2 the characteristic optical excitation spectra of a GSO:Ce ceramic and single crystal are compared. This shows that the excitation band positions are very similar. The low temperature (15 K) excitation spectrum indicates the existence of the known second Ce-center of which the emission is quenched at room temperature [3]. This verfies that adding cerium during ceramic processing causes the same two crystallographic sites to be occupied which are filled during crystal growth. For ceramics, however, the decrease of the excitation band intensity with decreasing wavelength is much more pronounced compared to the reference crystal. This may be explained by the special characteristic of GSO, that there is no sharp optical absorption edge of the host lattice [4,5]. The energy gap between the highest Ce states and the assumed conduction band edge of the

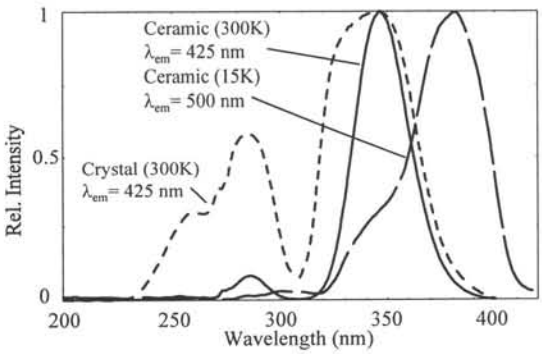

Fig. 2: Excitation spectra of GSO:Ce (0.5 mol%) ceramic and single crystal

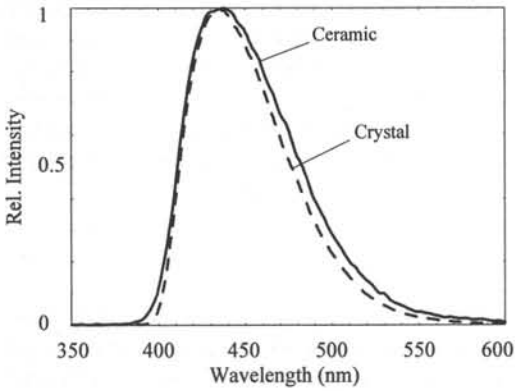

Fig. 3: X-ray excited emission spectra of GSO:Ce (0.5 mol%) ceramic and single crystal

GSO host lattice, being around 1.5 eV, contains something like a continuum of states. This may increase the liklihood that electrons in more excited Ce states will enter the conduction band where they are delocalized and mobile (ionization: Ce^{3+} to Ce^{4+}). This probability increases with decreasing excitation wavelength. In the case of a single crystal, the electrons may migrate for a certain time and distance, and will than be captured and deexcited by a Ce-ion. In the case of the polycrystalline ceramic, some of the migrating electrons will be captured by defect centers, i.e. located at the grain boundaries and deexcited by non-radiative transitions, which lowers the excitation band intensities. In addition, it has to be noted that the penetration depth of the exciting photons is much lower for the ceramics due to the high optical scattering, so, that surface layer defects may cause similar effects in the excitation spectra.

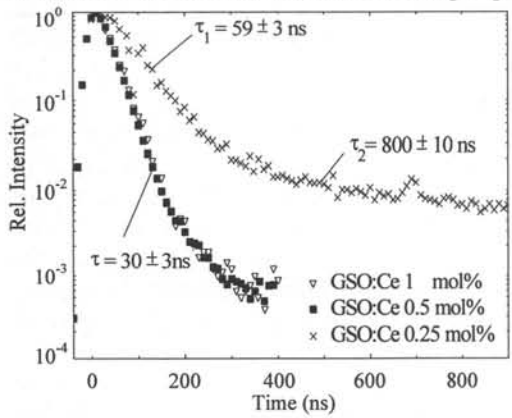

Fig. 4: Decay curve of GSO:Ce ceramics for excitation with 6.4 eV photons

The X-ray-excited emission spectra of GSO:Ce ceramics and single crystals are fully identical as demonstrated for X-ray excitation in Fig. 3. The absolute light yield was not measured but is expected to be lower for ceramics due to the non-transparent character and the higher propability of quenching centers located at the grain boundaries.

The decay kinetics of the emission is known to exhibit fast and slow decay components for excitation with photon energies higher than 6.1 eV [4,6]. Fig. 4 shows the decay curves for some GSO:Ce ceramics excited with 193nm (6.4 eV) photons. The various doped ceramics exhibit a primary decay of some ten nanoseconds, which is consistent with published single-crystal data [7], as well as, the measured Ce concentration dependence of the primary decay time and the luminescence light yield. Just as for single crystals, a secondary decay with similar time constants is observed for low Ce-doped ceramics. Surprisingly, however, for Ce-dopant concentrations $\geq$ 0.5 mol%, a single exponential decay is measured over three orders of magnitude without any indication of a slower secondary decay. An explanation has not yet been found and the results have to be confirmed by additional measurements, e.g. with γ-ray excitation. However, the role of grain boundaries may be considered as a barrier for very long-range energy transfer.

The pulse height response of GSO:Ce ceramics measured with a Co^{57} source (122 keV) varies considerably depending on the optical translucency of the ceramic bulk. For visualization, the energy spectrum of a 1.5 mm thick GSO:Ce ceramic is shown in Fig. 5 together with that of a 2 mm thick reference crystal, both with 0.5 mol% Ce. Although the spectra cannot be

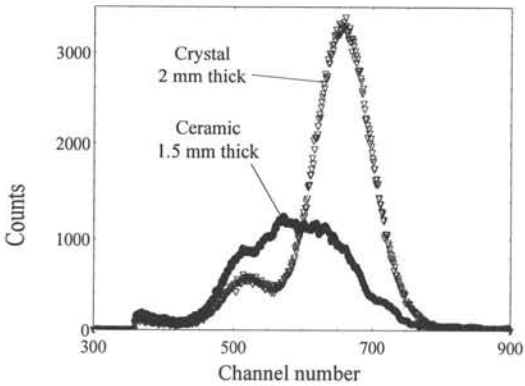

Fig. 5: Pulse-height spectra of GSO:Ce (0.5 mol%) ceramic and single crystal for Co^{57} source (122 keV)

compared exactly due to the different sample sizes, it demonstrates that the ceramic has the lower light yield and much worse energy resolution (FWHM of photopeak). However, the basic luminescence efficiency of the GSO:Ce ceramic is not expected to be very much lower than that of equally doped single crystals. The main drawback of the ceramic is the low optical quality of the bulk domintated by optical scattering which always leads to incomplete light collection for photon detection.

CONCLUSION

To our knowledge, this is the first report on luminescent cerium-doped gadolinium oxyorthosilicate ceramics with very high relative bulk densities. The fundamental luminescence characteristics of the ceramic samples are nearly identical to those of single crystals. The existence of the known two cerium centers could be observed, as well as, the characteristic emission and excitation bands. However, by a more detailed evaluation the ceramic specimens exhibit some differences, like a continuous decrease of the excitation band intensity with decreasing wavelength and the absence of secondary decay for cerium concentrations $\geq$ 0.5 mol%. The GSO:Ce ceramics in their present non-translucent optical quality are not well suited for spectroscopic purposes. For that reason, the optical quality of the GSO:Ce ceramic has to be improved by optimizing the ceramic processing. In addition, the decay dynamics has to be studied in greater detail using various excitation energies.

ACKNOWLEDGMENTS

The authors would like to thank Prof. G. Blasse for valuable discussions, R. Paul for fabricating the ceramic specimens and Dr. Ishibashi, Hitachi Chemical Co. LTD, for supplying a reference crystal.

REFERENCES

[1] C.L. Melcher and J.S. Schweitzer, Nucl. Instr. and Meth. A314, 212-214 (1992).
[2] T. Utsu and S. Akiyama, J. Cryst. Growth 109, 385-391 (1991).
[3] H. Suzuki, T.A. Tombrello, C.L. Melcher and J.S. Schweitzer, Nucl. Instr. and Meth. A320, 263-272 (1992).
[4] Z.A. Rachko, I.A. Tale, V.D. Ryzhikov, J.L. Jansons and S.F. Burochas, Nucl. Tracks. Radia. Meas., Vol. 21, No. 1, 121-124 (1993).
[5] D. Bouttet, C. Dujardin, C. Pedrini, W. Brunat, D. Tran Min, to be published.
[6] H. Suzuki, T.A. Tombrello, C.L. Melcher C.A. Peterson and J.S. Schweitzer, Nucl. Instr. and Meth. A346, 510-521 (1994).
[7] C.L. Melcher, J.S. Schweitzer, T. Utsu and S. Akiyama, IEEE Trans. Nucl. Sci. Vol. 37, No. 2, 161-164 (1990).

Ce^{3+} DOPED Lu_2O_3 AND Y_2O_3 SINGLE CRYSTALS: OPTICAL PROPERTIES OF NOVEL SCINTILLATOR MATERIALS

W. van Schaik, M. Raukas, S. Basun*, U. Happek and W.M. Yen
Department of Physics and Astronomy
The University of Georgia, Athens, GA 30602, U.S.A.
*A.F. Ioffe Phys. Tech. Institute, 194021 St. Petersburg, Russia

ABSTRACT

For the first time Ce^{3+} luminescence is observed in Lu_2O_3 and Y_2O_3 single crystals for UV excitation. The Ce^{3+} emission bands in these host lattices peak at 385 and 410 nm, respectively. For both crystals the decay time of the Ce^{3+} emission is 25 ns at room temperature. Furthermore, it is shown that absorption bands in the visible coincide with a band in the photoconductivity spectrum and can not be due to 4f-5d transitions of Ce^{3+}.

INTRODUCTION

In recent years a large number of investigations has been focused on Ce^{3+} doped materials, since they are good candidates for scintillators in nuclear physics or in medical applications. Until now, Ce^{3+} doped oxides such as Lu_2O_3 and Y_2O_3 have been studied in the form of powders, but the results in terms of luminescence efficiency were not very promising. This is rather surprising since Ce^{3+} is known to luminesce efficiently in a large number of host lattices. It has been suggested that the Ce^{3+} luminescence in these materials is quenched by photoionization [1].

To our knowledge no work has been done on single crystals of Lu_2O_3:Ce and Y_2O_3:Ce. We attribute this to the high melting point of these materials. Here we will report our results on the optical properties and photoconductivity characteristics of single crystals of these materials, grown with a laser heated pedestal growth technique. After growth the samples were annealed either in hydrogen atmosphere or in air.

RESULTS AND DISCUSSION

The 4f-4f transitions of Ce^{3+} are observed in the infrared absorption spectrum for crystals annealed in a reducing atmosphere. The spectral position and the number of observed lines is in agreement with earlier reports for powder samples [2]. After annealing in air no lines due to Ce^{3+} were observed in the infrared.

After pulsed laser excitation at either 280 nm and 337 nm blue luminescence is observed for both Lu_2O_3:Ce and Y_2O_3:Ce. The emission spectrum Y_2O_3:Ce at room temperature is presented in fig. 1. The emission bands peak at 385 and at 410 nm for Lu_2O_3:Ce and Y_2O_3:Ce, respectively. At low temperatures the emission band of Y_2O_3:Ce is clearly split in two bands, which reflects the ground state splitting of Ce^{3+}. The luminescence intensity does not strongly depend on the temperature in the range 10 to 300 K. This emission band is not observed for the samples which are annealed in air, nor for the undoped samples.

Proc. Int. Conf. on Inorganic Scintillators and Their Applications, SCINT95,
1996, Delft University Press, The Netherlands

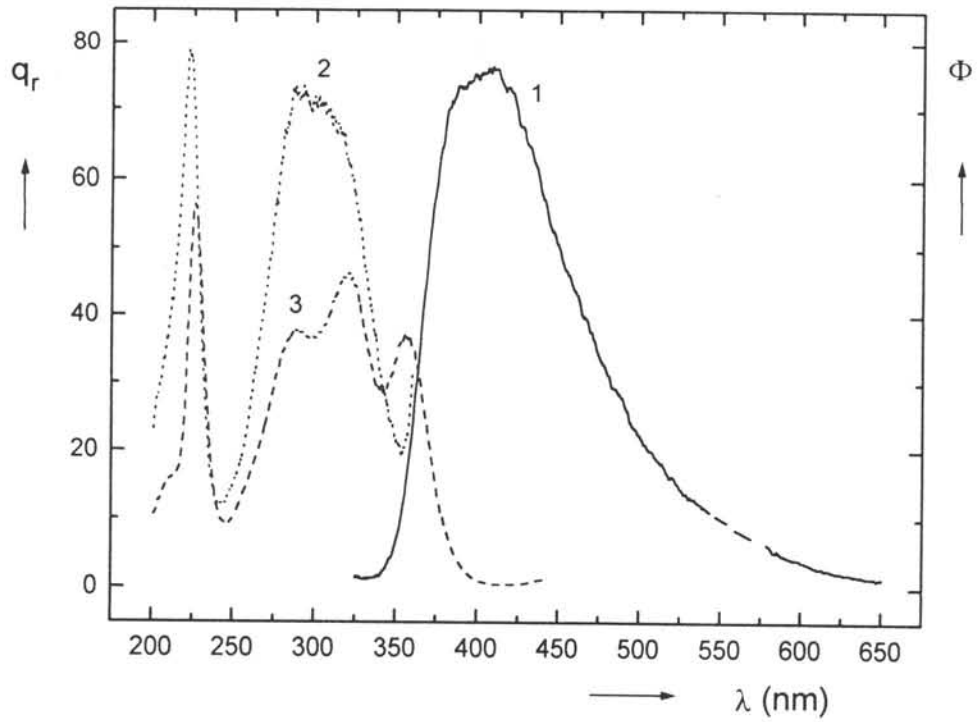

Fig. 1 Emission spectrum (1) of Y_2O_3:Ce at room temperature for λ_{exc}=280 nm. Φ gives the radiant power per constant wavelength interval. Excitation spectra of the Ce^{3+} luminescence in Y_2O_3 at room temperature. Spectrum 2 is recorded for λ_{em}=380 nm and spectrum 3 for λ_{em}=470 nm. q_r gives the relative quantum output in arbitrary units.

In fig. 1 the excitation spectrum of the Ce^{3+} emission in Y_2O_3:Ce is given. The excitation spectra recorded at the maximum of the emission band show for both crystals three bands in the UV, in addition to the host lattice excitation at wavelength shorter than 225 nm. Mentioned excitation bands are not observed for undoped crystals. The relative intensities of the excitation bands depend on the emission wavelength at which the excitation spectrum is recorded. This effect is especially pronounced for Y_2O_3:Ce. A well resolved excitation band centered at 355 nm appears in excitation spectra recorded at the long wavelength side of the emission band. Excitation at 355 nm results in a red shift of the emission maximum. These results show that the Ce^{3+} ion is incorporated on more than one site in both lattices. This is in agreement with the fact that both lattices offer two cation sites [3]. From the infrared absorption spectra we know that Ce^{3+} is present on both the C_2 and S_6 sites.

The decay curves recorded at the maximum of the emission band for both crystals can be fitted by a single exponential decay. The decay time of the Ce^{3+} emission in Lu_2O_3 is 25 ns at room temperature and 30 ns at 10 K. The decay time of the emission of Y_2O_3:Ce is 25 ns at 10 K and does not change with temperature. The decay time of the red shifted emission band in Y_2O_3:Ce for excitation at 355 nm is 40 ns at 10 K. In conclusion, the luminescence exhibits all the characteristics expected for Ce^{3+} doped in Lu_2O_3 and Y_2O_3.

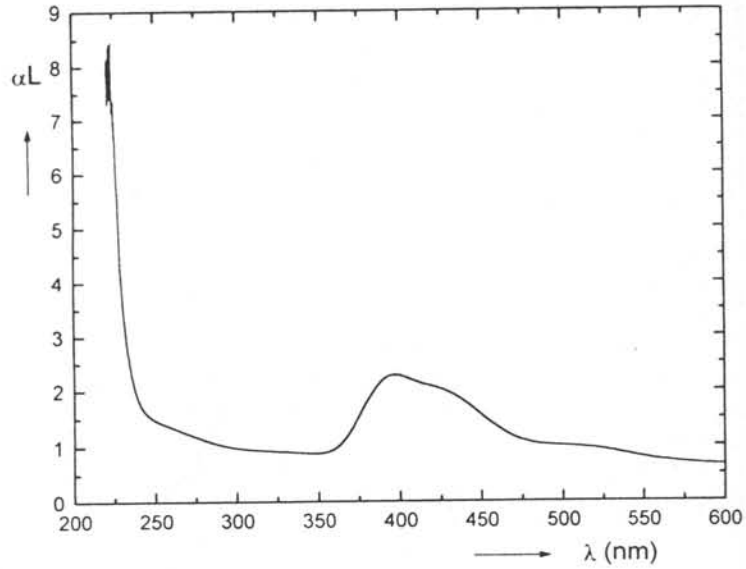

Fig. 2 Absorption spectrum of Y_2O_3:Ce at room temperature. The crystal was annealed in a reducing atmosphere.

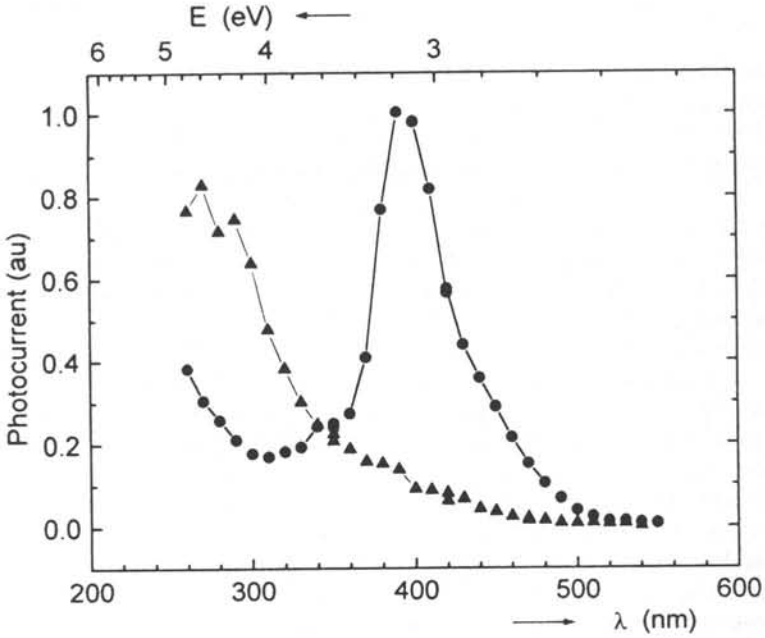

Fig. 3 Photoconductivity of Y_2O_3:Ce (dots) and undoped Y_2O_3 (triangles) at room temperature per incident photon in arbitrary units. Both crystals were annealed in a reducing atmosphere.

The absorption spectrum of Y_2O_3:Ce is given in fig. 2. The absorption spectra of Lu_2O_3:Ce is similar. At wavelengths shorter than 225 nm we observe an absorption band due to the host lattice. The spectra show features in the UV corresponding to the excitation bands in addition to a strong broad absorption band in the visible region. The absorption band at 400 nm is especially noteworthy. Assuming that the Ce^{3+} luminescence occurs from the lowest 5d level, this absorption band can not correspond to the observed luminescence, since the absorption band is red shifted relative to the short wavelength onset of the emission band. Excitation in this absorption band does not lead to luminescence in the visible region of the spectrum. Samples annealed in air do not show any of these features, but show a strong broad absorption band in the UV, which starts at around 400 nm. This band is ascribed to a ligand-to-metal charge transfer of Ce^{4+} [4].

In order to obtain more insight in the nature of the 400 nm absorption band we have studied the photoconductivity behavior. The photoconductivity spectrum of Y_2O_3:Ce is presented in fig. 3. The spectra are characterized by a band at 400 nm and by an increase of the photocurrent in the UV due to the band to band transition. This band structure in the photoconductivity spectrum is remarkable, since in general the signal due to photoionization is not expected to decrease with higher energies. It should be noted that excitation bands of the Ce^{3+} emission fit exactly into the gap of the photoconductivity spectrum.

The 400 nm photoconductivity band is not observed for the undoped samples, whereas for the samples containing Ce^{4+} it is nearly 2 orders of magnitude smaller. The photoconductivity results show that the absorption bands in the visible part of the spectrum can not be due to 4f-5d transitions of Ce^{3+}, since these are localized transitions, which are not expected to lead to photoconductivity. Moreover, it explains the fact that no Ce^{3+} luminescence is observed for excitation in these bands.

CONCLUSION

The absorption bands in the visible observed for Y_2O_3:Ce and Lu_2O_3:Ce are, in view of our photoconductivity results, not due to 4f-5d transitions. Tentatively we ascribe these absorption bands to an electron transfer state [1,5] of the couple $Ce^{3+} + Ce^{4+}$. This is a subject of further investigations. Finally we conclude, in contrast to earlier reports, that Ce^{3+} is luminescent in both Y_2O_3 and Lu_2O_3, but that the lowest 5d transition appears to be at higher energies than previously assumed.

We like to thank M. Weber, D. Cohen and G. Flinn for stimulating discussions, Lizhu Lu for growing the crystals, C. Melcher for supplying the starting material for the Lu_2O_3 samples and D. McClure for providing the photoconductivity equipment. This work is supported by grants from ARPA and NSF.

REFERENCES

[1] G. Blasse, W. Schipper and J.J. Hamelink, Inorg. Chim. Acta, **189** (1991) 77.
[2] G.A. Slack, S.L.Dole, V. Tsoukala and G.S. Nolas, J.Opt. Soc. Am. B, **11** (1994) 961.
[3] R.W.S. Wyckoff, Crystal Structures, vol. 2, 2nd ed., J. Wiley, New York 1965.
[4] W. van Schaik and G. Blasse, Chem. Mater., **4** (1992) 410.
[5] W. van Schaik, S. Lizzo, W. Smit and G. Blasse, J. Electrochem. Soc., **140** (1993) 216.

SOLID SOLUTIONS OF SCINTILLATORS: A WAY OF IMPROVING PROPERTIES

A.N.Belsky[1], A.V.Gektin[2], S.M.Klimov[1], J.C.Krupa[3], P.Martin[5], A.Mayolet[3], V.V.Mikhailin[1], C.Pedrini[4], A.N.Vasil'ev[1], E.I.Zinin[6]
[1]Physics Department, Moscow State University, 117234 Moscow, Russia
[2]Institute for Single Crystals, 310001 Kharkov, Ukraine
[3]Institute de Physique Nucleaire, 91406 Orsay France
[4]LPCML, University Lyon-1, 69622 Villeurbanne, Cedex France
[5]LURE, 91406Orsay France
[6]Budker Institute of Nuclear Physics, 630090 Novosibirsk, Russia

ABSTRACT

Luminescence spectra and decay kinetics under X-ray synchrotron radiation were investigated for the following solutions: $(Ce,La)F_3$, $(Ce,La)PO_4$, (Sr,Ca)S:Ce and Cs(I,Br). In addition to the monotonous change of luminescence parameters with the component concentration, the stepwise increase of luminescence yield and afterglow suppression was observed. These experimental data are explained by the modification of the spatial distribution of electronic excitations with the change of the concentration of components.

INTRODUCTION

The processes resulting in crystal scintillation are characterised by different spatial scales. The largest scale (above 100 nm) is determined by the exciting photon (γ or X-ray) absorption length. The smallest scale characterises by the structure of emission centres and traps (from 0.1 to 1 nm). The electronic excitation dynamics (their mean free paths, distances of interaction, etc.) presents intermediate scales from 1 to 100 nm. In an ideal crystal there are no structures with corresponding dimensions. On the other hand, in real crystals there are a lot of such structures: dislocations, enclosures with phase structure different from that of a host crystal, clusters, etc. It is natural to suppose that these structures influences on electronic excitation dynamics, since it is characterised by the same spatial dimension. Solid solutions should have structural fluctuations of this scale. In order to reveal the influence of crystal structure from middle scales on scintillation properties, series of solid solutions of different ionic crystals were studied.

EXPERIMENTAL RESULTS AND DISCUSSION

Recombination of electronic excitations in the case of clusterisation

Solid solutions discussed below consist of a single phase, since only one set of X-ray diffraction reflexions is observed, and the lattice constant increasing linearly with concentration. Investigation of local structure of ionic crystals solid solutions by EXAFS and XANES methods has revealed a presence of small clusters of one of the components, separated by a boundary region of mixed composition [1,2]. Their dimensions depend on both the component concentration and preparation conditions. We suppose that the boundaries of the clusters restrict the migration length of either correlated electron-hole pairs created

Proc. Int. Conf. on Inorganic Scintillators and Their Applications, SCINT95,
1996, Delft University Press, The Netherlands

simultaneously by a photon, or non-correlated pairs created by different photons in the same cluster. In this case both the probability of the exciton creation and the probability of simultaneous capture of an electron and a hole by an emission centre depends on cluster dimensions and can increase if these dimensions are compatible with the radius of the electron-hole interaction. It was shown [3] that the ratio between mean electron-hole after thermalisation and electron-hole interaction radius defines the relative probability of two channels: direct electron-hole recombination and electron-hole recombination after long migration stage (with possible trapping etc.).Therefore the restriction of the electron-hole migration during thermalisation should increase the fluorescence which includes the excitonic stage of energy transfer (like for Ce^{3+} emission centre) and reduces the afterglow which includes the trapping of charge carriers.

Variation of luminescence yield in solid solution

The cerium concentration for investigated solid solutions $Ca_{1-x}Sr_xS$-Ce is about 0.4 mol.%, therefore cerium ions do not affect the solution structure but serve as a probe which is sensitive to the changes of crystal structure and electron excitation distribution. It has been established [4] that the luminescence spectrum of cerium under high energy excitation is due to the emission of two types of centres: the first one with a cubic symmetry and the second one with a lower symmetry, providing a spectrum with the same profile but shifted by a value which increases with x. The shift is proportional to the displacement of Ce^{3+} ions from high-symmetry site, which is determined by the difference of inter-ion distances in CaS and SrS. Therefore it is possible to establish a correlation between the shift and the insertion site of the cerium in the solid solution.

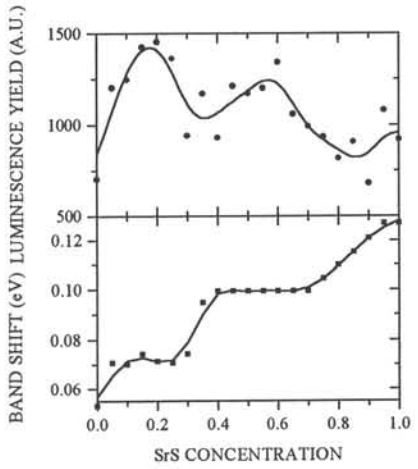

Fig 1. $Ca_{1-x}Sr_xS$-Ce luminescence yield (top panel) and band shift [1] (bottom panel)

Figure 1 shows that the luminescence increases at intermediate x and has two maxima in the regions where the band shift is constant. The increase of yield can be due to the limitation of electron migration by clusters. The most effective recombination will be in cases of compatible cluster dimensions and cerium capture radius. We can conclude that for $0.1<x<0.3$ and $0.4<x<0.7$ cluster dimensions fit this radius. The observed luminescence spectrum is therefore determined by cerium ions embedded into clusters. Since the cluster composition varies slightly, the band shift is constant in these concentration domains. According to the shift values, one can suppose that for $0.1<x<0.3$ domain cerium is mainly in clusters with increased concentration of CaS, whereas for $0.4<x<0.7$, of SrS.

Variation of luminescence decay in solid solution

Solid solutions of fluoride ($La_{1-x}Ce_xF_3$) and phosphates ($La_{1-x}Ce_xPO_4$) discussed below include cerium as a component of solid solution. Therefore in addition to effects of the solid solution local structure, one should expect the changes of cerium luminescence parameters due

to the increase of its concentration. The quenching due to interaction between closely located excited cerium ions is an example of such concentration effect [5].

Solid solutions of lanthanum and cerium phosphates have been synthesised recently. The emission spectra are typical for three-valent cerium. Decay kinetics and the lines corresponding to single exponential law with decay time of 18 ns are shown in Fig. 2. For cerium concentrations below 1% the long rising time presents. This rising time decreases with the increase of cerium concentration.

At the same time the fraction of the afterglow increases, and it reaches its maximum at x=0.2. For higher cerium concentrations there is no rising time, and afterglow decreases. For x=0.7 the decay curve becomes practically single exponential. For higher cerium concentrations the initial decay region becomes faster, probably due to the interaction of excited cerium ions.

The suppression of afterglow in $La_{1-x}Ce_xF_3$ is more effective. Decay curves were measured at the same conditions, and their absolute values are plotted in Fig. 3. Afterglow depends on the cerium concentration in a complicated way.

We have measured only a few crystals with different concentrations, so the presented results allow only to suppose the trends. For x close to zero or unity the afterglow level is about the same, whereas for $0.1<x<0.9$ domain this level is well below than the level for the limit concentrations.

In CeF_3 the afterglow appears for excitation energy above 7 eV and is determined by the duration of the electron migration in the conduction band after the ionisation of cerium ions[6]. For higher energies the afterglow is determined by the fraction of the separated electron-hole pairs. Strong decrease of the afterglow of 10 times for x=0.5 can be explained by the reduction of the electronic excitation migration length when clusters are created in solid solutions. We suppose that the region of maximum reduction of the $La_{1-x}Ce_xF_3$ afterglow shifts from 50% to 70% of Ce (as for $La_{1-x}Ce_xPO_4$).

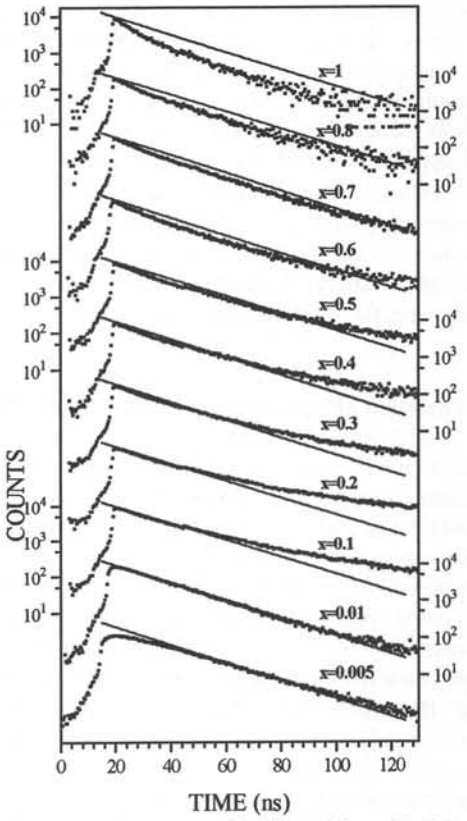

Fig. 2. Luminescence kinetics of $La_{1-x}Ce_xPO_4$ at X-ray excitation

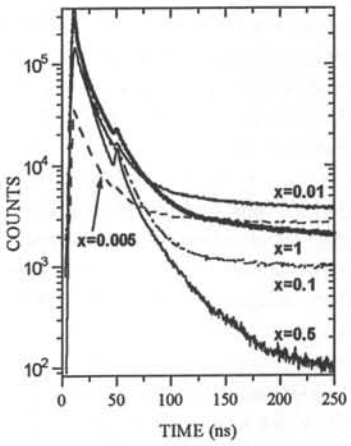

Fig. 3. Luminescence kinetics of $La_{1-x}Ce_xF_3$ at X-ray excitation

Modification of emission centre in solid solution

In $CsI_{1-x}Br_x$ solid solutions, ultraviolet luminescence results from the radiative decay of an exciton which can be localised at a defect of a crystal lattice [7]. Both the exciton and the defect are created by the exciting radiation. Therefore one can expect not only effects connected with distribution of electronic excitations but the dependence of centre creation probability and centre properties on the solid solution concentration.

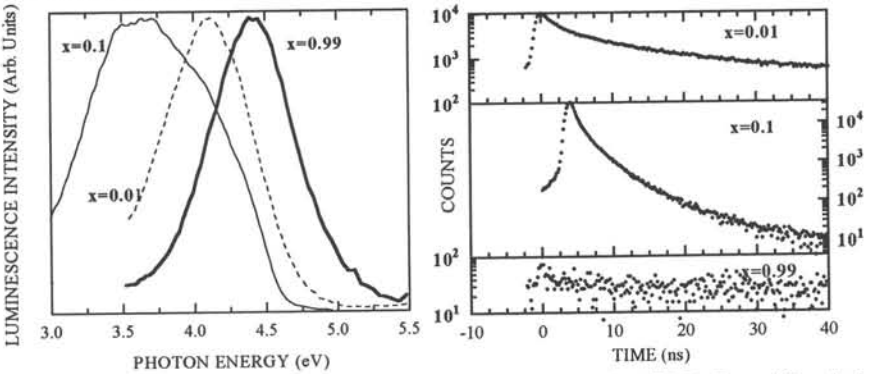

Fig. 4. Emission spectra (left panel) and kinetics (right panel) of $CsI_{1-x}Br_x$ solid solutions.

For solutions with x=0.1 the band maximum is observed at 3.7 eV instead of expected position between 4.1 and 4.5 eV. Decay kinetics for x=0.1 is much faster than the kinetics for x=0.01. Nevertheless, the increase of Br concentration to x=0.99 results in very slow decay.

Conclusion

The hypothesis that non-linear changes of solid solution properties can be explained by non-linear changes of crystal local structure was proposed. The proving of this hypothesis demands the answer on two important questions: dimensions and distribution of clusters as the function of solid solution concentration and the dynamic properties of electronic excitations in slightly disordered structures. Nevertheless, the increase of the luminescence yield and the suppression of the afterglow in solid solutions can be useful for the development of new scintillators.

References

[1] T.Murata, T.Matsukawa and S.Naoe, Sold State Comm. 66 (1988) 787
[2] A.N.Belsky,V.K.Fedorov,O.Krachni, V.V.Mikhailin, A.L.Rogalev, in: Defects in Insulating Materials, ed. by O.Kanert, J.-M.Spaeth, Singapore (1993) 1217
[3] I.A.Kamenskikh, V.V.Mikhailin, I.N.Spinkov, A.N.Vasil'ev, NIM, A282 (1989) 599
[4] A.N.Belsky, O.Krachni, V.V.Mikhailin, J. of Physics: Condensed Matter **5** (1993) 9417
[5] C.Pedrini, B.Moine, D.Bouttet, A.N.Belsky, V.V.Mikhailin, A.N.Vasil'ev and E.I.Zinin Chem.Phys.Lett., 206 (1993) 470
[6] C.Pedrini, A.N.Belsky, A.N.Vasil'ev, D.Bouttet, C.Dujardin, B.Moine, P.Martin and M.J.Weber, Materials Research Society Symposium Proceedings, vol 348 (1994) 225
[7] A.N.Belskiy, A.V.Gektin, V.V.Mikhailin, A.L.Rogalev, N.V.Shiran, A.N.Vasil'ev, E.I.Zinin, Rev. Sci. Instrum. 63 (1992) 806

THERMOLUMINESCENCE OF TERBIUM-DOPED GADOLINIUM OXYSULFIDE PHOSPHORS

F. Jermann, A. Jahnke, W. Rossner, B. C. Grabmaier, Siemens AG, Corporate Research and Development, D-81730 Munich, Germany

ABSTRACT

We investigate the defects of Gd_2O_2S:Tb powders and sintered powder compacts using thermoluminescence analysis. We study the influence of cerium codoping as well as the effect of subsequent annealing treatments at 800 °C in air and at 1300 °C in an argon atmosphere.
Several defect centers with energy depths between about 0.01 eV and 0.5 eV are observed by analysis of the glow peaks. A trap-filling analysis shows that at 15 K X-ray exposure temperature, glow peaks at low temperatures build up faster than those at higher temperatures.
Cerium codoping as well as annealing treatments lead to a considerable decrease of the glow peaks of the deepest traps. Simultaneously, the afterglow intensity of the corresponding phosphors decreases by about two orders of magnitude. Nevertheless, annealing treatments also form new traps with glow peaks at low temperatures.

INTRODUCTION

Gadolinium oxysulfide doped with terbium is a phosphor with a wide field of application due to its high conversion efficiency of exciting radiation. However, the phosphor quality depends on the synthesis technique influencing the number of defects. In the present paper, we investigate the defects in Gd_2O_2S:Tb with 1.0 mol% terbium using thermoluminescence analysis. A first detailed analysis has been carried out by S. Chatterjee et al [1]. They observed a complex glow spectrum with many peaks at temperatures between 100 and 400 K. Nevertheless, the origin of most glow peaks is still not clear. Moreover, the dependence of defect concentrations, defect types and the trap-related afterglow effect on the synthesis technique have hardly been investigated [2].
Afterglow is a phenomenon based on the trapping of charge carriers in phosphors. Electrons or holes excited during X-ray exposure are trapped by defects. After exposure, these charges may leave the traps by thermal or optical excitations and recombine radiatively. This process leads to a very slow decay (several milliseconds) of luminescence intensity in rare earth-doped Gd_2O_2S phosphors [2].
In this paper, we study the influence of several annealing treatments and cerium codoping on the thermoluminescence glow spectrum and the afterglow of Gd_2O_2S:Tb. We compare the relative glow peak intensities of the samples and calculate the energy depths as well as the frequency factors of the traps. The same trapping and recombination parameters (capture cross-section, thermal ionization rate, density of available sites, etc.) that control the trap emptying process also control the trap filling process. Thus, a study of the kinetics of trap filling can provide additional data relating to the charge storage properties of the material. So, we measure the dependence of the individual glow peak intensities on the X-ray dose applied before the beginning of the thermoluminescence heating procedure [3].

Proc. Int. Conf. on Inorganic Scintillators and Their Applications, SCINT95,
1996, Delft University Press, The Netherlands

EXPERIMENTAL DETAILS

Sample Preparation

Terbium-doped Gd_2O_2S powders were prepared as follows [4]. To give a rough description, as a first step homogeneous aqueous solutions of Gd_2O_3 and of Tb_4O_7 are mixed. Then a sulfur-containing initial product is precipitated. In the next step, this product is fired under a reducing atmosphere to get the Gd_2O_2S:Tb powder. Very fine grained powders (< 10 μm) are compacted by a dry pressing technique to form discs with 20 mm diameter. These compacts are densified to about 99% of the theoretical density by a specific sintering technique applying high pressures. Some samples are annealed in air at 800 °C or in an argon atmosphere at 1300 °C.

Sintered Gd_2O_2S powder compacts are doped with 1.0 mol% terbium. Additionally, we incorporate cerium as a codopant with concentrations from 10 to 100 mol ppm.

Thermoluminescence Measurements

Measurements are performed utilizing a helium refrigerator cryostat at temperatures between 15 K and 320 K. The thermoluminescence characteristics are studied after cooling the samples to 15 K. For trap filling the specimens are exposed to X-rays from a tube with a tungsten anode operated at U_X = 50 kV and generally I_X = 20 mA. Unless otherwise noted, the samples are exposed for t_X = 300 s. The glow curve of the ceramic is then obtained by heating the sample with a constant rate of β = 5 K/min and recording the luminescent intensity with a photomultiplier. The glow curve is obtained in steps of 1 K. In most cases, the delay between X-ray exposure and the onset of the glow curve measurement is 2 min.

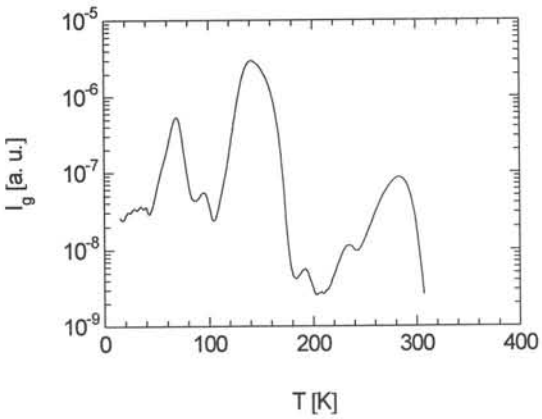

Figure 1: *Typical glow curve of Gd_2O_2S:Tb. Here the dose imparted to the sample is 61200 mAs (U_X = 50 kV).*

The differences between the samples in optical absorption and scattering are taken into account by normalizing the glow curve to the luminescence light yield during a test exposure with U_X = 40 kV and I_X = 5 mA. Thus, glow peak intensities of various samples can be compared directly .

The kinetics of trap filling are analyzed studying the build-up of thermoluminescence intensity as the 'dose' ($\equiv I_X t_X$) imparted to the sample is increased. Therefore, we vary the X-ray exposure time between 30 s and 3060 s. A plot of each glow peak intensity I_g versus exposure time t_X characterizes the trapping properties of the individual trapping centers.

Afterglow measurements are performed by recording the luminescence intensities I_0 at t = 0 and I_a approximately at t = 8 ms after X-ray exposure at room temperature. We denote the afterglow effect as the quantity $A = -\log(I_a/I_0)$.

RESULTS AND DISCUSSION

Glow Peaks in Gd_2O_2S:Tb

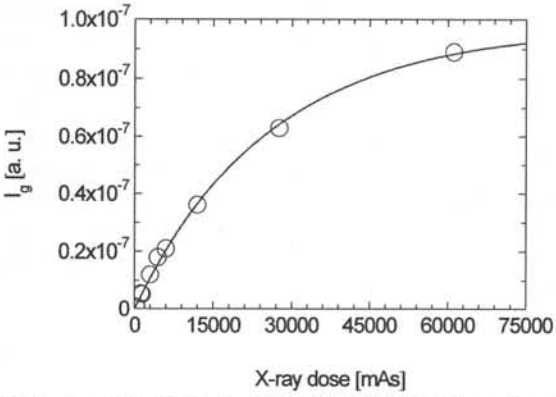

Figure 2: *Glow peak intensity of the 285 K-peak vs. X-ray dose imparted to the Gd2O2S:Tb sample (see Fig. 1). Circles: measured data; line: fit according to equation in text.*

The glow curves of Gd_2O_2S:Tb show a very complex structure (Fig. 1). The number of glow peaks strongly depends on the X-ray dose, imparted to the sample. At low doses many peaks with relatively low intensities can be detected. As the dose is increased, glow peaks of other defects may cover these low-intensity peaks. Thus, the number of peaks decreases with increasing dose imparted to the investigated sample. Sintered powder compacts and powders show very similar glow curves. Summarizing, we observe glow peaks at temperatures T_g = 43 K, 53 K, 68 K, 95 K, 139 K, 150 K, 192 K, 235 K, 285 K for a representative Gd_2O_2S:Tb sample without annealing treatment. Figure 2 shows the typical dependence of the glow peak intensity on the dose imparted to the sample. The measured data can be approximated well by the equation $I_g = I_{g,max}\,[1-\exp(-I_X t_X/\gamma)]$. The maximum glow peak intensities $I_{g,max}$ as well as the charge-capture parameters γ of most peaks are listed in Table 1. Generally, glow peaks at lower temperatures reach the steady-state intensity at shorter exposure times $t_X = \gamma/I_X$.

Since the peak temperatures do not move to higher temperatures at lower glow peak intensities I_g, we assume that all peaks can be described by first order kinetics [5, 6]. If possible, the trap depths E_A and the frequency factors S are calculated from the half width w and peak temperature T according to $E_A = 2\,k_B\,T\,(1.26\,T/w - 1)$ and $S = (2.67\,\beta/w)\,10^{T/w}$ [7, 1]. The values obtained coincide well with those reported in [1] for optical UV-excitation. If peaks are too bad separated to determine w, the initial rise method is used to estimate the trap depths. Of course, these E_A values are very rough estimations. E. g., the energy depth of the defect related to the 235 K peak differs from that obtained in [1] using the thermal cleaning technique by more than a factor of two.

T_g [K]	43	53	68	95	139	150	192	235	285
$I_{g,max}$ [a. u.]	> 20	> 44	512	54	3020	> 37	6	12	97
γ [mAs]	-	-	8217	13000	18100	-	17000	20700	25400
E_A [eV]	(0.05)	(0.06)	0.07	-	0.20	(0.19)	-	(0.24)	0.44
S [s^{-1}]	-	-	10^4	-	10^3-10^6	-	-	-	10^5-10^{10}

Table 1: *Maximum glow peak intensities $I_{g,max}$, charge-capture parameters γ, trap depths E_A, and frequency factors S for Gd_2O_2S:Tb. The intensities of the peaks at 43 K, 53 K, and 150 K are too low relative to neighboring peaks to determine the value of γ. Trap depths E_A and frequency factors S are determined according to Chen [7]. If a value is in brackets, the initial rise method is used [3] and the error is much larger because peaks are not really separated.*

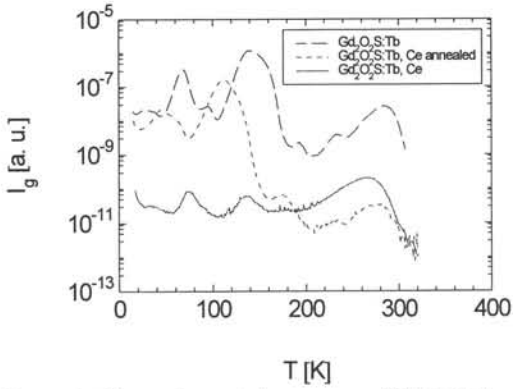

Figure 3: *Comparison of glow curves of Gd_2O_2S:Tb and Gd_2O_2S:Tb,Ce (annealing at 1300 °C).*

Influence of Cerium Doping

Additional doping of Gd_2O_2S:Tb with cerium strongly reduces the intensity of the glow peaks. A codoping with 50 ppm cerium shifts the glow curve by about two to three orders of magnitude (Fig. 3). The nature of the traps remains the same because trap depths and frequency factors do not change within measuring accuracy. At the same time, the afterglow is strongly reduced by cerium doping, as can be seen from Table 2. We find no correlation between the afterglow effect and a single glow peak only. Thus, we conclude that more than one trap contributes to the afterglow of Gd_2O_2S:Tb. Similar results have been reported for Gd_2O_2S:Pr [2]. Hence, most defect centers observed seem to be intrinsic defects of the Gd_2O_2S host lattice, and not specific for terbium-doped material.

cerium concentration [ppm]	*0*	*10*	*20*	*50*	*100*
afterglow coefficient A	2.7	3.1	3.3	3.8	4.4

Table 2: *Afterglow coefficient A vs. cerium codopant concentration of Gd_2O_2S:Tb,Ce.*

Effect of Annealing Treatments

Annealing treatments at 800 °C (in air) or 1300 °C (in argon) strongly reduce the intensity of the glow peaks above 180 K. This is illustrated in Fig. 3 with a cerium codoped sample. At temperatures below 180 K, new glow peaks with high intensities are observed. These peaks may refer to really new defects induced by the annealing process. The new peaks have activation energies E_A less than 0.1 eV and abnormally low frequency factors between 10^1 and 10^3 s^{-1}. These low values may point to a center-to-center recombination type [8]. However, these defects hardly influence the afterglow, i. e., the sample in Fig. 3 yields A = 4.1 after annealing at 1300 °C and A = 3.8 beforehand.

References

[1] S. Chatterjee, V, Shanker, P. K. Glosh, Solid State Commun. 80, 877 (1991)
[2] H.Yamada, A. Suzuki, Y. Uchida, M. Yoshida, H. Yamamoto, Y. Tsukuda, J. Electrochem. Soc. 136, 2713 (1989)
[3] S. W. S. McKeever, Thermoluminescence of solids, Cambridge University Press, 1985
[4] M. R. Royce, US Pat. 3.502.590, 1970
[5] P. W. Levy, PACT 3, 466 (1979)
[6] M. S. Rasheedy, A. M. A. Amry, J. Lumin. 63, 149 (1995)
[7] R. Chen, J. Appl. Phys. 40, 570 (1969)
[8] R. Chen, Y. Kirsh, Analysis of thermally stimulated processes, Pergamon Press, Oxford, 1981

OPTICAL AND MAGNETOOPTICAL INVESTIGATION OF THE X-RAY STORAGE PHOSPHOR $Cs_2NaYF_6:Ce^{3+}$

T. Pawlik and J.-M. Spaeth

University of Paderborn, Warburger Str. 100, 33098 Paderborn, Germany

ABSTRACT

We present $Cs_2NaYF_6:Ce^{3+}$ as a new promising X-ray storage phosphor and compare its figures of merit with those of other known phosphors. X-irradiation of pure and Ce-doped Cs_2NaYF_6 leads to several absorption bands in the visible region. The optical bands created by irradiation were investigated with the magnetic circular dichroism of the absorption (MCDA) and with MCDA-detected electron paramagnetic resonance.

EXPERIMENTAL RESULTS

Cs_2NaYF_6 has the cubic elpasolite structure. Cerium doped Cs_2NaYF_6 shows efficient emission at 360nm under X-ray and UV excitation. The emission is due to the allowed 5d-4f transitions of Ce^{3+}. In pure and Cerium doped Cs_2NaYF_6 X-irradiation at room temperature creates defects with several absorption bands in the visible region. After X-irradiation the luminescence of the activator Cerium at 360nm can be stimulated by bleaching into a radiation induced absorption band around 550nm [1]. The PSL emission and stimulation spectra of Cs_2NaYF_6: Ce^{3+} are shown in Fig. 1. The peak of the stimulation spectrum is situated at about 550nm, so a frequency-doubled Nd-YAG laser is the best source for the photostimulation. The PSL emission spectrum is identical with the prompt X-ray- induced luminescence of Ce^{3+} and the stimulation spectrum is very similar to the dominant radiation-induced absorption band. A comparison of the decay times of the PSL emisssion excited at 500 nm with a flash lamp of 5 ns pulse decay time and of the direct excitation of Ce^{3+} at 306 nm shows that the decay times of both emissions are identical within experimental error, i.e. 42 ns at room temperature. This is qualitatively the same result as found for $BaFBr:Eu^{2+}$: the bottleneck for the PSL decay time is the radiative life time of the activator ion. Below 100K the PSL decay time is dependent on temperature. Therefore a thermal activation must be involved in the PSL process. PSL effects have also been observed for other activators, e.g. Pr^{3+} and Sb^{3+}. For practical use, the PSL decay time of Pr^{3+} is too long (4 ms); that of Sb^{3+} is much faster. In Table I the conversion efficiency (CE) and stimulation energy (SE) for several X-ray storage phosphors including the commercially used BaFBr:Eu are presented.

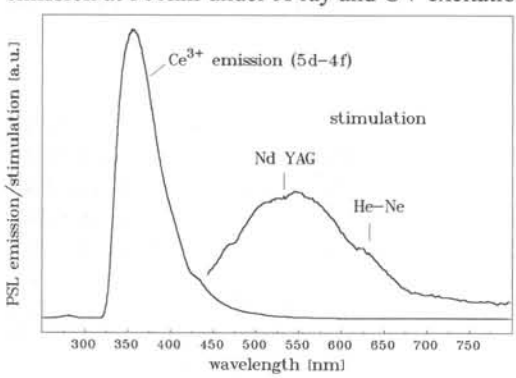

Fig.1: PSL stimulation and emission spectra of $Cs_2NaYF_6:Ce^{3+}$ at room temperature

Proc. Int. Conf. on Inorganic Scintillators and Their Applications, SCINT95,
1996, Delft University Press, The Netherlands

CE is the total amount of energy that can be released by PSL divided by the X-ray dose and SE is the energy required for the readout of the active centres [7].

Table 1: Efficiency of some X-ray storage phosphors.

Material	CE [pJ/mm^3/mR]	SE [µJ/mm^2]
BaFBr:Eu^{2+}	50	22
Cs_2NaYF_6:Ce^{3+}	15	90
KBr:In$^+$	4	10

From table 1 it is evident that the new material is promising but still inferior to BaFBr:Eu. However, improvements can probably be archieved by a variation of the composition.

RADIATION DEFECTS

No F centres have yet been reported in Cs_2NaYF_6, and it is, of course, speculated that the broad absorption band created by X-irradiation is due to F centres. In this crystal, an electron trapped at a F$^-$ site would have 4 nearest Cs^+ ions and one nearest Y^{3+} as well as one nearest Na^+ ion. Fig. 2 shows the MCDA spectrum and the MCDA-detected EPR-spectrum measured at 550 nm as a microwave-induced change of the MCDA (see e.g. [2]). An isotropic broad EPR line at g=2 (ν≈24GHz) with a half width of 67 mT is found superimposed on a narrow EPR line with a half width of 8 mT with opposite sign. The narrow line is slightly angular dependent. The two EPR lines cannot be measured separately by choosing different wavelenghts in the MCDA spectrum. The superimposed EPR spectra of Fig. 2 are measured always in all portions of the MCDA between 400 and 650 nm. However, the MCDA-EPR spectrum cannot be due to one centre only. When studying the dynamical behaviour of the MCDA in the middle of the narrow EPR line and in the flank of the broad EPR line, one can see that two different spin lattice relaxation times are involved. We tentatively assign the broad EPR line to F centres. The F-centre EPR line width in CsCl and CsBr is $\Delta B_{1/2}$ = 82.5 mT [3,4] and g=1.97 for CsCl, 1.96 for CsBr. Considering, that in CsBr and CsCl there are 8 nearest Cs^+ neighbours and here only 4 (the Cs^+ interactions will dominate the line width), it seems reasonable to assign the broad EPR spectrum to F centres. When measuring the MCDA-EPR-spectra over a wider field range we observe additional narrow resonance lines at lower field values. These resonances are strongly dependent on the microwave power. Fig. 3 shows several MCDA-EPR spectra measured with different levels of saturation. The additional EPR-lines appear approximately at $^B/_2$, $^B/_3$ ... where B=850mT is the field value of the

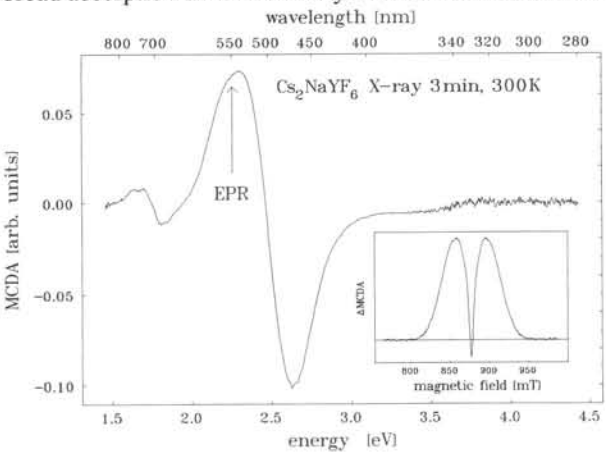

Fig. 2: MCDA and MCDA-EPR (inset) spectrum of the F-centre in X-irradiated Cs_2NaYF_6

narrow line. The low field resonances are due to forbidden ($\Delta m_S>1$) transitions of a defect with an electron spin S>1/2 and g≈2. Gd^{3+} (S=7/2) is a good candidate since trivalent rare earth ions are often found in elpasolite compound as accidental impurities. The Gd^{3+} content in the sample under investigation was determined by EPR. By comparison with a standard sample the concentration was found to be approximately 35 ppm.

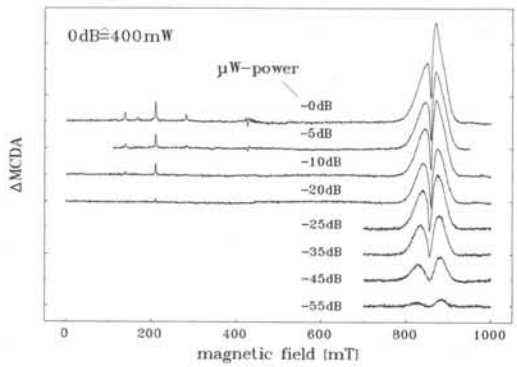

Fig. 3: MCDA-EPR-spectra of the F-centre measured with different microwave power values

Since the allowed optical transitions of Gd^{3+} usually lie in the UV-region, it is unlikely that a direct MCDA-EPR signal of Gd was observed in the MCDA at 575nm. It is more probable that the observed allowed and forbidden transitions appear because of a cross-relaxation effect between the F-centre and the paramagnetic Gd^{3+}. This is possible because there is an overlap of the EPR spectra of Gd^{3+} with that of the F-centre. The cross-relaxation effect is proportional to $1/R^6$ where R is the distance between the two paramagnetic defects. Thus it is likely that in irradiated Cs_2NaYF_6 the F-centers and Gd^{3+} ions are spatially correlated and therefore closer than expected from the statistical distribution (the average distance of Gd^{3+} ions in a statistical distribution is about 100Å at 35ppm). Similar cross-relaxation effects were observed for F-centres and Eu^{2+} in X-irradiated BaFBr:Eu [5]. A quantitative determination of the average distance using the cross relaxation effect has not yet been carrried out.

In a cerium doped sample additional paramagnetic MCDA bands are present before and after iradiation (Fig.4) . The MCDA-EPR spectrum shows a single line at 1850 mT corresponding to a g-factor of 0.929. By conventional EPR and ENDOR measurements this EPR-line was assigned to trivalent Ce^{3+} on a nonperturbed cubic Y^{3+} site [6]. The difference of the observed g-factor and the value of g=(-)1.429 expected for a $^2F_{5/2}$ ground-state can be explained by admixture of the low lying $^2F_{7/2}$ excited state. X-irradiation and PSL readout have no measurable effect on the Ce^{3+} concentration. The question arises whether in Ce-doped samples the F-centres are also correlated with the Ce^{3+} ions. However, in this case a cross-relaxation effect can not be expected since there is no overlap between the EPR lines of Ce^{3+} (g=0.93) and the F-centre. After X-irradiation Cs_2NaYF_6 at low temperatures strong thermo-luminescence bands are observed at 150K 220K and 350K. After annealing above 350K all PSL-active centres are destroyed. Thermoluminescence bands also appear just below room temperature. This is

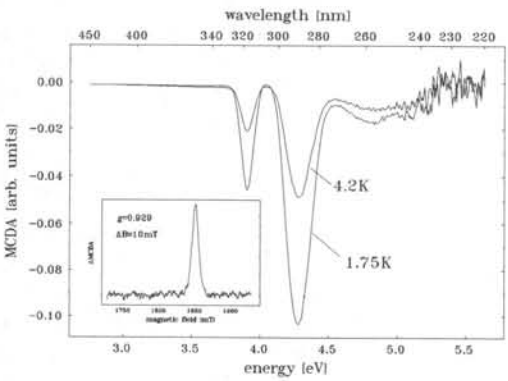

Fig. 4: MCDA and MCDA-EPR (inset) spectrum of the activator Ce^{3+} in Cs_2NaYF_6

consistent with the observation that about 30% of PSL-efficiency is lost in about 1 hour after X-irradiation at room temperature. We investigated the changes in the MCDA spectra of undoped Cs_2NaYF_6 after irradiation at 4.2K and subsequent annealing for several minutes at temperatures chosen such as to coincide with the peaks of the thermoluminescence (Figure 5). The annealing step at 156K leaves the 550nm MCDA-band unchanged. Comparing the PSL readout at 120K of a sample X-irradiated at 120K with that of a sample irradiated at 120K heated to 170K and read out at 120K, it is observed that the total PSL intensity is higher by a almost factor of 2 after the annealing, while the readout time is approximately the same. Thus it can be concluded that an annealing step at 170K beyond the first thermoluminescence peak leads to the formation of more PSL-active centres. After annealing at 225K the MCDA-band decreases to about 60%. Conventional EPR-measurements have shown that by X-irradiation at 77K a large concentration of V_K-centres is produced. These centres are stable to about 215K. Thus the TL-peak at 220K can be assigned to a recombination of F-centres and V_K-centres. The PSL efficiency is not affected by the recombination of these centres. Annealing up to 300K leads to a further decrease of the MCDA band to about 30% of its initial value along with a decrease in PSL efficiency. The shape of the MCDA changes considerably due to a new MCDA band appearing at 520nm. At low temperatures the new MCDA band decays very fast when the sample is bleached with 520nm light. After reheating to room temperature the 520nm band reappears. The decay is faster than the readout time of the PSL, therefore it is not likely that this MCDA band plays a role in the PSL process.

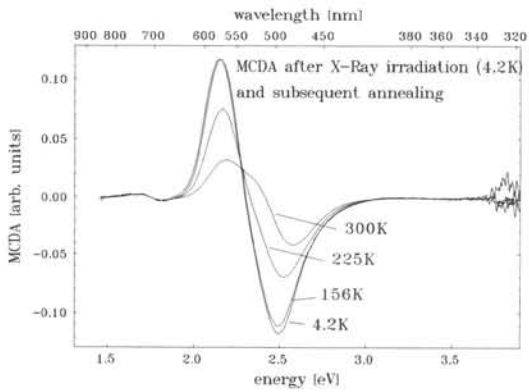

Fig. 5: MCDA spectra of undoped Cs_2NaYF_6 X-ray irradiated at 4.2K and annealed to the temperatures indicated in the figure.

CONCLUSION

$Cs_2NaYF_6:Ce^{3+}$ is a promising new storage phosphor. F-type electron centres are photostimulable centres. The corresponding hole centres could not yet be identified. No indications for a conversion of Ce^{3+} into Ce^{4+} after X-irradiation were found.

[1] J.- M. Spaeth, T. Hangleiter, F. K. Koschnick and T. Pawlik
Proceedings of the 7th EURODIM (1994)

[2] J.- M. Spaeth, J. R. Niklas and R. H. Bartram, Structural Analysis of Point Defects in Solids (Springer Series in Solid State Sciences 43) (1992)

[3] D. Schmidt, Ph.D. Thesis, Stuttgart (1966)

[4] F. Hughes and J. G. Allard, Phys Rev. **125**, 173 (1962)

[5] F. K. Koschnick, J.- M. Spaeth, R. S. Eachus, W. G. Mc Dugle and R. H. D. Nuttal Phys Rev Letters **67**, 3571 (1991)

[6] T. Pawlik, M.Otte, H. Overhof and J.-M. Spaeth
Proceedings of the 7th EURODIM (1994)

[7] Meijerink, A., Ph. D. Thesis, Utrecht (1990)

SCINTILLATION PROPERTIES OF Ce^{3+} DOPED $LiYF_4$ AND $LiLuF_4$ CRYSTALS

C.M. Combes, P. Dorenbos, C.W.E. van Eijk, C. Pedrini§, J.Y. Gesland§§
Delft University of Technology, Faculty of Applied Physics,
c/o IRI, Mekelweg 15, 2629 JB Delft, The Netherlands.
§Université Lyon 1, 69622 Villeurbanne Cedex, France.
§§Université du Maine, 72017 Le Mans Cedex, France.

ABSTRACT

The scintillation properties of $LiYF_4$ and $LiLuF_4$ crystals doped with different concentrations of Ce^{3+} were studied by means of X-ray induced emission spectra and γ-ray induced pulse-height spectra. The scintillation decay is dominated by a slow component. Optical absorption spectra exhibit five well-defined bands due to 4f-5d transitions in Ce^{3+}.

INTRODUCTION

$LiYF_4$ crystals doped with Ce have been studied 16 years ago because of their potential application as ultraviolet solid-state laser, see [1]. The scintillation properties of Ce doped $LiYF_4$ and $LiLuF_4$ were investigated in order to determine their suitability to provide a good thermal neutron detector. The presence of Lithium is required in the compound because of its ability to convert incident neutrons into secondary charged particles via the reaction : ${}^6_3Li + {}^1_0n \rightarrow {}^3_1H + {}^4_2\alpha$ with a Q-value of $4.78\,MeV$. The optical properties of Ce^{3+} in $LiYF_4$ and $LiLuF_4$ host crystals are very similar because of almost identical crystal structures. Their densities are 3.97 and $5.96\,g/cm^3$, respectively.

RESULTS AND DISCUSSION

Optical absorption spectra were recorded with two different set-ups. For a wavelength range from 150 to $300\,nm$, the measurements were performed in vacuum with a Deuterium lamp. A few crystals of Ce doped $LiYF_4$ and the crystal of Ce doped $LiLuF_4$ were measured with this set-up. For a wavelength range from 200 to $800\,nm$, a diode-array spectrophotometer (HP 8452A) was used to record optical absorption spectra of every crystal.

Every optical absorption spectrum exhibits five well-defined bands at $186\,nm$, $196\,nm$, $206\,nm$, $244\,nm$ and $292\,nm$ due to 4f-5d transitions in Ce^{3+}, see Figure 1. A calculation of the splitting of the 5d level in five bands is presented elsewhere [2]. The Ce doped $LiYF_4$ and Ce doped $LiLuF_4$ crystals were grown in different laboratories. The nominal Ce^{3+} concentrations are shown in Table 1. The actual Ce^{3+} concentrations of one Ce doped $LiYF_4$ crystal and of the Ce doped $LiLuF_4$ crystal, were determined by the method of mass spectroscopy in solution. By comparing the intensity of the optical absorption line at $244\,nm$ of each Ce doped $LiYF_4$ crystal with the reference crystal, the actual Ce^{3+} concentration was deduced, see Table 1. The error on the absorption coefficient, μ_{244nm}, is estimated to be 5%.

Proc. Int. Conf. on Inorganic Scintillators and Their Applications, SCINT95,
1996, Delft University Press, The Netherlands

Table 1: X-ray and γ-ray induced photon yields in $[photons/MeV]$ measured at room temperature, nominal Ce^{3+} concentration $(mol\%Ce)$, absorption coefficient μ_{244nm} (cm^{-1}) and actual Ce^{3+} concentration $(mol\%Ce)$ for the different Ce doped $LiYF_4$ and Ce doped $LiLuF_4$ crystals studied. *n.m.* means not measurable due to a very poor photopeak resolution. $\star$ indicates the concentrations which were determined by the method of mass spectroscopy in solution.

Crystal	Yield $[ph/MeV]$ X-rays	Yield $[ph/MeV]$ γ-rays ^{137}Cs	Nom. conc. $mol\%Ce^{3+}$	μ_{244nm} (cm^{-1})	Act. conc. $mol\%Ce^{3+}$
$LiYF_4$:Ce	3730	890	1.08	46.42	0.25
	6260	620	1.0	22.27	0.12
	6090	930	1.0	18.44	0.10 $\star$
	2180	*n.m.*	0.1	4.84	0.03
	2960	*n.m.*	0.3	4.56	0.02
$LiLuF_4$:Ce	3780	*n.m.*	1.0	15.52	0.10 $\star$

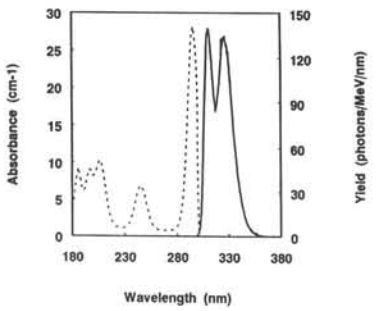

Figure 1: X-ray induced emission spectrum and optical absorption (dashed line) spectrum of $LiLuF_4$:0.1 $mol\%Ce$ at room temperature.

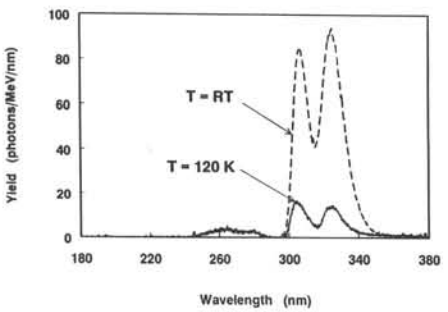

Figure 2: X-ray induced emission spectra of $LiYF_4$:0.02 $mol\%Ce$ recorded at room temperature and at T=120 K.

Details on the experimental set-ups employed to record X-ray induced emission spectra and γ-ray induced pulse height spectra are described elsewhere [3], as well as the methods to calculate the photon yields, either in $[photons/MeV$ X-ray energy] or in $[photons/MeV\,\gamma$-ray energy] . It is noted that under continuous X-ray excitation all scintillation decay components contribute to the obtained light yield, whereas with γ excitation, the yield depends on the electronic shaping time.

At room temperature, the X-ray induced emission spectra, of both Ce doped $LiYF_4$ and Ce doped $LiLuF_4$ crystals, exhibit at 305 and 325 nm Ce^{3+} emission bands caused by transitions from the lowest 5d level $^2D_{3/2}$ to the $^2F_{5/2}$ and $^2F_{7/2}$ levels of the $4f^1$ configuration, see Figures 1 and 2. In Figure 2, X-ray induced emission spectra recorded at room temperature (RT) and at 120 K are shown for the $LiYF_4$:0.02 $mol\%Ce^{3+}$ crystal. The luminescence observed at low temperature between 245 and 290 nm is attributed to Self-Trapped Exciton (STE) emission. It has also been observed in pure $LiYF_4$ between 200 and 450 nm by Hayes *et al*, see [5]. The spectral shape of STE emission in Ce doped

$LiYF_4$ is modified due to the presence of Ce^{3+} absorption bands at 244 and 292 nm. If the temperature increases from T~100 K to 160 K, both the STE emission and the Ce luminescence intensity decrease. Above T~160 K, the STE emission has disappeared and Ce luminescence intensity starts to increase from 1200 $photons/MeV$ at T~160 K to 4600 $photons/MeV$ at T~380 K, where a saturation is reached.

From previous studies on pure $LiYF_4$ and Er^{3+} or Pr^{3+} doped $LiYF_4$, see[4, 5], it is known that holes create F_2^- centres which are immobile below T~160 K. These centres trap electrons causing STE emission, which in the Ce doped crystals is partly reabsorbed by Ce^{3+} ions. Therefore both STE emission and Ce luminescence are observed but the overall emission intensity decreases as temperature is raised because of the increasing importance of non-radiative decay of the STE. Above T~160 K, the F_2^- centres are known to be mobile. Their probability of being trapped at Ce^{3+} ion sites, instead of creating STEs, increases with their mobility and hence with temperature. After, the electrons are trapped by the Ce^{4+} ions and luminescence follows.

γ-ray induced pulse height spectra were recorded employing a ^{137}Cs source and a shaping time of 1 μs. There is a factor of 4 to 10 difference between the light yields derived under X-ray and γ-ray excitation. This difference indicates that the scintillation process is dominated by components much longer than the 1 μs shaping time. A decay time component of ~100 ns was observed with the single photon counting technique.

Acknowledgements

The authors are grateful to H.W. Den Hartog (University of Groningen, The Netherlands), J.Y. Gesland (University of Maine, France) and P.A Rodnyi (St. Petersburg State Technical University, Russia) for providing the different crystals. These investigations have been supported by the Netherlands Technology Foundation (STW) and HCM project "Search for new and better scintillators for radiation detection".

References

[1] D.J. Ehrlich, P.F. Moulton, R.M. Osgood, Jr, Opt. Lett. Vol.4 (1979) p.184.

[2] J. Andriessen, H. Merenga, C.M. Combes, C.W.E. van Eijk, to be published for SCINT95, Delft, The Netherlands, abstract TU-X-13.

[3] P. Dorenbos, J.T.M. de Haas, R. Visser, C.W.E. van Eijk, R.W. Hollander, IEEE Trans. on Nucl. Sci. 40(4) (1993) p.424.

[4] G.M. Renfro, L.E. Halliburton, W.A. Sibley, R.F. Belt, J. Phys. C: Solid St. Phys. 13(1980) p.1941.

[5] W. Hayes, M. Yamaga, D.J. Robbins, B. Cockayne, J. Phys. C: Solid St. Phys. 13(1980) L1011.

EVALUATION OF $Ba_{0.9}Gd_{0.1-x}Ce_xF_{2.1}$ CRYSTAL SCINTILLATORS

M. KOBAYASHI[a], M. ISHII[b] B.P. SOBOLEV[c], Z.I. ZHMUROVA[c] and E.A KRIVANDINA[c]

a) KEK, National Laboratory for High Energy Physics, Tsukuba 305 Japan,
b) SIT, Shonan Institute of Technology, Fujisawa 251, Japan,
c) Instititue of Crystallography, Russian Academy of Science, Moscow 117333, Russia.

ABSTRACT

The effect of increasing Ce amount (x) from 0 to 0.05 was examined. The emission changes from the slow component (310 nm) of BaF_2 to that of Ce^{3+} (350 nm). The light intensity increases to 50% of BGO as the Ce amount (x) increases to 0.05. As the Ce amount increases, the dominant component of the decay time approaches to 30-40 nm, which is expected for Ce^{3+} luminescence. Quick spontaneous recovery of radaition damage was observed by addition of Ce.

1. INTRODUCTION

There is an ever increasing interest in heavy, fast and radiation-hard scintillators for electromagnetic (EM) calorimeters in high energy as well as nuclear physics experiments, medical diagnostics, nuclear well-logging, etc. BaF_2 has been extensively studied[1] as one of the best candidates for the use at high energies.

In the application for γ -ray detectors at high energies, however, there are two problems with BaF_2; first the slow component is much larger than the fast one, and second the unit radiation length X_o=2.03 cm is not short enough. Doping of various rare earths was studied by Woody et al.[2] and Sobolev et al.[3] with a primary aim of reducing the slow component. However, significant reduction was observed in not only the slow but also the fast components. Moreover, the radiation hardness was degraded except for La-doping, while the damage for Gd doping disappeared in 4 hours.

Good matching between Gd and Ce may be expected from the large light yield and the excellent radiation hardness of Gd_2SiO_5:Ce[4,5]. We examined the effects of adding a substantial amount of Gd and doping of small amount of Ce by expecting the increase in density, reduction in slow component, conversion of fast component of BaF_2 to again the fast scintillation of Ce^{3+}, large radiation hardness, etc. Although the amount of Gd is better to be as large as possible from the view point of shorter radiation length, it had to be kept below 20% so that the melt should be congruent [3]. From the viewpoint of crystal growth, only one $Ba_{0.9}Gd_{0.1}F_{2.1}$ composition of the whole series of $Ba_{1-y}Gd_yF_{2+y}$ solid solution has an important advantage. This crystal melts without decomposition (congruently). This anomalous behaviour of solid solution is a very important condition for the growth of perfect single crystals. Consequently, in the present study, we chose the mole fraction y at 10%, and changed the amount of Ce systematically. $Ba_{0.9}Gd_{0.1}F_{2.1}$ has a density of 5.11 g/cm^3 (compared with 4.89 g/cm^3 in BaF_2) and X_o=1.93 cm. We will report on the photoluminescence,

Proc. Int. Conf. on Inorganic Scintillators and Their Applications, SCINT95, 1996, Delft University Press, The Netherlands

Table 1 Result of $Ba_{0.9}Gd_{0.1-x}Ce_xF_{2.1}$ samples. Cut-off corresponds to transmittance of 10%. Intensity was measured with γ -ray isotopes.

	x	decay constants τ (ns) (relative intensity)			cutoff wavelngth(nm)	intensity (BGO=100)
N0	0	2.6(45%)	29(18%)	270(37%)	222	
N1	0.001	3.1(40%)	26(27%)	183(33%)	315	12
N2	0.003	2.7(35%)	21(24%)	157(41%)	322	15
N3	0.005	2.3(27%)	37(32%)	190(42%)	325	18
N4	0.01	2.8(28%)	37(32%)	177(40%)	326	22
N5	0.02	3.3(25%)	39(43%)	157(31%)	330	34
N6	0.03	4.2(23%)	43(51%)	201(26%)	331	39
N7	0.05	2.7(14%)	35(57%)	135(29%)	330	53

radioluminescence due to X-rays, scintillation light yield for γ -rays, decay constant, etc. for $Ba_{0.9}Gd_{0.1-x}Ce_xF_{2.1}$ scintillators.

The crystals were grown in Moscow by Bridgeman-Stockberger technique in a fluorinating atmosphere. The test samples have x=the amount of Ce in a range of 0 and 0.05 as listed in Table 1. The size was about 11.5 mm in diameter and 10 mm in length (14 mm for N0 sample). The parallel two faces were polished.

2. MEASURED RESULT

Transmission spectra of N0, N1 and N7 samples are compared in Fig. 1. The transmission spectrum of N0 shows many absorption lines at essentially the same positions as in undoped GSO[5]. They can be interpreted in terms of the transition of the ground state ($S_{7/2}$) of the $4f^7$ electrons of Gd^{3+} ions to the lowest-lying excited states of ^6D, ^6P and ^6I. These absorption lines are not seen any more due to absorption by Ce ions when even a smallest amount of Ce is added (x=0.001 in N1). The transmission spectra of N2-N6, which are not shown in the figure, lie between those of N1 and N7. The cutoff wavelength shifts from 320 nm in N1 to 335 nm in N7.

Excitation-emission spectra of N0 and N1 samples are compared in Fig. 2 for the surface emission for UV exciation. N2-N6 show spectra intermediate between N1 and N7. In the deep emission from inside in N1-N7 samples, the contribution of short wavelength below about 320 nm is suppressed due to small transmittance. The radioluminescence spectra due to X-rays (50kV, Cu) are also shown in Fig. 3. Both results from UV and X-ray excitations are consistent with each other. The emission in N0 is dominant at around 310 nm, similarly as the slow component in BaF_2. The emission occurs only at around 350 nm when Ce is added. When the Ce amount is very small (x=0.001), the emission has two peaks at around 310 and 350 nm.

Possible existence of phosphorescence in N0 (x=0) was suggested in [3]. We have measured phosphorescence of the present samples. We have found

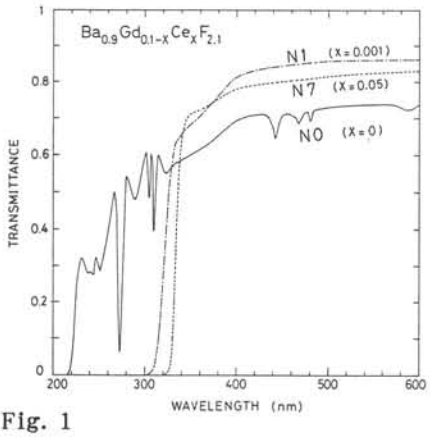

Fig. 1
Transmission spectra of N0, N1 and N7. Those of N2-N6 lie between N1 and N7.

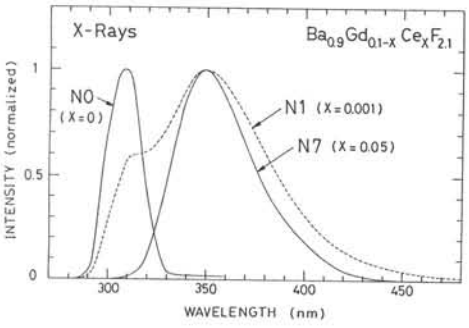

Fig. 3
Radioluminescence spectra of N0, N1 and N7 samples due to X-rays.

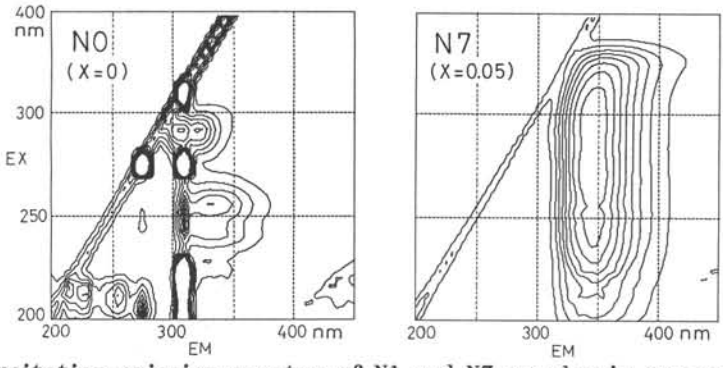

Fig. 2 Excitation-emission spectra of N1 and N7 samples in comparison.

that N0 shows significant phosphorescence with a time constant of roughly 10 ms at the emission wavelength of 310 nm. The phosphorescence is, however, reduced by two orders of magnitudes in N1 by adding a small amount of Ce. The phosphorescence was hardly detectable in N7. The phosphorescence in N0 was so significant that the bright spot irradiated by X-rays continued to be visiblly bright in the dark even after several minutes of switching off the X-rays.

Decay constant was measured by the conventional one photoelectron method in a separate scintillator scheme. The start pulse was taken from a small GSO:Ce scintillator while the stop pulse was the signal of the present sample mounted on a fast 2-inch phtomultiplier (Philips, XP2020). The decay time spectrum was fitted with three exponentials plus a constant background. The fitted result is compared in Table 1 for all the samples. We can see that the 30-40 ns component due to the luminescence of Ce increases and the slow component of 100-200 nm decreases as the Ce amount increases. For N7 the decay constant is shorter than 35 ns for 70% with the rest as slow as 135 ns.

Figure 4 gives a dependence of scintillation light output as a function of Ce amount. The light output was estimated by mounting the crystal on a 2-inch photomultiplier with bialkali photocathode (R329) and by measuring 0.662 MeV γ -rays from ^{137}Cs. The 0.662 MeV peak appeared as a peak on the background in the pulse height spectrum. The light output increases with the Ce amount reaching more than 50% of BGO. Comparison with BGO was made by measuring a BGO crystal of 10x10x30 mm^3 on the same measuring equipments. The above number (50%) may increase if the borosilicate glass window of the present PMT is changed to UV-transparent one to accept UV light below 350 nm efficiently. A typical pulse height spectrum of N7 sample for ^{22}Na γ -rays is given in Fig. 5. The FWHM resolution of 26% at 0.511 MeV gives about 160 photoelectrons per MeV deposited.

The radiation damage remains to be measured. We found, however, the following during the measurement of radioluminescence due to X-ray (50kV, 30A, Cu). The irradiated spot by X-rays (about 3 mm in diameter) got a colour of violet-brown after irradaition of several minutes. The colour was weaker for smaller x, being very faint in N1. For N0 (x=0), no colouring occured but bright phosphorescence spot appeared as described already. The violet-brown colour faded away with time and completely disappeared in several minutes in N1(x=0.001) to several tens of minutes in N7(x=0.05). The above fact indicates a possibility of spontaneous recovery of radiation damage when Ce is added. The effect of dramatical spontaneous recovery of Ce has actually been observed in GSO:Ce[5].

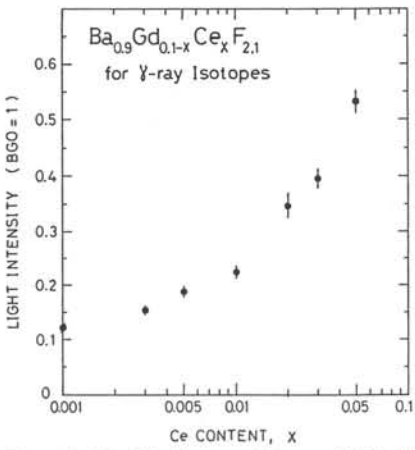

Fig. 4 Light intensities of N1-N7 samples measured with ^{137}Cs.

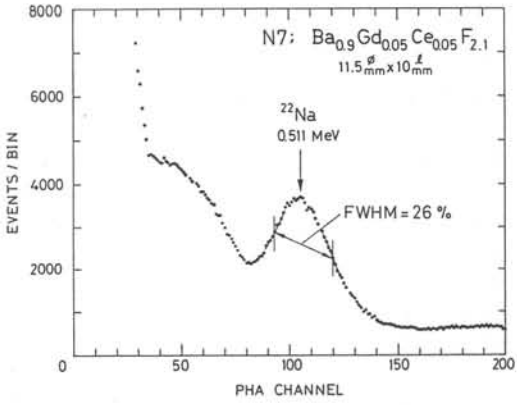

Fig. 5 Energy spectrum of ^{22}Na γ -rays measured with N7 sample.

References

1) For example, see G. Gratta, H. Newman and R.Y. Zhu, Ann. Rev. Nucl. Part. Sci. 14(1994)453, and the references therein.
2) C. Woody et al., IEEE Trans. Nucl. Sci. NS-36(1989)536.
3) B. Sobolev et al., Mat. Res. Soc. Symp. Proc. v.348(1994)277.
4) H. Ishibashi et al., IEEE Trans. Nucl. Sci. NS-36(1989)170.
5) M. Kobayashi and M. Ishii, Nucl. Instr. Meth. B82(1993)85.

OPTICAL AND SPECTRAL PROPERTIES OF THE Cd- CONTAINING BaF_2

M. Spriņģis, Ā. Veispāls, P. Kūlis, U. Rogulis, I. Tāle, J. Trokšs
Institute of Solid State Physics, University of Latvia, Ķengaraga Str., Rīga, Latvia

Abstract. The Cd is presented as an alternative to Pb for extraction of the oxygen from BaF_2. In Cd- containing crystals γ- irradiation induces new absorption bands at 295, 290 and 360 nm, caused by three different Cd- related defects: Cd^+_c, $Cd^+(x)$ and $Cd^+(1)$ respectively. These bands does not affect the crossluminescence (the fast component of UV emission) but diminishes the self- trapped exciton luminescence (slow componente of UV emission).

The application of the BaF_2 scintillators for photon calorimetry in high energy particle colliders requires use of large crystals transparent in the spectral region from 190 to 230 nm, where UV emission band (crossluminescence) with two maxima at 195 and 220 nm and extremely fast decay time (600- 800 ps) is located [1]. In addition to the fast luminescence band, the BaF_2 crystal has a slow emission component at 310 nm with a decay time of 600ns, caused by the self trapped excitons (STE) and being undesirable for high count rate applications [1].

Unfortunately, BaF_2 crystals, usually grown using the Bridgman method, have absorption bands around 200nm, caused by oxygen. To avoid a contamination of the crystal with the oxygen, so called "scavenger" is added to the starting material. This is another fluoride, that easily reacts with oxygen and subsequently evaporates from the melt.

The PbF_2 is mostly used as "scavenger" in the case of BaF_2. It was shown, that the Pb has also the absorption band at 205 nm and an extra scintillation emission band at 257nm, the main part of which consists of slow scintillation components (t~0.1ms) [1]. Thus, the absorption bands either of oxygen or Pb may be present in the case of deficit or in excess of Pb with respect to the amount of oxygen.

The addition of the CdF_2 in the melt is alternative to Pb technology to diminish the oxygen content in the BaF_2. The present report discuss the use of Cd for extraction of the oxygen and optical and magnetooptical characteristics of the Cd- related defects in BaF_2 -Cd crystals.

Three types of Cd-doped BaF_2 crystals, grown (in vacuum) by Bridgman method, have been examined. Part of the crystals (denoted as type I) contained approximately 10^{-2} at.% Cd. and at least an order of magnitude less another impurities. The impurity content of the other crystals (type II) was comparable to or exceeded (up to 10^{-1} at.% for alkali metal ions) the Cd (10^{-2} at.%) concentration. The crystals of the type III contained no detectable concentration of Cd (less than 10^{-4} at.%) and of order of 10^{-3} at.% for another impurities. The impurity content was controlled by atomic absorption and mass-spectrometry.

Unirradiated (as grown) samples of all the three types are transparent in the visible and UV spectral regions (Fig. 1a) and exhibit no significant absorption bands in the investigated crystals.

γ- irradiation (doses 10^3- 10^6 Gy) of the BaF_2 crystals of the types I and II results in creation of new absorption band centred at 290- 300nm (Fig.1b and Fig.1c correspondingly). An additional absorption band at the long wavelength side at 365 nm occurs for the crystal of the type II. The crystals of the type III show practically no induced absorption bands after the γ- irradiation.

Proc. Int. Conf. on Inorganic Scintillators and Their Applications, SCINT95,
1996, Delft University Press, The Netherlands

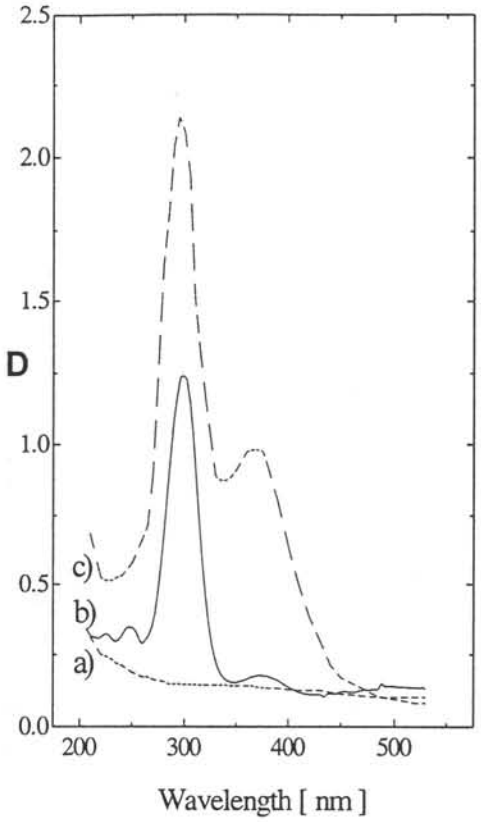

Fig.1. The spectra of optical absorption of the BaF_2 - Cd: a) unirradiated samples, b) typeI, γ- irradiated at 300 K,measured at 4.2 K
c) type II, γ- irradiated at 300 K, measured at 300 K

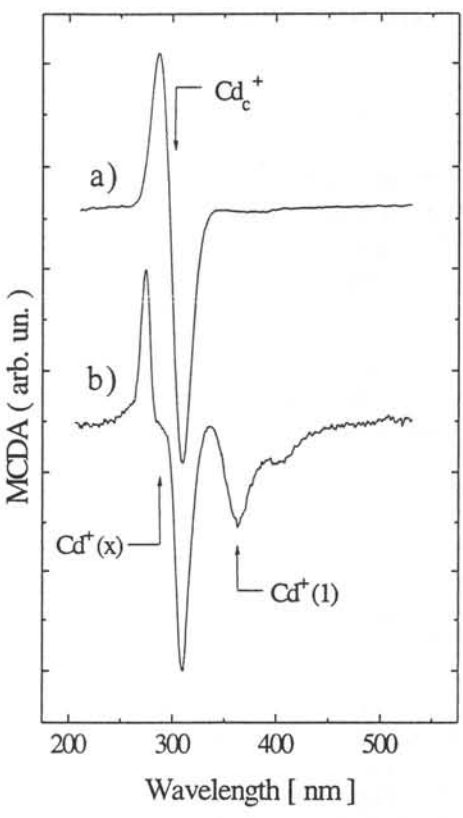

Fig. 2. The spectra of the MCD (at T=2K and B= 2T) of the BaF_2 - Cd crystals after γ- irradiation at 300 K :
a) of the type I,
b) of the type II.

We have investigated the defects created in the samples of BaF_2-Cd by use of the magnetooptical technique: the magnetic circular dichroism (MCD) and the MCD-optically detected EPR (OD EPR).

The samples of all the three types showed no MCD before the γ- irradiation. After the γ- irradiation, only two types of samples (I and II) have the MCD spectra, which we have identified as Cd- related defects by use of the method of the OD EPR. No signals of the magnetic circular dichroism have been observed, which we would attribute to Cd- defects in the crystals of the type III. We propose that in this case the impurity oxygen and Cd (added in the melt) concentrations were in such relation, that after the growth the crystal contains no Cd. In this case, the another impurities in concentration below 10^{-3} at.% create no significant changes in the absorption spectra after the γ- irradiation.

In the Fig.2 the spectra of the MCD are shown for the γ- irradiated BaF_2-Cd crystals of the type I (a) and of the type II (b). Qualitatively the same pattern of the OD EPR spectrum have been detected in whole the MCD bands. These spectra of the OD EPR are collected in the Fig. 3. and our analysis allows to identify them as caused by the different Cd- related defects, this analysis have been reported earlier in [2].

The corresponding MCD bands of Cd- related defects are scown in the Fig.2 by arrows. The whole MCD band of the derivative type is attributed to the Cd^{+}_{c} center (Cd^{2+} substituting Ba^{2+} and captured an electron) in the sample of the type I (Fig. 2a). We have

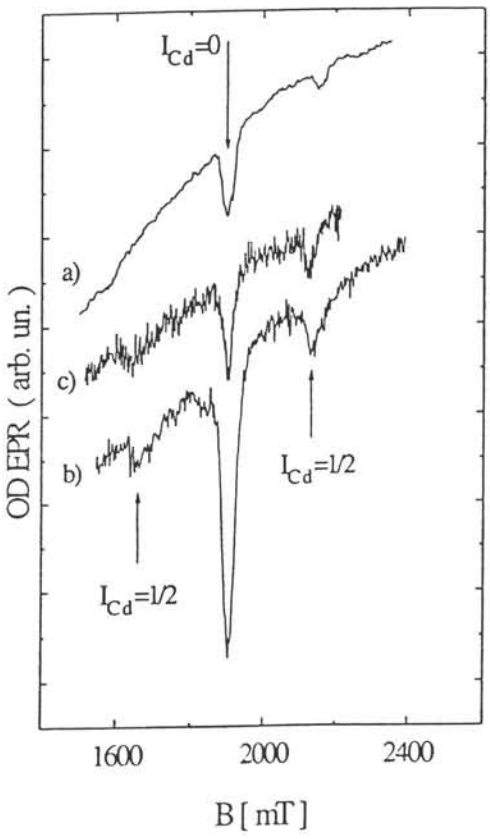

Fig. 3. The spectra of the OD EPR (at T=2K and ν = 53 GHz) :
a) type I, at 310 nm MCD band,
b) type II, at 300 nm MCD band,
c) type II, at 365 nm MCD band.

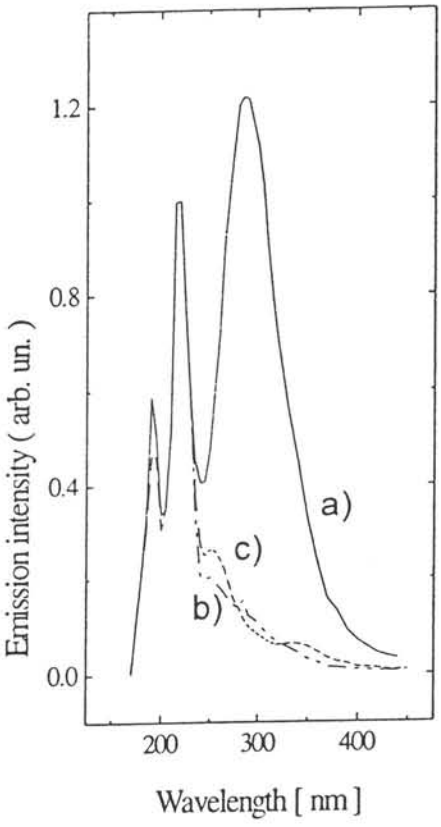

Fig. 4. The X- ray induced emission spectra of the BaF_2 - Cd crystals :
a) undoped, unirradiated sample,
b) Cd- doped, unirradiated sample of the type I,
c) Cd- doped, γ- irradiated sample of the type I.

interpreted the two MCD bands at about 275 nm and 310 nm to the perturbed Cd^{+}_{c} center (the nature of the perturbation stays unknown up to now) in the spectrum of the MCD of the sample of the type II. We have attributed the MCD band at 365 nm (as well as the little shoulder at the long- wavelength side, where the same spectrum of the OD EPR occurs) to the Cd^{+} (1) centers- an electron captured mostly on Cd^{2+} with the adjacent F- vacancy.

Excitation in the region of the discussed absorption bands at 290 nm and 295 nm results as well in photoluminescence bands at E~730 nm and 750 nm respectively, both with approximately the same half-width ~0.35 eV. The intensity of this luminescence increases insignificantly upon cooling from 300 K down up to 77 K. In the spectra of the X-ray induced luminescence these bands are about a factor of 100 weaker that the UV luminescence bands of the BaF_2 crystals.

Moreower, the presence of Cd does not affect significantly the crossluminescence in unirradiated and γ- irradiated crystals, but diminishes the intensity of the STE luminescence (Fig.4). As a result, the intensity of the STE luminescence in unirradiated samples is lower than that of crossluminescence, but comparable with the intensity of the crossluminescence in the γ- irradiated samples. No qulitative difference have been observed between the UV luminescence properties of the Cd- doped samples of the types I and II.

Thus, the Cd as an alternative to Pb allowed to diminish the oxygen content in BaF_2 and is perspective for production of high quality scintillators.

REFERENCES

[1] P. Schotanns et. al. IEEE Transact. on Nucl. sci., v.36, p.132-136 (1989).
[2] U.Rogulis et. al. Proceedings and Abstracts (p.291) of the EURODIM'94.

EMISSION PROPERTIES OF CERIUM-DOPED FLUORO-HAFNATE GLASSES STUDIED BY SYNCHROTRON RADIATION EXCITATION

E.G.Devitsin, N.Yu.Kirikova, V.E.Klimenko, V.A.Kozlov, V.N.Makhov, S.Yu.Potashov
Lebedev Physical Institute, 117924 Moscow, Russia

L.N.Dmitruk
General Physics Institute, 117334 Moscow, Russia

K.W.Bell, R.M.Brown, D.J.A.Cockerill, P.S.Flower, G.H.Grayer, P.W.Jeffreys, B.W.Kennedy, A.L.Lintern, M.Sproston
Rutherford Appleton Laboratory, OX11 0QX Oxon, UK

P.R.Hobson, T.J.Price
Brunel University, Middlesex UB8 3PH, UK

Abstract

The emission spectra of cerium-doped fluoro-hafnate glasses have been studied using X-ray synchrotron radiation excitation. It is suggested that the radiation resistance of such glasses can be improved by the shift of the scintillation emission spectrum to longer wavelengths where the transparency of glasses is much less affected by irradiation. Introducing oxygen-containing compounds into the raw material produced a strong transformation of the spectrum, such that the long wavelength emission band became the dominant one.

1 INTRODUCTION

Dense scintillating glasses are considered as a cheaper alternative to crystalline scintillators for electron/γ-ray detectors. Compared with cerium fluoride crystals, the cerium-doped fluoro-hafnate glasses have even shorter radiation lengths and comparable scintillation decay times [1]. The problem which has to be solved is to improve the radiation hardness of glasses with regard to the scintillation light collected. One approach for improving the radiation resistance is to shift the scintillation emission spectrum to longer wavelengths where the transparency of glasses is much less affected by irradiation.

In the present work a search for optimal compositions of cerium-doped fluoro-hafnate glasses with emission spectra shifted to longer wavelengths has been carried out using the technique of time-resolved spectroscopy with excitation by X-ray synchrotron radiation. It is assumed that during X-ray excitation, when one absorbed photon creates hundreds of electronic excitations, the conditions existing in the excited region of the sample are close to those in the 'real scintillator' after the passage of a high-energy particle.

2 EXPERIMENT

The glasses were produced in an argon atmosphere and then were cast into a brass mould.

The measurements have been carried out at the S-60 synchrotron radiation source in the Lebedev Physical Institute. The set-up allows the measurements of time-resolved emission spectra (in the range 120-520 nm) and decay kinetics (in the nanosecond range) under 'white' X-ray ($h\nu \approx 1$ keV) excitation. Emission light was detected from the irradiated surface of the sample. The latter was a freshly cleaved or polished plate with a thickness of several mm.

Proc. Int. Conf. on Inorganic Scintillators and Their Applications, SCINT95,
1996, Delft University Press, The Netherlands

3 RESULTS AND DISCUSSION

The typical emission spectrum of a fluoro-hafnate glass sample consists of two bands centered near 300 and 400 nm (Fig.1, curve 1). The short wavelength band (SWB) is usually the dominant one, and is due to radiative transitions from the lowest excited 5d-level (split by the crystal field) to the 4f ground state of Ce^{3+} ions situated in 'regular sites'. The spectral position of the band can be shifted to longer wavelengths in the case of stronger splitting (due to an increase of the local crystal field) of the 5d level of Ce. It is well known that for example for alkaline-earth fluorides the long wavelength shift of Ce^{3+} emission is observed in the series Ba→Sr→Ca due to the decrease of the crystal lattice parameter. This effect has been checked for fluoro-hafnate glasses by introducing Sr instead of Ba. This modification of the composition resulted in the shift of the SWB by 20-30 nm (Fig. 1, curve 2). Approximately the same shift was obtained for a high (20%) cerium concentration (Fig. 1, curve 3). Probably this effect is due to the agregation of Ce ions that can lead to the shift of the energy position of the 5d-4f transition. Unfortunately, it was technically impossible to cast a large sample with such a high concentration of Ce.

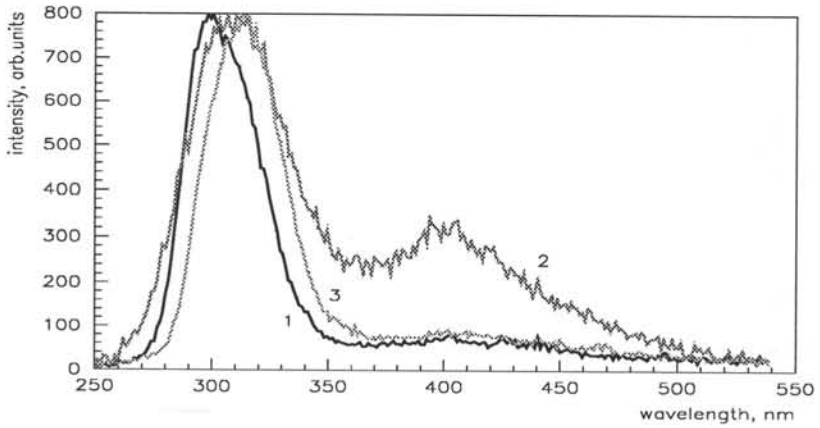

Fig.1. *Emission spectra of: 1 - 54Hf-20Ba-5Ce-2.5Al-17.5Li-1In (reference specimen), normalization factor $k_{norm}=1$; 2 - (23Hf-27Sr-8Y-5Ce-12Al-25Zn) + 2.0 mass.% $CePO_4$, $k_{norm}=3.1$; 3 - 65Hf-10Ba-20Ce-3Al-2In, $k_{norm}=1.1$.*

The longwavelength band (LWB) in Ce-containing compounds is usually attributed to the same 5d-4f transition in Ce^{3+} ions having another environment [2-5]. In particular, in CeF_3 [2,3] the LWB is due to the 5d-4f transitions in Ce^{3+} being in 'defect sites'. The latter are thought to occur near an anion vacancy stabilized by the O^{2-} ion. The Stokes shift of the emission band is considerably larger for the LWB than for the SWB. This is also very important for the increase of the transparency of the emission light.

Thus, an increase of the LWB yield can be achieved by introducing oxygen-containing compounds (CeO_2, $CePO_4$, etc.) into the raw material to create a large concentration of stable anion vacancies. This modification of the composition of glasses produced a strong redistribution of the emission intensity between the bands, such that the 400 nm band became the dominant one (Fig.2, curves 2,3). Unfortunately the effect was usually accompanied by a decrease of the total light yield, probably due to the formation of oxygen-containing defects (in the fluorine lattice) leading to the appearance of additional absorption bands and quenching centers.

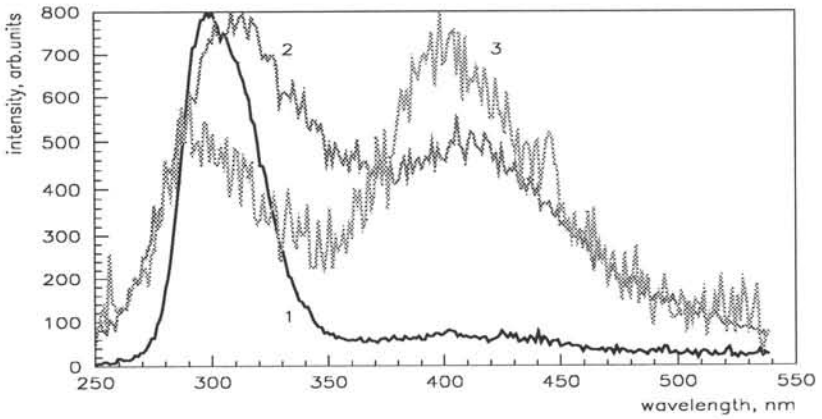

Fig.2. *Emission spectra of: 1 - 54Hf-20Ba-5Ce-2.5Al-17.5Li-1In (reference specimen), $k_{norm}=1$; 2 - (54Hf-20Ba-5Ce-2.5Al-17.5Li-1In) + 0.5 mass.% $CeBO_3$, $k_{norm}=4.1$; 3 - (54Hf-20Ba-5La-3Al-17Li-1In) + 5.0 mass % $CePO_4$, $k_{norm}=10.0$*

It is usually assumed that there is no direct excitation of the LWB during high-energy excitation because the concentration of defects is low compared with that of 'regular' Ce ions. The LWB emission occurs due to the energy transfer (mainly non-radiative) from the excited 'regular' Ce ions to Ce ions situated in 'defect sites' (see for example [6-8]). In case of strong quenching (and absorption) of the SWB emission, the total light yield will be low. Thus to obtain a high light yield in the LWB it is necesssary to excite directly the Ce ions emitting in the longwavelengths spectral range, i.e. to have a large concentration of such Ce ions. If we compare the emission spectra of different Ce-based scintillators (Fig. 3) we see that Ce^{3+} in fluorides emit mainly in SWB whilst in oxygen-based matrixes the Ce^{3+} emission band is situated in the longer wavelength region. Thus, the transformation of emission spectrum to longer wavelengths can be achieved for matrixes containing oxygen as an element of the lattice. In this case oxy-fluoro-hafnate glasses should be considered.

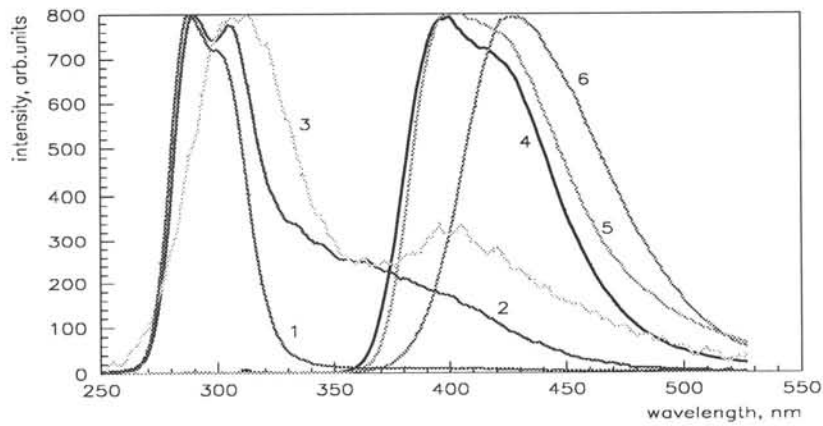

Fig.3. *Position of emission spectra of some Ce-based scintillators excited by X-ray synchrotron radiation: 1 - pure CeF_3; 2 - $La_{0.1}Ce_{0.9}F_3$; 3 - (23Hf-27Sr-8Y-5Ce-12Al-25Zn) + 2.0 mass.% $CePO_4$; 4 - LSO; 5 - YSO; 6 - GSO.*

4 CONCLUSIONS

X-ray synchrotron radiation was succesfully used for spectroscopic studies of the scintillation emission spectra of cerium-doped fluoro-hafnate glasses. It was shown that the composition modification of the raw material allows one to transform the emission spectrum to shift the latter to longer wavelengths, where the transparency of glasses is much less affected by irradiation. In particular, introducing oxygen-containing compounds leads to the strong redistribution of emission intensity between the bands such that the long wavelength emission became the dominant one. A search for the new composition of Ce doped hafnate glasses with higher light yield in the long wavelengths spectral range is now in progress.

This work was supported by the International Association for the Promotion of Cooperation with Scientists from the Independent States of the Former Soviet Union (INTAS), Agreement No.93-1104.

References

[1] . E.G.Devitsin, L.N.Dmitruk, V.A.Kozlov, A.A.Komar, M.I.Kotov, L.S. Popov and S.Yu.Potashov, Proc. Crystal-2000 Int. Workshop, Chamonix, France, Sept. 1992, p.401.

[2] . C.Pedrini, B.Moine, J.C.Gacon and B.Jacquier, J.Phys.: Condens. Matter 4(1992)5461.

[3] . A.J.Wojtowicz, E.Berman, Cz.Koepke and A.Lempicki, IEEE Trans.Nucl.Sci. NS-39(1992)494.

[4] . H.Suzuki, T.A.Tombrello, C.L.Melcher and J.S.Schweitzer, Nucl. Instr. and Meth. A320(1992)263.

[5] . H.Suzuki, T.A.Tombrello, C.L.Melcher and J.S.Schweitzer, IEEE Trans. Nucl. Sci. NS-40(1993)380.

[6] . B.Moine, C.Pedrini, D.Bouttet and P.Martin, Proc. Crystal-2000 Int. Workshop, Chamonix, France, Sept.1992, p.173.

[7] . E.G.Devitsin, N.M.Khaidukov, N.Yu.Kirikova, V.E.Klimenko, V.A.Kozlov, V.N.Makhov and T.V.Uvarova, Rad. Effects and Defects in Solids 133-134(1995).

[8] . M.A.Terekhin, I.A.Kamenskikh, V.N.Makhov, V.A.Kozlov, I.H.Munro, D.A.Shaw, C.M.Gregory and M.A.Hayes, this Proceedings.

SCINTILLATION MECHANISM OF K_2LaCl_5 DOPED WITH Ce^*

J.C. van 't Spijker, P. Dorenbos, C.W.E. van Eijk, K Krämer[§] , H.U. Güdel[§],
Delft University of Technology, Faculty of Applied Physics, c/o IRI, Mekelweg 15, 2629 JB Delft, The Netherlands
§ Institut für Anorganische Chemie der Universität Bern, Freierstraβe 3, 3000 Bern 9, Switzerland

ABSTRACT

Results are presented of a study of the scintillation properties of K_2LaCl_5 doped with Ce^{3+} at concentrations of 0, 0.1, 1 and 10 %. K_2LaCl_5:10%Ce shows a light yield of 50,000 ph/MeV. The non-proportionality curve is almost flat in the range from 10 keV to 1 MeV. The decay of the Ce emission is non-exponential and this can be explained by a diffusion mechanism involving V_k centres and Ce^{2+} centres.

INTRODUCTION

It is well known that the number of electron-hole pairs created by a γ quantum is larger when the bandgap of the material under study is smaller [1]. For chlorides the bandgap is in general smaller than for the fluorides and oxides under study in scintillation research. Therefore the chlorides are interesting to study. A much higher light output than for most known scintillators seems possible.
We present new results on K_2LaCl_5 doped with Ce^{3+}, which has a high light yield indeed. However the disadvantage of this material is the low stopping power in comparison with NaI:Tl. The density of K_2LaCl_5 is 2.54 g/cm^3 and Z_{eff}=44.1, whereas for NaI these values are respectatively 3.67 g/cm^3 and 50.8.

EXPERIMENTAL

The hygroscopic crystals of K_2LaCl_5:Ce were grown by the Bridgmann technique in quartz ampoules. Some of the crystals are not clear, they contain bubbles. The crystals were cut and polished in paraffin oil.
The scintillation properties were studied by means of X-ray and gamma ray excitation. The experimental techniques and conditions are described in [2]. The X-ray induced emission spectra are not corrected for the absorption in the crystal. To record the scintillation decay time on gamma ray excitation, the multi-hit method was used [3] employing XP2020Q tubes. The optical absorption spectra were measured using a HP8452-A diode array spectrophotometer and a quartz diffuser. The absorption coefficient $\mu(\lambda)$ is calculated using $\mu(\lambda)=\ln(T(\lambda)/T_{max})/d$, where $T(\lambda)$ is the transmission at wavelength λ, T_{max} is the maximum transmission and d the thickness of the crystal. The maximum transmission above 350 nm of the K_2LaCl_5 crystals is normally 80 % due to Fresnel reflection losses on the surfaces of the crystal. For some crystals the maximum transmission varied between 40-60% .

[a] These investigations have been supported by the Netherlands Technology Foundation (STW)

The optical excitation experiments were performed by a VUV set-up described by Schaart et al. [4] and at LURE (Laboratoire pour l'Utilisation du Rayonement Electromagnetique-Paris, France).
The excitation spectra were obtained, using for corrections a reference sample of sodium salicilate. In this way the spectra were corrected for the transmission of the system and the quantum efficiency of the photomultiplier tubes (PMTs). All experiments were performed at room temperature.

RESULTS

Figure 1 shows the X-ray induced emission spectra of K_2LaCl_5:Ce.. A broad emission band of the host lattice is visible from 250 to 550 nm. We attribute this luminescence to STE emission. Furthermore, the characteristic 5d-4f luminescence of Ce^{3+} is observed at 340 and 380 nm. In "pure" K_2LaCl_5 Ce emission is observed indicating that the material is contaminated with some Ce.
As reported before [5] for K_2LaCl_5:10%Ce the integral light yield of 50,000 ph/MeV is measured with X-ray induced emission experiments
The ^{60}Co γ scintillation decay time of K_2LaCl_5:10%Ce is presented in figure 2. It shows a non-exponential decay. There is a small fast exponential component with τ=48 ns, possibly fast Ce 5d-4f decay. The rest of the curve can be described by a $(1+at)^{-1.6}$ behaviour.
From pulse height experiments [5], employing a 662 keV ^{137}Cs source and a shaping time of 10 μs the absolute light yield of 35,000 ph/MeV was found.
The difference in the light yields obtained by the X-ray induced emission experiments and the pulse height experiments is attributed to the presence of afterglow and long decay components (> 10 μs). When the crystals are mounted on a PMT, they show a considerable afterglow, which disappears when they are heated at 400 °C.

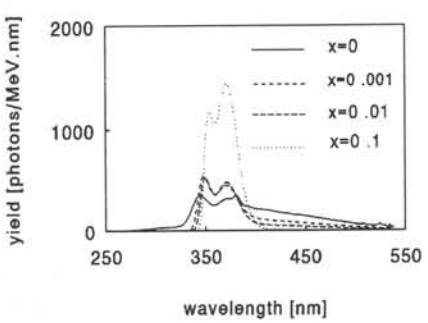

Figure 1: *X-ray induced emission spectra of* $K_2La_{1-x}Ce_xCl_5$.

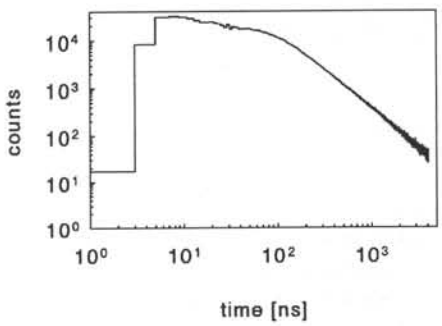

Figure 2: *Scintillation decay time of* K_2LaCl_5*:10%Ce, recorded with* ^{60}Co

In figure 3 the energy dependence of the light yield per MeV is shown, the so called non-proportionality curve. In the energy range of 10 keV-1 MeV the light yield per MeV is constant.
The energy dependence of the energy resolution is shown in figure 4. In this resolution there are several contributions [6]. There is a contribution of the PMT resolution and the resolution of the scintillator itself. The resolution of a PMT is due to statistics in the number of

photoelectrons and the spread in the gain. It can be calculated using [6], $R_M=2.36\sqrt{((1+v_M)/N)}$. Here R_M is the PMT resolution, v_M the fractional variance in the gain of the PMT and N the average number of photoelectrons generated by a γ quantum. For the XP2020Q tube which was used in the pulse height experiments v_M =0.09.

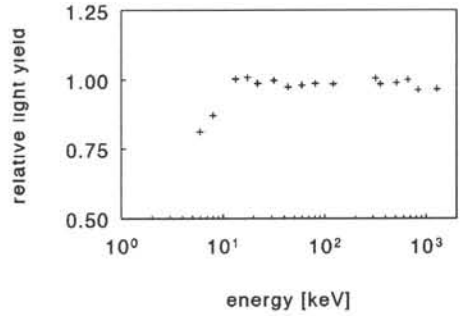

Figure 3: *Non-proportionality curve for K_2LaCl_5:10%Ce. All points are relative to the light yield per MeV for 662 keV γ radiation. The error in the range 10 keV-1 MeV is about 5%, below10 keV it is 8%.*

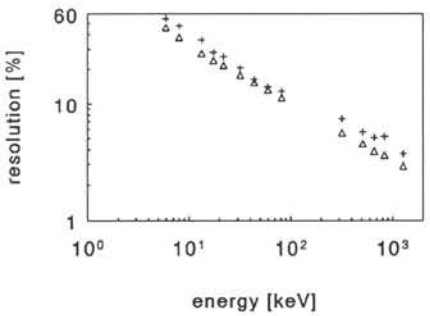

Figure 4: *Resolution curve for K_2LaCl_5:10%Ce (+). The PMT resolution is denoted with Δ. The error is about 10%*

In figure 5 the optical absorption spectra are shown of K_2LaCl_5 with Ce concentrations of 0, 0.1, 1 and 10 % .

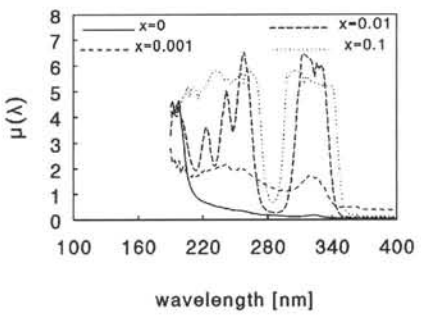

Figure 5: *Optical absorption spectra of $K_2La_{1-x}Ce_xCl_5$. For the Ce concentrations of 1 and 10 % the data above μ=5 cm^{-1} are not reliable. The thickness of a crystal is 0.75 (0%), 0.35 (0.1%), 1.20 (1%) and 0.60 (10%) mm.*

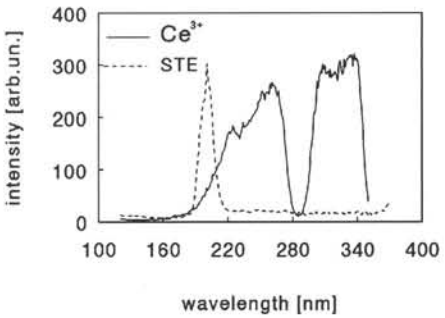

Figure 6: *Excitation spectra for STE (λ_{em} > 410 nm) and Ce (λ_{em}=-380 nm) for K_2LaCl_5:0.1%Ce. The error in the curve is 5%. The STE spectrum is multiplied by a factor for clarity.*

For all crystals the typical Ce 5d-4f absorption bands are observed at 224, 240, 260 and 320 nm. For the "pure" crystal these lines are weakly visible too, indicating that the crystal is contaminated with some Ce. From the absorption spectrum for the pure crystal a concentration of 0.01%Ce is deduced.

The absorption band below 200 nm is ascribed to the fundamental absorption band. Note that the absorption for K_2LaCl_5:0.1% Ce at wavelengths larger than 350 nm is higher than for the other crystals.

In figure 6 the excitation spectrum for the Ce and the STE luminescence are shown. For the Ce excitation spectrum at λ_{em}=380 nm, the typical 5d-4f absorption bands are visible, see figure 5. In the STE spectrum a small band at 200 nm, the fundamental absorption edge, is observed. Not a broad band is observed, probably due to quenching of the STE's at wavelengths near and below the bandgap [7].

DISCUSSION

Figure 1 shows that the light yield for the Ce emission increases with increasing Ce concentration due to an increase of the probability of energy transfer to the Ce centre.
The slow scintillation decay component shown in figure 2 can be described by a $(1+at)^{-1.6}$ behaviour. This indicates that a diffusion mechanism takes place.
A model to explain the energy transfer could be the following. After absorption of a γ quantum, electron-hole pairs are created. The holes are trapped forming V_k centres. The electrons can move freely in the lattice and can be trapped on Ce forming a Ce^{2+} centre, or near a V_k centre forming an STE.
At low Ce concentrations the STE and the Ce luminescence are both visible. With increasing Ce concentration the STE luminescence decreases and the Ce luminescence increases. With increasing Ce concentration more electrons can be trapped by the Ce, forming Ce^{2+} centres. After recombination with a V_k centre, which diffuses through the lattice, the Ce centre is excited and luminesces. In the K_2LaCl_5:10%Ce crystal this process is expected to be most efficient, which is confirmed by experiment. Obviously some other models could also explain the observed phenomena. More experiments are required.

REFERENCES

[1] Rodnyi P A, Dorenbos P, Van Eijk C W E, Phys. Stat. Sol. 1995, Vol 187, p. 15.
[2] Dorenbos P, de Haas J T M, Visser R, van Eijk C W E, Hollander R W, 1993 IEEE Trans. Nucl. Sci. NS-40, 424.
[3] Moses W W, Nucl. Instr. and Meth. 1993, A 336, p. 253.
[4] Schaart D R, Dorenbos P, van Eijk C W E, Visser R, Pedrini C, Moine B, Khaidukov N M, 1995, J. Phys. Condens. Matter 7, p. 3063.
[5] van 't Spijker J C, Dorenbos P, de Haas J T M, van Eijk C W E, Güdel HU, Krämer K, 1995 Rad. Meas. (228), in press.
[6] Dorenbos P, de Haas, J T M, van Eijk C W E, 1995 IEEE Trans. Nucl. Sci, in press.
[7] Williams R T, Song K, J. Phys. Chem. Solids, 1990, Vol 51, No 7 .p. 679.

DEVELOPMENT OF FAST SCINTILLATORS ON THE BASIS OF CsI DOPED WITH HOMOLOGICAL IMPURITIES

A.GEKTIN, N.SHIRAN, V.SHLYAHTUROV and A.BELSKY*
Institute for Single Crystals, Lenin ave 60, 310001, Kharkov, Ukraine
*Moscow State University, 117234, Moscow, Russia

ABSTRACT

Spectral and kinetic characteristics of UV-luminescence of mixed CsI_x-$CsBr_{1-x}$ single crystals (where x - ranges from 0 to 1) are presented. It has been shown that the doping of the CsI crystals with homological anion impurity is a method for affecting its spectral and kinetic characteristics.

INTRODUCTION

Due to the presence of fast ultraviolet luminescence at room temperature undoped CsI crystals are known to be rather effective scintillators [1,2]. The doping of these crystals with the small amounts of homological impurities (Rb, K, Br, Cl) preserves UV-luminescence, though leads to some changes in the spectral composition and in the decay kinetics [3,4].

The most significant feature of UV-luminescence of CsI crystals is the absence of its photoexcitation at least for energy up to 3 E_g (where E_g is the energy gap) [1,5]. This fact has been assumed as a basis for the suggestion about a correlated interaction of closely located electronic excitations (excitation cluster), the relaxation of which may condition the peculiarities of UV-luminescence [6,7]. There are no restrictions for the action of such a mechanism, therefore one may assume that it is to be observed not only in CsI, but also in other alkali halide crystals. The investigation of the properties in the crystal series *pure CsI, mixed CsI-CsBr, pure CsBr* must yield additional data necessary to verify the said hypothesis.

MATERIALS AND METHODS OF INVESTIGATION

The single crystals were grown by the Kiropulos (in a special atmosphere) and Stockbarger (in graphitized quartz crucible) methods. The luminescence spectra were measured by means of MDR-23 monochromator with the FEU-100 photomultiplier (PMT). The corrections for the monochromator dispersion and the PMT sensitivity were introduced. ^{241}Am was used as gamma-radiation source. Scintillation characteristics were measured by the single photon counting technique (^{22}Na and ^{137}Cs sources) with the gate width 100 ns (XP-2020Q PMT). The kinetic characteristics of UV-luminescence were determined in the process of excitation with synchrotron radiation by analogy with [6]. The time resolution was made 0.2 ns.

Proc. Int. Conf. on Inorganic Scintillators and Their Applications, SCINT95,
1996, Delft University Press, The Netherlands

EXPERIMENTAL RESULTS

Radioluminescence takes place for all the concentrations of the solution components, and the location of the maximum being shifted by 0.4 eV toward lower-energy region with transition from CsBr to CsI (Fig.1a). The character of this shift is close to linear (Fig.1b). However, the extrapolation to x=0 is incorrect: in pure CsBr crystals only

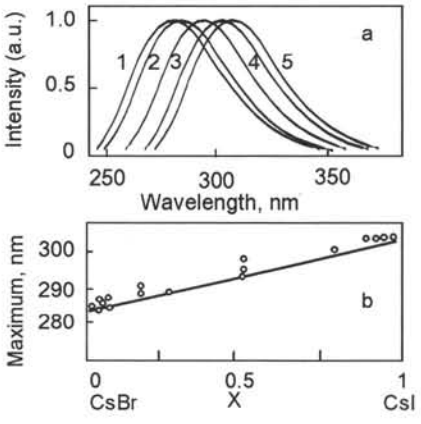

Fig.1. a) Radioluminescence spectra of mixed CsI_x-$CsBr_{1-x}$ crystals:
(a) x=0.01(1), x = 0.08 (2), x = 0.45 (3), x=0.8 (4), x = 1 (5).
(b) Maximum position of UV emission band on the content of mixed components.

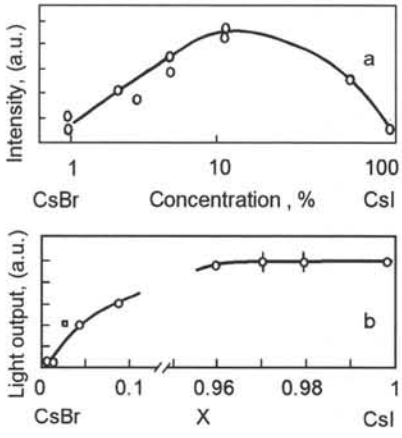

Fig.2. Concentration dependence of intensity (a) and light output (b) of CsI-CsBr crystals.

low-intensity luminescence with 250 nm maximum takes place; it is associated with core-valence transitions. The increase of the intensity of radioluminescence and light output of scintillations with the growth of x is shown in Fig.2. These data testify that the decrease of x from 1 up to 0.96 does not lead to the change of the light output. The luminescence decay kinetics has a complex character. The decay time constantly decreasing with the growth of the impurity concentration (Fig.3). The said effect is more pronounced with the rise of temperature [6]. Note that some decrease of decay times (in compare with pure CsI) is observed in the whole range of the solid solutions. The analysis of the pulse form shows that it may be approximated by exponents having 1-2 ns, 6-7 ns and ~25 ns component. As is evident, the shortest component is characterized by the largest changes in comparison with pure CsI. Moreover, it should be noted that for CsBr-CsI the behaviour of the I(t) curve (Fig.4) testifies the presence of a slow component. Its intensity is small, however, due to slow component presence the total light output in it exceeds the yield in the short component. The radioluminescence intensity of $CsBr_{0.98}$-$CsI_{0.02}$ is 4-6 times higher than ones of pure CsI, whereas this relation is inverse in the fast component (see Fig.2). For small Br^-—concentrations (x=0.96) in CsI-CsBr the luminescence at 280-300 nm may be excited not only by γ-quanta but also by photons with energy near 5.8 eV.

DISCUSSION

First of all it is necessary to dwell on the hypothesis about the dominant role of the correlated relaxation of defects and excitations closely located in the track in CsI crystals [4]. The doping of CsI crystals may affect both the peculiarities of the formation process of «excitation cluster» and the character of separate excitations. The estimation of the effective radius of «exciton-exciton» or «exciton-defect pair» interactions yields the value of the order of 1 nm [6]. Therefore the effect of a dopant may be

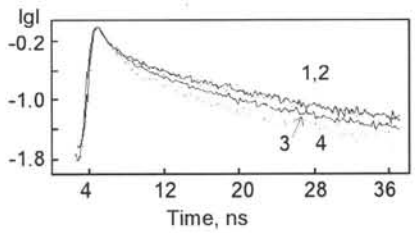

Fig.3. Decay curves of fast UV-emission in doped CsI_x-$CsBr_{1-x}$ crystals: x=1 (1), x = 0.99 (2), x = 0.92 (3), x=0.88(4). 300 K.

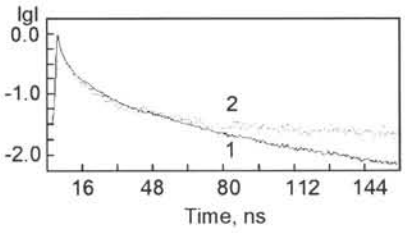

Fig.4. Decay curves of fast UV-emission in CsI crystal (1) and CsBr based crystal (x= 0.05) (2). 300 K.

essential only in the case of a high probability for impurity ions to be located within the regions of the crystal lattice involved in «excitation cluster». Therein 5-10 % concentration of the impurity is necessary. In this connection mixed crystals are the optimal object for investigations. The transition from pure CsI crystals to mixed ones is to be accompanied by the speed-up of the decay kinetics of fast UV-luminescence. Actually, Fig.3 shows that for small Br^-- content the curves I(t) are identical with the ones observed in pure CsI, whereas for x=0.88 the differences become essential.

In CsBr crystals containing traces of iodine impurity slow (millisecond) glow appears besides fast UV-luminescence practically within the same spectral range, i.e. two different mechanism of electronic excitation relaxation act simultaneously. This is confirmed by the possibility of their luminescence excitation at the tail of fundamental absorption in the region 5.8 eV. Moreover, additional thermostimulated peaks presence in glow curve at temperatures higher than 165 K [6]. The appearance of slow component may be associated with the relaxation of heteronuclear excitons as shown by EPR investigations [8]. Those are rather stable in the case of homological impurities with a smaller ionization potential presence.

It should be noted that mixed CsI-CsBr crystals possess a higher radiation stability than pure CsI if the Br^- - content not higher than 7%. In these samples there are no changes in transmission and scintillations parameters up to 10^5 Gy [9]. At higher Br^- - concentration the mixed crystals become unstable and it takes place the decomposition with aging [10].

CONCLUSION

It should be noted that the effect of fast ultraviolet luminescence is typical for the mixed crystals CsI-CsBr practically within the whole component concentration range. The

obtained data may be described in the frames of the hypothesis about the correlated relaxation of the defects and excitations closely located in the track. It has been shown that the doping of the crystal with a homological anion impurity is a method for affecting its spectral kinetic characteristics and radiation stability.

REFERENCES

[1] S.Kubota, H.Murakami, J.Ruan et al., NIM. A273 (1988) 645.

[2] V.V.Gavrilov, A.V.Gektin, N.V.Shiran, Sov. Opt. and Spectr. 66 (1989) 961.

[3] V.V.Gavrilov, A.V.Gektin, N.V.Shiran, Lett. JTP. 15 (1989) 27.

[4] A.V.Gektin, A.I.Gorelov, V.I.Rykalin et al., NIM. A294 (1990) 591.

[5] A.N.Belskyi, A.N.Vasiliev, V.V.Mikhailing et al., Rev. Sci. Instruments, 63 (1992) 806.

[6] A.V.Gektin, N.V.Shiran, A.N.Belskyi and A.N.Vasiliev, Nucl.Tracks Rad.Meas. 21 (1993)11.

[7] A.N.Belskyi, A.V.Gektin, V.V.Mikhailing et.al., Preprint ISC-90-26, Kharkov, Ukraine, (1990) 16 p.

[8] C.I.Delbecq, D.Shoemaker and P.Yuster, Phys.Rev. B7 (1973)3933.

[9] N.V.Shiran, T.A.Charkina, V.I.Goriletsky et al., Nucl.Tracks Rad.Meas. 21 (1993)107.

[10] A.V.Gektin, M.A.Rom, V.V.Shlyakturov and P.V.Mateichenko, Phys.Stat.Sol. A133 (1992)325.

LUMINESCENCE MECHANISMS IN CsI-BASED SCINTILLATORS

S.A.Chernov and R.G.Deych*
Institute of Solid State Physics University of Latvia
8 Kengaraga Str., Riga, LV-1063, Latvia
* Analogic Corp., 8 Centennial Dr., Peabody, MA 01960, USA

Abstract. The goal of presented work is to analyze the experimental data on kinetics of the scintillation rise and decay in pure and Na^+ or Tl^+ doped CsI crystals. The possible mechanisms of scintillation excitation in these crystals are discussed.

1. INTRODUCTION

Pure and Tl^+ or Na^+ doped CsI crystals are widely used as scintillators for detecting the ionizing radiation. The scintillation mechanism in Tl^+ and Na^+ doped CsI crystals is sufficiently well studied [1,2].

In pure CsI crystals the mechanism which leads to the excitation of scintillations at high temperatures is not established yet, the origin of the luminescence centre responsible for the scintillations is not clear too.

Recent publications have shown, however, that intense visible emission of CsI-Tl giving the main contribution to scintillations, is caused by the radiative annihilation of the self-trapped exciton (STE) localized near Tl^+ ion [3,4]. This fact was used for the explanation of the high scintillation yield of the scintillations in CsI [3]. Authors of [5] experimentally found a threshold of the scintillation excitation in pure CsI crystals.

The object of the present investigation is to discuss the mechanisms and the reasons of the high yield of the scintillations in Na^+ and Tl^+ doped CsI crystals as well as the possible origin of the luminescence centers, responsible for the scintillations in pure CsI crystal.

2. EXPERIMENTAL RESULTS AND DISCUSSION

The scintillation excitation mechanism is well understood in the case of CsI-Na crystal. Spectrally separated and reliable identified Na^0 and V_K absorption bands [6,7] enables us to investigate the transient absorption spectra relaxation in a wide temperature range and to compare these data with scintillation rise and decay characteristics under excitation with electron pulses (5 ns, 300 keV, 20 A/cm^2) [1]. This work has shown, that scintillations in CsI-Na occur as the result of V_K centers migration and their recombination with Na^0 centers, followed by the formation and radiative annihilation of the STE perturbed by Na^+ impurity. Thermal behavior of scintillation

Proc. Int. Conf. on Inorganic Scintillators and Their Applications, SCINT95,
1996, Delft University Press, The Netherlands

rise and decay times in CsI-Tl [2] is very similar to that observed in CsI-Na crystal. In our opinion, the interpretation of the scintillation mechanism in CsI-Na can be applied to CsI-Tl, as well. We have studied also the thermal annealing of induced absorption in the bands of V_K and Na^0 centers after electron irradiation in CsI-Na at 9 K (Fig. 1) [1].

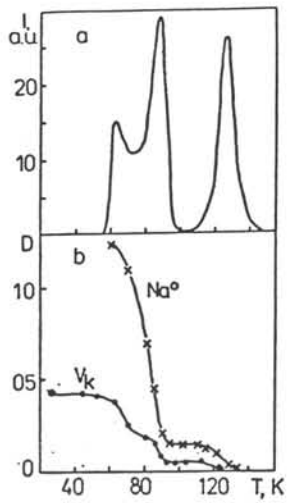

Fig. 1. Thermostimulated luminescence (a) and annealing of V_k and Na^0 centers (b) of CsI-Na crystal irradiated with electron pulse at 9 K.

Fig. 1 demonstrates that nearly 90% of Na^0 centers are destroyed at the temperature of V_k center destruction (TSL peaks 60 and 90 K [7]).

Therefore, the ratio of probabilities of recombination (A_r) and V_K-center capture (A_c) appears to be $A_r/A_c = 10$.

This result is quite different for crystals with NaCl-type structure, where $A_r/A_c < 1$ [8]. This peculiarity of CsI crystal determines the mechanism and a high yield of scintillations in CsI-Na and CsI-Tl crystals.

Recently CsI was suggested as a new fast scintilator [9]. However, the origin of the UV band providing the main contribution to scintillations in pure CsI at room temperature is yet to be established.

In order to clarify the origin of the fast emission in CsI, time-resolved spectroscopy method based on the electron accelerator with pulse duration 50 ps, electron energy 200 keV and pulse current density 100 A/cm^2 was used [10]. The result are shown in Fig. 2. The most important result is that the rise time of the emission coincides with the excitation pulse duration and was determined to be < 50 ps (Fig. 2a). It should be stressed, that this value is much smaller than the rise time of the STE emission and F-centre creation time in CsI (Fig. 2b). The STE and F-centre creation times are controlled by the free electron recombination with a self-trapped hole and are in the range of 300-500 ps under the experimental conditions [11]. The same lifetime of electrons in conduction band was obtained from the conductivity decay in CsI at 300 K [12]. Therefore, the recombination mechanism of the fast emission can be excluded from the consideration, i.e. the the emitting state cannot be formed via trapping and recombination of electrons and holes. We suggest that the emitting state arises from free exciton (FE) capture in the regions pertrubed by the lattice defect, impurity or STE.

According to the recent work [5] the yield of the UV luminescence drastically rises under excitation with photon energy higher than 20 eV. The excitation thershold of UV luminescence of CsI was explained as a result of interaction of two electron excitations [5]. In our opinion, the interaction of FE and STE may explain the existing experimental data on fast UV emission in CsI. Although the STE creation time due to the electron - V_k recombination in CsI is rather long (see Fig. 2b), a small fraction of STE concentration can be created as a consequence of the correlated relaxation of the interacting charge carriers [13]. Small yield of such STE and low probability of FE and STE interaction is a possible explanation of essiencially lower scintillation yield in pure CsI compared with CsI-Na and CsI-Tl.

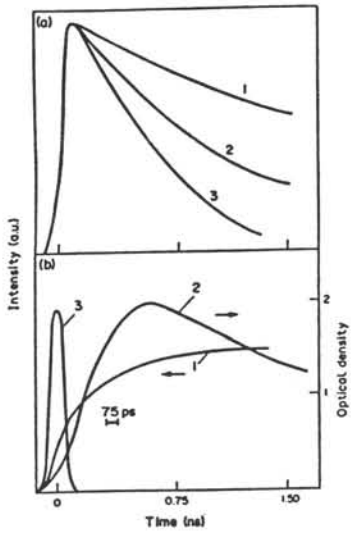

Fig. 2. Decay kinetics of CsI luminescence and absorption after excitation by 50 ps electron pulse: (a) fast u.v.-emission (305 nm) at 215 K (1), 293 K (2), 440 K (3); (b) luminescence of STE at 80 K (1), F-centre absorption at 293 K (2) and electron pulse shape (3).

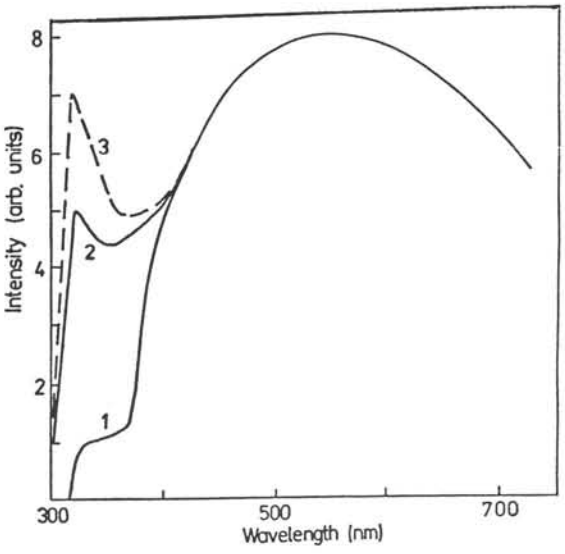

Fig. 3. Emission spectra of CsI(Tl) crystals with Tl^+ concentration (0.002-0.006) mol.% at the excitation by ionizing particle of various types:
1 - 30 keV X-ray [14]; 2 - 1,4 MeV protons; 3 - 2 MeV α-particles [15].

The probability of FE and STE interaction should increase with the increase of the energy density deposited by the radiation. Similar effects have been observed in CsI-Tl (Fig. 3) [14,15], when the contribution of the UV band to the total scintillation spectra increases with the rise of the excitation density.

3. CONCLUSIONS

1. In doped CsI crystals luminescence center is formed as a result of V_k center migration toward the electron trapping center (Na^o or Tl^o), followed by the formation and radiative annihilation of the STE perturbed by the Na^+ or Tl^+ impurity.

2. High yield of scintillations in CsI-Na and CsI-Tl is explained by the high probability of recombination of V_k center with Na^o or Tl^o center during the process of thermoactivated diffusion.

3. In pure CsI crystal a luminescence center is formed as a result of the interaction of a FE with a defect or a STE, formed as the result of the correlated relaxation of interacting carriers of opposite sighs (e-h pair).

1. N.L.Aluker, V.V.Gavrilov, R.G.Deich, S.A.Chernov, S.S.Etsin. Izv.Akad.Nauk Latv.SSR, ser.fiz.tekhn.nauk, 1982, N 4, 57.

2. L.M.Shamovski and A.A.Rogozin, Izv.AN USSR, ser. fiz., 1979, v. 43, N 6, 1115.

3. V.Nagirnyi, V.Stolovich, S.Zazubovich, V.Zapelin, M.Nikl, G.P.Pazzi and L.Salvini. J.Phys.Cond.Matter., 1995, v.7, 3637.

4. J.M.Spaeth, W.Meise and K.S.Song, J.Phys.Cond.Matter., 1994, v.6, 3999.

5. A.N.Belsky, A.N.Vasiljev, V.V.Mikhailin, A.V.Gektin, P.Martin, C.Pedrini and D.Bouttet. Phys.Rev.B, 1994, v. 49, N 18, 13197.

6. I.Mori, A.H.Kayal, C.Jaccard and M.A.Aegerter. Sol.St. Commun., 1980, v.34, N 5, 315.

7. T.Sidler, J.P.Pellaux, A.Nouailhat and M.A.Aegerter. Sol.St.Commun., 1973, v. 3, N 4, 479.

8. H.B.Dietrich, A.E.Purdy, R.B.Murray and R.T.Williams, Phys.Rev.B, 1973, v. 8, N 12, 5894.

9. Sh.Kubota, Sh.Sakuragi, S.Hashimoto and J.Ruan,.Nucl. Instr.Meth., 1988, v. A273, 275.

10. M.Abdrakhmanov, S.Chernov, R.Deich and V.Gavrilov. J.Lumin. 1992, v. 54, 197.

11. A.E.Aluker, R.G.Deich and G.S.Dumbadze. Pis'ma Zh. Techn. Fiz. 1988, v. 14, 2132.

12. B.P.Aduev, E.D.Aluker, V.N.Svaiko, Abstract VI Intern. Conf. "Radiation stimulated geterogen process", Russia, Kemerovo, 1995, 52.

13. T.Shibata, S.Iwai, T.Tokizaki, K.Tanimura, A.Nakamura and N.Itoh, Phys.Rev.B, 1994, v. 49, N 18, 13255.

14. P.Shotanus, R.Kammermans and P.Dorenbos. IEEE Trans. Nucl.Sci., 1990, v. NS-37, N 2, 177.

15. R.Gwin and R.B.Murray, Phys.Rev., 1963, v.131,N 2, 501.

PHOTO AND GAMMA-RAY INDUCED SCINTILLATIONS IN CsJ-Tl

B.Berzina
Institute of Solid State Physics, University of Latvia
8 Kengaraga St., LV-1063, Riga, Latvia

1. PROBLEM AND AIM

CsI-Tl is one of widely used inorganic scintillators available for registration of different types of radiation. Important requirements to scintillators are a short decay time (in order of ns) and a high scintillation yield. For CsI-Tl this yield is relatively high (10^4 photons per MeV), however the scintillation decay time is rather long (in order of μs) [1] . Recently observed renaissance of CsI-Tl scintillator seems to be caused mostly by its application together with a silicon photodiode sensitive to CsI-Tl emission [2].

At the same time a revival of an interest to the studies of the scintillation processes in CsI-Tl can be observed. Recent investigations of CsI-Tl using optically-detectable magnetic resonance (ODMR) methods [3] as well as detailed spectral, polarization and kinetic studies [4] were performed. Two main results of a great importance for the knowledge of the scintillation processes could be distinguished. The first of them is a proposal of a new model of impurity-related luminescence centers with self-trapped exciton (STE)-like structure, responsible for appearance of two highly overlapping visible emission bands in CsI-Tl [3,4]. The second one provides an evidence of the existence of the room temperature (RT) stable self-trapped hole (STH) stabilized at the impurity ion (V_{KA} centers) in doped CsI crystals [3].Just mentioned visible luminescence bands in CsI-Tl are mainly responsible for the gamma-ray [2,5] and x-ray [3] induced scintillations. The STE-like nature of these luminescence bands allows to explain the high yield of scintillations observed in CsI-Tl [4].

The aim of the present work is to study the exciton- and gamma-ray induced luminescence in order to extend the knowledge about the mechanisms of the scintillations in CsI-Tl.

2. EXPERIMENTAL AND RESULTS

A CsI-Tl crystal with Tl content of 7.2×10^{-3} mol fraction in a melt was used. The samples were put in a variable temperature cryostat.The spectral and the kinetic investigations were performed. Two different kind of excitations were used: i) a photoexcitation (a deuterium lamp or an electrical spark (10 kV) combined with a quartz prism monochromator) and ii) a gamma-ray excitation (Co^{60} source). The luminescence response passing through a grating monochromartor or a set of color glass filters was recorded by a photomultiplier coupled with a recorder or an oscilloscope. Further the gamma-ray excited luminescence is named gamma-scintillations, whereas the luminescence caused by the crystal excitation with light from the exciton absorption band is named ex-scintillations.

Fig.1 (a) shows three luminescence spectra of CsI-Tl at RT and (b) - temperature dependence of their relative yields normalized to unity yield at RT. These luminescence

Proc. Int. Conf. on Inorganic Scintillators and Their Applications, SCINT95,
1996, Delft University Press, The Netherlands

spectra are excited: 1 - by UV light from the low energy side of the exciton absorption band at 5.66 eV (ex-excitation), 2 - by light from the Tl-related absorption band at 4.49 eV and 3 - by gamma-rays from [2]. In all three spectra the visible broad luminescence band consisting of 2.55 and 2.25 eV single bands ([4] and our results) is predominant, whereas the temperature dependences of luminescence relative yields are different.

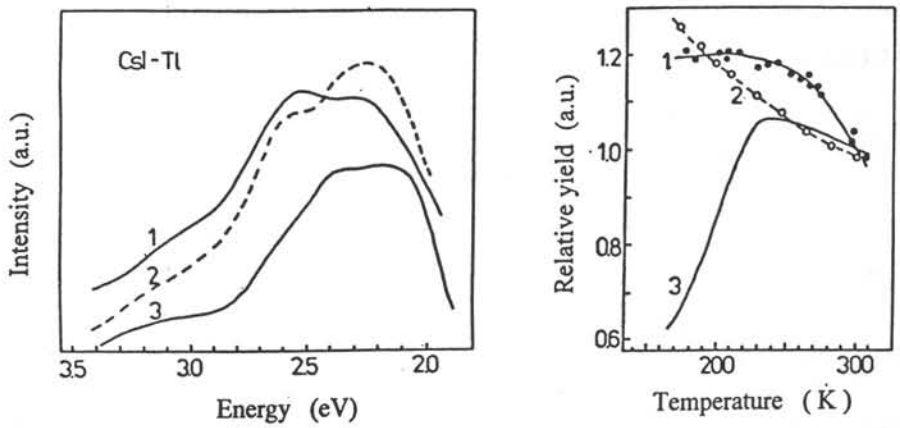

Fig.1. (a) Luminescence spectra of CsI-Tl at RT and (b) temperature dependence of relative yields of luminescence observed under three different excitations: 1 - UV light from the exciton absorption band at 5.66 eV (219 nm) ; 2 - UV light from the Tl-related absorption at 4.49 eV (276 nm) and 3 - gamma rays from [2]. All necessary corrections of spectra raised from apparatus are fulfilled. In a case of 5.66 and 4.49 eV excitation the yield of predominant broad visible luminescence band is registrated.

Fig.2 (a) reproduces some decay characteristics of ex- and gamma-scintillations attributed to the visible part of the luminescence spectra (Fig.1a). The direct excitation of Tl-related luminescence at 4.49 eV results in exponential temperature dependent decay component with the decay time common for both luminescence subbands (2.55 and 2.25 eV) at fixed temperatures within the region from RT down to 120K (Fig.2a,solid curve 1). Further temperature decrease results in difference of the decay times of the both subbands.The decay times of ex-scintillations are depicted by close circles. At RT ex-scintillations are formed by an exponential luminescence pulse with the rise time of 0.2 μs and the decay time larger than that produced by absorption in Tl-related bands (depicted by solid curve 1). Decrease of temperature leads to drastical rise of the decay time of ex-scintillations. A second faster component appears at at 170K and becomes predominant at temperatures below 120K. The decay time of the second component seems to be coincident with these observed under direct excitation of Tl-related centers. The spectra of the first and the second decay component of ex-scintillations are measured at 185K and 80K, correspondingly (Fig.2b). Both spectra describe the visible bands of Tl-related luminescence. At RT the gamma-scintillations consist of two exponential decay components with different decay times (Fig 2 a, empty circles). The decay time of the first faster component seems to be coincident with that of the first component from ex-scintillations appearing at RT region. The second component of gamma-scintillations has not an analog in ex-scintillations. The decrease of temperature results in decay time exponential rise of both components.

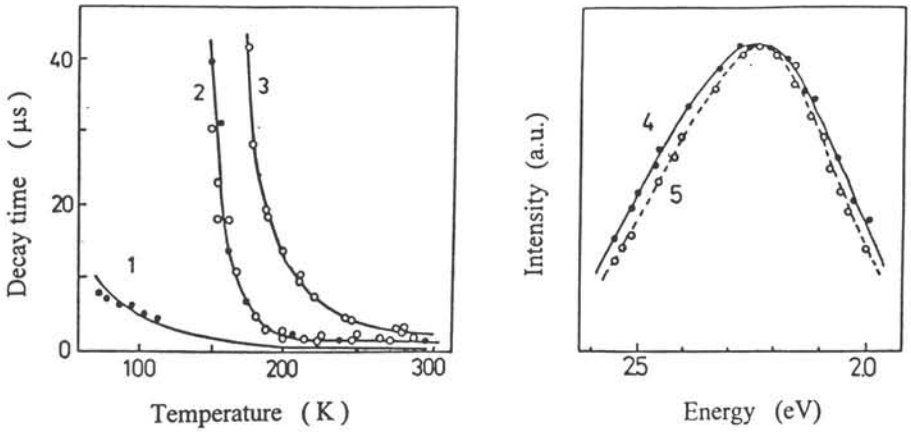

Fig.2. (a) Thermoevolution of decay times of several luminescence decay components measured at different excitations of CsI-Tl. 1, solid line - Tl-related luminescence caused by excitation at 4.49 eV ; 1,2, close circles - ex scintillations (5.66 eV excitation) and 2,3, empty circles - gamma-scintillations. (b) Luminescence spectra (uncorrected) of ex-scintillations: 4 - at 185K (close circles) and 5 - at 80K (empty circles).

3.DISCUSSION

The examined luminescence processes are illustrated in a terms of energy level scheme at Fig.3. CsI-Tl luminescence consists of four emission bands [4]. Two of them - the UV bands at 3,31 and 3.09 eV can be characterized with the structure of electronic states analogous to that of well studied Tl^+ center triplet states in alkali halides with NaCl structure [4]. These luminescence bands are highly quenched at RT. Other two overlapping visible emission bands 5.55 and 5.25 eV are predominant in ex- and gamma-scintillation spectra and, therefore, are a matter of present investigation.

The STE-like structure of Tl-related luminescence centers responsible for visible emission bands is being worked out now [3,4]. At present the hole component of these luminescence centers have been well established. From the ODMR investigations a hole center is estimated to be a V_{KA} center consisting of the I_2^- molecule ion trapped somewhere near the Tl^+ impurity [3]. The existence of two visible luminescence bands have been confirmed to be caused by two different types of V_{KA} and Tl^+ center location [3]. The electron component of the luminescence center is not yet clear. The excited electron seems to be bound to 7s or 6p Tl state [3] forming diffuse orbital of Tl^0 center, highly influenced and mixed with the molecular orbitals of the V_{KA} center. Therefore, the complex luminescence center seems to be a $V_{KA}Tl^0$ type center. The full process described can be illustrated at Fig.3: a photoexcitation - 4→5, the relaxation of the hole (4→6) and of the electron (5→7) components and emission (7→6)

Ex-scintillations. The photo-induced creation of excitons (e^0) (Fig.3, 1→2) results in the ex-scintillations predominantly composed by the emission of the $V_{KA}Tl^0$ centers (Fig.1a,1) within a temperature region from RT down at least to 80K (Fig.2b). The analysis of thermoevolution of the ex-scintillation decay (the existence of two different components

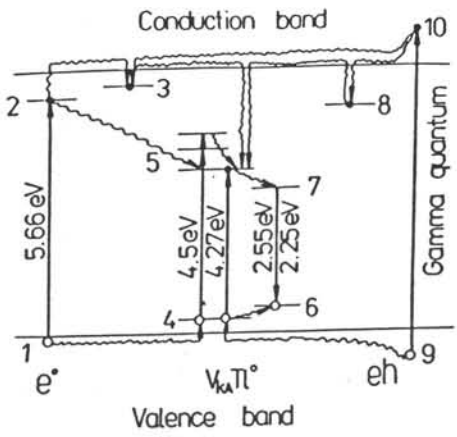

Fig.3. Illustration of processes responsible for ex- and gamma-scintillations.

Fig.2a,close circles) allow to propose two mechanisms responsible for the ex-scintillation creation. The first mechanism named an exciton mechanism can be considered as energy transfer from excitons to the impurity center resulting in the $V_{KA}Tl^{\circ}$ luminescence center formation (Fig.3.1→4, 2→5). It seems that this mechanism (represented by the second component of ex-scintillations) is working at low temperatures.The second proposed mechanism of the ex-scintillation creation is electron-hole (eh) energy transfer process working at the region of RT. This proposal is based on the existence of temperature-dependent slow decay component of ex-scintillations (Fig.2a,2). This mechanism can be considered to be caused by thermally-induced exciton dissociation resulting in an electron-hole pair creation.

A possible mechanism of this process can be regarded as a hole component trap by the Tl^{+} forming the $V_{KA}Tl^{+}$ center [3]. The electron passes to the conduction band from which it can be captured at an electron trap (Fig.3,3), and solely after its thermal release the electron can recombine with the $V_{KA}Tl^{+}$ center, resulting in the $V_{KA}Tl^{\circ}$ luminescence center creation (Fig.3, 2→3→5).

Gamma-scintillations. The electron-hole mechanism of the scintillation formation can be proposed basing on the analysis of thermoevolution of the luminescence decay components of gamma-scintillations (Fig.2a, empty circles). At least two types of the electron traps could be involved in this process, responsible for two slow components of gamma-scintillations, with one being from ex-scintillations. (Fig.3, 9→10, 10→8→7, 10→3→7, 9→4).

In summary it can be considered that in CsI-Tl the ex- and the gamma- scintillations are formed by the electron-hole recombination processes at RT. The fast hole capture near the Tl^{+} ions occurs [3] responsible for the high scintillation yield. The electron processes determine the slow decay time of scintillations in dopped CsI scintillators

References

1. C.W.E. van Eijk. Physical Processes in Fast Scintillators.St.Petersburg, Russia (Ed. by P.Rodnyi and C.W.E. van Eijk) 1994, p.1.
2. J.D.Valentine, W.W.Moses, S.E.Derenzo, D.K.Wehe and G.F.Knoll. Nucl.Instr.Meth. Phys.Res.A, 1993, **325**, 147.
3. J.M.Spaeth, W.Meise and K.S.Song. J.Phys.,Cond Matter., 1994, **6**, 3999.
4. V.Nagirnyi, S.Zazubovich, V.Zapelin, M.Nikl and G.P.Pazzini.Chem.Phys.Letters,1994 **227**, 533.
5. P.Schotanus,R.Kamermans and P.Dorenbos. IEEE Trans.Nucl.Sci., 1990, **37**, 177.

THE EFFECT OF Tl^+ DOPING ON LIGHT OUTPUT AND UNIFORMITY OF CsI(T1) CRYSTALS

Y.N. ZHENG , S.X. REN , F.Y. ZHANG
Beijing Glass Research Institute , Beijing 100062, CHINA

ABSTRACT

300mm long CsI(T1) crystals were grown by the Bridgman method. The relationship between T1+ doping level and light output of the ingots was investigated. A T1+ concentration of 400ppm was found to be most favorable. A further investigation analyzed the $T1^+$ distribution along the growth axis and the major factors which affect the uniformity. Large CsI(T1) crystals grown by the Bridgman method exhibit poorer uniformity as a result of uneven T1 distribution.

I. INTRODUCTION

CsI(Tl) crystal has high density and high light output (L.O.). It is muchless hygroscopic than NaI(Tl) and can be processed easily. These advantages have caused CsI(Tl) crystals to be used by more and more scientists.

We used the Bridgman method to produce CsI(Tl) crystals. Raw material purity, temperature gradient, crucible material, growing environment, growth rate and TlI doping rate have been investigated. In order to get large size blanks with both perfect structure and satisfactory scintillation properties, we studied the effect of TlI doping rate on L.O.. As a kind of impurity Tl+ diffuses along the growth axis when using Bridgman method. This factor influences the uniformity of CsI(Tl) crystals.

II. EXPERIMENTS

1. Crystal gowth

A series of ϕ 30 × 30 (mm3) CsI(T1) crystals with different T1I doping levels (20,50,100,200, ··· 1000ppm) were grown using the Brigman method in sealed vacuum

Proc. Int. Conf. on Inorganic Scintillators and Their Applications, SCINT95,
1996, Delft University Press, The Netherlands

quartz crucibles. The ingots were cut and polished to ϕ 1" × 1" samples. Large size CsI(Tl) crystals,65 × 65 × 300 × 75 × 75 (mm3) were successfully grown in vacuum furnances. The purity of CsI and TlI is 99.999% and 99.99% respectively.

2. Optical and Scintillation properties measurement

A Hitachi U-3210 spectrophotometer was used to measure the transmittance of crystals. Its wavelength accuracy is ± 0.3 nm and the photometric accuracy is ± 0.1%.

Light output and uniformity were tested at IHEP. The measurement has been done with an identical setup. Horiba ϕ 25.4 × 25.4 (mm3) CsI(Tl) crystal is the standard sample. measurement condition is as follows:

HV: 1KV PMT: R1847S

Shaping time: 1.6 μ s Air gap

In order to determine the uniformity, we measured the L.O. of 9 points along the crystal length.

3. Chemical and Spectrum Analysis

Atomic Absorption Method with accuracy of 30ppm and Himamazu Fluorescent Spectrophotometer were used to analyze the TlI concentration and relative scintillation intensity in crystals.

III. RESULT

The transmittance of small and large size CsI(Tl) crystals show that the absorption band edge moves from 305nm to 320nm when TlI doping rate reaches to 1000 ppm.

Fig.1 gives the relationship between TlI doping rate and L.O. . The Himamazu

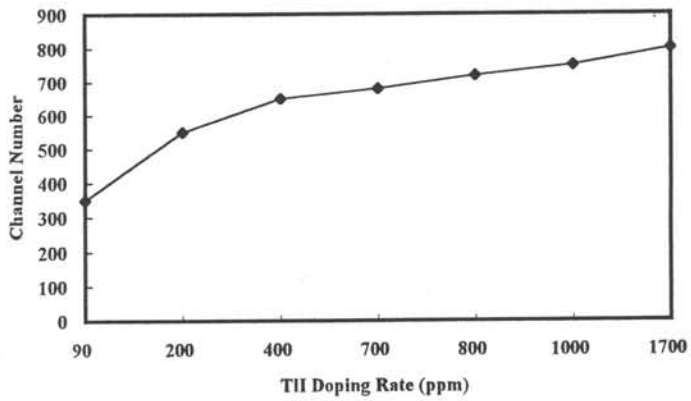

Fig.1. The relationship between TlI doping rate and light output. All samples size in ϕ 25.4 × 25.4 (mm3). The channal number of standard sample is 590.

Fluorescent Spetrophotometer was used to measure em- spectra of four ϕ 25.4 × 25.4 (mm3) samples. All these samples were excited at 302nm and the emission peak at about 524nm. The measurement accuracy is ± 3%. Table 1. lists their relative intensities.

Table 1. The Emission Pulse Height of Different TlI Doping Crystals. All Samples size in ϕ 25.4 × 25.4 (mm3).

Sample	1	2	3	4
TlI Doping Rate (ppm)	90	200	1000	1800
Relative Intensity (%)	38	44	57	59

The result of the small samples shows that at levels less than 500 ppm, the higher the TlI concentration the larger the light output and the higher the emission intensity. At doping levels between 500-2000 ppm, the pulse height has no significant increase. However, it is difficult to grow a complete large sized ingot above 800ppm. Bubbles and voids commonly appear at those levels.

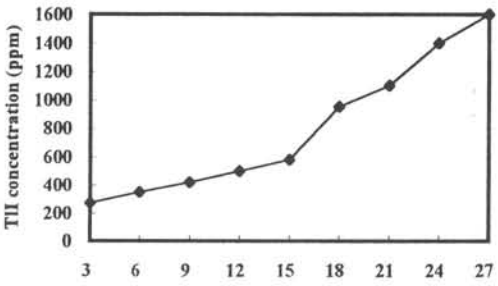

Fig.2. TlI distrabution of the CsI(Tl) blank sized in 60 × 60 × 300 × 70 × 70 (mm3) along growth axis.

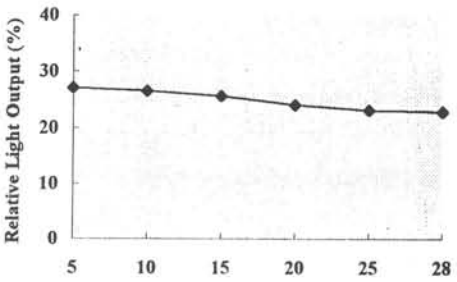

Fig.3. Light output of the 45 × 45 × 290 × 55 × 55 (mm3) CsI(Tl) crystal. The uniformity is 17% .

One full sized ingot was cut into 9 pieces equally spaced along the length with each sample being 2mm thick. The TlI concentration of the 9 samples was then measured using

atomic absorption spectroscopy. The analysis result in Fig.2 shows that the Tl+ concentration increases from bottom to top.

Uniformity of large size crystals was messured over 9 equally spaced points along the crystals. Figs.3 and 4 are the result. We found that polishing and wrapping actually affected the uniformity.

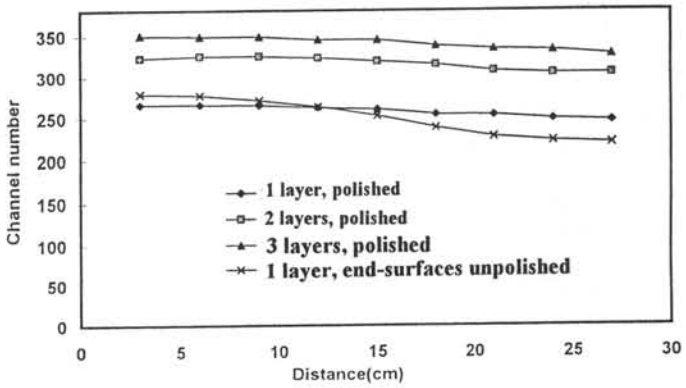

Fig.4. Light output and uniformity of 55 × 55 × 280 × 62 × 62 (mm3) CsI(Tl) crystal.

IV. DISCUSSION

The condensation factor of TlI in CsI is 0.1. Using Bridgman method to produce CsI(Tl) crystals, uneven TlI distrabution is unavoidable. In the ideal situation, it follows this formula:

$$C = k\, C_0 (1 - l/l_0)\, e^{kln(1-l/l_0)} \qquad (1)$$

C : TlI concentration in blank C_0 : TlI doping rate k = 0.1

l : Distance from bottom l_0 : Total length of blank

However, when we use the top (with larger cross section) of the crystal to match with PMT the higher TlI concentration compensated for the lower light collection efficiency. As the result, the uniformity improved.

Till now, the best uniformity of our products is 7%. In comparison, Czokraski grown CsI(T1) crystals which have an even Tl distribution exhibit a uniformity of less than 4%, much better than.Bridgman crystals.

V. REFERANCE

[1] H. -E. Kim , A.J. Moorhead , J. Am. Ceram. Soc. , 73 [3] 496-501 (1990) .

[2] Grassmann H. et al. , Nucl. Instrum. Methods , 223,323, (1985) .

[3] D. Cuinet ,et al. , Nucl. Instrum. Methods , A287, 614 (1989).

Localized excitons in activator absorption of alkali halide scintillators

A.N.Panova, B.V.Grinyov
Institute for Single Crystals, Acad. Sci. of Ukraine,
Lenin Av. 60, Kharkov, 310001

Summary

Empirical expressions have been proposed to evaluate changes in the energy state of halide excitons in alkali halides with admixtures of un-off heavy single-valent cations and in the energies of APES absorption maxima. On the basis of the closeness between calculated APES energy values and energies of activator absorption bands maxima for thallium-doped sodium, potassium, and cesium iodides showing the predominant long-wave luminescence at the excitation both in the bands mentioned and by ionizing radiation, the NaI-Tl, KI-Tl, and CsI-Tl scintillatiors can be classified as systems with indirect luminescence activation type.

The nature of short-wave (SL) and long-wave (LL) luminescence bands of NaI-Tl (3.7 and 3 eV), KI-Tl (3.7 and 3 eV) and CsI-Tl (3.33; 3.09 and 2.55; 2.25 eV) scintillation crystals is discussed over many years. A common feature of these crystals is an intensity redistribution of the luminescence bands mentioned and changes of their kinetic parameters at the excitation in the absorption A-band under temperature action or volume compression [1,2]. Starting from Seitz's emission centers model, those properties have been explained by a change in the energetic structure of the Tl^+ ion triplet state. While, it has been supposed [3] that the LL in KI-Tl is associated with the emission of self-trapped excitons perturbed by Tl^+ ion (APES). The energy transfer to APES occurs as a result of the activator excitation delocalization. The hypothese [3] about the association between LL and APES was confirmed recently by experiments on CsI-Tl [4]. In that work, LL bands are shown to be associated with transitions from the APES triplet state, while SL ones, with transitions from the Tl^+ ion triplet relaxed state. The states from which the emission originates are thermally associated and have a common minimum on the adiabatic potential surface.

Similarity in the spectral and kinetic characteristics change for NaI-Tl, KI-Tl, and CsI-Tl crystals allows to suggest that the nature of SL and LL in all these cases is the same. However, this assumption is insufficient to understand the APES excitation mechanism. It is of principal importance to elucidate if APES are manifested in the absorption of A-band associated with the triplet state of Tl^+ ion.

According to present wievs, the APES in alkali halides doped with s^2 ions manifest themselves as the absorption D-bands in the short-wave spectral range between C-band and first band of fundamental absorption. A semi-empiric D-state calculation for KCl-Tl (in the model of charge transfer accounting for three electron transition in a free Tl^+ ion) foretells the presence of three absorption D-bands for all alkali halide crystals containing s^2-ions [5]. Yet, according to [6], the LL (2.4 eV) not associated with transitions in Tl^+ ion in CsBr-Tl crystal is excited in four activator bands positioned in a short-wave spectral region as related to A-band. On that basis, the assumption has been made that D-bands are mixed with activator C and B ones and repeat the absorption spectrum of matrix exciton undergoing splittering and changes. These results show that, in contrast to [5], D-state may be considered in the frame of perturbed exciton model. By analogy with CsBr-Tl, the four short-wave activator absorption bands in CsI-Tl are

Proc. Int. Conf. on Inorganic Scintillators and Their Applications, SCINT95,
1996, Delft University Press, The Netherlands

related to D-bands, too. The causes of the LL excitation in B and C bands are not explained in [6].

The excitation of predominant LL in A, B, C, and D absorption bands of NaI-Tl, KI-Tl, and CsI-Tl suggests that either A, B, and C bands are mixed with D ones, or all activator bands are D-bands. These assumptions are supported at least by following facts: (1) at the excitation in A-band, the crystals store the light sum under formation of electron and hole colour centers [7-9], including V_k ones [9]; (2) the position of the anomalously intensive B-band (4.5 eV) in CsI-Tl does not fit into the scheme of genetic association with electron transitions in Tl^+ ion [10,11]. To interprete the activator absorption bands, a quantum-mechanical calculation of D-bands positions in the perturbed exciton model would be useful. But the micro-scale calculations of that type for a crystal with heavy ions are rather difficult and errors attain approximately ~1 eV what depreciates the calculated results.

Therefore, to interprete the absorption bands in Tl-activated crystals, we tried to estimate the energies of D-bands maxima using a empiric expressions instead of quantum-mechanical calculation. The estimation was performed under following assumptions:

- energy structure of D-bands repeats that of the matrix exciton absorption;
- the energy gap (ΔE) between each of the D-bands and the matrix exciton absorption band associated therewith is the same.

Under these assumptions

$$E^D = E^e - \Delta E \qquad (1)$$

where E^D, E^e are energies of D-band and exciton absorption band, respectively.

To calculate E^D reflecting the energy state change of an anionic exciton near a dopant ion, the following expression was used:

$$\Delta E = \Delta Q + \beta \Delta I \qquad (2)$$

where ΔI is the ionization potentials difference between metallic matrix component and activator dopant; ΔQ is difference between heat of formation of the matrix crystal and that of dopant salt with the same anion; β is a coefficient. To estimate ΔE for crystals containing the admixture of a heavy single-valent un-off cation,

$$\beta = 0.5\, R_i / R_h \qquad (3)$$

was used where R_h, R_i, are distances between metal and halide ions in vapor phase for matrix and dopant salt, respectively.

Using expressions (1) to (3), we had estimated ΔE for NaI-Tl, KI-Tl, and CsI-Tl, as well as for CsBr-Tl crystal having known D-bands positions [6].

The Q, I, R_h, and R_i values used to calculate ΔE are given in Table 1. In this table, ΔE values are also presented calculated according to expressions (2) and (3) for thallium doped cesium bromide, sodium, potassium, and cesium iodides.

The E^e values for above-mentioned crystal matrixes taken from publications [12-14] and calculated E^D values, as well as experimental energy values for the activator absorption bands maxima E_m are presented in Table 2. It is seen from this data that, for CsBr-Tl crystal, such a feature is characteristic: the calculated E^D values are coincident with E_m values only for that activator bands in which the LL is excited [6]. These bands are associated with the exciton absorption of matrix $4p^5 5s$, $4p^5 4d$ configurations. This confirms the assumption [6] about an association between LL and APES as well as the correctness of our approach to E^D estimation.

For thallium doped alkali iodides, the calculated E^D values are very close to E_m for all the activator absorption bands. Therewith, absorption A-bands of these crystals are associated with the low-energy component of $5p^5 6s$ doublet of the matrix exciton absorption.

Table 1.
Q, I, R_h and R_i parameters for thallium iodides, cesium and thallium bromides; in lower part, the calculated ΔE values for NaI-Tl, KI-Tl, and CsI-Tl crystals are given.

Crystals	NaI	KI	CsI	CsBr	TlI	TlBr
Q,eV	3.01	3.42	3.64	3.80	1.28	1.78
I,eV	5.14	4.32	3.89	3.89	6.10	6.10
R_h,Å	2.90	3.23	3.41	3.14	-	-
R_i,Å	-	-	-	-	2.87	2.68
ΔE,eV	1.26	1.37	1.44	1.09	-	-
Crystals	NaI-Tl	KI-TL	CsI-Tl	CsBr-Tl	-	-

The broad and intensive B-band (4.49 eV) of CsI-Tl crystal is associated with the $5p^5 5d$ doublet. It is just that fact which very probably is the cause of the B-band anomalous intensity in the absorption spectrum. Two weak bands at 4.82 and 5.02 eV are associated with weak Rydberg bands in the band-band transitions region. Interpretation of other bands is hindered by a significant overlapping of components corresponding to $5p^5 5d$ and $5p^5 6s$ configurations in the high-energy CsI exiton absorption band.

Table 2.
E^e , E^D and E_m values at 80 K for pure and thallium doped alkali metal iodides and cesium bromide.

Crystal	Determ by	E^e, E^D, E_m, eV								
			$4p^5 5s$	$4p^5 4d$		$4p^5 5s$,		$4p^5 4d$		
CsBr	exper		6.8	7.10; 7.18		7.39		7.67		
CsBr-Tl	calc		5.71	6.10; 6.09		6.30		6.58		
CsBr-Tl	exper	4.71(A)	5.75(D)	5.92(D)		6.30(D)		6.50(D)		
		$5p^5 6s$	$5p^5 5d$		Ridb.			$5p^5 5d$		$5p^5 6s$
CsI	exper	5.76	5.93 5.98		6.27	6.45		6.68	6.78	6.88
CsI-Tl	calc	4.32	4.49; 5.54		4.83	5.01		5.24	5.34	5.44
CsI-Tl	exper	4.26(A)	4.49(B)		4.82(D)	5.02(D)		5.21(D)	5.34(D)	5.43
		$5p^5 6s$	Ridb.	$5p^5 5d$				$5p^5 6s$		
KI	exper	5.8	6.42	6.68; 6.87				7.23		
KI-Tl	calc	4.43	5.05	5.31; 5.50				5.86		
KI-Tl	exper	4.40(A)	5.08(B)	5.32(C)	5.50(D)			-		
		$5p^5 6s$	($5p^5 5d$)			$5p^5 6s$				
NaI	exper	5.54	6.30	6.46		6.73				
NaI-Tl	calc	4.28	5.04	5.20		5.47				
NaI-Tl	exper	4.26(A)	4.96(B) ;5.21(C)			5.41(D)				

The weak B-band of KI-Tl is associated with the Rydberg one in the band-band region, C and D ones with $5p^5 5d$ doublet. Besides, the calculated $E^D = 5.86$ eV evidences the presence of one more D-band in KI overlapped with first exciton band (5.8 eV) of the fundamental absorption.

B and C absorption bands of NaI-Tl are associated with poorly resoluted maxima (perhaps those of $5p^5 5d$ doublet) on the long-wave tail of the high-energy component of $5p^5 6s$ configuration. The D-band is related with that component.
If our estimations of E^D are correct, then it follows from data of Table 2 that the main absorption centers in NaI-Tl, KI-Tl, and CsI-Tl scintillation crystals are iodine ions perturbed by Tl^+ ones. That allows to classify those crystals as systems with the indirect luminescence activation type.
To precise the nature of SL in scintillators considered, additional special studies are necessary. Yet, the thermal linkage between states responsive for the SL and LL of NaI-Tl and KI-Tl crystals, as well as the closeness of spectral and kinetic parameters of SL (≈ 3.7 eV; ≈ 10 ns) and self-trapped exciton emission in matrixes, (≈ 4 eV; ≈ 10 ns) suggest that the SL of activated crystals is associated also with APES. Energy structure of excited states of these APES seems to differ only slightly from that of matrix self-trapped excitons.

Conclusion

It can be concluded from the results obtained that the activator A, B, C, D absorption bands in the thallium-doped alkali iodides scintillation crystals are associated with the APES absorption. Under the ionising action, the hole capture on iodine ions perturbed by Tl^+ ion results in the V_{kA} centers formation. The latter are the main recombination centers in the scintillation process.

References:

[1] L. Nagli, Izv. AN Latv. SSR, ser. phys. i techn. nauk, N2, p. 50-56 (1966)

[2] A.N. Niylisk, I.K. Plyavin, Radiazionnaya Physika, N5, Riga, Zinatne, p. 147-177 (1967)

[3] J.M. Donahue, K. Teegarden, J. Phys. Chem. Solids, v.29, N12, p. 2141-2151 (1968)

[4] V. Nagirnyi, A. Stolovich, S. Zazubovich et al, Int. Symp. LUMDETR '94, Sept. 25-29, 1994, Tallinn, Estonia, p. 75

[5] T.Tsuboi, Sh.Sakoda, Phys. Rev.,v.22, N10, p.4972-4979 (1980)

[6] E.A. Vasilchenko, Thesis, Tartu (1974)

[7] V.N. Vishnevsky, N.S. Pidzyrailo, Izv. vuzov, Phisika, N7, p. 158-160 (1972)

[8] T.V. Lyakhotski, O.B. Kushnir, Ukrain, Phys. J., v.16, N7, p. 1209-1211 (1971)

[9] I.S. Bobkova, N.I. Ivanova, Opt. and Spectr., v.62, N1, p.91-93 (1987)

[10] R. Knox, Phys. Rev., v.115, p. 1095-1105 (1959)

[11] N.E. Lushchik, E.A. Vasilchenko, Trudy IPhA AN ESSR, N35, p. 150-157(1969)

[12] I.E. Eby, K.I. Teegarden, D.B. Dutten, Phys. Rev., v.116, N5, p. 1099-1105 (1959)

[13] K.I. Teegarden, G. Baldini, Phys. Rev., v.155, N3. p.896-907 (1966)

[14] T. Miyota, J. Phys. Soc. Japan, v.31, N2, p. 529-551 (1971)

ELECTRONIC AND IONIC PROCESSES IN CsI:Na^+, CsI:Tl^+ AND BaF_2 CRYSTALS

V.Zīraps
Institute of Solid State Physics, University of Latvia, 8 Kengaraga Str., LV-1063 Riga, Latvia

Abstract Electron and ion charge transport, localization, thermoactivated delocalization and interaction processes in the X-ray irradiated CsI, CsI:Na^+, CsI:Tl^+ and BaF_2 crystals above 90 K have been investigated by means of a complex of the electrical (conductivity, depolarization) and optical (luminescence, absorption) thermoactivation spectroscopy techniques. It is shown that the non-equilibrium conductivity at 90-300 K is with a predominant monopolar (electron) nature. In CsI:Na^+ the X-ray induced absorption band at 720 nm is composed and thermally bleaches (90-290 K) in about ten substages with the electron release and luminescence peaks. In BaF_2 the anion defect (vacancies, interstitials) thermal delocalization spectra at 300-700 K are with a quasi-continuous distribution nature: a very broad and overlapping ionic thermostimulated depolarization current peaks at 405 K, 450 K, 505 K, 540 k, 585 K and 630 K have been detected. The role of the thermoactivated ion diffusion-limited processes in the irradiated halide crystals above 300 K are very important in many relaxation phenomena.

Introduction. The scintillation properties of the CsI-based scintillator crystals strongly depends on the structural and impurity defect states and the interactions of electrons and holes with them. The parameters of the luminescence pulses depends on the activator ions (Na^+, Tl^+) and impurity ions distribution in CsI and on the preliminary thermal or deformation treatments [1]. In CsI:Na^+ the nature of the V_k-center and Na^0-centers and the role of the tunneling recombination luminescence (at 420 nm) of the pairs $\{Na^0...V_k\}$ have been established [2]. In this paper the thermally stimulated relaxation (TSR) processes in the X-ray irradiated (at 90 K or 290 K) crystals of CsI, CsI:Na^+, CsI:Tl^+ and BaF_2 have been investigated above 90 K or above 290 K by means of a complex of the *electrical* (ionic conductivity; thermally stimulated: current - TSC, depolarization current - TSDC, photostimulated current - PSC and X-ray excited current - XREC) and *optical* (luminescence - TSL, PSL, XREL; X-ray induced absorption) techniques.

Results and discussion. The TSR curves of CsI:Na^+ after X-ray irradiation at 90 K are shown in Fig.1 and Fig.2 (heating rate - 0.15 K/s). All the TSL (emission at 420 nm) peaks (Fig.1, curve 4) in the range 90-210 K are accompanied by the correlated charge transfer (TSC) peaks (curve 2) with the $T_m \approx$ 90 K, 103 K, 113 K, 122 K, 140K, 150 K, 170 K, 195 K, 220 K and 262 K and the thermal bleaching steps of the so-called *"Na^0-band"* (curve 3). Special experiments of the photostimulated TSC (after optical redistribution of electrons from the deep traps to the shallow ones) (curve 1) evidence that all the main peaks of the X-ray excited TSC and TSL (curves 2, 4) are with a predominant *electron* nature. It seems likely that these electrons are thermally delocalized from several kinds of traps associated with the sodium activator different localization sites and forms: about ten bleaching substages are resolved (curve 3) which all together forms a composed "Na^0-band".

These results evidence that in CsI:Na^+ the TSL at 420 nm arises via quasi-free *electron* recombination with the localized holes (V_{kA}-centers). The *efficiency of TSL* is characterized by the relation TSL/TSC (curve 5): during the TSR from 130 K to 250 K it decreases by more

Proc. Int. Conf. on Inorganic Scintillators and Their Applications, SCINT95,
1996, Delft University Press, The Netherlands

than three orders because of the hole deficiency on the activator centers and luminescence quenching. Similiar features of the TSR processes are observed in CsI:Tl⁺.

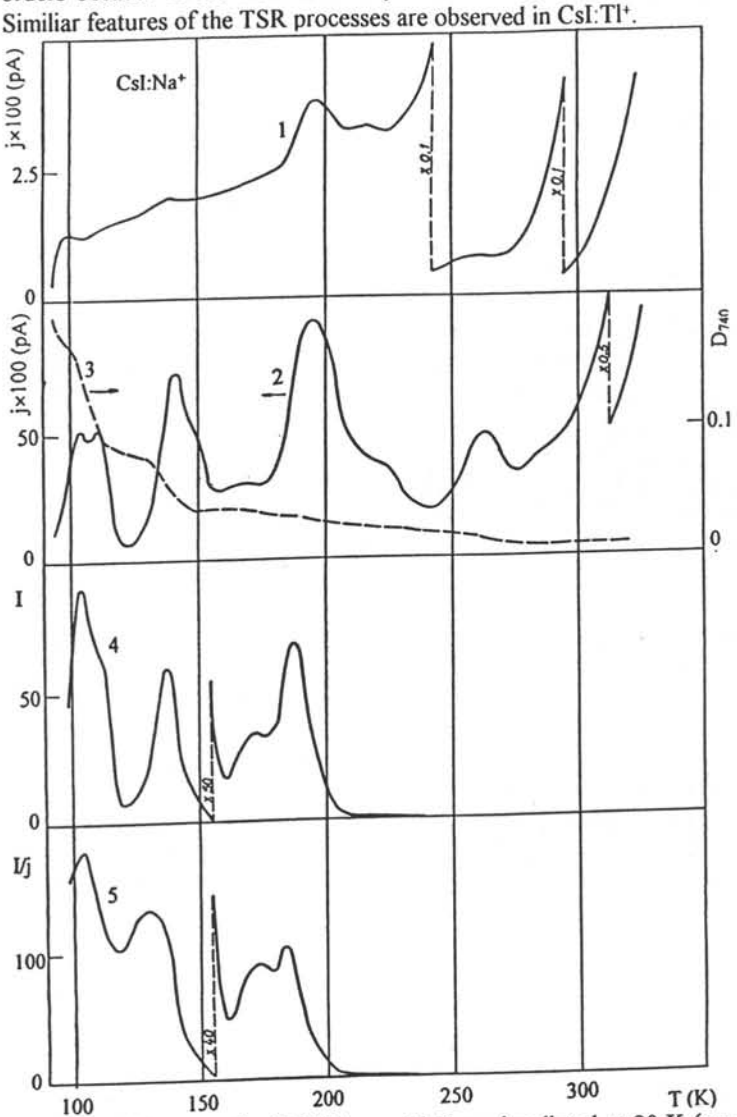

Fig. 1. The TSR curves for CsI:Na⁺ crystal X-ray irradiated at 90 K (curves 2-5) or X-ray irradiated at 290 K, cooled to 90 K and photostimulated at 90 K in the region of induced absorption bands of the localized electrons (curve 1): TSC (1); the simultaneously measured curves of TSC (2), TSL (4), thermal bleaching of the band at 740 nm (3) and efficiency of TSL (5).

During the TSR *holes* are freed from their traps and redistributed to the activator centers (Na^+ in CsI:Na^+ or Tl^+ in CsI:Tl^+) thus leading to several increase steps of the efficiency of luminescence (not only for TSL but also for PSL and XREL) at about 90 K, 120-140 K, 160 K and 180 K (see curve 5 on Fig.1).

The quasi-stationary X-ray excited (pulses - duration about 20 s) current (XEC) temperature dependences (Fig.2, curves 1, 2) and TSC (3) for CsI:Na^+ below 290 K have been measured (Fig.2). At the TSC (and TSL) peak temperatures the inertial component and the

pulse height of the XEC $\Delta j_x(T)$ strongly changes because of the correlated changes of the effective lifetime $\tau_n(T)$ of conduction electrons: $\Delta j_x(T) \sim \tau_n(T)$. These changes are determined by the sharp changes of the electron capture lifetime near T_m values when the quasi-level of Fermi passes the corresponding local energy level for the electron capture.

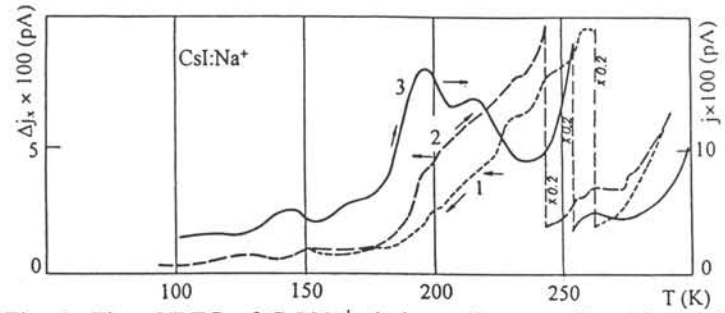

Fig. 2. The XREC of CsI:Na^+ during a linear cooling (1) and linear heating (0.15 K/s) (2) simultaneously with the TSC (3).

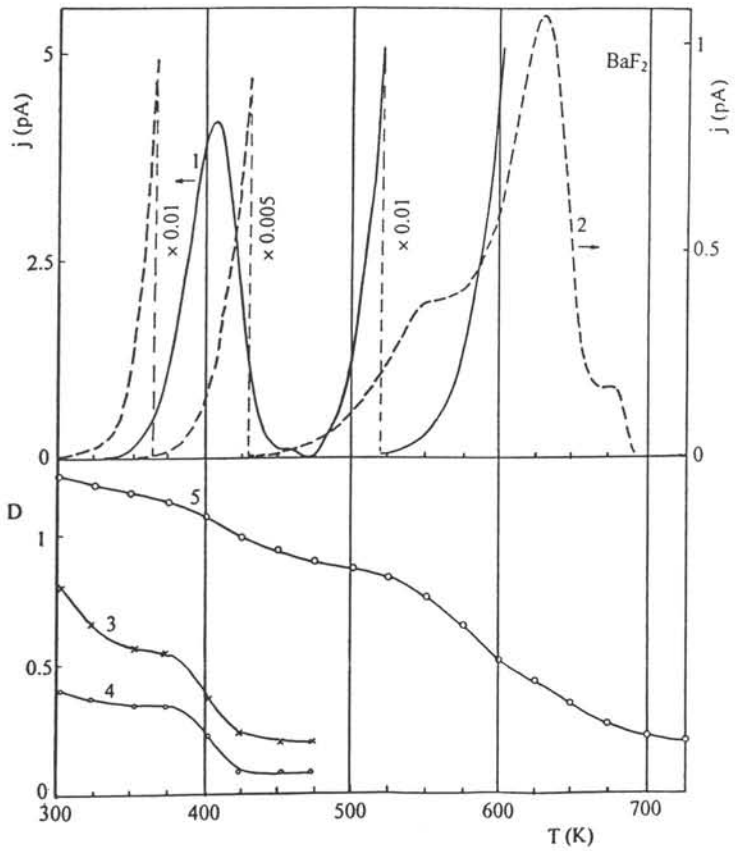

Fig. 3. The TSDC of BaF_2 thermally polarized under the field of -2 kV/cm at T_p<350 K (1) and T_p<500 K (2). The thermal bleaching curves of: F-band (3) and M-band (4) for γ-ray irradiated BaF_2 [3]; the X-ray induced band at 377 nm (5) for BaF_2:Cd [4].

A complex of the TSDC and ionic conductivity techniques is used to study, for the first time, the ionic space-charge (thermoelectret state) formation and decay - *ionic TSR processes in BaF_2* crystals in the temperature region (300-700 K) of the exponential rise of the ionic (anion vacancy and anion interstitial) conductivity. Some of these data (the anionic TSDC curves - 1 and 2) are shown in Fig.3 together with some thermal bleaching curves (taken from [3] and [4]) of the F-band (at 611 nm), M-band (720 nm) [3] and "Cd-band" (at 377 nm) [4]. A very broad and overlapping anionic TSDC peaks at $T_m \approx$ 405 K, 450 K, 505K, 540 K, 585 K and 630 K are resolved in the anion defect thermoactivated delocalization spectra if we use a set of the polarization temperatures below T_p = 350 K, 400 K, 450 K and 500 K. The first TSDC peak strongly correlates with the bulk anionic conductivity with a single activation energy of about 0.97 eV (delocalization of the F_i^-). It evidences that even in the nominally pure (optical) BaF_2 crystals there exist a very wide *energy spectrum for the anion defect localization-delocalization* which has rather *quasi-continuous distribution* nature.

As it is seen from Fig.3 in the same temperature region near T_m values of the anionic TSDC peaks the main thermal bleaching steps (stages) for the F-band (curve 3), M-band (4) and "Cd-band" (5) are observed. We believe that in the region of the high anionic conductivity above 300 K the *ionic thermoactivated relaxation processes* cause a very high *ionic disordering* of the BaF_2 lattice and thus initiate a new important class of the *"ion diffusion-limited thermoactivated relaxation processes"*. As a result of such two-step *ionic-ionic* or *ionic-electronic interactions* during the TSR of the irradiated crystal the thermal bleaching stages of the colour centers and localized electrons take place.

The main **conclusions** of these investigations are:

1. The *non-equilibrium electrical conductivity* (TSC, PSC and XREC) in the X-ray excited halide crystals (CsI, CsI:Na^+, CsI:Tl^+; BaF_2) at 90-300 K is with a predominant *monopolar (electron)* nature. All the TSC peaks are accompanied by a related activator TSL peaks and thermal bleaching stages of the induced absorption bands. The electron radiative recombination with the localized holes takes place.

2. In CsI:Na^+ crystal the X-ray induced (at 90 K) absorption *band at 720 nm* (traditionally related to Na^0-centers) is *composed* and thermally anneals in about ten substages resulted in the *electron release TSC* peaks at 90 K, 103 K, 113 K, 122 K, 140 K, 150 K, 170 K, 195 K, 220 K and 262 K. A *more complex sodium* and other electron traps formed by X-rays are important in such an activated system where a small sodium ion must replace a large cation.

3. The *electron recombination luminescence efficiencies* (TSL/TSC, PSL/PSC and XREL/XREC) for CsI:Na^+ and CsI:Tl^+ during the TSR from 90 K to 290 K decrease by more than three orders because of the hole deficiency rise on the activator centers. At the same time during the TSR *holes* are freed from their traps and redistributed to the activator centers: the efficiency increases at about 90 K, 120-140 K, 160 K and 180 K.

4. In BaF_2 crystal a very broad and overlapping *anionic TSDC peaks* at 405 K, 450 K, 505 K, 540 K, 585 K and 630 K have been detected in the anion vacancy and anion interstitial thermal delocalization spectra. In the irradiated halide crystals the *thermoactivated anion diffusion-limited processes* above 300 K are very important in many TSR phenomena.

References

[1] N.V.Shiran, T.A.Charkina, V.I.Goriletsky et al., Internat. Symposium Luminescent Detectors and Transformers of Ionizing Radiation, Proceedings, Riga, 1991, rep. B4.

[2] K.Imanaka, A.-H.Kayal, A.C.Mezger, and J.Rossel, phys. stat. sol. (b) **108**, 449 (1981).

[3] B.Narasimha, K.V.Rao, and R.N.P.Chaudhuri, phys. stat. sol.(a) **108**, K97 (1988).

[4] The data of Dr. P.Kulis (measured in Institute of Solid State Physics, University of Latvia) kindly given us to include in this figure.

PHOTO- AND THERMO-STIMULATED PROCESSES IN CsI-Tl SCINTILLATORS.

S.A.Chernov, A.I.Popov and L.E.Trinkler
Institute of Solid State Physics,University of Latvia
8 Kengaraga str., LV-1063, Riga, Latvia

CsI-Tl is a well known scintillator. The spectrum of its scintillations as well as that of photo- and X-luminescence are presented with two luminescence bands, peaking at 550 and 400 nm. Recent publications [1,2] have proposed a new convincing model, explaining the 550 nm band as the luminescence of the self-trapped exciton (STE), located near Tl^+ ion, contrary to early works, ascribing this band to thallium luminescence.

Such approach makes to review the concept of scintillation mechanism in CsI-Tl crystal. The scintillation mechanism in doped alkali halide crystals is determined by two processes:

1. Hole recombination luminescence (HRL)

$$e + p + Tl^+ \rightarrow V_k + Tl^0 \rightarrow STE + Tl^+ \rightarrow (Tl^+)^* \rightarrow Tl^+ + h\nu$$

2. Electron recombination luminescence (ERL)

$$e + p + 2Tl^+ \rightarrow V_k + Tl^0 + Tl^+ \rightarrow Tl^0 + Tl^{++} \rightarrow Tl^+ + (Tl^+)^* \rightarrow Tl^+ + Tl^+ + h\nu$$

In order to evaluate the contribution of these processes in CsI-Tl scintillations an attempt was done to elucidate the origine of 400 nm luminescence band rising under ionizing radiation. Spectra of photo- and thermo-stimulated luminescence (PSL and TSL) as well as kinetics of rise and decay of luminescence under electron pulses were measured.

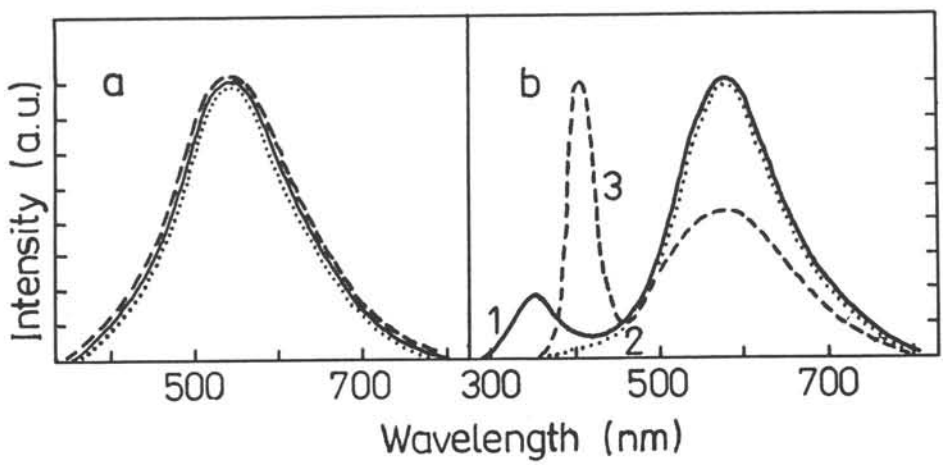

Figure 1. Photoluminescence of CsI-Tl excited by light with wavelength 200 nm (1), 225 nm (2) and 300 nm (3) at 300 K (a) and 80 K (b).

Fig.1. shows photoluminescence spectra under irradiation with light photons of different energies. At 80 K (Fig.1.b.) the band-to-band excitation (200 nm) causes the luminescence of STE in regular lattice (350 nm) and STE near Tl^+ ion (550 nm); excitation with a light from A absorption band (300 nm) rises the appearance of 550 and 405 nm bands

Proc. Int. Conf. on Inorganic Scintillators and Their Applications, SCINT95,
1996, Delft University Press, The Netherlands

of comparable intensity; and the D excitation (225 nm), creating an exciton near Tl^+ ion, is the reason of 550 nm luminescence band and a very weak band in the 400 nm area.

At 300 K (Fig.1.a.) the contribution of 400 nm band in the luminescence spectrum increases, compared with 80 K; luminescence spectra remains the same for all types of excitation. It enables to state that the 400 nm luminescence band arising under ionizing radiation is determined by the Tl^+ luminescence.

Results of kinetic measurements under electron pulses (with parameters: energy 270 keV, duration 10 ns, excitation density 10 MW/cm^2) at 300 K are shown at Fig.2.. Luminescence decay time for both bands is the same (700 ns). Comparing with the kinetics of the luminescence under A excitation [3], presenting the same components of the decay time for both bands at T>180 K, we get another reason for interpretation of the 400 nm band in cathodoluminescence as the emission of Tl^+ ion.

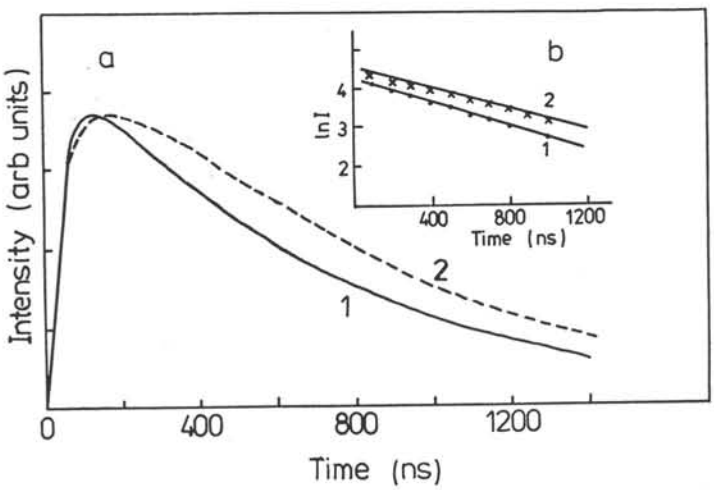

Figure 2. CsI-Tl luminescence rise and decay in 550 mn band (1) and 400 nm band (2) under electron pulse at 300 K (a); fitting of the luminescence decay in coordinates lnI versus t (b).

The process of Tl^+ excitation under ionizing irradiation can occur due to:

1. Electron recombination luminescence;

2. Thermoactivated energy transfer between two minima of the common potential surface (APES), connecting Tl^+ ion and STE near impurity. At high temperatures energy is transferred from STE near Tl^+ to Tl^+ ion,causing the excited state of thallium center $(Tl^+)^*$ [3].

In order to evaluate the contribution of these mechanisms the processes of photo- and thermo-stimulated luminescence were studied in 80-300 K temperature range. Preliminary irradiation was fulfilled with photons from D excitation band (225 nm). Light with λ>600 nm was used for PSL stimulation. Fig.3. shows the thermal evolution of 400 and 550 nm bands. The ratio of bands intensity for PSL and TSL processes rises drastically at T>180 K.. In the case of photoluminescence excited in D absorption band, that is to say when exciton is created near thallium impurity, the 400 nm band increases and the 550 nm band decreases in the same temperature region: T>180 K. This proves that the thermoactivated energy transfer between minima of APES connecting STE and Tl^+ centers is the main mechanism of 400 nm band excitation in the recombination processes.

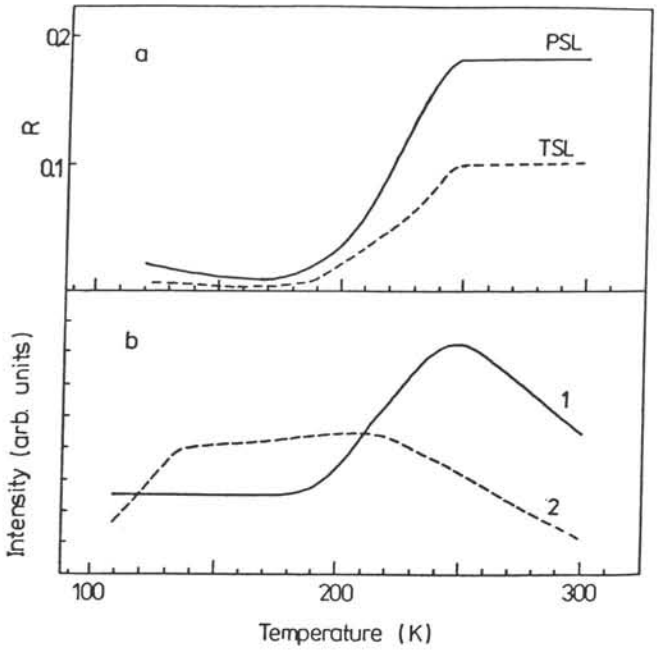

Figure 3. Thermal evolution of (a)-R ratio of 400 and 550 nm bands intensities in PSL and TSL; (b) - intensities of 400 and 550 nm bands in photoluminescence of CsI-Tl under excitation λ_{ex}=225 nm.

The negligible contribution of ERL into the excitation of Tl^+ luminescence reveals itself as a presence of a weak component in the luminescence rise of 400 nm band which is longer than HRL component similar for both bands and determined by V_k centers migration toward Tl^0 centers. The small ERL component can be ascribed to an electron release from some shallow trap and its recombination with V_{KA} or Tl^{++} center (if any).

Summing up the described above results, the following conclusions can be drawn:

1. 400 nm band in scintillation spectrum is due to Tl^+ ion luminescence.

2. Thermal evolution of thallium luminescence is determined by the thermoactivated energy transfer between minima of the APES, connecting STE near Tl^+ and $(Tl^+)^*$ states.

3. HRL is the main process contributing the scintillations in CsI-Tl, while the contribution of ERL is negligible.

REFERENCES

1. V.Nagirnyi, S.Zazubovich, V.Zapelin, M.Nikl and G.P.Pazzi // Chem. Phys. Letters, 1994, **V227**, 533.

2. J.M.Spaeth, W.Meise and K.S.Song // J.Phys, C.Cond. Matter, 1994, **V6**, 3999.

3. M.Nikl, J.Hlinka, E.Mihokova, K.Polak, P.Fabeni and G.P.Pazzi // Phil.Mahazine B, 1993, **V67**, N5, 627.

PRODUCTION OF CsJ(Na) MONOCRYSTALS WITH LOW LEVEL OF THE AFTERGLOW

I.P.Antoniv, I.V.Garapyn, R.I.Didyk
Physics Dept., Lviv University, Dragomanov str., 50,
290005, Lviv, Ukraine

Progress in computer tomography development is immediately related to technology development and to improvement of X-ray detector parameters and characteristics. The afterglow time value is one of the most significant parameters of scintillated detectors for tomography because it defines the device resolving density and the object irradiation time. According to present-day requirements afterglow time value must not exceed 0,1%.But the afterglow of production-type crystals is 0,5...5,0% after 6 ms /1,2/.Purification of crystals from impurities would make it possible to manufacture scintillators, which have not afterglow /2/, what , in particular, is of some considerable for applying such scintillators for detectors, operating in count condition.

The production of CsJ(Na) monocrystals with low level of the afterglow was the aim of our work. We proposed the method of commercial raw materials purification from oxygen containing impurities. By analogy with our previous work /3/ it involes the treatment of the melt in the presence of carbon sorbent. Then the reaction products are filtered out. Melt treatment as well as filtration takes place under the vacuum pumping conditions. Addition of NaJ in raw materials was performed in conditions, under which the contact with atmosphere was excluded.The monocrystals were grown from purified salt. The crystals dimensions were: 30 mm diameter,250 grams mass.

Monocrystals CsJ+0,2 mol% NaJ, obtained by Stokbarger method with pulling rate of 4 mm/hour in evacuated quartz ampoules from different raw materials - from commercial raw material "осч" mark (I); with adding carbon sorbent into the mixture (II) and from salt, which was purified according to above described method (III). Low content of oxygen containing impurities in monocrystals III by comparison with monocrystals I and II was confirmed by IR-spectroscopy method. For afterglow study the specimens with 15,0x3,0x1,8 mm^3 dimensions were cut from boules. Irradiation was carried out by X-ray (100 kV voltage on the tube, 10^{-3}s width of a pulse, time separation no worth than 0,01%, interval between impulses $4x10^{-2}$ s). The afterglow intensity after 2 ms was equal to 0,02% from maximum signal value at the irradiation moment.

It follows from Fig.1, that light yield of crystals glowing is defined by fast component of afterglow. But the prolonged component with afterglow time of 10^{-3} s must be taken into account as well. The smallest contribution of prolonged component into the light yield is for the specimen of crystal III and for the specimen of crystal I its contribution is more substantial. It is known /4/, that crystal afterglow time delay may be caused by presence of high temperature thermoglow peaks. Existence of the trapping levels noticeably influences the light yield and afterglow time values. This influence is defined by trapping level depth, trapping probability and thermal ionization probability. The presence of thermoglow peaks in crystallophosphores in room temperature region directly points to worsening of such properties of crystals as light yield and increase of sluggishness glow portion. We applied the thermoglow method since the

Proc. Int. Conf. on Inorganic Scintillators and Their Applications, SCINT95,
1996, Delft University Press, The Netherlands

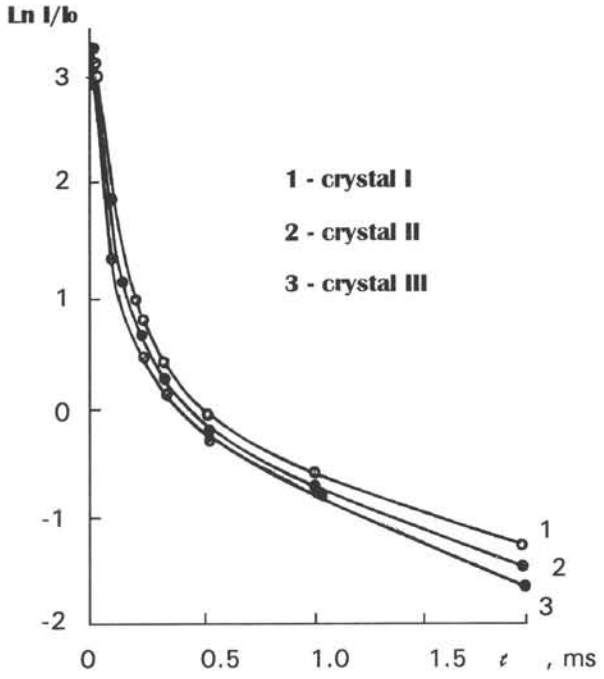

Fig. 1. CsJ(Na) monocrystals afterglow.

sluggishness component was observed in the crystals under study. The obtained results are presented on Fig. 2. It was found that two thermoglow hightemperature peaks at T_1=260 K, T_2=292 K are present in crystal I specimen by contrast to crystal III specimen. The activation thermal energies of those peaks are evaluated: E_1=0,43 eV, E_2=0,5 eV. So the delay of afterglow time in crystallophosphore I is caused by recombination processes on impurity centers what was confirmed by hightemperature TG peaks.

Foreign impurities have a significant effect on characteristics of luminophores. So, addition of copper, oxygen containing anions and iodine homologues causes the worsening of CsJ(Na) crystals resolving power and light yield decreasing /5/. The presence of CO_3^{2-} ions causes significant increase of screen prolonged afterglow /6/. Therefore the decrease of afterglow time in crystal III specimen in comparison with that in crystal I is caused by decrease of oxygen containing impurities amount. Really, the band with maximum 2148 sm^{-1} caused by CNO ions absorption is absent in IR-spectra of crystal I.

The afterglow time low values of investigated CsJ(Na) crystals and their negligible change due to used treatments (afterglow intensity after 2 ms was equal to 0,2 %) evidences about afterglow stability and this is a matter of interest for practical use.

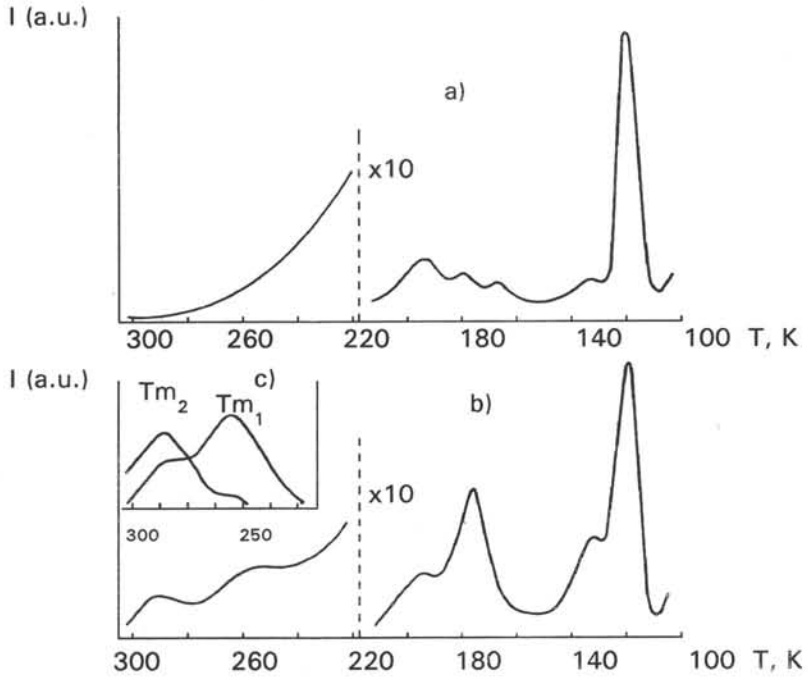

Fig. 2. Thermoglowing of CsJ(Na) monocrystals:a-crystal III; b - crystal I; c - high temperatures TG peaks, separated by fractional method (crystal I).

1. Kovaleva L.M., Kozlov S.N., Vinograd E.L. - Thesis of IX All-Union Conference "Sostojanije i perspectivy razrabotki i premenenija stsintilljatorov i scintilljatzionnych detektorov." - Kharkov, 1986, p.13.
2. Panova A.N. - Izvestija AN SSSR, ser.fiz., 1985, 49, №10, p. 1994-1998.
3. Antoniv I.P.,Garapyn I.V., Matvijchuk D.I. - Vysokochiostuje veshcestva, 1990, №3, p.175-177.
4. Zacharko Ja.M., Chepelev V.V.- Izvestija AN SSSR, ser,fiz., 1965, 29, №1, p.78-81.
5. Panova A.N., Shachova K.V.- J.prikladnoj spectroscopiji, 1974, 20,№4, p. 728-730.
6. Smolskaja L.P., Parfianovich I.A. - Thesis of IY-Union simposium "Luminestzentnyje prijomniki i preobrazovateli rentgenovskogo izlychenija", Irkytsk, 1982, p. 155.

LUMINESCENCE OF Pb^{2+} - DOPED CESIUM HALIDES AS POSSIBLE MATERIALS FOR SCINTILLATORS

R.Aceves[1], M.Barboza Flores[1], P.Fabeni[2], M.Gurioli[3], E.Mihokova[4], V.Nagirnyi[5], M.Nikl[4], G.P.Pazzi[2], R.Perez Salas[1], S.Zazubovich[1]*, and V.Zepelin[5]

[1]*CIF US, Universidad de Sonora, Hermosillo, Sonora, Mexico*

[2]*IROE of CNR, Florence, Italy*

[3]*LENS, Florence, Italy*

[4]*Institute of Physics, Prague, Czech Republic*

[5]*Institute of Physics, Tartu, Estonia*

Abstract. Spectral, kinetics and scintillation properties of Pb^{2+}-doped CsCl, CsBr and CsI crystals are reported. A strong interaction between excited states of Pb^{2+} ion and halogen states is justified for these systems. An aggregation of Pb^{2+} ions into $CsPbX_3$ (X=Cl, Br) microphase was found for CsX:Pb. The decay time of the excitonic emission of these microcrystals is of a ps order due to exciton superradiance effect. The mechanism of luminescence of such aggregated centres is discussed.

1. INTRODUCTION

On a complex investigation of an effective scintillation detector CsI:Tl it has been found that its main visible emission is caused by radiative decay of two configurations of an off-centre self-trapped exciton (STE) perturbed by Tl^+ ion [1,2]. A new model of luminescence centre in CsI:Tl has been suggested. According to this model, two pairs of minima of different nature coexists in the triplet RES. Two of them have the structure characteristic of a Tl^+ ion perturbed by the STE. Two others, which are responsible for the intensive visible emission, have the structure characteristic of the STE perturbed by Tl^+ ion. Similar features have also been found for CsCl:Tl and CsBr:Tl crystals.

It could be suggested that it is just the excitonic nature of the intensive visible emission of CsI:Tl that could explain its high scintillation efficiency. The scintillation process is assumed to be caused by recombination of V_K centres having migrated to Tl^0 and Tl^0 electrons, which leads to the creation of an exciton near Tl^+ ion and results in the visible excitonic-like emission of CsI:Tl. It is probable that the participation of impurity-perturbed exciton is of general importance for the scintillation process in doped crystals. For clarifying the role of impurity and halogen-ion mixed states in this process cesium halide crystals doped with lead seem to be of special interest, as a strong interaction of impurity and excitonic states could be expected for this system. These systems have been almost unstudied up to now. Only some contradictory data on the luminescence of CsCl:Pb, CsBr:Pb and CsI:Pb crystals have been published in [3]. It is expected that the study of the luminescence characteristics of these crystals will help clarification of the reasons and mechanisms of the mixing of the impurity and exciton states as well as the mechanism of scintillation process in these systems.

---

* On leave from: Institute of Physics, Riia 142, EE2400 Tartu, Estonia

Proc. Int. Conf. on Inorganic Scintillators and Their Applications, SCINT95,
1996, Delft University Press, The Netherlands

2. EXPERIMENTAL RESULTS

2.1. Optical properties of the main Pb^{2+} centres

Single CsCl:Pb, CsBr:Pb and CsI:Pb crystals were grown by using the Stockbarger-Bridgeman technique. The concentration of lead varied from 0.005% to 0.5% of PbX_2 (X=Cl,Br,I) in the melt. In the case of need, CsCl:Pb crystals were quenched from 430 °C, while CsBr:Pb and CsI:Pb crystals, from 500 °C. Set-ups for spectral and kinetics measurements have been described elsewhere [2,4]. All corrections to emission spectra are introduced.

Spectral characteristics of the all three systems investigated appeared to be extremely sensitive to the methods of crystal refining and growing as well as to the lead concentration in the crystal. However, a comparison of the spectral and kinetics data obtained on different crystals has allowed the distinguishing of the main emission bands, related to the main Pb^{2+} centres in the crystals investigated. Only these emission bands are reported in present paper.

CsCl:Pb crystal. Like in the case of CsX:Tl (X=Cl,Br,I) crystals, the emission spectrum of a quenched CsCl:Pb crystal is represented by two main groups of emission bands in ultra-violet and visible spectral regions. The ultra-violet emission consists of 3.55 eV band and a non-elementary band at 3.92-3.95 eV (Fig.1a, curve 1). Respective excitation spectra are shown in curve 2 and 2'. Two decay components - the slow one (SC) with the decay time τ=2 ms and the fast one (FC) with τ=4 ns, were detected in the decay of the 3.55 eV emission. These ultra-violet bands can be ascribed to the triplet A emission of the main Pb^{2+} centres, split due to the presence of cation vacancy v_c^- near Pb^{2+} ion.

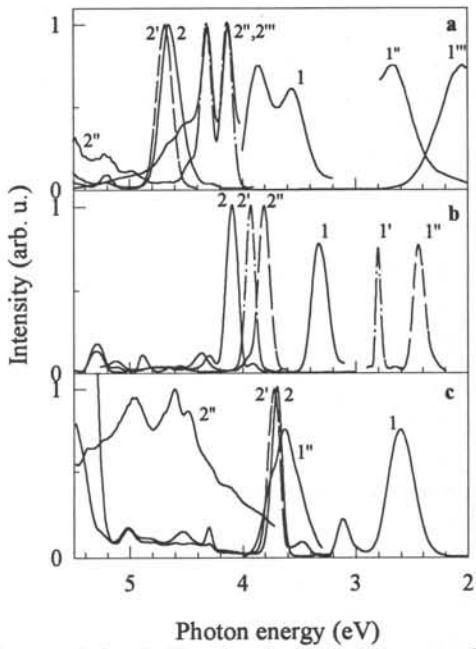

Fig. 1. Emission (1-1'') and excitation (2-2'') spectra of CsCl:Pb (a), CsBr:Pb (b) and CsI:Pb (c) crystals at 4.2 K. For notations see the text.

The visible emission consists of several bands two of which, peaking at 2.65 and 2.05 eV (curves 1'',1'''; corresponding excitation spectra - curves 2'',2'''), can very probably be ascribed to Pb^{2+}-perturbed STE in CsCl:Pb crystal. These emissions are intense, respective low-energy absorption bands are practically dominanting ones in the absorption spectrum of CsCl:Pb measured at 295 K in [4]. The decay time of the 2.05 eV emission is 45 μs at 4.2 K, being close to the ones found for STE in Tl^+-doped cesium halides.

CsBr:Pb crystal. Three main emission bands peaking at 3.32 eV (Fig. 1b, curve 1), 2.8 eV (curve 1') and 2.43 eV (curve 1'') were observed in CsBr:Pb crystals on excitation in 4.1 eV (curve 2), 3.95 eV (curve 2') and 3.8 eV (curve 2'') bands, respectively. The ratio of the intensities of these emission bands is the same in all the samples investigated. Hence, they undoubtedly belong to the same Pb^{2+} centres in the crystal. At 4.2 K two components with τ_{SC}=1.1 ms and τ_{FC}=26 ns were observed in the decay of the 3.32 eV band. The light sum ratio S_{FC}/S_{SC}=4. Two components with τ_{SC}=7 ms and τ_{FC}=24.5 ns (S_{FC}/S_{SC}=0.1) were observed in the decay of the 2.43 eV band. At T>30K τ_{SC} decreases exponentially with temperature increasing. Consequently, the emission bands described could be connected with the triplet

excited state of Pb^{2+} centre. However, their small halfwidths (0.16 eV, 0.09 eV and 0.11 eV for the 3.32 eV, 2.8 eV and 2.43 eV bands, respectively) as well as very fast decay of the 2.8 eV emission at 4.2 K (2.6 μs) points to a strong covalent interaction between the excited impurity and halogen ions, which may lead to the formation of molecular-type bounds between them. This feature may explain the fact that no trace of impurity-perturbed exciton emission has been found in CsBr:Pb crystal.

CsI:Pb crystal. Two most intense emission bands peaking at 3.1 eV and 2.6 eV (Fig. 1c, curve 1) were observed in CsI:Pb crystals on excitation in 3.7 and 3.72 eV bands, respectively (curves 2,2'). In the decay of the 2.6 eV emission one SC with τ_{SC}=2.1 ms and two FCs with τ_{FC1}=26.5 ns and τ_{FC2}=6.5 ns were found. Probably, both these emission bands are caused by radiative decay of triplet A state of Pb^{2+} centres, split due to v_c^- near Pb^{2+} ion. However, the excitation spectra of the 2.6 eV and the 3.1 eV emission bands are not typical of ns^2 ions in alkali halides, showing a number of weaker excitation bands at the energies higher than 3.7 eV (curves 2,2'). This situation is similar to the case of CsI:Tl crystal where a very strong interaction between impurity excited states and excitonic states has been found [1,2].

The ultra-violet emission peaking at 3.62 eV is the dominanting one in all the CsI:Pb crystals investigated (curve 1''). It has a poorly-structured excitation spectrum covering the whole region between 3.7 end 6.0 eV (curve 2''). Two components with τ_1=0.55 μs and τ_2=5.6 μs were found in the decay kinetics of this emission at 4.2 K. Their light sum ratio S_2/S_1=2 as well as decay times are independent of excitation energy. The position of the emission described is very close to that of STE in CsI crystal [2]. Possibly, to explain this emission an energy transfer from impurity to excitonic states has to be considered.

Thus, from the very first measurements it may be concluded that lead-doped cesium halide crystals are characterized by a very strong interaction between impurity and excitonic states. This interaction grows stronger in the row CsCl→CsBr→CsI. In view of the results obtained for Tl^+-doped cesium halides [1,2] it is clear that the systems investigated are of special interest for the study of scintillation process in activated crystals.

2.2. Optical properties of extended Pb^{2+}-based aggregates in CsX hosts (X=Cl,Br,I).

Absorption bands present at λ ~ 500-530 nm in CsBr:Pb and 400-420 nm in CsCl:Pb [4] in as grown crystals can be erased by a usual quenching procedure and restored by annealing at 150 - 250 °C for several (tens of) hours (for CsBr:Pb see Fig. 2). The influence of annealing temperature and treatment duration can be seen, namely, the peak broadens and shifts to high-energy side at lower annealing temperature and shorter time (for CsBr:Pb in Fig. 2,b,c). The photoluminescence excited within these annealing-related absorption bands, peaking at about 420 nm and 540 nm, shows subnanosecond decay times in CsCl:Pb and CsBr:Pb, respectively. At low temperatures higher spectral resolution (<0.5 nm) reveals a rather structured character of these emissions even at non-resonant excitation (<390 nm), further changes in spectra are observed at elevated temperatures. These features might be explained with temperature dependent interplay between free and localized exciton states. The fast component is present up to RT, even if its intensity is decreased by about two orders with respect to that at 4.2 K.

Based on a comparison with the bulk $CsPbCl_3$ single crystal emission [5], the 420 nm emission in CsCl:Pb was ascribed to nm-sized $CsPbCl_3$-like aggregates and the above-mentioned broadening and the high-energy shift were ascribed to the quantum size effect. The same conclusion (i.e. creation of nanocrystals of $CsPbBr_3$-like phase) can be drawn for CsBr:Pb, because excitonic absorption transition at about 531 nm [6] as well as a complex excitonic emission in the 533-540 nm region at 4.2 K [7] have been reported for the bulk

$CsPbBr_3$. In CsBr:Pb, clear influence of the quantum confinement effect was evidenced in the emission of $CsPbBr_3$-like aggregates, as can also be inferred from Fig. 2,b,c.

Under X-ray excitation, in CsCl:Pb no emission of $CsPbCl_3$-like phase was detected at RT and low concentration of 0.01% of Pb^{2+} in the melt [8]. In the case of heavily doped and annealed CsBr:Pb(0.5%) (Fig. 2c), the emission of $CsPbBr_3$-like phase is present at 80 K under X-ray excitation (inset of Fig. 2) together with self-trapped host lattice exciton (STE) emission at about 340 nm [9]. However, the former emission is quenched at RT (inset of Fig. 2) and the resulting emission is only the STE one modified by the absorption of Pb^{2+}-aggregated phase. The energy can be transferred to $CsPbX_3$-like aggregates both in radiative and nonradiative ways, because their excitation spectra extend from exciton absorption peaks down to 200 nm [4]. A detailed γ(X-ray)-excited decay kinetics study at low temperatures is necessary to determine the importance of all possible energy transfer paths.

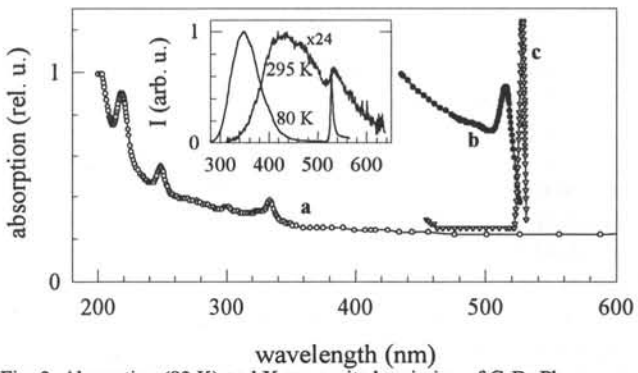

Fig. 2. Absorption (82 K) and X-ray excited emission of CsBr:Pb. a) Absorption of quenched CsBr:Pb(0.05%). b) Absorption of quenched and annealed CsBr:Pb(0.1%), 15 hours at 175 °C. c) Absorption of quenched and annealed CsBr:Pb(0.5%), 65 hours at 240 °C. In the inset, X-ray excited emission of the sample described in c) is given at 82 and 295 K.

No respective processes in photoluminescence were found in annealed CsI:Pb crystals.

For $CsPbX_3$-like nanocrystals in Pb^{2+}-doped CsX hosts (X=Cl,Br), the following general conclusions can be drawn:

1) At T=80-100 K the estimated photoluminescence efficiency is relatively high (>0.5) and efficient transfer from STE and cross-luminescence processes is made possible due to an extended overlap between these emissions and excitation spectra of $CsPbX_3$-like nanocrystals.
2) Because of the subnanosecond decay time of $CsPbX_3$-like phase emission, the conversion of UV luminescence processes to the visible region of spectra is accomplished "without delay".
3) At RT $CsPbX_3$-like phase emission is severely quenched.

This work was supported in part by CONACyT (Mexico, Grant No. D1520-E9201), DGICSA-SEP (Mexico), FOMES (Universitad de Sonora, Mexico) and NATO Linkage Grant HTECH.LG 931435. Dr. S.Zazubovich is grateful to CONACyT for a Catedra Patrimonial de Excelencia Nivel II grant.

[1] V.Nagirnyi, S.Zazubovich, V.Zepelin, M.Nikl, G.P.Pazzi, Chem. Phys. Letters **227**, 533 (1994).
[2] V.Nagirnyi, A.Stolovich, S.Zazubovich, V.Zepelin, E.Mihokova, M.Nikl, G.P.Pazzi, L.Salvini, J.Phys.: Cond. Matter **7**, 3637 (1995)
[3] S.Radhakrishna, J.Luminescence **12/13**, 409 (1976).
[4] M.Nikl, K.Nitsch, K.Polak, G.P.Pazzi, P.Fabeni, D.S.Citrin, M.Gurioli: Phys. Rev. B51, 5192 (1995).
[5] M.Nikl, E.Mihokova, K.Nitsch, K.Polak, M.Rodova, M.Dusek, G.P.Pazzi, P.Fabeni, M.Gurioli: Chem.Phys.Lett. 220, 14 (1994).
[6] K.Heidrich, H.Kunzel, J.Treusch: Sol.St.Comm. 25, 887 (1978).
[7] I.P.Pashuk, N.S.Pidzyrailo, M.G.Matsko: Sov.Phys.Sol.St. 23, 1263 (1981).
[8] M.Nikl, K.Nitsch, I.Dafinei, P.Lecoq, G.P.Pazzi, P.Fabeni, M.Gurioli: MRS Proceedings Series (Scintillators and Phosphors) 348, 155 (1994).
[9] Pooley et al: J.Phys.C 3, 1815 (1970).

RADIATION DEFECTS AND ENERGY TRANSFER TO DOPANT IN ALKALI IODIDES

G.Vâle
Institute of Solid State Physics, University of Latvia,
8 Kengaraga Str., LV-1063, Riga, LATVIA

Abstracts.- Peculiarities of colour centre production and recombination in doped alkali halides are examined. Two types of scintillation material (instant and storage) with a dopant ion as the scintillation centre are offered, both based on the interaction of unrelaxed H centres with dopant ions in different states. The radiation defects in doped crystals are spatially distributed in the vicinity of dopants.
Key words: scintillators, colour centres, dopants, alkali halides, radiation defects.
Running head: radiation defects in doped alkali halides.

THE STATEMENT OF THE PROBLEM

In this report we are regarding the radiation defect production, migration and recombination in doped alkali halides from the viewpoint what role the colour centres could play in the scintillation response. Our attention to classical alkali halides is drawn mainly as to model systems for better understanding of basic mechanisms involved in the scintillation process. We hope the present investigation will be helpful for the development of the physics of much more complicated systems as well. The requirements to the scintillation material are very diversified and depend on their application field. But a general and the most important requirement is a fast and high light output. It should be noted that the most common opinion is that dopants can also act as traps for electrons and holes thus producing afterglow and the accumulation of radiation defects. Both are responsible for the limited use of the scintillation material.

We have focused our attention primarily on the exciton decay in the defect pair of {F,H} centres and their role in the scintillation process. It should be mentioned that the quantum yield of this decay reaction is high and in some cases becomes dominant (for instance, at higher temperatures in chlorides). We are looking for the ways how to make this exciton decay serve as the basis for a fast and high energy transfer to the dopant with the luminescence of the latter.

For this purpose KCl, KBr, KJ crystals doped with Tl^+,In^+, Ag^+, (Ag^-,Na^+,F) and (Tl^+.F) in concentrations of (1-5) 10^{17} cm^{-3} have been investigated. The last two dopants were produced by means of additive coloration and subsequent thermal treatment.
The spectral measurements were made on standard apparatus.

THE COLOUR CENTRE PRODUCTION IN DOPED CRYSTALS

It was found [1] that in 20 ps after the radiation pulse there are only local F and moving H centres as a result of exciton decay, and the concentration of the survived F centres depends on time and temperature as it is evident from Fig.1 for pure KJ (Curves 1,2).

Proc. Int. Conf. on Inorganic Scintillators and Their Applications, SCINT95,
1996, Delft University Press, The Netherlands

Surprisingly, there is a very good agreement between the PSL response and the production of F centres by ns e-beam pulse irradiation. There is no doubt that the starting point of F centre production in doped crystals as in pure ones is the exciton decay in the {F,H} pair, yet in doped crystals the survival of the F centre is determined by a complementary H centre captured by the dopant ion, forming different kinds of dopant hole centres (D^{++}, $D^{++}v_c$, D^{+}..H etc.).

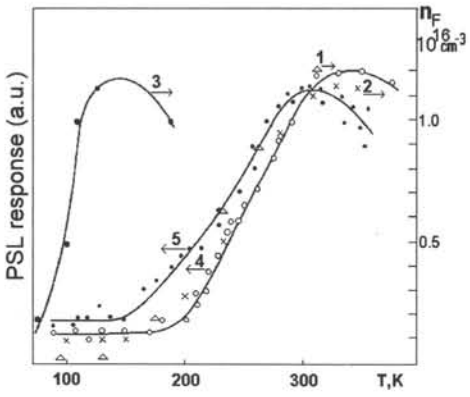

Fig.1 The production of F centres for KJ in ps (1), ns (2) and stat. (3) range. PSL response for Tl (4) and In (5) in KJ

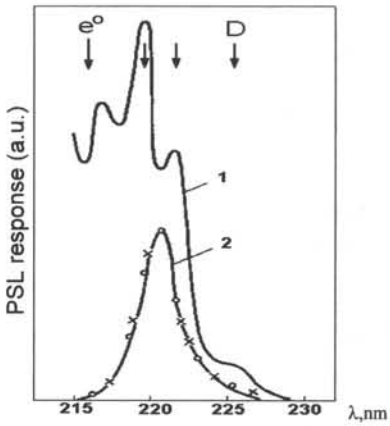

Fig.2 The production spectra of F (1) and Tl^0 (2) for KJ:Tl at LNT.

It allows to draw a principal conclusion that dopant hole centre formation occurs in a subnanosecond's time as a result of the interaction of an unrelaxed H centre with a dopant. And this is because the PSL temperature dependence characterizes the production efficiency of primary F centres.

Another important conclusion may be drawn from the F centre production spectra by monochromatic UV light, which gives information about excitations taking an active part in the F centre production. In pure crystals those are excitons. In doped crystals a complex structure of the production spectra of F centres has been observed (Fig.2). In the spectral range from the anion exciton absorption maximum where the free excitons are produced in a regular lattice to the local dopant absorption bands, two (or more) narrow exciton-like bands are observed. The origin of the bands could be interpreted as exciton absorption at discrete distances from the dopant ion, and therefore the decay of such an exciton with F centre formation from the dopant takes place at corresponding distances, too. We could conclude that the radiation defects in doped crystals are spatially disposed in near vicinity of dopants.

THE COLOUR CENTRE RECOMBINATION LUMINESCENCE

The destruction spectra of the dopant electron centres (Fig.3 for Ag^o centres in KCl:Ag) show a markedly expressed exciton behaviour. It can be explained in terms of the interaction of unrelaxed H centres, produced in the exciton decay, with Ag^o atoms. A similar behaviour occurs when H centre recombines with F centre near the dopant ion (Tl^+.F in KJ).

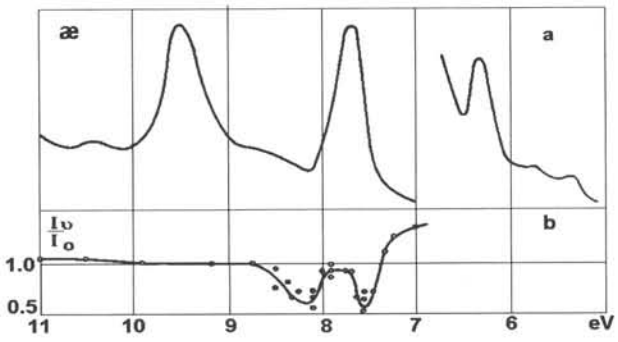

The Tl^+ inner luminescence is always observed. The resonant energy transfer from the exciton, formed in the recombination process, to the dopant ion takes place in the excited state.

Fig.3 The destruction spectra of Ag^o centres (b); and (a) - absorption spectra for KCl:Ag.

THE ASPECTS OF APPLICATION

The peculiarities of colour centre production and recombination as disclosed above imply that the investigated doped crystals could be used as:

a) scintillator (KJ:Tl^+,F), for instant detection of radiation based on the interaction between unrelaxed H and F centres near the dopant. It seems, that in such a system almost all the absorbed energy is transformed into scintillations. No defect accumulation could be detected after a kGy X-ray dose;

b) photostimulable scintillation storage materials (KBr, KBr.KJ and RbBr) with high and fast PSL response, limited only by the inner centre luminescence decay of the dopant 10^{-7} sec for Tl^+). The low dose of detection of X-rays (10^{-4} Gy), high density of write-in and read-out (10^6 bit/cm^2), easy laser scanning by means of a computer with subsequent data processing as well as repeated use of materials make them attractive for X-ray CT (computer tomography);

c) UV light PS scintillation storagematerial (KBr:Ag^-,Na^+,F) with a wide variety of detectable parameters. Besides the properties mentioned above there is also a possibility to detect the UV light polarisation degree and wavelength, the spectral conversion of the UV image into a visible one, optical processing of mathematical and logical data.

THE CONCLUSIONS

There is a good reason to think that in doped systems the basic reaction of radiation defect production - anion exciton decay on {F,H} pair - takes place at some discrete distances from it, and the complementary unrelaxed H centre forms a dopant hole centre in a sub-ns time range. As a result in doped systems the radiation defects are spatially distributed in near vicinity of the dopants.

The recombination of unrelaxed H centres with F centre near the dopant with high and fast output provides inner luminescence of the latter, i.e. scintillations. The disclosed peculiarities of radiation defect production and recombination in doped crystals make possible their use as instant and PS storage scintillation materials with a dopant as the scintillation centre with wide variety of possibilities for data processing and transformarion.

[1] M.Hirai, Y.Suzuki, H.Hattori, T.Ehara and E.Kitamura, J.Phys.Soc.Jpn. 56 (1987) 298.
[2] Y.Suzuki, T.Tasaki, M.Hirai, Int.Conf. in Defects in Ins. Materials, Abstr. (1992) 299.

THE X-RAY STORAGE PHOSPHORS RbI:Tl^+ AND KBr:In^+ AND OTHER In^+ AND Ga^+ DOPED ALKALI HALIDES

Th. Hangleiter*, U. Rogulis†, C. Dietze*, J.-M. Spaeth*
P. Willems‡, L. Struye‡, P.J.R. Leblans‡

*Fachbereich Physik, University of Paderborn, D-33095 Paderborn, Germany
†Institute of Solid State Physics, University of Latvia, Riga, Latvia
‡Agfa-Gevaert N.V., Septestraat 27, B-2640 Mortsel, Belgium

ABSTRACT: The X-ray storage phosphors KBr:In^+ and RbI:Tl^+ show similar properties as the well-known phosphor BaFBr:Eu^{2+}. The radiation damage defects as well as the photostimulated In^+ or Tl^+ emissions were investigated with optical measurements and optically detected magnetic resonance methods between 1.5 K and 300 K. The photostimulation luminescence was also measured in In^+ and Ga^+ doped RbBr, RbI, CsBr and CsI crystals.

INTRODUCTION

X-ray storage phosphors such as BaFBr doped with Eu^{2+} were intensively investigated in the last years. With special interest the radiation-induced defects were studied to understand the mechanism of the photostimulation process. The X-ray information is stored in electron traps usually as F centres and in hole centres. In the case of KBr:In^+ it was assumed that after X-irradiation F- and In^{2+}-pairs are formed [1,2], which can be excited and read-out by stimulation of the F-absorption band. In Tl^+ doped RbI V_K centres stabilised nearby the activator Tl^+ were postulated to be the relevant hole centres [3].

EXPERIMENTAL RESULTS

Single crystals with an activator dopant concentration of 100 to 1000 ppm in the melt were grown with the Bridgman method under inert gas. The radiation defects were produced by X-irradiation with 60 kV, 15 mA for approximately 10 to 60 min at low temperatures or at room temperature. We measured the radiation defects with optical absorption, luminescence, optically detected magnetic resonance (ODMR) and electron paramagnetic resonance (EPR).

a) RbI:Tl^+

RbI:Tl^+ crystals were X-irradiated at 80 K. Fig.1 shows the spectrum of the magnetic circular dichroism (MCD) at 1.5 K. After X-irradiation F centres, V_K centres and Tl^{2+} centres are produced. Additionally Tl^0 centres can be detected by their optical absorption at 2.27 eV (546.3 nm) [3]. The V_K centres were identified with optically detected electron paramagnetic resonance (ODEPR) using the MCD or conventional EPR. The V_K centres disappear after annealing at 150 K and the Tl^{2+} bands (see fig.1) increase as a consequence of the annealing out of V_K centres. The disappearance of V_K can also be shown with thermoluminescence and EPR. However, no disturbed V_K centres like V_{K_A}(Tl) could be detected. The highest intensity of the photostimulated luminesence can be achieved after X-irradiation at low temperatures and annealing to 150 K. At 180 K the Tl^0 centres recombine with Tl^{2+} centres and the MCD signal of Tl^{2+} becomes smaller.

Proc. Int. Conf. on Inorganic Scintillators and Their Applications, SCINT95,
1996, Delft University Press, The Netherlands

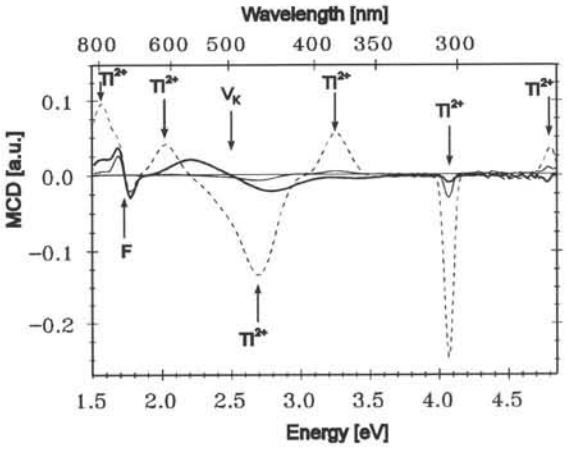

Fig. 1. Spectrum of the magnetic circular dichroism of RbI:Tl^+ at 1.5 K (a) after X-irradiation at 80 K (solid thick line), (b) after annealing at 150 K (broken line), (c) after annealing at 220 K (thin line)

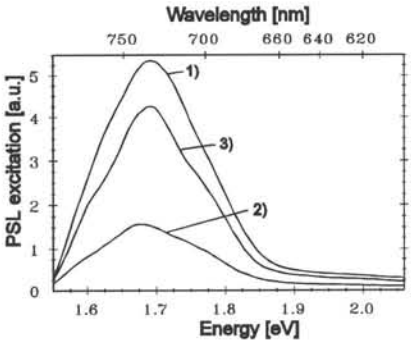

Fig. 2. PSL excitation spectrum of RbI:Tl^+ at 80 K detected at 433 nm. The crystal was X-irradiated, annealed at 220 K (1), bleached at 305 nm (2) and annealed again at 150 K (3).

If Tl^{2+} is bleached with 305 nm (4.07 eV) light, the MCD of the Tl^{2+} centres vanishes. At the same time the photostimulated luminescence (PSL) excited in the F band decreases. EPR measurements show that V_K centres are created by this process at low temperatures (below 150 K). After this procedure warming the crystal to 150 K destroys the V_K centres again, which can be seen in the thermoluminescence spectrum, then the PSL signal is restored to about 80% of its original value (recovery effect, shown in fig.2). The MCD of Tl^{2+} comes back. This indicates that Tl^{2+} is the primary hole centre.

At temperatures above 150 K the Tl^{2+} centre recombines with the F centre as a consequence of photo-exciting in the F band giving rise to the Tl^+ luminescence, i.e. the PSL effect. On the basis of the bleaching experiments at 80 K we assume the following processes to occur in RbI:Tl^+:

Exciting of Tl^{2+} at 80 K:

$$Tl^{2+} + h\nu\ (305\ nm) \longrightarrow \left(Tl^{+}\right)^{*} + V_K$$

$$\longrightarrow Tl^{+} + h\nu(433\ nm) + V_K$$

$$Tl^{+} + V_K \xrightarrow{150\ K} Tl^{2+} \qquad \textit{"recovery-effect"}$$

Photostimulated luminescence (PSL):

$$F + h\nu\ (735\ nm) + Tl^{2+} \longrightarrow \left(Tl^{+}\right)^{*}$$

$$\longrightarrow Tl^{+} + h\nu(433\ nm)$$

In RbI:Tl^+ there is no replenishment effect [5].

b) KBr:In^+

X-irradiation of KBr:In^+ at low temperatures (< 120 K) produces F centres, In^0 and V_K centres, which can be detected with MCD and ODEPR [4]. In KBr crystals with a higher In^+ concentration also In^{2+} centres were found. The V_K centres decay at temperatures above 150 K [6] and only the In^{2+} centres remain as hole centres. By bleaching the In^{2+} (315 nm) at 80 K the In^{2+} centres decrease and new V_K centres are generated. In contrast to RbI:Tl^+ no In^{2+} centres are restored upon annealing to higher temperatures. The PSL spectra after different annealing steps (fig.3) show that the PSL signal is much higher before the V_K centres are destroyed. This means that the V_K centre is the dominant hole centre at low temperatures.

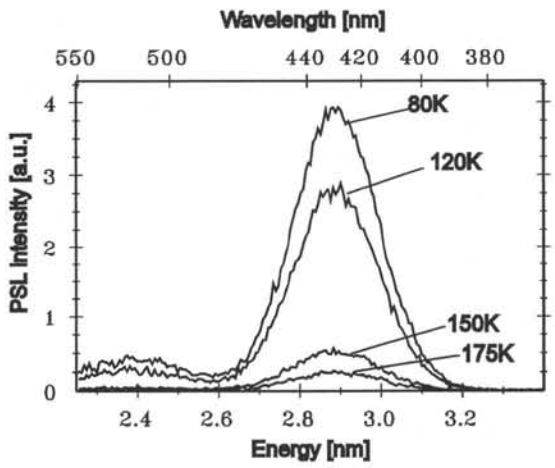

Fig. 3. PSL spectrum of KBr:In^+ at 80 K excited at 605 nm. The crystal was X-irradiated at 80 K (1), gradually annealed to 120 K (2), 150 K (3) and 175 K (4).

After X-irradiation at room temperature only In^{2+}, In^0 and F centres are found. Further hole centres could not be detected until now.

The replenishment effect in KBr:In^+ depends on the In^+ concentration. Apart from this the effects in KBr:In^+ are similar as in RbI:Tl^+.

c) RbBr, RbI, CsBr and CsI crystals doped with In^+ and Ga^+

RbBr, RbI, CsBr and CsI crystals were doped with 200 to 1000 ppm Indium or Gallium in the melt. The maximum of the PSL excitation is at longer wavelength than that in BaFBr:Eu^{2+} (see table 1). CsI:Ga^+ shows no storage effect. The values for the ratio of the conversion efficiency and the stimulation energy of Ga^+ doped RbBr and CsBr are in the same order of magnitude as commercial X-ray storage screens (for details of the figures of merit CE/SE see [7]).

	stimulation wavelength [nm]	max. of the PSL [nm]	max. of the PSL stimulation [nm]	conversion efficiency (CE) [pJ/mm^2/mR]	stimulation energy (SE) [μJ/mm^2]	CE/SE * 10^3
BaFBr:Eu^{2+} screen	633[1)]	390	550	20.4	15.7	1300
BaFBr:Eu^{2+} screen	680[2)]	390	550	14.4	28	510
RbBr:In^+	680[2)]	490	700	1.9	25.0	77
RbBr:Ga^+	680[2)]	550	705	5.6	3.9	1470
RbI:Ga^+	680[2)]	620	770	3)	3)	3)
	856[2)]	620	770	0.0024	131	0.0183
CsBr:In^+	680[2)]	504	700	3.0	23.0	140
CsBr:Ga^+	680[2)]	515	685	5.4	4.3	1370
CsI:Ga^+	680[2)]	-	-	-	-	-

Tab. 1. Data of some In^+ and Ga^+ doped X-ray storage phosphors in comparison with a standard BaFBr:Eu^{2+} X-ray storage phosphor screen. [1)] *HeNe-laser,* [2)] *laser diode,* [3)] *not measurable with the 680 nm laser diode.*

CONCLUSION

RbI:Tl^+ shows no PSL via Tl^+-emission after low temperature X-irradiation. It could be shown that Tl^{2+} is the responsible hole centre for the PSL process in RbI:Tl^+. The situation differs in KBr:In^+ where V_K centres are the relevant hole centres at temperatures below 140 K. The In^{2+} centre could be identified as the hole centre at room temperature. It is also shown that RbBr and CsBr crystals doped with Ga^+ are very efficient X-ray storage phosphors.

REFERENCES

[1] I. Plavina, I. Tale and A. Tale, Proc. of the LUMDETR'91, Riga, **D4** (1991)

[2] P.F. Braslavets, A. Kalnins, I. Plavina, A.I. Popov, B.I. Rapoport and A. Tale, phys. stat. sol.(b) **170**, 395 (1992)

[3] M. Thoms, H. von Seggern and A. Winnacker, J. Appl. Phys. **76**, 1800 (1994)

[4] U. Rogulis, I. Tale, Th. Hangleiter and J.-M. Spaeth, J. Phys.: Condens. Matter **7**, 3129 (1995)

[5] Th. Hangleiter, F.-K. Koschnick, J.-M. Spaeth, R.H.D. Nuttall and R.S. Eachus, J. Phys.: Condens. Matter **2**, 6837 (1990)

[6] D. Schoemaker, Phys. Rev. B **7**, 786 (1973)

[7] A. Meijerink, submitted to Mat. Chem. Phys.

RADIATION DAMAGE IN SILVER HALIDES

A.Alzugbi, D.Millers, L.Grigorjeva
Institute of Solid State Physics of University of Latvia
Kengaraga Str. 8, Riga, LV-1063, Latvia

Abstract. Short-lived absorption due to radiation defects was observed for all $AgBr_{1-x}Cl_x$ crystals studied. Radiation defects creation efficiency dependence on temperature was observed for compositions $0,15 \geqslant x \geqslant 0$ whereas for $0,25 \leqslant x \leqslant 1$ did not. Radiation defects creation in AgBr involves some multiphonon process.

INTRODUCTION

Radiation defects in some insulators can be created by subthreshold mechanism. In details subthreshold mechanism is studied for alkali halides [1] only. The main idea of subthreshold mechanism operating is as follows. Electronical excitations (excitons) were created in insulator by irradiation. During the excitons relaxation its interaction with phonons take place and nonradiative decay of some excitons may result in the pairs of radiation defects. On the one hand excitons self-trapping in material is indicating strong exciton-phonon interaction and in these materials radiation defects creation by subthershlod mechanism is possible. On the other hand in AgBr only free excitons were observed [2], i.e. no direct evidence of strong exciton-phonon interaction is, however in AgBr important radiation damage take place under irradiation by light, as it is known from photography.

Since in $AgBr_{1-x}Cl_x$ excitons for $x = 1$ (AgCl) are self-trapped, for $x = 0$ (AgBr) free and for intermediate x coexistence of self-trapped and free excitons is possible [2] these solid solutions are suitable for radiation damage mechanism study. If radiation damage in silver halides take place intrinsic defects $Ag^{++}V_c^-$ (hole associated with cation vacancy) and Ag_i^0 (interstitial silver atom) were created [3] as primary defects pairs.

EXPERIMENT

Time resolved absorption spectroscopy was used for radiation defects creation study. Pulsed electron beam (pulse width 10 ns, energy of electrons 270 KeV) was used as excitation source. Xenon flash-lamp was used as probing light source, probing light passes throught the sample, grating monochromator and was registrated by photodetector. Signal from photodetector output was displayed on storage oscilloscope. Time resolution of optical signal registration was 25 ns.

RESULTS AND DISCUSSION

Primary results of our experiments were kinetics of a probing light passing throught the sample. Induced absorption

Proc. Int. Conf. on Inorganic Scintillators and Their Applications, SCINT95,
1996, Delft University Press, The Netherlands

spectra and optical density dependence on temperature were obtained from the different sets of kinetics.

Kinetics. Transient induced absorption was observed in all samples investigated. This absorption reaches maximal optical density at the end of irradiation pulse indicating fast process of radiation defects production. After irradiation pulse transient absorption decay was complete within microseconds. Decay kinetics does not obey to first or second order processes and is not a simple sum of two these processes. Transient absorption decays to 0,5 of its maximum level during some time interval Δt (half-life) and this time interval was used as characteristic parameter of kinetics.

Absorption spectra. Induced absorption spectra for all $AgBr_{1-x}Cl_x$ were similar. In AgCl main absorption peak was at 1,3 eV and was shiffed to lower energies in $AgBr_{1-x}Cl_x$. The larger band shift correspond to lager bromine concentration. For $AgBr_{0,85}Cl_{0,15}$ absorption peak position is out of spectral range (i.e. below 0,8 eV) of equipment used, however optical density rise within 1,1-0,8 eV even for AgBr gives clear evidence induced absorption band realy is. This absorption band in AgCl it is due to $Ag^{++}V_c^-$. Absorption band peaking at 2,75 eV possibly is due to Ag_i^0 [3]. It is assumed in $AgBr_{1-x}Cl_x$ similar radiation defects were created. Mentioned above shift of main absorption band in $AgBr_{1-x}Cl_x$ is caused by different anionic environment of $Ag^{++}V_c^-$.

Radiation defects creation efficiency. Since irradiation pulse width was 10 ns and complete decay of transient absorption was observed within microseconds, it was assumed during the irradiation pulse only a small fraction of radiation defects created can recombine. In this case maximum level of optical density D induced by a single irradiation pulse is proportional to radiation defects creation efficiency. Thus the D is a good relative parameter for obtaining dependence of radiation defects creation efficiency on temperature.

Estimation of absolute value of $Ag^{++}V_c^-$ creation efficiency was possible. Concentration of $Ag^{++}V_c^-$ was estimated from induced absorption band peaking at 1,3 eV in AgCl. In calculations oscillator strength 1,0 for this absorption band was used however its real value may be smaller. Electron flux during the simple irradiation pulse was $\sim 1{,}2 \cdot 10^{12}$ cm^{-2}, irradiated surface area of sample was 0,8x1,4 cm^2, penetration depth of electron is 0,2 mm. Estimation shown radiation defects creation efficiency in AgCl exceeds 0,007, i.e. more than one exciton from 150 may decay on radiation defects.

Dependence of radiation defects creation efficiency on temperature for some $AgBr_{1-x}Cl_x$ solid solutions is shown on fig. 1. Radiation defects creation efficiency in these solid solutions for $0 \leqslant x \leqslant 0{,}15$ shown dependence on temperature, whereas for $0{,}25 \leqslant x \leqslant 1$ does not. Ahreniuss plot of radiation defects crea-tion efficiency increase give a straight lines for AgBr, $AgBr_{0,97}Cl_{0,03}$, $AgBr_{0,85}Cl_{0,15}$ and corresponding activation energies are 0,074 eV, 0,019 eV and 0,016 eV. Consequently in AgBr in radiation defects creation multiphonon process was involved, whereas in $AgBr_{0,97}Cl_{0,03}$ and $AgBr_{0,85}Cl_{0,15}$ activation energies is close to optical phonon energy.

Noticeable dependence on temperature of induced absorption half-life was observed only for AgBr (fig. 1). Important is half-life rise within temperature range 160-350 K. To higher

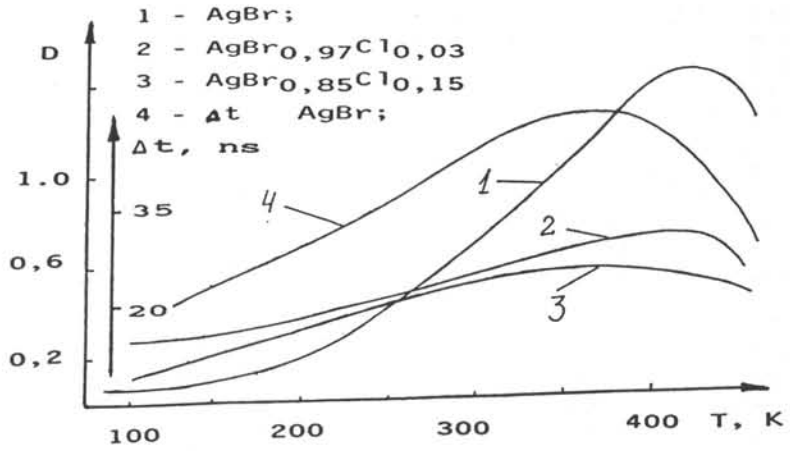

Fig. 1. Dependence of radiation defects creation efficiency and transient absorption half-life time on temperature.

temperature corresponds longer half-life. This result can find the explanation if between radiation defects as created distance increase at higher temperatures.

Comparision of dependencies on temperature of radiation defects creation efficiency and induced absorption half-life for AgBr shown not only radiation defects separation enhanced its creation efficiency, at higher temperatures probability of nonradiative electronic excitations decay on radiation defects increases.

CONCLUSION

Strong interaction between electronic excitations and phonons in AgBr is possible. This interaction is complicated, involves multiphonon process and as temperature rise may result in both enhanced probability of electronic excitations nonradiative decay and better spatial separation of radiation defects as created.

LITERATURE

1. K.S.Song, C.H.Leung and R.T.Williams, J.Phys.-Cond. Matt., 1, 1989, 683.

2. H.Yashioka, M.Yamaga, J.Phys.Soc.Japan, **54**, 2,1985, 841.

3. L.G.Grigorjeva, D.K.Millers, E.A.Kotomin, V.G.Artjushenko and A.V.Nomoev, Opt.Spectrosc.(USSR), **67**, 3, 1989, 357.

Some scintillation properties of HgI_2 single crystals

B.V. Shulgin, S.I. Gorkunova, V.L. Petrov, D.B. Shulgin, G.I. Pilipenko
Experimental Physics Department, Urals State Technical University
620002, Ekaterinburg, Russia

V.V. Osipov
Institute of Electrophysics, Russian Academy of Science
620019, Ekaterinburg, Russia

In this work we present some results of investigation on scintillatin properties of red HgI_2 single crystals. α-, β-, γ- Excitation measurements discovered no scintillations for HgI_2 specimens. But we discovered the effective scintillations for HgI_2 single crystals under high power pulse e-beam excitation [1] and discovered super fast scintillation under the excitation by high intensity synchrotron radiation (SR).

HgI_2 single crystals were grown by G.Rodionova and professor Yu.M.Smirnov (Tver State University, Russia). HgI_2 crystals had size 6x6x1 mm or 15x15x5 mm, are red, tetragon modification, space groupe $P4_2/nmc$. For HgI_2 ϵ=9.2, ρ=6,38 g/cm^3, melting point is 250 °C, Z_{eff} =67,3.

The conditions of excitation by pulse e-beam

The e-beam scintillation of HgI_2 single crystals were excited under irradiation of specimens by pulsed (time duration 2 ns) high-current density electron beams (current density up to j=300 A/cm^2, average electron energy E=160-200 keV of compact electron accelerator (600x250x200 mm) RADAN type. The spectra of scintillations were measured by the CCD-detector adapted to a computer. A spectral range from 300 to 800 nm was analyzed. The error of wavelength measure was less than 1,2 nm. The time resolution of apparatus was 0,3 μs,- so we analyzed the long components of scintillation only.

The conditions of excitation by SR

The synchrotron radiation pulses of VEPP-3 storage ring (Institute of Nuclear Physics, Novosibirsk, Russia) was used for the excitation. The pulse parameters are: Gaussian form (σ =0,43), flux density 10^{14}-10^{17} photon$\cdot$ s^{-1}cm^{-2}, frequency 4MHz, excitation photons energy 3-62 keV, the duration of pulse of excitation $\ll$100 ps. Stroboscopic electronic-optical chronography method based on a dissector LI-602 type (time resolution 10^{-11} s) to register fast processes were used [2]. The fluorescence kinetic parameters were defind based upon the fact that the experimental decay curve represents a convolution of the sample scintillation function f(t) and well known Gauss excitation function. The determination of f(t) was based on the assumption that the function represents itself as a sum of two exponents, while the microsecond-range component was taken to be independent of time. The parameters of the exponents were chosen so that calculated convolute fitted the experimental one in the best possible way [2].

Results.

Under e-beam excitation HgI_2 had emission max 575-580 nm, Fig 1, decay time 2,1=-0,007 μs, efficiency 10.1% to CsI-Tl. We discovered 3 groups of luminescence peaks for HgI_2 at 300 K with the position (nm) (I) 564,7; 569,6; 574,2; 578,8; 583,9; 589,4; 593,9; (II) 563,7; 568,3; 573; 577,3; 582,1; 587,9; 592,7; 597,2 and (III) 566,5; 571,4; 576; 581,2; 586,1; 590,6; 595,1. The complicated emission spectra above-edge-luminescence of HgI_2 (with main maxima at 575-580 nm for Eg=582-585 nm at 300 K) are due to edge luminescence of nonrelaxed exciton or electron-hole recombination near defects with

Proc. Int. Conf. on Inorganic Scintillators and Their Applications, SCINT95,
1996, Delft University Press, The Netherlands

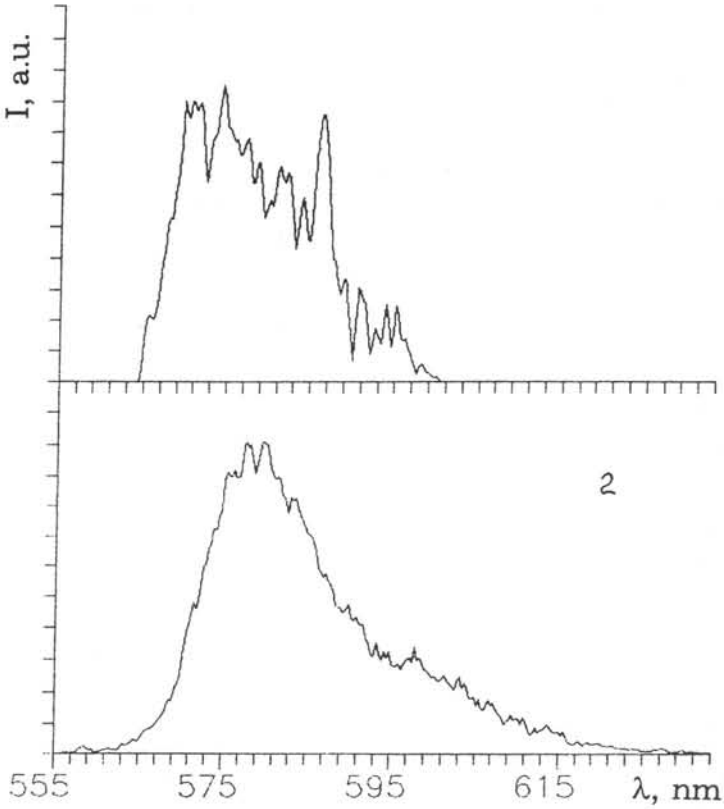
I, a.u.
2
555
575
595
615
λ, nm

Fig. 1.

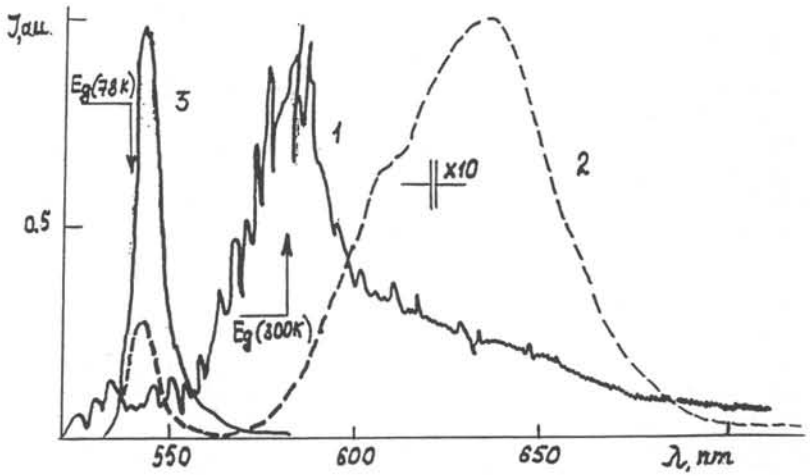
J,a.u.
Eg(78K)
3
1
x10
2
0.5
Eg(300K)
550
600
650
λ, nm

Fig. 2.

phonon assistence (phonon B_1g, 143 cm^{-1}, or combination of phonons A_{1g}, 129 cm^{-1}, and B_{1g}, 29 cm^{-1}).

Under SR excitation (300 K) the luminescence spectrum of HgI_2 have 3 bands: 534, 584 and 630 nm (curve 1 on Fig 2). The band 584 nm (decay time <100 ps) is due to edge luminescence of nonrelaxed excitons. The structure of 584 nm band is due to exciton - phonon interaction. The band 534 nm is due to super edge luminescence (it was found before [3], for laser excitation [3]). Band 630 nm (decay time 1.1 μs (30%) and >10 μs (70%) is due to defects (impurities).

Cooling specimens of HgI_2 (78 K) leads to increasing of output of (536 nm) edge- and (608 and 630 nm) impurity- luminescence, curve 2 on Fig2. Curve 3 on Fig 2 corresponds to the luminescence spectrum of super fast component of scintillation (<100 ps). This super fast process is probably due to capture of exciton on defects of lattice.

The discover of super short (fast) component (<100 ps) of scintillation of red HgI_2 (exciting by SR) give the possibility to increase the loading ability of electronic tract of registration pulse X-ray (SR) signals.

The calculated coefficients of light collection $K_{L,C}$ for HgI_2 crystals with mirror surface and rough side surface for different thickness are:

thickness, mm	$K_{L,C}$(mirror surface)	$K_{L,C}$(rough surface)
2	0.096	0.331
4	0.091	0.237
10	–	0.140

The 2-4 mm thickness of HgI_2 crystals would be enough for registration 100 kev X-ray with efficiency 0.974 and for registration γ -radiation 1-5 MeV with the efficiency 0.12-0.39.

Acknoledgments. – This work was made in coauthorship with V.A. Pustovarov.

REFERENSES

1. Solomonov V.I., Shulgin B.V., Osipov V.V. et al. Pisma v Journal Technical Physics, 1995, v.21, N10, pp.29-33.

2. Pustovarov V.A., Krymov A.L., Zinin E.I. NIM, 1995, v.A359, pp.336-338.

3. Akopjan I.Ch., Novikov B.V. et al. Pisma v JETP, 1973, v.17, N8, pp.419-421.

4. Shulgin B.V., Pustovarov V.A., S.I.Gorkunova, E.I.Zinin, Pisma v Journal Technical Physics, 1995, v.21, N16, pp.63-66.

Inorganic Hydrogenous Scintillators for Neutron Detection

J. Bart Czirr
Mission Support Incorporated
455 North University Avenue
Suite 206
Provo, Utah 84601 U.S.A.
(801) 374-6722
(801) 374-6652 Fax
E-Mail: msiz15@aol.com

Manuel Berrondo
Brigham Young University
Physics & Astronomy, 263 FB
Provo, Utah 84602 U.S.A.
(801) 378-4635
E-Mail: berrondom@plasma.byu.edu

Abstract

We have grown and tested a series of Tl-doped ammonium-salt crystalline scintillators for use as neutron detectors. The advantages of these materials over organic scintillators include higher hydrogen density, higher scintillation efficiency and improved linearity in response to heavy charged particles. The emission decay time is typical of Tl-doped alkali-halide scintillators. Response data and production techniques will be presented. Other ammonium based scintillators will be described.

INTRODUCTION

Our group has been involved for several years in a search for improved hydrogenous scintillators for neutron spectroscopy in the MeV energy range. Commercially available plastic and liquid scintillators are fast and efficient and have been widely used in neutron spectroscopy where time of flight techniques are feasible. These scintillators, however, suffer from severe non-linearities and low light output in their response to internally generated protons from n, p elastic collisions--limitations which have reduced their usefulness in a variety of other applications. Low light output and non-linearity appear to be a result of the organic basis of these scintillators. For this reason, we have investigated a number of inorganic hydrogenous scintillators with the hope of overcoming the inherent limitations of organic materials [1].

INORGANIC HYDROGENOUS SCINTILLATORS

Our investigations have included fourteen different materials, ten of which are based upon ammonium salts doped with thallium. We were initially attracted to the ammonium compounds because of their high hydrogen density (similar to existing organic scintillators), and ability to form transparent crystals. Although all of the ammonium salts formed clear crystals, only a few were found to yield significant scintillation light output. The most efficient scintillators were ammonium bromide and ammonium iodide doped with thallium.

Proc. Int. Conf. on Inorganic Scintillators and Their Applications, SCINT95,
1996, Delft University Press, The Netherlands

Table I lists the fourteen materials investigated. The Relative Pulse Height for each material was measured with 5-MeV alpha particles and is listed relative to BC408 plastic scintillator (PH=1.0). Table II lists several characteristics of the most promising materials.

Table I
Hydrogenous Materials Investigated

MATERIAL	FORMS CRYSTAL	RELATIVE PULSE HEIGHT (∝)
BC408 plastic	–	1.0
Ammonium tartrate (Ce)	Y	0 (no Ce incorporated)
Ammonium tartrate (Tl)	Y	0
Ammonium aluminum sulfate (Tl)	Y	0
Ammonium chloride (Tl)	Y	0 (too slow)
Ammonium bromide (Tl)	Y	5.5
Ammonium iodide (Tl)	Y	~3
Lanthanum acetate (Ce)	N	–
Cerium acetate	N	–
Ammonium formate (Tl)	Y	0
Ammonium sulfate (Tl)	Y	0.38
Ammonium sulfamide (Tl)	Y	0
Amm. dihydrogen phosphate (Tl)	Y	0.13
Methyl ammonium bromide (Tl)	Y	?
Ammonium halides (Na)	Y	0

Table II
Viable Hydrogenous Scintillators

Material	Structure	Hydrogen Density ($x10^{22}$ cm^{-3})	Pulse Decay Time (ns)	Alpha Pulse Height	Gamma Pulse Height	α/β Ratio
BC408	plastic	5.3	5	1.0	---	0.09
NaI (Tl)	NaCl (fcc)	0	200	---	1.0	0.35
NH_4Br (Tl)	CsCl	6.0	1000	5.5	0.6	0.18
NH_4I (Tl)	NaCl	4.2	200	~ 3	0.4	0.15
$(NH_4)_2SO_4$(Tl)	rhombic	6.5	?	0.4	0.05	0.14

FABRICATION OF AMMONIUM SCINTILLATORS

We initially grew sizeable crystals of ammonium chloride, bromide and iodide by aqueous evaporation and by vapor transport. The vapor transport method produced large single crystals, but we were unable to incorporate sufficient thallium to optimize the light output. Our later crystals have been grown from the melt in a pressurized system at 625°C. At this temperature, the corresponding thallium halide is also molten and easily incorporated in the crystal. The highest thallium concentration (in the melt) used to date is 0.5% by weight.

CONCLUSIONS

The high hydrogen density and light output of ammonium bromide point to this material as the preferred scintillator for neutron spectroscopy applications. For example, ammonium bromide could be used to replace the plastic scintillator in dual-signal spectrometers in order to improve the neutron energy resolution [2]. If a combination neutron and gamma detector is desired, ammonium iodide provides a suitable compromise material. The density and effective atomic number are similar to that of NaI (for gamma detection), but the ammonium compound is 67% hydrogen, for neutron detection. In addition, the ammonium halides are weakly or non-hygroscopic.

Our near term goal in this project is to increase the light output of the ammonium-based scintillators by determining the optimum Tl concentration. In addition, we will refine our fabrication techniques to produce large, clear, single crystals from the melt.

If time-of-flight techniques are available, the fast timing characteristics of organic scintillators can provide the best energy resolution. In other situations, the superior light output and linearity of the ammonium halides can be used in a self-contained dual-signal spectrometer to give useful neutron spectra information in the MeV energy range.

REFERENCES

[1]A.P. Mamedov and L.Y. Panova, *Optics and Spectroscopy*, 50, 150 (1981) .
[2]J.B. Czirr and G.L. Jensen, *Nuclear Instruments and Methods in Physics Research*, A349, 532 (1994).

SCINTILLATION CRYSTALS ZnSe(Te): PREPARATION, PROPERTIES, APPLICATIONS

V.D.Ryzhikov, Yu.A.Borodenko, S.N.Galkin, L.P.Gal'chinetskii,
E.A.Danshin, K.A.Katrunov, E.M.Selegenev, V.I.Silin
Institute for Single Crystals of the National Academy of
Sciences, 60 Lenin Ave., 310001 Kharkov, Ukraine

Using the Bridgman technique, ZnSe(Te) crystals have been grown and their physico-chemical and optoelectronic parameters studied. It is established that on the base of ZnSe(Te) crystals, efficient "scintillator - Si photodiode" detectors of ionizing radiation can be developed.

Preparation technology of scintillation crystals ZnSe(Te) is based on the known method of crystal growth from the melt [1] using the Bridgman technique in vertical compression furnaces under inert gas (argon) pressure up to 5.10^6 Pa. Growth rate is 2-5 mm/hour, with temperature in the melt zone - up to 1850 K; crystals are grown in graphite crucibles. After growth, crystals are annealed in a vapour of Zn for enhancement and spectral stabilization of luminescence in the 610-640 nm region.

To determine optimum technological parameters of the preparation process of ZnSe(Te), we have studied in detail physical chemistry, thermodynamics and kinetics of interaction of the components in the system ZnSe - ZnTe, by accounting for the composition of the gaseous medium and construction materials of the growth equipment [2,3]. The technology developed by us allows one to obtain reproducibly two types of ZnSe(Te) crystals (mass up to 600 g, diameter up to 40 mm), which are called conventionally "fast" and "slow" scintillators. The main characteristics of these crystals are presented in Tables 1 and 2.

Table 1. Main parameters of scintillation crystals ZnSe(Te).

Parameter	Value
Melting point, K	1773-1793 (depending on [Te])
Density ρ, g/cm^3	5.42
Effective atomic number Z	33
Emission maximum λ_m at 300 K, nm:	
"fast" scintillator	610
"slow" scintillator	640
Refractive index for λ_m=610-640 nm	2.58-2.61
Attenuation coefficient at λ_m, cm^{-1}	0.05-0.15
Decay time τ, μs:	
"fast" scintillator	1 - 3
"slow" scintillator	30-70
Afterglow,%	< 0.05 after 3 ms
Light yield,photons/MeV γ	8.10^4
Light output in relation to CsI(Tl),%, for X-rays with E < 100 keV (CsI(Tl)=100):	
at 4 mm thickness	up to 100
at 2 mm thickness	up to 170
Matching coefficient between scintillator and photodiode	up to 0.9

Proc. Int. Conf. on Inorganic Scintillators and Their Applications, SCINT95,
1996, Delft University Press, The Netherlands

Table 2. Exitation radiation absorption depth in ZnSe(Te) (calculated data)

	X-, γ-radiation keV			β-particles MeV			α-particles MeV		
	50	100	150	0.5	1.0	5.0	1	5	10
90% absorption depth, mm	1.4	7.5	17	0.1	0.3	2.7	0.002	0.015	0.043

ZnSe(Te) crystals are not toxic, not hygroscopic and can resist without degradation of working parameters γ-irradiation (^{60}Co, 1.24 MeV) up to 10^5 Gy and temperatures up to 400 K.

Studies of photoluminescence (PL) and radioluminescence (RL) spectra have shown that, apart from the edge luminescence region (not considered here because it is not used in the "scintillator-photodiode" detectors), the luminescence spectrum of ZnSe(Te) above 77 K is concentrated between 500 and 700 nm (Fig.1) and consists of three bands: I (not elementary, consists of two overlapping bands with λ_m=605 nm and λ_m=635 nm at 80 K), II (λ_m=560 nm) and III (λ_m=505 nm). At 300 K only band I is observed with λ_m=610 nm for "fast" scintillators and λ_m=640 nm for "slow" ones. At 77 K, "fast" scintillators are characterized by bands I (605 nm) and II, and "slow" scintillators - I(635 nm) and III. An intermediate case is also possible ($3\mu s < \tau < 50\mu s$), when all three bands are visible with corresponding relative intensities.

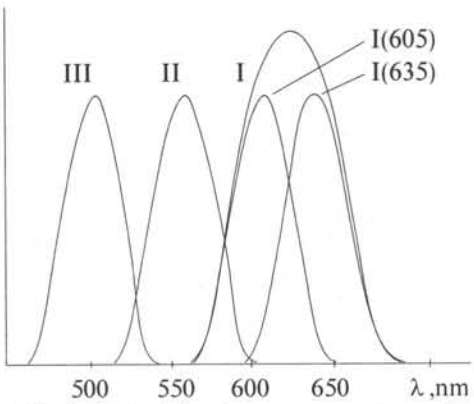

Fig.1. Typical luminescence spectrum of ZnSe and ZnSe(Te)

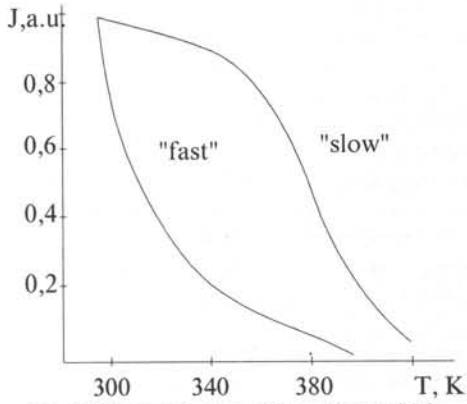

Fig.2. Thermal quenching of Band I in ZnSe(Te)

As it is seen from Fig.2, "fast" scintillators are characterized by rapid decay of luminescence at T > 273 K, while thermal quenching of of the band I of "slow" scintillators becomes significant only at T > 350 K.

Studies of PL, RL and PL exitation spectra [4-7], studies of luminescence centres and intrinsic point defects (IPD) by other experimental and calculation techniques [4-12] leads to a conclusion that in ZnSe and ZnSe(Te) crystals, formation of the radiative recombination centres is governed not only by the isovalent dopant (ID) Te_{Se}, but also by the O_{Se} ID. Background concentration of oxygen even in specially undoped ZnSe crystals can be higher than 10^{20} cm^{-3} [7,9,13].

The presence of Zn_i and Te_{Se} favours, due to volume compensation of local elastic stresses and compensation of charge (for the Zn_i - O_{Se} pair), an increase of $[O_{Se}]$ by four orders of magnitude [7,9]. These data, as well as the results of [10], are evidence that in ZnSe and ZnSe(Te) matrices, thermodynamically stable Zn_i + O_{Se}

complexes are present, the concentration of which does significantly increase after annealling of ZnSe(Te) in Zn vapour.

It was assumed earlier [1,4-6,8,10] that donor-acceptor complexes (DAC) V_{Zn} + Te_{Se} + Zn_i based on the close pair V_{Zn} -Zn_i could be emission recombination centres in the region of 640 nm at 300 K. Accounting for the IVD O and its influence upon PL, RL and CL of ZnSe crystals, as well as interaction of O_{Se} with IPD and Te_{Se} allows one to construct more exactly the scheme of radiative recombination in ZnSe and ZnSe(Te) in the 500-700 nm region, which explains consistently the nature of all the luminescence bands and their temperature dependence between 77 and 420 K in the non-doped crystals. This scheme is presented in Fig.3. It is shown [9] that when the temperature is increased above 77 K, V''_{Zn} and $Zn_i^{\bullet\bullet}$ begin to be more and more dominating. Therefore, while at temperatures of 77 K and lower, luminescence is determined by the transitions $Zn_i^{\bullet}$ -$(V'_{Zn} + Te_{Se}^{\times})'$ (band III) and $(Zn_i^{\bullet} + O_{Se}^{\times})^{\bullet}$ - V'_{Zn} (band II) together with the transitions $Zn_i^{\bullet\bullet}$ - $(V''_{Zn} + Te_{Se}^{\times})''$ (band I, 635 nm) and $(Zn_i^{\bullet\bullet} + O_{Se}^{\times})^{\bullet\bullet}$ - V''_{Zn} (band I, 605 nm), at T > 77 K, a temperature increase leads to a greater contribution of the latter two which are responsible for band I; at T > 300 K only these transitions are observed.

As it is shown in [8], thermal stability of DAC with IVD Te determines thermal stability of band I (635) - see Fig.2 - and high radiation stability of ZnSe(Te).
A favourable combination of the main optical and electronic parameters together with good spectral matching to the silicon photodiode allowed us to develop, based on ZnSe(Te), a vide variety of mono- and multielement detectors of ionizing radiation of the "scintillator-photodiode" type (SELDI detectors). Their main parameters are: range of the detected dose rates (X-ray and gamma) - 10^{-5} - 10^{6} R/h; energy range - 10 keV - 10 MeV; radiation sensitivity- more than 30nA·min·R^{-1}·cm^{-2};

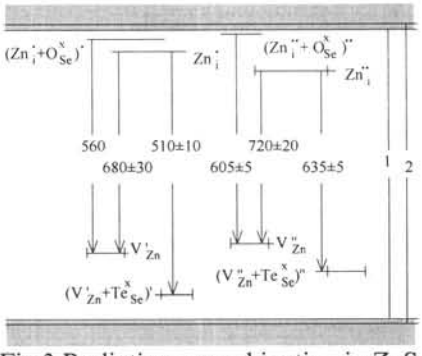

Fig.3.Radiation recombination in ZnSe and ZnSe(Te); λ_m in nm.
1 - Eg=2,68eV(300K);2 - 2,8eV(77K).

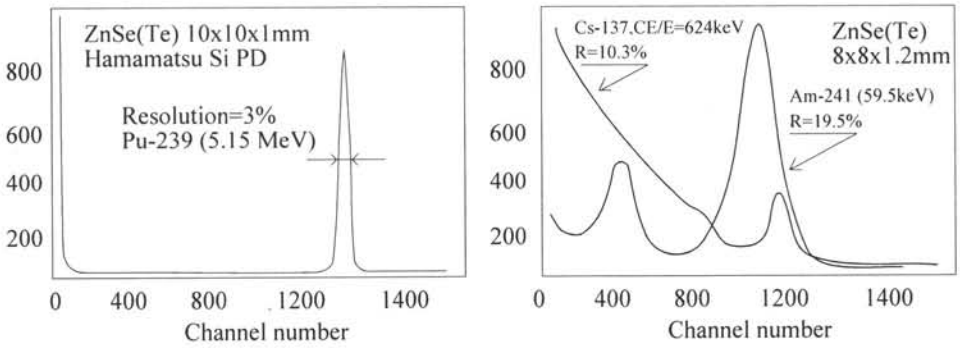

Fig.4.Spectrometric curve for α-particles (5,15MeV), CE/E-particles, γ-radiation (59,5 keV)

volume 0.5-2 cm^3; no sensitivity towards magnetic fields; no need for high voltage; number of channels - 1,2,4,8,16,32; input window area of a channel - 1.5 mm^2 -170 mm^2 (e.g., 2 x 0.7, 2 x1.4, 4 x1.4).

Tests have shown that SELDI detectors are promising for dosimetry and radiation monitoring, in defectoscopy, industrial and medical tomography and non-destructive testing, devices for customs control,etc. In the X-ray energy range up to 150 keV ZnSe(Te)-based detectors have significant advantages over CsI(Tl) due to the absence of afterglow. Favourable combination of low ρ and Z values, high light yield and high radiation stability make ZnSe(Te) a promising material for spectrometry of α- and β-particles, as well as soft X-, γ-rays (Fig.4).

Acknowledgments

The authors express their gratitude to L.N.Lisetski for fruitful discussions, and to N.G.Starzhinskii, A.Koval', O.Zelenskaja and V.P Sokhin for presenting some of the experimental data.

References

1. V.D.Ryzhikov. Scintillation crystals of semiconducting compounds $A^{II}B^{VI}$: growth, properties, application. Moscow, NIITEKHIM, 1989, 124 pp. (in Russian).
2. S.N.Galkin, L.P.Gal'chinetskii, Yu.N.Dmitriev e.a. Zhurn. Neorg.Khimii, 35, 3178 (1990). (in Russian).
3. S.N.Galkin, L.P.Gal'chinetskii e.a. Ibid., 38, 711 (1993).
4. V.D.Ryzhikov et al. Ukr.Fiz.Zhurnal, 33, 818 (1988). (in Russian).
5. R.Baltramejunas,V.D.Ryzhikov e.a. Physica B, 185, 245 (1993).
6. B.Embergenov, N.E.Korsunskaya, V.D.Ryzhikov e.a. Phys. Techn. Semiconductors, 27, 1240 (1993).
7. L.P.Gal'chinetskii, I.A.Karetnikov, V.E.Mashchenko e.a. Zhurn. Prikl. Spektroskop., 58, 488 (1993). (in Russian).
8. L.P.Gal'chinetskii, Yu.N.Dmitriev, E.D.Kovtun e.a. Izv.AN SSSR - Neorgan.Mat., 25, 1632 (1989). (in Russian).
9. N.K.Morozova, V.D.Ryzhikov e.a. Zinc Selenide: Preparation and Optical Properties. Moscow, Nauka, 1992.
10. Yu.N.Dmitriev, V.D.Ryzhikov, and L.P.Gal'chinetskii. Thermodynamics and isovalent doping of crystals of semiconducting compounds of A B type. Preprint IMK-90-16. Kharkov, Institute for Single Crystals, 1990, 52 pp.
11. G.D.Watkins. In: Radiation Effects in Semiconductors. Bristol-London 1977, p.95.
12. A.N.Georgobiani, Yu.V.Ozerov, I.M.Tiginianu. Izv.AN SSSR, ser. phys.,46, No.8, 50 (1982). (in Russian).
13. M.P.Kulakov e.a. Izv.AN SSSR, Neorg.Mater., 26,2280 (1990). (in Russian).

Scintillation materials for high-current pulse e-beam registration (visualisation)

G.A. Mesyats, V.I. Solomonov, V.V. Osipov, S.G. Mikhaylov
Institute of Electrophysics, Russian Academy of Science
620019, Ekaterinburg, Russia
B.V. Shulgin, V.L. Petrov
Experimental Physics Department,Urals State Technical University
620002, Ekaterinburg, Russia

Abstracts. – The optical materials of different types as materials for high-current pulse e-beam registration have been investigated (standard AHC, crystals of diamond, HgI_2, halides, chalcogenides, oxides, some glasses, ceramics and plastic scintillators).

1. INTRODUCTION

The optical materials of different types have been investigated for high current pulse e-beam registration. Th intensity of e-beam scintillations is at 4-6 orders more than intensity of classical cathodo- and X-ray luminescence. So the high curret pulse e-beam excitation method may be used for a new scintillation spectroscopy method of solids. It is shown on example of diamond.

2. EXPERIMENTAL DETAILS

The e-beam scintillations of investigated materials were excited under irradiation of specimens by pulsed, high current density electron beam (time duration 2 ns, electron energy E=100-200 keV, current density j=100-300 A/cm^2) of compact electron accelerator (600×250×200 mm) RADAN type. The schematic diagram of devices is presented on Fig. 1. On this Fig. 1 position 2 is position for specimen (diamond-gem), AHC, oxides etc.). The spectra of scintillations were measured by CCD-detector adapted to a computer. A spectral range 300-800 nm was analysed. The error of wavelength measurement was less then 1.2 nm. The time resolution of apparatus was 0.3 μs [1].

3. MATERIALS AND RESULTS

For pulse registration or visualisation of high current pulse e^-–beam we have used some different inorganic insulator and semiconductor materials:
standard AHC scintillators;diamond; HgI_2; AHC; Halides;Chalcogenides;Silicon oxide and silicates (SiO_2, Gd_2SiO_5–Ce, Y_2SiO_5–Ce,Tb, Sc_2SiO_5(Gd), $Lu_2SiO_5(Ce)$, Na_2ZrSiO_5, $BaZrSi_3O_9$, $Be_3Al_2Si_6O_{18}$); $La_2Be_2O_5$; Al_2O_3 and aluminates;niobates, tantalates, vanadates;tungsten compounds;$Be-P-$glass, $Ce-P-$glass.
Using high power e-beam excitation we measured the emission bands, rise and decay time and efficiency of scintillation materials (for crystals, ceramic, films, powder and glass).

Diamond. The spectrum of e-beam (pulse, high power) luminescence (of e-beam scintillation) of diamond is at Fig 2. This is high resolution spectrum (su-

Proc. Int. Conf. on Inorganic Scintillators and Their Applications, SCINT95,
1996, Delft University Press, The Netherlands

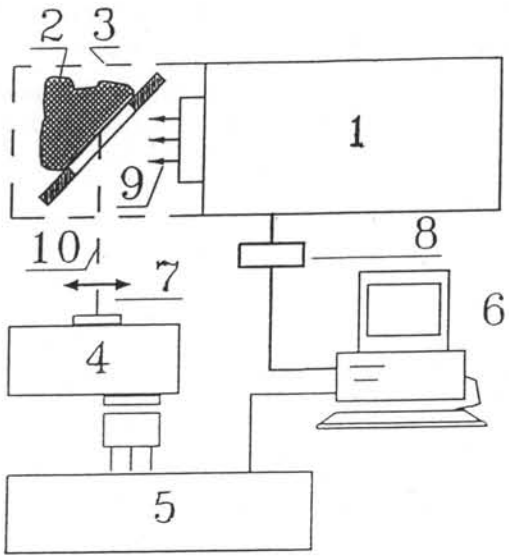

Fig.1. The schematic diagram of devices.
1 - compact e-beam accelerator; 2 - gem; 3 - metallic chamber; 4 - polychromator; 5 - CCD-detector; 6 - computer; 7 - lens; 8 - instance block; 9 - e-beam; 10 - luminescence flux.

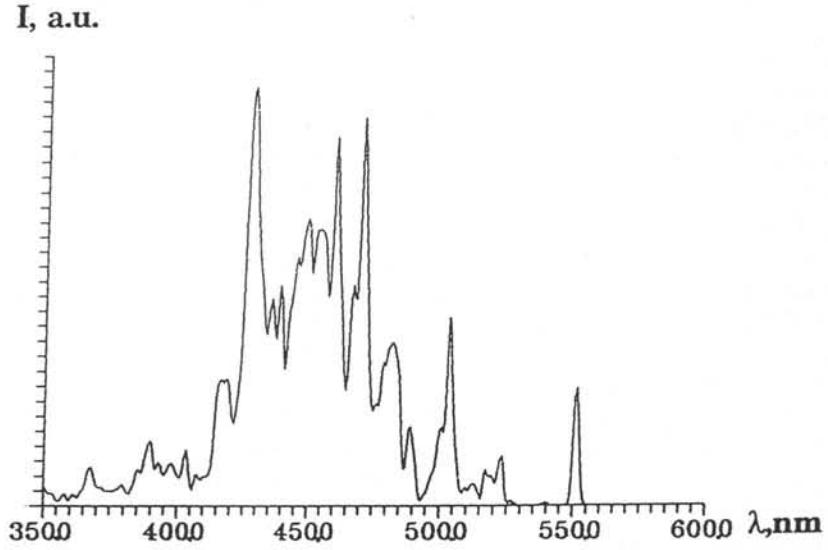

Fig.2. The luminescence spectrum of diamond under high power e-beam excitation for the pulse recording.

perposition of two bands at 450 and 520 nm) with some components of electron-phonon interaction.

There are 4 sets of lines. The first one have zero-phonon line 415,2 nm with phonon vibration repetitions with Stockes and antistockes (news) components; E_{ph} =40 meV. The second set of lines (known as S2) have zero-phonon lines A(523,3), B(489,1), C(477,6) and lines D(472,5 and E(470,5 nm) with phonon energy E_{ph} =40meV. The third set of line have zero-phonon line 503,2 nm with E_{ph} =40 meV with stockes and antistockes components. We discavered the new fourth set of line with zero-phonon line 445 nm. Probably it is the antistockes components of S2-series. The presents of antistockes components showes probably to the presents of Rebane hot luminescence in e-beam scintillations of diamond specimens.

The sets of spectral lines af e-beam luminescence spectrum of diamond correspond to impurity defects of N3, H3 and S2 type. So, the investigated diamonds are the mixed A+B1 type. All analyzed specimens of diamond were identified due to high power e-beam devices with high excitation and good spectral resolution.

HgI_2. Under e-beam excitation HgI_2 had edge luminescence of nonrelaxed exciton or electron-hole recombination near defects with phonon assistance, band 575-580 nm at 300 K, decay time 2.1±0.007 μs and efficiency 10.1% to $CsI - Tl$ [2,3].

Another materials. We discovered the effective e-beam scintillations for $Y(Ta,Nb)O_4$ (λ =350-420 nm) (usually no α-, β-, γ- scintillations), and effective IR-scintillation materials InP (λ =855 nm), GaAs (λ =790-890 nm), $MgAl_2O_4$ (λ =675-725 nm), and effective new e-beam scintillation materials as $Bi_{12}GeO_{20}$ (λ =390-490 nm), $Bi_2Ga_4O_9$ (λ =610-710 nm), $LiF - Mg,Ti$ (λ =420 nm), $LiF - U,Cu,Fe$ (λ =530-540 nm), $NaF - PbF_2$ (λ =380-440 nm), NaF-U,Li (λ =560 nm) and $NH_4Hal - Eu$ (with complicated emission spectra).

CONCLUSION

For all materials the intensity of e-beam pulse luminescence (e-beam scintillations) was at 4-6 order more than intensity of classical cathodoluminescence or pulse X-ray luminescence. So, high power e-beam excitation method may be used as precise spectroscopy method of solids.

Acknoledgement. - The authors are grateful to Kargin Yu.F., Volkov V.V., Scorikov V.M., Kidibaev M., Kuketaev T.

REFERENCES

1. G.A. Mesyats, S.G. Mikhailov, V.V. Osipov, V.I. Solomonov Pisma v Jurnal Tekhnicheskoi Fiziki, 1992, **18**(3). 87-90.
2. Solomonov V.I., Shulgin B.V., Osipov V.V. et al. Pisma v Jurnal Tekhnicheskoi Fiziki, 1995, **21**(10), 29-33.
3. Shulgin B.V., Pustovarov V.A., S.I.Gorkunova, E.I.Zinin, Pisma v Jurnal Tekhnicheskoi Fiziki, 1995, **21**(16), 63-66.

PART VI

Materials Preparation and Crystal Growth

RELATION BETWEEN REAL CRYSTALLINE STRUCTURE AND PROPERTIES OF SCINTILLATORS

Klassen N.V., Shmurak S.Z., Shmyt'ko I.M., Kulakov A.B., Emel'chenko G.A..,
Red'kin B.S., Kosenko A.V., Rybchenko S.I., Savchenko I.B.,Sinizin V.V., Gurov A.F.
Institute of Solid State Physics, 142 432,
Chernogolovka, Moscow Region, Russia

INTRODUCTION

Concerning the width of a forbidden gap between valence and conductivity band, most of heavy scintillators can be referred to wide gap semiconductors (like zinc sulfide). The latter are applied in various light emitting and light detecting devices for many years, so their optical and other physical properties have been investigated rather well [1]. All of these properties are severely dependent on the content of various defects in their crystalline structure: extrinsic (impurities) and intrinsic (vacancies and interstitials, dislocations, stacking faults, grain boundaries, etc.). Several most important characteristics of wide gap semiconductors (light emission effectiveness, light absorption spectrum, degradation in time) are determined by behavior of point defects and dislocations [2,3]. Due to this dependence several parameters, characterizing the content of structural defects, are included usually into a list of technical requirements to the quality of semiconducting material and much attention is paid to the control of these defects.

On the other hand, in the most part of publications on science and technology of crystalline scintillators structural defects except of dopants and contaminations are left without attention. For cesium iodide this can be reasonable for the first approach, because the structure of this material can be distorted severely by hot forging or extrusion without significant changes in scintillation parameters. But in the case of other materials (especially lead containing scintillators) relatively week variations in the substructure of lattice defects can induce significant changes in the most important characteristics of the crystals. This paper is a review of research work on lead tungstate and lead fluoride scintillators, made by a large group of specialists of the Institute of Solid State Physics. These results demonstrate the importance of taking into consideration the influence of structural defects on scintillators physical properties. The actuality of lead tungstate studies can be well supported by the selection of this crystal to be the basic material for CMS Electromagnetic Calorimeter of LHC Project and is illustrated by a large number of papers on lead and other tungstates, presented at this Conference.

INFLUENCE OF POINT DEFECTS AND DEVIATIONS FROM STOICHIOMETRY ON LEAD TUNGSTATE PROPERTIES

Usually bulk lead tungstate single crystals are grown from the melt by Czochralski or Bridgeman techniques. Our studies showed, that the region of lead tungstate homogeneity on the phase diagram lead oxide - tungsten oxide is rather narrow. If deviations from 50/50 composition exceed 0.5%, segregations of structural inhomogeneities are observed. In accordance with the phase diagram of this system [4], the excess amount of lead oxide induces the segregation of double lead tungstate Pb_2WO_5 and eutectics Pb_2WO_5 -$PbWO_4$ and PbO-Pb_2WO_5 . On the other hand, the excess amount of tungsten oxide induces the

Proc. Int. Conf. on Inorganic Scintillators and Their Applications, SCINT95,
1996, Delft University Press, The Netherlands

segregation of eutectic composition $PbWO_4$ - WO_3 . Surely, all these segregations deteriorate optical quality of crystals because of light scattering and absorption. In addition we have found, that Pb_2WO_5 segregations bring severe danger to mechanical stability of lead tungstate crystals. The reason lies in a phase transformation, proceeding in double lead tungstate in the vicinity of 240°C. During cooling of as grown Pb_2WO_5 the optically homogeneous colorless material at this temperature region is abruptly transformed to yellowish powder in explosion-like way (what reveals essential volume effect of the transition).

Deviations from stoichiometry composition of the raw material are well revealed by differential thermal analysis: the heat flow curves during heating or cooling of nonstoichiometric powder reveal distinct peculiarities at temperatures, corresponding to the melting points of the eutectics mentioned above.

Deviations from stoichiometry in the range less, than 0.5%, when the crystal remains optically homogeneous, increase slightly the light yield of gamma scintillations and modify the light excitation spectra of luminescence [5]. In the luminescence excitation spectra additional bands appear in the transparency region (longer than 320 nm). This means that slight stoichiometry distortions generate new optically active centers (naturally, for lead and tungstate excess the nature of these centers is different, what is confirmed by the differences in the spectral shape of the new bands - see fig.1).

Large doses of gamma irradiation from Co^{60} source (about 10 Mrad - this level is critical for LHC) induce variations of light yield of scintillations and of excitation spectra of

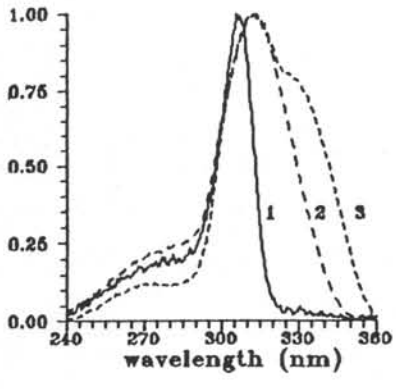

Fig.1.LES,300 K. 1-stoichiometric powder, 2-0.3% PbO excess, 3-0.3% WO3 excess.

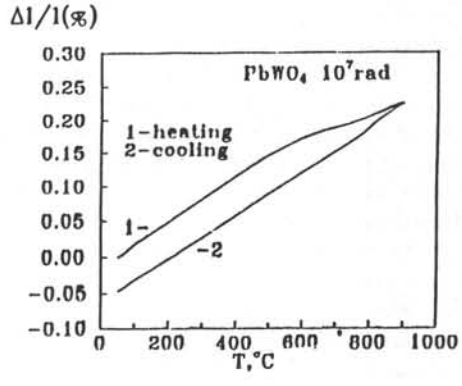

Fig.2. Anomaly of thermal expansion of lead tungstate crystal, irradiated by 10 Mrad.

light emission [5]. It's worth noting, that changes in the excitation spectra are close to those, induced by stoichiometry distortions. Thus we may conclude that at this level of irradiation new intrinsic structural defects are created (more probably these are point defects or their complexes). Some crystals demonstrate slight increase of the light yield of gamma scintillations after irradiation [5]. This means, that the interpretation of the effect of irradiation as the creation of new absorption centers is too simple to be adequate for lead tungstate. At least in some samples the irradiation creates additional defects, which induce positive changes in the ratio of radiative and nonradiative recombination.

Infrared spectroscopy of lead tungstate before and after irradiation showed that the most significant structural changes induced by irradiation occur with the vibration modes, connected with lead ions, whereas the modes, connected with tungstate and oxygen

displacements, are much more stable [6]. Thus the sublattice of lead ions is more strongly distorted by gamma irradiation. Dilatometry measurements of the crystals, irradiated up to 10 Mrad, demonstrated significant expansionof their volume. This is one more evidence for the creation of new structural defects by gamma irradiation.

INFLUENCE OF STRUCTURAL TRANSFORMATIONS ON MECHANICAL STABILITY AND SCINTILLATION PROPERTIES

Lead tungstate crystals differ from tungstates of the second group metals (calcium, zinc and cadmium) by much smaller scintillation output and much faster decay time of scintillations (see, for example,[7]). But this is valid for room temperature, whereas at temperatures lower than 200 K, light yields and decay times of these materials are much closer to each other. This occurs due to sharp increase of the light yield and of the decay time of lead tungstate, which take place during cooling from 250 to 180 K. By means of dilatometry, calorimetry and X-ray diffractometry measurements we have found, that in the temperature range, close the region of the sharp change of scintillation parameters, new structural transformation takes place in lead tungstate crystals . In dilatometry this transformation reveals itself by a distinct change of crystal dimensions in a temperature range from 200 K to 270 K [5].. Calorimetry measurements demonstrate increase of the specific heat in the region from 220 to 290 K. (fig.3), whereas X-ray diffraction reveals changes of interatomic spacing in the same temperature region (fig.4). All these effects are well observed after keeping the crystals at low temperature for several hours. Taking into account possible hysteresis of structural transformations, we may assume, that all these measurements reveal the same group of phase transitions in lead tungstate. These results give us an opportunity to propose a new mechanism of temperature quenching of scintillations in lead tungstate, induced by existence of structural transformation in the temperature range from 200 to 290 K. At this temperature region the crystalline lattice of lead tungstate looses its stability. Generally speaking, the loss of lattice stability facilitates ionic displacements. This process can induce additional mechanism for the energy transfer from electronic excitations to the lattice, enhancing nonradiative recombination and thus decreasing the yield of light emission. Testing of this assumption needs further studies.

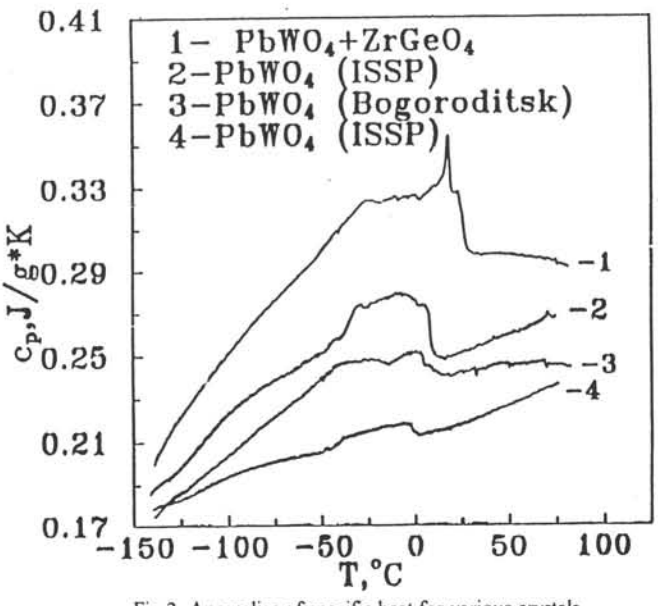

Fig.3. Anomalies of specific heat for various crystals

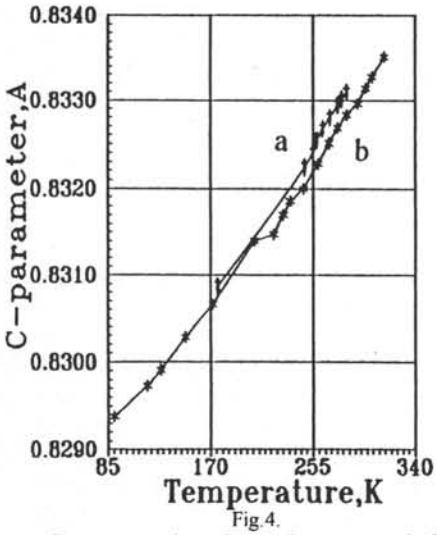

Fig.4.
Temperature dependence of c-parameter in first cooling (a) and after keeping of the sample at 77 K in 12 hours (b).

The same assumption about the negative influence of structural nonstabilities on the yield of light emission can be used for better understanding of severe difference in the rate of temperature quenching of light emission in cubic and orthorhombic lead fluoride [8]. Cubic lead fluoride is nonequilibrium at temperatures lower than 300°C, so we can assume, that electron excitations can induce local transformations of atomic configuration to equilibrium orthorhombic type. Generally speaking, these transformations, followed by displacements of atoms, can facilitate the transfer of electron energy to the lattice.

This structural transformations can be used for explanation of the nature of additional X-ray diffraction reflexes, found in lead tungstate earlier [3,9]. Significant decrease of the angular width of the new reflexes with the increase if the diffraction angle shows, that these inclusions have geometry of thin plates (the thickness of the order of 10 nm) (figs.5,6). . The existence of new phases in a form of thin plate-like inclusions can result in other kind variations of scintillation properties. For example, such inclusion can induce local electrostatic field, separating nonequilibrium charge carriers and inducing long tails of their recombination.

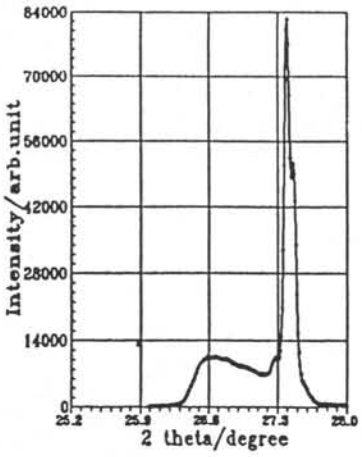

Fig.5. X-ray diffraction splitting by secondary phase inclusion at small diffaction angle

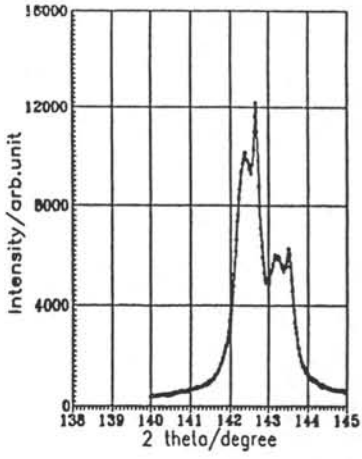

Fig.6.X-ray diffraction splitting by secondary phase inclusion at big diffraction angle

On the other hand, the new structural transformation, found in lead tungstate, can be used for understanding of anomalously high brittleness of these crystals, which creates serious problems for the producers of lead tungstate scintillators. Extrapolating the straight line, separating high pressure and normal phases of lead tungstate, to zero pressure, we'll get the value, close to 100°C [4]. Taking into account the approximate character of this extrapolation, we may assume, that the new phase, existing close to 0°C, has the same nature,

as the high pressure phase. Thus we can conclude, that any local increase of pressure (induced by cutting, lapping or another kind of processing) is able to induce the structural transformation, what will result in local volume change and give rise to cracking.

So looking for possible ways of stabilization of lead tungstate structure can solve two problems simultaneously: to increase scintillation light yield by elimination of additional mechanism of nonradiative recombination and to improve mechanical stability of the crystals due to excluding of additional source of internal stresses.

INFLUENCE OF SURFACE PROCESSING ON LIGHT EMISSION CHARACTERISTICS

X-ray diffractometry of lead tungstate surfaces, subjected to mechanical polishing and annealings in various conditions, in the angular range, when regular reflexes are not seen, reveals new reflexes, corresponding to structural modifications, unknown earlier (fig.7). For the regular reflexes, corresponding to usual sheelite structure, significant broadening by mechanical polishing is observed. This broadening is eliminated by annealing (fig.8). Spectroscopy of excitation of light emission shows, that the layer adjacent to the surfaces does not emit any light [5]. Layer by layer chemical polishing of the distorted material

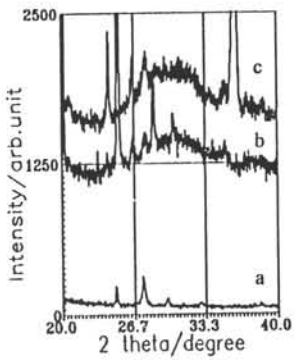

Fig.7.Low angle part of the diffraction spectra of optically polished sample (a), after annealing in Pb_2WO_5 (b) and in WO_3 powder (c).

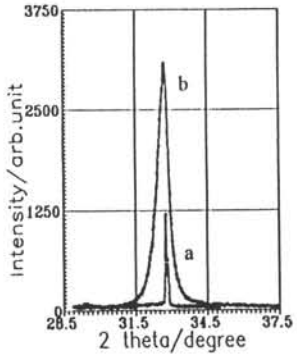

Fig.8 . Diffraction spectra of the rational cut after optical polishing (a) and after annealing at 600 °C (b)

recovers gradually the emission ability, and full recovery occurs after the removal of 100 mcm layer.

The same recovery effect is achieved by the crystal annealing: after several hours heating at temperatures not less than 650°C the effectiveness of surface light emission is close to chemically polished surface. ([5], figs.1,2). The strong decrease of light emission ability, induced by mechanical treatment of the surface, correlates with severe decrease of X-ray excited luminescence in crystals, subjected to plastical deformation by uniaxial compression [3,9]. This decrease can be attributed to creation of new channels of nonradiative recombination, induced by deformation and bound with dislocations, point defects, etc. The recovery of crystalline structure at the surface vicinity, produced by annealing, can proceed in the way of mutual annihilation of dislocations with opposite signs, interstitials and vacancies, etc.

Influence of annealing of lead tungstate crystals turns out to be strongly dependent on the ambient atmosphere and chemical nature of substances being in contact with the crystal

[10]. For example, annealing of the surface in mechanical contact with quartz plate results in more descrete form of the excitation spectrum, than after chemical polishing (fig9). Three maxima can be resolved (at 275, 290 and 310 nm). Differences in the surface optical spectra, obtained for various contacting substances, proves the participation of diffusion in the annealing process.

The defects in the surface layer can influence significantly the properties of scintillator as a whole. First of all - because of light reabsorption during multiple internal reflections from the surface. On the other hand, for small size crystals, used for position sensitive scintillating detectors, the surface layer can be an essential portion of the whole volume.

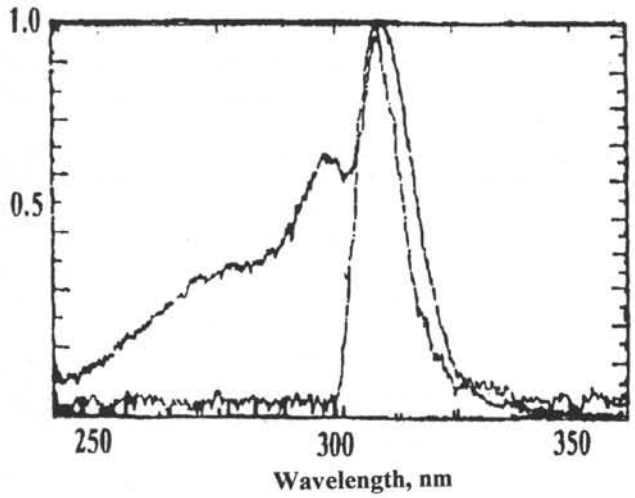

Fig.9. Influence of annealing in contact with quartz on luminescence excitation spectra.

It's worth noting, that the results of annealing are strongly dependent on the pressure of oxygen in the ambient atmosphere. Say, annealing with decreased partial pressure of oxygen results in segregation of precipitates, forming rather long curved lines On the contrary, annealing in increased content of oxygen leads to disappearance of this lines. This effect can be explained by diffusion of oxygen, leading to the loss (in the first case) or to the capture of oxygen by the crystal. If some amount of oxygen ions escape from the crystal, precipitates of lead or tungsten oxides can be segregated at dislocations, arranging dark lines. When the oxygen ions are returned to the crystal, these precipitates are dissolved again. The diffusion coefficients of lead and tungsten are much lower, so they can participate in local redistribution of stoichiometry (of the order of tens of micrometers) without changes in the total composition. Nevertheless this redistribution can produce significant modifications of optical and other characteristics.

It turned out, that oxygen mobility in lead tungstate is highly anisotropic (this was found by measurements of ionic conductivity). In a direction normal to tetragonal axis the mobility is about 10 times bigger, than along the axis. This anomaly can be understood by examining of the atomic construction of lead tungstate unit cell: planes, constructed from oxygen ions, are oriented normally to this axis (fig.10). Surely, this anisotropy of oxygen behavior should be taken into account during annealing and other treatments.

All the manipulations, mentioned above, do not produce essential changes in light emission spectra. Weak sensitivity of the spectra of light emission can be understood, by taking into consideration the results of papers [11,12]. Authors of these papers came to conclusion, that the main part of light emission is connected with various states of WO_4 tetrahedrons. On the other hand, studies of vibration spectra of lead tungstate [6] showed, that the sublattice of these tetrahedrons is much more stable in comparison with the

sublattice of lead ions. It can be assumed, that low stability of lead sublattice is a result of flexibility of lead valency value (it can be easily changed from 2 to 4). This peculiarity of lead can result in wide variety of possible configurations of the closest neighbors of lead ions in the lattice. In calcium, cadmium and zinc tungstates WO_4 tetrahedrons play the main role in light emission as well [13]. Then what is the reason of such a huge difference between the efficiencies and decay times of light emission for lead tungstate and other tungstates? If the emission process in all of these compounds proceeds without severe differences, then we should assume, that much less values of emission efficiency and decay times for lead tungstate result from much higher nonradiative recombination during the delivery of electron excitations to the centers of light emission. Much higher nonradiative recombination for lead tungstate can be explained by low stability of lead sublattice (easy creation of point defects, structural transformations).

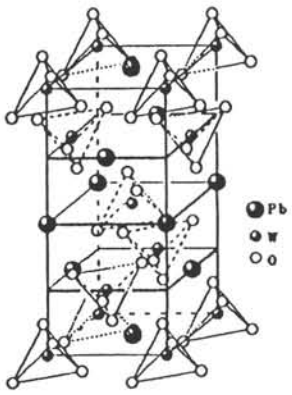

Fig.10. Unit cell of tetragonal lead tungstate. In the upper part oxygen plane is seen

May be the same reason of low lattice stability resulting in intence nonradiative losses of electron excitations during their delivery to emission centers explains small efficiency of light emission of lead fluoride at room temperature [8]. Our studies showed, that when the centers of light emission in lead fluoride are excited directly by resonant optical photons, the emission is rather high. On the other hand, at interband excitation the emission is smaller by many times. This is the case either for Tb and Sm centers or for the light emission centers, introduced in orthorhombic lead fluoride by plastical deformation. But when Tb or Sm doped crystals are transformed by deformation to orthorhombic state, interesting evolution of light excitation spectra occurs (fig. 11)[14]. In a cubic phase and in orthorhombic phase just after the transformation the excitation spectrum of terbium emission remained narrow. But after several days of relaxation a wide pedestal started to grow, achieving maximum after about 10 days. This broadening of excitation spectrum can be explained by the participation of delivery of electron excitations to the emission centers from the outer volume of the crystal. For example, this delivery can take place via dislocations, which came into contact with the Tb centers in the process of relaxation.

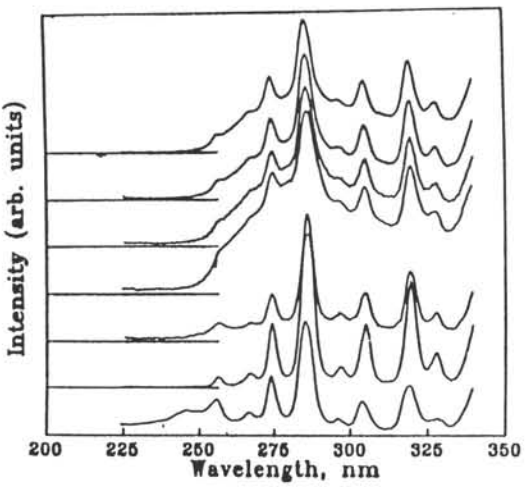

Fig.11. Evolution of luminescence excitation spectra of Tb doped lead fluoride after transformation to orthorombic phase. Low. initial cubic, then after 0,1,5,10,15 ,20 days from the transformation

The results presented above create a hope, that scintillation properties of

lead based compounds can be improved significantly by proper arrangement of their real structure.

This studies were supported by INTAS Grant No 93-12-39.

REFERENCES

1. Physics and Chemistry of II-YI Compounds . ed. M.Aven and S.S.Prener. North Holland Publishing Company, Amsterdam, 1967.
2.N.V.Klassen, Yu.A.Ossipyan. J.Physique, 40, Supplement, cb-91.
3.N.V.Klassen, "Scintillator and Phosphor Materials", ed. M.Weber, P.Lecoq, R.Ruchti, C.Woody, W.Yen, R-Y. Zhu., p.247, San Francisco, 1994.
4.. L.L.Y.Chang, J.Amer.Ceram.Soc., v.54,p.357, 1971.
5. S.Z.Shmurak et.al. - this issue.
6. A.V.Bazhenov, I.S.Smirnova, et.al. - this issue.
7. S.E.Derenzo and W.W.Moses, Heavy Scintillators for Scientific and Industrial Applications
Proc. of Crystal 2000 International Workshop, Chamonix, 1992., p.125.
8.. D.I.Alov, A.V.Bazhenov et.al. - MRS 1994 Spring Meeting "Scintillator and Phosphor Materials", p.259, San-Francisco, 1994.
9. P.Denes, N.Klassen, et.al. Physical Processes in Fast Scintillators, Record of International Workshop PHYSCI 94, eds. P.Rodnyi and C.van Eijk, S-Petersburg, 1994, .118.
10..N.V.Klassen, S.I.Mahonin, S.I.Rybchenko, S.Z.Shmurak - to be published.
11. Reut E.G. Optika I Spectroscopia, v.50, 821-823, 1981.
12. Korzhik M.V., Pavlenko V.B., Katchanov V.A.,Peigneux J.P., Poulet M. MRS 1994 Spring Meeting "Scintillator and Phosphor Materials", S-Francisco, 1994, report P 1.8.
13. Influence of Structural Defects on Physical; Properties of Tungstates, L'vov 1978. ed. M.V.Pashkovskii.
14. N.V.Klassen, S.Z.Shmurak, A.V.Soloviev et.al. Phusical Processes in Fast Scintillators. Record of International Workshop PHYSCI 94, eds. P.Rodnyi and C. van Eijk, S-Peterburg, 1994.

Preparation of Shaped Scintillation Crystals under Non-Wetting Conditions

Shiro SAKURAGI
Union Materials Inc., Oshido Tone-Machi Ibaragi, 300-16 JAPAN

Shaped scintillation crystals of CsI(Tl) and NaI(Tl) were prepared by Bridgeman method applying the purification treatment of Reactive-gas Atomosphere Processing (RAP) method. The removal of water by RAP method causes non-wetting relation between the crystal and the crucible. Consequently, the crystal is easily taken out from the crucible and has the nearly equal shape of detector which is required by end users. This technological progress will bring great advantage for producing scintillation crystals of high quality, low cost and energy saving.

1.Introduction

Generally, inorganic scintillation crystals are made using Vertical Bridgeman(VB) or Vertical Gradient Freezing(VGF) method by which the molten material is held in a crucible (container). When there is a chemical reaction between the liquid and the container, that is a " wetting " environment between them, the liquid is crystallized and then the two solids strongly adhere to each other, and good crystal cannot be obtained. So, getting over the problem of "wetting " conditions for VB/VGF method is quite important point.

Almost all the cause of wetting conditions come from a very small quantity of water which is residual one within the environment. Fortunately, this water can be removed by the purification process named as RAP method mainly applied to prepare metallic halide crystals[1-3]. In the course of Reactive-gas Atomosphere Processing (RAP) method, the residual water is removed perfectly using two steps process. The first one is vacuum evacuation of the crucible and raw material and the second step one is the chemical reaction between the residual water and halogen gas. In this chemical reaction, the residual water is converted into gaseous form and evacuated by vacuum pump. We applied RAP method for the preparation of CsI(Tl) and NaI(Tl) using graphite crucible and consequently solved the wetting problem.

2. Non-Wetting Conditions by RAP method

The raw materials of metallic halides contain several tens of ppm as residual water. When growing KCl crystal using a quartz (SiO_2) crucible without reduction of residual water, there may occur some chemical reaction between KCl, H_2O and SiO_2 corresponding to formula (1), resulting some compound like K_2SiO_3.

$$2KCl + H_2O + Si_2 \rightarrow K_2SiO_3 + 2HCl \quad \cdots\cdots\cdots(1)$$

After crystallization, resulting material was analyzed by Electron Probe Micro

Proc. Int. Conf. on Inorganic Scintillators and Their Applications, SCINT95,
1996, Delft University Press, The Netherlands

Analysis (EPMA) on the sticked part between KCl crystal and SiO_2 crucible. Figure 1 shows this result, in which analysed elements were limited to Si, K and Cl. The analysis point was shifted from SiO_2(A) side to KCl one (F). In the points A, B, the dominant element is Si, but in C, D regions, Si decreases and K, Cl increases. Finally at the point F, 20 μm away from quartz crucible, there are only K and Cl without Si. These data implies that there are some compounds layer between SiO_2 and KCl as mentioned in equation (1) likely K_2SiO_3. This intermediate layer between KCl and SiO_2 acts as a glue to adhere strongly each other and we never get a desired crystal. In RAP method, residual wateris removed down to ppm level from halides powder by means of chemical reaction. The preparation of large KCl crystal with Cl_2 gas was done successfully using quartz crucible for the development of high quality CO_2 laser windows.[4] In the case of CsI, the residual water may be removed using CI_4 or HI at temperature around 200℃ by the chemical reactions described below:

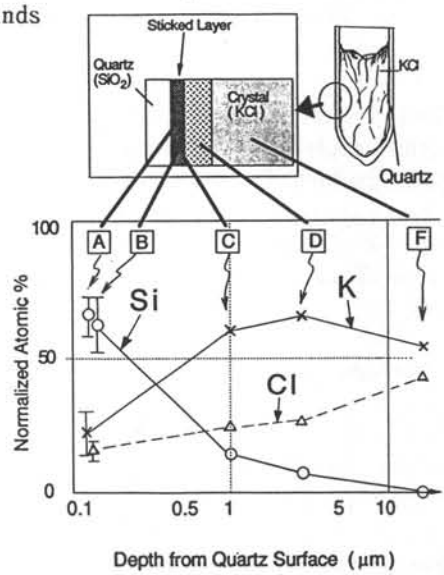

Figure 1. EPMA analysis of sticked layer between KCl and SiO_2

$$CsI + H_2O \rightarrow CsOH + HI \quad \cdots\cdots(2)$$

$$2CsOH + CI_4 \rightarrow 2CsI + CO_2 + 2HI \quad \cdots(3)$$

$$CsOH + HI \rightarrow CsI + H_2O \quad \cdots\cdots(4)$$

RAP method was also applied to fluorides to high quality materials and reactive-gas of HF, CCl_4 and CBr_4 were used to remove such anion impurities of OH^-, NO_3^-, HCO_3^- and CO_2^{2-} from halides [5,6].

3. Application of RAP to CsI(Tl) and NaI(Tl)

NaI(Tl) and CsI(Tl) are well-known scintillators from long ago. But, up to now the methods for their production are almost done under wetting conditions. There are some exceptions of RAP-application for mass production of CsI by BDH Ltd., and HORIBA Ltd.,. These corporations supplied about 8000 pieces of CsI(Tl) crystals with RAP method for CLEO-II γ-ray detector at Cornell University in 1988. But thinking about big difference of volume between a cylindrical ingot and a detector shape, there remains problems about much labor and material losses from the stand point of cost down.

In these situations, we tried to develop shaped scintillation crystals of CsI(Tl) and NaI (Tl) using graphite crucible by applying RAP method. Once we can get a shaped crystal, it is expected that the material loss from machining will decrease and consequently labor cost will decrease drastically.

The experimental conditions are as follows. Starting CsI powder of 6N grade was purchased from Chemetall Ltd., and NaI powder of 4N grade was from Mitsui Toatsu Chemical Ltd.,. The graphite crucible was machined from the high purity semiconductor grade materials (ET-10P) which was produced by Ibiden Ltd,.. The inner shape of the graphite crucible for HB furnace was 4×7cm area at the face and 5×7cm at the end face with 25cm of length. Figure 2 shows the schematic arrangement of CsI(Tl) growing furnace by HB method. A graphite crucible with a charge of 2.5Kg of CsI powder and 0.2% of TlI was placed in a quartz container.

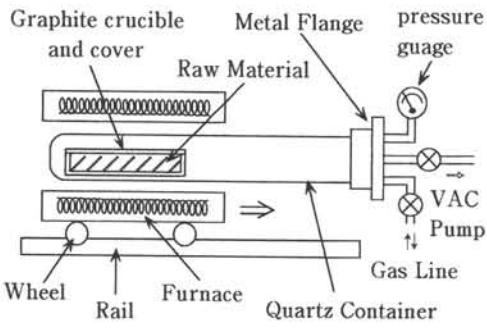

Figure 2. Schematic figure of CsI(Tl) and NaI(Tl) growing furnace by Horizontal Bridgeman Method. (HB)

The outgasing from raw material was done in high vacuum ($<10^{-5}$Torr) at about 250℃ for 5 hours. After this, HI or CCl_4 was introduced in the container up to about 100Torr and Ar gas was added to halogen gas up to 400Torr . CsI powder was melted with this atomosphere during 2 to 3 hours and chemical reaction described in equations (2),(3) and (4) was proceeded in this process. The horizontal furnace was moved at a rate of 2mm/Hr and temperature gradient near interface of solid and liquidwas about 10℃/cm.

About NaI(Tl),the procedure of preparation was nearly equal to CsI (Tl). But, the very hygroscopic NaI must be charged into the crucible in a dry box so as to avoid heavy water adsorption.

4. Results and Discussions

The most difficult part arises from the way to obtain completely dehydrated graphite crucible. If dehydration of the graphite crucible is not sufficient enough, continuous release of small amount of gases occurs during crystallization. Once we have got the completely dryed environment, RAP method proceed effectively to get non-wetting conditions between the molten CsI (Tl) and the graphite crucible.

Figure 3. CsI(Tl) crystals obtained by VB method (upper) and HB method (lower) with length about 25cm

Figure 3 shows two different shaped of CsI(Tl) crystals. The upper one was prepared by VB method with the size of $4\times4cm^2$ initial part, $5\times5cm^2$ of end part and 25cm length. The lower one was prepared by HB method with the size of $4\times3cm^2$ (top part), $5\times3cm^2$ (end part) with 25cm length. They both were taken

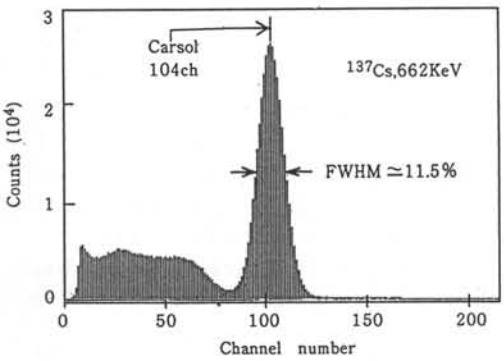

Figure 4. Energy spectrum from a ^{137}Cs source measured with CsI(Tl) Tapered crystal by VB

out easily from graphite crucible. But they have some bubbles, inclusions and mist are observed at end parts of both crystals probably induced by growth conditions in the final stage of the crystallization process. In the case of NaI(Tl), non-wetting condition has also been realized.

The result of characterization of CsI(Tl) sample obtained by VB is displayed in Figure 4. The crystal is cut at the initial side 15cm away from that position. The two faces are polished and the crystal found totally transparent through 15cm length. Energy spectrum obtained from this crystal with 662KeV photons is shown in Figure 4. The measurement are done using a 3 inches photomultiplier (Hamamatsu R594), the full width at half maximum (FWHM) energy resolution being about 11.5%. These data show that our shaped crystals are comparable to ordinary prepared crystal.

5. Concluding Remarks

We realized CsI(Tl) and NaI(Tl) shaped crystals under non-wetting conditions by RAP method. There still remains some items to be done about technical improvement towards large scale production. The conception for preparation of shaped crystals under non-wetting condition is quite important not only for scintillation crystals but also for various kinds of crystals from a point of view of resources, energy and labor saving.

Finally, I would like to propose the suitable word when explaining the " non-wetting " state between various kinds of liquids and the surface of a solid at high temperature. That word is " liquinertness ". This is formed by combining two words " liquid " and "inert ". The so-created word " liquinertness " expresses the situation in which there is repellent relation between a solid and liquid, namely they are "liquinert" to each other.

References

[1] H. Gruendig : Z.Physik 158 (1960) 577
[2] M. Lebl and J. Trnka : Z. Physik 186 (1965) 128
[3] G. Rosenberger : " Ultrapurity " (Marcel Dekker, New York,1972) 3
[4] Shiro Sakuragi, Niro Sakai, Haruo Kotani and Takeo Miyata : ICALEO'84 Proceedings Vol. 44 (1984) 291
[5] R.C. Pastor and A.C. Pastor : Mat. Res. Bull. 10 (1975) 117
[6] R.C. Pastor and K. Arita : Mat. Res. Bull. 10 (1975) 493

ON SOME PECULIARITIES OF CESIUM IODIDE CRYSTALS

L.M.Shamovsky, A.Rogozhin, VIMS, Ecodetector-VIMS Ltd, Staromonetny per. 31, 109017, Moscow, Russia

Abstract. Some peculiarities of CsI crystallization are analized concerning possible polimorphic transition of the material near the melting point and formation of solid state solutions with activating dopants. The crystal structure and the impurity distribution inhomogeneities are supposed to influense the quality of cesium iodide scintillators.

Cesium iodide is one of the most extensively used scintillation material. CsI (undoped), CsI(Tl), CsI(Na) are well known (see e.g.[1] and references therein), but $CsI(CO_3)$ was also reported to have good scintillation properties [2]. Besides, one can find in literature information about luminescence properties of CsI(Ga), CsI-In [3], CsI-CsBr and other systems. There are various methods to produce luminescent materials with CsI-matrix. Obviously, the properties of the scintillator strongly depends on the method of its obtaining.

It is well known that cesium iodide, as well as cesium bromide and cesium chloride, has at normal conditions the CsCl-type structure unlike the majority of alkali halides which have the NaCl-type structure. According to [4] the specific volume of cesium halides must change with crystallization by 10% which is the minimum value of all alkali halides. Indeed, CsCl crystallizes at 919 K into NaCl-type lattice with such a diminishing of the specific volume and with the significant decrease in enthalpy, ΔH=20,38 kJ/mol [5]. At 743 K CsCl exibits a solid-state polimorphic transformation from the NaCl-type structure to the CsCl-type structure with additional diminishing in volume by 17,6% and with liberating of the yeat of 2,93 kJ/mol. This transformation is the reason why CsCl crystals being grown from the melt are usually unperfect samples of poor optical quality.(We nevertheless have obtained optically perfect strain hardened polycrystal samples of CsCl using plastic deformation methods). To obtain optically clear single crystals of CsCl M.Midoricawa *et al.*used a melt-growth technique under high inert gas pressure. With increasing the pressure P of inert gas they managed to shift the phase transformation point until it coinsides with the melting point at T=933 K and P=970 kg/cm^2 . Thus the material was "made" to crystallize directly in the stable form.

Actually an anomalous big value of the volume decrease of 28,5% is observed for the cesium iodide transfer between the melt and the solid phase[4]. It is possible that this anomaly is due to the two-stage process of the CsI crystallization. In the first stage CsI is transformed from the melt to the unstable face-centered NaCl-type modification. In the process the specific volume diminishes by the value of approximately 10% as in the case of CsCl and the significant decrease of enthalpy occurs. In the second stage the solid state transition to the body-centered CsCl-type structure is attended with the volume change of the relatively big value although with the relatively small change of the enthalpy. This is possibly due to the the fact that the mentioned polimorphic transition occurs at the expense of the anions approaching each other by 18,6%, whereas the cation-anion distance increases by 3,3%. The attempts to detect this phase transition by means of the differential thermal analysis have not been successful. This appears understandable if the polimorphic transition occurs in the immediate vicinity of the melting point, probably within 1-2 K - interval.

Taking the values of the specific heat released and of the volume change at the CsI phase transition as in the case of CsCl one can obtain for T= 905 K: $\Delta P/\Delta T \approx 4 \cdot 10^5$ Pa/K. We used elevated inert gas pressure growing technique to obtain CsI(Tl) and CsI(Na)

Proc. Int. Conf. on Inorganic Scintillators and Their Applications, SCINT95,
1996, Delft University Press, The Netherlands

crystals and it was found that the scintillation light output drastically decreased for CsI(Na) crystals grown under the inert gas pressure higher than $8 \cdot 10^5$ Pa. The crystallysation of CsI directly into the low-temperature form is a plausible explanation of the effect. The CsI-NaI is a strongly unisomorphic system with eutectic and without mutual solubility of the components[6,7]. The components not only significantly differ in ionic radii of the cations but also in crystal structure as NaI has the lattice of the NaCl type. Thus CsI(Na) phosphor can not be produced by means of the crystallization from solutions without some special temperature treatment [3]. According to our assumption CsI crystallizes firstly in the unstable form. NaI is slightly soluble in it as the components of the solid state solution are isostructural although they differ by 66% in elementary volumes. That is why a limited amount of sodium ions enter the lattice of CsI. But if we "make" CsI crystallize directly in the CsCl type lattice by increasing the inert gas pressure upon the melt the solid state solution cannot be formed.

An anomalous behavior of CsI near the melting point results in the relatively high viscosity of the material near the crystallization front presenting a problem for initiation of a single centre of crystallization and for removing gas bubbles which staying in the crystal originate the formation of light scattering centers. A great amount of the gas inclusions in their passage through the viscous crystallization zone leave channel tracks behind them. And of course, the polymorphic transformation of the host crystal ruptures the crystal structure leading to the nonuniform distribution of the impurities which tend to locate near defects and grain borders. All these defects are well observed by means of electron microscopy (two examples are given in Fig.1).

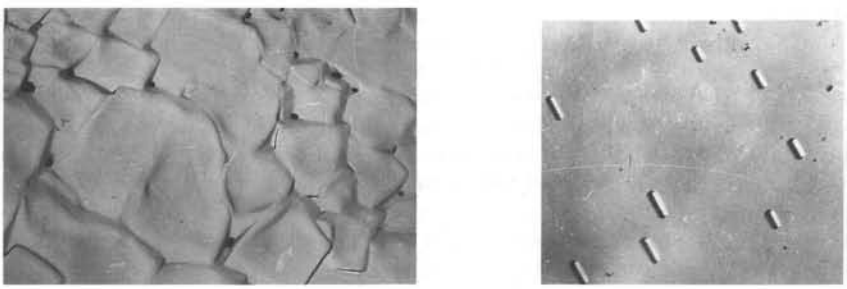

a b

Fig.1. a- microblocks in CsI(Tl) forming as a result of polimorphic transformation (x 16000);
b- NaI-phase inclusions in CsI(Na) along [110] (x 20000).

The structure and the nature of the luminescent centers and the luminescence mechanisms in CsI(Tl) and CsI(Na) have been discussed for many years (see e.g. [7] and references therein). For both systems the existense of more than one types of luminescent centers has been established. For example, there exist at least four bands in Cs(Tl) photoluminescence spectra with maximums at 405 nm, 490 nm, 560 nm and 595 nm. The recombination luminescence spectra are also complicated containing some overlapping bands. The band at 405 nm which is due to electron transitions in the Tl^+ - center never occurs in the recombination luminescence whereas the main scintillation yellow band results from off-impurity center of the type of an exiton perterbed by the impurity. There are many arguments in favour of the contention that the significant amount of thallium ions being responsible for the principle yellow luminescence do not

enter a regular substitutional solid state solution [3,7]. For example, in [3] it was assumed that the 560 nm band is connected with the thallium ions associations localized near near some surface and linear defects in the crystal. L.M. Shamovsky[7] offered the hypothesis about anomalous solid state solutions in alkali halide crystals. Following this model TlI can enter the CsI crystal lattice as regular two-dimentional "buildings in" due to the fact that the dimensions of the unit cell a_{CsI} x $2a_{CsI}\sqrt{2}$ are nearly equal to the dimensions of one of the loops of the α-TlI lattice built by two TlI moleculs.

As for CsI(Na), there is no doubt that we are dealing with undirect activation. At least three types of luminescent centers occur in CsI(Na) [7,8] but as it was already pointed out it is hardly possible that they enter a substitutional or interstitional solid state solution. (However, the possibility of forming the anomalous interstitial solid state solutions similar to that in CsI(Tl) was proposed [7]).

In such conditions with cesium iodide crystallyzing through intermediate polymorphic transition and with the rather poor solubility of the components the impurities tend to an uneven distribution in the crystal readily locating near structure defects and forming clusters or precipitated phases. Such inhomogeneities are the main cause of the fact that the energy resolution of CsI(Na) and CsI(Tl) is more often worse compared to NaI(Tl). The understanding of the origins of this inhomogeneities allows to develop means for their eliminating.

REFERENCES

1. Van Eijk C.W.E. Record of the Intrnational workshop PHYSCI'94, St.-Petersburg, 1994, pp.1-12.
2. Goryletsky V.I., Eidelman L.G., Panova A.N. *et al.* Nucl. Nracks Radat. Meas.,1993, vol. 21, N 1, pp. 109-110.
3. Birman T.A., Gourvitch A.M., Iliyna M.A., Tombak M.I. Izv. Akad. Nauk SSSR, ser. phys., 1977, v. 41, n 7, pp. 1394-1402 (in Russian).
4. Ubbelohde A.R. Melting and crystal structure. Clarendon Press: Oxford, 1965.
5. Thermodinamic constants of substances, edited by V.Glushko, VINITI, Moscow , 1965-1973 (in Russian).
6. Hartmanova M., Urusovskaya A.A., Hanic F., Sebestova E. Czech. J. Phys., 1981,B 31, pp. 620-634.
7. Shamovsky L.M. Crystallophosphors and scintillators in geology, Nedra: Moscow, 1985 (in Russian).
8. Panova A.N. Udovitchenko L.V., Shahova K.V. Izv. Akad. Nauk SSSR, ser. phys. 1974, v. 38, N 6, pp. 1244-1246 (in Russian).

RECENT PROGRESS ON THE R & D OF LARGE SIZE CsI(Tl) AND $PbWO_4$ CRYSTALS

Z. W. Yin and Z. L. Xue, Shanghai Institute of Ceramics (SIC), 1295 Ding Xi Road, Shanghai 200050, China.

ABSTRACT

A summary of some experimental results and the recent progress on the R & D of large size CsI(Tl) and $PbWO_4$ crystals.

INTRODUCTION

Since early 1994, SIC, Shanghai, joined with Beijing Glass Research Institute (BGRI), Beijing, has been in collaboration with KEK, Japan and SLAC, USA respectively to carry out the R&D program aiming at the large size scintillator crystal of thallium doped cesium iodide, CsI(Tl), to be used for their ECAL of the B-Factory experiments. Furthermore, SIC, with BGRI, has also been in collaboration with ETHZ, Swiss and CMS/CERN to proceed the research on the lead tungstate crystal, $PbWO_4$, a kind of new developed scintillating crystal to be used for the ECAL in the CMS/LHC which has been approved by the CERN Council on December, 1994. In this paper, the current status as well as some experimnetal results and progress achieved in the past year on these two kinds of crystal will be presented.

LARGE SIZE CsI(Tl) CRYSTAL

Current status

A modified Bridgman method developed by SIC was employed to grow the large size CsI(Tl) crystals. The pure and Tl doped CsI raw materials provided from Chemetall were being used in the growth of crystals. The average crystal dimension for KEK B-Factory is 55^2x65^2x300 mm^3 and for BABAR (SLAC) Detector is $46^2x60^2x(300\sim330)$ mm^3. 30 cm long fullsized crystals have been successfully grown both in SIC and BGRI. Tables 1 and 2 show respectively the performance of fullsized crystals recently grown for KEK and BABAR experiments.

Table 1. Light output (L.O.) and uniformity of ten tapered Tl doped CsI crystals for KEK B-Factory Experiment.

Crystal No.	JJS004	JJS005	JJS006	JJS007	JJS008
L.O. (%)	29.0	29.0	29.6	29.2	30.0
Uniformity (%)	3.0	4.0	5.2	3.3	9.0

(to be continued)

Proc. Int. Conf. on Inorganic Scintillators and Their Applications, SCINT95, 1996, Delft University Press, The Netherlands

Crystal No.	JJS009	JJS010	JJS011	JJS012	JJS013
L.O. (%)	30.0	29.7	32.5	29.4	28.5
Uniformity (%)	7.0	2.0	6.3	4.9	6.9

Crystals were wrapped with one layer of thick Teflon (170 μ) + Al film (12 μ).

Table 2. Light output and uniformity of four tapered Tl doped CsI crystals for BABAR Detector.

Crystal No.	S_1	S_3	85	87
L.O. (%)	19.1	24.4	20.2	18.9
Uniformity (%)	1.6	4.1	3.2	10.3

Crystals were wrapped with one layer of thick Teflon (170 μ) + Tyvac (~200 μ) + Al film (12 μ).

The data of the light output and the uniformity (both in percentage) listed in Tables 1 and 2 were obtained by comparing with the specified reference crystals, ϕ25x25 mm^3, supplied by KEK and SLAC respectively measured in their same conditions.

Influence of doping on the performance of the crystals

Thallium distribution in the crystal was determined by X-ray Fluorescence Spectroscopy (XFS). Tl contents in different sections of a crystal with different original doping, namely, 100, 200, 300 and 400 ppm (wt), were tested and the experimental results are shown in Fig. 1. It shows that Tl always concentrates at the upper part of the crystal. About the first 80% of the total crystal length, the Tl content is almost evenly distributed and the higher the original Tl doping, the higher the Tl content in this part of the crystal.

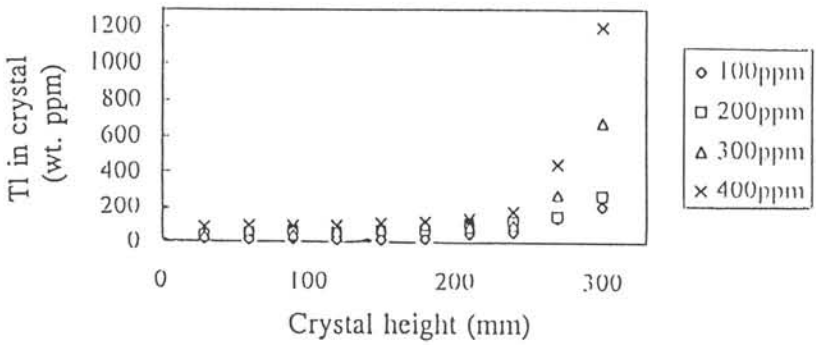

Fig. 1. Tl content along different height of CsI(Tl) crystals with different amount of original Tl doping: 100, 200 300 and 400 ppm (wt).

After cut the top part, i.e., the high Tl content part from the crystal and mechanically processed, then measured their uniformity curves, as shown in Fig.2, which tell us that along with the increase of the amount of Tl doping, besides the light output being increased, its uniformity has also been improved. It is seemly that higher original Tl doping (higher than 400 ppm) would continuously increase the light output of the crystal.

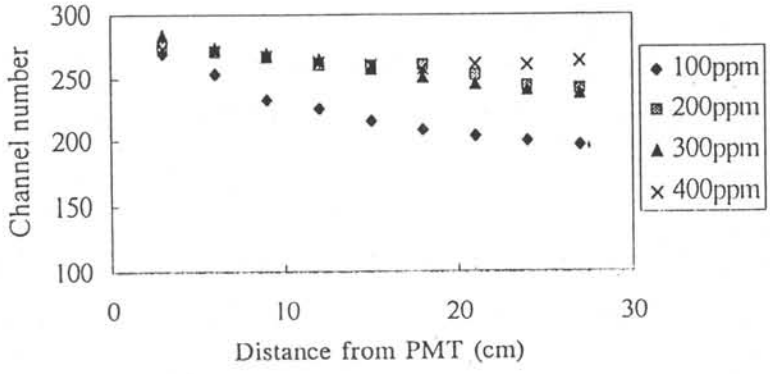

Fig. 2. Uniformity curves of the above four crystals with different amount of Tl doping.

LEAD TUNGSTATE $PbWO_4$ (PWO) CRYSTALS

Current status

The investigation on $PbWO_4$ crystals has been carried out by JCCG (SIC and BGRI) from the beginning of 1994. Now, fullsized PWO crystals in the length of 23 cm have been grown by the modified Bridgman method. Table 3 shows the performance of some of the new-grown PWO crystals.

Table 3. The performance of some new-grown PWO crystals.

Crystal No.	Dimension (mm)	X-ray excited peak w.l. (nm)	Method of wrapping	L. O. p.e./MeV	Uniformity (%)
38	26^2x26^2x190	508	1 layer of Teflon (120μ)	9.7	10.5
39	(26x22)x(22x 21)x210	506	"	10.0	8.5
43	23^2x19^2x230	505	"	15.0	8.0

Effect of annealing on scintillating property of PWO crystals

Lead tungstate ($PbWO_4$) single crystal belongs to the tetragonal system and is of the Scheelite type. Although the crystal is not very difficult to grow in large size, yet it is not easy to be grown perfectly and to have the crystal to be mechanically processed due to its anisotropy and possessing the cleavages on the planes of (101) and (112)[1]. Therefore, annealing is necessary to remove the large stress in the as-grown crystals before the mechanical processing.

The PWO crystals were experienced with annealing under the temperatures in the range of 850 to 950 °C in different atmospheres. After having been properly annealed, the crystals not only can bear the cutting, grinding and polishing, but also can be obviously improved in their scintillating properties[2]. Another annealing effect on the crystal is that the scattering particles in the grown crystal can be evidently eliminated and the crystal becomes more transparent.

Two crystal samples (N0. 34 and No. 35, 45 and 120 mm long respectively) were taken to study the effect of annealing in different atmosphere on the scintillating properties of the PWO crystals. For No. 34, the crystal experienced two days annealing at 920 °C in high vacuum condition (10^{-4} τ). For No. 35, the crystal first experienced one day annealing at 920 °C in oxygen-rich atmosphere. After measuring its transmittance, L.O. and X-ray excited emitting peak wavelength, the crystal then experienced the high vacuum annealing same as that for No. 34 for one day and its properties were measured again. Finally, the crystal experienced another oxygen-rich annealing to see what happened on its properties. The experimental results are shown in Table 4 and Fig. 3.

Table 4. Effect of different annealing conditions on the performance of the PWO crystals.

Crystal No.	Annealing condition	X-ray excited emitting peak wavelength (nm)	Light output (p.e./MeV)
34	Vacuum (10^{-4} τ), 920 °C, 48 hrs.	464	16.0
35	Before annealing	463	9.0
	Oxygen-rich, 920 °C, 24 hrs.	510	11.7
	Vacuum (10^{-4} τ), 920 °C, 24 hrs.	451	5.4
	Oxygen-rich, 920 °C, 24 hrs.	517	5.5

On the scintillation mechanism of PWO crystals

There are literatures [3][4] already existed on scintillation mechanism of the PWO crystals. However, the literature seems to be contradictious to the recent experimental results as shown in Table 4. For example, it was pointed out by Korzhik that the blue light is produced by WO_4^{2-} scintillation center, while the green light is produced by WO_3+F centers. Our experimental result, however, shows that PWO crystals, annealed with an oxygen-rich atmosphere, have an yellowish color and emit a light with its peak at 510 ~ 520 nm (green

light). On the other hands, with vacuum annealing, the emitting peak will shift to 450 ~ 470 nm (blue light) and its transmittance, particularly in the wavelength region below 500 nm, is increased, where oxygen might escape to form oxygen vacancies.

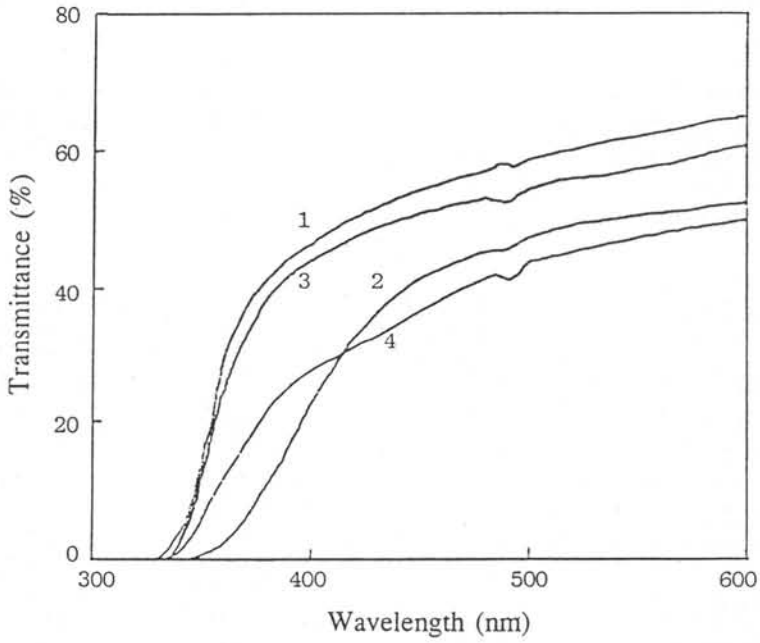

Fig. 3. Effect of different annealing conditions on the transmittance of PWO crystals.

Curves: 1-Crystal No. 34, vacuum annealed; 2-Crystal No. 35, oxygen-rich annealed; 3-Crystal of Curve 2, vacuum annealed; 4-Crystal of Curve 3, oxygen-rich re-annealed.

REFERENCES:

[1] PWO Crystal Group, Shanghai Institute of Ceramics, Chinese Academy of Sciences, "The thermal expansion of the PWO crystals", presented at the $PbWO_4$ Crystal Seminar at Jiading, Shanghai, China, April 10-12, 1995.

[2] Ibid, "Notes on annealing and mechanical processing of the PWO crystals.

[3] M.V. Korzhik et al., "The scintillation mechanism in $PbWO_4$ crystals", Mat. Res. Symp. Proc., Material Research Society, 348, 285-290 (1994).

[4] P. Lecoq et al., "Lead tungstate ($PbWO_4$) scintillators for LHC EM-Calorimetry", CERN-PPE/94-225, December 14, 1994.

GROWTH OF CRYSTALS OF YTTRIUM - ALUMINUM PEROVSKITES WITH RARE EARTH ELEMENTS

S.À. Smirnova, All-Russian Research Institute for Synthesis of Materials
Aleksandrov, Russia
M.V. Korzhik, Institute for Nuclear Problems, Minsk, Belarussia

ABSTRACT

Yttrium - aluminum perovskites with rare-earth elements, crystal growth peculiarity and its influence on their scintillation properties will be discussed

INTRODUCTION

Yttrium-aluminum perovskite crystals (YAP) activated by rare-earth elements are promising materials for scintillators of wide purposes. Having the excellent physical characteristics - high density, hardness, melting temperature and refractive index, they sustain thermal and mechanical loads. This makes them irreplaceable in a number of applications. The manufacturing of large and high quality YAP crystals is rather difficult, and will be discussed below.

The compounds with perovskite structure of $RAlO_3$ composition (where R= Y, La - Lu) form in that part of the phase diagram of R_2O_3 - Al_2O_3, which is considered as an area of unstable phase formation. They are stable in narrow thermal ranges, which much complicates their synthesis. Stability of oxide compounds with perovskite structure (space group D_{2h}^{16}) is determined by dimensional ratios of ion radii of yttrium being in twelve oxide coordination, and aluminum, and oxygen. Distortions of different sorts arise in the structure of aluminum perovskite depending on its individual peculiarities. They can cause polymorphic transitions with change of temperature conditions, which is especially characteristic for $GdAlO_3$ crystals. The closeness of **a** and **b** parameters of the elementary perovskite cell promotes twinning and cracking of crystals, together with their spontaneous reorientation. All these factors are necessary to take into account during crystal growth.

DISCUSSION

YAP crystals were grown with cerium, praseodymium, holmium, erbium and lutetium partially or complete (for Gd, Er, Lu) substituting yttrium. Crystals were grown by the method of horizontal oriented crystallization (HOC, Bagdasarov method). The choice of this method was not accidental. It appeared, that it is possible to produce better crystals by the HOC method in vacuum, than by the Czochralski method. Growth of crystals of high structural perfection is possible under conditions of free melt convection (without forced mixing). The double melt purification from impurities typical for this method (caused by the evaporation of impurities from the melted surface which occurs especially in vacuum and by

Proc. Int. Conf. on Inorganic Scintillators and Their Applications, SCINT95,
1996, Delft University Press, The Netherlands

segregation pushing impurities out from the crystallization front) also promotes formation of crystals free from defects.

Crystals were grown in molybdenum crucibles of boat-like form with dimensions 60×70×16 mm and 0.3 mm wall thickness. The oriented seed was inserted into a narrow boat spout. Powder-like oxides of the appropriate metals were used as mixture. Important for manufacturing of good quality crystals is the preliminary processing of initial components. The best results were obtained after melting their stochiometric blends in air in a set-up with high-frequency heating for the formation of polycrystalline ingots.

The crystallization cycle includes: the creation of a vacuum not worse than 1×10^{-5} Pa in the growth chamber, a temperature increase up to the melting temperature, crystal seeding, crystallization by slow passing of the crucible through the heating zone, crystal cooling and annealing.

The search for the optimal conditions for the manufacturing of good quality YAP crystals activated with various rare-earth elements (REE) was conducted by variation of the speed of the crucible movement through the heating zone (from 2 up to 12 mm/h), the width of the melting zone, form of crystallization front, modes of crystal cooling and annealing.

The main reasons, which complicates the growth of all YAP crystals, are: the narrow range of stability, upset of stochiometric ratio of components, propensity to doubling and cracking.

If one addresses the phasediagram of Y_2O_3 - Al_2O_3 [1], it is possible to see that from the three oxide compounds of the various structures which can be formed, the narrowest range of steady phase formation is for the perovskite aluminates. For the manufacturing of the crystals it is necessary not only to get into this narrow interval of the corresponding temperatures and compositions, but also to maintain it during the total growth cycle, which is rather difficult. For example, the crystals of yttrium-aluminum garnets formed in the same system can be produced not only under significant deviations in the melt stochiometry, but also with varying temperature modes.

The upset of the stochiometric component ratio during growth is caused by the growth method itself and by the physical-chemical properties of the melt. In conditions of high vacuum ($P=1\times10^{-5}$ Pa) there is evaporation from the melt surface. Thus aluminum oxide, having higher vapor pressure in comparison with yttrium oxide and REE, evaporates more intensively. As a result, the melt is enriched with yttrium oxide (and REE), the phase balance is shifted in the party of compounds with the higher contents of REE oxides, in particular of the monoclinic $Y_4Al_2O_9$ phase. The phase concentrates in a kind of a thin rim on the crystal bottom, because it has greater density, and serves as a source of additional tension and cracks in a crystal. To avoid these troubles, the growth is performed from a melt in which a small excess of aluminum oxide is on purpose entered.

We note, that the growth of YAP crystals under conditions of excess aluminum oxide in the melt requires certain skills, because it is easily possible to run into the other extreme and to produce a crystal with aluminum oxide inclusions.

All YAP crystals have the tendency to twinning. The twins are formed usually along the direction of crystal growth closer to the lateral crucible walls. The doubling at the crystal center is very characteristic. Beginning from the seed the double dissects a crystal over the whole length forming two blocks rotated 1.5 - 2 angular degrees relatively to the [001] direction.

It is possible to remove twinning by growing the crystal along the optimal crystallographic direction [001] and using a certain seeding procedure. However, we could not avoid the formation of the doubles with the help of the above-mentioned procedures during production of gadolinium aluminate crystals.

Rather large and good quality crystals with impurities of Ce (1% mass.), Pr (1-3% mass.), Ho (1% mass.), Er (1-30% mass.) were manufactured as a result of the performed experiments. The crystals have the form of plates with the dimensions of non-defective areas not less than 50×50×20 mm. The crystals with complete substitution of Y to Gd are applicable for research, but they contain doubles. We could not produce $LuAlO_3$ crystals. In all experiments, garnet ($Lu_3Al_5O_{12}$), lutetium oxide (Lu_2O_3), and lutetium aluminate ($Lu_4Al_2O_9$) were formed (determined with X-ray analysis) from melts of stochiometry blend with excess or deficit of aluminum oxide. The garnet phase and about 20 % lutetium oxide predominated in the spout part of a crystal. $Lu_3Al_5O_{12}$ dominates in the middle accounting for 60-65% of the mass, and the remainder was of $Lu_4Al_2O_9$. The end part was represented mainly by lutetium aluminate of $Lu_4Al_2O_9$ and $Lu_3Al_5O_{12}$ composition (35-40% mass.).

Some curious detail was observed. Parameters of the lutetium garnet elementary cell from various parts of the crystals produced under different conditions were measured. It was established, firstly, that the elementary cell parameters (ECP) of $Lu_3Al_5O_{12}$ formed during lutetium aluminate synthesis was always much larger than of those ones produced from the garnet melt (11.926 ÷ 11.950 and 11. 9140±0005 Å, respectively). Secondly, ECP of synthesized $Lu_3Al_5O_{12}$ increase with increasing amount of lutetium oxide phase in the sample. There is the impression, that only a part of lutetium is included in the garnet structure, and not in dodecahedron, but in octahedron substituting aluminum.

In conclusion we note, that the activity on growth and research of YAP crystals with rare-earth elements is proceeding and it will be directed to the production of large qualitative crystals for scintillator usage.

REFERENCES

1. Compounds of rare-earth elements, Nauka, Moscow, 1983.

PREPARATION OF SINGLE PHASE $LuAlO_3$ -Ce SCINTILLATOR CRYSTALS

A.G.Petrosyan, and C.Pedrini*,
Institute for Physical Research, Armenian National Academy of Sciences, 378410 Ashtarak-2, Armenia, and
*Laboratoire de Physico-Chimie des Materiaux Luminescents, Universite Claude Bernard Lyon1, CNRS n^0 442, Bat 205, 69622 Villeurbanne Cedex, France

ABSTRACT

The vertical Bridgman technique has been applied to growth of $LuAlO_3$ -Ce scintillator crystals. Conditions were found to obtain clear single crystals free of twins, light scattering and traces of a second phase. Material thermal stability, melting behavior, and Ce incorporation have been studied. By employing spectral emission analysis a value of k=0,17 for partition coefficient of Ce ions was determined.

INTRODUCTION

Developments in inorganic scintillators [1,2] place special requirements on material science and preparation techniques of current materials of interest. Cerium-activated lutetium orthoaluminate ($LuAlO_3$ -Ce) has been reported in two recent papers [3,4] as a promising scintillator crystal material for nuclear detection applications where high stopping power, fast decay and high light yield are the prime considerations. The attractive features of $LuAlO_3$ -Ce are high density, (8,34g/cc), high effective Z, short-wave (visible-near ultraviolet) luminescence and short decay times.

The current status of $LuAlO_3$ crystals assumes important optimization of Ce doping level, control of Ce ion charge state and control of impurities added unintentionally. In addition, improvements in general preparation techniques of this unstable perovskite phase are desirable for larger size and better optical quality. Adaptation of different techniques could provide complementary results to achieve these goals. In the present study for single crystal preparation we have applied the vertical Bridgman technique. Material thermal stability, melting behavior and Ce incorporation were studied in view of optimization of the growth conditions leading to good quality single phase material.

CRYSTAL GROWTH

$LuAlO_3$ -Ce single crystals have been grown by the vertical Bridgman technique employing resistance heating and molybdenum containers under an atmosphere consisting of Ar and H_2 . The Ce content in the initial melts was between 0,2 and 0,7 at.% with respect to Lu. Growth rates of 1-3 mm per hour have been used. Single crystals have been prepared by the selective self-seeding process, described in details in [5]. In brief, it is based on the material behavior concerning (i) solid structures that develop as a function of supercooling (ΔT^-), (ii) the degree of supercooling that can be exhibited by melts of $LuAlO_3$ composition as a function of the superheating extent (ΔT^+) and the holding time (t) in the molten state, and (iii) the perovskite phase thermal behavior in between spontaneous solidification temperature (T_{SP})

Proc. Int. Conf. on Inorganic Scintillators and Their Applications, SCINT95,
1996, Delft University Press, The Netherlands

and the melting point (T_m). Crystallization scheme employed suppresses growth of 3:5 (garnet) and 2:1 (monoclinic) phases and provides nucleation and growth of the perovskite phase.

3 to 4N purity lutetium and cerium oxides have been used. Prefired powders were mixed with vacuum melted crystalline alumina and melted in Mo crucibles. Ce concentration in the melts was 0,2-0,7 at.% with respect to Lu. The melts were holded under enclosed atmosphere consisting of Ar and H_2 above critical $t\Delta T^+$ values (typically 60 min and 60° K respectively) and subsequently solidified at rates 1-3 mm per hour. Crystal cooling rates were around 150 K/h. Colorless, optically transparent (free of twins and light scattering) crystals have been obtained. A small amount of 2:1 phase has been detected in the first portions of the solid which disappears as the growth of 1:1 phase proceeds on spontaneous section. The single crystal part contains no traces of a second phase as checked by X-ray diffraction. No visible attack on the crucible metal has been detected. It is further assumed that by using tungsten resistance heating elements and of a mixture of H_2 and Ar, the partial pressure of O_2 and therefore the fraction of possible Ce^{4+} ions are very low. The spectroscopy of grown crystals is typical of cerium-doped orthoaluminates possessing the perovskite-type structure. Fluorescence and scintillator properties are presented elsewhere at this conference [6].

THERMAL BEHAVIOR

$LuAlO_3$ readily decomposes if heated from room temperature to temperatures above 1000° C at a rate increasing with raising of the treatment temperature [7]. The observation that self-seeded growth occurs in Bridgman geometry following nucleation of the perovskite phase and melt supercooling removal, suggests stability of the perovskite phase between T_{SP} and T_m . Dissimilar stability levels being exhibited by $LuAlO_3$ during crystal growth and in annealing experiments can be explained in terms of the phases formed as a function of the temperature route and of the temperature raising rate as shown in Table 1 and Fig.1.

Table I.
Phases observed after heat treatment of single phase $LuAlO_3$ as indicated.

Temperature route	Temperature raising rate (°K/min)	Annealing temperature/duration, °C (min)	Phases observed at T_R (X-ray)
$T_R \rightarrow T_{an}$	100	1700(5)	3:5 + oxide
$T_R \rightarrow T_{an}$	2000	1700(5)	1:1 only
$T_R \rightarrow T_m + 20^0C$	100	1980(5)	3:5 + 2:1
$T_{SP} \rightarrow T_m + 20^0C$	100	1920(5)	1:1 only

T_R - room temperature, T_{an} - annealing temperature, T_m - melting temperature, T_{SP} - spontaneous solidification temperature.

The rate of raising from room temperature to that in between 1600°C and 1850°C exerts detectable influence upon decomposition degree. Samples rapidly raised to the annealing point decompose if treated for more than 40 min, whilst in the case of slow-rate raising only around 5 min are necessary for complete decomposition of the initial charge suggesting that in the latter case decomposition is progressing below 1600°C. Decomposition

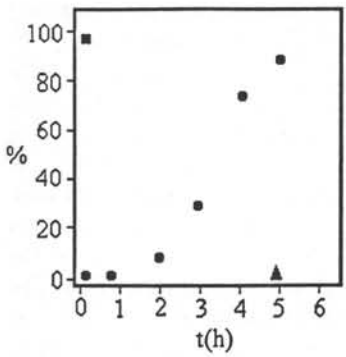

Fig.1 Degree of decomposition (%) of $LuAlO_3$ at 1700°C as a function of the annealing time (t): (●) raised from T_R at 2000°K/min, (■) raised from T_R at 100°K/min, (Δ) raised from T_{SP} at a rate 100°K/min.

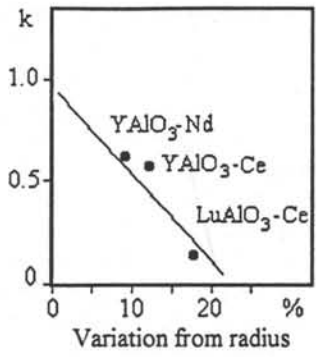

Fig.2. Distribution coefficients in orthoaluminate hosts as a function of the size mismatch

starts from the surface followed by formation of an opaque ceramic-like layer (of 3:5 + oxide) gradually increasing in height with increase of the treatment duration that is typical for a diffusion favoured process. This behavior is not in agreement with conventional nucleation process of phase transition within the sample volume and needs further studies.

The perovskite phase held at 1700° C (directly after solidification at T_{SP}) for 5 hours, exhibited no signs of decomposition (Fig. 1). Congruent melting behavior (T=1900 ±15 ° C) is observed in the case of raising from T_{SP}. Note that in the course of slow temperature raise from T_R, the material decomposes and the melting point measured is ~1960° C (Table 1). The difference in thermal stability and melting behavior observed as a function of the temperature route, suggests that cooling to room temperature produces a change in material properties that decreases stability exhibited upon subsequent heating. A better understanding of thermal behavior achieved by employing both different temperature raising rates and routs, suggests that revision of the existing phase diagrams is necessary.

Ce INCORPORATION

Triply charged cerium ions substitute for 12-fold coordinated Lu^{3+} ions at sites with C_S symmetry. A limiting factor for Ce incorporation is the size difference between Ce^{3+} (1,13A,VIII) and Lu^{3+} (0,97A, VIII) ions which is around 17,5% with respect to Lu. An additional limiting factor is isodimorphism of involved solid solution components ($LuAlO_3$ is orthorhombic while $CeAlO_3$ is rhombohedral).

Ce analysis were performed by spectral emission technique employing standard samples with fraction of Ce between 0,05 and 1 at.%. A value of k = 0,17 ± 0,05 has been determined for the distribution or partition coefficient by measuring the Ce content in single crystal and in the rapidly solidified melt both near to the interface. Close to this values of k have been measured by graphical solution of distribution curves of Ce measured along the crystal height of 3 cm which are monotonic and correspond to complete melt stirring approximation.

Fig.2 shows k values of rare-earth dopants in orthorhombic crystals as a function of variation of the dopant ion size from that of the host ion. Data from references [8,9] for Czochralski grown crystals of $YAlO_3$-Nd (k=0,65) and $YAlO_3$-Ce (k=0,6) have been used. The decrease of k values against the size mismatch is typical for systems involving isoelectric substitutions with close values of electronegativities.

CONCLUSIONS

In this article we have presented the results concerning application of the vertical Bridgman technique to growth of $LuAlO_3$-Ce scintillator crystals. Optimization of the major growth parameters has provided clear single phase crystals free of twins and light scattering. Material thermal stability region and congruent melting have been depicted. The difference in stability levels being exhibited during crystal growth and in annealing experiments is explained in terms of the phases formed as a fiunction of the temperature route and of the temperature raising rate. Distribution coefficient value of $k = 0,17 \pm 0,05$ for Ce incorporation has been measured by spectral emission analysis.

Acknowledgments

This work was partially supported by NATO grant HTECH. CRG 940392.

References

1. C.W.E. van Eijk,. Proceedings of the International Workshop on Physical Processes in Fast Scintillators, September 30 - October 3. 1994 St.Petersburg, Russia, p.1.
2. M.J.Weber. To be published in the Proceedings of the V International Conference on Calorimetry in High Energy Physics.
3. W.W.Moses, S.E.Derenzo, A.Fyodorov, M.Korzhic, A.Gektin, B.Minkov, and V.Aslanov, IEEE Trans.Nucl.Sci. NS-42 (submitted for publication).
4. A.Lempicki, M.H.Randles, D.Wisniewski, M.Balcerzyk, C.Brecher, and A.J.Wojtowicz, IEEE Trans.Nucl.Sci. NS-42 (submitted for publication).
5. A.G.Petrosyan, J.Crystal Growth 139 (1994) 372.
6. C.Dujardin, C.Pedrini, D.Bouttet, J.W.M.Verweij, A.G.Petrosyan, A.Belsky, A.Vasil'ev, E.I.Zinin, and P.Martin (this conference).
7. I.A.Bondar, A.K.Shirvinskaya, V.F.Popova, I.V.Mochalov, and A.O.Ivanov, Dokl.Akad.Nauk SSSR 246 (1979) 132.
8. P.Korczak, and C.B.Staff, J.Crystal Growth 20 (1973) 71.
9. E.G. Gumanskaya, O.A.Egorycheva, M.V.Korzik, S.A.Smirnova, V.B.Pavlenko, and A.A.Fedorov, Opt.Spectr. 72 (1992) 215.

OPTIMIZATION OF BASIC MATRIX COMPOSITION OF SCINTILLATING FLUORIDE HAFNATE Ce_3^+-DOPED GLASS

L.N.Dmitruk, S.Ch.Batygov, N.N.Vinogradova
General Physics Institute, 117317 Moscow, Russia
E.G.Devitain, V.A.Kozlov, S.Yu.Potashov
Lebedev Physical Inst., 117924, Moscow, Russia
V.D.Fedorov
All-Russian Chemical Technlogy Inst., Moscow, Russia

23 August 1995

Abstract

Crystallisation behaviour and properties of scintillating HfF_4- based glasses with increased concentration of Ce were studied. Most stable compositions were determined. It is shown that the addition of Ce as $CeCl_3$ enables to get stable glasses with concentrations of Ce_3^+ up to 12-13 at.% and almost double light yield compared to known fluoride compositions. The crystallisation behaviour of glasses doped with some Ce oxide compounds was also studied for which a shift of emission line to the long-wave range of the spectrum is observed.

1 INTRODUCTION

Fluoride Hafnate glasses are interesting as a fast heavy scintillator for gamma-ray detectors [1]-[2]. The advantage of glasses over crystalline scintillators is smaller technological cost, particularly in the production of large-size spieces.

In the present work the possibility of improving glass properties by composition modification is studied. One of approaches was a search for compositions with an increased Ce_3^+ concentrations. The problem is that this concentration increase gives rise to glass crystallisation [3]. Another approach was an attempt to change the local environment of the Ce ion by addition of Ce_3^+ as chloride and oxide compounds.

2 EXPERIMENT

At present a big number of fluoride glass forming systems is known [4]. Proceeding from the physical properties (density, hygroscopy, etc.) and glass forming properties the following systems have been chosen: I. $HfF_4 - BaF_2 - CeF_3 - AlF_3 - Li(Na, Cs)F$; II. $HfF_4 - BaF_2 - CeF_3 - AlF_3 - YF_3 - Zn(Cd)F_2$. The ranges of components concentration variation in system I were, mol.%: 5-15 CeF_3, 45-65 HfF_4, 10-25 BaF_2, 0-17 $Li(Na, Cs)F$. In system II - 2-10 CeF_3, 20-30 HfF_4, 20-28 BaF_2, 6-15 YF_3, 0-10 AlF_3, 20-33 $Zn(Cd)F_2$. The glass stability was estimated using the cooling rate under which crystallisation took place. For the samples which were obtained as glasses at the cooling rates of $< 40°C$ the light yield and emission spectra under X-ray and synchrotron excitation was determined.

Proc. Int. Conf. on Inorganic Scintillators and Their Applications, SCINT95,
1996, Delft University Press, The Netherlands

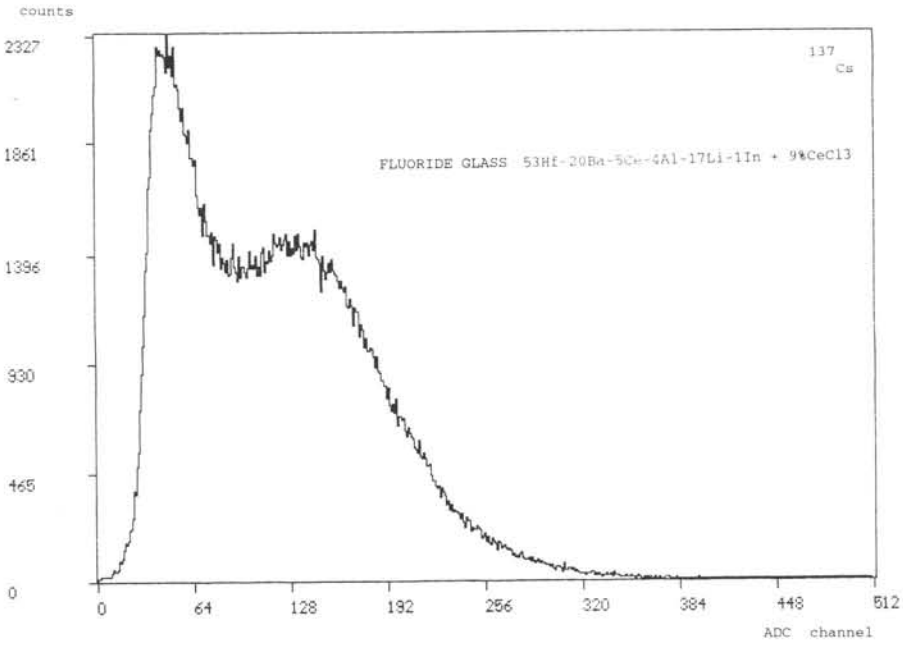

Fig.1 Pulse-height spectrum of the fluoride-chloride glasses, obtained using ^{137}Cs source.

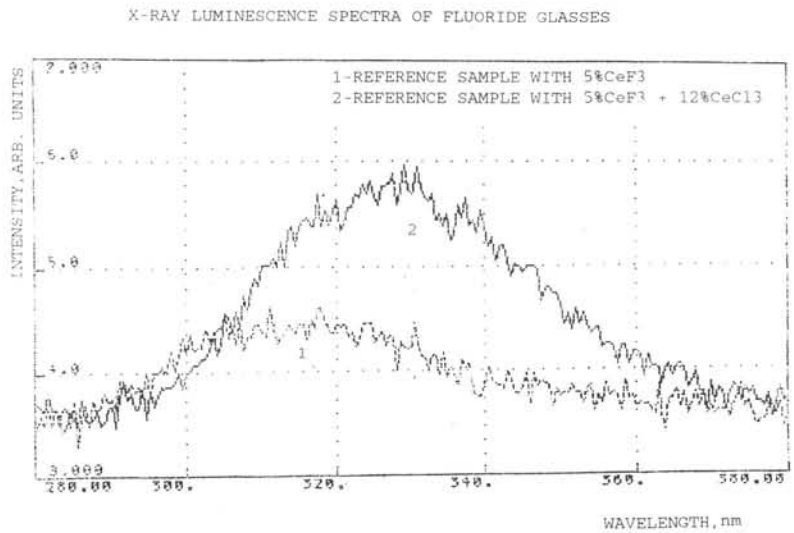

Fig.2 Emission spectra under the X-rays excitation. 1 -fluoride glass and 2 -fluoride-chloride glass (10% $CeCl_3$).

3 RESULTS AND DISCUSSION

A substantial drop of the glass-forming properties of the basic compositions I and II occurs with an increase of CeF_3 concentration. Out of all the samples from this system the most stable was the one where LiF is replaced by CsF in the relation close to the composition of the eutectic in the LiF-CsF system. The light yield of such glasses exceeds that of the basic composition glasses. In system II it is possible to obtain stable glasses at a CeF_3 content up to 7-8%. However these glasses have both a lower density and light yield. The replacement of ZnF_2 by CdF_2 increases the density, but the suppression of Ce luminescence takes place. The emission spectra and decay times of glasses I and II with increased concentrations of CeF_3 are close to basic compositions.

The introduction of $CeCl_3$ makes it possible to obtain stable glasses with 12-13 at.% Ce. In Fig.1 the emission spectrum under X-ray excitation of glass with $CeCl_3$ is shown. Its light yield is almost a factor of 2 graeter than that of a basic glass. In addition a shift of the emission spectrum to lower region is observed.

The following Ce oxide compounds were added in the glass: CeP_2O_7, $CeAlO_3$, $Ce(MoO_4)_3$, $CeGaO_3$, Ce_2SiO_5. The stable crystallisation of glasses was obtained for aluminate, silicate, galate concentrations $< 0.5 - 0.7\%$. The maximum concentrations were reached for Ce phosphate (7 wt.%) and molybdate (4 wt.%). The results of an emission spectra study described in [5] has shown that the modification of the fluoride glasses with oxide dopants leads to a considerble spectral redistribution of emission energy to the region about 400 nm. This result is interesting from the viewpoint of radiation hardness improvement.

4 CONCLUSION

In the fluoride hafnate systems studied the preparation of high Ce concentration glasses is a complicated goal due to crystallisation. The developed compositions with high stability (fractional replacement of LiF by CeF_3) enables to increase the light yield by 15-20 % compared to standard compositions. More promising are the mixed fluoride-chloride glasses. In this system it is possible to obtain glasses with a Ce_3^+ concentration of 12-13 at.% and a light yield up to almost 1% $NaI(Tl)$. A more detailed study of the fluoride-chloride glasses and those with the oxide dopings is one of the promising ways to increase the light yield and radiation hardness.

5 ACKNOWLEDGMENTS

We would like to express our gratitude to Dr. R.Brown and his colleagues from RAL for useful discussions and support in our work.

REFERENCES

[1] E.G.Devitsin et al.:*CRYSTAL 2000 Proceedings.* Chamonix, Sep.1992, p.401.

[2] P.E.Hobson et al.:*CRYSTAL 2000 Proceedings.* Chamonix, Sep.1992, p.343.

[3] L.N.Dmitruk et al.:*Glass Physics and Chemistry (in Russian)*, V19,1992,1,p.22.

[4] M.Poulain: *Proceedings of the 9-th Intern. Sympos. on non-oxide glasses.* Hangzhou, China, May 1994, p.140.

[5] E.G.Devitsin et al.:*Proceedings of SCINTILLATOR-95 Conf..* Delft, Netherlands, August 1995.

THE PRODUCTION OF LARGE, INEXPENSIVE BLOCKS OF SCINTILLATING FLUOROHAFNATE GLASS.

P R Hobson, T Price,
Department of Physics, Brunel University, Uxbridge, Middlesex, UB8 3PH, UK
D Bowen, T Cliff,
Johnson Matthey plc, Orchard Road, Royston, Hertfordshire, SG8 5HE, UK
B Kinsman, R Smith,
Merck Ltd, Merck House, Poole, Dorset, BH15 1TD, UK
R M Brown, P S Flower, P W Jeffreys, M Sproston,
Rutherford Appleton Laboratory, Chilton, Didcot, Oxford, OX11 0QX, UK
K J McKinlay, J M Parker,
Department of Engineering Materials, Sheffield University, Mappin Street, Sheffield, S10 1JD, UK

ABSTRACT

Fluoride glasses are generally made in small volumes for high value products such as optical fibres. Ce-doped fluorohafnate glass scintillators for particle physics experiments require large scale production. By careful attention to glass composition and fabrication we have made blocks of 2x3x14 cm^3 and are developing the use of cheap fluorides, of adequate quality for glass making.

INTRODUCTION

Homogeneous electromagnetic calorimeters for experiments at the Large Hadron Collider at CERN must be fast, radiation resistant and affordable [1]. Lead silicate glasses cannot be used due to the high radiation levels that will be encountered. Cerium doped fluorhafnate glasses are a candidate scintillator that has been investigated in detail recently [2]. Their optical, scintillation and radiation damage properties are discussed elsewhere in these proceedings [3]. Here we concentrate on the technical aspects of making large blocks at a commercial cost approaching \$1/cm^3.

METHOD

Fluorohafnate glass batches consist of pure fluorides weighed to an accuracy of at least 0.1% of the batch weight in a sealed dry box to reduce contamination by water and dust. They are transferred into a controlled atmosphere glove box inside a sealed container. Where oxide contamination of the raw materials is suspected, an excess of a fluorinating agent is added. Glasses are melted in a platinum/5% gold crucible inside a silica liner attached to the glove box. The melting chamber atmosphere can be separately controlled, allowing the melt redox to be varied with time. To make a glass free of black reduced species an air/N_2 atmosphere was used during initial melting. Subsequently the air was switched off. With large melts the response of the melt redox equilibrium to such changes was slow but improved on stirring. Fig. 1 illustrates the enhanced UV transmission associated with this melt schedule, arising from the reduction of Fe impurities to the Fe^{2+} state [4].

Melts were cast into aluminium which is largely unaffected by the hot fluoride melt and has a high thermal conductivity. The casting temperature was above the glass liquidus temperature to avoid premature crystallisation. For the large blocks, the mould mass and initial temperature were selected knowing the thermal mass of the fluoride melt and the thermal diffusivities of both melt and mould. These factors define the interface temperature after casting and its subsequent evolution. This temperature should be near the glass transition to avoid sticking, thermal shock cracking and to maximise the rate of heat transfer. Subsequent annealing is also important to reduce the risk of subsequent block fracture and requires carefully controlled cooling of the block.

Early work concentrated on glass composition development to give a maximum scintillation yield with a minimum radiation length, but the requirement to make blocks at least 2 cm thick meant turning to more stable glass forming compositions. Compositions closer to the ZBLAN (Zr, Ba, La, Al and Na fluorides) and ZBLALi glasses used for optical fibres were therefore adopted. Samples have been made in sizes from 1 to 84 cm^3. The smaller samples were used for preliminary testing and the larger blocks for developing the manufacturing technology and for bulk yield tests.

Proc. Int. Conf. on Inorganic Scintillators and Their Applications, SCINT95,
1996, Delft University Press, The Netherlands

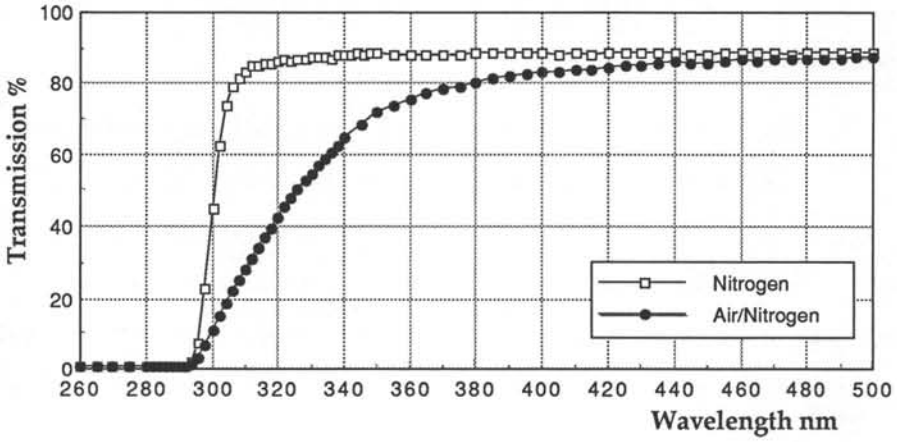

Fig. 1. Showing the effect of melting atmosphere schedule on UV transmission

RESULTS AND DISCUSSION

As part of the optimisation process, a series of glasses containing different alkali metal fluorides was studied (Table 1). Glasses based on NaF have the most suitable properties and allowed blocks measuring 2x3x6 cm3 to be cast while similar blocks containing LiF partially crystallised. NaF containing glasses are however slightly less dense than those containing LiF. In a second melt series the Al atom was replaced by the heavier In atom which should have a small beneficial effect on radiation length. Because In exists in 2 oxidation states and can therefore act as a trap for electronic defects radiation hardness also improved but at the expense of scintillation yield [3].

RF	LiF	NaF	KF	CsF
T_g/K	538	552	562	563
T_x-T_g/K	112	127	78	109
Scin. yield	10.3%	9.6%	8.0%	8.3%

Table 1. Glass transition temperature, T_g, stability parameter (T_x-T_g, where T_x is the crystallisation onset temperature measured by DSC), and scintillation yield of HBLA glasses doped with RF

In our glasses some impurities (e.g. Zr) can be tolerated at the 1% level without reducing performance. Thus eliminates an expensive stage in HfF_4 purification, viz. the removal of residual Zr. Critical impurities are those transition metals and lanthanides with absorption bands in the Ce^{3+} emission region at 325 nm. Typically their concentration must be < 10 ppm [4]. Our early experience with impure (i.e. inexpensive) HfF_4 was that it contained Fe at levels 2 orders of magnitude higher than acceptable. Recently an alternative supply of $HfCl_4$ has been located in which Ti is the only important impurity. Further purification, and the final fluorination process, reduced the Ti concentration without significant cost. Tests on several $HfCl_4$ batches have shown a remarkably constant Ti level, low enough for our application.

Fluoride glasses have large volume shrinkages as they are cooled from their glass transformation temperature (T_g). One consequence is that the glasses shrink away from the moulds during cooling so lowering the rate of heat transfer. This also means that considerably more surface preparation is needed subsequently to produce optical quality blocks. A further consequence is that small bubbles trapped during casting grow and act as optical scattering centres. This was a particular problem with NaF free glasses, probably because of their high T_g and also their viscosity during casting allowing more bubbles to be trapped but was almost eliminated by using HBLAN compositions.

The cooling rate of the centre of large 2x3x14 cm^3 blocks is low for several reasons. Firstly insulating gaps of up to 0.5mm occur at the mould glass interface as a result of the shrinkage already discussed. Secondly the thermal diffusivity of fluoride glass is low because of the high inherent structural

disorder (which reduces the thermal conductivity) and the high specific heat per unit volume of the melt arising from its dense structure and the large amount of heat taken to break down the glassy network above T_g, in addition to the Dulong and Petit specific heat. Finally the infrared transparency of the material and the low temperatures involved means that radiative heat transfer is inoperative during cooling. On the other hand the low melt viscosity encourages convection in the centre of the block. The slower the melt cooling rate, the more likely are crystals to grow particularly if nucleating agents such as oxide impurities are present.
Blocks of good optical quality have been made and tested in a high energy proton beam. The scintillation light output from one end of a laterally excited block has been measured. Fig. 2 shows a comparison with a lead tungstate single crystal, the main competitor for this application.

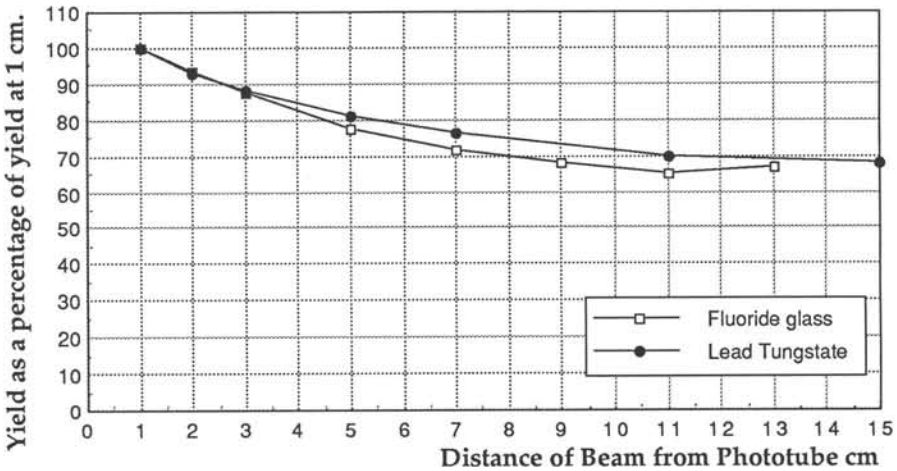

Fig. 2 Showing the scintillation yield of a glass block irradiated at various positions along its length, and in comparison with the equivalent yield from a lead tungstate crystal.

CONCLUSIONS

Large, high quality optical blocks of fluoride glasses can be manufactured giving useful scintillation yields. Although radiation hardness is not ideal improvements can be made by adding suitable dopants. Costs can be significantly reduced by the appropriate choice of raw materials.

ACKNOWLEDGEMENTS

We would like to thank L.N.Dmitruk from the General Physics Institute in Moscow for many helpful discussions and for supplying some of the HfF_4 used in these tests.

This work has been supported by the Particle Physics and Astronomy Research Council

REFERENCES

[1] CMS. The Compact Muon Solenoid . Letter of intent. CERN/LHCC 92-3.
[2] E.G. Devitsin et al., Heavy Scintillators for Scientific and Industrial Applications, Edited by F. de Notaristefani et al., Editions Frontiere, Gif-sur-Yvette, 1993, 401-406.
[3] P R Hobson et al., Dense, Fast, Radiation-tolerant Fluorohafnate Glass Scintillators for Electromagnetic Calorimeters in High Energy Physics, published in this proceedings.
[4] France, F., Carter, S. and Parker, J.M., Phys. Chem. Glasses, 27, 32-41 (1983).

PRECISION MACHINING, POLISHING AND MEASUREMENT OF MECHANICAL AND TOXICOLOGICAL PROPERTIES OF LEAD TUNGSTATE CRYSTALS FOR THE CMS ELECTROMAGNETIC CALORIMETER

Craig R. Wuest, Baruch A. Fuchs, Xiaorong Shi
Lawrence Livermore National Laboratory
P. O. Box 808
Livermore, CA 94551 USA

We have developed new machining and polishing techniques that have previously been applied to large scintillating crystal arrays for high energy physics experiments such as the Barium Fluoride Electromagnetic Calorimeter for the GEM Detector at SSCL, the CsI Electromagnetic Calorimeter for the BaBar Detector at PEP-II B Factory at SLAC and the 110,000 crystal CMS Lead Tungstate Electromagnetic Calorimeter at LHC at CERN. We discuss earlier results achieved with diamond machining and polishing methods and present new results on diamond machining of lead tungstate crystals. Additionally we present new results on mechanical properties of lead tungstate including toxicological data important for the safe handling and processing of this material.

INTRODUCTION

New machining and polishing techniques have been developed at Lawrence Livermore National Laboratory (LLNL) for large scintillating crystals that optimize crystalline surfaces while minimizing sub-surface damage or stress. Surface optimization is critical to ensure long term stability of crystals in calorimeter applications where they may be subject to many years of radiation exposure, temperature cycling and confinement without the ability to replace or repair degraded or damaged crystals. Our studies on barium fluoride crystals produced fully crystalline surfaces using diamond-loaded pitch lapping techniques [1]. These crystalline surfaces were verified by Atomic Force Microscopy (AFM) and Rutherford Back-scattering (RBS) analyses. Surface roughness of about 10–20 angstroms and sub-micron mechanical tolerances were demonstrated on large crystals. Mass production techniques were also developed for machining and polishing up to five 50 cm long crystals at one time. The technology was found to be applicable for a number of new crystal detectors proposed at high energy physics colliders including most recently the Compact Muon Solenoid Detector Lead Tungstate Electromagnetic Calorimeter (CMS ECAL) at LHC [2].

LLNL has an active program of study on lead tungstate (PWO) as part of our responsibility within the CMS ECAL Program. This includes the development of a specialized cutting and polishing machine for proper characterization of PWO boules immediately after removal from the furnaces and prior to cutting the crystals to their final long, tapered trapezoidal shapes. Crystals are to be inspected using a transmissometer to ensure the requisite optical quality. In addition the endfaces of the crystal need to be polished to a high quality to enhance light collection properties, which are dependent on high reflectivity mirrored front and rear surfaces. These mirrored surfaces might be applied in the form of a reflective coating, in which case the quality of the surface is critical for the long term stability of the coating. Additionally a polished optically flat surface is required for a high quality bonding of the photodetector to the crystal (the CMS ECAL will use avalanche photodiodes). We present work on machining PWO crystals applicable to the development of this special endface cutting and polishing machine.

PWO machining produces PWO wastes, typically fine chips of the material mixed into cutting oil and solvents. We are concerned with the safety of the personnel who will come into contact with these waste products as well as the environmental implications of disposal of lead-containing wastes. In order to provide quantitative answers to the question of lead contamination of personnel, machines and the environment we have begun a program of study of PWO solubility in cutting oils.

LLNL is working in collaboration with ECAL collaboration members at CERN and elsewhere to develop the thermal model of the ECAL along with the proper monitoring system and we are also working to design the support structure for the large number of crystals. Because of this responsibility we are making measurements of fundamental crystal properties in order to properly understand the thermal and mechanical behavior of the CMS ECAL.

LEAD TUNGSTATE SURFACE PREPARATION AND ANALYSIS

Surface preparation is critical to the performance of crystals for a number of reasons. First, an improperly prepared (machined, ground, polished, lapped) crystal suffers from induced stresses and deformations in the first few hundred microns of the surface. These stresses can manifest themselves in the formation of cracks (crazing) over long times, or more quickly when subjected to extremes of heat, radiation, humidity, etc.. Surface stresses can be minimized using well-known polishing and lapping techniques that *gently* bring the surface to a final finish. These techniques have been developed at LLNL for barium fluoride and also applied to cerium fluoride, lead fluoride and

Proc. Int. Conf. on Inorganic Scintillators and Their Applications, SCINT95,
1996, Delft University Press, The Netherlands

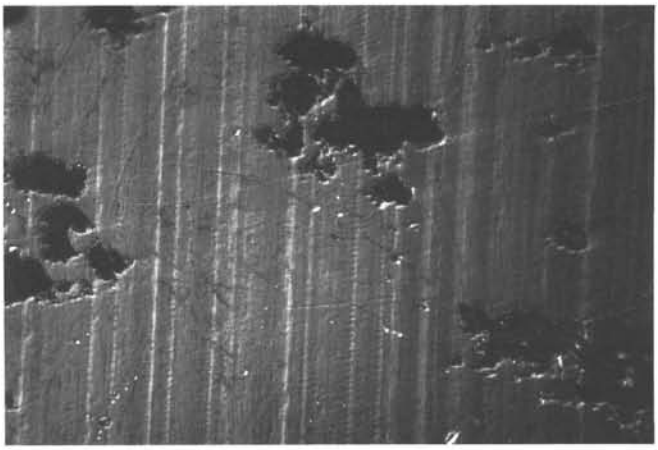

Figure 1. Photograph (179x) of single point diamond turning of PWO showing regions of both plastic flow and fracture.

PWO. Improper surface preparation can introduce contaminants into the surface of the crystal. Under certain conditions these contaminants can migrate into the bulk of the crystal and cause areas of radiation susceptibility. Because these scintillator materials emit their light typically in the blue or near UV, surface finish is especially important for good light transport properties.

We have previously described surface preparation techniques explored at LLNL, including ion beam milling, diamond turning with a single point diamond tool, and various polishing/lapping techniques [1]. In general we have found that ion beam milling provides the best crystalline surface, however, the uniformity of the surface, as well as the surface finish is not very good. In terms of surface finish, diamond-turned surface finishes can be quite impressive – 6 Å RMS finishes have been demonstrated on barium fluoride. However, RBS analysis of diamond-turned surfaces reveal that they are amorphous, presumably due to plastic flow of the material under the action of the diamond tool. Figure 1 shows a diamond turned sample of PWO. We observe that the material exhibits localized areas of plastic flow interspersed with areas of fracture. We conjecture that improved PWO growing and annealing methods might lead to fully diamond-turnable crystal surfaces.

In the meantime another polishing technique – pitch lapping with diamond abrasives – provides the best combination of surface finish (10-20 Å RMS) and surface crystallinity for most crystals. The technique is applied after more standard polishing techniques and is a simple lap prepared with a low melting temperature synthetic pitch. Grooves are formed in the pitch in a pattern to allow cutting fluids, abrasives and ground material to be washed away during the lapping process. The key to the process is a final polish with an abrasive of very uniformly sized diamond, 0.5 μm or 0.25 μm diameter, imbedded in the pitch. In addition, a non-aqueous cutting fluid such as low viscosity oil, or ethylene glycol is used to uniformly disperse the diamond and to carry away waste material. Water is not a good fluid for diamond polishing because of the tendency of diamond to agglomerate in water. These polishing techniques are simple to implement and are essentially extensions of standard polishing techniques already in practice in the US and elsewhere. These techniques are easily transferred to industry both in the US and abroad. LLNL engineers and physicists have successfully worked with our counterparts at the Shanghai Institute of Ceramics and the Beijing Glass Research Institute to develop this capability [3]. Figure 2 shows examples of improper (as received from the crystal grower) and proper (diamond-loaded pitch lap) polishing of PWO.

MEASUREMENTS OF LEAD TUNGSTATE MECHANICAL PROPERTIES

Measurements of PWO mechanical properties are being made at LLNL to better define the CMS ECAL structural and thermal systems. We have measured the coefficient of thermal expansion of a small ~ 1 cm x 1 cm x 0.5 cm crystal sample cut from a larger crystal. Measurements were made using a DuPont 9900 Thermal Mechanical Analysis system and the sample was cycled from dry ice temperature (-38 degrees Centigrade) to +100 degrees Centigrade. In the sample we prepared, the crystal's principle, or "a" axis is about 19 degrees off from the actual growth axis, which corresponds to the direction of the 0.5 cm sample dimension. Thus we measure a superposition of components of linear expansion along the two principle axes of the crystal. The coefficient of thermal expansion is linear in the range of 15 degrees to 30 degrees, the range of expected minimum and maximum temperature in the ECAL. The results give a coefficient of thermal expansion of 10.0 x 10^{-6}/°C and 11.5 x 10^{-6}/°C for the two 1 cm long sides in the range of 15 - 30 °C. This can be compared with measurements from the Shanghai Institute of Ceramics which give 9.58 x 10^{-6}/°C at 100 °C perpendicular to

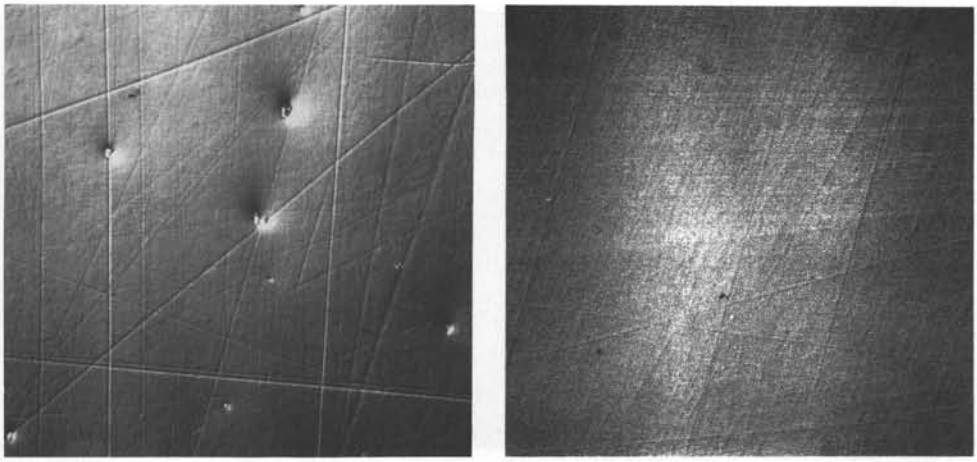

Figure 2. Photographs (x179) of two polished PWO surfaces. On the left is the as-received crystal with large surface scratches and inclusions of polishing debris. Poor surfaces such as this exhibit large amounts of subsurface damage and stress. The large scratches and pits make application of high quality reflective coatings difficult. On the right is a PWO surface polished at LLNL using diamond-loaded pitch lapping. The surface roughness is ~15-20 Å RMS.

the "a" axis and 22.7 x 10^{-6}/°C parallel to the "a" axis. Earlier work by Krishna Rao and Deshpande give 8.13 x 10^{-6}/°C and 19.73 x 10^{-6}/°C perpendicular and parallel to the "a" axis, respectively, at 30 °C [4]. Our result, measured perpendicular to the growth axis and 19 degrees offset from the "a" axis is consistent with previous measurements.

We have measured the Young's Modulus of compression of a right circular cylinder of PWO with dimensions 1 cm in diameter and 2 cm long. The sample was prepared with the cylinder axis in the direction of the growth axis of the crystal from which it was taken. To prevent stress from building up in localized regions of the crystal due to non-uniform loading, the sample was prepared as a cylinder with very parallel faces. The sample was measured on an Instron Model 1125, 20k pound test machine using a 20k pound load cell set to the 500 pound load range. A spherical seat was installed at the bottom platen to correct for any remaining deviation from parallelism between the top and bottom surfaces. Three MTS 0.3 inch 15% extensometers were installed on the test sample to provide average strain data. Figure 3 shows the setup. Three runs were made at room temperature with a constant crosshead travel of 0.002 inches (50 microns)/minute. The first run loaded the sample to 250 pounds. The second run inadvertently began with the crosshead loading the sample to 2100 pounds prior to the error being detected. The sample developed a slight internal fracture but did not break. The third run took the sample to 500 pounds to determine if the modulus had changed. The results of the third run are shown in Figure 3. No large change in modulus was observed between the first and third runs and the results for the modulus were measured to be 9.0 x 10^6 psi and 9.27 x 10^6 psi (62.1 GPa and 64.0 GPa), respectively. For comparison the modulus of aluminum alloy is 10 x 10^6 psi and lead silicate glass is 9 x 10^6 psi. Our result is comparable to measurements made by researchers at CERN and École Polytechnique [5].

MEASUREMENTS OF LEAD SOLUBILITY FROM LEAD TUNGSTATE

We have also made measurements of lead solubility in cutting oil. Two experiments have been performed. The first (qualitative) measurement was made using chips of PWO mixed with hydrocarbon cutting oil (Drakeol 7) used in the diamond turning study. The sample included 0.5 cc of chips ranging in size from about 1-20 microns. The chips were immersed in 20 cc of cutting oil. The sample was aged for 43 days at room temperature and then analyzed. In the analysis the cutting oil was separated from the solid material by centrifugation at 4000 rpm for 10 minutes. 0.2 gram of oil was then wet ashed in concentrated HNO_3/H2SO_4 in a closed Teflon digestion vessel to destroy any organic material. The total volume of material was then evaporated to approximately 0.5 g to which 100 ng of thallium was added as an internal standard. Following volume adjustment to a final volume of 10 ml, the presence of lead was determined by inductively coupled plasma mass spectrometry (ICP-MS). A clean sample of unused cutting oil was also measured in the same manner for comparison. The results show that the amount of lead is 160 ng/g for the unexposed oil and 530 ng/g for the exposed oil. Both measurements have an uncertainty of about 10%.

In a second ongoing quantitative experiment a PWO cube, 1 cm on a side, is being continuously exposed to cutting oil in a polyethylene bottle. Small amounts of exposed and unexposed oil will be measured over regular periods approximately once per month for the next few months. Occupational

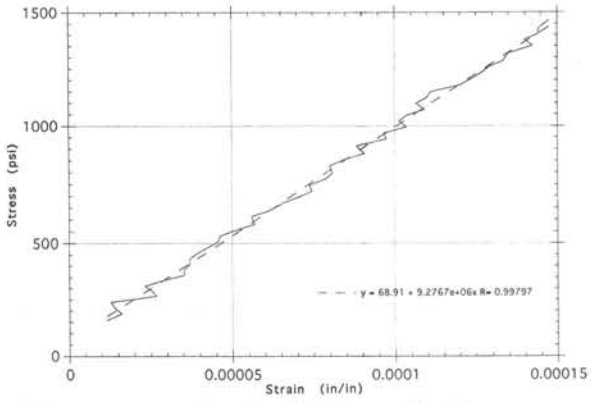

Figure 3. Photograph of the Young's Modulus test setup and results of a 500 pound load run.

health and safety regulations at LLNL do not specify a limit on skin contact with lead because elemental lead is not readily absorbed through the skin. Exposure limits are available for ingestion of lead. The US EPA limit for lead exposure in drinking water is 15 ng/g. Environmental regulations at LLNL also define lead wastes as containing greater than 200 ng/g of lead [6]. The oil waste can also contain organo-lead compounds, which might be absorbed through the skin or inhaled. Thus we see that the PWO solubility in cutting oil poses a problem for handling and disposal by LLNL standards. Proper collection, processing and disposal of this lead-containing hydrocarbon oil waste is necessary. Protective gloves should be used to prevent ingestion via hand to mouth.

CONCLUSIONS

LLNL is contributing to the understanding of PWO as part of the effort to build the CMS ECAL sub-system. We have seen that PWO is a material that challenges our abilities to produce a high quality electromagnetic calorimeter. Our diverse program of study encompasses many aspects important to this effort including materials properties, machining, polishing, fundamental physical constants and personnel and environmental safety. We intend to continue this program of study during the R&D phase of CMS to develop machines for production factories and to provide input to mechanical and thermal models of the ECAL.

ACKNOWLEDGEMENTS

We gratefully acknowledge the work of Phil Miller and Terry Duewer for lead solubility measurements, Scott Preuss for measurements of Young's Modulus, and Mervyn Lawrence for measurements of thermal expansion. This work was performed under the auspices of the US Department of Energy by the Lawrence Livermore National Laboratory under Contract W-7405-ENG-48.

REFERENCES

1. C. R. Wuest, et al., "Precision Machining and Polishing of Scintillating Crystals for Large Calorimeters and Hodoscopes," UCRL-JC-114014 REV1, *Proc. Spring Meeting Materials Research Society*, San Francisco, CA, April, 1994.

2. "The Compact Muon Solenoid Technical Proposal," CERN/LHCC 94-38, December, 1994.

3. Z. W. Yin, "Research and Development Works on BaF2 Crystals in Shanghai Institute of Ceramics," *Proc. Spring Meeting Materials Research Society*, San Francisco, CA, April, 1994.

4. K. V. Krishna Rao, V. T. Deshpande, "Thermal Expansion and Chemical Bond," *Proc. 6th Int. Symp. Thermal Expansion*, Plenum Press, p. 43-56 (1978) and "Proceedings of the May, 1995 CMS ECAL Engineering Group Meeting at CERN," unpublished.

5. M. Lebeau and J. Badier, private communication.

6. "LLNL 1994-1995 Discharge Permit," issued by the City of Livermore, CA.

DIAGNOSTICS OF SCINTILLATING CRYSTALS BY MEANS OF SPECIALLY DESIGNED SPECTROPHOTOMETER

A.V.Bazhenov, A.V.Gorbunov, N.V.Klassen
Institute of Solid State Physics, 142432 Chernogolovka, Russia

Parameters of scintillating crystals (light yield, spectral distribution of light emission and attenuation, mechanical strength, radiation hardness, etc.) as usual are strongly dependent on the history of crystals: quality of raw material preparation, procedures of crystals growth, annealing and processing. Variations of these conditions can modify the content of impurities, create inclusions of secondary phases, induce elastic stresses, resulting in severe decrease of scintillator quality. The problem of production of large amounts of big size scintillating crystals with reproducible parameters induces the need to develop adequate and economic techniques for fast, but informative diagnostics of crystals. We have designed a special compact spectrophotometer which permits to get a lot of information about scintillating crystals. This device is essentially cheaper than commercial spectrometers. A lot of information about the defects produced during the crystal preparation was obtained, resulting in the opportunity to optimize the preparation processes.

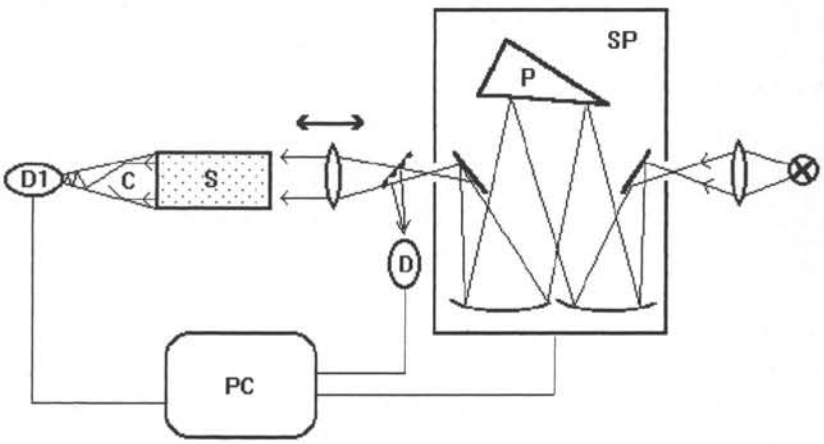

Fig.1. Optical scheme of spectrophotometer SP: P - quartz prism with Al mirror, S - sample, C - quartz cone, D - incident light detector, D1 - transmitted light detector, PC - IBM personal computer.

The optical scheme of the spectrophotometer is shown in Fig.1. The geometry of a monochromator SP is typical for grating devices. However, instead of a diffraction grating a quartz prism P with an aluminum mirror is used as a dispersive element. On the one hand, low dispersion means low spectral resolution. But it turns out to be quite adequate for scintillating crystals which show as a rule no sharp spectral peculiarities. On the other hand, this technical solution gives a few important benefits:

1. low dispersion results in high output light intensity;
2. there exists no problem with diffraction orders;
3. the very wide spectral range (near ultraviolet - visual - near infrared).

The main optical parameters of the spectrometer are: spectral range 200-800 nm, the maximal spectral resolution - from 3 nm in ultraviolet to 30 nm in near-infrared, light aperture 1:3, focal length 175 mm. The monochromator sizes are 35x30x27 cm, the sizes of illuminator compartment - 37x22x20 cm^3. The overall length of the spectrometer is limited by the size of sample compartment which strongly depends on sample sizes.

A probable variant of the photoregistration system could use a diode array or an other multichannel detector in the plane of the exit slit. This would allow, in particular, to see the wide range spectrum on a computer display in quasi-real-time mode. Fig.1 shows the case of two-channel registration with D1 as transmitted light detector and D as incident light detector. This variant, besides of essentially lower price, has other advantages. Its mechanics includes the prism rotation by means of a computer-controlled stepper motor (a standard serial interface RS232 is used) and simplified sine mechanism only.

In addition to usual measurements of optical transmission spectra (scheme 1 in Fig.2) it allows with the help of simple accessories to measure:

a. both external and internal reflection spectra (including multiple internal reflection (see scheme 2 in Fig.2));

b. the homogeneity of optical transmission along the axis of a long-size sample by moving it across the testing light beam (Fig.2, scheme 3);

c. the spectra of light scattering related with structural inhomogeneities both in the volume and at the surface layer of a crystal (Fig.2, scheme 4);

d. the luminescence or scintillation spectra (Fig.2, scheme 5);

e. the optical luminescence excitation spectra (the same as Fig.2, scheme 4, but a filter must be placed in front of the detector to cut off the incident light).

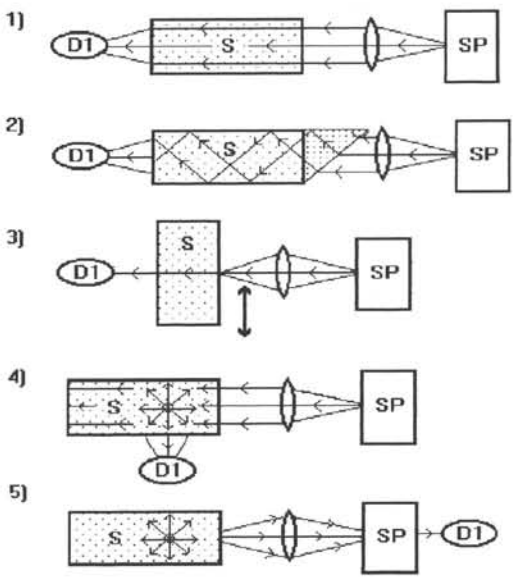

Fig.2. A set of possible experiments with the spectrophotometer: 1) transmission spectra, 2) multiple internal reflection spectra, 3) the optical homogeneity of long samples, i.e. variation of transmission spectra along crystal length, 4) volume/surface scattering spectra or luminescence excitation spectra, and 5) light emission (either luminescence or scintillation) spectra.

The development of a special attachment is planned for both visualization of the internal stress distribution and measurement of the stress magnitude by means of birefringence: due to the large optical anisotropy of lead tungstate this is not an easy task.

The spectral resolution of the spectrometer is illustrated in Fig.3 which shows the spectrum of Hg-He low pressure lamp. Both the graduation curve $\lambda(n_{stp})$ and the dispersion curve $d\lambda/dn_{stp}$ of the spectrometer are shown in Fig.4. Here n_{stp} is the number of motor step.

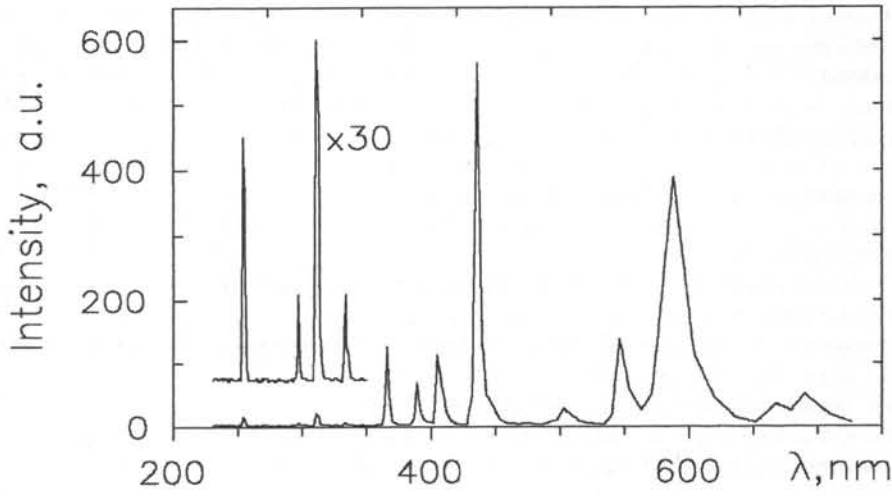

Fig.3. The spectrum of Hg-He-lamp measured with this spectrometer. Slit widths are 10 μm.

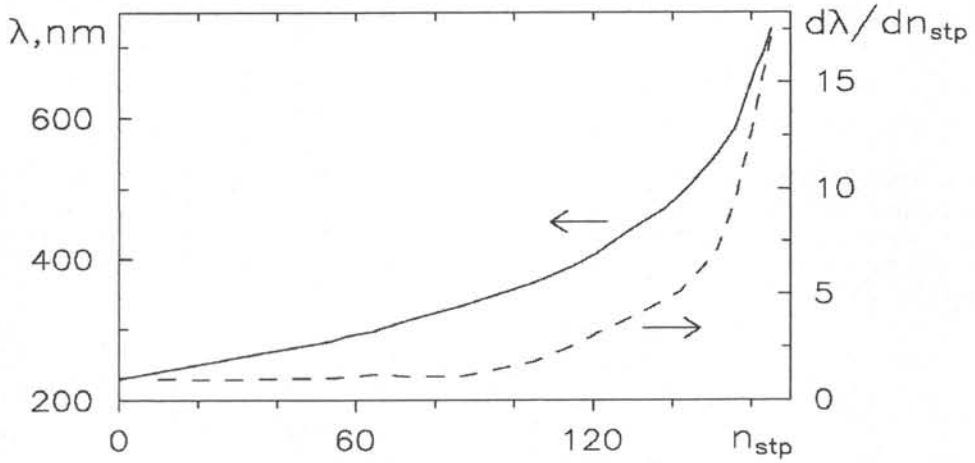

Fig.4. Wavelength λ (dense curve) and dispersion $d\lambda/dn_{stp}$ (dashed curve) as functions of motor step number n_{stp}

Thus, a cheap and compact, large aperture and low- dispersion multifunctional spectrophotometer has been designed which permits to get a lot of useful information about optical properties of scintillating crystals in the spectral range from near ultraviolet to near infrared.

The work was supported by INTAS Grant No.93 1239.

APPLICATION OF PHOTOELASTICITY TO QUALITY INSPECTION OF SCINTILLATING CRYSTALS

M. Lebeau, CERN, Geneva, Switzerland
G. Majni, N. Paone, D. Rinaldi, Università degli Studi di Ancona, Italy

The birefringence under strain of scintillating crystals is studied to determine their photoelastic properties. The basic physics of photoelasticity and some experimental data obtained on a simple work-bench are presented. The industrial on-line check of crystal built-in mechanical tensions — an important aspect of quality inspection — is put in perspective.

1. BASICS OF PHOTOELASTICITY

In optically anisotropic materials the refraction index depends on the light propagation direction (birefringence). Most of photoelastic materials are normally isotropic and show optical anisotropy when mechanically stressed. The commonly used expression of photoelastic properties is the photoelastic constant f_σ, a material dependent quantity.

In a photoelastic material the two light waves phase difference is expressed by:

$$\Delta = \omega(t_1 - t_2) = 2\pi b(\sigma_1 - \sigma_2)/f_\sigma \qquad (1)$$

where b = depth of the sample, σ_1, σ_2 = principal stresses, f_σ = photoelastic constant.

The experimental equipment to perform the measurements of f_σ is shown in fig. 1 (plane polariscope). If the sample produces a rotation θ of one of the two outcoming wave planes, the wave intensity is expressed by:

$$y = a\sin\theta\cos\theta\,[\cos\omega(t - t_2) - \cos\omega(t - t_1)] = a\sin 2\theta\,\sin[\omega(t_1 - t_2)/2]\,\sin\omega[t - (t_1 + t_2)/2] \quad (2)$$

Extinction occurs when principal stress directions are along the polariser or analyser axes:

$\sin 2\theta = 0 \rightarrow \theta = n\pi$ with $n = 0, 1, 2, \ldots$ and when:

$\sin[\omega(t_1 - t_2)/2] = 0 \rightarrow \omega(t_1 - t_2)/2 = n\pi$ with $n = 0, 1, 2, \ldots$ (3), then:

$$\omega(t_1 - t_2)/2 = n\pi = \pi b(\sigma_1 - \sigma_2)/f_\sigma \quad (4) \qquad \text{or:} \qquad \sigma_1 - \sigma_2 = \frac{\Delta}{2\pi}\,\frac{f_\sigma}{b} = nf_\sigma/b \qquad (5)$$

i. e. when the difference between the principal stresses is constant (isochromatic fringes).The experiment is performed with monochromatic light (f_σ proportional to λ). We observe symmetric fringes of order $n = \pm 0, 1, 2, 3, \ldots$ in dark field. In light field we observe symmetric fringes of order $\pm 0.5, 1.5, 2.5, \ldots$ The sign $\pm$ indicates compression or traction.

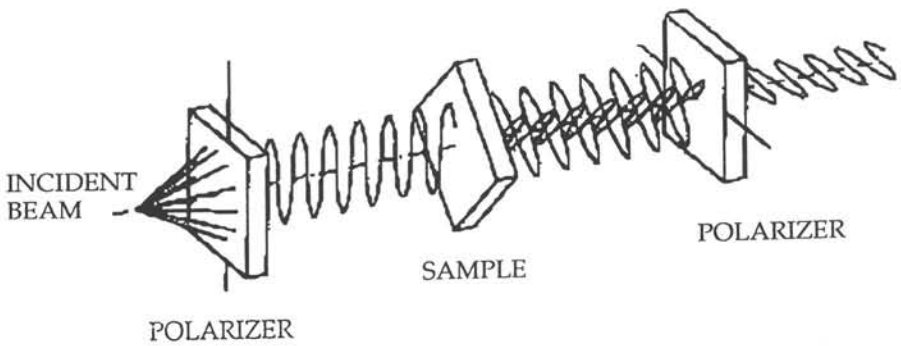

Fig. 1

Proc. Int. Conf. on Inorganic Scintillators and Their Applications, SCINT95,
1996, Delft University Press, The Netherlands

2. EXPERIMENTAL SET-UP AND MEASUREMENT PROCEDURE

2.1 Loading system

A pure bending produces a uniform stress gradient and a fringe pattern (fig. 2). The crystal sample is a freely supported beam, loaded by two vertical equal forces, orthogonal to the beam axis. The bending moment M_f is constant between the two points of application of the forces (6). The principal stress σ_1 distribution is represented by $\sigma_f(y)$, and $\sigma_2 = \sigma_3 = 0$ (7). The moment of inertia is $J = bh^3/12$ and the maximum of σ_f is given by (8):

$$M_f = \frac{P}{2}\frac{\ell}{3} \quad (6) \qquad \sigma_f(y) = \frac{M_f}{J}y \quad (7) \qquad \sigma_{f\,max} = \frac{P\ell}{bh^2} \quad (8)$$

2.2 Polariscope operating principle

The polariser is turned parallel to σ_1 direction and the analyser parallel or perpendicular. The photoelastic constant f_σ is calculated by the position y of a dark fringe of order n:

$$\sigma_1 = n\frac{f_\sigma}{b} \quad (9) \qquad f_\sigma = \frac{2P\ell}{nh^3}y \quad (10)$$

Eq. (10) has been used in two different ways:

1. identify the n^{th} fringe and measure its position y,
2. determine the fringe order n at the border of the loaded beam, i.e. at $y = \pm(h/2)$.

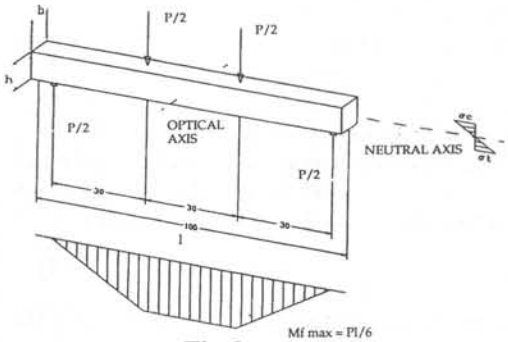

Fig. 2

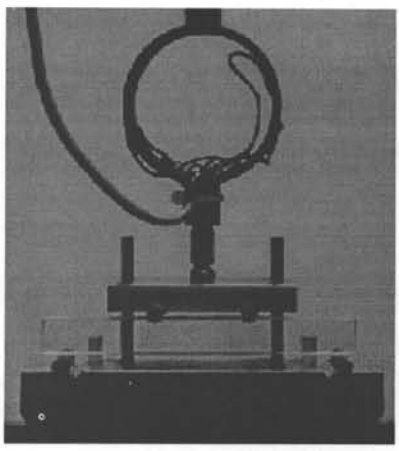

Fig. 3

2.3 Data acquisition

A loading screw instrumented with 4 strain gauges and a Wheatstone bridge calibrated with an accuracy better than 0.5% loads the sample as represented by fig. 3. A 768 x 512 pixels optical system with an 8 bit A/D converter produces a digital image. Images are acquired with a large magnification (135 mm lens, f#2.8) to improve the system resolution. Illumination is achieved by a sodium lamp (λ = 589.3 nm).On each image, the lateral dimensions of the loaded crystal is measured with high accuracy. To define the scale in pixels/mm the digital image processor is calibrated. Then an intensity profile is measured across the fringe axis. On each image, an average profile is obtained from several measures. Fig. 4 shows a photoelastic image of a Plexiglas sample used to verify the measurement procedure. The resolution is 15 pixels/mm. The best precision is obtained by proper adjustment of the contrast, of the gain and of the sample illumination over the 8 bits dynamic range of the grey levels.

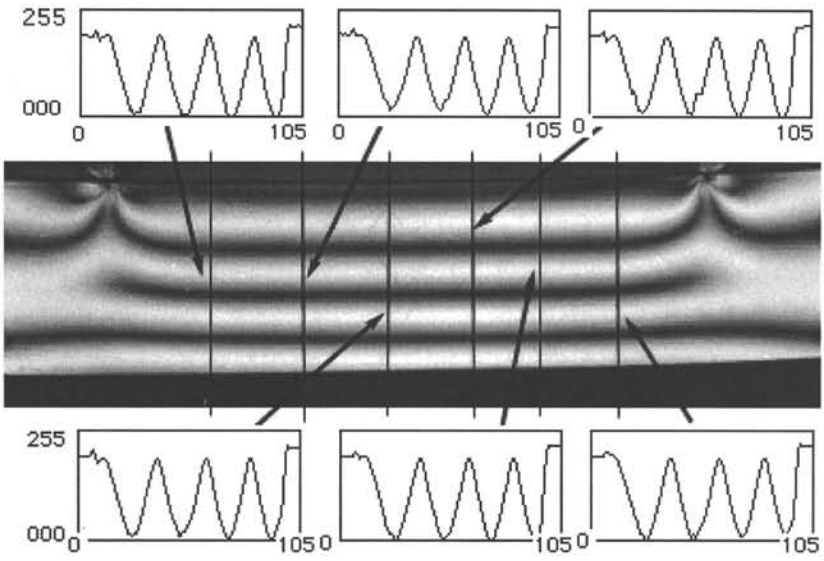

Fig. 4

3. RESULTS

3.1 $PbWO_4$ and CeF_3

With the described set up the $PbWO_4$ and CeF_3 samples do not show observable interference patterns: a photoelastic constant can not be measured. However, in a different configuration an optical pattern typical of the crystal intrinsic birefringence has been observed in the case of $PbWO_4$ (uniaxial). Pattern alterations of biaxial type depending on mechanical tensions need further study for practical applications.

3.2 BGO

In the case of BGO ($Bi_4Ge_3O_{12}$), the photoelastic coefficient could be measured:

$f_\sigma = 124.98 \pm 3.19$ N/mm for $\lambda = 589.3$ nm (fig. 5a, b)

3.3 QUARTZ

Although not a scintillator, a quartz sample of 15 x 15 x 200 mm^3 was studied for reference. Fig. 6a shows a light field picture under high external load (1200 N). We see a fringe emerging in the upper edge. Fig. 6b is the dark field picture of the same external load condition. This picture shows two fringes.

3.4 BaF_2

In sample #1, the image without load shows a curved line inside the sample (fig. 7a). This fact can be explained in term of polycrystallinity which probably causes a tensional state close to the monocrystal interface. Fringe patterns result, but it is impossible to calculate f_σ because, until breaking, only the n = 0 fringe appeared in dark field (fig. 7b).

In the case of BaF_2 sample #2, with load P = 0 no fringe is observed and no internal strain is assumed. Applying an increasing load fringes become visible both in dark field and in light field as shown in fig. 8a and fig. 8b. New measurements, especially on polycrystallinity of the samples, are in progress.

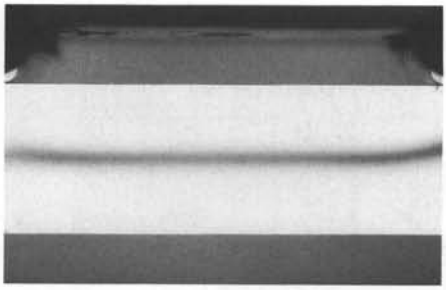

Fig. 5a

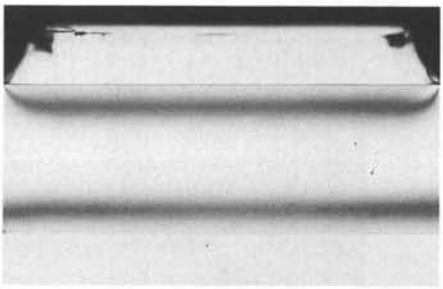

Fig. 5b

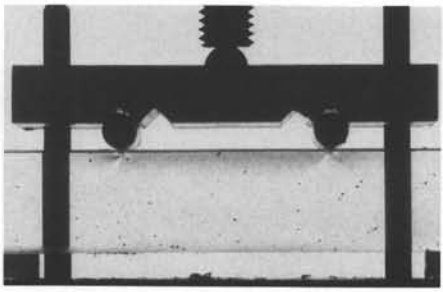

Fig. 6a

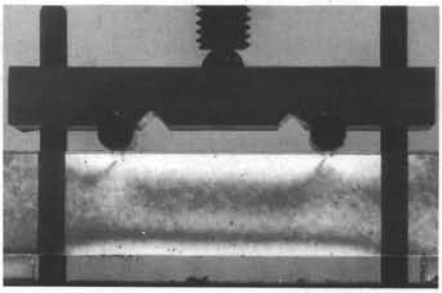

Fig. 6b

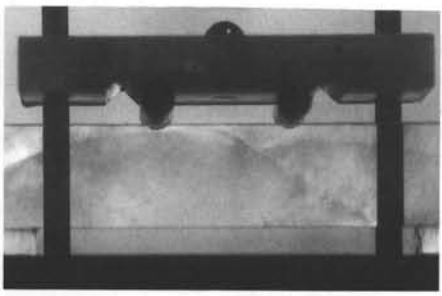

Fig. 7a

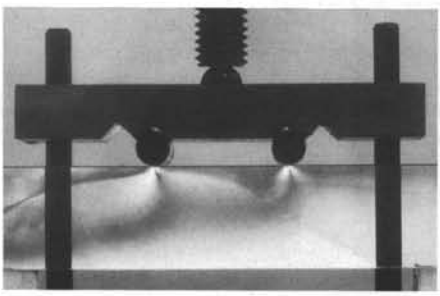

Fig. 7b

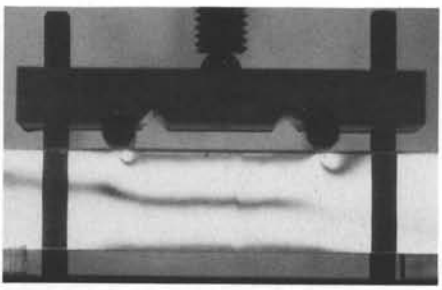

Fig. 8a

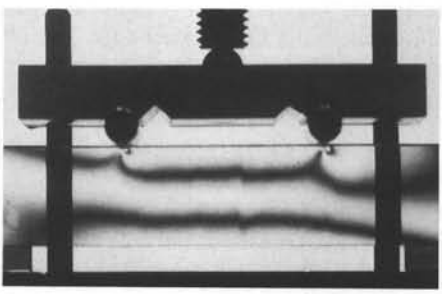

Fig. 8b

CHARACTERIZATION OF IMPURITIES IN BaF_2 SCINTILLATOR BY ABSORPTION AND LUMINESCENCE SPECTROSCOPY.

L.Trinkler, B.Berzina, M.Reichling* and J.Sils
Institute of Solid State Physics, University of Latvia, 8 Kengaraga str., LV-1063 Riga, Latvia
*Fachbereich Physik, Freie Universitat, Berlin, Arnimallee 14, 14195 Berlin, Germany

The used method of the absorption and luminescence spectroscopy allowed to detect the presence of lead impurities in BaF_2 crystal sample. The main contribution to photoluminescence results from single Pb^{2+} ions. In the same time the spectroscopic measurements imply the presence of the oxygen contamination.

Barium fluoride is a widely used scintillator material and its properties are degraded by the presence of unwanted impurities. Therefore a detailed knowledge about the origin, nature and content of unwanted components is of key importance for the further development of scintillators. The purpose of the present work is to detect the origin of unwanted impurities in the synthesized nominally pure BaF_2 crystals by means of optical spectroscopy. Spectra of absorption, photoluminescence and its excitation, as well as X-luminescence were measured. Spectroscopic measurements were complemented with laser mass spectrometric analysis, allowing detection of impurities with a concentration limit of $>10^{-5}$ at%.

The usual technique including Specord UV VIS spectrophotometer, grating and VUV monochromator, hydrogen discharge and deuterium lamps, photomultiplier and recorder was used for absorption and luminescence measurements. The laser mass spectrometry technique is described in [1]. X-ray source was a tube with a tungsten anode, operating at 50 kV, 10 mA.

Laser mass spectrometry showed a presence of lead impurities in BaF_2 samples with a concentration of $5 \cdot 10^{-2}$ at% (10^{19} cm^{-3}). No other types of impurities were found. It should be mentioned, however, that oxygen contamination can not be detected by the equipment used.

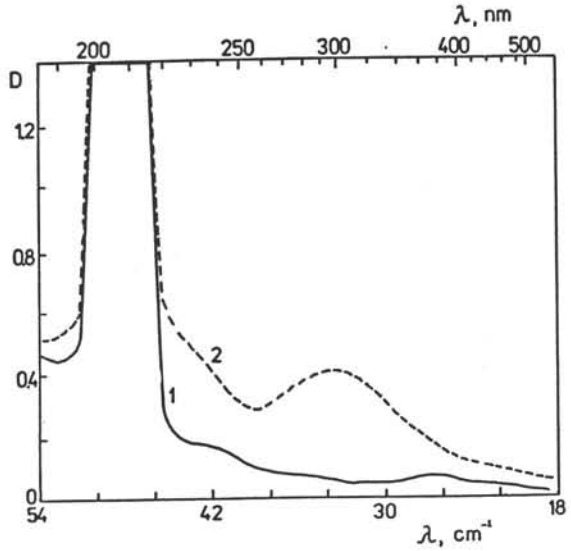

Fig.1. Absorption spectra of a 0.7 mm thick BaF_2 sample at 300K: 1-freshly cut crystal; 2-after X-irradiation.

Proc. Int. Conf. on Inorganic Scintillators and Their Applications, SCINT95, 1996, Delft University Press, The Netherlands

The presence of lead impurities in BaF_2 crystal is easily to be explained as resulting from the procedure of crystal growth. To facilitate the removal of oxygen-related impurities, PbF_2 is added to the melt. The resulting lead oxide PbO and an excess of PbF_2 normally evaporate from the melt. However, under certain conditions of synthesis it is possible to obtain crystals doped with lead ions. A high concentration of lead impurities, found in the samples under investigation, probably also implies the presence of oxygen , if PbO remained in the crystal.

The oxygen ion enters the fluorite lattice in pair with the charge compensating fluorine vacancy, forming the O^{2-} - v_F dipoles. Also the results of our spectroscopic studies prove the presence of lead impurities and support the hypothesis of oxygen contamination.

The pure BaF_2 crystals are transparent up to 9 eV. The absorption spectrum of freshly cut BaF_2 crystal under study has an intense band at 206 nm and a number of weaker bands at longer wavelengths (Fig.1, curve 1). Excitation in the 206 nm absorption band gives a luminescence band peaking at 260 nm (257 nm at 80 K), as shown in Fig.2. by curves 1 and 2. The excitation spectrum of this luminescence band includes also a wide band in the region of 145 - 175 nm (Fig.2, curve 3). The position of luminescence and excitation bands as well as the halfwidth of the luminescence band (0.6 eV at 300 K, 0.4 eV at 80 K) allows to ascribe unambiguously the luminescence to Pb^{2+} ions, substituting Ba^{2+} ions in the lattice site [2,3]. The absorption of the mercury like Pb^{2+} ion is characterized with A, B, C and D bands. The 206 nm band observed in absorption and excitation spectra is the A band corresponding to $^1A_{1g}$ -> $^3T_{1u}$ transition of the lead ion; the 145 - 175 nm excitation band is a superposition of B ($^1A_{1g}$ -> ^3E, $^3T_{2u}$; 154 nm) and C ($^1A_{1g}$ -> $^1T_{1u}$; 164 nm) bands, overlapping due to high concentration of Pb^{2+} luminescence centers. The 260 nm luminescence band represents the A luminescence ($^1T_{1u}$ -> $^1A_{1g}$).

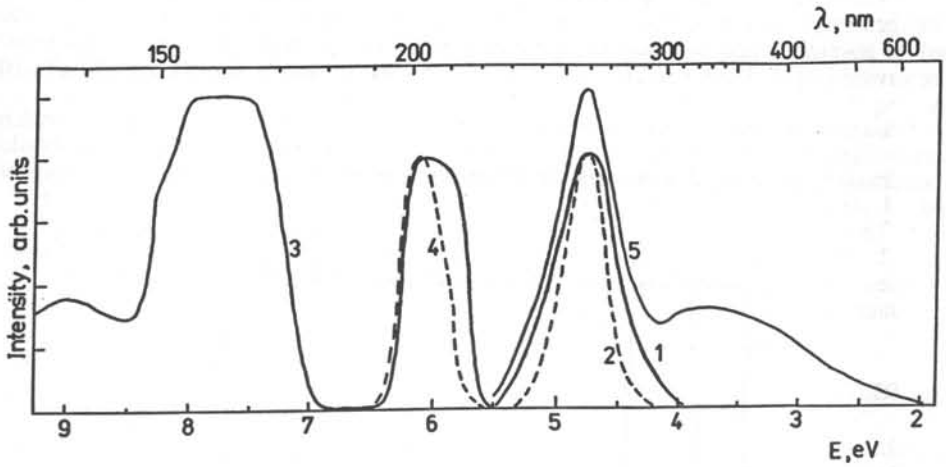

Fig.2. Spectral properties of BaF_2: 1 - photoluminescence under 210 nm excitation at 300 K; 2 - the same at 80 K; 3 - excitation of A luminescence band at 300 K; 4 - A excitation band at 80 K; 5 - X-luminescence at 300 K.

The weak background of the absorption spectrum presumably results from the oxygen contamination. The absorption (5.2; 6.1; 7.2; 8.6 eV) and photoluminescence (2.38 eV) of oxygen -vacancy dipoles in BaF_2 crystals are described in [4]. Two of the mentioned absorption bands are observed in the spectrum of BaF_2 sample under investigation: one of them at 235 nm, and another one in the region of 200 nm, overlapped by the intense absorption band of Pb^{2+} ion. Irradiation with 235 nm light causes the weak luminescence at 520 nm, proving the presence of the small amount of the oxygen - vacancy centers in the sample.

Other longwave absorption bands can be ascribed to the lead aggregate centers due to high lead concentration. Similarly lead aggregate and precipitate centers are formed in alkali

halide crystals at high concentrations of impurity, providing absorption bands at the long wavelength side of A absorption band of Pb^{2+} center [5].

The scintillation emission spectrum shown in Fig.2, curve 5 was measured by irradiating the sample with X-rays. The cut off at 220 nm is due to the sensitivity limit of the photomultiplier. The scintillation spectrum is in good agreement with data of Schotanus et al [6], dealing with BaF_2 doped with 2 ppm of Pb. The larger contribution of the lead band (257 nm) to the scintillations for our sample compared with intrinsic luminescence band 310 nm can be explained by higher impurity concentration. The additional contribution in the 400 - 500 nm region can be ascribed to luminescence of different cluster centers, including intrinsic defects, lead and oxygen impurities.

After X-irradiation the absorption spectrum of the crystal shows new band peaking and 300 nm, see Fig.1, curve 2. It is unlikely that the origin of the 300 nm absorption band is connected with lead ions with excess or lack of electrons. Although there are reports about the appearance of Pb^{+}, Pb^{2+}-Pb^{+} and $Pb^{0}(2)$ centers under X-irradiation their absorption bands are situated at longer wavelength [7]. Another possibility to explain the appearance of the new absorption bands involves the participation of a fluorine vacancy. Crystals with the fluorite structure with oxygen contaminations have many variations of mutual displacement of O^{2-} ions, charge compensating fluorine vacancies v_F and impurities . Crystal lattice imperfections are precursors of color centers, appearing under X-irradiation. X-rays produce electrons and holes. Some electrons are captured by vacances, forming F or F-type centers. At room temperatures (RT), however, F centers are not stable, they aggregate in clusters, sometimes near impurities.

No references has been found concerning the 300 nm absorption band in BaF_2 crystal. But for similar CaF_2 crystal Radzhabov [8] showed, that at RT the X- coloration is provided by F_2H^{+} centers, consisting of an electron bound to a pair of anion vacancies, perturbed by an oxygen impurity. One of the absorption bands of this center is situated at 310 nm. Several types of F center clusters perturbed by an impurity in BaF_2 are described in [9]. Some of them have absorption bands in the 300 nm region. Likewise, the 300 nm absorption band appearing under X-irradiation in BaF_2 crystal, tentatively can be explained by a cluster of F-type centers, perturbed by a lead or oxygen ion.

In summary the following conclusions can be drawn:

1. Spectroscopic measurements allow the detection of lead impurities in the BaF_2 crystal. The main contribution to photoluminescence results from single Pb^{2+} ions.

2. Spectroscopic measurements of BaF_2 samples implies the presence of oxygen impurities in the freshly cut crystal in the form of O^{2-} - v_F dipoles, and participation of F-type center clusters in color center formation.

REFERENCES

1. G.I.Ramendik, O.I.Krjuchkova Laser mass spectrometric analysis of solid state. Moscow, 1987, Preprint of GEOHI Institute of Academy of Sciences of USSR.
2. V.A.Arhangelskaya, N.E.Lushchik, V.M.Reiterov, H.A.Soovik and L.M.Trofimova Opt. spectrosc.(USSR) (1979), 47, N 4, 708.
3. V.A.Arhangelskaya, V.M.Reiterov and L.M.Trofimova J.Appl. Spectr. (USSR) (1980), **32**, N 1,103.
4. E.Radzhabov and P.Figura phys. stat sol(b) (1994) 186,K37.
5. C.Zaldo and F.Agullo-Lopez J.Chem.Solids (1983), 44, N 12, 1099 .
6. P.Schotanus, P.Dorenbos, C.W.E. van Eijk and R.W.Hollander IEEE Trans.Nucl.Sci. (1989), **36**, N 1, 132.
7. M.Fockele, F.Lohse, J.-M.Spaeth and R.H.Bartram J.Phys. Condens.Matter (1989), **1**, 13.
8. E.Radzhabov phys. stat. sol.(b) (1993), **180**, 513.
9. O.A.Krasilshchikova, A.N.Taraschan and A.H.Platonov Color and luminescence of natural fluorite. (in Russian), Kiev, Nauk. dumka, 1986, 224 p.

ENERGY RANGE OF X-RAY DETECTORS BASED ON NEW SCINTILLATION MATERIALS

M.Globus, B.Grinyov, L.Halina, I.Kirichenko, O.Shilov
Institute for Single Crystals, Kharkov, 310001, Ukraine

Abstract

The energy range of applicability is estimated for some nontraditional scintillators which combine certain essential advantages with a low value of the effective atomic number and a rather strong reabsorption of fluorescence light.

I. INTRODUCTION

The $Y_3Al_5O_{12}$, $YAlO_3$ and Al_2O_3 crystals are known to gain scintillator properties when doped with cerium (the two former crystals) or titanium (the latter one) [1,2]. The scintillators have important advantages: a short radiation time (70 *ns* for $Y_3Al_5O_{12}$, 30-40 *ns* for $YAlO_3$), chemical and mechanical stability. On the other hand, a rather strong reabsorption of fluorescence light and a low value of the effective atomic number restrict the X-ray energy region of applicability. This region will be estimated below from the condition that the maximal scintillator length, allowable with regard to reabsorption, must exceed the X-ray free path length, l, with respect to photoabsorption.

II.THE MINIMAL AND MAXIMAL LENGTHS OF SCINTILLATOR

Let us characterize the scintillator substance by the effective atomic number, Z, the number of atoms per unit volume, N, and the X-ray free-path length,l. For the convenience of further estimations some arbitrary fixed values of these quantities are introduced: $Z^* = 30$, $N^* = 5 \cdot 10^{22}$ cm, $l^* = 0.225$ cm. (Naturally, the result is independent of the choice of these values). A well-known formula for the free-path length with respect to photoabsorption [3] can be rewritten in the form

$$l(E) = l^* \frac{N^*}{N} \left(\frac{Z^*}{Z} \right)^5 \left(\frac{E}{E^*} \right)^{3.5} \qquad (1)$$

for a photon with the energy E in the range $0.0136Z^2$ keV< E << mc^2= 511 keV. The quantity (1) plays the role of the lower boundary of the scintillator length, L (the crystal size parallel to the X-ray incidence direction).

Now we will estimate the upper boundary of L for an ordinary case where the photoreceiver is attached to the scintillator face perpendicular to the X-ray incidence direction, i.e. to the size L. The upper boundary, L_{max}, corresponds to the case where the scintillation light energy coming to the photoreceiver, $E\eta\tau$, is diminished by reabsorption down to the discrimination threshold value, E_{th}. Here η is the conversion efficiency of the scintillator and τ is the light collection coefficient for the scintillation point, most remote from the photoreceiver. If all the faces of the scintillator are polished and the face opposite to the photoreceiver has the reflection coefficient close to unity, then:

$$\tau = (1-\nu)e^{-\beta kL}, \quad \nu = \left[1 - \left(\frac{n'}{n} \right)^2 \right]^{1/2}, \quad \beta = -\frac{\ln \nu}{1-\nu} . \qquad (2)$$

Here k stands for the absorption coefficient at the scintillation light frequency; n is the refraction index of the scintillator and n' is that of the coupling liquid filling the space

Proc. Int. Conf. on Inorganic Scintillators and Their Applications, SCINT95,
1996, Delft University Press, The Netherlands

between the scintillator and the photoreceiver. Equating $E\eta\tau$ to E_{th} with allowance for (2), one obtains the upper boundary of the scintillator length:

$$L_{\max}(E)=\frac{1}{\beta k}\ln\frac{E\eta(1-\nu)}{E_{th}}=\frac{1}{\beta k}\ln\frac{E}{\tilde{E}_{th}}. \qquad (3)$$

Here E_{th} is the threshold value of the scintillation energy fraction which achieves the photoreceiver and $\tilde{E}_{th}$ is the threshold X-ray energy in the case of the same scintillator with a small size L ($L\,k<<1$). The quantity $\tilde{E}_{th}$ as well as

$$E_{th}=\eta(1-\nu)\tilde{E}_{th} \qquad (4)$$

is the discrimination threshold of the scintillation detector system (any of them can be used depending on the considerations of convenience).

III. THE MAXIMAL X-RAY ENERGY

The scintillation detector can be used in the X-ray energy range within which $L_{max}(E) > l(E)$. Equating the quantity (3) to (1), one obtains the maximal permissible value of X-ray energy, $\bar{E}$, and the corresponding scintillator length, $\bar{L}$:

$$\bar{E}=\tilde{E}_{th}F\left(\beta k l^{*}\left(\frac{\tilde{E}_{th}}{E^{*}}\right)^{7/2}\frac{N^{*}}{N}\left(\frac{Z^{*}}{Z}\right)^{5}\right), \qquad (5)$$

$$\bar{L}=(\beta k)^{-1}\ln\left(\bar{E}/\tilde{E}_{th}\right). \qquad (6)$$

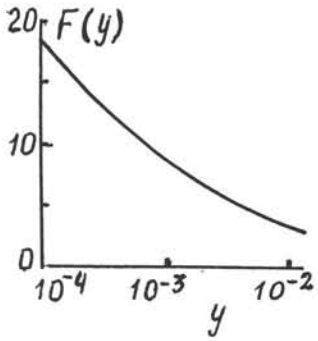

Plot of the function F=F(y).

The function $F=F(y)$, given by the equation $y = \ln F/F^{3.5}$, is plotted in the figure. For $E < \bar{E}$, the scintillator length L can be chosen between the lower and upper boundaries (1) and (3), the optimal L value coinciding with the middle of the interval between them.

An example is given below. Let the scintillator $YALO_3(Ce)$ with the parameters n=1.961, Z=28.3, N/N^{*}=1.96 be joined to a photomultiplier without an optical contact (n' =1) so that β=1.08. For various $\tilde{E}_{th}$ and k, the formulae (5) and (6) give the following values of the maximal gamma-ray energy and the corresponding scintillator length:

Table. The upper boundary of the energy interval, within which X-rays can be detected by the scintillator, and the corresponding scintillator length

$\tilde{E}_{th}$, keV	k, cm^{-1}	$\bar{E}$, keV	$\bar{L}$, cm
10	0.4	294	7.8
10	0.8	238	3.7
50	0.2	300	8.2
50	0.4	236	3.6
50	0.8	182	1.5

The scintillation detector system can be used to detect X-rays in the energy range

$$\widetilde{E}_{th} < E < \overline{E} . \qquad (7)$$

As seen from the Table, this interval is narrowed as the discrimination threshold and the fluorescence light absorption increase. For the X-ray energy within the interval (7), the optimal scintillator length can be estimated as follows:

$$L_{opt} \approx \overline{L} \frac{E - \widetilde{E}_{th}}{\overline{E} - \widetilde{E}_{th}} . \qquad (8)$$

IV. CONCLUSION

The X-ray energy region of the scintillation detector applicability is given by Equs. (5) and (7). For every energy within this region, the boundaries of the allowable interval of the scintillator length are defined by Equs. (1) and (3).

REFERENCES

[1]. R.Antratar, P.Schaner, J.Phys. E., v.4, N 8, p.707. 1978.

[2]. R.Antratar, P.Schaner, S.Kvapil, Scanning, v.5, N 1, p.91. 1983.

[3]. M.Globus, Nucl. Tracks and Radiation Measur., v.21, N 1, p.131. 1993.

INTERNET ACCESS TO DATA FOR SCINTILLATION COMPOUNDS†

William W. Moses, Alex C. West, Stephen E. Derenzo, and Marvin J. Weber, Lawrence Berkeley National Laboratory, University of California, Berkeley, CA 94720

INTRODUCTION

The LBL Pulsed X-Ray Facility has scintillation data on a large variety of inorganic scintillators. We offer this information on *all* compounds that we have tested. The only restrictions / favors that we ask users of this data are:

1) The data is intended for research use and may not be sold.

2) If any portion of the data is used in a publication, that the following text appear somewhere in the publication:

> "This work was supported in part by the Director, Office of Energy Research, Office of Health and Environmental Research, Medical Applications and Biophysical Research Division of the U.S. Department of Energy under contract No. DE-AC03-76SF00098, and in part by Public Health Service Grant No. R01 CA48002 awarded by the National Cancer Institutes, Department of Health and Human Services."

Please note that the University of California and the U.S. Department of Energy make no warranty as to the accuracy of this data. If you have questions, comments, suggestions, etc., please send email to wwmoses@lbl.gov.

HOW TO CONNECT

(1) Establish an FTP connection to "**scint.lbl.gov**" .
(2) Log in using the user name "**anonymous**" .
(3) Give your email address as the password.

GENERAL ORGANIZATION

There are two general types of files — summary files and data files. Summary files are found in the top level directory, while data files are located in subdirectories. Files are ASCII text with a TAB character delimiting columns and a <CR> (carriage return) delimiting rows.

Compound Summary

The first summary file is "compounds.dat", which contains a list of the chemical formula and / or name of each measured compound. Note that each sample is identified by a unique number that identifies it. This files also list some of the pertinent physical properties, such as the color, the density, and the attenuation length for 511 keV photons. Unless otherwise noted, all of these samples are in powdered form and are contained in quartz cuvettes with 5 mm outer diameter, 0.3 mm wall thickness, and 50 mm length.

†This work was supported in part by the Director, Office of Energy Research, Office of Health and Environmental Research, Medical Applications and Biophysical Research Division of the U.S. Department of Energy under contract No. DE-AC03-76SF00098, and in part by Public Health Service Grant No. R01 CA48002 awarded by the National Cancer Institutes, Department of Health and Human Services.

Proc. Int. Conf. on Inorganic Scintillators and Their Applications, SCINT95,
1996, Delft University Press, The Netherlands

Luminosity Summary

The summary files "luminosity.dat" record the apparent luminosity of these compounds. Two "luminosity.dat" files exist, one for data taken at a synchrotron light source with monochromatic x-rays (NSLS) and one for data taken at LBL with the pulsed x-ray source. The data is kept separate due to the different nature of the experiments. For both experiments, the sample is exposed to an x-ray source and the resulting scintillation photon rate determined with a photomultiplier tube (PMT). The "true" luminosity cannot be determined with powdered samples unless the optical attenuation length of the powder is known and corrected for. As we do not know this attenuation length, we merely assume that it is the same for all samples, and thus make no correction. A more complete discussion of this issue is given in [1] and [2]. In addition, more accurate estimates of the luminosity are obtained if a correction is made for the differing x-ray attenuation length in the sample. This is straightforward when monochromatic x-rays are used, as at the synchrotron source, and so the NSLS data has this correction made. It is complex when polychromatic x-rays are used, as with the pulsed x-ray source, so this correction is not made for the LBL data. The following discussion pertains to the LBL data - see [1] and [2] for a complete discussion of the NSLS data.

The Luminosity (defined as scintillation photon count rate per unit x-ray flux) protocol is as follows. The background count rate in the photomultiplier tube (PMT_Dark_Rate) is measured with the x-ray source turned on but no sample (or cuvette) in the x-ray beam. There is a weak background luminosity due to scintillation from the quartz cuvettes (Cuvette_Luminosity) — this is determined by placing an empty cuvette in the x-ray beam and measuring both the photomultiplier tube count rate (Raw_Cuvette_Rate) and the anode current in the x-ray tube (Current) in microamperes. Thus,

Cuvette_Luminosity = (Raw_Cuvette_Rate – PMT_Dark_Rate) / Current .

A sample is placed in the x-ray beam and the photomultiplier tube count rate (Raw_Rate) and the anode current in the x-ray tube (Current) measured. The apparent luminosity of the compound is then computed by correcting for the dark rate and the cuvette luminosity, or

Luminosity = [(Raw_Rate – PMT_Dark_Rate) / Current] – Cuvette_Luminosity .

No individual data files are kept for the Luminosity measurements — all relevant data is kept in the "luminosity.dat" files. For reference, with the pulsed x-ray source the luminosity of BGO is typically 1,600 counts/second/microampere and the background luminosity from dark current and the cuvette is typically 50 counts/second/microampere.

Decay Time Summary

The summary file "lifetime.dat" file contains an entry for each fit that has been performed on the decay time data. The function that is used to is usually a sum of n exponential decay components plus a constant background. More explicitly, the form of the fit is:

$$Fit(t) = Background + \sum_{i=1}^{n} \frac{Fraction_i}{\tau_i} \cdot \exp(-\frac{t}{\tau_i}) \quad .$$

The impulse response of the system (typically about 120 ps fwhm) is deconvolved from the data, and in some cases an exponential rise time is included in the fit. A goodness of fit (chi squared per degree of freedom) is included to help evaluate the fit. Decay times that are much longer than the repetition period of the x-ray source (typically 10 microseconds) are difficult to separate from the background due to PMT dark current, as neither has any apparent time structure. In many cases though, the background due to dark current is subtracted. There is another component of the Background that is due to excitation by "background" x-rays that are uncorrelated in time to the main pulse of x-rays (for details, see [3]). In most cases, no effort is made to differentiate this background from very long decay components.

Decay Time Data

Individual data files are kept for each decay time measurement. They are located in the "lifetime" subdirectory, or in subdirectories therein (arranged by compound number). The file name consists of the sample number, the date the data was taken, and the type of TDC used to take the data with, all separated by periods. Thus, the file name for BGO (sample #5) data taken on 6/15/95 with the Highland M-690 TDC is 0005.061595.M690 . Each file contains a header that describes in detail the run conditions under which the data was accumulated. The data is accumulated in fixed width bins (typically 20 ps), but has undergone a logarithmic compression so the width of the time bin divided by the difference the time bin is from time zero is approximately a constant (roughly 1%), which reduces the size of the data set considerably. Each data file consists of three columns - the time (in ns), the Count_Rate (listed in terms of counts per original bin), and a Weight factor (the number of original bins that have been merged to obtain this compressed bin). The total number of counts that went into this bin is then Count_Rate * Weight. More details on this compression are given in [4].

Emission Spectrum Data

Individual data files are kept for each emission spectrum measurement. They are located in the "spectrum" subdirectory or in subdirectories therein (arranged by compound number). The file name consists of the sample number, the date the data was taken, and the blaze of the monochromator grating used to acquire data, all separated by periods. Thus, the file name for BGO (sample #5) data taken on 6/15/95 with a grating blazed for 300 nm is 0005.061595.300 . Each file contains a header that describes the detailed run conditions under which the data was accumulated. The relative quantum efficiency of the monochromator / photomultiplier tube combination has been calibrated; these correction factors are included in each data file.

Wavelength Resolved Decay Time Data

For a few of the samples with multiple emission peaks, the wavelength resolved decay time is collected. These data are located in the "wr_lifetime" subdirectory. The file name consists of the sample number, the date the data was taken, and the designator WRDT, all separated by periods. Thus, the file name for BGO (sample #5) data taken on 6/15/95 is 0005.061595.WRDT . Each file contains a header that describes in detail the run conditions under which the data was accumulated. As with the lifetime data, the data is accumulated in fixed width bins but has undergone a logarithmic compression so the width of the time bin divided by the difference the time bin is from time zero is approximately 1%. Each data file consists of two columns that contain the time (in ns) and a Weight factor (the number of original bins that have been merged to obtain this compressed bin), followed by a column containing the Count_Rate (defined the same way as data in the Decay Time section) for each emission wavelength, selected using a monochromator.

REFERENCES

[1] S.E. Derenzo, W.W. Moses, J.L. Cahoon, et al. Prospects for new inorganic scintillators. IEEE Trans. Nucl. Sci. NS-37: pp. 203-208, 1990.

[2] S.E. Derenzo, W.W. Moses, J.L. Cahoon, et al. X-ray fluorescence measurements of 412 inorganic compounds. Proceedings of The IEEE Nuclear Science Symposium, pp. 143-147, (Edited by G. T. Baldwin), Santa Fe, NM, 1991.

[3] S.C. Blankespoor, S.E. Derenzo, W.W. Moses, et al. Characterization of a pulsed x-ray source for fluorescent lifetime measurements. IEEE Trans. Nucl. Sci. NS–41: pp. 698–702, 1994.

[4] W.W. Moses, S.E. Derenzo, M.J. Weber, et al. Scintillator Characterization using the LBL Pulsed X-ray Facility. Rad. Meas. (in press), 1995.

PART VII

Light Detection

READOUT OF FAST, LOW LIGHT YIELD SCINTILLATORS WITH AVALANCHE PHOTODIODES

C. Schmelz[1], S. Bradbury[1], I. Holl[1], E. Lorenz[1], M. Merck [3], D. Renker[4],.S. Ziegler[2]
[1] Max-Planck-Institut für Physik, München, Germany
[2] Nuklearmedizinische Klinik Rechts der Isar der Techn. Universität München, Germany
[3] Max Planck Institut für Extraterrestrische Physik, Garching, Germany
[4] Paul Scherrer Institut, Villigen, Switzerland

ABSTRACT: Avalanche photodiodes (APDs) have several advantages in the readout of scintillators over photomultipliers (PMs) and photodiodes (PDs), particularly in applications where fine granularity is needed and/or high rates of fast (1-500 ns), low light level signals are to be expected. In this paper, properties of APDs will be discussed and compared to those of PMs and PDs. On recent tests and possible applications of APDs will be reported as well as directions for the future development of APDs for the fast, low light level readout will be given.

I. INTRODUCTION

Many nuclear detectors are based on devices that emit light such as scintillation counters or Cerenkov radiators. In common to all of these detectors is a small light yield and a short emission time ranging from nsec (Cerenkov light, plastic scintillators) to a few μsec (high Z inorganic scintillators for γ detection). The classical readout element for these detectors are photomultipliers (PMs). Whenever a very large detection area or very low light level detection, (e.g. single photon counting at high speed) are required, PMs are still unsurpassed due to their low noise. PMs do however have limitations such as a large volume or sensitivity to magnetic fields. Since about 10 years silicon photodiodes (PDs) have been used as a replacement for PMs in some systems having a large number of individual channels or being operated in magnetic fields (examples are given in refs.[1] to [6]). The main advantages of PDs over PMs are their compactness, complete insensitivity to magnetic fields, high stability due to unity gain and high quantum efficiency. A severe restriction on the use of a PD readout comes from the large noise, caused both by the leakage current of typically 1-10 nA/cm^2 diode area and the series noise of the PD-preamplifier system. This noise can normally only be reduced by introducing long filter time constants unsuitable for high rate applications. Silicon photodiodes with internal avalanche amplification can overcome some of the drawbacks. Early APD designs were characterised by small size, high excess noise, non uniformity in gain, high temperature dependence of avalanche gain, high voltage (> 500 V), low sensitivity to blue light or high capacitance. In addition widespread operation tolerances and insufficient reliability under severe operation conditions such as under high radiation backgrounds or accidental exposure to ambient light made them difficult to use in the past. Recently, new techniques such as ion implantation, deep Ga diffusion or epitaxial growth have resulted in the production of large area APDs with low noise, high stability, high reliability and narrow operational tolerances.

APDs could be used particularly where PDs are at their limit in high rate applications, e.g. where signals are well above the one photoelectron level but fast readout is needed. The advantages of APDs over PDs are lower noise for fast readout and lower (typically by a factor 10-100) 'nuclear counter effect' (see chapter IIIc).

We have studied the readout of fast scintillators by using some commercially available APDs. In this paper we first briefly discuss the operating principles and noise properties of APDs and then present the results of a series of tests which demonstrate that APDs can be quite successful in the fast, low noise readout of scintillators. Furthermore a short overview of requirements for some future applications is given.

Proc. Int. Conf. on Inorganic Scintillators and Their Applications, SCINT95,
1996, Delft University Press, The Netherlands

II. THEORY AND PROPERTIES OF APDS.

A) STRUCTURE OF APDS:

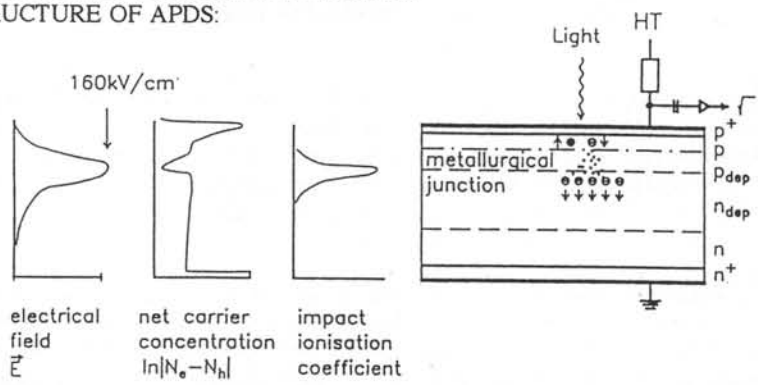

Fig. 1: Cross section (not to scale) of a blue enhanced APD. To the left the electrical field distribution, the charge carrier concentration and the impact ionisation coefficient is depicted (courtesy of Advanced Photonics).

For most scintillator applications one would prefer blue enhanced p-on-n APDs which have higher quantum efficiency (QE) for blue light than the classical n-on-p APDs. Figure 1 shows a cross section of a p-on-n APD. Incident photons are mostly converted into electron-hole pairs in the (depleted) p-layer. The photoelectrons will be accelerated to the depleted, high field pn-junction which is often called metallurgical junction or avalanche zone. Due to special doping profiles (see fig. 1) the electrical field is very high in this region. When the electrons reach the avalanche zone, they will be multiplied by impact ionisation. Finally the electron cloud drifts towards the ohmic contact at the n++ side while holes, moving in the opposite direction, are not accelerated enough in order to create also electron-hole pairs.

Classical APDs are more sensitive to red light. This is due to their design structure with a n-doped layer on top. The photons have to traverse the n layer before reaching the p-zone . Consequently only photons with a sufficiently long enough absorption length in silicon (i.e. of long wave length up to $\approx 1\mu$) can penetrate far enough, while most of the short wavelength light is already absorbed in the front n-doped layer and cannot be amplified.

Table 1 gives an overview over the properties of some types of APDs.

TABLE 1: Properties of some tested APDs:

type	manufacturer	Ø of sensor	bias for gain=50	I_{dark} gain=50	capaci-tance	t_{rise} [ns]	t_{fall} [ns]
C30916E	EGG(RCA)	1.5 mm	280 V	20 nA	< 10 pF	3	3
C30994E	EGG(RCA)	3x3 mm^2	400-500 V	150-200 nA	12-14 pF	?	?
S5344-SPL2060	Hamamatsu	3 mm	144 V	6 nA	≈ 120 pF	< 1	4
S5344-SPL5402	Hamamatsu	3 mm	280 V (g=100)	20 nA (g=100)	34 pF	< 1	?
S 5345-SPL2061	Hamamatsu	5 mm	145 V	320 nA	≈ 320 pF	< 1	8
S2384-SPL4053	Hamamatsu	3 mm	152 V	0.6 nA	≈ 40 pF	< 1	5
TL 15 CA 2	Ad.Photonics	15 mm	2216 V	6000 nA	≈ 110 pF	≈ 6	2

For most of our tests we used the Hamamatsu type S5344 which was very rugged, needed a low operation voltage and was easy to optically couple to scintillators; the only drawback was a high capacitance (120 pF), which has now been reduced in the new types (SPL5402) to 34 pF. Another advantage for high energy physics (HEP) applications was the very thin active p-layer (= reduced red sensitivity) being sensitive to signals from the passage of charged particles, see discussion about the so-called nuclear counter effect.

B) NOISE CONSIDERATIONS:

At room temperature and above semiconductor light detectors are in general more noisy than PMs. Dominant noise sources are the leakage current and the parallel capacitance of the diode and the amplifier. Noise suppression is normally achieved by limiting the bandwidth of the readout circuits. In the case of large area PIN photodiodes one uses filter time constants in the range of a few μsec for best performance at low light levels while for APDs with internal gain the best low noise response is shifted towards shorter readout times because both the parallel and series noise are reduced by the internal amplification process (which is itself another source of noise).

The noise in APDs can be calculated in good approximation by formula (1):

$$ENC^2 = \frac{1}{8}\left[2q\left(\frac{I_{ds}}{g^2} + I_{db}F\right)\cdot\tau + 4kTR_s\frac{C_{tot}^2}{g^2}\cdot\frac{1}{\tau}\right] \qquad (1)$$

with:

ENC	= equivalent noise charge	F	= excess noise factor
q	= electron charge	τ	= filter time constant, assume $\tau = \tau_{diff} = \tau_{int}$
g	= avalanche gain	k	= Stefan-Boltzmann constant
I_{ds}	= component of dark current that is not amplified (surface leakage and n-layer bulk current)	T	= absolute temperature
		R_S	= (APD + amplifier) series noise resistance
I_{db}	= component of dark current that is amplified (bulk current from the p-layer)	C_{tot}	= parallel capacitance (APD + cable + preamp)
		the parallel noise term $2q\,(I_{ds}/g^2 + I_{db}F)\,\tau$ is $\sim\tau$	
		the series noise term $4\,k\,T\,R_s\,C^2/(g^2\,\tau)$ is $\sim 1/\tau$	

F is the so-called excess noise factor which expresses the broadening of the noise distribution of I_{db} due to the statistics of the avalanche process. It can be seen from formula 1 that the surface leakage current contributes rather little to the parallel noise ($\sim\tau$) because in the APD only the electrons of the p-layer, e.g. the signal and the bulk current, are amplified by avalanche multiplication. This is one of the main differences compared to the PIN-PD, where surface-leakage currents are one of the main noise sources. On the other hand the thermally generated bulk dark current in front of the avalanche zone is amplified and contributes fully to the noise. Due to the avalanche multiplication the shot noise of this type of dark current is increased by the excess noise factor F which has for the best current APDs a value of 2 to 3 for a gain of 50-100. One of the most important challenges in future APD designs is to raise the gain while keeping F low by proper field distributions in the avalanche region. Formula 1 shows that the second contribution to the total noise comes from the series noise which is given by the product of the total series resistance and the sum of the parallel capacitances of the APD, the connecting cable and the preamplifier, but again divided by the gain. The other challenge for future designs is to keep both C low (not always possible) and to raise the gain. In general the optimum working condition for minimal noise as a function of τ occurs when the first term in formula 1 is comparable to the second one.

It should be mentioned that part of the excess noise has its origin in the hole multiplication which is not exactly zero even for modern designs. The suppression of this multiplication is another challenge for APD designs.

Taking formula 1 one can calculate the signal/noise-ratio in an APD for a signal generating n photoelectrons in front of the gain zone:

$$S/N = \frac{n}{\sqrt{ENC^2 + (F-1)n}} \qquad (2)$$

ENC is the above calculated equivalent noise charge and (F-1)n is the excess noise caused by the avalanche multiplication of the signal itself.

As we have seen in chapter IIa, APDs from different suppliers have quite different properties, which are useful for different applications. For example the Hamamatsu S5344 has a very low dark current, while the EG&G C30994 has a very low capacity. On hand of a small test we discuss briefly the consequences of these two properties for the fast readout of

LSO- or BGO-crystals in PET applications. The crystal under test (4x4x12 mm^3) was wrapped in reflective material and optically coupled to the APD. The signals were amplified by a charge sensitive preamplifier (Canberra 2003BT), shaped by a filter amplifier (EG&G Ortec 579) and then fed into a multi-channel-analyser (MCA). For timing measurements two of such units, looking front to front to a positronium source, were coupled to a TDC and generated after appropriate delay the 'Start' and 'Stop' signals.

LSO emits in average 30000 photons/MeV with a characteristic decay time τ of approximately 42 ns, whereas BGO emits only about 6000 photons/MeV with a τ of 300 ns. Let us assume that we want to detect 511 KeV annihilation γs which produce signals of 15000 or 3000 photons respectively. Let us further assume that 20 % of the emitted photons are converted into photoelectrons such that $\approx$ 3000 or 600 primary photoelectrons form a signal within 42 or 300 ns, respectively. Integrating the charge of these pulses will result in a signal with regard to the integration time as depicted in figure 2 together with the calculated ENC. Figure 3. shows the corresponding S/N ratio, again as a function of the shaping time.

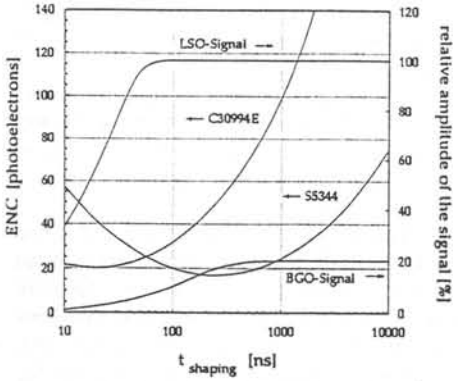

Fig. 2: Pulse height and ENC in units of photoelectrons as a function of the integration time ($\approx$ shaping-time).

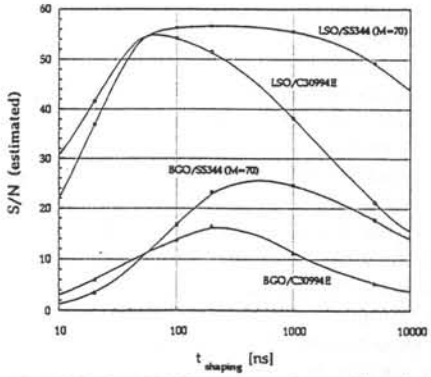

Fig. 3: S/N (511 KeV-gammas) as a function of the shaping time, for LSO and BGO read out by the S5344 and the C30994 .

The S/N curves in figure 3 show that the S5344 is far superior with respect to low noise for shaping times >50 ns for LSO and >100 ns for BGO, whereas the C30994 is better suited in the case of a very fast readout. This manifests itself also in a somewhat better time resolution of the C30994 compared to the S5344 in LSO- and BGO-readout because one has to use short shaping times for timing [8-11]. On the other hand the S5344 readout gives a superior energy resolution for shaping times > 50 ns for LSO and > 100 ns for BGO.

III. SOME TESTS WITH APDS

A) EVALUATION OF RADIATION HARDNESS

It is important to discuss briefly the impact of radiation damage because APDs are very interesting readout elements of scintillators in HEP applications. Radiation damage will normally influence the parallel noise (first term in eq. 1.), in particular by an increase of the surface leakage current, therefore one expects that the impact of radiation damage should be less critical for APDs than for PIN-PDs.

Some radiation hardness tests were carried out with the APD S5344 in comparison to a PIN-PD (Hamamatsu S1790) by exposing them both to a ^{60}Co γ source (70krad/h) and a 70 MeV proton beam. Both devices were fully biased during irradiation. The results are depicted in figure 4.

In both devices a substantial increase in dark current occurred. While the PD showed a serious degradation in resolution (tested by the widening of the 60 KeV γ -line from an Americium source), no degradation was observed in the APD. It should be noted that

immediately after the exposure the PD degradation was much higher and the diode needed ≈24 h for recovery albeit to a worse noise level than before the exposure, while the APD was fully operational immediately after the radiation exposure. This is of importance for operation at storage rings where partial beam losses during filling or tuning can give rise to short term extreme high radiation levels. In a second test, the APD was exposed to an intense 70 MeV proton beam of an integrated flux of 10^{13} protons/cm^2. The dark current increased by a factor of 300. After 2 days this fell to a value of 170. In order to speed up the recovery the diode was annealed for one day at 250°C and the dark current increase fell to a value of 30 after which the diode could be used for measurements with some noise degradation.

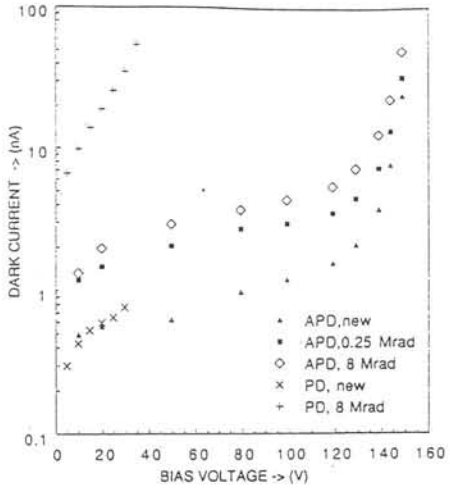

Fig. 4: Increase in dark current after 0.25, 2 and 8 Mrad γ-exposure.

If our test is exemplary it can be concluded that one can work at least up to a level of 8 Mrad γ (electron)-exposure with this type of APD without significant noise degradation, but an exposure of around 200 krad to highly ionising protons can seriously affect their performance.

A method of minimising the influence of a large leakage current on the noise is to work with the shortest possible filter time constant even at the expense of higher series noise. For certain applications it may be worthwhile to select APDs with a thin depleted volume and a large capacitance in order to keep the bulk current within acceptable limits. This translates the problem to one of a low noise amplifiers.

B) SENSITIVITY TO MAGNETIC FIELDS:

Many applications require the installation of detectors inside magnetic fields. APDs offer a clear advantage over PMs. As reported in ref. [14] APDs tested in fields up to 5 Tesla show less than 1% change in gain.

C) NUCLEAR COUNTER EFFECT

In many applications, particularly in high energy physics experiments, the light sensors may be traversed by charged particles. This can give rise to large false signals. In PDs the entire depleted volume is active while in an APD only the depleted volume in front of the gain zone is of importance while the volume behind the zone contributes very little. An APD configuration, as shown in fig. 1, is in general more suitable than the 'reach through' structure. For example, particles passing through the high C version of the S5344 produce only about 1.5 % of the signal generated in the depletion volume of a standard 200 μm PD such as the Hamamatsu S1790, i.e., only about 3 μm of the depleted layer of the S5344 are 'sensitive' to charged particles.

D) NOISE MEASUREMENT WITH γ-QUANTA:

To roughly estimate the noise performance of APDs, one can use γ's from a ^{55}Fe-source or light pulses from a laser or a LED. γ's from ^{55}Fe have an average energy of 5.96 KeV thereby generating approximately 5.96 KeV/3.6 eV = 1600 primary photoelectrons when being absorbed in the active layer of the APD. This signal can be used as a calibration standard and the line broadening for an estimate of the noise performance of the APD. Fig. 5 shows a typical ^{55}Fe -spectrum detected by a new low capacitance version of the S5344. The line shape can be somewhat asymmetric which might have its origin in the spread of the γ

absorption in depth. Some of the γ's are not absorbed in the depletion layer before the avalanche zone, but in or even behind the zone. Those signals are not fully or not at all amplified by the avalanche process and show up as a non-gaussian broadening and a tail on the left side of the peak. For best estimates only the right side of the distribution should be used for noise calculations. When taking the distribution of figure 5 we derive a broadening to about 67 electrons, which corresponds to a FWHM of 160. This includes the excess noise factor and noise contributions from the preamplifier. This result demonstrates the good noise performance of the new type of S5344 and gives hope that future APD designs might reach a noise of only a few electrons and hence being almost as good as photomultipliers but with much higher quantum efficiency.

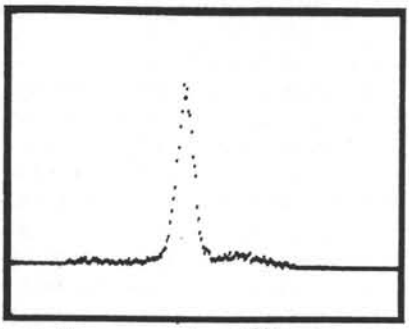

Fig. 5: Energy spectra of ^{55}Fe, detected by a new type of S5344 (C = 34 pF);τ = 20 nsec.

IV. APPLICATIONS IN HIGH ENERGY PHYSICS

There exist a multitude of applications for possible APD readout of scintillators in HEP. Whenever the light yield is above a few hundred photons and these can be concentrated onto a small area then it should be possible to replace PMs by APDs. The main area of application are a) for scintillators that have to be read out in magnetic fields, b) where compactness is a premium, c) where fine granularity is necessary. and d) extreme high rate per channel is not required.

Examples are the readout of fine granularity beam hodoscopes of plastic scintillators or the readout of fast, low light yield scintillating crystals for γ calorimetry. A description for the readout of pure CsI crystals is given if ref. [7]. In this reference the problem of coupling of a large cross section crystal to a 3 mm APD is discussed. A possible solution is offered in form of a fluorescent flux concentrator.

For other examples for crystal readout by APDs we refer the reader to the various contributions to this conference from the CMS collaboration. The APD's high sensitivity at low noise levels and fast readout speed was a decisive argument to consider them for the readout of CMS γ calorimeter of $PbWO_4$ crystals, which have on one hand a very short radiation length and a short scintillation decay time but on the other hand a very low light yield.

Further detaiis about the possible implementation of APDs in high energy physics detectors can be found in refs. [7, 8, 14].

V. AN EXAMPLE FOR NUCLEAR MEDICAL APPLICATIONS

Scintillation detectors have found widespread use in medical applications. One area is the detection of γ-rays of several hundred KeV in positron-emission-tomography (PET), where 511 KeV-annihilation γ's are detected by opposite scintillation crystals with a high spatial resolution of a few millimeters. APDs can offer a significant advantage over PMs as APDs can be miniaturised down to a few mm Ø and hence guarantee not only high spatial resolution, but also short dead times, which result from the 1:1-coupling of APD and crystal. State of the art PET systems with PM readout of a matrix of BGO-crystals are based on the Anger weighting principle. This method leads to long dead times and pile up-effects. With such a system at most a spatial resolution of 5 mm (FWHM), a timing resolution of about 5-10 ns (FWHM) and an energy resolution for the 511 KeV-γ's of 20-30 % (FWHM) can be reached. A system, in which photomultipliers (PM) are replaced by APDs in a 1:1-coupling to BGO-crystals was first proposed by [11] in 1985 by using the APD C30994E. This BGO/APD-detector resulted in a significant improvement in spatial resolution of 1.9 mm,

FWHM but significant degradation in time resolution (12-20 ns, FWHM). Recently we carried out a small test on the basis of the APD S5344 coupled to LSO crystals of fine granularity [9, 10]. The result was an overall improvement in performance which is compared in table 2 to the BGO/PM- and the BGO/C30994E-configuration.

Table 2: Prototype PET-performance of different detector-configurations:

	LSO/S5344	BGO/C30994E	BGO/PM
spatial resolution*) [mm, FWHM]	2.3	1.9	~ 5
timing resolution [ns, FWHM]	~ 3	~ 15-20	~ 10
energy resolution [%, FWHM]	~ 15 (662 KeV)	~ 25 (511 KeV)	~ 25 (511 KeV)

*) geometry of crystals was slightly different e.g. the cross-section was 4x4 mm^2 for the LSO-crystal coupled to the S5344 and 3x5 mm^2 for the BGO-crystal coupled to the C30994E.

Further improvements of the APD S5344, like reducing the relatively high capacity of 120 pF to less than 40 pF (now available as prototype) without increasing the low dark current, should lead to a timing resolution of the LSO/S5344-detector of ≈ 2 ns FWHM at shaping times of 10-20 ns. Also the energy resolution should be improved to 10-12 % FWHM for 662 KeV.

Further details on the studies for future PET applications can be found in ref. [9] and in a separate presentation of this conference, ref. [15].

VI. A POSSIBLE APPLICATION IN ASTROPHYSICS

Scintillation radiation detectors are widely used in research satellites. Since these detectors need to be light-weighted, low voltage devices of low power consumption and of high shock resistance, APDs might be an attractive replacement for photomultipliers. Here we present as example a possible scintillation detector for the wide angle γ detector GLAST, the successor of EGRET. Fig. 6 shows a simplified design concept. The main elements of GLAST are a multilayer Si-strip detector and a segmented CsI(Tl) γ calorimeter. Cosmic γ-rays are converted with a certain probability in the silicon tracker and the initial energy is measured in the calorimeter. The e^+e^- track allows to determine both the incident direction and thus extrapolate back to the source and to predict the impact point on the calorimeter. An important task in detecting γs is to separate them from the many orders larger charged cosmic ray background which carries no information on the incident direction.

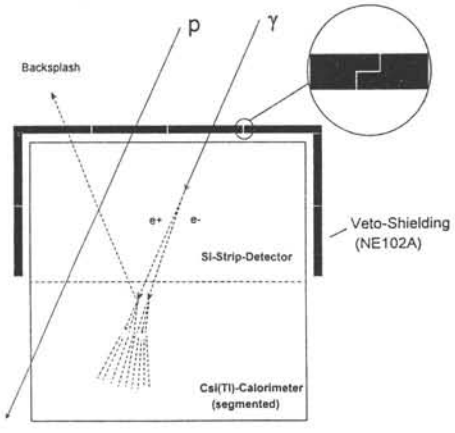

Fig. 6: Schematic (not to scale) of GLAST.

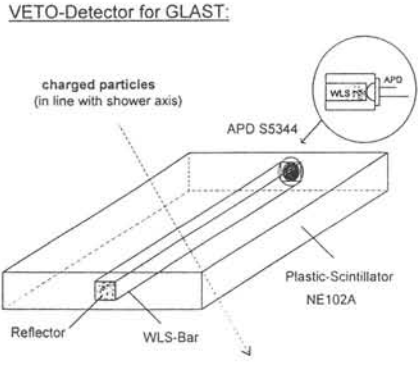

Fig. 7: Readout of the veto-scintillator-tile by a wavelength-shifter bar coupled to an APD.

Previous γ satellites used a plastic scintillator veto shield read out by PMs. The large size of GLAST would create considerable problems due to the increased veto rate from

accidentals and also from a considerable suppression of rare high energy γ-rays due to back scatter. A way out might be to replace the continuous veto shield by segmented elements which can be correlated to the active CsI cells. We have carried out a feasibility test for the readout of a 18x18x1 cm^3 plastic scintillator. The actual readout was formed by a wavelength shifter bar coupled to the original 140 pF version of the S5344. The unit was exposed to cosmic muons and triggered by two, 10x4 cm^2, coincidence counters positioned above and below the scintillator. Figure 7 shows the principle, figure 8 the test set-up and figure 9 the resulting pulse height spectrum for passing muons.

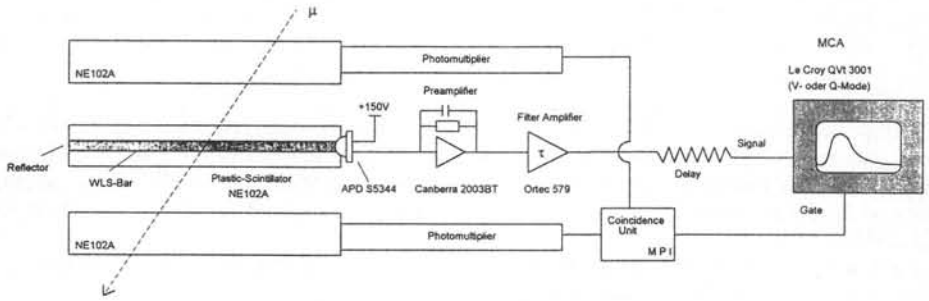

Fig. 8: Set-up for measuring the pulse height spectrum of cosmic muons

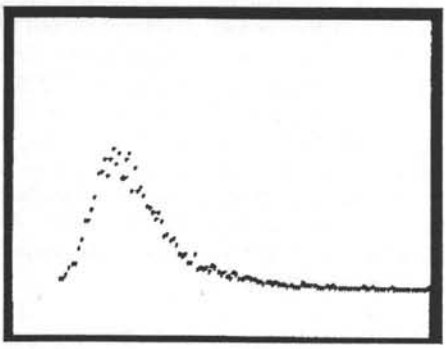

Fig. 9: Pulse height spectrum of cosmic muons passing the test unit (APD gain 100, $\tau = 20$ nsec)

The mean pulse height in figure 9 corresponds to about 250 photoelectrons, i.e. to about 5 times the noise. This is not yet fully acceptable but some improvements should be possible, such as using a low C version of the S5344 or a better optical coupling.

As another example for a forthcoming application in astrophysics we refer to ref. [7], where the design of a high granularity camera in connection with an image intensifier for an air Cerenkov telescope is discussed.

VII. FUTURE DIRECTION

The various test results allow one to define new targets for future improved APDs. Table 3 lists some requirements for four classes of potential applications. These applications are deliberately chosen on the borderline of achievable performances and could be considered as basis for next generation APDs. In common to all applications is the requirement for high gain and low noise at fast filter time constants. The four chosen areas are: the readout of high Z, low light yield, fast scintillators in high energy physics (HEP) γ calorimetry, high resolution PET, readout of fast plastic scintillators and a high resolution camera for air Cerenkov telescopes in cosmic ray physics.

VIII. CONCLUSIONS

In summary the discussed examples and tests have shown the advantages which can be offered by modern APDs in applications where fast, low-noise readout of scintillators is needed. The low noise at a readout time below 100 nsec is a significant advance over the PIN PD readout. Therefore APDs have a large potential for future applications. The detection of

single photons is still out of reach for room temperature applications. Due to size limitations APDs are better suited to the readout of small scintillators. For large ones one has to use intermediate elements such as wavelength shifter bars or fluorescent flux concentrators (FFCs). Beside the efforts to improve the quality of APDs there exists a clear need for the development of new fast preamplifiers with better noise performance.

TABLE 3: Requirements for APDs for four areas of applications

Device for	HEP γ calorimeter	PET	plastic scint. detectors	camera for air C-telescopes
area	≈ 05-2 cm^2	≈ 3-10 mm^2	≈ 0.5-2 cm^2	≈ 10 mm^2
device capacitance per 10 mm^2 area	< 200 pF	< 50 pF	< 50 pF	< 30 pF
typical gain	50-100	100	50-100	100-300
noise/10mm^2 area and τ =20 nsec	200 e	50 e	30 e	< 6 e cooled
excess noise factor at g=100	2-3	≈ 2	2-3	< 2
upper rate limit	>10^6(10^7)/sec	10^5/sec	>10^6	-
radiation hardnes	very high 10-100 Mrad >10^{14} n/cm^2	modest	modest	-
resistance against high peak loads	high	-	modest	very high > 10^8 phot./μsec
nuclear counter eff.	small 2-5 μ active layer	-	modest	-
blue sensitivity	QE > 50 % (λ=400nm) ->		->	->
temperature stab. at g = 100	< 0.5 %/°C	->	->	->
$\Delta g/\Delta U$ (g=100)	< 10%/1%	->	->	->
operation voltage	< 300 V	->	->	->
optical coupling	needed (n≥1.5)	->	->	->

IX. ACKNOWLEDGEMENTS

We thank Dr. Yamamoto, Hamamatsu Photonics for the modified APDs and Crismatec and Schlumberger-Doll for some of the crystals tested. We thank also our colleagues from the Paul Scherrer Institute for the help to carry out the radiation damage studies.

X. REFERENCES

[1] G. Blanar et al.; *Nuc. Inst. Meth.*; A 203 (1982) 213
[2] H. Grassmann et al.; *Nuc. Inst. Meth.*; A 235 (1985) 319
[3] J. Groom; *Nuc. Inst. Meth.*; 219 (1984)
[4] E. Lorenz et al.; *Nuc. Inst. Meth.*. A 249 (1986) 235
[5] R. Sumner; *Nuc. Inst. Meth.*; A 265 (1988) 252
[6] C. Bebek et al.; *Nuc. Inst. Meth.*, A 265 (1988) 258
[7] E. Lorenz et al.: *Nuc. Inst. Meth.;* A344, (1994), 64
[8] I. Holl et al.: Some Studies of Avalanche Photodiode Readout of fast Scintillators. *IEEE NSS*, Norfolk, VA, Oct. 1994.
[9] C. Schmelz et al.: Feasibility Study of an APD Readout for a High Resolution PET with nsec Time Resolution. *IEEE MIC,* Norfolk, VA, Oct. 1994.
[10] C. Schmelz: Diploma thesis, Technical University, Munich, 1994, unpublished.
[11] R. Lecomte et al.: *IEEE Trans. Nucl. Sci.* 32, No. 1, 1985, 482-486.
[12] R. Lecomte et al.: *Nuc. Inst. Meth.;* A278, (1989), 585-597.
[13] C.L. Melcher et al: *Nuc. Inst. Meth.;* A314, (1992), 212-214.
[14] D. Renker et al.: *Paul Scherrer Institut Report* TM-13-94-02. August 1994.
[15] S. I. Ziegler et al.: APD Readout of LSO for High Resolution PET. Cont. to this conf.
[16] P. F. Michelson: GLAST. A Next Generation High-Energy Gamma-Ray Telescope. Proc. Int. Workshop *Towards a Major Atmospheric Cerenkov Detector III*, Tokyo, 1994

AVALANCHE PHOTODIODE READOUT OF LUTETIUM-OXYORTHO-SILICATE FOR HIGH RESOLUTION POSITRON EMISSION TOMOGRAPHY

S.I. Ziegler[1], C. Schmelz[1,2], E. Lorenz[2], D. Renker[3]
[1]Nuklearmedizin TU München, [2]Max-Planck-Institut München, Germany,
[3]Paul Scherrer Institut, Villigen, Switzerland

ABSTRACT

High resolution positron scanners with three-dimensional data acquisition specially designed for imaging small animals are essential for the noninvasive evaluation of new tracers. High spatial resolution, good efficiency, adequate count rate linearity and small dimensions can best be realized in tomograph designs based on small detector units with one-to-one coupling of crystals and light sensors. Lutetium-oxyorthosilicate (LSO) crystals are very promising for applications in positron emission tomography because of their high light yield, fast decay time and good detection efficiency.

New, low noise, UV enhanced avalanche photodiodes (Hamamatsu S5344, 3.0 mm dia.) were coupled to small (4.0 mm x 4.0 mm x 9.5 mm) LSO scintillation crystals. The signals of the avalanche photodiodes were fed into transimpedance preamplifiers and fast filter amplifiers. All measurements were performed at room temperature. The energy resolution for 662 keV gamma quanta was 11% (FWHM). Timing measurements, performed with two opposing detector units viewing a positron source (^{22}Na, 1.0 mm dia.), yielded a spread of 2.6 ns (FWHM). In a setup simulating a ring of detectors with a diameter of 10 cm spatial resolution was 2.3 mm (FWHM) with little degradation across the field-of-view.

Our measurements showed that this compact detector module combines adequate energy resolution with improved time resolution. The unique features of this very thin readout device make it feasible to design a multi-layer detector module for small diameter positron tomographs facilitating depth of interaction detection.

INTRODUCTION

Positron emission tomography (PET) offers the advantage of measuring the biodistribution of a labelled substance invivo. Based on the tracer principle it is a very sensitive tool for metabolic imaging in combination with modern radiochemistry. Examples of invivo biochemistry already performed in humans are glucose metabolism, innervation, or blood flow. Before new tracers can be used in humans they have to be evaluated and characterized in animal experiments. The idea of dedicated designs of tomographs with specially adapted performance specifications originates from the necessity to reduce the number of animals needed in these validation studies [1-4]. Commercial tomographs consist of BGO-block detectors and photomultiplier tubes with Anger-type readout. High resolution volume imaging devices require high detection efficiency, spatial resolution, count rate linearity and isotropic resolution across the field-of-view. The use of one-to-one coupling for a high granularity device is advantageous for this application compared to the block detectors.

Small rings or tubular geometry ensure high detection efficiency and less effect of angular misalignment of the annihilation photons but have the disadvantage of variable resolution across the field-of-view of the camera. This dependency can be eliminated by implementing depth-of-interaction detection. Fast scintillators are preferred since they allow narrower coincidence windows and therefore reduce the random count rate.

With the development of new, fast avalanche photodiodes (APD) closely packed detector modules become feasible [5]. Due to their internal amplification these readout devices are

Proc. Int. Conf. on Inorganic Scintillators and Their Applications, SCINT95,
1996, Delft University Press, The Netherlands

specially suited for application in scintillator readout. Small area APDs are available and can be directly coupled to the scintillation crystal.

LSO [6] has been shown to be superior to BGO in the PET application because of its high light yield, fast decay time and comparable attenuation length for 511keV quanta.

MATERIALS AND METHODS

UV-enhanced, modified Hamamatsu APD S5344 were used in this study. The main features are summarized in table 1.

Table 1: APD parameters and characteristics

	S5344mod	next generation
sensitive area	3 mm dia.	3 mm dia.
bias	148 V at gain 70	290 V at gain 100
leakage current	10 nA at gain 70	10 nA at gain 100
capacitance	130 pF	34 pF
rise time	< 1 ns	< 1 ns

LSO crystals of the size 4mmx4mmx9.5mm were wrapped in several layers of white Teflon tape and directly coupled to the APDs using thin silicon rubber discs.

Transimpedance preamplifiers were used and their signals fed into fast filter amplifiers (EGG-Ortec model 579). The amplifier signals were analysed by an ADC (LeCroy model qVt) or constant fraction discriminators (EGG-Ortec model 934). All measurements were performed under normal laboratory conditions with average temperatures of 22-24°C.

Energy resolution was measured with a ^{137}Cs source. For timing measurements two identical detector channels were aligned directly opposing each other, facing a pointlike (1mm dia.) ^{22}Na positron source, each detector at a distance of 5cm from the source. With this setup the spatial resolution was tested by monitoring the coincidence count rate as a function of source position across the fiel-of-view. By rotating one of the detector modules we could simulate an offset line-of-response in a tomograph.

RESULTS

The detection efficiency of these detector modules was 38% at a 350 keV energy threshold. Since this is caused by the short length of the crystals but not by the crystal material itself, a structure consisting of two layers of these scintillators would have an efficiency of 70-80% and therefore be comparable to current designs.

Fig. 1 shows the energy spectrum for 662keV gamma quanta. The FWHM of the photopeak was 11% at a gain of 70 and a filter time constant of 20 ns.

Timing resolution at a threshold of 350 keV was 2.6 ns FWHM measured with two identical channels and 511 keV gamma quanta (fig. 2).

Only little degradation of the 2.3 mm (FWHM) spatial resolution was noticed for different lines-of-response, as expected due to the small detector length. Fig. 3 shows the distributions for different angles between the detector pair.

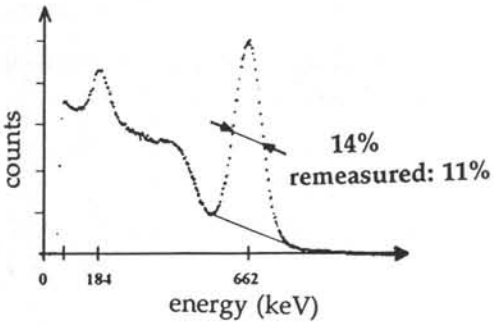

Fig. 1 Energy spectrum of ^{137}Cs

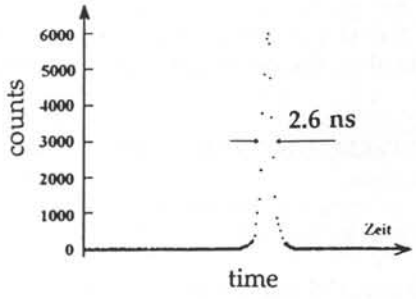

Fig. 2 Timing spectrum using pointlike ^{22}Na source

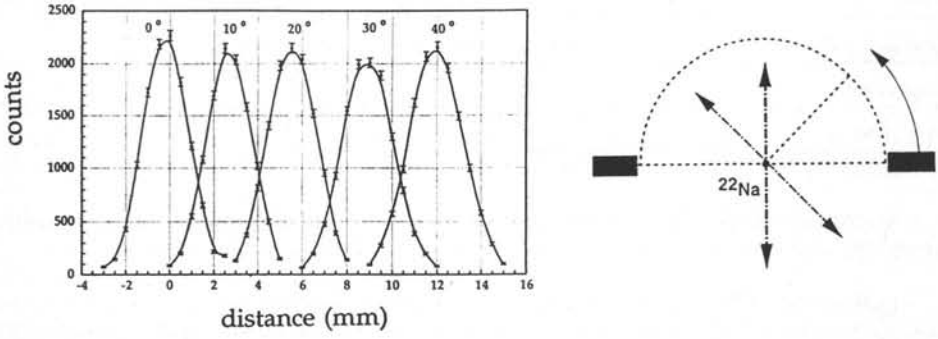

Fig. 3 Pointspread functions for different lines-of-response in a circular detector setup.

^{176}Lu content in LSO exhibits a natural background above 350 keV. The crystal samples used in these tests had noise rates of 20 per second at a threshold of 350 keV.

DISCUSSION

The readout of scintillation crystals with APDs has several advantages compared to photomultipliers: Because of their small size a high granularity detector module can be achieved. Coupling small LSO crystals to compact position sensitive photomultipliers could in principle give similar spatial resolution. Since the crystal-modules can not be stacked, timing as well as energy resolution can be expected to be less favourable because of the necessary crystal length.

Current APD designs are quite sensitive to small changes in the bias voltage and therefore need specially stabilized voltage supplies. New APDs with less gain dependance are being developed and will be even better suited for the PET application where thousands of detector channels have to function reliably in a clinical research environment.

A BGO-APD detector module was used in a PET-prototype before [3]. In this design a timing resolution of 20ns was tolerated to maintain the energy resolution of better than 25%. We have shown that by using the combination of LSO and fast APDs this compromise diminishes.

CONCLUSIONS

Our results show that the use of APDs in PET applications with high spatial and temporal resolution is feasible. New designs become available if arrays of APDs can be directly coupled to a two-dimensional array of LSO crystals. Several layers of such modules will enhance the detection efficiency per channel and facilitate depth-of-interaction detection. Also, Compton discrimination and collimation by event description becomes possible. Therefore, we expect the combination of LSO crystals and APD readout to gain importance in nuclear medicine applications in the near future.

ACKNOWLEDGEMENTS

We thank Dr. C.L. Melcher, Schlumberger (Ridgefield, CT, USA) for the provision of LSO crystals and Dr. Yamamoto, Hamamatsu Photonics (Hamamatsu, Japan) for the modification of APDs.

REFERENCES

[1] Rajeswaran S, Bailey DL, Hume, SP, Townsend DW, Geissbuehler A, Young , Jones T: 2D and 3D Imaging of Small Animals and the Human Radial Artery with a High Resolution Detector for PET. IEEE Trans Med Imag 1992;11:386-391

[2] Tavernier S, Bruyndonckx P, Shuping Z: A Fully 3D Small PET Scanner. Phys Med Biol 1992;37:635-643

[3] Lecomte R, Martel C, Cadorette J: Study of the Resolution Performance of an Array of Discrete Detectors with Independent Readouts for Positron Emission Tomography. IEEE Trans Med Imag 1991;10:347-357

[4] Watanabe M, Uchida H, Okada H, Shimizu K, Satoh N, Yoshikawa E, Ohmura T, Yamashita T, Tanaka E: A High Resolution PET for Animal Studies. IEEE Trans Med Imag 1992;11:577-580

[5] Lorenz E, Natkaniec S, Renker D, Schwartz B: Fast Readout of Plastic and Crystal Scintillators by Avalanche Photodiodes. Nucl Instr and Meth 1994;A344:64-72

[6] Melcher CL, Schweitzer JS: A Promising New Scintillator: Cerium-Doped Lutetium Oxyorthosilicate. Nucl Instr and Meth 1992;A314:212-214

[7] Watanabe M, Omura T, Kyushima H, Hasegawa Y, Yamashita T: A Compact Position-Sensitive Detector for PET. 1994 IEEE Conference Record:1652-1656

A SILICON DRIFT DETECTOR USED FOR THE READ-OUT OF A CsI(Tl) SCINTILLATOR

H. Valk[1], E. A. Hijzen[1], J. T. M. de Haas[1], R. W. Hollander[1], C. W.E van Eijk[1], P. M. Sarro[2], L. K. Nanver[2], A. van den Bogaard[2]
Delft University of Technology, The Netherlands
[1]Department of Applied Physics, Radiation Technology Group
[2]Delft Institute of Microelectronics and Submicron Technology (DIMES)

Abstract - A silicon drift detector was used as scintillation light sensor. The energy spectrum of a ^{137}Cs source was recorded using a CsI(Tl) crystal and compared with the spectrum obtained for the same crystal with a photomultiplier.

INTRODUCTION

In the past the use of photodiodes for the read-out of scintillation light has been studied [1-3]. Drift detectors have also been proposed as light sensors [4]. In this paper we present the silicon drift detector [5] as detector for scintillation light. These detectors are made at DIMES. The advantage of a drift detector over a normal photodiode of the same size is the smaller detector capacitance which reduces the total noise of the system. Drift detectors share with photodiodes features like reduced operation voltages, no internal amplification and a maximum quantum efficiency at longer wavelengths.
In a first attempt we mounted a CsI(Tl) scintillator on a drift detector. Its high light yield of 55,000 ph/MeV and emission peak at 565 nm [6] make it an attractive scintillator for read-out by means of a silicon detector.

PRINCIPLE OF OPERATION OF THE DRIFT DETECTOR

In figure 1 the schematic layout of a (circular) drift detector is shown. A single anode (n^+ region) is surrounded by several cathode rings (p^+ regions) on a high-ohmic silicon wafer. On the opposite side of the wafer a continuous cathode (p^+ implantation) provides a large entrance window for scintillation light. By applying different voltages to the cathodes a drift field can be created inside the drift detector which causes the photon induced electrons to drift towards the anode, indicated by the arrows in Figure 1. The drift time depends on the size of the detector and the biasing voltage and is of the order of microseconds. Due to the structure of the drift detector an increase in detector size will hardly increase the detector capacitance, which is usually around ~ 10^2 fF. Drift detector sizes of 55 cm^2 have been reported by Rehak [7].
In combination with a scintillator the optimum shaping time of the drift detector, usually around 2 μs for direct X-ray detection, may have to be increased if a slow decay component exists. For CsI(Tl) on a drift detector the optimum shaping time was found to be 6 μs, determined by the ~ 7 μs decay component of CsI(Tl).
Neither CsI(Tl) nor the drift detector are suitable to measure time information. For energy measurement, however, the long decay time and the long drift time, which impose a long shaping time, do not pose a problem. The combination is attractive for energy measurement.

Proc. Int. Conf. on Inorganic Scintillators and Their Applications, SCINT95,
1996, Delft University Press, The Netherlands

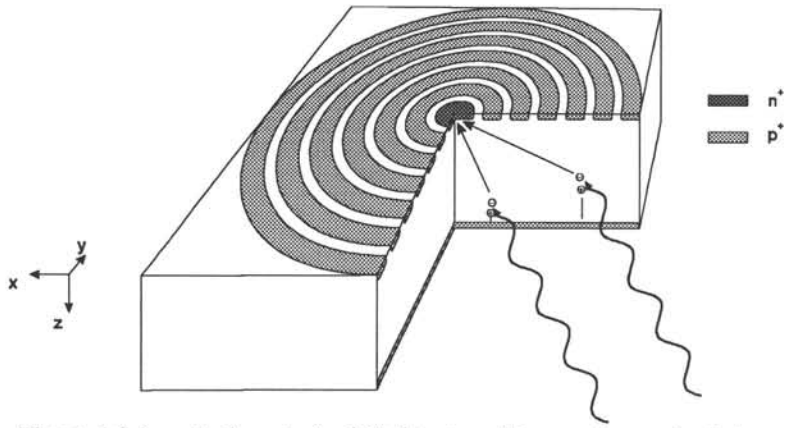

Figure 1 *Schematic layout of a drift detector with a continuous backplane*

EXPERIMENTAL SET-UP

We used a circular drift detector with an effective diameter of 7.5 mm and a continuous backplane. The entrance window of our detector was not optimised for the detection of light and in going to shorter wavelengths we expect a decrease in the quantum efficiency starting around 500 nm.
On top of the drift detector a CsI(Tl) crystal was mounted with a diameter of 5 mm and a height of 7.5 mm. The crystal was wrapped in Teflon leaving only one side free, which was contacted to the drift detector using Viscasil. In a reference measurement the same crystal was mounted on a XP2254B photomultiplier tube.

RESULTS AND DISCUSSION

We first used the bare drift detector and a ^{241}Am source, in order to obtain an absolute reference for the light yield. The 59.5 keV γ-ray will generate $1.65 \cdot 10^4$ electron-hole pairs in the drift detector. By comparing the peak position with that of the 662 keV γ-peak of ^{137}Cs the number of electron-holes was calculated to be $1.79 \cdot 10^4$, which corresponds to an overall photon detection efficiency of 50 %.
Measurements with a ^{137}Cs source and a CsI(Tl)-drift detector were done at room temperature. In Figure 2 the measured spectrum is shown. The best energy resolution was found for a shaping time of 6 μs, where the resolution of the 662 keV γ-peak was 7.6 %. The measurement with the photomultiplier tube showed an energy resolution of 6.7 % and a yield of 9720 phe/MeV. Thus the energy resolution using a drift detector is slightly worse than with a photomultiplier tube.
At 6 μs shaping time the preamplifier and the drift detector contribute 136 rms. electrons and 159 rms. electrons to the signal respectively. Together with the inherent energy resolution of the CsI(Tl) crystal of 6.6 %, this leads to an expected energy resolution of 7.1 %. The discrepancy between this value and the measured 7.6 % is probably caused by electrical interference for we also observed increased drift detector noise figures for measurements with the ^{241}Am source.

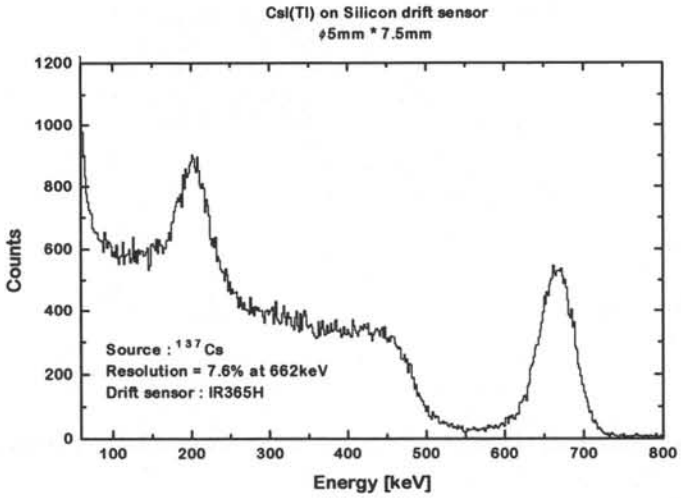

***Figure 2** Energy spectrum of ^{137}Cs (662 keV γ) measured with a combination of CsI(Tl) and a drift detector*

CONCLUSIONS

The non-optimized drift detector shows an energy resolution of 7.6 %, which is only slightly worse than that obtained using the XP2254B photomultiplier tube (6.7 %). The energy resolution can be improved by using an improved setup, an optimized entrance window (shallow p-type dead layer), cooling the drift detector and integrating a JFET in the anode. The silicon drift detector is an interesting low-noise alternative for the standard photodiode in cases where the time information is not important.

REFERENCES

[1] I.Holl, E.Lorenz, G.Mageras, A measurement of the light yield of common inorganic scintillators, IEEE Trans. Nucl. Sci. 35(1), 1988, p. 105

[2] J.C.C.Melle, G.J.Nieuwenhuizen, R.J.Meijer, P.F.Box, P.Decowski, R.Kamermans, Pulse shape analysis of CsI(Tl)-PD signals induced by 6-20 MeV α-particles and protons, NIM A277, 1989, p. 584

[3] P.Schotanus, P.Dorenbos, V.D.Ryzhikov, Detection of CdS(Te) and ZnSe(Te) scintillation light with silicon photodiodes, IEEE Trans. Nucl. Sci. 39(4), 1992, p. 546

[4] B.S.Avset, J.Ellison, L.Evensen, G.Hall, T-E.Hansen, S.Roe, R.Wheadon, Silicon drift photodiodes, Nucl. Instr. and Meth. A288, 1990, p. 131

[5] E.A.Hijzen, Design and fabrication of silicon drift detectors, thesis, Delft University Press, Delft, to be published 1995

[6] R.Visser, Energy transfer in fluoride scintillators, thesis, Delft University Press, Delft, 1993, ISBN 90-6275-933-5/CIP

[7] P.Rehak, A 55 cm^2 cylindrical silicon drift detector, presentation at the 7th European Symposium on Semiconductor Detectors, Schloβ Elmau, Germany, May 1995

CsI:Tl FOR SOLID STATE X-RAY DETECTORS

H. Wieczorek, G. Frings, P. Quadflieg, U. Schiebel,
Philips GmbH Forschungslaboratorien, Weißhausstraße 2, 52066 Aachen, Germany
T.F.v. Bergen, F.M. Dreesen, M.A.C. Ligtenberg, T. Poorter,
Philips Medical Systems Nederland B.V., Jan Campertstraat 5, 6416 SG Heerlen, The Netherlands

ABSTRACT

A well known concept of a flat panel X-ray detector consists of an a-Si:H photodetector array with an X-ray sensitive phosphor layer on top. CsI:Tl is the material of choice for such a digital imaging system since its light output is high, its emission spectrum is well adapted to the optical absorption of amorphous silicon photodiodes, and the intrinsic structure of the CsI layer gives a good spatial resolution. The requirements for the CsI:Tl layer, the possible signal and noise performance, and first measurement results on this solid state detector are discussed.

FLAT PANEL X-RAY DETECTORS

Present systems for X-ray imaging use an image intensifier tube to convert and amplify X-ray signals into visible light that is detected by an imaging tube or by a CCD camera. These imaging systems are bulky vacuum tubes with a curved input screen and an electron optics amplification stage. This set-up has the disadvantage of geometrically distorted pictures and veiling glare. The image quality could be considerably improved with a digital imaging system providing possibilities of image enhancement and a rigid correspondence of object and image pixels for fixed pattern noise correction. Furthermore, for certain medical applications like bed side imaging a flat and light detector would be much better suited. For these reasons there is a continuing effort to develop a solid state dynamic X-ray image sensor with digital readout.

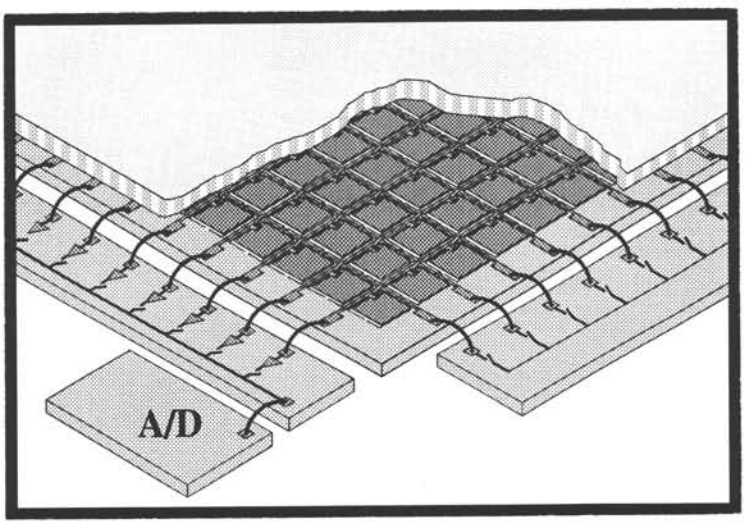

Fig. 1: Large area detector array with a-Si:H photodiodes and overlying CsI:Tl layer

Proc. Int. Conf. on Inorganic Scintillators and Their Applications, SCINT95,
1996, Delft University Press, The Netherlands

The fabrication of large area image sensors has been made available by the development of amorphous silicon technology for flat panel displays [1,2]. Photodiode arrays with an active area of up to 26 x 26 cm^2 and with a pixel size down to 127 x 127 μm^2 have already been developed [3]. An X-ray detector is built by covering the image sensor with an appropriate phosphor layer (Fig. 1). The incoming X-ray quanta are converted into visible light, these photons are absorbed in the a-Si:H photodiodes generating electron-hole pairs, and the photogenerated charge is stored on the diode capacitance of every pixel in the detector. After one frame time, the charge is electronically read out via thin-film transistors adjacent to each diode, transferred into a charge-sensitive readout amplifier, multiplexed and digitised for input into an image acquisition system [4].

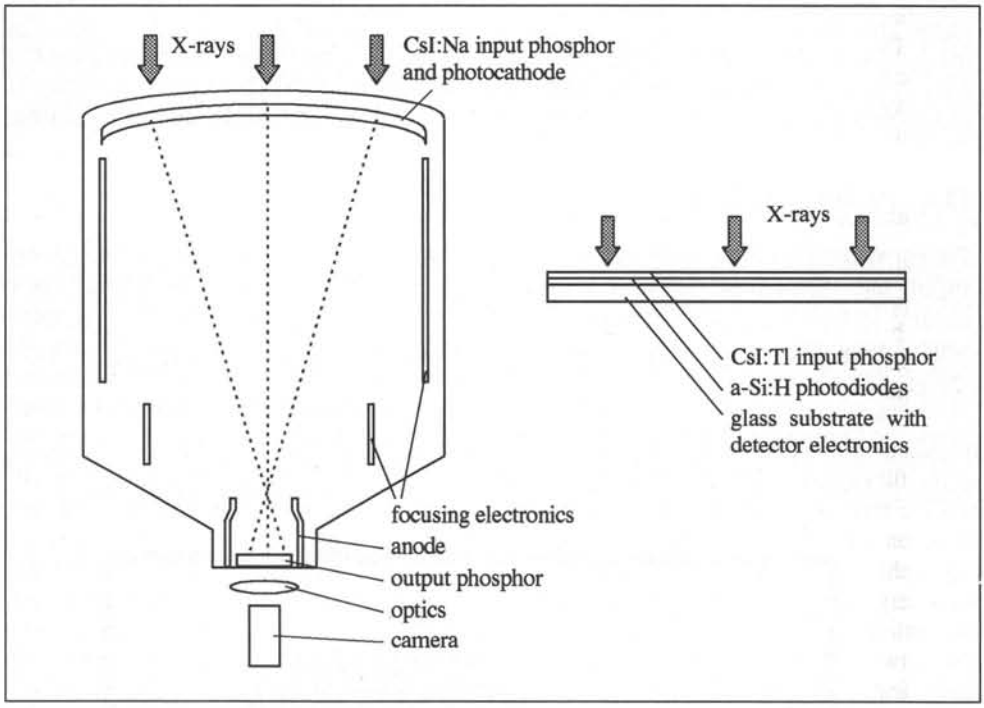

Fig. 2: Crossection of image intensifier (left) and flat panel X-ray detector (right)

SENSOR REQUIREMENTS

Compared to the traditional image intensifier - TV camera chain, this new device is flat and lightweight, it does not need electron optics in a vacuum tube, input screen and output section of the detector are in direct contact, and there is no image distortion due to the detector geometry (Fig. 2). There is, however, no signal amplification as in the traditional image intensifier, and the electronic noise that is added by the readout process of the photodiodes and the readout amplifiers is higher than that of an imaging tube or a CCD camera. For fluoroscopic examinations where an extremely low dose is applied, it is therefore difficult to provide the same signal-to-noise ratio as in present image intensifiers. A fluoroscopic image quality comparable to present systems can only be achieved when the detector signal is high

and the electronic noise is kept low. The only possible way to increase the signal is to absorb the X-ray quanta impinging on the detector and convert them into signal charge as efficiently as possible. This can be done by using thick phosphor layers with strong X-ray absorption, a high photon gain, and a good spectral match between the phosphor emission spectrum and the photodiode absorption spectrum. Absorption of a large fraction of the impinging X-ray quanta has the additional advantage of a high detective quantum efficiency and low X-ray shot noise. The electronic readout noise has to be kept low by a special detector and amplifier development.

Besides these requirements for signal and noise in the thin film detector, the spatial resolution of the new imaging system should be comparable or better than that of traditional image intensifier systems or intensifying screens. The modulation transfer function of an image intensifier is limited by the overall performance of the intensifier tube, including the electron optics. The phosphor itself, a relatively thin structured layer of CsI:Na, has a much better MTF than the imaging system. If, however, thick phosphor layers are applied in order to increase the X-ray absorption, the MTF may be limited by the phosphor layer itself and a compromise between signal and spatial resolution has to be found.

X-ray absorption and emission efficiency

X-ray quanta are absorbed mainly by photoelectric absorption, a process that depends on the fourth power of the atomic number. Therefore, compounds that contain heavy elements have always been preferred for X-ray detection. The maximum efficiency and the photon gain for an X-ray phosphor can be calculated using a model based on a statistical analysis of electron-hole pair generation [5].

Among the traditional X-ray phosphors there is $CaWO_4$ which has been used for many years in screen-film systems. It has a relatively low theoretical photon gain of 31 000 photons / MeV and the measured light output is still lower. Its X-ray absorption is less than ideal for the detection of diagnostic X-rays due to its K-absorption edge at 70 keV. The rare-earth oxysulphides like Gd_2O_2S:Tb, Gd_2O_2S:Pr,Ce,F or La_2O_2S:Tb are much better suited for the mid-energy range since their K-absorption edge lies at 50 keV or below and the X-ray absorption is much stronger in the range between 50 keV and 70 keV. Their photon gain is about twice as high as that of $CaWO_4$. Similar values of 62 000 photons / MeV are theoretically achieved by CsI:Na, the standard input screen phosphor for image intensifier tubes, and for CsI:Tl. Barium based compounds like BaFCl:Eu and $BaSO_4$:Eu have a photon gain of about 45 000 photons / MeV. The maximum photon gain of 94 000 photons / MeV is calculated for (Zn,Cd)S:Ag, a previously used input screen material for image intensifiers and for direct viewing screens.

Spectral match

The light emitted by the phosphor layer is absorbed and converted into electric charge in the amorphous silicon photodiodes on the flat panel X-ray detector. In order to get a high signal, the spectral range of phosphor emission and photodiode absorption should coincide as far as possible. Amorphous silicon photodiodes show the highest sensitivity in the range between 400 nm and 700 nm, with the maximum at about 580 nm, depending on the a-Si:H layer thickness (Fig. 3). Of the phosphors mentioned above, only (ZnCd)S:Ag, Gd_2O_2S:Tb,

La_2O_2S:Tb and CsI:Tl show an appropriate emission spectrum with the maximum intensity between 530 nm and 550 nm wavelength. The other phosphors were mostly optimised for film-screen combinations or for combination with a photocathode and show their main emission in the violet part of the spectrum. They can therefore not efficiently be used for X-ray detectors based on amorphous silicon photodiodes.

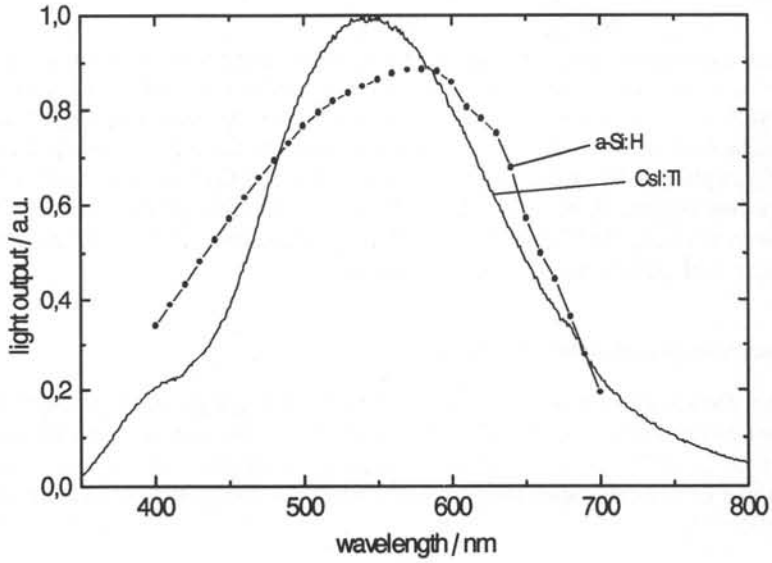

Fig. 3: Normalised CsI:Tl emission spectrum and quantum efficiency of a-Si:H pin diode

Spatial resolution

Even when a phosphor contains heavy elements, a layer thickness of several hundred microns is needed for an effective energy absorption. For spatial resolution reasons, it is desirable to use relatively dense and thin layers to prevent a wide spread of the light generated within the phosphor layer. While powder phosphors show only a packing density of approximately 50%, more than 90% packing density are achieved by production of ceramic layers from materials like Gd_2O_2S:Pr,Ce,F [6] or by vapour deposition of a phosphor layer. The latter technique is only possible with alkali halide type phosphors, among them CsI:Na, the material presently used in image intensifier tubes, and CsI:Tl.

Powder phosphors embedded in a binder layer and ceramic phosphors show a higher spatial resolution than a fully transparent phosphor layer because of the multiple scattering of light at the phosphor grains that stops the spreading out of the light cone over a large area. A much better contrast is achieved by a special vapour deposition technology for polycrystalline phosphors where small cracks are formed in a direction perpendicular to the surface of the layer, resulting in a layer that consists of a multitude of crystalline pillars with an average diameter of a few micron [7]. By total reflection of light at the crack interfaces, light channelling and an impressively improved contrast, compared to powder phosphors, is achieved.

Fig. 4 shows for comparison the MTF of different phosphor screens and a typical image intensifier tube, measured at one line pair per millimetre. The X-ray absorption is given as a relative measure of the phosphor thickness and the signal gain. Powder phosphor intensifying screens have been produced with different absorption to optimise either for high light output or for a good spatial resolution. Four samples of powder phosphor screens are given, with the two thinner screens based on $CaWO_4$ and the thicker ones based on Gd_2O_2S:Tb [8,9]. The MTF decreases strongly from 80% to values between 40% and 55% when the X-ray absorption is increased. One has to bear in mind that these film-screen combinations generally use two intensifying screens, one at the front side and one at the back side of the film. The absorption and the light output of a single screen are therefore much lower than that of the whole system. In contrast to these powder phosphor screens, the MTF of a typical image intensifier with a much thicker CsI:Na input screen of typically 300 - 400 µm thickness is higher than 60%. This MTF value is mainly determined by the electron optics, and the pure screen MTF is about 20% higher, showing the outstanding performance of the CsI evaporation method. It is the spatial resolution of the image intensifier system that we have to reach in the flat panel X-ray detector in order to get pictures of comparable quality.

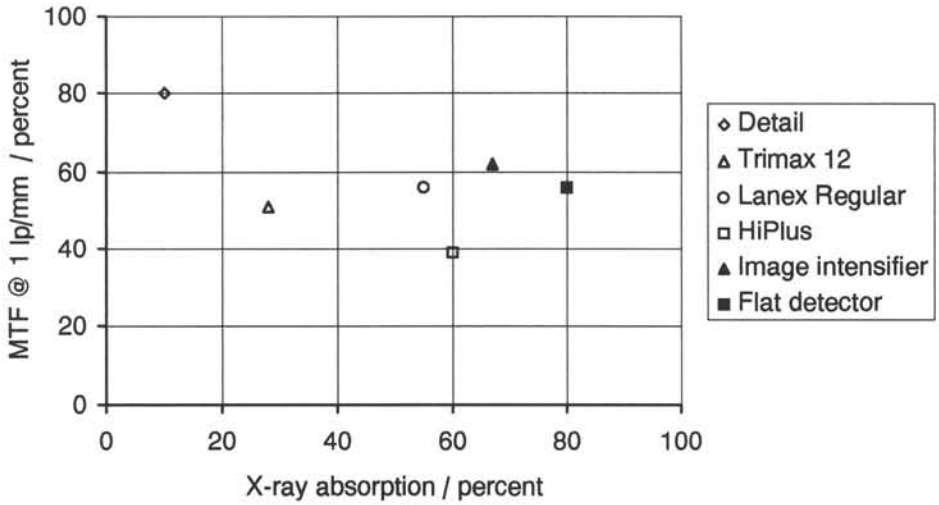

Fig. 4: MTF @ 1 lp / mm versus X-ray absorption for four different powder phosphor screens, a CsI:Na layer, a standard image intensifier and a prototype flat panel detector

Properties of CsI:Tl

Summing all the information given above, thallium doped caesium iodide is the material of choice for the flat panel X-ray detector application. It is the only X-ray phosphor that can be vacuum evaporated in thick layers with high packing density, pillar growth and therefore good spatial resolution, giving a high signal due to an appropriate photon gain and an excellent spectral match with the absorption spectrum of amorphous silicon. Furthermore, it can be deposited at moderate temperatures, and therefore it is possible to evaporate the phosphor layer directly on the detector array. This gives a much better spatial resolution than a separate CsI:Tl screen coupled to the detector panel.

DETECTOR PERFORMANCE

In the following, we will compare the performance of present image intensifier systems with the expected performance of a new flat panel X-ray detector and with measurements on prototype X-ray detector arrays. In the new detector concept, there is electronic noise due to the readout system that may be comparable to or even greater than the quantum shot noise in the fluoroscopic modes. Therefore, the system performance has to be evaluated in this low dose region. Typical values for the radiation incident on the detector in fluoroscopic applications are an average X-ray dose rate of 10 nGy per frame and a tube voltage of 75 kV with 1.5 mm Cu filter, giving an effective X-ray energy of 60 keV. The average quantum flux under these conditions is 12.3 X-ray quanta per pixel, referring to prototype detectors with a pixel size of 200 x 200 μm^2 as described in [4].

With the average X-ray dose rate of 10 nGy per frame there are regions in the image where the dose may be ten times lower. We want to view these regions without serious interference by noise, meaning that the X-ray detector should show nearly quantum limited operation even at the lowest dose levels of interest. The signal given by the absorption of one X-ray quantum has therefore to be equal or larger than the electronic noise of detector and readout circuit.

Comparison: image intensifier tube

Present image intensifier systems use CsI:Na input screens with a thickness of 300 - 400 µm. 67% of the X-ray quanta are stopped in the CsI layer, but because of K-escape and partial reabsorption, only 58% of the X-ray energy is effectively absorbed and can be converted into photons. Depending on the type of screen, 1500 - 2000 photons per absorbed X-ray quantum are extracted from the CsI:Na layer. Roughly 10% of these photons give rise to emission of photoelectrons from the photocathode applied on the input screen, and the photoelectrons are again converted into photons with a gain of 1000 - 2000 photons in the output screen. In the last stage, when the light emitted from the output phosphor is converted into electric charge in the camera tube, the efficiency of charge generation is less than 1% due to lens coupling and camera efficiency (Fig. 2). A typical value for the signal gain is 10 000 electrons / 10 nGy, referring to an area of 200 x 200 μm^2. This level is high enough for image intensifier systems since the electronic noise given by the plumbicon camera is less than 200 electrons and that of a CCD readout system is even lower. Compared to signal and X-ray shot noise, this noise level is low enough and cannot be seen in the imaging sequences even at fluoroscopic X-ray doses.

Signal and noise

This is different in a solid state X-ray detector since the readout of the signal from a large area detector cannot be performed without adding electronic noise. The X-ray absorption and the signal gain in the detector must be optimised for an appropriate signal-to-noise ratio if the detector has to be quantum limited even in low dose fluoroscopic regions.

Increasing the caesium iodide thickness from normally used 300 - 400 µm to 500 - 600 µm gives typically 80% absorption of X-ray quanta and 72% absorption of energy, accounting for K-fluorescence and partial reabsorption. According to solid state theory [5], the generation of one electron-hole pair in CsI needs 2.5 times the bandgap energy of 6.4 eV, or 16 eV. Assuming full extraction of the photons with the aid of a reflector layer on top of the phosphor, this results in a theoretically possible gain of 3 375 photons per absorbed X-ray

quantum of 60 keV energy. The quantum efficiency of light absorption in optimised amorphous silicon nip photodiodes is roughly 65%, calculated for the emission spectrum of CsI:Tl and the angular distribution of a Lambertian light source. With these values, we get an overall signal of 2 200 electrons per absorbed X-ray photon or 21 650 electrons per pixel and frame under a dose rate of 10 nGy / frame. With an active photodiode area of 47% as in the prototype detector arrays described in [4], this would give a signal of 10 150 electrons per frame. We have indeed measured values as high as 14 000 electrons, probably due to the reflection of photons from parts of the detector array outside the active diode area (Fig. 1). Extending the active photodiode area to 70% of the area available, we do expect far more than 15 000 electrons signal. It is interesting to see that even without a photoelectron amplification stage, a signal height comparable to or larger than in image intensifier systems is possible due to the good optical coupling of the phosphor layer to the large area photodiode array.

The electronic noise that is added in the detector readout consists mainly of two components, the transistor switching noise and the readout amplifier noise [4]. The first noise source is due to the switching of the readout transistor in each detector pixel. It is proportional to the square root of the photodiode capacitance and amounts to 700 electrons noise for a pixel capacitance of 1.6 pF. The amplifier noise is proportional to the parasitic capacitance at the detector readout lines and increases therefore with the size of the diode array. For an optimised 1k x 1k detector we expect a value of 600 - 700 electrons so that both components of the electronic noise would add up to less than 1 000 electrons. This is lower than the signal generated by a single X-ray quantum so that nearly quantum limited operation is possible down to dose rates of the order of 1 nGy / frame.

Spatial resolution

We have measured the MTF of 550 µm thick phosphor layers directly evaporated on prototype detector arrays using a lead grid. Under appropriate evaporation conditions, we got an MTF of 61% at a spatial frequency of 1 lp / mm. This value is comparable to the MTF of image intensifier systems with a considerably thinner CsI layer. When a reflector layer is applied at the top of the CsI layer, the MTF is reduced to 56%, a spatial resolution adequate for many film-screen systems. We expect even higher MTF values when the active photodiode area is increased to approximately 70% of the pixel area, resulting in a lower fraction of light reflected from the diode array into the phosphor layer and back to the photodiodes. With these MTF values and the high signal level of approximately 15 000 electrons / 10 nGy an acceptable compromise between signal height and spatial resolution has been found.

LUMINESCENCE MECHANISM AND AFTERGLOW PROBLEMS

One drawback of CsI:Tl for this application is its high amount of afterglow. This signal retardation is due to trapping of either electrons or holes that hinders the radiant recombination of these carriers. After the thermal emission of trapped carriers, recombination luminescence can be observed a long time after the end of the X-ray illumination pulse.

Though CsI:Tl has been investigated for some decades now, neither the mechanism of luminescence nor the afterglow mechanism have been clarified. It is still unclear whether afterglow in thallium doped caesium iodide is an intrinsic effect or whether it is caused by oxygen-containing impurities or stress caused by structural defects [10]. With the knowledge

of the luminescence mechanisms, there could possibly be a way to reduce the afterglow level by adding of codopants or by other measures [11].

CsI:Tl shows two broad emission peaks centred at 550 nm and 420 nm wavelength. The main peak at 550 nm was first interpreted by electron capturing at Tl^+, thermal emission of self-trapped holes to the valence band, migration to Tl^0 centres and recombination at the thallium ion [12]. Later interpretations tried to explain the symmetry properties of A-band emission at different excitation energies by the Jahn-Teller effect or by spin-orbit coupling of different states [13,14]. Newest papers show that the two main peaks consist of three or four emission bands, interpreted as different minima in the adiabatic potential surface of the excited state of the Tl^+ ion [15] or as partly A-band emission and partly triplet luminescence of self trapped excitons perturbed by the Tl^+ ion [16, 17]. Other papers stress the role of Tl-bound excitons as well, differ, however, in the interpretation of the possible role of self trapped holes and electrons as sources of afterglow [18,19]. Obviously, there is a lot of interesting work to do to clarify the luminescence and afterglow mechanism in CsI:Tl. Possibly, even a way will be found to reduce the afterglow and enhance the image quality of solid state X-ray detectors.

---

[1] R.A. Street, I. Fujieda, R. Weisfield, S. Nelson, P. Nylen, Mat. Res. Soc. Symp. Proc. 258, 1145 (1992)

[2] M.J. Powell, I.D. French, J.R. Hughes, N.C. Bird, O.S. Davies, C. Glasse, J.E. Curran, Mat. Res. Soc. Symp. Proc. 258, 1127 (1992)

[3] L.E. Antonuk, J.M. Boudry, Y. El-Mohri, W. Huang, J.H. Siewerdsen, J. Yorkston, R.A. Street, SPIE Vol 2432, 216 (1995)

[4] U. Schiebel, N. Conrads, N. Jungs, M. Weibrecht, H. Wieczorek, T. Zaengel, M.J. Powell, I.D. French, C. Glasse, Medical Imaging 1994: Physics of Medical Imaging, Proc. SPIE Vol. 2163, 129 (1994)

[5] D.J. Robbins, J. Electrochem. Soc. 127, 2694 (1980)

[6] Y. Ito, H. Yamada, M. Yoshida, H. Fujii, G. Toda, H. Takeuchi, Y. Tsukuda, Jpn. J. Appl. Phys. 27, L 1371 (1988)

[7] A.L.N. Stevels, W. Kühl, Medicamundi 19, 3 (1974)

[8] A.E. Burgess, Med. Phys. 5, 199 (1978)

[9] M.G. Fisher, Photographic Science and Engineering 26, 32 (1982)

[10] Ya.A. Zakharin, L.V. Kovaleva, L.L. Nagornaya, N.M. Naumenko, V.G. Protsenko, Yu.A. Tsirlin, L.N. Shpilinskaya, Iz. Akad. Nauk SSSR, Seriya Fizicheskaya 41, 1413 (1977)

[11] B.C. Grabmeier, J. Lumin. 60&61, 967 (1994)

[12] R. Gwin, R.B. Murray, Phys. Rev. 131, 508 (1963)

[13] D.J. Simkin, T.F. Belliveau, V.S. Sivasankar, K. Schmitt, P.W.M. Jacobs, J. Lumin. 31&31, 320 (1984)

[14] M.J. Stillman, P.W.M. Jacobs, K. Oyama Gannon, D.J. Simkin, phys. stat. sol. (b)124, 261 (1984)

[15] M. Nikl, J. Hlinka, E. Mihokova, K. Polak, P. Fabeni, G.P. Pazzi, Philos. Mag. B 67, 627 (1993)

[16] V. Nagirnyi, S. Zazubovich, V. Zepelin, M. Nikl, G.P. Pazzi, Chem. Phys. Letters 227, 553 (1994)

[17] V. Nagirnyi, A. Stolovich, S. Zazubovich, V. Zepelin, E. Mihokova, M. Nikl, G.P. Pazzi, L. Salvini, J. Phys.: Condens. Matter 7, 3637 (1995)

[18] J.M. Spaeth, W. Meise, K.S. Song, J. Phys.: Condens. Matter 6, 3999 (1994)

[19] G. Blasse, Chem. Mater. 6, 1465 (1994)

LOW-CROSSTALK MULTI-CHANNEL PMTs FROM UV TO IR

Esso Flyckt, Philips Photonics, BP520, F-19106 Brive, France

Abstract

The Philips Photonics multi-channel PMT family has been extended to cover many new UV, green, red and IR applications. High cathode sensitivity is obtained by using a pre-deposited bialkali photocathode on a sapphire window for the UV part of the spectrum, and on a clear-glass or fibre-optic window for the blue part of the spectrum. For the green and red parts of the spectrum, several new tubes have been introduced with an S20 photocathode on a clear-glass or fibre-optic window. These tubes are produced using transfer technology, resulting in a cathode sensitivity comparable to that of second generation image intensifiers. This technology facilitates increasing the photocathode thickness to produce an S25 cathode for applications up to 900 nm or making an S1 cathode for applications at 1060 nm or a solar-blind UV cathode on a sapphire window.

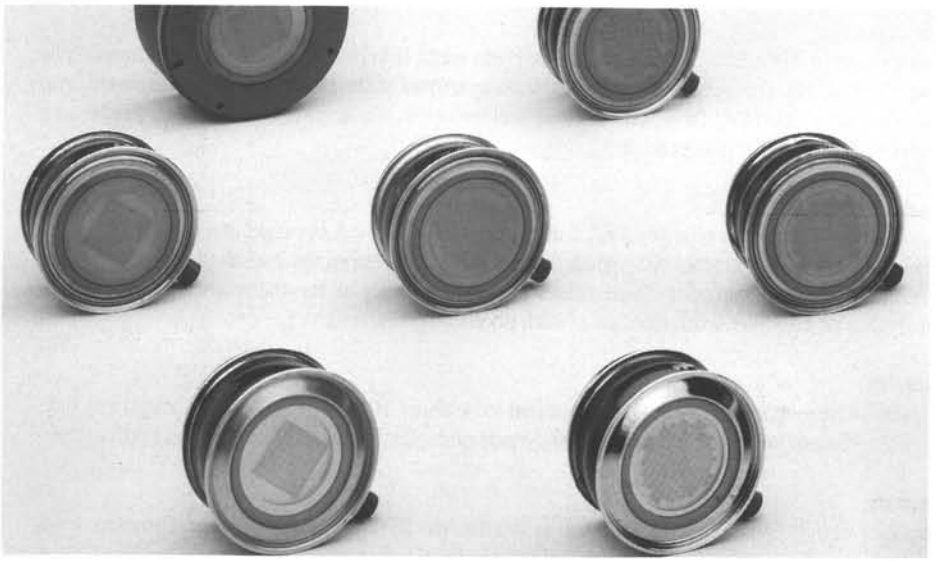

I. INTRODUCTION

Conventional single-channel photomultipliers have been criticized for many years for their large size and sensitivity to (even moderate) magnetic fields. The introduction of scintillating and wavelength-shifting fibres with diameters of 0.5 - 2 mm has further stressed the need for pixel detectors with pixels of 1 - 10 mm^2 that can detect signals of one to ten photoelectrons. This has encouraged the use of Avalanche Photodiodes (APDs) when their noise, until now worse than phototubes, can be tolerated. This is not the case for very low light level applications with scintillating fibres or new PET scanner arrays composed of very small scintillator rods. Therefore, a phototube approach will remain the only option for many years to come, be it the Philips Photonics multi-channel photomultiplier (MC-PMT) family, the similar Hamamatsu metal-dynode tube family [1], or the new multi-channel ceramic photomultiplier [2]. Other options include electron-bombarded silicon or APD arrays in tubes, the Position Sensitive Hybrid PMT, promoted by DEP [3], or the similar but less developed (VAPD) promoted by Advanced Photonix [4]. Multi-channel versions of microchannel plate photomultipliers (MCP-PMTs) have also been made over the years [5] but still suffer from a limited life – a total processed charge of 0.1 - 0.2 C/cm^2 halving their original gain.

Proc. Int. Conf. on Inorganic Scintillators and Their Applications, SCINT95,
1996, Delft University Press, The Netherlands

II. THE MC-PMT

Design principles

The basic design of the Philips Photonics patented low-crosstalk metal-foil multiplier has been extensively reported in [6 - 8]. The primary design target was that the resulting MC-PMTs should have normal PMT characteristics of gain, time response, noise and linearity and be able to read out all channels in parallel with extremely low crosstalk.

Multiplier gain

The gain of the 10-stage foil-multiplier reaches 10^6 (the same as conventional PMTs) at a supply voltage of 1000 - 1200 V. In addition, the gain of the MC-PMT's first dynode is high enough to clearly resolve the single photoelectron peak [7]. Already, the gain spread between pixels in the MC-PMT is approaching the gain spread in a random sample of 64 or 96 conventional PMTs (about 5:1), and a typical value of 3:1 looks feasible in the future.

Time response

The anode pulse rise time is 5 ns and the anode pulse width (FWHM) is 8 ns. The signal transit time is only 15 ns due to proximity focusing and the compactness of the multiplier, so the single-electron transit time jitter (FWHM) for a *pixel* channel is in the order of a nanosecond – all very similar to a conventional PMT's time response [6-7].

Noise

The *anode* dark current is typically 5 nA and in the order of 100 pA per pixel at a gain of 10^6 and is dominated by leakage currents rather than thermoelectric noise from the bialkali photocathode. For the S20, S25 and S1 cathodes, these values are slightly higher as the thermionic noise increases strongly due to the lower work function of such photocathodes.

Linearity

The *pixel* pulse height linearity has been reported to be about 100 pC [9-10] which, though less than that of a well-designed linear focused (large) dynode multiplier, is still adequate in most applications.

Crosstalk

This major design parameter has been well satisfied in the XP1700 family of tubes. Crosstalk from one pixel into *all eight* neighbours is only ~35 %. In the 64-channel staggered-pixel version, where the pixels are further apart in one direction, it falls to ~ 12 %. These values are for 430 nm blue light from a ϕ2 mm fibre centrally coupled to a 2.54 x 2.54 mm^2 pixel. It is of course possible to reduce crosstalk further by only using 32 out of 64, or 48 out of 96 pixels - but at increased cost per channel. For extensive discussions on crosstalk and how it is defined and measured, see [8] and [11].

Photocathodes

The pre-deposited bialkali photocathode has a cathode sensitivity at 400 nm of typically 65 mA/W on glass windows. This is lower than today's 80 - 100 mA/W for in-situ cathode processing. However, as glass window tubes with values approaching 75 mA/W are already made, we anticipate this to be a typical value in the future. For fibre-optic windows absorbing blue light this will be more difficult to reach. The response of the bialkali cathode falls off sharply on the green side of the spectrum and is less suitable for wavelength-shifting fibre applications. Therefore, Philips Photonics is introducing an S20 cathode made in the transfer technology. This photocathode has a typical peak sensitivity of 60 mA/W at 500 nm and is still useful up to 800 nm. In transfer technology, the cathode thickness can be tailored into what is called a thin S20 cathode, peaking at 450 nm, or made gradually thicker as S25 cathode versions peaking from 550 up to 650 nm with good response up to 900 nm. These new cathodes significantly extend the XP1700 family.

Magnetic field response
The foil-multiplier of the XP1700 was not designed to work in strong magnetic fields but to provide minimum crosstalk. However, it is immune to an axial magetic field of 80-100 gauss [11-12].

Temperature stability
The MC-PMT family with a bialkali cathode and antimonized CuBe multiplier has a gain temperature stability similar to conventional PMTs of about - 0.3 %/°C. Silicon-based APDs, hybrid tubes and VAPDs are clearly at a disadvantage in this respect.

Life
At Gran Sasso, three tubes have worked at average anode currents of 30 - 70 μA for about 100 hours with no evident gain degradation. The gain of another tube has halved after 200 hours. This indicates a lifetime of at least 50 C [13]. Some other examples indicate a lifetime of up to 100 C.

III. APPLICATIONS

Typical *rough imaging* applications where the XP1700 family is contributing to science are:

- On the summit of Gran Sasso, Italy where the clear-glass 96-pixel version is looking for fast Cherenkov light in the upper atmosphere from ultra-high-energy gamma rays [14].
- At CERN, Geneva, in several scintillating fibre detectors for high-energy physics.
- At NIH, where the 64-pixel tube gives enhanced vision in a confocal microscope.
- At UCLA, for reading out scintillator blocks via clear fibres of a new animal PET scanner and for a new interoperative β-probe.

IV. PRICES

The ratio of price/performance is determining which type of multi-channel phototube will be more economic than APDs, say. The graph (right) shows price trends for the MC-PMTs discussed here. It is likely that the metal-dynode technology [1] will show a similar trend as both are PMT technologies operating at 1000 V. Whether 10 kV hybrid tubes and VAPDs can match such prices is unclear today as they also depend on unclear yields and prices of high-ohmic silicon and APD arrays. Even today's single-channel APD prices will have to fall considerably to be competitive.

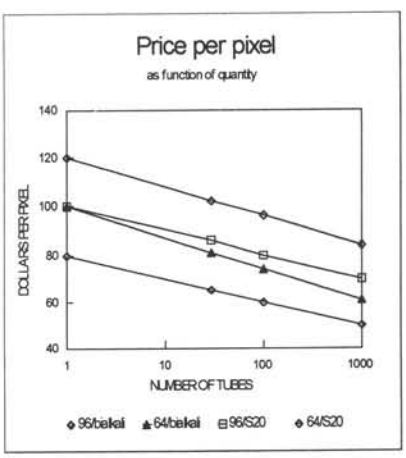

V. FUTURE IMPROVEMENTS

The useful area to total area ratio of the MC-PMT is still poor and therefore a hurdle in some applications. As soon as the market demands it, square or rectangular shapes with more pixels per tube may be necessary for PET scanners. For gamma ray telescopes and some new X-ray applications, more pixels per tube in a 12 x 12 or larger array with the same pixel size would be of interest, and in some applications smaller pixels would be desirable – and more of them. There are no fundamental obstacles to make a larger 200 pixel tube. Making the pixels smaller is however limited by the density of signal connections and their increased electrical interference.

VI. CONCLUSIONS

After significant improvements in manufacture, the low-crosstalk MC-PMT family of tubes can now be regarded as a state-of-the art product of 64 or 96 PMTs in one envelope. By extending the family with versions able to operate from UV to IR, many new applications are envisaged.

References

[1] Kyushima H. et al., IEEE transactions on Nuclear Science, Vol.41, No 4, pages 725-729, 1994.

[2] Comby G., Karolak M., Piret Y.; SCINT95 proceedings, Delft 1995.
"Performance of multi-channel ceramic photomultiplier"

[3] Boksma L., Glazenborg R.; SCINT95 proceedings, Delft 1995.
"Photon detection with (position sensitive) Hybrid PhotoMultiplier Tubes"

[4] Cushman P. & Rusack R., Conference Records of the 1992 IEEE Nuclear Science Symposium & Medical Imaging Conference, Orlando, Florida, October 1992.

[5] Boutot J.P.,"Workshop on MCP Photomultipliers and Related Devices", LBL, 1976.

[6] Boutot J.P. et al., IEEE transactions on Nuclear Science NS-34, pages 449-452, 1987.

[7] Comby G. & Meunier R., Nucl. Instr. and Meth. A269, pages 246-260, 1988.

[8] "XP1700 multi-channel photomultipliers", Philips Photonics, D-XP1700-TP93, 1993.

[9] Cushman P., University of Minnesota, Private communication on linearity test results.

[10] Müller T., UCLA, Private communication on linearity test results.

[11] Majewski S. et al., Conference Records of the 1991 IEEE Nuclear Science Symposium & Medical Imaging Conference, November 1991, Santa Fe, New Mexico, pages 324-330.

[12] Salomon M., Conference Records of the 1991 IEEE Nuclear Science Symposium & Medical Imaging Conference, November 1991, Santa Fe, New Mexico, pages 346-348.

[13] Morello C., INFN Torino, Private communication, July 1995.

[14] Aglietta M. et al., "Imaging of Atmospheric EAS Cherenkov Light at EAS-TOP", Il Nuovo Cimento, Vol. 15C, N.3, 1992.

The author would like to thank J-P Boutot and J-C Rebuffie of Philips Photonics, Brive, France for many useful remarks and detailed contributions.

LIGHT YIELD AND RESPONSE FUNCTION OF YAP:Ce MULTI-CRYSTAL DETECTORS

HIRESPET Collaboration
F.de Notaristefani, $R.Pani, L.M.Barone, *K.Blazek, %D.Bollini, @A.Del Guerra, $G.De Vincentis, &G.Di Domenico, ~M.Galli, &M.Giganti, $T. Malatesta, *P.Maly, $R.Pellegrini, $A.Pergola, &A.Piffanelli, $F.Scopinaro, +A.Soluri, F.Vittori, @G.Zavattini
INFN- Dept. of Physics - University of Rome "La Sapienza" Italy-(*) PRECIOSA CRYTUR. Turnov Czech Republic-(+) ITBM CNR Italy (%)Dept. of Physics - University of Bologna Italy (@)Dept. of Physics - University of Ferrara Italy ($) Dept. of Experimental Medicine - University of Rome "La Sapienza" Italy (&) Institute of Radiology - University of Ferrara Italy(~) ENEA INN-FIS Bologna Italy

ABSTRACT

The use of PSPMT (Position Sensitive Photo Multiplier Tube) in Nuclear Medicine imaging has recently produced some major steps forward in this field. However, a reasonable number of light photons and a narrow PSF (Point Spread Function) are needed in order to maximize PSPMT performances, this implies the use of multi-crystal scintillation detector. In this work the response function and the light yield of a number of YAP:Ce multi-crystal detectors are studied. The light output of the crystal needles shows a strong dependence on the size of the needle itself. The light output relative to NaI(Tl) ranged between 5% and 30%. The energy resolution varied between 25% and 90% at 140 keV incident photon energy. Studies were carried out coupling the scintillation crystals to a conventional PMT and to a PSPMT Hamamatsu R2486.

INTRODUCTION

Position Sensitive Photo Multiplier Tubes (PSPMT) induced a substantial improvement in spatial resolution for radiation imaging application. This field needs a detection system with high efficiency at photon energies higher than 80 keV, large detection area, high spatial resolution and low cost. Up today only detection systems based on scintillation crystals and PMT's allowed to satisfy such requirements. Recently, the detection principle of PET has introduced the use of arrays of crystal pillars coupled to a multi-anode PSPMT. In the multi-anodes PMT the spatial resolution is related to single anode dimension (some millimeters), the scintillation crystal is configured as a two dimensional array of pillars. In this way it is possible to obtain very high detection efficiency, high rate and a spatial resolution comparable with that of a standard gamma-camera. For Single Photon Emission imaging (SPET) the use of crossed-wire anode PSPMT, coupled to a flat crystal, is more suitable because of the continuous position linearity requirement. These PSPMT's have intrinsic spatial resolution up to 0.3 mm, they are limited on active area (less than 80 cm^2) and on spatial resolution if coupled with planar crystals. Only using thin crystals spatial resolution of about 2-3 mm is achievable, but with low detection efficiency [1]. The only way to fully take advantage of the intrinsic characteristics of PSPMT is the use of multi-crystal arrays to obtain high detection efficiency, narrow PSF and a reasonable light output. The goal of the future developments is to find a multi-crystal perfectly matching the detection requirements of PSPMT. Advantages and disadvantages of multi-crystal detectors in comparison with standard flat

Proc. Int. Conf. on Inorganic Scintillators and Their Applications, SCINT95,
1996, Delft University Press, The Netherlands

scintillation crystals are analyzed in detail. YAP:Ce multi-crystal array first proposed by Pani et al. [2],[3] represents the first attempt in this direction. In particular the detector response function of a number of YAP:Ce multi-crystal detectors for application in Nuclear Medicine is tested and discussed.

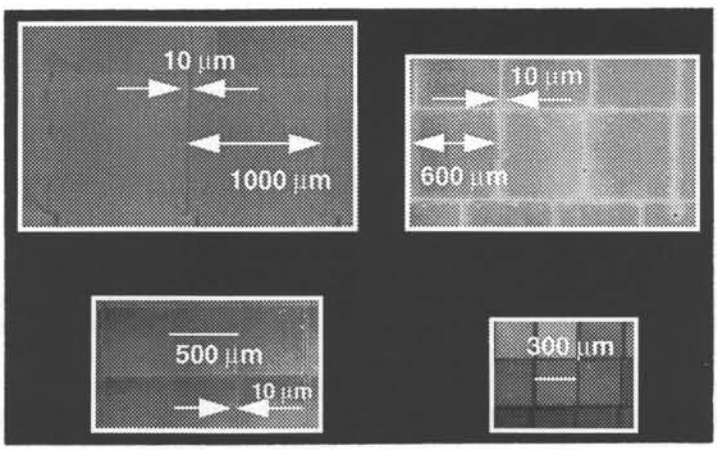

Fig. 1 Photograph of YAP:Ce needles cross sections

EQUIPMENT AND METHOD

In order to analyze the YAP:Ce light yield and energy resolution response, scintillation crystals were coupled to a standard bi-alkali photomultiplier tube EMI 9765B and irradiated by different free calibrated radioactive point sources at different photon energies under the same geometrical irradiation condition i.e. at 10 cm Source-Detector-Distance.
In order to achieve reference measurements two scintillation planar crystals of YAP:Ce and NaI(Tl) were made with the same housing. The response of YAP:Ce multi-crystal arrays was also tested irradiating crystal on top and lateral face, by a collimated Tc-99m source. Collimation diameter of 1 mm and 0.2 mm were used. To analyze at the same time the detector response function of multi-crystal arrays and the spatial resolutions, crystals were coupled to a PSPMT Hamamatsu R2486-06. The readout electronics consisted of 32 independent chains of preamplifiers and amplifiers in which the signal from wire anodes was multiplexed and digitized producing independent spectrometric responses. PSPMT has 7.5 cm of diameter with a measured active area of 50 mm diameter. The basic detection principle of the PSPMT is described elsewhere [5]. $YAlO_3$:Ce is a scintillation crystal with the structure of Perovskit. It has density value of 5.37 g/cm^3, and a relatively high atomic number (Z= 39) that make it very interesting for X-gamma ray applications [4].
The scintillation emission maximum of YAP:Ce is situated at 370 nm with a decay time of about 25 ns. Furthermore its characteristics of high hardness and no hygroscopicity can allow crystal machining to various shapes and geometry. The multi-crystal scintillation detectors made and tested, are shown in fig.1. They consist of arrays with a number of YAP:Ce scintillation elements ranging between 5x5 and 22x11. Crystal lengths varied between 1 mm and 28 mm. A thin dielectric reflective layer is deposited together a thin metal layer for optical

insulation. The elements are glued to one block. The total thickness of dead layer between scintillation elements resulted about 10 μm. The control of light tightness was made removing the top face layers, exciting one scintillation element by UV light (360 nm) and measuring light from neighbouring crystals. By this measurement, less than 1% cross talk of light was measured.

IMAGE FORMING PRINCIPLE IN MULTI-CRYSTAL SCINTILLATION CAMERA

For incident photon energies up to some hundred keV the spatial resolution is mainly due to the contributions of different factors with different weights depending on the photon energy, crystal properties, shape and on PMT characteristics. In Anger camera the spatial resolution along one axis (σ_x) is related to Point Spread Function (PSF) (eq.1) and to the number of photoelectrons emitted from photocathode.

$$\sigma_x^2 = \frac{\sigma^2}{N} \qquad (1)$$

where $N = \sum_i n_i$, σ = standard deviation of PSF and n_i is the number of photoelectrons collected by the i^{th} wire anode in the case of PSPMT. It also represents the quadratic sum of standard deviations relative to the following distributions :

- light photons directly impinging on photocathode into the solid angle subtended by wire anode (Planar Crystal).
- light photons reflected inside the crystal before to strike photocathode.
- cloud of electrons intrinsically created during the multiplication process in the PSPMT.

Furthermore the light distribution on photocathode can be affected by radiation transport effects into the crystal and by other minor effects that can be neglected for simplicity. To understand the influence of charge distribution spread on spatial resolution. Fig. 2 shows three curves calculated on the basis of equation 1 at different values of light yield relative to a standard response of NaI(Tl). Charge distribution collected by wire anode represent the Detector Response Function (DRF). PSPMT DRF FWHM has an intrinsic minimum value (σ_0) of about 7 mm. The values of light yield correspond to 60, 120 and 360 photoelectrons generated by PSPMT bi-alkali photocathode at NaI(Tl) emission wave length and 140 keV photon energy. Experimental spatial resolution values obtained from multi-crystal detectors are shown in the figure framed by a rectangle. Intrinsic charge spread of PSPMT leads spatial resolution of crystal needles. The empty rectangle represents the expected spatial resolution values from crystal arrays by new generation compact Hamamatsu PSPMT R5600. In the case of planar crystal (< 4 - 5 mm total thickness for both crystal and glass window) FWHM of light distribution leads spatial resolution. The ratio between number of light photons directly impinging on photocathode and reflected light photons into the planar crystal is correlated to position discrimination and pulse height. In fact reflections into the crystal improves energy resolution, but impair position discrimination and spatial resolution. As shown in fig.2 Sodium Iodine crystal, can carry out only 30% of relative light output with an energy resolution of 15% at 140 keV if reflections are minimized. The major limitation of planar crystals was the use of very thin thickness to obtain narrow PSF, compromising the detection efficiency. Furthermore, position linearity range resulted shorter than intrinsic one of PSPMT due to large planar crystal PSF.

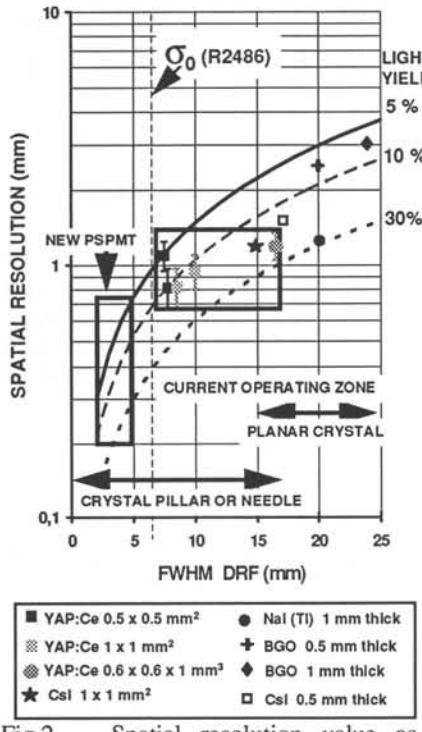

Fig.2 Spatial resolution value as a function of charge distribution.

The advantages of planar crystals resulted: low cost, large area availability and sufficient energy resolution for nuclear medicine application (better than 25% at 140 keV). Crystal needles (1 mm or less cross section) have spatial resolution responses mainly depending on light output. In this case reflections are utilized to concentrate and transport the light, and light output depends on crystal length and on base area. In contrast with planar crystals, multi-crystal arrays, have to maximize reflections to improve pulse height without affecting the light spread. As shown in fig. 2 the measured responses of crystal needles are confined in a range between 5% and 30% of relative light output corresponding to a length between 30 and 1 mm. The YAP:Ce needle of 1 mm length represents a limit between planar and needle response function carrying out the same light output obtained from NaI(Tl), the same energy resolution, but better spatial resolution. The major advantages of multi-crystal arrays are : spatial resolution of about 1 mm of FWHM, high detection efficiency and position linearity range equal to PSPMT intrinsic one.

The disadvantages are: high costs, inhomogeneities of light response of crystal needles and principally the poor energy resolution as will be analyzed in the following.

Energy transport effect on image forming

YAP:Ce attenuation coefficients at 140 keV, give the same radiation absorption contribution for photoelectric and Compton effect. Thus, at the gamma emission energy of Tc-99m we expect a larger contribute of Compton photon re-absorption or escape than NaI(Tl) and CsI(Tl). On contrary the low energy of K_α X ray (about 15 keV) of YAP:Ce and its small fluorescent yield (about 0.36) reducing the energy deposition spread due to fluorescent x-ray re-absorption. In fact for X and gamma ray imaging systems, at photon energies below 140 keV , spatial resolution less than 1 mm can be affected by attenuation length of fluorescent X-ray in the material. Fig. 3 and fig. 4 show the two re-absorption processes in a multi-crystal detector due to photoelectric and Compton effects respectively. As an example we can compare 0.8 mm of attenuation length of BGO K_α X-ray (80 keV average value and 0.6 fluorescent yield) with 0.13 mm of YAP:Ce K_α X-ray. In planar crystals the escape of characteristic X-rays produces on the energy spectrum the escape peak. Its intensity depends on crystal thickness at 140 keV. Usually 3 mm thickness is able to minimize the escape from the entrance surface in NaI(Tl), BGO and CsI(Tl) crystals.

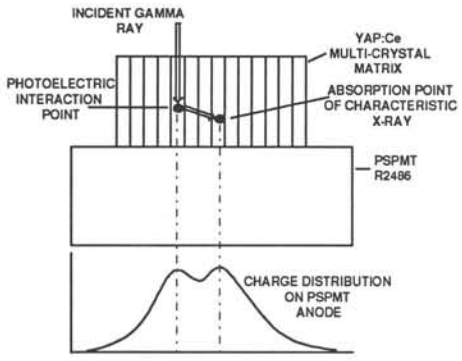

Fig. 3 Re-absorption process of X-rays in YAP:Ce multi-crystal detector.

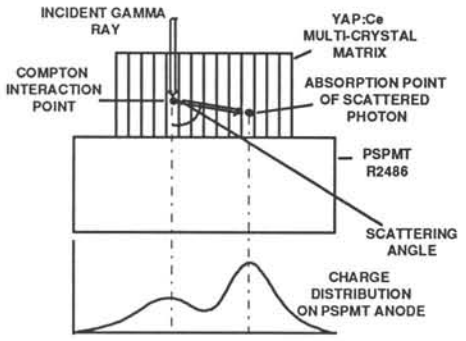

Fig. 4 Re-absorption process of Compton photon in YAP:Ce multi-Crystal detector.

In gamma camera, the presence of escape peak on energy spectrum produces or a loss of detected events or an increasing of incident Compton photons detection (false events) for narrow and large energy window respectively. In crystal pillars or needles X-ray escape from lateral surfaces and the intensity of this phenomena strictly depends on collimation aperture diameter and on cross section of the crystal. Crystal needle of CsI(Tl) with a cross section less than 1x 1 mm^2 and 10 mm length (irradiating the top face) can produce an escape peak intensity of about 50% of photopeak at 140 keV incident energies. Placing lead layers between neighbouring crystals energy resolution gets worse because of the increasing of escape peak. However, isotropic emission of X-rays involves in the re-absorption process mainly the 8 neighbouring needles, so that it limits the worsening of spatial resolution. Furthermore when the difference between incident photon and X-ray energy is large it scarcely affects the centroid of light distribution. In YAP:Ce multi-crystal arrays this effect is negligible and its contribution on centroid has been evaluated to be less than 100 μm. On contrary because of the low photofraction of YAP:Ce the contribution due to Compton photon re-absorption into the multi-crystal array is higher than other scintillation crystals . It can produce a wide distribution of counts around the peak of image. How much this phenomenon can affect image contrast and spatial resolution has to be evaluated.

RESULTS.

The first measurements of light output of multi-crystal arrays were carried out by free point sources. In fig.5 the energy response of different crystal lengths is shown. Curves show the dependence on crystal length of light output. From these results the energy linearity response seems little affected from the point in which the radiation interaction occurs inside the crystal when needle top face is irradiated. The dependence on YAP:Ce needle length of light output is better shown in fig.6. It was obtained irradiating the top face of crystal matrices by a Tc-99m collimated source. The light output goes down abruptly between 1 mm and 3 mm of crystal length starting from 30% of relative light yield.

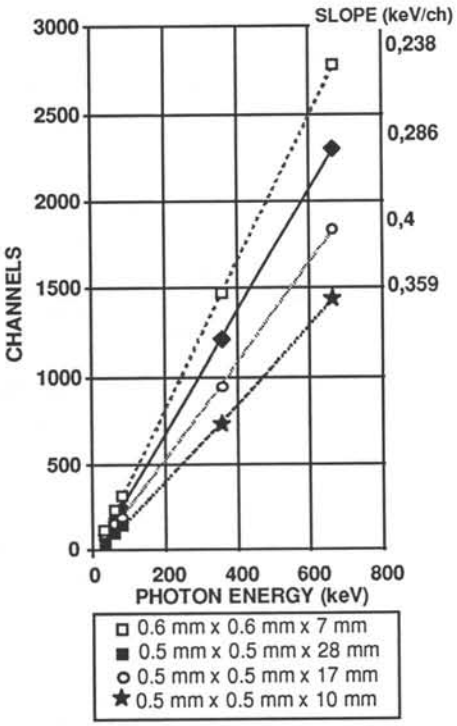

Fig.5 Energy response of YAP:Ce needles

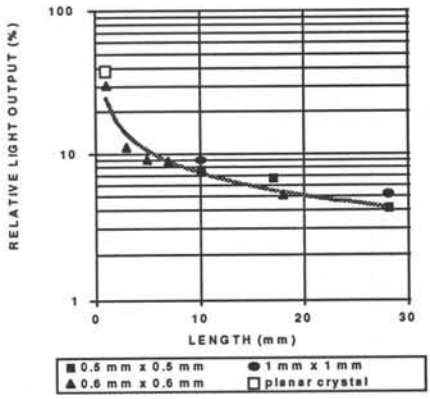

Fig.6 Light output vs crystal length at 140 keV photon energy.

It is worth to remark how crystals with different cross sections have approximately the same response indicating the prevalence of length with respect to the cross section in affecting light output. YAP:Ce crystal arrays were then irradiated along their length (by a collimated Tc-99m source) and light output was measured as a function of the distance between irradiation point and photocathode glass window (see fig. 7). In this case is clearly shown how the light output can range within a factor two between bottom and top.

When the needle cross section goes down to 0.3 x 0.3 mm^2 this effect becomes more strong. The interaction probability density affects the light output as schematically shown in fig.8. Depending on photon energy and crystal length the photopeak can be asymmetric on the right zone. The probability distribution of photon interactions inside the crystal can more affect the energy resolution than the mean value of peak. In Fig.9 the variation of photopeak mean value in function of incident gamma ray energy is show in terms of photoelectrons/keV.

The value (photoelectrons/keV) increases inversely with crystal length. The agreement with constancy of the value is within 5% at 10 mm of crystal length. The energy resolution response as a function of YAP:Ce needle length (Tc-99m collimated source and crystal irradiation) is shown in fig. 10.

A value ranging between 25% and 40% corresponding to 10 mm length seems the best situation for application in Nuclear Medicine with a detection efficiency comparable to an Anger camera. The effect of interaction probability density on energy resolution, is well visible in fig. 11 where all normalized values of energy resolution were plotted as a function of relative light output.

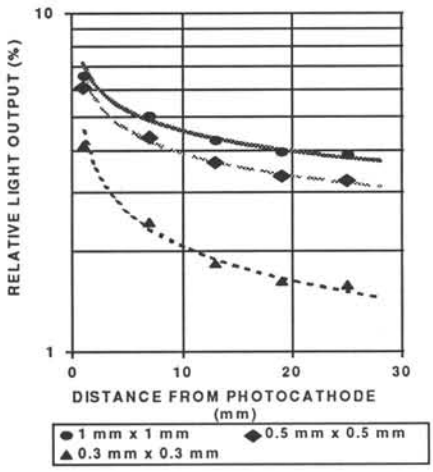

Fig 7 Light output as function of interaction point.

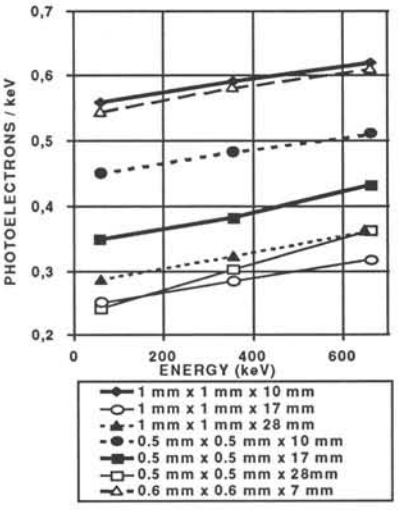

Fig. 9 Energy resolution

The data disagree from the slope inversely proportional to the square root of number of light photons ($N^{-1/2}$). The normalized values of energy resolution obtained from lateral irradiation of the crystals by Tc-99m collimated source are shown in fig.12. All data agree with ($N^{-1/2}$) slope indicating how is relevant the dependence on interaction probability density of energy resolution.

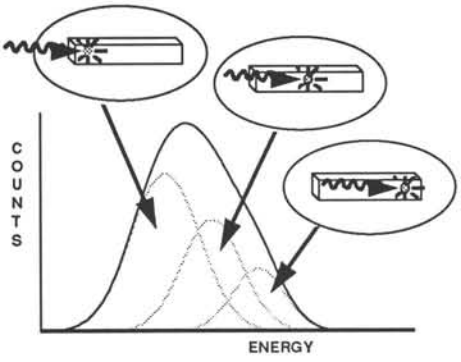

Fig. 8 Different contributions of light output to photopeak

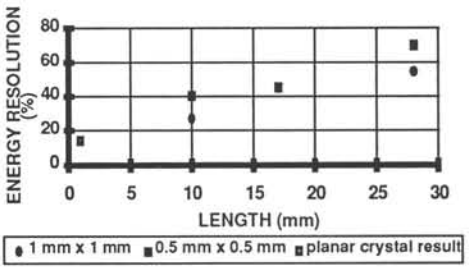

Fig. 10 Normalized energy resolution of YAP:Ce needles at 140 keV

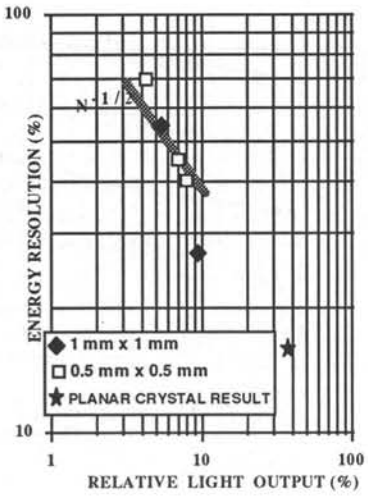

Fig.11 Normalized energy resolution obtained irradiating the crystal top face

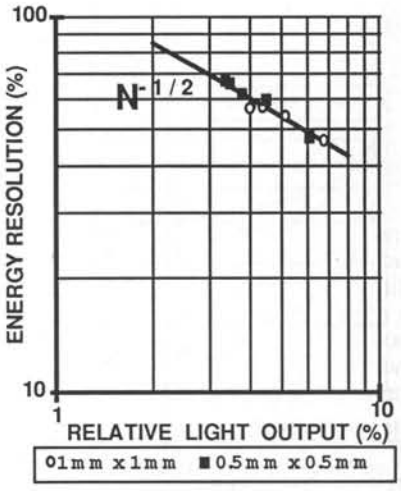

Fig. 12 Normalized energy resolution obtained at 140 keV irradiating crystal lateral surface

CONCLUSION

Multi-crystal scintillation detectors match very well detection characteristics of PSPMT. They maximize the ratio between detection efficiency and spatial resolution. Furthermore they maximize PSPMT active area. YAP:Ce multi-crystal arrays carried out very good responses of spatial resolution and detection efficiency. However spatial resolution was strongly limited by intrinsic spread of charge of PSPMT. This problem seems to be solved by next generation PSPMT that will be able to stress the intrinsic imaging capability of YAP:Ce needles. The major limitation is the energy resolution. Its improvement represents the future goal in the development of next generation gamma cameras based on PSPMT.

REFERENCES

[1] R Pani, F.Scopinaro, G.Depaola, R. Pellegrini, A.Soluri Physica Medica Vol.IX N. 2-3 1993. ,233-36

[2] R. Pani, K. Blazek, F. De Notaristefani, P.Maly, R. Pellegrini, A. Pergola , F. Scopinaro, A. Soluri Nucl. Instr. & Meth. A348 1994., 551

[3]K. Blazek, F. De Notaristefani, P.Maly, R.Pani, R. Pellegrini, A. Pergola , F. Scopinaro, A. Soluri IEEE Trans. on Nucl. Sci.1995., 42 5.

[4]A.Baccaro, K. Blazek, F. De Notaristefani, P.Maly, R.Pani, R. Pellegrini, A. Soluri J.A. Mares in print on Nucl. Instr. & Meth. 1995.

[5]L.M.Barone, K.Blazek,D.Bollini,A.Del Guerra, F.De Notaristefani, G.De Vincentis, G.Di Domenico, M.Galli, P.Maly,R.Pani , R.Pellegrini, A.Pergola, A.Piffanelli, F.Scopinaro, A.Soluri, F.Vittori. Nucl. Instr. & Meth. A360 1995 302-306

PERFORMANCES OF MULTI-CHANNEL CERAMIC PHOTOMULTIPLIERS

G. Comby, M. Karolak, Y. Piret, J.P. Mouly - DAPNIA C.E. SACLAY
91191 GIF sur YVETTE - France
E. Kuzmin -JINR-141980 - DUBNA Moscow Region - Russia

Ceramic electron multipliers with real metal dynodes and independent channels were constructed using multilayer ceramic technology. Tests of these prototypes show their capability to form sensitive detectors such as photomultipliers or light intensifiers. Here, we present results for the photocathode sensitivity, dynode activation, gain, linearity range and dynamic characteristics as well as the effect of 3-year aging of the main operational functions. The advantages provided by the ceramic components are discussed. These results motivate the development of a compact 256 pixel ceramic photomultiplier.

1-INTRODUCTION:

The multi-channel photomultipliers that have appeared in the last 10 years have provided new solutions to fast imaging problems at very low luminosities. To adapt these photo-detectors to such applications by optimizing their geometry and dimensions, simplifying their operation and facilitating their production, we proposed using multi-layer ceramic technology for manufacturing these new components (1). In (2), we reported the main results of a feasibility study which showed good conformity with all the PM dynamic operating functions and gave an optimistic forecast for the performance of an industrially-developed detector.

This article extends these data and gives the first values for the analog and temporal characteristics of these ceramic PMs.

2-CERAMIC PHOTOMULTIPLIER PROTOTYPE DESIGN (CMP)

2.1-*Ceramic electron multiplier block (CEM)*

We have described the structure and the fabrication procedure for ceramic photomultipliers (1), (2). The production of the new CEM has again made it possible to test the techniques used in multilayer ceramic technology both for obtaining new cavity shapes and sizes as well as precision and reproducibility of conductive layers to form real metallic dynodes.

Improved understanding of the problems involved has allowed NTK TECHNICAL CERAMICS (3) better selection and scheduling of the basic fabrication procedures. The results are interstage insulation values consistently above 200 Gohms at 200 volts and more uniform gains for the gold-plated dynode channels.

To increase the stage gains to usable levels, we deposited an (Sb-Cs) type layer, known to have high emmisivity and widely used industrially, on the walls of each cavity. Antimony deposition on the dynodes was done by electroplating using DALIC industrial products (4). This procedure does not change the operating characteristics evaluated above.

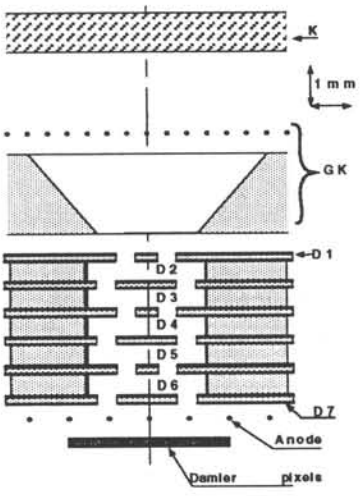

Fig.1. Schematic of CPM electrode and dynode arrangement

2.2- *Activation of antimony-plated CEMs*

To provide simple, autonomous mountings that facilitate repeated measurements for determining aging characteristics, and to benefit from specialized industrial photoelectric techniques, we decided to construct photomultipliers. Thus, our results go beyond the simple objective of dynode activation. Antimony-plated CEMs with measured gains were sent to

Proc. Int. Conf. on Inorganic Scintillators and Their Applications, SCINT95,
1996, Delft University Press, The Netherlands

PHILIPS PHOTONIQUE (5) where they were incorporated in standard PM XP4722 structures to evaporate a photocathode and activate the multiplier.

A schematic electrode arrangement is shown in Figure 1. The input stage consists of the photocathode K and the GK electrode. The multiplier is made up of dynodes 1 to 6. The electrode 7, the grid-anode and the damier-pixels form the output stage. The 4 damier-pixels are antimony vacuum-deposited; their emissivity serves to estimate the efficiency of the activation process.

3-CPM CHARACTERIZATION

3.1- *Photocathode*

The CPM fabrication steps, i.e., photocathode production and multiplier activation, are now carried out simultaneously in the glass envelope. Experience has shown that both material characteristics and electrode geometry can affect photocathode sensitivity. The sensitivities at 407 nm of bialkali (Sb-K-Cs) photocathodes with both compact mountings and new materials are given in Table T1. Although they have not been optimized, these values establish the compatibility of the multiplier components (ceramic and electro-metal plating) with those of tube activation (alkali metals and photocathode). This compatibility is strengthened by the practically complete stability of a SbCs-type photocathode of PMC 3 over 42 months.

Table 1:PHOTOCATHODE SENSITIVITY AT 407 nm (mA/W)						
PMC 7 45	PMC 11 58	PMC 12 41	PMC13 40	PMC 16 47	PMC 17 61	PMC 18 68

3.2 *Dynode gain*

The gain, Gi of each dynode-cavity is given by: $Gi(v) = C_{(i-1)i}(v) * S_i(v)$, where $C_{(i-1)i}(v)$ is the electron collection factor between stages (i-1) and i and $S_i(v)$ is the secondary emission factor of dynode i. The ratio $T(i-1)i(v)=C(i-1)i(v)/C(i-1)i(200)$ represents the electron transfer efficiency relatively to operating conditions for an interdynode voltage Vid = 200 volts. The T(i-1)i(v) values of each dynode for the same CPM are given in Figure 2. There is a plateau with a slight slope which indicates an efficient transfer of secondary electrons (>90%) for Vid < 200 V. The small scatter in the parameters can be interpreted as due to good geometric reproducibility of the channel structure. The average curve T(v) specifies the electron propagation in this structure. Table T2 gives, for each of the 5 CPMs, the electrode type, the antimony plating technique used: (VD) for vacuum deposition, (EP) for electroplating, and the corresponding gains for an interstage voltage, Vid, = 200 V.

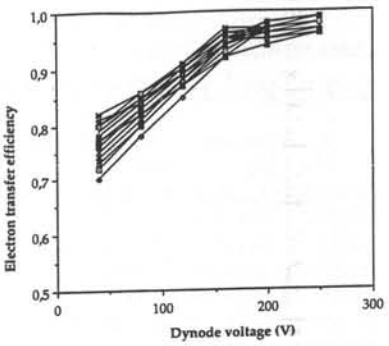

fig.2. channel electron transfer efficiency

PMC Label	ELECTRODE METAL	GK STEEL	DYN1 GOLD	DYN2 GOLD	DYN3 GOLD	DYN4 GOLD	DYN5 GOLD	DYN6 GOLD	DAMIER ALUMINIUM
13	Sb layer		EP	EP	EP	EP	EP	EP	VD
	Gain		4,25	2,1	1,6	1,4	1,6	1,9	10
14	Sb layer		EP	EP	EP	EP	EP	EP	VD
	Gain		6,7	1,8	1,8	1,5	1,5	1,8	6
15	Sb layer	EP	EP	EP	EP	EP	EP	EP	VD
	Gain	2,2	1	2,2	1,4	1,5	1,2	1,3	7
16	Sb layer	VD	EP	EP	EP	EP	EP	EP	VD
	Gain	1,8	1	2	1,3	1,6	1,5	1,4	12
17	Sb layer	EP	EP	EP	EP	EP	EP	EP	VD
	Gain			2	1,7	1,7	1,6	2,2	5

The vacuum depositions give the best efficiency, in particular those for the CMP13 and 14 damier-pixels. Nevertheless, the yield from the EP-Sb layer on the D1 dynode (CPM14) reaches the same values as those of the associated VD-Sb damier-dynode. The very different emissivities of the VD type layers of the GK electrode and damier (CPM16) show the influence of the sublayer. The low gains observed for the innermost dynodes indicate poor diffusion of the products coupled with insufficient preparation of the metal surfaces.

Although these results are limited, it can be stated that there are physical-chemical conditions providing an electrolytic antimony deposit with a usable emission yield. These conditions are also closely related to electrode type and geometry and thus require a specific process. This designates the transfer technique - which is widely used for producing microchannel image intensifiers - for activating and assembling the CPMs freed of a glass envelope studied here .The gain dependence of the 4 channels on the voltage Vm applied to the multiplier is shown in Figure 3. At this stage we have true photomultiplier with stable operation. Although the gains are limited due to non-optimization of the production steps and the reduced number of stages, we can evaluate the main analog and dynamic characteristics of these new components.

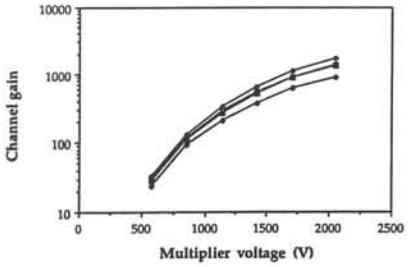

fig.3. Gain of the 4 channels vs multiplier voltage

3.3 *Dynamic parameters*

To explore the dynamic characteristics we used a test bench including a LED emitting very short light flashes at 450 nm directed by optical fibers to the studied CPM and a standard Philips XP2020 PM. This was used as a reference as its specifications and performances are well known. The anode pulses of these 2 PMs observed under 50 ohms by means a Hewlett-Packard oscilloscope (6) for cathode voltages of -1500 and -1900 volts, respectively, are shown in Figure 4. From the similarity of these pulses, we derive a CPM rise time very close to that of the XP2020 and below 2 ns.

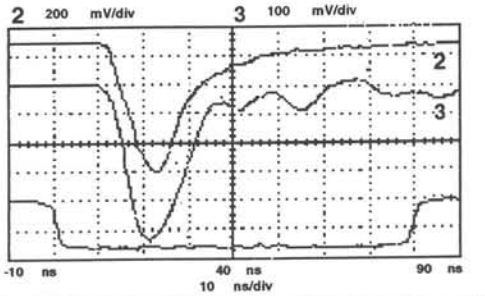

fig.4. Anodic pulses of (2) XP2020, (3) CPM, on 50 ohms load

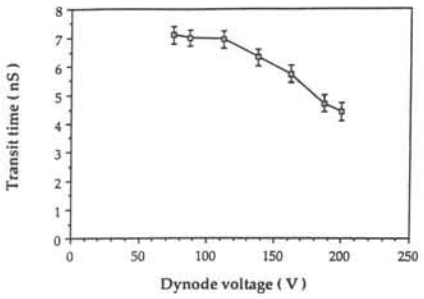

fig.5. CPM transit time versus dynode voltage

The variation of the CPM transit time with the voltage Vid applied to all the stages is shown in Figure 5.The tight dynode spacings (0.25 mm) establish strong electric fields which fast collect the electrons to generate short latency-times: from 7 to 4.5 ns depending of the dynode voltage.

3.4 *Linearity*

It might be thought that the small dynode area (2-3 mm^2/cavity) involved in the electron multiplication would restrict the linearity range of these multipliers. Thanks to the light sources performances, which allow adjusting the flash intensities with practically no degradation of the time characteristics we can establish the correlation between the main light power measured using a semiconductor detector (7) and the corresponding charge of the anodic pulses. The results reported figure 6 for a dynode voltage Vid= 200 volts show a linear dependance until 260 pC per pulse. The absence of any saturation index indicates a higher limit.

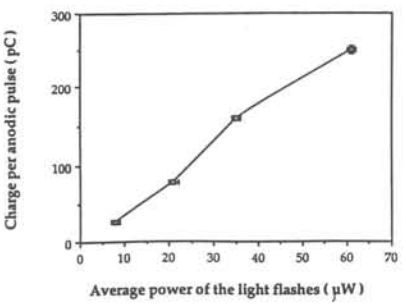

fig.6. Anodic pulse charge versus the mean power of the light flashes

4-CEM POTENTIALITIES

One of the initial motivations in this development was to produce multiplier blocks that were autonomous with respect to vacuum, dynode interconnection and detector mechanical assembly problems.This autonomy allows designing various components that do not require a vacuum envelope and can be placed side by side to provide large detection surfaces or even volumes. The suggestion made on completion of this study that a feasibility study be made for constructing a 256 channel CPM is in this direction (2).

But the use of this ceramic multiplier largely goes beyond the photosensor field (PMs and light intensifiers) and is applicable to all the fields where electrons are the indicators of a physical event (calorimetry (8), ion analysis, vacuum-sensors, etc.)

The constituents of these components ensure that they are highly resistant, with ultra-high vacuum properties and suitable for integration in advanced technology equipment.

5-CONCLUSION

These results complete and reinforce the conclusion of the preceding studies. Analysis of the main analog and dynamic characteristic shows that the behavior of these CPMs is identical to that standard metal dynode PMs. In particular, these CEM allow to built fast detectors with transit time of 5ns, a high dynamic rate and a linear range greater than 250 pC/pulse. Issuing from a masse production technique, these components enable to facilitate the detector manufacture and, then, to cut down the production cost.

To make these multipliers completely operational, the activation conditions, which are now well known, must be extended to the innermost dynodes. This fabrication process development phase exceeds the capabilities of a simple research laboratory. It requires the competence and motivation of the photoelectric industry .

ACKNOWLEDGMENTS

This ceramic PM study and development program carried out in DAPNIA/DSM was made possible by the financial support of L'ANVAR-ILE-DE-FRANCE (9). We wish to thank in particular Madame Nottin and Messieurs Chianelli and Gerard, the *Delegués Regionaux* as well as Mr. Haissinski, the head of DAPNIA department .

REFERENCES

(1) G. Comby and F. Lehar, A ceramic multichannel electron multiplier for a new multichannel PM, presented at the Int. Workshop on Heavy Scintillators for Scientific and Industrial Applications, Chamonix, 1992.
(2) G. Comby, F. Lehar, E. Chassaing, G. Lorthioir, Status of the ceramic multichannel PM tube, Nucl. Instr. and Meth. A 343 (1994) 263-267
(3) NTK TECHNICAL CERAMICS, 14-18 Takatsuji-cho, Mizuao-ku, Nagoya, Japan. and NGK SPARK PLUGS (FRANCE) SA, 220 Brd. Jean Jaures, 92100, Boulogne-Billancourt, France.
(4) DALIC, ZI de Plagué, 41 rue des Eaux, 35500, Vitré, France.
(5) PHILIPS PHOTONIQUE, 4 rue du Port-aux-Vins, BP 317, 92156, Suresnes Cedex, France and Avenue R. Roncier, BP 520, 19106, Brive la Gaillarde, France.
(6) Oscilloscope HP 54 542A - 2 GSA/S - 500 MHz - Hewlett Packard.
(7) Optical Power Meter, Model 840 HandHeld - Newport / Klinger - CA / USA
(8) G.S. Bitsadze et al., Module of electromagnetic secondary emission flight type calorimeter, Nucl. Instr. and Meth. A 334 (1993) 399-408.
(9) ANVAR. ILE -DE-FRANCE, 15 cité Malesherbes, 75009 Paris, France.

LOW TEMPERATURE TEST OF PHOTOMULTIPLIER TUBES

H.M.Araújo, V.Yu.Chepel, M.I.Lopes, R.Ferreira Marques and A.J.P.L.Policarpo
LIP-Coimbra and Departamento de Física da Universidade de Coimbra - Portugal

Two photomultiplier tubes with bialkali photocathodes and quartz windows (2-inch Philips XP2020Q and $1^1/_8$-inch Hamamatsu R1668) were tested at low temperature, down to -160°C, illuminated in the UV and VUV regions. The photomultipliers were used as vacuum diodes to study in detail the effects associated with the photocathode. An abrupt decrease in quantum efficiency for all wavelengths was observed at a temperature depending on the photomultiplier type, magnitude of the photocurrent, applied voltage, and illuminated area. Changes of the spectral sensitivity were also observed at VUV wavelengths.

INTRODUCTION

The increasing prospects in practical applications involving liquefied rare gases as radiation detecting media, as scintillators in particular [1,2], have led to the need of operating photomultiplier tubes (PMTs) at low temperature, specially those designed for the vacuum ultraviolet (VUV) region and low light intensities. In particular, PMTs with K_2SbCs bialkali photocathodes are still among the most attractive for these purposes in view of their high quantum efficiency and low dark noise. Thus, the performance of PMTs at low temperature, ensured by manufacturers usually down to -30 °C, was object of several studies [3-8]. However, these experiments were all carried out in the visible region of the spectrum and no studies could be found in literature for the UV and VUV light.

Apart from the expected reduction of thermionic emission, two main effects of low temperature on bialkali PMTs have been reported, the first being the smooth shift of its spectral sensitivity to shorter wavelengths with decreasing temperature and the second the sharp drop in response at low temperature. The former is related to the intrinsic processes that lead to the photoelectron emission, and the later has been suggested to be due to charge accumulation in the emitting layer caused by the increase of its resistivity, which is much larger that in other types of photocathodes even at room temperature. This problem can be surmounted by depositing a metal pattern under the photocathode layer, but at expense of some quantum efficiency.

In the present work, we investigated two bialkali PMTs with quartz windows down to -160°C, with wavelengths ranging from 340 nm to 170 nm. Special attention was devoted to the effects associated with the photocathode.

EXPERIMENTAL APPARATUS

Two head-on photomultipliers were studied: the popular 2-inch Philips XP2020Q (SN:12607) and a factory calibrated $1^1/_8$-inch Hamamatsu R1668 (SN:BA1076). Both were used as vacuum diodes, without multiplication. The dynode stages and anode were shorted to the same positive voltage while the photocathode was kept at ground potential. The electrodes of the electro-optic input system were kept at the voltages recommended for optimum collection. The cathode to first dynode voltages were +300V for the XP2020Q and +150V for

Proc. Int. Conf. on Inorganic Scintillators and Their Applications, SCINT95,
1996, Delft University Press, The Netherlands

the R1668. A Keithley 602 electrometer was used to measure the current from photocathode to ground, with typical values extending from few pA to more than 100 pA.

The set-up used to cool the photomultiplier is shown in fig.1. The PMT (1) is placed in a sealed brass compartment closed by a 3mm-thick quartz window (2) mounted in a stainless steel flange (3). The chamber is cooled by a flux of cold N_2 flowing inside a copper tube wound around it (4). A very small flux of N_2 gas at room temperature is allowed into the chamber by a gas inlet (5), conducted along a thin tube (6) leaving by gas outlet (7); the dry nitrogen environment prevents VUV light absorption and condensation of water vapour or other species on the PMT window, avoids sparks from electrical contacts, and helps to decrease temperature gradients between the PMT ends. Temperature is monitored by two copper-constantan thermocouples (8) glued to the PMT window and base with silicone sealant. These, together with the electrical wires connected to the contact pins (9), leave the chamber through a small silicone-sealed hole. The stainless steel tube in the upper part of fig.1 connects the cryostat to an ARC VM-502 vacuum monochromator. A Resonance Ltd. D_2ArCM-L deuterium dc lamp is used as the UV/VUV light source. The monochromator and stainless steel tube up to the quartz window are evacuated to a pressure of about 10^{-6} mbar. Uniform illumination of the PMT window is ensured, as checked by analysing the beam profile with photographic paper. A measurement of irradiance at the position of the photocathode was accomplished with the calibrated R1668.

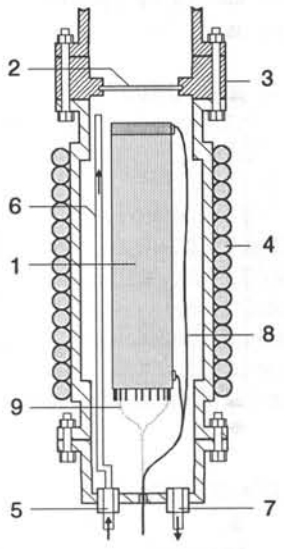

Fig.1: The cryostat

The procedure in each test is as follows. The positive voltage is applied to the PMT at least 12 hours before running. The lamp is switched on 1 hour in advance, and a small flow of nitrogen is allowed into the chamber to purge of contaminations. After the start of the cooling process, the pressure in the dewer and the flux of room temperature nitrogen are controlled to achieve a cooling rate of about 1 °C/min. The temperature difference between both ends of the PMT is typically kept smaller that 10°C. Thermal equilibrium of the photocathode is readily achieved, contrarily to what happens with the dynodes, in which case a value of half an hour is quoted [5]. Data is read in intervals not larger than ~5 °C. In each measurement the leakage current (ohmic leakage through the glass between pins of PMT) is read after the measurement of the photocurrent by diverting the mirror of the monochromator from the beam path. After reaching -160°C, the chamber is allowed to warm freely, and the reading process continues to verify if the response retraces the previous path.

RESULTS AND DISCUSSION

Figs. 2 and 3 show some results obtained with the XP2020Q PMT. These data were taken with illumination of a central 30 mm-diameter area of the photocathode which is 42 mm in diameter. A set of curves of response for different wavelengths and the same irradiance is plotted against the temperature in fig. 2. Similar behaviour was observed in the wavelength range between 185 nm and 340 nm. The variation of the relative response with temperature at a fixed wavelength and for different irradiances is shown in fig.3. At room temperature, the

photocurrent ranges from 7.1 pA to 125 pA. The response measured during the warming process retraced the previous path with a temperature hysteresis smaller than 6°C.

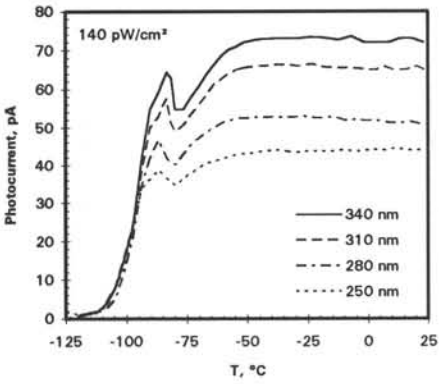

Fig. 2: Dependence on temperature of the response of XP2020Q for several wavelengths in the UV region.

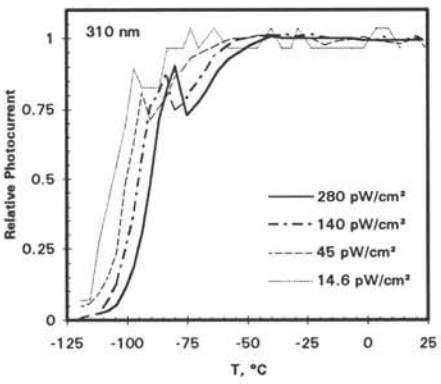

Fig. 3: Dependence on temperature of the response of XP2020Q for different irradiances at 310 nm.

These data allow to conclude that the temperature at which the relative response drops to any given value depends on the logarithm of the initial photocurrent. This feature seems to be consistent with an exponential increase of the photocathode resistivity with decreasing temperature [9]. The minimum of the response curves around -80°C remains to be explained. The existence of an abrupt drop in the PMT response, observed in the present work at all irradiances and wavelengths used, is in agreement with our previous tests carried out with another XP2020 with a pulsed illumination source in the visible range, although the temperature at which that drop occurred was lower in the previous tests (at about -110°C) [8]. This difference can be explained by a smaller current drawn from the photocathode in the case of the pulsed illumination.

Concerning the Hamamatsu R1668, its relative response as a function of temperature is plotted in fig.4 for two cases: full illumination of the photocathode, whose effective diameter is 25 mm, and irradiation of a 10 mm-diameter central area. Both runs were performed at 310 nm and at the same irradiance. As one can see, this PMT also exhibits an abrupt drop in response but at a temperature lower than the XP2020Q. This critical temperature was found to depend on the photocurrent measured at room temperature in a way much alike that observed with the XP2020Q. At higher temperatures, the sensitivity slightly increases with decreasing temperature, the rate of increase being always smaller than 0.06% /°C.

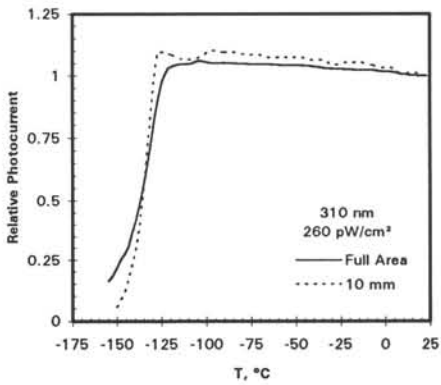

Fig. 4: Dependence on temperature of the response of R1668 for different illuminated areas at the same irradiance.

Fig.5 shows the response of both PMTs as a function of temperature at λ=170 nm. Note the large increase of sensitivity just below room temperature observed at this particular wavelength for the XP2020Q, which was not observed with any PMT with light in the region between 185 nm and 340 nm. The tests were repeated with extra care to avoid light absorption from gaseous contamination but the same results were obtained. It is worthwhile to refer that such strong variation of response near room temperature could explain disagreements found in the literature between calibrations of this PMT at short wavelengths [10].

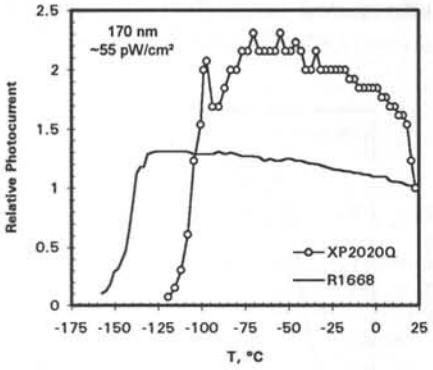

Fig. 5: Relative response of both PMTs versus temperature at 170 nm.

An attempt to understand the PMTs response as a function of temperature is being carried out. This could lead to a more quantitative explanation of the behaviour of bialkali PMTs, namely in the temperature range of interest for scintillation detectors using liquefied noble gases. In particular, factors like initial photocurrent, applied voltage and illuminated area could be related to the evolution of response with cooling [9]. Concerning the behaviour in the VUV region, further investigation is required. Since 170 nm is close to the wavelength at which liquid xenon scintillates, this unexpected increase of quantum efficiency opens good prospects for the use of an XP2020Q in scintillation counting.

ACKNOWLEDGEMENTS

This work was performed in the framework of the project PBIC/S/DIV/1880/95. H.M.Araújo was supported by a research grant FMRH/BIC/1231/94 from JNICT. The authors thank Hamamatsu Photonics K.K., and in particular Mr D. Castrillo from its representative in Spain, for the support given during these investigations.

REFERENCES

[1] V.Yu.Chepel, Nucl. Tracks Radiat. Meas. 21 (1993) 47-51.
[2] D.Y.Akimov *et al.*, Nucl. Instr. and Meth. A327 (1993) 155-158.
[3] R.B.Murray and J.J.Manning, IRE Trans. Nucl. Sci. NS-7 (1960) 80-86.
[4] W.Budde and P.Kelly, Appl. Opt. 10 (1971) 2612-2616.
[5] A.S.Singh and A.G.Wright, IEEE Trans. Nucl. Sci. NS-34 (1987) 434-7.
[6] J.E.McMillan and R.J.O.Reid, J. Phys. E: Sci. Instrum. 22 (1989) 377-382.
[7] M.Ichige, T.Doke, Y.Doi, Y.Yoshimura, Nucl. Instr. and Meth. A327 (1993) 144-147.
[8] V.Y.Chepel *et al.*, Appl. Radiat. Isot. 46 (1995) 495-496.
[9] H.M.Araújo, V.Yu.Chepel, M.I.Lopes, R.Ferreira Marques and A.J.P.L.Policarpo (in preparation).
[10] P.Dorenbos *et al.*, Nucl. Instr. and Meth. A325 (1993) 367-369.

PHOTON DETECTION WITH (POSITION SENSITIVE) HYBRID PHOTOMULTIPLIER TUBES

Ir. L.W. Boskma, R.J. Glazenborg, Ing, R.J. Schomaker, Ing.
September 1995
Delft Electronische Producten (DEP), PO Box 60, 9300 AB Roden,
The Netherlands tel: 31-5908-18808 fax: 31-5908-13510

1 ABSTRACT

The Hybrid Photomultiplier Tube (HPMT) has been developed at request of the physics world in their search for detectors with a high quantum yield, low noise, photon counting capabilities and magnetic field insensitivity. Presently a wide range of detectors is available that outperforms traditional Photomultipliers in many respects.

The HPMT is a vacuum tube in which the latest technologies of photocathodes and photodiodes are combined. Photoelectrons are accelerated by a high voltage and bombard a reversely biased PIN diode, in which they create many electron-hole pairs. The resulting charge pulse can be amplified and further processed. This device does not suffer the statistical fluctuations common for electron multiplication processes in a PMT. An energy resolution up to 17 photoelectrons is presented, together with striking figures for dynamic range and temporal behavior. Latest developments concern the development of pixellated tubes, fast timing tubes, tubes made of fully non-magnetic materials and tubes with other silicon structures.

2 PRINCIPLE

The HPMT is a vacuum tube with a photocathode coupled to a silicon PIN diode. Photoelectrons, generated in the photocathode, are accelerated towards the PIN diode with several kV and create a track of electron/hole pairs near the surface of the silicon chip. As the diode is reversely biased, electrons and holes are collected on the electrodes which results in a charge pulse that can be amplified with side-on electronics.

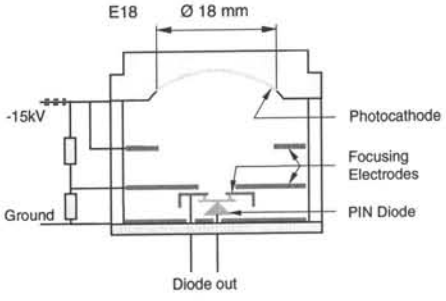

Fig. 1

Electrostatically focused
Hybrid Photomultiplier Tube

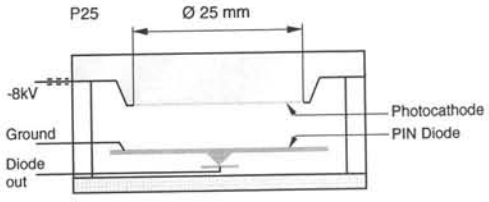

Fig. 2

Proximity focused
Hybrid Photomultiplier Tube

Proc. Int. Conf. on Inorganic Scintillators and Their Applications, SCINT95,
1996, Delft University Press, The Netherlands

Figures 1 and 2 show the two basic tube layouts, which differ in electron focusing. Electrons will leave a point on the photocathode with an energy of a few eV oriented in random directions. Focusing is necessary to collect all these electrons on about the same spot on the diode plane. Of course this is especially relevant in pixellated versions.
Fig. 1 shows the electrostatically focused version. In this concept a large photocathode can be combined with a small diode, thus giving the fastest timing, and a high photo-electron resolution.
Fig. 2 shows the proximity focused version, which is totally insensitive to strong magnetic fields.

3 GAIN

The gain is linear with the high voltage following the formula G = (HV-V(th)) / 3.6, where "HV" is the applied high voltage, "V(th)" the threshold voltage and "3.6" the energy, expressed in V, necessary to create an electron/hole pair. For an acceleration voltage of 15 kV and a threshold of 2 kV this will give a typical gain number of 3500 electrons per photo-electron (Fig. 3). It should be noted that the gain stability of such a device is much better compared to conventional Photomultipliers. This is because the gain is linear rather than exponential with the high voltage, and the gain is virtually independent of the environmental temperature.

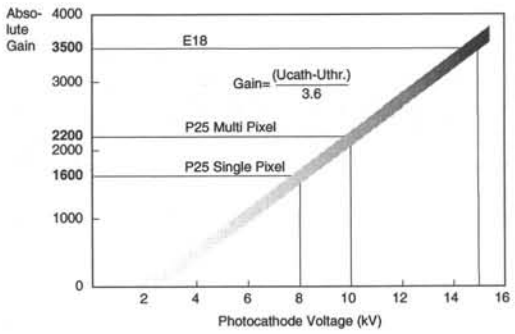

Fig. 3 Gain versus acceleration voltage

The dynamic range has been measured on proximity focused devices. Fig. 4 shows both the output pulse height and the output pulse integrated charge as a function of the number of photoelectrons per pulse. Eight orders of magnitude are achievable linearly. This means that signals varying from single photoelectron counting until output currents of about 10 mA can be handled by one device, with the same voltage settings.

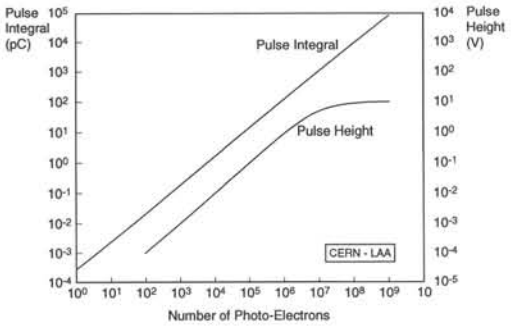

Fig. 4 Dynamic range

4 PHOTOCATHODES

A number of highly efficient photocathodes have been developed for these devices. Thin S20 and bialkali photocathodes are optimized to make the ideal read-out for e.g. scintillators. Fig. 5 gives the spectral response (Quantum efficiency versus wavelength) of some examples of available photocathodes. Especially developed for the HPMT are a low darkcount bialkali photocathode and a high QE (>30%) S20 version for UV. Special windows, e.g. for solar blind 250 nm photocathodes, can easily be implemented at low cost due to the photocathode transfer technique.
An important advantage to PMT's is the high photoelectron collection efficiency: the fraction of the photoelectrons in an HPMT that does not lead to a pulse is considerably smaller than in a PMT and the photocathode response is within 10% uniform over the full active area.

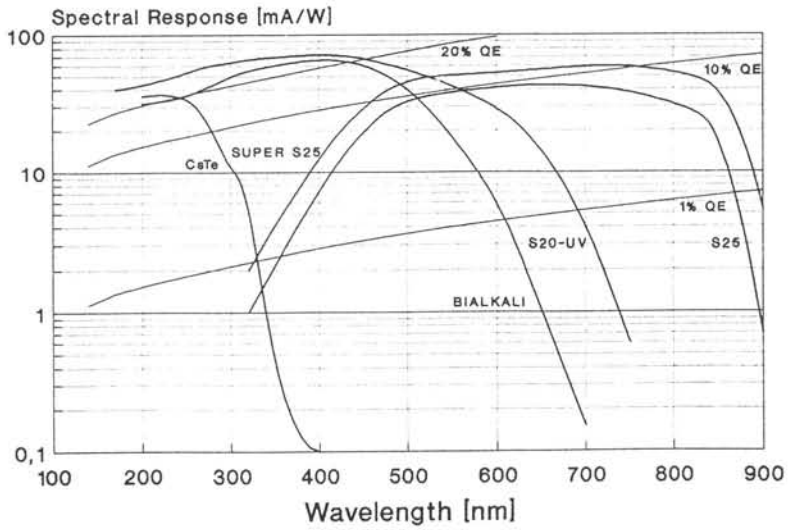

Fig. 5 Typical HPMT photocathodes

5 SIGNAL CHARACTERISTICS

The HPMT is a real low noise device. Three signal determining factors are discussed. The first one is the photoelectron resolution. The second factor is the thermal electron emission from the photocathode (darkcounts), and the third one is the collection of second order factors like the silicon read-out noise and cosmics.

5.1 Gain variation and Photoelectron resolution

Because of the absence of electron multiplication stages, the counting statistics of an HPMT are much better than in regular PMT's. In fact, since the relative photon to photon gain variations are extremely low, a peaked pulse height distribution is obtained with separate peaks for separate photo-electron numbers.

The noise of a HPMT/preamp system , expressed as equivalent photoelectrons, is depending on the electron gain and on the chip capacity. A high acceleration voltage, combined with a low capacity (e.g. small chip), will of course give the best results, a voltage of 7 kV already leads to <20% FWHM resolution (the chip capacitance will contribute to the electronics noise of the preamplifier). Fig. 6 shows photoelectron response distributions in an electrostatically focused version with integrated preamplifier, as measured by DEP. The lightsource is a triggered LED which results in 3 and 10 photo-electrons average. See also ref. 2.

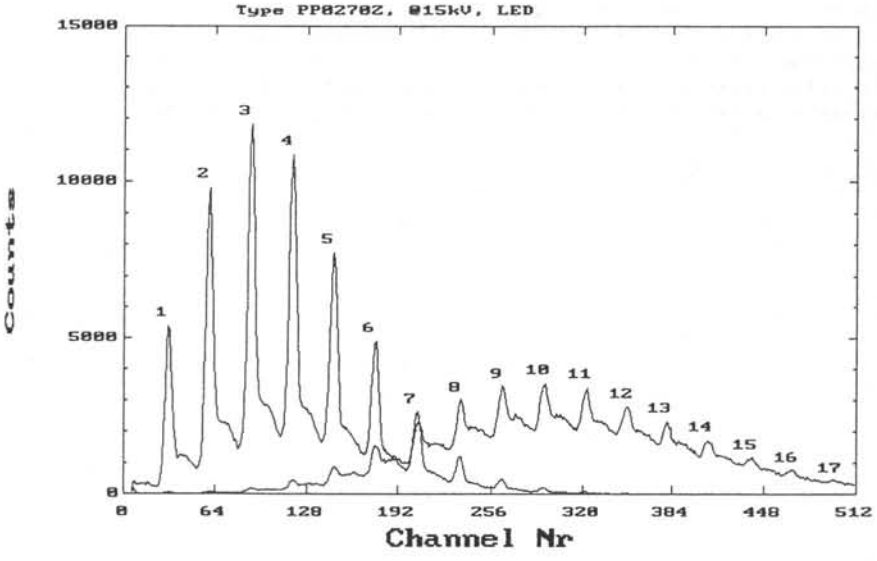

Fig. 6 Photo-electron resolution of the electrostatically focused HPMT

Fig. 7 shows one of the photoelectron spectra as measured by the BaBar collaboration on a 25 mm proximity focused device. This plot is taken from ref. 3.

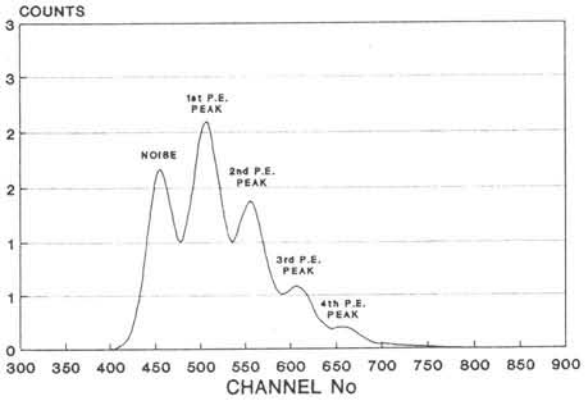

Fig. 7 Photoelectron resolution of proximity focused ø25 mm HPMT.

People familiar with Photomultipliers will recognize from these plots that HPMT's here fully outperform PMT's due to the extremely low noise. The best photon counting PMT's presently available barely show the second photoelectron peak. As the mechanisms leading to these plots are crucial, we will discuss these in some more detail.

The width (FWHM) of the peaks in such plots is set by fluctuations in gain (thus by chip capacity) and leakage current (shot noise). The shape of the valley in the plots with narrow peaks (fig. 6) is set by backscattered photoelectrons that re-enter the diode under a lower angle or with partial energy deposition, e.g. due to photon emission. The best point to evaluate the noise is behind the preamplifier. The level here is the amplifier offset noise plus a value per picofarad input (chip) capacity. In order to compare this with the signal of a photoelectron, this noise can be expressed in keV. For electrostatically focused versions with integrated preamplifier this noise level is typically 1.5 keV (FWHM), thus much lower than the signal of a single photon. For the worst case, a proximity focused version, with a large capacity chip (e.g. 200 pF) and an optimized amplifier, a noise equivalent to 8 keV is achieved (if the tube is operated at 8 keV, this means that the width is equivalent to the signal of 1 photoelectron). This is important, as the number of photoelectrons in e.g. a Cherenkov counter, may be only a few.

The ratio of the height of the peaks is determined by the average number of photoelectrons per pulse, which in turn is determined by the stability and statistics of the light source and the statistics of the photo-electric effect in the photocathode.

5.2 Darkcounts

The thermal electron emission of the photocathode is a noise source in photon counting applications, and by far the most dominant contribution in darkcounts. The signal from such an electron cannot be distinguished from a single photo-electron. The countrate is depending on the type of photocathode and on the temperature and is simular to PMT darkcounts.

Cosmics may add spurious signals. These are however comparable with the effect in silicon strip detectors, as the aborption will take place in the diode rather than in the thin photocathode. The signal level thus is far below the photoelectron level.
Although the frequency of interaction of cosmic rays with the photocathode is almost zero due to the small thickness, they may in theory create some Cherenkov light in the photocathode input window which could lead to a photoelectron.
Also incidentally small electrical discharges in the tubes may give spurious signals which cannot be distinguished from real signals. The annoying effect of afterpulsing is not present in HPMT's.
At room temperature a S20 photocathode will give in total a few hundred counts per second per cm^2, for a bialkali this is considerably lower. In first approximation cooling decreases these figures with a factor of 2 for every 7 °C. It should be clear that darkcounts add to the first photoelectron peak in figures 6 and 7.

5.3 Additional factors

The thermal noise from the silicon itself is in the order of tenths of photo-electrons. As the signal is a few thousands electrons, this source is negligible. As the gain is linear with the applied high voltage, voltage fluctations will give rise to gain fluctuations which are proportional, rather than exponential with the voltage fluctuations, as is the case with PMT's. This contributes to the high stability of this device.

6 MAGNETIC FIELD BEHAVIOR

The main reason for developing proximity focusing HPMT's is the need in the physics world for detectors that do not suffer the magnetic field problems as they are present in fine mesh PMT's.
Fig. 8 shows the normalized gain versus the magnetic field up to 1.6 Tesla, for several angles between the tube axis and the magnetic field. The modulation occurs because the spiraling electron trajectories lead to variable impinging angles on the chip and thus to variable effective thicknesses of the threshold layer (see for calculations ref. 1).

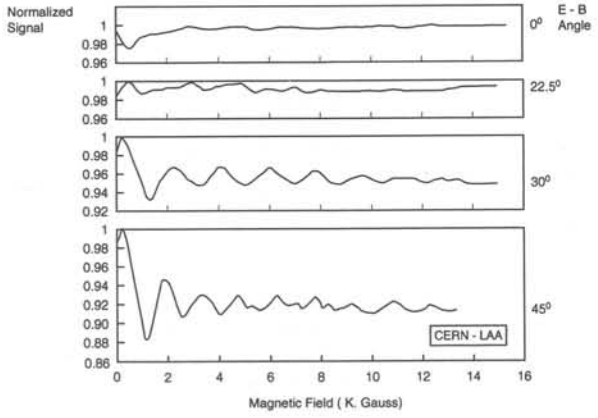

Fig. 8 Gain versus magnetic field

PMT's, including fine mesh versions, are always sensitive to magnetic fields, especially if tilted, because their gain mechanism (bouncing over dynode structures) is heavily influenced by the magnetic field. Recent tests with HPMT's have proven that operation up to 2.5 Tesla is still without loss of gain. No loss is foreseen in stronger magnetic fields.

7 TIMING PROPERTIES

In e.g. time-of-flight detectors, fluorescence studies and range-finding, fast timing characteristics are crucial. Small chips combined with a tube design with small electron transit time differences, give the shortest rise and fall times. Figures 9 and 10 show the output pulse for each design.

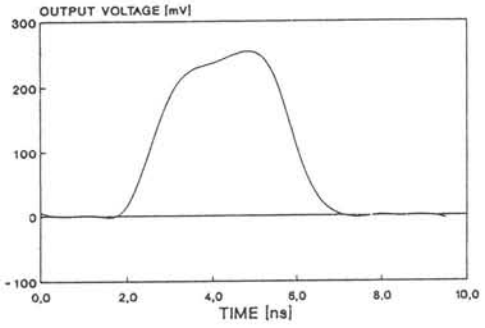

Fig. 9 Pulse of electrostatically focused HPMT (ø18 mm cathode, ø2 mm chip)

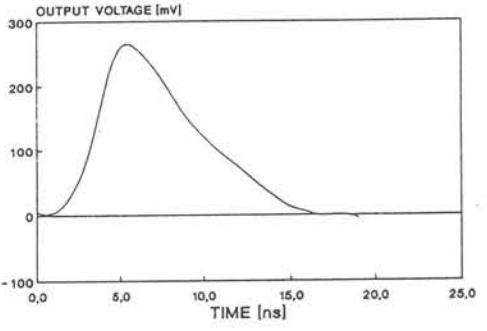

Fig. 10 Pulse of proximity focused HPMT (ø25 mm)

Proximity focused devices have no transit time differences at all. As a result of improvements in diode design, tube design and photocathode processing an extremely small pulse delay variation across the tube of only 20 ps has been achieved. Rise and fall times were both in the order of 4 ns. The time resolution as a function of the number of photons per pulse is given in fig. 11. See for details refs. 3 and 5. This makes these devices quite suitable for time of flight detectors and for fast triggers.

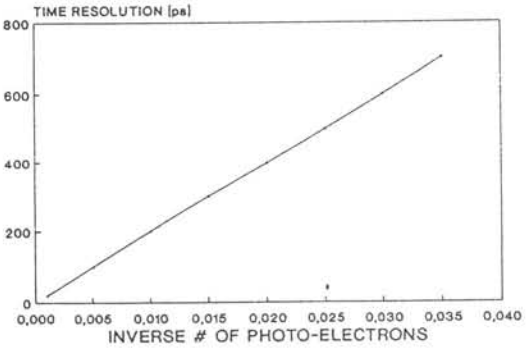

Fig. 11 (ref. 5) Time resolution versus number of photons per pulse

8 PIXELLATION

A large, INFN funded, project in 1992/1993 proved the feasibility of backside bombarded, pixellized PIN diodes. In 1994 DEP introduced a 25 mm, proximity focused HPMT with 7 pixels which is now widely used by CERN and other institutes. Fig. 12 shows the layout and the response uniformity (ref. 4).

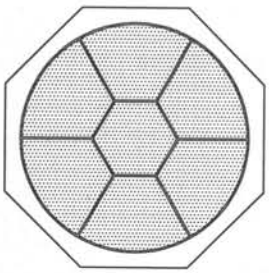

Fig. 12a pixel layout 7 pixel HPMT

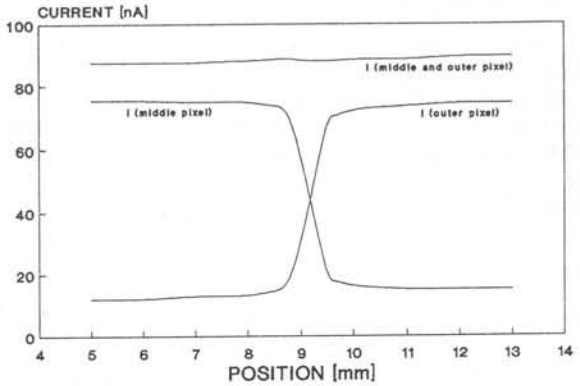

Fig. 12b Scan in 100 µm steps

9 COMMERCIAL STATUS

ø18 mm electrostatic, ø18 mm and ø25 mm proximity focused versions, as well as a 7-pixel ø25 mm proximity focused version are commercially available now. These tubes can be supplied with a wide range of photocathodes, and with side electronics as high voltage power supplies and preamplifiers, which makes them easy to handle and flexible devices for e.g. spectroscopy. Presently DEP is further improving pixellation and contacting technology in order to produce devices with much more, e.g. 9, 25, 37 or 61, pixels. The primary focus is towards gamma imaging and scintillating fiber readout at lower costs per channel.

ACKNOWLEDGMENTS

The development of this technology and these devices is the direct result of a long term fruitful collaboration between CERN, INFN, Canberra and DEP. A substantial part of the development work has been funded by INFN Italy.

REFERENCES

1 H. Arnoudon et al, NIM A342 (1994), 558-570
2 C. D'Ambrosio et al, CERN, NIM A332 (1993), 134-141
C. D'Ambrosio et al, CERN, NIM A345 (1994), 279-283
3 M. Calvi et al, Univ. Rome / INFN , submitted to NIM, (May 1995) "Characterization of Large Area Proximity Focused Hybrid Photodiodes"
4 P. Cushman, Minnesota Univ. Private communication, data from proximity HPMT evaluation
5 P. Benetti et al. "Speed properties of the Hybrid Photodiode Tube", Submitted to NIM, July 1995

A position-sensitive photomultiplier based on a CsI-photocathode and a microgap gas detector

J. van der Marel[1], A. van den Bogaard[2], C.W.E. van Eijk[1], R.W. Hollander[1], N.J. Noordhoek[1], P.M. Sarro[2] and V.C.F.B. Scheerhoorn[1]

Delft University of Technology, Delft, The Netherlands,
[1] *Radiation Technology Group, Faculty of Applied Physics.*
[2] *Delft Institute of Microelectronics and Submicrontechnology.*

Abstract

We are developing microgap gas chambers (MGC's) with two-dimensional read-out. The MGC can be used for the position-sensitive detection of soft X-rays directly in the detection gas, but also for the position-sensitive read-out of solid photocathodes like CsI. We have coupled a semi-transparant CsI-photocathode to an MGC and detected and amplified the light of a Hg UV light source.

1 Introduction

Cesiumiodide (CsI) is seen as a promising solar-blind photocathode for the VUV. It is less sensitive to air than most photocathode materials and can resist dry gases. This property makes CsI suitable as a photocathode in a gas-filled photomultiplier (PM) (rather an electron multiplier). The last few years a lot of research has been performed on reflective CsI-photocathodes for use in multiwire proportional chambers (MWPC's). This detector would provide a relatively cheap large area (UV-)light position-sensitive detector. A CsI-photocathode can also be read-out by other (gas-filled) devices.

The Microgap Chamber (MGC) is a gas-filled radiation detector introduced by Angelini et al [1] in 1993 for the detection of fast charged particles and soft X-rays. Electrons liberated by the radiation in the detector gas drift to the microgap plane, are amplified in the gas, and subsequently are collected on small metallic strips. Electrons can also be produced in a semi-transparant CsI-photocathode. The combination of photocathode and MGC results in a microgap photomultiplier (MGPM). The very narrow structures of an MGC result in a fast avalanche charge collection and high acceptable count rates. The division of anode and cathode in two separate planes makes it easy to apply two-dimensional read-out.

These properties and the fact that CsI is only sensitive in the VUV make the MGPM very suitable for the position-sensitive read-out of fast cross luminescence crystals like $KMgF_3$ and BaF_2 in high count rate environments.

2 The Microgap Chamber

In figure 1 an MGC is schematically drawn. The detector exists of a silicon wafer with an insulating SiO_2 layer. This layer is covered by an aluminium film that is kept on ground potential (cathode). On the film small SiO_2 strips are made and on top of these small aluminium strips are positioned which are kept on positive high voltage (anode). Opposite to the microgap plane a drift electrode (a metallized foil for soft X-ray detection and charged particles or a semi-transparant photocathode for light detection) is positioned that is kept on negative high voltage. The whole detector is placed in a gas and due to the electric field configuration electrons liberated in the gas or in the photocathode drift to the anode and are multiplied in the intense electric field between anode and cathode. The photocathode-microgap plane distance can be $< 1\,mm$. Then the transit time is $< 20\,ns$. The gas is usually a mixture of a noble gas and a poly-atomic organic quenching gas. The MGC needs a large concentration of quenching gas for stable operation. For more details about the lay-out see ref. [2]. The detector used in this research has a pitch of $200\,\mu m$ for both anode and cathode and has a total size of $1 \times 1\,cm^2$.

This MGC has an excellent stability and a fast avalanche charge collection ($\sim 2.5\,ns$). Gas gains up to 4000 and a position resolution of better than $125\,\mu m$ have been measured (see refs. [2, 3]).

3 CsI-photocathodes

Reflective CsI-photocathodes have been thoroughly investigated in the past few years. The quantum efficiency (QE) measured by several authors is not very consistent, depending on the fabrication and the

Proc. Int. Conf. on Inorganic Scintillators and Their Applications, SCINT95,
1996, Delft University Press, The Netherlands

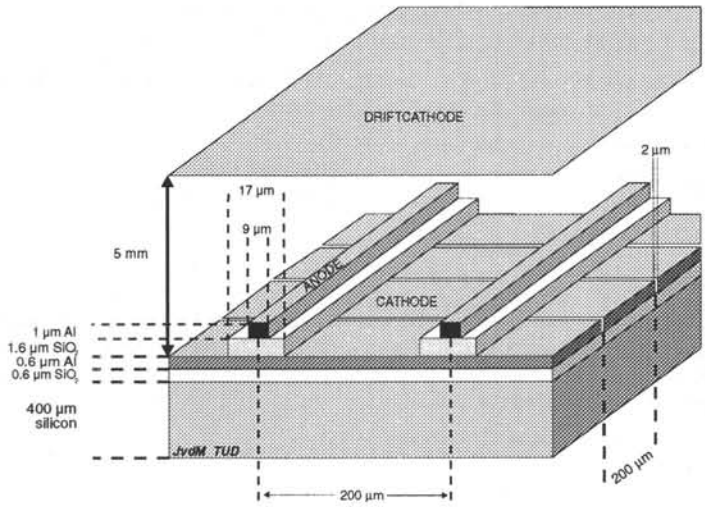

Figure 1: Schematic cross section of the microgap chamber

method of measurement [4, 5, 6, 7, 8, 9]. In figure 2 a curve for the QE of a reflective photocathode is plotted [11]. For comparison the emission spectrum of a $KMgF_3$ scintillation crystal is shown.

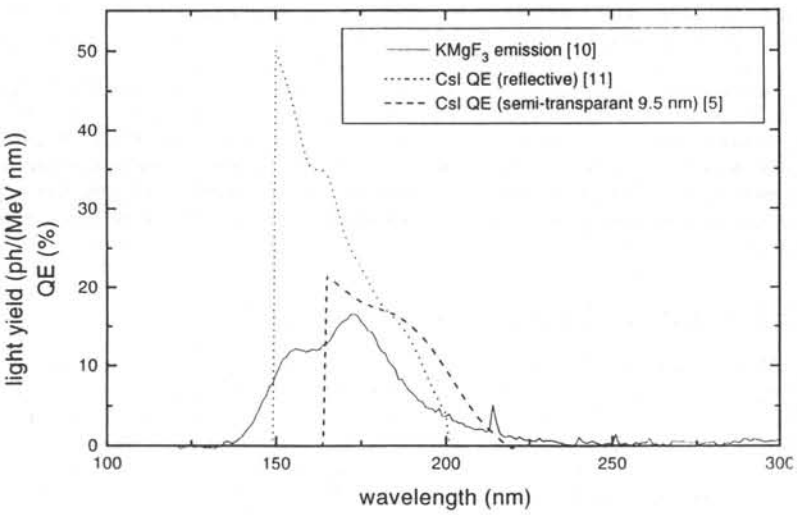

Figure 2: The emission spectrum of a $KMgF_3$ crystal and the quantum efficiency for a reflective and a semi-tranparant CsI-photocathode

For application in an MGPM a semi-transparant photocathode is needed. The QE of a semi-transparant CsI-photocathode measured by Lu [5] is also drawn in figure 2. According to Lu the optimal thickness is 9.5 nm of CsI.

CsI is a good insulator, so the window has to be coated with a thin metallic film to prevent charging of the photocathode. The photocathode used in this research is made on a 6 mm thick quartz face plate with a 5 nm Ni coating at the CsI side. The CsI-layer is 12.5 nm thick. The transmission of the Ni coating is 57 % and the cut-off wavelength of the quartz is $\sim$ 170 nm, so only light with a wavelength larger than 170 nm can be detected.

4 UV-light detection

A schematic of the MGPM in the test set-up is shown in figure 3. Three gas compositions were used: 60 % argon/ 40 % dimethylether (DME), 90 % xenon/ 10 % CO_2 and 40 % xenon/ 60 % CO_2.

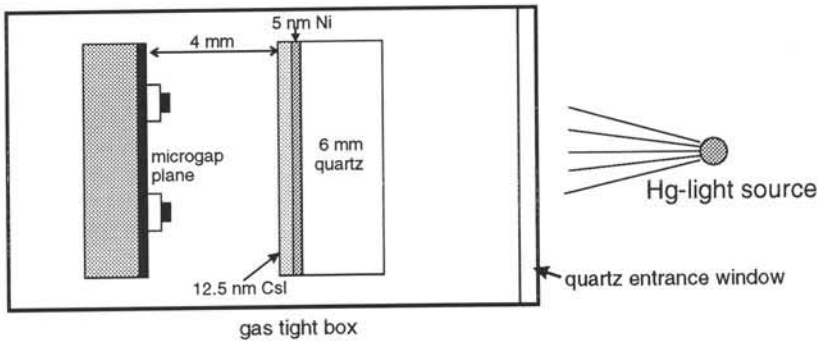

Figure 3: Schematic of the test set-up for the microgap photomultiplier

The MGPM is illuminated with a low-pressure Hg-lamp through a quartz window. The photocurrent has been measured as a function of the electric field E_d to find plateau values for the different gases. For that purpose the anodes and cathodes of the MG plane are connected together, so that a parallel plate chamber configuration is obtained. Addition of DME, which has a cut-off wavelength of 195 nm, to the argon in the gas box reduced the photocurrent to < 1 %. This demonstrates that the photocathode is only sensitive to the 185 nm and not to the 254 nm line of the Hg-light source as can be expected from figure 2.

Next a voltage was applied to the anode and the anode-cathode current was registered. Increasing the anode-cathode voltage shows a significant increase in current. Using the previously measured photocurrent as reference value for a measurement without amplification, the gas gain is computed. In figure 4 the resulting curve for Xe/CO_2 90/10 is drawn. The gas gain has also been determined from pulse height spectra of 6 keV X-rays, absorbed in the detector gas. This curve is also plotted in figure 4. In the X-ray case there is no significant difference in gain between $E_d = 1.25\,kV/cm$ and $E_d = 2\,kV/cm$. The agreement between the two curves is obvious. For the other gases the two methods of measuring the gas gain give similar results.

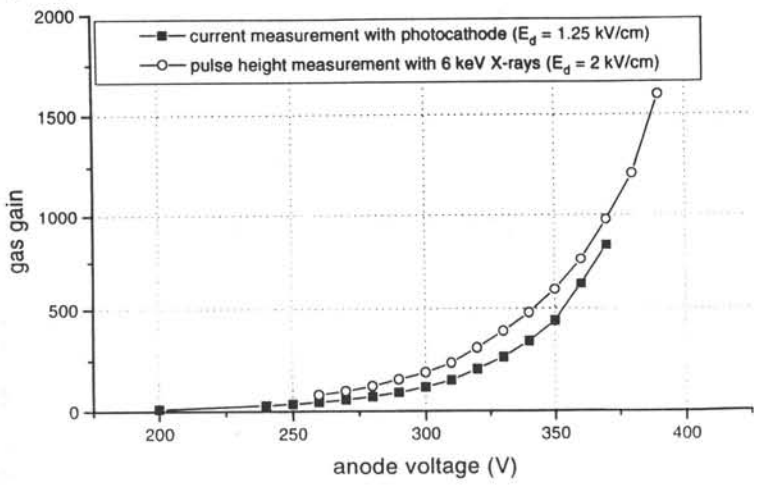

Figure 4: Gas gains in 90 % xenon, 10 % CO_2 measured in two different ways

Attempts have been made to detect the light of a $KMgF_3$ and a BaF_2 scintillator crystal. Unfor-

tunately these scintillators have a low light yield in the wavelength region where the CsI has a high quantum efficiency and, as the light collection in the face plate is rather poor, the noise of the detector was too large to detect the small signals.

5 Conclusions

A MGPM has been build and successfully operated in current mode up to a gain of almost 1000 by irradiating the photocathode with a low-pressure Hg UV light source. There is a good agreement between the gain measured with this method and pulse height measurements of avalanches caused by absorption of 6 keV X-rays of a ^{55}Fe-source in the detector gas. With the MGPM in current mode it is possible to make a one-dimensional position-sensitive photomultiplier. For a two-dimensional device it is necessary to operate in pulse mode. Then the x and y-coordinates of the center of gravity of the light cloud of a scintillation event can be registered. Pulse mode operation is also required to obtain energy and timing information. The combination of an MGPM operated in pulse mode and fast cross luminescence scintillators like $KMgF_3$ and BaF_2 would provide a fast and compact position-sensitive detector for γ-rays. Pulse mode operation has been tested by detecting the light of such scintillators but the number of photoelectrons was too low to cause a signal that was large enough to come out of the detector noise. Future investigations of the MGPM should be focused on improvement of the signal-to-noise ratio. In the first step we will replace the face plate by a continuous quartz or MgF_2 window. It would be even better to have the CsI-photocathode directly on the scintillator. Furthermore we will use thinner metal coatings. Obviously we will continue our general work on the MGC to increase the amplification and reduce detector and electronics noise.

References

[1] F. Angelini et al. Nucl. Instr. and Meth. A 335 (1993) 69.

[2] J. van der Marel et al. Development of micrsotrip and microgap gas chambers on silicon. Proc. of the International Workshop on Micro-strip Gas Chambers, Legnaro (Italy), 13-14 October 1994.

[3] J. van der Marel et al. Two-dimensional microgap ga chambers on silicon. Proc. of the Vienna Wire Chamber Conference, Vienna, 13-17 February 1995, to be published in Nucl. Instr. and Meth. A.

[4] J. Séguinot et al. Nucl. Instr. and Meth. A 297 (1990) 133.

[5] C. Lu et al. Nucl. Instr. and Meth. A 343 (1994) 135.

[6] R. Aleksan et al. Nucl. Instr. and Meth. A 340 (1994) 293.

[7] A. Breskin et al. Nucl. Instr. and Meth. A 344 (1994) 537.

[8] D.F. Anderson et al. Nucl. Instr. and Meth. A 323 (1992) 626.

[9] G. Malamud et al. Nucl. Instr. and Meth. A 335 (1993) 136.

[10] R. van Sonsbeek and J. de Haas. private communication.

[11] V.C.F.B. Scheerhoorn. CsI-fotokathodes, fabricage en QE-metingen, master thesis TU Delft, in preparation.

OPTIMIZATION OF LIGHT COLLECTION IN OXIDE AND ALKALI-HALIDE SCINTILLATORS IN A WIDE RANGE OF THE LONGITUDINAL-TO-TRANSVERSE SIZE RATIO

M.E. Globus and B.V. Grinyov
Institute for Single Crystals, Kharkov, 310001, Ukraine

Abstract

Light collection is explored in a wide range of the longitudinal-to-transverse size ratio with allowance for a true angle distribution of the reflected light. An optimal choice of the reflector type is grounded.

I. INTRODUCTION

Light collection in scintillators and their spectrometric characteristics essentially depend on the ratio of the longitudinal scintillator size, h, to the transverse one, a (Fig.1). With this in view, we explored theoretically and optimized light collection in scintillation detectors based on inorganic single crystals. As example, $Bi_4Ge_3O_{12}$ (BGO), $CdWO_4$ (CWO) and NaI(Tl) are considered. In the case of a large h-to-a ratio (schematically shown in Fig.1) the light collection efficiency drastically depends on the shape of the indicatrix of the light scattering on the diffuse reflecting surface. The scattering indicatrix has a strong maximum in the direction of the mirror reflection which amounts upon the average to about 75% of the total intensity of the scattered light [1]. This peculiarity of the reflection indicatrix extremely promotes light collection for $h/a>>1$ since the light fraction, obeying the mirror reflection law, achieves the photomultiplier (PMT) window much sooner than the rest of the scattered light (see Fig.1). Earlier we have developed a mathematical approach which permits one to calculate light collection with taking into account the both fractions of the reflected light [2]. (The usual approach [3,4] makes no allowance for the dependence of the light scattering indicatrix on the incidence direction and, hence, for its mirror-type maximum).

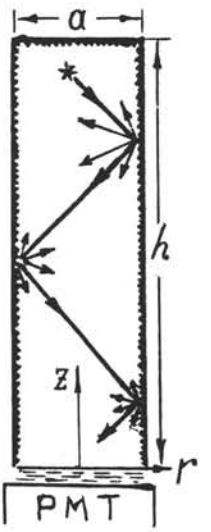

Fig.1. Light propagation in a crystal with the rough surface.

We have used the developed approach to calculate light collection in a wide range of the h-to-a ratio in order to trace general regularities and to ground the optimal choice of the reflector type.

II. SCINTILLATOR PARAMETERS AND SPECTROMETRIC CHARACTERISTICS

The light collection coefficient, τ, is defined as a fraction of the scintillation light energy which achieves the photoreceiver (PMT or photodiode). The quantity $\tau=\tau(\mathbf{r})$ as a function of the scintillation point $\mathbf{r}$ is characterized by the averaged value $\bar{\tau} = \int \tau(\mathbf{r}) d\mathbf{r} / V$ and the dispersion $\sigma = \left[\overline{\tau(\mathbf{r})^2} - \bar{\tau}^2\right]^{1/2} / \bar{\tau}$ (V is the scintillator volume). In more detail the nonuni-

Proc. Int. Conf. on Inorganic Scintillators and Their Applications, SCINT95,
1996, Delft University Press, The Netherlands

formity of τ (**r**) is described by the difference, δ_z , between the τ values taken at the opposite scintillator points $z = h$ and $z = 0$ (Fig.1) and averaged over the cross section (perpendicular to the z-axis). Similarly, $\delta_\perp$ is introduced as the difference between the values taken at the boundary of the cross section and at its center, the averaging being performed over the z-axis.

The intrinsic resolution, R_0 , is defined as follows:

$$R_0 = \left[(2.35\sigma)^2 + R_\lambda^2\right]^{1/2} \qquad (1)$$

where the first summand is the contribution of the light collection nonuniformity and the second one originates from the energy dependence of the conversion efficiency. For NaI(Tl) $R_\lambda \approx 4.5\%$, for BGO and CWO $R_\lambda = 0$. The total resolution of the detector, R, includes the intrinsic resolution R_0 and the PMT contribution:

$$R = (R_0^2 + A/CE)^{1/2}, \quad C = \eta\bar{\tau}c \; . \qquad (2)$$

Here E is the γ-quantum energy and C denotes the relative light output, proportional to τ and to the conversion efficiency of the substance, η. Due to the choice of the constant c the light output C is normalized to unity for the cylindrical NaI(Tl) crystal ϕ40x40 mm with the rough reflecting surface.

The enumerated spectrometric characteristics depend as well on the sizes of the scintillator (indicated in Fig.1) as on its optical parameters: the absorption coefficient for the fluorescence light, k; the refraction index of the scintillator, n, and that of the coupling liquid, $n_1 = 1.5$; the reflection coefficient ρ. For BGO $n = 2.15$, $k = 0.025$ cm^{-1}, for CWO $n = 2.35$, $k = 0.025$ cm^{-1}, for NaI(Tl) $n = 1.85$, $k = 0.005$ cm^{-1}. The ratio of the conversion efficiency of BGO and CWO to that of NaI(Tl) is taken to be 0.15 and 0.40, respectively.

Three versions of the scintillator reflector were considered: the totally rough reflecting surface with $\rho = 0.95$; the totally polished surface, only the top face (opposite to the PMT) being covered by the reflector with the reflection coefficient $\rho = 0.95$; a combined reflector with the rough top ($\rho = 0.95$) and the polished rest of the surface, the latter being provided by the outer reflector with $\rho = 0.7$ without optical contact. (In the last case a high value of ρ is not as important as in the former cases).

III. RESULTS OF CALCULATIONS

Table demonstrates light collection characteristics for three substances and two versions of the scintillator shape: a cylinder with the dimensions $\varnothing\, a \times h$ and a rectangular prism $a \times a \times h$. For a cylinder the three above-mentioned versions of the reflecting surface are considered: totally rough; totally polished (in this case the result is independent of the cross-section shape and size and, hence, coincides for the cylinder and prism with the same h); the combined version.

As seen from Table, the cases of the rough-surface prism and cylinder with the same sizes do not strongly differ from one other (the cylinder has a somewhat worse intrinsic resolution R_0).In the both cases the axial nonuniformity of τ generally predominates over the transverse one and mainly determins R_0. In the case of the totally polished surface the transverse nonuniformity is absent at all.

But in the case of a cylinder with the combined reflector and not too large h/a the transverse nonuniformity predominates and noticeably affects R_0 . This is due to the rays which are emitted in a large space angle towards the rough top being totally reflected from the polished side surface. After scattering from the rough top the rays turn towards the PMT window and make a noticeable contribution to the light output. The space angle of such rays increases as the scintillation point approaches the side surface. As a consequence, τ

Table. Light-collection and spectrometric characteristics of the scintillators: rectangular prism with the sizes $a \times a \times h$ and the cylinder $\varnothing\, a \times h$ (a=40 mm, h is varied). The total resolution is given depending on the γ-ray energy E (in MeV). All characteristics are expressed in percent.

h, mm	$\bar{\tau}$	δ_z	$\delta_\perp$	C	R_0	R (0.661)	R (2.614)	$\bar{\tau}$	δ_z	$\delta_\perp$	C	R_0	R (0.661)	R (2.614)
	Prism							Prism or cylinder						
	Rough reflecting surface							Polished surface						
BGO														
20	45	0	2	15.4	2.5	9.2	5.1	27	0	0	9.2	0.1	11.5	5.8
40	39	0	2	13.2	2.3	9.9	5.4	26	0	0	8.8	0.3	11.8	5.9
80	31	-5	1	10.5	4.8	11.9	7.3	22	-2	0	7.9	1.2	12.5	6.4
120	25	-14	1	8.7	11.5	16.5	12.9	21	-4	0	7.2	2.8	13.3	7.1
160	22	-27	1	7.4	21.8	25.3	22.7	19	-7	0	6.5	5.0	14.6	8.5
CWO														
20	41	0	2	33.3	2.9	6.7	4.2	22	0	0	17.9	0.1	8.3	4.2
40	34	-1	2	27.8	2.9	7.2	4.4	21	0	0	17.0	0.3	8.5	4.3
80	27	-6	2	21.8	5.1	9.1	6.3	19	-2	0	15.5	1.2	9.0	4.7
120	22	-13	1	18.1	11.3	13.9	12.0	17	-4	0	14.0	2.6	9.7	5.4
160	19	-26	1	15.5	20.8	22.6	21.3	16	-7	0	12.7	4.6	10.8	6.7
NaI(Tl)														
40	64	-2	1	101	4.9	6.0	5.2	40	0	0	62.2	4.5	6.3	5.0
80	56	-6	1	87.5	6.6	7.6	6.9	38	0	0	60.5	4.5	6.4	5.0
120	49	-13	1	76.5	11.6	12.3	11.8	37	0	0	58.3	4.5	6.4	5.1
160	43	-23	1	67.6	18.7	19.2	18.8	36	-1	0	57.2	4.5	6.5	5.1
	Cylinder													
	Rough reflecting surface							Rough top, polished side						
BGO														
20	45	0	-6	15.7	5.4	10.4	7.0	36	1	8	12.2	7.0	12.2	8.6
40	38	-1	-6	13.5	5.4	10.8	7.1	30	1	6	10.1	4.8	12.0	7.3
80	30	-9	-7	10.8	7.9	13.6	9.6	24	-1	3	8.1	3.2	12.7	7.0
120	24	-21	-8	8.8	12.8	17.5	14.2	20	-6	2	6.6	4.5	14.3	8.2
160	20	-39	-8	7.5	27.3	30.0	28.0	18	-10	2	6.2	8.5	16.4	11.0
CWO														
20	38	0	-6	32.4	5.5	8.2	6.2	31	1	7	25.6	6.1	9.2	7.0
40	31	-1	-6	27.0	5.5	8.6	6.4	25	1	5	20.5	4.1	8.7	5.6
80	24	-7	-7	21.4	7.7	10.8	8.6	20	-1	3	16.0	2.7	9.1	5.2
120	19	-18	-7	15.0	16.0	18.4	16.6	16	-4	2	12.5	4.2	10.7	6.4
160	16	-32	-8	13.4	26.9	28.5	27.3	15	-9	2	11.8	8.0	12.9	9.5
NaI(Tl)														
40	64	-2	-5	100	6.5	7.4	6.7	48	2	19	75.8	16.1	16.6	16.2
80	54	-6	-6	86	8.4	9.2	8.6	44	1	14	68.7	12.7	13.4	12.9
120	47	-14	-7	74	12.4	13.1	12.6	41	0	11	64.0	10.3	11.2	10.5
160	42	-23	-7	66	19.5	19.9	19.6	39	-3	10	61.1	9.2	10.2	9.5

increases with the radial coordinate r. The space angle increases as well with a decrease in the distance of the scintillation point from the rough top. As seen from Table , this leads to a partial compensation of the decreasing z-dependence of τ which becomes strong for $h/a>>1$. On the other hand, the radial nonuniformity of τ diminishes with an increase in h/a. So, the combined version becomes preferable in the range of large enough h-to-a ratios. In this region the version of the totally polished surface may gain an advantage as well. However, the partially polished reflecting surface or, all the more, the totally polished one provides a lower light output than the totally rough reflector, and, hence, a larger PMT contribution to the total resolution R (the second summand in (2)). But the PMT

contribution diminishes with an increase in the γ-ray energy, E, or in the conversion efficiency, η (η grows in the row BGO - CWO - NaI(Tl)).

It follows that the partially or totally polished surface becomes preferable with an increase in h/a, E and η. This regularity is demonstrated by Table where the conversion efficiency η is taken into account by the light output C.

IV. CONCLUSION

The calculation results permit one to indicate the regions of the sizes and the γ-ray energy, E, where one of the three versions of the reflecting surface is preferable. For example, Fig.2 shows the boundary between such regions for the totally rough and totally polished surfaces of cylinder scintillators (the region of the polished surface lies on the right-hand side from the boundary).

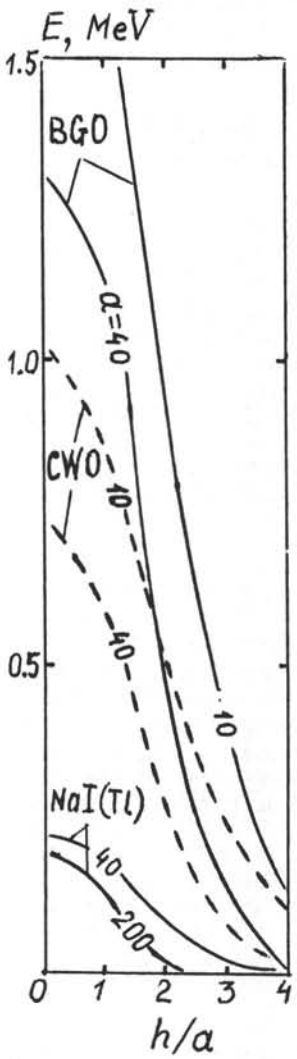

Fig.2. Boundary between the regions where the totally rough reflecting surface or the totally polished one is preferable for cylinder scintillators.

REFERENCES

[1]. M.Globus, Pribory and Teknika experimenta, N1, pp.54-56.1981.

[2]. M.Globus, Nucl. Tracks and Radiation Measur., v.21, N 1, pp.131-133. 1993.

[3]. S.E.Derenzo and J.K. Rilers, IEEE Trans. Nucl. Sci., v.NS-29, N.1, pp.191-194. February 1982.

[4]. C.Carrier and R.Lecomte, Nucl. Instrum. Methods, A292(3), pp.685-692.1990; A294(1-2), pp.355-364. 1990.

USE OF A NEURAL NETWORK TO EXPLOIT LIGHT DIVISION IN A TRIANGULAR SCINTILLATING CRYSTAL

C. Morel [a], S. Delorme [b], R. Frei [b], C. Joseph [b], J.-F. Loude [b]
[a] Division of Nuclear Medicine, Geneva University Hospital, CH-1211 Geneva, Switzerland
[b] Institute for Nuclear Physics, University of Lausanne, CH-1015 Lausanne, Switzerland

ABSTRACT

This work presents a novel way of exploiting light division in a scintillating crystal to localise the point of interaction using a neural network. Because sensitivity at the centre of a positron tomograph would be significantly increased for a spherical geometry compared to a cylinder with the same area of detection, we explored the possibility of developing a position-sensitive triangular block detector that might be used ultimately as an element of a spherical shell. With 3 PMTs coupled on each side of a triangular BaF_2 crystal of about 8 $cm^2 \times 1$ cm, we obtain spatial resolutions less than 4 mm fwhm over the whole surface of the triangle and energy resolutions of about 14% fwhm for 662 keV impinging photons. Experimental measurements are compared with Monte Carlo simulations and prospects for different configurations are discussed.

I. INTRODUCTION

Positron Emission Tomography (PET) is an in vivo imaging technique in which a radiopharmaceutical labelled with a positron emitting isotope is administered to the patient. The positron resulting from isotope decay annihilates with an electron in the surrounding body tissue, producing two 511 keV photons travelling in opposite directions. A positron tomograph composed of a number of adjacent detector rings is used to detect in coincidence pairs of annihilation photons. The resulting information allows an image of the density of the annihilation points to be constructed approximating the spatial distribution of the tracer.

Although the sensitivity of current cylindrical positron tomographs has been improved [1], most of the radiopharmaceutical administered to a patient is of no use because of the small geometrical acceptance of the detector. With the same detection area, a spherical geometry would significantly increase the sensitivity at the tomograph centre. A spherical tessellation may be approximated by an assembly composed of only a few classes of nearly equilateral triangles. Thus, we explored the possibility of developing a position-sensitive triangular block detector and found that a multilayer neural network can easily localise the point of interaction.

II. MULTILAYER NEURAL NETWORK

A multilayer neural network may be considered as a black box that performs a non-linear vectorial process described by a transfer function. It is built of layers comprising independent formal neurons [2] such that only neurons belonging to neighbouring layers are interconnected. Each neuron works out a potential by calculating the weighted sum of its inputs and produces at the output the transformation of its potential by a non-linear continuous function. The final output of the network is then determined by the input signal that is propagated throughout the layers downwards to the output.

A multilayer neural network has to undergo a supervised learning of the transfer function it is to produce. Learning the transfer function means modifying the weights associated to each neuron input. This is achieved by minimising a quadratic error function calculated from the difference between the effective output of the network and its desired output for a given input signal [3]. Appropriate learning of the transfer function is obtained by iteration of this minimisation procedure over a great number of pairs of input signals and desired outputs of the network.

Proc. Int. Conf. on Inorganic Scintillators and Their Applications, SCINT95,
1996, Delft University Press, The Netherlands

III. MEASUREMENTS

To learn a transfer function that describes scintillation light distributions in a given scintillating crystal, a great number of input/desired output pairs must be obtained, consisting of light output measurements from the set of photodetectors for known irradiation positions. To irradiate the crystal, we use a vertical collimated beam of 662 keV photons positioned by a x-y horizontal table. The x-y table is operated by step motors and the positioning precision of the collimator is better than 300 μm in both directions. The exit hole of the collimator has a diameter of 0.6 mm and is 26.4 mm away from the scintillator surface. A small CdTe detector with a sensitive area (1×1 mm^2), located in a fixed position at the same distance from the collimator, is used as a reference point to localise the position of the beam in the plane of the scintillator. The beam impinging on the scintillator surface sampled with this CdTe detector appears to be nearly circular with a Gaussian profile measuring 1.3 mm fwhm (Fig. 1).

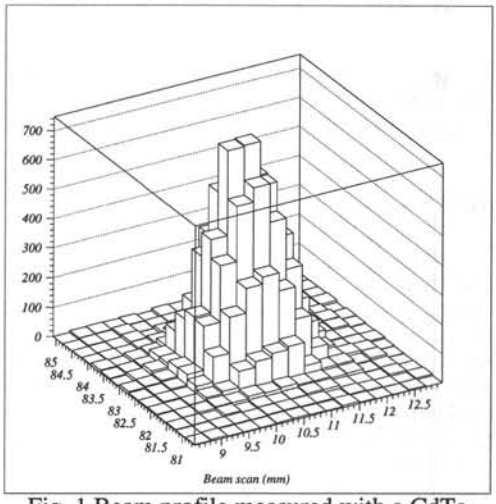

Fig. 1 Beam profile measured with a CdTe gamma detector.

This irradiation setup is used to map the light output of an equilateral triangular BaF_2 crystal, 10 mm thick and 37.5 mm high, for a set of discrete beam positions. BaF_2 was chosen for its timing properties as we also plan to investigate the possibility of combining a position-sensitive triangular block detector with time-of-flight measurements. The triangle has polished surfaces. Each side is optically coupled to three UV sensitive Hamamatsu R760 PMTs using silicon grease. The scintillating triangle with its PMTs, as well as the CdTe detector, are housed in a light tight box that has an aluminium entrance window 500 μm thick facing the beam. The gains of the PMTs are adjusted so that signal amplitudes obtained for symmetric positions of irradiation are approximately equal. A discriminator threshold set on the sum of the PMT pulse heights is used to trigger total energy events by gating the charge ADCs LRS 2249W that digitise the PMT signals.

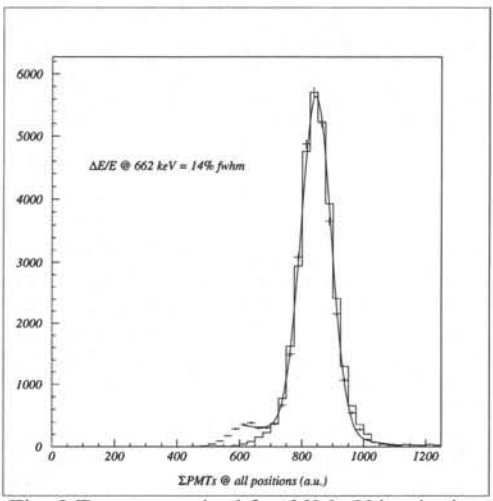

Fig. 2 Events acquired for 662 keV impinging photons (crosses) with a discrimination threshold set in the Compton region compared to Monte Carlo total energy events (line) simulating the experimental setup.

We mapped the light output of the scintillating triangle using a set of 31 discrete beam positions with a distance of 5 mm between neighbouring ones. The energy resolution of the block detector is about 14% fwhm for 662 keV impinging photons (Fig. 2) and depends only slightly on the position of the beam. We then used a learning set of 1000 events per irradiation position to train a network comprising 4 hidden layers of 10 neurons each. All connection weights are updated at the end of each iteration and training is stopped after 50 million iterations. Another independent set measured with the same irradiation positions is then used by this trained neural network to reconstruct the beam positions (Fig 3a). The spatial resolution obtained with this method is less

than 4 mm fwhm over the whole surface of the triangle and goes down to less than 2 mm fwhm near the summits of the triangle.

IV. MONTE CARLO SIMULATIONS AND PROSPECTS

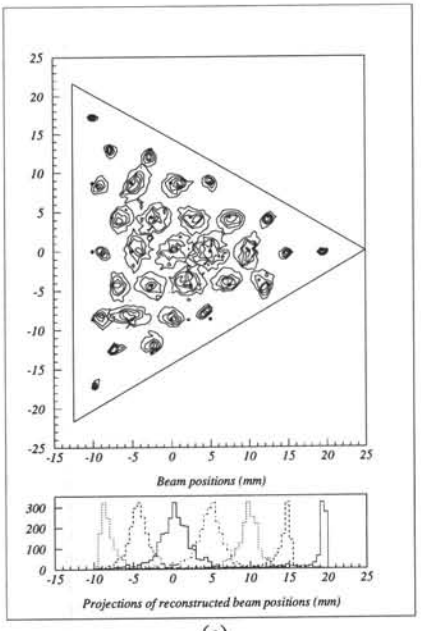

(a)

(b)

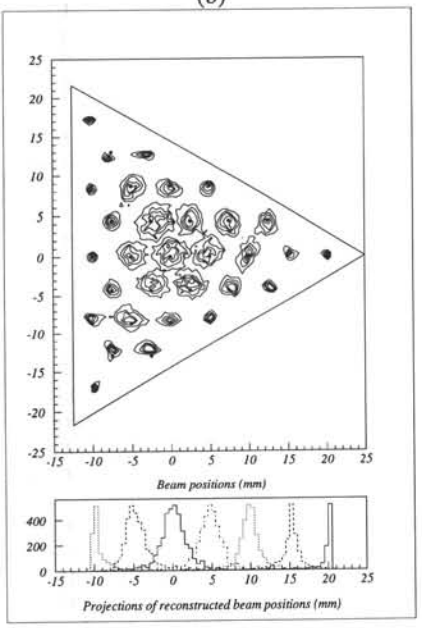

A program using the Monte Carlo method was developed to simulate the experimental setup. It reproduces the geometry of the crystal and its scintillating and optical properties, including scintillation light self-absorption. Scintillation photons are tracked from their point of emission until they reach a photodetector coupled to the crystal or are refracted outside the crystal. Photoelectric interactions and multiple Compton scattering are taken into account for the build-up of the total energy peak. The momentum of scattered photons is generated using the Klein-Nishina formula. Both fast and slow scintillation components of BaF_2 are introduced to generate data corresponding to the experimental setup. We simulate a beam of 662 keV photons having an axially symmetric distribution with a Gaussian profile of standard-deviation 0.5 mm. Distributions of reconstructed positions computed for a Monte Carlo learning set comprising 1000 events for each of 31 irradiation positions are similar to measurements (Fig. 3b). A good agreement is also observed between actual pulse height spectra and the ones obtained by Monte Carlo (Fig. 2). However to make it agree, the Monte Carlo program had to take into account partial retrodiffusion into the scintillator of the light entering the semitransparent photocathode of the PMTs, as suggested in *Ref.* 4.

A Monte Carlo training set of 50'000 events was generated without light retrodiffusion for a beam of 511 keV photons and irradiation positions uniformly distributed over the surface of the triangle. Once trained with this set, the neural network was used to compute reconstructed position distributions for another set of 31 irradiation positions generated with exactly the same procedure, except that impinging photon coordinates are no more spread around the irradiation position, but concentrated on single points. Using this, we obtain spatial resolutions of about 2 mm fwhm nearly uniformly over the crystal (Fig. 3c). At the centre of gravity of the triangle, this 2 mm fwhm spatial resolution is degraded up to 2.5 mm fwhm when the photon beam is spread as for the training set. Changing slightly the shape of the triangle does not make significant differences to spatial resolutions obtained with the same method.

As a scintillator, BaF_2 has fast timing properties, but a fairly low stopping power

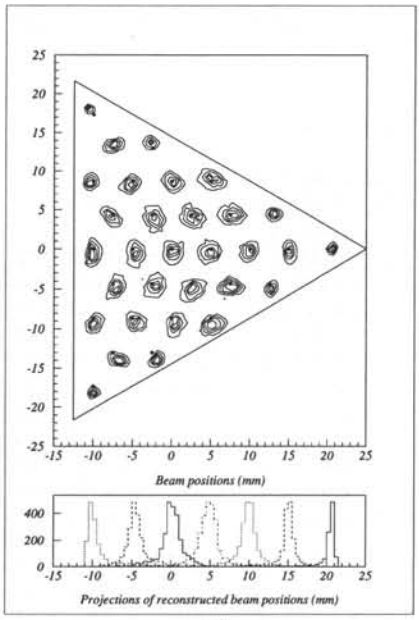

(c)

Fig. 3 Contour lines and projections of reconstructed position distributions computed for (a) real data, (b) Monte Carlo data simulating the experimental setup and (c) Monte Carlo data generated without light retrodiffusion. Each position distribution is potted using 5 equidistant contour lines. Irradiation positions are represented by black dots. Reconstructed position distributions corresponding to irradiation positions situated along the horizontal median of the triangle are projected onto the horizontal axis to estimate spatial resolutions.

compared to BGO. Furthermore, it emits in the UV region which makes the use of solid state photodetectors difficult and at present impossible. We used the Monte Carlo generator to estimate the effect of varying scintillator characteristics. Providing there is no diffraction centres in the crystal, we observed that spatial resolutions are mostly affected by the scintillator light yield and depend roughly on the square root of the number of scintillation photons. As an example, a light yield of 50'000 ph/MeV would bring spatial resolutions down to about 1 mm fwhm for 511 keV photons. On the other hand, having diffraction centres in the crystal would degrade its spatial resolutions. This fact is clearly related to the blurring of some spatial information contained in the scintillation light distributions by diffraction processes. Besides high stopping power and fast timing properties, the ideal scintillator has therefore to provide high light yield with good spectral matching to solid state photodetectors and as low diffraction centres as possible.

A possible future positron tomograph design might exhibit spherical symmetry and be built of closely-packed triangular blocks of scintillating crystal with avalanche photodiodes directly deposited on their sides. A dedicated analogue circuit, one per block, would receive the photodetector pulse heights and propagate them throughout the integrated architecture of a trained multilayer neural network downwards to its outputs to estimate the spatial three coordinates of the interaction point. Furthermore, a fast PMT coupled to the rear side of each block detector could be utilised to measure the time-of-flight of the annihilation photons detected in coincidence.

ACKNOWLEDGEMENTS

We are indebted to Prof. B. Delaloye, former head of the Autonomous Division of Nuclear Medicine of the Centre Hospitalier Universitaire Vaudois, and Prof. A. Donath, head of the Division of Nuclear Medicine of the Geneva Cantonal University Hospital, for their efficient support of this work. This work was partially funded as the 1993 Special Project of the Rectors of the University of Lausanne.

REFERENCES

[1] D. Townsend et al., "Performance characteristics of PET scanners operated in 3D mode", in *Proc. of the 1995 International Meeting on Fully 3D Image Reconstruction in Radiology and Nuclear Medicine*, Aix-les-Bains, France, 1995, pp. 225-229.

[2] W.S. McCulloch and W. Pitts, "A logical calculus of the ideas immanent in nervous system", *Bull of Math. Biophysics*, **5** (1943) 115.

[3] D.E. Rumelhart, G.E. Hinton and R.J. Williams, "Learning representations by backpropagating errors", *Nature*, **323** (1986) 533.

[4] *Photomultiplier tubes, principles & applications,* Philips Photonics, 1994, F-19106 Brive, pp. 4-9 and 4-10.

List of Participants

Allain, J.L.	Crismatec	France
Alov, D.L.	Institute of Solid State Physics	Russia
Andriessen, H.	Delft University of Technology	The Netherlands
Antoniv, I.P.	Lviv State University	Ukraine
Araujo, H.	University of Coimbra	Portugal
Auffray, E.	Solid State Physics	France
Baccaro, S.	ENEA, Casaccia, Sez. INFN Roma 1	Italy
Balcerzyk, M.	N. Copernicus University	Poland
Batenchuk, M.	Lviv State University	Ukraine
Belsky, A.N.	Moscow State University	Russia
Berrondo, M.	Brigham Young University	USA
Berzina, B.	University of Latvia	Latvia
Blasse, G.	Utrecht University	The Netherlands
Bom, V.R.	Delft University of Technology	The Netherlands
Bos, J.J.	Delft University of Technology	The Netherlands
Boskma, L.	DEP Delft Instruments	The Netherlands
Bouttet, D.	Universite Lyon 1	France
Brown, B.	Rutherford Appleton Laboratory	United Kingdom
Carelov, S.V.	Urals State Technical University	Russia
Chen, G.	Beijing Glass Research Institute	P.R. China
Chernov, S.	University of Latvia	Latvia
Chipaux, R.	CEA DSM/DAPNIA	France
Coenen, J.G.C.	Shell Research B.V.	The Netherlands
Combes, C.M.	Delft University of Technology	The Netherlands
Comby, G.	C.E.A.	France
Czirr, J.B.	Mission Support Incorporated	USA
Dafinei, I.	CERN	Switzerland
Devitsin, E.G.	Lebedev Physical Institute	Russia
Deych, R.	Analogic Corp.	USA
Dirker, J.	Delft University of Technology	The Netherlands
Dmitruk, L.N.	General Physics Institute	Russia
Domenico, G. Di	University of Ferrara	Italy
Dorenbos, P.	Delft University of Technology	The Netherlands
Dujardin, Ch.	Universite Lyon 1	France
Eijk, C.W.E. van	Delft University of Technology	The Netherlands
Engelsman, M.	Delft University of Technology	The Netherlands
Eriksson, L.	Karolinska Institute	Sweden
Evans, H.	UK Defence Research Agency	United Kingdom
Fabeni, P.	IROE	Italy
Fedorov, V.D.	All.Russian Research Institute	Russia
Flower, P.	Rutherford Appleton Laboratory	United Kingdom
Flyckt, E.	Philips Photonics	France

Gal'chnetskii, L.P.	Institute for Single Crystals	Ukraine
Gektin, M.	Institute for Single Crystals	Ukraine
Geochemistry	Russia	
Globus, M.	Institute for Single Crystals	Ukraine
Goebbels, J.	Federal Institute	Germany
Gorbunov, S.V.	Urals State Technical University	Russia
Grabmaier, B.C.	Siemens AG	Germany
Grigorjeva, L.	University of Latvia	Latvia
Grinev, B.V.	Institute for Single Crystals	Ukraine
Haas, J. de	Delft University of Technology	The Netherlands
Hangleiter, Th.	Universitaet-GH Paderborn	Germany
Hanney, R.	Merck Ltd.	United Kingdom
Hill, G.	Levy Hill Laboratories Ltd	United Kingdom
Hobson, P.R.	Brunel University	United Kingdom
Hollander, R.W.	Delft University of Technology	The Netherlands
Jermann, F.	Siemens AG	Germany
Jones, T.	MCR Clinical Sciences Centre	United Kingdom
Klassen, N.V.	Institute of Solid State Physics	Russia
Kniest, F.	BICRON	The Netherlands
Knitel, M.J.	Delft University of Technology	The Netherlands
Kobayashi, M.	KEK, National Laboratory	Japan
Kolobanov, V.	Moscow State University	Russia
Korbel, V.	Deutsches Elektronen Synchrotron	Germany
Korzhik, M.V.	Institute for Nuclear Problems	Belorussia
Kruzhalov, A.V.	Ural State Technical University	Russia
Kulik, A.	University of South Carolina	USA
Kvapil, J.	Preciosa-Crytur Turnov	The Czech Republic
Lebeau, M.	CERN	Switzerland
Lecoq, P.	CERN - PPE	Switzerland
Leliveld, K.J.	Stichting FOM	The Netherlands
Lempicki, A.	Boston University	USA
Lioubinskii, V.	Cryos Ltd.	Ukraine
Makhov, V.N.	Lebedev Physical Institute	Russia
Mangnus, A.	Eindhoven Univ. of Technology	The Netherlands
Marel, J. van der	Delft University of Technology	The Netherlands
Mares, J.A.	Czech Academy of Sciences	The Czech Republic
Mareschal, J.	Crismatec	France
Marsman, M.	Delft University of Technology	The Netherlands
Masopust, J.	Preciosa-Crytur a.s.	The Czech Republic
Matyas, R.	Preciosa-Crytur Turnov	The Czech Republic
McKinlay, K.	Sheffield University	United Kingdom
Meijvogel, K.	Delft University of Technology	The Netherlands
Melcher, C.	Schlumberger	USA
Merenga, H.	Delft University of Technology	The Netherlands

Mestais, C.	CEA - LETI	France
Millers, D.	University of Latvia	Latvia
Moine, B.	Universite Lyon	France
Morel, C.	Geneva University Hospital	Switzerland
Moses, W.W.	Lawrence Berkeley Lab.	USA
Moszynski, M.	Soltan Inst. for Nuclear Studies	Poland
Mürk, V.	Institute of Physics	Estonia
Musselwhite, C.M.	Hilger Analytical	United Kingdom
Nagirnyi, V.	Institute of Physics	Estonia
Nagornaya, L.	Institute for Single Crystals	Ukraine
Nedelko, S.	Taras Shevchenko Kyiv University	Ukraine
Nikl, M.	Czech Academy of Sciences	The Czech Republic
Nishimura, H.	Osaka City University	Japan
Nosenko, A.	West Ukrainian Physical Society	Ukraine
Novotny, R.	University Giessen	Germany
Ogorodnikov, I.N.	Urals State Technical University	Russia
Pani, R.	University of Rome "La Sapienza"	Italy
Pawelke, J.	Forschungszentrum Rossendorf EV	Germany
Pawlik, Th.	University of Paderborn	Germany
Pazzi, G.P.	IROE	Italy
Pédrini, Ch.	University Lyon 1	France
Pellegrini, R.	University of Rome	Italy
Petrosyan, A.G.	Institute for Physical Research	Armenia
Petrov, V.L.	Ural State Technical University	Russia
Petrov, S.A.	Durham University	United Kingdom
Polak, K.	Czech Academy of Sciences	The Czech Republic
Poorter, T.	Philips Medical Systems	The Netherlands
Popov, A.	University of Latvia	Latvia
Provorova, A.M.	All Russian Research Institute	Russia
Radzhabov, E.	Academy of Sciences of Russia	Russia
Rhodes, N.	Rutherford Appleton Laboratory	United Kingdom
Rivet, A.	Crismatec	France
Rodnyi, P.A.	Dept. of Experimental Physics	Russia
Rogozhin, A.	Ecodetector VIMS, Ltd.	Russia
Rossner, W.	Siemens AG	Germany
Sakuragi, S.	Union Materials Inc.	Japan
Schaik, W. van	University of Georgia	USA
Schmelz, Chr.	Max-Planck-Institute fuer Physik	Germany
Schotanus, P.	Scionix Holland	The Netherlands
Schwarz, L.	University of Greifswald	Germany
Shiran, N.	Institute for Single Crystals	Ukraine
Shulgin, B.V.	Ural State Technical University	Russia
Spijker, H.C. van 't	Delft University of Technology	The Netherlands
Springis, M.	University of Latvia	Latvia

Tamai, K.	KEK, National Laboratory	Japan
Tavernier, S.	University of Brussel	Belgium
Trinkler, L.	University of Latvia	Latvia
Tulach, L.	Preciosa-Crytur Turnov	The Czech Republic
Vale, G.	University of Latvia	Latvia
Valk, H.	Delft University of Technology	The Netherlands
Vasil'ev, A.N.	Moscow State University	Russia
Verburg, P.	Teledyne Brown Engineering	The Netherlands
Verweij, J.W.M.	LPCML	France
Vittori, F.	University of Rome "La Sapienza"	Italy
Voloshinovskii, A.	Lviv State University	Ukraine
Weber, M.J.	Lawrence Berkeley Laboratory	USA
Wieczorek, H.	Philips	Germany
Wienhard, K.	Max-Planck-Institut	Germany
Willems, P.	Agfa Gevaert	Belgium
Williams, R.T.	Wake Forest University	USA
Wisniewski, D.	N. Copernicus University	Poland
Wojtowicz, A.J.	N. Copernicus University	Poland
Woody, C.	Brookhaven National Lab.	USA
Wyon, Ch.	LETI/CEA	France
Xue, Z.	Shanghai Institute of Ceramics	P.R. China
Yin, Z.	Shanghai Institute of Ceramics	P.R. China
Zheng, Y.	Beijing Glass Research Institute	P.R. China
Ziegler, S.	Technische Universitaet Muenchen	Germany
Ziraps, V.	University of Latvia	Latvia

Author Index

Subject Index

Materials Index